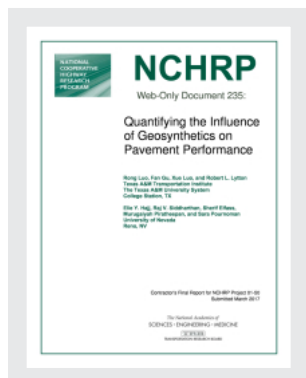


This PDF is available at <http://nap.edu/24841>

SHARE



Quantifying the Influence of Geosynthetics on Pavement Performance (2017)

DETAILS

841 pages | 8.5 x 11 | PAPERBACK

ISBN 978-0-309-46328-7 | DOI 10.17226/24841

GET THIS BOOK

FIND RELATED TITLES

CONTRIBUTORS

Rong Luo, Fan Gu, Xue Luo, Robert L. Lytton, Elie Y. Hajj, Raj V. Siddharthan, Sherif Elfass, Murugaiyah Piratheepan, and Sara Pournoman; National Cooperative Highway Research Program; Transportation Research Board; National Academies of Sciences, Engineering, and Medicine

SUGGESTED CITATION

National Academies of Sciences, Engineering, and Medicine 2017. *Quantifying the Influence of Geosynthetics on Pavement Performance*. Washington, DC: The National Academies Press. <https://doi.org/10.17226/24841>.

Visit the National Academies Press at NAP.edu and login or register to get:

- Access to free PDF downloads of thousands of scientific reports
- 10% off the price of print titles
- Email or social media notifications of new titles related to your interests
- Special offers and discounts



Distribution, posting, or copying of this PDF is strictly prohibited without written permission of the National Academies Press. (Request Permission) Unless otherwise indicated, all materials in this PDF are copyrighted by the National Academy of Sciences.

Copyright © National Academy of Sciences. All rights reserved.

NCHRP

Web-Only Document 235:

Quantifying the Influence of Geosynthetics on Pavement Performance

Rong Luo, Fan Gu, Xue Luo, and Robert L. Lytton
Texas A&M Transportation Institute
The Texas A&M University System
College Station, TX

Elie Y. Hajj, Raj V. Siddharthan, Sherif Elfass,
Murugaiyah Piratheepan, and Sara Pournoman
University of Nevada
Reno, NV

Contractor's Final Report for NCHRP Project 01-50
Submitted March 2017

ACKNOWLEDGMENT

This work was sponsored by the American Association of State Highway and Transportation Officials (AASHTO), in cooperation with the Federal Highway Administration, and was conducted in the National Cooperative Highway Research Program (NCHRP), which is administered by the Transportation Research Board (TRB) of the National Academies of Sciences, Engineering, and Medicine.

COPYRIGHT INFORMATION

Authors herein are responsible for the authenticity of their materials and for obtaining written permissions from publishers or persons who own the copyright to any previously published or copyrighted material used herein.

Cooperative Research Programs (CRP) grants permission to reproduce material in this publication for classroom and not-for-profit purposes. Permission is given with the understanding that none of the material will be used to imply TRB, AASHTO, FAA, FHWA, FMCSA, FRA, FTA, Office of the Assistant Secretary for Research and Technology, PHMSA, or TDC endorsement of a particular product, method, or practice. It is expected that those reproducing the material in this document for educational and not-for-profit uses will give appropriate acknowledgment of the source of any reprinted or reproduced material. For other uses of the material, request permission from CRP.

DISCLAIMER

The opinions and conclusions expressed or implied in this report are those of the researchers who performed the research. They are not necessarily those of the Transportation Research Board; the National Academies of Sciences, Engineering, and Medicine; or the program sponsors.

The information contained in this document was taken directly from the submission of the author(s). This material has not been edited by TRB.

The National Academies of
SCIENCES • ENGINEERING • MEDICINE



TRANSPORTATION RESEARCH BOARD

The National Academies of **SCIENCES • ENGINEERING • MEDICINE**

The **National Academy of Sciences** was established in 1863 by an Act of Congress, signed by President Lincoln, as a private, non-governmental institution to advise the nation on issues related to science and technology. Members are elected by their peers for outstanding contributions to research. Dr. Marcia McNutt is president.

The **National Academy of Engineering** was established in 1964 under the charter of the National Academy of Sciences to bring the practices of engineering to advising the nation. Members are elected by their peers for extraordinary contributions to engineering. Dr. C. D. Mote, Jr., is president.

The **National Academy of Medicine** (formerly the Institute of Medicine) was established in 1970 under the charter of the National Academy of Sciences to advise the nation on medical and health issues. Members are elected by their peers for distinguished contributions to medicine and health. Dr. Victor J. Dzau is president.

The three Academies work together as the **National Academies of Sciences, Engineering, and Medicine** to provide independent, objective analysis and advice to the nation and conduct other activities to solve complex problems and inform public policy decisions. The National Academies also encourage education and research, recognize outstanding contributions to knowledge, and increase public understanding in matters of science, engineering, and medicine.

Learn more about the National Academies of Sciences, Engineering, and Medicine at www.national-academies.org.

The **Transportation Research Board** is one of seven major programs of the National Academies of Sciences, Engineering, and Medicine. The mission of the Transportation Research Board is to increase the benefits that transportation contributes to society by providing leadership in transportation innovation and progress through research and information exchange, conducted within a setting that is objective, interdisciplinary, and multimodal. The Board's varied committees, task forces, and panels annually engage about 7,000 engineers, scientists, and other transportation researchers and practitioners from the public and private sectors and academia, all of whom contribute their expertise in the public interest. The program is supported by state transportation departments, federal agencies including the component administrations of the U.S. Department of Transportation, and other organizations and individuals interested in the development of transportation.

Learn more about the Transportation Research Board at www.TRB.org.

TABLE OF CONTENTS

LIST OF FIGURES	vi
LIST OF TABLES	xi
CHAPTER 1. INTRODUCTION	1
Introduction.....	1
Objective	1
Research Scope and Approach	1
Organization of the Report	4
CHAPTER 2. SYNTHESIS OF CURRENT KNOWLEDGE	5
Laboratory Characterization of Granular Materials with Geosynthetics.....	5
Modeling of Pavements with Geosynthetics	6
Design Methods for Pavements with Geosynthetics	7
CHAPTER 3. RESEARCH PLAN	9
Full-Scale Laboratory Testing	9
Triaxial Laboratory Testing.....	10
Finite Element Modeling	11
Development of ANN Models of Critical Strains and Stresses.....	11
Performance Data Collection of In-Service Pavement Sections with Geosynthetics.....	12
CHAPTER 4. EXPERIMENTS, MODELING, AND FINDINGS	13
Introduction.....	13
Geosynthetic Application and Reinforcement Mechanisms.....	13
Available Test Methods for Evaluating Geosynthetic Properties Related to Pavement Performance	14
Selection of Test Methods for Determining Geosynthetic Properties	15
Direct Tension Test to Determine Geosynthetic Sheet Stiffness.....	15
Pullout Test to Determine Geosynthetic-Aggregate/Soil Interfacial Properties	16
Laboratory Methodology for Quantifying Influence of Geosynthetics	17
Influence of Geosynthetics on Cross-Anisotropic Properties of UGMs.....	17
Influence of Geosynthetics on Permanent Deformation Properties of UGMs.....	24
Analytical Model for Quantifying the Influence of Geosynthetics	30
LST Test on Pavement Layers with Geosynthetics	34
Experimental Plan and Setup	35
Data Analysis Methodologies	43
Flexible Pavement.....	43
Rigid Pavement.....	65
Finite Element Modeling of Pavements with Geosynthetics.....	77
Characterization of Materials Used in LST Test	80
Development of Nonlinear Cross-Anisotropic User-Defined Material Subroutine.....	85
Development of Goodman Model Friction Subroutine	87
Numerical Modeling Techniques for Geosynthetic-Reinforced Pavement Structures	88
Effect of Geosynthetic Reinforcement on Pavement Responses	89
Parametric Study of Material Properties on Pavement Performance.....	93
Comparison of Finite Element Simulations with LST Measurements	98
ANN Approach for Predicting Pavement Performance.....	105
Experimental Computational Plan for ANN Models.....	106
Development of ANN Models	107

Determination of Modified Material Properties.....	113
Prediction of Pavement Performance.....	117
Validation of the Proposed ANN Approach	120
CHAPTER 5. INTERPRETATIONS, APPRAISAL, AND APPLICATIONS	124
Introduction.....	124
LST Testing Program.....	124
Measurement of Geosynthetic-Aggregate/Soil Interfacial Slippage	127
Determination of Geosynthetic-Aggregate/Soil Interfacial Properties.....	129
Impact of Geosynthetics on Cross-Anisotropy and Permanent Deformation of UGMs	129
Mechanistic-Empirical Permanent Deformation Model for Unreinforced and Geosynthetic-Reinforced UGMs	132
Analytical Model for Quantifying Influence of Geosynthetics	134
Development of Finite Element Model for Geosynthetic-Reinforced Pavement.....	135
Predictions of Geosynthetic-Reinforced Pavement Performance.....	136
CHAPTER 6. SUMMARY AND SUGGESTED RESEARCH.....	145
Summary	145
Suggested Research	146
REFERENCES	148
ATTACHMENT A. STANDARD METHOD OF TEST FOR DETERMINING THE PERMANENT DEFORMATION PROPERTIES OF GEOSYNTHETIC- REINFORCED AND UNREINFORCED GRANULAR MATERIAL	153
ATTACHMENT B. STANDARD METHOD OF TEST FOR DETERMINING THE CROSS-ANISOTROPIC RESILIENT MODULUS OF GEOSYNTHETIC- REINFORCED AND UNREINFORCED GRANULAR MATERIAL	157
FINAL REPORT APPENDICES	165
APPENDIX A. REVIEW OF AVAILABLE TEST METHODS FOR DETERMINING PERFORMANCE-RELATED GEOSYNTHETIC PROPERTIES	A-1
APPENDIX B. DETERMINATION OF GEOSYNTHETIC-AGGREGATE INTERFACIAL PROPERTIES USING PULLOUT TEST.....	B-1
APPENDIX C. LABORATORY EVALUATION OF INFLUENCE OF GEOSYNTHETICS ON CROSS-ANISOTROPY AND PERMANENT DEFORMATION OF UNBOUND GRANULAR MATERIAL	C-1
APPENDIX D. ANALYTICAL MODEL FOR QUANTIFYING INFLUENCE OF GEOSYNTHETICS.....	D-1
APPENDIX E. INSTRUMENTATION PLANS FOR FLEXIBLE PAVEMENT EXPERIMENTS	E-1
APPENDIX F. SUMMARY CHARTS FOR FLEXIBLE PAVEMENT EXPERIMENTS	F-1
APPENDIX G. FLEXIBLE PAVEMENT EXPERIMENTS: COMPARISON OF TEST MEASUREMENTS.....	G-1
APPENDIX H. INSTRUMENTATION PLANS FOR RIGID PAVEMENT EXPERIMENTS	H-1
APPENDIX I. ANALYSIS METHODOLOGIES OF LST TEST DATA.....	I-1
APPENDIX J. SUMMARY CHARTS OF RIGID PAVEMENT EXPERIMENTS	J-1
APPENDIX K. RIGID PAVEMENT EXPERIMENTS: COMPARISON OF TEST MEASUREMENTS	K-1

APPENDIX L. CHARACTERIZATION OF MATERIALS USED IN LST TEST.....	L-1
APPENDIX M. COMPARISON OF FINITE ELEMENT SIMULATIONS WITH LST MEASUREMENTS.....	M-1
APPENDIX N. DEVELOPMENT OF ARTIFICIAL NEURAL NETWORK MODELS FOR PREDICTING GEOSYNTHETIC-REINFORCED PAVEMENT PERFORMANCE.....	N-1
APPENDIX O. VALIDATION OF ARTIFICIAL NEURAL NETWORK APPROACH FOR PREDICTING GEOSYNTHETIC-REINFORCED PAVEMENT PERFORMANCE.....	O-1
APPENDIX P. LIST OF GEOSYNTHETIC-REINFORCED IN-SERVICE PAVEMENT SECTIONS IDENTIFIED FROM LONG-TERM PAVEMENT PERFORMANCE (LTPP) DATABASE AND TEXAS PAVEMENT MANAGEMENT INFORMATION SYSTEM (PMIS).....	P-1
APPENDIX Q. EXAMPLES OF PROGRAM RUNS OF THE COMPOSITE GEOSYNTHETIC-BASE COURSE MODEL.....	Q-1

LIST OF FIGURES

Figure 1.1. Compatibility of Proposed Program with AASHTOWare Pavement ME Design	3
Figure 4.1. Mechanisms of Geosynthetics in Pavement	14
Figure 4.2. Schematic Plot of the Pullout Test	16
Figure 4.3. Pullout Force versus Geosynthetic Displacement in a Pullout Test	17
Figure 4.4. Schematic Plot of Aggregate Specimens with/without Geosynthetic	18
Figure 4.5. Configuration of Rapid Triaxial Test	19
Figure 4.6. Effect of Stress Level on Reduction of Permanent Strain	24
Figure 4.7. Illustration of the Stress-Related Terms in the Proposed Model	26
Figure 4.8. Comparison of Lab-Measured and Proposed Model-Predicted Permanent Deformation Curves	27
Figure 4.9. Validation of Prediction Accuracy of Proposed Permanent Deformation Model	28
Figure 4.10. Effect of Type of Geosynthetic on Permanent Deformation of UGM	29
Figure 4.11. Effect of Location of Geosynthetic on Permanent Deformation of UGM	29
Figure 4.12. Schematic Plot of Geosynthetic Reinforcement on UGM Specimen	31
Figure 4.13. Comparison of Resilient Moduli Predicted by Analytical Models with Measured Values	34
Figure 4.14. FWD Loading Plate Used in the LST Experiments: (a) Top View; (b) Bottom View	36
Figure 4.15. Plastic Sheet Covering the Wave-Absorbing Material in the LST	36
Figure 4.16. Completed Large-Scale Test Setup for Flexible Pavement Experiment	37
Figure 4.17. Instrumentation Plan for Flexible Pavement Experiment 4: (a) Profile View at X = 0 inch; (b) Plan View at Z = 0 inch	39
Figure 4.18. Instrumentation Plan for Rigid Pavement Experiment 9: (a) Profile View at Y = 0 inch; (b) Plan View at Z = 0 inch	40
Figure 4.19. Placement of the 4-inch Earth Pressure Cell in the Subgrade	41
Figure 4.20. (a) In-Place Asphalt Strain Gauge; (b) Final In-Place Asphalt Strain Gauge with Temperature Sensor	42
Figure 4.21. LST Configuration for Flexible Pavements with Thin CAB (Experiments 1, 3, and 5) Showing Only Earth Pressure Cells across Geosynthetic	47
Figure 4.22. Vertical Stresses at the Centerline of the Loading Plate for Thin CAB Layer (Experiments 1, 3, and 5)	48
Figure 4.23. Vertical Stresses at the Edge of the Loading Plate for Thin CAB Layer (Experiments 1, 3, and 5)	49
Figure 4.24. Horizontal Stresses at the Edge of the Loading Plate for Thin CAB Layer (Experiments 1, 3, and 5)	50
Figure 4.25. LST Configuration for Flexible Pavements with Thick CAB (Experiments 2, 4, and 6) Showing Only Earth Pressure Cells across Geosynthetic	50
Figure 4.26. Vertical Stresses at the Centerline of the Loading Plate for Thick CAB Layer (Experiments 2, 4, and 6)	51
Figure 4.27. Vertical Stresses at the Edge of the Loading Plate for Thick CAB Layer (Experiments 2, 4, and 6)	52
Figure 4.28. Horizontal Stresses at the Edge of the Loading Plate for Thick CAB Layer (Experiments 2, 4, and 6)	53

Figure 4.29. LST Configuration for Flexible Pavements with Thin CAB (Experiments 1, 3, and 5) Showing Only the Instrumentations on and around Geosynthetic	54
Figure 4.30. LST Configuration for Flexible Pavements with Thick CAB (Experiments 2, 4, and 6) Showing Only the Instrumentations on and around Geosynthetic	55
Figure 4.31. Horizontal Strains in the Geosynthetic Reinforcements—Flexible Pavements: (a) Experiment 3 (geogrid); (b) Experiment 5 (geotextile)	56
Figure 4.32. Horizontal Strains in the Geosynthetic Reinforcements—Flexible Pavements: (a) Experiment 4 (geogrid); (b) Experiment 6 (geotextile)	57
Figure 4.33. Tensile Strains at the Centerline of the Load and at the Bottom of the AC Layer (Experiments 1, 3, and 5).....	57
Figure 4.34. Tensile Strains at the Centerline of the Load and at the Bottom of the AC Layer (Experiments 2, 4, and 6).....	58
Figure 4.35. Vertical Displacements of the Geosynthetic and Adjacent Unbound Material in Experiments 3 and 5 for Various Load Levels: (a) 9 kip; (b) 12 kip; (c) 16 kip	60
Figure 4.36. Horizontal Displacements of the Geosynthetic and Adjacent Unbound Material in Experiments 1, 3, and 5 for Various Load Levels: (a) 9 kip; (b) 12 kip; (c) 16 kip	61
Figure 4.37. Horizontal Slippage of the Geosynthetic and Adjacent Unbound Material in Experiments 3 and 5 for Various Load Levels—Flexible Pavements	62
Figure 4.38. Vertical Displacements of the Geosynthetic and Adjacent Unbound Material in Experiments 4 and 6 for Various Load Levels: (a) 9 kip; (b) 12 kip; (c) 16 kip	63
Figure 4.39. Horizontal Displacements of the Geosynthetic and Adjacent Unbound Material in Experiments 2, 4, and 6 for Various Load Levels: (a) 9 kip; (b) 12 kip; (c) 16 kip	64
Figure 4.40. Horizontal Slippage of the Geosynthetic and Adjacent Unbound Material in Experiments 4 and 6 for Various Load Levels—Flexible Pavements	65
Figure 4.41. LST Configuration for Rigid Pavements (Experiments 7, 9, and 10) Showing Only Earth Pressure Cells across Geosynthetic—Profile View	68
Figure 4.42. LST Configuration for Rigid Pavements (Experiments 7, 9, and 10) Showing Only Earth Pressure Cells across Geosynthetic—Plan View at 8 inches below Pavement Surface.....	68
Figure 4.43. Vertical Stresses at the Centerline of the Loading Plate for Rigid Pavements (Experiments 7, 9, and 10—Dry and Wet)	69
Figure 4.44. Vertical Stresses at Two Similar Locations in the CAB across the Joint and at 8 inches from the Centerline of the Loading Plate for Rigid Pavements (Experiments 7, 9, and 10—Dry and Wet)	70
Figure 4.45. Vertical and Horizontal Stresses at the Edge of the Loading Plate in the X-direction (Parallel to the Edge of the PCC Slab) for Rigid Pavements (Experiments 7, 9, and 10—Dry and Wet)	71
Figure 4.46. LST Configuration for Rigid Pavements (Experiments 7, 9, and 10) Showing Only Strain Gauges on Geosynthetic—Profile View	72
Figure 4.47. LST Configuration for Rigid Pavements (Experiments 7, 9, and 10) Showing Only Strain Gauges on Geosynthetic—Plan View at 10 inches below Pavement Surface	72
Figure 4.48. Horizontal Strains in the Geogrid Reinforcement (Experiment 9)—Rigid Pavement (Dry and Wet)	73

Figure 4.49. Tensile Strains in the X-direction (Parallel to the Edge of the PCC Slab) at the Centerline of the Load and at the Bottom of the PCC Layer (Experiments 7, 9, and 10)	74
Figure 4.50. LST Configuration for Rigid Pavements (Experiments 7, 9, and 10) Showing Only the LVDT Used for Assessing Slippage at the PCC Edge—Profile View	76
Figure 4.51. LST Configuration for Rigid Pavements (Experiments 7, 9, and 10) Showing Only the LVDT Used to Assess Slippage at the PCC Edge—Plan View at 6 inches below Pavement Surface.....	76
Figure 4.52. PCC-CAB Interface Slippage at the Edge of the PCC Slab (Experiments 7, 9, and 10): (a) Dry Condition; (b) Wet Condition	77
Figure 4.53. Typical Geosynthetic-Reinforced Flexible Pavement Structure in LST Test	78
Figure 4.54. Meshed Geosynthetic-Reinforced Pavement Structure in ABAQUS	78
Figure 4.55. Typical Geosynthetic-Reinforced Rigid Pavement Structure in LST Test	79
Figure 4.56. Meshed Geosynthetic-Reinforced Rigid Pavement Structure in ABAQUS	80
Figure 4.57. Comparison between the Measured Dynamic Moduli and the Fitted Dynamic Moduli	83
Figure 4.58. Direct Tension Test for Determining Sheet Stiffness of Geosynthetics.....	84
Figure 4.59. Relationships between Tensile Force and Tensile Strain for Geosynthetics.....	85
Figure 4.60. Flowchart of the Developed UMAT Subroutine	87
Figure 4.61. Simulation of Lateral Confinement in Geosynthetic-Reinforced Pavement Structure.....	89
Figure 4.62. Surface Deflections of Flexible Pavement Structures with and without Geosynthetic	90
Figure 4.63. Vertical Stress Distribution within Geosynthetic-Reinforced and Unreinforced Flexible Base Layer	91
Figure 4.64. Tensile Bending Stresses at the Bottom of the PCC Slab for the Geosynthetic-Reinforced and Unreinforced Rigid Pavements	92
Figure 4.65. Tensile Stresses at the Top of the PCC Slab for the Geosynthetic-Reinforced and Unreinforced Rigid Pavements	93
Figure 4.66. Sensitivity of Model-Predicted Pavement Responses to Subgrade Modulus.....	95
Figure 4.67. Sensitivity of Model-Predicted Pavement Responses to Geosynthetic Sheet Stiffness.....	97
Figure 4.68. Sensitivity of Model-Predicted Pavement Responses to Thickness of Base Course	98
Figure 4.69. Location of Instruments in Flexible Pavement Structures	99
Figure 4.70. Location of Instruments in Rigid Pavement Structures.....	100
Figure 4.71. Comparison of Measured and Predicted Surface Deflections for Pavement Structures with and without Geosynthetic	101
Figure 4.72. Comparison of Measured and Predicted Tensile Strains at the Bottom of Asphalt Layer for Pavement Structures with and without Geosynthetic.....	102
Figure 4.73. Comparison of Measured and Predicted Vertical Stresses within the Base and Subgrade for Pavement Structures with and without Geosynthetic.....	103
Figure 4.74. Comparison of Measured and Predicted Surface Deflections for Rigid Pavement Structures with and without Geosynthetic	104
Figure 4.75. Comparison of Measured and Predicted Vertical Stresses within the Base and Subgrade for Rigid Pavement Structures with and without Geosynthetic	104

Figure 4.76. Illustration of Three-Layered Neural Network Architecture.....	108
Figure 4.77. Comparison of Tensile Strain at the Bottom of the Asphalt Layer	109
Figure 4.78. Comparison of Average Vertical Strain in the Asphalt Layer	110
Figure 4.79. Comparison of Average Vertical Strain in the Base Layer	111
Figure 4.80. Comparison of Vertical Strain at the Top of the Subgrade	112
Figure 4.81. Comparison of Vertical Strain at 6 inches below the Top of the Subgrade	113
Figure 4.82. Flowchart of the Process of Predicting Pavement Performance	115
Figure 4.83. Geosynthetic-Reinforced Pavement Structures for Case Studies.....	116
Figure 4.84. Effect of Geosynthetic Location and Geosynthetic Type on Fatigue Cracking	118
Figure 4.85. Effect of Geosynthetic Location and Geosynthetic Type on Rutting Depth.....	119
Figure 4.86. Effect of Geosynthetic Location and Geosynthetic Type on IRI	119
Figure 4.87. Flowchart of the Process of Validating the Proposed ANN Approach.....	121
Figure 4.88. Comparison of Rutting Depth between ANN Approach Prediction and Field Measurement for Pavement Section 16-9032	122
Figure 4.89. Comparison of Fatigue Cracking between ANN Approach Prediction and Field Measurement for Pavement Section 16-9032.....	123
Figure 4.90. Comparison of IRI between ANN Approach Prediction and Field Measurement for Pavement Section 16-9032.....	123
Figure 5.1. Measured Horizontal Displacements of Geogrid and UGM When Geogrid Was Placed in the Middle of the Base Course.....	127
Figure 5.2. Measured Horizontal Displacements of Geogrid and UGM When Geogrid Was Placed at the Bottom of the Base Course.....	128
Figure 5.3. Measured Horizontal Displacements of Geotextile and UGM When Geotextile Was Placed in the Middle of the Base Course	128
Figure 5.4. Measured Horizontal Displacements of Geotextile and UGM When Geotextile Was Placed at the Bottom of the Base Course	129
Figure 5.5. Horizontal and Vertical Moduli of Unreinforced UGM at Each Stress State	130
Figure 5.6. Effect of Geosynthetics on Horizontal Modulus of UGM	130
Figure 5.7. Effect of Geosynthetics on Vertical Modulus of UGM.....	131
Figure 5.8. Effect of Geosynthetics on Anisotropic Ratio of UGM	131
Figure 5.9. Effect of Geosynthetic Reinforcement on Reducing Permanent Strain of UGMs.....	132
Figure 5.10. Comparison of Lab-Measured and Proposed-Model-Predicted Permanent Strain Curves for Unreinforced UGMs.....	133
Figure 5.11. Comparison of Lab-Measured and Proposed Model-Predicted Permanent Strain Curves for Geogrid-Reinforced UGMs.....	133
Figure 5.12. Comparison of Lab-Measured and Proposed-Model-Predicted Permanent Strain Curves for Geotextile-Reinforced UGMs	134
Figure 5.13. Effect of Geosynthetic Sheet Stiffness on Predicted Horizontal Modulus of UGM	135
Figure 5.14. Effect of Geosynthetic Sheet Stiffness on Predicted Vertical Modulus of UGM	135
Figure 5.15. Effect of Base Modulus on Average Compressive Strain in Base Layer.....	137
Figure 5.16. Effect of Base Modulus on Compressive Strain at the Top of Subgrade.....	137
Figure 5.17. Effect of Subgrade Modulus on Average Compressive Strain in Base Layer	138
Figure 5.18. Effect of Subgrade Modulus on Compressive Strain at the Top of Subgrade.....	138

Figure 5.19. Effect of Tensile Sheet Stiffness of Geogrid on Average Compressive Strain in Base Layer	139
Figure 5.20. Effect of Tensile Sheet Stiffness of Geogrid on Compressive Strain at the Top of Subgrade.....	139
Figure 5.21. Effect of Base Modulus on Rutting Depth of Geosynthetic-Reinforced and Unreinforced Pavements	140
Figure 5.22. Effect of Base Modulus on Fatigue Cracking of Geosynthetic-Reinforced and Unreinforced Pavements	140
Figure 5.23. Effect of Base Modulus on IRI of Geosynthetic-Reinforced and Unreinforced Pavements	141
Figure 5.24. Effect of Subgrade Modulus on Rutting Depth of Geosynthetic-Reinforced and Unreinforced Pavements	141
Figure 5.25. Effect of Subgrade Modulus on Fatigue Cracking of Geosynthetic- Reinforced and Unreinforced Pavements	142
Figure 5.26. Effect of Subgrade Modulus on IRI of Geosynthetic-Reinforced and Unreinforced Pavements	142
Figure 5.27. Effect of Sheet Stiffness of Geogrid on Rutting Depth of Reinforced Pavements	143
Figure 5.28. Effect of Sheet Stiffness of Geogrid on Fatigue Cracking of Reinforced Pavements	143
Figure 5.29. Effect of Sheet Stiffness of Geogrid on IRI of Reinforced Pavements	144

LIST OF TABLES

Table 2.1. Summary of Finite Element Model Studies on Geosynthetic-Reinforced Pavements	7
Table 2.2. Summary of Design Methods for Pavements with Geosynthetics	8
Table 3.1. LST Experiment Design for Flexible Pavement.....	10
Table 3.2. LST Experiment Design for Rigid Pavement.....	10
Table 3.3. Loading Protocol for Flexible and Rigid Pavement in LST Experiments.....	10
Table 4.1. Triaxial Test Protocol for Determining Cross-Anisotropic Properties.....	20
Table 4.2. Influence of Geosynthetic on Material Properties—Geosynthetic Location: Mid-Height.....	21
Table 4.3. Influence of Geosynthetic on Material Properties—Geosynthetic Location: One-Quarter below the Middle	22
Table 4.4. Influence of Geosynthetic on Material Properties—Geosynthetic Location: Bottom.....	23
Table 4.5. Proposed Permanent Deformation Test Protocol—Proposed Stress Levels for Calibration of Model Coefficients	26
Table 4.6. Proposed Permanent Deformation Test Protocol—Proposed Stress Levels for Validation of Model Coefficients	27
Table 4.7. Determination of Model Coefficients for the UGM with and without Geosynthetics.....	28
Table 4.8. General Description of the Instrumentation Plan in LST	38
Table 4.9. Selected Laboratory Tests for Material Characterization.....	81
Table 4.10. Determined Prony-Series Model Coefficients for the Plant-Mixed, Laboratory-Compacted (PMLC) Asphalt Concrete.....	82
Table 4.11. Cross-Anisotropic Properties of the UGM Used in LST Test.....	83
Table 4.12. Comparison of Geosynthetic Sheet Stiffness Values between Laboratory Test and Manufacturer’s Specifications	85
Table 4.13. Computed Critical Strains for Geosynthetic-Reinforced and Unreinforced Flexible Pavement Structures	92
Table 4.14. Selected Input Parameters for Geosynthetic-Reinforced Pavement Structures.....	106
Table 4.15. Selected Input Parameters for Unreinforced Pavement Structures.....	107
Table 4.16. Material Properties of Geosynthetic-Reinforced Pavements for Case Studies—Material Properties of Control Pavement.....	117
Table 4.17. Material Properties of Geosynthetic-Reinforced Pavements for Case Studies—Material Properties for Geosynthetic Products	117
Table 4.18. Determination of Modified Material Properties for Case Studies	117
Table 5.1. Summary of Specifics of LST Experiments on Flexible Pavements.....	125
Table 5.2. Summary of Specifics of LST Experiments on Rigid Pavements.....	126

CHAPTER 1. INTRODUCTION

Introduction

Geosynthetics are available in a wide range of forms and materials and are used in many applications. Geosynthetics are often used by highway agencies in conjunction with unbound base layers (i.e., within the layer or as a subgrade/base interface layer) to enhance the performance of flexible and rigid pavements. Although much research has been performed on the properties of these materials and their use in pavement structures, limited research has dealt with the methodologies of quantifying their influence on pavement performance in a manner that would allow incorporation into the mechanistic-empirical pavement design and analysis procedures. The AASHTOWare Pavement ME Design software provides a methodology for the analysis and performance prediction of pavements. However, use of geosynthetics in pavement layers and their influence on distress models have not been included in Pavement ME Design.

Procedures that quantify the influence of geosynthetics on pavement performance will help in determining the payoff of using these materials and selecting the appropriate material for a specific application. However, such information is not readily available. As a result, the research in this project was initiated to (a) evaluate those tests currently used for characterizing geosynthetics and identify how tests relate to performance, and (b) develop a methodology for quantifying the influence of geosynthetics on performance for use in pavement design and analysis. This information can be incorporated into the Pavement ME Design software, thus allowing a rational analysis and design procedure of flexible and rigid pavements in which geosynthetics are used in conjunction with unbound bases and subbases.

Objective

The objective of this research project was to develop a methodology for quantifying the influence of geosynthetics on pavement performance for use in pavement design and analysis. The methodology should be consistent with the Pavement ME Design framework to facilitate incorporation into the AASHTOWare Pavement ME Design software. This project focused on the use of geosynthetics in unbound base/subbase layers or as a base/subgrade interface layer for flexible and rigid pavements.

Research Scope and Approach

The project was divided into six components: (a) full-scale laboratory testing of typical asphalt and concrete pavement sections in an instrumented large-scale tank (LST); (b) laboratory triaxial testing of different base courses with geosynthetics at different locations within the test samples; (c) finite element computations to match the results of the full-scale tests; (d) use of the same finite element program to develop full factorial sets of pavement data to construct the Artificial Neural Network (ANN) models of the critical strains and stresses in pavements; (e) generation of a new model of permanent deformation to predict pavement performance; and (f) comparison of the predicted performance of pavements with and without geosynthetics embedded in the unbound base courses.

The deliverables of this project included a computer subroutine written for incorporation into the Pavement ME Design software to predict the performance of pavements with geosynthetics. This computer program was named “Composite Geosynthetic–Base Course Model” and was supported by other major deliverables, including testing protocols that produced the geosynthetic property and modified base course property inputs for the Pavement ME Design software that were needed to accurately predict their influence on pavement performance. These predictive relations were based on full-scale measurements made in an LST of typical flexible and rigid pavements under static and dynamic loading. The complete set of measured data in electronic form was another major deliverable of this project. Summaries of these data are presented in Appendices E through K. The measurements and observations were matched closely with computations made with a finite element computer program equipped with interface elements. Multiple runs with the finite element program over a wide range of pavement variables produced the data for constructing ANN models of the critical strains and stresses in pavements used to predict the performance of those pavements. The permanent deformation models of the base course and the subgrade were replaced with other models that fit the data more reliably and incorporated the stress state levels. These are the subroutines referred to above. These new models of the critical stresses and strains and permanent deformation were used to compute the roughness and the principal distresses of pavements. The computation of the critical stresses in rigid pavements for predicting transverse cracking showed that these stresses are insensitive to the type or location of geosynthetics (see discussions in Chapter 4). This result indicates that geosynthetics will have negligible influence on this type of rigid pavement distress. However, there is a strong likelihood that the ability of geogrids to reduce the permanent deformation of base courses, as shown in Chapter 4, will be able to improve pavement performance by reducing the joint faulting and roughness in these rigid pavements. The calibration of these critical stresses and strains and permanent deformations to these different measures of flexible pavement performance were left unchanged, relying on the validity of the calibration that was done in the existing version of the Pavement ME Design software. Verification of these relations was accomplished to the extent possible with existing in-service pavement sections with embedded geosynthetics. The relationship between the existing model in the Pavement ME Design software and the Composite Geosynthetic–Base Course Model developed in this project is illustrated in Figure 1.1. Examples of using the Composite Geosynthetic–Base Course Model to analyze pavement structures with/without a geosynthetic layer are provided in Appendix Q.

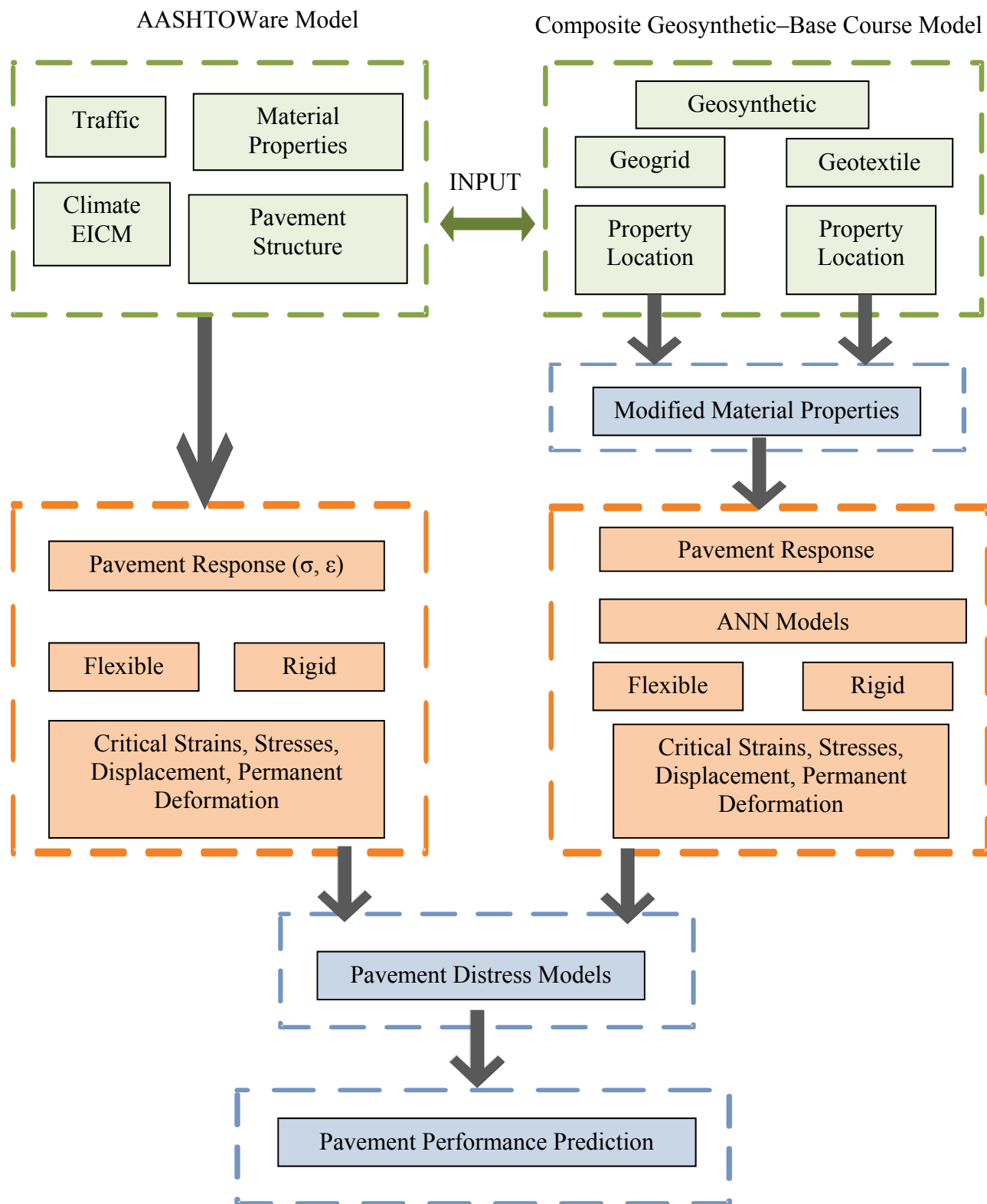


Figure 1.1. Compatibility of Proposed Program with AASHTOWare Pavement ME Design

Organization of the Report

This report is organized into six chapters:

- The first chapter presents the introduction and research approach used in this research project.
- The second chapter presents a synthesis of current knowledge of quantification of influence of geosynthetics on pavement performance.
- The third chapter presents a research plan of this project.
- The fourth chapter presents the experiments, models, and major findings. These include the tests that were conducted to determine the effects of both geogrids and geotextiles on the anisotropic properties of unreinforced, unbound base courses; the results of the LST tests on both flexible and rigid pavements; the identification of the conditions under which slippage occurred between the base course and the geosynthetic material; the close correspondence between the stresses, strains, and displacements that were observed in the LST tests and modeled in the finite element program; the important properties of geosynthetics that affected the performance of a pavement; the method of converting the properties of an unreinforced base course and geosynthetics into a composite input value to the ANN models of reinforced base/subbase courses; the use of the pullout resistance test to obtain design values of the interaction coefficient between the base course and geosynthetics; the improved prediction of permanent deformation of base courses under repeated loading by replacing the current Pavement ME Design model with the new, recently developed model; and the comparison of the critical strains, stresses, and displacements in a pavement with a reinforced base versus one without a reinforced base. The commentary in this chapter provides an overview, while many of the corresponding details are contained in a number of appendices introduced in the chapter.
- The fifth chapter presents interpretation, appraisal, and application of the findings discussed in the second chapter. It gives examples of the application of the new models to specific pavement conditions, traffic levels, and geosynthetic placement in different locations within and beneath the base course.
- The sixth chapter presents conclusions and suggested further research.

The main body of the report is written to give an accurate overview of the approach taken and the results of this project. More detailed discussions of the topics in the report are contained in Appendices A through Q.

CHAPTER 2. SYNTHESIS OF CURRENT KNOWLEDGE

Geogrids and geotextiles have been the most commonly used geosynthetic products for enhancing pavement performance (1–5). Beneficial effects of the geosynthetic layer have been identified on the responses of pavements under traffic loading through two major mechanisms (6–13):

- Lateral confinement, which is produced by the interface frictional interaction and interlocking between base course aggregates and the geosynthetic layer. Significant tensile stress is generated in the geosynthetic layer when a spread motion is created by traffic loading, which in turn reduces the vertical stress and shear stress dramatically due to the increased base course stiffness.
- Vertical membrane effect. The inward shear stress caused by membrane deformation reduces the outward shear stress generated by repetitive wheel loading. As a result, the vertical stress is then reduced and distributed widely around the geosynthetic layer.

In addition to the above major reinforcement mechanisms, the layer separation provided by geotextiles is another important function that prolongs pavement service life. Layer separation reduces the base course contamination, which significantly increases the resilient modulus of the base course and then increases the pavement service life.

To extend the use of geosynthetics in pavements, there is a need to incorporate geosynthetic material into pavement design. Accurate prediction of geosynthetic-reinforced pavement performance is a key to pavement design in this respect. The Pavement ME Design software is usually used to predict the pavement performance by taking into account a variety of factors, such as pavement structure, material property, traffic, and climate. However, it does not include geosynthetic material for pavement design. Thus, it is desirable to develop a methodology to incorporate geosynthetic material into the Pavement ME Design software so that the performance of geosynthetic-reinforced pavements can be accurately predicted. Generally, there are three critical steps involved to achieve this target: (a) laboratory characterization of geosynthetic-reinforced unbound granular material, (b) numerical modeling of geosynthetic-reinforced pavement, and (c) prediction of geosynthetic-reinforced pavement performance using the computed pavement responses.

Laboratory Characterization of Granular Materials with Geosynthetics

Many studies have been conducted to characterize the effect of geosynthetic reinforcement on the vertical resilient modulus of the unbound granular materials (UGMs). It was found that the geosynthetic did not have a significant effect on enhancing the vertical resilient modulus of the reinforced UGMs when the specimen was fabricated as a 15-cm-diameter and 30-cm-high cylinder (14) or a 20-cm-diameter and 40-cm-high cylinder (15). In contrast, Rahman et al. (16) reported that the geosynthetic was effective at improving the resilient modulus of the reinforced UGMs when the specimen size was reduced to a dimension of 15-cm diameter and 20-cm height. Therefore, it was inferred that the effect of the geosynthetic reinforcement on the resilient modulus of the UGMs depended on the dimensions of the UGM specimen. Yang and Han (17) developed an analytical model to predict the resilient modulus of the geosynthetic-reinforced UGMs at any given dimensions. According to this analytical model,

the geosynthetic was more effective in increasing the resilient modulus of the UGMs with a larger diameter and a smaller height. McDowell et al. (18) and Schuettpelz et al. (19) showed that the geosynthetic provided the reinforcing effect in an area that is typically approximately 3 cm to 7.5 cm in thickness on both sides of the geosynthetic. Since the geosynthetic reinforcement influence zone had such a small range, quantifying the influence of geosynthetics on the vertical resilient modulus of the UGMs with a 30-cm height or more would be inappropriate.

Recent studies revealed that the UGMs exhibit cross-anisotropic resilient behavior (i.e., the resilient moduli in the vertical plane were different from the horizontal resilient moduli, while the resilient moduli in the horizontal plane were the same in all directions) (20, 21). The cross-anisotropic nature of the UGMs was demonstrated to be a major factor that influences pavement performance (22). Therefore, quantifying the influence of geosynthetics on the resilient properties of UGMs should focus on evaluating the effect of geosynthetics on the cross-anisotropic properties of the base course—an effort that was not identified in any of the literature that was reviewed in this study.

Compared to the increase of the resilient modulus, the reduction of the permanent deformation of UGM is a more important benefit of the geosynthetic reinforcement. Perkins et al. (23), Wayne et al. (24), and Nazzal et al. (14) found that the geosynthetic considerably reduced the permanent deformation of the UGMs using the repeated load triaxial tests. Moghaddas-Nejad and Small (15) and Abu-Farsakh et al. (25) showed that for a particular confining stress, the reduction of the permanent deformation by the geosynthetic increased rapidly with the increase of the deviatoric stress, until a peak was reached, and then it decreased gradually. This finding indicated that the stress level significantly influenced the effects of the geosynthetic on the reduction of the permanent deformation of the UGMs. It was known that the stress induced by the traffic load was non-uniformly distributed in the base course of pavements. Therefore, quantifying the effect of stress level on the permanent deformation characteristics of the geosynthetic-reinforced UGMs was critical to accurately predicting the pavement performance. The permanent deformation of the base layer was directly related to the rutting of flexible pavements and the faulting of the joints in rigid pavements. Since the present Pavement ME Design does not permit the use of permanent deformation of the base layer to predict either the erosion or the faulting of the joints in rigid pavements, a major revision of the structural subsystem of the rigid part of the Pavement ME Design is required.

Modeling of Pavements with Geosynthetics

The influence of geosynthetics on pavement structures has been evaluated using finite element models. Specifically, the finite element models were constructed to compute pavement responses (stresses, strains, and deformations) of pavements (with/without a geosynthetic layer) under different loading configurations. These pavement responses were used to evaluate the influence of using the geosynthetic layer as base reinforcement (2, 3, 9, 26–29). The elements addressed in the finite element models included geosynthetic geometric characteristics, traffic loading, constitutive models of materials, and interface condition. Table 2.1 summarizes the features of the finite element models constructed for geosynthetic-reinforced pavements and the

corresponding modeling techniques. All the pavements represented in Table 2.1 were flexible pavements; no models were found for rigid pavements.

Table 2.1. Summary of Finite Element Model Studies on Geosynthetic-Reinforced Pavements

Developer	Geometry	Surface Constitutive Model	Base Constitutive Model	Geosynthetic Constitutive Model	Interface Model	Subgrade Constitutive Model
Barksdale and Brown (30)	Axial symmetric	Isotropic nonlinear elastic	Anisotropic linear elastic	Isotropic linear elastic membrane	Linear elastic-plastic	Isotropic
Dondi (31)	Three dimension	Isotropic linear elastic	Isotropic elastoplastic D-P	Isotropic linear elastic membrane	Elastic-plastic Mohr-C	Isotropic elastoplastic Cam-Clay
Wathugala et al. (32)	Two dimension	Isotropic elastoplastic D-P	Isotropic elastoplastic D-P	Isotropic, elastoplastic membrane	None	Isotropic elastoplastic HiSS
Perkins (3)	Three dimension	Anisotropic elastic-perfectly plastic	Isotropic plastic	Anisotropic elastic-plastic membrane	Mohr-C	Isotropic plastic
Saad et al. (27)	Three dimension	Isotropic linear elastic	Isotropic elastic-plastic D-P	Isotropic linear elastic membrane	Perfect bonding	Isotropic elastoplastic Cam-Clay
Luo (33)	Two dimension	Isotropic linear elastic	Isotropic linear elastic	Isotropic linear elastic truss element	Perfect bonding	Isotropic linear elastic
Kwon (4)	Two dimension	Isotropic linear elastic	Anisotropic nonlinear elastic	Isotropic elastic membrane	Linear elastic element	Isotropic linear elastic

Design Methods for Pavements with Geosynthetics

Empirical and mechanistic-empirical design methods have been developed for pavements with geosynthetics (1, 34). The empirical design approaches for geosynthetic-reinforced pavements were based on relating the laboratory testing results to the field conditions. The limitation of the empirical design method was that it could be applied only to the limited field conditions from which the data were taken. Compared to the empirical design methods, the mechanistic-empirical design methods were based on finite element models and were more reliable for geosynthetic-reinforced pavement design (3, 4, 29, 35, 36). Table 2.2 presents a

summary of the design methods for pavements with geosynthetics. Design methods were not found in the literature for rigid pavements with geosynthetics.

Table 2.2. Summary of Design Methods for Pavements with Geosynthetics

Developer	Design Method	Geosynthetic Reinforcement Modification	Distress Mode	Practice Support	Mechanics Support
Barksdale and Brown (30)	Mechanistic-empirical	Isotropic, linear elastic model using membrane element	Surface deformation	Field results	Finite element model
Webster (35)	Empirical	Direct extrapolation from field test results	Rut depth	Field results	None
Perkins et al. (34)	Mechanistic-empirical	Isotropic, linear elastic model using membrane element	Surface deformation	Field results	Finite element model
Giroud and Han (11)	Empirical	Bearing capacity factor, bearing capacity mobilization coefficient, stress distribution angle	Stresses at the base course/subgrade interface, rut depth	Field wheel load test, laboratory cyclic plate loading test	None
Kwon (4)	Mechanistic-empirical	Anisotropic, nonlinear elastic model using membrane element	Vertical strain on the top of subgrade, vertical deflection	Full-scale test results	Finite element model

CHAPTER 3. RESEARCH PLAN

The research plan included six components: (a) full-scale laboratory testing of typical asphalt and concrete pavement sections in an instrumented LST; (b) laboratory triaxial testing of different base courses with geosynthetics at different locations within the test samples; (c) finite element computations to match the results of the full-scale tests; (d) use of the same finite element program to develop full factorial sets of pavement data to construct ANN models of the critical strains and stresses in pavements; (e) generation of a new model of permanent deformation to predict pavement performance; and (f) comparison of the predicted performance of pavements with and without geosynthetics embedded in the unbound base courses.

Full-Scale Laboratory Testing

The full-scale laboratory testing plan was designed to capture the effect of two types of geosynthetics on the response of both rigid and flexible pavement sections under static and dynamic loads. Two distinctive mechanisms by which geosynthetics affected the performance of pavements were reported: (a) stiffening the entire base course, and (b) more efficiently spreading the tire load. The two geosynthetics were selected to illustrate these two separate mechanisms on both asphalt and concrete pavements.

According to the literature, the benefits of geosynthetics in asphalt pavements have depended on the thickness of the crushed aggregate base (CAB) layer and the location of the geosynthetic within that layer (13, 37–41). Generally, geosynthetics were reported to be more effective in flexible pavements when placed at the base-subgrade interface of thin base sections (such as 6 inches) and near the midpoint of thicker base layers (such as 10 or more inches). Thus, two different base thicknesses (6 and 10 inches) along with two different locations for the geosynthetic were included in the test matrix for flexible pavement. Table 3.1 provides a summary of the LST experiments conducted on the flexible pavement structure.

A second test matrix was developed to capture the influence of geosynthetics on rigid (Portland cement concrete [PCC]) pavement responses. For the rigid pavement experiments, the thicknesses of the PCC layer and CAB layer were kept at 6 and 8 inches, respectively. The testing plan for PCC included only a typical base thickness since the PCC slab itself supplies most of the pavement's structural capacity. Table 3.2 provides a summary of the LST experiments conducted on the rigid pavement structure.

Generally, two types of loading with three different intensities were applied to each pavement structure. The flexible pavement structure was subjected to repeated dynamic loads of 9, 12, and 16 kips for different cycles, with a pulse duration of 0.1 second followed by a rest period of 0.9 second in each loading cycle. The pavement structure was then allowed to recover under 100-lb seating load for 300 seconds. A static load of 6, 9, and 12 kip was then applied for 300 seconds with a rest period between two load levels of 30 minutes. The rigid pavement structure was subjected to the same dynamic load but only for 25 cycles with a 180-second recovery period. The static load was almost similar but was applied for 180 seconds with a rest period of 300 seconds. The loading and rest periods were longer with the flexible pavement structure to permit complete viscoelastic recovery. Table 3.3 provides a summary of the loading protocol for all of the flexible and rigid pavement experiments. Following each loading level, a

rest period was imposed to allow the pavement to rebound from the applied loading strains accumulated in the previous test. All loads were applied through a loading plate to the surface of the pavement layer. For the flexible pavement structure, the loading plate was located at the center of the LST, while for the rigid pavement structure, the plate was placed at the edge of the concrete slab. The measurements made in all of the test pavements included the surface deflections, vertical and horizontal strains and stresses, and relative displacement between the geosynthetic and the surrounding unbound base course.

Table 3.1. LST Experiment Design for Flexible Pavement

Experiment		Asphalt Layer Thickness (inch)	CAB Layer Thickness (inch)	Reinforcement	
ID	No.			Type	Location
AC-Contr-B06	1	6	6	None (Control)	N/A
AC-Contr-B10	2	6	10	None (Control)	N/A
AC-Grid-B06	3	6	6	Geogrid	Base-Subgrade Interface
AC-Grid-B10	4	6	10	Geogrid	Middle of the Base
AC-Textile-B06	5	6	6	Geotextile	Base-Subgrade Interface
AC-Textile-B10	6	6	10	Geotextile	Middle of the Base

Note: AC = asphalt concrete; N/A = not applicable.

Table 3.2. LST Experiment Design for Rigid Pavement

Experiment		Concrete Layer Thickness (inch)	CAB Layer Thickness (inch)	Reinforcement	
ID	No.			Type	Location
PCC-Contr-IS	7	6	8	None (Control)	N/A
PCC-Grid-IS	9	6	8	Geogrid	Middle of the Base
PCC-Textile-IS	10	6	8	Geotextile	Middle of the Base

Note: N/A = not applicable.

Table 3.3. Loading Protocol for Flexible and Rigid Pavement in LST Experiments

Load Type	Target Load Level (kips)		Loading Duration		Rest Period	
	AC	PCC	AC	PCC	AC	PCC
Dynamic (0.1-sec Loading + 0.9-sec Rest Period)	9		80 Cycles	25 Cycles	5 Minutes	3 Minutes
	12		100 Cycles			
	16		150 Cycles			
Static	6	5	5 Minutes	3 Minutes	30 Minutes	5 Minutes
	9					
	12					

Triaxial Laboratory Testing

The research team tested two different base courses under triaxial laboratory conditions according to protocols for resilient modulus and permanent deformation testing that were developed before this project to obtain the anisotropic properties of a base course material. One

was a base course that was used in the LST tests at the University of Nevada, Reno, and the other was a limestone base course commonly used in Texas. Both geotextiles and geogrids were placed at three different locations within the samples, and their effects on the anisotropic properties and permanent deformation properties of the base courses were measured. The protocols that were used in these tests include measurements of the resilient modulus, anisotropic ratio, and permanent deformation with repeated loading.

Finite Element Modeling

The finite element program ABAQUS that was available in the computer system was used to model the effects of loading in the different tests that were performed in the LST. The computer program was capable of representing anisotropy, stress dependency, and plasticity zones (42). It also included a Goodman-type interface element that was capable of modeling the slippage and interaction between the base course and the geosynthetics (43). This program was used to match, to the extent possible, the measured results of the LST tests.

The mechanical effects of geosynthetics on the properties of an unbound base course were two-fold. They affected the stiffness, anisotropic ratio, and permanent deformation of the base course as measured in the triaxial test. They also provided the membrane effect on increasing the confining pressure and reducing the vertical strain in the base course and subgrade. Although only the stiffening effect was measured in the triaxial test, both the stiffening and the membrane effects were combined in the finite element analyses.

Development of ANN Models of Critical Strains and Stresses

Using the finite element program that successfully matched the measurements in the LST tests, the researchers made a large number of runs covering a wide range of pavement variables. In flexible pavements, the variables included various thicknesses of the asphalt, base, and subgrade; various levels of moduli of each layer; various anisotropic ratios of the base course; and several levels of sheet stiffness and locations of geosynthetics. No ANN models of critical stresses were developed for rigid pavements because the finite element model computations, as illustrated in Chapter 4, showed that critical stresses were insensitive to the type and location of geosynthetics.

In all cases for flexible pavements, one load level was used: the 9-kip load. The anisotropic ratios used in the computations spanned the range that was measured in the triaxial tests of the two base courses. In this way, the alteration of the anisotropic ratios by the embedded geosynthetics was accounted for. In each case, the critical strains and stresses in pavements were calculated. These strains or stresses were used in Pavement ME Design to predict pavement distresses and roughness. The load-related pavement distresses that were predicted in flexible pavements were roughness, rutting, and fatigue cracking. A new permanent deformation model replaced the permanent deformation model of the base course and subgrade in the Pavement ME Design software because of its superior predictions at different stress states and numbers of load repetitions in the repeated load triaxial tests. ANN models were developed for each of the critical strains and stresses in flexible pavements using the extensive computed database that was generated with the finite element program. These stresses were inputs in the new permanent

deformation model. When geosynthetics were used in the design of a flexible pavement, these ANN models could be used in place of the current models in the Pavement ME Design software, as indicated schematically in Figure 1.1.

The material property inputs to the Composite Geosynthetic–Base Course Model developed in this project included separate properties of the unreinforced, unbound base course and the sheet stiffness of the geosynthetic. These properties could be inputs at Level 1, 2, or 3.

- Level 1: Base course input data included the stress-dependent coefficients for both the vertical modulus and the shear modulus, the anisotropic ratio, a shear interaction coefficient between the base course and the geosynthetic, and the suction-vs.-water content characteristic curve of the base course. The permanent deformation model required two exponents in addition to the input required by the Pavement ME Design software. The geosynthetic properties included the sheet stiffness and its location within the base course. If geogrids were used, the aperture needed to be at least 1.2 times the maximum size of the aggregate of the base course.
- Level 2: Base course input data included a modulus; a Poisson's ratio; an anisotropic ratio of the unreinforced, unbound base course; and a shear interaction coefficient between the base course and the geosynthetic. The geosynthetic input data included the sheet stiffness and its location within the base course.
- Level 3: Base course input data included a selection of typical base courses with tabulated material properties. A typical tabulated shear interaction coefficient was used. The geosynthetic input data included the sheet stiffness and its location within the base course. The separate properties of the base course and geosynthetic were combined to make a composite material, the properties of which were used in the ANN models to calculate the critical strains and stresses of pavements. The rules for making this conversion into a composite material are given in Chapter 4.

Performance Data Collection of In-Service Pavement Sections with Geosynthetics

The research team identified the in-service pavement sections with embedded geosynthetics from the Long-Term Pavement Performance (LTPP) database and other databases from local highway agencies. The collected pavement structure and performance information was listed as follows:

- Pavement structure data, including layer thickness, construction dates, material design information, and falling weight deflectometer data.
- Traffic data from the identified pavement sections, which should be compatible with the input of the traffic module in the Pavement ME Design software.
- Climatic data or weather station information from the identified pavement sections.
- Performance data from the identified pavement sections, including fatigue cracking, rutting, and international roughness index.

CHAPTER 4. EXPERIMENTS, MODELING, AND FINDINGS

Introduction

This chapter on the experiments, modeling, and findings of the research project reviews the tests that were used commercially and identifies the geosynthetic properties that were most relevant to pavement performance prediction. Triaxial laboratory tests at multiple stress states were run to demonstrate the effect of geosynthetics on the measured cross-anisotropic properties of the base courses in which they were embedded. LST tests were conducted with different base course thicknesses and asphalt layer thicknesses, and a single concrete layer thickness. Because pavement edges and joints were of prime importance to concrete pavement performance, the loads were applied at the edge of the concrete pavement. The slippage that was observed between the geosynthetics and base courses revealed the part of the data from a pullout test that was most useful in characterizing the contribution of geosynthetics to reinforcing a base course.

Finite element models of each pavement layer and the interfaces between the geosynthetic and base course were used to determine the properties of each layer that were needed to replicate the LST measurements. In general, the comparisons of the predicted and measured results were excellent. In order to provide the Pavement ME Design software with the capability to include the effects of embedded geosynthetics, ANN models predicting the critical strains in asphalt pavements were prepared. The models could reproduce the results of thousands of runs with the analytical software, representing a wide variety of pavement structures and layer material properties. Because of the insensitivity of critical stresses in concrete pavements to either type or location of geosynthetics, no ANN models were developed for rigid pavements.

Geosynthetic Application and Reinforcement Mechanisms

Geogrids and geotextiles have been the most commonly used geosynthetic products in unbound base layers (i.e., within the layer or as a subgrade/base interface layer) as a means of enhancing the performance of flexible and rigid pavements. Beneficial effects of the geosynthetic layer were identified in the responses of pavements under traffic loading through two major mechanisms (see Figure 4.1):

- Lateral confinement, which was produced by the interface frictional interaction and interlocking between base course aggregates and the geosynthetic layer. Significant tensile stress was generated in the geosynthetic layer when a spreading motion was created by traffic loading, which in turn reduced the vertical stress and shear stress dramatically due to the increased base course stiffness (2, 43).
- Vertical membrane effect. The inward shear stress caused by membrane deformation reduced the outward shear stress generated by repetitive wheel loading. As a result, the vertical stress was reduced and distributed widely around the geosynthetic layer (6).

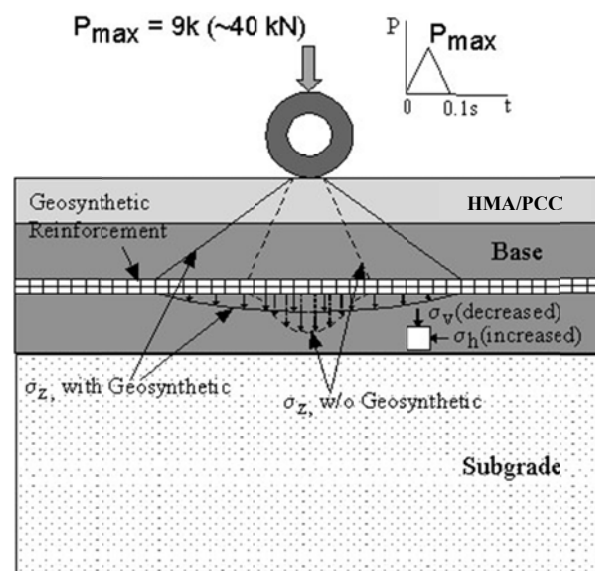


Figure 4.1. Mechanisms of Geosynthetics in Pavement

In addition to the above major reinforcement mechanisms, the layer separation provided by geotextiles was another important function that prolonged the pavement service life. Layer separation reduced the base course contamination (2), which significantly increased the resilient modulus of the base course and then increased the pavement service life.

Available Test Methods for Evaluating Geosynthetic Properties Related to Pavement Performance

The geosynthetic properties that were related to pavement performance included the physical properties, mechanical properties, and interface properties between the geosynthetic layer and aggregates/soils. Many test methods were conducted to evaluate the pavement performance-related geosynthetic properties. The test standards and the corresponding geosynthetic properties are listed below. Specifically, test standards for evaluating geogrid properties included:

- Tex-621-J, to measure the aperture size, which must be at least 50 percent greater than the maximum aggregate size in the base course gradation (5).
- ASTM D1777, to measure the dimensions of the geogrid ribs.
- ASTM D5818, to determine the resistance to installation damage.
- ASTM D6637, to measure the rib tensile stiffness.
- ASTM D7737, to measure the junction strength and junction efficiency.
- ASTM D7748, to measure the flexural rigidity.
- ASTM D6706, to determine the geogrid-aggregate/soil shear interfacial properties.

Test standards for evaluating geotextile properties included:

- ASTM D5199, to measure the sheet thickness.
- ASTM D4751, to measure the apparent opening size, which should be smaller than the 15 percent passing particle size.
- ASTM D4491, to measure the permeability, which affects the drainage function.

- ASTM D5493, to measure the permittivity, which influences the filtration function.
- ASTM D4595, to measure the tensile stiffness.
- ASTM D6241, to determine the California bearing ratio (CBR) puncture strength.
- ASTM D6706, to determine the geotextile-aggregate/soil interfacial properties.

Selection of Test Methods for Determining Geosynthetic Properties

A comprehensive review of available test methods for determining the performance-related geosynthetic properties is provided in Appendix A. The criteria of test method selection included the following:

- The test method should have the characteristics of simple operation, short test time, and low cost.
- The test method should be repeatable and reliable.
- The test method should be applicable to different types of geosynthetics.
- The determined geosynthetic properties should be directly related to pavement performance.
- The determined geosynthetic properties should be capable of being input into the finite element program.

Based on the selection criteria above, the direct tension test and the pullout test were determined to be the best tests to measure the tensile sheet stiffness of geosynthetics and determine the geosynthetic-aggregate/soil interfacial properties, respectively, both of which significantly affected the performance of geosynthetic-reinforced pavements.

Direct Tension Test to Determine Geosynthetic Sheet Stiffness

The geosynthetic sheet stiffness was closely related to the performance of geosynthetic reinforcement on unbound aggregates (49). Specifically, an increase in the tensile stiffness of the geosynthetic increased the resilient modulus of the geosynthetic-reinforced unbound aggregates. In addition, it reduced the permanent deformation of the material. Two test standards, ASTM D6637 and ASTM D4595, as mentioned above, were employed to measure the force-strain relationships of geogrids and geotextiles, respectively, through the direct tension test. The sheet stiffnesses of geogrids and geotextiles were determined using Equations 4.1 and 4.2, respectively. Note that the sheet stiffness at a small strain stage (i.e., tensile strain was less than 1 percent) was typically considered a key value in base reinforcement applications.

$$M = \frac{Ea}{s} = \frac{\Delta T}{\Delta \varepsilon} \text{ (Geogrid)} \quad (4.1)$$

$$M = Et = \frac{\Delta T}{\Delta \varepsilon} \text{ (Geotextile)} \quad (4.2)$$

where M is the sheet stiffness of the geosynthetic; E is the tensile modulus of the geosynthetic; a is the cross-section area of the geogrid rib; s is the spacing of the geogrid ribs; t is the thickness of the geotextile; ΔT is the applied incremental tensile force; and $\Delta \varepsilon$ is the corresponding incremental tensile strain.

Pullout Test to Determine Geosynthetic-Aggregate/Soil Interfacial Properties

The interaction between aggregates and the geosynthetic layer was commonly quantified using the pullout test (49). Figure 4.2 is a schematic plot of the pullout test. The geosynthetic embedded in the base course was pulled out of the aggregate layer by a tensile pullout force. The pullout force was recorded and the displacement of the geosynthetic was measured using linear variable differential transformers (LVDTs). Typical pullout test data are shown in Figure 4.3. The pullout force versus geosynthetic displacement curve had three stages: linear stage, nonlinear stage, and critical stage. Each stage had different mechanisms of aggregate-geosynthetic interaction. The pullout test data in the three stages were interpreted to determine the interfacial shear modulus between the geosynthetic and the aggregates, as shown in Equation 4.3.

$$G(x) = \frac{G}{1 + \frac{1}{\tau_{\max} \delta_s} [A \cosh(\beta x) + B \sinh(\beta x) + C]} \quad (4.3)$$

where $G(x)$ is the interfacial shear modulus as a function of the geosynthetic embedded location; G is the shear modulus of the base aggregates; δ_s is the thickness of the shear zone; τ_{\max} is the maximum shear stress applied on the geosynthetic-aggregate interface; and β , A , B , and C are model coefficients that can be determined from the pullout test data. The details of developing the interfacial shear modulus model are presented in Appendix B.

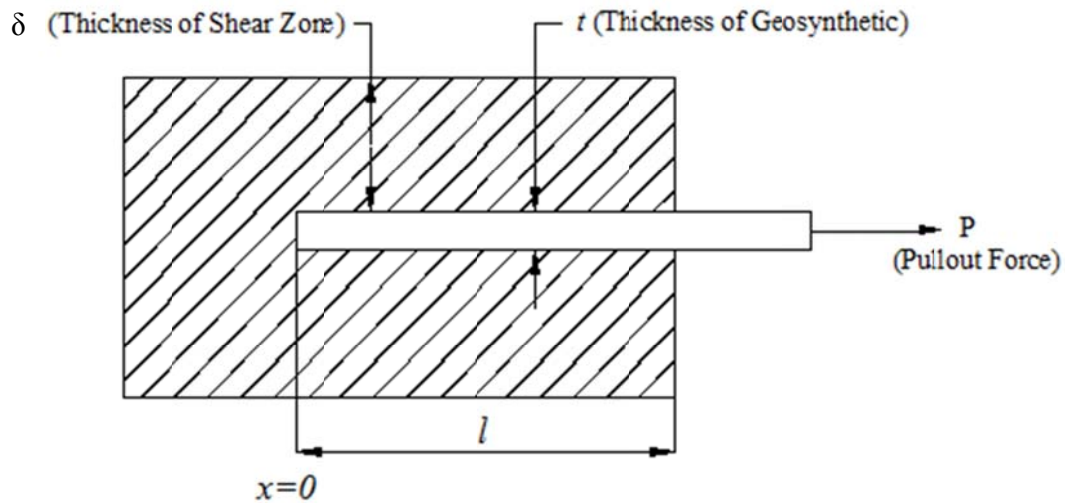


Figure 4.2. Schematic Plot of the Pullout Test

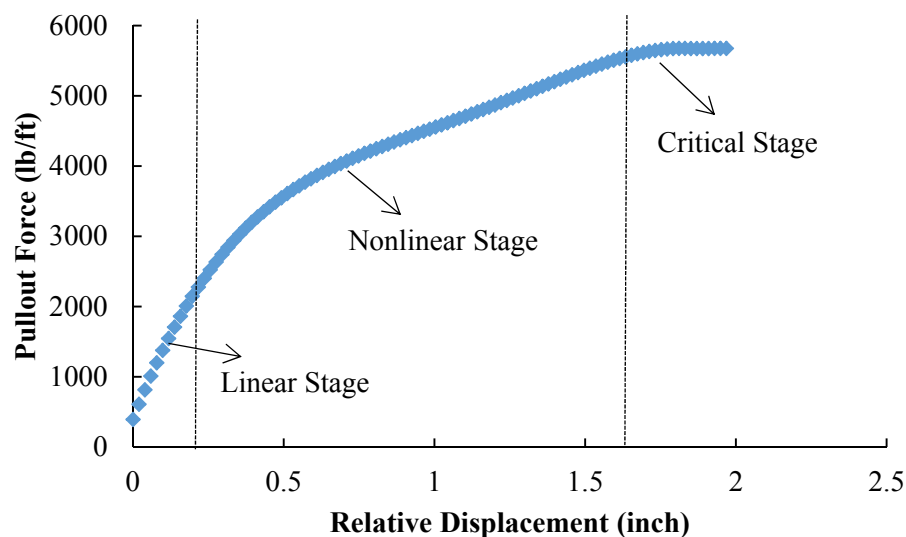


Figure 4.3. Pullout Force versus Geosynthetic Displacement in a Pullout Test

Laboratory Methodology for Quantifying Influence of Geosynthetics

The application of geosynthetics had the potential ability to reduce the thickness of the base courses, improve performance, and extend the service life of the pavement structure. Accurate and efficient laboratory characterizations of geosynthetic-reinforced materials were important for including geosynthetic products in pavement design. To develop a laboratory methodology compatible with the current Pavement ME Design software, it was necessary to quantify the characteristics of geosynthetic reinforcement in terms of the resilient properties and permanent deformation properties of the geosynthetic-reinforced UGMs.

Influence of Geosynthetics on Cross-Anisotropic Properties of UGMs

UGMs were found to exhibit cross-anisotropic resilient behavior (i.e., the properties in the vertical plane were different from the properties in the horizontal plane, while the properties in the horizontal plane were the same in all directions) (21, 50). The cross-anisotropic nature of the base course was demonstrated to be a major factor that influences pavement performance (51). Therefore, quantifying the influence of geosynthetics on the resilient properties of UGMs required the evaluation of the effect of geosynthetics on the cross-anisotropic properties of the base course.

One crushed granite material was used in the evaluations in this project. Three types of geogrids and one type of geotextile were selected to reinforce the UGMs. Appendix C elaborates on the material information, including the aggregate gradation, moisture-dry density relationship, and geosynthetic properties. The aggregate specimens were fabricated as 6-inch-diameter and 6-inch-high cylinders at the optimum moisture content using a modified compaction effort (ASTM D1557-12). The influence of the geosynthetic layer depended on its location within the base course. To evaluate this effect, the geosynthetic layer was placed in the middle of the specimen, one-quarter below the middle of the specimen, and at the bottom of the specimen, respectively (see Figure 4.4).

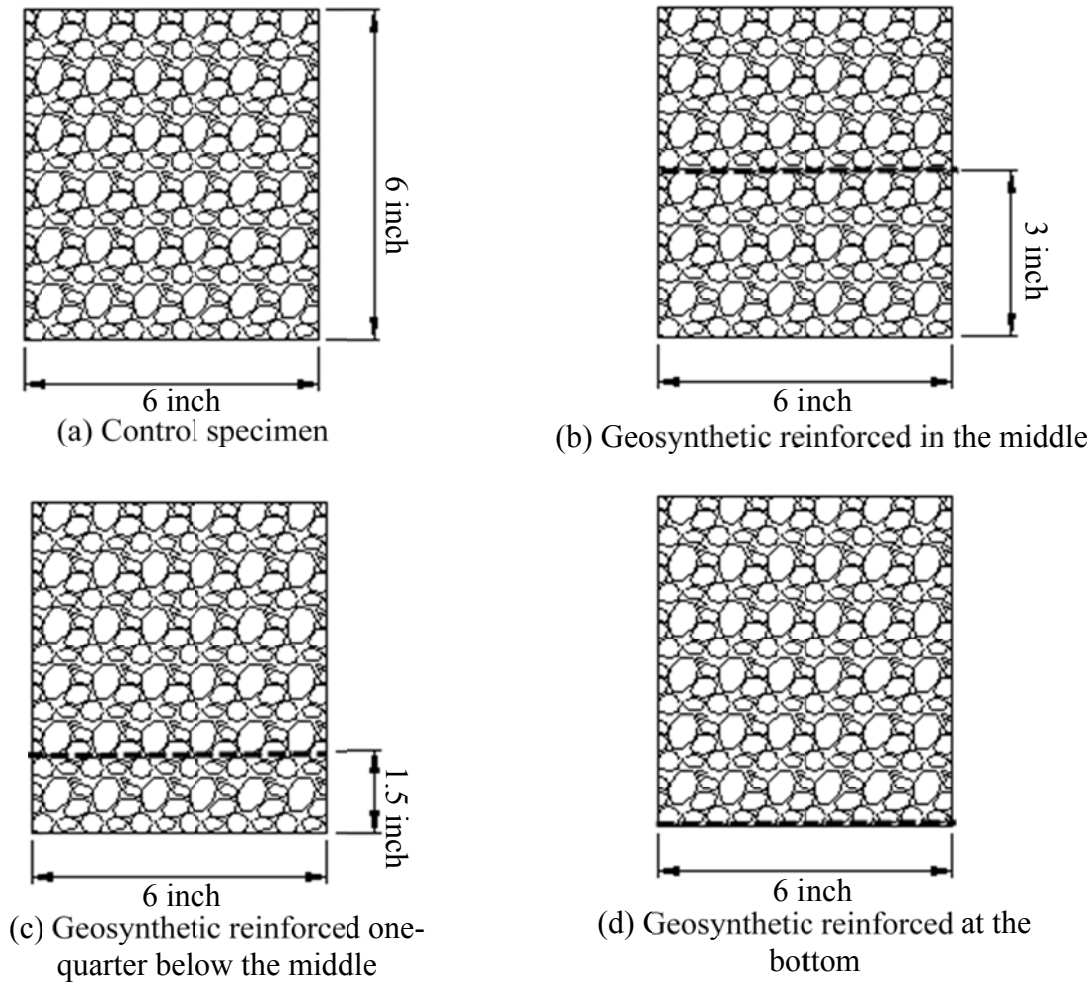


Figure 4.4. Schematic Plot of Aggregate Specimens with/without Geosynthetic

Triaxial tests were conducted on both the unreinforced aggregate specimens and geosynthetic-reinforced aggregate specimens using the rapid triaxial test (RaTT) cell with the Universal Testing Machine (see Figure 4.5). During each test, LVDTs measured the axial and radial deformations of the specimen. The test data were used to calculate the following five anisotropic properties of each specimen:

- Resilient modulus of the aggregate matrix in the radial direction, E_r .
- Resilient modulus of the aggregate matrix in the axial direction, E_z .
- Shear modulus of the aggregate matrix in the axial plane, G_{rz} .
- Poisson's ratio of the aggregate matrix in the axial plane, ν_{rz} .
- Poisson's ratio of the aggregate matrix in the radial plane, ν_{rr} .

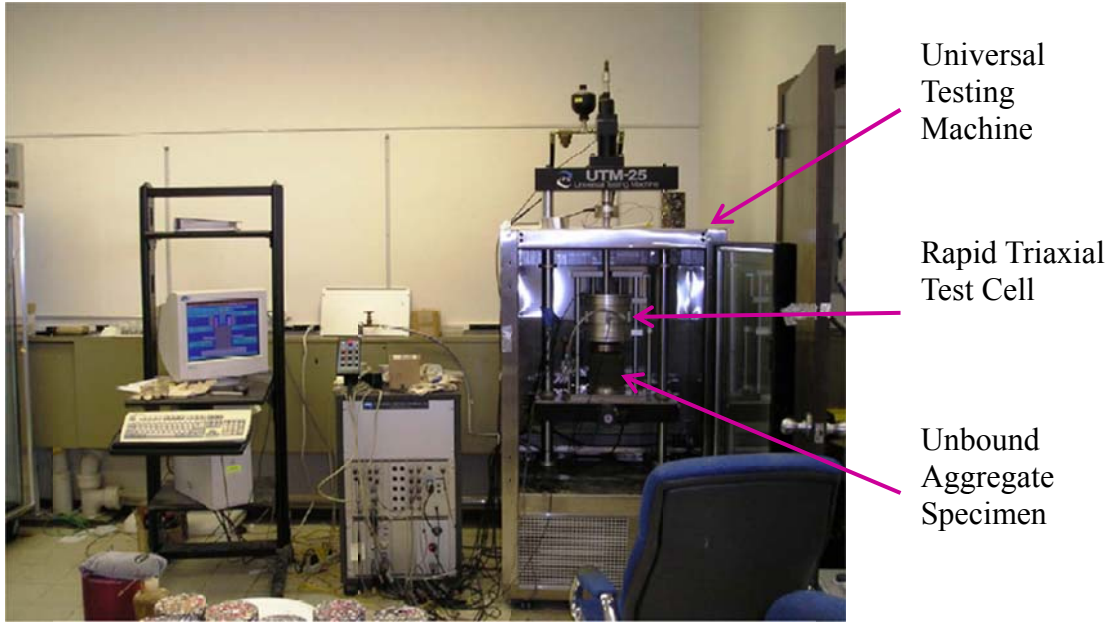


Figure 4.5. Configuration of Rapid Triaxial Test

The loading protocol used in the triaxial test was developed based on the constitutive equations of the cross-anisotropic aggregate specimens, as shown in Equation 4.4, which is rewritten in the incremental form in Equation 4.5 for the small strain protocol.

$$\begin{bmatrix} \frac{1}{E_r} & -\frac{\nu_{rz}}{E_r} & -\frac{\nu_{rr}}{E_r} \\ -\frac{\nu_{rz}}{E_r} & \frac{1}{E_z} & -\frac{\nu_{rz}}{E_r} \end{bmatrix} \begin{Bmatrix} \sigma_r \\ \sigma_z \\ \sigma_r \end{Bmatrix} = \begin{Bmatrix} \varepsilon_r \\ \varepsilon_z \end{Bmatrix} \quad (4.4)$$

$$\begin{bmatrix} \frac{1}{E_r} & -\frac{\nu_{rz}}{E_r} & -\frac{\nu_{rr}}{E_r} \\ -\frac{\nu_{rz}}{E_r} & \frac{1}{E_z} & -\frac{\nu_{rz}}{E_r} \end{bmatrix} \begin{Bmatrix} \Delta\sigma_r \\ \Delta\sigma_z \\ \Delta\sigma_r \end{Bmatrix} = \begin{Bmatrix} \Delta\varepsilon_r \\ \Delta\varepsilon_z \end{Bmatrix} \quad (4.5)$$

where σ_r is the stress in the radial direction; σ_z is the stress in the axial direction; ε_r is the strain in the radial direction; and ε_z is the strain in the axial direction.

According to the cross-anisotropic constitutive relation, three stress modes were used in the loading protocol, including the compression, shear, and extension modes (20). A total of 10 static stress states associated with corresponding dynamic stresses in the three stress modes were employed in the triaxial test, as shown in Table 4.1. In each stress state, every loading cycle of the dynamic stress consisted of 1.5 seconds of loading and 1.5 seconds of unloading. A stable resilient strain was achieved after 25 repetitions in the dynamic loading.

Table 4.1. Triaxial Test Protocol for Determining Cross-Anisotropic Properties

Stress State	Static Stress (psi)		Dynamic Stress (psi)					
			Compression		Shear		Extension	
	σ_z	σ_r	σ_z^c	σ_r^c	σ_z^s	σ_r^s	σ_z^e	σ_r^e
1	5.8	3.6	0.7	0	1.5	-0.7	-0.7	0.7
2	7.3	3.6	1.5	0	1.5	-0.7	-1.5	0.7
3	10.2	5.8	1.5	0	1.5	-0.7	-1.5	1.5
4	18.9	8.7	2.9	0	2.9	-1.5	-1.5	1.5
5	21.8	10.2	2.9	0	2.9	-1.5	-1.5	1.5
6	24.7	14.5	2.9	0	2.9	-1.5	-2.9	2.9
7	31.9	17.4	4.4	0	4.4	-2.2	-2.9	2.9
8	36.3	20.3	4.4	0	4.4	-2.2	-2.9	2.9
9	36.3	17.4	4.4	0	4.4	-2.2	-2.9	2.9
10	36.3	15.2	4.4	0	4.4	-2.2	-2.9	2.9

The measured axial and radial strains in every loading mode were analyzed using the system identification method to back-calculate the five cross-anisotropic properties— E_r , E_z , G_{rz} , ν_{rz} , and ν_{rr} —based on the constitutive model presented in Equations 4.4 and 4.5. The results of the calculated cross-anisotropic properties are presented in Appendix C. The cross-anisotropic properties of the control specimens were compared to those of the geosynthetic-reinforced specimens by calculating the normalized material property ratio of the control specimen to the reinforced specimen. Tables 4.2, 4.3, and 4.4 show examples of the comparison results of the aggregate specimens with a geosynthetic layer at the different locations. In these tables, the parameter AR represents the anisotropic ratio, which is the ratio of horizontal modulus to vertical modulus.

Table 4.2. Influence of Geosynthetic on Material Properties—Geosynthetic Location: Mid-Height

Stress State	Geosynthetic Type	$\frac{E_{r-\text{geosynthetic}}}{E_{r-\text{control}}}$ (%)	$\frac{E_{z-\text{geosynthetic}}}{E_{z-\text{control}}}$ (%)	$\frac{G_{rz-\text{geosynthetic}}}{G_{rz-\text{control}}}$ (%)	$\frac{AR_{\text{geosynthetic}}}{AR_{\text{control}}}$ (%)
1	Geogrid	123	120	127	103
	Geotextile	153	92	110	166
2	Geogrid	117	131	129	89
	Geotextile	157	109	107	144
3	Geogrid	126	120	113	105
	Geotextile	144	98	99	147
4	Geogrid	118	121	108	98
	Geotextile	131	100	110	131
5	Geogrid	124	116	116	107
	Geotextile	132	104	103	127
6	Geogrid	122	115	113	106
	Geotextile	127	99	104	128
7	Geogrid	112	111	114	101
	Geotextile	124	103	104	120
8	Geogrid	111	112	117	99
	Geotextile	124	95	99	131
9	Geogrid	121	109	122	111
	Geotextile	117	98	103	119
10	Geogrid	110	110	126	100
	Geotextile	122	102	103	120

**Table 4.3. Influence of Geosynthetic on Material Properties—Geosynthetic Location:
One-Quarter below the Middle**

Stress State	Geosynthetic Type	$\frac{E_{r-\text{geosynthetic}}}{E_{r-\text{control}}}$ (%)	$\frac{E_{z-\text{geosynthetic}}}{E_{z-\text{control}}}$ (%)	$\frac{G_{rz-\text{geosynthetic}}}{G_{rz-\text{control}}}$ (%)	$\frac{AR_{\text{geosynthetic}}}{AR_{\text{control}}}$ (%)
1	Geogrid	121	110	118	110
	Geotextile	132	85	109	155
2	Geogrid	109	122	120	89
	Geotextile	125	97	101	129
3	Geogrid	112	124	115	90
	Geotextile	118	102	109	115
4	Geogrid	119	120	114	99
	Geotextile	122	95	117	128
5	Geogrid	108	119	121	91
	Geotextile	124	99	104	125
6	Geogrid	111	115	106	96
	Geotextile	115	91	94	126
7	Geogrid	113	124	127	91
	Geotextile	106	103	108	103
8	Geogrid	119	108	117	110
	Geotextile	109	95	104	114
9	Geogrid	115	110	114	104
	Geotextile	107	89	108	120
10	Geogrid	109	108	111	101
	Geotextile	110	87	101	126

Table 4.4. Influence of Geosynthetic on Material Properties—Geosynthetic Location: Bottom

Stress State	Geosynthetic Type	$\frac{E_{r-\text{geosynthetic}}}{E_{r-\text{control}}}$ (%)	$\frac{E_{z-\text{geosynthetic}}}{E_{z-\text{control}}}$ (%)	$\frac{G_{rz-\text{geosynthetic}}}{G_{rz-\text{control}}}$ (%)	$\frac{AR_{\text{geosynthetic}}}{AR_{\text{control}}}$ (%)
1	Geogrid	110	109	105	101
	Geotextile	104	97	116	107
2	Geogrid	107	112	98	96
	Geotextile	104	93	112	112
3	Geogrid	109	110	89	99
	Geotextile	108	95	115	114
4	Geogrid	103	105	102	98
	Geotextile	94	102	106	93
5	Geogrid	103	98	105	105
	Geotextile	107	96	102	111
6	Geogrid	99	103	100	96
	Geotextile	116	103	103	113
7	Geogrid	95	97	109	98
	Geotextile	104	95	97	109
8	Geogrid	102	96	107	107
	Geotextile	106	93	97	114
9	Geogrid	105	95	109	110
	Geotextile	102	92	97	110
10	Geogrid	95	98	102	97
	Geotextile	97	93	98	104

As Tables 4.2 and 4.3 illustrate, the modulus ratios, $\frac{E_{r-\text{geosynthetic}}}{E_{r-\text{control}}}$, $\frac{E_{z-\text{geosynthetic}}}{E_{z-\text{control}}}$, and

$\frac{G_{rz-\text{geosynthetic}}}{G_{rz-\text{control}}}$, of the geogrid-reinforced specimens were larger than 100 percent in every stress

state, which showed that the geogrid increased E_r , E_z , and G_{rz} of the aggregate matrix specimen. However, a review of the existing studies conducted on the effects of geosynthetic reinforcement on UGMs revealed that the geogrid had only a slight influence on the vertical modulus E_z when the specimens were fabricated as 6-inch-diameter and 12-inch-high cylinders (14, 15). In this study, researchers found that the application of geogrids increased the vertical modulus of UGMs by approximately 10–20 percent when the specimens were fabricated as 6-inch-diameter and 6-inch-high cylinders. It was inferred that the benefits of geosynthetic reinforcement were significantly influenced by the dimension of the UGM specimen. This phenomenon also explained why geogrid-related increases in the resilient modulus of base courses were found in in-service reinforced pavement sections and full-scale pavement sections by back-calculating the modulus of the reinforced base course using falling weight deflectometer (FWD) data (53).

In contrast to the geogrid, the application of a geotextile slightly reduced the vertical modulus of the UGM specimen but significantly raised the horizontal modulus. As a result, the geotextile increased the anisotropic ratio of the specimen by 20~60 percent, which indicated that the geotextile made the specimen more isotropic (54).

Compared to Tables 4.2 and 4.3, the test results in Table 4.4 demonstrate that placing the geosynthetic at the bottom of the UGM specimen did not show any benefits related to an increase in the cross-anisotropic properties.

Influence of Geosynthetics on Permanent Deformation Properties of UGMs

Rutting or accumulated permanent deformation has been the primary distress for unbound aggregate bases in flexible pavements. It may also be a major factor in the faulting of jointed concrete pavements. Many studies on in-service or large-scale pavement sections found that the application of geogrids significantly reduced the rutting distress of the flexible pavements (8, 55, 56). In the laboratory, the permanent deformation behavior of UGMs with and without geosynthetics was characterized by the repeated load triaxial tests (see Figure 4.5). It was known that the permanent deformation behavior of UGMs was mainly affected by the stress level (57). The stress level also significantly influenced the effects of the geosynthetic on the reduction of the permanent strain of UGMs (25). In this study, the reduction of the permanent strain (RPS) was defined as:

$$RPS(\%) = \frac{\text{permanent strain without geosynthetic} - \text{permanent strain with geosynthetic}}{\text{permanent strain without geosynthetic}} \times 100\% \quad (4.6)$$

As shown in Figure 4.6, the RPS of the geogrid-reinforced UGM was only 13.5 percent when the deviatoric shear stress σ_d was 10 psi. This indicated that the effect of geogrid reinforcement was not significant when the deviatoric shear stress was small. When the deviatoric shear stress reached 19 to 28 psi, the RPS increased to a value between 28.4 and 36.5 percent, which indicated that the reduction of permanent deformation was greater at high deviatoric shear stress levels.

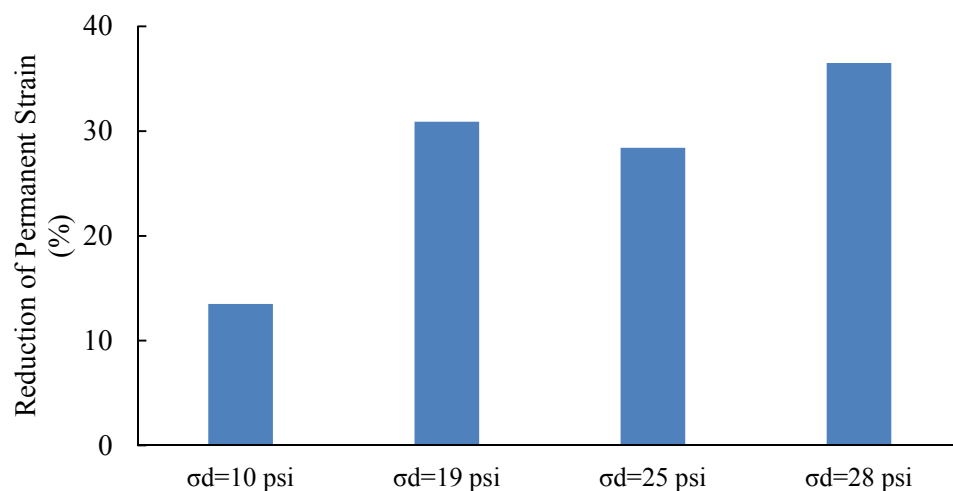


Figure 4.6. Effect of Stress Level on Reduction of Permanent Strain

In order to characterize the stress-dependent permanent deformation behavior of UGMs with and without geosynthetics, a new permanent deformation model was proposed, as shown in Equations 4.7 to 4.9. The proposed model was able to determine the accumulated permanent deformation at any specific stress state and number of load repetitions.

$$\varepsilon_p = \varepsilon_0 e^{-\left(\frac{\rho}{N}\right)^\beta} \left(\sqrt{J_2}\right)^m (\alpha I_1 + K)^n \quad (4.7)$$

$$\alpha = \frac{2 \sin \phi}{\sqrt{3}(3 - \sin \phi)} \quad (4.8)$$

$$K = \frac{c \cdot 6 \cos \phi}{\sqrt{3}(3 - \sin \phi)} \quad (4.9)$$

where J_2 is the second invariant of the deviatoric stress tensor; I_1 is the first invariant of the stress tensor; ε_0 , ρ , β , m , and n are model coefficients; and c and ϕ are cohesive shear strength and friction angle, respectively. In this model, the two terms, $\sqrt{J_2}$ and $\alpha I_1 + K$, were incorporated into the Tseng-Lytton model (58), which was used to reflect the influence of a stress state on the permanent deformation of the UGM.

Figure 4.7 illustrates the concept of the permanent deformation model. The Drucker-Prager plastic yield criterion (59), which was widely applied to rock, concrete, and other pressure-dependent materials, was the basis of this model. As shown in Figure 4.7, the black dot represents the current stress state in the $(I_1 - \sqrt{J_2})$ plane; the parameter $\sqrt{J_2}$ represents the softening effects of the deviatoric shear stress on the UGM, and a higher $\sqrt{J_2}$ yields a larger permanent deformation. Thus, the power coefficient m in Equation 4.7 was always a positive number. In addition, the term $(\alpha I_1 + K)$ indicated the hardening/strengthening effect of the hydrostatic stress on the UGM, which was highly affected by the material cohesion and internal friction angle. A higher $(\alpha I_1 + K)$ value resulted in a smaller plastic deformation; thus, the power coefficient n in Equation 4.7 was always a negative number.

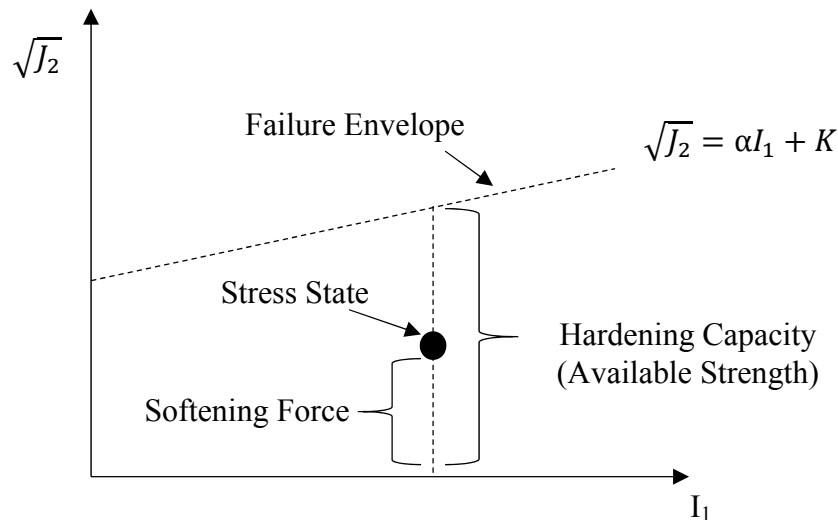


Figure 4.7. Illustration of the Stress-Related Terms in the Proposed Model

Table 4.5 shows the seven stress levels designed to determine the coefficients of the proposed rutting model. Stress States 1, 2, 3, and 4 employed the same I_1 but different J_2 , whereas Stress States 1, 5, 6, and 7 applied the same J_2 with various I_1 . This test protocol allowed for quantifying the influence of I_1 and J_2 on the permanent deformation behavior of UGMs with and without geosynthetics, individually. Note that Stress State 4 represented a hydrostatic state, which could also be used to verify that the plastic behavior of UGMs was marginal under the hydrostatic condition. Table 4.6 presents the other two stress states used to validate the determined coefficients in the permanent deformation model.

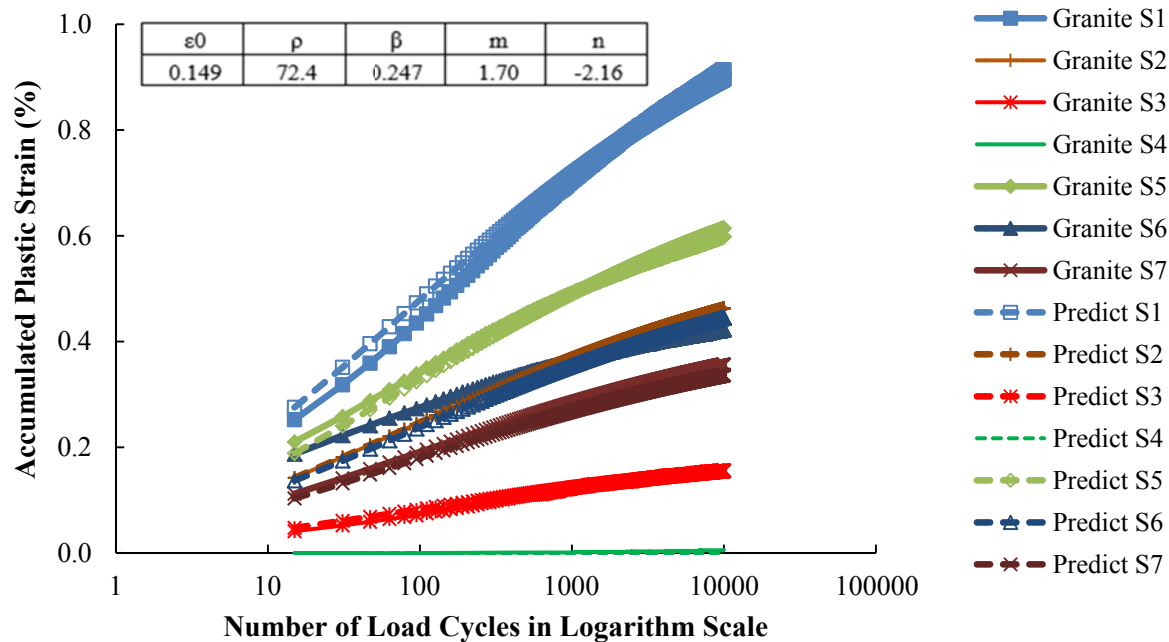
Table 4.5. Proposed Permanent Deformation Test Protocol—Proposed Stress Levels for Calibration of Model Coefficients

Stress State	Confining Pressure, σ_3 (psi)	Deviatoric Stress, σ_d (psi)	Bulk Stress, I_1 (psi)	Second Invariant of Shear Stress Tensor, J_2 (psi ²)
1	4.0	28.0	40.0	261.3
2	7.0	19.0	40.0	120.3
3	10.0	10.0	40.0	33.3
4	13.3	0	40.0	0
5	7.0	28.0	49.0	261.3
6	10.0	28.0	58.0	261.3
7	13.0	28.0	67.0	261.3

Table 4.6. Proposed Permanent Deformation Test Protocol—Proposed Stress Levels for Validation of Model Coefficients

Stress State	Confining Pressure, σ_3 (psi)	Deviatoric Stress, σ_d (psi)	Bulk Stress, I_1 (psi)	Second Invariant of Shear Stress Tensor, J_2 (psi ²)
8	5.0	25.0	40.0	208.3
9	15.0	28.0	73.0	261.3

The coefficients of the model were determined by fitting the measured permanent deformation curves using the solver function in the software Excel. Figure 4.8 presents the comparisons of laboratory-measured and model-predicted accumulated permanent strains at different stress levels for the tested specimens. Stress state is abbreviated as “S” in the legend of Figure 4.8. The recorded permanent strain started from the 15th load cycle. The root-mean-square errors (RMSEs) were calculated to evaluate the goodness of model fit at various stress states. In general, a smaller RMSE indicated a better goodness of fit (60). The determined RMSE at each stress level was relatively small, which indicated that the model accurately captured the trend of the measured permanent deformation curves.

**Figure 4.8. Comparison of Lab-Measured and Proposed Model-Predicted Permanent Deformation Curves**

Test data from Stress States 8 and 9 shown in Table 4.6 were used to validate the prediction accuracy of the rutting model. These stress states were not used in determining the model coefficients. Figure 4.9 compares the measured permanent deformation curves for Stress States 8 and 9 to the permanent deformation curves predicted by the model. The predictions of the model had small RMSE values, which showed that the model had a high accuracy. The model was able to quantify the effect of the stress level on the permanent deformation behavior

of the UGM with and without geosynthetics. Table 4.7 lists the model coefficients determined for the tested UGM with and without geosynthetics.

Table 4.7. Determination of Model Coefficients for the UGM with and without Geosynthetics

Material Type	Permanent Deformation Model Coefficients				
	ε_0	ρ	β	m	n
Unreinforced	0.149	72.4	0.247	1.70	-2.16
TX-Geogrid Reinforced	0.079	48.3	0.174	1.68	-2.10
BX-Geogrid Reinforced	0.082	31.2	0.182	1.64	-2.01
Geotextile Reinforced	0.112	60.4	0.261	1.76	-2.18

Note: TX = triangular geogrid; BX = rectangular geogrid.

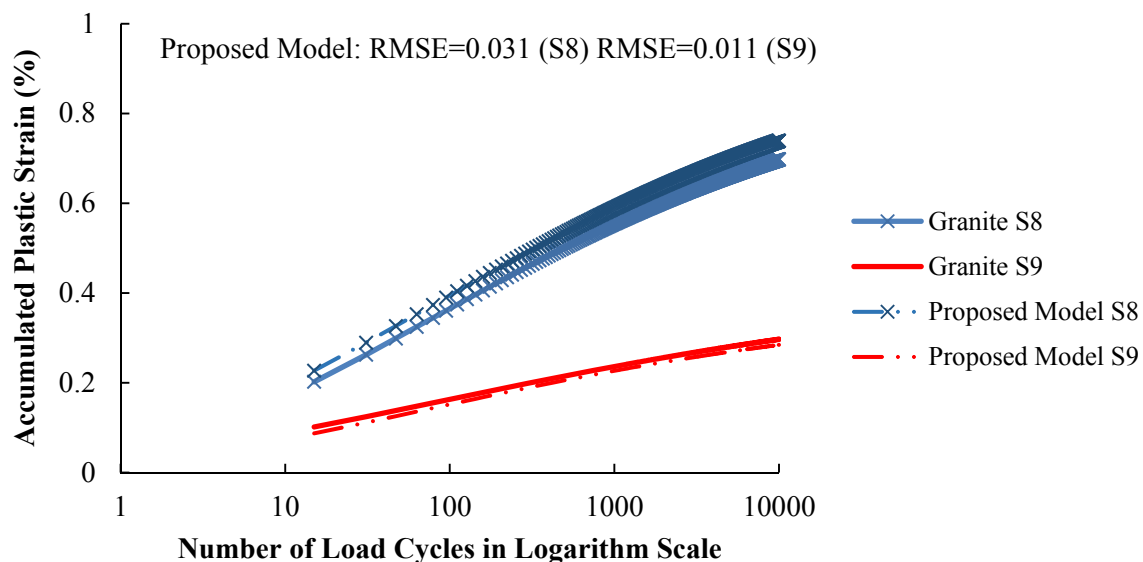


Figure 4.9. Validation of Prediction Accuracy of Proposed Permanent Deformation Model

This study also evaluated the effects of the type of geosynthetic and location of geosynthetic on the permanent deformation behavior of UGMs. Figure 4.10 shows an example of the influence of the type of geosynthetic on the permanent deformation of the UGM. In Figure 4.10, TX denotes a type of geogrid with triangular apertures, while BX denotes another type of geogrid with rectangular apertures. Figure 4.10 demonstrates that the geogrid with the triangular apertures reduced the permanent deformation of the UGM more than the geogrid with the rectangular apertures. The aperture openings for the triangular (23 mm) and rectangular (25 mm) geogrids were similar. This finding was consistent for all of the tested stress states (see Appendix C). Since the maximum size of aggregates in the UGMs was 19 mm, the apertures of the TX and BX geogrids were around 1.21 and 1.32 times the maximum aggregate size, respectively. Figure 4.11 presents an example of the effect of the location of the geosynthetic on

the permanent deformation behavior of the UGM. It was found that the geogrid placed in the middle of the UGM had a greater effect on the RPS than the geogrid placed at one-quarter below the middle of the UGM. The geogrid placed at the bottom did not show any improvement on the resistance to permanent deformation. Some studies reported that the pavement structure with the geogrid placed at the interface between the base layer and subgrade had less permanent deformation than the unreinforced pavement (27, 56). This finding was due to the fact that the application of the geogrid also reduced the vertical compressive stresses in the base layer and subgrade because of the membrane effect, thereby reducing the permanent deformation of the pavement structure.

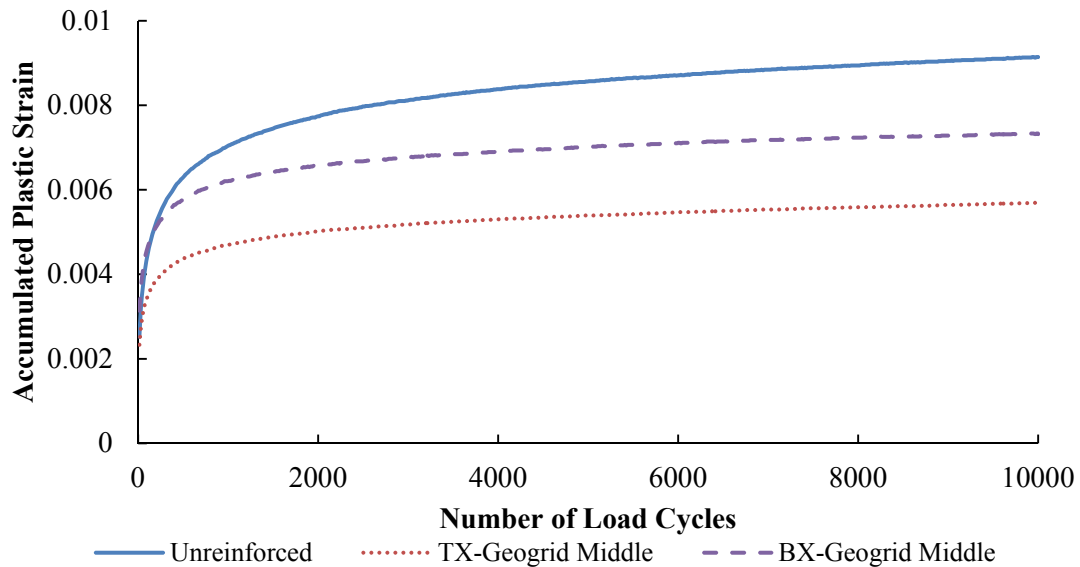


Figure 4.10. Effect of Type of Geosynthetic on Permanent Deformation of UGM

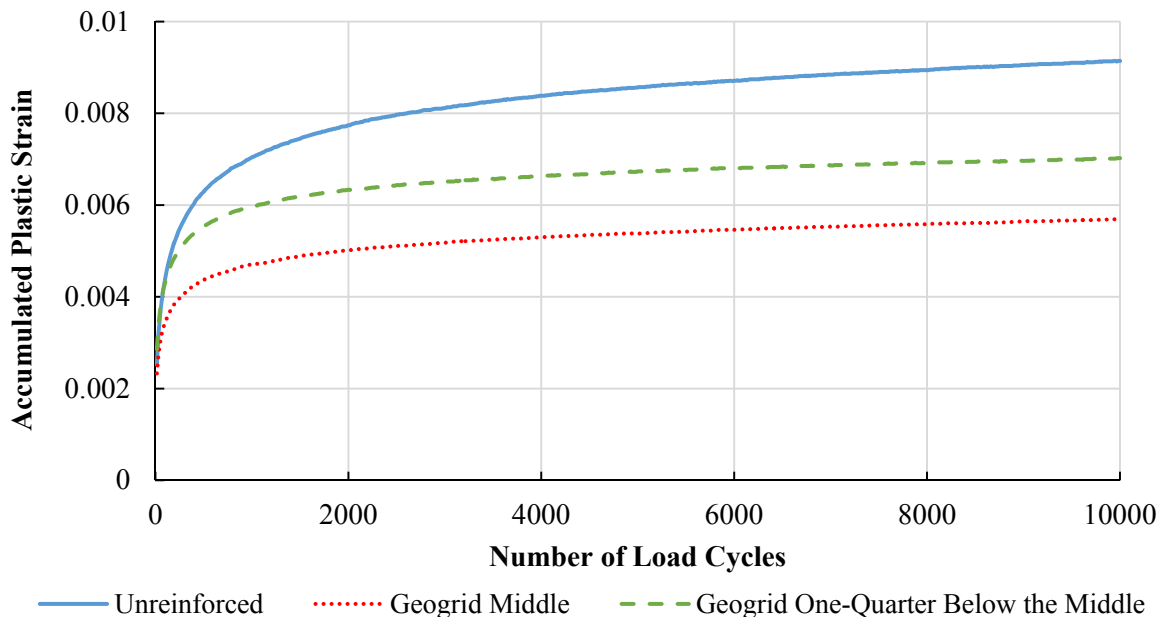


Figure 4.11. Effect of Location of Geosynthetic on Permanent Deformation of UGM

Analytical Model for Quantifying the Influence of Geosynthetics

The repeated load triaxial tests indicated that the placement of geosynthetics influenced the cross-anisotropic properties (i.e., the vertical and horizontal modulus) and the permanent deformation properties of the UGM. An analytical model was proposed to predict the vertical and horizontal moduli and the permanent deformation of the geosynthetic-reinforced UGM when it was subjected to a triaxial load. Figure 4.12a shows a schematic plot of a geosynthetic-reinforced UGM specimen in the triaxial load test. The geosynthetic-reinforced specimen was compressed in the axial direction and normally expanded in the lateral direction due to the plastic and resilient deformation. As shown in this figure, the lateral movement of the UGM was restrained by the geosynthetic. The shear stress was generated due to the relative lateral displacement between the geosynthetic and aggregate, which resulted in the stretch of the embedded geosynthetic. Note that the lateral movements of the aggregate and geosynthetic were identical. Figure 4.12b shows the difference in lateral movement between the geosynthetic and aggregate during the test. A coefficient α was employed to account for the difference in radial displacement between the geosynthetic and aggregate, as shown in Equation 4.10.

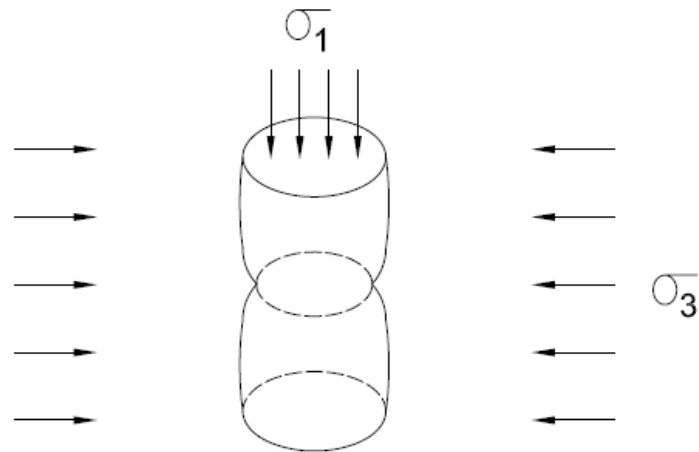
$$\alpha = \frac{\varepsilon_{rr}^a}{\varepsilon_{rr}^g} \quad (4.10)$$

where ε_{rr}^a is the aggregate radial tensile strain at the interface between the geosynthetic and aggregate; and ε_{rr}^g is the geogrid radial tensile strain. Note that the value of α was normally larger than 1, which meant that the aggregate had a larger lateral movement than the geosynthetic. The analytical solution to determine the coefficient α is shown in Equations 4.11 and 4.12 (61).

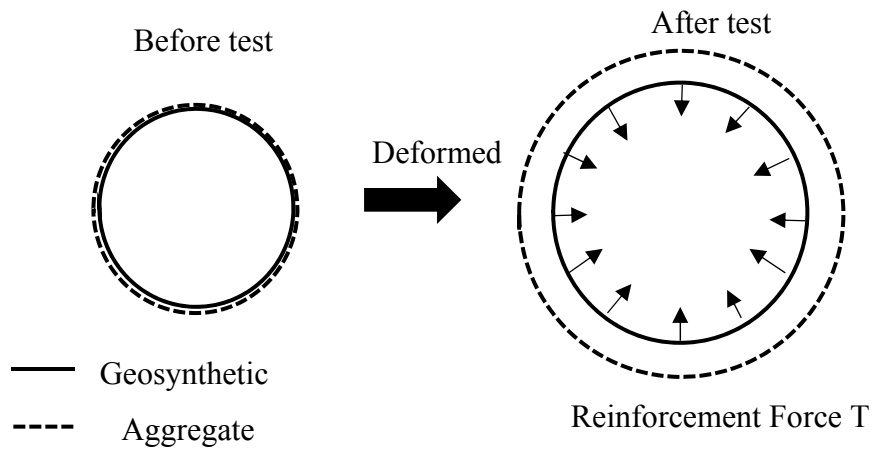
$$\beta \cdot J_0\left(\beta \frac{D}{2}\right) - \frac{2}{D} \cdot J_1\left(\beta \frac{D}{2}\right) = \sigma_3 \quad (4.11)$$

$$\beta = \left[\frac{2G_a(\alpha - 1)(1 - \nu_g^2)}{\delta M} \right]^{1/2} \quad (4.12)$$

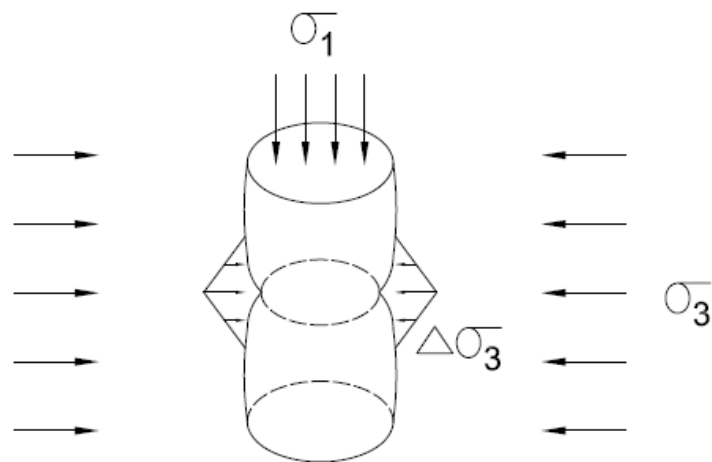
where $J_i(x)$ is the Bessel function of order i ; D is the diameter of the aggregate specimen (i.e., $D = 6$ inches); and G_a is the shear modulus of the aggregate. Equation 4.12 is an implicit equation for the coefficient α . The stretch of the geosynthetic generated a reinforcement force T to confine the UGM specimen through the aggregate particle interlock and interface friction (17). Figure 4.12c shows that the reinforcement force T was equivalent to a triangularly distributed additional confining stress, $\Delta\sigma_3$, which only acted on a 6-inch geosynthetic-reinforced influence zone (19). This distribution took into account the phenomenon that the influence of the geosynthetic reinforcement decreased with the distance between the aggregate and geosynthetic, and the geosynthetic reinforcement was negligible when the material was far away from the geosynthetic.



(a) Displacement Pattern of UGM Restraint by Geosynthetic



(b) Difference in Radial Movement of Geosynthetic and Aggregate



(c) Equivalence of Reinforcement Force to Additional Stress $\Delta\sigma_3$

Figure 4.12. Schematic Plot of Geosynthetic Reinforcement on UGM Specimen

Equation 4.13 was used to calculate the maximum equivalent additional stress $\Delta\sigma_{3\max}$.

$$\Delta\sigma_{3\max} = \frac{2M}{(1-\nu_g)\delta\alpha} \cdot \left[\frac{(\sigma_3 + \Delta\sigma_{3\max})}{E_H} - \frac{\nu_{13}\sigma_1}{E_V} - \frac{\nu_{33}(\sigma_3 + \Delta\sigma_{3\max})}{E_H} + 0.85\varepsilon_0 e^{-\left(\frac{\rho}{N}\right)^p} \left(\sqrt{J_2}\right)^m (\alpha I_1 + K)^n \right] \quad (4.13)$$

where σ_1 is the axial stress applied to the specimen; σ_3 is the initial confining pressure; ν_{13} is the Poisson's ratio to characterize the effect of axial stress on lateral strain; ν_{33} is the Poisson's ratio to characterize the effect of lateral stress on lateral strain; E_H is the horizontal modulus of the specimen; E_V is the vertical modulus of the specimen; ν_g is the Poisson's ratio of the geosynthetic; and δ is the thickness of the influence zone (i.e., $\delta = 6$ inches). In Equation 4.13, the only unknown parameter was the maximum additional confining stress, $\Delta\sigma_{3\max}$. An iteration method was utilized to solve for this parameter.

Since the thickness of the influence zone δ was a constant, the calculated maximum additional confining stress, $\Delta\sigma_{3\max}$, could be used to determine the distribution function of the equivalent additional confining stress, $\Delta\sigma_3(z)$, along the depth, z , of the specimen. The determined equivalent additional confining stress distribution, $\Delta\sigma_3(z)$, was then input into Equation 4.14 to calculate the modified vertical modulus of the base course, $E_{V-Modified}(z)$, in the influence zone.

$$E_{V-Modified}(z) = k_1 P_a \left[\frac{I_1 + \Delta\sigma_3(z)}{P_a} \right]^{k_2} \left(\frac{\tau_{oct}}{P_a} + 1 \right)^{k_3} \quad (4.14)$$

where I_1 is the first invariant of the stress tensor; τ_{oct} is the octahedral shear stress; P_a is the atmospheric pressure; and k_1 , k_2 , and k_3 are regression coefficients. The effective vertical modulus of the entire geosynthetic-reinforced UGM specimen, $E_{V-Effective}$, was calculated using Equation 4.15, which took into account the variation of the location of the geosynthetic in the UGM specimen.

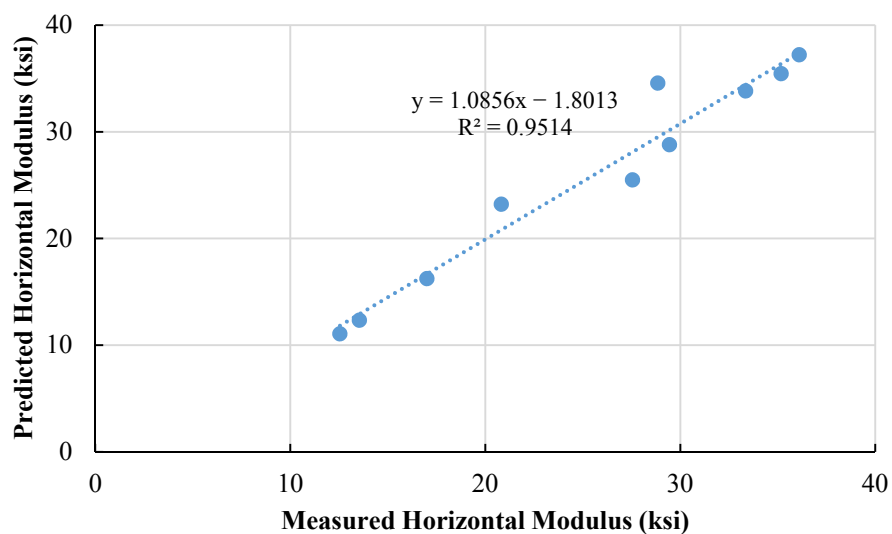
$$E_{V-Effective} = \begin{cases} \frac{E_{V-UGM} (h - \delta) + \int_0^{\delta} E_{V-Modified} (z) dz}{h} & \left(\frac{\delta}{2} < l < h - \frac{\delta}{2} \right) \\ \frac{E_{V-UGM} \left(h - \frac{\delta}{2} - l \right) + \int_0^{\frac{\delta}{2} + l} E_{V-Modified} (z) dz}{h} & \left(l < \frac{\delta}{2} \right) \\ \frac{E_{V-UGM} \left(h - \frac{\delta}{2} - l \right) + \int_0^{\frac{\delta}{2} + h - l} E_{V-Modified} (z) dz}{h} & \left(l > h - \frac{\delta}{2} \right) \end{cases} \quad (4.15)$$

where E_{V-UGM} is the vertical modulus of the unreinforced base course; h is the thickness of the base course; and l is the distance between the geosynthetic layer and the bottom of the base course. The effective horizontal modulus of the geosynthetic-reinforced UGM specimen, $E_{H-Effective}$, was calculated using Equation 4.16.

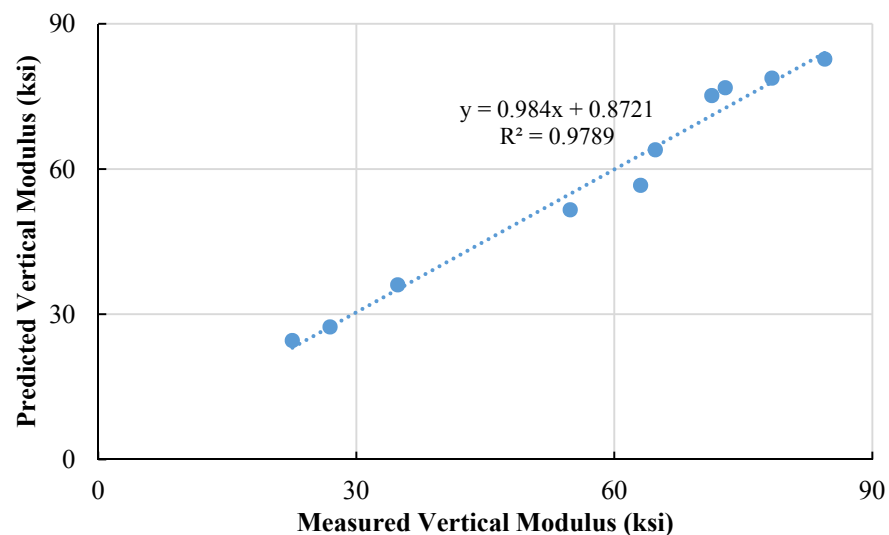
$$E_{H-Effective} = n \cdot E_{V-Effective} \quad (4.16)$$

where n is the ratio of the horizontal modulus to the vertical modulus, which is determined from the repeated load test. Similarly, inputting the determined equivalent additional confining stress distribution, $\Delta\sigma_3(z)$, into Equation 4.7 allowed for prediction of the permanent deformation of the geosynthetic-reinforced UGM at any given stress level. The detailed derivations of the above analytical models are presented in Appendix D.

Figure 4.13 shows the comparison of the resilient moduli of geogrid-reinforced UGMs predicted by the proposed analytical models and those measured from the laboratory tests. The horizontal and vertical resilient moduli predicted by the analytical models matched the measured values with R-squared values of 0.96 and 0.98, respectively. This finding indicated that the proposed analytical models were able to accurately predict both the horizontal and vertical moduli of geogrid-reinforced UGMs.



(a) Predicted Horizontal Moduli vs. Measured Horizontal Moduli



(b) Predicted Vertical Moduli vs. Measured Vertical Moduli

Figure 4.13. Comparison of Resilient Moduli Predicted by Analytical Models with Measured Values

LST Test on Pavement Layers with Geosynthetics

A comprehensive experimental program, complemented with a detailed numerical model, was designed to capture the mechanism of the interaction between the geosynthetic and the surrounding unbound materials. The measured data obtained from the LST experimental program were used to validate and improve the numerical model.

Experimental Plan and Setup

Test Matrix Experimental Setup

One of the largest tank containers in the United States was used to execute the experimental program. This modular cylindrical container, which measured 8 ft in diameter, was divided into three segments; each segment was 3 ft high. Two of the three segments, measuring 6 ft high, along with the base plate were assembled in the laboratory. A 12-inch-diameter actual FWD loading plate (see Figure 4.14) was used to apply the load on the surface of the pavement layer to better simulate actual tire loading conditions. The ratio of the diameter of the LST to the diameter of the loading plate was deemed sufficient to minimize the interference from the LST boundaries.

Since the experimental program would include dynamic loading applied onto a pavement structure prepared in a steel container, there was concern about introducing measurement errors in the data collected from the sensors due to reflection of the waves at the boundary. A common technique to minimize such error was to install wave-absorbing material on the inside walls of the steel tank container. A field experiment was performed by the research team to determine the best commercially available wave-absorbing material. The team tested four damping materials (insulation foam, cushion pad, fiberglass, and bubble wrap). It was concluded that fiberglass provided the best absorbing mechanism, so it was selected for this project. The kraft-faced fiberglass insulation was installed in one layer with the kraft side facing inside. After installing the fiberglass material, researchers placed a plastic sheet on the inside of the LST (see Figure 4.15). This sheet provided a frictionless boundary similar to what is expected in the field as well as the numerical model.

A hydraulic ram capable of delivering 60,000 lb was used to apply the dynamic and the static loads. The ram was modified by attaching a Moog-252 spool valve that could be electronically controlled to provide just the required flow to the ram to achieve the target dynamic load at the target frequency. The control mechanism also allowed researchers to apply the static load in a controlled manner. The system was connected to a hydraulic pump along with accumulators to ensure adequate flow of hydraulic fluid necessary for the repeated cycles of loading. The ram was mounted onto a stiff beam connected between two vertical columns comprising the reaction frame.

A computer running a real-time operating system connected to a National Instrument (NI) four-slot SCXI-1001 chassis populated with two NI SCXI-1320 conditioners was used to control the servo valve. A 20,000-lb interface pancake-type load cell along with a Unimeasure string pot were attached to the ram and electronically connected to the controller. The controller design was a proportional-integral-derivative controller. This control loop feedback mechanism was used to control the ram in either force or displacement control mode. Careful calibration of the gain was essential to ensure the proper operation of the entire loading system. Figure 4.16 shows the completed test setup for a selected flexible pavement experiment.



Figure 4.14. FWD Loading Plate Used in the LST Experiments: (a) Top View; (b) Bottom View



Figure 4.15. Plastic Sheet Covering the Wave-Absorbing Material in the LST



Figure 4.16. Completed Large-Scale Test Setup for Flexible Pavement Experiment

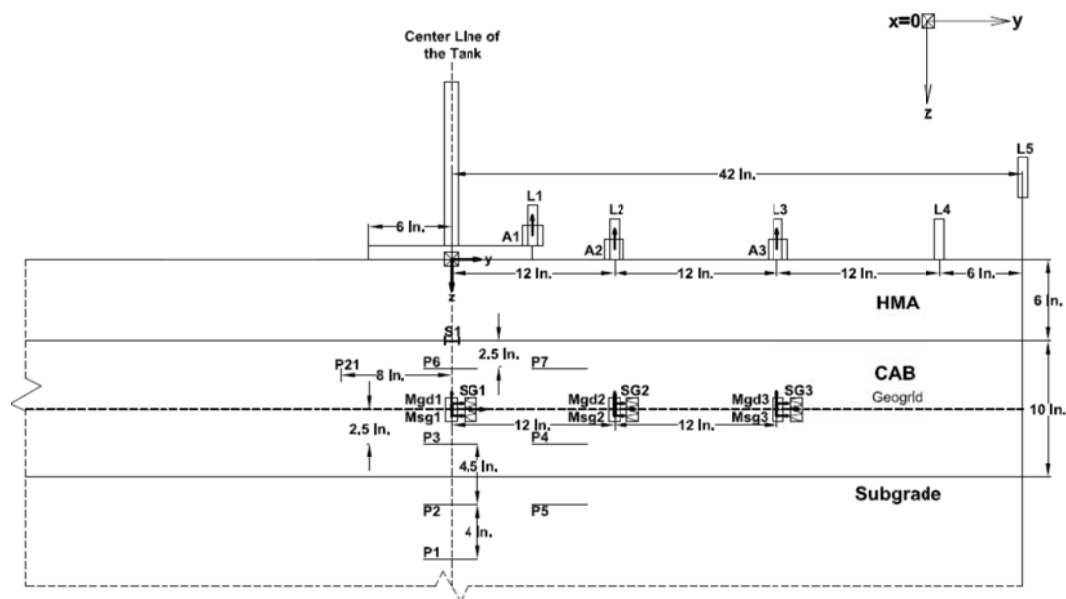
Sensors and Instrumentation Plans

Various sensor types were used in this project to capture the geosynthetic mechanism and pavement response to loading. Non-vibrating-wire Geokon Total Earth Pressure Cells, Model 3500, were used to capture the total vertical and horizontal stresses at different locations within the pavement. These cells were 4 inches in diameter with capacities that ranged between 250 and 600 kPa. Two Kyowa 1-inch load cells were also used to measure the total horizontal stresses over a small area. Four Novotechnik TR-100 LVDTs with a range from 0 to 4 inches were used to capture surface deflection of the pavement layer. During the flexible pavement experiments, one LVDT was used to measure the top deflection of the base material through a hole, which was drilled through the asphalt layer, to provide data that could be used for assessing the deformation of the base layer only. Texas Measurements strain gauges for asphalt (PMFLS-60-50) and concrete (PML-60) were used to capture the response of the pavement under dynamic and static loading as well as to provide a comprehensive picture of the pavement responses (stress, strain, and deformation) when combined with surface deformation data. Texas Measurements YMFLA-2 (2-mm) strain gauges were used to capture the strain in the geogrid and the geotextile. Micro-electro-mechanical systems-based accelerometers capable of measuring acceleration up to 5 g in three directions were used to capture the possible interface slippage at the interface of the geosynthetic and surrounding unbound materials as well as the deformation shape of the geosynthetic material. This measurement was achieved by calibrating the surface deflection recorded from the LVDT with back-calculated deflection using acceleration data recorded from the surface accelerometers. The calibrated scheme was then used to back-calculate the deflection of the geosynthetic material as well as the surrounding unbound materials at different locations. In each experiment, an extensive network of sensors was installed at different locations in the LST for flexible and rigid pavements. Table 4.8 describes the general instrumentation plan used

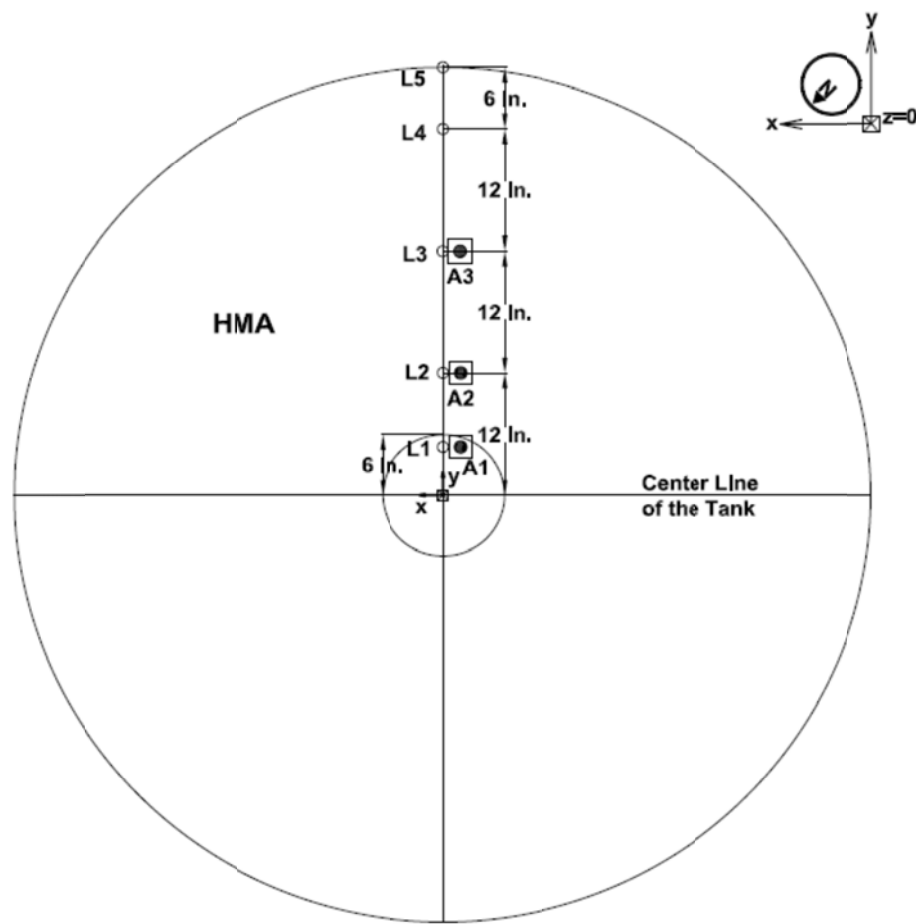
in the various experiments. Figure 4.17 and Figure 4.18 illustrate a typically instrumented experiment for a reinforced flexible and rigid pavement, respectively. Specific instrumentation diagrams for each of the completed experiments are provided in detail in Appendices E and H.

Table 4.8. General Description of the Instrumentation Plan in LST

Instrumentation	Location	Type of Measurements	Installation Techniques
Strain Gauges for Geosynthetics	Geogrid	Strain distribution	All surfaces were prepared before attaching the strain gauges. For geogrids: the strain gauges were glued on the ribs using epoxy adhesive. For geotextiles: the strain gauges were attached using the silicone adhesive impregnation technique, which involved impregnating the geosynthetic filaments with a thin film of elastic silicon adhesive before attaching the strain gauge.
	Geotextile		
Total Earth Pressure Cells	Above and below geosynthetic, at the centerline and at the edge of the loading plate	Vertical and horizontal stress distributions	Earth pressure cells (EPCs) were installed with the flat surfaces horizontal to measure vertical stresses. These EPCs rested on a thin layer of fine sand to ensure uniform pressure distribution.
Accelerometers	Geosynthetic	Dynamic deformation of geosynthetic	Accelerometers were embedded in place.
	Interface between geosynthetic and base or subgrade	Slip at the interface	
Strain Gauges for AC or PCC	Bottom of AC or PCC	Tensile strain	Strain gauge was placed on top of the base prior to the placement and compaction of the AC layer or PCC.
LVDTs	Pavement surface	Pavement surface deflections	Linear position sensors were attached to a stationary beam, acting as a reference frame. The moving tip rested on the top of the pavement layer.



(a)



(b)

Figure 4.17. Instrumentation Plan for Flexible Pavement Experiment 4: (a) Profile View at X = 0 inch; (b) Plan View at Z = 0 inch

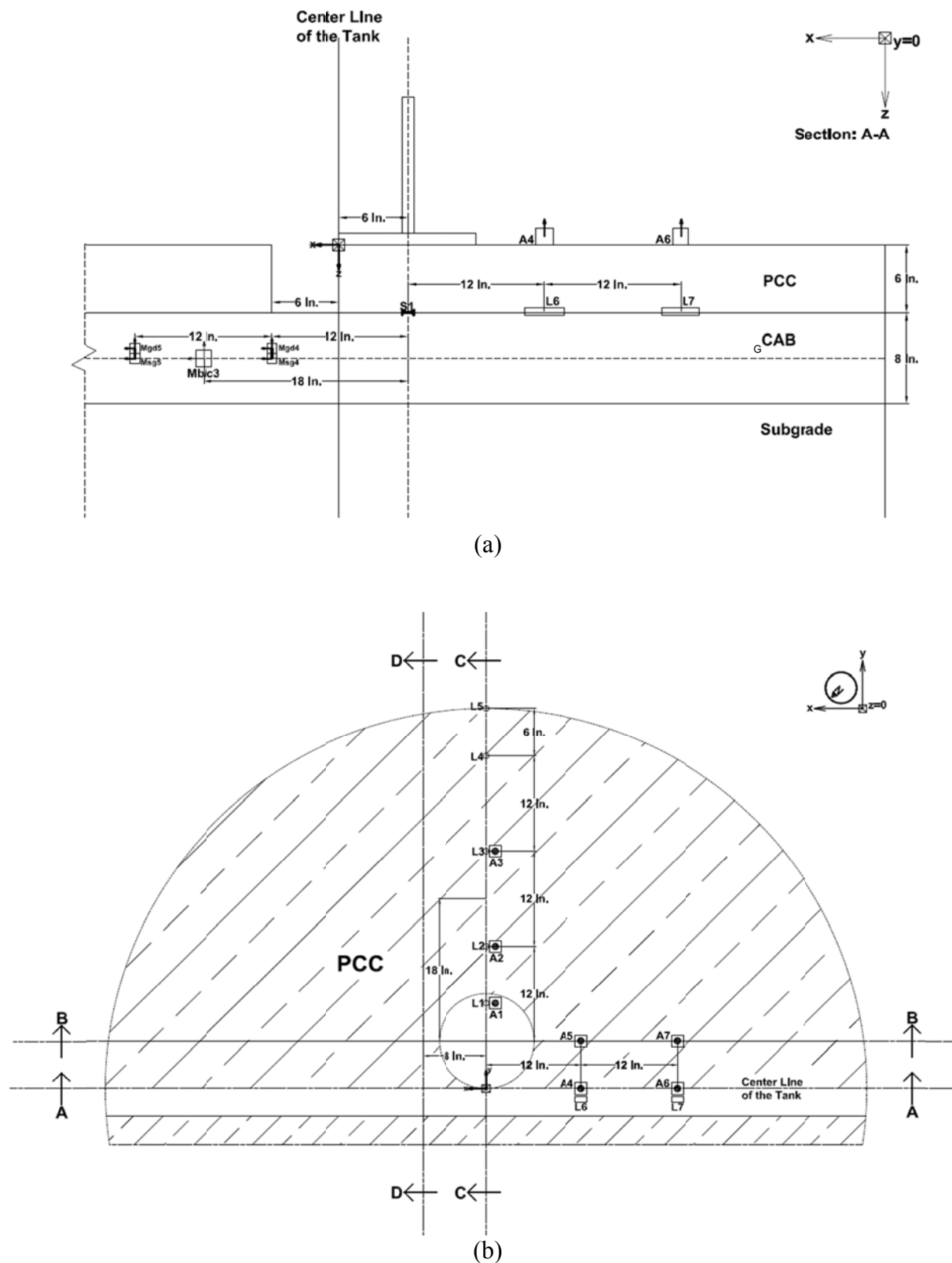


Figure 4.18. Instrumentation Plan for Rigid Pavement Experiment 9: (a) Profile View at Y = 0 inch; (b) Plan View at Z = 0 inch

The instrumentation for the subgrade layer consisted of two 4-inch total earth pressure cells placed at a depth of 6 inches and 2 inches below the subgrade surface. This placement was done after compacting the subgrade to the finish grade and then using a pickaxe and a shovel to excavate around the center of the tank to the desired depth. The pressure cells were then placed carefully on a leveled surface of a thin layer of compacted fine material. Next, the subgrade material was placed carefully on top of the cell and compacted by hand using a steel tamper plate. Figure 4.19 shows the placement of the pressure cell in the subgrade.



Figure 4.19. Placement of the 4-inch Earth Pressure Cell in the Subgrade

The instrumentation in the CAB was the most extensive and therefore required the most attention. Five earth pressure cells, three 4-inch cells, two 1-inch cells, and four accelerometers were placed in the CAB. Due to the sensitivity of the instrumentation, the CAB could not be compacted using the mechanical rammer. Therefore, this stage was accomplished by placing and mechanically compacting the CAB, and then excavating around the locations of placement to the desired depth and placing the earth pressure cells. To locate the direct center of the tank, three strings were tied along the diameter of the tank, each oriented differently, and the intersection point of the strings was used as the direct center. A bed of fine aggregates was placed around the pressure cells to protect against sharp, coarse rocks puncturing the cells during testing. Once all the various instrumentation sensors were placed, the excavated base material was then mixed with appropriate water content and recompact manually using a steel tamper plate.

To measure the differential displacement between the base and the geosynthetic, three accelerometers were embedded in the subgrade (for 6-inch aggregate base) or in the aggregate base (for 8- and 10-inch aggregate base), while three other accelerometers were placed on top of the geosynthetic immediately above the three subgrade/base accelerometers. Absolute displacements of the subgrade/base and the geosynthetic were assessed by integrating the output acceleration. Differential displacements were assessed by subtracting the absolute displacements.

In addition to the accelerometers, strain gauges were placed directly on the ribs of the geogrid, or the fabric of the geotextile, next to the accelerometers in the X and Y directions to measure strain induced in the reinforcement from surface loading. The installation was done after the geosynthetic was in place to assure accurate placement. All gauges were installed according to specifications. For the geogrid, once the locations were selected, the ribs were smoothed using an ultra-fine sandpaper and then cleaned with fast-evaporating acetone. Using the Tokyo Sokki-cyanoacrylate adhesive, the strain gauges were attached and allowed to dry. For the geotextile, once the locations were identified, the area was first cleaned with fast-evaporating acetone before applying Liquid Nail to the geotextile and immediately securing the gauge in place. Once the

glue dried, the gauges were covered with rubber cement to protect from damage that might occur while placing the CAB. The locations of the strain gauges were decided based on consistency. One gauge was placed directly on each rib adjacent to the accelerometer in the local X and Y directions.

The instrumentation used in the asphalt concrete consisted of one strain gauge and two temperature sensors used for monitoring temperature during placement. A small amount of heated asphalt binder was placed over the area of application and allowed to cool for 20 minutes. After cooling, a small amount of a fine-graded asphalt mix was placed over the asphalt binder. This was used to ensure (a) a proper support for the strain gauge, and (b) a good bond between the strain gauge and the asphalt layer. Once the strain gauge was placed, a steel plate was placed on top, and a static pressure was used to compact the gauge into the asphalt patch. The asphalt mixture was then placed directly over the strain gauge. Figure 4.20 shows the installed asphalt strain gauge on top of the compacted CAB layer. A similar practice was followed for the installation of the PCC strain gauge to ensure that the gauge was completely encapsulated in concrete and complete strain transfer was occurring from the PCC slab. A fresh amount of concrete was placed on top of the CAB, on which the embedded concrete strain gauge was placed. Care was taken to secure the strain gauge in the desired location and orientation along with the attached lead wire cable before the concrete was poured. A small patch of the concrete material was poured carefully over the gauge before pouring the entire slab.



Figure 4.20. (a) In-Place Asphalt Strain Gauge; (b) Final In-Place Asphalt Strain Gauge with Temperature Sensor

Data Acquisition

An NI data acquisition system comprised of two 12-slot SCXI-1001 chassis populated with 20 NI SCXI-1320 conditioners Hz was used to acquire the sensor data. This 80-data-channel system was capable of sampling data at frequencies that ranged from 1 to 3000 Hz. Such a system was applicable for acquiring data from a wide range of sensors, including strain gauges, displacement transducers, load cells, pressure cells, and accelerometers. Data from experiments involving dynamic loading were acquired at 1024 Hz to accommodate the requirements for the double-integration algorithm for assessing the displacements and slippage (refer to Appendix I for further details). Data from experiments with static loading were acquired at 32 Hz. Once acquired, the data were stored locally on the computer hard drive in CSV format, which could be imported and manipulated by most software packages for data analysis.

Data Analysis Methodologies

The laboratory testing program for flexible and rigid pavements included a series of instrumentation that included accelerometers, LVDTs, earth pressure cells, and strain gauges. The instrumentation program was designed to assess several aspects of the influence of the base reinforcement on pavement responses under a variety of realistic pavement loading conditions. A database of pertinent pavement responses with and without reinforcement collected under dynamic and static pavement loading conditions was assembled. The pavement response database was used to assess the validity and applicability of the finite element numerical modeling of reinforced pavement structures. In particular, the instrumentation plan focused on the mechanisms associated with the interaction between the geosynthetic and the unbound materials including (a) assessment of the deflection profile of the geosynthetic; (b) investigation of the slippage at the interface between the unbound material and the geosynthetic; (c) stress transfer across the geosynthetic; and (d) load-induced strains in the geosynthetic. While the last two aspects could be addressed based on direct measurements from pressure cells (vertical and horizontal) and strain gauges, the first two aspects needed to be evaluated based on the deflections at many interior locations within the pavement. The slippage investigation at the interface required measurements of the deflections in the geosynthetic and in the adjacent unbound material to examine the relative movements between the two.

As mentioned earlier, the role of the geosynthetic affecting the load transfer across the geosynthetic itself was generally referred to as shell/membrane action. The deformed shape of the geogrid or geotextile located within the unbound pavement layers during the application of the pulse loading was important to evaluate the shell/membrane action of the reinforced layer. The dynamic (instantaneous) deformation of the geosynthetic could be related to the change in vertical stress that could occur across the reinforced CAB layer. Accordingly, high-gain accelerometers were used, with the recording measurements being twice integrated to get the displacement under dynamic loading. It was important to find the best methodology for the double integration of accelerometer readings to get the displacement. Subsequently, these displacements obtained from the integration could be used to assess shell/membrane action of the embedded geogrid or geotextile. The detailed data analysis methodologies are presented in Appendix I.

Flexible Pavement

The database of pavement responses generated from the LST testing was substantial and covered many aspects of the geosynthetic-unbound material interaction. Therefore, a recap of pertinent key factors that had significant influence on the measured data is provided below. Such information was very useful when navigating through the collected data and during the interpretation process of the various results.

- Experiments 1, 3, and 5 included a 6-inch CAB and represented, respectively, the testing for the control (i.e., no base reinforcement), geogrid-reinforced base, and geotextile-reinforced base. The geosynthetic was located in both Experiments 3 and 5 at the bottom of the CAB layer (i.e., 12 inches below the pavement surface).
- Experiments 2, 4, and 6 included a 10-inch CAB and represented, respectively, the testing for the control (i.e., no base reinforcement), geogrid-reinforced base, and

- geotextile-reinforced base. The geosynthetic was located in both Experiments 4 and 6 at the middle of the CAB layer (i.e., 11 inches below the pavement surface).
- The stiffness properties of the geogrid and geotextile differed depending on the direction of testing. Overall, at the strain levels expected under the LST loading conditions, the average stiffness on a per-foot basis of the geotextile was considerably larger (as much as 80 percent) than the geogrid.
 - Unlike the geogrid, the geotextile used in the experiments was a woven continuous carpet-like roll and acted as a separator between the unbound materials present above and below the reinforcement. Geogrid reinforcement, on the other hand, had a cell-like configuration, which provided a better interlocking of the unbound materials across the interface.
 - The presentation of the results in this section included the earth pressure cell data measured above and below the geosynthetic. The locations of the earth pressure cells were not at the same equal distance above and below the geosynthetic for the 6- and 10-inch aggregates bases.
 - Unlike earth pressure cells, measurements made by the accelerometers, strain gauges, and LVDTs could be considered as 1-point measurements. The majority of the pressure cells used in the LST experiments were 4 inches in diameter (a couple of the pressure cells were 1 inch in diameter and were mainly used for measurements of the horizontal pressure), and the fluid present within the flexible diaphragm gave the average induced pressure within the entire surface area of the cell.
 - Studies showed that in many typical pavement configurations without reinforcements, there could be a reduction in horizontal stresses in the CAB, especially near the centerline of the loaded area and directly below the AC surface layer. This phenomenon was governed by the thickness and stiffness of the various pavement layers.
 - The earth pressure cells used to measure horizontal stresses in the CAB were located laterally away from the axis of loading and at 8 inches from the centerline (under the edge of the plate) in all experimental tests.
 - While an AC layer of 6 inches was targeted for all the LST experiments, measurements from the post-test core specimens revealed variations in the in-situ AC layer thickness within an individual experiment and among the various experiments. Such variation in the AC layer thickness could have an influence on the various measured pavement responses and should be kept in mind when interpreting the LST test results.

Stress Distributions Across the Reinforcements

First, the collected earth pressure cell data were reviewed. Figure 4.21 presents an abridged version of the LST configuration showing only the earth pressure cells in the CAB for the pavement with the thin (i.e., 6-inch) CAB (Experiments 1, 3, and 5). The locations of the earth pressure cells are provided with modified identifications to facilitate the interpretation of the results. For example, the subscripts “Center” and “Edge” refer to the pressure cells on the centerline and under the edge (8 inches from the centerline) of the loading plate, respectively.

The superscripts “Above” and “Below” refer to the pressure cells above and below the geosynthetic. The horizontal stress in the CAB under the edge of the loading plate is referred to as $\sigma_{B-Horiz}$.

A review of the assembled results with a focus on assessing the influence of the reinforcement indicated many noteworthy observations. A summary of the important results and interpretations are presented below.

Figure 4.22a and Figure 4.22b show the load-induced vertical stress measurements along the centerline of the load for above and below the reinforcement location, respectively. Similarly, Figure 4.23a and Figure 4.23b show the vertical stress measurements along the edge of the load for above and below the reinforcement location, respectively. Figure 4.22c shows the difference in the vertical stresses above and below the reinforcement location at the centerline and edge of the loading plate, respectively. As expected, the vertical stresses above and below the reinforcement location consistently increased with the increase in the applied load level. The form of the relationship between the vertical stress and the load level could be used to investigate the presence and extent of the nonlinearity in unbound materials. This check for the possible presence of nonlinearity could be readily undertaken with all datasets generated in the LST testing program.

At the centerline of the load, lower vertical stresses (above and below the reinforcement location) were observed in the experimental tests with reinforcements when compared to the control experiment. These reductions in vertical stresses due to CAB reinforcement were slightly higher with the geogrid reinforcement. On the other hand, except for the vertical stress above the geogrid, higher vertical stresses (above and below the reinforcement location) were observed at the edge of the loading plate in the experimental tests with reinforcements when compared to the control experiment.

At the centerline of the load, the vertical stresses above the reinforcement location (i.e., in the middle of the 6-inch CAB) were consistently found to be lower than those measured below the reinforcement location (i.e., 2 inches below the subgrade surface), even though the pressure cells located above were closer to the pavement surface. This observation may be attributed to a substantial reduction in the compressive horizontal stresses due to bending of the pavement layers under loading and, accordingly, a reduction in the CAB stiffness at this location. The difference in the vertical stresses at the centerline of the load and across the geosynthetic location was found to be the highest in the case of no reinforcement (i.e., control experiment). The lowest difference was observed when the geotextile was used, and it was more pronounced at the higher load level of 16 kip (see Figure 4.23c).

Unlike the observations at the centerline of the load, the vertical stresses along the edge of the loading plate and above the reinforcement location were found to be higher than those measured below the reinforcement location (i.e., in the subgrade layer) for both the control and geotextile-reinforced base. A different behavior was observed with the geogrid when compared to the geotextile-reinforced base, where the vertical stresses at the edge of the loading plate were slightly lower below the geogrid when compared to the vertical stresses above it. The difference in the vertical stresses at the edge of the loading plate and across the geosynthetic location was found to be significant for the control and geotextile-reinforced base, with a higher difference being observed in the latter case.

Figure 4.24 shows the horizontal stresses in the CAB layer measured along the edge of the loading plate. Noticeably lower horizontal stresses were observed with the reinforced base layer when compared to those measured in the control experiment (i.e., no reinforcement). The difference in behavior between the geogrid and geotextile was minor.

Figure 4.25 presents an abridged version of the LST configuration showing only the earth pressure cells in the CAB for the pavement with the thick (i.e., 10-inch) CAB (Experiments 2, 4, and 6). Similar to the thin pavement case, the locations of the earth pressure cells are provided with modified identifications to facilitate the interpretation of the results. As noted before, it should be kept in mind that the relative offsets of the pressure cells above the reinforcements are not exactly the same between the experiments with thin and thick CAB.

Figure 4.26a and Figure 4.26b show, for the thick CAB layer, the load-induced vertical stress measurements along the centerline of the load for above and below the reinforcement location, respectively. Similarly, Figure 4.27a and Figure 4.27b show the vertical stress measurements along the edge of the load for above and below the reinforcement location, respectively. Figure 4.27c shows the difference in the vertical stresses above and below the reinforcement location at the centerline and edge of the loading plate for the thick CAB layer. Similar to the case of the thin CAB, the vertical stresses above and below the reinforcement location consistently increased with the increase in the applied load level.

At the centerline of the load, higher and lower vertical stresses were observed, respectively, above and below the reinforcement location in the experimental tests for the thick CAB with reinforcements when compared to the control experiment. On the other hand, noticeably lower vertical stresses above the reinforcement location were observed at the edge of the loading plate in the experimental tests with reinforcements when compared to the control experiment in the thick CAB layer. The reduction in the vertical stress at the edge of the loading plate was more significant in the case of the geotextile when compared to the geogrid-reinforced base. The reduction in the vertical stress at the centerline of the load and across the geosynthetic location was substantial in the case of the geogrid when compared to the geotextile. Unlike at the locations along the centerline of the load, the differences in stresses across the geosynthetics were not substantial, especially in the case of the geogrid. It should be noted that the experiment on the thin CAB layer with geogrid (i.e., Experiment 3) did not show any noticeable difference in vertical stresses across the geogrid at all load levels.

The horizontal stress measurements in the thick CAB layer measured along the edge of the loading plate are shown in Figure 4.28. Unlike the case of the thin CAB layer, substantially higher horizontal stresses were observed in the reinforced base layer when compared to those measured in the control experiment (i.e., no reinforcement). The observed horizontal stresses were also higher in the case of the geogrid when compared to the geotextile-reinforced base. It should be noted that the measurements of the horizontal stresses in the case of the control experiment (i.e., Experiment 2) were made with a 4-inch-diameter pressure cell as opposed to a 1-inch-diameter cell, as in the case of the reinforced experiments (Experiment 4 and 6). This difference in the type of pressure cells might have influenced the horizontal stress measurements in the control experiment. As noted before, the average induced pressure within the entire surface area of the pressure cell was being measured, which might partially explain the reason behind the low observed magnitudes for the horizontal stresses in the control experiment.

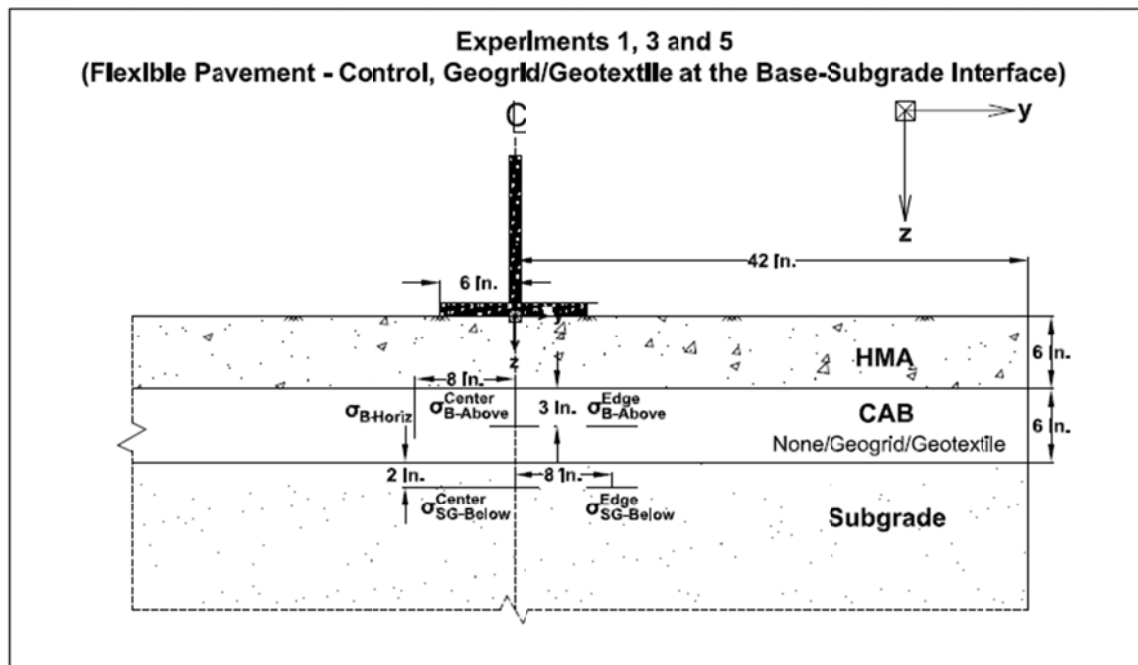
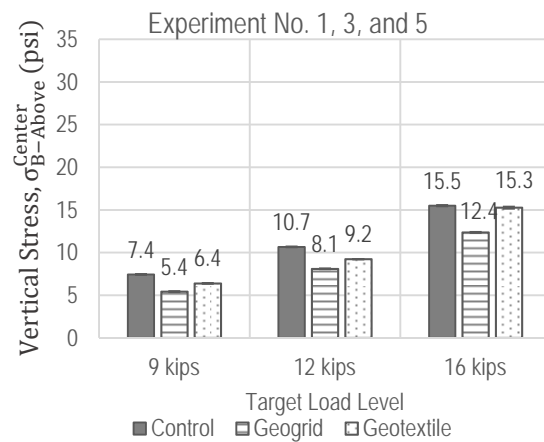


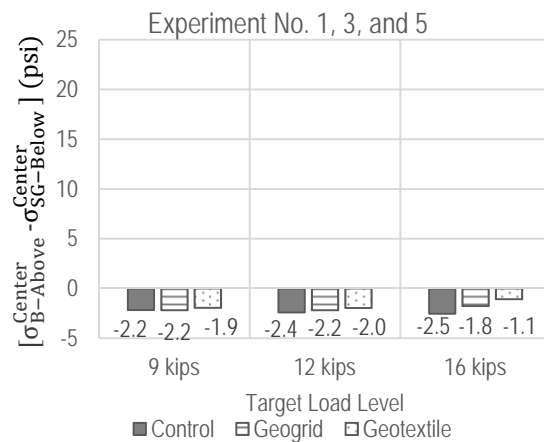
Figure 4.21. LST Configuration for Flexible Pavements with Thin CAB (Experiments 1, 3, and 5) Showing Only Earth Pressure Cells across Geosynthetic



(a)

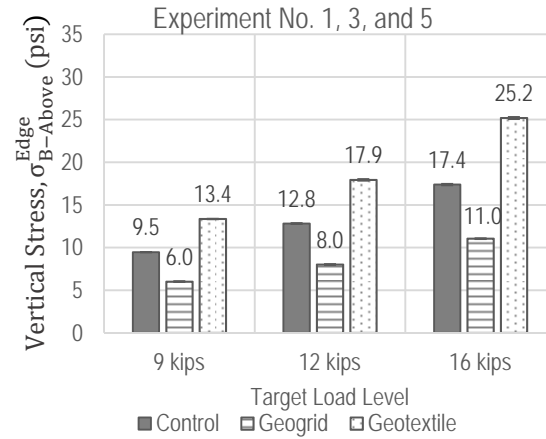


(b)

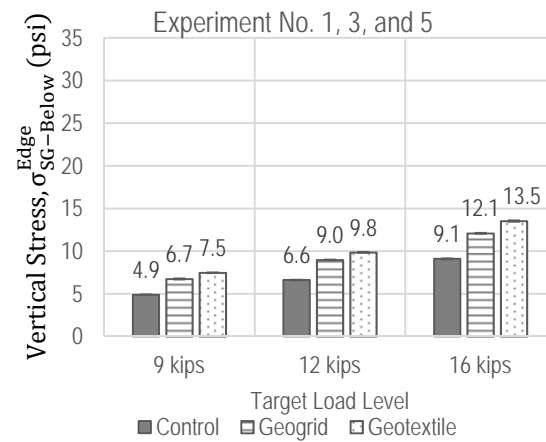


(c)

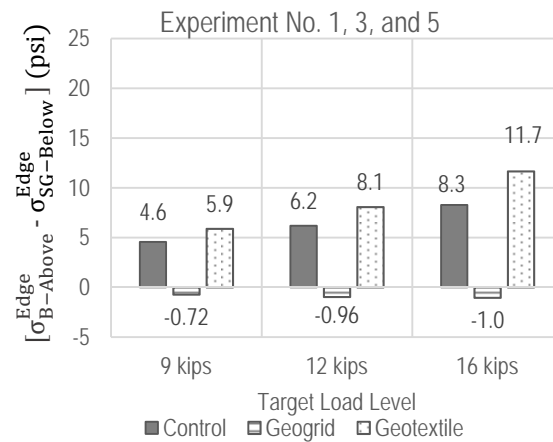
Figure 4.22. Vertical Stresses at the Centerline of the Loading Plate for Thin CAB Layer (Experiments 1, 3, and 5)



(a)



(b)



(c)

Figure 4.23. Vertical Stresses at the Edge of the Loading Plate for Thin CAB Layer (Experiments 1, 3, and 5)

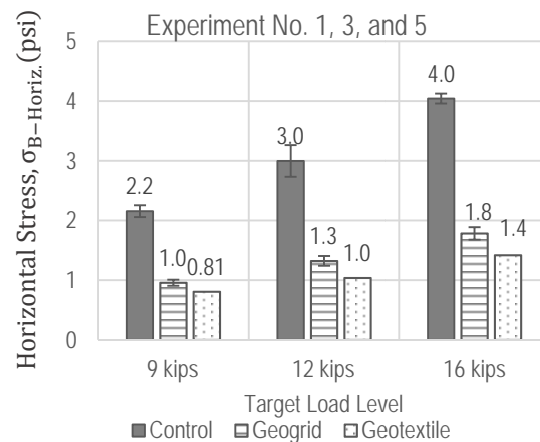


Figure 4.24. Horizontal Stresses at the Edge of the Loading Plate for Thin CAB Layer (Experiments 1, 3, and 5)

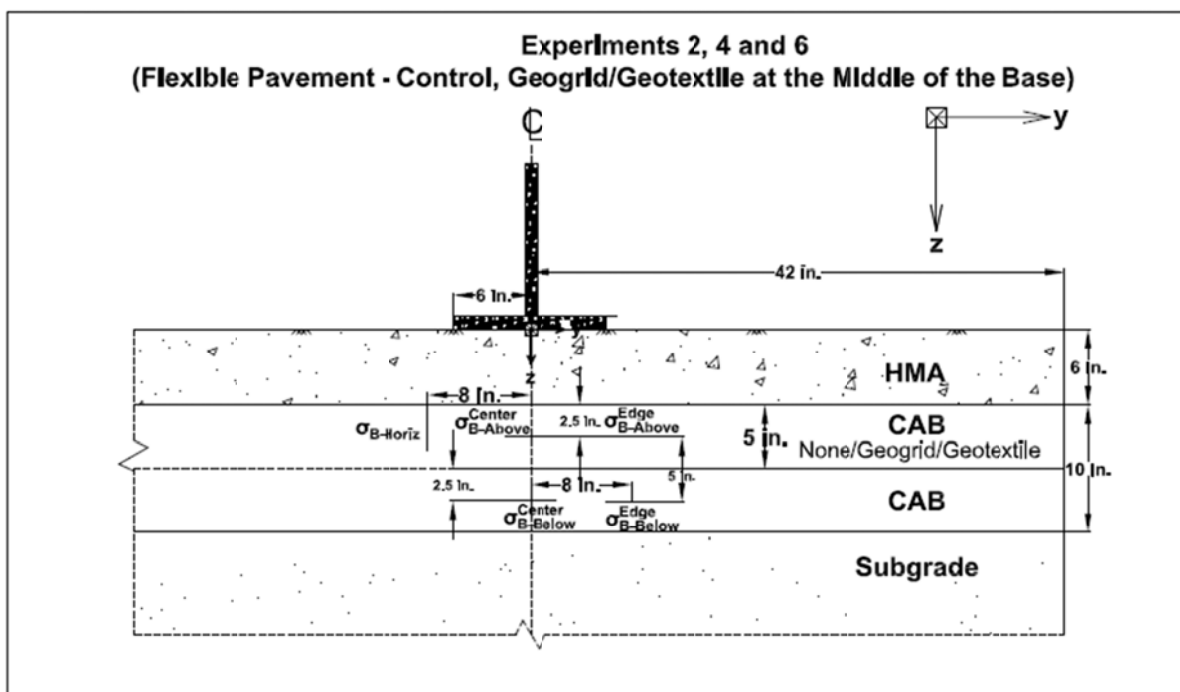
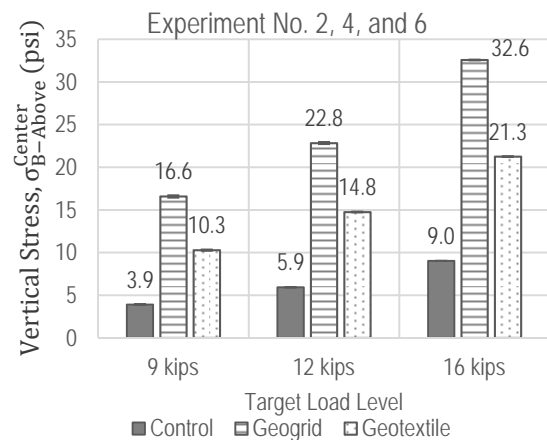
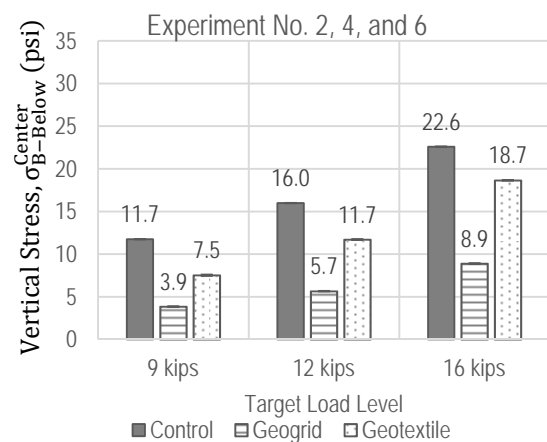


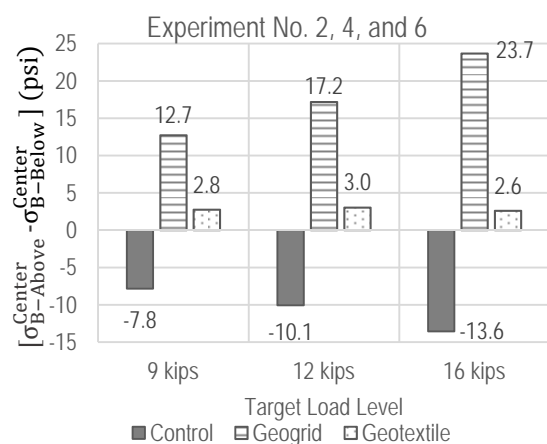
Figure 4.25. LST Configuration for Flexible Pavements with Thick CAB (Experiments 2, 4, and 6) Showing Only Earth Pressure Cells across Geosynthetic



(a)

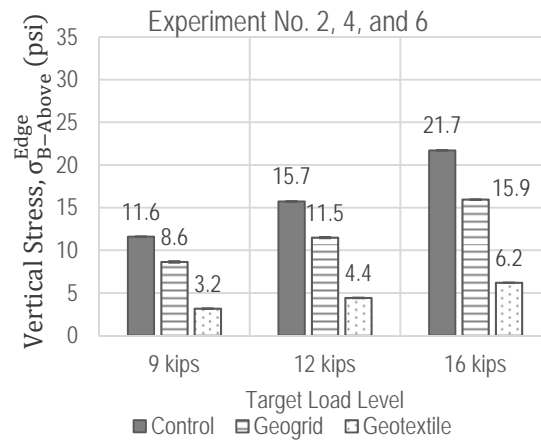


(b)

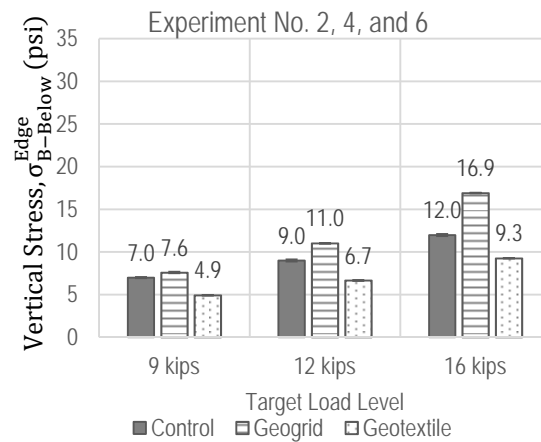


(c)

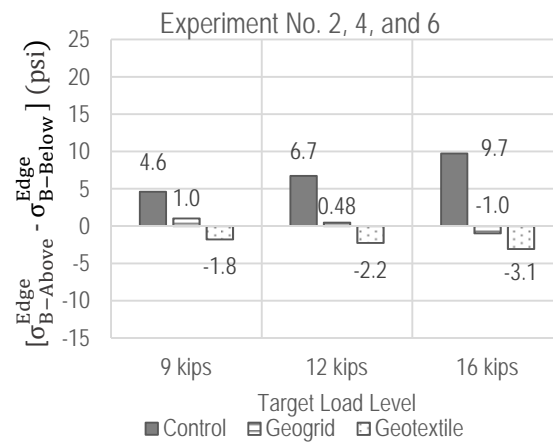
Figure 4.26. Vertical Stresses at the Centerline of the Loading Plate for Thick CAB Layer (Experiments 2, 4, and 6)



(a)



(b)



(c)

Figure 4.27. Vertical Stresses at the Edge of the Loading Plate for Thick CAB Layer (Experiments 2, 4, and 6)

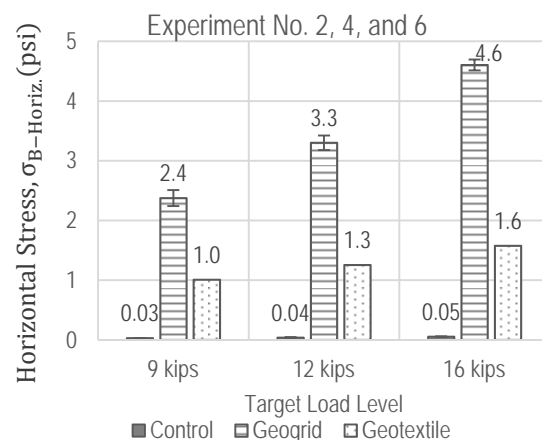


Figure 4.28. Horizontal Stresses at the Edge of the Loading Plate for Thick CAB Layer (Experiments 2, 4, and 6)

Strain Measurements in the Geosynthetic and at the Bottom of the AC Layer

Figure 4.29 and Figure 4.30 present abridged versions of the LST configuration showing only the instrumentations on and around the geosynthetics for thin and thick CAB layers, respectively. The instrumentations shown in the figures are the strain gauges on the reinforcements (designated as SG1 through SG3) and the accelerometers located on and below the geosynthetics. A number of factors that can influence the strain response are listed below and should be considered when interpreting the strain gauge results.

- The strain gauges were glued to the top of the ribs in the case of geogrids and on the top surface of the geotextile. The X- and Y-axes represent the tangential and radial directions, respectively.
- When the embedded geosynthetics deform under the applied surface load, tensile strains are expected because of the membrane effect. However, locally, when the geogrid, for instance, undergoes bending, there will be tension and compression induced at the bottom and top of the geogrid, respectively. The strain measurements made at the top of the geogrid rib will reflect the net effect of these two deformation mechanisms (membrane and bending).
- The laboratory testing of the geosynthetic materials revealed an anisotropic behavior for both the geogrid and geotextile with a noticeable difference in stiffness between the main and cross direction. The stiffness ratio between the two perpendicular directions can be as much as 2.5. Accordingly, the assumption of the existence of an axisymmetric condition for the flexible pavement may not be strictly true.
- In Experiments 2 and 4, the geosynthetic was at the interface between the subgrade and the CAB layer, while in Experiments 4 and 6, it was fully surrounded by the CAB. When the all-around crushed aggregates from the base are interlocked with the geogrid, a significant interaction between the ribs and the aggregates is expected. Accordingly, the strain measurements are expected to reflect this localized complex nonlinear interaction, which is also expected to be influenced by the loading cycles and load levels.

- While a 6-inch AC layer was targeted for all of the LST experiments, there were variations in the thickness of the AC layers within the individual experiments and among the various experiments. It is anticipated that the differences in the in-situ AC layer thickness values will influence the measured responses, and in particular the measured tensile strains at the bottom of the AC layer.

The above factors indicated that care should be taken when interpreting the strain data measurements. Figure 4.31 and Figure 4.32 show the measured horizontal strain data on the geosynthetics for both thin (6-inch CAB layer) and thick (10-inch CAB layer) pavements for all load levels, respectively. Higher strains were observed at the centerline of the load when compared to those measurements at locations away from the load. The increase in load levels did not result in a proportional increase in the measured strains.

The horizontal strain at the bottom of the AC layer was a critical input to the assessment of the long-term performance of flexible pavements. The strain measurements at the bottom of the AC layer are presented in Figure 4.33 and Figure 4.34 for thin and thick pavements, respectively. Unlike in the case of the strains in geosynthetics, the AC strain responses were very consistent and the measurements increased proportionally with the increase in applied load levels. The load-induced tensile strains for the control experiment were observed to be between the strain measurements from the reinforced base experiments. The measured tensile strains at the bottom of the AC layer were consistently higher in the case of the geogrid-reinforced base (Experiments 3 and 4) compared to the geotextile-reinforced base (Experiments 5 and 6).

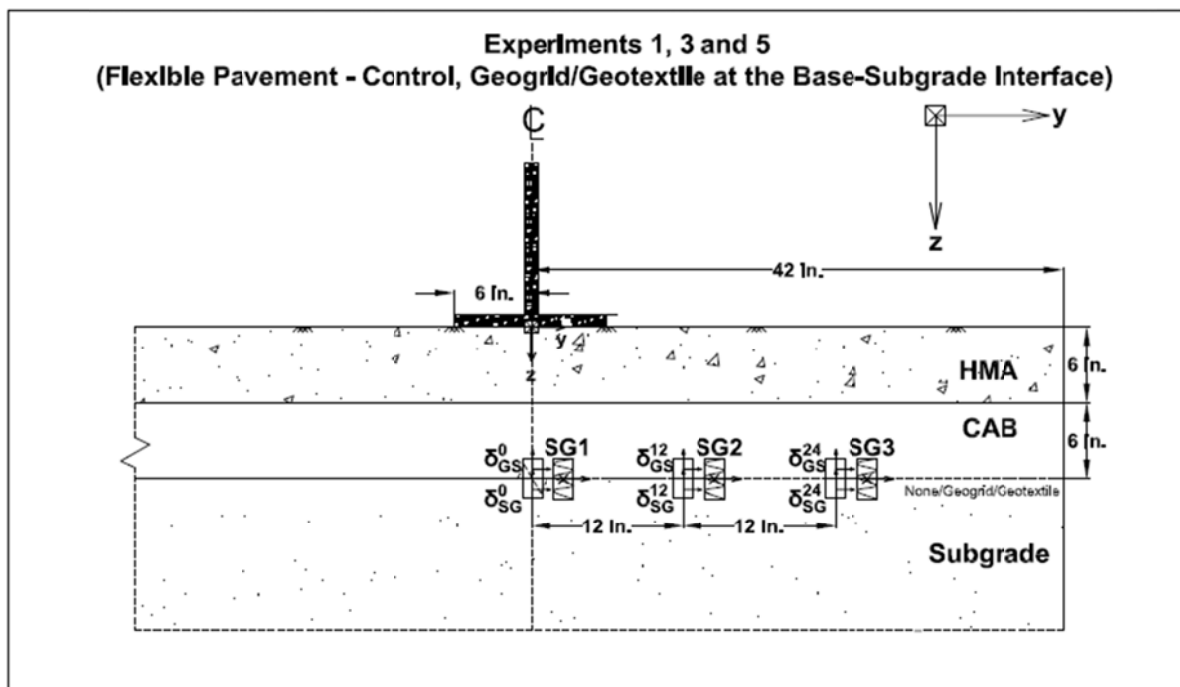


Figure 4.29. LST Configuration for Flexible Pavements with Thin CAB (Experiments 1, 3, and 5) Showing Only the Instrumentations on and around Geosynthetic

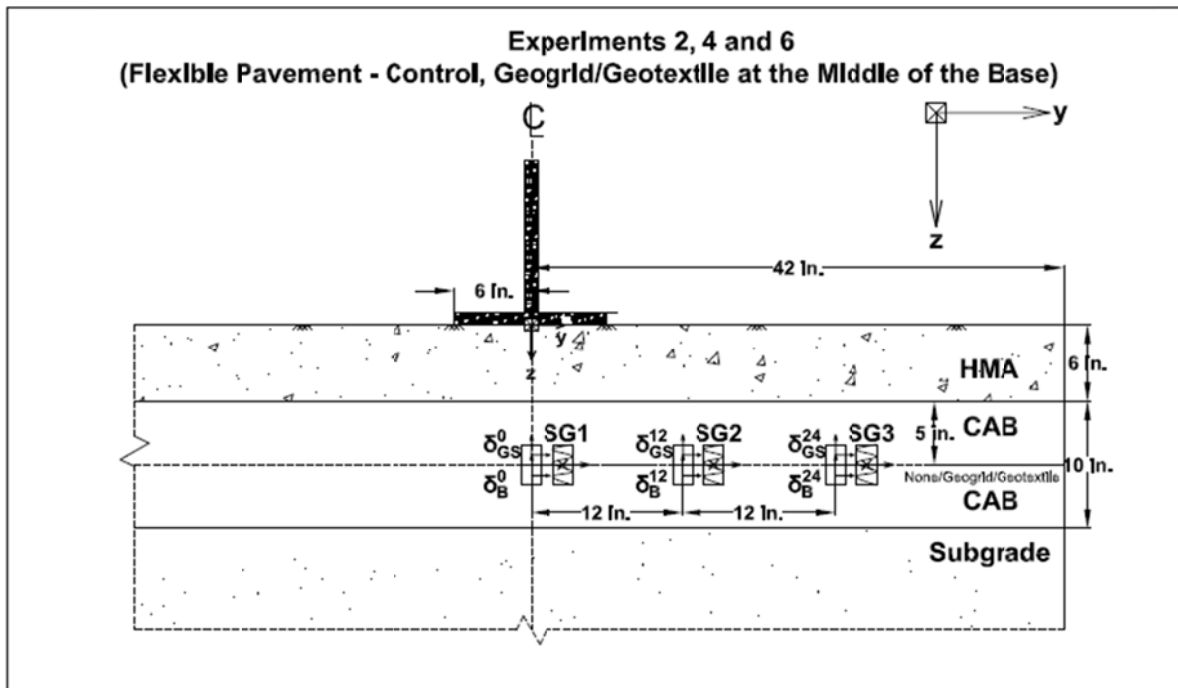


Figure 4.30. LST Configuration for Flexible Pavements with Thick CAB (Experiments 2, 4, and 6) Showing Only the Instrumentations on and around Geosynthetic

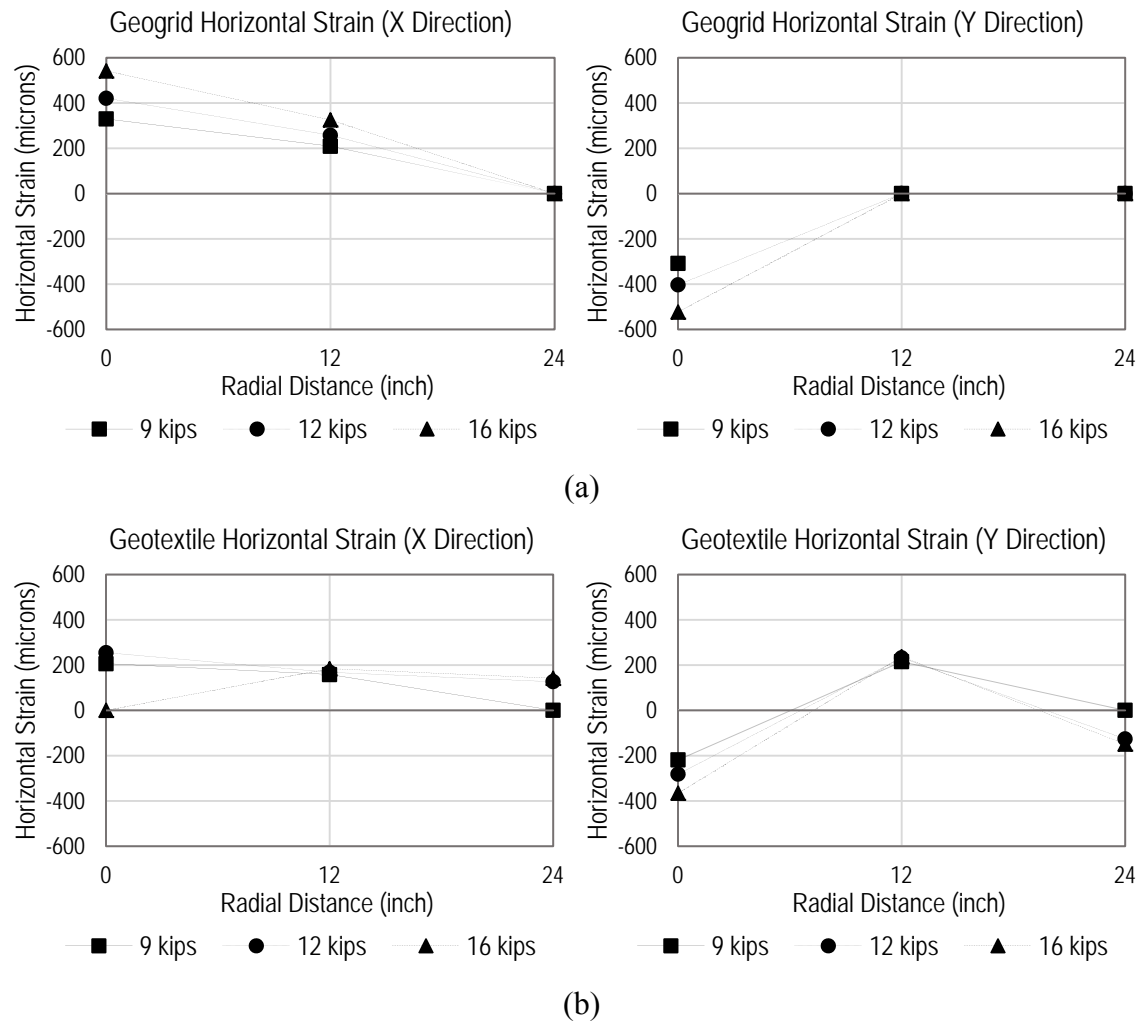


Figure 4.31. Horizontal Strains in the Geosynthetic Reinforcements—Flexible Pavements:
(a) Experiment 3 (geogrid); (b) Experiment 5 (geotextile)

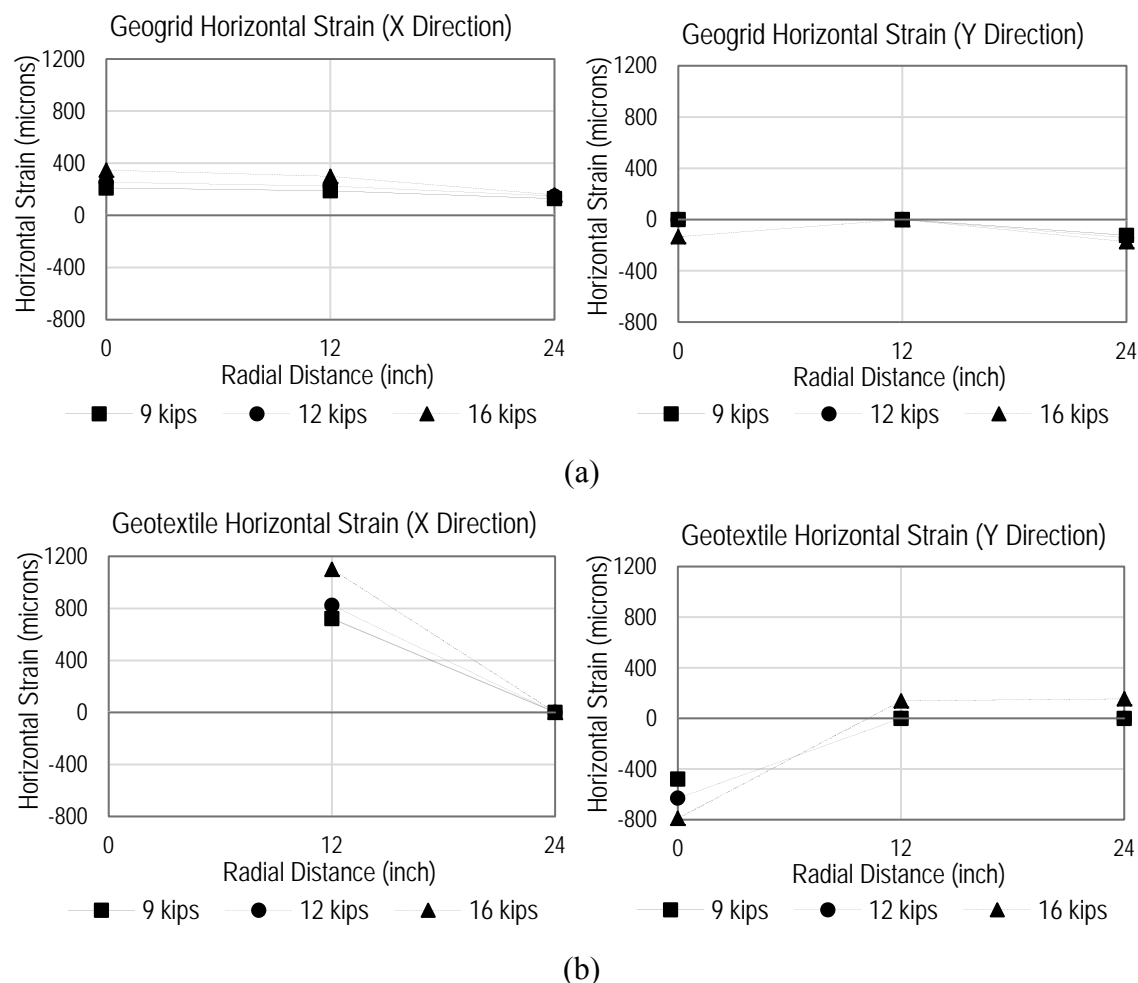


Figure 4.32. Horizontal Strains in the Geosynthetic Reinforcements—Flexible Pavements: (a) Experiment 4 (geogrid); (b) Experiment 6 (geotextile)

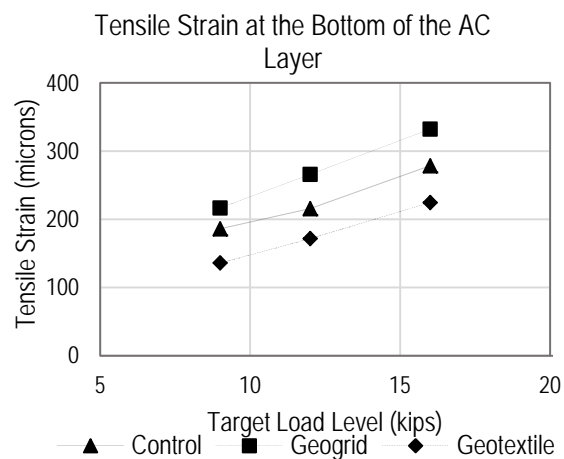


Figure 4.33. Tensile Strains at the Centerline of the Load and at the Bottom of the AC Layer (Experiments 1, 3, and 5)

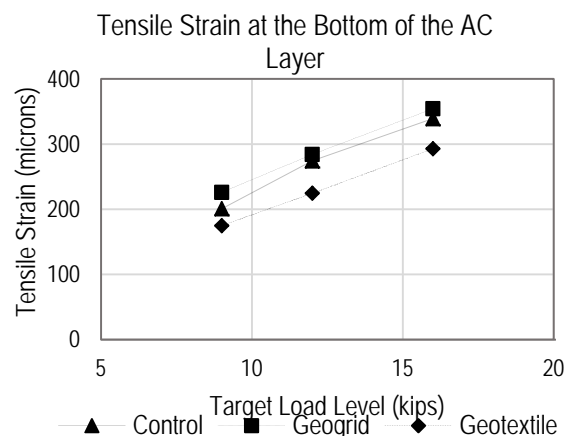


Figure 4.34. Tensile Strains at the Centerline of the Load and at the Bottom of the AC Layer (Experiments 2, 4, and 6)

Deformation of the Geosynthetic and Interface Slippage

The vertical deformed shape of the geosynthetic could be determined using the vertical displacements at various locations of the geosynthetic. As mentioned previously, the vertical displacements at the interior locations could be obtained using the proposed calibrated double-integration procedure. However, since these computed displacements were not direct measurements, caution should be exercised when synthesizing the observed measurements, particularly if a lack of proportionality in load level increase was present for any type of response.

Figure 4.35 shows the computed load-induced vertical displacements for all load levels in Experiments 3 and 5. The accelerometers were located on the geosynthetic and in adjacent underlying unbound material; hence, two displacement values were available at each of the radial distances. A review of the data in the figures revealed that all computed displacements indicated proportionality with the applied load level except the displacements from the experiment with the geotextile at 9- and 12-kip load levels. Therefore, the results of this test could not be directly used in the data interpretation. The computed vertical displacements at various radial distances on the geosynthetic describe the deformed shape of the geosynthetic itself under loading. In general, minimal differences in vertical displacements between the geosynthetic and the adjacent unbound material were observed at the various load levels, thus lending credibility to the implemented double-integration procedure.

Figure 4.36 shows the horizontal displacements of the geosynthetics as a function of radial distance and for all load levels in the case of the thin CAB layer. To evaluate the role of geosynthetics on the horizontal movement, the results of the control experiment (Experiment 1) are also included. The results showed that there was substantial outward movement under the edge of the plate in the case of the control experiment, while much lower or negligible inward movements were computed with the geosynthetics. This was an important observation since the geosynthetics reduced the horizontal displacement under the edge of the plate substantially.

An important aspect of the geosynthetic-unbound material interaction was the possible slippage at the interface. Figure 4.37 shows the observed horizontal slippage in the thin CAB experiments, computed as the difference in horizontal displacements between the geosynthetic

and the adjacent unbound material. The potential horizontal slippage was calculated at all applied load levels. As noted above, the results for the geotextile-reinforced base under a 12-kip load should be omitted. The data in Figure 4.37 indicated the potential presence of slippage between the geosynthetic and the underlying subgrade material, especially under the edge of the loading plate. This slippage was also observed to be higher with the increase in the applied load level. The slippage between the geogrid and the underlying subgrade material under the 9-kip load was negligible and increased with the 12- and 16-kip load levels. On the other hand, slippage was detected at the 9- and 16-kip load levels for the geotextile case.

Similar plots are presented for the experiments with the thick CAB layer (i.e., Experiments 2, 4, and 6) in Figure 4.38 to Figure 4.40. Although the vertical displacements of the geogrid at 16 kip did not follow the proportionality criterion noted above, the localized nonlinear interaction between the geogrid and the surrounding aggregates could explain the anomaly. Similar to the experiments with the thin CAB layer, minimal differences in vertical displacements between the geosynthetic and the adjacent aggregate base material were observed at the various load levels.

The results for the horizontal displacements (see Figure 4.39) were analogous to those observed in thin CAB layer cases, where a substantial outward movement under the edge of the plate was seen for the control experiment, while much lower or negligible inward movements were computed with the geosynthetics. On the other hand, the data in Figure 4.40 indicated the potential presence of slippage between the geotextile and the adjacent aggregate base material, especially under the edge of the loading plate. However, the slippage estimates were negligible with the geogrid reinforcement when placed in the middle of the 10-inch CAB layer.

The measured slippage from the LST test showed that the maximum relative displacement between the geosynthetic and aggregate was less than 0.04 inch. This suggested that the interface slippage that normally occurred in the geosynthetic-reinforced aggregates was in the linear stage (see Figure 4.3).

In general, the observed difference in the behavior between the geogrid and geotextile as a function of load level, pavement structure, and geosynthetic location within the CAB layer warranted the appropriate modeling of the geosynthetic-unbound material layer interface to better capture any influence that the reinforcement may have on pavement responses.

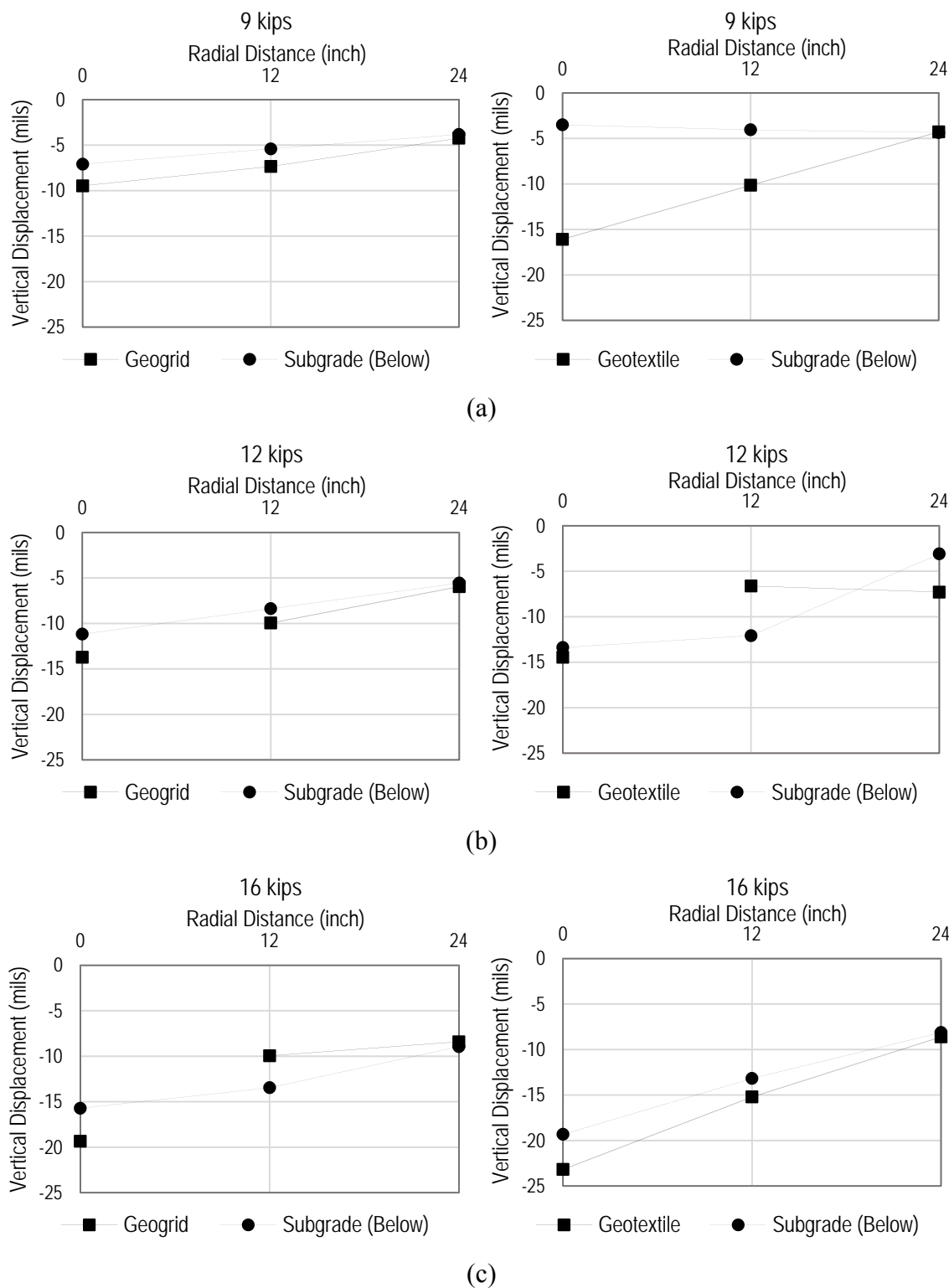


Figure 4.35. Vertical Displacements of the Geosynthetic and Adjacent Unbound Material in Experiments 3 and 5 for Various Load Levels: (a) 9 kip; (b) 12 kip; (c) 16 kip

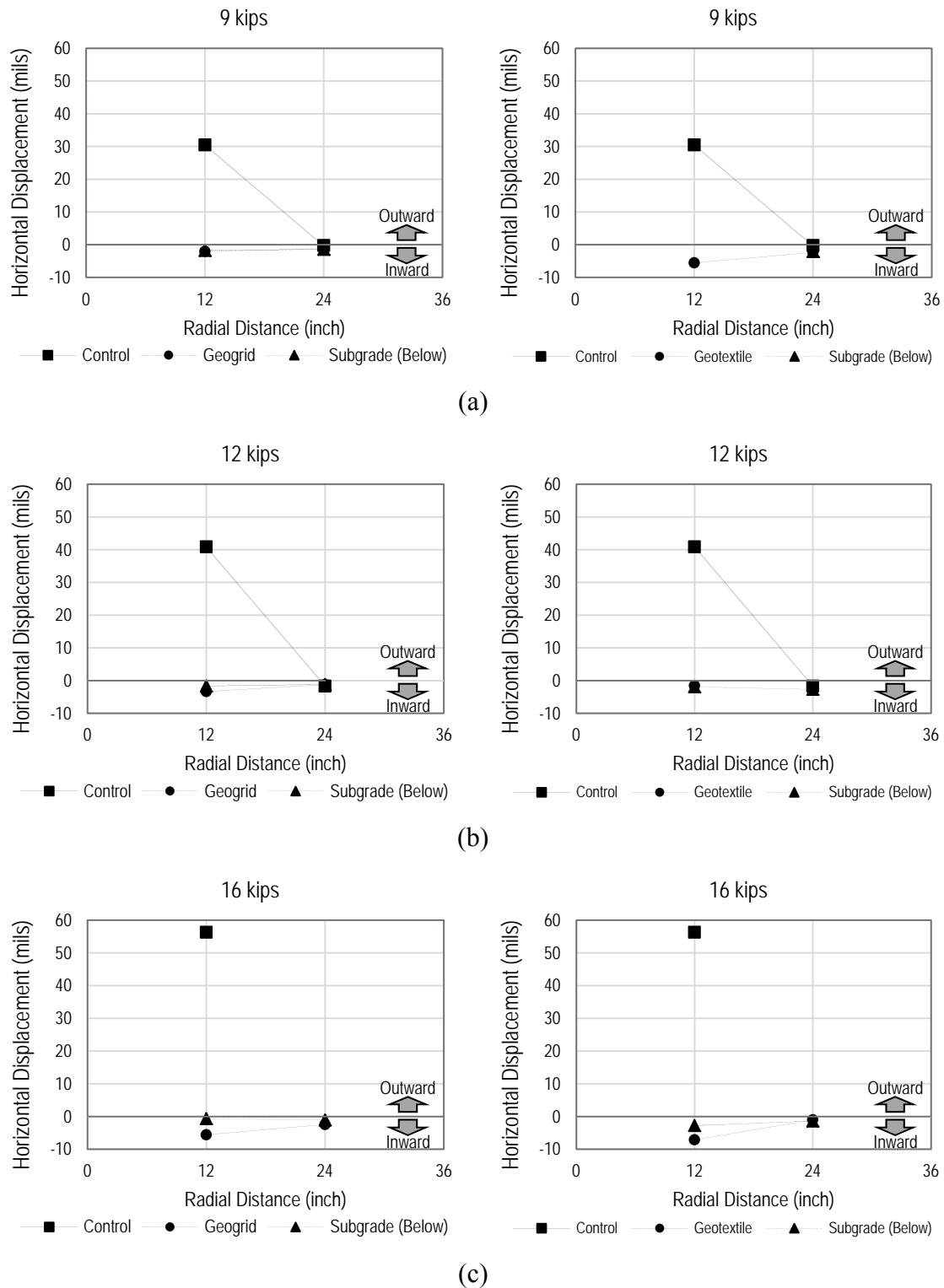


Figure 4.36. Horizontal Displacements of the Geosynthetic and Adjacent Unbound Material in Experiments 1, 3, and 5 for Various Load Levels: (a) 9 kip; (b) 12 kip; (c) 16 kip

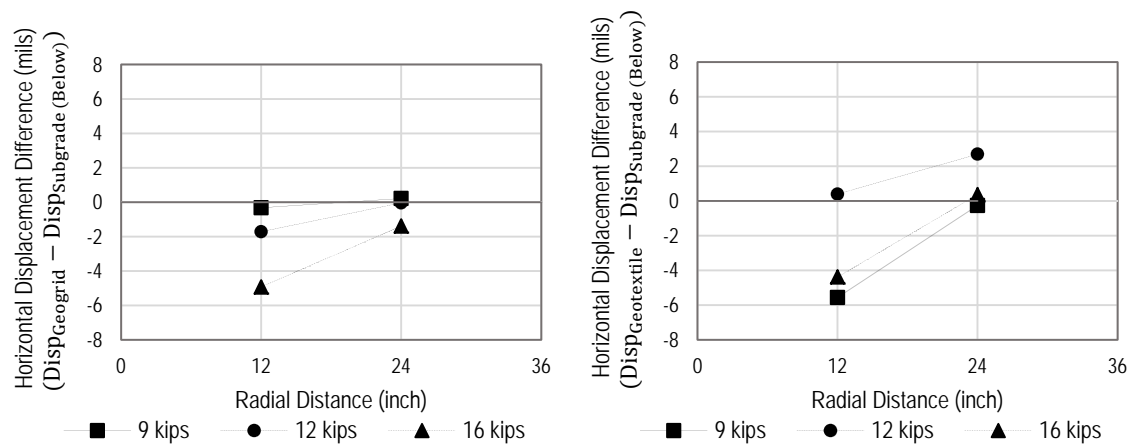


Figure 4.37. Horizontal Slippage of the Geosynthetic and Adjacent Unbound Material in Experiments 3 and 5 for Various Load Levels—Flexible Pavements

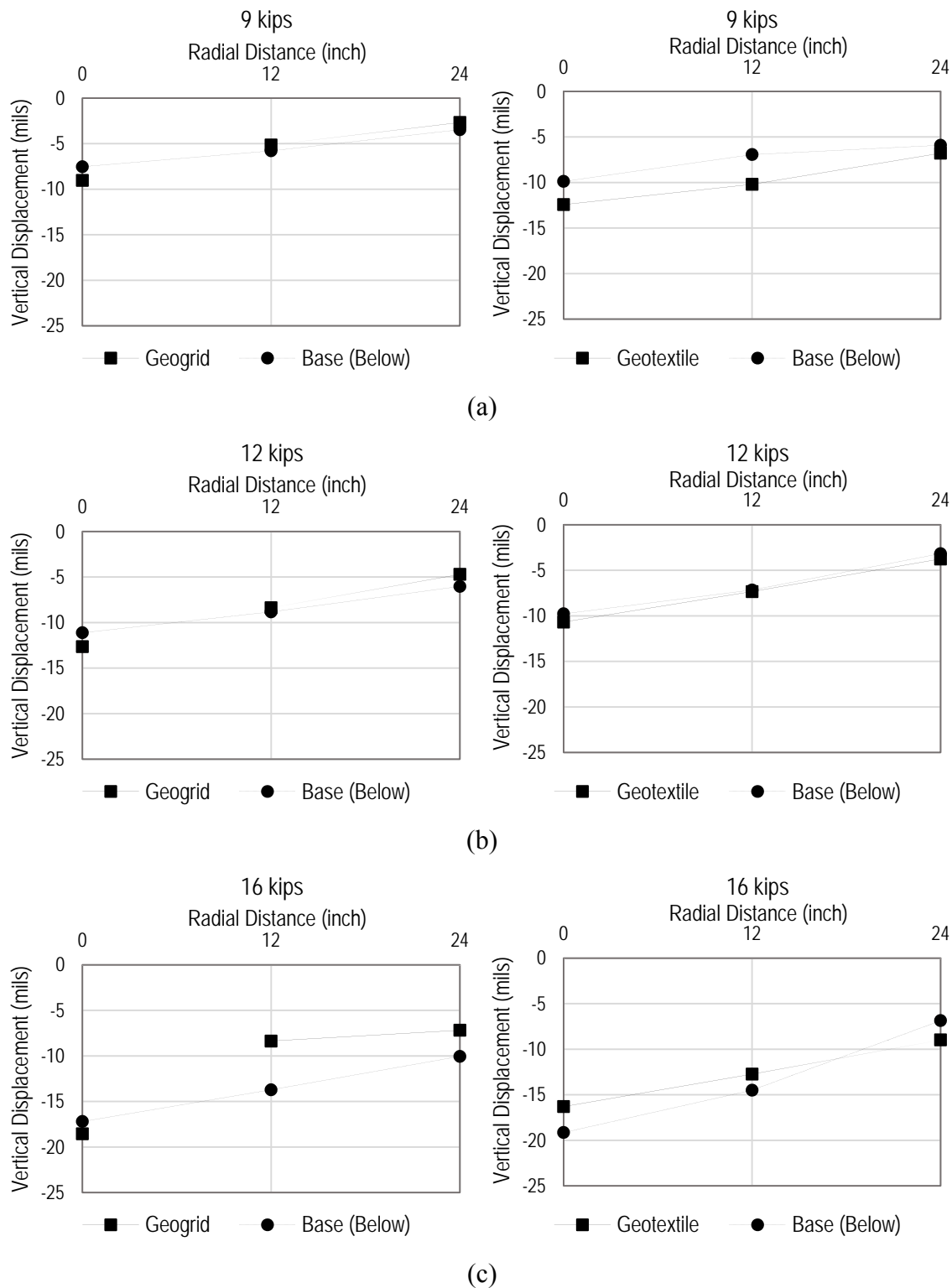


Figure 4.38. Vertical Displacements of the Geosynthetic and Adjacent Unbound Material in Experiments 4 and 6 for Various Load Levels: (a) 9 kip; (b) 12 kip; (c) 16 kip

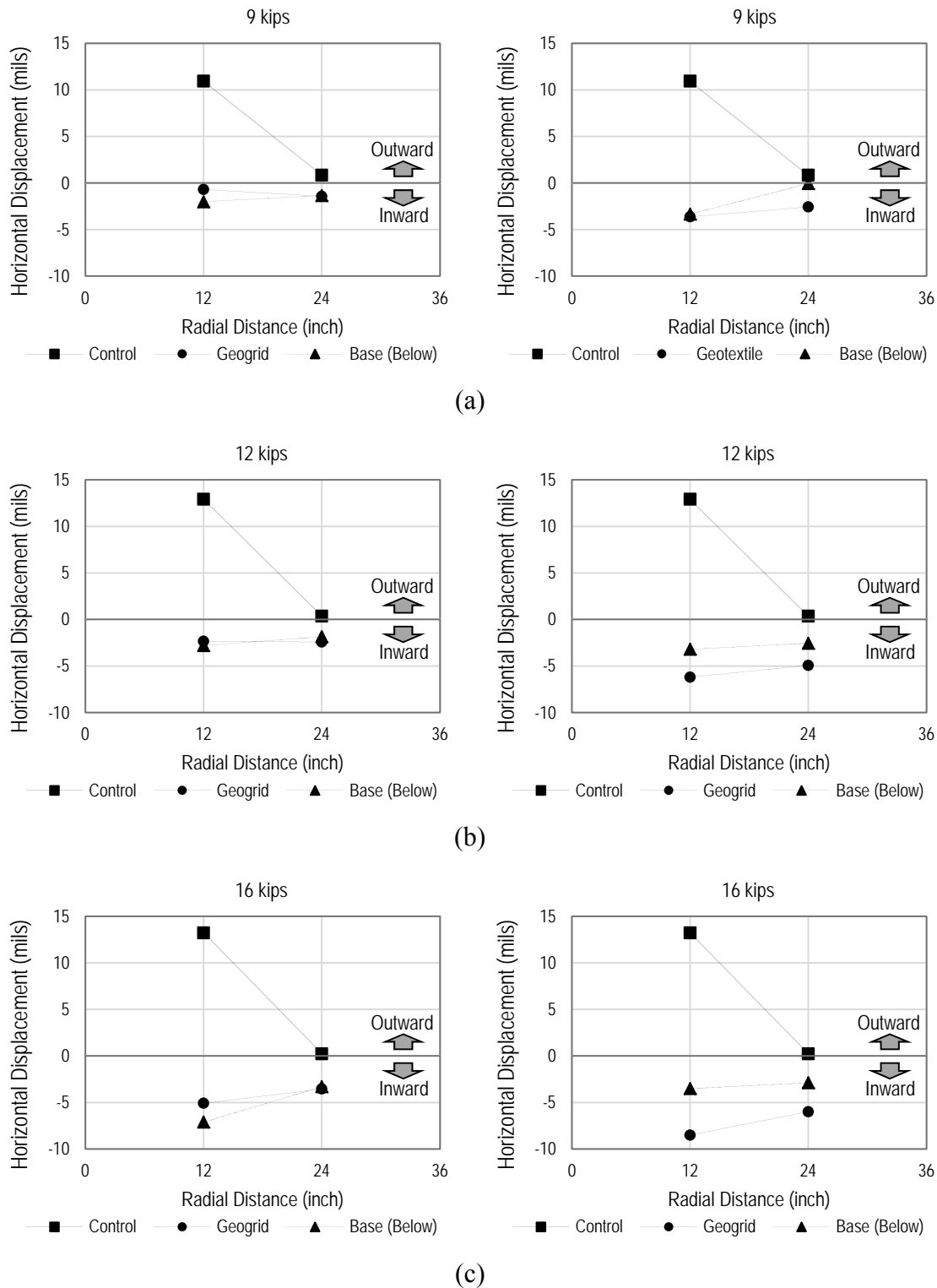


Figure 4.39. Horizontal Displacements of the Geosynthetic and Adjacent Unbound Material in Experiments 2, 4, and 6 for Various Load Levels: (a) 9 kip; (b) 12 kip; (c) 16 kip

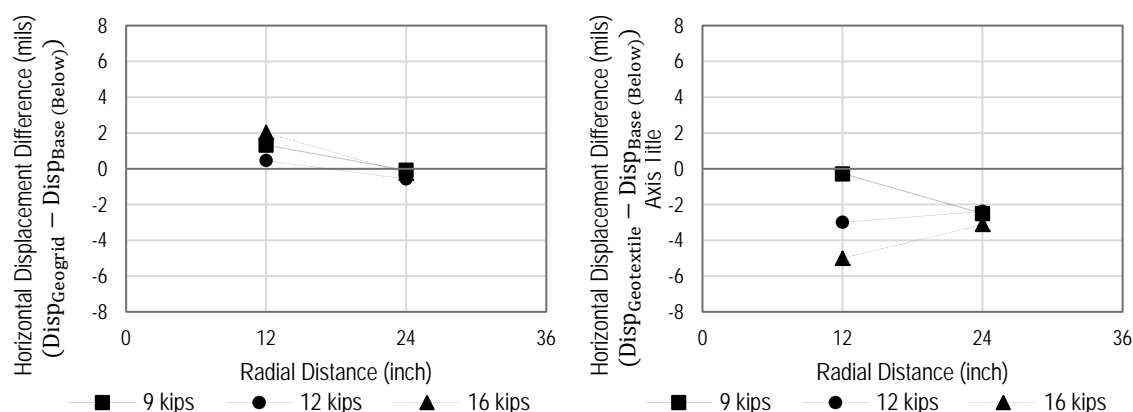


Figure 4.40. Horizontal Slippage of the Geosynthetic and Adjacent Unbound Material in Experiments 4 and 6 for Various Load Levels—Flexible Pavements

Rigid Pavement

Similar to the flexible pavement results section, a recap of pertinent key factors that had significant influence on the measured data is first provided below. Such information was very useful when navigating through the collected data and during the interpretation process of the various results.

- Experiments 7, 9, and 10 included a 6-inch PCC layer on top of an 8-inch CAB layer and represent, respectively, the testing for the control (i.e., no base reinforcement), geogrid-reinforced base, and geotextile-reinforced base. Both the geogrid and geotextile were located at the middle of the CAB layer (i.e., 10 inches below the pavement surface).
- With the focus given to the edge of the PCC slab, the surface layer was constructed in two segments with a gap of 6 inches in between, and the loading was applied near the edge of one of the slabs (referred to as loaded slab). Various instrumentations (earth pressure cells, strain gauges, and accelerometers) were positioned in an attempt to characterize many aspects of pavement responses at the edge of the slab.
- Since pumping of the CAB layer through the joints was an important design concern, especially in the presence of moisture, load pulses resumed after introducing additional moisture to the CAB (referred to as wet experiments) and after the tests with dry CAB (i.e., at the optimum moisture content) were completed. The purpose of this activity was to investigate the roles of geosynthetics and excess moisture on pumping of the CAB at the joints.
- The presence of the gap between the loaded and unloaded slabs along with the application of the load at the edge of the loaded slab represented a complex loading condition. This loading condition was non-axisymmetric and was coupled with the loaded slab independently undergoing possible rocking because of its high stiffness around the axis that was parallel to the edge of the slab (along the gap direction). Therefore, the responses under such circumstances were expected to be difficult to illustrate.

- Unlike with the tests on flexible pavements, a number of instruments malfunctioned. This problem limited the scope of the data interpretation described below.
- The presentation of the results of the stress distribution across the geosynthetic was based on earth pressure cell data measured above and below the geosynthetic. The locations of the earth pressure cells were 2 inches above and below the geosynthetic.
- Unlike earth pressure cells, measurements made by the accelerometers, strain gauges, and LVDTs could be considered as 1-point measurements. The majority of the pressure cells used in the LST experiments were 4 inches in diameter (a couple of the pressure cells were 1 inch in diameter and were mainly used for measurements of the horizontal pressure), and the fluid present within the flexible diaphragm indicated the average induced pressure within the entire surface area of the cell.
- The earth pressure cells used to measure horizontal stresses in the CAB were located laterally away from the axis of loading and at approximately 8 inches from the centerline (under the edge of the plate) in all experimental tests.
- The PCC layer of 6 inches was targeted for all the LST experiments; measurements from the core specimens showed consistently uniform thickness for the surface layer.

Stress Distributions Across the Reinforcements

First, the collected earth pressure cell data were reviewed. Figure 4.41 (section through the Y-axis) and Figure 4.42 (plan view at a depth of 8 inches) present the abridged versions of the LST configuration showing only the earth pressure cells in the CAB layer for the rigid pavement in Experiments 7, 9, and 10. The locations of the earth pressure cells are provided with modified identifications to facilitate the interpretation of the results. For example, the subscripts “B-Above” and “B-Below” refer to the pressure cells in the base above and below the geosynthetic, respectively. The superscript “Loaded-Center” refers to the pressure cells at the centerline of the load on the loaded side of the concrete slab, while “YD” represents the Y-direction. The horizontal stress is referred to as $\sigma_{B-Horiz}$ and was measured at only one location in the CAB layer (above the geosynthetic location and in the X-direction).

A review of the assembled results with a focus on assessing the influence of the reinforcement indicated many noteworthy observations. A summary of the important results and interpretations is presented below.

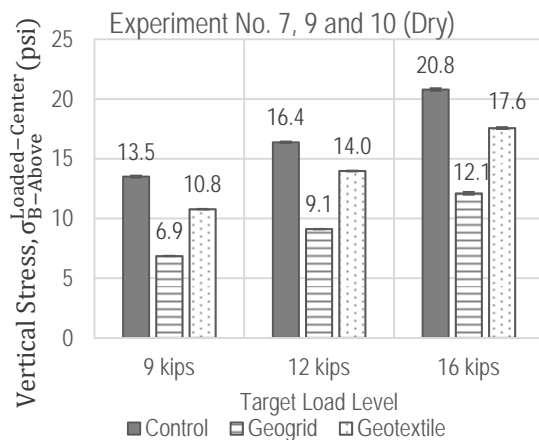
Figure 4.43a and Figure 4.43c show the load-induced vertical stress measurements along the centerline of the load for above and below the reinforcement location, respectively. Figure 4.43e shows the difference in the vertical stresses above and below the reinforcement location. The results for the CAB at the optimum moisture content (referred to as dry CAB) and partially saturated (referred to as wet CAB) are presented side by side on the left and right of the figure, respectively. The corresponding figures for the wet CAB are Figure 4.43b, Figure 4.43d, and Figure 4.43f, respectively. As expected, the vertical stresses above and below the reinforcement location consistently increased with the increase in the applied load level. As noted earlier, the form of the relationship between the vertical stress and the load level could be used to investigate the extent of the nonlinearity in the unbound materials.

The vertical stresses for the dry tests above the reinforcement location were highest in the control experiment, followed by the geotextile-reinforced base and then the geogrid-reinforced

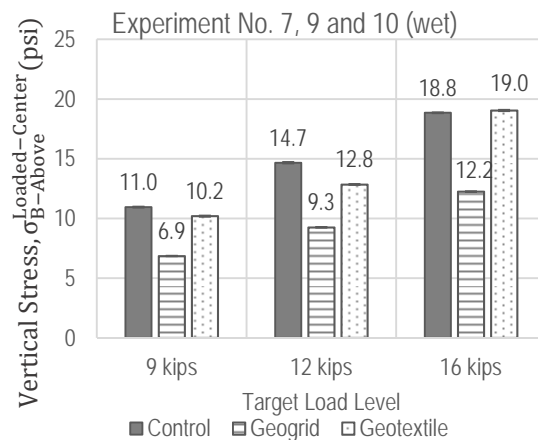
base. In contrast, a reverse trend was observed for the vertical stresses below the reinforcement location. A substantial reduction in the vertical stress (from above to below the reinforcement location) was observed in the control experiment, while the lowest reduction was observed across the geogrid, thus revealing the impact of the geogrid on the stress transfer across the reinforcement. In all cases, the vertical stresses in the wet CAB were similar to those in the dry CAB, indicating a very limited influence on the level of moisture introduced to the CAB during testing.

Data were available in the CAB at two similar locations to assess load transfer across the concrete joint (i.e., the 6-inch gap/discontinuity in the concrete slab). These locations were below the reinforcement location at a depth of 12 inches from the surface and at 8 inches on the opposite sides of the centerline. Figure 4.44 presents the load-induced vertical stresses in the CAB layer at these specific locations for all load levels. It should be noted that some data were not available because of instrumentation malfunction. As expected, much higher vertical stresses were induced in the location under the loaded slab when compared with the results from beneath the unloaded slab. The stresses in the case of the control experiment (i.e., no reinforcement) were consistently in between those measured with the geogrid- and geotextile-reinforced base. The highest stresses were observed within the geogrid-reinforced base layer. Similar to the stress transfer across the geosynthetic, only a very limited influence was seen with the introduction of the specific moisture level to the CAB layer.

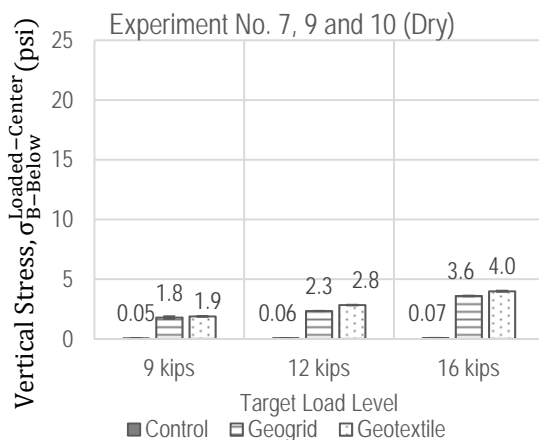
Vertical and horizontal stresses in the CAB layer were also measured at the edge of the loading plate in the X-direction (parallel to the edge of the slab) and above the geosynthetic location (see Figure 4.45). The data indicated higher vertical stresses in the geotextile than in the CAB without any reinforcement (i.e., control experiment). Though the horizontal stresses were lower than the vertical stresses in all cases, significantly lower horizontal stresses were measured in experiments with a geotextile-reinforced base. The difference in behavior when additional moisture was introduced to the CAB layer was noticeable in the experiment with the geotextile.



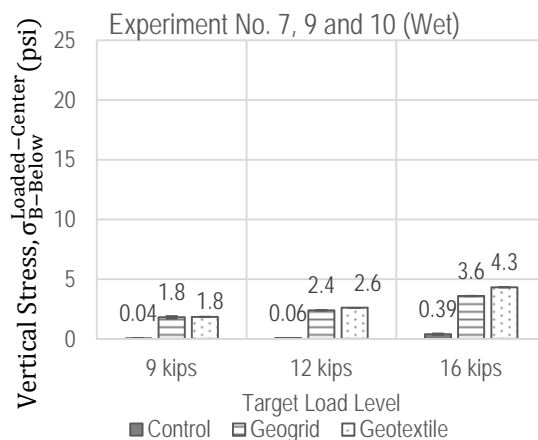
(a)



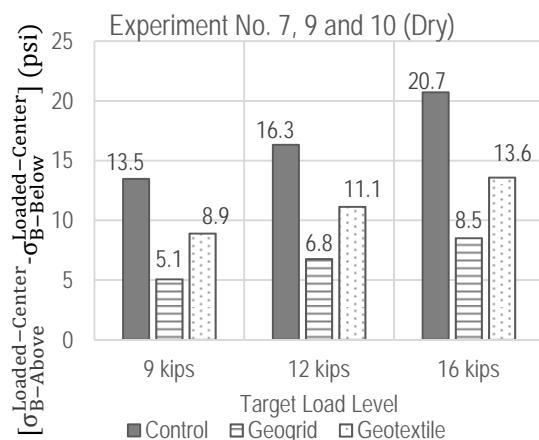
(b)



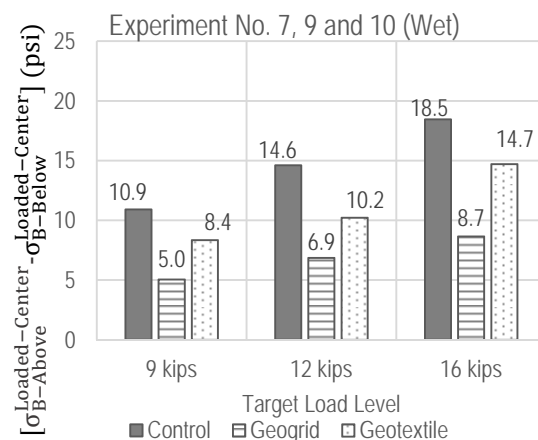
(c)



(d)



(e)



(f)

Figure 4.43. Vertical Stresses at the Centerline of the Loading Plate for Rigid Pavements (Experiments 7, 9, and 10—Dry and Wet)

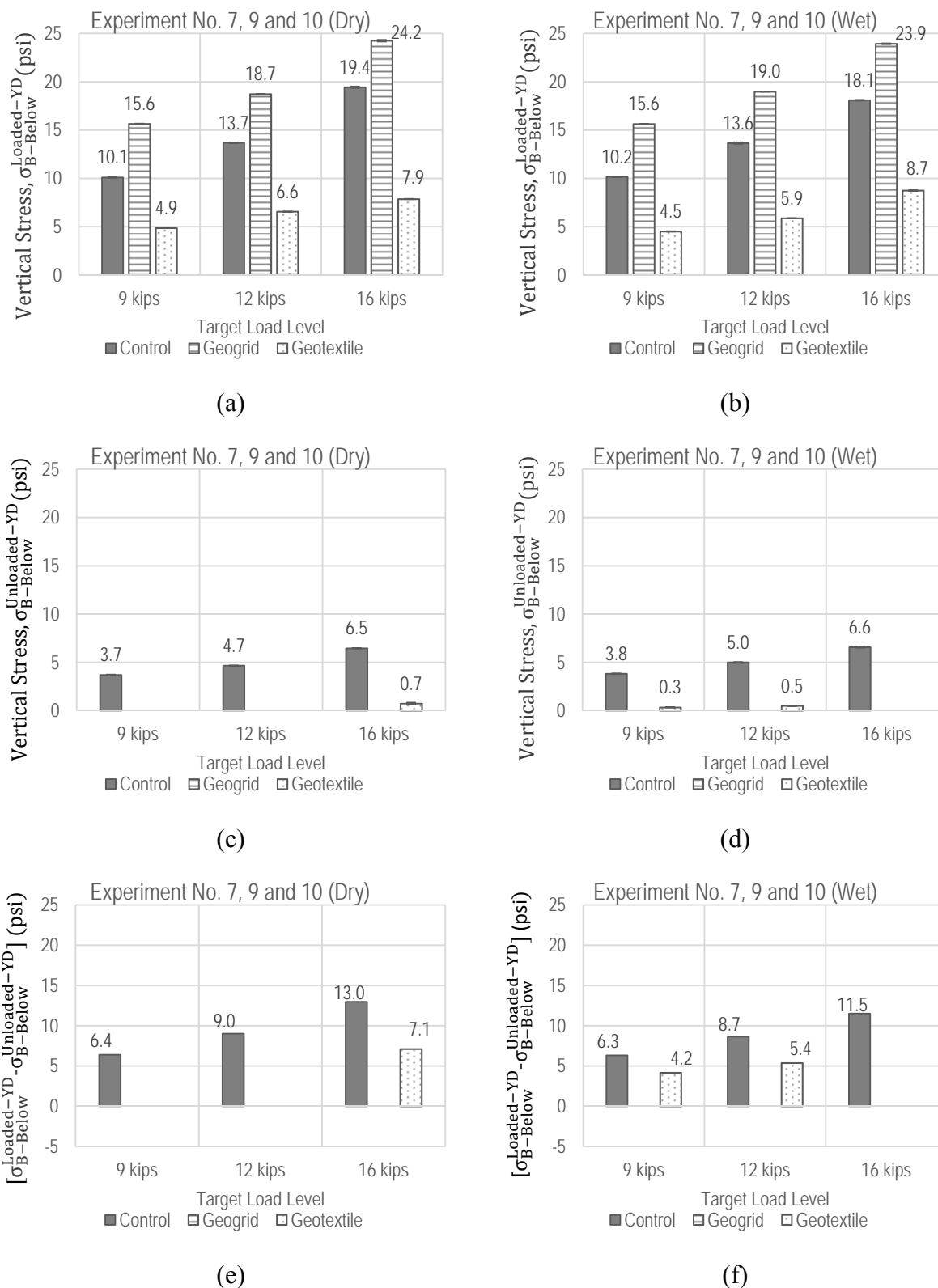


Figure 4.44. Vertical Stresses at Two Similar Locations in the CAB across the Joint and at 8 inches from the Centerline of the Loading Plate for Rigid Pavements (Experiments 7, 9, and 10—Dry and Wet)

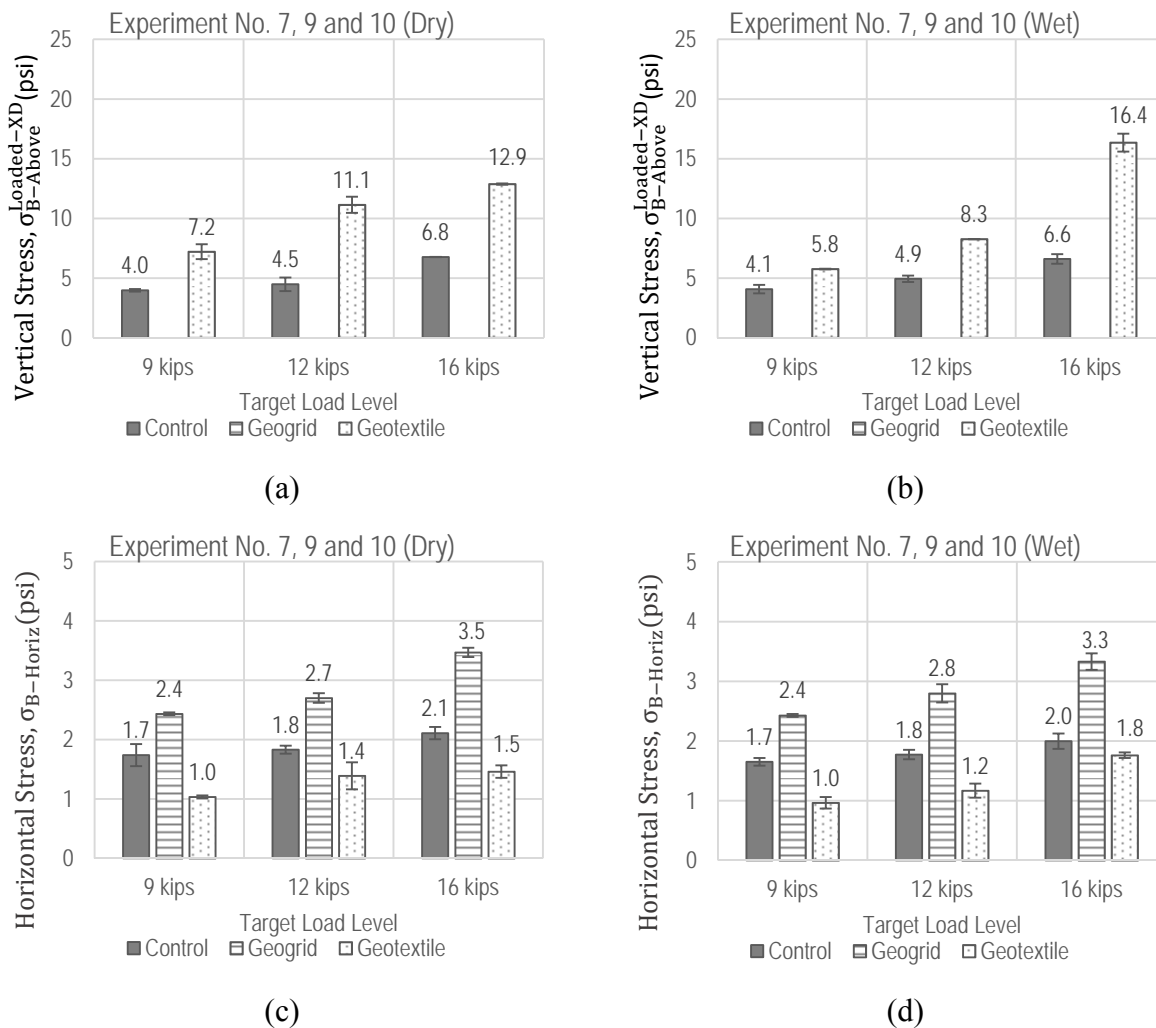


Figure 4.45. Vertical and Horizontal Stresses at the Edge of the Loading Plate in the X-direction (Parallel to the Edge of the PCC Slab) for Rigid Pavements (Experiments 7, 9, and 10—Dry and Wet)

Strain Measurements in Geosynthetic

The normal strain measurements in the geosynthetics were made in two radial directions: X (parallel to the edge of the slab) and Y (perpendicular to the edge of the slab). Figure 4.46 (elevation view) shows the strain gauges SG1 through SG3, which measured the strains in the Y-direction. Figure 4.47 is a plan view at a depth of 10 inches below the pavement surface and shows the remaining strain gauges (SG4 and SG5), which measured normal strains in the X-direction.

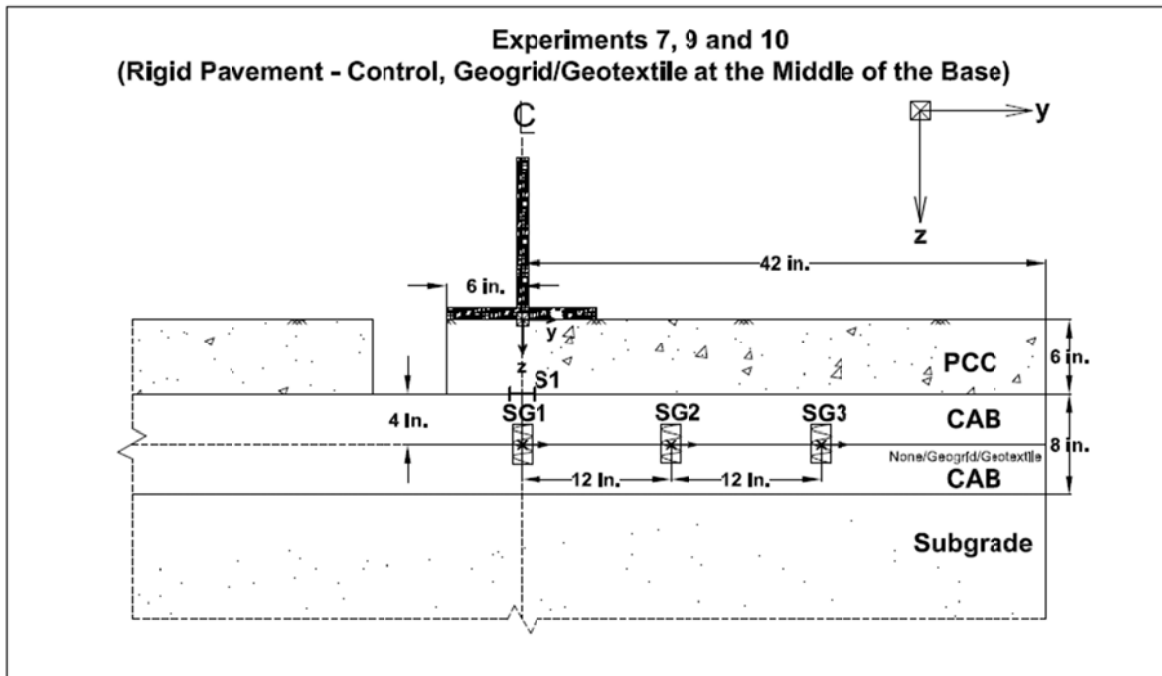


Figure 4.46. LST Configuration for Rigid Pavements (Experiments 7, 9, and 10) Showing Only Strain Gauges on Geosynthetic—Profile View

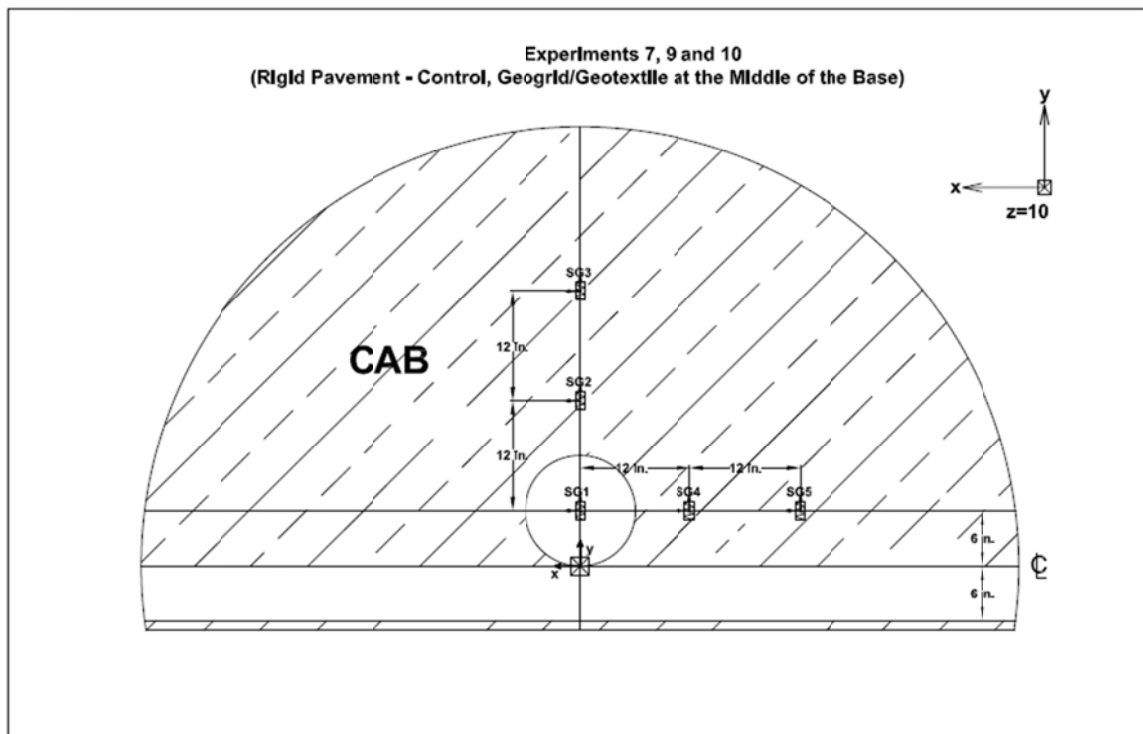


Figure 4.47. LST Configuration for Rigid Pavements (Experiments 7, 9, and 10) Showing Only Strain Gauges on Geosynthetic—Plan View at 10 inches below Pavement Surface

Figure 4.48 shows the strain measurements obtained for all loaded levels with dry and wet CAB as a function of the radial strain measured from the centerline of the load. It should be

noted that the measurements on the geotextile were not available due to malfunction of the strain gauges. The normal strains on the geogrid in the X-direction were consistently higher under the edge of the loading plate (i.e., at a radial distance of 12 inches in Figure 4.48a and Figure 4.48b) for all load levels. Compressive strains were indicated at 24 inches away from the centerline of the load, which is the farthest point where measurements were made. The strains in the Y-direction, measured by SG1 through SG3, are given in Figure 4.48c and Figure 4.48d. No substantial difference was observed between the dry and wet tests for the strain measurements below the edge of the loading plate for the various load levels. In general, for both dry and wet testing conditions, the strains in the X-direction at 12 and 24 inches from the centerline of the load were observed to be higher than those in the Y-direction at the same distance from the load. Furthermore, while tensile strains were observed in the X-direction, compressive strains were measured in the Y-direction at the 12- and 24-inch radial distances.

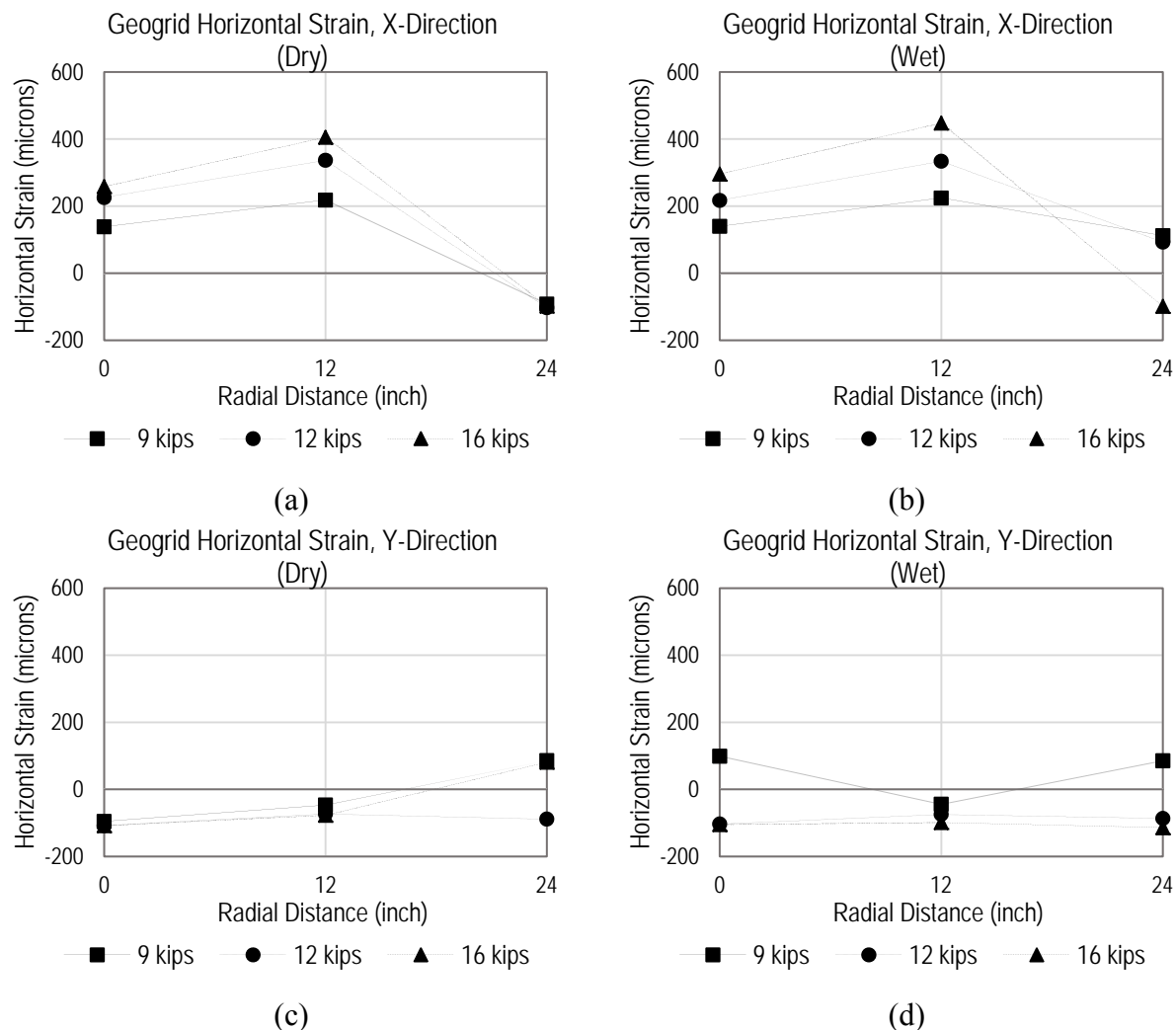


Figure 4.48. Horizontal Strains in the Geogrid Reinforcement (Experiment 9)—Rigid Pavement (Dry and Wet)

Concrete strain gauges embedded at the bottom of the PCC slab were used to assess the normal strains developed due to surface loading. A positive strain reflected a tensile response associated with a beam action, while a negative strain reflected a compression response due to reversed beam action. Figure 4.49 shows the measured normal strains in the X-direction at the bottom of the PCC slab under the center of the loading plate for both dry and wet conditions. The data obtained from the embedded gauges in the dry structure indicated that adding a geogrid layer to the pavement structure increased the tensile strain when compared to a structure without any geosynthetic reinforcement (i.e., control). This behavior was reversed in the wet structure, reflecting lower tensile strains due to the presence of the geogrid layer. Meanwhile, adding a geotextile layer reversed the tensile strain to a compressive strain, in the dry as well as the wet structure, indicating a reversed beam action. Since these data were not expected and were somewhat controversial, care should be taken when interpreting the concrete strain gauge results. There was no evidence that the captured data were indeed a behavior of the reinforced structure and not an error due to installation. It was believed that a couple of possible installation scenarios might have caused the reversed beam action in Experiment 10. The first scenario was if the gauge accidentally rested on a piece of aggregate of relatively significant size within the concrete mixture, which happened to be in the middle of the gauge. This aggregate would have forced the gauge to arch upward when the pavement was loaded, especially due to the discontinuity in the PCC slab. A second scenario was if the gauge moved during concrete placement and changed its orientation or levelness. It should be noted that these scenarios were just speculation, and no solid data were available to prove or disprove them.

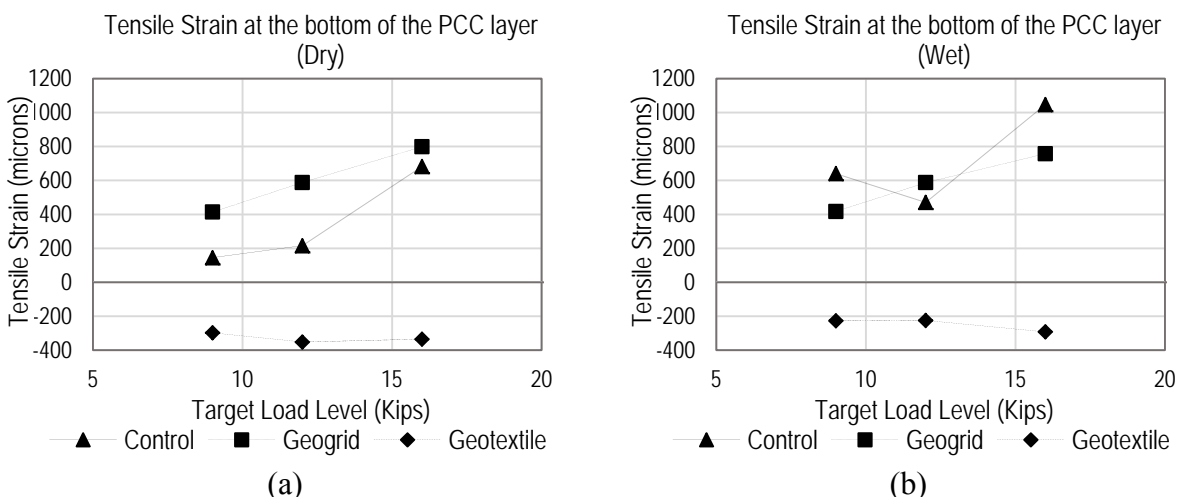


Figure 4.49. Tensile Strains in the X-direction (Parallel to the Edge of the PCC Slab) at the Centerline of the Load and at the Bottom of the PCC Layer (Experiments 7, 9, and 10)

PCC-CAB Interface Slippage

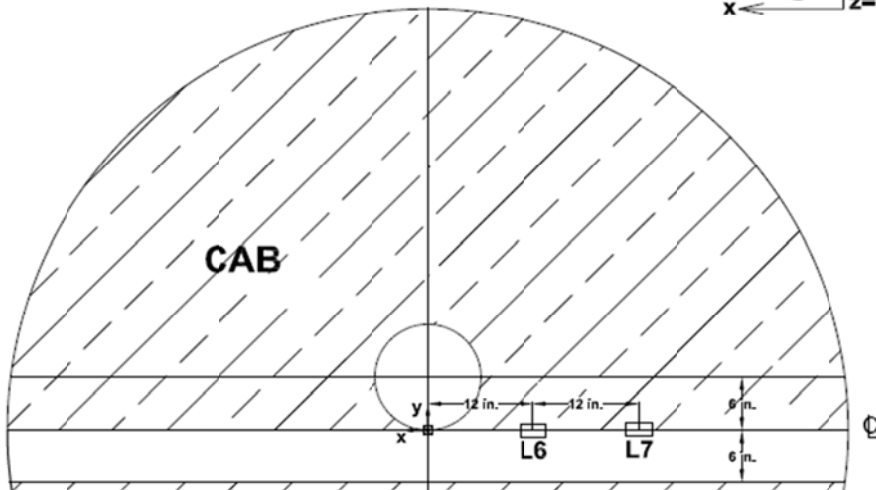
While the technique of double integrating the acceleration records collected from paired accelerometers embedded at the same location in two different materials produced good results in the flexible pavement experiments, it was not as successful in the rigid pavement experiments when used to assess the slippage at the interface between the bottom of the slab and the

supporting base layer. The data collected were not reliable to carry out the integration algorithm, which might be attributed to difficulties associated with the installation of the accelerometers. Accordingly, two LVDTs were added in each experiment to provide a direct measurement of such potential slippage. These LVDTs were placed in the 6-inch gap between the two slabs and were attached in a way that allowed measuring the relative movement between the PCC and the CAB. This was achieved by attaching the LVDT body to the PCC while securing the tip of its shaft to a fixed point in the CAB. Figure 4.50 (elevation view) and Figure 4.51 (plan view) show the locations of the LVDTs at 12 and 24 inches from the centerline of the load along the edge of the loaded slab. While one of the two LVDTs (L7 at 24 inches from the centerline of the load) did not consistently produce dependable data due to loss of anchor of the LVDT shaft tip, good-quality data were produced with L7 and carefully examined.

Figure 4.52 shows the PCC-CAB slippage measurements at the various load levels for both dry and wet testing for all experiments. Based on the data in Figure 4.52, it could be generally concluded that potential slippage between the PCC and the CAB occurred but at different rates and amplitudes. The negative sign associated with all the data collected from L6 indicated that the LVDT shaft moved inward toward the LVDT body. This finding showed that the relative movement between the CAB and the PCC was inward. In other words, the CAB was moving away from the center of the loading more than the PCC slab due to loading. The following specific observations were also made:

- For the dry condition of the pavement structure without any geosynthetics, the same small amount of slippage was observed at the 9-kip and the 12-kip load level. However, this amount was slightly more than doubled when the load increased to 16 kip. In the case of the wet condition, almost the same moderate amount of slippage was observed at all load levels with a slight increase as the load increased.
- For the dry and wet conditions of the pavement structure with geogrid-reinforced base, similar minor slippage was observed and remained almost unchanged as the load increased from 9 to 16 kip.
- For the dry condition of the pavement structure with geotextile-reinforced base, significant slippage was observed and increased modestly as the load increased from 9 to 12 kip. Unfortunately, data at 16 kip were not available. In the case of the wet condition, minor slippage was observed at 9 kip, and the slippage increased significantly when the structure was subjected to 12 kip. Again, data at 16 kip were not available.
- For the dry condition, the addition of the geogrid either kept the same magnitude of slippage or slightly reduced it when compared to the control experiment, while the addition of the geotextile significantly increased the magnitude.
- For the wet condition, the addition of the geogrid reduced the slippage at all load levels when compared to the control experiment, while the addition of the geotextile reduced the slippage at 9 kip but significantly increased it at 12 kip.

Experiments 7, 9 and 10
(Rigid Pavement - Control, Geogrid/Geotextile at the Middle of the Base)



The diagram illustrates a rigid pavement cross-section. The main structure is a semi-circular slab labeled 'CAB'. The base is labeled 'C'. The diagram includes dimensions: a 12 in. horizontal distance from the centerline to the center of the base, and a 6 in. vertical distance from the base to the center of the slab. A coordinate system is shown in the top right corner with the origin at the center of the base, the x-axis pointing left, and the y-axis pointing up. A circular inset in the top right corner shows a top-down view of the slab with a diagonal line and an arrow pointing towards the center.

Copyright National Academy of Sciences. All rights reserved.

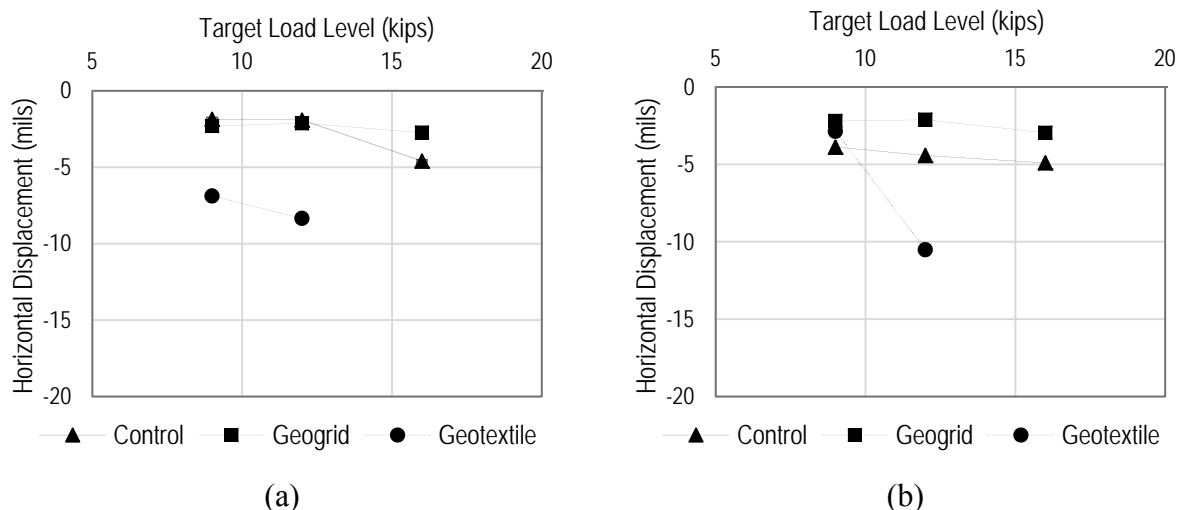


Figure 4.52. PCC-CAB Interface Slippage at the Edge of the PCC Slab (Experiments 7, 9, and 10): (a) Dry Condition; (b) Wet Condition

Finite Element Modeling of Pavements with Geosynthetics

The finite element models were developed using the software ABAQUS to simulate the LST test results (42). They were constructed for pavement structures with and without a geosynthetic layer in order to determine the critical responses of the pavement to different loading conditions. These pavement responses were used to predict the pavement performance. Figure 4.53 shows a typical geosynthetic-reinforced flexible pavement structure used in the LST test. It consisted of a 6-inch hot mix asphalt (HMA) layer, a 6-inch unbound aggregate base course, a 0.08-inch geosynthetic layer, and a subgrade. The geosynthetic layer was placed between the base course and the subgrade. The pavement structure was subjected to dynamic loading cycles with loading amplitudes of 9 kip, 12 kip, and 16 kip, respectively. The loading zone was applied with a circular loading foot with a radius of 6 inches. Figure 4.54 presents the finite element mesh of the geosynthetic-reinforced flexible pavement structure in ABAQUS. The cylindrical flexible pavement structure in the LST test was simplified as an axisymmetric model. Fine mesh was used near the load. The HMA layer, base course, and subgrade were represented as 8-node biquadratic homogeneous solid elements with reduced integration. The geosynthetic layer was represented by the 3-node quadratic membrane element. The interface between the geosynthetic layer and the aggregate/soil layer was characterized by the Goodman element (43).

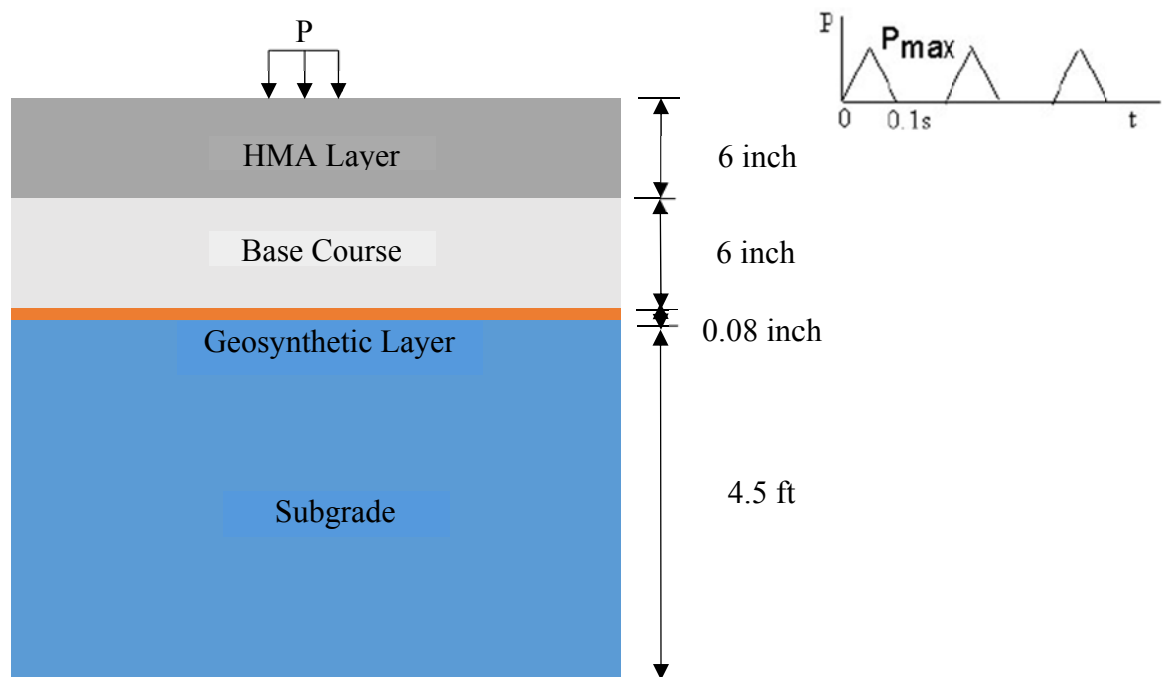


Figure 4.53. Typical Geosynthetic-Reinforced Flexible Pavement Structure in LST Test

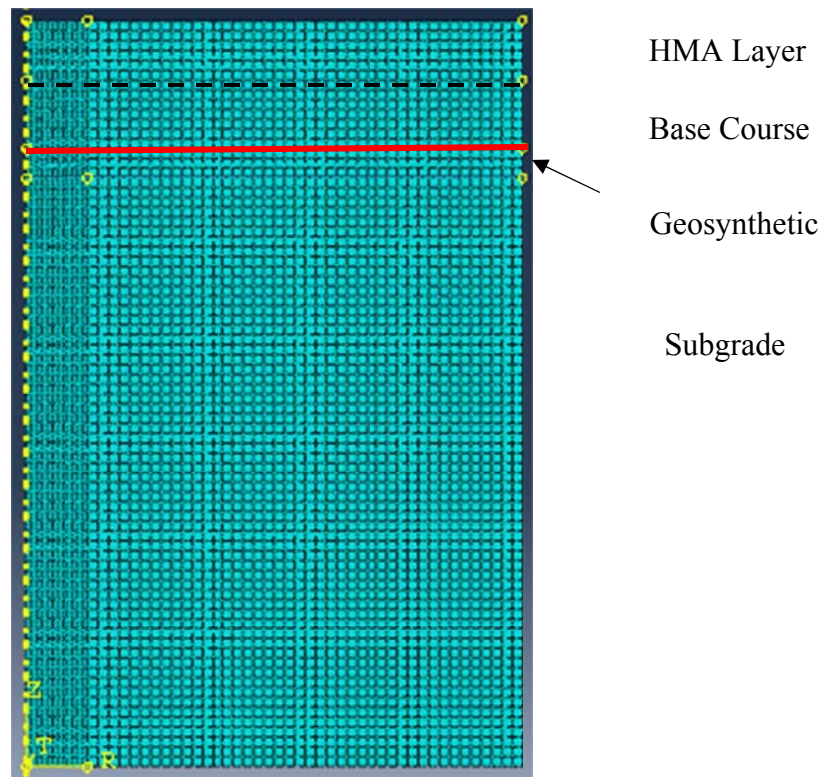


Figure 4.54. Meshed Geosynthetic-Reinforced Pavement Structure in ABAQUS

Figure 4.55 presents a typical geosynthetic-reinforced rigid pavement structure used in the LST test. The structure consisted of a 6-inch PCC layer, an 8-inch unbound granular base, a 0.08-inch geosynthetic layer, and a subgrade. The geosynthetic layer was placed in the center of the base course. The same loading configuration used with the flexible pavement was applied to the rigid pavement. Since a 6-inch gap existed between the two concrete slabs, the geosynthetic-reinforced rigid pavement could not be simulated as an axisymmetric structure. Figure 4.56 shows the meshed three-dimensional geosynthetic-reinforced rigid pavement model in ABAQUS.

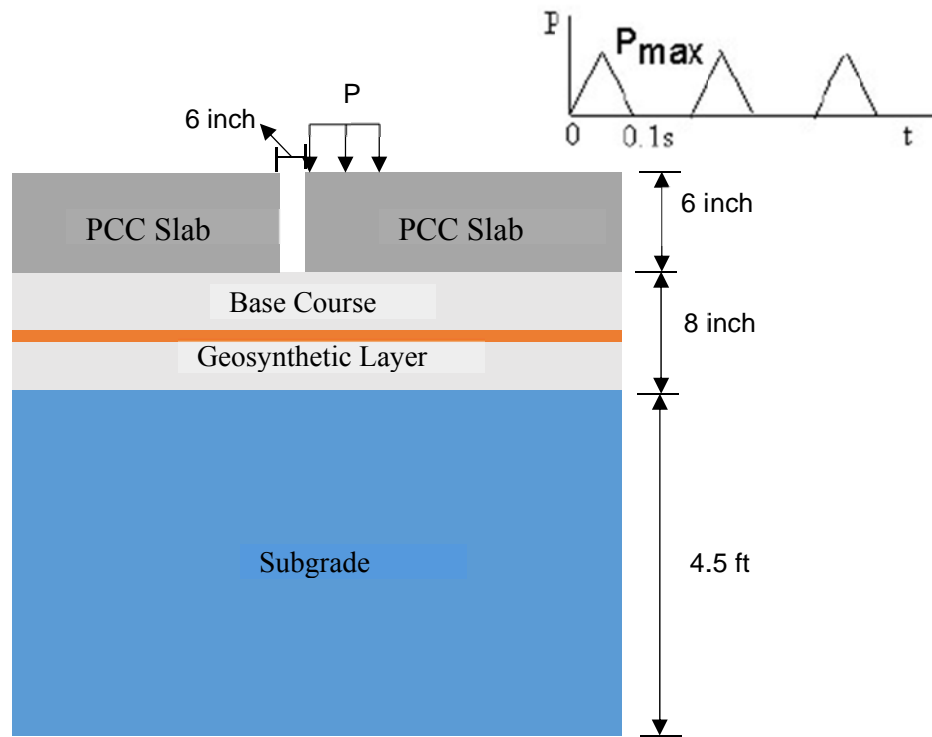


Figure 4.55. Typical Geosynthetic-Reinforced Rigid Pavement Structure in LST Test

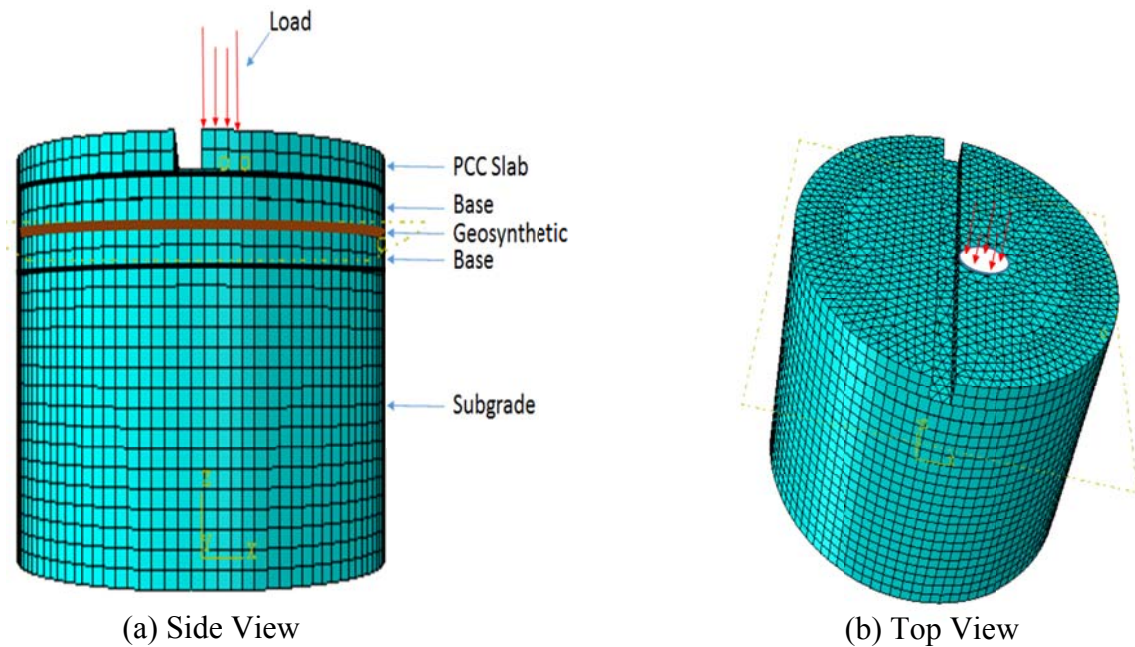


Figure 4.56. Meshed Geosynthetic-Reinforced Rigid Pavement Structure in ABAQUS

Characterization of Materials Used in LST Test

In this study, the HMA layer was characterized as a viscoelastic material, the PCC slab was a linear elastic material, the base layer with and without geosynthetic was defined as a nonlinear cross-anisotropic elastic material, and the subgrade was assumed to be a linear elastic material. Table 4.9 presents the selected laboratory tests used to characterize the materials in the LST test and the corresponding input parameters to the finite element models. The dynamic modulus test was used to characterize the viscoelastic behavior of asphalt concrete. The compressive strength test was employed to estimate the elastic modulus of the PCC slab (62). The nonlinear cross-anisotropic properties of the geogrid-reinforced and unreinforced base material were determined using the rapid triaxial test. The tensile sheet stiffness of the geogrid material was measured by the direct tension test. The elastic modulus of the subgrade was estimated using the California bearing ratio test (62).

Table 4.9. Selected Laboratory Tests for Material Characterization

Material Type	Constitutive Model	Lab Test	Model Input
HMA	Viscoelastic	Dynamic modulus test	Prony-series parameters (G_i , K_i , and τ_i), Poisson's ratio
PCC	Elastic	Compressive strength test	Young's modulus, Poisson's ratio
Base course	Nonlinear cross-anisotropic	Rapid triaxial test	Inputs of the developed subroutine
Geosynthetic	Elastic	Direct tension test	Tensile sheet stiffness, Poisson's ratio
Subgrade	Elastic	CBR test	Young's modulus, Poisson's ratio

In the software ABAQUS, Prony-series models were used to characterize the time-dependent viscoelastic behavior of the hot mix asphalt, as shown in Equations 4.17 and 4.18.

$$G(t) = G_0 \left(1 - \sum_{i=1}^n G_i \left(1 - e^{-t/\tau_i} \right) \right) \quad (4.17)$$

$$K(t) = K_0 \left(1 - \sum_{i=1}^n K_i \left(1 - e^{-t/\tau_i} \right) \right) \quad (4.18)$$

where $G(t)$ and $K(t)$ are relaxation shear modulus and bulk modulus; G_0 and K_0 are instantaneous shear modulus and bulk modulus; and G_i , K_i , and τ_i are the input coefficients. The method of fitting the Prony-series parameters with the dynamic modulus test result is as follows. The relaxation modulus of a linearly viscoelastic material can be expressed as:

$$E(t) = E_\infty^a + \sum_{i=1}^n \left(E_i^a e^{-\frac{t}{\tau_i}} \right) \quad (4.19)$$

where $E(t)$ is the relaxation elastic modulus; and E_∞^a , E_i^a , and τ_i are the regression coefficients in the model. Accordingly, the storage and loss moduli can be expressed by Equations 4.20 and 4.21. The magnitude of the dynamic modulus is given in Equation 4.22.

$$E'(\omega) = E_\infty^a + \sum_{i=1}^n \frac{\omega^2 \tau_i^2 E_i^a}{1 + \omega^2 \tau_i^2} \quad (4.20)$$

$$E''(\omega) = \sum_{i=1}^n \frac{\omega \tau_i E_i^a}{1 + \omega^2 \tau_i^2} \quad (4.21)$$

$$|E^*| = \sqrt{E'^2 + E''^2} \quad (4.22)$$

where $E'(\omega)$ and $E''(\omega)$ are the storage and loss modulus, respectively; ω is the angular velocity; and $|E^*|$ is the magnitude of the dynamic modulus. By fitting the dynamic modulus test

result, the unknown parameters in Equation 4.19 could be determined based on the least square error criterion. As observed in Equations 4.17 and 4.19, the form of the Prony-series model in ABAQUS was slightly different from the model used for fitting the dynamic modulus test result. Parameter conversions between Equations 4.17 and 4.19 were required and are provided in Equations 4.23–4.27. Table 4.10 lists the determined Prony-series model coefficients used to characterize the asphalt concrete in ABAQUS. Figure 4.57 compares the fitted dynamic moduli with the measured ones, showing that the fitted dynamic moduli accurately matched the dynamic modulus test result.

$$E_0 = E_\infty + \sum_{i=1}^n E_i^a \quad (4.23)$$

$$E_i = \frac{E_i^a}{E_0} \quad (4.24)$$

$$G_0 = \frac{E_0}{2(1+\nu)} \quad (4.25)$$

$$K_0 = \frac{E_0}{3(1-2\nu)} \quad (4.26)$$

$$G_i = K_i = E_i \quad (4.27)$$

where E_0 is the instantaneous elastic modulus, and ν is the Poisson's ratio.

Table 4.10. Determined Prony-Series Model Coefficients for the Plant-Mixed, Laboratory-Compacted (PMLC) Asphalt Concrete

<i>i</i>	Prony-Series Coefficients		
	G_i	K_i	τ_i
1	0.362	0.362	4.09E-06
2	0.363	0.363	2.56E-04
3	0.1765	0.1765	7.71E-03
4	0.074	0.074	2.10E-01
5	0.0165	0.0165	3.88E+00
6	0.0057	0.0057	6.53E+01

Note: Elastic parameters: instantaneous modulus = 2630 ksi; Poisson's ratio = 0.35.

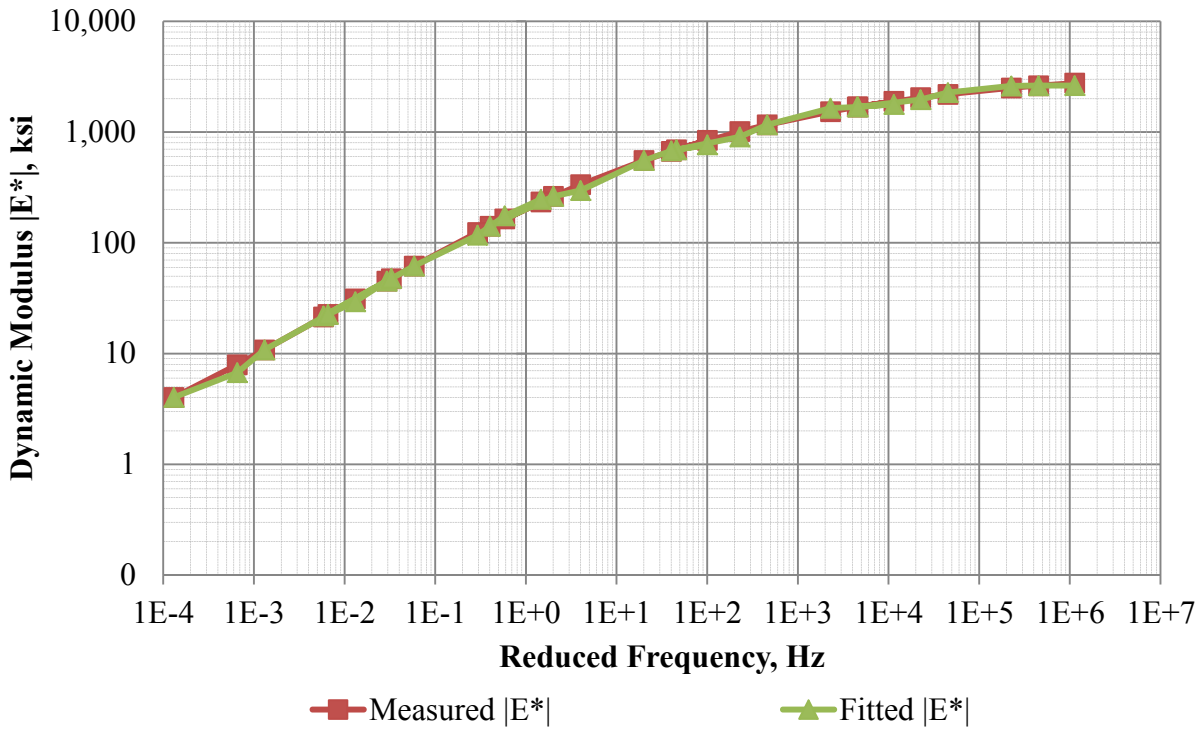


Figure 4.57. Comparison between the Measured Dynamic Moduli and the Fitted Dynamic Moduli

As stated in the previous section, the RaTT was employed to determine the cross-anisotropic properties of the UGM used in the LST test. The test data are given in Appendix L. The constitutive models of the UGM used in this study are shown in Equations 4.28 to 4.30 (22).

$$E_y = k_1 P_a \left(\frac{I_1}{P_a} \right)^{k_2} \left(\frac{\tau_{oct}}{P_a} + 1 \right)^{k_3} \quad (4.28)$$

$$n = \frac{E_x}{E_y} \quad (4.29)$$

$$m = \frac{G_{xy}}{E_y} \quad (4.30)$$

where I_1 is the first invariant of the stress tensor; τ_{oct} is the octahedral shear stress; P_a is the atmospheric pressure; k_1 , k_2 , and k_3 are regression coefficients; E_x is the horizontal resilient modulus; E_y is the vertical resilient modulus; and G_{xy} is the shear modulus in the $x - y$ plane. Table 4.11 presents the cross-anisotropic properties of the UGM determined in the LST test.

Table 4.11. Cross-Anisotropic Properties of the UGM Used in LST Test

Parameters	k_1	k_2	k_3	n	m	ν_{xy}	ν_{xx}
Determined Values	1545	0.75	-0.1	0.45	0.35	0.17	0.43

The direct tension tests were conducted to determine the sheet stiffness of geosynthetic products used in the LST tests (see Figure 4.58). Figure 4.59 shows the relationships between the tensile force and the tensile strain for the tested geogrid and geotextile. MD is the abbreviation for machine direction. XMD is the abbreviation for cross-machine direction. Both the geogrid and geotextile had smaller sheet stiffnesses in the machine direction than in the cross-machine direction. The ductility of geosynthetics in the machine direction was much higher than that in the cross-machine direction. The sheet moduli at 2 percent strain and 5 percent strain were compared to the data in the manufacturer's specifications, as shown in Table 4.12. Researchers found that all of the determined geosynthetic sheet moduli were higher than the data in the manufacturer's specifications.



(a) Tensile Test Setup for Geogrid



(b) Tensile Test Setup for Geotextile

Figure 4.58. Direct Tension Test for Determining Sheet Stiffness of Geosynthetics

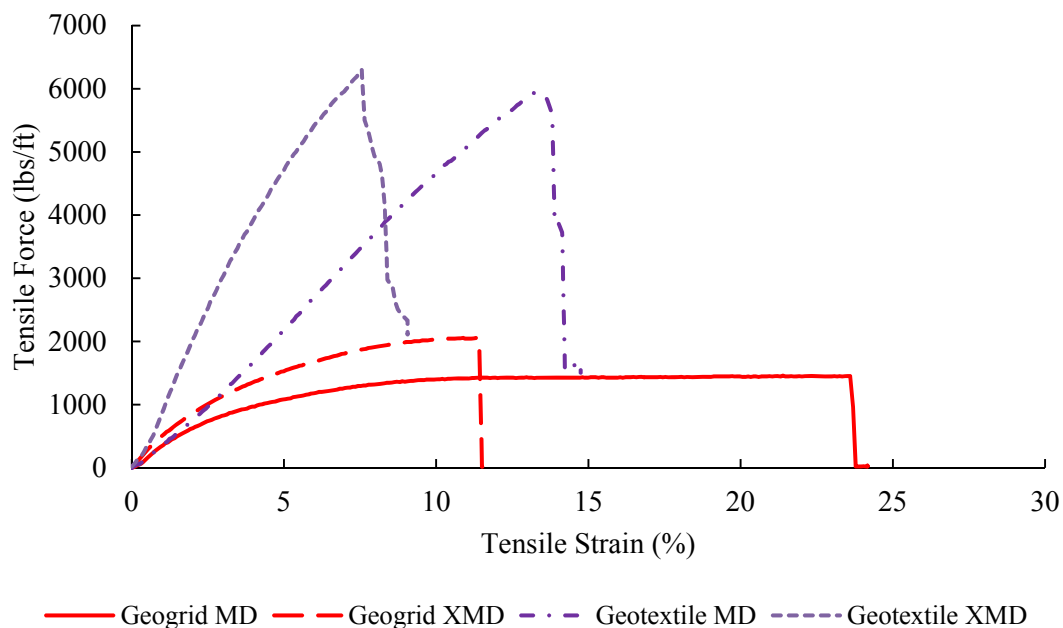


Figure 4.59. Relationships between Tensile Force and Tensile Strain for Geosynthetics

Table 4.12. Comparison of Geosynthetic Sheet Stiffness Values between Laboratory Test and Manufacturer's Specifications

Geosynthetic Type	Mechanical Properties—Test		Mechanical Properties—Specification	
	Sheet Stiffness @ 2% Strain (lb/in)	Sheet Stiffness @ 5% Strain (lb/in)	Sheet Stiffness @ 2% Strain (lb/in)	Sheet Stiffness @ 5% Strain (lb/in)
Geogrid MD Value	2650	1840	1713	1348
Geogrid XMD Value	3608	2563	2569	2232
Geotextile MD Value	3175	3589	NA	NA
Geotextile XMD Value	8419	7818	7505	NA

Note: NA = not available.

Development of Nonlinear Cross-Anisotropic User-Defined Material Subroutine

A user-defined material (UMAT) subroutine was developed to characterize the nonlinear cross-anisotropic behavior of the UGM in the software ABAQUS. The UMAT subroutine adopted the direct secant modulus approach to determine the nonlinear resilient modulus solution in each iteration. The trial vertical modulus was computed using Equation 4.31 in each iteration (63).

$$E_y^i = (1 - \lambda) E_y^{i-1} + \lambda E_{ycomputed}^i \quad (4.31)$$

where E_y^i is the vertical modulus output from the i^{th} iteration; E_y^{i-1} is the vertical modulus output from the $(i-1)^{\text{th}}$ iteration; λ is the damping factor; and $E_{ycomputed}^i$ is the vertical modulus computed in Equation 4.28 at the i^{th} iteration. The convergence criteria are shown in Equations 4.32 and 4.33 (64).

$$Error_i = \frac{|E_y^i - E_y^{i-1}|}{|E_y^i|} \leq 2\% \quad (4.32)$$

$$Error_c = \frac{\sum_{i=1}^n (E_y^i - E_y^{i-1})^2}{\sum_{i=1}^n (E_y^i)^2} \leq 0.5\% \quad (4.33)$$

where $Error_i$ is the individual error for each node; $Error_c$ is the cumulative error for the entire model; and n is the number of nodes in the model. The secant modulus nonlinear solution technique was less complicated than the tangent stiffness approach, but it was adequate to provide good convergence of the iterations. Figure 4.60 shows the flowchart of the developed UMAT subroutine.

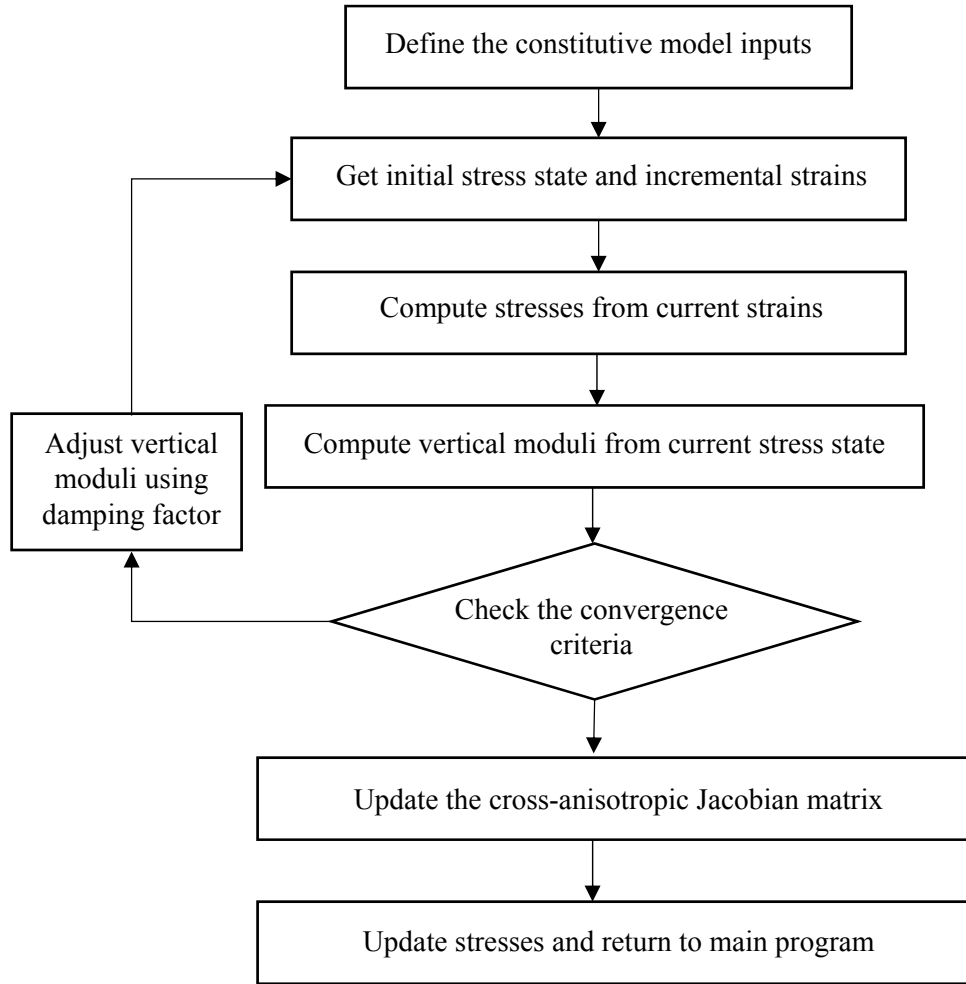


Figure 4.60. Flowchart of the Developed UMAT Subroutine

Development of Goodman Model Friction Subroutine

When surfaces of the geosynthetic and aggregate/soil were in contact, they usually transmitted shear and normal stresses across their interface. In this study, the interface element between the geosynthetic surface and the aggregate/soil surface was characterized using the Goodman model (4), which is shown in Equation 4.34.

$$\begin{bmatrix} d\tau \\ d\sigma_n \end{bmatrix} = \begin{bmatrix} k_s & 0 \\ 0 & k_n \end{bmatrix} \begin{Bmatrix} du_r \\ dv_r \end{Bmatrix} \quad (4.34)$$

where τ is the shear stress; σ_n is the normal stress; u_r is the relative shear displacement; v_r is the relative normal displacement; k_s is the shear stiffness; and k_n is the normal stiffness. The interface slippage condition was quantified by the shear stiffness, k_s . If the geosynthetic-aggregate/soil interface was fully bonded, the shear stiffness was assigned a large value, for example, $k_s = 1 \times 10^8$ lb/in. If the slippage occurred at the geosynthetic-aggregate/soil interface,

the shear stiffness, k_s , was determined using the pullout test data. This tangential contact behavior was defined by the user subroutine FRIC in the ABAQUS software.

Numerical Modeling Techniques for Geosynthetic-Reinforced Pavement Structures

As mentioned previously, the reinforcement mechanisms of a geosynthetic included the lateral confinement and the vertical membrane effect. In ABAQUS, the vertical membrane effect was simulated by assigning the geosynthetic as a membrane element. However, the numerical model could not directly characterize the lateral confinement, which effectively reinforced the base material. In the numerical model, the lateral confinement of a geosynthetic was equivalent to an additional confining stress distributed in the geosynthetic influence zone, which affected the resilient modulus of the base course. For the sake of simplicity, the lateral confinement was simulated in this study by assigning the geosynthetic-reinforced base material a higher modulus value. Figure 4.61 illustrates the schematic plot to simulate the lateral confinement in the geosynthetic-reinforced pavement structure. As shown in Figure 4.61a, the shaded area is an influence zone. Previous studies reported that the influence zone ranged from 4 to 6 inches (18, 19, 65). The range of influence zone was herein assumed to be 6 inches in height when the geosynthetic was placed in the middle of the base course. In this range, the geosynthetic-reinforced base material had a higher modulus than the unreinforced material. The analytical models shown in Equations 4.13 and 4.14 were used to determine the modulus of the base material in the influence zone. The base material outside of the influence zone was considered an unreinforced material. The findings of the laboratory test evaluation indicated that placing the geosynthetic layer in the middle of the base material affected its horizontal and vertical modulus, while placing the geosynthetic layer at the bottom exerted a minor influence on the modulus of the base material. Therefore, no influence zone was assumed in the model when the geosynthetic was placed at the bottom of the base course, as shown in Figure 4.61b. This simulation represented the modulus of the base material to be the same as that of the unreinforced material.

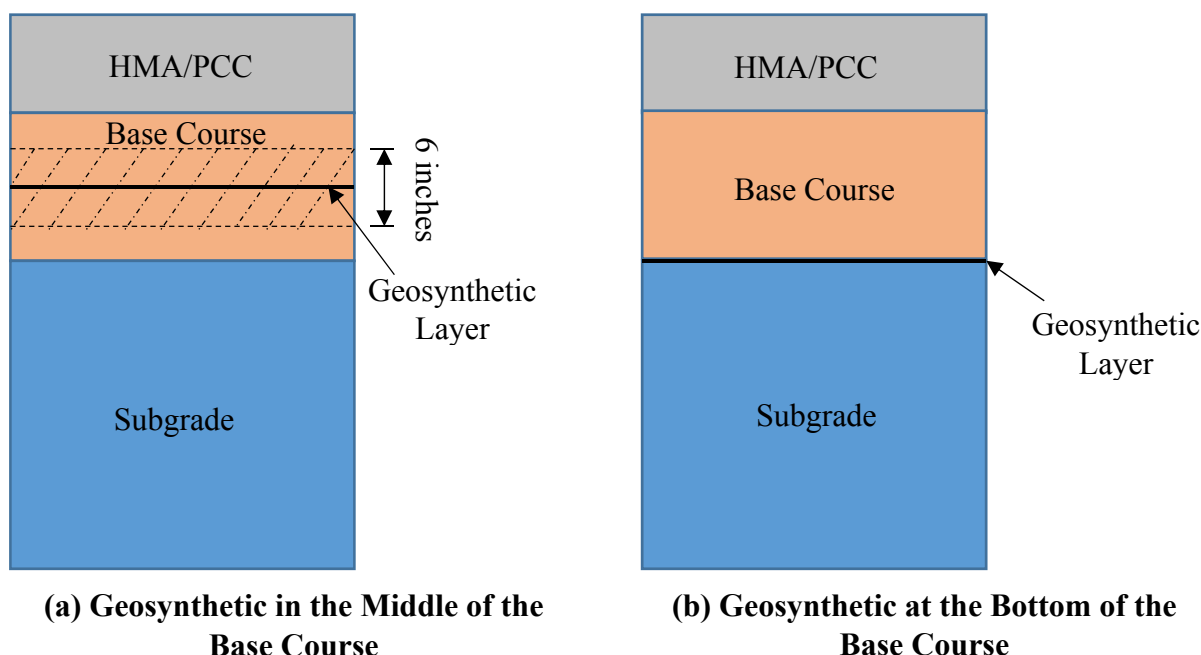


Figure 4.61. Simulation of Lateral Confinement in Geosynthetic-Reinforced Pavement Structure

Effect of Geosynthetic Reinforcement on Pavement Responses

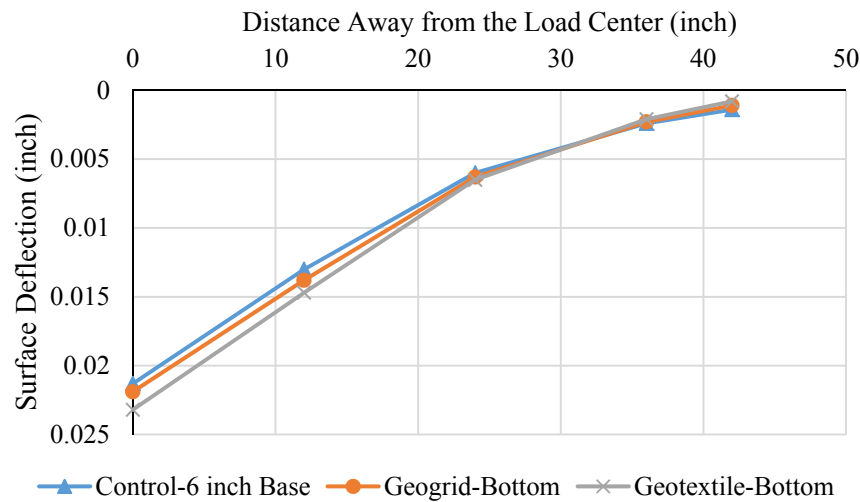
The current Pavement ME Design software predicts pavement performance based on the following computed critical responses by the embedded finite element program (62).

- For flexible pavements:
 - Horizontal tensile strain at the bottom of the asphalt layer for fatigue cracking.
 - Vertical compressive strains within the asphalt layer, base course, and subgrade for rutting.
- For rigid pavements:
 - Tensile bending stress at the bottom of the slab for bottom-up transverse cracking.
 - Tensile stress at the top of the slab for top-down transverse cracking.
 - Differential deflections across a joint for faulting.

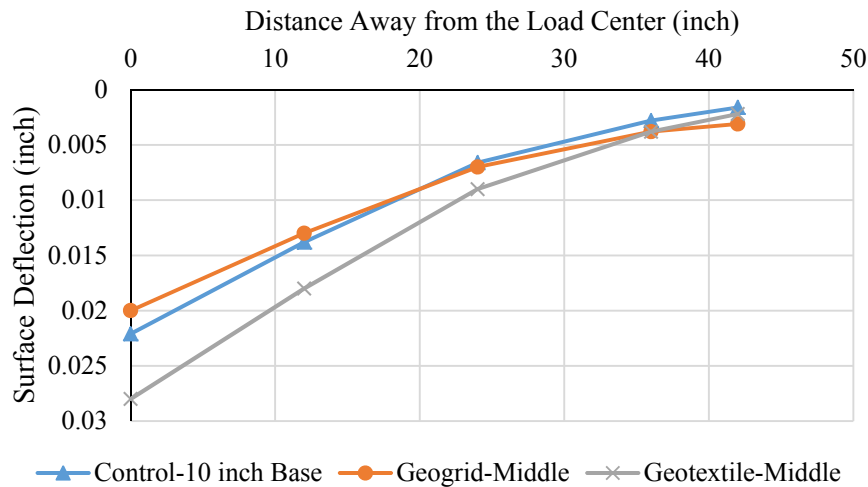
In this study, the critical responses of pavement with and without geosynthetics were computed based on the developed user subroutines and the proposed modeling techniques. The pavement models selected were similar to the pavement structures shown in Figures 4.53 and 4.55, respectively. The flexible pavement structures included a 6-inch base course with the geogrid or geotextile placed at the bottom, a 10-inch base course structure with the geogrid or geotextile placed in the middle, and the corresponding unreinforced structures. The rigid pavement structures included an 8-inch base course with the geogrid or geotextile placed in the center or at the bottom of the base course, and the corresponding control structure.

Figures 4.62a and 4.62b compare the surface deflections of the geosynthetic-reinforced flexible pavement models with those of the unreinforced pavement models when they were

subjected to a 9-kip load on a circular area with the radius of 6 inches. The figure shows that placing the geogrid and geotextile at the bottom of the base course cannot reduce the surface deflections of the flexible pavement, while placing the geogrid in the middle of the base course only slightly decreases the surface deflections. The surface deflections of flexible pavement with the geotextile in the middle of the base layer are much larger than those of the unreinforced pavement. There are two reasons for this phenomenon. One is that placing the geotextile in the middle slightly reduces the vertical modulus of the base material. The other is that the slippage that occurs between the geotextile surface and the aggregate layer decreases the bonding coefficient of the geotextile-aggregate interface.



(a) Surface Deflections of Flexible Pavement Structures with 6-inch Base Course



(b) Surface Deflections of Flexible Pavement Structures with 10-inch Base Course

Figure 4.62. Surface Deflections of Flexible Pavement Structures with and without Geosynthetic

Distributions of the vertical stress beneath the load center within the flexible base layer are plotted in Figures 4.63a and 4.63b. The geogrid and geotextile-reinforced flexible pavement

structures diminished the vertical compressive stresses within the base layer by 2–3 psi. The decrease of vertical compressive stresses within the base layer was beneficial for reducing the permanent deformation of the base materials.

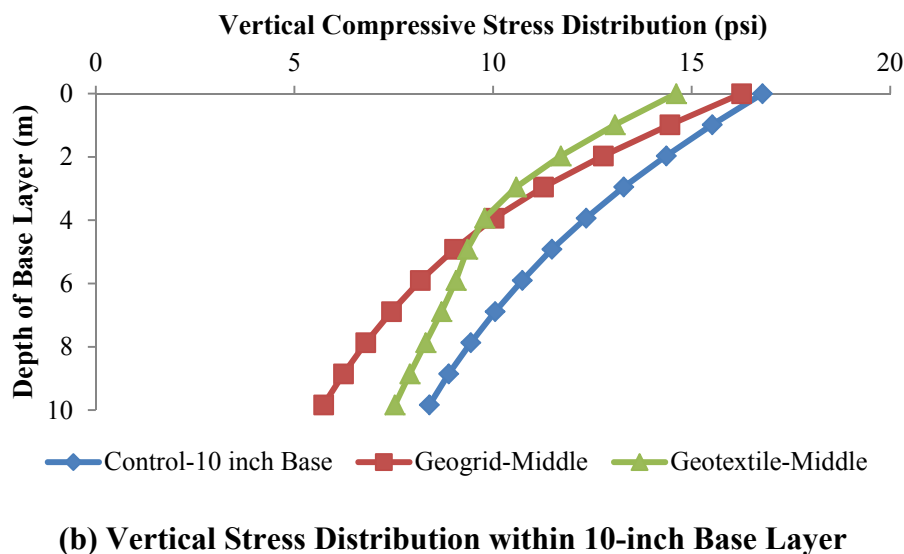
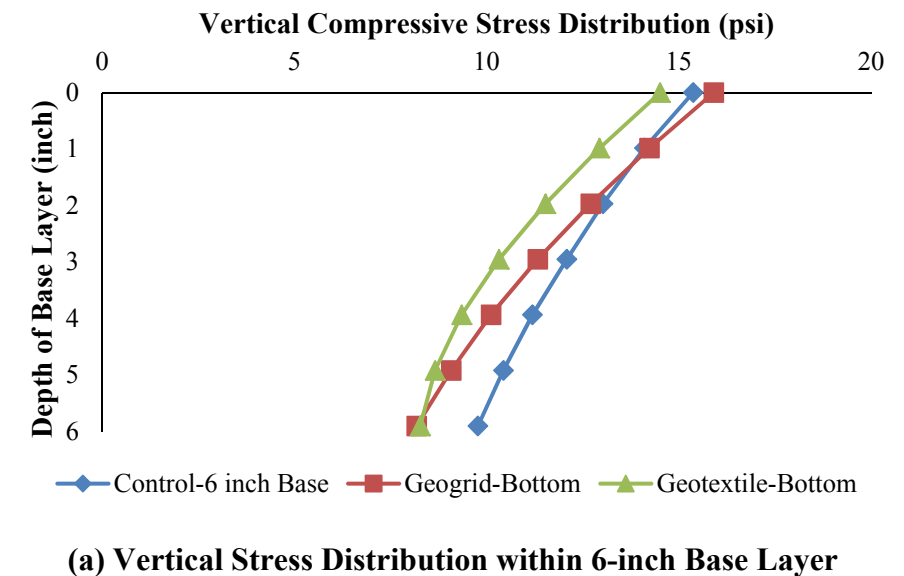


Figure 4.63. Vertical Stress Distribution within Geosynthetic-Reinforced and Unreinforced Flexible Base Layer

In addition, Table 4.13 presents the computed critical strains in the geosynthetic-reinforced and unreinforced flexible pavements. As the table shows, the geosynthetic reinforcement did not reduce the tensile strain at the bottom of the asphalt layer. This finding indicated that the application of a geosynthetic did not significantly influence the fatigue cracking performance of flexible pavements. In contrast, placing the geogrid and geotextile in the middle of the base course could decrease the average compressive strain in the unreinforced base layer by 17 percent and 10 percent, respectively. The geogrid and geotextile reinforced at

the bottom of the base course did not affect the compressive strain in the base layer, but they both diminished the compressive strain at the top of the subgrade significantly. This finding demonstrated that a geosynthetic reinforced in the middle of the base course reduced the permanent deformation of the base layer, while a geosynthetic reinforced at the bottom of the base course helped decrease the permanent deformation of the subgrade.

Table 4.13. Computed Critical Strains for Geosynthetic-Reinforced and Unreinforced Flexible Pavement Structures

Pavement Structure	Tensile Strain at the Bottom of AC ($\mu\epsilon$)	Average Compressive Strain in Base Layer ($\mu\epsilon$)	Compressive Strain at Top of Subgrade ($\mu\epsilon$)
Control—6-inch Base	214	719	677
Geogrid—Bottom	231	735	421
Geotextile—Bottom	243	681	353
Control—10-inch Base	215	645	516
Geogrid—Middle	205	539	462
Geotextile—Middle	255	579	524

Figure 4.64 presents the load-induced tensile bending stresses at the bottom of the PCC slab for the geosynthetic-reinforced and unreinforced rigid pavements. As the figure shows, the geosynthetics slightly reduced the tensile bending stress at the bottom of the PCC slab. The tensile bending stress at the bottom of the PCC slab was not sensitive to the location and the type of geosynthetic.

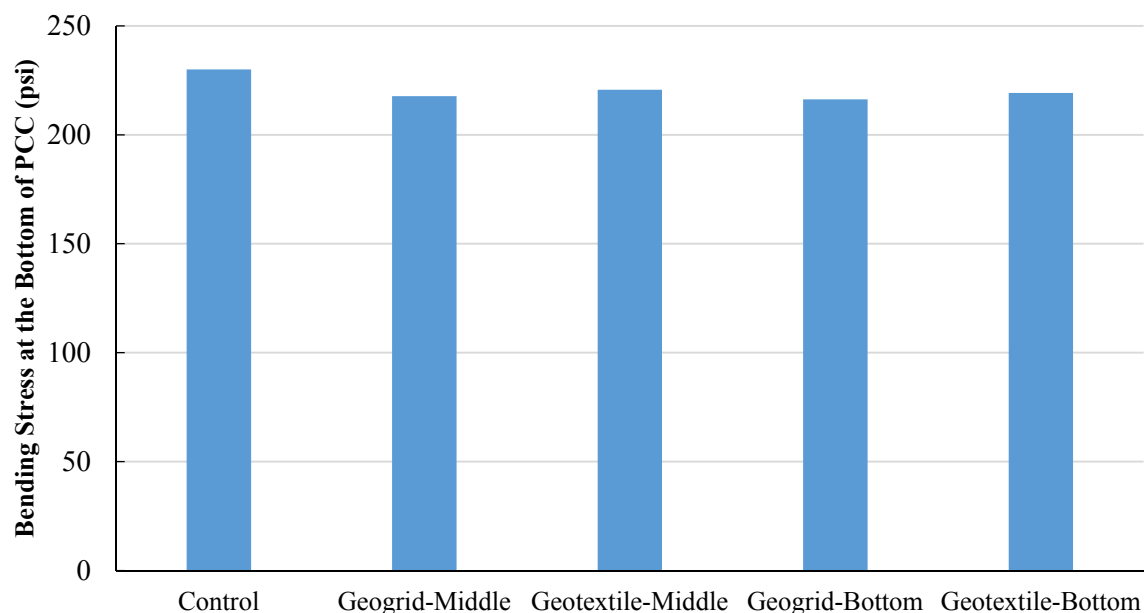


Figure 4.64. Tensile Bending Stresses at the Bottom of the PCC Slab for the Geosynthetic-Reinforced and Unreinforced Rigid Pavements

Figure 4.65 shows the load-induced tensile stress at the top of the PCC slab for the geosynthetic-reinforced and unreinforced rigid pavements. There was no significant difference observed among the geosynthetic-reinforced and unreinforced rigid pavements. This finding indicated that the influence of geosynthetic type and geosynthetic location on the tensile stress at the top of the PCC slab is negligible.

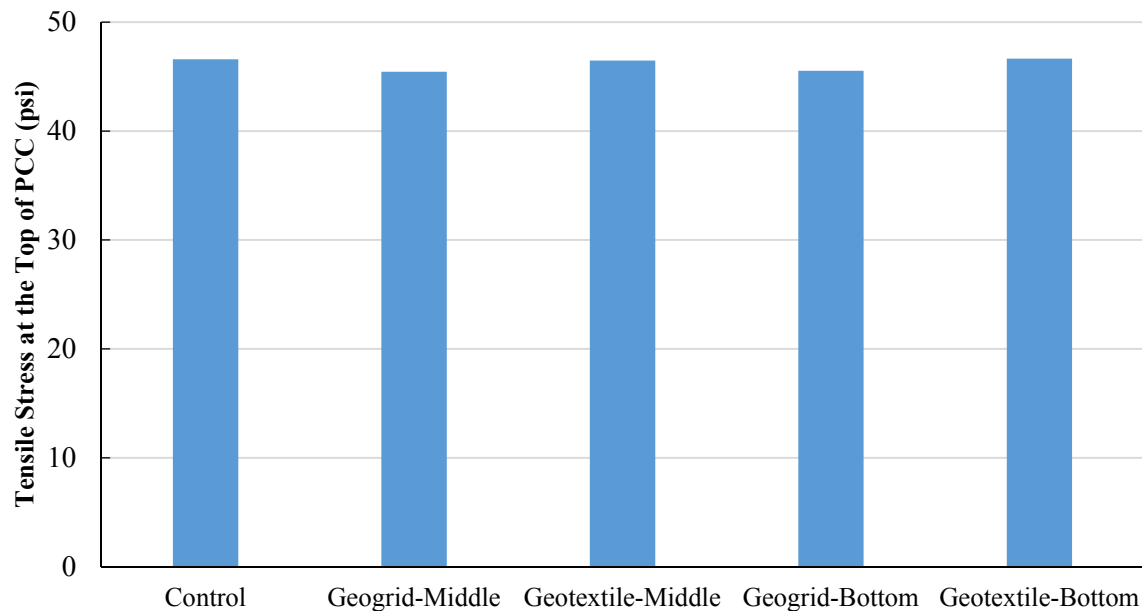


Figure 4.65. Tensile Stresses at the Top of the PCC Slab for the Geosynthetic-Reinforced and Unreinforced Rigid Pavements

Parametric Study of Material Properties on Pavement Performance

The sensitivity analysis of the pavement responses predicted by the finite element model was conducted by varying the material properties, such as the subgrade modulus and the geosynthetic sheet stiffness, and the thickness of the base course. Researchers found that the primary advantage of geosynthetic reinforcement was the reduction of the vertical compressive strain in the base course and at the top of the subgrade. Therefore, the pavement responses studied in the sensitivity analysis specifically referred to these two critical strains. The unreinforced pavement structure consisted of a 4-inch HMA layer and a 6-inch base course; the subgrade was analyzed as the control group, which was reinforced by a geosynthetic (geogrid or geotextile) placed in the middle or at the bottom of the base course.

Figures 4.66a and 4.66b show the sensitivity of the model-predicted pavement responses to the variations in the subgrade modulus. The selected subgrade moduli were 5 ksi, 15 ksi, and 25 ksi, which represented the poor, fair, and good quality of the subgrade, respectively. The increase in subgrade modulus remarkably decreased the vertical strain at the top of the subgrade but slightly increased the vertical strain within the base layer. The placement of the geosynthetic was effective at reducing these two critical strains. The reduction of the critical strains due to the geosynthetic reinforcement was normalized using Equation 4.35.

$$\text{Normalized reduction of strain} = \frac{\text{Strain}_{\text{Control}} - \text{Strain}_{\text{Geosynthetic}}}{\text{Strain}_{\text{Control}}} \times 100\% \quad (4.35)$$

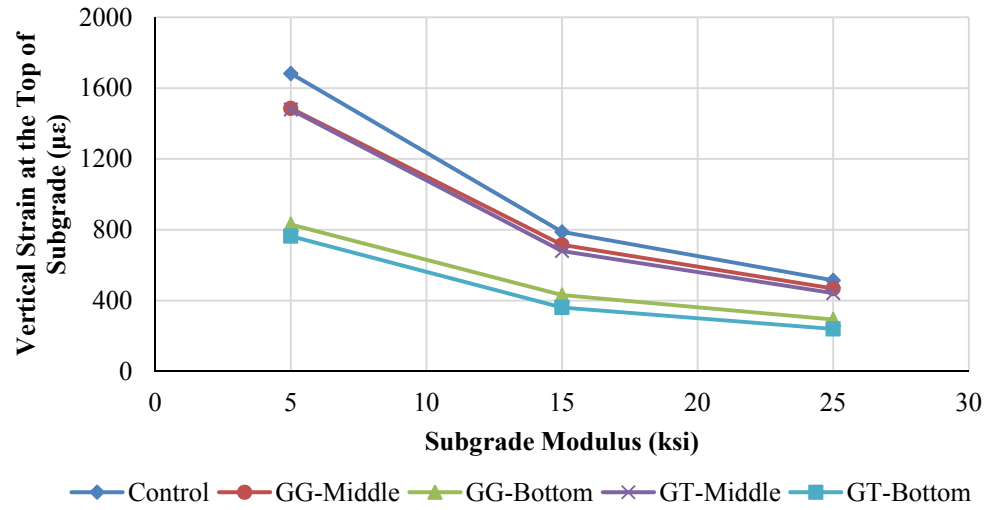
where $\text{Strain}_{\text{Control}}$ is the computed critical strain in the control model; and

$\text{Strain}_{\text{Geosynthetic}}$ is the computed critical strain in the geosynthetic-reinforced model.

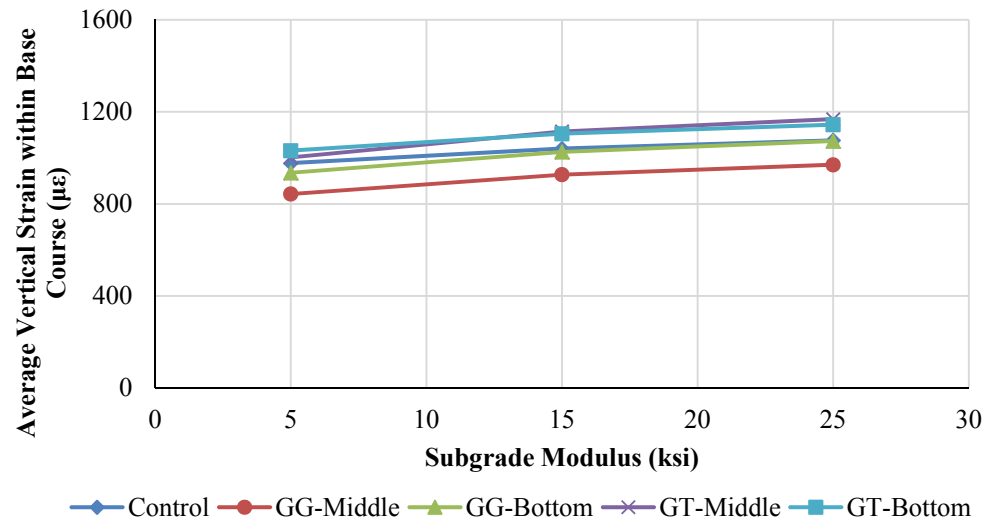
Figure 4.66c indicates that the reduction of the vertical strain at the top of the subgrade was significant when the geogrid or geotextile was placed at the bottom of the base course. The increase in subgrade modulus did not influence the normalized reduction of the subgrade vertical strain due to the presence of the geotextile but slightly decreased the reduction percentage due to the presence of the geogrid. Figure 4.66d illustrates that the geosynthetic reinforced in the middle of the base course effectively reduced the vertical strain, while the geosynthetic located at the bottom of the base course slightly increased the base vertical strain. With the increase in the subgrade modulus, the normalized reduction of the base vertical strain due to the geosynthetic decreased by approximately 5 percent. This finding indicated that geosynthetic reinforcement was more effective when it was placed over a weaker subgrade, which normally had a lower resilient modulus.

Figures 4.67a and 4.67b show the sensitivity of the pavement responses predicted by the model to the variation of the geosynthetic sheet stiffness. Both the vertical strain at the top of the subgrade and the average vertical strain within the base layer decreased with the geosynthetic sheet stiffness. This finding indicated that the geosynthetic with a higher sheet stiffness was more efficient at reducing the permanent deformation of the pavement structure.

Figure 4.68 indicates that the developed geosynthetic-reinforced and unreinforced pavement models were also sensitive to the thickness of the base course in predicting the vertical strains in the base layer and the subgrade. The figure shows that increasing the thickness of the base course reduced both the vertical compressive strain at the top of the subgrade and the vertical strain within the base course. The geosynthetic reinforcement was more effective for a thin base layer in terms of the percent reduction of vertical strains in the base and subgrade.

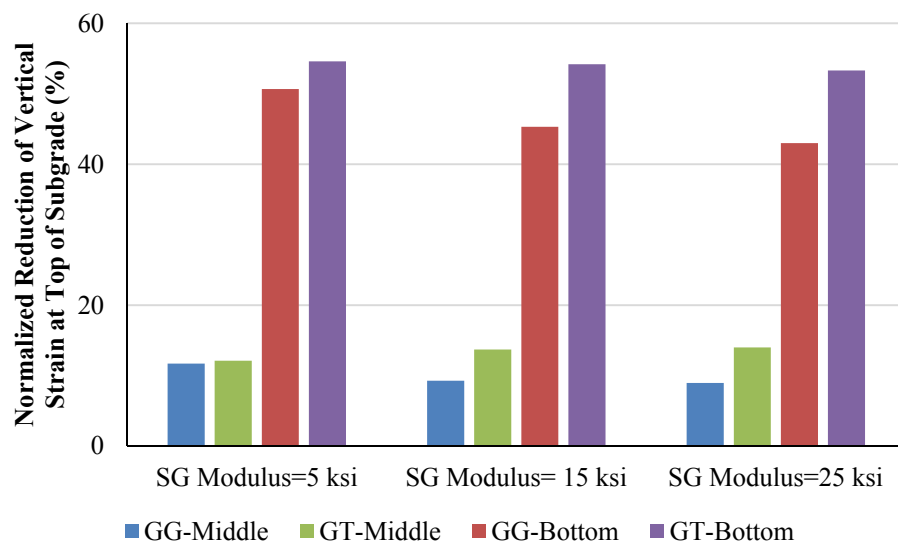


(a) Computed Vertical Strain at the Top of Subgrade

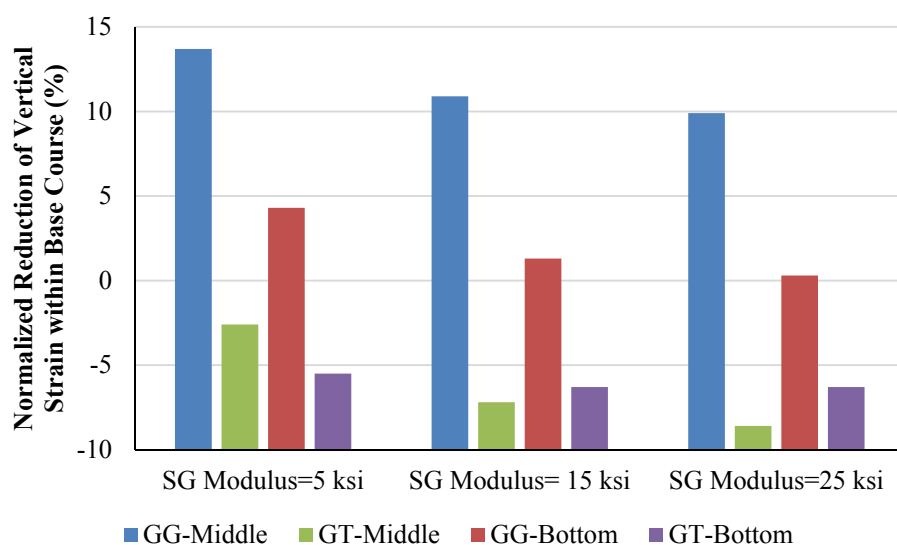


(b) Computed Average Vertical Strain within Base Course

Figure 4.66. Sensitivity of Model-Predicted Pavement Responses to Subgrade Modulus

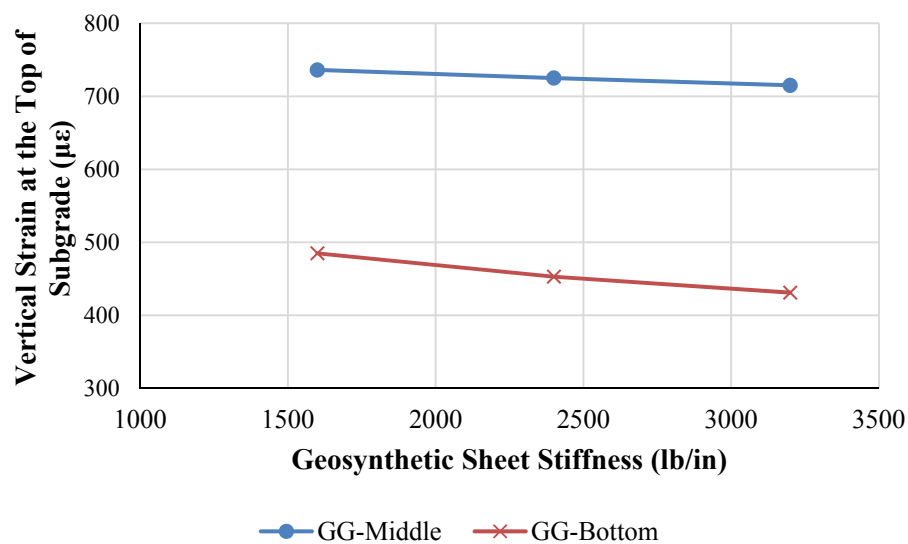


(c) Normalized Reduction of Vertical Strain at the Top of Subgrade

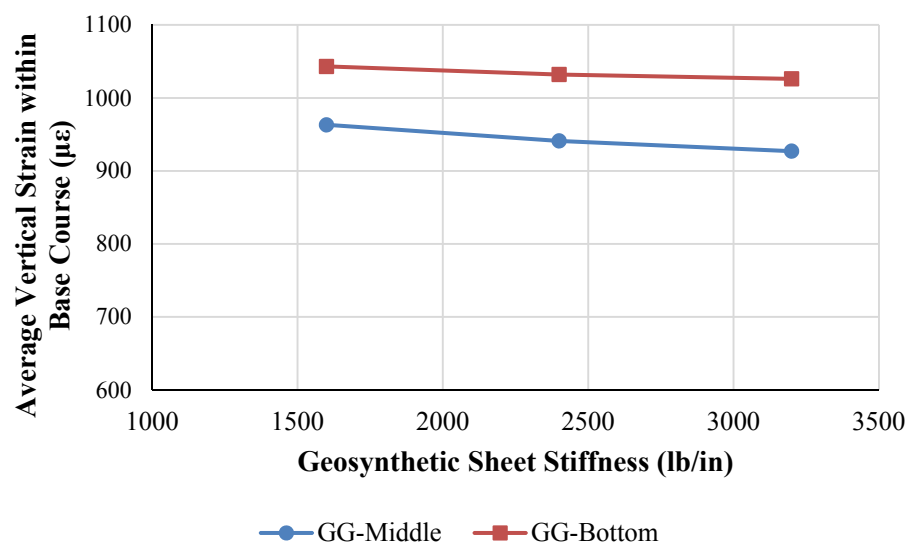


(d) Normalized Reduction of Vertical Strain within Base Course

Figure 4.66. Sensitivity of Model-Predicted Pavement Responses to Subgrade Modulus (Continued)

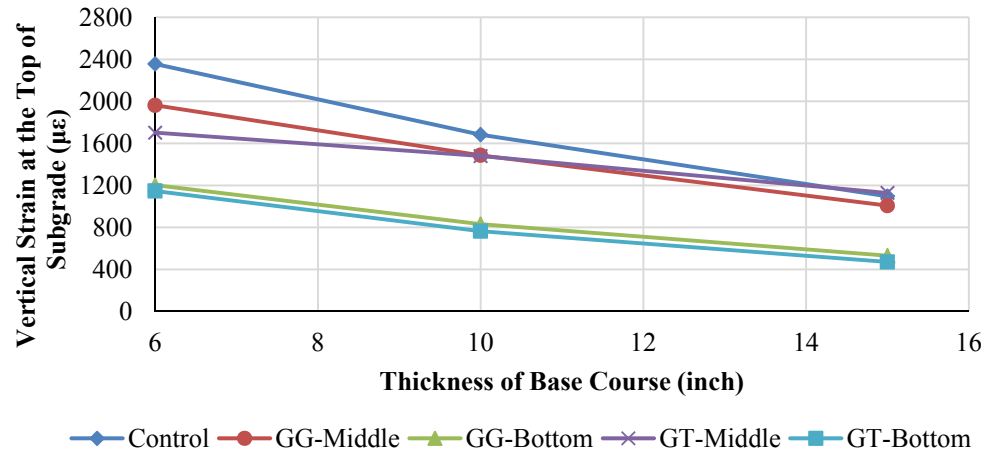


(a) Vertical Strain at the Top of Subgrade

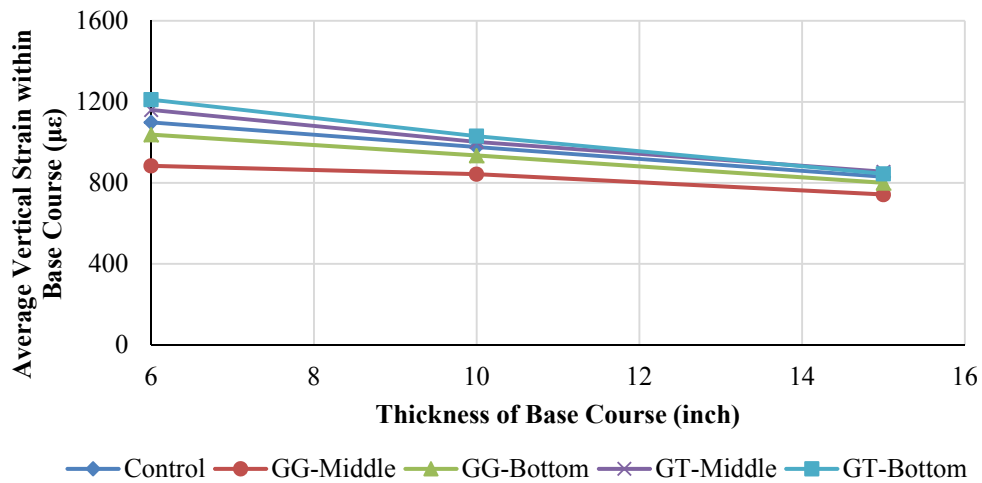


(b) Average Vertical Strain within the Base Course

Figure 4.67. Sensitivity of Model-Predicted Pavement Responses to Geosynthetic Sheet Stiffness



(a) Computed Vertical Strain at the Top of Subgrade

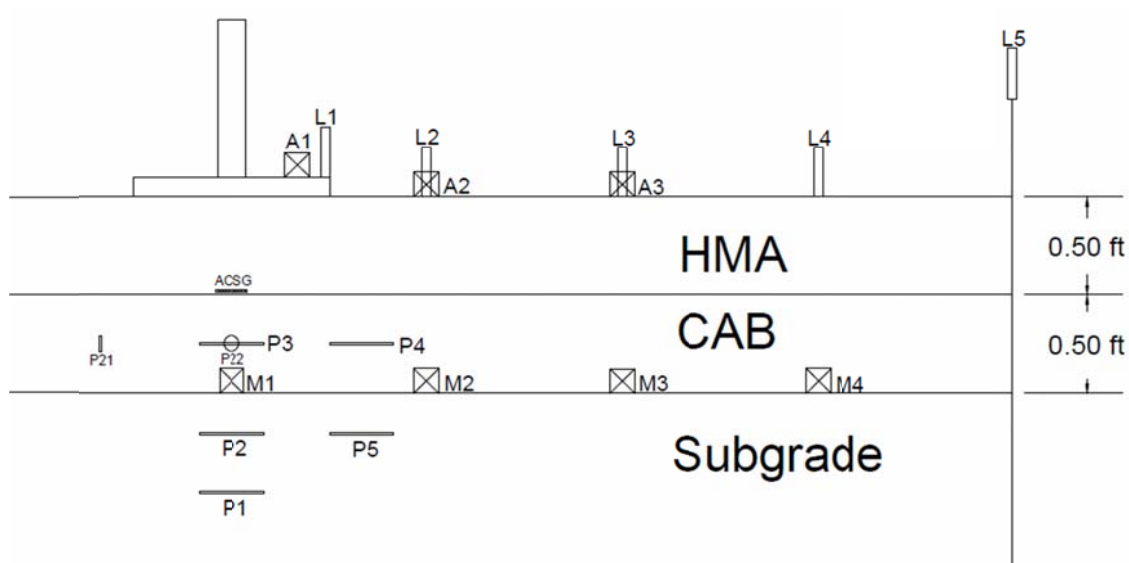


(b) Computed Average Vertical Strain within Base Course

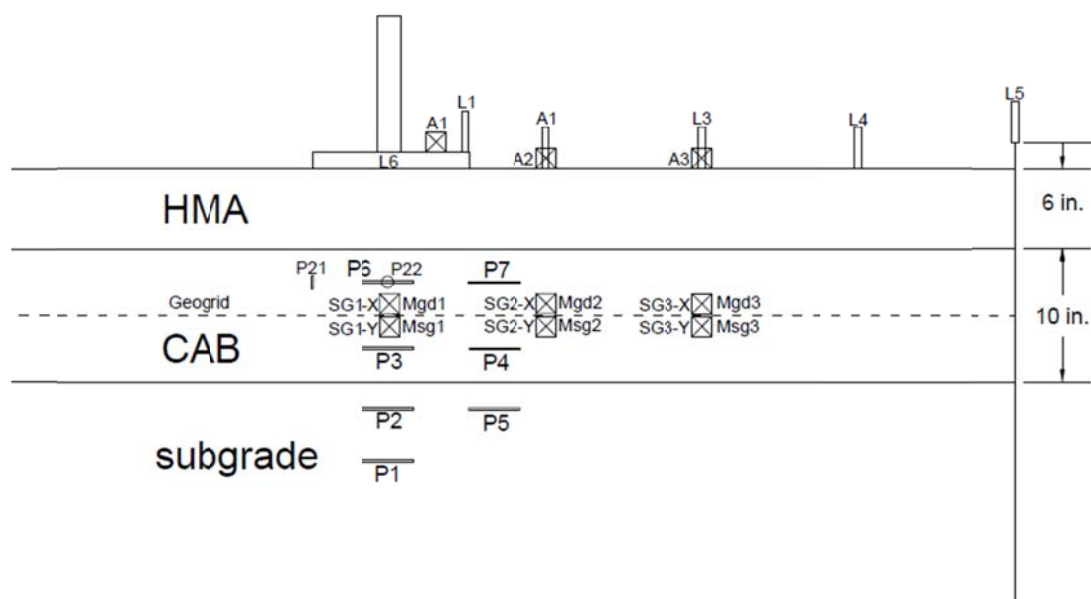
Figure 4.68. Sensitivity of Model-Predicted Pavement Responses to Thickness of Base Course

Comparison of Finite Element Simulations with LST Measurements

The finite element simulation results of the developed geosynthetic-reinforced and unreinforced pavement models were validated by comparing them to the LST test measurements in terms of the surface deflection, tensile strain at the bottom of the asphalt layer, and vertical pressures within the base and subgrade layers. The detailed comparison processes are presented in Appendix M. Figures 4.69 and 4.70 illustrate the location of the instruments, such as the LVDTs, the tensile strain gauge, and the pressure sensors, in the flexible and rigid pavement structures, respectively.



(a) Flexible Pavement with a 6-inch Base Course



(b) Flexible Pavement with a 10-inch Base Course

Figure 4.69. Location of Instruments in Flexible Pavement Structures

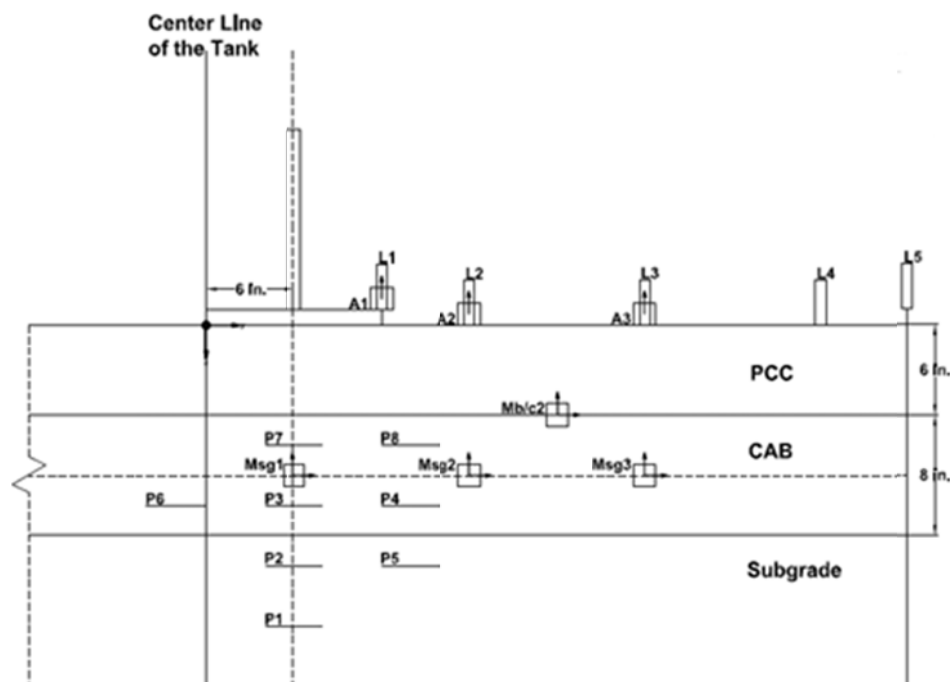
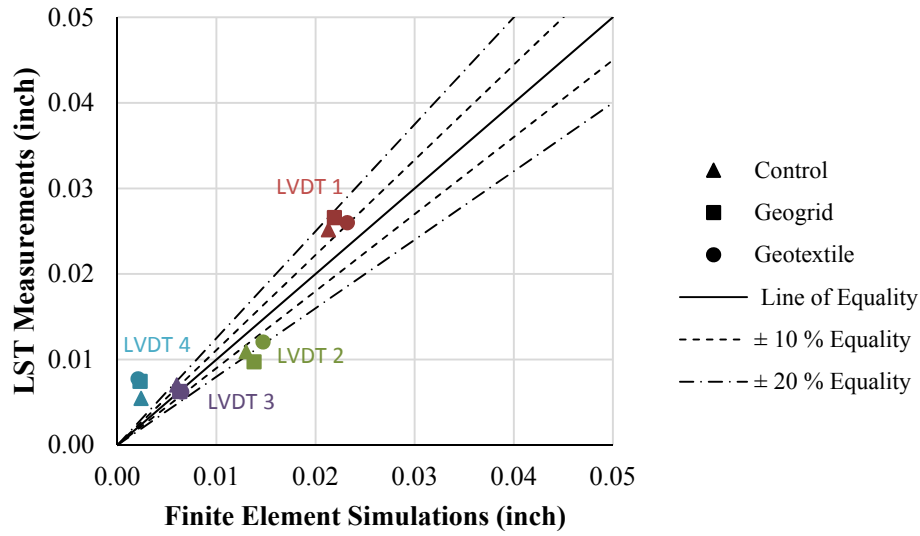
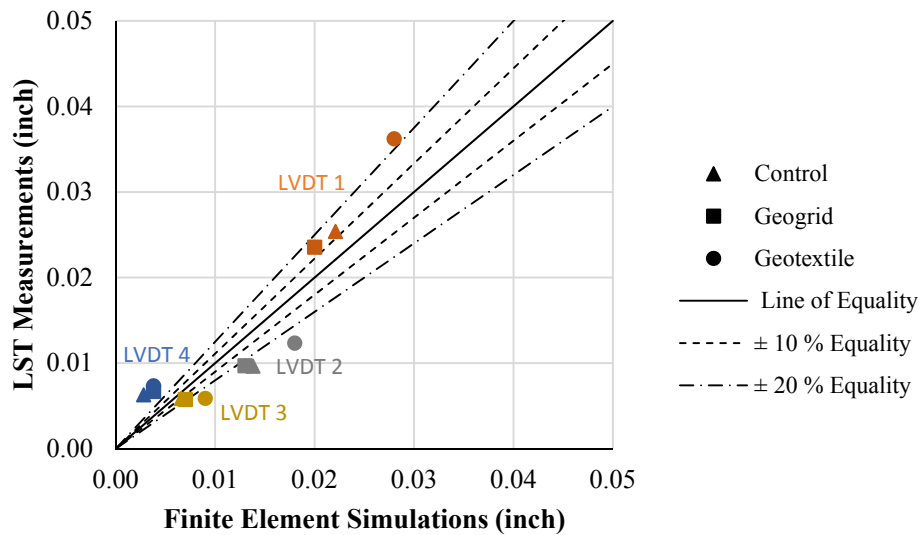


Figure 4.70. Location of Instruments in Rigid Pavement Structures

Figure 4.71 shows the comparison of the surface deflections predicted by the finite element models and the LST test measurements when the flexible pavement structures were subjected to a 9-kip load. The model-predicted surface deflections were in agreement with the LST measurements from LVDTs 1, 2, and 3. The deviation between the measured surface deflection by LVDT 4 and that predicted by the finite element model existed because the surface deflection at this location was too small to be accurately captured by the LVDT. This finding indicated that the developed geosynthetic-reinforced and unreinforced pavement models were highly accurate when predicting the pavement surface deflections. The comparison of the tensile strain at the bottom of the asphalt concrete is plotted in Figure 4.72. The figure shows that the developed finite element models accurately predicted the tensile strain in the geogrid-reinforced and unreinforced pavement structures but slightly overestimated the tensile strain in the geotextile-reinforced pavement structures. Figure 4.73 presents a comparison between the predicted vertical pressures within the base and subgrade layer and the measured results for the flexible pavements. Most of the measured pressure values were captured by the developed finite element models, except the measurement of pressure cells P1 and P7. A number of possible explanations existed for these discrepancies. For instance, for sensor P1, the stress-dependent behavior of the subgrade was not taken into account (see Figures 4.73a and 4.73b). For sensor P7, shown in Figure 4.73b, the measured pressure being lower than the predicted pressure might have been due to arching over the sensor.

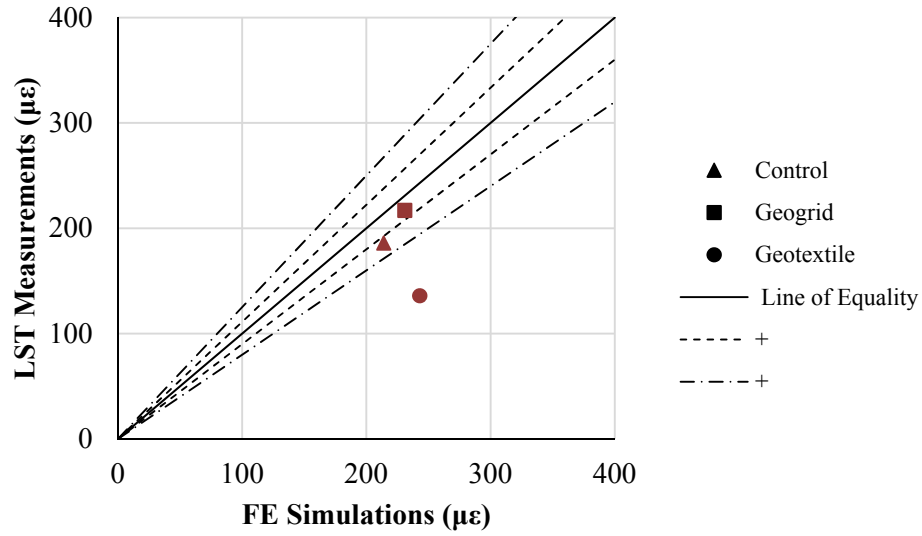


(a) Pavement Structures with 6-inch Base Course

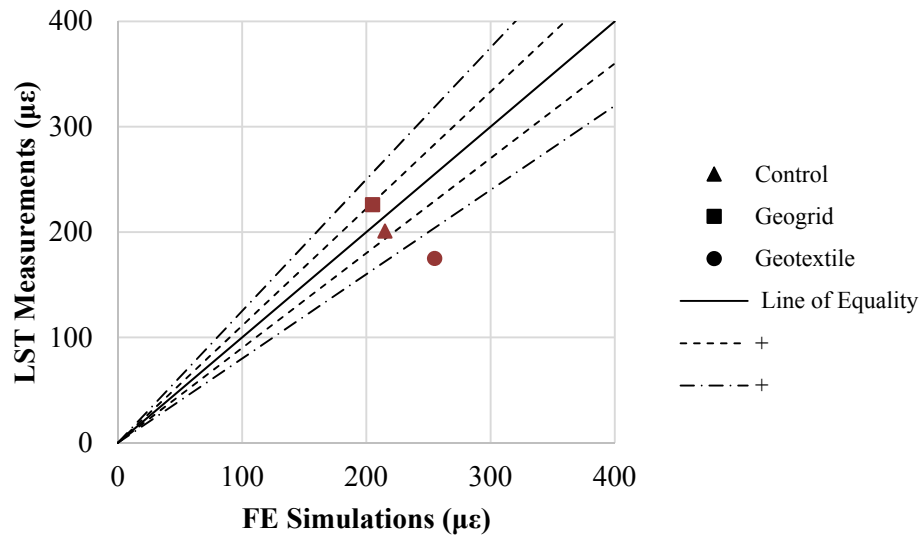


(b) Pavement Structures with 10-inch Base Course

Figure 4.71. Comparison of Measured and Predicted Surface Deflections for Pavement Structures with and without Geosynthetic

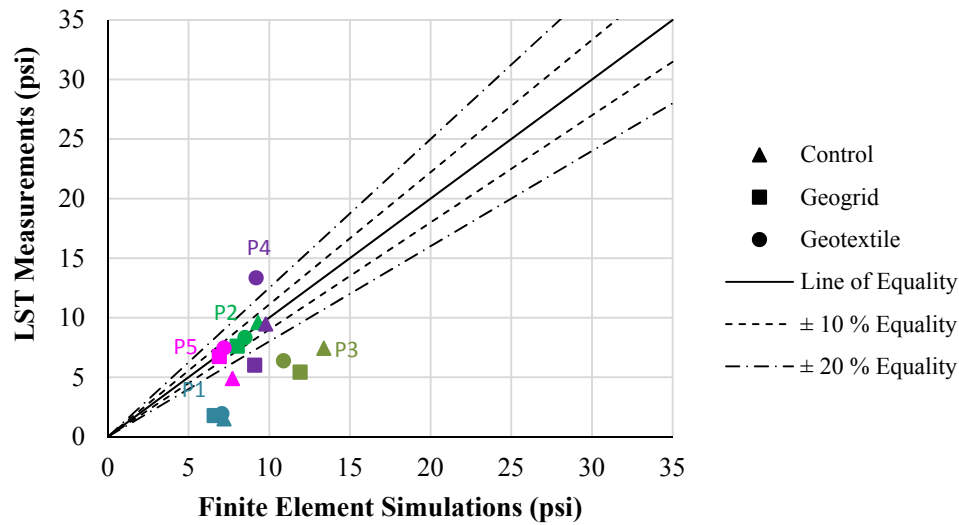


(a) Pavement Structures with 6-inch Base Course

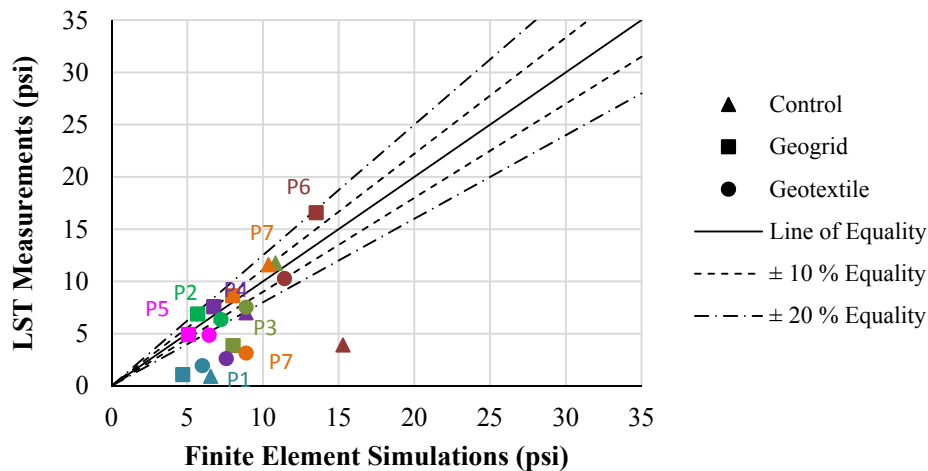


(b) Pavement Structures with 10-inch Base Course

Figure 4.72. Comparison of Measured and Predicted Tensile Strains at the Bottom of Asphalt Layer for Pavement Structures with and without Geosynthetic



(a) Pavement Structures with 6-inch Base Course



(b) Pavement Structures with 10-inch Base Course

Figure 4.73. Comparison of Measured and Predicted Vertical Stresses within the Base and Subgrade for Pavement Structures with and without Geosynthetic

Figure 4.74 compares the measured surface deflections of rigid pavements with those predicted by the finite element models. The figure shows that the surface deflections predicted by the finite element models were in agreement with the measurements of LVDTs 1 and 2 but did not match the measurements of LVDTs 3 and 4. The measured surface deflections from LVDTs 3 and 4 were negative, which indicated that the PCC slab moved upward at the far end near the tank wall. This movement might be because of the boundary conditions at the edge of the PCC slab. Figure 4.75 shows the comparison of the measured and predicted vertical pressures

in the base and subgrade. Note that some of the pressure sensor data (e.g., P1, P3, P6, and P8) were removed due to poor quality. The figure shows that the geogrid and geotextile effectively reduced the vertical compressive stresses in the base course when they were placed in the center of the base course but had a negligible influence on reducing the vertical compressive stresses in the subgrade.

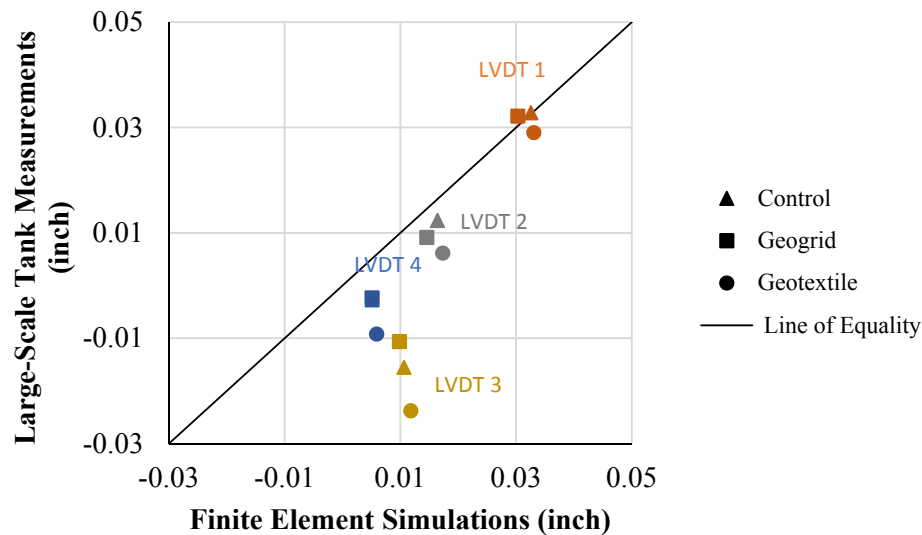


Figure 4.74. Comparison of Measured and Predicted Surface Deflections for Rigid Pavement Structures with and without Geosynthetic

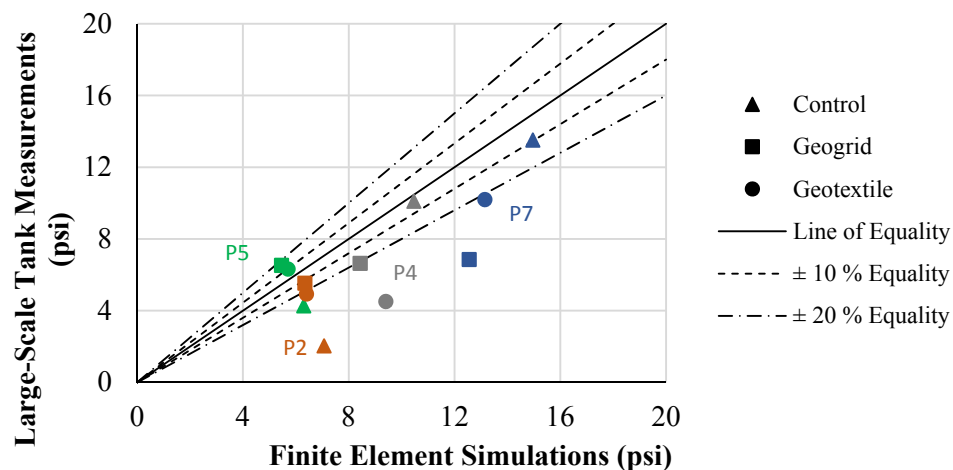


Figure 4.75. Comparison of Measured and Predicted Vertical Stresses within the Base and Subgrade for Rigid Pavement Structures with and without Geosynthetic

In summary, the finite element simulation results were in good agreement with the LST test measurements for both the reinforced and unreinforced pavement structures. Consideration of the paving material characterization, the geosynthetic-aggregate/soil interface characterization,

and the reinforcement influence zone was important to develop accurate numerical models of geosynthetic-reinforced pavement structures.

ANN Approach for Predicting Pavement Performance

The current Pavement ME Design software predicted pavement performance based on the computed critical pavement responses from a linear isotropic and layered elastic program. In other words, the determination of critical pavement responses was the key to forecasting pavement performance. The finite element models developed in this project were sufficiently accurate to compute the critical responses of geosynthetic-reinforced pavement structures. However, these models were developed using the software ABAQUS, which was not compatible with the Pavement ME Design embedded software DARWin-ME. Furthermore, replacing the current Pavement ME Design software with the developed finite element models to compute the critical responses of the arbitrary user-inputted geosynthetic-reinforced pavement structures was impractical. Therefore, there was a need to predict the responses of any given geosynthetic-reinforced pavement structure based on computation with the developed finite element models for a wide range of geosynthetic-reinforced pavement structures.

To satisfy this need, the ANN approach was used in this study to predict the critical responses of geosynthetic-reinforced pavement structures. The ANN models allowed for establishing the correlations between the input variables, X_i , and the output variables, Y_j , through the inter-connected neurons (i.e., weight factor, w_{ji}) (66). Note that the input variables, X_i , and the output variables, Y_j , were usually normalized to x_i and y_j , respectively, and were values between 0 and 1. In this study, the output variables, Y_j , represented the computed critical pavement responses, including the tensile strain at the bottom of the asphalt concrete and the compressive strain within the asphalt concrete, base layer, and subgrade. The selection of the input parameters, X_i , was based on the sensitivity analysis of the developed finite element models. The identified input parameters to the ANN models included the layer thickness, the modulus of the paving material, the location of the geosynthetic, and the type of geosynthetic. The correlations developed by the ANN models between the normalized input parameters, x_i , and the normalized output variables, y_j , are shown in Equation 4.36.

$$y_j = f\left(\sum_{i=1}^n w_{ji}x_i\right) \quad (4.36)$$

where f is a transfer function, which normally uses a sigmoidal, Gaussian, or threshold functional form; and w_{ji} is the unknown weight factors. Developing a neural network model specifically requires the determination of the weight factors, w_{ji} , as in Equation 4.36. The ANN model determined these weight factors, w_{ji} , through two major functions: training and validating. The training dataset was used to determine the trial weight factors, w_{ji} , and the validating dataset was employed to examine the accuracy of the model prediction. A robust ANN model

normally required a large database of input and output variables (67). Thus, generating the input and output variable database was the first step in developing an ANN model.

Experimental Computational Plan for ANN Models

To generate the database of the numerical model inputs and the corresponding computed critical pavement responses, researchers computed multiple cases based on the developed geosynthetic-reinforced and unreinforced finite element models. Tables 4.14 and 4.15 show the selected input parameters as well as their values for the geosynthetic-reinforced pavement structures and the corresponding unreinforced pavement structures, respectively. Based on these experimental computational plans, the number of computed geosynthetic-reinforced pavement models was 5,832, and the number of computed unreinforced pavement models was 486. As shown in Table 4.14, two geosynthetic types (geogrid and geotextile) and two geosynthetic locations (middle and bottom of base course) were taken into account in the computation of the multiple cases. The pavement response database was divided into five categories, including:

- The geogrid placed in the middle of the base layer (GG-M).
- The geogrid placed at the bottom of the base layer (GG-B).
- The geotextile placed in the middle of the base layer (GT-M).
- The geotextile placed at the bottom of the base layer (GT-B).
- The unreinforced one (NG).

Each category of pavement response corresponded to one set of neural network models.

Table 4.14. Selected Input Parameters for Geosynthetic-Reinforced Pavement Structures

Influential Factors	Level	Input Values
Load Magnitude	1	9 kip
HMA Thickness	3	2, 4, and 6 inches
HMA Modulus	3	300, 450, and 600 ksi
Base Thickness	3	6, 10, and 15 inches
Base Vertical Modulus	3	20, 40, and 60 ksi
Base Anisotropic Ratio	2	0.35 and 0.45
Geosynthetic Location	2	Middle and Bottom of Base Course
Geosynthetic Type	2	Geogrid and Geotextile
Geogrid Sheet Stiffness	3	1200, 2400, and 3600 lb/in
Geotextile Sheet Stiffness	3	1800, 3600, and 5400 lb/in
Subgrade Modulus	3	5, 15, and 25 ksi

Note: The number of total cases was 5,832.

Table 4.15. Selected Input Parameters for Unreinforced Pavement Structures

Influential Factors	Level	Input Values
Load Magnitude	1	9 kip
HMA Thickness	3	2, 4, and 6 inches
HMA Modulus	3	300, 450, and 600 ksi
Base Thickness	3	6, 10, and 15 inches
Base Vertical Modulus	3	20, 40, and 60 ksi
Base Anisotropic Ratio	2	0.35 and 0.45
Subgrade Modulus	3	5, 15, and 25 ksi

Note: The number of total cases was 486.

Development of ANN Models

A three-layered neural network architecture consisting of one input layer, one hidden layer, and one output layer was constructed, as shown in Figure 4.76. The input parameters are listed in Tables 4.14 and 4.15, except the geosynthetic location and the geosynthetic type. The output variables were the critical pavement responses, including the tensile strain at the bottom of the asphalt concrete and the compressive strains within the asphalt concrete, base course, and subgrade. The hidden layer assigned 20 neurons to establish the connection between the output layer and the input layer. In this study, the transfer function used a sigmoidal functional form, which is shown in Equation 4.37 (68).

$$f(I_i) = \frac{1}{1 + \exp(-\phi I_i)} \quad (4.37)$$

where I_i is the input quantity; and ϕ is a positive scaling constant, which controls the steepness between the two asymptotic values 0 and 1. The constructed neural network structure was programmed using the software MATLAB R2013a (69). The training algorithm used the Levenberg-Marquardt back propagation method to minimize the mean squared error (MSE) (70). The gradient descent weight function was employed as a learning algorithm to adjust the weight factors, w_{ji} (71).

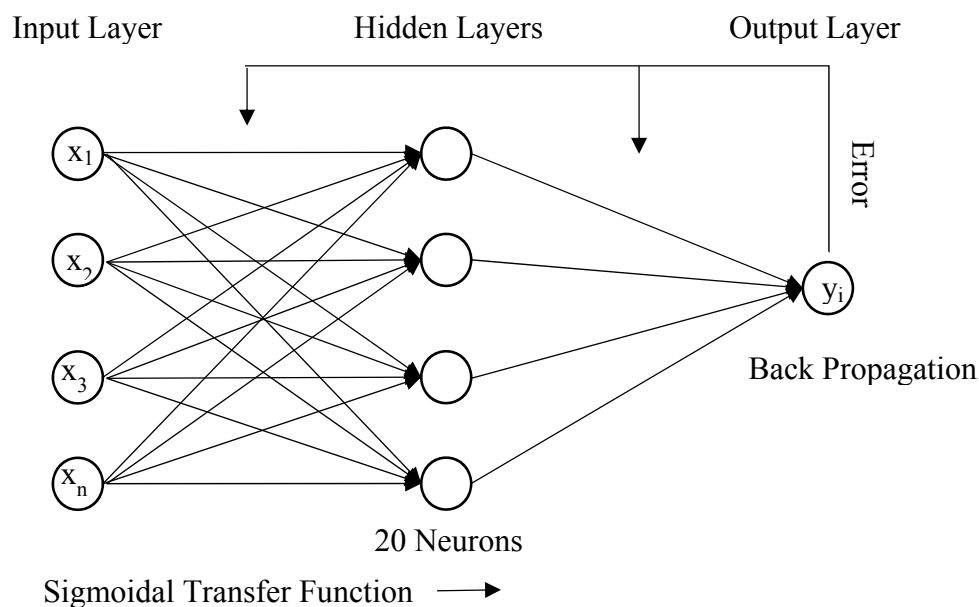


Figure 4.76. Illustration of Three-Layered Neural Network Architecture

The pavement response database was first randomly divided into a training dataset and a validating dataset as the ratio of 80 percent and 20 percent, respectively. The training dataset was used to determine the weight factors, w_{ji} , and the validating dataset was employed to examine the prediction accuracy of the developed neural network. Figures 4.77–4.81 show the comparisons between the pavement responses computed by the finite element model and the responses of the pavement with a GG-M structure predicted by the ANN model. As the figures illustrate, the ANN model predictions were in good agreement with the finite element model computational results. This finding indicated that the ANN models accurately predicted all of the pavement responses from the validating dataset after the training process. The comprehensive comparisons between the pavement responses computed by the finite element model and those predicted by the ANN model are presented in Appendix N. The developed ANN models could be used to interpolate the critical responses of any given geosynthetic-reinforced and unreinforced pavement structure.

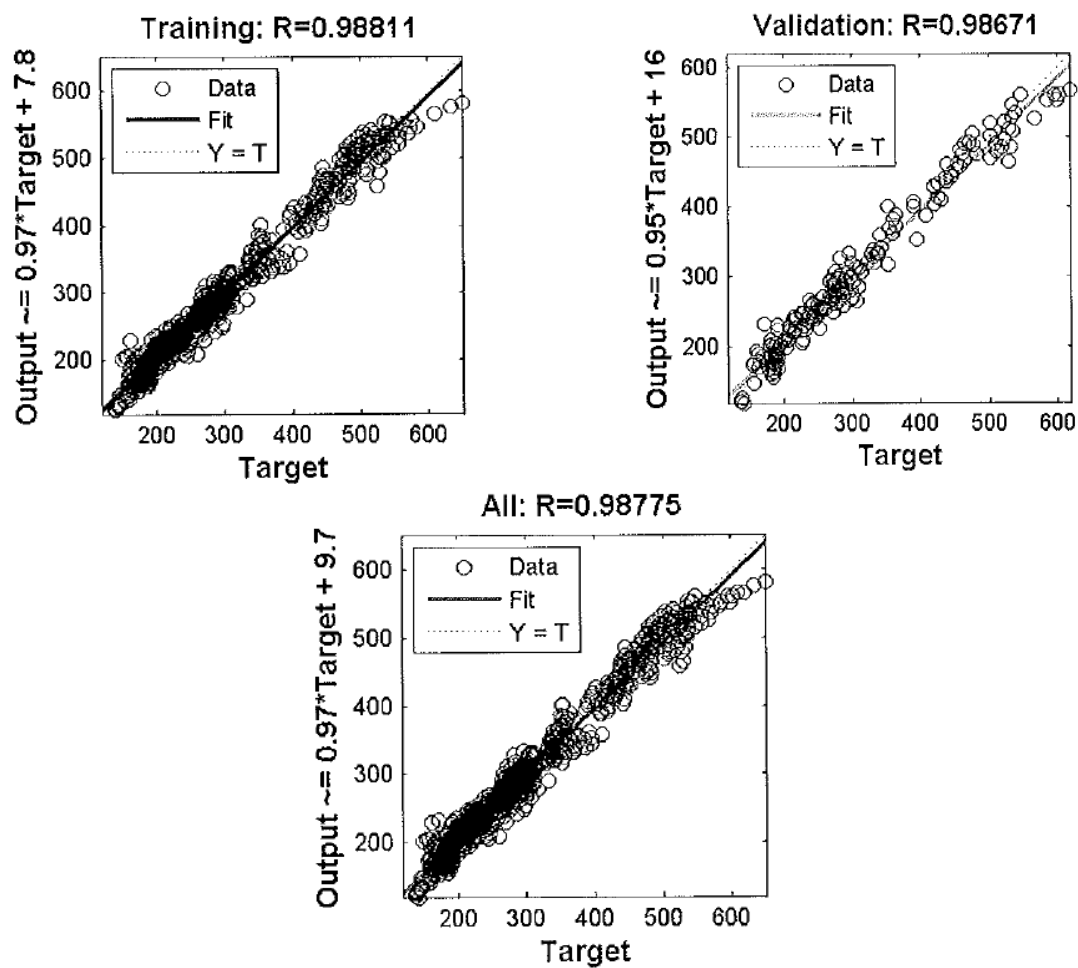


Figure 4.77. Comparison of Tensile Strain at the Bottom of the Asphalt Layer

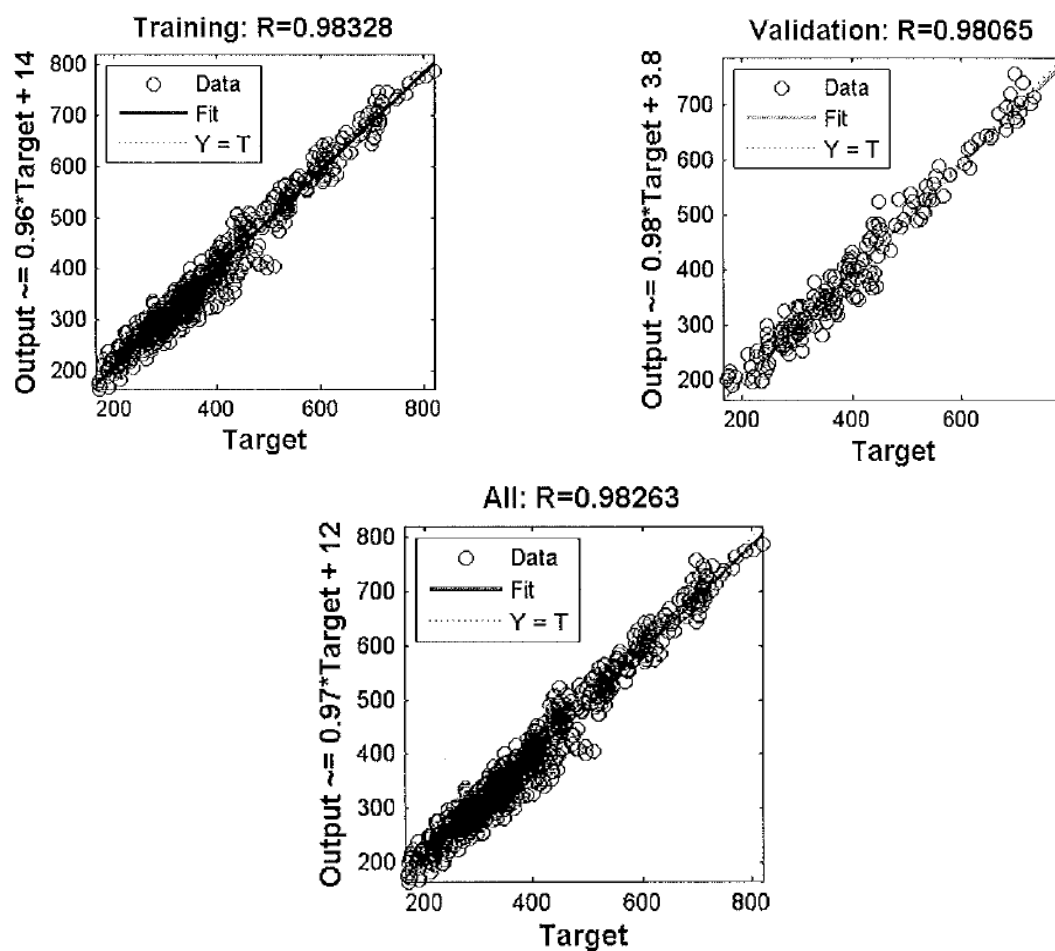


Figure 4.78. Comparison of Average Vertical Strain in the Asphalt Layer

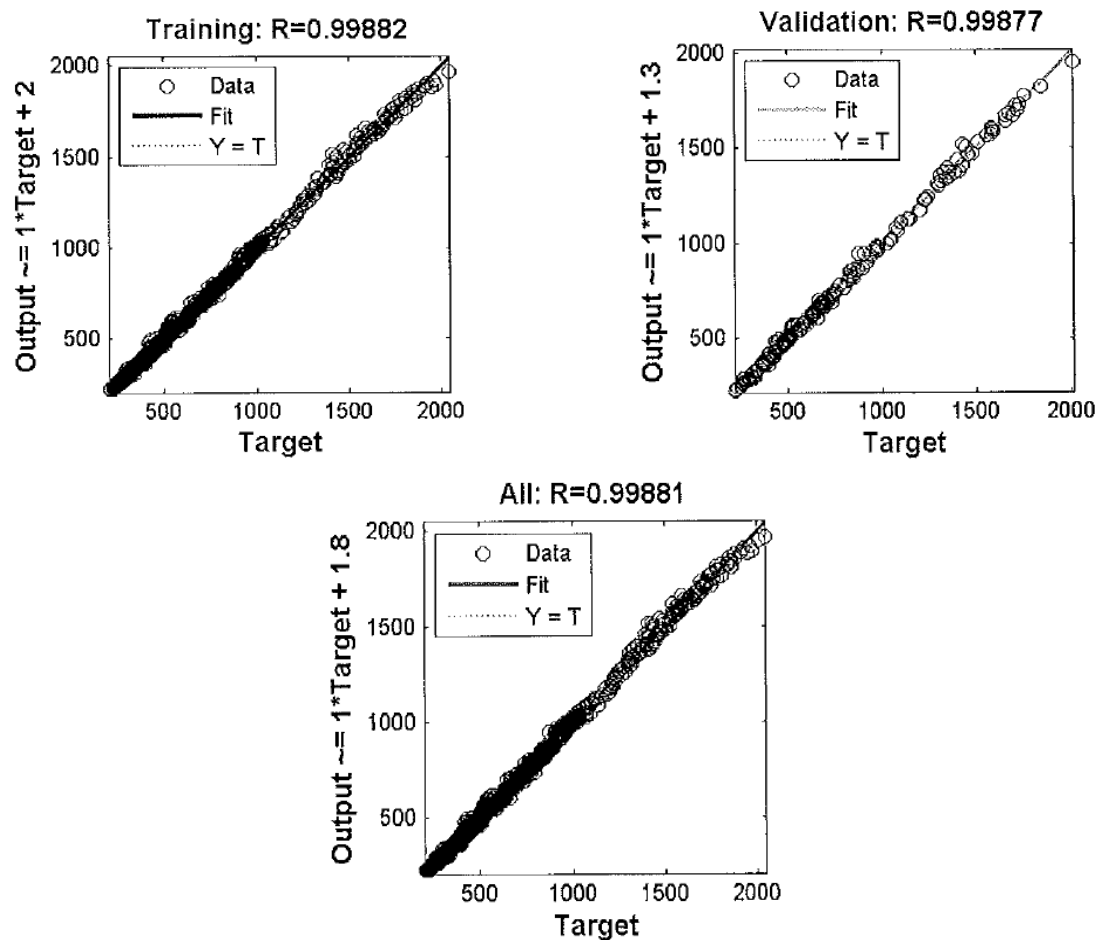


Figure 4.79. Comparison of Average Vertical Strain in the Base Layer

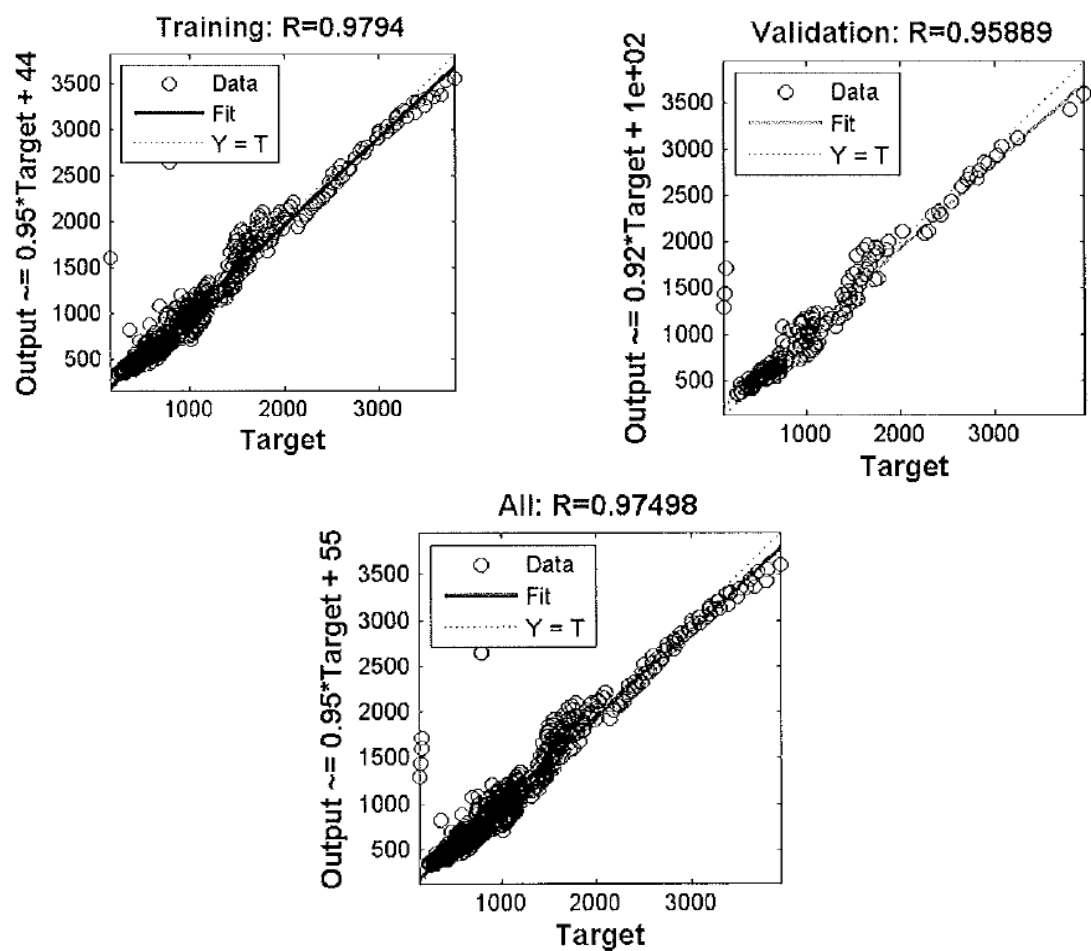


Figure 4.80. Comparison of Vertical Strain at the Top of the Subgrade

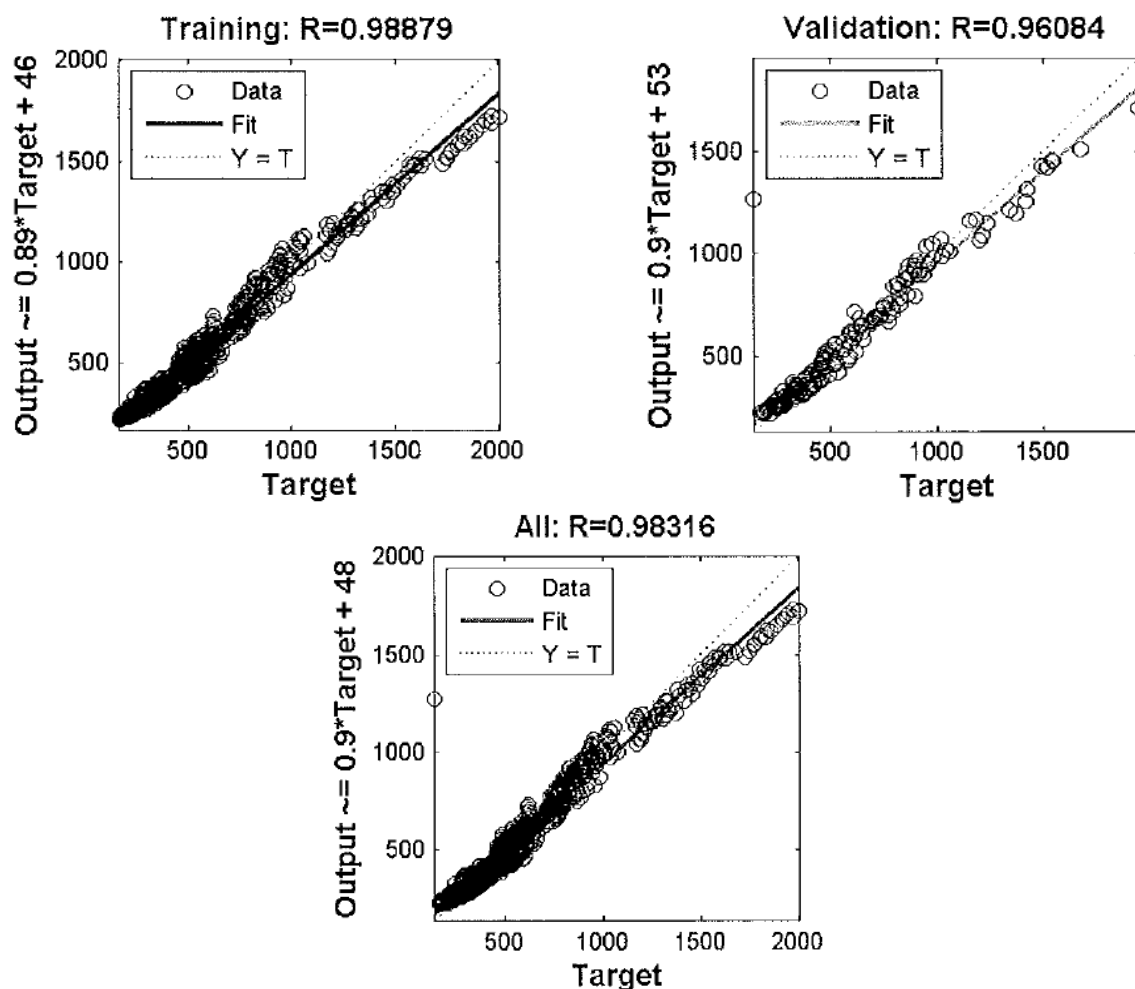


Figure 4.81. Comparison of Vertical Strain at 6 inches below the Top of the Subgrade

Determination of Modified Material Properties

The performance of geosynthetic-reinforced flexible pavements included fatigue cracking, permanent deformation, and international roughness index (IRI) (51). The aforementioned ANN-model-predicted critical pavement responses could be used to predict the pavement performance using the distress models in the current Pavement ME Design software. However, this method ignored the influence of traffic and climate on pavement performance. To eliminate this defect, the material properties of geosynthetic-reinforced pavement structures had to first be made equivalent to a combination of modified material properties (e.g., modified base modulus and modified subgrade modulus) of an unreinforced pavement structure. The determined modified material properties were then input into the Pavement ME Design software to predict the pavement performance. In this approach, the influence of traffic and climate on the pavement performance was taken into account by the Pavement ME Design software. Figure 4.82 presents a flowchart to determine the modified material properties for a geosynthetic-reinforced pavement structure. When the user input the geosynthetic-reinforced pavement structure information (e.g., layer thickness and material properties), the program would automatically generate a control structure with the same layer thickness and the equivalent material properties. The ANN models

were selected to predict the responses of the geosynthetic-reinforced and the control pavement structures. Subsequently, the responses of the geosynthetic-reinforced pavement structure were compared to those of the control structure. Equation 4.38 presents the convergence criterion used in this flowchart.

$$\frac{|\varepsilon_{\text{geosynthetic}} - \varepsilon_{\text{control}}|}{\varepsilon_{\text{control}}} \leq 10\% \quad (4.38)$$

where $\varepsilon_{\text{geosynthetic}}$ represents the response of the geosynthetic-reinforced pavement structure; and $\varepsilon_{\text{control}}$ represents the response of the control structure. If the responses of the geosynthetic-reinforced pavement structure did not match those of the control structure, the material properties (i.e., base material and subgrade modulus) of the control structure would be modified. The iteration would end when the comparison of the critical responses passed the convergence criterion. The program would then output the modified material properties of the control structure, which were the inputs for the Pavement ME Design software. The program was written using C# language to be compatible with the current Pavement ME Design software.

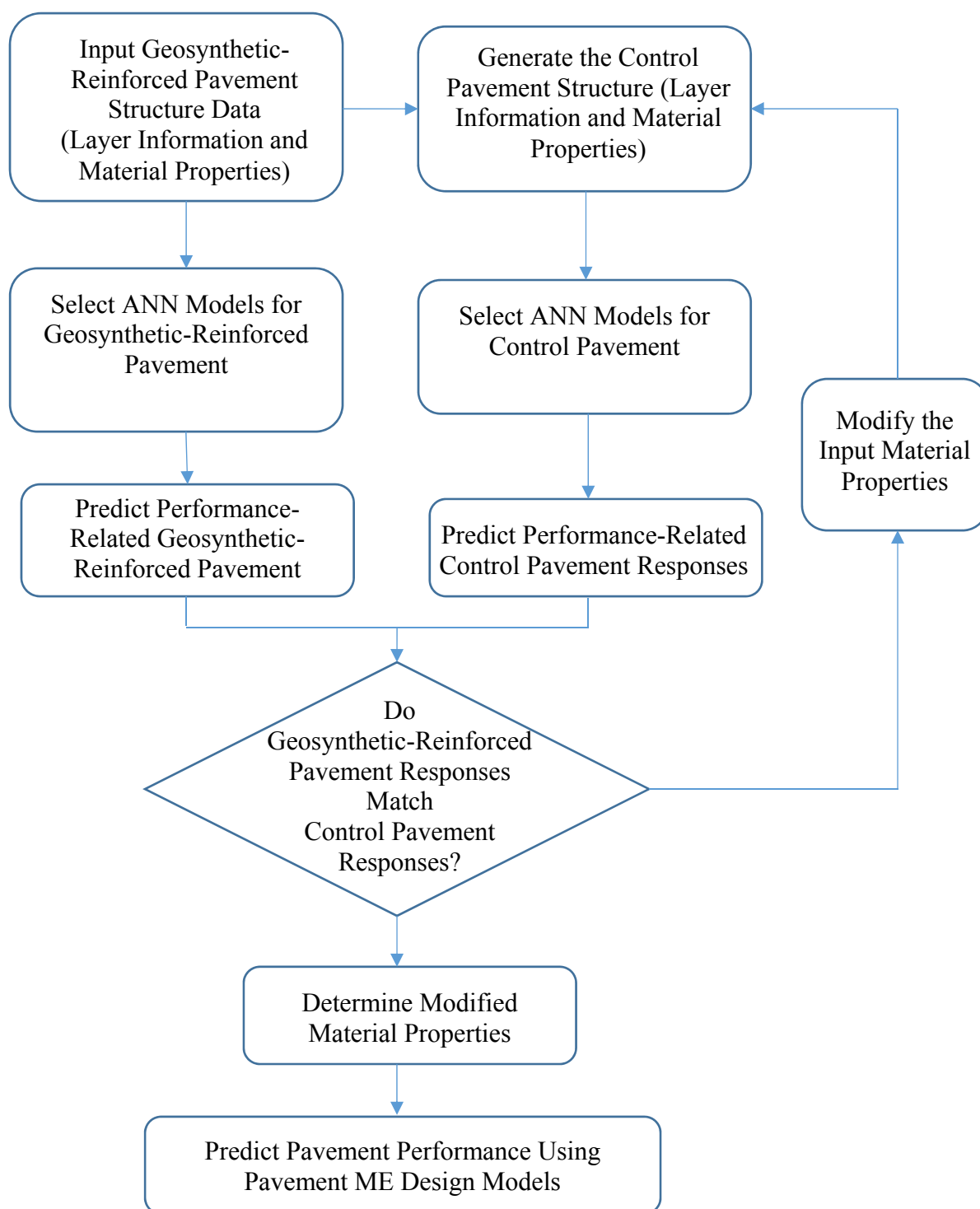


Figure 4.82. Flowchart of the Process of Predicting Pavement Performance

Case studies were performed on flexible pavements with geosynthetics (i.e., geogrid or geotextile) placed in the middle or at the bottom of the base course. Figure 4.83 presents the geosynthetic-reinforced pavement structures analyzed in this study. The material properties of the geosynthetic-reinforced pavements are shown in Tables 4.16 and 4.17. The modified material properties of the control pavement structure were determined using the aforementioned approach, as presented in Table 4.18. As shown in Figure 4.83, placing the geogrid in the middle or at the bottom of the base course was equivalent to increasing the moduli of the base course and subgrade. Placing the geotextile at the bottom of the base course was comparable to increasing the subgrade modulus. It was also noteworthy that the geotextile placed in the middle of the base course could not reinforce the pavement structure but significantly reduced the base course modulus. The determined modified material properties could serve as the inputs of the Pavement ME Design software for predicting the performance of geosynthetic-reinforced pavement structures.

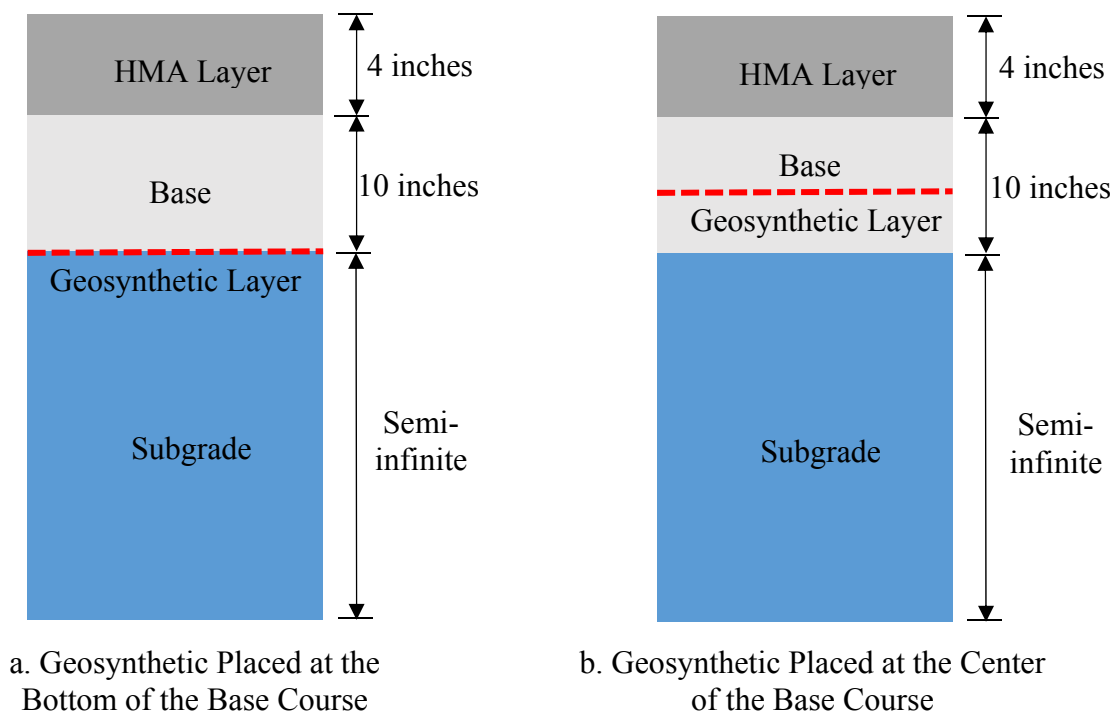


Figure 4.83. Geosynthetic-Reinforced Pavement Structures for Case Studies

**Table 4.16. Material Properties of Geosynthetic-Reinforced Pavements for Case Studies—
Material Properties of Control Pavement**

Material Type	Thickness (inch)	Vertical Modulus (ksi)	Anisotropic Ratio	Poisson's Ratio
Asphalt Concrete	4	300	N/A	0.35
Base Course	10	30	0.4	0.4
Subgrade	N/A	10	N/A	0.4

**Table 4.17. Material Properties of Geosynthetic-Reinforced Pavements for Case Studies—
Material Properties for Geosynthetic Products**

Material Type	Location	Thickness (inch)	Sheet Stiffness (lb/in)	Poisson's Ratio
Geogrid	Middle of Base Course	0.08	2400	0.3
Geogrid	Bottom of Base Course	0.08	2400	0.3
Geotextile	Middle of Base Course	0.08	3600	0.3
Geotextile	Bottom of Base Course	0.08	3600	0.3

Table 4.18. Determination of Modified Material Properties for Case Studies

Material Type	Location	Modified Base Course Modulus (ksi)	Modified Subgrade Modulus (ksi)
Geogrid	Middle of Base Course	32.1	15.1
Geogrid	Bottom of Base Course	30.8	20.7
Geotextile	Middle of Base Course	24.3	10.0
Geotextile	Bottom of Base Course	30.0	18.7

Prediction of Pavement Performance

The pavement structures shown in Figure 4.83 were assumed to be constructed in College Station, Texas. The two-way average annual daily truck traffic was 2,000. The vehicle class distribution and growth followed the default values. The climate information was collected from the weather station in College Station, Texas. The Pavement ME Design software was used to predict the performance of geosynthetic-reinforced and unreinforced pavements. Figures 4.84–4.86 show the effect of geosynthetic type and geosynthetic location with the base course on the flexible pavement performance. As shown in Figure 4.84, the greatest amount of fatigue cracking

occurred with the geotextile placed in the center of the base course, and it was dramatically higher than that in the unreinforced pavement section. This finding indicated that placing the geotextile in the center of the base course significantly reduced the fatigue life of the pavement structures. Compared to other pavement structures, the least amount of fatigue cracking occurred with the geogrid at the bottom of the base course, though this section only slightly outperformed the unreinforced pavement section. As shown in Figure 4.85, the greatest amount of rutting still occurred with the geotextile in the center of the base course. Compared to the control pavement, placing the geogrid in the center or at the bottom of the base course, or placing the geotextile at the bottom of the base course, could effectively reduce the accumulated permanent deformation of the pavement structure. As Figure 4.86 illustrates, the pavement with the highest IRI was the one with the geotextile in the center of the base course. The lowest IRI was provided by the geogrid at the bottom of the base course. These example calculations indicated that the major benefit of geosynthetics on the performance of flexible pavements was derived from a reduction in rutting and roughness. The placement of a geogrid at the bottom of the base course would achieve the most beneficial effect.

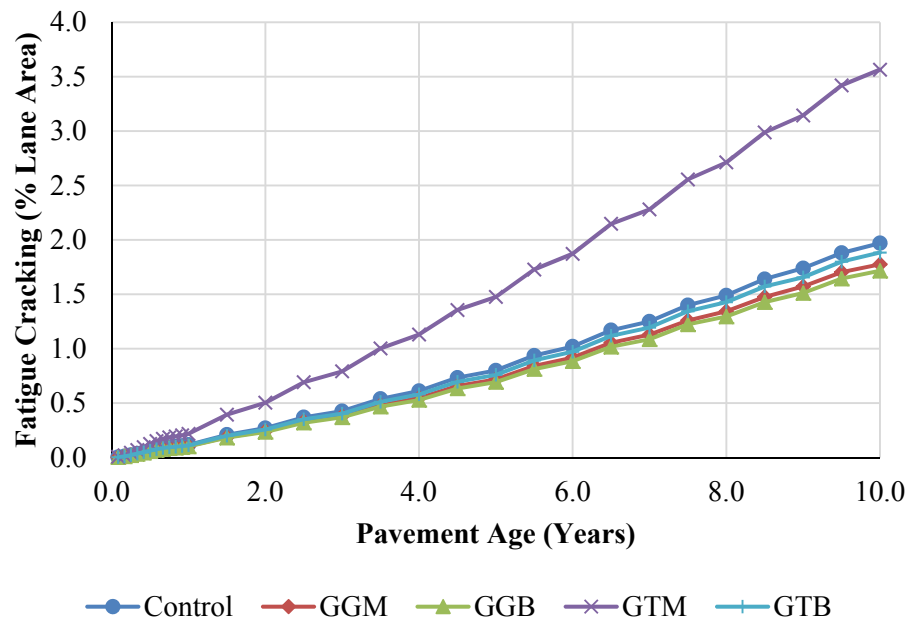


Figure 4.84. Effect of Geosynthetic Location and Geosynthetic Type on Fatigue Cracking

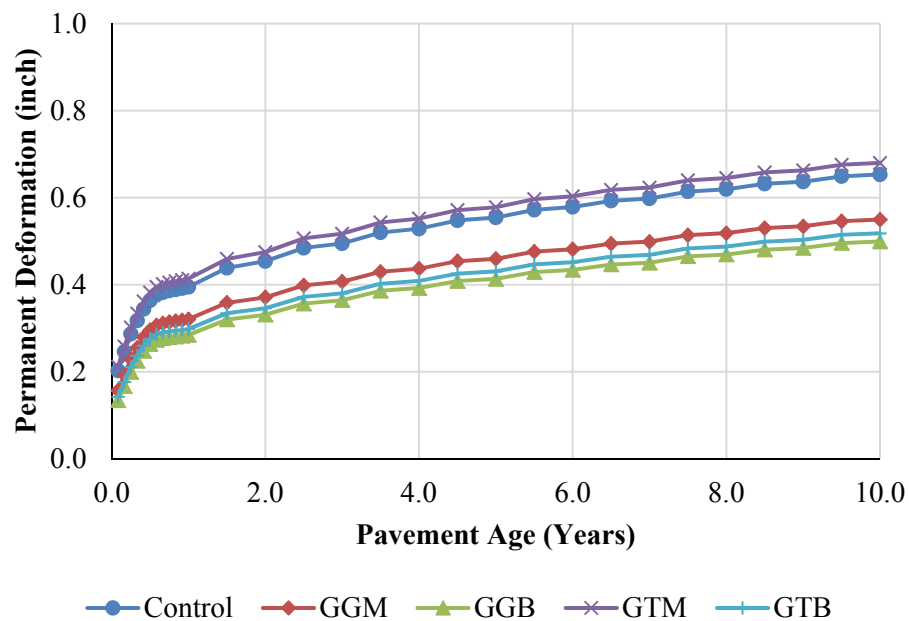


Figure 4.85. Effect of Geosynthetic Location and Geosynthetic Type on Rutting Depth

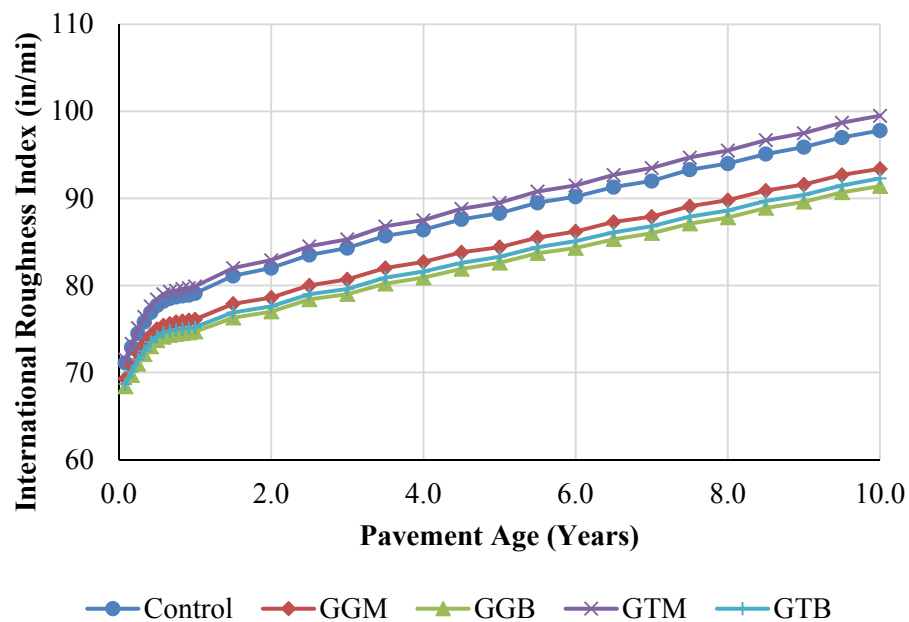


Figure 4.86. Effect of Geosynthetic Location and Geosynthetic Type on IRI

Validation of the Proposed ANN Approach

Using the proposed ANN approach, a geosynthetic-reinforced pavement with any given material properties needed to be made equivalent to an unreinforced pavement with the modified material properties to obtain the identical pavement responses. The process of validating the proposed ANN approach is illustrated in Figure 4.87 and involved the following steps:

- Identify the in-service geosynthetic-reinforced pavement sections from the LTPP database and Texas Pavement Management Information System (PMIS). This study focused on the in-service pavement sections with the placement of geosynthetics in conjunction with the unbound base courses.
- Collect the pavement structure data, including layer thickness, construction dates, material design information, and falling weight deflectometer data.
- Collect the traffic data from the identified pavement sections, which should be compatible with the input of the traffic module in the Pavement ME Design software.
- Collect the climatic data or weather station information from the identified pavement sections.
- Collect the performance data from the identified pavement sections, including fatigue cracking, rutting, and IRI.
- Employ the proposed ANN approach to determine the modified material properties of an unreinforced pavement.
- Input the unreinforced pavement structure data, the collected traffic data and climatic data, and the determined modified material properties into the Pavement ME Design software to predict the pavement performance (i.e., fatigue cracking, rutting, and IRI).
- Compare the predicted pavement performance with that measured in the field.

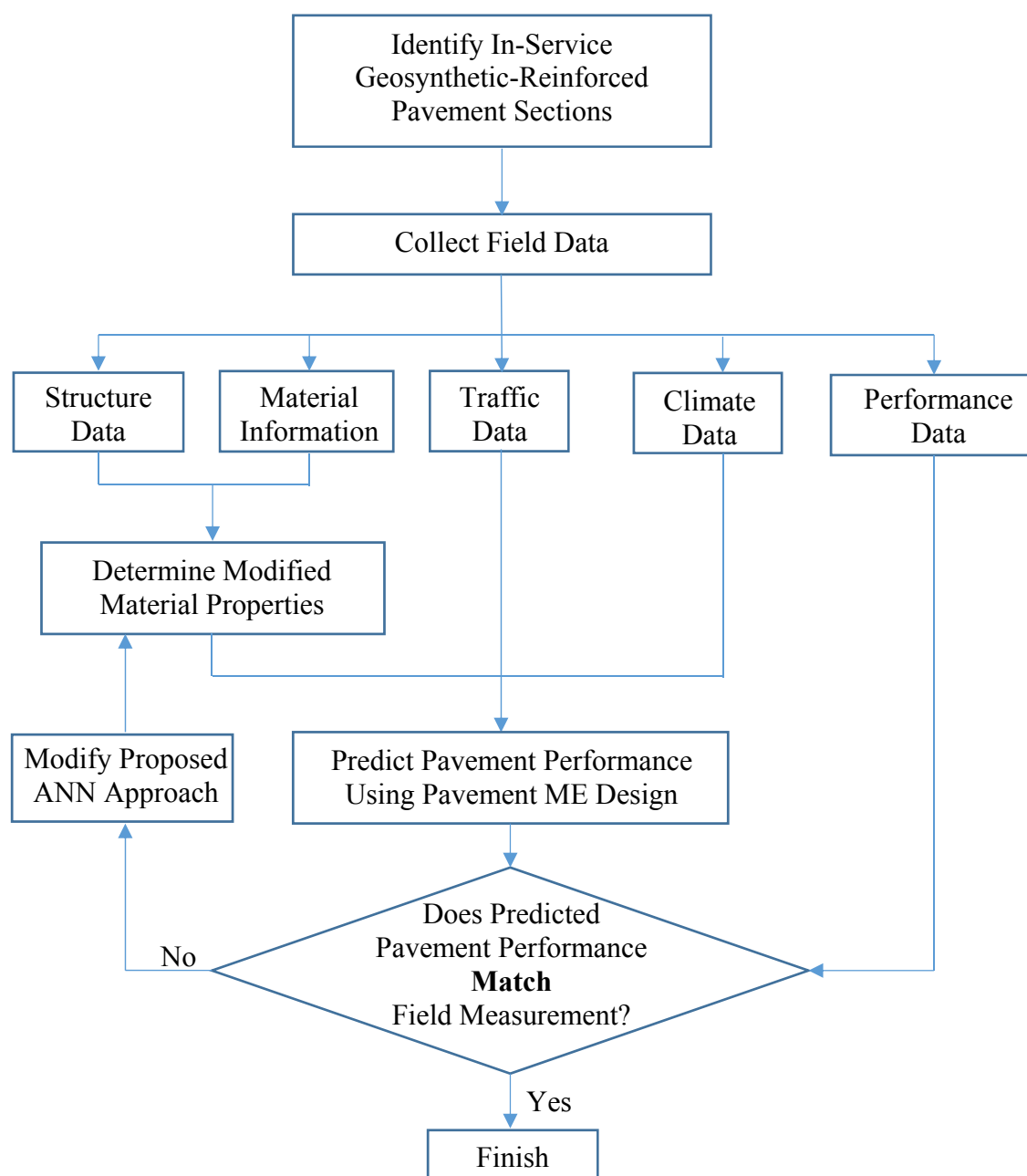


Figure 4.87. Flowchart of the Process of Validating the Proposed ANN Approach

After a thorough review of the in-service pavement sections in the LTPP database and PMIS, researchers found 74 pavement sections containing geosynthetics in the LTPP database and 51 pavement sections containing geosynthetics in the PMIS. A full list of the identified pavement sections is presented in Appendix P. Of these identified pavement sections, most had stabilized base courses, which were not under consideration in this study. Of the remaining pavement sections, five were from the LTPP database and five were from the PMIS.

Researchers used Pavement Section 16-9032 from the LTPP database as an example to validate the proposed ANN approach. Section 16-9032 consisted of a 6-inch hot-mixed and

dense-graded asphalt concrete, a 23.2-inch crushed gravel unbound base, and a semi-infinite subgrade, which was classified as AASHTO 7-5 soil. A 0.1-inch woven geotextile was placed at the interface between the unbound base and subgrade. The comparisons of geosynthetic-reinforced pavement performance between the predictions from the proposed ANN approach and the field measurements are presented in Figures 4.88–4.90. The figures show that the predicted rutting depth and IRI results were in good agreement with the field measurements. The fatigue cracking of the geosynthetic-reinforced pavement was slightly overestimated by the proposed ANN approach. These findings indicated that the proposed ANN approach was capable of accurately predicting the performance of geosynthetic-reinforced pavements. Figures 4.88–4.90 also present the predicted performance of the control pavement and demonstrate that the geotextile placed at the base/subgrade interface had beneficial effects on reducing the rutting and IRI of flexible pavements. The comparisons of the geosynthetic-reinforced pavement performance between the ANN approach predictions and the field measurements for other identified pavement sections are detailed in Appendix O.

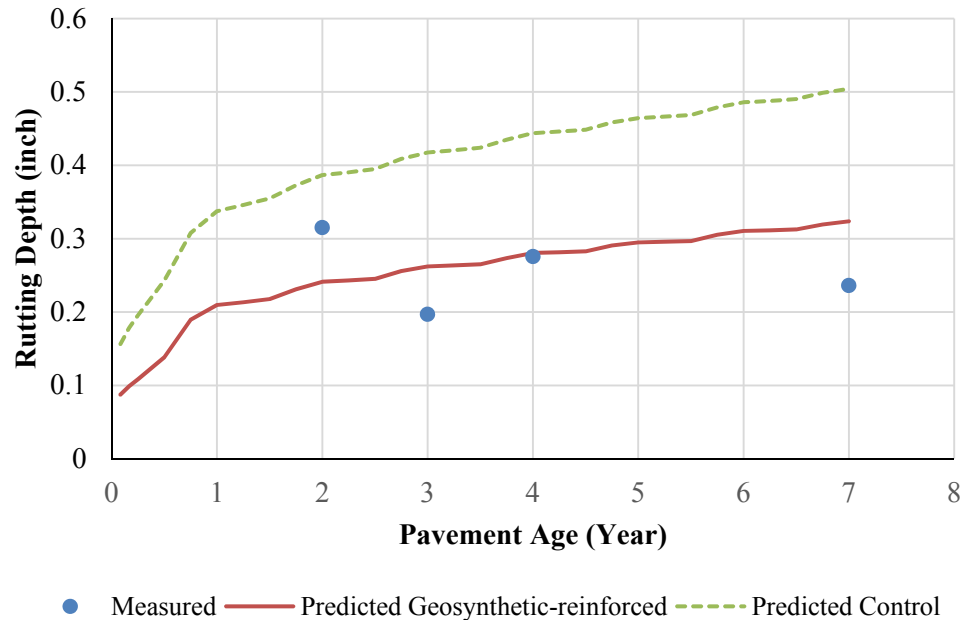


Figure 4.88. Comparison of Rutting Depth between ANN Approach Prediction and Field Measurement for Pavement Section 16-9032

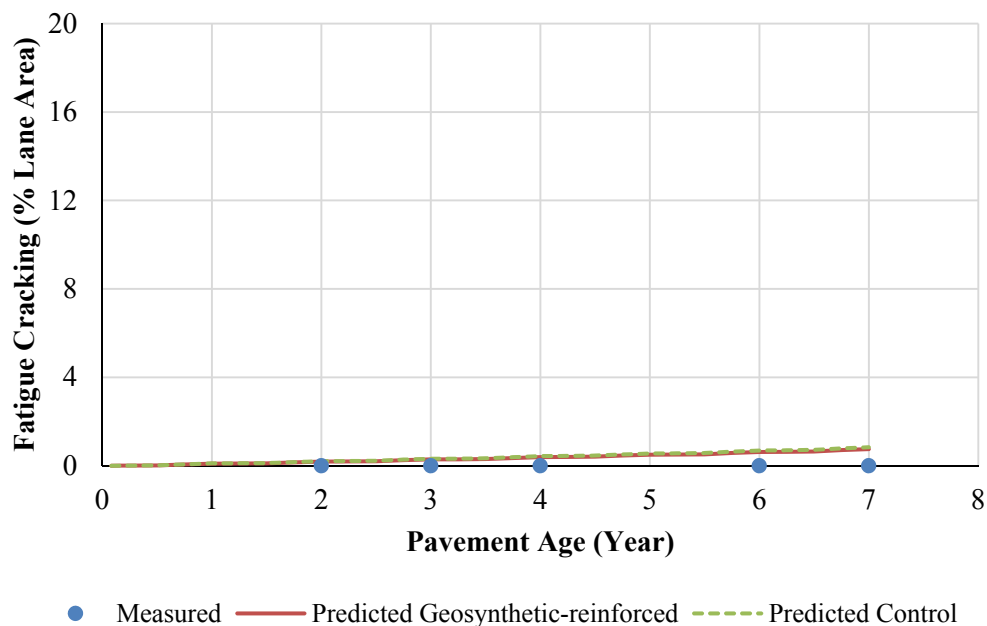


Figure 4.89. Comparison of Fatigue Cracking between ANN Approach Prediction and Field Measurement for Pavement Section 16-9032

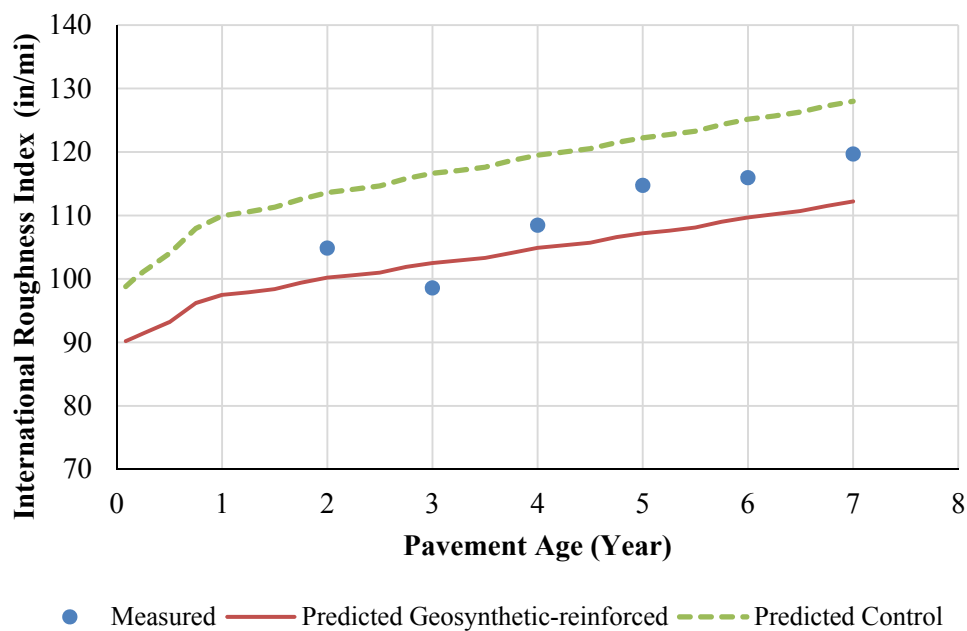


Figure 4.90. Comparison of IRI between ANN Approach Prediction and Field Measurement for Pavement Section 16-9032

CHAPTER 5. INTERPRETATIONS, APPRAISAL, AND APPLICATIONS

Introduction

This project developed a methodology for quantifying the influence of geosynthetics on pavement performance. This methodology included the development of the two laboratory test protocols for evaluating the impact of geosynthetics on cross-anisotropy and permanent deformation of UGMs, analytical models for quantifying the impact of geosynthetics, finite element models for computing the critical stresses and strains that control the performance of geosynthetic-reinforced pavements, and ANN models for predicting the performance of geosynthetic-reinforced pavements. One LST testing program with extensive instrumentation was conducted, and the measurements were used to validate the developed finite element models by comparing the measured pavement responses with those predicted by the models.

LST Testing Program

An LST testing program was conducted on flexible and rigid pavements using an 8-ft-diameter by 6-ft-high circular steel tank. Tables 5.1 and 5.2 summarize the specifics of the LST experiments on flexible pavements and rigid pavements, respectively. A database of pertinent pavement responses with and without reinforcement of the base layer collected under realistic pavement loading conditions was assembled. The established database was then used in the numerical investigation (model and input parameters, etc.) of the LST to assess the validity and applicability of the finite element numerical modeling of pavement structures with geosynthetic-reinforced bases. In particular, data critical to the validation of the numerical modeling of the interaction of a geosynthetic layer with the surrounding medium were examined and included:

- The stress distributions across the geosynthetic under dynamic loading in both the AC and PCC pavements.
- The strain measurements in the geosynthetic and at the bottom of the surface layer (AC or PCC) under dynamic loading.
- The deformed shape of the geosynthetic and the slippage at the interface between the geosynthetic and the unbound material under dynamic loading.
- The slippage between the bottom of the PCC slab and the supporting unbound granular material base layer at the edge of the loaded slab.

The LST testing program confirmed that a careful representation of the geosynthetic material was necessary for the overall numerical modeling of reinforced pavement structures. An appropriate modeling of the geosynthetic material should be able to capture the mechanism of the behavior of the reinforcement in the base layer under dynamic loading. This mechanism was observed to be different between the selected geogrid and geotextile materials evaluated as part of this study. These differences are explained and illustrated in Chapter 4. The effects of these mechanism differences were incorporated in the ANN models that were developed in this project. The extensive LST database assembled in this study would serve as a valuable resource for the verification of future numerical modeling of reinforced base layers in pavement structures.

Table 5.1. Summary of Specifics of LST Experiments on Flexible Pavements

Experiment		Surface Layer Thick. (inch)	CAB Layer Thick. (inch)	Reinforcement		Instrumentation		
ID	No			Type	Location	Transducer type	Location	Quantity
AC-Contr-B06	1	6	6	None (Control)	N/A	LVDT	Surface	5
						Accelerometer (1D)	Surface	3
						Accelerometer (2D)	Middle of the base	3 (V and H)
						Pressure cell	Middle of the base, 2 in. and 6 in. below the subgrade	5 (V), 2 (H)
						Asphalt strain gauge	At the bottom of the HMA	1
AC-Contr-B10	2	6	10	None (Control)	N/A	LVDT	Surface	5
						Accelerometer (1D)	Surface	3
						Accelerometer (2D)	Middle of the base	3
						Pressure cell	Middle of top and bottom half of the base, 2 in. and 6 in. below the subgrade	5 (V), 2 (H)
						Asphalt strain gauge	At the bottom of the HMA	1
AC-Grid-B06	3	6	6	Geogrid	Base-Subgrade Interface	LVDT	Surface	6
						Accelerometer (1D)	Surface	3
						Accelerometer (2D)	Middle of the base (on geogrid and in the base)	3 (G), 3 (B)
						Pressure cell	Middle of the base, 2 in. and 6 in. below the subgrade	5 (V), 2 (H)
						Asphalt strain gauge	At the bottom of the HMA	1
						Strain gauge	On geogrid (X and Y directions)	3
AC-Grid-B10	4	6	10	Geogrid	Middle of the Base	LVDT	Surface	6
						Accelerometer (1D)	Surface	3
						Accelerometer (2D)	Middle of the base (on geogrid & in the base)	3 (G), 3 (B)
						Pressure cell	Middle of top and bottom half of the base, 2 in. and 6 in. below the subgrade	5 (V), 2 (H)
						Asphalt strain gauge	At the bottom of the HMA	1
						Strain gauge	On geogrid (X and Y directions)	3
AC-Textile-B06	5	6	6	Geotextile	Base-Subgrade Interface	LVDT	Surface	6
						Accelerometer (1D)	Surface	3
						Accelerometer (2D)	Middle of the base (on geogrid and in the base)	3 (G), 3 (B)
						Pressure cell	Middle of the base, 2 in. and 6 in. below the subgrade	5 (V), 2 (H)
						Asphalt strain gauge	At the bottom of the HMA	1
						Strain gauge	On geotextile (X and Y directions)	3
AC-Textile-B10	6	6	10	Geotextile	Middle of the Base	LVDT	Surface	6
						Accelerometer (1D)	Surface	3
						Accelerometer (2D)	Middle of the base (on geogrid and in the base)	3 (G), 3 (B)
						Pressure cell	Middle of top and bottom half of the base, 2 in. and 6 in. below the subgrade	5 (V), 2 (H)
						Asphalt strain gauge	At the bottom of the HMA	1
						Strain gauge	On geotextile (X and Y directions)	3

Note: V = vertical, H = horizontal, B = base, and G = geogrid/geotextile.

Table 5.2. Summary of Specifics of LST Experiments on Rigid Pavements

Experiment		Surf. Layer Thick. (inch)	CAB Layer Thick. (inch)	Reinforcement		Instrumentation		
ID	No			Type	Location	Transducer type	Location	Quantity
PCC-Contr-IS	7	6	8	None (Control)	N/A	LVDT	Surface and top of the base (H)	5(V), 2(H)
						Accelerometer (1D)	Surface	7
						Accelerometer (2D)	Middle of the base, embedded in concrete at the interface, top of the base	8(B), 2 (C)
						Accelerometer (3D)	Embedded in concrete at the interface, top of the base	1(B), 1(C)
						Pressure cell	Middle of top and bottom half of the base, 2 in. and 6 in. below the subgrade	10 (V), 1 (H)
						Concrete strain gauge	At the bottom of the PCC	1
PCC-Grid-IS	9	6	8	Geogrid	Middle of the Base	LVDT	Surface and top of the base (H)	5(V), 2(H)
						Accelerometer (1D)	Surface	7
						Accelerometer (2D)	Middle of the base on geogrid and in the base, embedded in concrete at the interface and top of the base	8(B), 2(C), 4 (G)
						Accelerometer (3D)	Embedded in concrete at the interface, top of the base	2(B), 1(C), 1(G)
						Pressure cell	Middle of top and bottom half of the base, 2 in. and 6 in. below the subgrade	10 (V), 1 (H)
						Concrete strain gauge	At the bottom of the PCC	1
						Strain gauge	On geogrid (X and Y directions)	5
PCC-Textile-IS	10	6	8	Geotextile	Middle of the Base	LVDT	Surface and top of the base (H)	5(V), 2(H)
						Accelerometer (1D)	Surface	7
						Accelerometer (2D)	Middle of the base on geotextile and in the base, embedded in concrete at the interface and top of the base	8(B), 2(C), 4 (G)
						Accelerometer (3D)	Embedded in concrete at the interface, top of the base	2(B), 1(C), 1(G)
						Pressure cell	Middle of top and bottom half of the base, 2 in. and 6 in. below the subgrade	10 (V), 1 (H)
						Concrete strain gauge	At the bottom of the PCC	1
						Strain gauge	On geotextile (X and Y directions)	5
						LVDT	Surface and top of the base (H)	5(V), 2(H)

Note: V = vertical, H = horizontal, B = base, G = geogrid/geotextile, and C = concrete.

Measurement of Geosynthetic-Aggregate/Soil Interfacial Slippage

The slippage at the geosynthetic-aggregate/soil interface significantly affected the geosynthetic-UGM interaction. The horizontal slippage was calculated as the difference in horizontal displacements between the geosynthetic and the adjacent UGM using the calibrated double-integration procedure that is explained in Appendix I. Figures 5.1–5.4 show the measured interfacial slippage for the geogrid-reinforced and geotextile-reinforced pavement structures, respectively. Slippage at the geogrid interface only occurred when the geogrid was placed at the bottom of the base course. It increased as the load level increased. Slippage at the geotextile interface occurred when the geotextile was placed at the bottom and in the middle of the base course. This slippage was greater than with the geogrids and also increased with load level when the geotextile was placed in the middle of the base course.

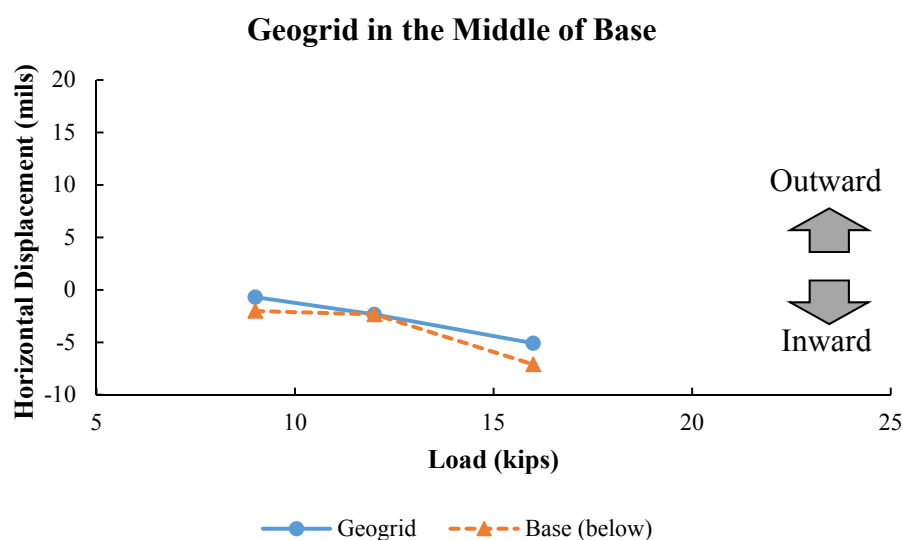


Figure 5.1. Measured Horizontal Displacements of Geogrid and UGM When Geogrid Was Placed in the Middle of the Base Course

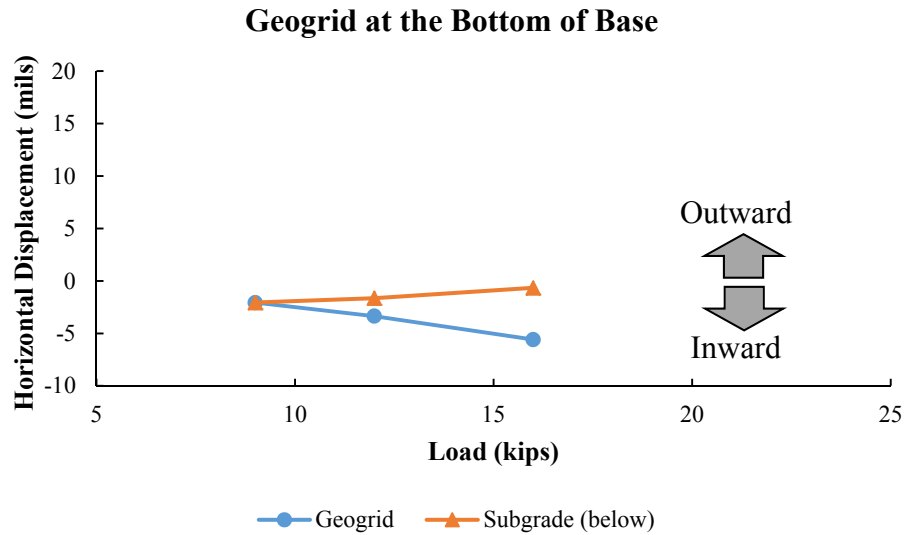


Figure 5.2. Measured Horizontal Displacements of Geogrid and UGM When Geogrid Was Placed at the Bottom of the Base Course

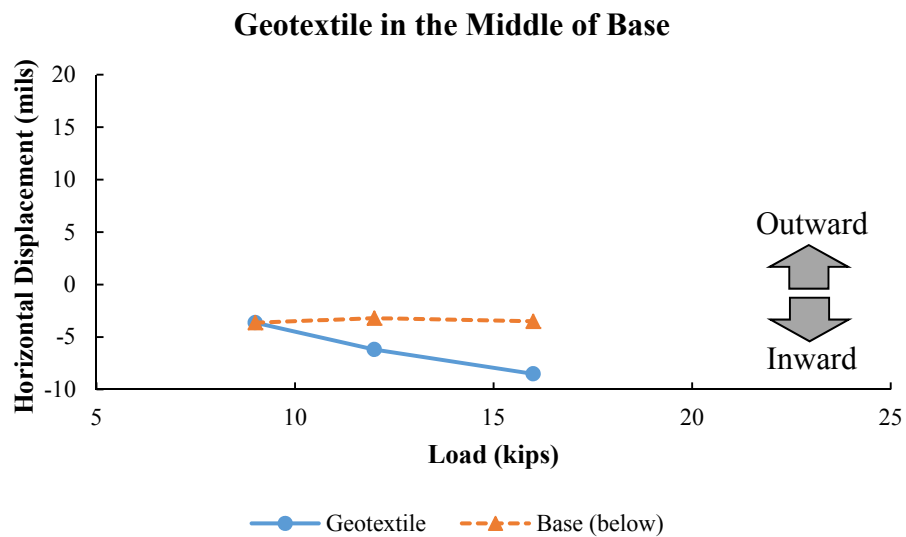


Figure 5.3. Measured Horizontal Displacements of Geotextile and UGM When Geotextile Was Placed in the Middle of the Base Course

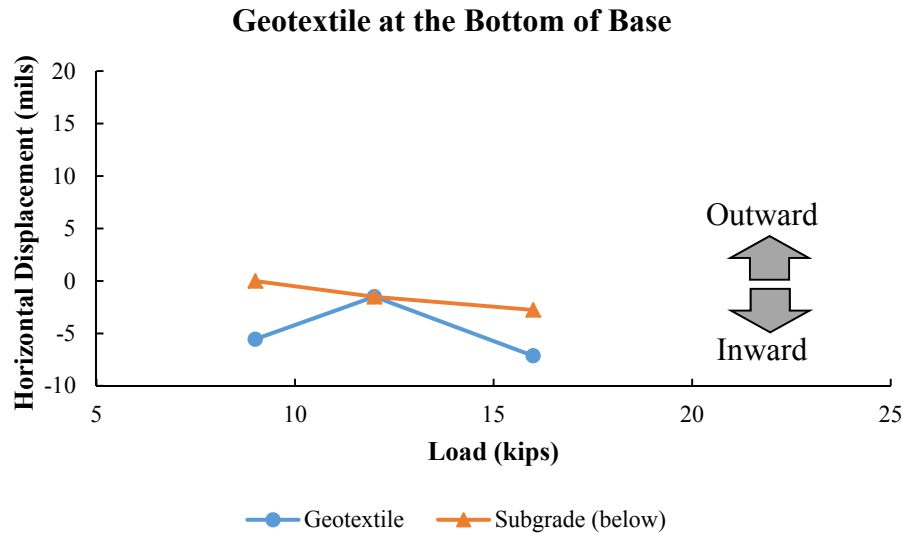


Figure 5.4. Measured Horizontal Displacements of Geotextile and UGM When Geotextile Was Placed at the Bottom of the Base Course

Determination of Geosynthetic-Aggregate/Soil Interfacial Properties

The interfacial shear stiffness was an important property for characterizing the geosynthetic-aggregate/soil interaction behavior. This property depended on the slippage condition between the geosynthetic and the surrounding aggregates. An analytical solution was derived to determine the interfacial shear stiffness under various slippage conditions using the pullout test data. The details of this solution are found in Appendix B. The measured slippage from the LST tests showed that the maximum horizontal relative displacement between the geosynthetic and aggregates was less than 0.04 inch. This finding demonstrated that the interface slippage normally occurred in the geosynthetic-reinforced aggregates when the relative displacement was in the linear stage of the pullout test.

Impact of Geosynthetics on Cross-Anisotropy and Permanent Deformation of UGMs

The impact of geosynthetics on cross-anisotropy and permanent deformation of UGMs was evaluated using the rapid triaxial test. The geosynthetic reinforcement was influenced by the geosynthetic type, the sheet stiffness, and the geosynthetic location. In general, the geogrid increased both the vertical and horizontal modulus but not the anisotropic ratio of the UGM, while the geotextile only increased the horizontal modulus, which resulted in an increase in the anisotropic ratio of the UGM. Figure 5.5 shows the horizontal and vertical resilient moduli of the unreinforced UGM at each stress state shown in Table 4.1 in Chapter 4. Figures 5.6–5.8 show the effects of geogrids and geotextiles on the cross-anisotropy of UGMs.

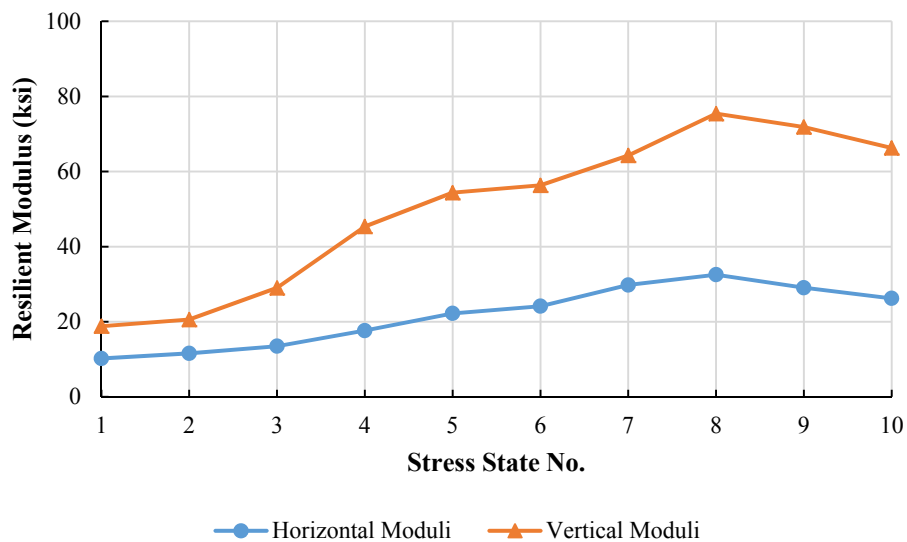


Figure 5.5. Horizontal and Vertical Moduli of Unreinforced UGM at Each Stress State

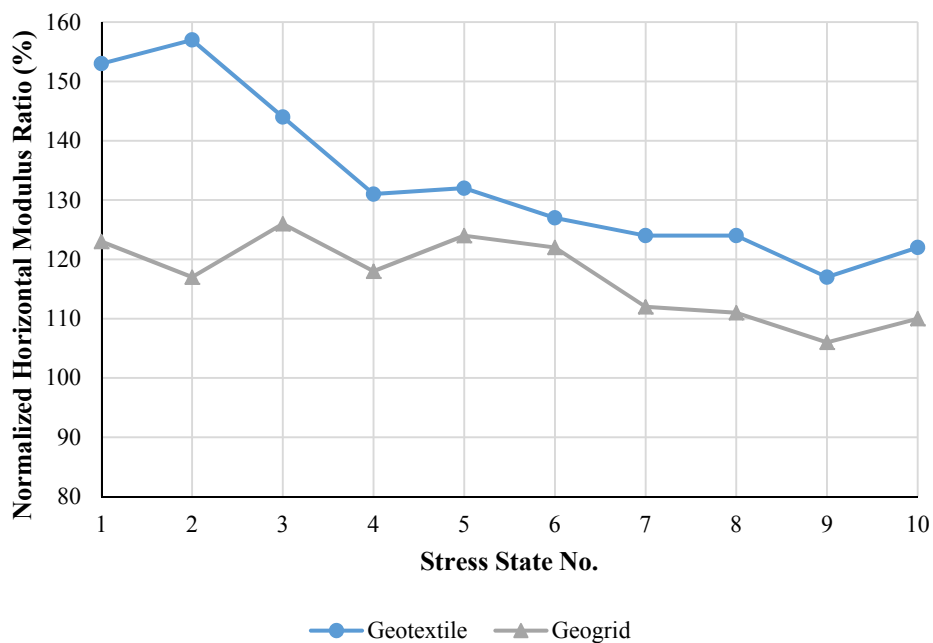


Figure 5.6. Effect of Geosynthetics on Horizontal Modulus of UGM

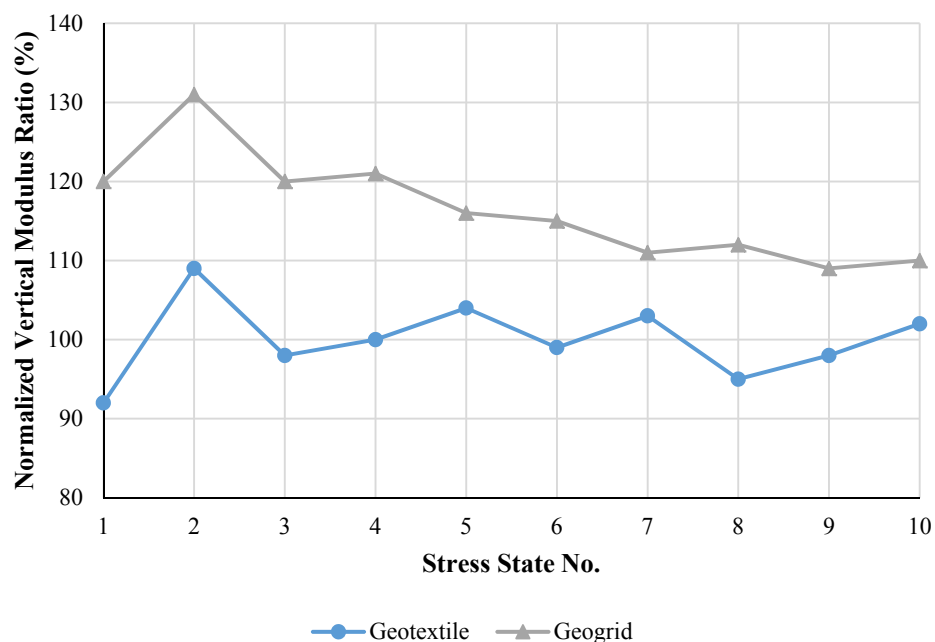


Figure 5.7. Effect of Geosynthetics on Vertical Modulus of UGM

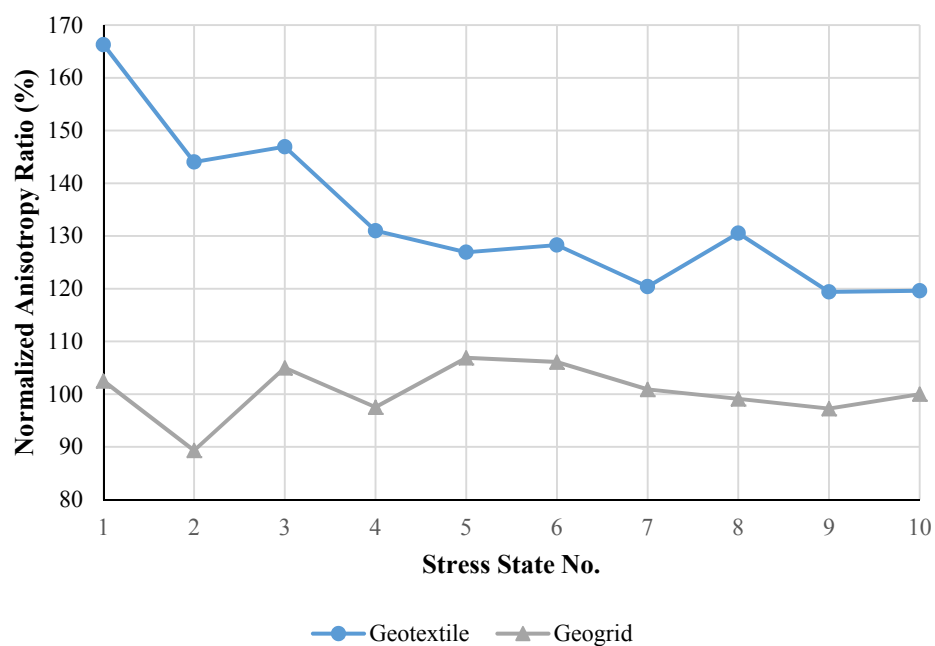


Figure 5.8. Effect of Geosynthetics on Anisotropic Ratio of UGM

Compared to the increase in the resilient modulus, the reduction of the permanent deformation of the UGM was a more important benefit of the geosynthetic reinforcement. Figure 5.9 shows the effect of geosynthetic reinforcement on the permanent deformation of the UGM when it was subjected to the different deviatoric stress levels. A description of the selected geosynthetics and the relevant geosynthetic material is found in Appendix C. Researchers found that the geogrid was much more effective than the geotextile at reducing the permanent

deformation of the UGM. The effect of geogrid reinforcement was not significant in reducing the permanent deformation until the deviatoric shear stress reached a threshold level (e.g., $\sigma_d = 19$ psi in this study).

The accurate and efficient laboratory characterization of a geosynthetic-reinforced UGM provided a sound basis for including the geosynthetic material in the Pavement ME Design software. The impact of geosynthetics on cross-anisotropy and permanent deformation of UGMs would further influence the performance of geosynthetic-reinforced pavement structures.

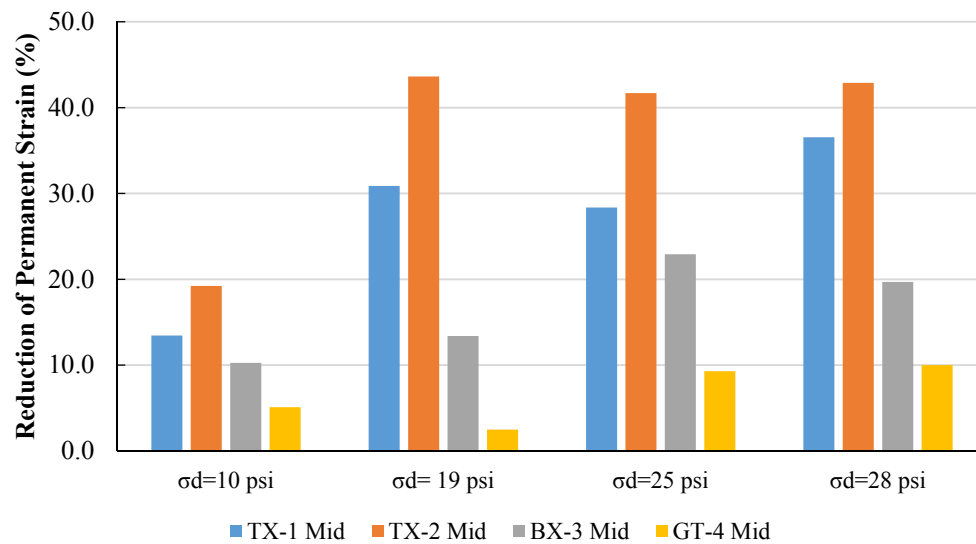


Figure 5.9. Effect of Geosynthetic Reinforcement on Reducing Permanent Strain of UGMs

Mechanistic-Empirical Permanent Deformation Model for Unreinforced and Geosynthetic-Reinforced UGMs

Based on the Drucker-Prager plastic yield criterion, a new mechanistic-empirical rutting model was developed to evaluate the stress-dependent permanent deformation characteristics of geosynthetic-reinforced and unreinforced UGMs. The model is found in Equation 4.7 in Chapter 4. Figures 5.10–5.12 compare the model-predicted permanent strain curves with the laboratory-measured ones at different stress states for both unreinforced and geosynthetic-reinforced UGMs. The stress states used in this testing protocol are tabulated in Table 4.3 in Chapter 4. Figures 5.10–5.12 illustrate that all of the determined RMSE values were relatively small, which indicates that the developed model accurately captured the influence of stress level on the permanent strain of the geosynthetic-reinforced and unreinforced UGMs. Figures 5.10–5.12 also present the determined coefficients of the developed rutting model. These model coefficients can be used to predict the permanent deformation of UGMs at any stress levels and numbers of load repetitions.

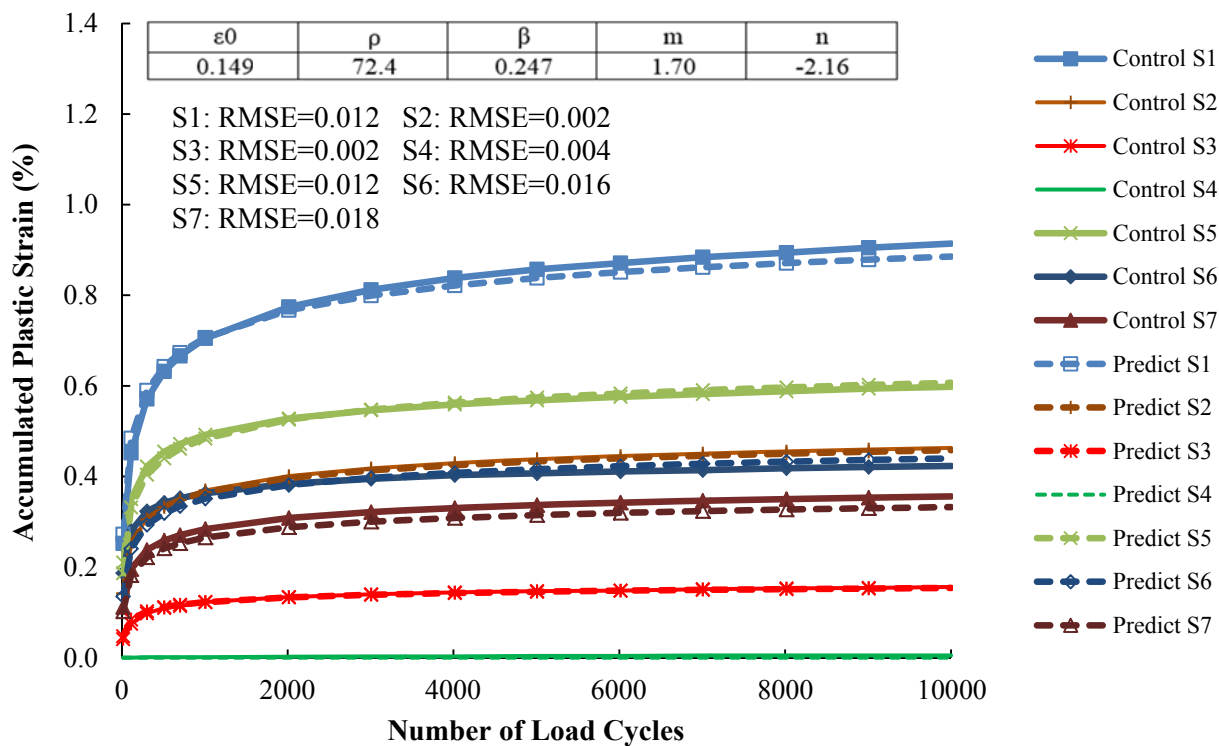


Figure 5.10. Comparison of Lab-Measured and Proposed-Model-Predicted Permanent Strain Curves for Unreinforced UGMs

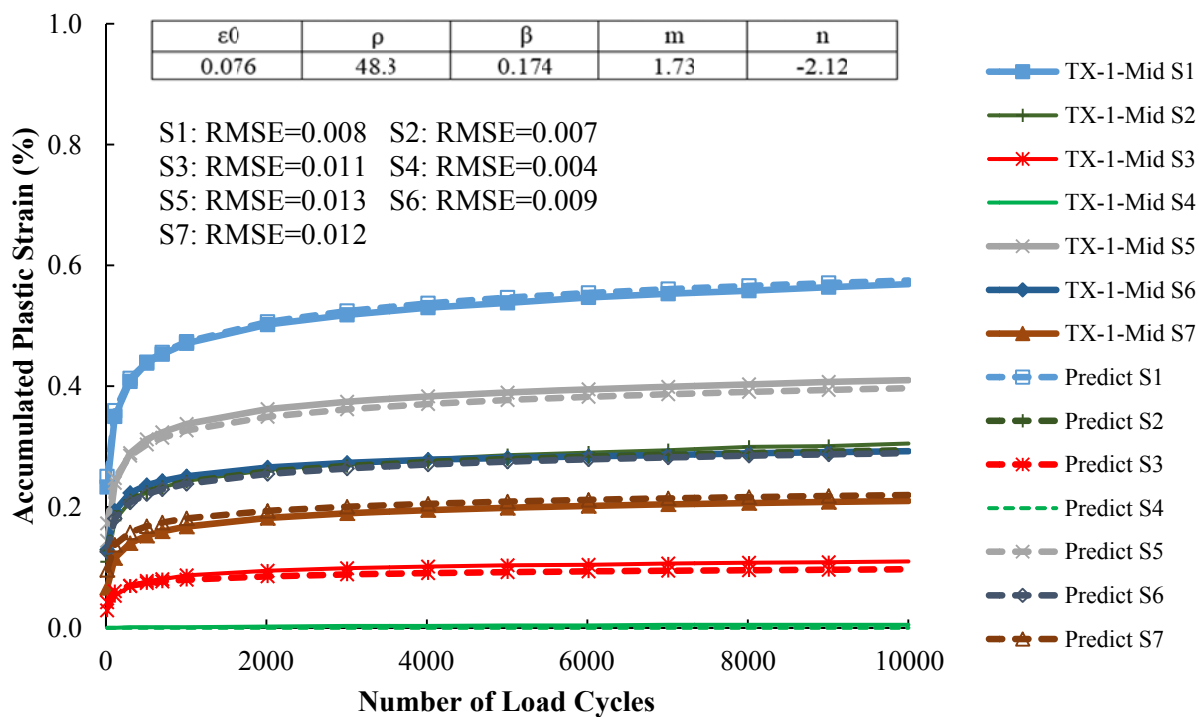


Figure 5.11. Comparison of Lab-Measured and Proposed Model-Predicted Permanent Strain Curves for Geogrid-Reinforced UGMs

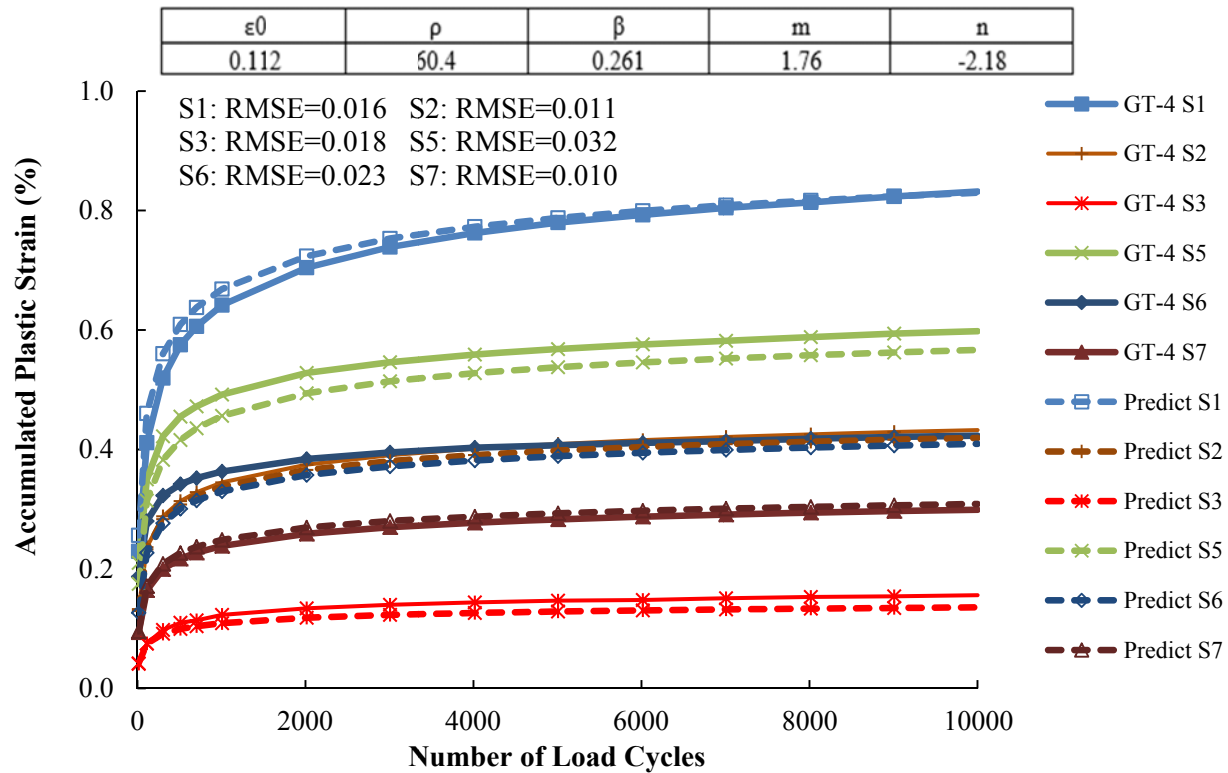


Figure 5.12. Comparison of Lab-Measured and Proposed-Model-Predicted Permanent Strain Curves for Geotextile-Reinforced UGMs

Analytical Model for Quantifying Influence of Geosynthetics

An analytical model was developed to predict the vertical and horizontal moduli and the permanent deformation of the geosynthetic-reinforced UGMs when subjected to a triaxial stress state. In this model, the effect of lateral confinement due to the shear restraint of the geosynthetic was equivalent to an additional confining stress, which was triangularly distributed along the side of a UGM specimen. The developed analytical model was also capable of quantifying the influence of the tensile sheet stiffness and the location of the geosynthetic within the base course. Figures 5.13 and 5.14 show the effect of the tensile sheet stiffness of the geosynthetic on the horizontal and vertical moduli of the UGM.

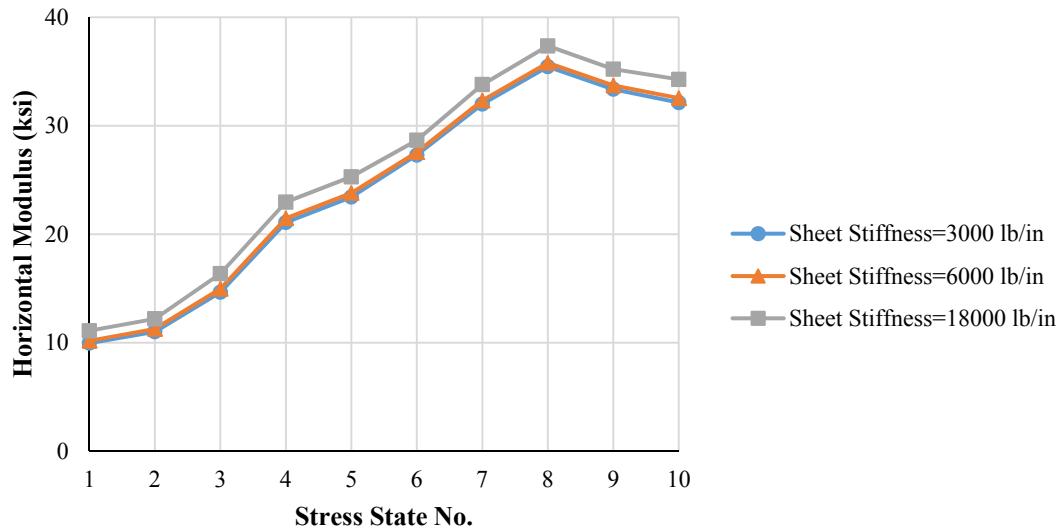


Figure 5.13. Effect of Geosynthetic Sheet Stiffness on Predicted Horizontal Modulus of UGM

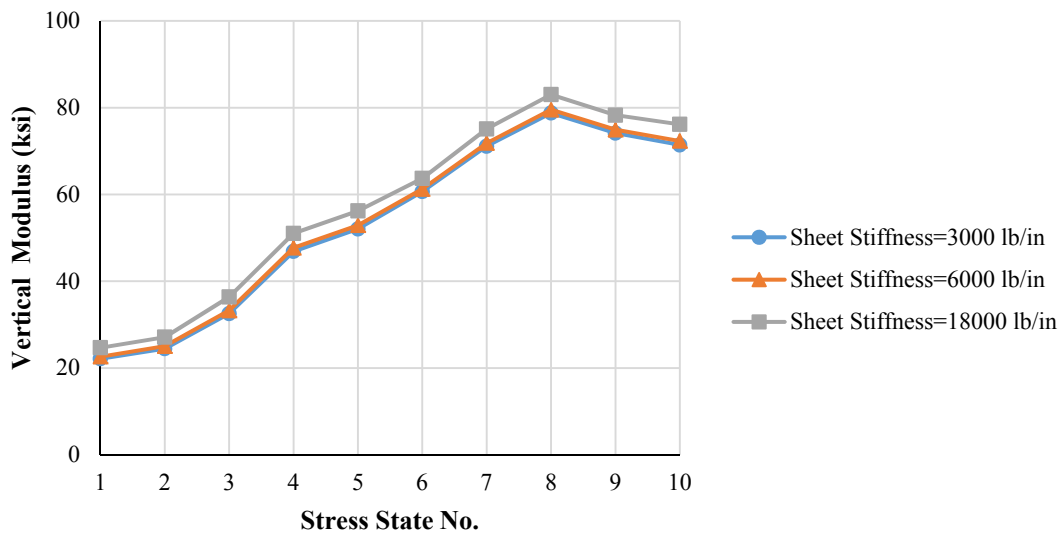


Figure 5.14. Effect of Geosynthetic Sheet Stiffness on Predicted Vertical Modulus of UGM

Development of Finite Element Model for Geosynthetic-Reinforced Pavement

A geosynthetic reinforced the granular material through two major mechanisms: (a) lateral confinement to reinforce the UGM near the geosynthetic, and (b) the membrane effect to reduce the vertical stresses in the base and subgrade. The finite element models were developed to simulate the geosynthetic-reinforced pavement structures by taking into account these two mechanisms, and to evaluate the effect of material and geometric factors on the performance of geosynthetic-reinforced pavements.

In the finite element model, the lateral confinement was equivalent to an increase in the horizontal and vertical moduli of the UGM in the geosynthetic influence zone. The membrane

effect was simulated by defining the geosynthetic as a membrane element and characterizing the geosynthetic-aggregate/soil interface interaction using the Goodman model (43). The developed geosynthetic-reinforced pavement models were successfully validated by comparing the predicted pavement responses to the LST measurements. These finite element models were also able to quantify the effect of layer thickness, layer modulus, geosynthetic sheet stiffness, and geosynthetic location on pavement performance. The finite element modeling technique provided a sound basis for predicting the critical stresses and strains that control the performance of geosynthetic-reinforced pavements. Using this approach, a large database of critical pavement responses was established for a wide range of geosynthetic-reinforced pavement structures. This database was used in developing ANN models of the critical strains in pavement structures.

Predictions of Geosynthetic-Reinforced Pavement Performance

The ANN models were used to predict the responses of geosynthetic-reinforced pavement structures when they were subjected to a standard single-axle load (i.e., 18,000-lb single-axle load). The established database of geosynthetic-reinforced pavement responses was used to train and validate the ANN models with the following critical strains:

- Horizontal tensile strain at the bottom of the asphalt layer for fatigue cracking.
- Vertical compressive strains within the asphalt layer, base course, and subgrade for rutting.

The developed ANN models were accurate and efficient in predicting these critical responses of arbitrary user-inputted geosynthetic-reinforced pavement structures. Compared to the finite element method, the major advantage of the ANN approach was that it was compatible with the Pavement ME Design software and greatly reduced computer run times. Figures 5.15 and 5.16 compare the effect of the base modulus on the predicted critical responses of unreinforced and geogrid-reinforced pavements as shown in Figure 4.83 in Chapter 4. The ANN models were sensitive to the variation of the base modulus. The compressive strain in the base course and subgrade decreased with an increasing base modulus. Figures 5.17 and 5.18 show the sensitivity of the subgrade modulus to the critical responses of the unreinforced and geogrid-reinforced pavements as predicted by the ANN models. The compressive strain at the top of the subgrade decreased, while the average compressive strain in the base layer slightly increased with an increasing subgrade modulus. The effects of the tensile sheet stiffness of the geogrid on the predicted critical pavement responses are shown in Figures 5.19 and 5.20. The geogrid with a higher tensile sheet stiffness achieved more beneficial effects in reducing the compressive strain in the base layer and subgrade.

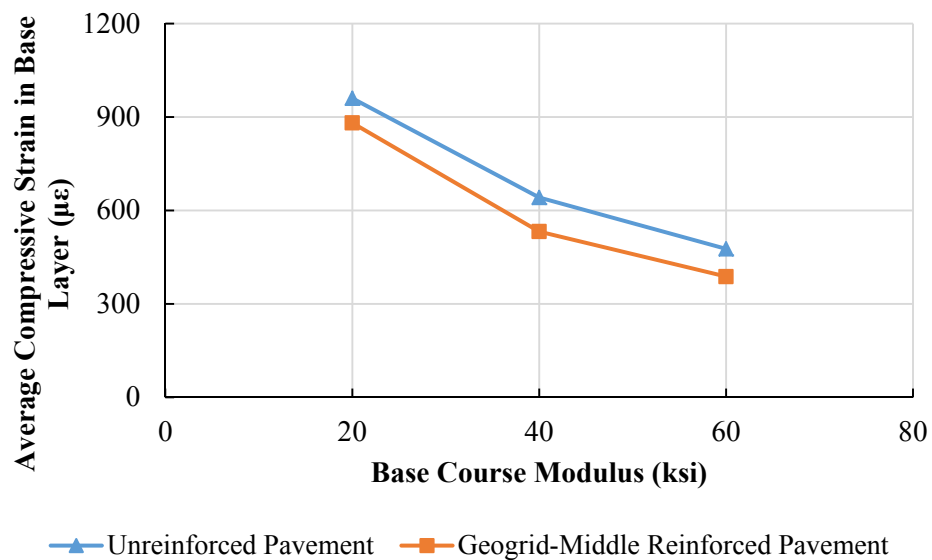


Figure 5.15. Effect of Base Modulus on Average Compressive Strain in Base Layer

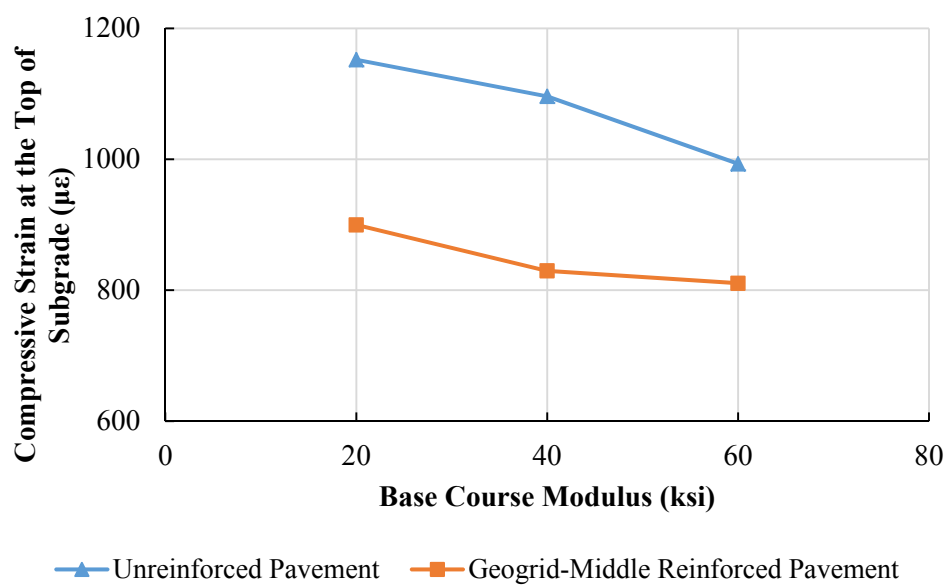


Figure 5.16. Effect of Base Modulus on Compressive Strain at the Top of Subgrade

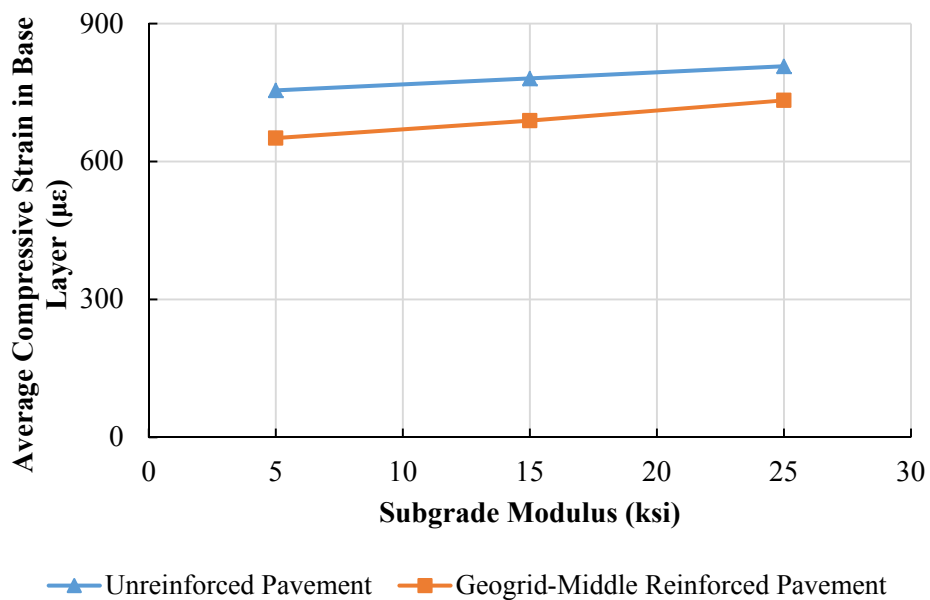


Figure 5.17. Effect of Subgrade Modulus on Average Compressive Strain in Base Layer

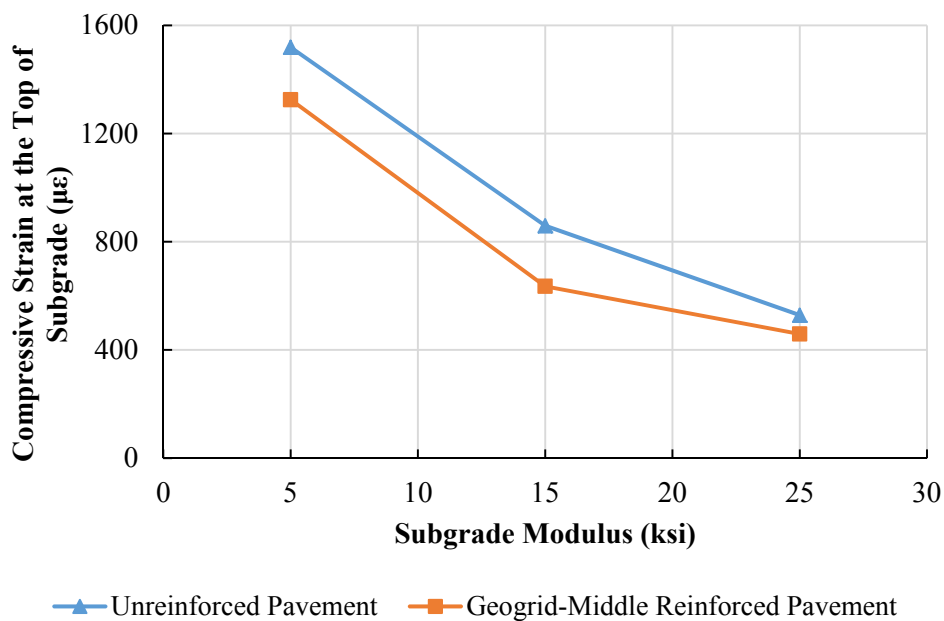


Figure 5.18. Effect of Subgrade Modulus on Compressive Strain at the Top of Subgrade

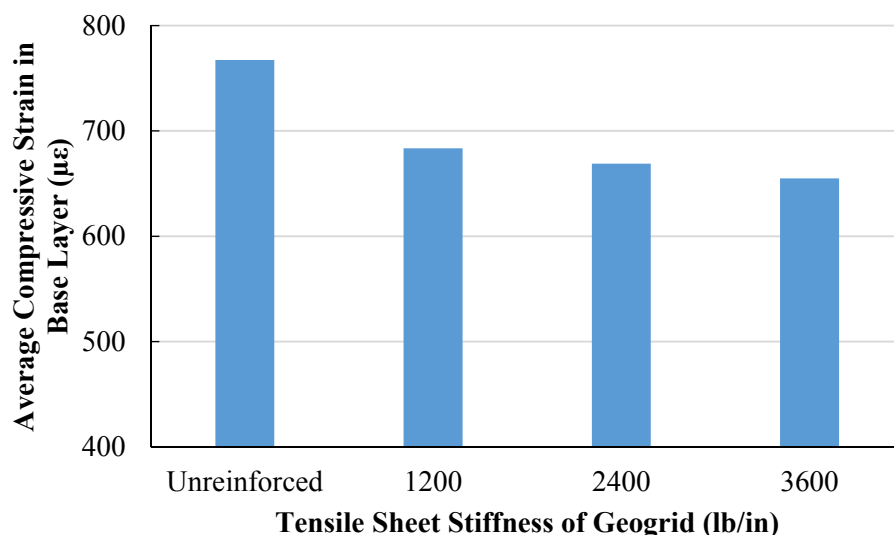


Figure 5.19. Effect of Tensile Sheet Stiffness of Geogrid on Average Compressive Strain in Base Layer

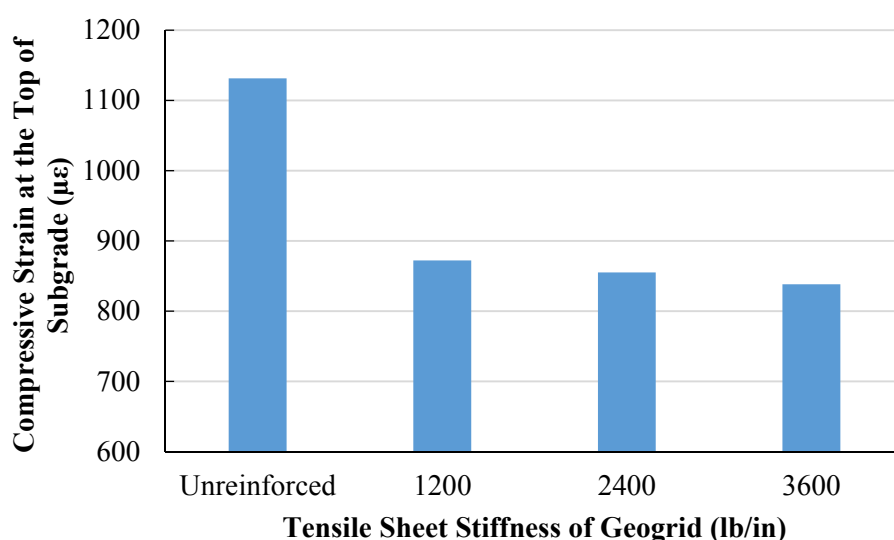


Figure 5.20. Effect of Tensile Sheet Stiffness of Geogrid on Compressive Strain at the Top of Subgrade

The performance of geosynthetic-reinforced flexible pavements includes fatigue cracking, permanent deformation, and IRI. These pavement performance measures are significantly influenced by traffic and climate factors, which have been taken into account in the current Pavement ME Design software. In this study, the geosynthetic-reinforced pavement structure with the input material properties was first made equivalent to an unreinforced pavement structure with the modified input material properties to achieve the identical critical responses. The modified material properties were then input into the Pavement ME Design software to predict the performance of the geosynthetic-reinforced pavement. The calibration of this approach relied on the validity of the calibration that was done in the existing versions of the

Pavement ME Design software. Figures 5.21–5.23 compare the effect of the base modulus on the predicted performance of geosynthetic-reinforced and unreinforced pavements after 10-year service in College Station, Texas. The geogrid placed in the middle of the base course was effective at reducing the rutting damage and IRI of pavement while slightly reducing the fatigue cracking of the pavement. The geogrid had a more beneficial effect on pavement performance when it was placed in the base course with a smaller resilient modulus. Figures 5.24–5.26 show the sensitivity of the subgrade modulus on the predicted performance of geosynthetic-reinforced and unreinforced pavements. The geogrid was more effective at reducing the rutting and IRI when the subgrade had a smaller resilient modulus. Figures 5.27–5.29 present the effect of the tensile sheet stiffness of the geogrid on the predicted pavement performance. The rutting depth, fatigue cracking, and IRI slightly decreased with increasing sheet stiffness of the geogrid.

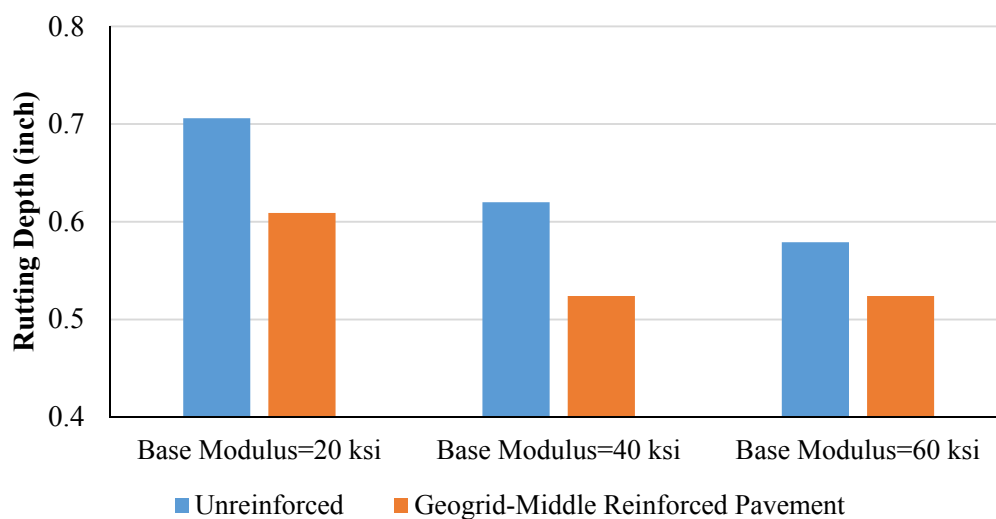


Figure 5.21. Effect of Base Modulus on Rutting Depth of Geosynthetic-Reinforced and Unreinforced Pavements

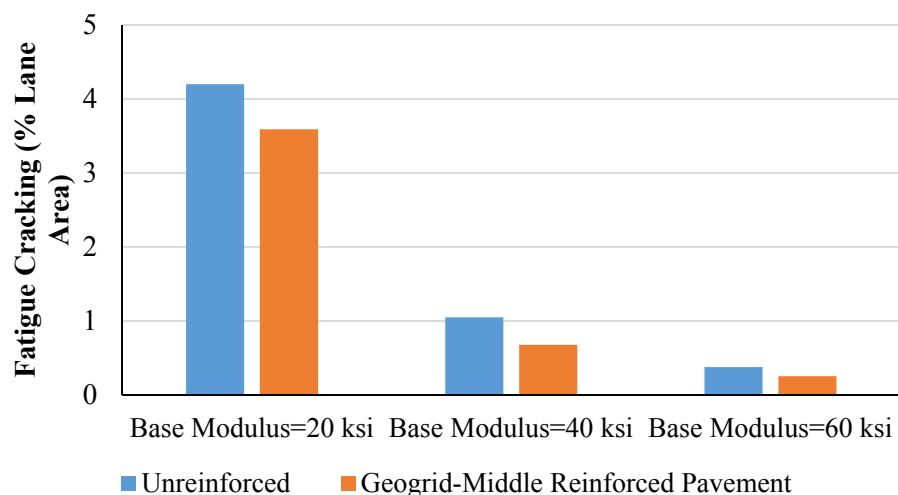


Figure 5.22. Effect of Base Modulus on Fatigue Cracking of Geosynthetic-Reinforced and Unreinforced Pavements

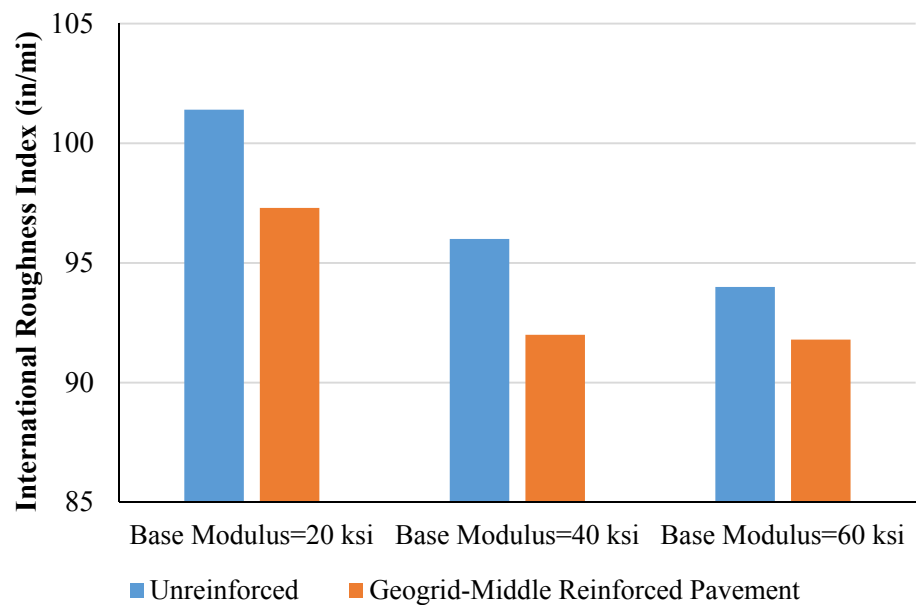


Figure 5.23. Effect of Base Modulus on IRI of Geosynthetic-Reinforced and Unreinforced Pavements

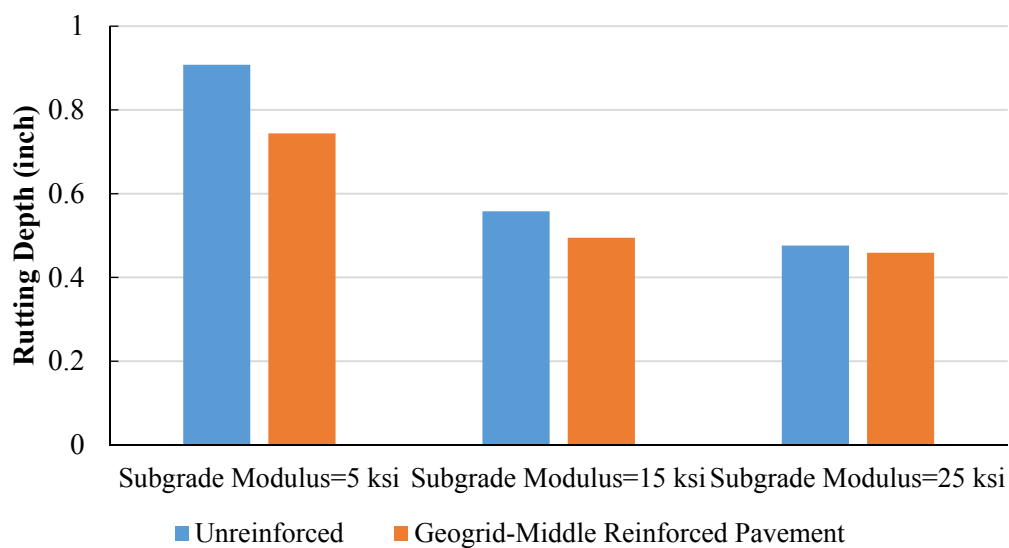


Figure 5.24. Effect of Subgrade Modulus on Rutting Depth of Geosynthetic-Reinforced and Unreinforced Pavements

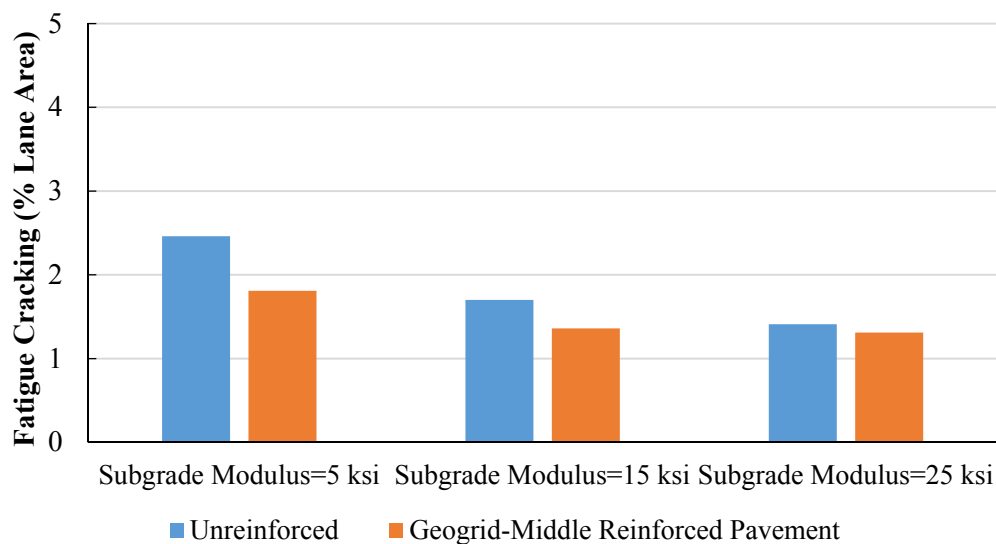


Figure 5.25. Effect of Subgrade Modulus on Fatigue Cracking of Geosynthetic-Reinforced and Unreinforced Pavements

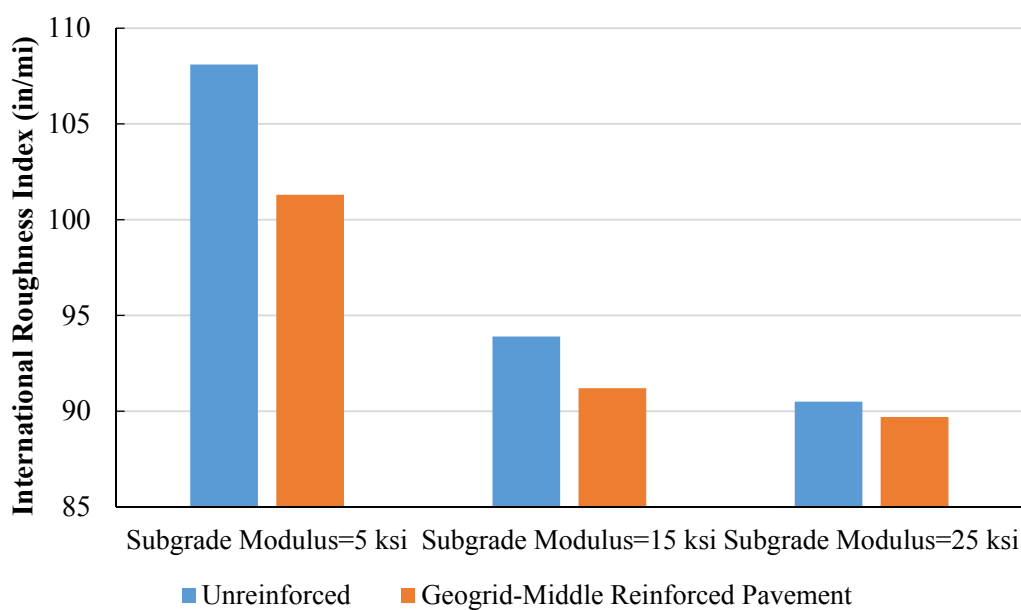


Figure 5.26. Effect of Subgrade Modulus on IRI of Geosynthetic-Reinforced and Unreinforced Pavements

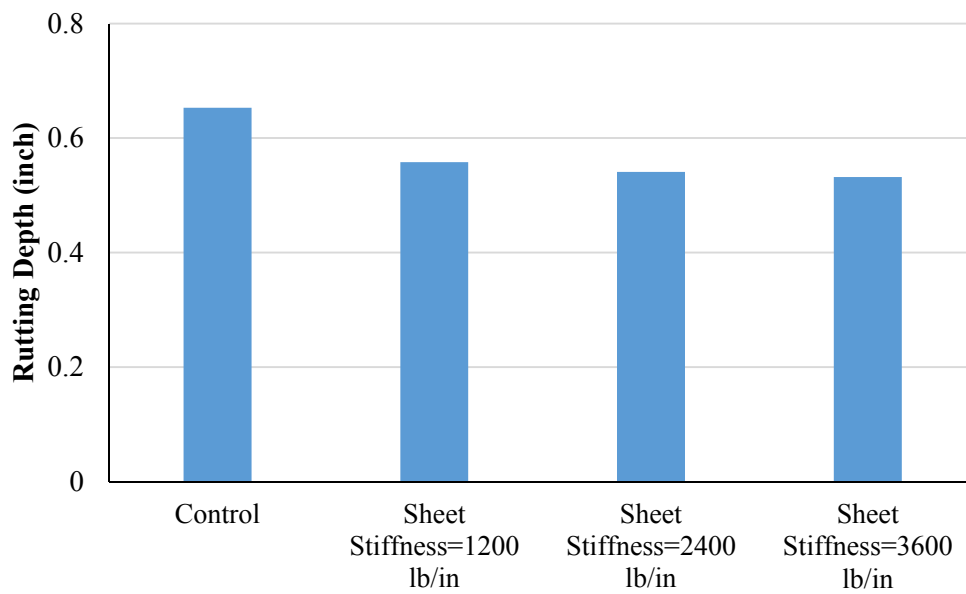


Figure 5.27. Effect of Sheet Stiffness of Geogrid on Rutting Depth of Reinforced Pavements

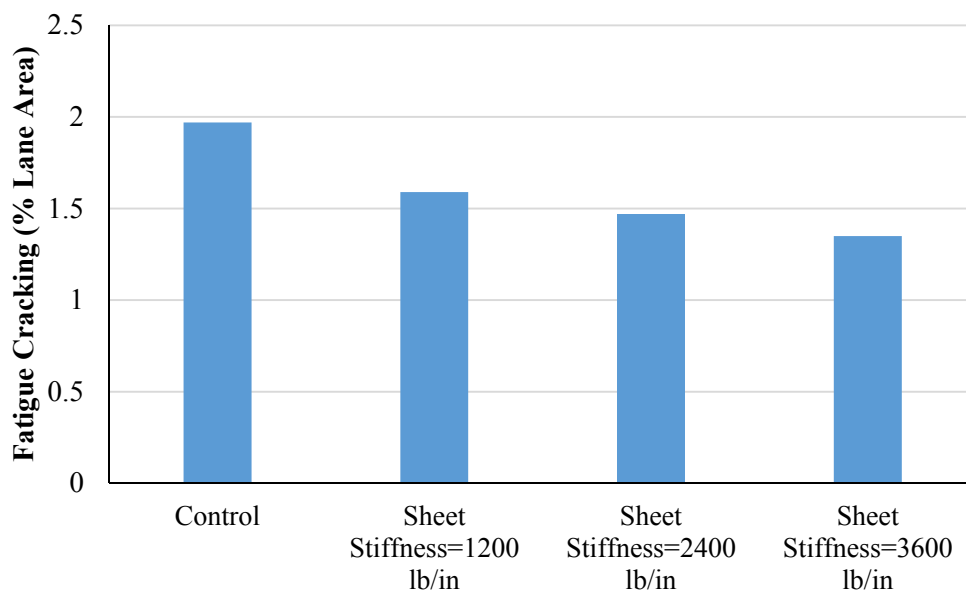


Figure 5.28. Effect of Sheet Stiffness of Geogrid on Fatigue Cracking of Reinforced Pavements

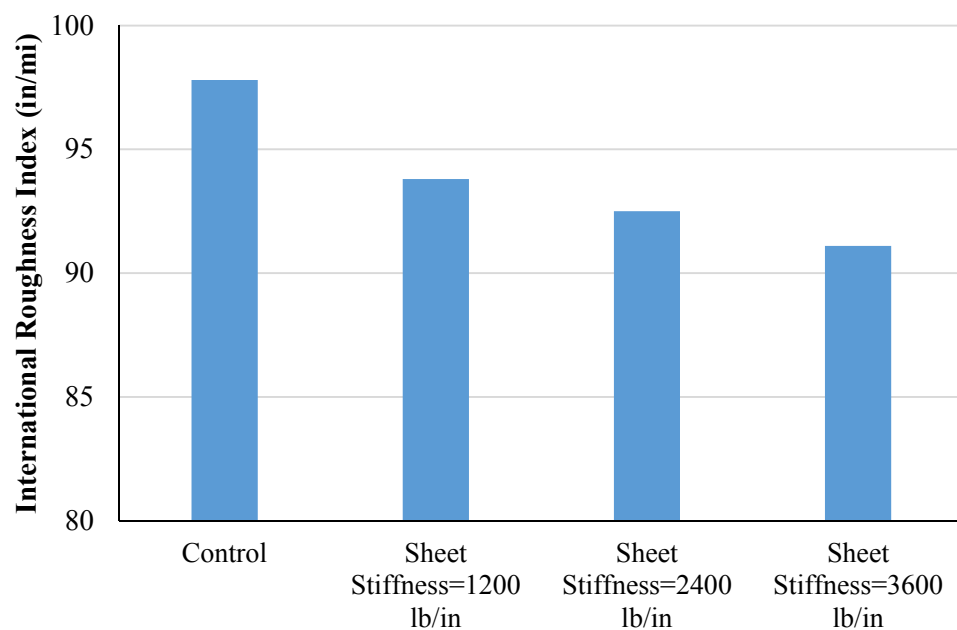


Figure 5.29. Effect of Sheet Stiffness of Geogrid on IRI of Reinforced Pavements

CHAPTER 6. SUMMARY AND SUGGESTED RESEARCH

Summary

A well-designed LST testing protocol with extensive instrumentations was conducted on flexible and rigid pavements using an 8-ft-diameter by 6-ft-high circular steel tank. The implemented testing program differed from previous studies, which traditionally assessed the influence of the base reinforcement on pavement performance under repetitive surface loading until failure. Instead, the experimental program focused on the following distinctive characteristics of the geosynthetic, which were essential for proper modeling of the geosynthetic material for base reinforcement, and ultimately for enhanced predictions of the performance of pavements with geosynthetic-reinforced base courses:

- The stress distributions across the geosynthetic under dynamic loading in both the AC and PCC pavements.
- The strain measurements in the geosynthetic and at the bottom of the surface layer (AC or PCC) under dynamic loading.
- The deformed shape of the geosynthetic and the potential slippage at the geosynthetic and the unbound aggregate material interface under dynamic loading.
- The potential slippage between the bottom of the PCC slab and the supporting CAB layer at the edge of the loaded slab.

Upon completion of the testing program, a database of pertinent pavement responses with and without reinforcement of the base layer collected under realistic pavement loading conditions was assembled. The established database was then used in the numerical investigation (model and input parameters, etc.) of the LST data to assess the validity and applicability of the finite element numerical modeling of geosynthetic-reinforced pavement structures.

Building upon the results of the finite element numerical validation, the Composite Geosynthetic–Base Course Model was developed as a subroutine for the AASHTOWare Pavement ME Design software. Both types of geosynthetics were included in the model: geogrids and geotextiles. The subroutine supplemented the Pavement ME Design software by making it possible to predict the performance of pavements when they were supported by unbound base/subbase courses that were reinforced with geosynthetics. The model required the input of the material properties of the unreinforced, unbound base course and the selected geosynthetics. It also required the input of the location of the geosynthetics within or beneath the base course. The input geosynthetic material property was its sheet stiffness measured at low strain levels (approximately 1 percent). The model also required the input of the shear interaction coefficient, which was determined by laboratory testing and indicated the degree to which the embedded geosynthetic restrained the surrounding unbound base course material. Internal to the subroutine, the model converted the two separate sets of material properties into a composite reinforced base course material property.

This composite material property was used in a series of ANN models that were created in this project to predict the critical strains and stresses used in the current version of the Pavement ME Design software to predict several measures of pavement performance. The asphalt pavement performance measures are roughness (IRI), rutting, and fatigue cracking.

The ANN models were generated from large computed databases of the critical strains and stresses in asphalt pavements. No ANN models were developed for concrete pavements because of the insensitivity of critical stresses in concrete pavements to either type or location of geosynthetics. The databases incorporated the calculated values of the strains and stresses as they varied within a wide range of layer thickness, layer modulus, base course anisotropic ratio, embedded geosynthetic sheet stiffness, and geosynthetic location within or beneath the base course. The finite element program that was used to create these databases was capable of representing anisotropy, stress-dependent material properties, and small plastic deformation zones. The finite element program also had interface elements to represent the interaction, including the slippage, of the base course with the geosynthetic.

The use of this finite element program was undertaken only after it had demonstrated the ability to match closely the measured displacements, strains, and stresses in the LST tests of typical asphalt and concrete pavements.

Triaxial laboratory test methods were used to determine the resilient modulus and repeated load permanent deformation properties of the base course both with and without embedded geosynthetics. The test protocol was arranged to extract the anisotropic and stress-dependent properties of a base course as well as of a base course that was altered by geosynthetic reinforcing. The resilient modulus and repeated load permanent deformation test protocols have been prepared in the standard AASHTO format and are presented in Attachments A and B.

A method was developed to use these same test results to determine analytically the shear interaction coefficient. It was also determined that a commonly used geosynthetic test, the pullout resistance test, may be used to determine the shear interaction coefficient.

Suggested Research

Based on the findings of this project, the following topics are suggested for future research:

- Exploring the massive data generated by the LST tests: Much useful information and data were generated by the LST tests, only a fraction of which was used directly in this project. The experience that was gained in the instrumentation, measurement, and data interpretation has been documented and can be found in Appendices E through K. The data have extensive implications for material characterization, modeling, and improved performance prediction. As an example, models of faulting and erosion in concrete pavements can be substantially improved with the data observed and recorded and the permanent deformation models developed in this project. Inclusion of these results in the Pavement ME Design software will require a major revision of the concrete pavement structural subsystem within that software.
- Expanding the range of material properties for the developed subroutine: The input to the Composite Geosynthetic–Base Course Model requires unbound base course material properties and geosynthetic properties. These properties can be provided at any of three levels of data refinement. There is a need to have a wider range of these properties covering all of the more commonly used base courses and geosynthetics

- available to pavement designers in an electronically accessible catalog. This catalog would make this subroutine more extensively used and useful.
- Extending the capabilities of the developed subroutine: Extending the ability of the Composite Geosynthetic–Base Course Model to include modified or stabilized materials is the next step to make this development more extensively applicable. These modified or stabilized models will be able to use the same three levels of input properties. The calibration of these models is expected to be considerably different from that of the unbound models. The research team has located a number of in-service pavements with stabilized base courses reinforced with geosynthetics in the LTPP database, which can be used for the calibration process.
 - Developing relations between soil suction and water content of the base course: The effects of the ambient moisture in the base course on the resulting performance of the pavement it supports suggest that a highly productive area for future research is to develop the soil-water characteristic curves (SWCCs; relation between the soil suction and the water content of the base course) of the more commonly used base courses. The SWCCs are critical for the following applications:
 - Allowing the Pavement ME Design software to consider the effect of this important variable in the design of both asphalt and concrete pavements as it varies with climatic and ground water conditions.
 - Being used in quality control (QC) and quality assurance (QA) processes during construction. The research focus on the moisture effects on the base courses will require the development of the soil-dielectric characteristic curve (SDCC) of base courses in addition to the SWCC. Having the SDCC available during construction permits the use of ground penetrating radar (GPR) as a QC/QA measurement technique. The advantage of using GPR for compaction QC/QA is that measurements can be made at highway speeds with approximately 1-ft spacing between individual measurements. Verifying compaction water content and density with a GPR-created strip map provides a better overview of the construction production quality than randomly selected sampling, as is done at present. Also, it can be done much more quickly with no loss of accuracy.

REFERENCES

1. Berg, R.R., Christopher, B.R., and Perkins, S.W. (2000). Geosynthetic Reinforcement of the Aggregate Base/Subbase Courses of Flexible Pavement Structures. *GMA White Paper II*, Geosynthetic Materials Association, Roseville, MN, 176p.
2. Perkins, S. W. (2001). Mechanical-Empirical Modeling and Design Model Development of Geosynthetic-Reinforced Flexible Pavement. *Final Report, No. FHWA/MT-01-002/99160-1A*, Federal Highway Administration, Washington, D.C., 171p.
3. Perkins, S. W. (2001). Numerical Modeling of Geosynthetic Reinforced Flexible Pavements. *Final Report, No. FHWA/MT-01-003/99160-2*, Federal Highway Administration, Washington, D.C., 112p.
4. Kwon, J. (2007). *Development of a Mechanistic Model for Geogrid Reinforced Flexible Pavements*. Ph.D. Dissertation, University of Illinois at Urbana-Champaign, Urbana, Illinois.
5. Zornberg, J. G., Prozzi, J. A., Gupta, R., Luo, R., McCartney, J. S., Ferreira, J. Z., and Nogueira, C. (2008). Validating Mechanisms in Geosynthetic Reinforced Pavements. *Research Report FHWA/TX-08/0-4829-1*, Center for Transportation Research, The University of Texas at Austin, Austin, Texas.
6. Giroud, J. P. and Noiray, L. (1981). Geotextile-Reinforced Unpaved Roads. *Journal of Geotechnical Engineering Division, ASCE*, Vol. 107, No. 9, pp. 1233–1254.
7. Giroud, J. P., Ah-Line, A., and Bonaparte, R. (1984). Design of Unpaved Roads and Traffic Areas with Geogrids. *Proceedings of the Symposium on Polymer Grid Reinforcement*, Thomas Telford, London, England, pp. 116–127.
8. Perkins, S.W., and Ismeik, M. (1997). A Synthesis and Evaluation of Geosynthetic-Reinforced Base Course Layers in Flexible Pavements: Part I Experimental Work. *Geosynthetics International*, Vol. 4, No. 6, pp. 549–604.
9. Perkins, S.W., and Ismeik, M. (1997). A Synthesis and Evaluation of Geosynthetic-Reinforced Base Course Layers in Flexible Pavements: Part II Analytical Work. *Geosynthetics International*, Vol. 4, No. 6, pp. 605–621.
10. Holtz, R.D., Christopher, B.R., and Berg, R.R. (1998). Geosynthetic Design and Construction Guidelines, *FHWA-HI-98-038*, Washington, D.C., 460p.
11. Giroud, J.P., and Han, J. (2004). Design Method for Geogrid-Reinforced Unpaved Roads-I. *Journal of Geotechnical Engineering, ASCE*, Vol. 130, No. 8, pp. 775–786.
12. Kwon, J., and Tutumluer, E. (2009). Geogrid Base Reinforcement with Aggregate Interlock and Modeling of Associated Stiffness Enhancement in Mechanistic Pavement Analysis. *Transportation Research Record: Journal of the Transportation Research Board*, No. 2116, pp. 85–95.
13. Al-Qadi, I. L., Dessouki, S., Tutumluer, E., and Kwon, J. (2011). Geogrid Mechanism in Low-Volume Flexible Pavements: Accelerated Testing of Full Scale Heavily Instrumented Pavement Sections. *International Journal of Pavement Engineering*, Vol. 12, No. 2, pp. 121–135.

14. Nazzal, M., Abu-Farsakh, M., and Mohammad, L. (2007). Laboratory Characterization of Reinforced Crushed Limestone under Monotonic and Cyclic Loading. *Journal of Materials in Civil Engineering*, Vol. 19, No. 9, pp. 772–783.
15. Moghaddas-Nejad, F., and Small, J. C. (2003). Resilient and Permanent Characteristics of Reinforced Granular Materials by Repeated Load Triaxial Tests. *Geotechnical Testing Journal*, Vol. 26, No. 2, pp. 152–166.
16. Rahman, M., Arulrajah, A., Piratheepan, J., Bo, M., and Imteaz, M. (2014). Resilient Modulus and Permanent Deformation Responses of Geogrid-Reinforced Construction and Demolition Materials. *Journal of Materials in Civil Engineering*, Vol. 26, No. 3, pp. 512–519.
17. Yang, X., and Han, J. (2013). Analytical Model for Resilient Modulus and Permanent Deformation of Geosynthetic-Reinforced Unbound Granular Material. *Journal of Geotechnical and Geoenvironmental Engineering*, Vol. 139, No. 9, pp. 1443–1453.
18. McDowell, G. R., Harireche, O., Konietzky, H., Brown, S. F., and Thom, N. H. (2006). Discrete Element Modelling of Geogrid-Reinforced Aggregates. *Proceedings of the Institution of Civil Engineers: Geotechnical Engineering*, Vol. 159, No. 1, pp. 35–48.
19. Schuettelpelz, C., Fratta, D., and Edil, T. B. (2009). Evaluation of the Zone of Influence and Stiffness Improvement from Geogrid Reinforcement in Granular Materials. *Transportation Research Record: Journal of the Transportation Research Board*, No. 2116, pp. 76–84.
20. Adu-Osei, A., Little, D. N., and Lytton, R. L. (2001). Cross-Anisotropic Characterization of Unbound Granular Materials. *Transportation Research Record: Journal of the Transportation Research Board*, No. 1757, pp. 82–91.
21. Ashtiani, R. (2009). *Anisotropic Characterization and Performance Prediction of Chemically and Hydraulically Bounded Pavement Foundations*. Ph.D. Dissertation, Texas A&M University, College Station, Texas.
22. Oh, J., Lytton, R. L., and Fernando, E. (2006). Modeling of Pavement Response Using Nonlinear Cross-Anisotropy Approach. *Journal of Transportation Engineering*, Vol. 132, No. 6, pp. 458–468.
23. Perkins, S. W., Christopher, B. R., Cuelho, E. L., Eiksund, G. R., Hoff, I., Schwartz, C. W., Svano, G., and Want, A. (2004). Development of Design Methods for Geosynthetic Reinforced Flexible Pavements. *Report No. DTFH61-01-X-00068*, 263p.
24. Wayne, M., Boudreau, R. L., and Kwon, J. (2011). Characterization of Mechanically Stabilized Layer by Resilient Modulus and Permanent Deformation Testing. *Transportation Research Record: Journal of the Transportation Research Board*, No. 2204, pp. 76–82.
25. Abu-Farsakh, M., Souci, G., Voyiadjis, G. Z., and Chen, Q. (2012). Evaluation of Factors Affecting the Performance of Geogrid-Reinforced Granular Base Material Using Repeated Load Triaxial Tests. *Journal of Materials in Civil Engineering*, Vol. 24, No. 1, pp. 72–83.
26. Perkins, S. W., and Edens, M. Q. (2003). A Design Model for Geosynthetic-Reinforced Pavements. *International Journal of Pavement Engineering*, Vol. 4, No. 1, pp. 37–50.
27. Saad, B., Mitri, H., and Poorooshasb, H. (2006). 3D FE Analysis of Flexible Pavement with Geosynthetic Reinforcement. *Journal of Transportation Engineering*, Vol. 132, No. 5, pp. 402–415.

28. Prozzi, J. A., and Luo, R. (2007). Using Geogrids to Minimize Reflective Longitudinal Cracking on Pavements over Shrinking Subgrades. *Transportation Research Record: Journal of the Transportation Research Board*, No. 2004, pp. 99–110.
29. Kwon, J., Tutumluer, E., and Al-Qadi, I. L. (2009). Validated Mechanistic Model for Geogrid Base Reinforced Flexible Pavement. *Journal of Transportation Engineering*, Vol. 135, No. 12, pp. 915–926.
30. Barksdale, R. D., and Brown, S. F. (1988). Potential Benefits of Geosynthetics in Flexible Pavements. *Final Report, No. E-20-672*, National Cooperative Highway Research Program, National Research Council, Washington D.C., 626p.
31. Dondi, G. (1994). Three-Dimensional Finite Element Analysis of a Reinforced Paved Road. *Fifth International Conference on Geotextiles, Geomembranes and Related Products*, Singapore, pp. 95–100.
32. Wathugala, G. W., Huang, B., and Pal, S. (1996). Numerical Simulation of Geosynthetic-Reinforced Flexible Pavements. *Transportation Research Record: Journal of the Transportation Research Board*, No. 1534, pp. 58–65.
33. Luo, R. (2007). *Minimizing Longitudinal Pavement Cracking Due to Subgrade Shrinkage*. Ph.D. Dissertation, The University of Texas at Austin, Austin, Texas.
34. Perkins, S. W., Christopher, B. R., Cuelho, E. L., Eiksund, G. R., Hoff, I., Schwartz, C. W., Svano, G., and Want, A. (2004). Development of Design Methods for Geosynthetic Reinforced Flexible Pavements. *Final Report No. DTFH61-01-X-00068*, Federal Highway Administration, Washington, D.C.
35. Webster, S. L. (1991). Geogrid Reinforced Base Course for Flexible Pavements for Light Aircraft: Literature Review and Test Section Design. *Interim Report, NO. DOT/FAA/RD-90/28*, 40p.
36. Bhutta, S. A. (1998). *Mechanistic-Empirical Pavement Design Procedure for Geosynthetically Stabilized Flexible Pavements*. Ph.D. Dissertation, Virginia Polytechnic Institute and State University, Blacksburg, Virginia.
37. Aran, S. (2006). Base Reinforcement with Biaxial Geogrid—Long Term Performance. *Transportation Research Record: Journal of the Transportation Research Board*, No. 1975, pp. 115–123.
38. Chan, F., Barksdale R., and Brown, S. (1989). Aggregate Base Reinforcement of Surfaced Pavements. *Geotextile and Geomembranes*, Vol. 8, No. 3, pp. 165–189.
39. Haas R., Walls, J., and Carroll, R.G. (1988). Geogrid Reinforcement of Granular Bases in Flexible Pavements. *Transportation Research Record: Journal of the Transportation Research Board*, No. 1188, pp. 19–27.
40. Moghaddas-Nejad, F., and Small, J.C. (1996). Effect of Geogrid Reinforcement in Model Track Tests on Pavement. *Journal of Transportation Engineering*, Vol. 122, No. 6, pp. 468–474.
41. Perkins, S.W. (1999). Mechanical Response of Geosynthetic-Reinforced Flexible Pavements. *Geosynthetic International*, Vol. 6, No. 5, pp. 347–381.
42. ABAQUS. (2010). ABAQUS Standard User's Manual. Abaqus Inc., Providence, RI.

43. Goodman, R.E., Taylor, R.L., and Brekke, T.L. (1968). A Model for the Mechanics of Jointed Rock. *Journal of Soil Mechanics and Foundation Division, ASCE*, Vol. 94, No. SM3, pp. 637–659.
44. Christopher, B. R., Berg, R. R., and Perkins, S. W. (2001). Geosynthetic Reinforcement in Roadway Sections. Final Report, NCHRP Synthesis for NCHRP Project 20-7, Task 112, 119p.
45. Loulizi, A., Al-Qadi, I.L. Bhutta, S.A., and Flintsch, G.W. (1999). Evaluation of Geosynthetics Used as Separators. *Transportation Research Record: Journal of the Transportation Research Record*, No. 1687, pp. 104–111.
46. Texas Department of Transportation. (1999). Testing Geogrids. Tex-621-J, TxDOT, Austin, Texas.
47. Narejo, D.B. (2003). Opening Size Recommendations for Separation Geotextiles Used in Pavements. *Geotextiles and Geomembranes*, Vol. 21, No. 4, pp. 257–264.
48. Perkins, S.W. (1999). Geosynthetic Reinforcement of Flexible Pavements: Laboratory Based Pavement Test Sections. *Report No. FHWA/MT-99-001/8138*, Montana Department of Transportation, Helena, Montana, 140p.
49. Perkins, S.W., and Cuelho, E.V. (1999). Soil-Geosynthetic Interface Strength and Stiffness Relationships from Pullout Tests. *Geosynthetic International*, Vol. 6, No. 5, pp. 321–346.
50. Adu-Osei, A. (2000). Characterization of Unbound Granular Layers in Flexible Pavements. Ph.D. Dissertation, Texas A&M University, College Station, Texas.
51. Tutumluer, E., and Thompson, M. (1997). Anisotropic Modeling of Granular Bases in Flexible Pavements. *Transportation Research Record: Journal of the Transportation Research Board*, No. 1577, pp. 18–26.
52. ASTM. (2012). Standard Test Methods for Laboratory Compaction Characteristics of Soil Using Modified Effort. *ASTM D1557-12*, American Society for Testing and Materials, West Conshohocken, Pennsylvania.
53. Kinney, T.C., Stone, D.K., and Schuler, J. (1998). Using Geogrids for Base Reinforcement as Measured by Falling Weight Deflectometer in Full-Scale Laboratory Study. *Transportation Research Record: Journal of the Transportation Research Board*, No. 1611, pp. 70–77.
54. Tarefder, R.A. Ahmed, M.U., and Islam, M.R. (2014). Impact of Cross-Anisotropy on Embedded Sensor Stress-Strain and Pavement Damage. *European Journal of Environmental and Civil Engineering*, Vol. 18, No. 8, pp. 845–861.
55. Kinney, T.C., Abbott, J., and Schuler, J. (1998). Benefits of Using Geogrids for Base Reinforcement with Regard to Rutting. *Transportation Research Record: Journal of the Transportation Research Board*, No. 1611, pp. 86–96.
56. Al-Qadi, I.L., and Appea, A.K. (2003). Eight-Year Field Performance of Secondary Road Incorporating Geosynthetics at Subgrade-Base Interface. *Transportation Research Record: Journal of the Transportation Research Board*, No. 1849, pp. 212–220.
57. Tutumluer, E. (2013). Practices for Unbound Aggregate Pavement Layers. *NCHRP Synthesis 445*, Transportation Research Board, National Research Council, Washington, D.C., 180p.

58. Tseng, K.H., and Lytton, R.L. (1989). Prediction of Permanent Deformation in Flexible Pavements Materials: Implication of Aggregates in the Design, Construction, and Performance of Flexible Pavements. *ASTM STP 1016*, American Society for Testing and Materials, pp. 154–172.
59. Drucker, D.C., and Prager, W. (1952). Soil Mechanics and Plastic Analysis for Limit Design. *Quarterly of Applied Mathematics*, Vol. 10, No. 2, pp. 157–165.
60. Gauch, H.G., Hwang, J.T., and Fick, G.W. (2003). Model Evaluation by Comparison of Model-Based Predictions and Measured Values. *Agronomy Journal*, No. 95, pp. 1442–1446.
61. Lytton, R.L. (2015). Analytical Model for Quantifying Influence of Geosynthetics on Performance of Granular Material. *Unpublished Work*. Department of Civil Engineering, Texas A&M University, College Station, Texas.
62. AASHTO. (2008). Mechanistic-Empirical Pavement Design Guide: A Manual of Practice, Interim Edition. American Association of State Highway and Transportation Officials, Washington, D.C.
63. Tutumluer, E. (1995). Predicting Behavior of Flexible Pavements with Granular Bases. Ph.D. Dissertation, Georgia Institute of Technology, Atlanta.
64. Kim, M., Tutumluer, E., and Kwon, J. (2009). Nonlinear Pavement Foundation Modeling for Three-Dimensional Finite Element Analysis of Flexible Pavements. *International Journal of Geomechanics*, Vol. 9, No. 5, pp. 195–208.
65. Perkins, S.W. (2004). Development of Design Methods for Geosynthetic-Reinforced Flexible Pavements. *Report No. DTFH61-01-X-00068*, FHWA, U.S. Department of Transportation, Washington, D.C., 263p.
66. Haykin, S.S. (1999). *Neural Networks: A Comprehensive Foundation*. Prentice Hall, Upper Saddle River, NJ.
67. Wu, Z., Hu, S., and Zhou, F. (2014). Prediction of Stress Intensity Factors in Pavement Cracking with Neural Networks Based on Semi-Analytical FEA. *Expert Systems with Applications*, Vol. 41, pp. 1021–1030.
68. Ceylan, H., Bayrak, M.B., and Gopalakrishnan, K. (2014). Neural Networks Applications in Pavement Engineering: A Recent Survey. *International Journal of Pavement Research and Technology*, Vol. 7, No. 6, pp. 434–444.
69. Demuth, H., and Beale, M. (1998). *Neural Network Toolbox for Use with MATLAB*. The MathWorks, Natick, MA.
70. More, J. (1978). The Levenberg-Marquardt Algorithm: Implementation and Theory. *Numerical Analysis*, Vol. 630, pp. 105–116.
71. Amari, S. (1998). Natural Gradient Works Efficiently in Learning. *Neural Computation*, Vol. 10, No. 2, pp. 251–276.

**ATTACHMENT A. STANDARD METHOD OF TEST FOR DETERMINING THE
PERMANENT DEFORMATION PROPERTIES OF GEOSYNTHETIC-REINFORCED
AND UNREINFORCED GRANULAR MATERIAL**

Standard Method of Test for

Determining the Permanent Deformation Properties of Geosynthetic-Reinforced and Unreinforced Granular Material



AASHTO Designation: T xx-xx

1. SCOPE

- 1.1. The test method described is applicable to unbound granular materials and geosynthetic-reinforced granular materials prepared for testing by compaction in the laboratory.
 - 1.2. The values of permanent deformation properties determined from this procedure recognize the stress-dependent nonlinear characteristics of granular material.
 - 1.3. Permanent deformation properties can be used with structural response analysis models to predict the permanent deformation of unbound base courses and geosynthetic-reinforced base courses under a certain number of load repetitions.
 - 1.4. *This standard may involve hazardous materials, operations, and equipment. This standard does not purport to address all of the safety concerns associated with its use. It is the responsibility of the user of this standard to consult and establish appropriate safety and health practices and determine the applicability of regulatory limitations prior to use.*
-

2. REFERENCED DOCUMENTS

- 2.1. AASHTO Standards:
 - T 307, Determining the Resilient Modulus of Soils and Aggregate Materials
 - T 296, Unconsolidated, Undrained Compressive Strength of Cohesive Soils in Triaxial Compression
-

3. SIGNIFICANCE AND USE

- 3.1. The permanent deformation test provides a basic relationship between stress and permanent deformation of pavement materials for the structural analysis and performance prediction of layered pavement systems.
 - 3.2. The permanent deformation test provides a means of characterizing pavement construction materials, including unbound granular materials, and geosynthetic-reinforced (i.e., geogrid and geotextile) granular materials, under a variety of conditions (i.e., moisture, density, etc.) and stress states that simulate the conditions in a pavement subjected to moving wheel loads.
-

4. APPARATUS

- 4.1. *Triaxial Pressure Chamber*—The pressure chamber is used to contain the test specimen and the confining fluid during the test. A typical triaxial chamber suitable for use in the permanent deformation test of granular material shall be as described in T 307.

- 4.2. *Loading Device*—The loading device shall be a top-loading, closed-loop, electro-hydraulic, or electro-pneumatic testing machine with a function generator that is capable of applying repeated cycles of haversine-shaped load pulse with 0.1-second loading and 0.9-second unloading periods.
- 4.3. *Specimen Response Measuring Equipment*—The measuring system for all materials shall consist of two linear variable deformation transducers (LVDTs) mounted on the top or both sides of the specimen. The LVDT requirement shall be as described in T 307.
- 4.4. *Specimen Preparation Equipment*—Use of different methods of compaction is necessary to prepare specimens of different materials and to simulate desired field conditions. The specimen compaction equipment and compaction procedures shall be as described in T 307.

5. PREPARATION OF TEST SPECIMENS

- 5.1. Use 150-mm-diameter and 150-mm-height (or 300-mm-height) specimens for tests on granular material specimens.
- 5.2. Cut the geosynthetic product in a circle with a diameter of 150 mm.
- 5.3. Prepare laboratory-compacted specimens/reconstituted test specimens of granular materials to approximate the in-situ wet density and moisture content. Place the geosynthetic at a certain location during compaction.
- 5.4. Ensure that the moisture content of the laboratory-compacted specimen does not vary by more than ± 0.5 percent for granular materials from the in-situ moisture content obtained.
- 5.5. Protect the prepared specimens from moisture change by applying the triaxial cell or the triaxial membrane and testing within five days of completion. Prior to storage, and directly after removal from storage, weigh the specimen to determine if there was any moisture loss. If moisture loss exceeds 0.5 percent, then do not test the prepared specimen.

6. PROCEDURE

- 6.1. Place the laboratory-compacted geosynthetic-reinforced or unreinforced specimens in the triaxial chamber.
- 6.2. Connect the air pressure line to the triaxial chamber and apply the specified preconditioning confining pressure of 41.4 kPa to the test specimen. Maintain a contact stress of 10 percent ± 0.7 kPa of the maximum applied axial stress during each stress level.
- 6.3. Begin the test by applying 500 repetitions of a load equivalent to a maximum axial stress of 103.4 kPa and 103.4 kPa confining pressure according to Stress Level 0 in Table 1. This is a preconditioning step to eliminate the effects of the interval between compaction and loading and to eliminate the initial loading versus reloading.
- 6.4. Apply a specified axial load to the top of the triaxial cell piston rod for 10,000 cycles according to the stress level shown in Table 1.
- 6.5. Test each granular material specimen for only one stress level. Condition the specimen by Stress Level 0 in Table 1 prior to the permanent deformation test.

Table 1—Permanent Deformation Testing Protocol for Geosynthetic-Reinforced and Unreinforced Granular Material

Stress Level	Confining Pressure		Max. Axial Stress		Cyclic Stress		Contact Stress		No. of Load Applications
	kPa	psi	kPa	psi	kPa	psi	kPa	psi	
0*	103.4	15	103.4	15	93.0	13.5	10.3	1.5	500
1	27.6	4.0	192.9	28.0	173.6	25.2	19.3	2.8	10,000
2	48.2	7.0	130.9	19.0	117.8	17.1	13.1	1.9	10,000
3	68.9	10.0	68.9	10.0	62.0	9.0	6.9	1.0	10,000
4	48.2	7.0	192.9	28.0	173.6	25.2	19.3	2.8	10,000
5	68.9	10.0	192.9	28.0	173.6	25.2	19.3	2.8	10,000
6	89.6	13.0	192.9	28.0	173.6	25.2	19.3	2.8	10,000

*Note: Stress Level 0 is for preconditioning of granular material.

7. CALCULATION OF RESULTS

- 7.1. Perform the calculations to obtain the curves of permanent strain versus the number of load cycles for each tested stress level.
- 7.2. Determine the permanent deformation properties in Equations 1 to 3 using the least square error criteria.

$$\varepsilon_p = \varepsilon_0 e^{-\left(\frac{\rho}{N}\right)^\beta} \left(\sqrt{J_2}\right)^m (\alpha I_1 + K)^n \quad (1)$$

$$\alpha = \frac{2 \sin \phi}{\sqrt{3}(3 - \sin \phi)} \quad (2)$$

$$K = \frac{c \cdot 6 \cos \phi}{\sqrt{3}(3 - \sin \phi)} \quad (3)$$

where:

J_2 = the second invariant of the deviatoric stress tensor;

I_1 = the first invariant of the stress tensor;

$\varepsilon_0, \rho, \beta, m$, and n = permanent deformation properties;

c = cohesion of granular material; and

ϕ = internal friction angle of granular material.

8. REPORT

- 8.1. The report shall include the following:
 - 8.1.1. Source of granular material.
 - 8.1.2. Type of geosynthetic.
 - 8.1.3. Geosynthetic location.
 - 8.1.4. Permanent strain curve for each tested stress level.
 - 8.1.5. Determined permanent deformation properties and fitted permanent strain vs. load repetition curves.

**ATTACHMENT B. STANDARD METHOD OF TEST FOR DETERMINING THE
CROSS-ANISOTROPIC RESILIENT MODULUS OF GEOSYNTHETIC-REINFORCED
AND UNREINFORCED GRANULAR MATERIAL**

Standard Method of Test for

Determining the Cross-Anisotropic Resilient Modulus of Geosynthetic-Reinforced and Unreinforced Granular Material



AASHTO Designation: T xx-xx

1. SCOPE

- 1.1. This test method described is applicable to unbound granular materials and geosynthetic-reinforced granular materials prepared for testing by compaction in the laboratory.
 - 1.2. The values of the cross-anisotropic resilient modulus determined from this procedure are a measure of the elastic modulus of the unbound granular materials and geosynthetic-reinforced granular materials recognizing the stress-dependent nonlinear characteristics.
 - 1.3. Cross-anisotropic resilient modulus can be used with structural response analysis models to calculate the geosynthetic-reinforced or unreinforced pavement structural response to wheel loads, and with pavement design procedures to design geosynthetic-reinforced and unreinforced pavement structures.
 - 1.4. *This standard may involve hazardous materials, operations, and equipment. This standard does not purport to address all of the safety concerns associated with its use. It is the responsibility of the user of this standard to consult and establish appropriate safety and health practices and determine the applicability of regulatory limitations prior to use.*
-

2. REFERENCED DOCUMENTS

- 2.1. AASHTO Standards:
 - T 307, Determining the Resilient Modulus of Soils and Aggregate Materials
-

3. SIGNIFICANCE AND USE

- 3.1. The cross-anisotropic resilient modulus test provides a basic relationship between stress and horizontal and vertical resilient moduli of pavement materials for the structural analysis and performance prediction of layered pavement systems.
 - 3.2. The cross-anisotropic resilient modulus test provides a means of characterizing the cross-anisotropy nature of pavement construction materials, including unbound granular materials, and geosynthetic-reinforced (i.e., geogrid and geotextile) granular materials, under a variety of conditions (i.e., moisture, density, etc.) and stress states.
-

4. APPARATUS

- 4.1. *Rapid Triaxial Test (RaTT) Cell*—The pressure cell is used to contain the test specimen and the confining fluid during the test. A typical RaTT cell suitable for use in the cross-anisotropic resilient modulus test of granular material is shown in Figure 1.

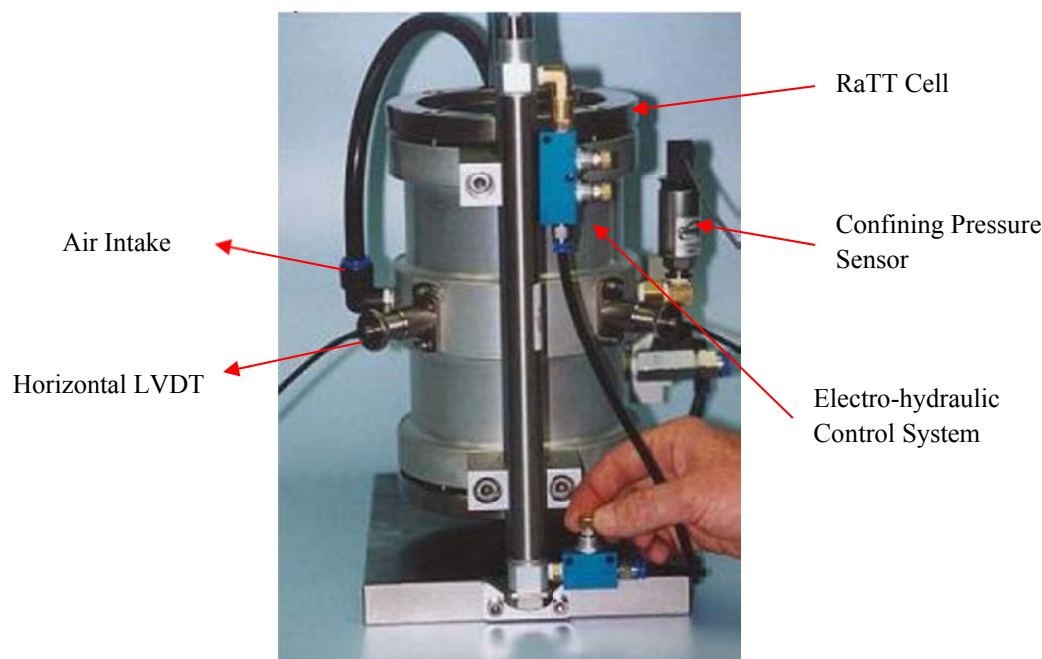


Figure 1—Typical Rapid Triaxial Test Cell for Cross-Anisotropic Resilient Modulus Test

- 4.2. *Loading Device*—The loading device shall be a top-loading, closed-loop, electro-hydraulic, or electro-pneumatic testing machine with a function generator that is capable of applying repeated cycles of haversine-shaped load pulse with 1.5-second loading and 1.5-second unloading periods.
- 4.3. *Confining Pressure System*—The confining pressure shall be controlled by an electro-pneumatic system with a function generator that is capable of applying haversine-shaped confining pressure.
- 4.4. *Specimen Response Measuring Equipment*—The measuring system for all materials shall consist of two linear variable deformation transducers (LVDTs) mounted on the top of the specimen and two (or three) LVDTs on the lateral direction of the specimen. The LVDT requirement shall be as described in T 307.
- 4.5. *Specimen Preparation Equipment*—Use of different methods of compaction is necessary to prepare specimens of different materials and to simulate desired field conditions. The specimen compaction equipment and compaction procedures shall be as described in T 307.

5. PREPARATION OF TEST SPECIMENS

- 5.1. Use 150-mm-diameter and 150-mm-height specimens for tests on granular material specimens.
 - 5.2. Cut the geosynthetic product in a circle with a diameter of 150 mm.
 - 5.3. Prepare laboratory-compacted specimens/reconstituted test specimens of granular materials to approximate the in-situ wet density and moisture content. Place the geosynthetic at a certain location during compaction.
 - 5.4. Ensure that the moisture content of the laboratory-compacted specimen does not vary by more than ± 0.5 percent for granular materials from the in-situ moisture content obtained.
 - 5.5. Protect the prepared specimens from moisture change by applying the triaxial cell or the triaxial membrane and testing within five days of completion. Prior to storage, and directly after removal from storage, weigh the specimen to determine if there was any moisture loss. If moisture loss exceeds 0.5 percent, then do not test the prepared specimen.
-

6. PROCEDURE

- 6.1. Place the laboratory-compacted geosynthetic-reinforced or unreinforced specimens in the RaTT cell as shown in Figure 2.
- 6.2. Connect the air pressure line to the RaTT cell and apply the specified preconditioning confining pressure of 41.4 kPa to the test specimen. Maintain a contact stress of 10 percent \pm 0.7 kPa of the maximum applied axial stress during each stress level.
- 6.3. Begin the test by applying 500 repetitions of a load equivalent to a maximum axial stress of 103.4 kPa and 103.4 kPa confining pressure according to Stress Level 0 in Table 1. This is a preconditioning step to eliminate the effects of the interval between compaction and loading and to eliminate the initial loading versus reloading.
- 6.4. Apply a specified axial load to the top of the triaxial cell piston rod for 100 cycles according to stress sequence and loading mode shown in Table 1. Meanwhile, apply a specified confining pressure to the lateral direction of the test specimen according to Table 1.

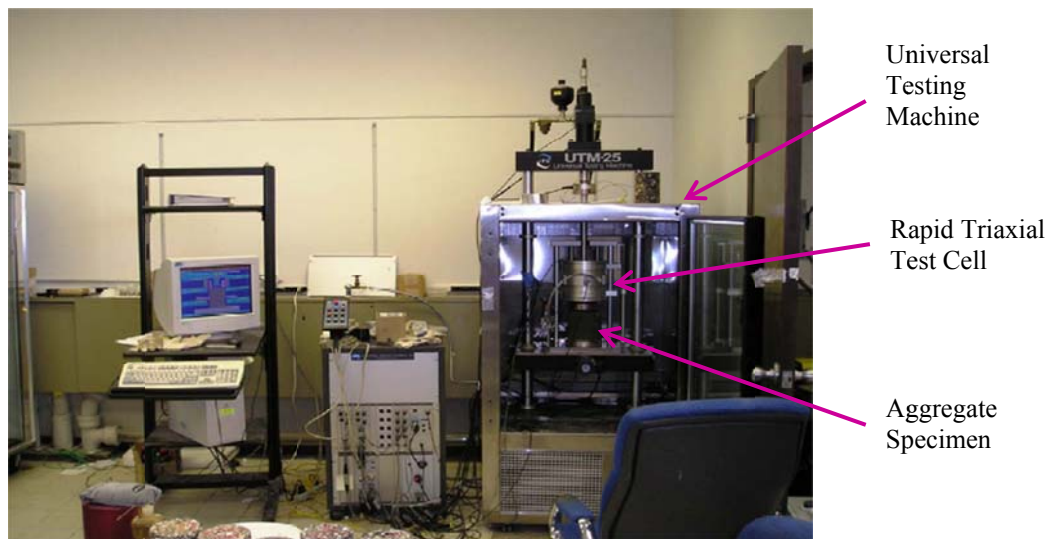


Figure 2—Configuration of Cross-Anisotropic Resilient Modulus Test

Table 1—Cross-Anisotropic Resilient Modulus Testing Protocol for Geosynthetic-Reinforced and Unreinforced Granular Material

Stress Sequence	Static Stress (kPa)		Dynamic Stress (kPa)						No. of Load Applications
	Axial	Lateral	Compression		Shear		Extension		
			Axial	Lateral	Axial	Lateral	Axial	Lateral	
0*	206.8	103.4							500
1	40	25	5	0	10	−5	−5	5	100
2	50	25	10	0	10	−5	−10	5	100
3	70	40	10	0	10	−5	−10	10	100
4	130	60	20	0	20	−10	−10	10	100
5	150	70	20	0	20	−10	−10	10	100
6	170	100	20	0	20	−10	−20	20	100
7	220	120	30	0	30	−15	−20	20	100
8	250	140	30	0	30	−15	−20	20	100
9	250	120	30	0	30	−15	−20	20	100
10	250	105	30	0	30	−15	−20	20	100

*Note: Stress Level 0 is for preconditioning of granular material.

7. CALCULATION OF RESULTS

- 7.1. Determine the cross-anisotropic resilient modulus shown in Equation 1 using the system identification method (see Annex A).

$$\begin{bmatrix} \frac{1}{E_x} & -\frac{\nu_{xy}}{E_x} & -\frac{\nu_{xx}}{E_x} \\ -\frac{\nu_{xy}}{E_x} & \frac{1}{E_y} & -\frac{\nu_{xy}}{E_x} \end{bmatrix} \begin{Bmatrix} \sigma_x \\ \sigma_y \\ \sigma_x \end{Bmatrix} = \begin{Bmatrix} \varepsilon_x \\ \varepsilon_y \\ \varepsilon_x \end{Bmatrix} \quad (1)$$

where:

σ_x = the stress in the lateral direction;

σ_y = the stress in the axial direction;

ε_x = the resilient strain in the lateral direction;

ε_y = the resilient strain in the axial direction;

E_x = the resilient modulus in the lateral direction;

E_y = the resilient modulus in the axial direction;

ν_{xx} = the Poisson's ratio in the lateral plane; and

ν_{xy} = the Poisson's ratio in the axial plane.

8. REPORT

- 8.1. The report shall include the following:
- 8.1.1. Source of granular material.
 - 8.1.2. Type of geosynthetic.
 - 8.1.3. Geosynthetic location.
 - 8.1.4. Determined cross-anisotropic resilient modulus for the tested stress levels.

Annex A—System Identification Method

The objective of the system identification method is to estimate the system characteristics using only input and output data from the system to be identified. The model is identified when the error between the model and the real process is minimized in some sense; otherwise, the model must be modified until the desired level of agreement is achieved.

The system identification method requires the accurately measured output data of the unknown system, a suitable model to represent the behavior of the system, and an efficient parameter adjustment algorithm that converges accurately and rapidly. An algorithm can be developed for adjusting model parameters on the basis of Taylor's series expansion. Let the mathematical model of some process be defined by n parameters:

$$f = f(p_1, p_2, \dots, p_n; x, t) \quad (\text{A-1})$$

where x and t are independent spatial and temporary variables. Then any function

$f_k(p_1, p_2, \dots, p_n; x_k, t_k)$ can be expanded in a Taylor's series as:

$$f_k(p + \Delta p) = f_k(p) + \nabla f_k \cdot \Delta p + \delta^2 \quad (\text{A-2})$$

Assuming $f_k(p + \Delta p)$ to be the actual output of the system and $f_k(p)$ to be the output of the model for the most recent set of parameters, the error between the two outputs becomes:

$$\left. \begin{aligned} e_k &= f_k(p + \Delta p) - f_k(p) \\ &= \nabla f_k \cdot \Delta p \\ &= \frac{\partial f_k}{\partial p_1} \Delta p_1 + \frac{\partial f_k}{\partial p_2} \Delta p_2 + \dots + \frac{\partial f_k}{\partial p_n} \Delta p_n \end{aligned} \right\} \quad (\text{A-3})$$

where e_k represents the difference between the actual system output and the model output for each observed point k . If the error is evaluated at m values ($m \geq n$) of the independent variables, m equations will be generated as:

$$\frac{e_k}{f_k} = \sum_{i=1}^{i=n} \frac{\partial f_k}{\partial p_i} \frac{p_i}{f_k} \frac{\Delta p_i}{p_i} \quad (\text{A-4})$$

This can be collected into a matrix form as:

$$r = F \alpha \quad (\text{A-5})$$

where:

$$r_k = \frac{e_k}{f_k} \quad (\text{A-6})$$

$$F_{ki} = \frac{\partial f_k}{\partial p_i} \frac{p_i}{f_k} \quad (\text{A-7})$$

$$\alpha_i = \frac{\Delta p}{p_i} \quad (\text{A-8})$$

The r vector is completely determined from the outputs of the model and the real system. The matrix F is called the sensitivity matrix, and its elements F_{ki} reflect the sensitivity of the output f_k to the parameter p_i . It is generated by the differentials of the output f_k with respect to the parameter p_i .

The unknown vector α reflects the relative changes of the parameters. Once the vector α is obtained, a new set of parameters is determined as:

$$p_i^{r+1} = p_i^r (1 + \alpha) \quad (\text{A-9})$$

where r is the iteration number. The iteration process is continued until the desired convergence is reached. Applying the algorithm described above to the rapid triaxial testing model results in four unknown parameters ($E_y, E_x, \nu_{xy}, \nu_{xx}$) and two outputs ($\Delta \varepsilon_x, \Delta \varepsilon_y$). The model strains (model output) can be determined from the values of the parameters, which can be guessed initially from the system output. The difference between the measured strains and the model strains (model output) represents the error, which can be improved through the parameter adjustment routine until a desired criterion is achieved.

The F matrix, α vector, and r vector can be derived from Equation A-4 as follows:

$$F = \begin{bmatrix} \frac{\partial(\Delta \varepsilon_x)}{\partial E_x} \cdot \frac{E_x}{\Delta \varepsilon_x} & \frac{\partial(\Delta \varepsilon_x)}{\partial \nu_{xy}} \cdot \frac{\nu_{xy}}{\Delta \varepsilon_x} & \frac{\partial(\Delta \varepsilon_x)}{\partial \nu_{xx}} \cdot \frac{\nu_{xx}}{\Delta \varepsilon_x} & \frac{\partial(\Delta \varepsilon_x)}{\partial E_y} \cdot \frac{E_y}{\Delta \varepsilon_x} \\ \frac{\partial(\Delta \varepsilon_y)}{\partial E_x} \cdot \frac{E_x}{\Delta \varepsilon_y} & \frac{\partial(\Delta \varepsilon_y)}{\partial \nu_{xy}} \cdot \frac{\nu_{xy}}{\Delta \varepsilon_y} & \frac{\partial(\Delta \varepsilon_y)}{\partial \nu_{xx}} \cdot \frac{\nu_{xx}}{\Delta \varepsilon_y} & \frac{\partial(\Delta \varepsilon_y)}{\partial E_y} \cdot \frac{E_y}{\Delta \varepsilon_y} \end{bmatrix} \quad (\text{A-10})$$

$$\alpha = \begin{bmatrix} \frac{E_x^{r+1}}{E_x^r} & \frac{\nu_{xy}^{r+1}}{\nu_{xy}^r} & \frac{\nu_{xx}^{r+1}}{\nu_{xx}^r} & \frac{E_y^{r+1}}{E_y^r} \end{bmatrix}^T \quad (\text{A-11})$$

$$r = \begin{bmatrix} \frac{\Delta \varepsilon_x^m - \Delta \varepsilon_x^{\wedge}}{\Delta \varepsilon_x^{\wedge}} \\ \frac{\Delta \varepsilon_y^m - \Delta \varepsilon_y^{\wedge}}{\Delta \varepsilon_y^{\wedge}} \end{bmatrix} \quad (\text{A-12})$$

where:

$\Delta \varepsilon_x^m$ = measured (actual system) radial strain,

$\Delta \varepsilon_y^m$ = measured (actual system) axial strain,

$\Delta \varepsilon_x^{\wedge}$ = calculated (model) radial strain, and

$\Delta \varepsilon_y^{\wedge}$ = calculated (model) axial strain.

To generate enough elements in the sensitivity matrix and to control the number of row degeneracy, the three stress regimes (triaxial compression, triaxial shear, and triaxial extension) are combined to give one F matrix and one r matrix at each stress state. Thus, at each stress state, they can be written as:

$$\begin{bmatrix} F^{TC} \\ F^{TS} \\ F^{TE} \end{bmatrix} \left\{ \alpha \right\} = \begin{bmatrix} r^{TC} \\ r^{TS} \\ r^{TE} \end{bmatrix} \quad (\text{A-13})$$

where:

F^{TC} = sensitivity matrix for triaxial compression regime,

F^{TS} = sensitivity matrix for triaxial shear regime,

F^{TE} = sensitivity matrix for triaxial extension regime,

r^{TC} = r vector for triaxial compression regime,

r^{TS} = r vector for triaxial shear regime, and

r^{TE} = r vector for triaxial extension regime.

Four of the five material properties ($E_y, E_x, \nu_{xy}, \nu_{xx}$) can be determined by the above algorithm.

QUANTIFYING THE INFLUENCE OF GEOSYNTHETICS ON PAVEMENT PERFORMANCE

FINAL REPORT APPENDICES

TABLE OF CONTENTS

Appendix A. Review of Available Test Methods for Determining Performance-Related Geosynthetic Properties	A-1
Appendix B. Determination of Geosynthetic-Aggregate Interfacial Properties Using Pullout Test	B-1
Appendix C. Laboratory Evaluation of Influence of Geosynthetics on Cross-Anisotropy and Permanent Deformation of Unbound Granular Material	C-1
Appendix D. Analytical Model for Quantifying Influence of Geosynthetics.....	D-1
Appendix E. Instrumentation Plans for Flexible Pavement Experiments.....	E-1
Appendix E1. Experiment No. 1 (Control—Thin Base)	E-2
Appendix E2. Experiment No. 2 (Control—Thick Base).....	E-14
Appendix E3. Experiment No. 3 (Geogrid—Thin Base).....	E-25
Appendix E4. Experiment No. 4 (Geogrid—Thick Base).....	E-37
Appendix E5. Experiment No. 5 (Geotextile—Thin Base)	E-50
Appendix E6. Experiment No. 6 (Geotextile—Thick Base)	E-62
Appendix F. Summary Charts for Flexible Pavement Experiments.....	F-1
Appendix F1. Summary Charts for Flexible Pavement Experiments: Dynamic Loading—Thin Base: No. 1 (Control), No. 3 (Geogrid), and No. 5 (Geotextile)	F-2
Appendix F2. Summary Charts for Flexible Pavement in Experiments: Static Loading—Thin Base: No. 1 (Control), No. 3 (Geogrid), and No. 5 (Geotextile)	F-37
Appendix F3. Summary Charts for Flexible Pavement Experiments: Dynamic Loading—Thick Base: No. 2 (Control), No. 4 (Geogrid), and No. 6 (Geotextile)	F-62
Appendix F4. Summary Charts for Flexible Pavement Experiments: Static Loading—Thick Base: No. 2 (Control), No. 4 (Geogrid), and No. 6 (Geotextile).....	F-96
Appendix G. Flexible Pavement Experiments: Comparison of Test Measurements.....	G-1
Appendix G1. Flexible Pavements: Comparison of Test Measurements: Dynamic Loading—Thin Base: No. 1 (Control), No. 3 (Geogrid), and No. 5 (Geotextile)	G-2
Appendix G2. Flexible Pavements: Comparison of Test Measurements: Static Loading—Thin Base: No. 1 (Control), No. 3 (Geogrid), and No. 5 (Geotextile)	G-7
Appendix G3. Flexible Pavements: Comparison of Test Measurements: Dynamic Loading—Thick Base: No. 2 (Control), No. 4 (Geogrid), and No. 6 (Geotextile)	G-11
Appendix G4. Flexible Pavements: Comparison of Test Measurements: Static Loading—Thick Base: No. 2 (Control), No. 4 (Geogrid), and No. 6 (Geotextile)	G-16
Appendix H. Instrumentation Plans for Rigid Pavement Experiments	H-1
Appendix H1. Experiment No. 7 (Control)	H-2
Appendix H2. Experiment No. 9 (Geogrid)	H-19
Appendix H3. Experiment No. 10 (Geotextile).....	H-36
Appendix I. Analysis Methodologies of Large-Scale Tank Test Data	I-1
Appendix J. Summary Charts of Rigid Pavement Experiments.....	J-1
Appendix J1. Summary Charts for Rigid Pavement Experiments: Dynamic Loading—Dry and Wet: No. 7 (Control), No. 9 (Geogrid), and No. 10 (Geotextile)	J-2

Appendix J2. Summary Charts for Rigid Pavement Experiments: Static Loading—Dry and Wet: No. 7 (Control), No. 9 (Geogrid), and No. 10 (Geotextile)	J-54
Appendix K. Rigid Pavement Experiments: Comparison of Test Measurements.....	K-1
Appendix K1. Rigid Pavements: Comparison of Test Measurements: Dynamic Loading—Dry and Wet: No. 7 (Control), No. 9 (Geogrid), and No. 10 (Geotextile).....	K-2
Appendix K2. Rigid Pavements: Comparison of Test Measurements: Static Loading—Dry and Wet: No. 7 (Control), No. 9 (Geogrid), and No. 10 (Geotextile)	K-12
Appendix L. Characterization of Materials Used in Large-Scale Tank Test.....	L-1
Appendix M. Comparison of Finite Element Simulations with Large-Scale Tank Measurements	M-1
Appendix N. Development of Artificial Neural Network Models for Predicting Geosynthetic-Reinforced Pavement Performance	N-1
Appendix O. Validation of Artificial Neural Network Approach for Predicting Geosynthetic-Reinforced Pavement Performance	O-1
Appendix P. List of Geosynthetic-Reinforced In-Service Pavement Sections Identified from Long-Term Pavement Performance (LTPP) Database and Texas Pavement Management Information System (PMIS).....	P-1
Appendix P1. LTPP Sections with Geotextile.....	P-11
Appendix P2. LTPP Sections with Geogrid	P-74
Appendix P3. Texas PMIS Sections with Geosynthetics	P-99
Appendix P4. Collection of FWD Data from Identified Pavement Sections	P-166
Appendix P5. Collection of Geosynthetic Information	P-180
Appendix Q. Examples of Program Runs of the Composite Geosynthetic–Base Course Model	Q-1

APPENDIX A. REVIEW OF AVAILABLE TEST METHODS FOR DETERMINING PERFORMANCE-RELATED GEOSYNTHETIC PROPERTIES

The geosynthetic properties that are related to pavement performance include the physical properties, mechanical properties, and interface properties between the geosynthetic layer and aggregates/soils. Many test methods have been conducted to evaluate the pavement performance-related geosynthetic properties. In general, these test standards and the corresponding geosynthetic properties are summarized below. Test standards for evaluating geogrid properties include:

- Tex-621-J, to measure the aperture size, which must be at least 50 percent greater than the maximum aggregate size in the base course gradation (1, 2).
- ASTM D1777, to measure the dimensions of the geogrid ribs (3).
- ASTM D5818, to determine the resistance to installation damage (4).
- ASTM D6637, to measure the rib tensile stiffness (5).
- ASTM D7737, to measure the junction strength and junction efficiency (6).
- ASTM D7748, to measure the flexural rigidity (7).
- ASTM D6706, to determine the geogrid-aggregate/soil shear interfacial properties (8).

Test standards for evaluating geotextile properties include:

- ASTM D5199, to measure the sheet thickness (9).
- ASTM D4751, to measure the apparent opening size, which should be smaller than the 15 percent passing particle size (10, 11).
- ASTM D4491, to measure the permeability, which affects the drainage function (12).
- ASTM D5493, to measure the permittivity, which influences the filtration function (13).
- ASTM D4595, to measure the tensile stiffness (14).
- ASTM D6241, to determine the California bearing ratio (CBR) puncture strength (15).
- ASTM D6706, to determine the geotextile-aggregate/soil interfacial properties (8).

A comprehensive review of available test methods for determining the performance-related geosynthetic properties is provided in Table A-1. The criteria of test method selection include the following:

- The test method should have the characteristics of simple operation, less time consumption, and low cost
- The test method should be repeatable and reliable
- The test method should be applicable to different types of geosynthetic
- The determined geosynthetic properties should be directly related to pavement performance
- The determined geosynthetic properties should be capable of being input into the finite element program.

Based on the selection criteria above, the best tests to measure the tensile sheet stiffness of geosynthetics and to determine the geosynthetic-aggregate/soil interfacial properties are direct tension test and pullout test, respectively. These two properties significantly affect the performance of geosynthetic-reinforced pavements.

Table A-1. Geosynthetic Properties Affecting Pavement Performance and Corresponding Standard Tests

Material Type	Property	Test Standard	Features				Findings Reported in Literature
			Time Consuming	Expensive	Repeatability	Compatibility with Finite Element Model	
Geogrid	Rib Thickness	ASTM D1777	No	No	Yes	Yes	Thicker rib is preferred (16).
	Rib Stiffness	ASTM D6637	No	No	Yes	Yes	Stiffer rib is highly recommended (17).
	Rib Shape	N/A	No	No	Yes	No	Square or rectangular ribs are better than round one (17).
	Aperture Shape	N/A	No	No	Yes	No	Triangular aperture can provide more tensile strength than square aperture (18).
	Aperture Size	TEX-621-J	No	No	Yes	No	Related to base aggregate size and the recommended value range is 25–50 mm (2, 17).
	Aperture Rigidity	ASTM D6637	No	No	Yes	No	Higher stiffness is recommended (19).
	Percent Open Area	TEX-621-J	No	No	Yes	No	One important parameter for mechanical interlock capacity of geogrid (20).
	Flexural Rigidity	ASTM D7748	No	No	Possible	No	Influence the load distribution in the geogrid structure (21).
	Junction Strength	ASTM D7737	No	No	Possible	No	Require a minimum strength (17).

	Junction Efficiency	ASTM D7737	No	No	Possible	No	70% is recommended as the minimum value (2).
	Tensile Strength	ASTM D6637	No	No	Yes	No	A key property in current design methods (2).
	Pullout Resistance	ASTM D6706	No	Yes	Yes	Yes	Related to interface coefficient (22).
	Wide-Width Strip Tensile Modulus	ASTM D4595	No	No	Yes	Yes	Directly related to lateral confinement (23).
	Resistance to Installation Damage	ASTM D5818	Yes	No	Possible	No	Influence the benefit ratio contributed to the pavement performance (2).
Geotextile	Thickness	ASTM D5199	No	No	Yes	Yes	Related to the ability to resist damage and to distribute concentrated stresses (24).
	Apparent Opening Size	ASTM D4751	No	No	Yes	No	Apparent opening size smaller than the 15% passing particle size (11).
	Permeability	ASTM D4491	Yes	No	Yes	No	Related to drainage function; optimum value is not known (25).
	Permittivity	ASTM D5493	Yes	No	Possible	No	Related to filtration function (2).
	Transmissivity	ASTM D6574	Yes	No	Possible	No	Related to lateral drainage function (2).
	Flexural Rigidity	ASTM D7748	No	No	Possible	No	Higher stiffness is preferred (26).

	Pullout Resistance	ASTM D6706	No	Yes	Yes	Yes	Related to interface coefficient (27).
	Wide-Width Strip Tensile Modulus	ASTM D4595	No	No	Yes	Yes	Related to reinforcement function (27).
	CBR Puncture Strength	ASTM D6241	No	No	Yes	No	Related to the ability to withstand damage (24).
	Resistance to Installation Damage	ASTM D5818	Yes	No	Possible	No	Influence the benefit ratio contributed to the pavement performance (2).

References

1. TxDOT. (1999). Testing Geogrids. Tex-621-J, Texas Department of Transportation, Austin, Texas.
2. Zornberg, J.G., Prozzi, J.A., Gupta, R., Luo, R., McCartney, J.S., Ferreira, J.Z., and Nogueira, C. (2008). Validating Mechanisms in Geosynthetic Reinforced Pavements. Report No. FHWA/TX-08/0-4829-1, Center for Transportation Research, The University of Texas at Austin, Austin, Texas.
3. ASTM. (2002). Standard Test Method for Thickness of Textile Materials. ASTM D1777-96, American Society for Testing and Materials (ASTM), West Conshohocken, Pennsylvania.
4. ASTM. (2000). Standard Practice for Obtaining Samples of Geosynthetics from a Test Section for Assessment of Installation Damage. ASTM D5818-95, American Society for Testing and Materials (ASTM), West Conshohocken, Pennsylvania.
5. ASTM. (2010). Standard Test Method for Determining Tensile Properties of Geogrids by the Single or Multi-Rib Tensile Method. ASTM D6637-10, American Society for Testing and Materials (ASTM), West Conshohocken, Pennsylvania.
6. ASTM. (2011). Standard Test Method for Individual Geogrid Junction Strength. ASTM D7737-11, American Society for Testing and Materials (ASTM), West Conshohocken, Pennsylvania.
7. ASTM. (2014). Standard Test Method for Flexural Rigidity of Geogrids, Geotextile and Related Products. ASTM D7748-14, American Society for Testing and Materials (ASTM), West Conshohocken, Pennsylvania.
8. ASTM. (2001). Standard Test Method for Measuring Geosynthetic Pullout Resistance in Soil. ASTM D6706-01, American Society for Testing and Materials (ASTM), West Conshohocken, Pennsylvania.
9. ASTM. (2012). Standard Test Method for Measuring the Nominal Thickness of Geosynthetics. ASTM D5199-12, American Society for Testing and Materials (ASTM), West Conshohocken, Pennsylvania.
10. ASTM. (1999). Standard Test Method for Determining Apparent Opening Size of a Geotextile. ASTM D4751-99, American Society for Testing and Materials (ASTM), West Conshohocken, Pennsylvania.
11. Narejo, D.B. (2003). Opening Size Recommendations for Separation Geotextiles Used in Pavements. *Geotextiles and Geomembranes*, Vol. 21, No. 4, pp. 257–264.
12. ASTM. (2014). Standard Test Method for Water Permeability of Geotextiles by Permittivity. ASTM D4491-99, American Society for Testing and Materials (ASTM), West Conshohocken, Pennsylvania.
13. ASTM. (2006). Standard Test Method for Permittivity of Geotextiles under Load. ASTM D5493-06, American Society for Testing and Materials (ASTM), West Conshohocken, Pennsylvania.
14. ASTM. (2011). Standard Test Method for Tensile Properties of Geotextiles by the Wide-Width Strip Method. ASTM D4595-11, American Society for Testing and Materials (ASTM), West Conshohocken, Pennsylvania.

15. ASTM. (2014). Standard Test Method for Static Puncture Strength of Geotextile and Geotextile-Related Products Using a 50-mm Probe. ASTM D6241-14, American Society for Testing and Materials (ASTM), West Conshohocken, Pennsylvania.
16. Webster, S.L. (1991). Geogrid Reinforced Base Course for Flexible Pavements for Light Aircraft: Literature Review and Test Section Design. Interim Report, No. DOT/FAA/RD-90/28, 40p.
17. Han, J., Zhang, Y., and Parsons, R.L. (2011). Qualifying the Influence of Geosynthetics on Performance of Reinforced Granular Base in Laboratory. *Geotechnical Engineering Journal of the SEAGS & AGSSEA*, Vol. 42, No. 1, pp. 74–83.
18. Dong, Y.L., Han, J., and Bai, X.H. (2011). Numerical Analysis of Tensile Behavior of Geogrids with Rectangular and Triangular Apertures. *Geotextiles and Geomembranes*, Vol. 29, pp. 83–91.
19. Ling, H.I., and Liu, Z. (2001). Performance of Geosynthetic-Reinforced Asphalt Pavement. *Journal of Geotechnical and Geoenvironmental Engineering, American Society of Civil Engineers*, Vol. 127, No. 2, pp. 178–184.
20. Simac, R.M. (1990). Connections for Geogrid Systems. *Geotextiles and Geomembranes*, Vol. 9, pp. 537–546.
21. Moghaddas-Nejad, F., and Small, J.C. (1996). Effect of Geogrid Reinforcement in Model Track Tests on Pavement. *J. Transp. Eng., ASCE*, Vol. 122, No. 6, pp. 468–474.
22. Cuelho, E.V., and Perkins, S.W. (2005). Resilient Interface Shear Modulus from Short-Strip, Cyclic, Pullout Tests. *Proceedings of the Sessions of the Geo-Frontier Conference, American Society of Civil Engineers*, Vol. 166, pp. 2863–2873.
23. Al-Qadi, I.L., Dessouki, S., Tutumluer, E., and Kwon, J. (2011). Geogrid Mechanism in Low-Volume Flexible Pavements: Accelerated Testing of Full Scale Heavily Instrumented Pavement Sections. *International Journal of Pavement Engineering*, Vol. 12, No. 2, pp. 121–135.
24. Giroud, J.P. (1984). Geotextiles and Geomembranes. *Geotextiles and Geomembranes*, Vol. 1, pp. 5–40.
25. Loulizi, A., Al-Qadi, I.L., Bhutta, S.A., Flintsch, G.W. (1999). Evaluation of Geosynthetics Used as Separators. *Transportation Research Record: Journal of the Transportation Research Board*, No. 1687, pp. 104–111.
26. Bhosale, S., and Kambale, B.R. (2008). Laboratory Study for Evaluation of Membrane Effect of Geotextile in Unpaved Road. *Proceedings of the 12th International Conference of International Association for Computer Methods and Advances in Geomechanics (IACMAG)*, Goa, India, pp. 4385–4391.
27. Paulson, J.N. (1987). Geosynthetic Material and Physical Properties Relevant to Soil Reinforcement Applications. *Geotextiles and Geomembranes*, Vol. 6, pp. 211–223.

APPENDIX B. DETERMINATION OF GEOSYNTHETIC-AGGREGATE INTERFACIAL PROPERTIES USING PULLOUT TEST

The interaction between aggregates and the geosynthetic layer is commonly quantified using the pullout test (*1*). Figure B-1 is a schematic plot of the pullout test. The geosynthetic embedded in the base course is pulled out of the aggregate layer by a tensile pullout force. The pullout force is recorded and the displacement of the geosynthetic is measured using linear variable differential transformers (LVDTs). The typical pullout test data are shown in Figure B-2, in which the pullout force versus geosynthetic displacement curve has three stages—linear stage, nonlinear stage, and critical stage—each with different mechanisms of aggregate-geosynthetic interaction. The pullout test data in the three stages were interpreted in this project to determine the interfacial shear modulus between the geosynthetic and the aggregates, which are detailed as follows. The purpose of developing the following equations was to determine from readily available test data the effective properties of geosynthetics as they interact with base course material. This provides valuable supplemental information that is useful input to the modifications to the Pavement ME Design software.

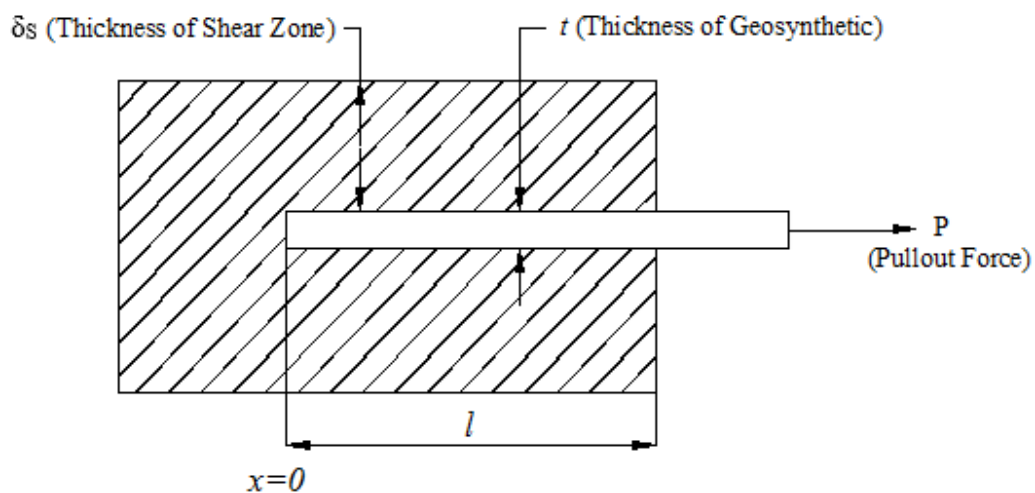


Figure B-1. Schematic Plot of the Pullout Test

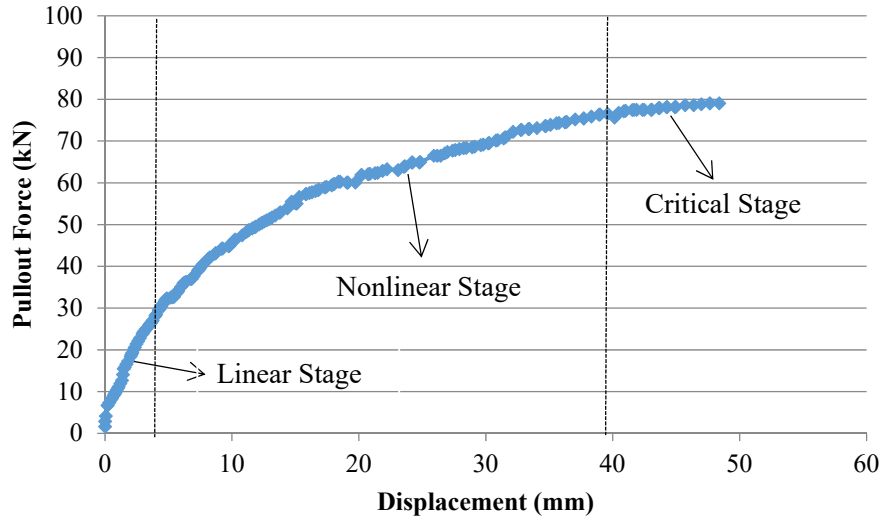


Figure B-2. Pullout Force versus Geosynthetic Displacement in a Pullout Test

Stage 1: Linear without Slipping

In Stage 1, the geosynthetic experiences a small amount of displacement under the pullout force. In this stage, the pullout force has a linear relationship with the geosynthetic displacement and no slipping occurs at the interface. Taking the geogrid as an example for the calculation of the interfacial shear modulus, a differential equation is first established based on the force equilibrium principle:

$$\frac{Ea}{s} \frac{\partial^2 u(x)}{\partial x^2} - \frac{2G}{\delta_s} u(x) = 0 \quad (\text{B-1})$$

where E is the elastic modulus of the geogrid; a is the width of the rib; s is the rib spacing; G is the interfacial shear modulus in the linear stage; δ_s is the thickness of the shear zone; and $u(x)$ is the geogrid displacement at different locations.

The boundary conditions for solving Equation B-1 are listed in Equations B-2 through B-4:

$$x = 0 : u(x = 0) = 0 \quad (\text{B-2})$$

$$x = l : u(x = l) = u_l \quad (\text{B-3})$$

$$x = l : P = P_l = \frac{Ea}{s} \frac{\partial u(x)}{\partial x} \quad (\text{B-4})$$

With these boundary conditions, a possible solution to Equation B-1 is:

$$u(x) = A \cosh(\beta x) + B \sinh(\beta x) \quad (\text{B-5})$$

where A , B , and β are unknown coefficients to be determined. Substituting Equation B-5 into Equation B-1 yields:

$$\left(\frac{Ea}{s}\beta^2 - \frac{2G}{\delta_s}\right)[A \cosh(\beta x) + B \sinh(\beta x)] = 0 \quad (\text{B-6})$$

Since $[A \cosh(\beta x) + B \sinh(\beta x)] \neq 0$, Equation B-6 can be rewritten as:

$$\beta^2 = \frac{2Gs}{Ea\delta_s} \quad (\text{B-7})$$

Using the boundary conditions, Equations B-2 and B-3, A and B are solved as:

$$A = 0 \quad (\text{B-8})$$

$$B = \frac{u_l}{\sinh(\beta l)} \quad (\text{B-9})$$

Therefore, the geogrid displacement function $u(x)$ can be expressed as:

$$u(x) = u_l \frac{\sinh\left(\sqrt{\frac{2Gs}{Ea\delta_s}}x\right)}{\sinh\left(\sqrt{\frac{2Gs}{Ea\delta_s}}l\right)} \quad (\text{B-10})$$

Substituting Equation B-10 into Equation B-4 yields:

$$P_l = \frac{Ea}{s}\beta \cosh(\beta l) \frac{u_l}{\sinh(\beta l)} \quad (\text{B-11})$$

By solving Equation B-11 for β and then solving Equation B-7, the thickness of the interface shear zone δ_s is determined:

$$\delta_s = \frac{2Gs}{Ea\beta^2} \quad (\text{B-12})$$

Since the pullout force has a linear relationship with the corresponding geosynthetic displacement, G can be assigned as the shear modulus of the base aggregate, which is obtained in the triaxial test.

Stage 2: Nonlinear without Slipping

In Stage 2, the pullout force shows a nonlinear relationship with the geosynthetic displacement and no slipping occurs on the aggregate/geosynthetic interface. The differential formulation for the geogrid is constructed in Equation B-13:

$$\frac{Ea}{s} \frac{\partial^2 u(x)}{\partial x^2} - \frac{2G(x)}{\delta_s} u(x) = 0 \quad (\text{B-13})$$

where $G(x)$ is the interfacial shear modulus as a function of location, which can be formulated as:

$$G(x) = \frac{1}{\frac{1}{G} + \frac{u(x)}{\tau_{\max} \delta_s}} \quad (\text{B-14})$$

where τ_{\max} is the maximum shear stress to be determined in Stage 3. Substituting Equation B-14 into Equation B-13 yields:

$$\frac{\partial^2 u(x)}{\partial x^2} - \frac{2Gs u(x)}{Ea \delta_s + \frac{Ea G u(x)}{\tau_{\max}}} = 0 \quad (\text{B-15})$$

The boundary conditions are listed in Equations B-16 through B-18:

$$x = 0 : u(x = 0) = 0 \quad (\text{B-16})$$

$$x = l : u(x = l) = u_l \quad (\text{B-17})$$

$$x = l : P = P_l = \frac{Ea}{s} \frac{\partial u(x)}{\partial x} \quad (\text{B-18})$$

A solution of $u(x)$ is proposed in Equation B-19:

$$u(x) = A \cosh(\beta x) + B \sinh(\beta x) + C \quad (\text{B-19})$$

Then Equation B-15 becomes:

$$\beta^2 [A \cosh(\beta x) + B \sinh(\beta x)] - \frac{2Gs [A \cosh(\beta x) + B \sinh(\beta x) + C]}{Ea \delta_s + \frac{Ea G}{\tau_{\max}} [A \cosh(\beta x) + B \sinh(\beta x) + C]} = 0 \quad (\text{B-20})$$

Using the boundary conditions in Equations B-16 to B-18, the three unknown parameters A , B , and C are obtained:

$$A = \frac{u_l \beta \cosh(\beta l) - \frac{P_l s}{Ea} \sinh(\beta l)}{\beta [\cosh^2(\beta l) - \sinh^2(\beta l) - \cosh(\beta l)]} \quad (\text{B-21})$$

$$B = \frac{\frac{P_l s}{Ea} [\cosh(\beta l) - 1] - u_l \beta \sinh(\beta l)}{\beta [\cosh^2(\beta l) - \sinh^2(\beta l) - \cosh(\beta l)]} \quad (\text{B-22})$$

$$C = \frac{\frac{P_l s}{Ea} \sinh(\beta l) - u_l \beta \cosh(\beta l)}{\beta [\cosh^2(\beta l) - \sinh^2(\beta l) - \cosh(\beta l)]} \quad (\text{B-23})$$

Substituting Equation B-19 into Equation B-14 yields:

$$G(x) = \frac{G}{1 + \frac{1}{\tau_{\max} \delta_s} [A \cosh(\beta x) + B \sinh(\beta x) + C]} \quad (\text{B-24})$$

where G is the shear modulus of the base aggregates, and β_s , δ , A , B , and C are determined by Equations B-11, B-12, B-21, B-22, and B-23, respectively.

Stage 3: Critical State

In Stage 3, the friction stress on the aggregate/geosynthetic interface reaches the maximum shear stress, and the interface is at a critical state of slipping. Based on the force equilibrium, τ_{\max} can be calculated as follows:

$$\tau_{\max} = \frac{P_{\max}}{2ls} \quad (\text{B-25})$$

Therefore, the aggregate-geogrid interfacial shear modulus at different locations can be determined using Equation B-24 based on the pullout test data. The aggregate-geotextile interfacial shear modulus can also be determined using the same method.

When the interface slippage is in the linear stage, a simplified equation for the interfacial shear stiffness in the linear stage is expressed as:

$$k_s = \frac{\Delta P}{2l \cdot \Delta u_r} \quad (\text{B-26})$$

where k_s is the interfacial shear stiffness, ΔP is the incremental applied pullout force, l is the embedded length of geosynthetic, and Δu_r is the incremental relative displacement. The Large-Scale Tank test measurements presented in this report indicate that the maximum relative displacement between the geosynthetic and aggregate is less than 0.04 inch. This suggests that the interface slippage normally occurring in the geosynthetic-reinforced aggregates is in the linear stage.

References

1. Perkins, S.W., and Cuelho, E. V. (1999). Soil-Geosynthetic Interface Strength and Stiffness Relationships from Pullout Tests. *Geosynthetic International*, Vol. 6, No. 5, pp. 321–346.

APPENDIX C. LABORATORY EVALUATION OF INFLUENCE OF GEOSYNTHETICS ON CROSS-ANISOTROPY AND PERMANENT DEFORMATION OF UNBOUND GRANULAR MATERIAL

The application of geosynthetics has potential abilities to reduce the thickness of base courses, improve performance, and extend the service life of pavement structures. Accurate and efficient laboratory characterizations of geosynthetic-reinforced materials are important for including geosynthetic products in pavement design. To develop a laboratory methodology compatible with the current Pavement ME Design, it is necessary to quantify the characteristics of geosynthetic reinforcement in terms of the resilient properties and permanent deformation properties of the geosynthetic-reinforced unbound granular material (UGM).

Mechanistic Models for Geogrid-Reinforced UGMs

Cross-Anisotropic Properties of Reinforced UGMs

UGMs exhibit cross-anisotropy characteristics. The constitutive model used to characterize the cross-anisotropic behavior is shown in Equation C-1.

$$\begin{bmatrix} \frac{1}{E_x} & -\frac{\nu_{xy}}{E_x} & -\frac{\nu_{xx}}{E_x} \\ -\frac{\nu_{xy}}{E_x} & \frac{1}{E_y} & -\frac{\nu_{xy}}{E_x} \end{bmatrix} \begin{Bmatrix} \sigma_x \\ \sigma_y \\ \sigma_x \end{Bmatrix} = \begin{Bmatrix} \varepsilon_x \\ \varepsilon_y \\ \varepsilon_y \end{Bmatrix} \quad (\text{C-1})$$

where σ_x is the stress in the horizontal direction; σ_y is the stress in the vertical direction; ε_x is the strain in the horizontal direction; ε_y is the strain in the vertical direction; E_x is the resilient modulus in the horizontal direction; E_y is the resilient modulus in the vertical direction; ν_{xx} is the Poisson's ratio in the horizontal plane; and ν_{xy} is the Poisson's ratio in the vertical plane. E_x , E_y , ν_{xx} , and ν_{xy} are the cross-anisotropic properties of UGMs.

Stress-Dependent Permanent Deformation Properties of Reinforced UGMs

A new mechanistic-empirical rutting model is proposed to evaluate the stress-dependent permanent deformation characteristics of geogrid-reinforced and unreinforced UGMs, as shown in Equation C-2. The proposed rutting model is able to determine the accumulated permanent deformation at any specific stress state and number of load repetitions.

$$\varepsilon_p = \varepsilon_0 e^{-\left(\frac{\rho}{N}\right)^\beta} \left(\sqrt{J_2}\right)^m (\alpha I_1 + K)^n \quad (\text{C-2})$$

$$\alpha = \frac{2 \sin \phi}{\sqrt{3}(3 - \sin \phi)} \quad (\text{C-3})$$

$$K = \frac{c \cdot 6 \cos \phi}{\sqrt{3}(3 - \sin \phi)} \quad (\text{C-4})$$

where J_2 is the second invariant of the deviatoric stress tensor; I_1 is the first invariant of the stress tensor; ε_0 , ρ , β , m , and n are model coefficients; and c and ϕ are the cohesive shear strength and friction angle, respectively. In this model, the two terms, $\sqrt{J_2}$ and $\alpha I_1 + K$, are incorporated into the Tseng-Lytton model (1) and used to reflect the influence of a stress state on the permanent deformation characteristics of UGMs.

The concept of the proposed rutting model is illustrated in Figure C-1. The Drucker-Prager plastic yield criterion (2) was applied in this study. As shown in Figure C-1, the black dot represents the current stress state in the $I_1 - \sqrt{J_2}$ plane. The term of $\sqrt{J_2}$ represents the softening effects of the deviatoric shear stress on the UGM, and a higher $\sqrt{J_2}$ yields a larger permanent deformation. Thus, the power coefficient m is always a positive number. In addition, the term $\alpha I_1 + K$ indicates the hardening effect of the hydrostatic stress on the UGM, which is highly affected by the material cohesion and internal friction angle. A higher $\alpha I_1 + K$ value results in a smaller plastic deformation, so the power coefficient n is always a negative value.

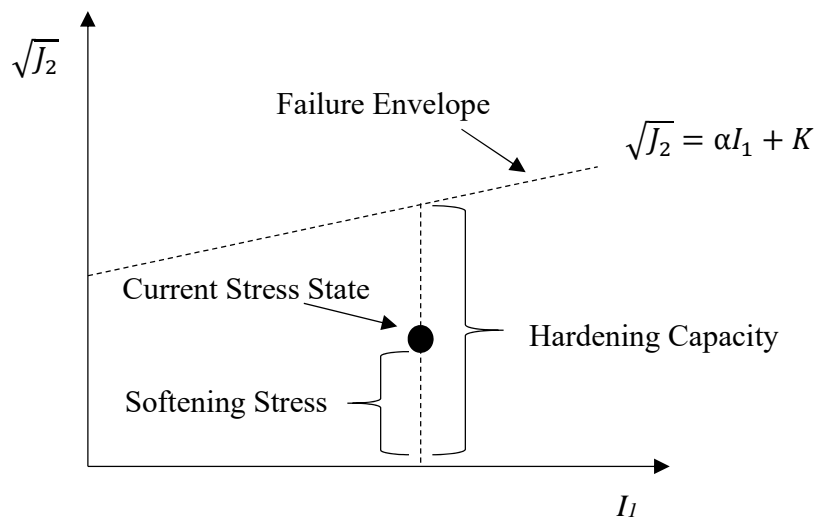


Figure C-1. Illustration of the Proposed Rutting Model Based on Drucker-Prager Plastic Yield Criterion

Materials and Experiment

Materials

Aggregate

One crushed granite material was used in this study. The gradation of the selected aggregate material is shown in Table C-1. It has a maximum dry density of $2.16 \times 10^3 \text{ kg/m}^3$ and an optimum water content of 6.7 percent. The compacted aggregate specimen has a cohesion of 20.2 kPa and an internal friction angle of 51.3 degrees.

Table C-1. Gradation of Crushed Granite Aggregate

Sieve Size (mm)	25.4	19.0	12.7	9.5	4.75	2.36	1.18	0.6	0.075
Passing Percentage (%)	100	97	86	68	46	30	20	15	4.1

Geosynthetic

Three types of geogrids, TX-1, TX-2, and BX-3, and one type of geotextile, GT-4, were selected to reinforce the UGMs. “TX” denotes that the aperture shape of the geogrid is triangular. “BX” means the aperture shape of the geogrid is rectangular. “GT” means the geosynthetic product is a geotextile. The physical and mechanical properties of the selected geogrids and geotextiles are shown in Tables C-2 and C-3, respectively.

Table C-2. Physical and Mechanical Properties of the Selected Geogrids

Geogrid Type	Aperture Shape	Aperture Dimension (mm)	Tensile Sheet Stiffness ^a (kN/m)	
			MD ^b	XMD ^c
TX-1	Triangle	40×40×40	225	225
TX-2	Triangle	40×40×40	300	300
BX-3	Rectangle	25×33	300	450

^a Tensile sheet stiffness values are at 0.5% tensile strain for TX geogrid and at 2% tensile strain for BX geogrid.

^b MD=machine direction.

^c XMD=cross-machine direction.

Table C-3. Material Properties of the Selected Geotextile GT-4

Material Properties	Test Method	Unit	Minimum Average Roll Value
Test Modulus @ 2% strain	ASTM D4595	kN/m	1313.3
Flow Rate	ASTM D4491	l/min/m ²	3055.5
Permittivity	ASTM D4491	sec ⁻¹	1.0
Apparent Opening Size	ASTM D4791	mm	0.43
Pore Size O ₉₅	ASTM D6767	microns	350 ³
Pore Size O ₅₀	ASTM D6767	microns	185 ³
Factory Seam Strength	ASTM D4884	kN/m	43.8
UV Resistance (at 500 hours)	ASTM D4355	% strength retained	80

Geosynthetic-Reinforced and Unreinforced Aggregate Specimens

The geosynthetic-reinforced and unreinforced aggregate specimens were fabricated as 15-cm diameter and 15-cm-high cylinders at the optimum water content using a modified compactive effort. The effect of the geogrid depends upon its location within the base course. To evaluate this effect, the geogrid was placed in the middle of the specimen, one-quarter below the middle of the specimen, and at the bottom of the specimen, as shown in Figure C-2.

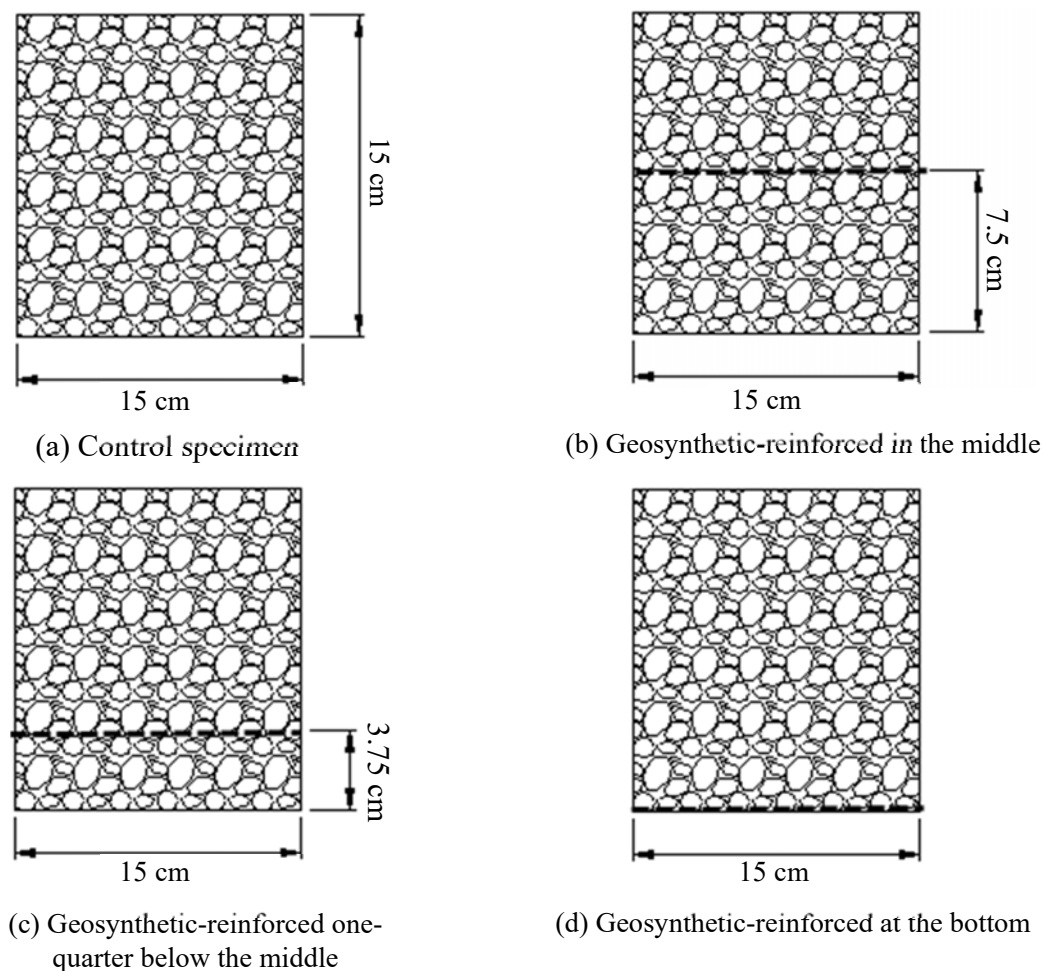


Figure C-2. Geosynthetic Location in UGM Specimen

Test Methods

Cross-Anisotropy Test

The cross-anisotropy tests were conducted on both the geogrid-reinforced and unreinforced aggregate specimens using the universal testing machine (UTM) with a rapid triaxial test (RaTT) cell. Figure C-3 shows the configuration of the cross-anisotropy test. Prior to testing, the RaTT cell was moved downward to encompass the specimen. The confining pressure was applied directly to the specimen by the RaTT cell via a pneumatic bladder. The dynamic axial load was applied to the specimen through the loading frame of the UTM. In pre-conditioning, the confining pressure was controlled at 103.4 kPa, and a 103.4 kPa deviatoric axial load was applied for 500 repetitions. Table C-4 shows the cross-anisotropy test protocol developed by Texas A&M University (3). According to the cross-anisotropic constitutive model, three stress modes were used in the loading protocol, including the compression, shear, and extension modes, which are detailed below.

Table C-4. RLT Test Protocol for Determining Cross-Anisotropic Properties of Geosynthetic-Reinforced and Unreinforced UGM

Stress State	Static Stress (kPa)		Dynamic Stress (kPa)					
			Compression		Shear		Extension	
	σ_y	σ_x	σ_y^c	σ_x^c	σ_y^s	σ_x^s	σ_y^e	σ_x^e
1	40	25	5	0	10	-5	-5	5
2	50	25	10	0	10	-5	-10	5
3	70	40	10	0	10	-5	-10	10
4	130	60	20	0	20	-10	-10	10
5	150	70	20	0	20	-10	-10	10
6	170	100	20	0	20	-10	-20	20
7	220	120	30	0	30	-15	-20	20
8	250	140	30	0	30	-15	-20	20
9	250	120	30	0	30	-15	-20	20
10	250	105	30	0	30	-15	-20	20

Compression Mode

In the compression mode, the radial stress was kept constant while the axial stress was dynamically cycled in an increment of $\Delta\sigma_y$, as illustrated in Equation C-5.

$$\begin{bmatrix} \frac{1}{E_x} & -\frac{\nu_{xy}}{E_x} & -\frac{\nu_{xx}}{E_x} \\ -\frac{\nu_{xy}}{E_x} & \frac{1}{E_y} & -\frac{\nu_{xy}}{E_x} \end{bmatrix} \begin{Bmatrix} \Delta\sigma_x^c \\ \Delta\sigma_y^c \\ \Delta\sigma_x^c \end{Bmatrix} = \begin{Bmatrix} \Delta\epsilon_x^c \\ \Delta\epsilon_y^c \end{Bmatrix} \quad (C-5)$$

where $\Delta\epsilon_x^c$ is the change in the radial strain due to an infinitesimal change in the axial stress

$\Delta\sigma_y^c$; $\Delta\epsilon_y^c$ is the change in the axial strain due to an infinitesimal change in the axial stress $\Delta\sigma_y^c$; and $\Delta\sigma_x^c$ is zero.

Shear Mode

In the shear mode, an increment of the dynamic axial stress, $\Delta\sigma_y^s$, was applied to the sample while the radial stress was reduced by a small change in the dynamic stress, $\Delta\sigma_x^s$, such that $\Delta\sigma_x^s = -\frac{1}{2}\Delta\sigma_y^s$. Equation C-6 is constructed for the shear mode.

$$\begin{bmatrix} \frac{1}{E_x} & -\frac{\nu_{xy}}{E_x} & -\frac{\nu_{xx}}{E_x} \\ -\frac{\nu_{xy}}{E_x} & \frac{1}{E_y} & -\frac{\nu_{xy}}{E_x} \end{bmatrix} \begin{Bmatrix} \Delta\sigma_x^s \\ \Delta\sigma_y^s \\ \Delta\sigma_x^s \end{Bmatrix} = \begin{Bmatrix} \Delta\epsilon_x^s \\ \Delta\epsilon_y^s \end{Bmatrix} \quad (C-6)$$

The change in the first stress invariant, ΔI_1 , is calculated to be zero, as shown in Equation C-7:

$$\Delta I_1 = \Delta \sigma_y^s + 2\Delta \sigma_x^s = \Delta \sigma_y^s - 2 \times \frac{1}{2} \Delta \sigma_y^s = 0 \quad (\text{C-7})$$

The incremental change of the second deviatoric stress invariant, ΔJ_2^s , is written as:

$$\begin{aligned} \Delta J_2^s &= \frac{1}{3} \Delta I_1^2 - \Delta I_2 \\ &= - \left[\Delta \sigma_y^s \Delta \sigma_x^s + (\Delta \sigma_x^s)^2 + \Delta \sigma_x^s \Delta \sigma_y^s \right] \\ &= \frac{3}{4} (\Delta \sigma_y^s)^2 \end{aligned} \quad (\text{C-8})$$

where ΔI_2 is the incremental change of the second stress invariant. The change in the strain energy, ΔE^s , is given in the following equation:

$$\Delta E^s = \frac{1}{2} (\Delta \sigma_x^s \Delta \epsilon_x^s + \Delta \sigma_y^s \Delta \epsilon_y^s + \Delta \sigma_x^s \Delta \epsilon_x^s) = \frac{1}{2} \Delta \sigma_y^s (\Delta \epsilon_y^s - \Delta \epsilon_x^s) \quad (\text{C-9})$$

Since the total work on a deformable body is path independent due to the law of energy conservation, the work performed on the unit volume, dW , is formulated in terms of stress invariants, as shown in Equation C-10:

$$\oint dW = \oint \frac{I_1 dI_1}{9E_y} \left[1 + 2 \frac{E_y}{E_x} - 4\nu_{xy} \frac{E_y}{E_x} - 2\nu_{xx} \frac{E_y}{E_x} \right] + \frac{dJ_2}{2G_{xy}} \quad (\text{C-10})$$

Since the first stress invariant, ΔI_1 , is zero, the change in the strain energy, ΔE^s , is formulated in Equation C-11 based on Equation C-10:

$$\Delta E^s = \frac{\Delta J_2^s}{2G_{xy}} \quad (\text{C-11})$$

By substituting Equations C-8 and C-9 into Equation C-11, the shear modulus in the vertical plane is then determined, as shown in Equation C-12:

$$G_{xy} = \frac{3}{4} \frac{\Delta \sigma_y^s}{(\Delta \epsilon_y^s - \Delta \epsilon_x^s)} \quad (\text{C-12})$$

Extension Mode

In the extension mode, the static axial stress σ_y was reduced by a small change in the dynamic stress $\Delta \sigma_y^e$, and the radial stress σ_x was increased by a small dynamic stress $\Delta \sigma_x^e$. Therefore, in each loading cycle, the aggregate specimen was loaded to $(\sigma_y^e - \Delta \sigma_y^e, \sigma_x^e + \Delta \sigma_x^e)$ and was unloaded to (σ_y^e, σ_x^e) . The constitutive equation is constructed for the extension mode in Equation C-13.

$$\begin{bmatrix} \frac{1}{E_x} & -\frac{\nu_{xy}}{E_x} & -\frac{\nu_{xx}}{E_x} \\ -\frac{\nu_{xy}}{E_x} & \frac{1}{E_y} & -\frac{\nu_{xy}}{E_x} \end{bmatrix} \begin{Bmatrix} \Delta\sigma_x^e \\ \Delta\sigma_y^e \\ \Delta\sigma_x^e \end{Bmatrix} = \begin{Bmatrix} \Delta\epsilon_x^e \\ \Delta\epsilon_y^e \end{Bmatrix} \quad (\text{C-13})$$

where $\Delta\epsilon_x^e$ is the change in the radial strain due to $\Delta\sigma_x^e$ and $\Delta\sigma_y^e$; and $\Delta\epsilon_y^e$ is the change in the axial strain due to $\Delta\sigma_x^e$ and $\Delta\sigma_y^e$.

As seen in Table C-2, 10 stress states were associated with corresponding dynamic stresses. At each stress state, every loading cycle of the dynamic stress consisted of 1.5 seconds of loading and 1.5 seconds of unloading. The LVDTs measured the vertical and horizontal deformations of the specimen. The test data were used to calculate the anisotropic properties of geogrid-reinforced and unreinforced aggregate specimens using the system identification method.

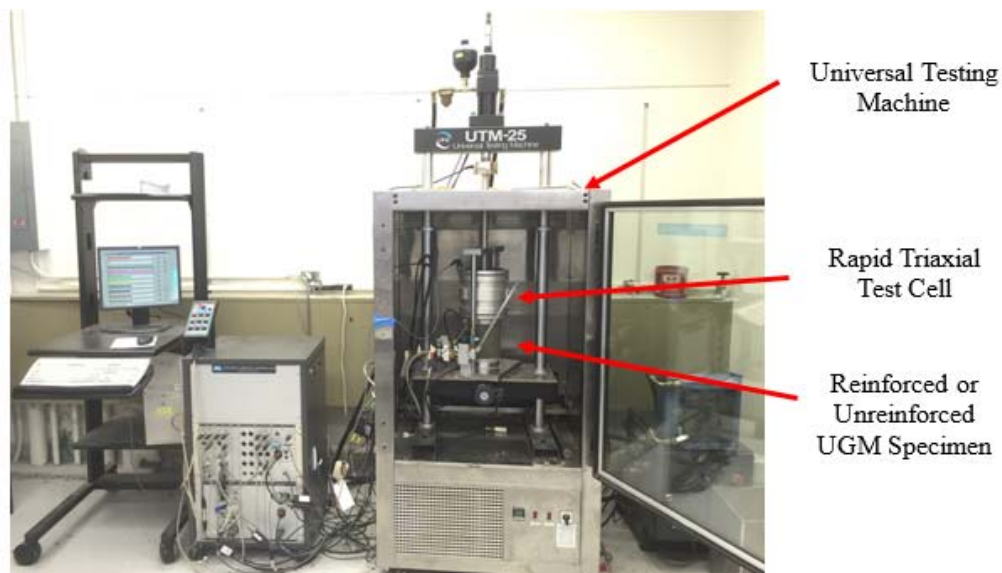


Figure C-3. Configuration of the Repeated Load Triaxial Test

Permanent Deformation Test

Compared to the cross-anisotropy test, the permanent deformation test used the same UTM configuration (see Figure C-3) but a different test module. The axial load follows a haversine shape with 0.1-second load period and 0.9-second rest period in every load cycle. After pre-conditioning, the specimens were subjected to 10,000 cycles of repeated load at a specified stress level. The LVDTs only measured the vertical deformations of the specimen. The test data were used to determine the permanent deformation properties of geogrid-reinforced and unreinforced aggregate specimens.

To evaluate the effect of stress level on the geogrid reinforcement of UGM specimens, a new permanent deformation test protocol was developed, as shown in Table C-5. The proposed

test protocol includes seven stress states (i.e., Stress States 1–7) for model calibration and two stress states (i.e., Stress States 8 and 9) for model validation. Stress States 1, 2, 3, 4, and 9 apply the same I_1 with various J_2 , whereas Stress States 1, 5, 6, 7, and 9 employ the same J_2 but different I_1 . This test protocol allows quantifying the influence of the two stress terms, I_1 and J_2 , on the permanent deformation behavior of geogrid-reinforced and unreinforced UGM specimens, individually.

Table C-5. RLT Test Protocol for Determining Permanent Deformation Properties of Geosynthetic-Reinforced and Unreinforced UGMs

Stress State	Confining Pressure, σ_3 (kPa)	Deviatoric Stress, σ_d (kPa)	Bulk Stress, I_1 (kPa)	Second Invariant of Shear Stress Tensor, J_2 (kPa ²)	Comments
1	27.6	192.9	275.6	12406.0	Model Calibration
2	48.2	130.9	275.6	5712.5	
3	68.9	68.9	275.6	1582.4	
4	91.9	0	275.6	0	
5	48.2	192.9	337.6	12406.0	
6	68.9	192.9	399.6	12406.0	
7	89.6	192.9	461.6	12406.0	
8	34.5	172.3	275.6	9890.0	Model Validation
9	103.4	192.9	503.0	12406.0	

Test Results

Impact of Geosynthetic on Cross-Anisotropy Characteristics of UGMs

The measured vertical and horizontal resilient deformations in the cross-anisotropy test were analyzed using the system identification method to back-calculate the vertical and horizontal resilient moduli, E_y and E_x , respectively, based on the constitutive model presented in Equation C-1. The determined vertical and horizontal moduli and anisotropic ratio of the geosynthetic-reinforced specimens were compared to those of the unreinforced specimens (the control) by calculating the normalized modulus ratio of the geosynthetic-reinforced specimen to the unreinforced specimen, as shown in Equations C-14–C-16.

$$\text{Normalized Horizontal Modulus Ratio} = \frac{E_{x-\text{geo}}}{E_{x-\text{control}}} \quad (\text{C-14})$$

$$\text{Normalized Vertical Modulus Ratio} = \frac{E_{y-\text{geo}}}{E_{y-\text{control}}} \quad (\text{C-15})$$

$$\text{Normalized Anisotropic Ratio} = \frac{AR_{\text{geo}}}{AR_{\text{control}}} \quad (\text{C-16})$$

where E_{x-geo} is the horizontal resilient modulus of the geogrid-reinforced specimen; $E_{x-control}$ is the horizontal resilient modulus of the unreinforced specimen; E_{y-geo} is the vertical resilient modulus of the geogrid-reinforced specimen; $E_{y-control}$ is the vertical resilient modulus of the unreinforced specimen; AR_{geo} is the anisotropic ratio of the geosynthetic-reinforced specimen; and $AR_{control}$ is the anisotropic ratio of the unreinforced specimen. The comparison results are shown in Table C-5.

Table C-6 shows that the normalized horizontal and vertical modulus ratios of all three types of geogrid-reinforced specimens are larger than 100 percent at every stress state, which indicates that the geogrid increases both the vertical and horizontal moduli of the UGM specimen since the total elastic deformation of the specimen is restricted due to the adding of the geogrid in the UGMs. However, the inclusion of the geogrid does not influence the anisotropy ratio of the UGM. Compared to the geogrid TX-1, the geogrid TX-2 provides slightly higher horizontal and vertical modulus ratios at most of the stress states, which demonstrates that the geogrid with a higher sheet stiffness is more beneficial for the reinforcement. Compared to the geogrid TX-1 and TX-2, the geogrid BX-3 provides comparable reinforcement on the horizontal and vertical resilient moduli of UGM. This indicates that the aperture shape of the geogrid does not significantly affect the resilient modulus of the UGM specimen. Different from the geogrids, the geotextile only reinforces the horizontal modulus of the UGM specimen, which results in the increase in anisotropic ratio of the UGM.

Tables C-6, C-7, and C-8 also present the effect of geogrid location on the horizontal and vertical resilient moduli of the UGM. The normalized modulus ratios when the geogrid is placed in the middle or one-quarter below the middle of the specimen are larger than 100 percent at every stress state, while those of the specimen with the geogrid placed at the bottom of the specimen fluctuate around 100 percent. This indicates that placing the geogrid in the middle or one-quarter below the middle of the specimen increases the vertical and horizontal moduli, but placing the geogrid at the bottom cannot reinforce the UGM neither vertically nor horizontally. Compared to the geogrid placed in the middle of the specimen, the geogrid placed one-quarter below the middle of the specimen provides slightly smaller normalized vertical and horizontal modulus ratios at most of the stress states, which indicates that the geogrid placed in the middle of the specimen has a slightly better reinforcement effect. It must be noted that the bottom of the UGM specimen interfaces with an aluminum platen, which differs from the interface between a pavement base layer with the subgrade. Thus, placing a geogrid at the bottom of the UGM specimen and at the bottom of the base layer may introduce different effects on the UGM performance, which needs to be studied based on pavement structural analysis in the future.

**Table C-6. Influence of Geosynthetic on Cross-Anisotropic Properties
(Geosynthetic Location: Mid-Height)**

Stress State	Geosynthetic Type	$\frac{E_{x-geo}}{E_{x-control}}$ (%)	$\frac{E_{y-geo}}{E_{y-control}}$ (%)	$\frac{AR_{geo}}{AR_{control}}$ (%)
1	TX-1	115	119	97
	TX-2	119	124	96
	BX-3	123	120	103
	GT-4	153	92	166
2	TX-1	112	120	93
	TX-2	119	125	95
	BX-3	117	131	89
	GT-4	157	109	144
3	TX-1	107	112	96
	TX-2	115	110	105
	BX-3	126	120	105
	GT-4	144	98	147
4	TX-1	119	119	100
	TX-2	124	122	102
	BX-3	118	121	98
	GT-4	131	100	131
5	TX-1	120	117	103
	TX-2	118	120	98
	BX-3	124	116	107
	GT-4	132	104	127
6	TX-1	115	118	97
	TX-2	121	115	105
	BX-3	122	115	106
	GT-4	127	99	128
7	TX-1	108	107	101
	TX-2	114	112	102
	BX-3	112	111	101
	GT-4	124	103	120
8	TX-1	103	102	101
	TX-2	107	109	98
	BX-3	111	112	99
	GT-4	124	95	131
9	TX-1	108	105	103
	TX-2	110	109	101
	BX-3	121	109	111
	GT-4	117	98	119
10	TX-1	106	103	103
	TX-2	105	107	98
	BX-3	110	110	100
	GT-4	122	102	120

**Table C-7. Influence of Geosynthetic on Cross-Anisotropic Properties
(Geosynthetic Location: One-Quarter below the Middle)**

Stress State	Geosynthetic Type	$\frac{E_{x-geo}}{E_{x-control}}$ (%)	$\frac{E_{y-geo}}{E_{y-control}}$ (%)	$\frac{AR_{geo}}{AR_{control}}$ (%)
1	TX-1	113	112	101
	TX-2	109	115	95
	BX-3	121	110	110
	GT-4	132	85	155
2	TX-1	108	110	98
	TX-2	112	116	97
	BX-3	109	122	89
	GT-4	125	97	129
3	TX-1	114	113	101
	TX-2	107	115	93
	BX-3	112	124	90
	GT-4	118	102	116
4	TX-1	107	117	91
	TX-2	109	122	89
	BX-3	119	120	99
	GT-4	122	95	128
5	TX-1	114	110	104
	TX-2	110	115	96
	BX-3	108	119	91
	GT-4	124	99	125
6	TX-1	108	110	98
	TX-2	112	106	106
	BX-3	111	115	97
	GT-4	115	91	126
7	TX-1	106	105	101
	TX-2	105	107	98
	BX-3	113	124	91
	GT-4	106	103	103
8	TX-1	109	106	103
	TX-2	114	103	111
	BX-3	119	108	110
	GT-4	109	95	115
9	TX-1	110	105	105
	TX-2	108	109	99
	BX-3	115	110	105
	GT-4	107	89	120
10	TX-1	105	106	99
	TX-2	108	111	97
	BX-3	109	108	101
	GT-4	110	87	126

**Table C-8. Influence of Geosynthetic on Cross-Anisotropic Properties
(Geosynthetic Location: Bottom)**

Stress State	Geosynthetic Type	$\frac{E_{x-geo}}{E_{x-control}}$ (%)	$\frac{E_{y-geo}}{E_{y-control}}$ (%)	$\frac{AR_{geo}}{AR_{control}}$ (%)
1	TX-1	98	102	96
	GT-4	104	97	107
2	TX-1	103	98	105
	GT-4	104	93	112
3	TX-1	103	102	101
	GT-4	108	95	114
4	TX-1	97	100	97
	GT-4	94	102	92
5	TX-1	102	103	99
	GT-4	107	96	111
6	TX-1	103	101	102
	GT-4	116	103	113
7	TX-1	101	96	105
	GT-4	104	95	109
8	TX-1	97	102	95
	GT-4	106	93	114
9	TX-1	101	97	104
	GT-4	102	92	111
10	TX-1	98	102	96
	GT-4	97	93	104

Impact of Geosynthetic on Permanent Deformation Characteristics of UGM

The proposed mechanistic-empirical rutting model was employed to quantify the permanent deformation characteristics of geogrid-reinforced and unreinforced UGMs at various stress states. The model coefficients were determined using the solver function in Microsoft Excel to fit the measured permanent strain curves from Stress States 1–7. Figures C-4 and C-5 compare the model-predicted permanent strain curves with the laboratory-measured ones at different stress states for both unreinforced and geogrid-reinforced UGMs. The root-mean-square error (RMSE) values were calculated to evaluate the goodness of the model fitting. In general, a small RMSE value indicates a high goodness of fitting (4). The figures show that all of the determined RMSE values were relatively small, which indicates that the proposed model accurately captures the influence of stress level on the permanent deformation of the geogrid-reinforced and unreinforced UGMs.

Figures C-4 and C-5 also present the determined coefficients of the proposed rutting model, which were used to predict the plastic strain curves of the UGMs at Stress States 8 and 9 in this study. To examine the accuracy of the proposed rutting model, the model-predicted permanent strain curves were compared to the laboratory-measured permanent strain curves from Stress States 8 and 9, as shown in Figure C-6. The model predictions had small RMSE values for

both geogrid-reinforced and unreinforced UGMs at the two stress states, which indicates that the proposed rutting model is accurate to predict the stress-dependent permanent deformation characteristics of geogrid-reinforced and unreinforced UGMs. Table C-9 lists the determined model coefficients for the geogrid-reinforced and unreinforced UGMs tested in this study. The determined model coefficients can be used to predict the permanent deformation of UGMs at any stress levels and number of load repetitions.

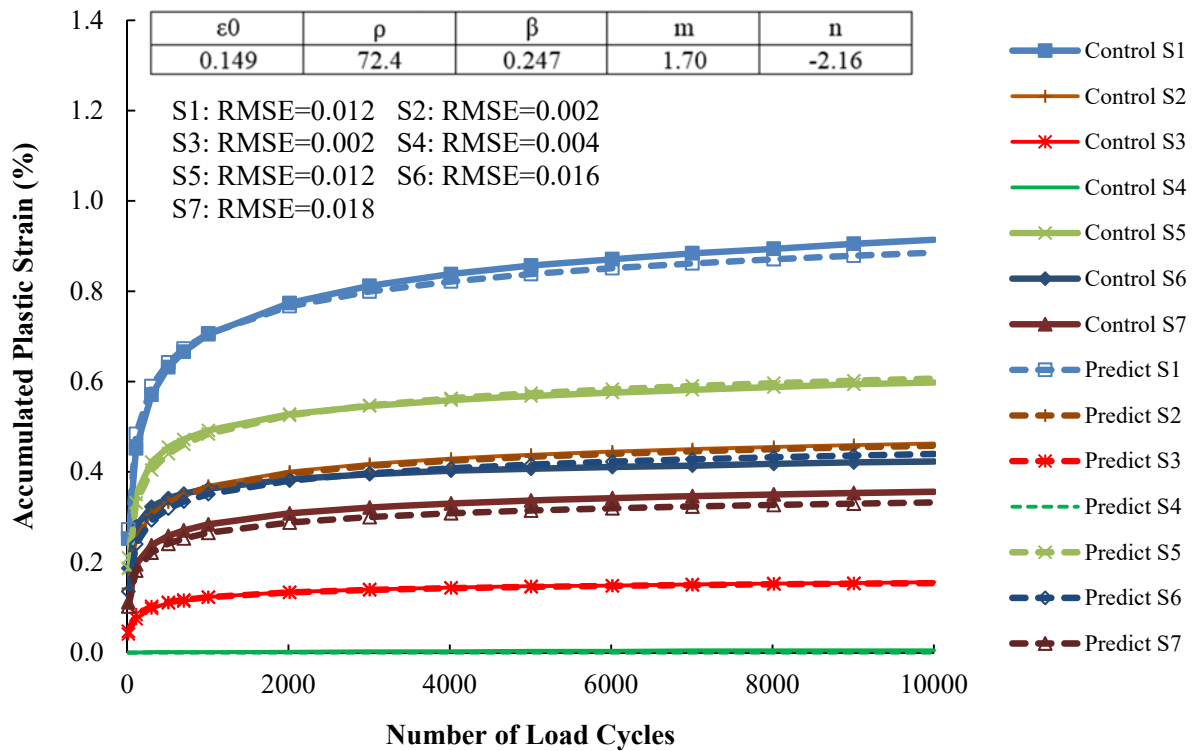


Figure C-4. Comparison of Lab-Measured and Proposed-Model-Predicted Permanent Deformation Curves for Unreinforced UGM

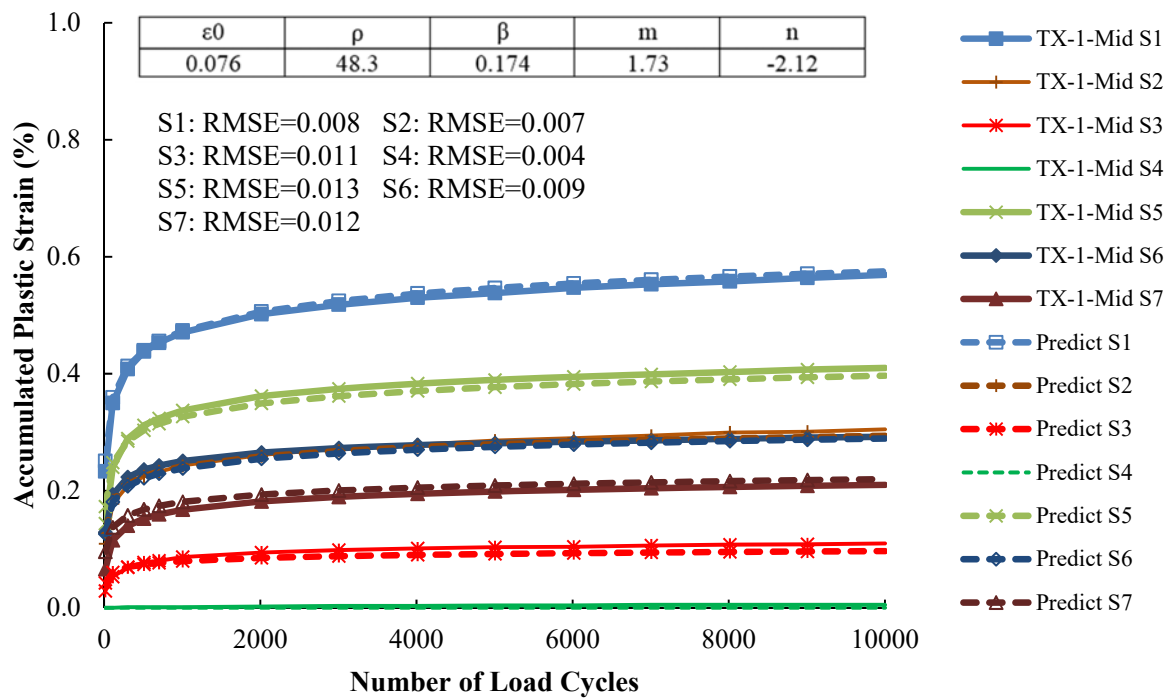


Figure C-5. Comparison of Lab-Measured and Proposed-Model-Predicted Permanent Deformation Curves for Geogrid-Reinforced UGM

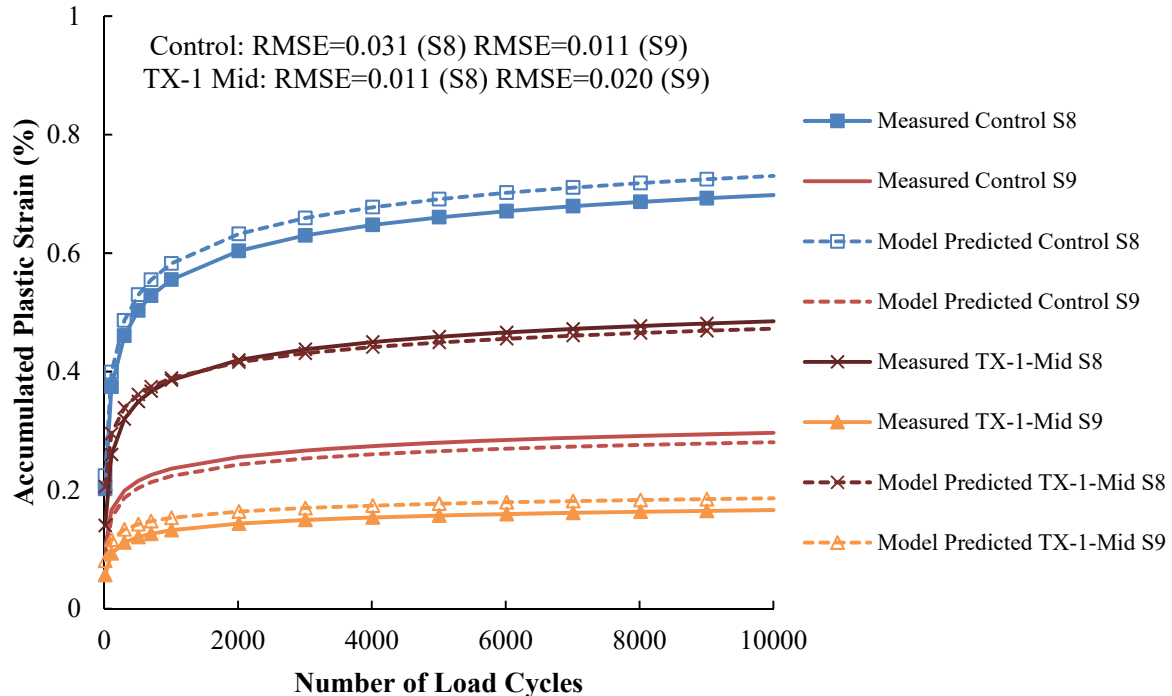


Figure C-6. Validation of Prediction Accuracy of Proposed Model for Geogrid-Reinforced and Unreinforced UGMs

Table C-9. Determination of Model Coefficients for Geogrid-Reinforced and Unreinforced UGMs

Material Type	Permanent Deformation Model Coefficients				
	ϵ_0	ρ	β	m	n
Unreinforced	0.149	72.4	0.247	1.70	-2.16
TX-1 Middle	0.076	48.3	0.174	1.73	-2.12
TX-2 Middle	0.068	82.1	0.165	1.84	-2.21
BX-3 Middle	0.082	31.2	0.182	1.64	-2.01
TX-2 One-Quarter below Middle	0.093	62.5	0.159	1.62	-2.03
TX-2 Bottom	0.142	35.1	0.294	1.79	-2.26
GT-4 Middle	0.112	60.4	0.261	1.76	-2.18

References

1. Tseng, K.H., and Lytton, R.L. (1989). Prediction of Permanent Deformation in Flexible Pavements Materials: Implication of Aggregates in the Design, Construction, and Performance of Flexible Pavements. *ASTM STP 1016*, American Society for Testing and Materials (ASTM), West Conshohocken, Pennsylvania.
2. Drucker, D.C., and Prager, W. (1952). Soil Mechanics and Plastic Analysis for Limit Design. *Quarterly of Applied Mathematics*, Vol. 10, No. 2, pp. 157–165.
3. Adu-Osei, A., Little, D.N., and Lytton, R.L. (2001). Cross-Anisotropic Characterization of Unbound Granular Materials. *Transportation Research Record: Journal of the Transportation Research Board*, No. 1757, pp. 82–91.
4. Gauch, H.G., Hwang, J.T., and Fick, G.W. (2003). Model Evaluation by Comparison of Model-Based Predictions and Measured Values. *Agronomy Journal*, No. 95, pp. 1442–1446.

APPENDIX D. ANALYTICAL MODEL FOR QUANTIFYING INFLUENCE OF GEOSYNTHETICS

The repeated load triaxial test studies indicate that the placement of geosynthetics influences the cross-anisotropic properties (i.e., the vertical and horizontal modulus) and the permanent deformation properties of the UGM. An analytical model is proposed to predict the vertical and horizontal modulus and the permanent deformation of the geosynthetic-reinforced UGM when it is subjected to a triaxial load. Figure D-1a shows a schematic plot of a geosynthetic-reinforced UGM specimen in the triaxial load test. The geosynthetic-reinforced specimen is compressed in the axial direction and normally expands in the lateral direction due to the plastic and resilient deformation. The figure shows that the lateral movement of the UGM is restrained by the geosynthetic. The shear stress is generated due to the relative lateral displacement between the geosynthetic and aggregate, which results in the stretch of the embedded geosynthetic. Note that the lateral movement of the aggregate and geosynthetic cannot be identical. Figure D-1b shows the difference in lateral movement between the geosynthetic and aggregate during the test. A coefficient α was employed to account for the difference of radial displacement between geosynthetic and aggregate, as shown in Equation D-1.

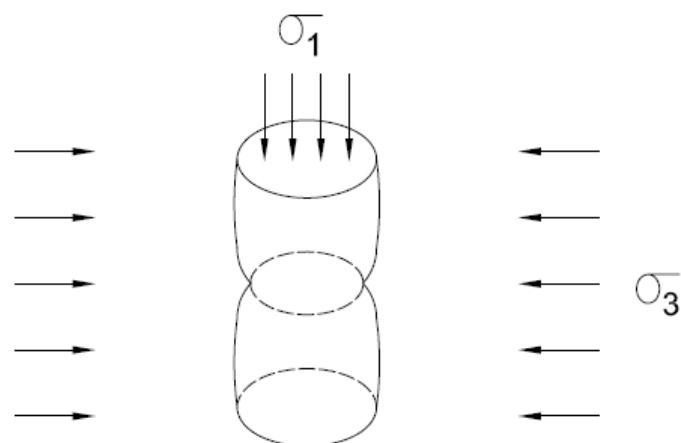
$$\alpha = \frac{\epsilon_{rr}^a}{\epsilon_{rr}^g} \quad (\text{D-1})$$

where ϵ_{rr}^a is the aggregate radial tensile strain at the interface between the geosynthetic and aggregate, and ϵ_{rr}^g is the geogrid radial tensile strain. Note that the value of α is normally larger than 1, which illustrates that the aggregate has a larger lateral movement than the geosynthetic. The analytical solution to determine the coefficient α is shown in Equations D-2 and D-3 (1).

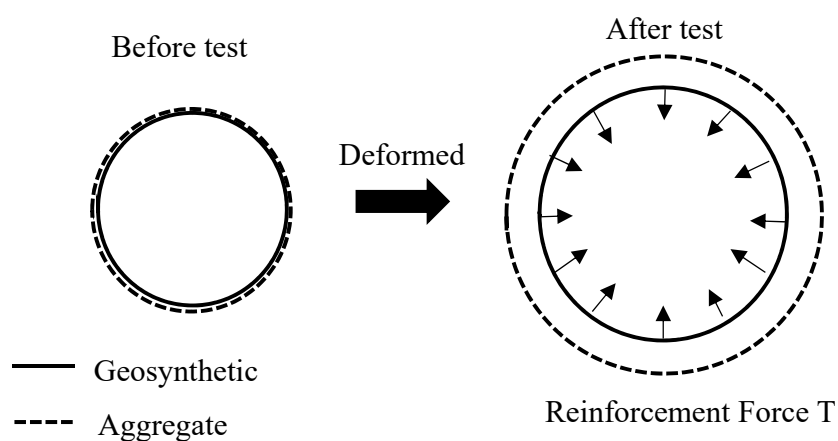
$$\beta \cdot J_0\left(\beta \frac{D}{2}\right) - \frac{2}{D} \cdot J_1\left(\beta \frac{D}{2}\right) = \sigma_3 \quad (\text{D-2})$$

$$\beta = \left[\frac{2G_a(\alpha-1)(1-\nu_g^2)}{\delta M} \right]^{1/2} \quad (\text{D-3})$$

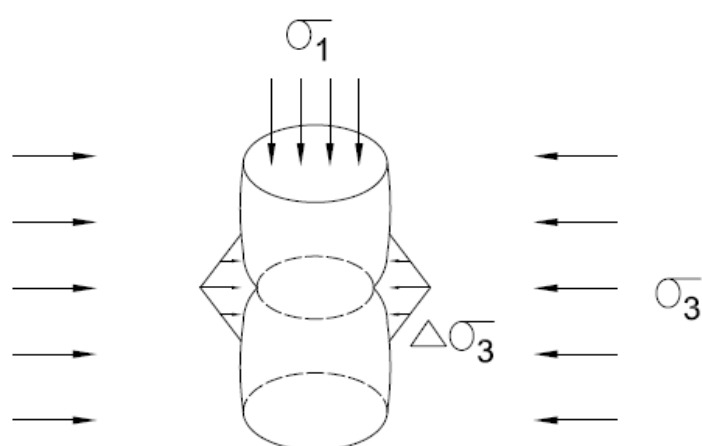
where $J_i(x)$ is the Bessel function of order i , D is the diameter of the aggregate specimen (i.e., $D = 6$ inches), and G_a is the shear modulus of the aggregate. Equation D-2 is an implicit equation for the coefficient α . The stretch of the geosynthetic generates a reinforcement force T to confine the UGM specimen through the aggregate particle interlock and interface friction (2). Figure D-1c shows that the reinforcement force T is equivalent to a triangularly distributed additional confining stress $\Delta\sigma_3$, which only acts on a 6-inch geosynthetic-reinforced influence zone (3). This distribution takes into account the phenomenon that the geosynthetic reinforcement influence decreases with the distance between the aggregate and geosynthetic, and the geosynthetic reinforcement is negligible when the material is far away from the geosynthetic.



(a) Displacement Pattern of UGM Restraint by Geosynthetic



(b) Difference in Radial Movement of Geosynthetic and Aggregate



(c) Equivalence of Reinforcement Force to Additional Stress $\Delta\sigma_3$

Figure D-1. Schematic Plot of Geosynthetic Reinforcement on UGM Specimen

Under an axisymmetric plane-stress condition, the reaction force T is determined by Equation D-4.

$$T = \frac{M}{(1 - \nu_g^2)} \cdot (\epsilon_{rr}^g + \nu_g \epsilon_{\theta\theta}^g) \quad (\text{D-4})$$

where M is the geosynthetic sheet stiffness, ν_g is the Poisson's ratio of the geosynthetic, ϵ_{rr}^g is the geosynthetic tensile strain in the radial direction, and $\epsilon_{\theta\theta}^g$ is the geosynthetic tensile strain in the circumferential direction. By assuming that the geosynthetic expands uniformly in both the radial and the circumferential directions, Equation D-4 is simplified as:

$$T = \frac{M}{(1 - \nu_g)} \cdot \epsilon_{rr}^g \quad (\text{D-5})$$

If the equivalent additional confining stress $\Delta\sigma_3$ is triangularly distributed in the influential zone, the maximum additional confining stress $\Delta\sigma_{3\max}$ can be calculated by Equation D-6.

$$\Delta\sigma_{3\max} = \frac{2T}{\delta} = \frac{2M}{(1 - \nu_g)\delta} \cdot \epsilon_{rr}^g \quad (\text{D-6})$$

where δ is the thickness of the influential zone (i.e., $\delta = 6$ inches). Substituting Equation D-1 into Equation D-6 yields:

$$\Delta\sigma_{3\max} = \frac{2M}{(1 - \nu_g)\delta\alpha} \cdot \epsilon_{rr}^a \quad (\text{D-7})$$

In Equation D-7, the aggregate radial tensile strain ϵ_{rr}^a is the summation of the radial elastic strain $\epsilon_{3,r}^a$ and the radial plastic strain $\epsilon_{3,p}^a$. The radial elastic strain $\epsilon_{3,r}^a$ is calculated by the generalized Hooke's law, as shown in Equations D-8.

$$\epsilon_{3,r}^a = \frac{(\sigma_3 + \Delta\sigma_{3\max})}{E_H} - \frac{\nu_{13}\sigma_1}{E_V} - \frac{\nu_{33}(\sigma_3 + \Delta\sigma_{3\max})}{E_H} \quad (\text{D-8})$$

where σ_3 is the axial stress applied to the specimen, σ_1 is the initial confining pressure, ν_{13} is the Poisson's ratio to characterize the effect of axial strain on lateral strain, ν_{33} is the Poisson's ratio to characterize the effect of lateral strain on lateral strain, E_H is the horizontal modulus of the specimen, and E_V is the vertical modulus of the specimen. Equation D-9 is used to calculate the axial plastic strain $\epsilon_{1,p}^a$.

$$\epsilon_{1,p}^a = \epsilon_0 e^{-\left(\frac{\rho}{N}\right)^\beta} \left(\sqrt{J_2}\right)^m (\alpha I_1 + K)^n \quad (\text{D-9})$$

where $J_2 = \frac{1}{3}[\sigma_1 - (\sigma_3 + \Delta\sigma_{3\max})]^2$, $I_1 = \sigma_1 + 2(\sigma_3 + \Delta\sigma_{3\max})$, and ε_0 , ρ , β , m , and n are permanent deformation properties for the unreinforced specimen. The relationship between the radial plastic strain $\varepsilon_{3,p}^a$ and the axial plastic strain $\varepsilon_{1,p}^a$ is shown in Equation D-10.

$$\varepsilon_{3,p}^a = \frac{1}{2} \varepsilon_{1,p}^a \left(\frac{1 + \sin \psi}{1 - \sin \psi} \right) \quad (\text{D-10})$$

where ψ is the dilation angle of the specimen. Assuming that the dilation angle ψ is 15 degrees, Equation D-10 is simplified as:

$$\varepsilon_{3,p}^a = 0.85 \varepsilon_{1,p}^a \quad (\text{D-11})$$

Substituting Equations D-8, D-9, and D-11 into Equation D-7 yields:

$$\Delta\sigma_{3\max} = \frac{2M}{(1-\nu_g)\delta\alpha} \left[\frac{(\sigma_3 + \Delta\sigma_{3\max})}{E_H} - \frac{\nu_{13}\sigma_1}{E_V} - \frac{\nu_{33}(\sigma_3 + \Delta\sigma_{3\max})}{E_H} + 0.85\varepsilon_0 e^{-\left(\frac{\rho}{N}\right)^\beta} \left(\sqrt{J_2}\right)^m (\alpha I_1 + K)^n \right] \quad (\text{D-12})$$

In Equation D-12, the only unknown parameter is the maximum additional confining stress, $\Delta\sigma_{3\max}$. An iteration method is utilized to solve for this parameter.

Since the thickness of the influence zone, δ , is a constant, the calculated maximum additional confining stress, $\Delta\sigma_{3\max}$, can be used to determine the distribution function of equivalent additional confining stress, $\Delta\sigma_3(z)$, along the depth, z , of specimen. The determined equivalent additional confining stress distribution, $\Delta\sigma_3(z)$, is then input into Equation D-13 to calculate the modified vertical modulus of the base course, $E_{V-Modified}(z)$, in the influence zone.

$$E_{V-Modified}(z) = k_1 P_a \left[\frac{I_1 + \Delta\sigma_3(z)}{P_a} \right]^{k_2} \left(\frac{\tau_{oct}}{P_a} + 1 \right)^{k_3} \quad (\text{D-13})$$

where I_1 is the first invariant of the stress tensor; τ_{oct} is the octahedral shear stress; P_a is the atmospheric pressure; and k_1 , k_2 , and k_3 are regression coefficients. The effective vertical modulus of the entire geosynthetic-reinforced UGM specimen, $E_{V-Effective}$, is calculated using Equation D-14, which takes into account the variation of the location of the geosynthetic in the UGM specimen.

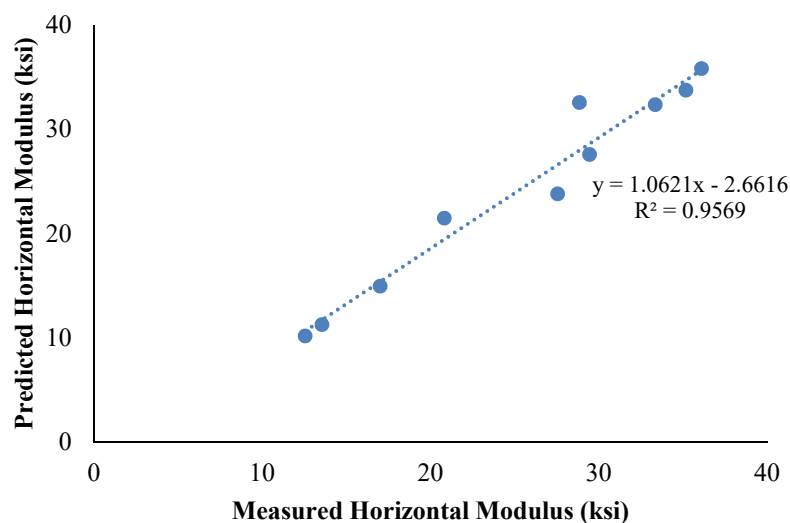
$$E_{V-Effective} = \begin{cases} \frac{E_{V-UGM} (h - \delta) + \int_0^{\delta} E_{V-Modified} (z) dz}{h} & \left(\frac{\delta}{2} < l < h - \frac{\delta}{2} \right) \\ \frac{E_{V-UGM} \left(h - \frac{\delta}{2} - l \right) + \int_0^{\frac{\delta}{2} + l} E_{V-Modified} (z) dz}{h} & \left(l < \frac{\delta}{2} \right) \\ \frac{E_{V-UGM} \left(h - \frac{\delta}{2} - l \right) + \int_0^{\frac{\delta}{2} + h - l} E_{V-Modified} (z) dz}{h} & \left(l > h - \frac{\delta}{2} \right) \end{cases} \quad (D-14)$$

where E_{V-UGM} is the vertical modulus of the unreinforced base course, h is the thickness of the base course, and l is the distance between the geosynthetic layer and the bottom of the base course. The effective horizontal modulus of the geosynthetic-reinforced UGM specimen, $E_{H-Effective}$, is calculated using Equation D-15.

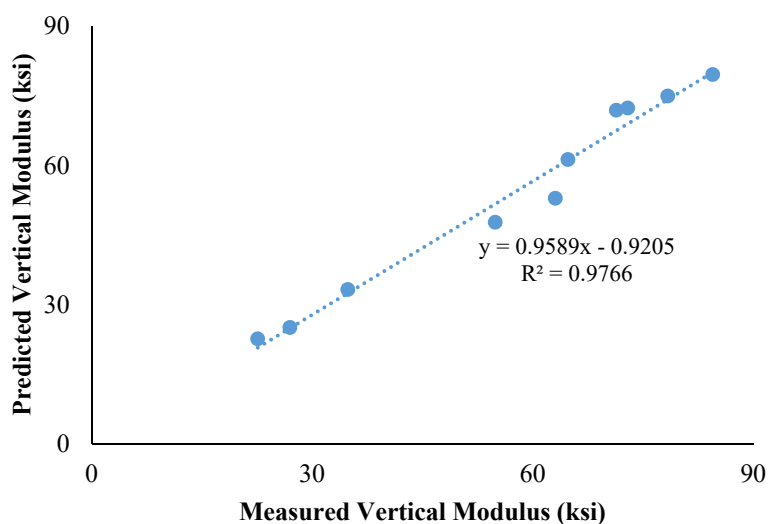
$$E_{H-Effective} = n \cdot E_{V-Effective} \quad (D-15)$$

where n is the ratio of the horizontal modulus to the vertical modulus, which is determined from the repeated load test. Similarly, inputting the determined equivalent additional confining stress distribution, $\Delta\sigma_3(z)$, into Equation D-9 can predict the permanent deformation of geosynthetic-reinforced UGMs at any given stress levels.

Figure D-2 shows the comparison of the resilient moduli of geogrid-reinforced UGMs predicted by the proposed analytical models and those measured from the laboratory tests. The horizontal and vertical resilient moduli predicted by the analytical models match the measured values with R-squared values of 0.96 and 0.98, respectively. This indicates that the proposed analytical models can accurately predict both the horizontal and vertical moduli of the geogrid-reinforced UGMs.



(a) Predicted Horizontal Moduli vs. Measured Horizontal Moduli



(b) Predicted Vertical Moduli vs. Measured Vertical Moduli

Figure D-2. Comparison of Resilient Moduli Predicted by Analytical Models with Measured Values

References

1. Lytton, R.L. (2015). Analytical Model for Quantifying Influence of Geosynthetics on Performance of Granular Material. *Unpublished Work*. Department of Civil Engineering, Texas A&M University, College Station, Texas.

2. Yang, X., and Han, J. (2013). Analytical Model for Resilient Modulus and Permanent Deformation of Geosynthetic-Reinforced Unbound Granular Material. *Journal of Geotechnical and Geoenvironmental Engineering*, Vol. 139, No. 9, pp. 1443–1453.
3. Schuettpelz, C., Fratta, D., and Edil, T.B. (2009). Evaluation of the Zone of Influence and Stiffness Improvement from Geogrid Reinforcement in Granular Materials. *Transportation Research Record: Journal of the Transportation Research Board*, No. 2116, pp. 76–84.

APPENDIX E. INSTRUMENTATION PLANS FOR FLEXIBLE PAVEMENT EXPERIMENTS

Appendix E1. Experiment No. 1 (Control—Thin Base)

Experiment ID	Exp1-AC-Contr-B06
Description	Flexible pavement; no reinforcement; 6-inch aggregate base

Average Asphalt Layer Thickness (inch)	5.82
Asphalt Layer Temperature (°F)	79.0
Average CAB Layer Thickness (inch)	6.00

Pressure Cell ID	Pressure Cell Diameter	X Coordinate (in)	Y Coordinate (in)	Z Coordinate (in)	Comments
P1	4 inch	0	0	18	P1 measures vertical pressure at 6 inches below the subgrade surface.
P2	4 inch	0	0	14	P2 measures vertical pressure at 2 inches below the subgrade surface.
P3	4 inch	0	0	9	P3 measures vertical pressure at 3 inches below the base surface at the center of the load.
P4	4 inch	0	8	9	P4 measures vertical pressure at 3 inches below the base surface and 8 inches from the center of the load.
P5	4 inch	0	0	14	P2 measures vertical pressure at 2 inches below the subgrade surface and 8 inches from the center.
P6	N/A	N/A	N/A	N/A	N/A
P7	N/A	N/A	N/A	N/A	N/A
P21	1 inch	0	-8	9	P21 measures horizontal pressure at 3 inches above the subgrade surface and 8 inches from the center of the load.
P22	1 inch	8	0	9	P22 measures horizontal pressure at 3 inches above the subgrade surface and 8 inches from the center of the load.

Strain Gauge	X Coordinate (in)	Y Coordinate (in)	Z Coordinate (in)	Comments
S1 (ACSG)	0	0	6	Strain at the centerline of the load and at the bottom of the asphalt layer.

LVDT ID	X Coordinate (in)	Y Coordinate (in)	Z Coordinate (in)	Comments
LVDT 1	0	6	0	At the pavement surface and 6 inches from the centerline of the load. Note: because of the plate configuration, the measurement is considered to be at the centerline of the load
LVDT 2	0	12	0	At the pavement surface and 12 inches from the centerline of the load.
LVDT 3	0	24	0	At the pavement surface and 24 inches from the centerline of the load.
LVDT 4	0	36	0	At the pavement surface and 36 inches from the centerline of the load.
LVDT 5	0	48	0	On top of the Large-Scale Tank rim.
LVDT 6	-7.5	0	6	At 7.5 inches from the centerline of the load (in negative X-direction), measuring base deflection.

Accelerometer	Accelerometer ID	X Coordinate (in)	Y Coordinate (in)	Z Coordinate (in)	Comments
A1	A1_Z	0	6	0	At the pavement surface and 6 inches from the centerline of the load. Note: because of the plate configuration, the measurement is considered to be at the centerline of the load.
A2	A2_Z	0	12	0	At the pavement surface and 12 inches from the centerline of the load.
A3	A3_Z	0	24	0	At the pavement surface and 24 inches from the centerline of the load.
M1	M1_Y	0	0	12	On top of the subgrade and at the centerline of the load. Measurement is in Y-direction.
M1	M1_Z	0	0	12	On top of the subgrade and at the centerline of the load. Measurement is in Z-direction.
M2	M2_Y	0	12	12	On top of the subgrade and 12 inches from the centerline of the load. Measurement is in Y-direction.
M2	M2_Z	0	12	12	On top of the subgrade and 12 inches from the centerline of the load. Measurement is in Z-direction.
M3	M3_Y	0	24	12	On top of the subgrade and 24 inches from the centerline of the load. Measurement is in Y-direction.
M3	M3_Z	0	24	12	On top of the subgrade and 24 inches from the centerline of the load. Measurement is in Z-direction.
M4	M4_Y	0	36	12	On top of the subgrade and 24 inches from the centerline of the load. Measurement is in Y-direction.
M4	M4_Z	0	36	12	On top of the subgrade and 24 inches from the centerline of the load. Measurement is in Z-direction.

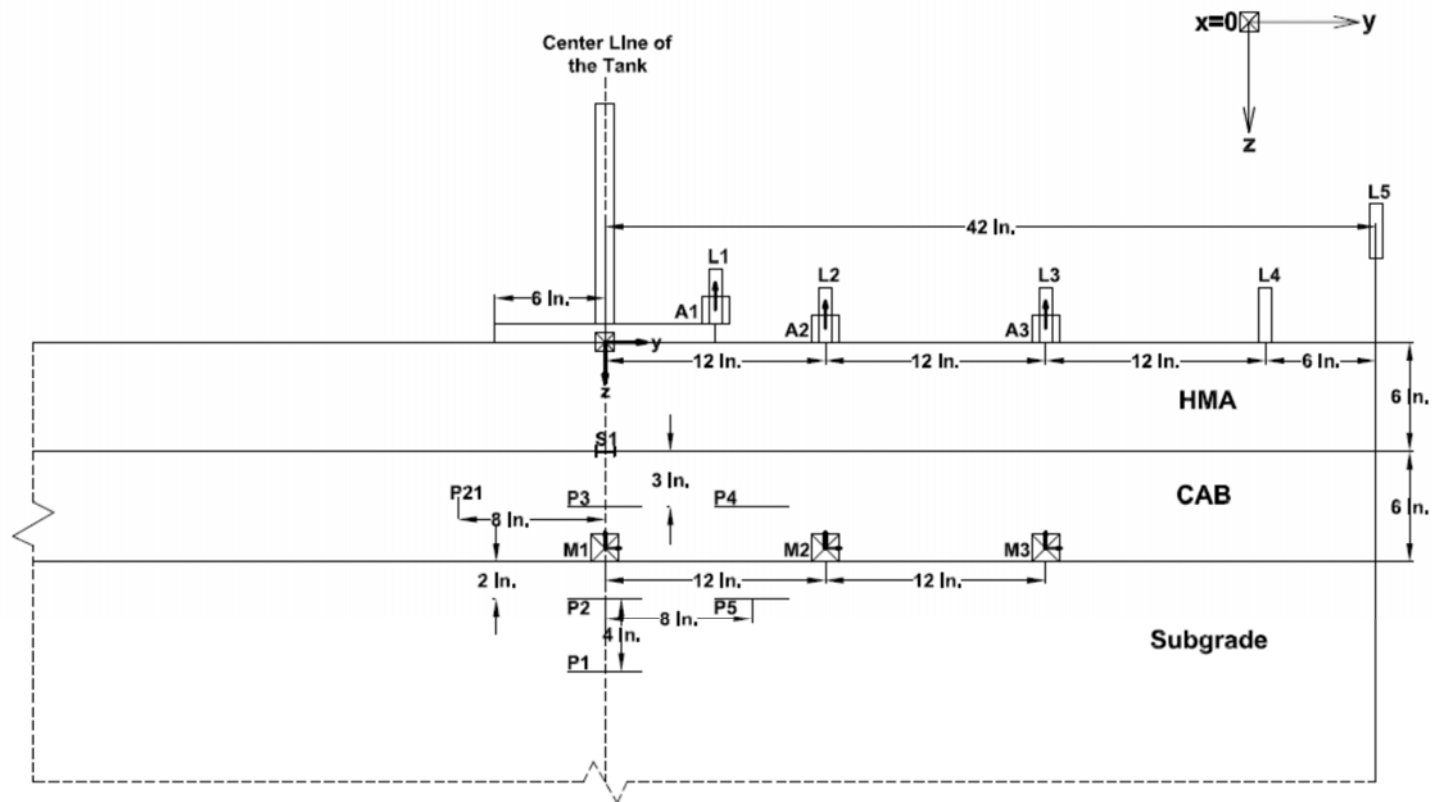


Figure E1-1. Instrumentation plan for experiment No. 1—Profile view, $X = 0$ inch

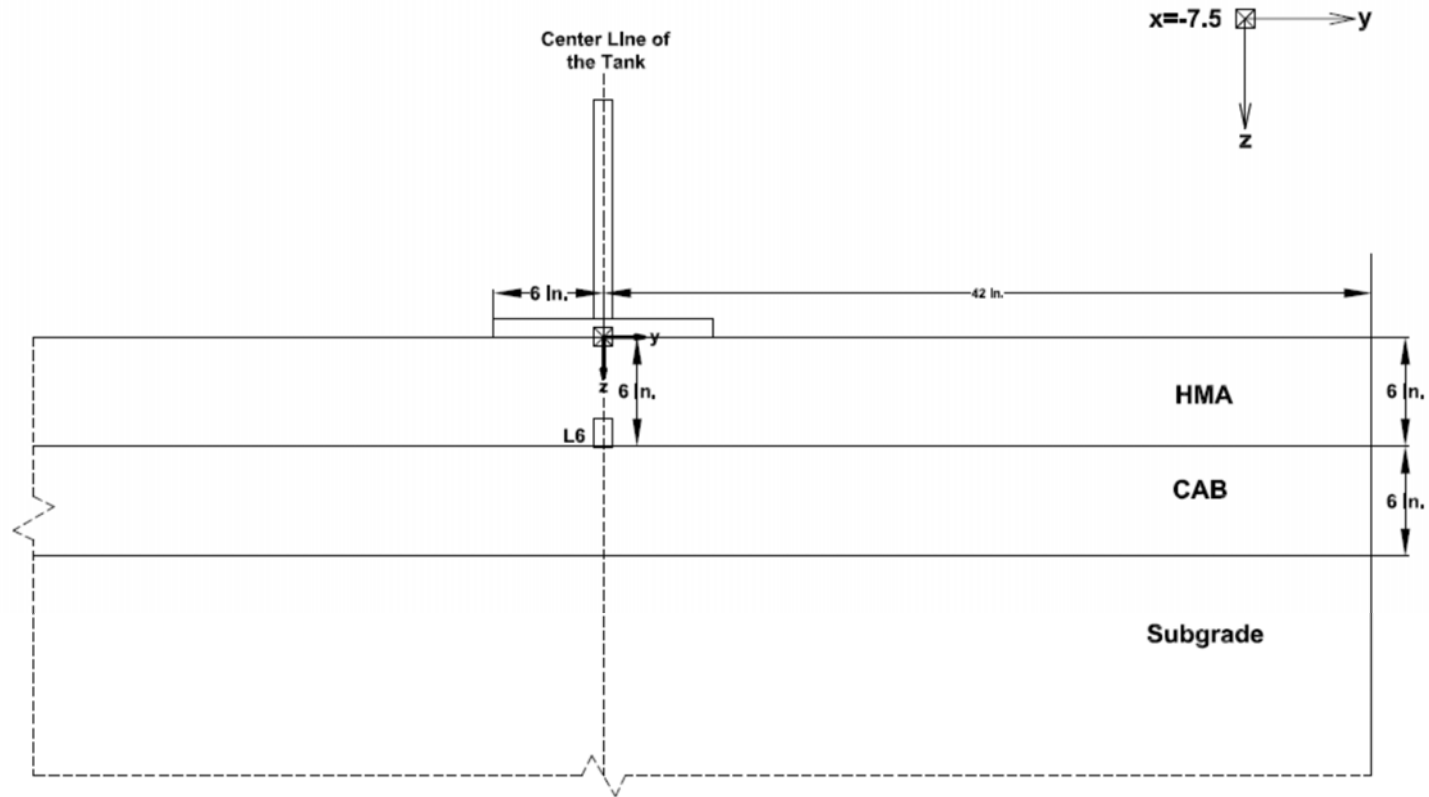


Figure E1-2. Instrumentation plan for experiment No. 1—Profile view, $X = -7.5$ inches

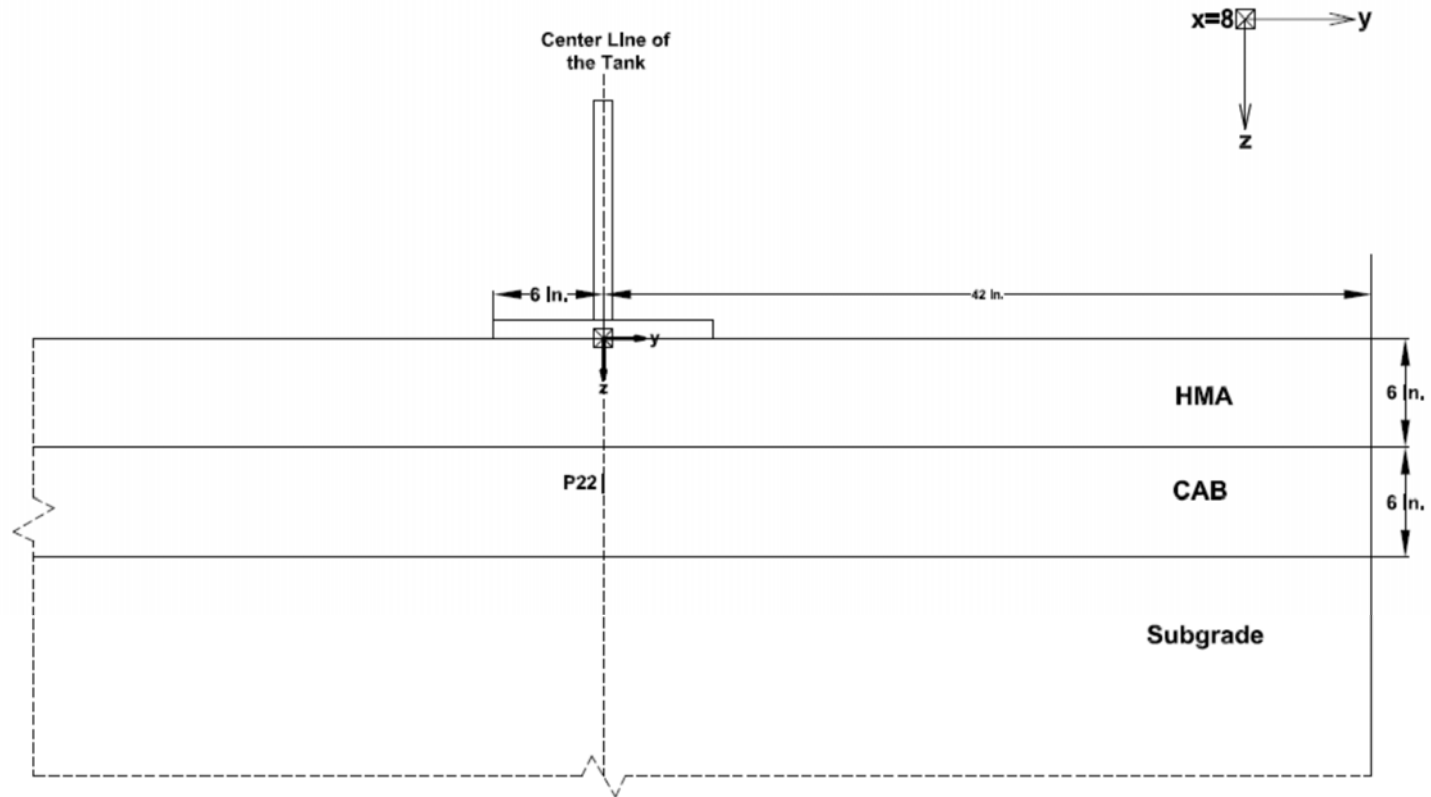


Figure E1-3. Instrumentation plan for experiment No. 1—Profile view, X = 8 inches

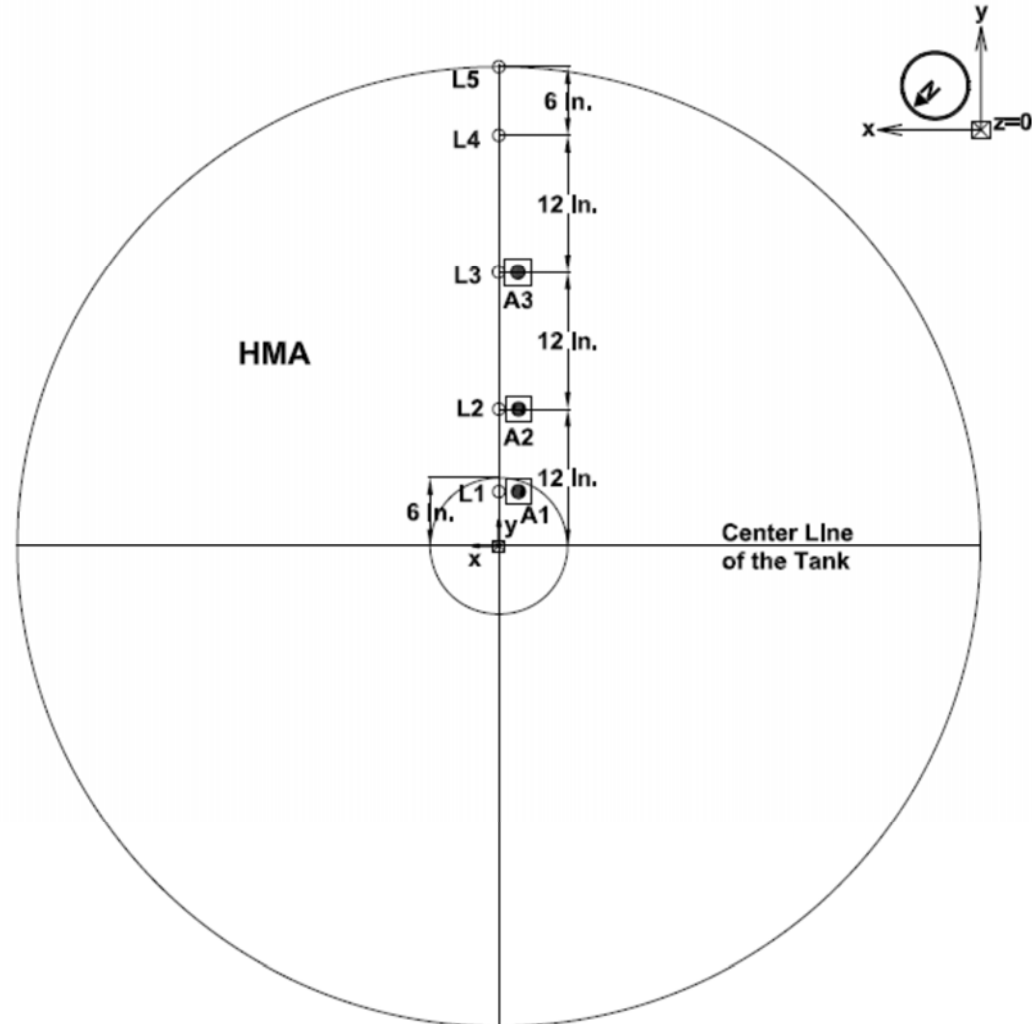


Figure E1-4. Instrumentation plan for experiment No. 1—Plan view, $Z = 0$ inch



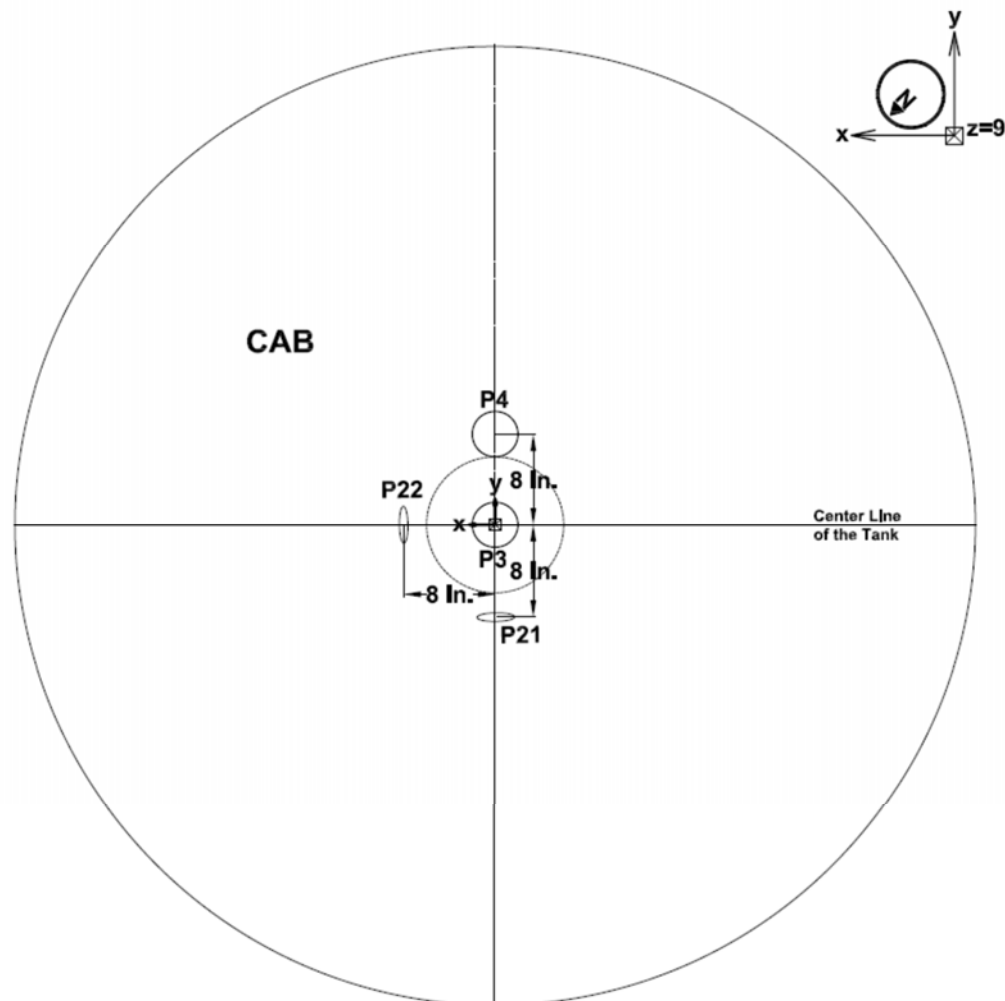


Figure E1-6. Instrumentation plan for experiment No. 1—Plan view, Z = 9 inches

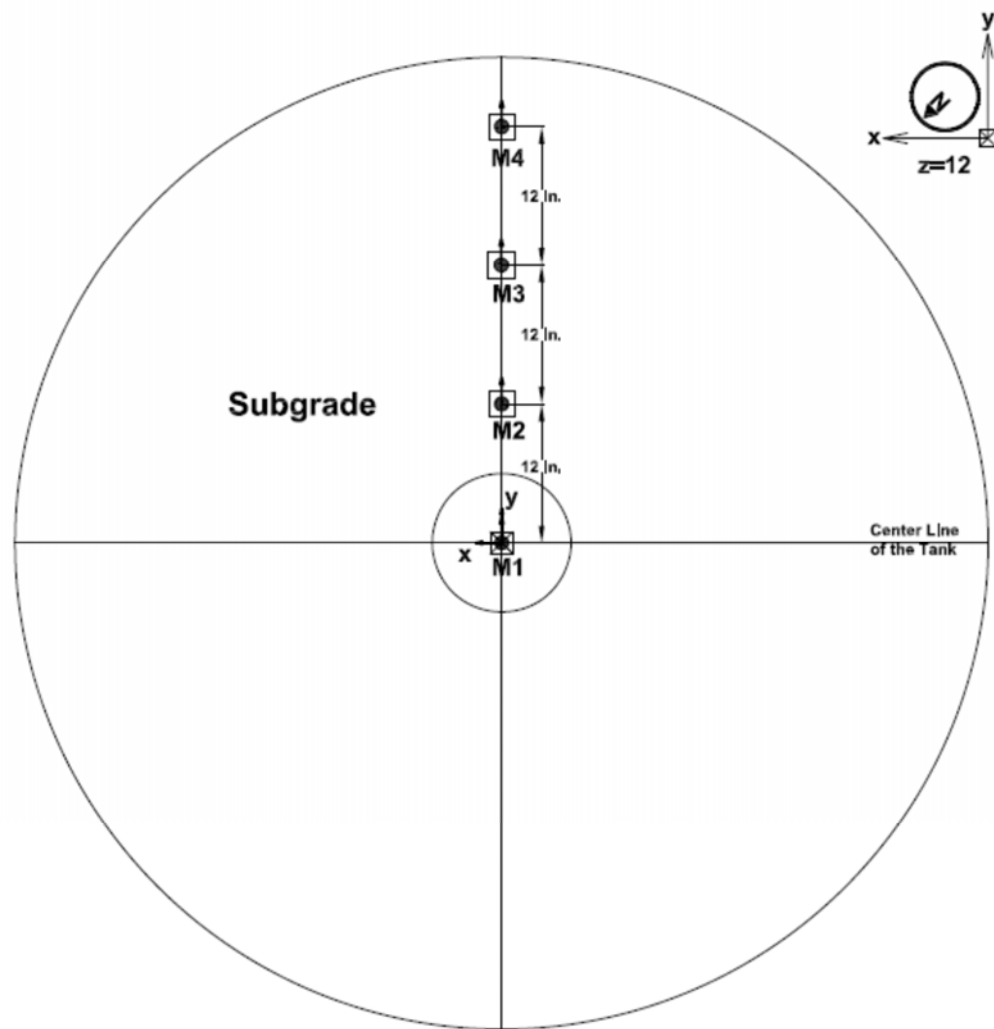


Figure E1-7. Instrumentation plan for experiment No. 1—Plan view, $Z = 12$ inches

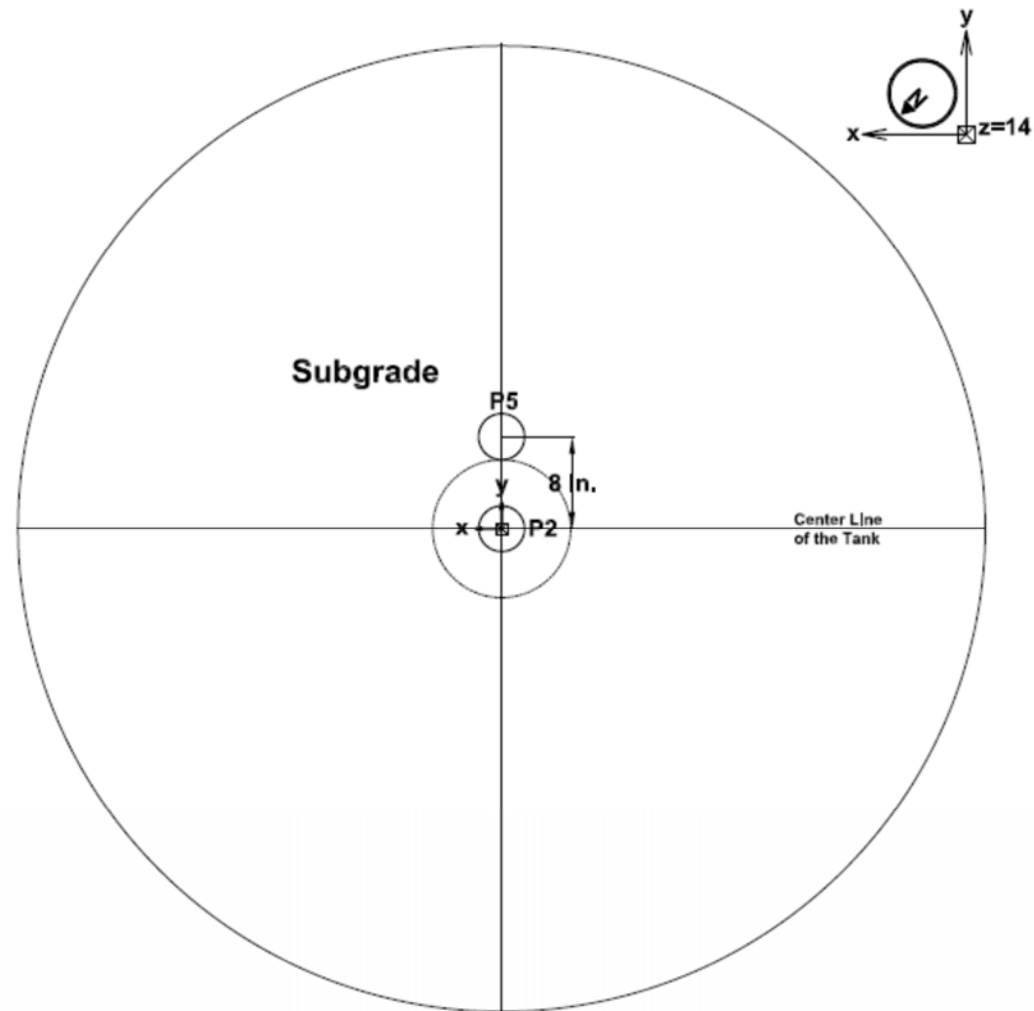


Figure E1-8. Instrumentation plan for experiment No. 1—Plan view, $Z = 14$ inches

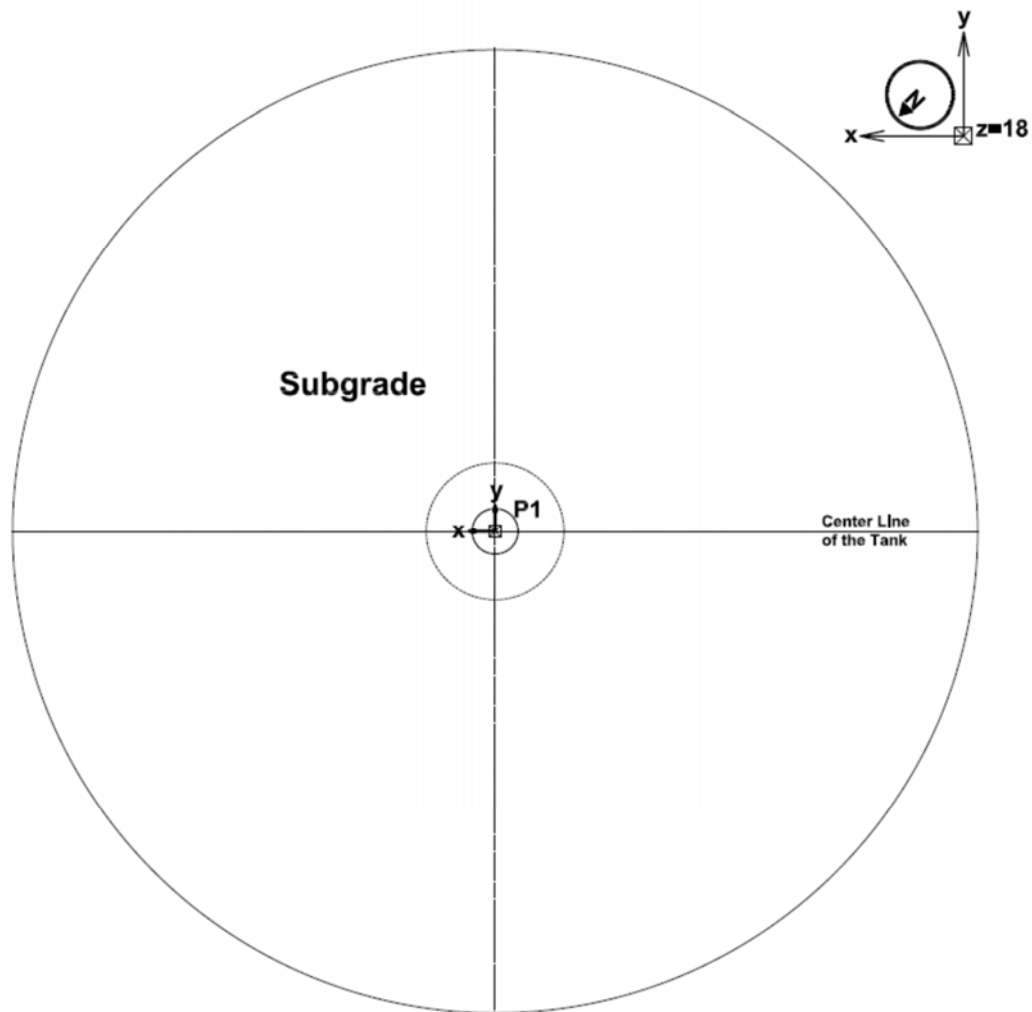


Figure E1-9. Instrumentation plan for experiment No. 1—Profile view, $Z = 18$ inches

Appendix E2. Experiment No. 2 (Control—Thick Base)

Experiment ID	Exp2-AC-Contr-B10
Description	Flexible pavement; no reinforcement; 10-inch aggregate base

Average Asphalt Layer Thickness (inch)	5.6
Asphalt Layer Temperature (°F)	79.5
Average CAB Layer Thickness (inch)	10.00

Pressure Cell ID	Pressure Cell Diameter	X Coordinate (in)	Y Coordinate (in)	Z Coordinate (in)	Comments
P1	4 inch	0	0	22	P1 measures vertical pressure, 6 inches below the subgrade surface.
P2	4 inch	0	0	13.5	P2 measures vertical pressure, 2.5 inches above the subgrade surface.
P3	4 inch	0	0	8.5	P3 measures vertical pressure, 2.5 inches below the base surface.
P4	4 inch	0	8	8.5	P4 measures vertical pressure, 2.5 inches below the base surface and 8 inches from the center of the load.
P5	4 inch	0	-8	8.5	P5 measures horizontal pressure, 2.5 inches below the base surface and 8 inches from the center of the load.
P21	1 inch	0	8	13.5	P21 measures vertical pressure, 2.5 inches above the subgrade surface and 8 inches from the center of the load.
P22	1 inch	8	0	8.5	P22 measures horizontal pressure, 2.5 inches below the base surface and 8 inches from the center of the load.

Strain Gauge	X Coordinate (in)	Y Coordinate (in)	Z Coordinate (in)	Comments
S1	0	0	6	Strain, the centerline of the load and the bottom of the asphalt layer.

LVDT ID	X Coordinate (in)	Y Coordinate (in)	Z Coordinate (in)	Comments
LVDT 1	0	6	0	At the pavement surface and 6 inches from the centerline of the load. Note: because of the plate configuration, the measurement is considered to be the centerline of the load.
LVDT 2	0	12	0	At the pavement surface and 12 inches from the centerline of the load.
LVDT 3	0	24	0	At the pavement surface and 24 inches from the centerline of the load.
LVDT 4	0	36	0	At the pavement surface and 36 inches from the centerline of the load.
LVDT 5	0	48	0	On top of the Large-Scale Tank rim.

Accelerometer	Accelerometer ID	X Coordinate (in)	Y Coordinate (in)	Z Coordinate (in)	Comments
A1	A1_Z	0	6	0	At the pavement surface and 6 inches from the centerline of the load. Note: because of the plate configuration, the measurement is considered to be the centerline of the load.
A2	A2_Z	0	12	0	At the pavement surface and 12 inches from the centerline of the load.

Accelerometer	Accelerometer ID	X Coordinate (in)	Y Coordinate (in)	Z Coordinate (in)	Comments
A3	A3_Z	0	24	0	At the pavement surface and 24 inches from the centerline of the load.
M1	M1_Y	0	0	11	In the middle of the base and is the centerline of the load. Measurement is in Y-direction.
M1	M1_Z	0	0	11	In the middle of the base and is the centerline of the load. Measurement is in Z-direction.
M2	M2_Y	0	12	11	In the middle of the base and 12 inches from the centerline of the load. Measurement is in Y-direction.
M2	M2_Z	0	12	11	In the middle of the base and 12 inches from the centerline of the load. Measurement is in Z-direction.
M3	M3_Y	0	24	11	In the middle of the base and 24 inches from the centerline of the load. Measurement is in Y-direction.
M3	M3_Z	0	24	11	In the middle of the base and 24 inches from the centerline of the load. Measurement is in Z-direction.

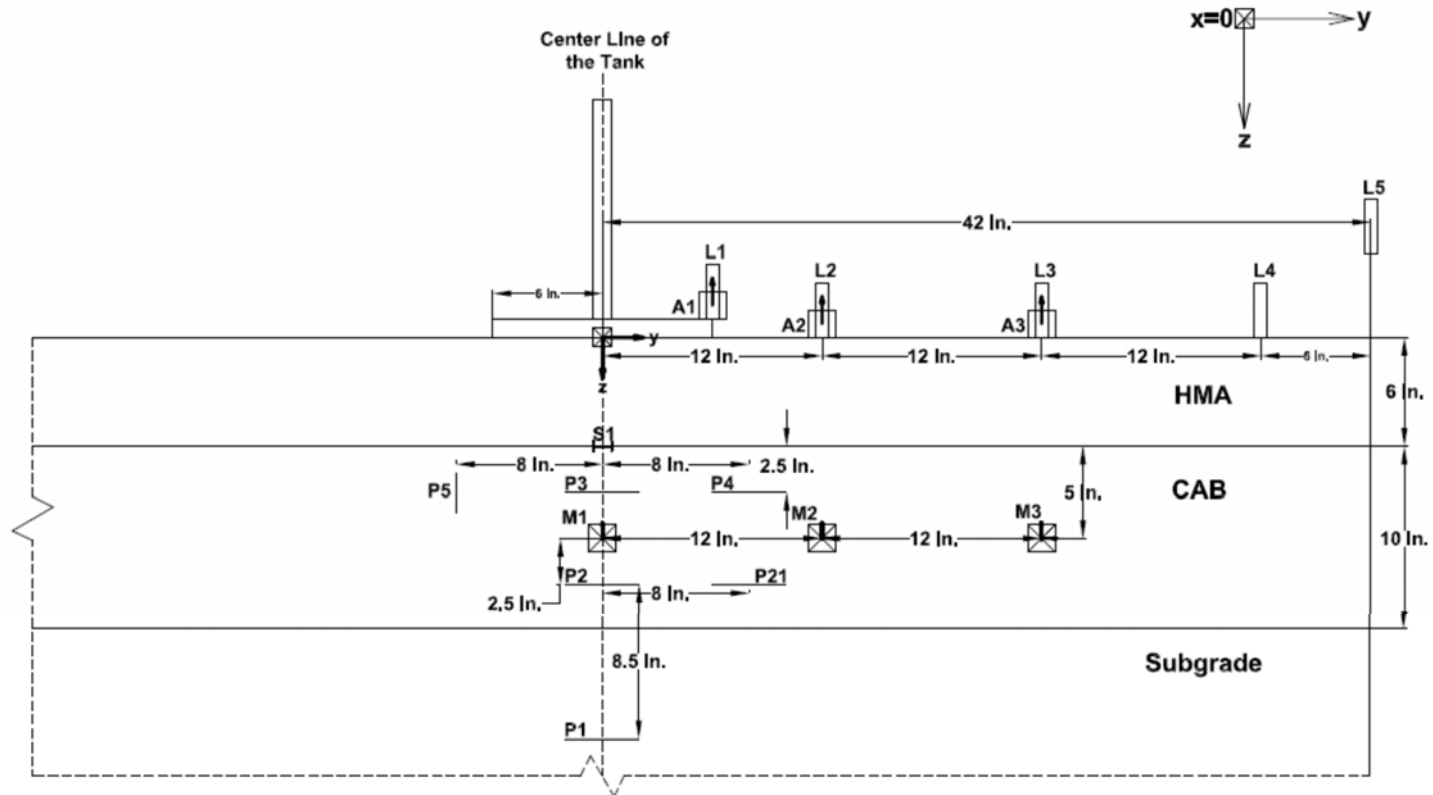


Figure E2-1. Instrumentation plan for experiment No. 2—Profile view, $X = 0$ inch

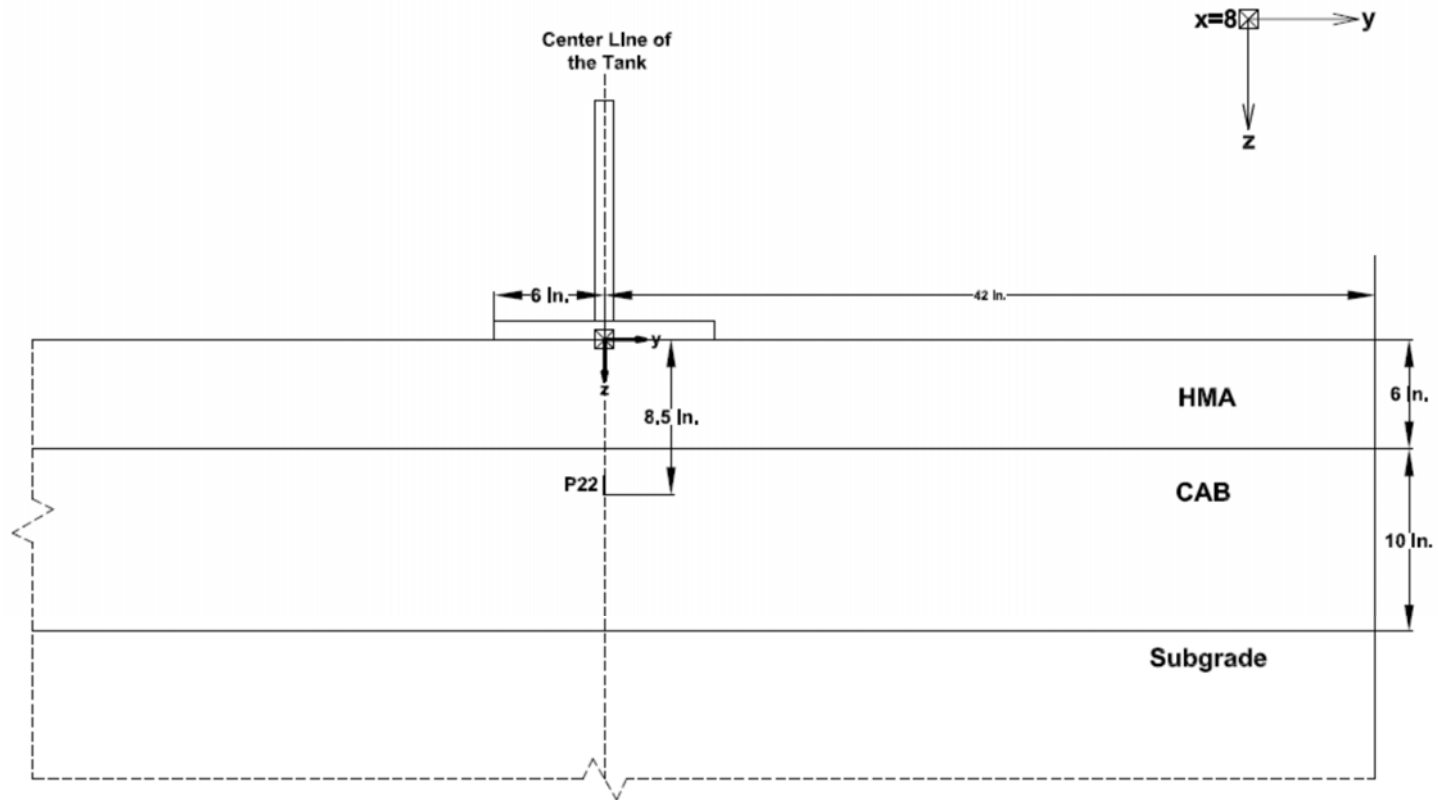


Figure E2-2. Instrumentation plan for experiment No. 2—Profile view, X = 8 inches

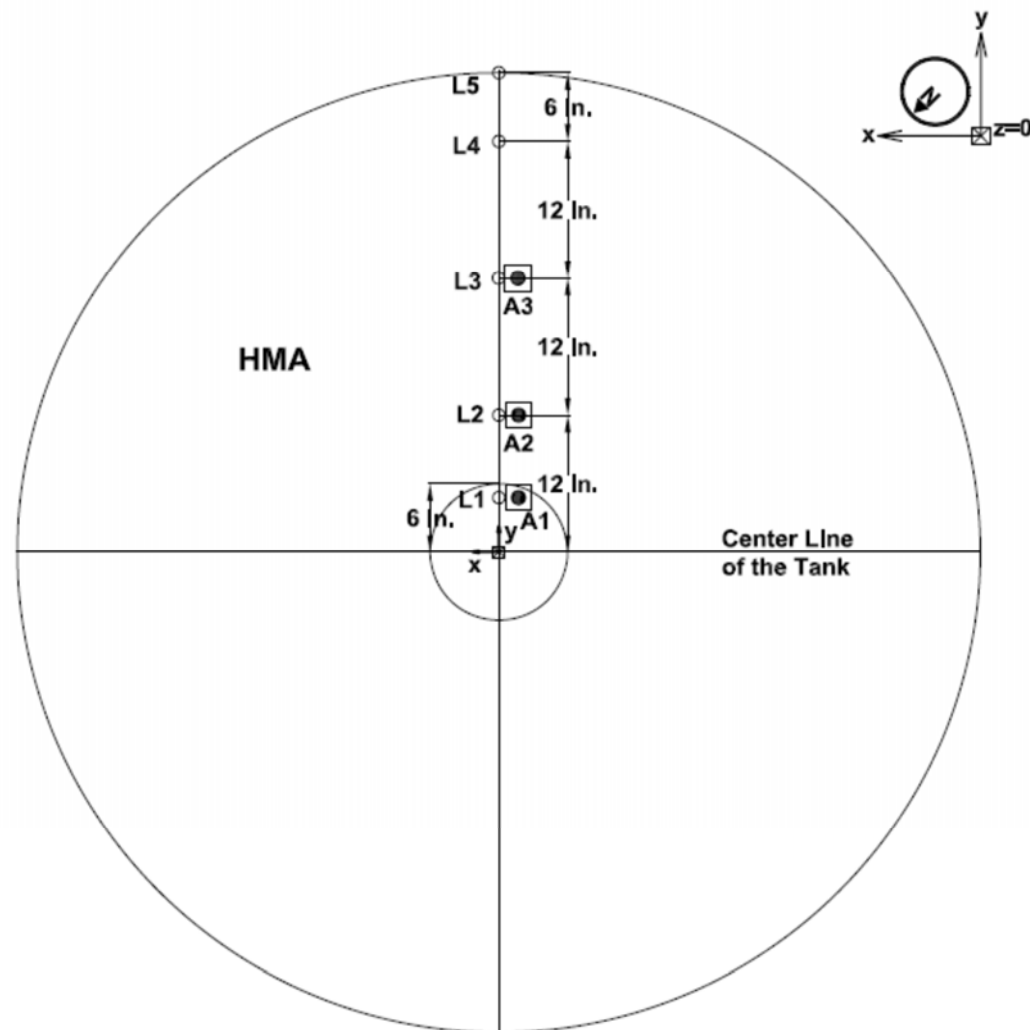


Figure E2-3. Instrumentation plan for experiment No. 2—Plan view, $Z = 0$ inch

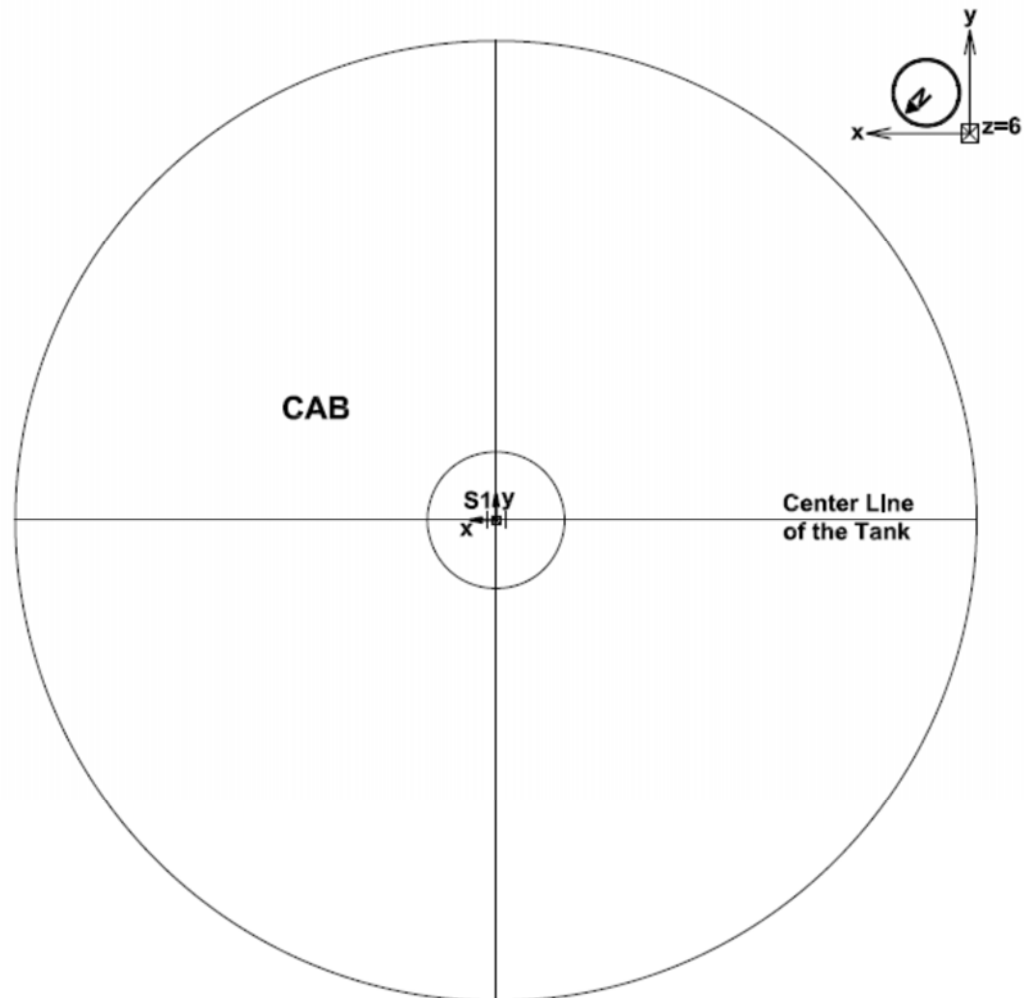


Figure E2-4. Instrumentation plan for experiment No. 2—Plan view, Z = 6 inches

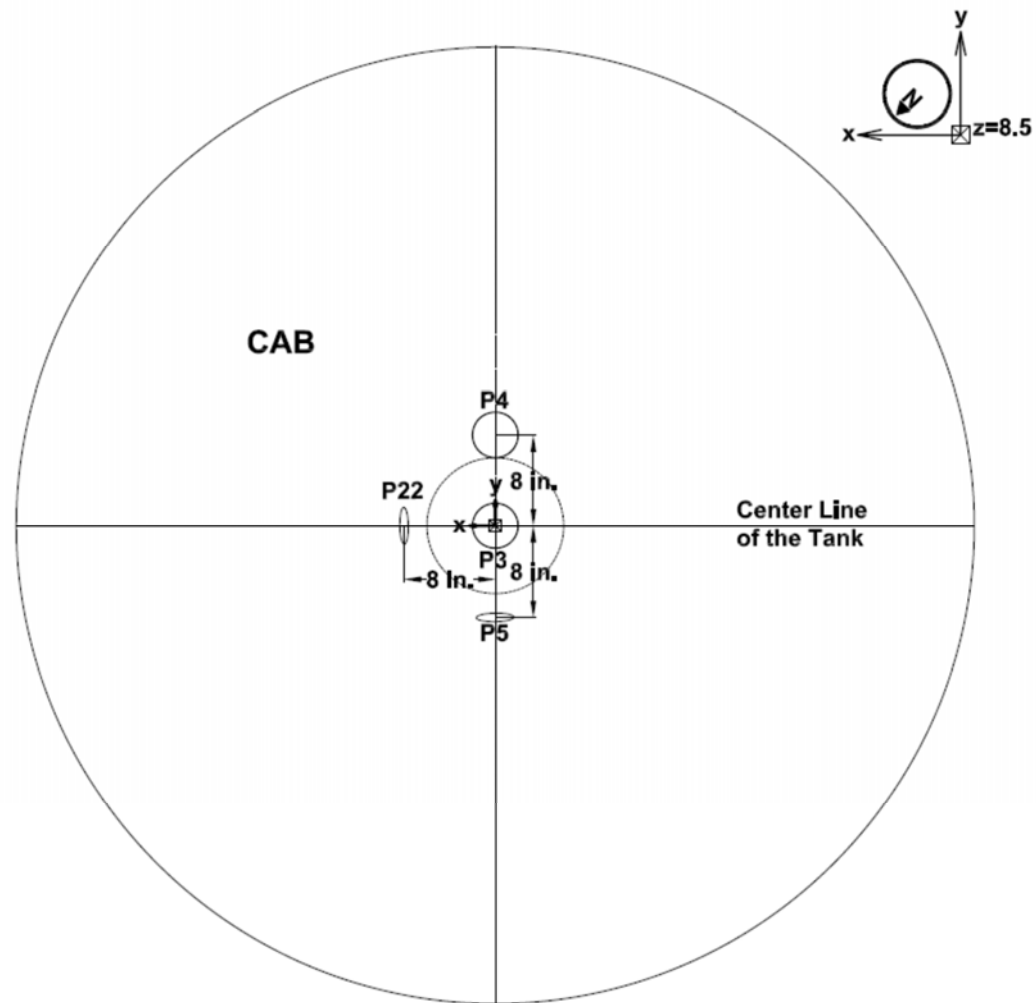


Figure E2-5. Instrumentation plan for experiment No. 2—Plan view, $Z = 8.5$ inches

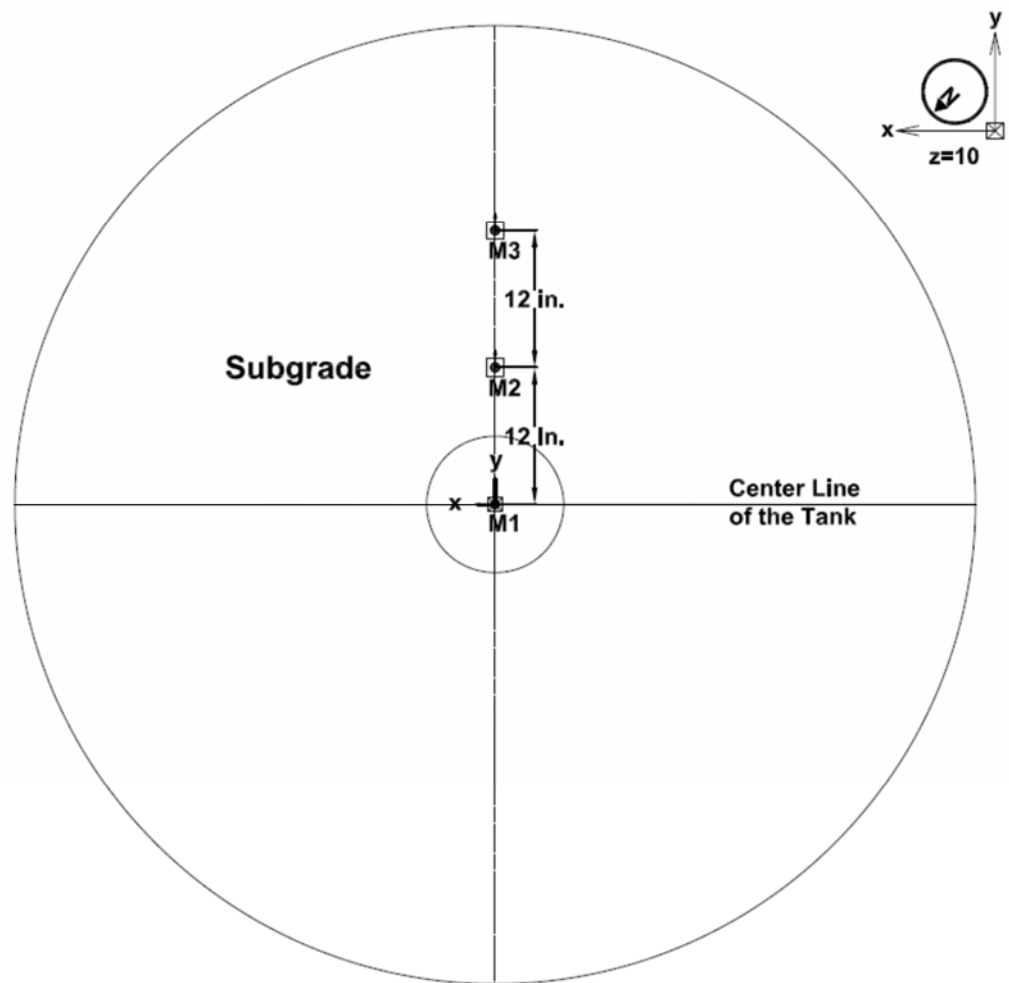


Figure E2-6. Instrumentation plan for experiment No. 2—Plan view, $Z = 10$ inches

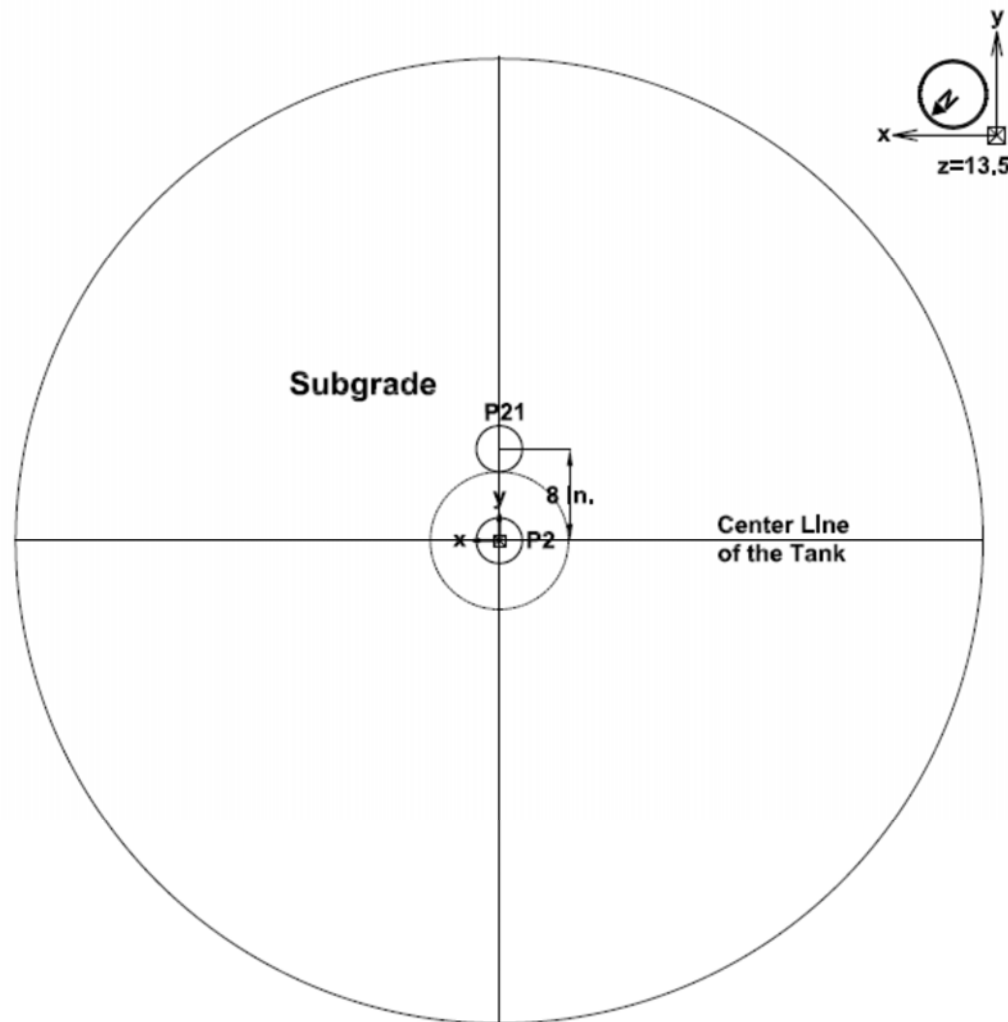


Figure E2-7. Instrumentation plan for experiment No. 2—Plan view, $Z = 13.5$ inches

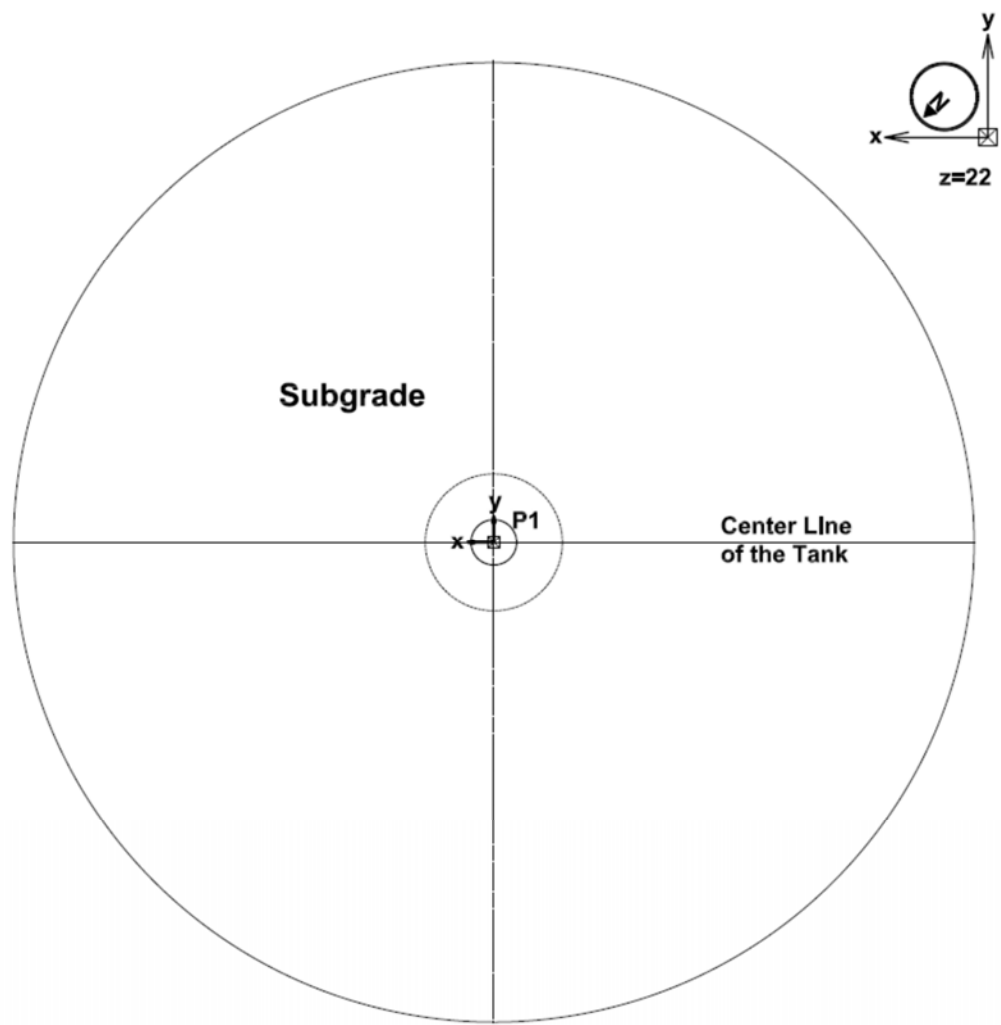


Figure E2-8. Instrumentation plan for experiment No. 2—Profile view, Z = 22 inches

Appendix E3. Experiment No. 3 (Geogrid—Thin Base)

Experiment ID	Exp3-AC-Grid-B06
Description	Flexible pavement; geogrid reinforcement, 6-inch aggregate base

Average Asphalt Layer Thickness (inch)	5.7
Asphalt Layer Temperature (°F)	79.5
Average CAB Layer Thickness (inch)	6.00

Pressure Cell ID	Pressure Cell Diameter	X Coordinate (in)	Y Coordinate (in)	Z Coordinate (in)	Comments
P1	4 inch	0	0	18	P1 measures vertical pressure at 6 inches below the subgrade surface.
P2	4 inch	0	0	14	P2 measures vertical pressure at 2 inches below the subgrade surface.
P3	4 inch	0	0	9	P3 measures vertical pressure at 3 inches below the base surface at the center of the load.
P4	4 inch	0	8	9	P4 measures vertical pressure at 3 inches below the base surface and 8 inches from the center of the load.
P5	4 inch	0	0	14	P2 measures vertical pressure at 2 inches below the subgrade surface and 8 inches from the center.
P6	N/A	N/A	N/A	N/A	N/A
P7	N/A	N/A	N/A	N/A	N/A
P21	1 inch	0	-8	9	P21 measures horizontal pressure at 3 inches above the subgrade surface and 8 inches from the center of the load.
P22	1 inch	8	0	9	P22 measures horizontal pressure at 3 inches above the subgrade surface and 8 inches from the center of the load.

LVDT ID	X Coordinate (in)	Y Coordinate (in)	Z Coordinate (in)	Comments
LVDT 1	0	6	0	At the pavement surface and 6 inches from the centerline of the load. Note: because of the plate configuration, the measurement is considered to be at the centerline of the load.
LVDT 2	0	12	0	At the pavement surface and 12 inches from the centerline of the load.
LVDT 3	0	24	0	At the pavement surface and 24 inches from the centerline of the load.
LVDT 4	0	36	0	At the pavement surface and 36 inches from the centerline of the load.
LVDT 5	0	48	0	On top of the Large-Scale Tank rim.
LVDT 6	-7.5	0	6	At 7.5 inches from the centerline of the load (in negative X-direction), measuring base deflection.

Strain Gauge	X Coordinate (in)	Y Coordinate (in)	Z Coordinate (in)	Comments
S1	0	0	6	Strain at the centerline of the load and at the bottom of the asphalt layer.
SG1-X	0	0	12	Strain on geogrid.
SG1-Y	0	0	12	Strain on geogrid.
SG2-X	0	12	12	Strain on geogrid.
SG2-Y	0	12	12	Strain on geogrid.
SG3-X	0	24	12	Strain on geogrid.
SG3-Y	0	24	12	Strain on geogrid.

Accelerometer	Accelerometer ID	X Coordinate (in)	Y Coordinate (in)	Z Coordinate (in)	Comments
A1	A1_Z	0	6	0	At the pavement surface and 6 inches from the centerline of the load. Note: because of the plate configuration, the measurement is considered to be at the centerline of the load.
A2	A2_Z	0	12	0	At the pavement surface and 12 inches from the centerline of the load.
A3	A3_Z	0	24	0	At the pavement surface and 24 inches from the centerline of the load.
Msg1	M1_Y	0	0	12	In the subgrade, at the base/SG interface, and at the centerline of the load. Measurement is in Y-direction.
Msg1	M1_Z	0	0	12	In the subgrade, at the base/SG interface, and at the centerline of the load. Measurement is in Z-direction.
Msg2	M2_Y	0	12	12	In the subgrade, at the base/SG interface, and 12 inches from the centerline of the load. Measurement is in Y-direction.
Msg2	M2_Z	0	12	12	In the subgrade, at the base/SG interface, and 12 inches from the centerline of the load. Measurement is in Z-direction.
Msg3	M3_Y	0	24	12	In the subgrade, at the base/SG interface, and 24 inches from the centerline of the load. Measurement is in Y-direction.
Msg3	M3_Z	0	24	12	In the subgrade, at the base/SG interface, and 24 inches from the centerline of the load. Measurement is in Z-direction.
Mgd1	M1_Y	0	0	12	At the centerline of the load. Measurement is in Y-direction. Attached to geogrid.
Mgd1	M1_Z	0	0	12	At the centerline of the load. Measurement is in Z-direction. Attached to geogrid.
Mgd2	M2_Y	0	12	12	12 inches from the centerline of the load. Measurement is in Y-direction. Attached to geogrid.
Mgd2	M2_Z	0	12	12	12 inches from the centerline of the load. Measurement is in Z-direction. Attached to geogrid.
Mgd3	M3_Y	0	24	12	24 inches from the centerline of the load. Measurement is in Y-direction. Attached to geogrid.
Mgd3	M3_Z	0	24	12	24 inches from the centerline of the load. Measurement is in Z-direction. Attached to geogrid.

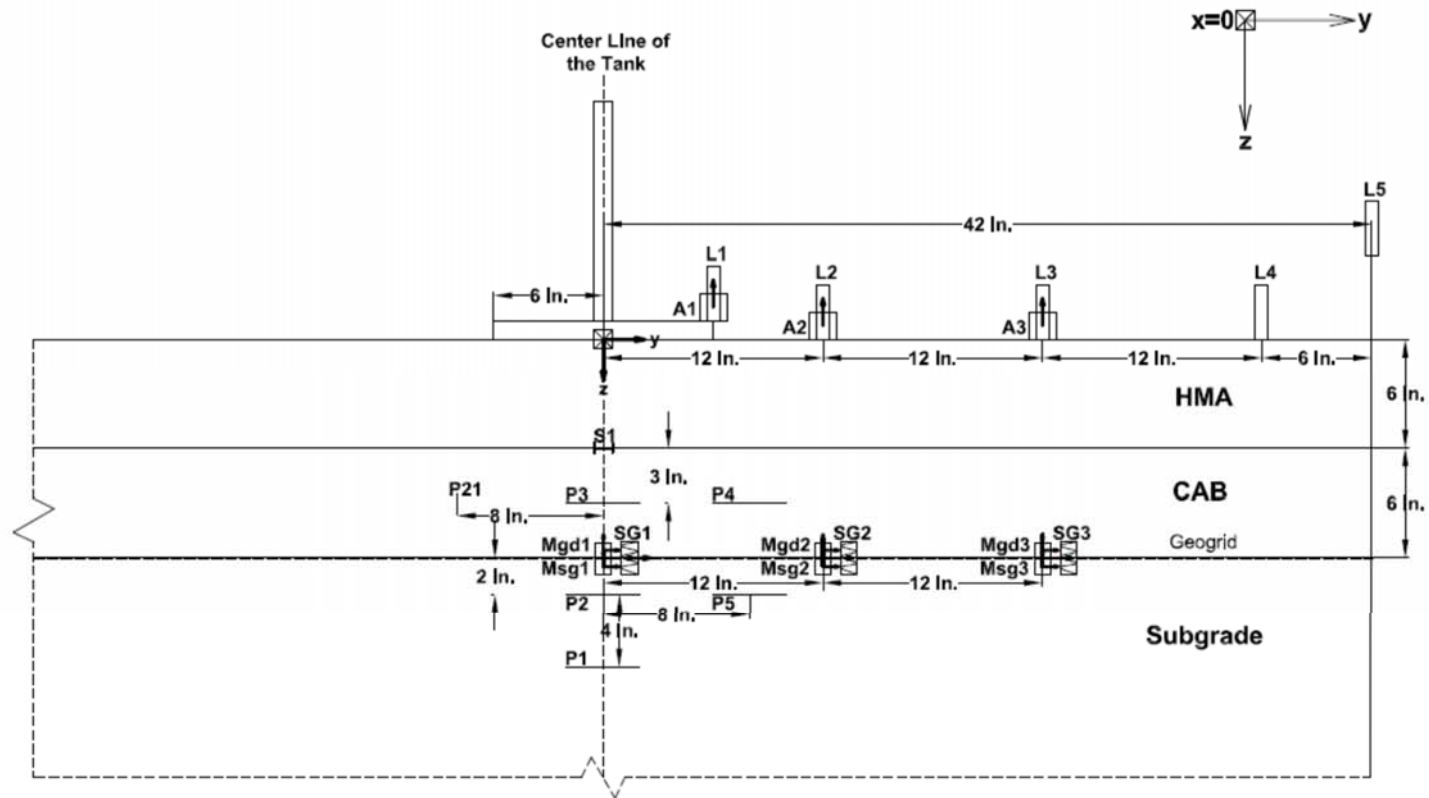


Figure E3-1. Instrumentation plan for experiment No. 3—Profile view, X = 0 inch

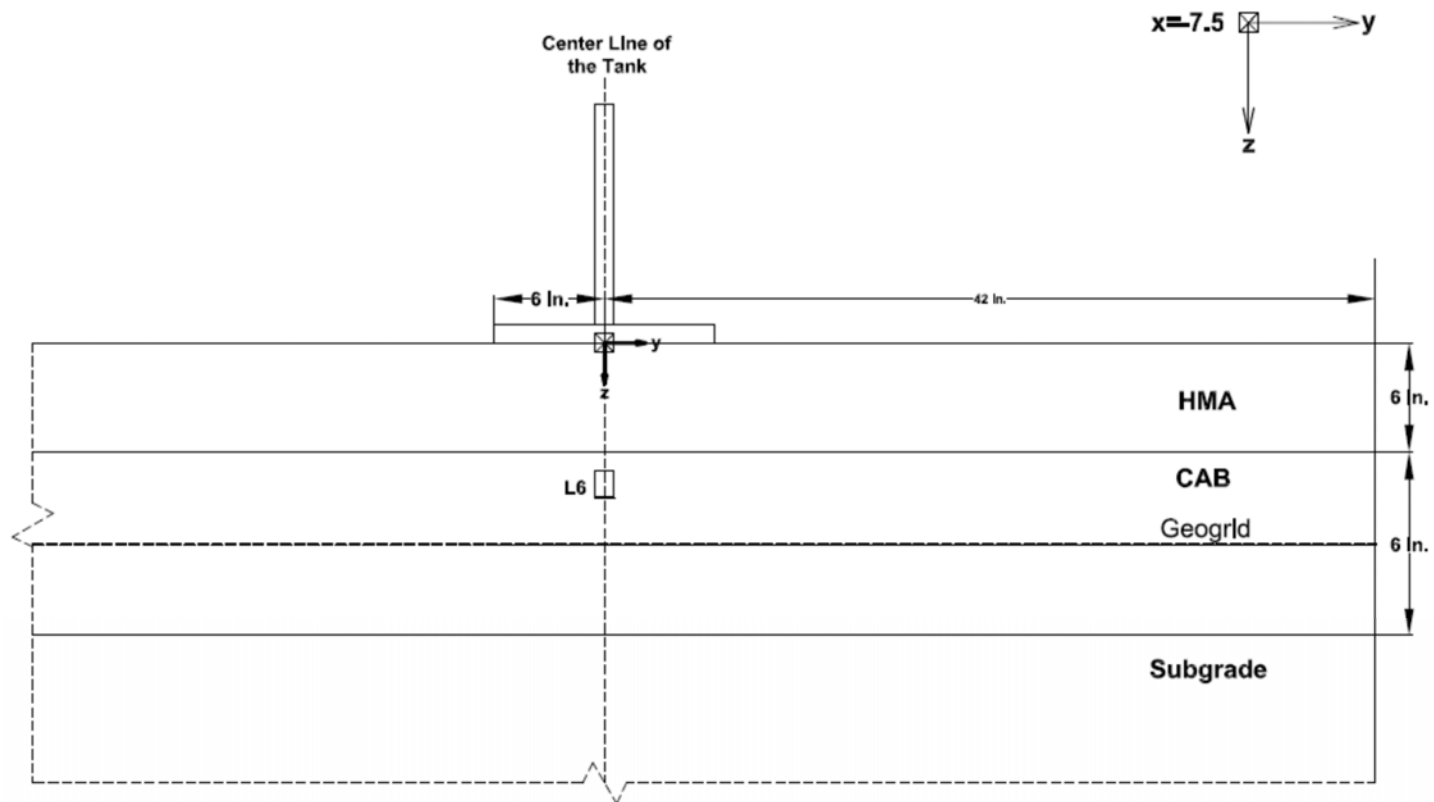


Figure E3-2. Instrumentation plan for experiment No. 3—Profile view, $X = -7.5$ inches

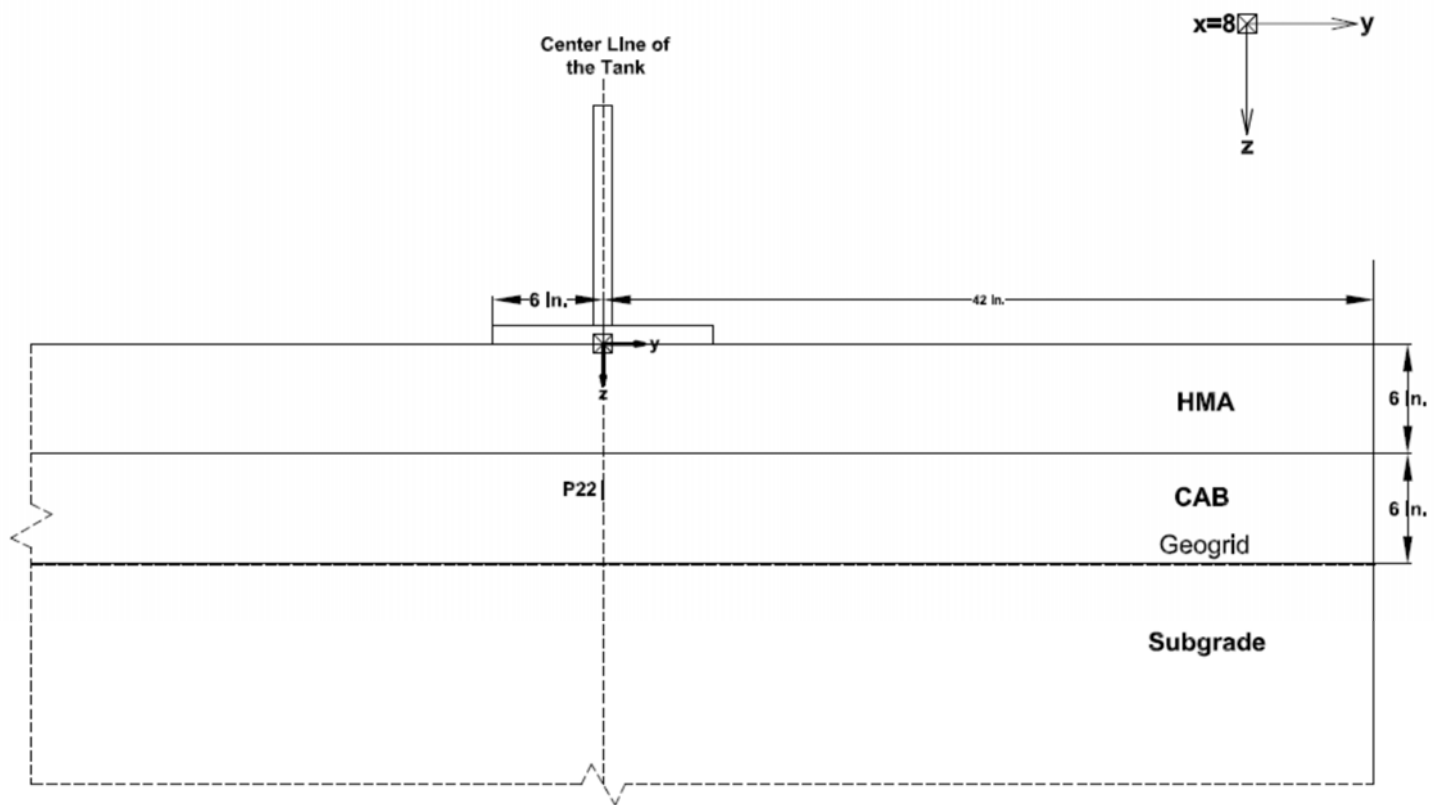


Figure E3-3. Instrumentation plan for experiment No. 3—Profile view, X = 8 inches

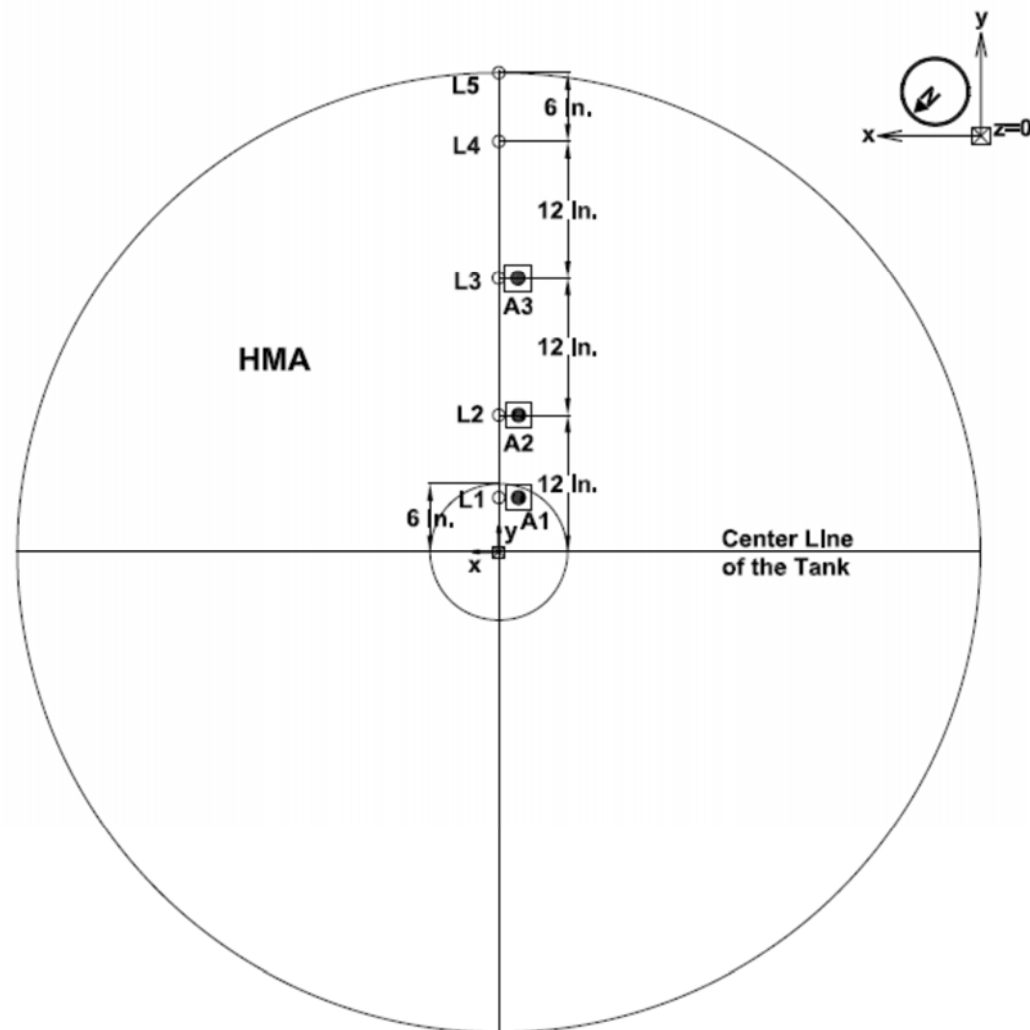


Figure E3-4. Instrumentation plan for experiment No. 3—Plan view, $Z = 0$ inch

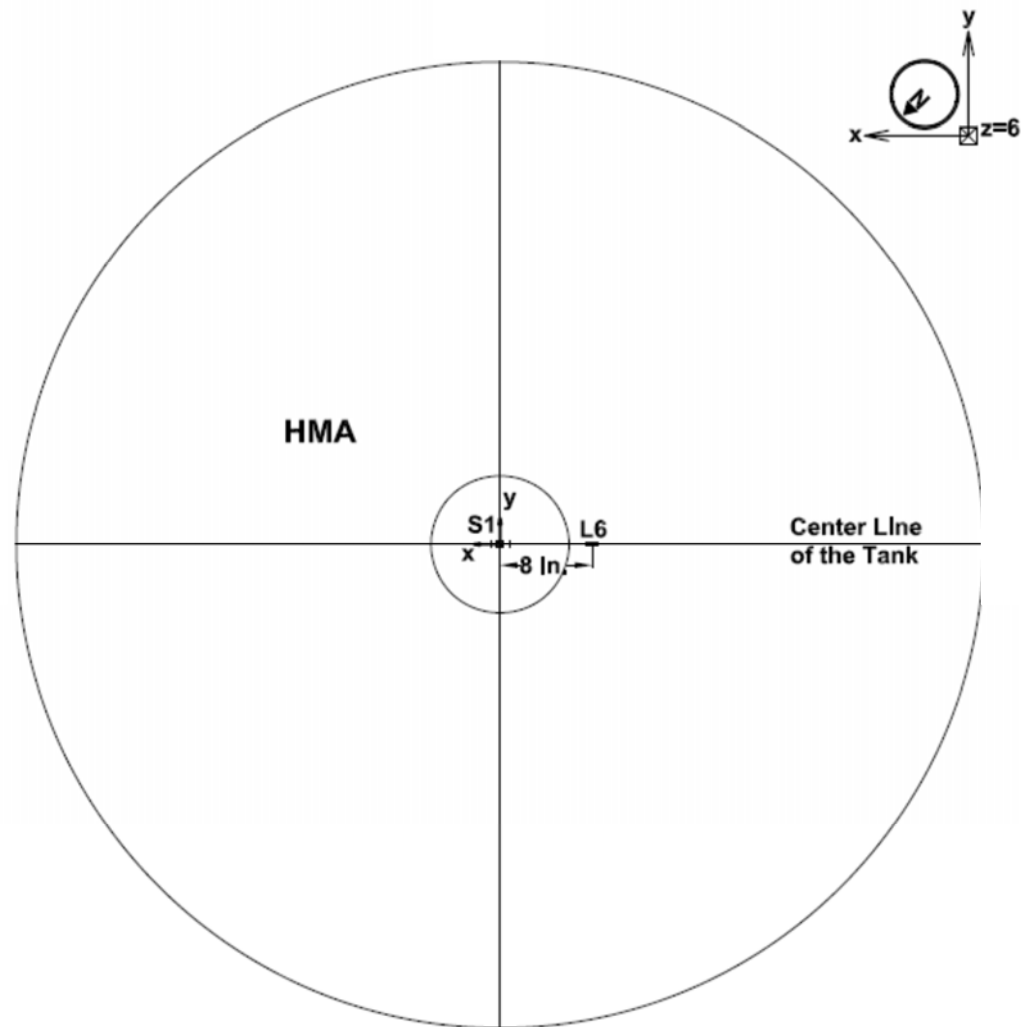


Figure E3-5. Instrumentation plan for experiment No. 3— Plan view, Z = 6 inches

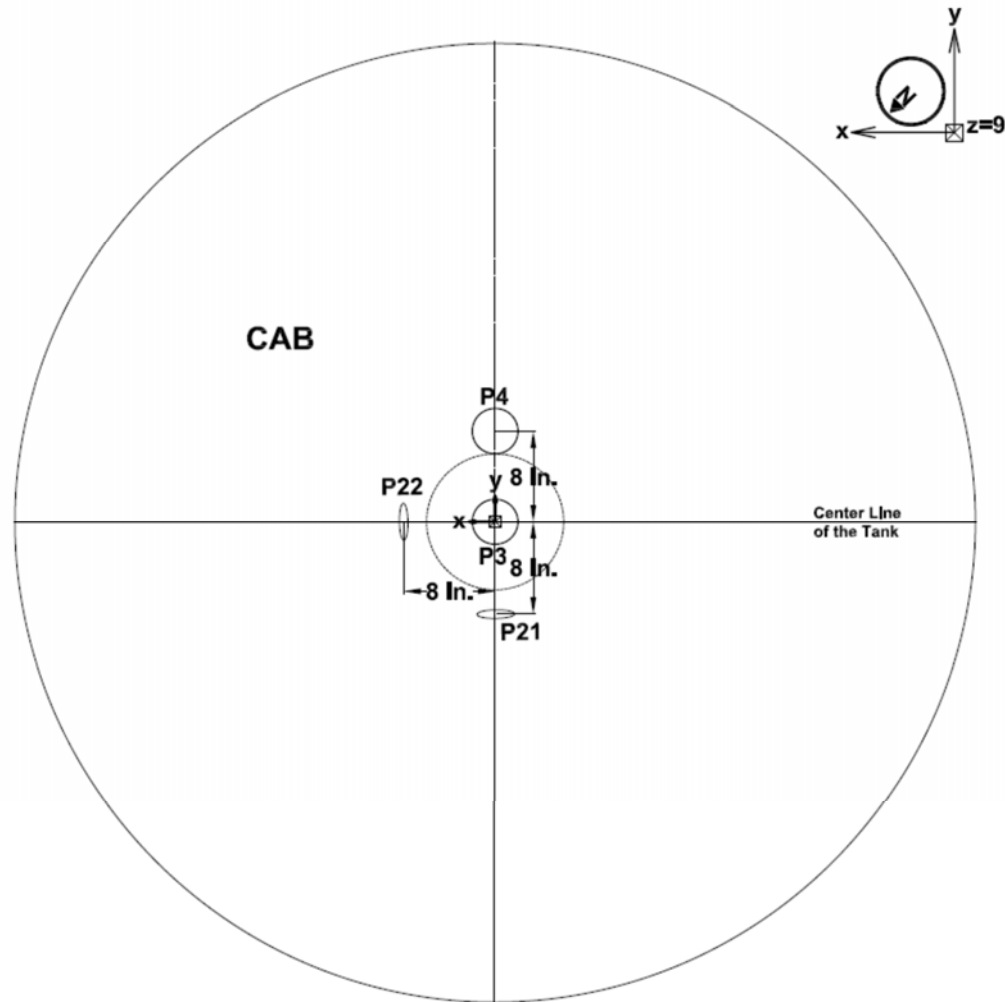


Figure E3-6. Instrumentation plan for experiment No. 3— Plan view, $Z = 9$ inches

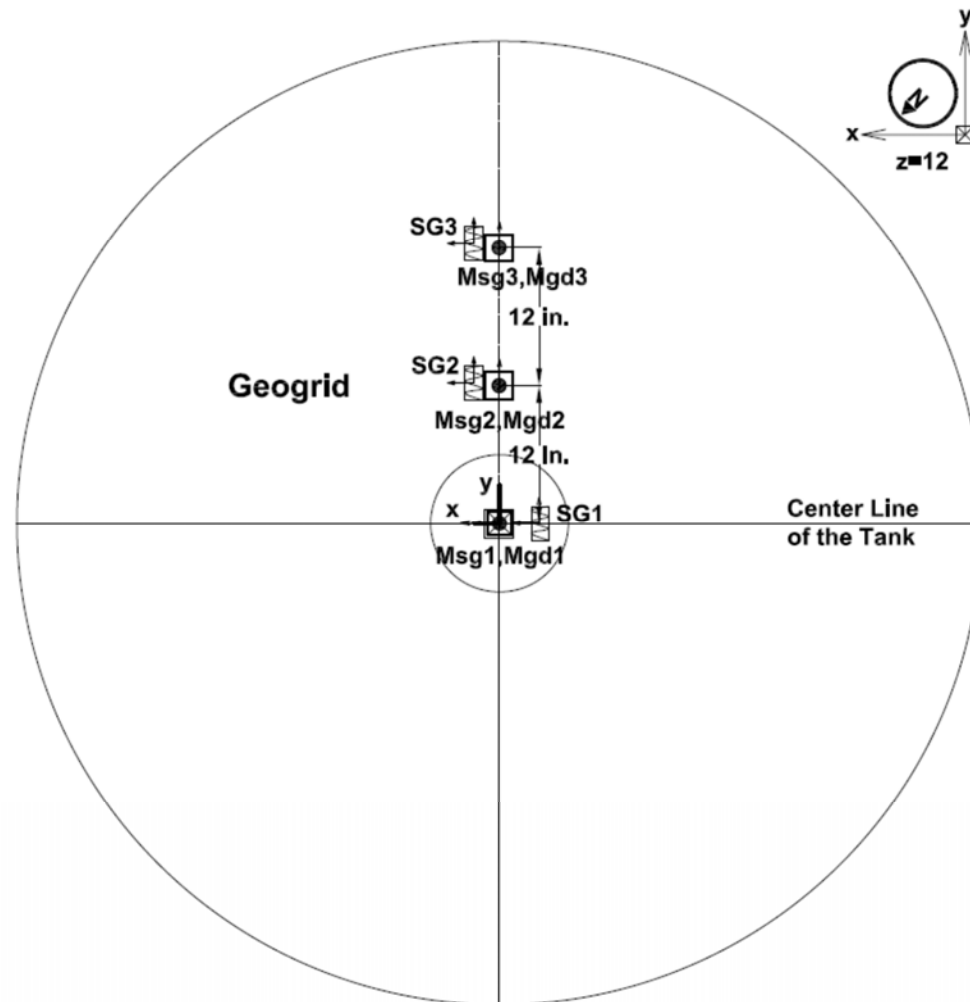


Figure E3-7. Instrumentation plan for experiment No. 3—Plan view, $Z = 12$ inches

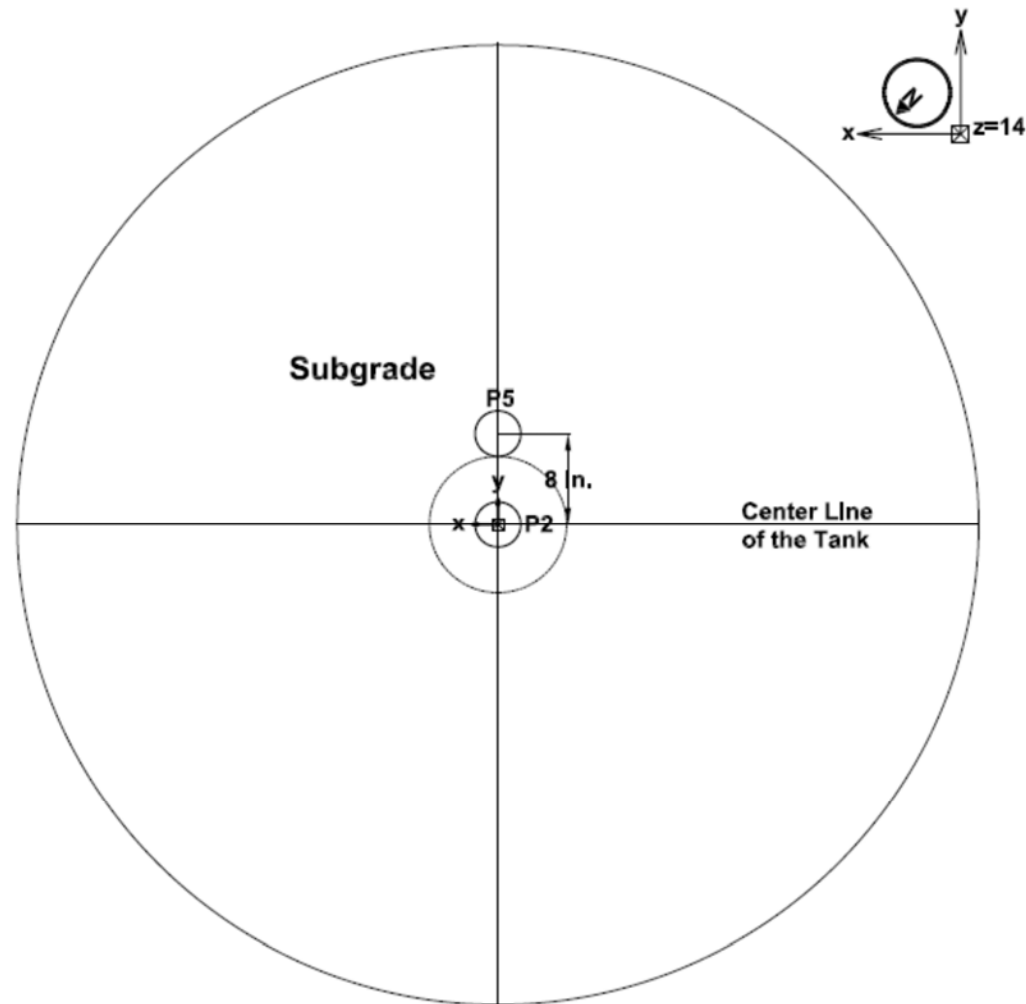


Figure E3-8. Instrumentation plan for experiment No. 3—Plan view, $Z = 14$ inches

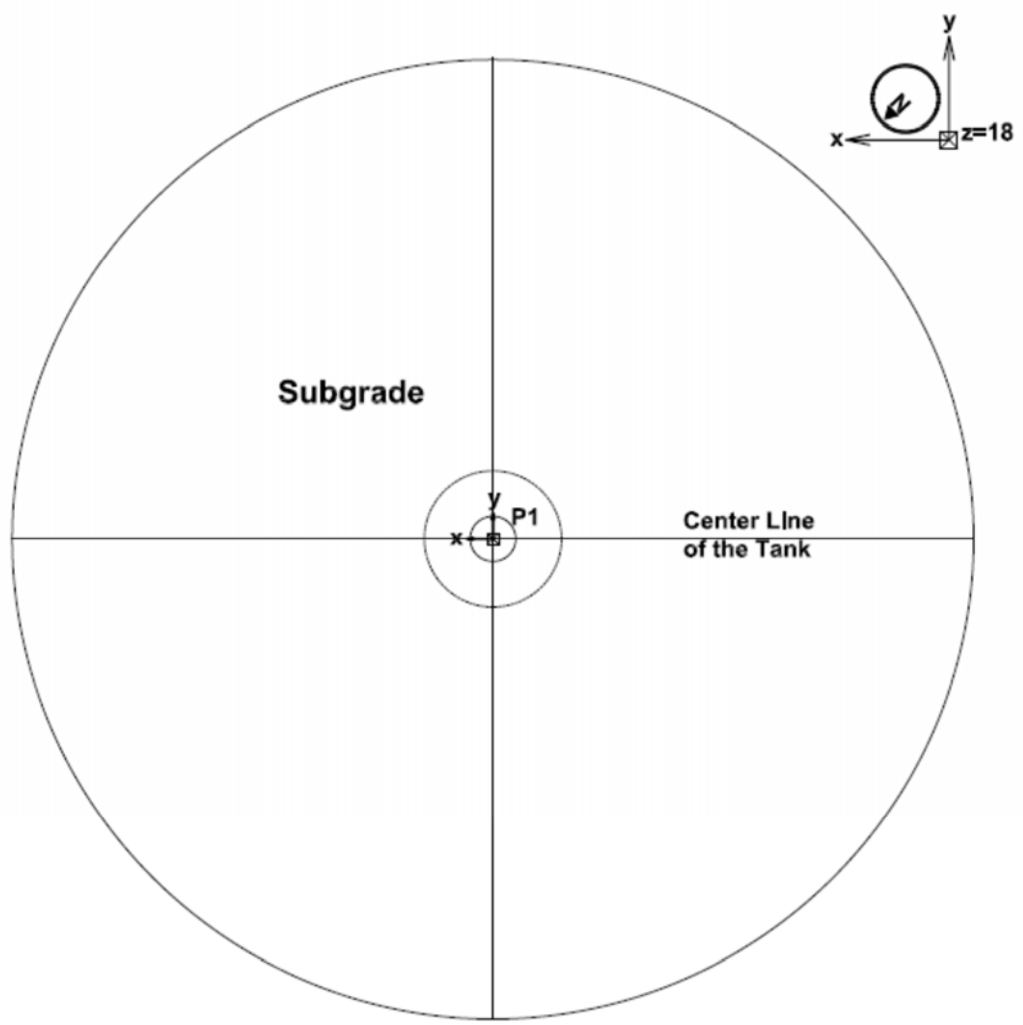


Figure E3-9. Instrumentation plan for experiment No. 3—Profile view, Z = 18 inches

Appendix E4. Experiment No. 4 (Geogrid—Thick Base)

Experiment ID	Exp4-AC-Grid-B10
Description	Flexible pavement; geogrid reinforcement; 10-inch aggregate base

Average Asphalt Layer Thickness (inch)	5.65
Asphalt Layer Temperature (°F)	79.0
Average CAB Layer Thickness (inch)	10.00

Pressure Cell ID	Pressure Cell Diameter	X Coordinate (in)	Y Coordinate (in)	Z Coordinate (in)	Comments
P1	4 inch	0	0	22	P1 measures vertical pressure at 6 inches below the subgrade surface.
P2	4 inch	0	0	18	P2 measures vertical pressure at 2 inches below the subgrade surface.
P3	4 inch	0	0	13.5	P3 measures vertical pressure at 7.5 inches below the base surface.
P4	4 inch	0	8	13.5	P4 measures vertical pressure at 7.5 inches below the base surface and 8 inches from the center of the load in the positive Y-direction.
P5	4 inch	0	8	18	P5 measures vertical pressure at 2 inches below the subgrade surface and 8 inches from the center.
P6	4 inch	0	0	8.5	P6 measures vertical pressure at 2.5 inches below the base surface at the center of the load.
P7	4 inch	0	8	8.5	P7 measures vertical pressure at 2.5 inches below the asphalt surface and 8 inches from the center.
P21	1 inch	0	-8	8.5	P21 measures horizontal pressure at 2.5 inches above the subgrade surface and 8 inches from the center of the load in the negative y-direction.
P22	1 inch	8	0	8.5	P22 measures horizontal pressure at 2.5 inches below the base surface and 8 inches from the center of the load in the positive x-direction.

LVDT ID	X Coordinate (in)	Y Coordinate (in)	Z Coordinate (in)	Comments
LVDT 1	0	6	0	At the pavement surface and 6 inches from the centerline of the load. Note: because of the plate configuration, the measurement is considered to be at the centerline of the load.
LVDT 2	0	12	0	At the pavement surface and 12 inches from the centerline of the load.
LVDT 3	0	24	0	At the pavement surface and 24 inches from the centerline of the load.
LVDT 4	0	36	0	At the pavement surface and 36 inches from the centerline of the load.
LVDT 5	0	48	0	On top of the Large-Scale Tank rim.
LVDT 6	-7.5	0	6	At 7.5 inches from the centerline of the load (in negative X-direction), measuring base deflection.

Strain Gauge	X Coordinate (in)	Y Coordinate (in)	Z Coordinate (in)	Comments
S1	0	0	6	Strain at the centerline of the load and at the bottom of the asphalt layer.
SG1-X	0	0	12	Strain on geogrid.
SG1-Y	0	0	12	Strain on geogrid.
SG2-X	0	12	12	Strain on geogrid.

Strain Gauge	X Coordinate (in)	Y Coordinate (in)	Z Coordinate (in)	Comments
SG2-Y	0	12	12	Strain on geogrid.
SG3-X	0	24	12	Strain on geogrid.
SG3-Y	0	24	12	Strain on geogrid.

Accelerometer	Accelerometer ID	X Coordinate (in)	Y Coordinate (in)	Z Coordinate (in)	Comments
A1	A1_Z	0	6	0	At the pavement surface and 6 inches from the centerline of the load. Note: because of the plate configuration, the measurement is considered to be at the centerline of the load.
A2	A2_Z	0	12	0	At the pavement surface and 12 inches from the centerline of the load.
A3	A3_Z	0	24	0	At the pavement surface and 24 inches from the centerline of the load.
Msg1	M1_Y	0	0	11	In the middle of the base and at the centerline of the load. Measurement is in Y-direction.
Msg1	M1_Z	0	0	11	In the middle of the base and at the centerline of the load. Measurement is in Z-direction.
Msg2	M2_Y	0	12	11	In the middle of the base and 12 inches from the centerline of the load. Measurement is in Y-direction.
Msg2	M2_Z	0	12	11	In the middle of the base and 12 inches from the centerline of the load. Measurement is in Z-direction.
Msg3	M3_Y	0	24	11	In the middle of the base and 24 inches from the centerline of the load. Measurement is in Y-direction.
Msg3	M3_Z	0	24	11	In the middle of the base and 24 inches from the centerline of the load. Measurement is in Z-direction.
Mgd1	M1_Y	0	0	11	In the middle of the base and at the centerline of the load. Measurement is in Y-direction. Attached to geogrid.
Mgd1	M1_Z	0	0	11	In the middle of the base and at the centerline of the load. Measurement is in Z-direction. Attached to geogrid.
Mgd2	M2_Y	0	12	11	In the middle of the base and 12 inches from the centerline of the load. Measurement is in Y-direction. Attached to geogrid.
Mgd2	M2_Z	0	12	11	In the middle of the base and 12 inches from the centerline of the load. Measurement is in Z-direction.
Mgd3	M3_Y	0	24	11	In the middle of the base and 24 inches from the centerline of the load. Measurement is in Y-direction. Attached to geogrid.
Mgd3	M3_Z	0	24	11	In the middle of the base and 24 inches from the centerline of the load. Measurement is in Z-direction. Attached to geogrid.

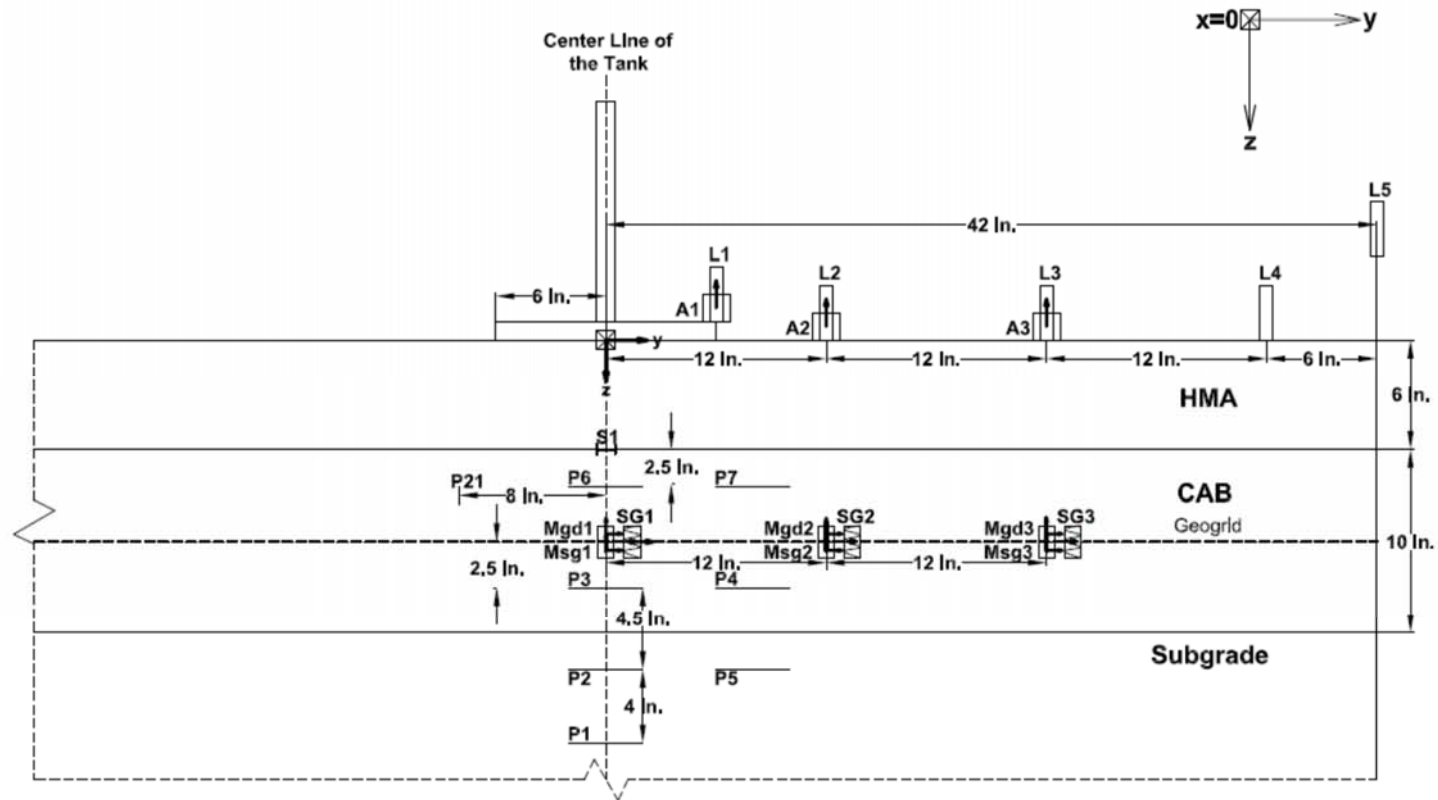


Figure E4-1. Instrumentation plan for experiment No. 4—Profile view at X = 0 inch



Figure E4-2. Instrumentation plan for experiment No. 4—Profile view at X = -7.5 inches

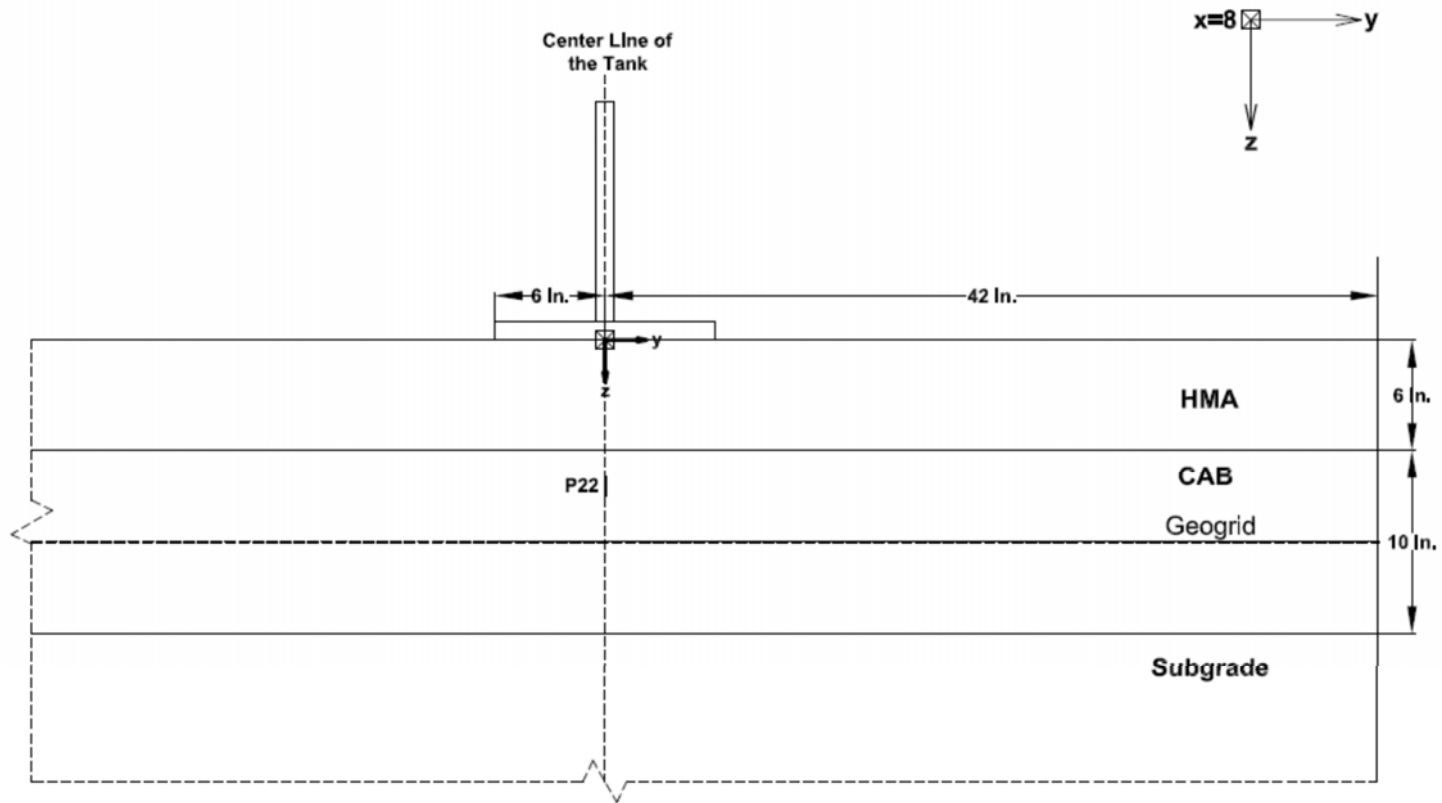


Figure E4-3. Instrumentation plan for experiment No. 4—Profile view at X = 8 inches

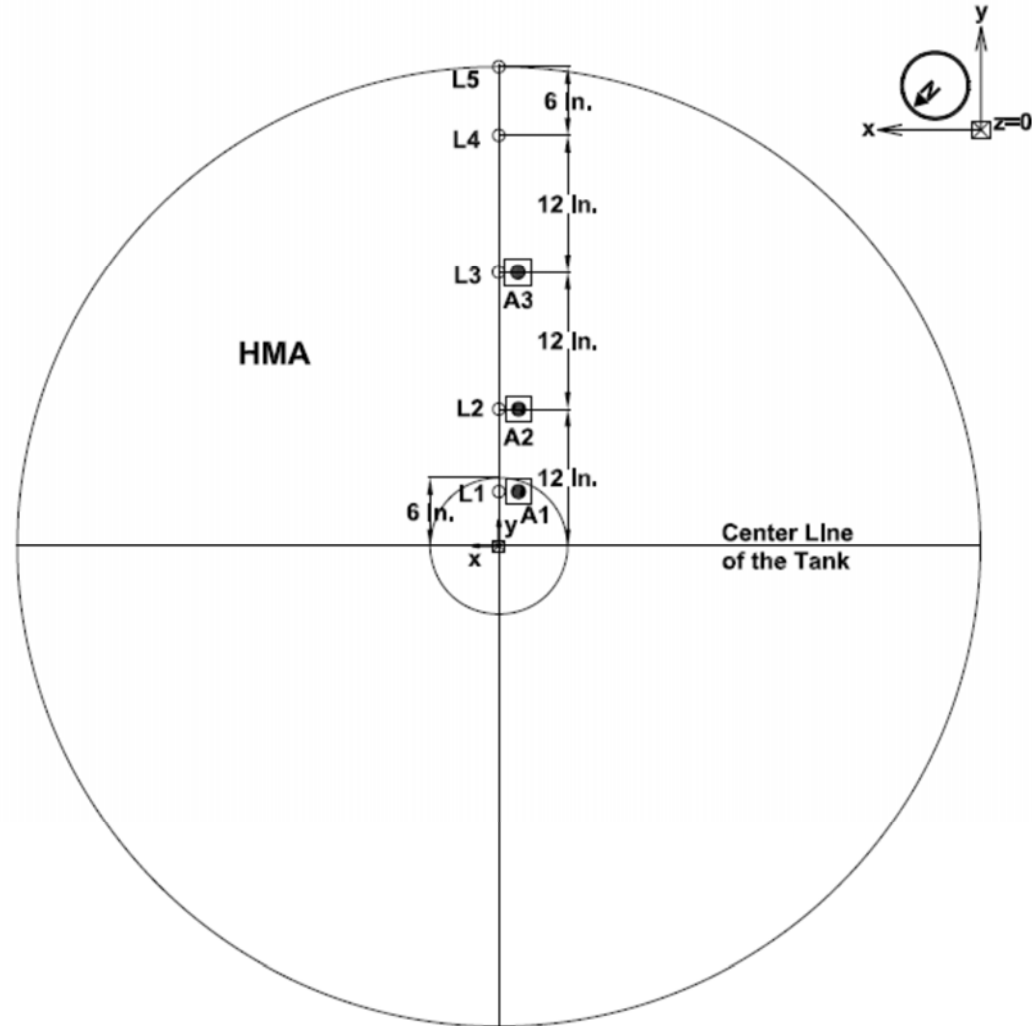


Figure E4-4. Instrumentation plan for experiment No. 4—Plan view at $Z = 0$ inch

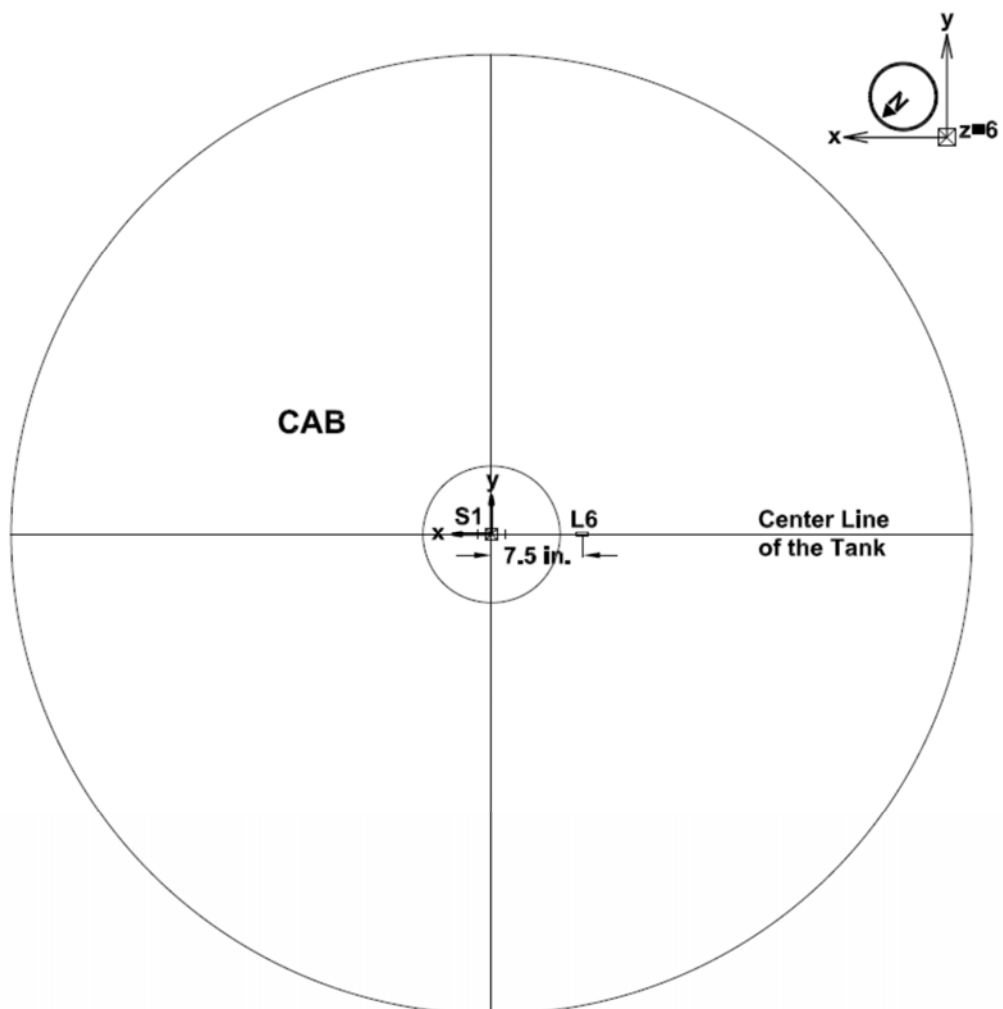


Figure E4-5. Instrumentation plan for experiment No. 4—Plan view at Z = 6 inches



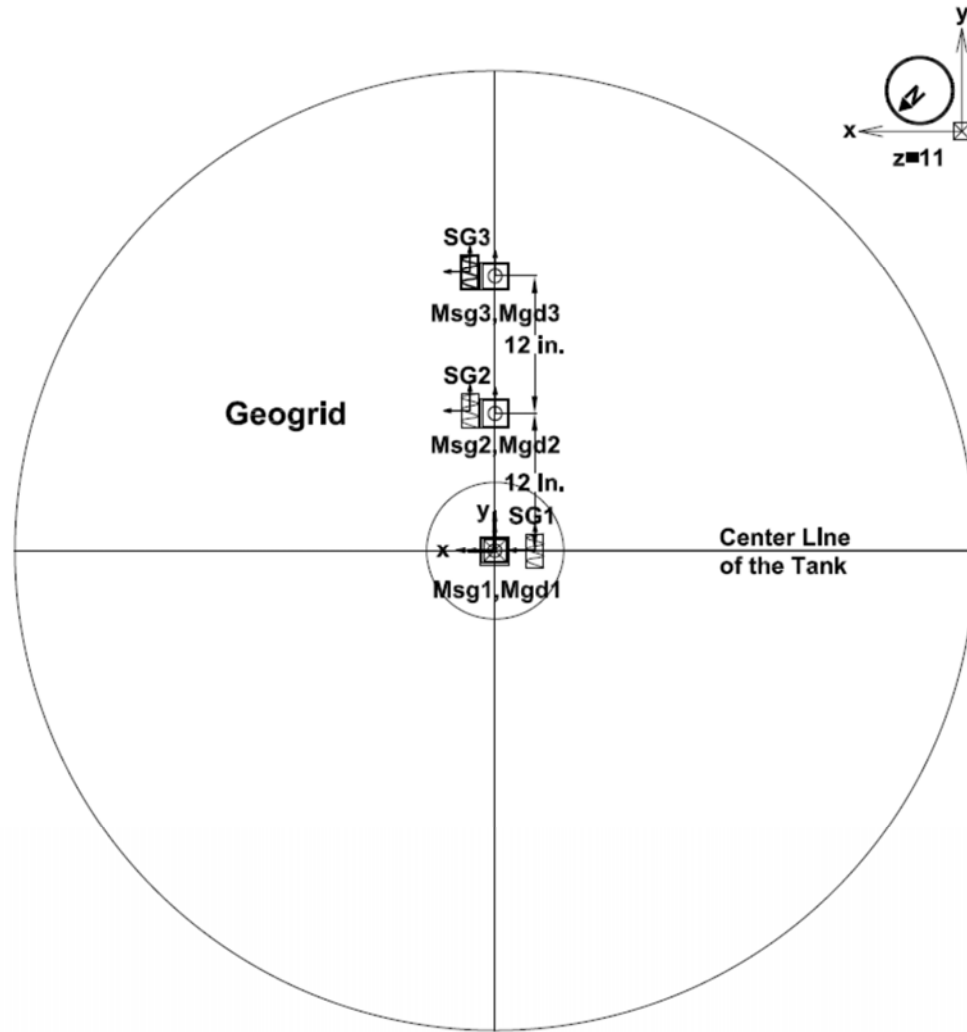


Figure E4-7. Instrumentation plan for experiment No. 4—Plan view at $Z = 11$ inches

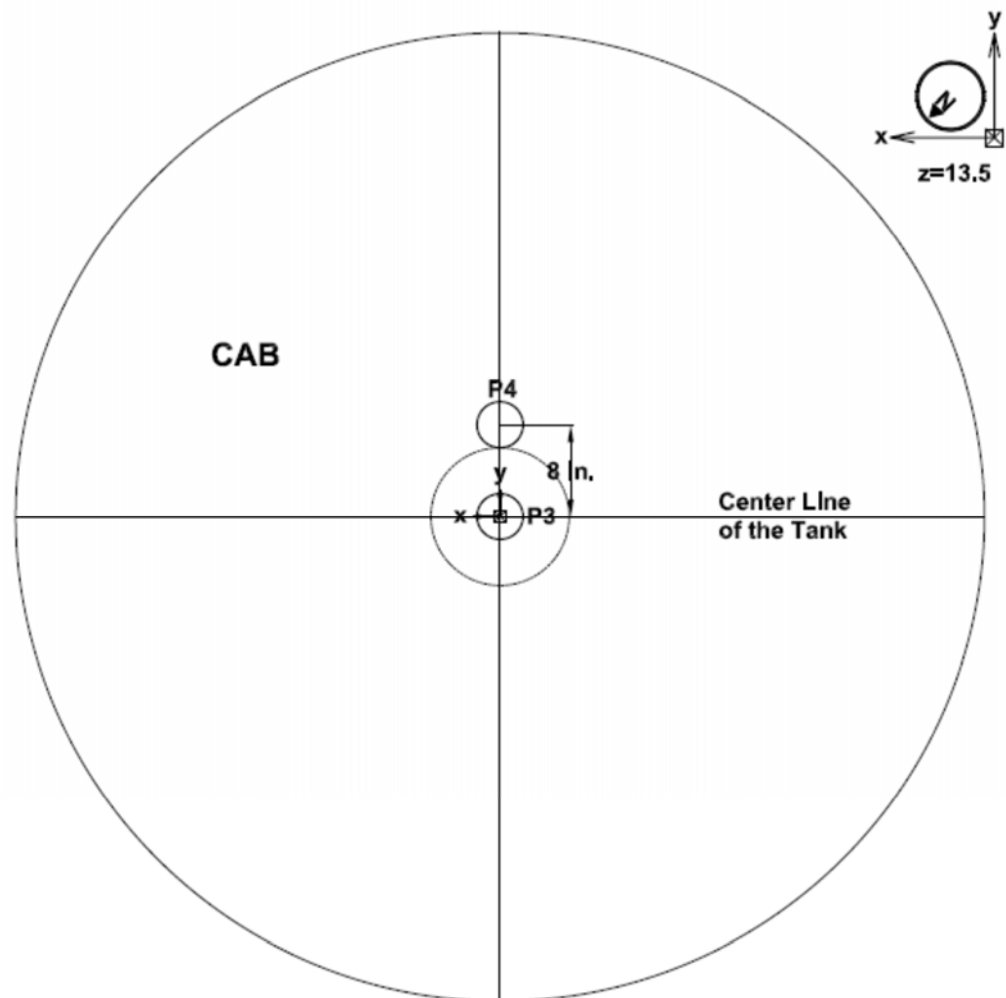


Figure E4-8. Instrumentation plan for experiment No. 4—Plan view at $Z = 13.5$ inches

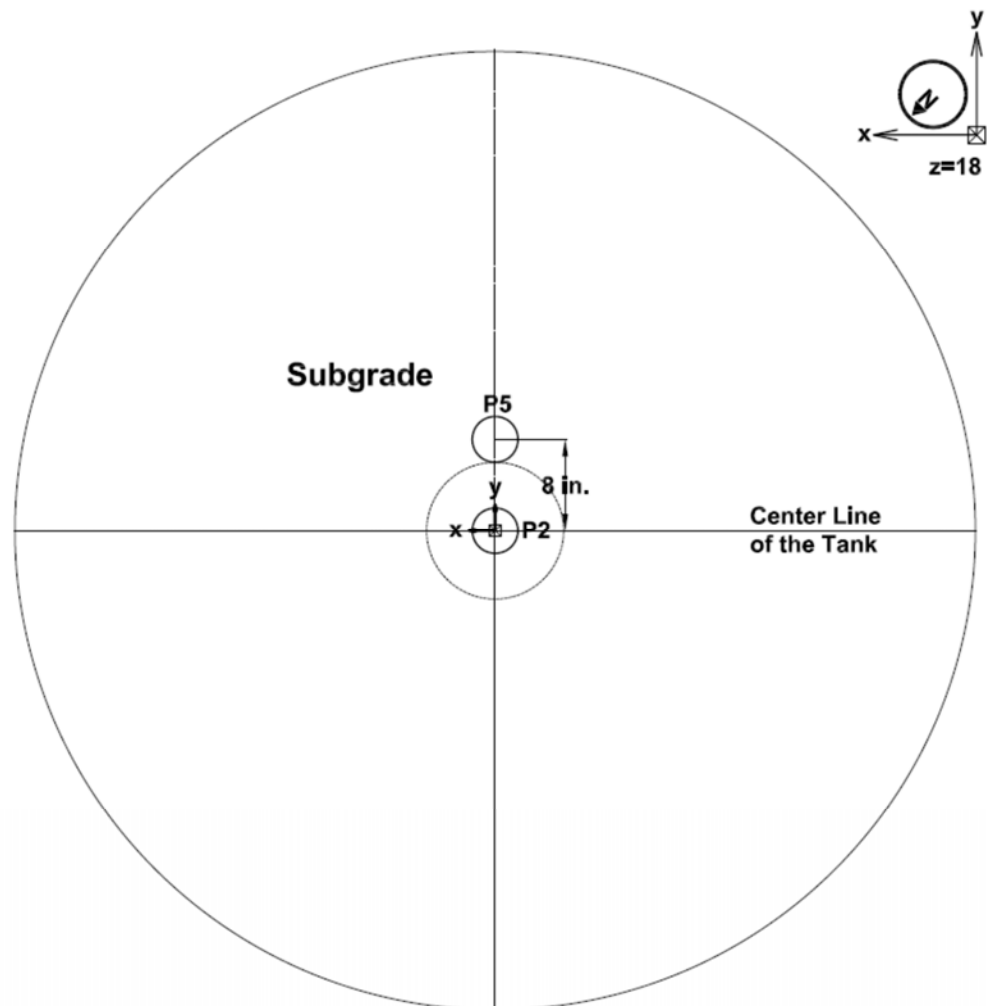


Figure E4-9. Instrumentation plan for experiment No. 4—Profile view at $Z = 18$ inches

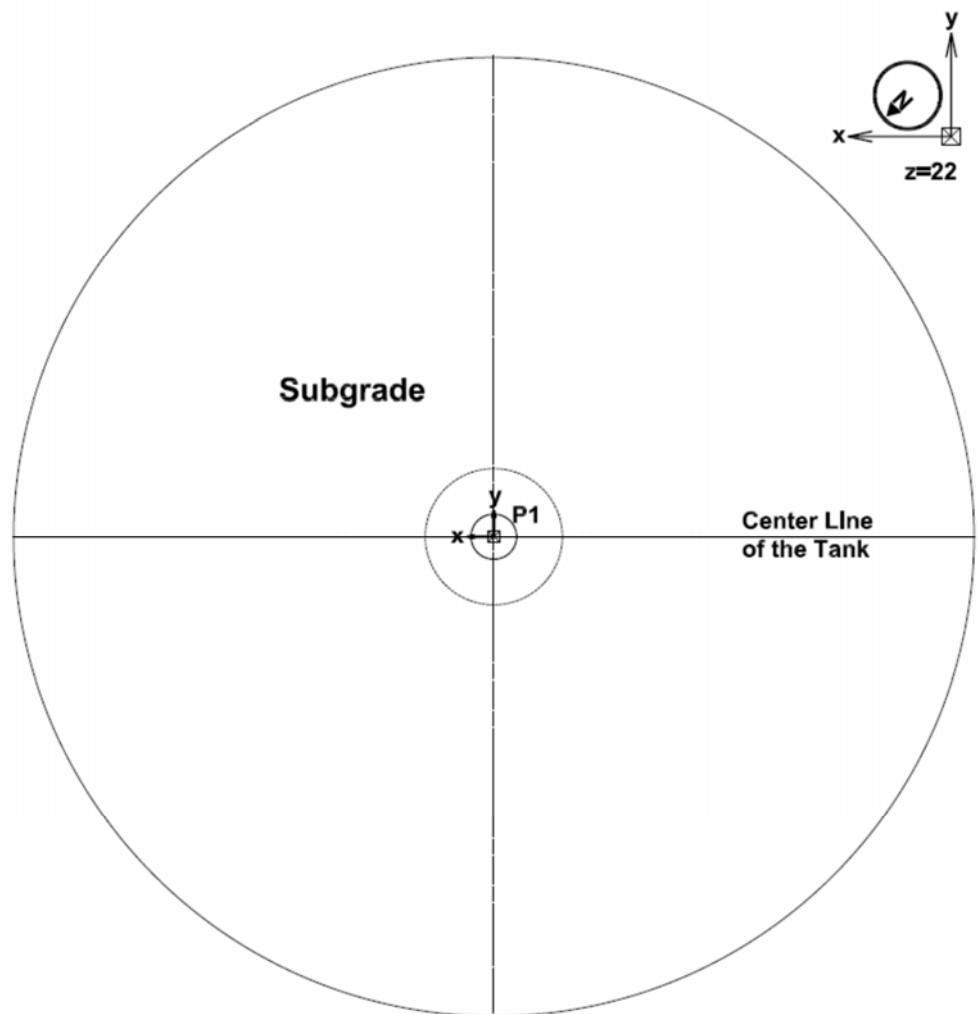


Figure E4-10. Instrumentation plan for experiment No. 4—Profile view at $Z = 22$ inches

Appendix E5. Experiment No. 5 (Geotextile—Thin Base)

Experiment ID	Exp5-AC-Textile-B06
Description	Flexible pavement; geotextile reinforcement, 6-inch aggregate base

Average Asphalt Layer Thickness (inch)	5.94
Asphalt Layer Temperature (°F)	79.0
Average CAB Layer Thickness (inch)	6.00

Pressure Cell ID	Pressure Cell Diameter	X Coordinate (in)	Y Coordinate (in)	Z Coordinate (in)	Comments
P1	4 inch	0	0	18	P1 measures vertical pressure at 6 inches below the subgrade surface.
P2	4 inch	0	0	14	P2 measures vertical pressure at 2 inches below the subgrade surface.
P3	4 inch	0	0	9	P3 measures vertical pressure at 3 inches below the base surface at the center of the load.
P4	4 inch	0	8	9	P4 measures vertical pressure at 3 inches below the base surface and 8 inches from the center of the load.
P5	4 inch	0	0	14	P2 measures vertical pressure at 2 inches below the subgrade surface and 8 inches from the center.
P6	N/A	N/A	N/A	N/A	N/A
P7	N/A	N/A	N/A	N/A	N/A
P21	1 inch	0	-8	9	P21 measures horizontal pressure at 3 inches above the subgrade surface and 8 inches from the center of the load.
P22	1 inch	8	0	9	P22 measures horizontal pressure at 3 inches above the subgrade surface and 8 inches from the center of the load.

LVDT ID	X Coordinate (in)	Y Coordinate (in)	Z Coordinate (in)	Comments
LVDT 1	0	6	0	At the pavement surface and 6 inches from the centerline of the load. Note: because of the plate configuration, the measurement is considered to be at the centerline of the load.
LVDT 2	0	12	0	At the pavement surface and 12 inches from the centerline of the load.
LVDT 3	0	24	0	At the pavement surface and 24 inches from the centerline of the load.
LVDT 4	0	36	0	At the pavement surface and 36 inches from the centerline of the load.
LVDT 5	0	48	0	On top of the Large-Scale Tank rim.
LVDT 6	-7.5	0	6	At 7.5 inches from the centerline of the load (in negative X-direction), measuring base deflection.

Strain Gauge	X Coordinate (in)	Y Coordinate (in)	Z Coordinate (in)	Comments
S1	0	0	6	Strain at the centerline of the load and at the bottom of the asphalt layer.
SG1-X	0	0	12	Strain on geotextile.
SG1-Y	0	0	12	Strain on geotextile.
SG2-X	0	12	12	Strain on geotextile.
SG2-Y	0	12	12	Strain on geotextile.
SG3-X	0	24	12	Strain on geotextile.

Strain Gauge	X Coordinate (in)	Y Coordinate (in)	Z Coordinate (in)	Comments
SG3-Y	0	24	12	Strain on geotextile.
SG1-A	0	0	12	Strain on geotextile, measuring at 45 degrees to the y-axis.
SG2-A	0	12	12	Strain on geotextile, measuring at 45 degrees to the y-axis.
SG3-A	0	24	12	Strain on geotextile, measuring at 45 degrees to the y-axis.

Accelerometer	Accelerometer ID	X Coordinate (in)	Y Coordinate (in)	Z Coordinate (in)	Comments
A1	A1_Z	0	6	0	At the pavement surface and 6 inches from the centerline of the load. Note: because of the plate configuration, the measurement is considered to be at the centerline of the load.
A2	A2_Z	0	12	0	At the pavement surface and 12 inches from the centerline of the load.
A3	A3_Z	0	24	0	At the pavement surface and 24 inches from the centerline of the load.
Msg1	M1_Y	0	0	12	In the subgrade, at the base/SG interface, and at the centerline of the load. Measurement is in Y-direction.
Msg1	M1_Z	0	0	12	In the subgrade, at the base/SG interface, and at the centerline of the load. Measurement is in Z-direction.
Msg2	M2_Y	0	12	12	In the subgrade, at the base/SG interface, and 12 inches from the centerline of the load. Measurement is in Y-direction.
Msg2	M2_Z	0	12	12	In the subgrade, at the base/SG interface, and 12 inches from the centerline of the load. Measurement is in Z-direction.
Msg3	M3_Y	0	24	12	In the subgrade, at the base/SG interface, and 24 inches from the centerline of the load. Measurement is in Y-direction.
Msg3	M3_Z	0	24	12	In the subgrade, at the base/SG interface, and 24 inches from the centerline of the load. Measurement is in Z-direction.
Mgd1	M1_Y	0	0	12	At the centerline of the load. Measurement is in Y-direction. Attached to geotextile.
Mgd1	M1_Z	0	0	12	At the centerline of the load. Measurement is in Z-direction. Attached to geotextile.
Mgd2	M2_Y	0	12	12	12 inches from the centerline of the load. Measurement is in Y-direction. Attached to geotextile.
Mgd2	M2_Z	0	12	12	12 inches from the centerline of the load. Measurement is in Z-direction. Attached to geotextile.
Mgd3	M3_Y	0	24	12	24 inches from the centerline of the load. Measurement is in Y-direction. Attached to geotextile.
Mgd3	M3_Z	0	24	12	24 inches from the centerline of the load. Measurement is in Z-direction. Attached to geotextile.

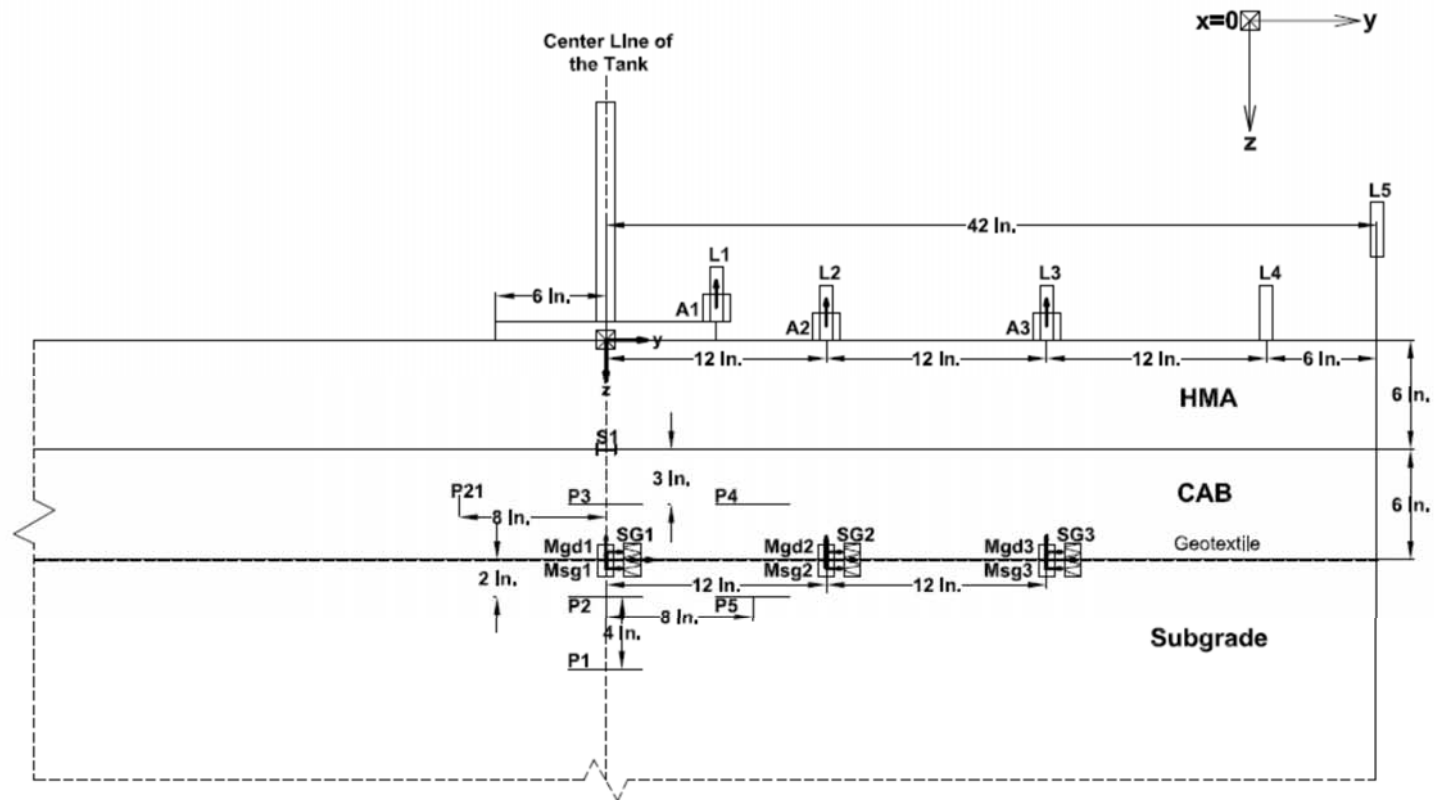


Figure E5-1. Instrumentation plan for experiment No. 5—Profile view, X = 0 inch

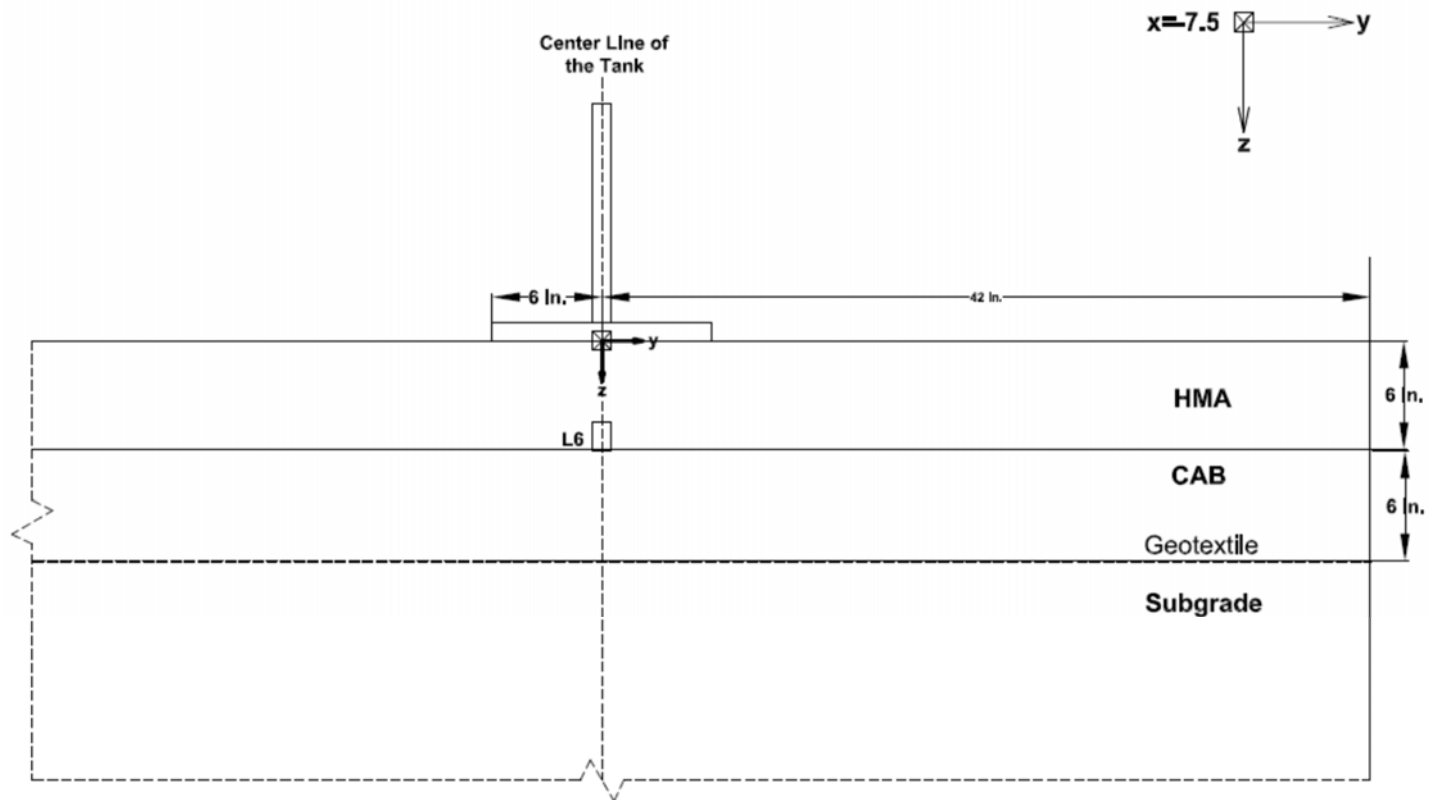


Figure E5-2. Instrumentation plan for experiment No. 5—Profile view, $X = -7.5$ inches

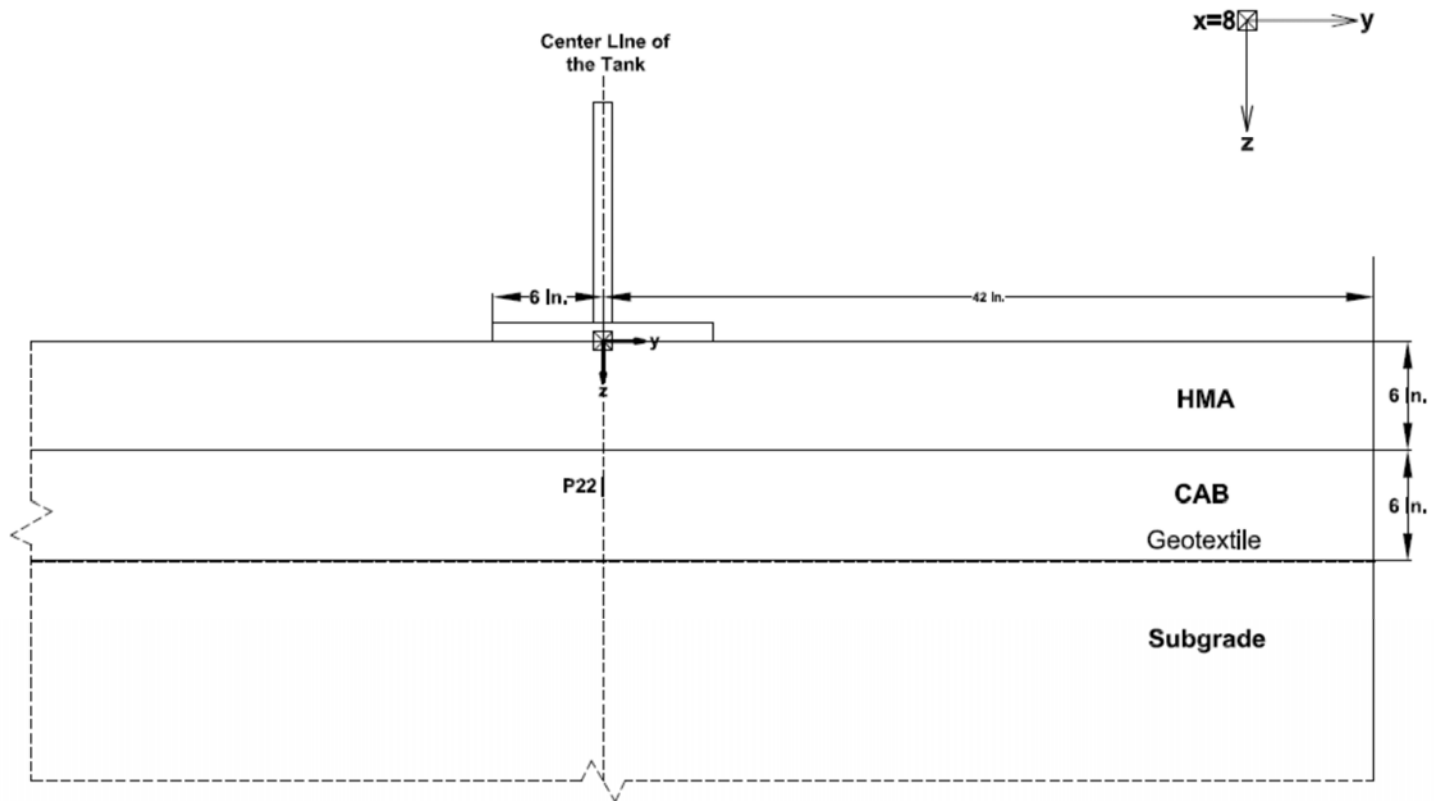


Figure E5-3. Instrumentation plan for experiment No. 5—Profile view, X = 8 inches

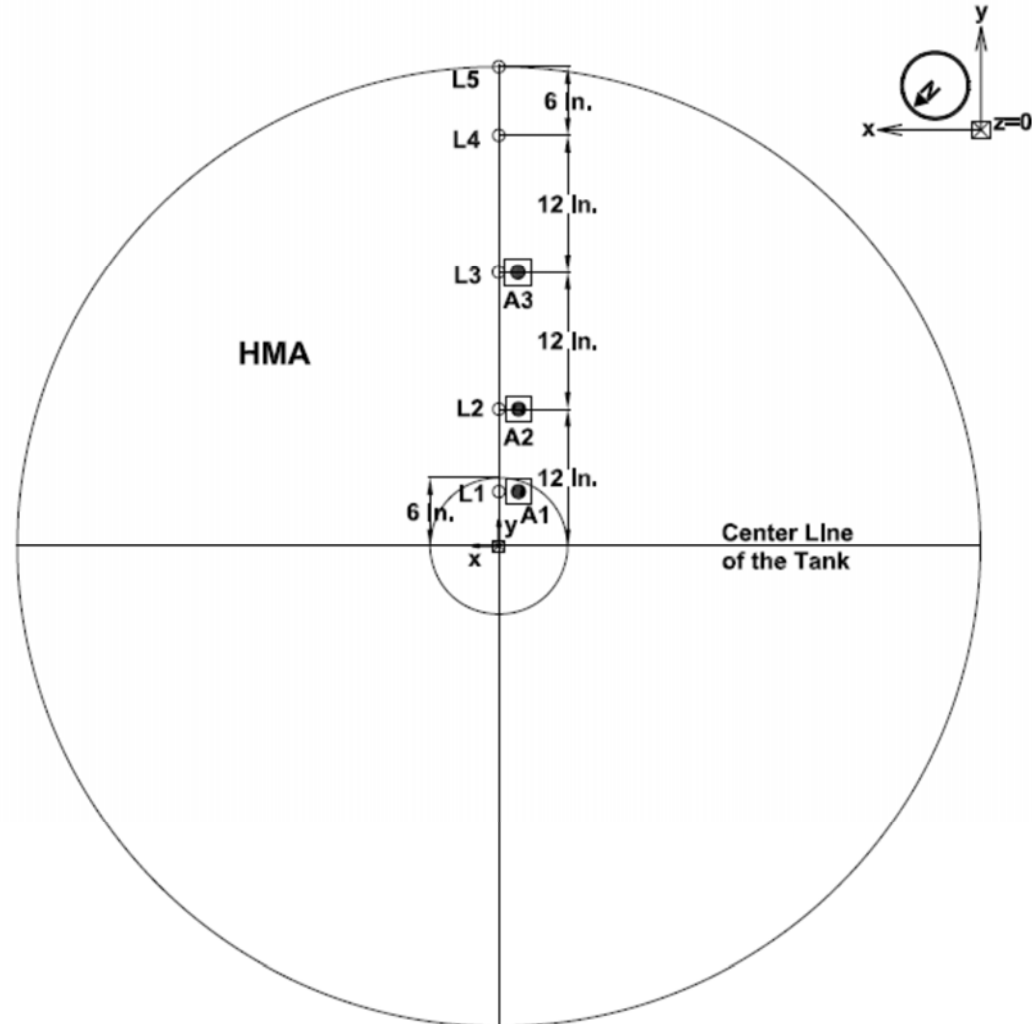


Figure E5-4. Instrumentation plan for experiment No. 5—Plan view, $Z = 0$ inch

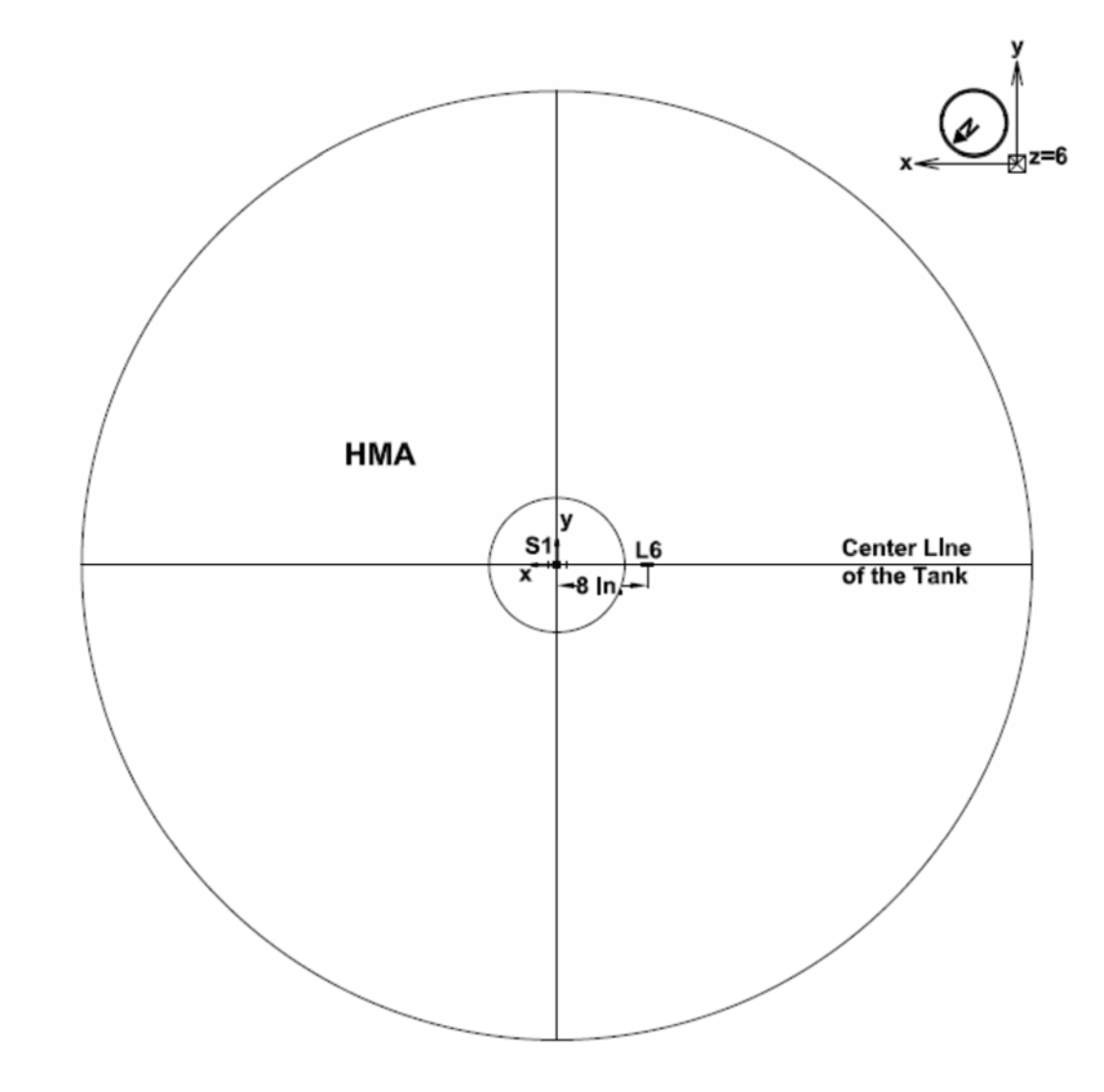


Figure E5-5. Instrumentation plan for experiment No. 5—Plan view, Z = 6 inches

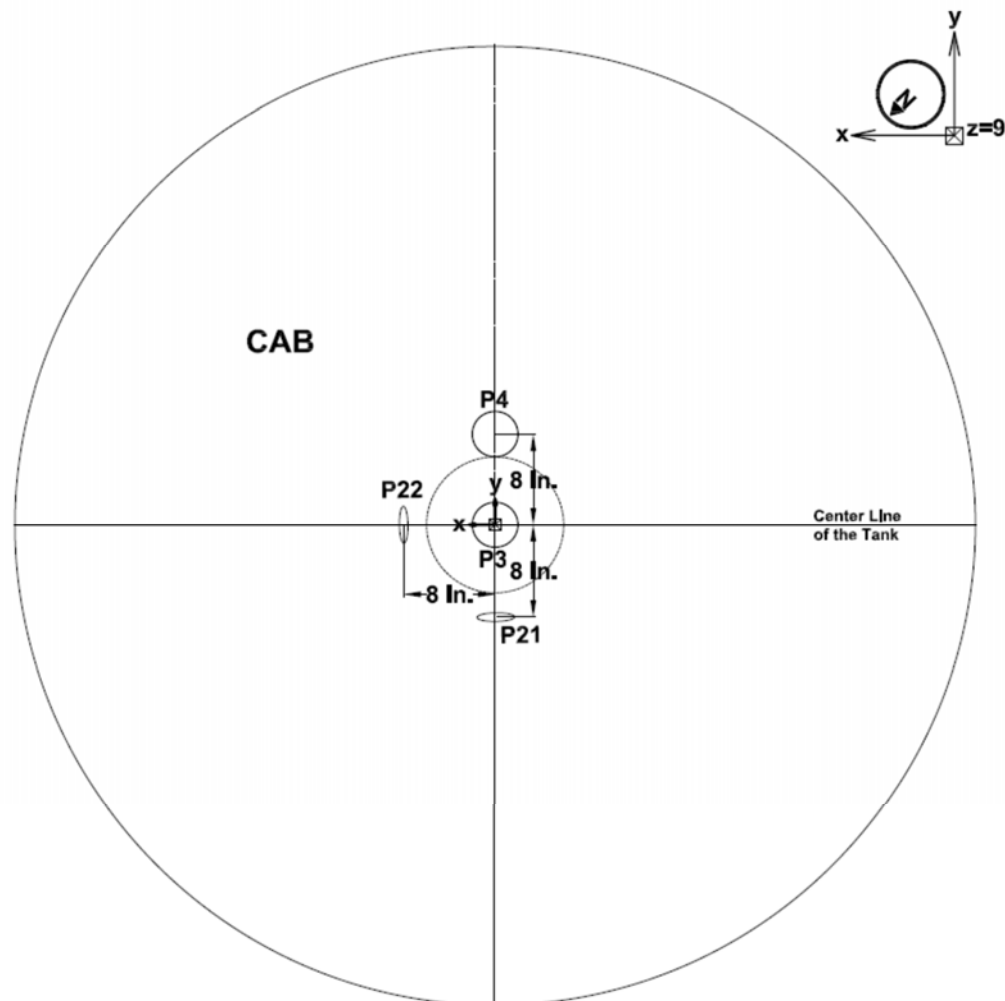


Figure E5-6. Instrumentation plan for experiment No. 5—Plan view, Z = 9 inches

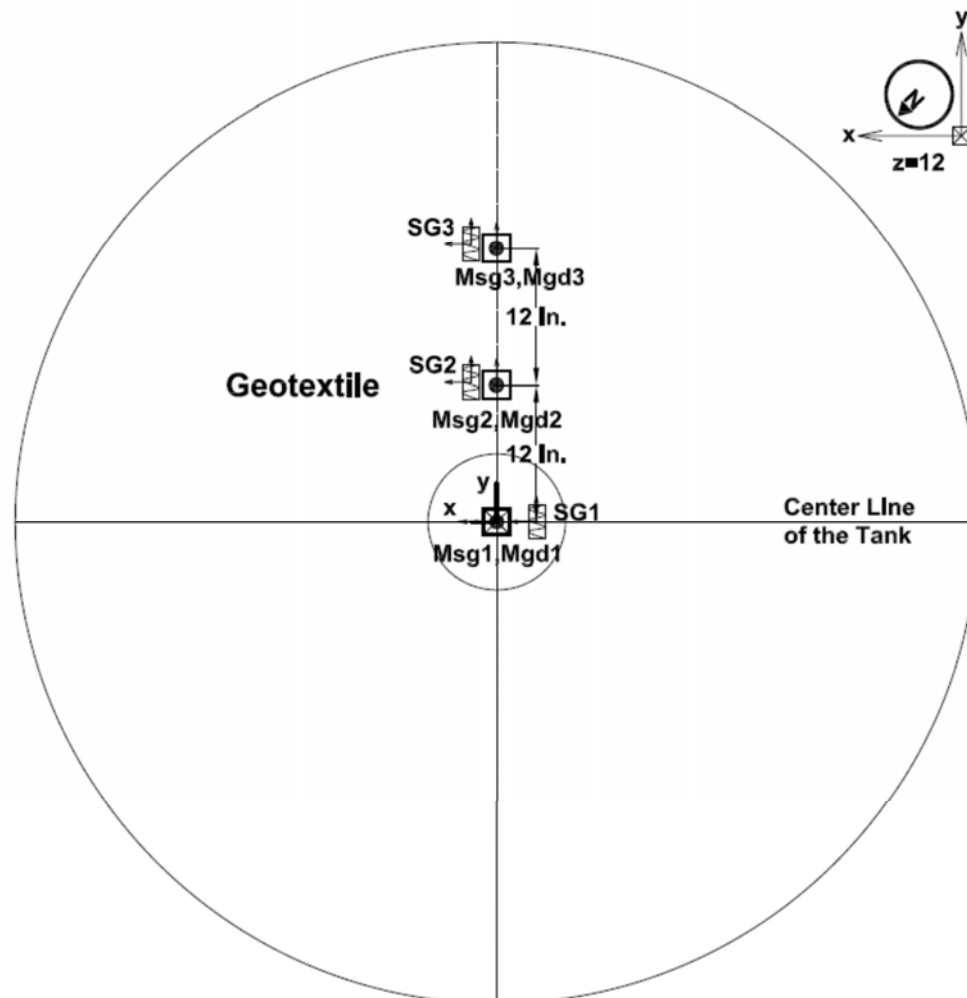


Figure E5-7. Instrumentation plan for experiment No. 5—Plan view, $Z = 12$ inches

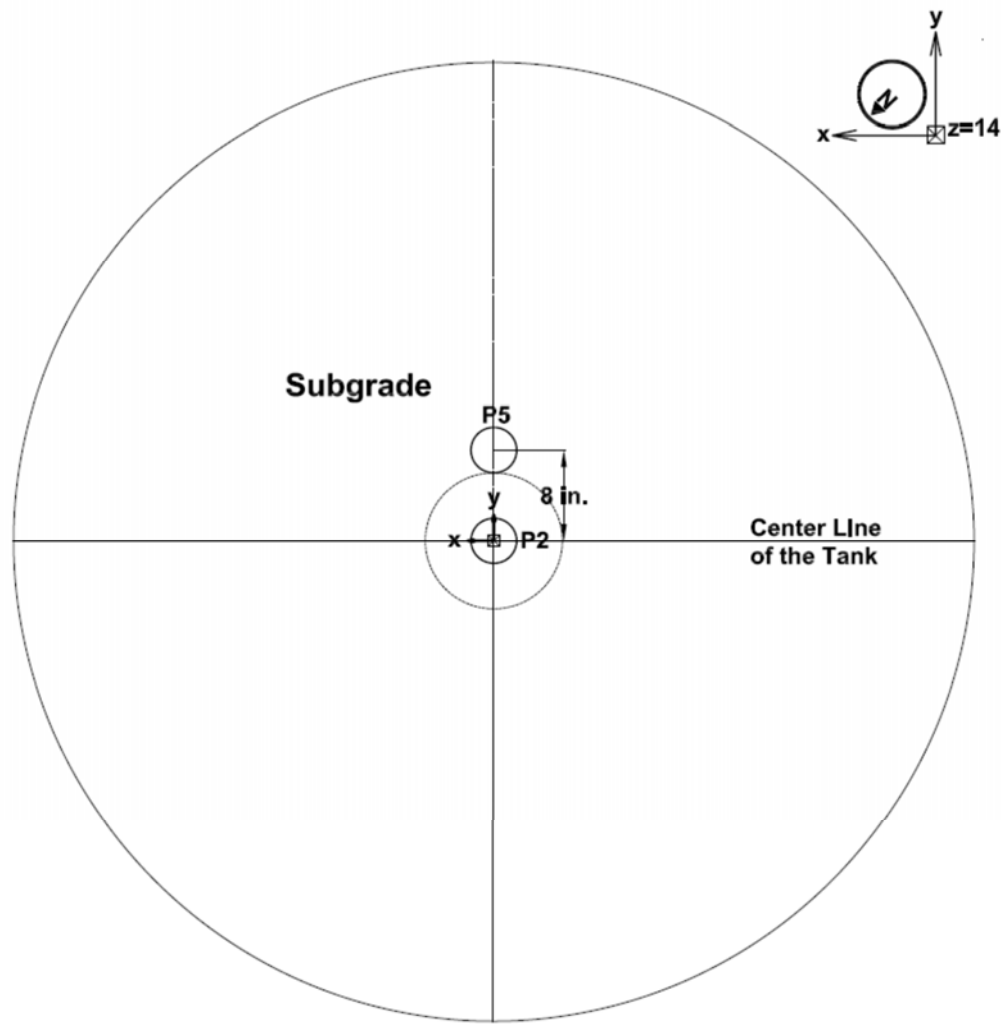


Figure E5-8. Instrumentation plan for experiment No. 5—Plan view, Z = 14 inches

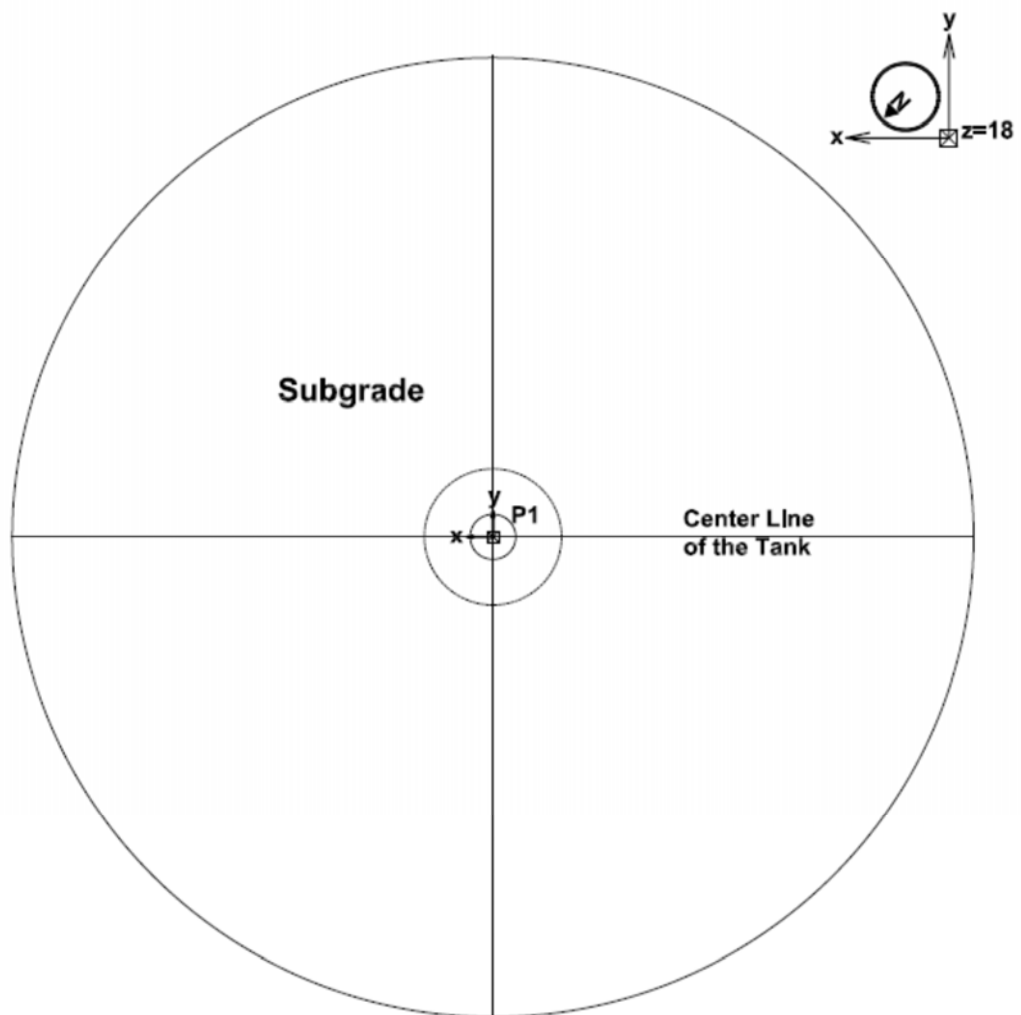


Figure E5-9. Instrumentation plan for experiment No. 5– Profile view, Z = 18 inches

Appendix E6. Experiment No. 6 (Geotextile—Thick Base)

Experiment ID	Exp6-AC-Textile-B10
Description	Flexible pavement; geotextile reinforcement; 10-inch aggregate base

Average Asphalt Layer Thickness (inch)	5.90
Asphalt Layer Temperature (°F)	78.5
Average CAB Layer Thickness (inch)	10.00

Pressure Cell ID	Pressure Cell Diameter	X Coordinate (in)	Y Coordinate (in)	Z Coordinate (in)	Comments
P1	4 inch	0	0	22	P1 measures vertical pressure at 6 inches below the subgrade surface.
P2	4 inch	0	0	18	P2 measures vertical pressure at 2 inches below the subgrade surface.
P3	4 inch	0	0	13.5	P3 measures vertical pressure at 7.5 inches below the base surface.
P4	4 inch	0	8	13.5	P4 measures vertical pressure at 7.5 inches below the base surface and 8 inches from the center of the load in the positive Y-direction.
P5	4 inch	0	8	18	P5 measures vertical pressure at 2 inches below the subgrade surface and 8 inches from the center.
P6	4 inch	0	0	8.5	P6 measures vertical pressure at 2.5 inches below the base surface at the center of the load.
P7	4 inch	0	8	8.5	P7 measures vertical pressure at 2.5 inches below the asphalt surface and 8 inches from the center.
P21	1 inch	0	-8	8.5	P21 measures horizontal pressure at 2.5 inches above the subgrade surface and 8 inches from the center of the load in the negative y-direction.
P22	1 inch	8	0	8.5	P22 measures horizontal pressure at 2.5 inches below the base surface and 8 inches from the center of the load in the positive x-direction.

LVDT ID	X Coordinate (in)	Y Coordinate (in)	Z Coordinate (in)	Comments
LVDT 1	0	6	0	At the pavement surface and 6 inches from the centerline of the load. Note: because of the plate configuration, the measurement is considered to be at the centerline of the load.
LVDT 2	0	12	0	At the pavement surface and 12 inches from the centerline of the load.
LVDT 3	0	24	0	At the pavement surface and 24 inches from the centerline of the load.
LVDT 4	0	36	0	At the pavement surface and 36 inches from the centerline of the load.
LVDT 5	0	48	0	On top of the Large-Scale Tank rim.
LVDT 6	-7.5	0	6	At 7.5 inches from the centerline of the load (in negative X-direction), measuring base deflection.

Strain Gauge	X Coordinate (in)	Y Coordinate (in)	Z Coordinate (in)	Comments
S1	0	0	6	Strain at the centerline of the load and at the bottom of the asphalt layer.
SG1-X	0	0	12	Strain on geotextile.
SG1-Y	0	0	12	Strain on geotextile.

Strain Gauge	X Coordinate (in)	Y Coordinate (in)	Z Coordinate (in)	Comments
SG2-X	0	12	12	Strain on geotextile.
SG2-Y	0	12	12	Strain on geotextile.
SG3-X	0	24	12	Strain on geotextile.
SG3-Y	0	24	12	Strain on geotextile.
SG1-A	0	0	12	Strain on geotextile, measuring at 45 degrees to the y-axis.
SG2-A	0	12	12	Strain on geotextile, measuring at 45 degrees to the y-axis.
SG3-A	0	24	12	Strain on geotextile, measuring at 45 degrees to the y-axis.

Accelerometer	Accelerometer ID	X Coordinate (in)	Y Coordinate (in)	Z Coordinate (in)	Comments
A1	A1_Z	0	6	0	At the pavement surface and 6 inches from the centerline of the load. Note: because of the plate configuration, the measurement is considered to be at the centerline of the load.
A2	A2_Z	0	12	0	At the pavement surface and 12 inches from the centerline of the load.
A3	A3_Z	0	24	0	At the pavement surface and 24 inches from the centerline of the load.
Msg1	M1_Y	0	0	11	In the middle of the base and at the centerline of the load. Measurement is in Y-direction.
Msg1	M1_Z	0	0	11	In the middle of the base and at the centerline of the load. Measurement is in Z-direction.
Msg2	M2_Y	0	12	11	In the middle of the base and 12 inches from the centerline of the load. Measurement is in Y-direction.
Msg2	M2_Z	0	12	11	In the middle of the base and 12 inches from the centerline of the load. Measurement is in Z-direction.
Msg3	M3_Y	0	24	11	In the middle of the base and 24 inches from the centerline of the load. Measurement is in Y-direction.
Msg3	M3_Z	0	24	11	In the middle of the base and 24 inches from the centerline of the load. Measurement is in Z-direction.
Mgd1	M1_Y	0	0	11	In the middle of the base and at the centerline of the load. Measurement is in Y-direction. Attached to geotextile.
Mgd1	M1_Z	0	0	11	In the middle of the base and at the centerline of the load. Measurement is in Z-direction. Attached to geotextile.
Mgd2	M2_Y	0	12	11	In the middle of the base and 12 inches from the centerline of the load. Measurement is in Y-direction. Attached to geotextile.
Mgd2	M2_Z	0	12	11	In the middle of the base and 12 inches from the centerline of the load. Measurement is in Z-direction.
Mgd3	M3_Y	0	24	11	In the middle of the base and 24 inches from the centerline of the load. Measurement is in Y-direction. Attached to geotextile.
Mgd3	M3_Z	0	24	11	In the middle of the base and 24 inches from the centerline of the load. Measurement is in Z-direction. Attached to geotextile.

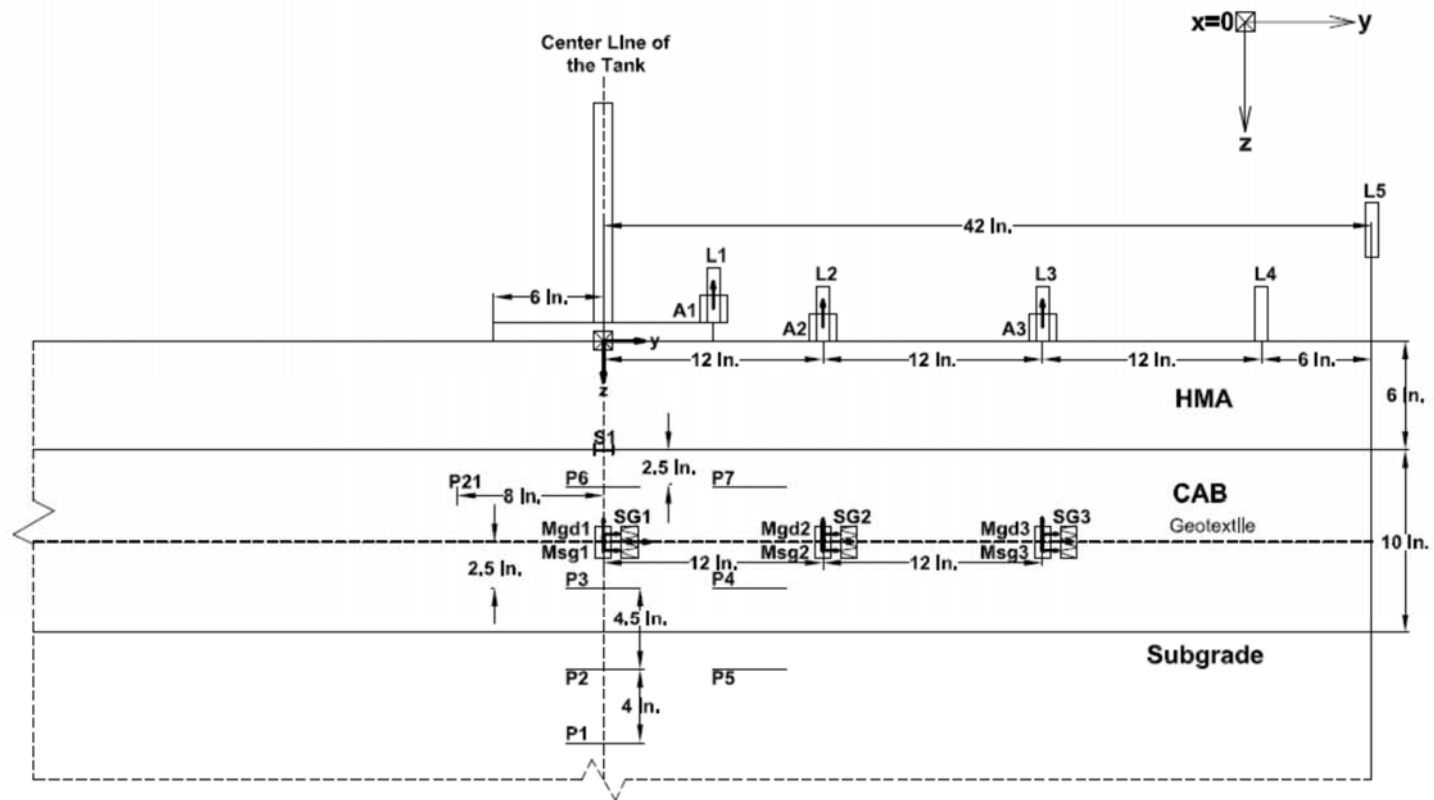


Figure E6-1. Instrumentation plan for experiment No. 6—Profile view at X = 0 inch

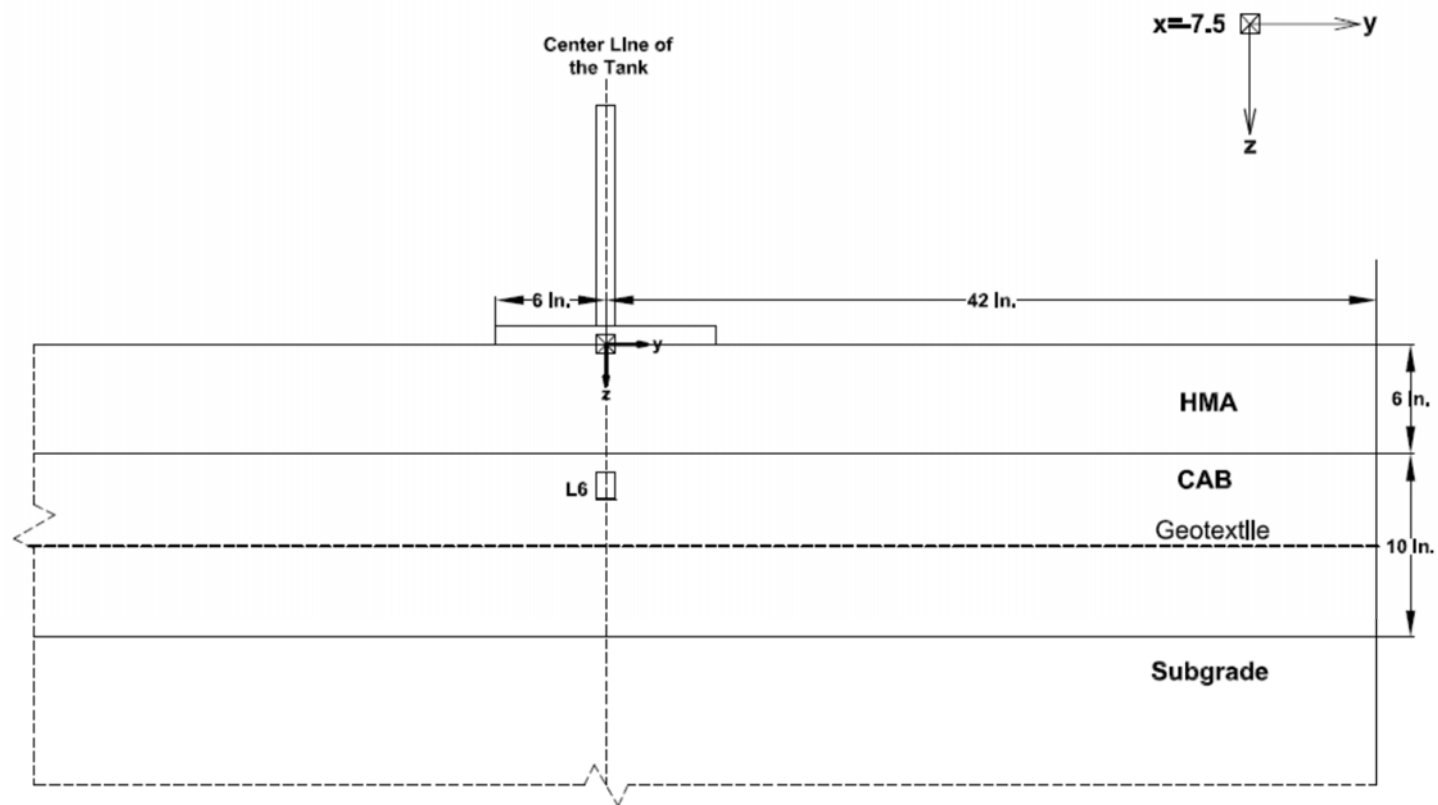
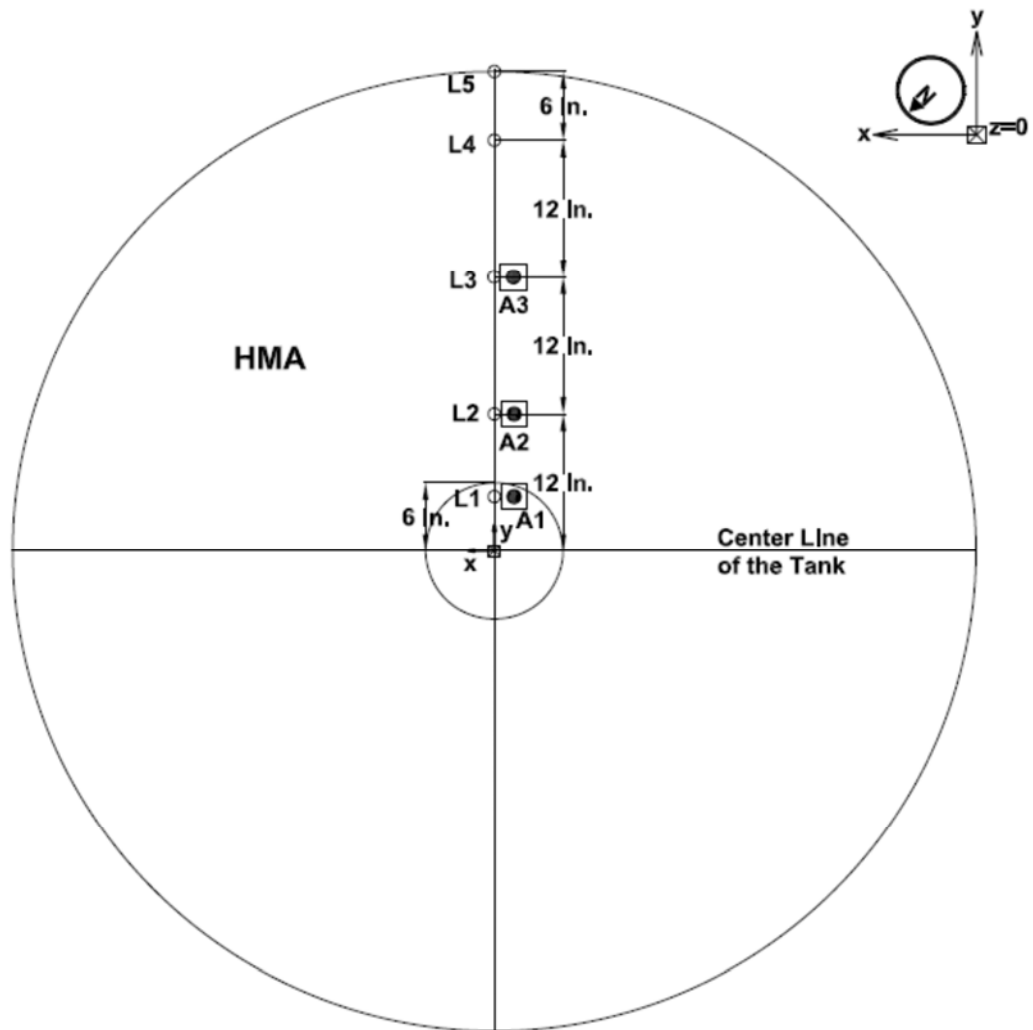


Figure E6-2. Instrumentation plan for experiment No. 6—Profile view at $X = -7.5$ inches



Figure E6-3. Instrumentation plan for experiment No. 6—Profile view at X = 8 inches



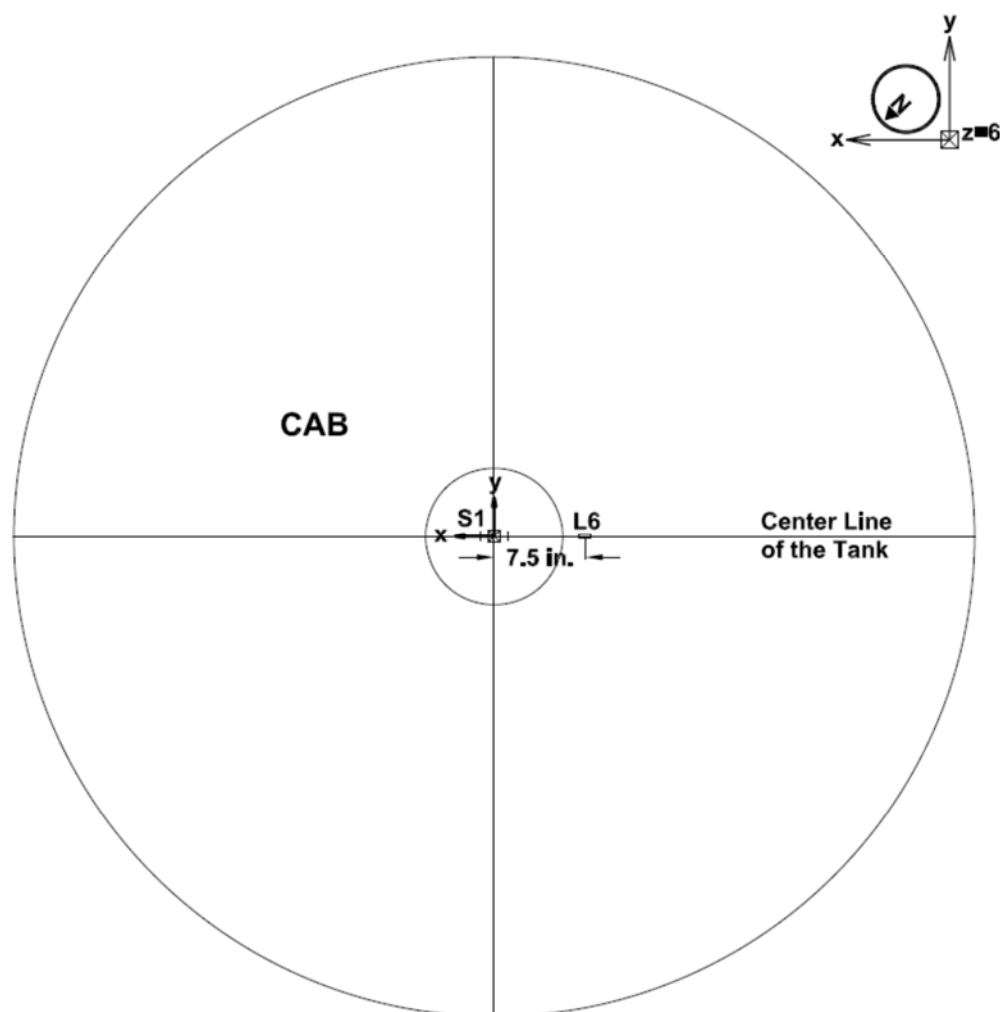


Figure E6-5. Instrumentation plan for experiment No. 6—Plan view at Z = 6 inches

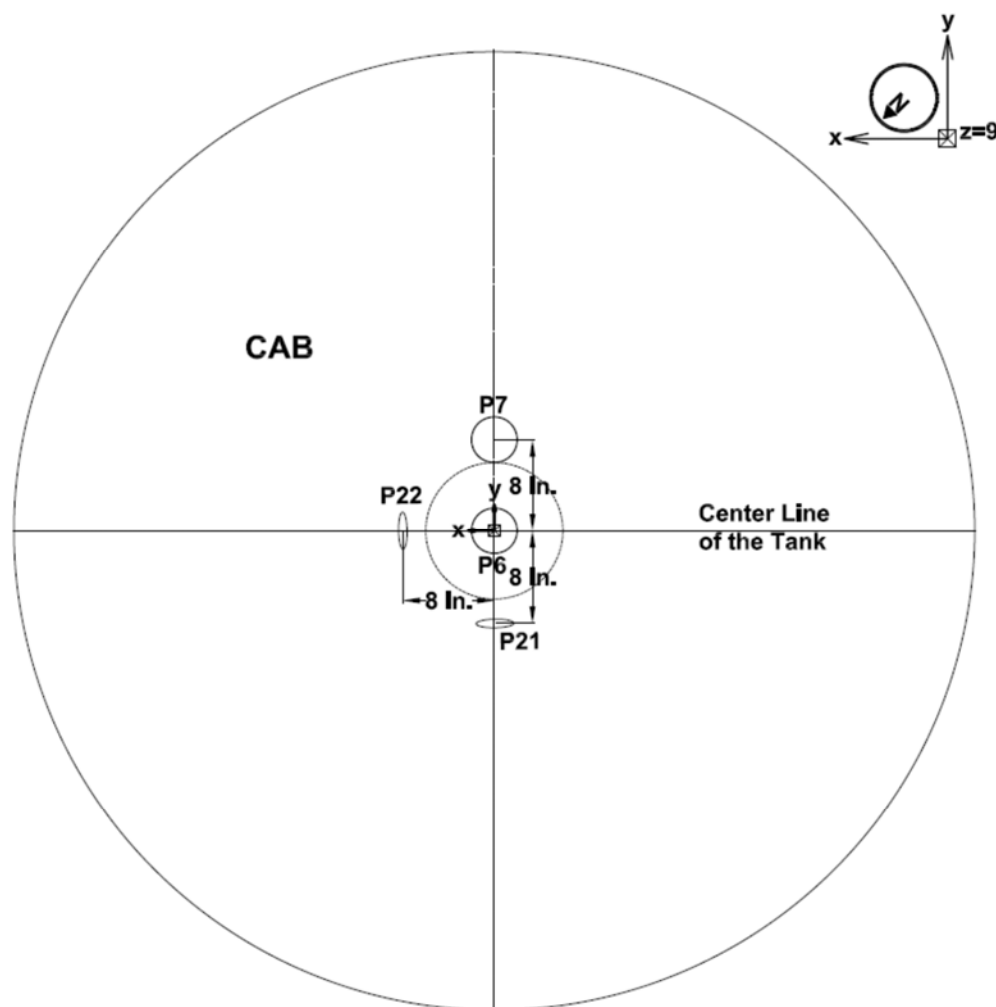


Figure E6-6. Instrumentation plan for experiment No. 6—Plan view at $Z = 9$ inches

Copyright National Academy of Sciences. All rights reserved.

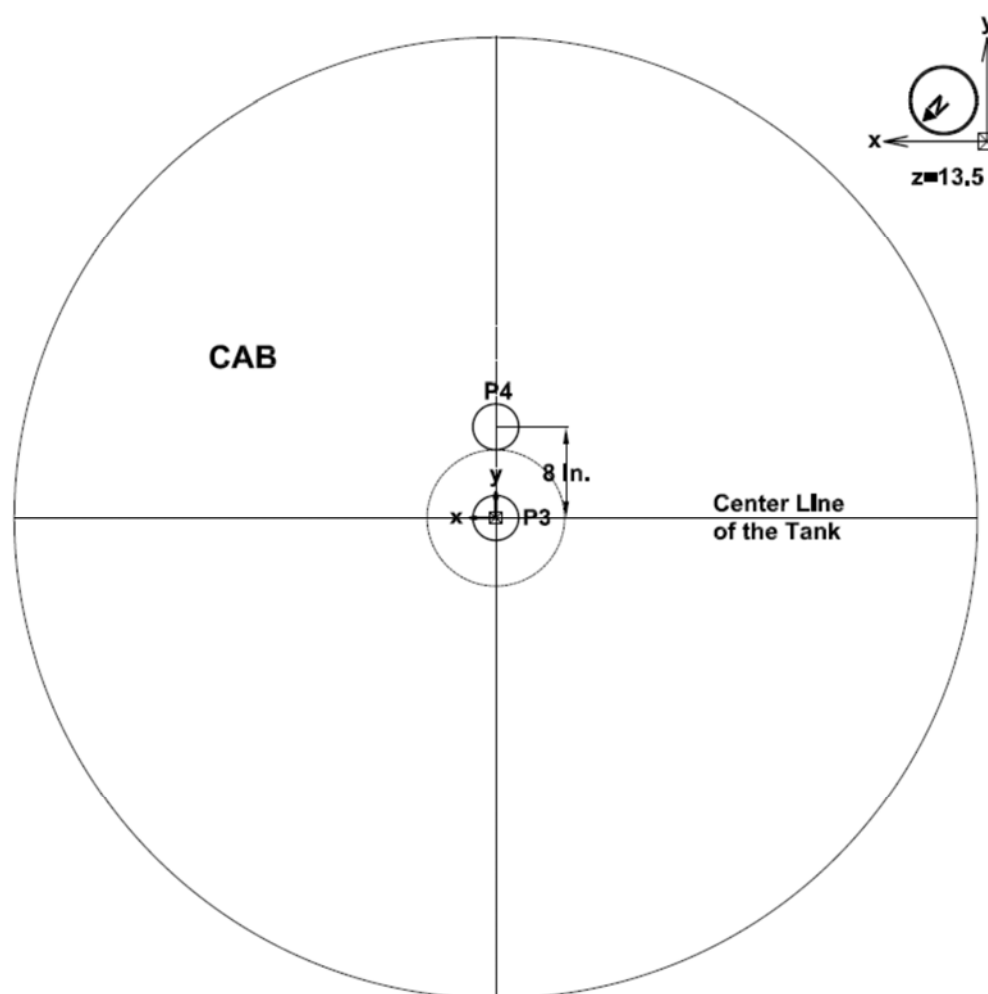


Figure E6-8. Instrumentation plan for experiment No. 6—Plan view at $Z = 13.5$ inches

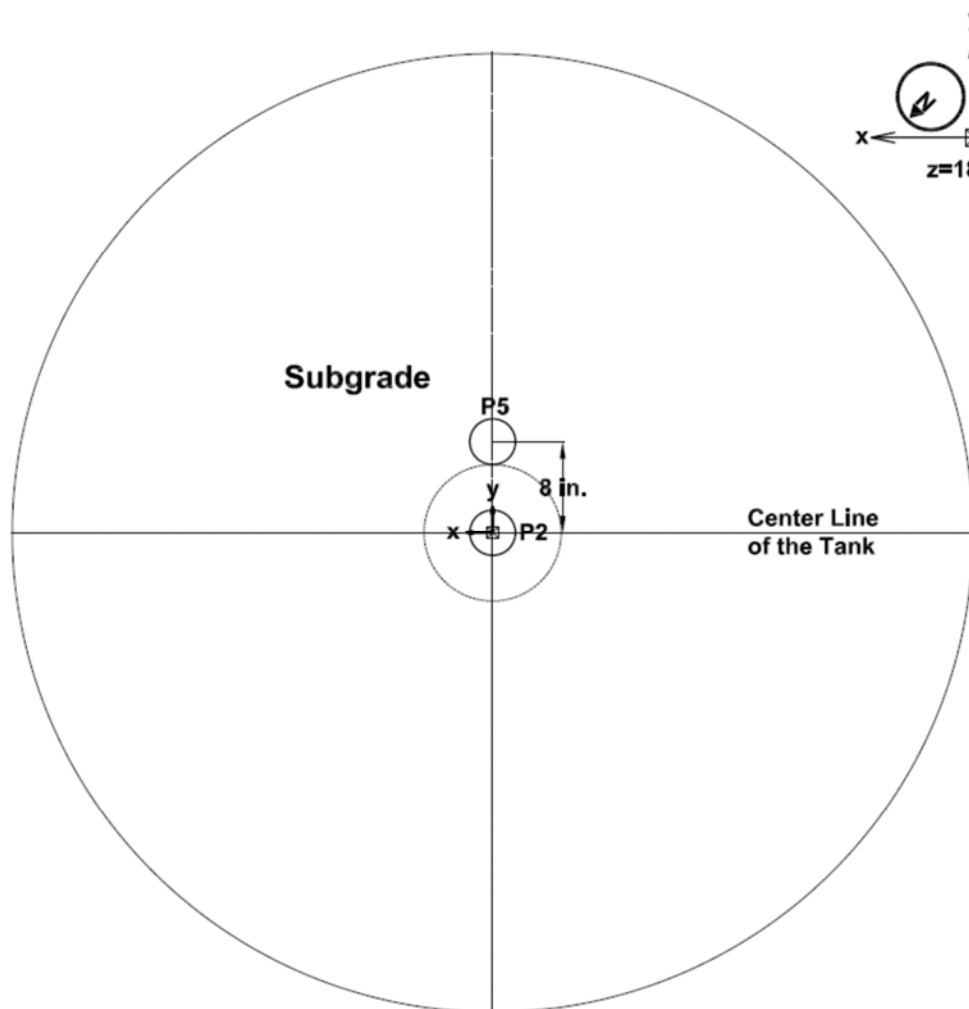


Figure E6-9. Instrumentation plan for experiment No. 6—Profile view at $Z = 18$ inches

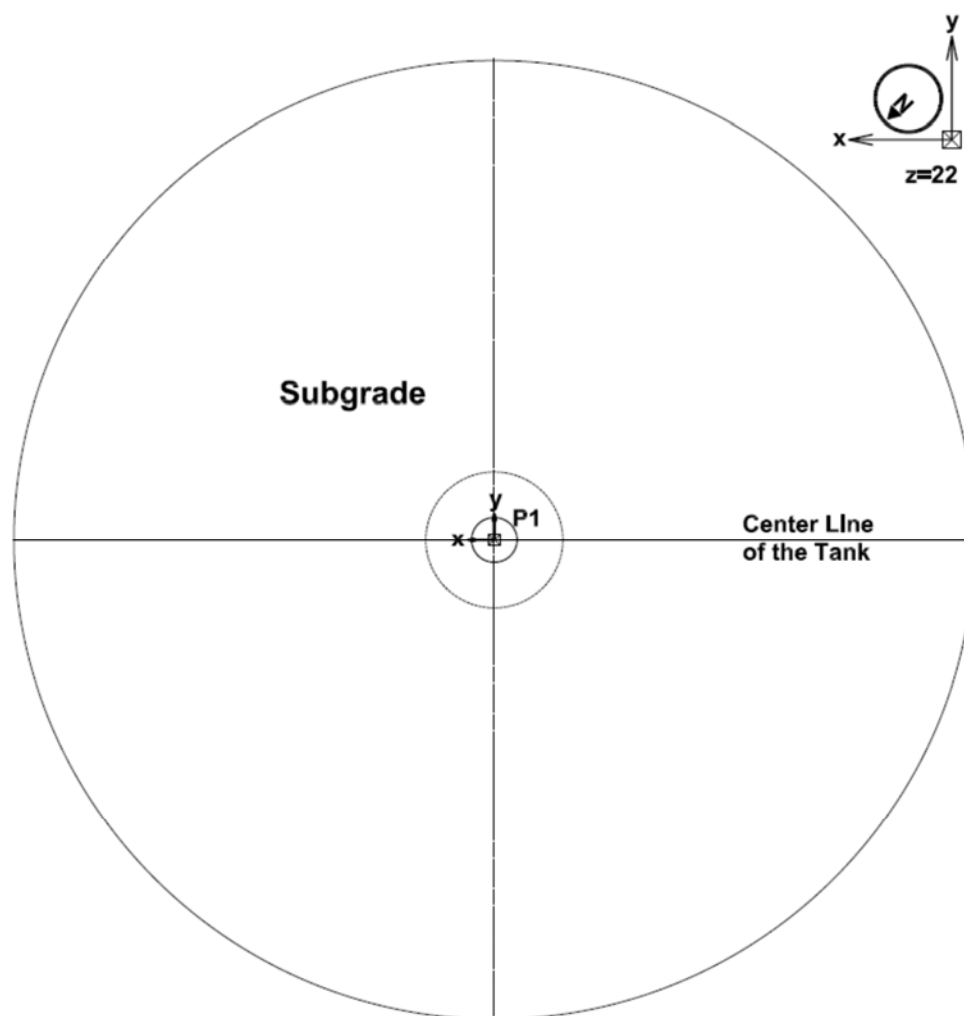


Figure E6-10. Instrumentation plan for experiment No. 6—Profile view at $Z = 22$ inches

APPENDIX F. SUMMARY CHARTS FOR FLEXIBLE PAVEMENT EXPERIMENTS

**Appendix F1. Summary Charts for Flexible Pavement Experiments: Dynamic Loading—
Thin Base: No. 1 (Control), No. 3 (Geogrid), and No. 5 (Geotextile)**

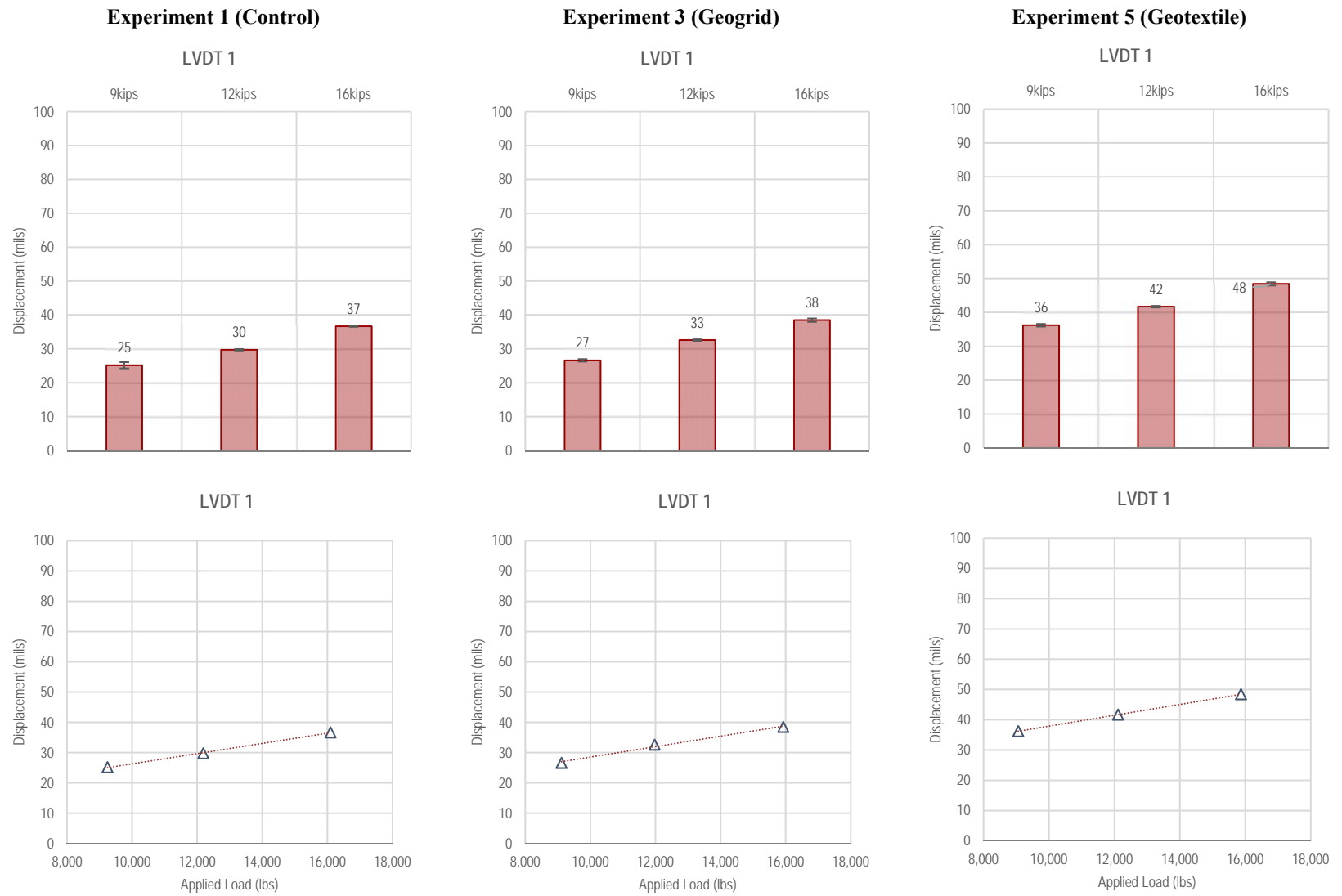


Figure F1-1. Summary of LVDT 1 measurements—Dynamic Loading

F-3

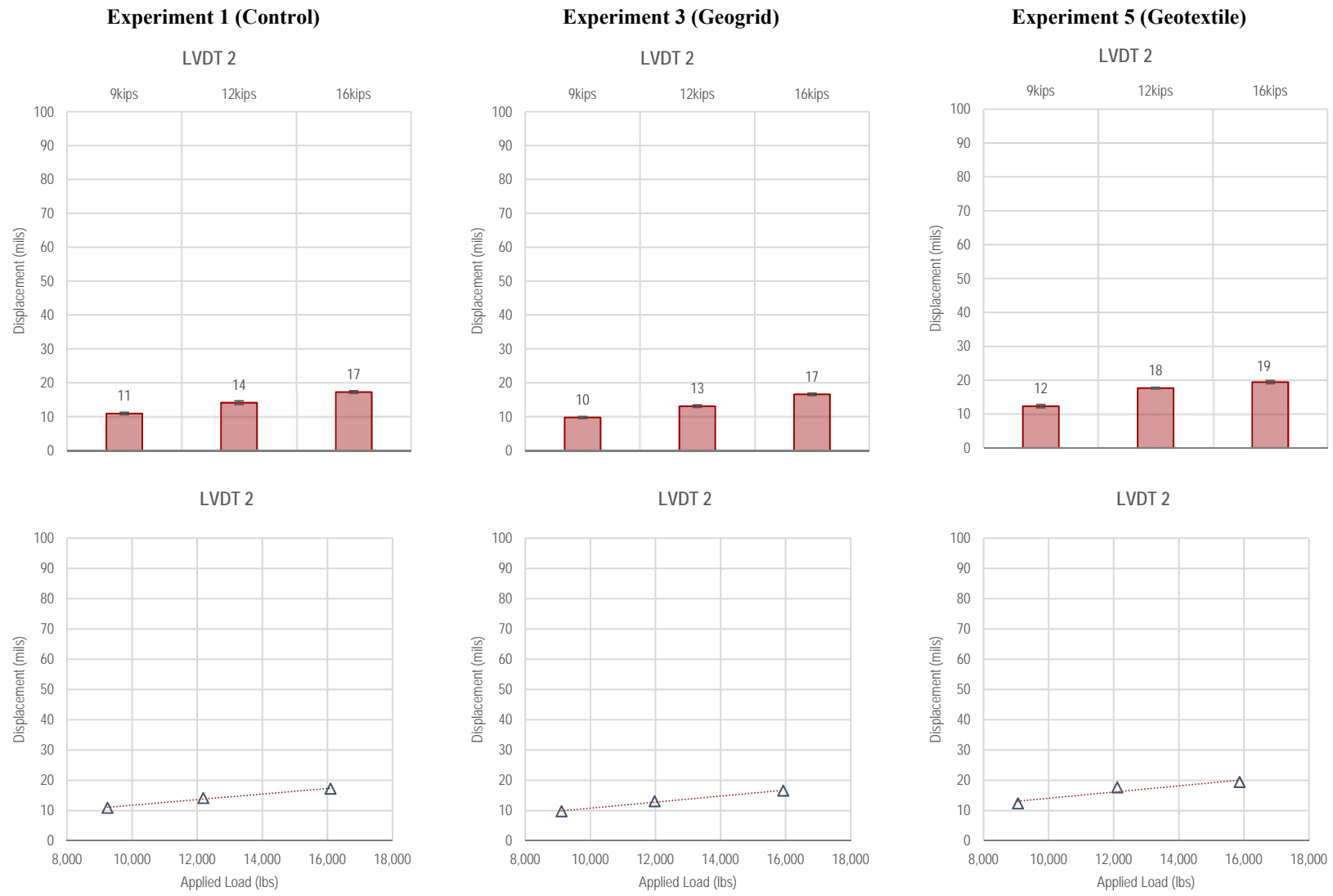


Figure F1- 2. Summary of LVDT 2 measurements—Dynamic Loading

F-4

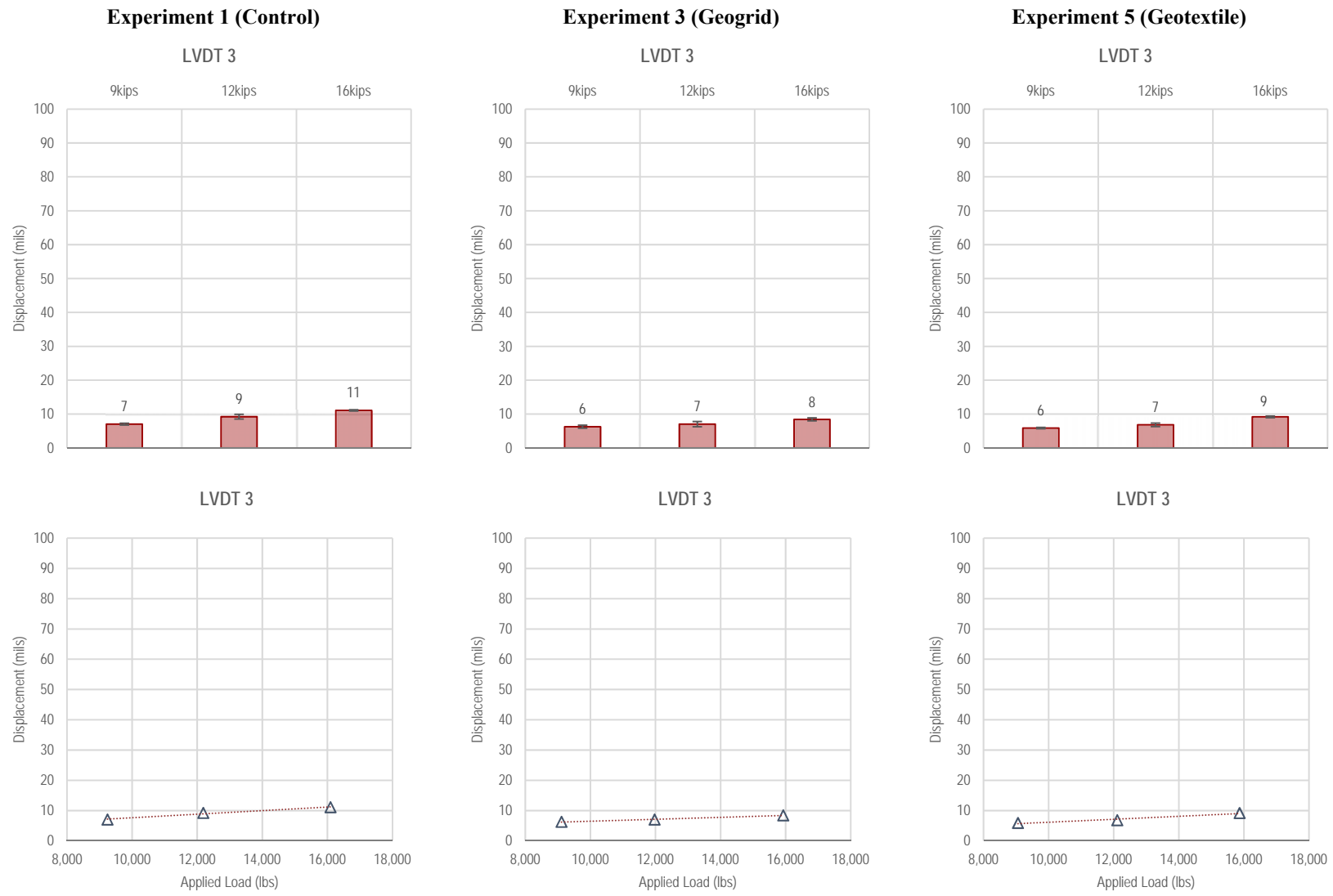


Figure F1-3. Summary of LVDT 3 measurements—Dynamic Loading

F-5

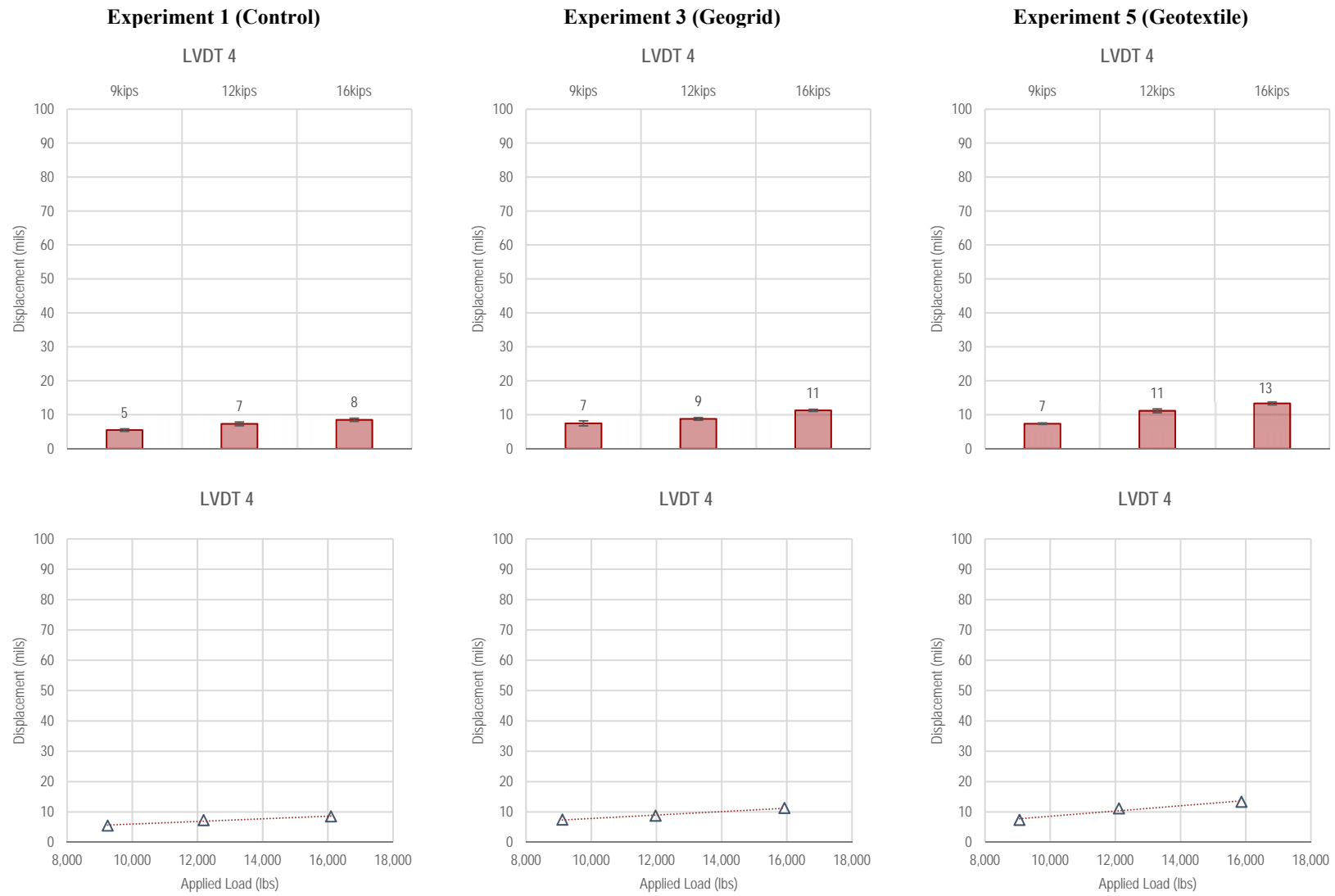


Figure F1-4. Summary of LVDT 4 measurements—Dynamic Loading

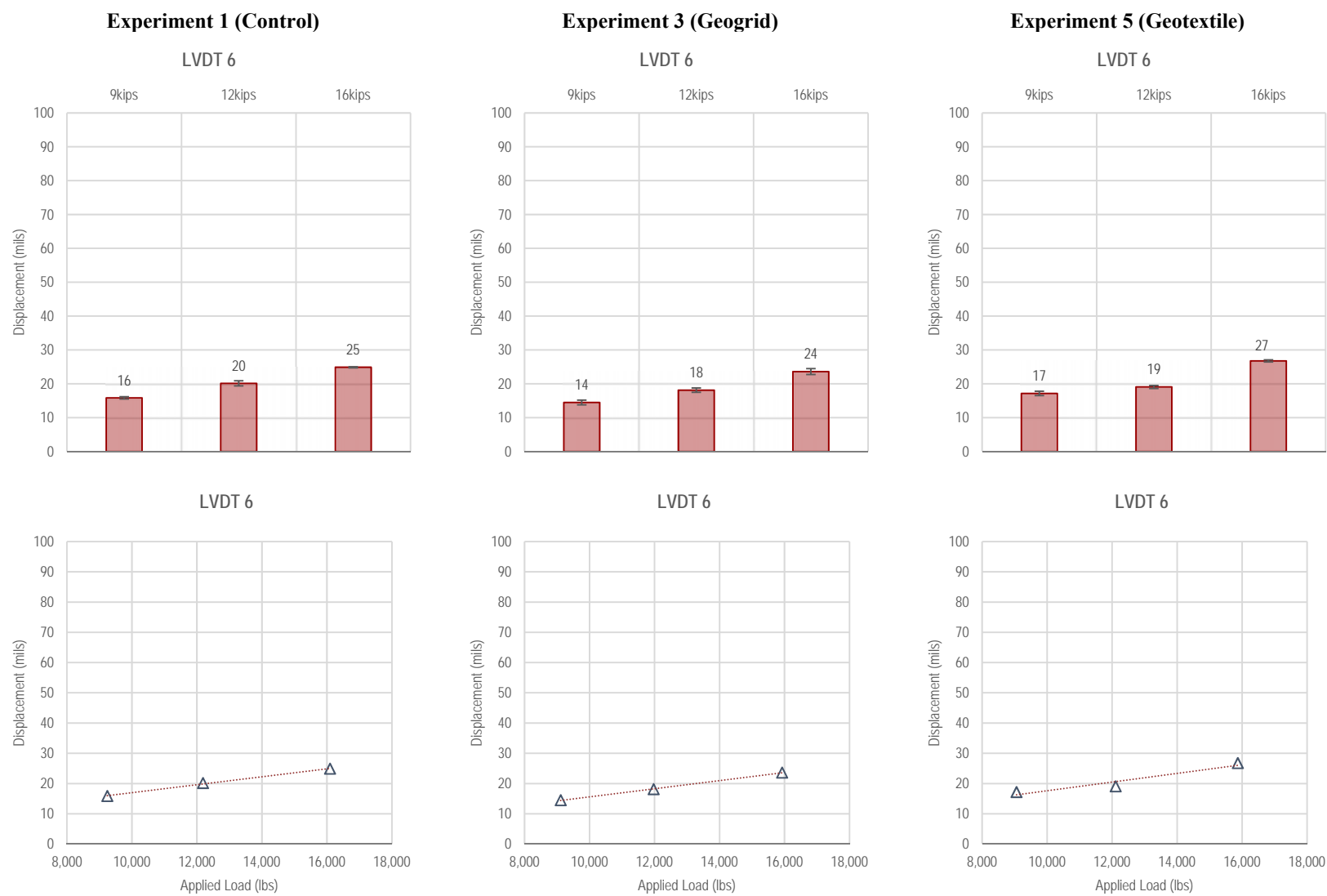


Figure F1-5. Summary of LVDT 6 measurements—Dynamic Loading

F-7

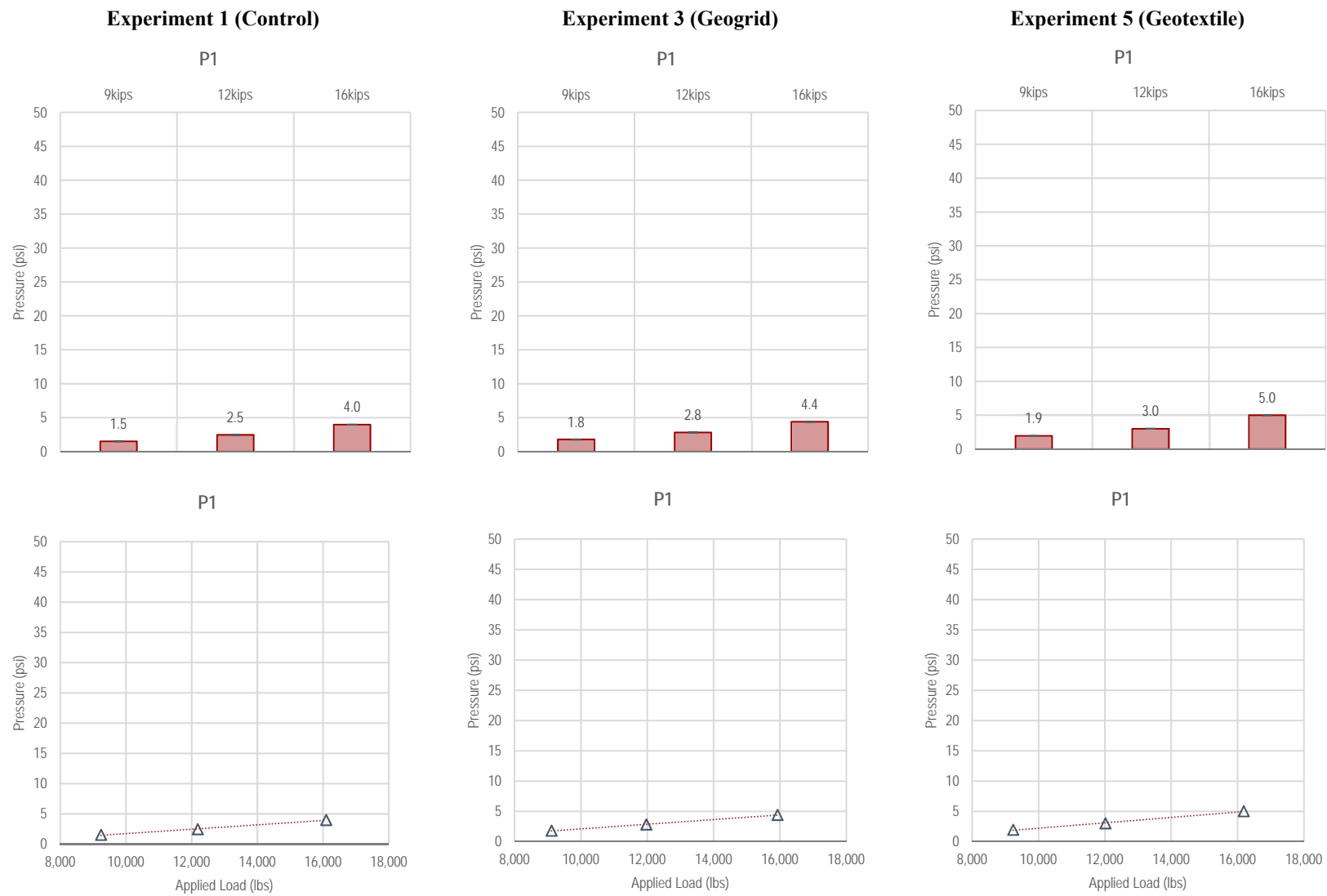


Figure F1-6. Summary of P1 measurements—Dynamic Loading

F-8

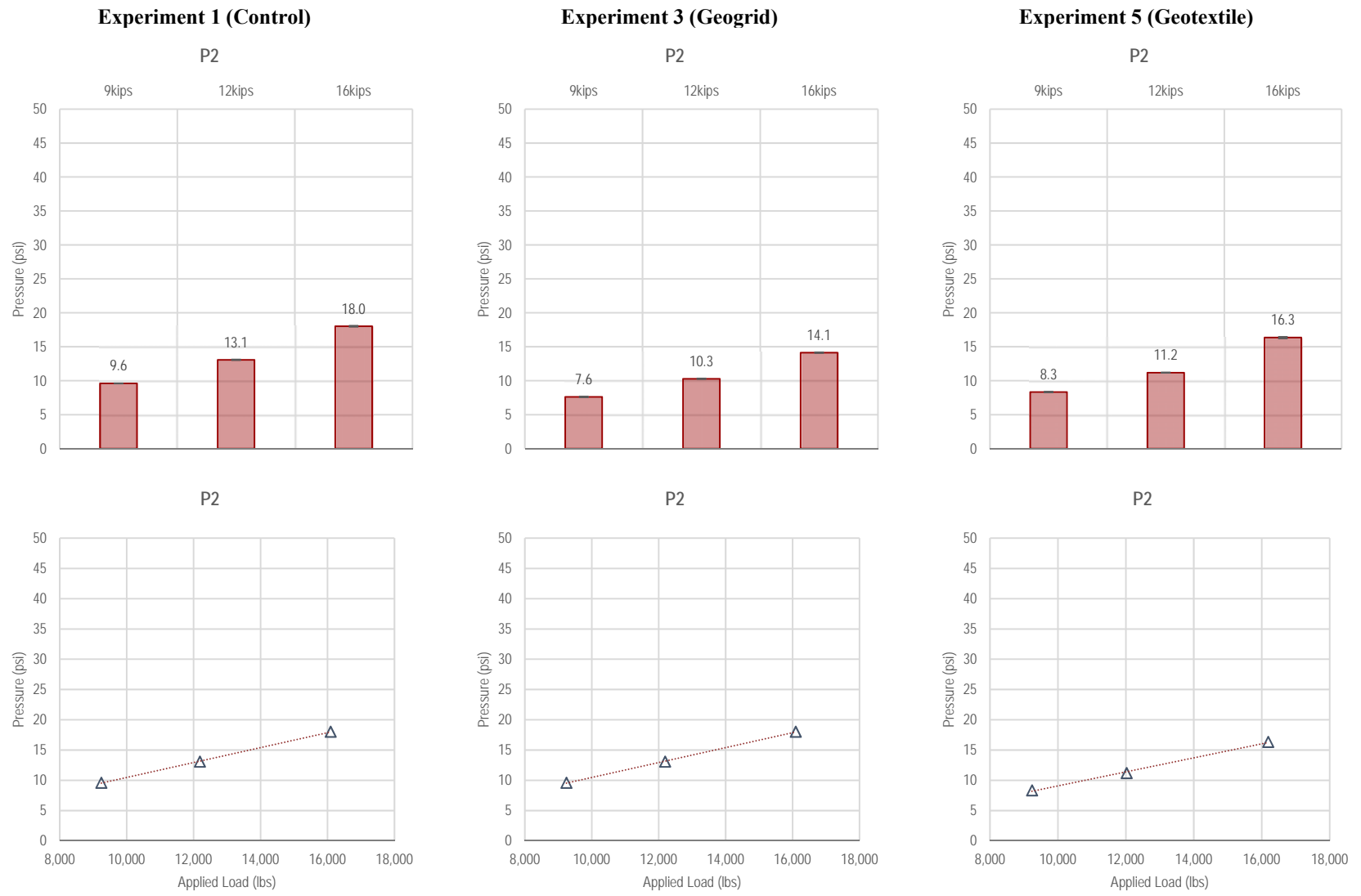


Figure F1-7. Summary of P2 measurements—Dynamic Loading

F-9

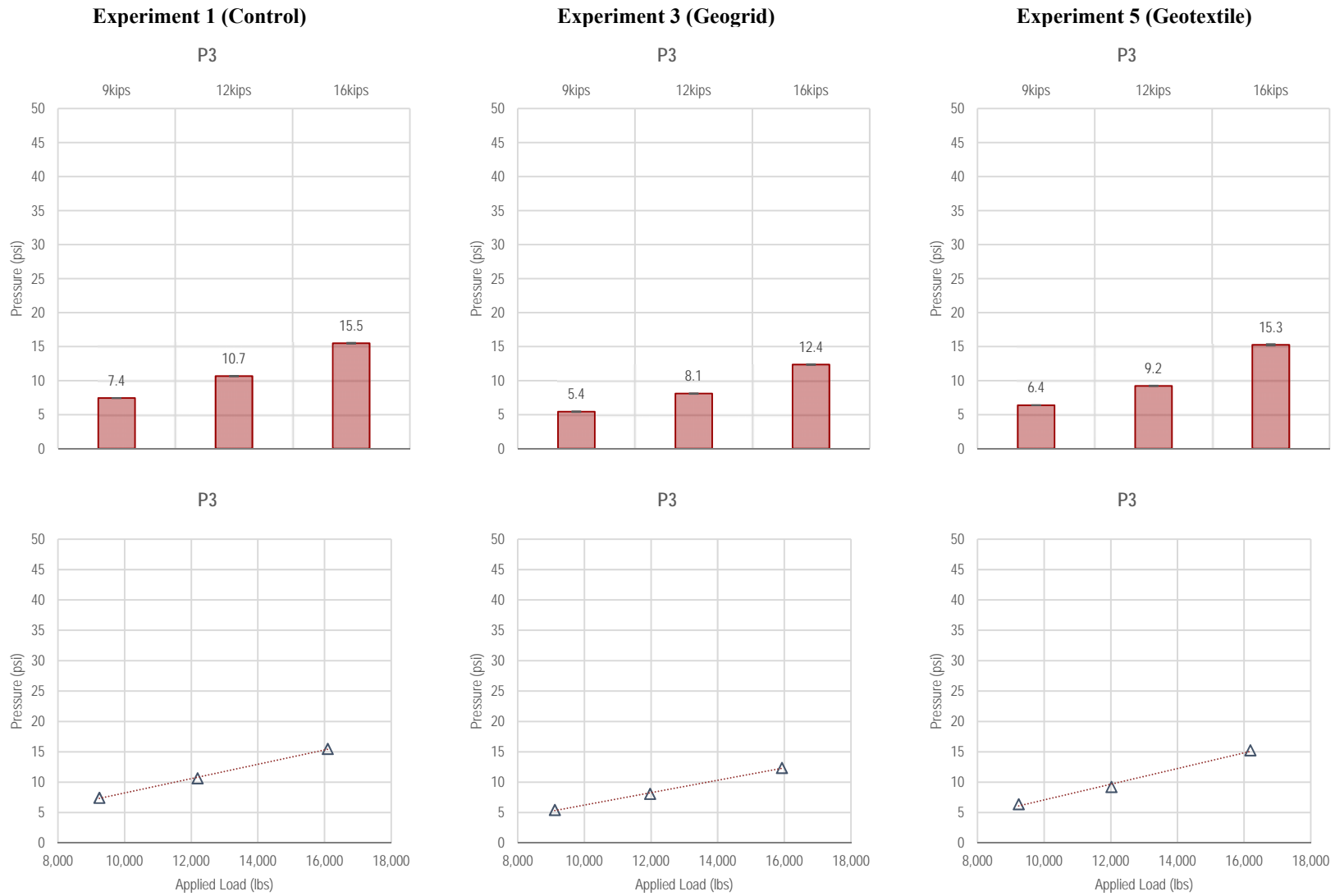


Figure F1-8. Summary of P3 measurements—Dynamic Loading

F-10

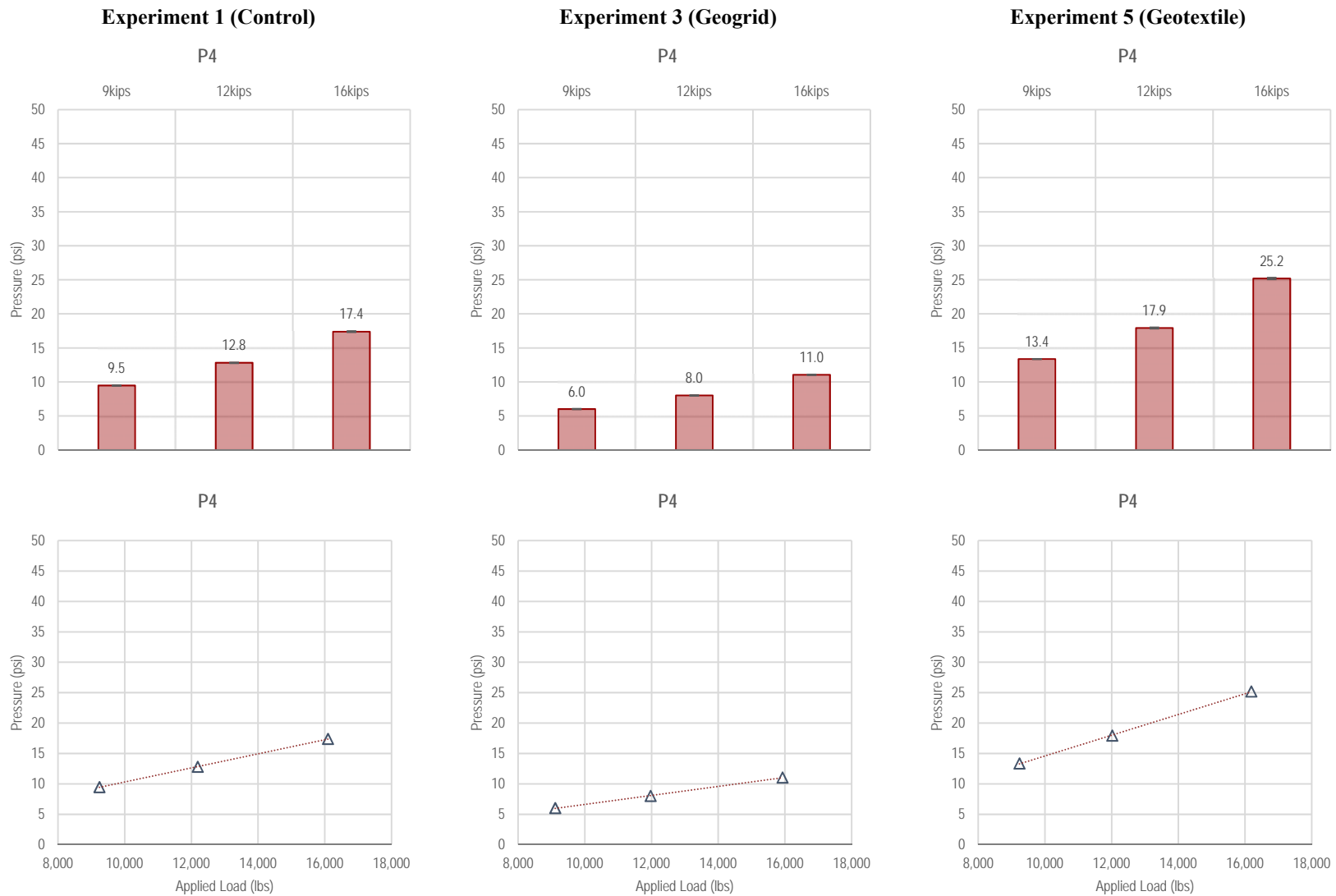


Figure F1-9. Summary of P4 measurements—Dynamic Loading

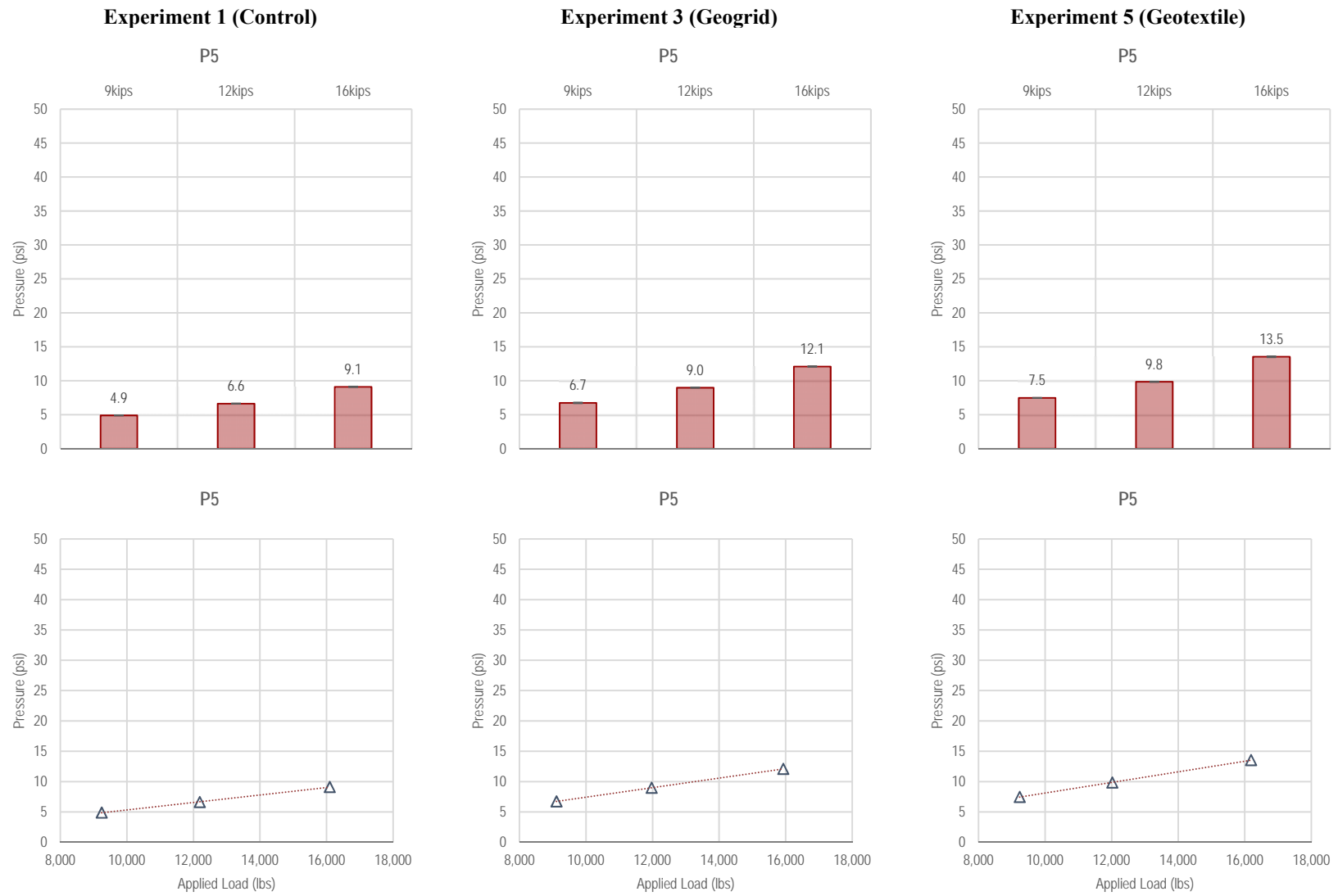


Figure F1-10. Summary of P5 measurements—Dynamic Loading

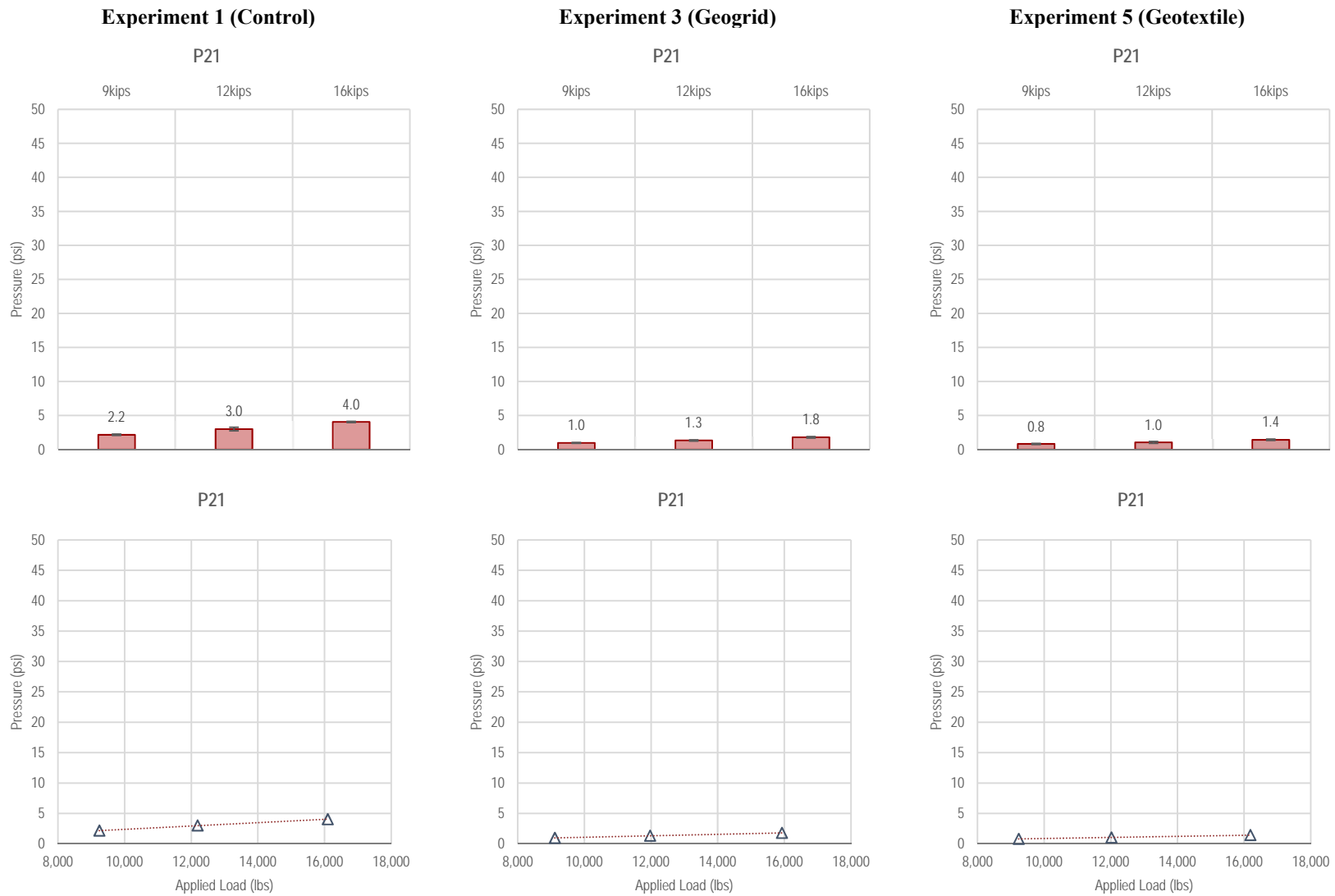


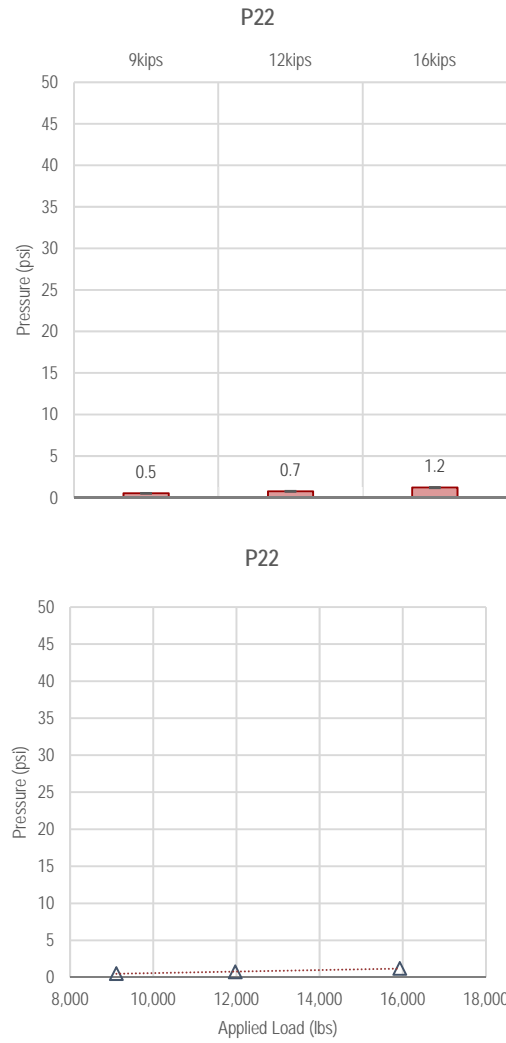
Figure F1-11. Summary of P21 measurements—Dynamic Loading

F-14

Experiment 1 (Control)

Not Available

Experiment 3 (Geogrid)



Experiment 5 (Geotextile)

Not Available

Not Available

Figure F1-12. Summary of P22 measurements—Dynamic Loading

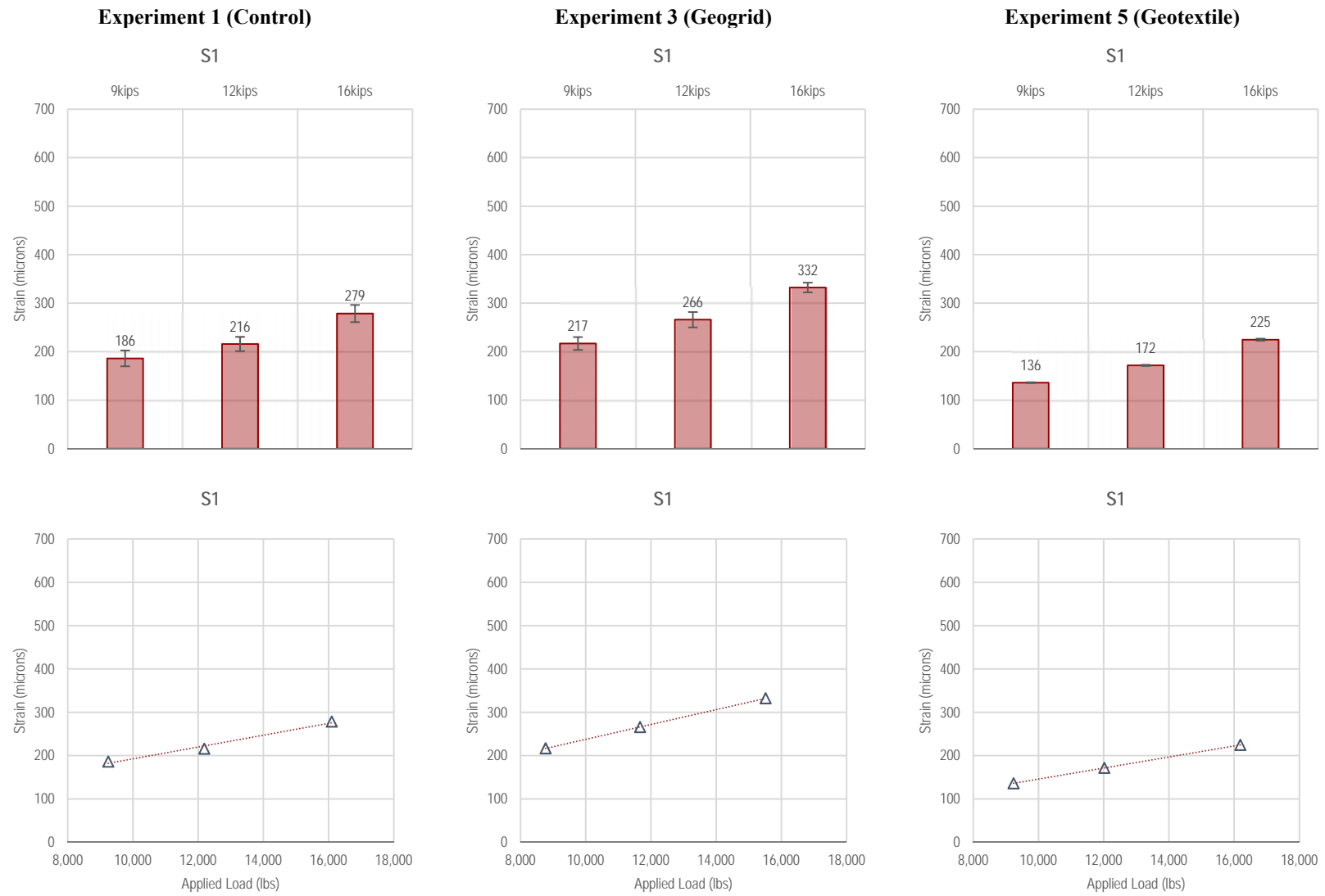


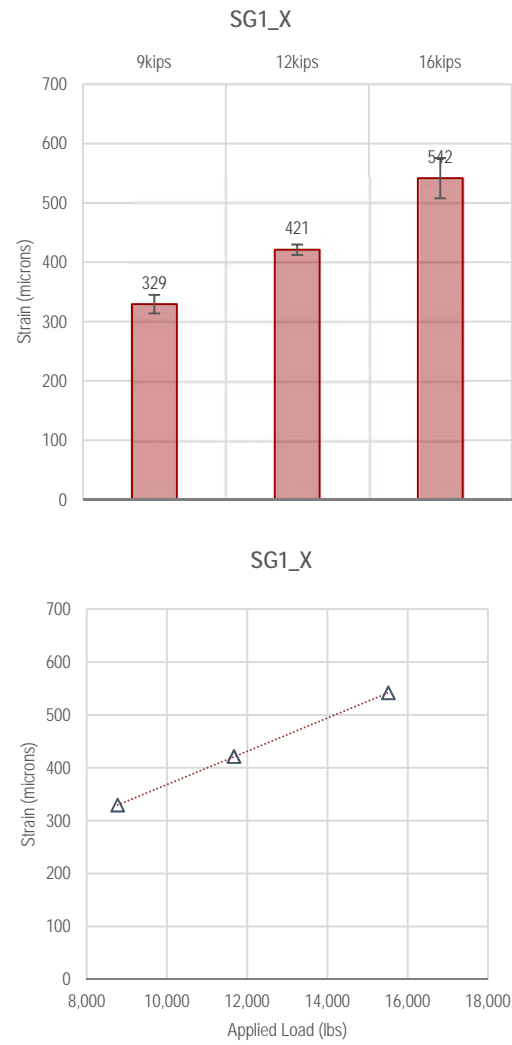
Figure F1-13. Summary of S1 measurements—Dynamic Loading

F-15

Experiment 1 (Control)

Not Available

Experiment 3 (Geogrid)



Experiment 5 (Geotextile)

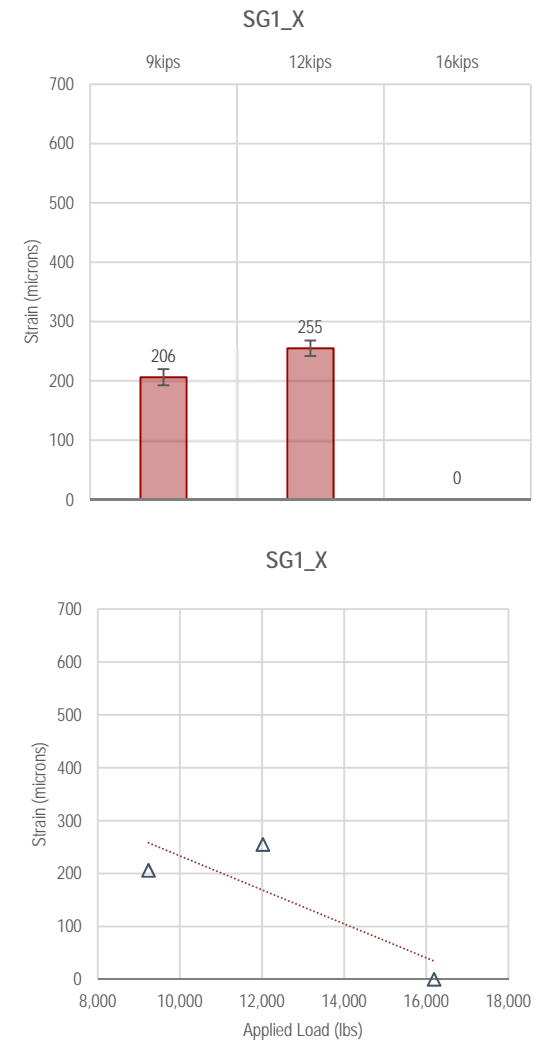
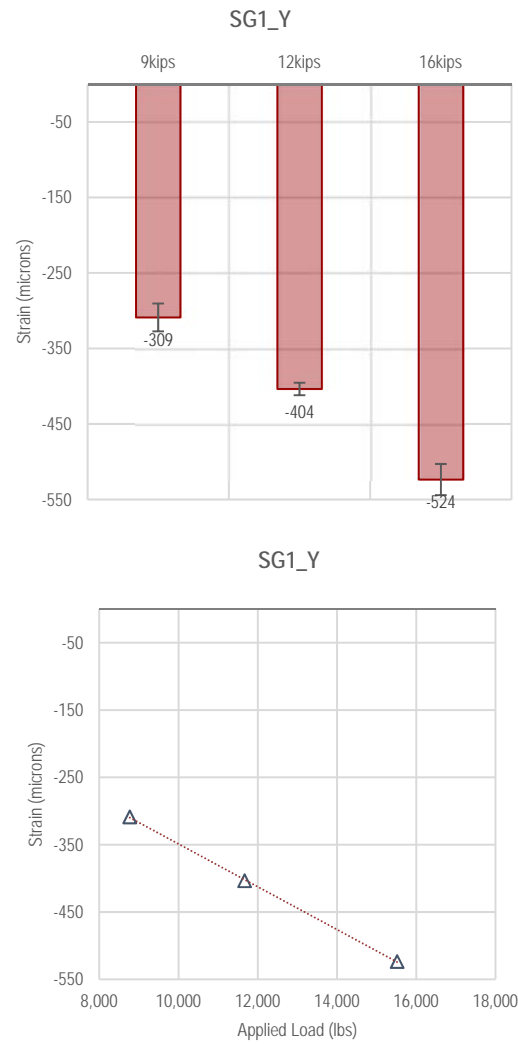


Figure F1-14. Summary of SG1_X measurements—Dynamic Loading

Experiment 1 (Control)

Not Available

Experiment 3 (Geogrid)



Experiment 5 (Geotextile)

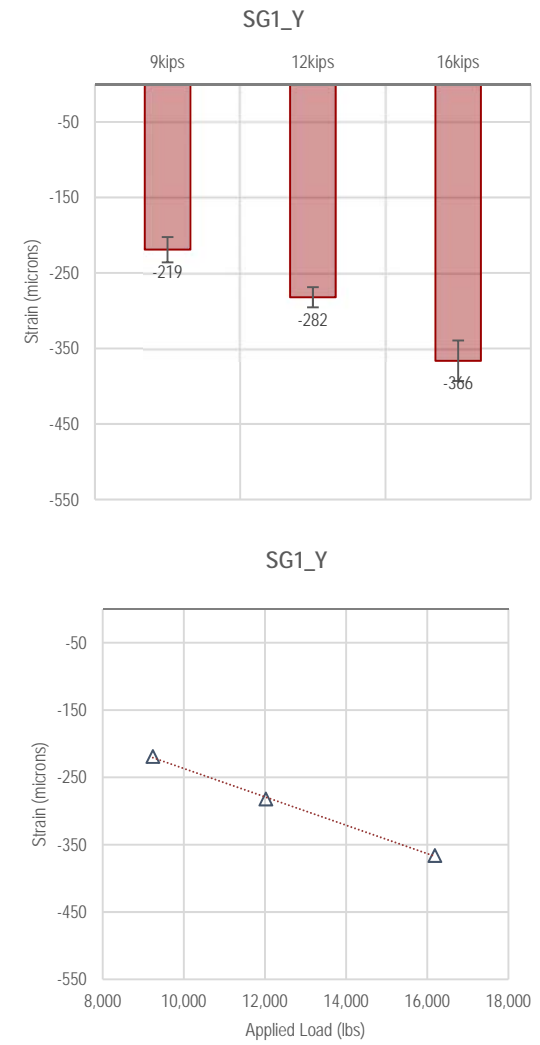
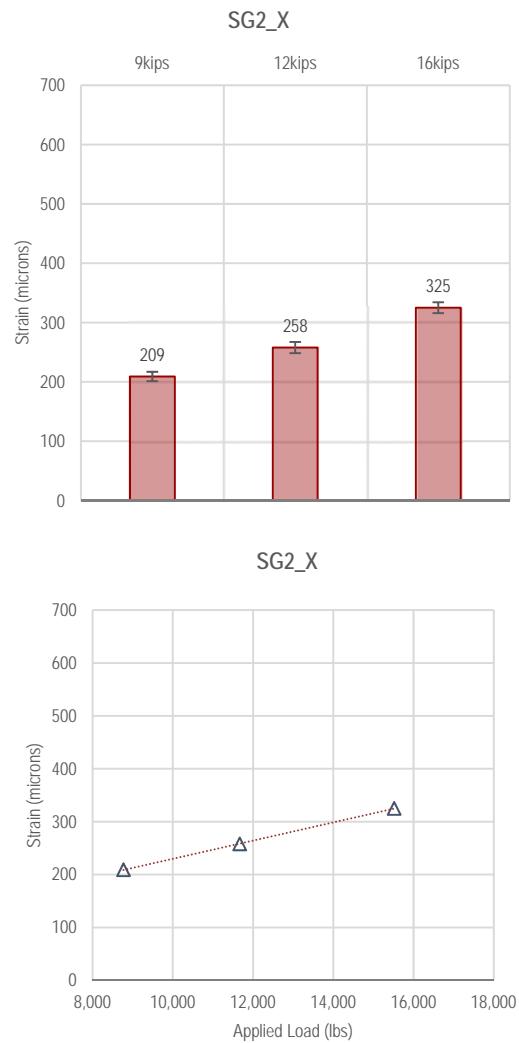


Figure F1-15. Summary of SG1_Y measurements—Dynamic loading

Experiment 1 (Control)

Not Available

Experiment 3 (Geogrid)



Experiment 5 (Geotextile)



Not Available

Figure F1-16. Summary of SG2_X measurements—Dynamic Loading

F-19

Experiment 1 (Control)

Not Available

Not Available

Experiment 3 (Geogrid)

Not Available

Not Available

Experiment 5 (Geotextile)

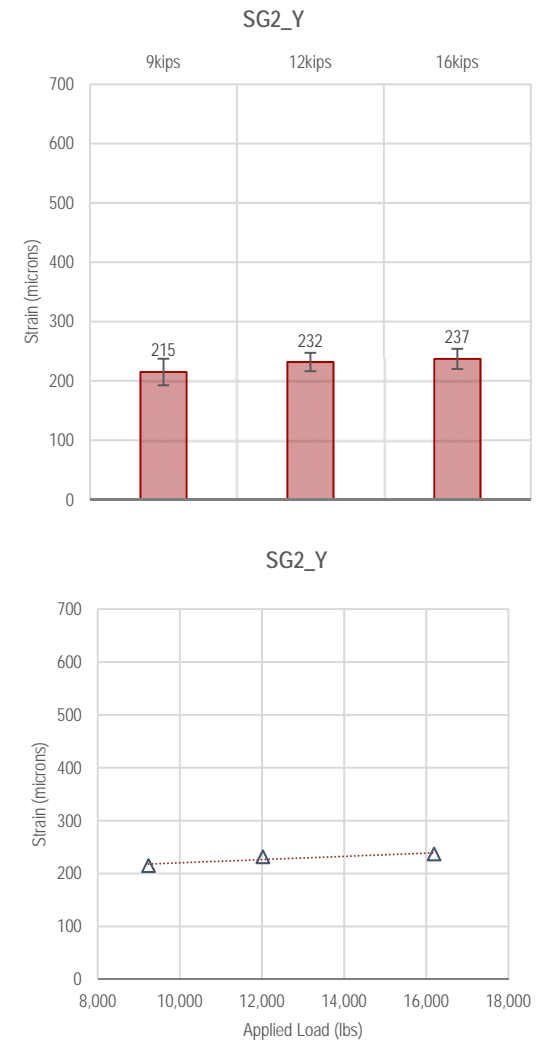


Figure F1-17. Summary of SG2_Y measurements—Dynamic Loading

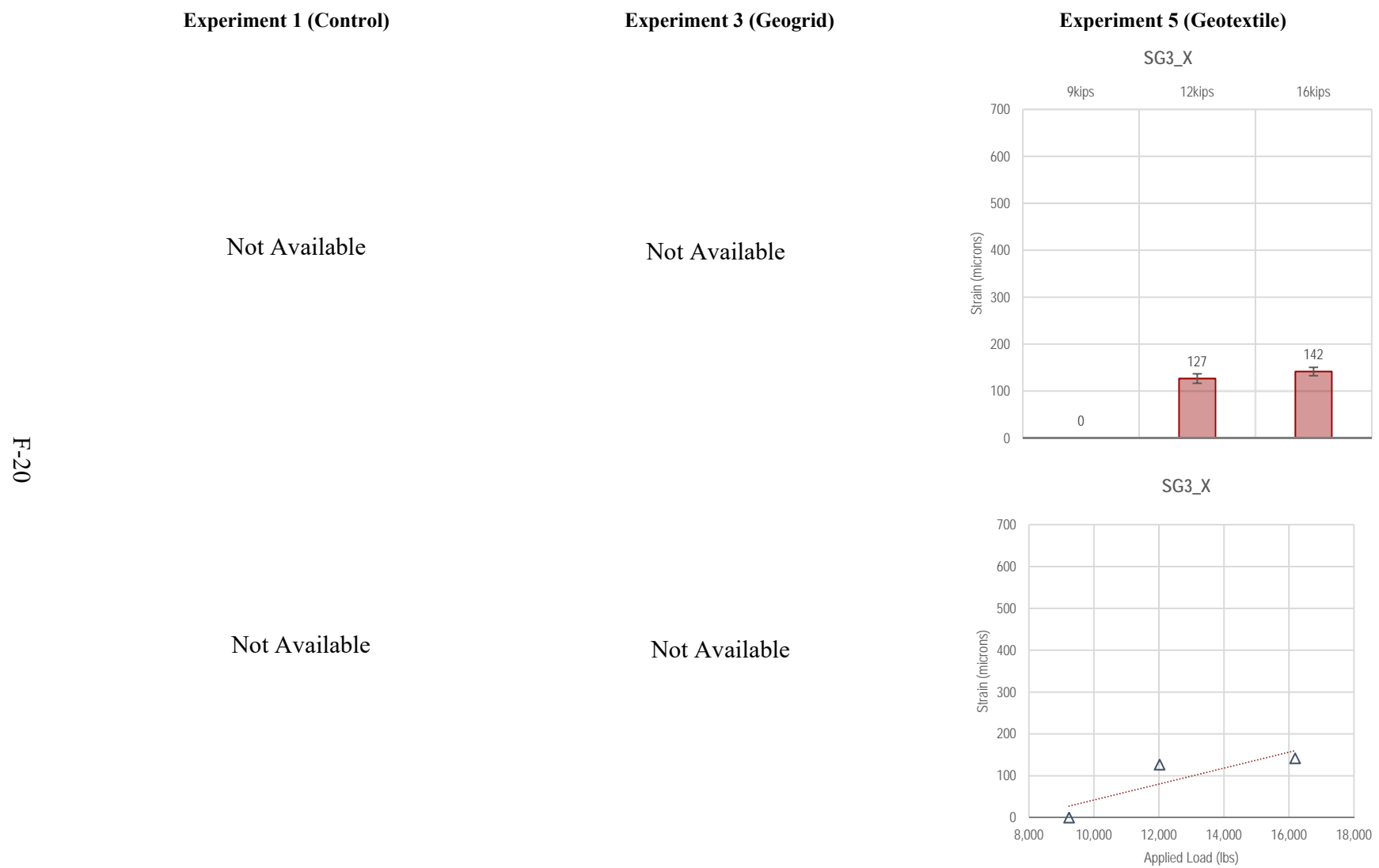


Figure F1-18. Summary of SG3_X measurements—Dynamic Loading

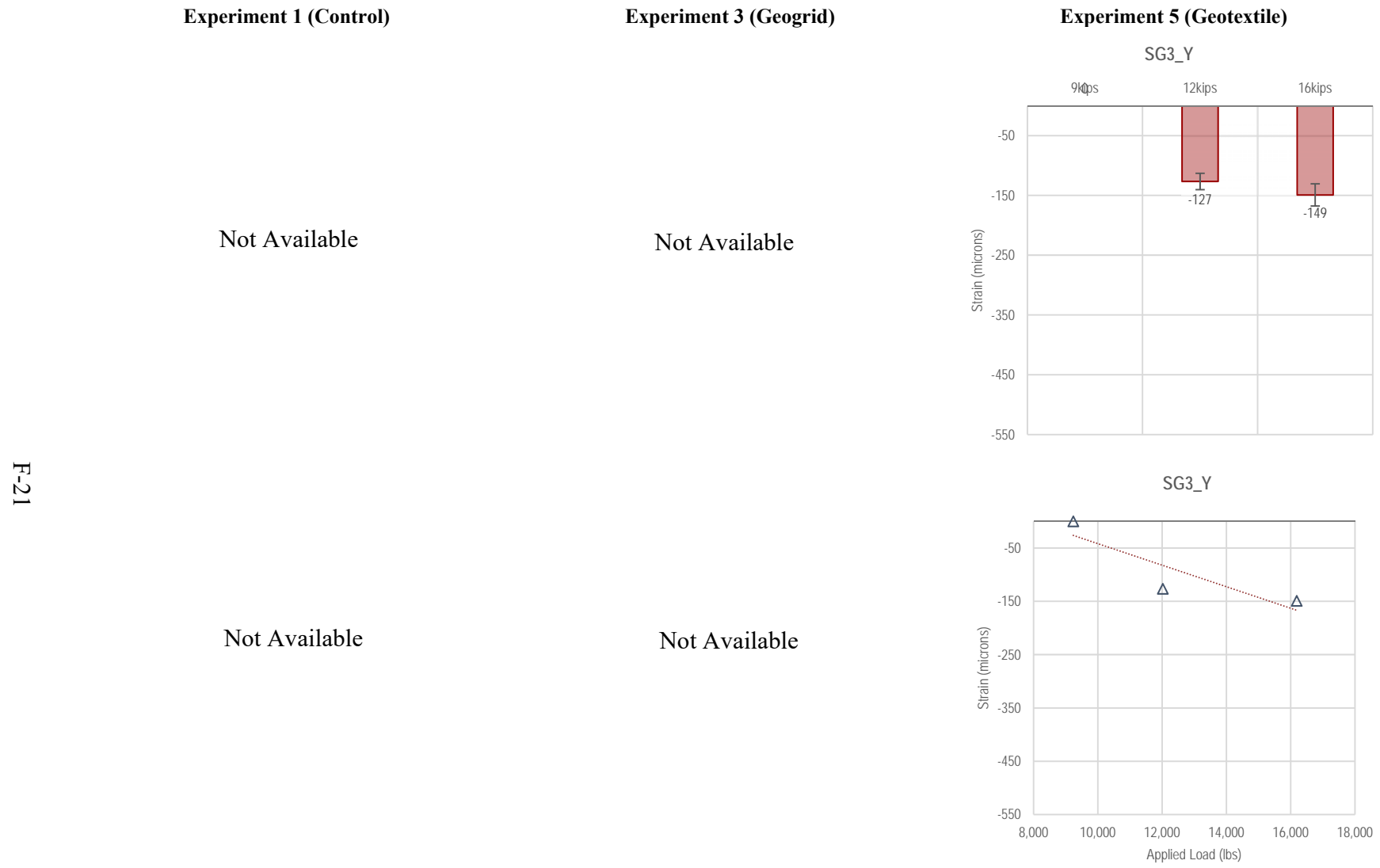


Figure F1-19. Summary of SG3_Y measurements—Dynamic Loading

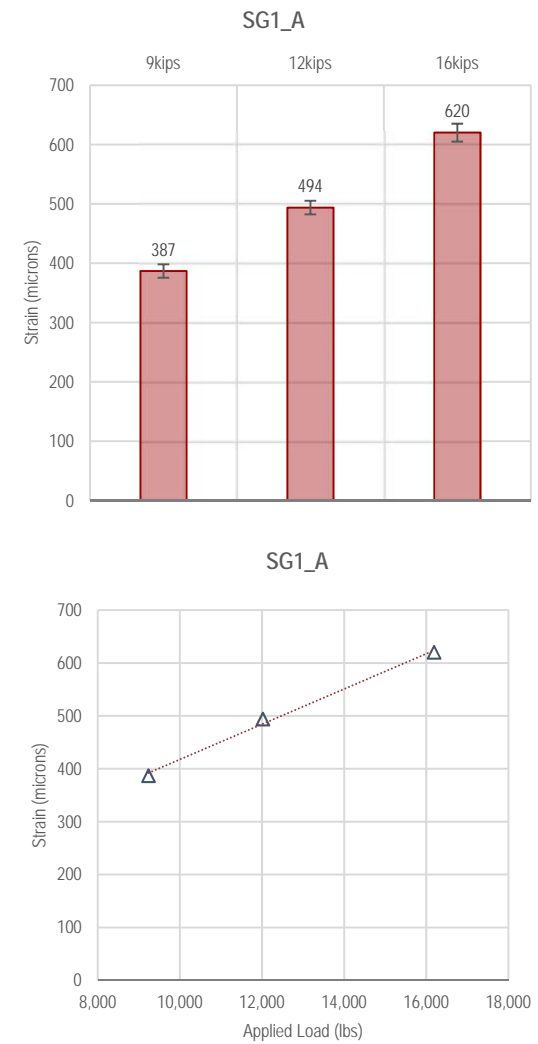
Experiment 1 (Control)

Experiment 3 (Geogrid)

Experiment 5 (Geotextile)

Not Available

Not Available



Not Available

Not Available

Figure F1-20. Summary of SG1_A measurements—Dynamic Loading

F-23

Experiment 1 (Control)

Not Available

Experiment 3 (Geogrid)

Not Available

Experiment 5 (Geotextile)

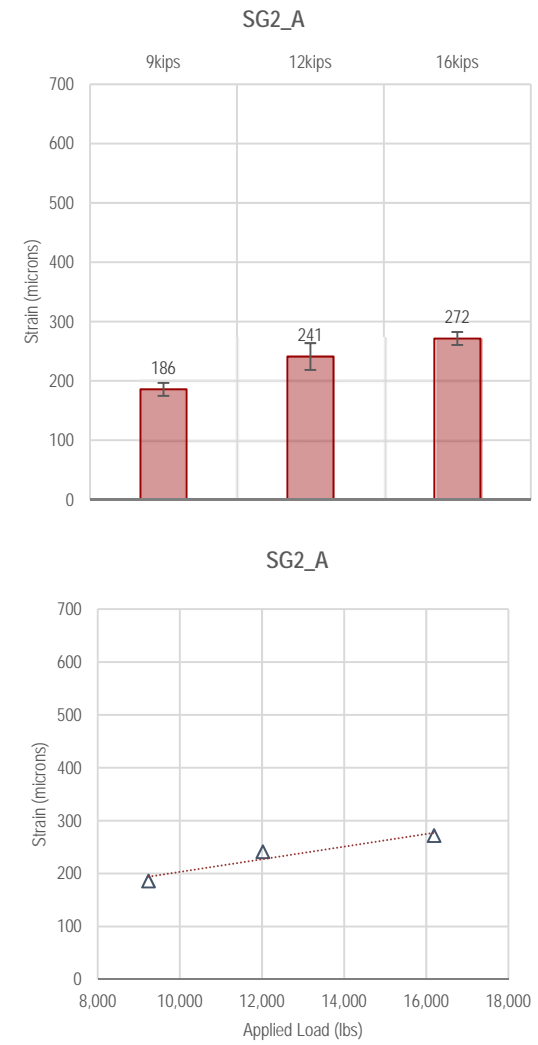


Figure F1-21. Summary of SG2_A measurements—Dynamic Loading

Experiment 1 (Control)

Experiment 3 (Geogrid)

Experiment 5 (Geotextile)

Not Available

Not Available

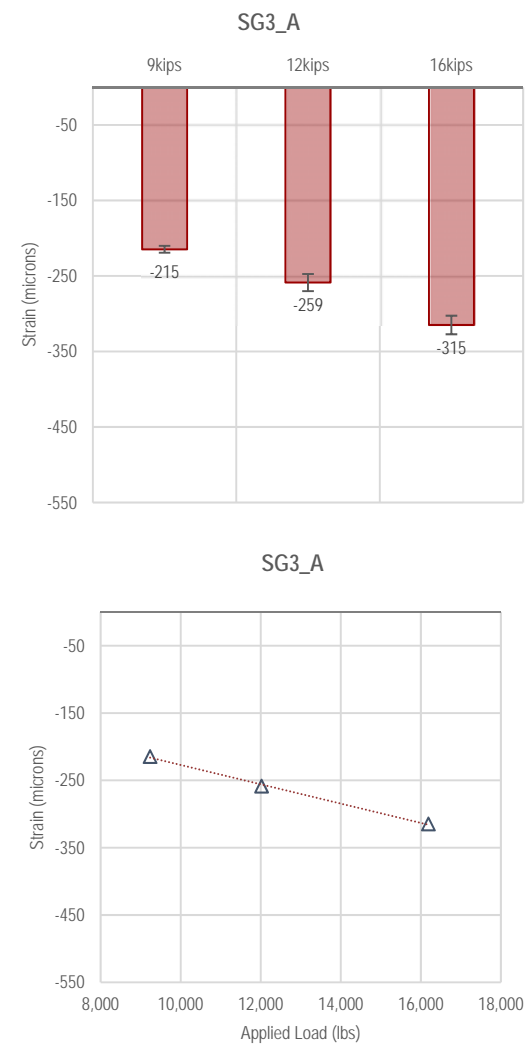


Figure F1-22. Summary of SG3_A measurements—Dynamic Loading

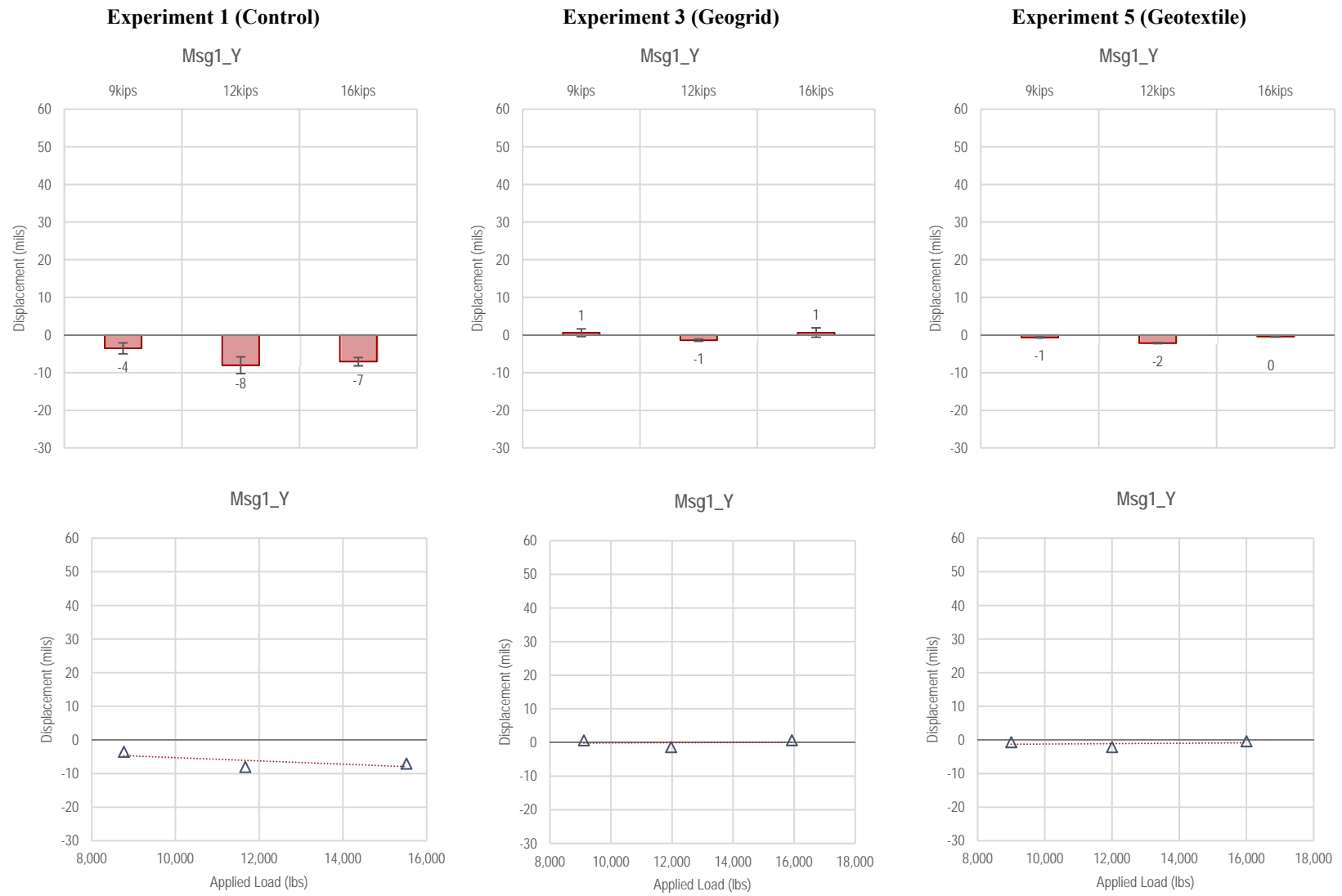


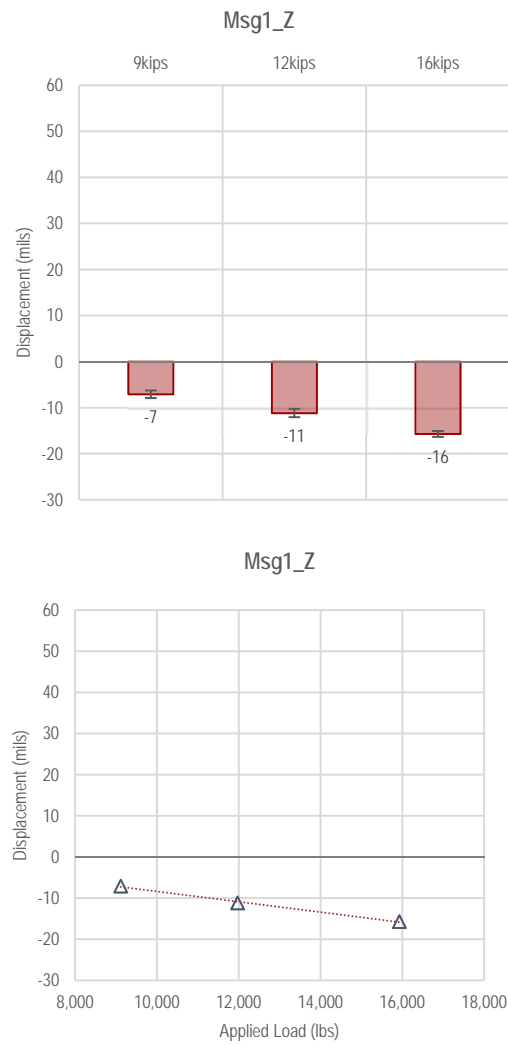
Figure F1-23. Summary of Msg1_Y measurements—Dynamic Loading

F-25

Experiment 1 (Control)

Not Available

Experiment 3 (Geogrid)



Experiment 5 (Geotextile)

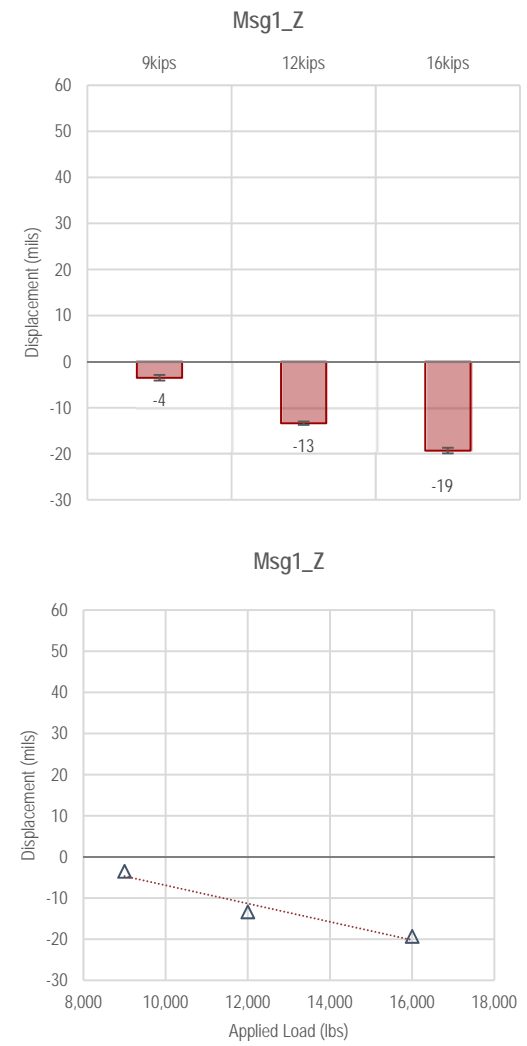


Figure F1-24. Summary of Msg1_Z measurements—Dynamic Loading

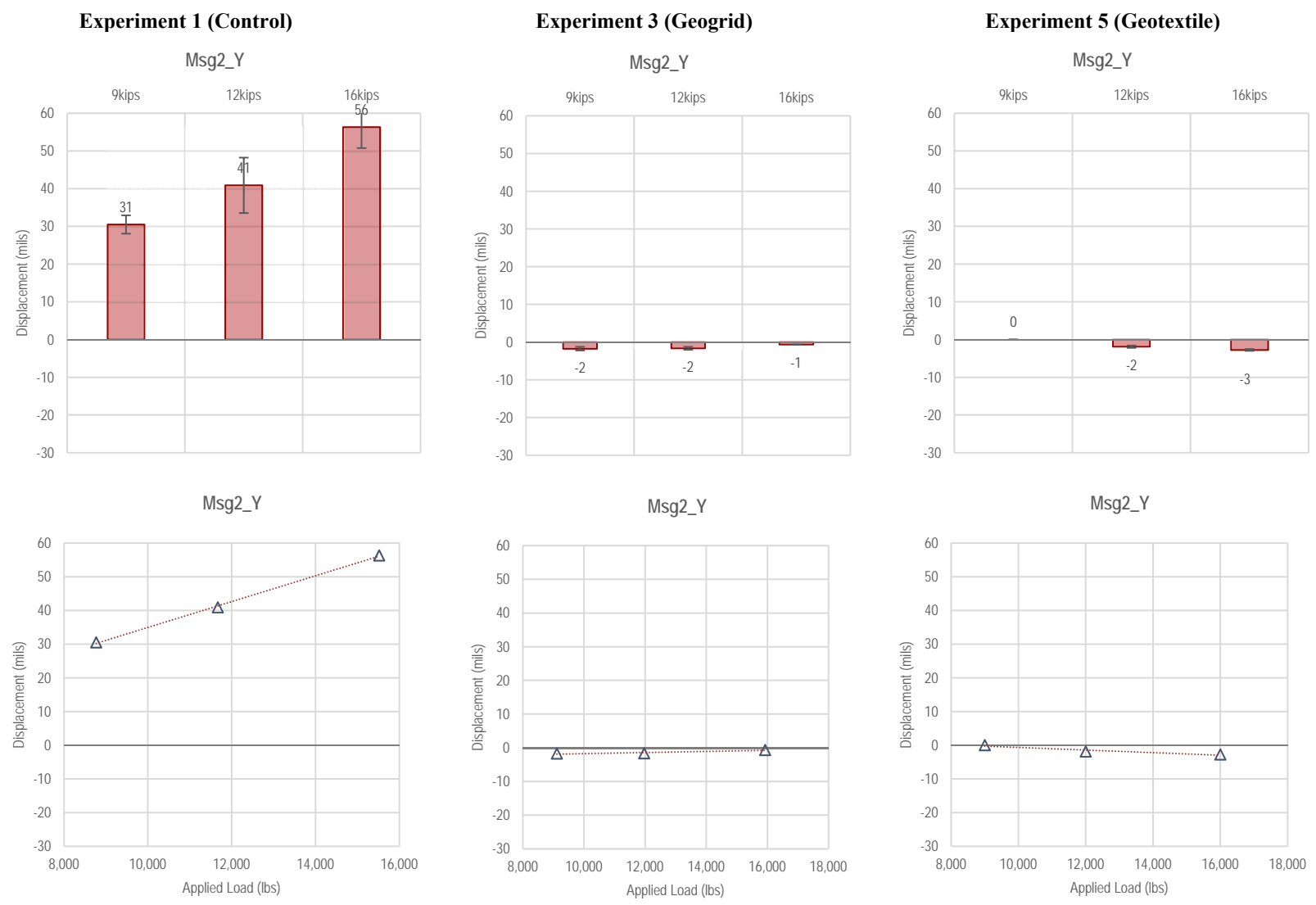
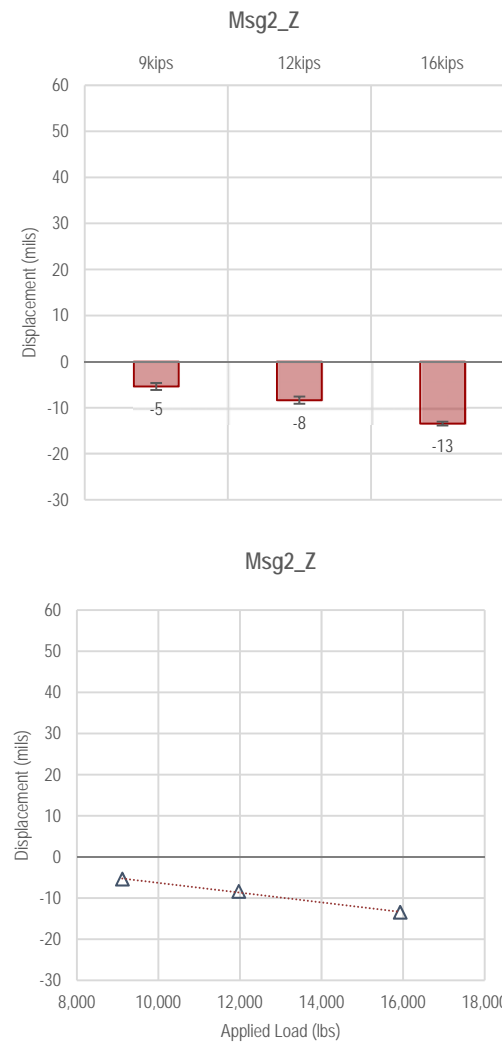


Figure F1-25. Summary of Msg2_Y measurements—Dynamic Loading

Experiment 1 (Control)

Not Available

Experiment 3 (Geogrid)



Experiment 5 (Geotextile)

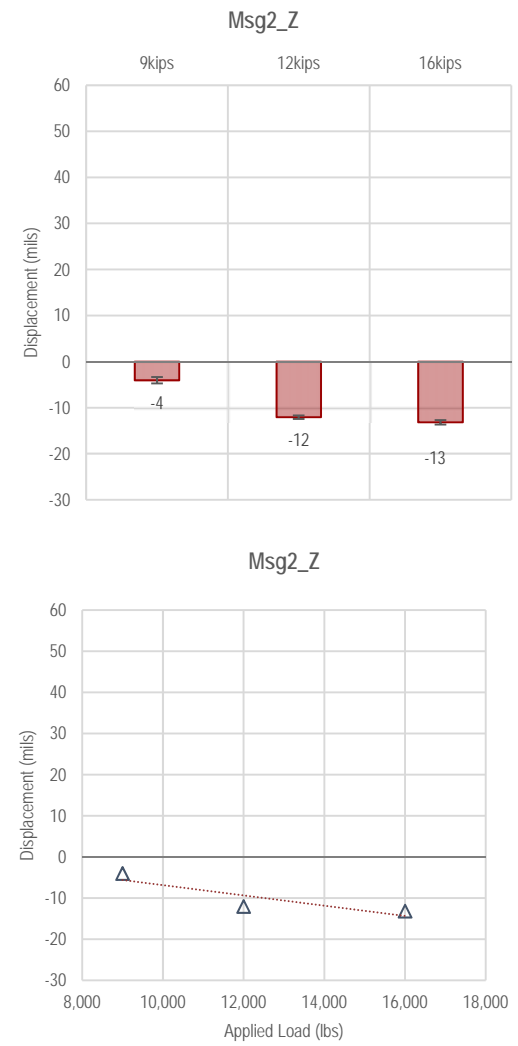


Figure F1-26. Summary of Msg2_Z measurements—Dynamic Loading

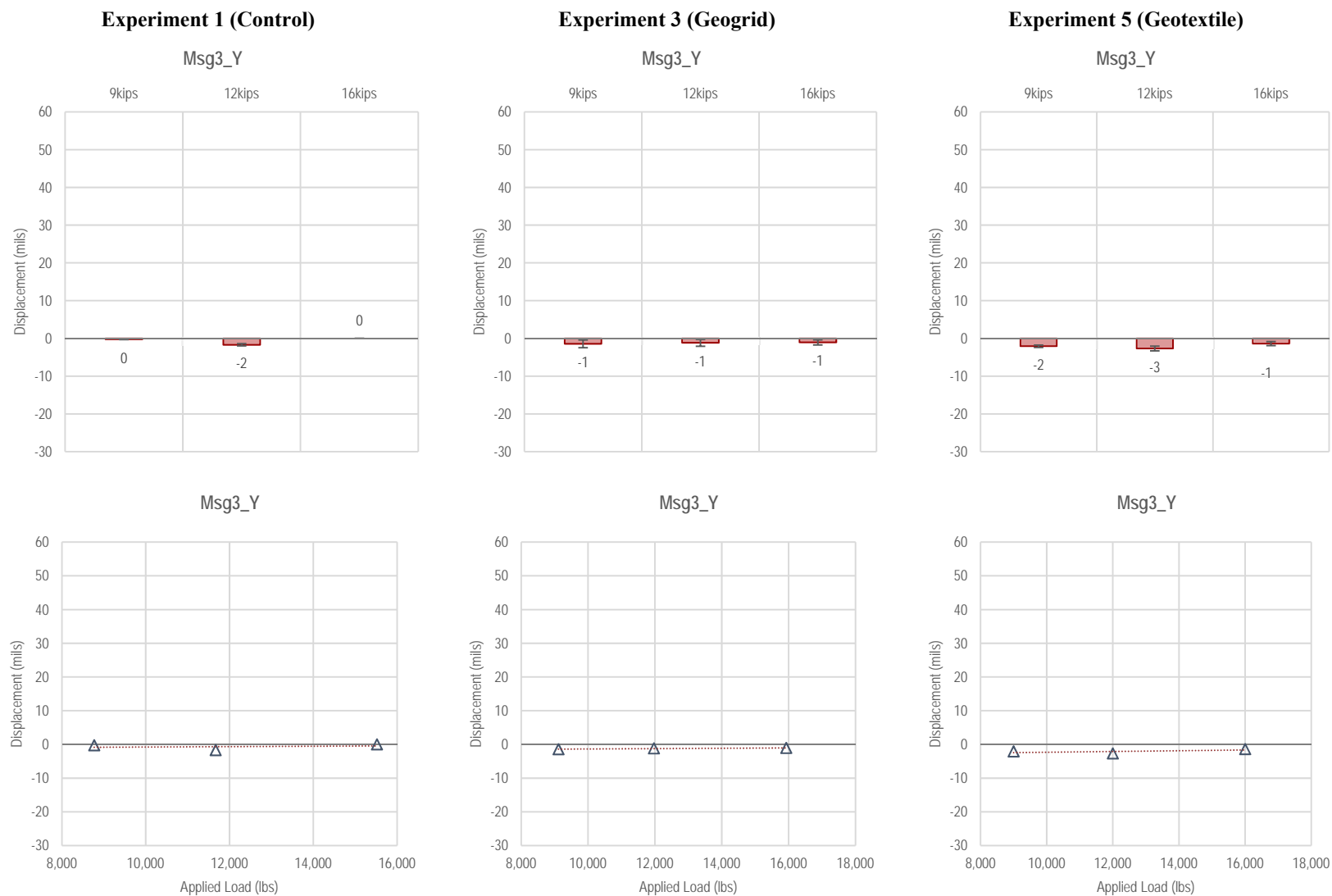


Figure F1-27. Summary of Msg3_Y measurements—Dynamic Loading

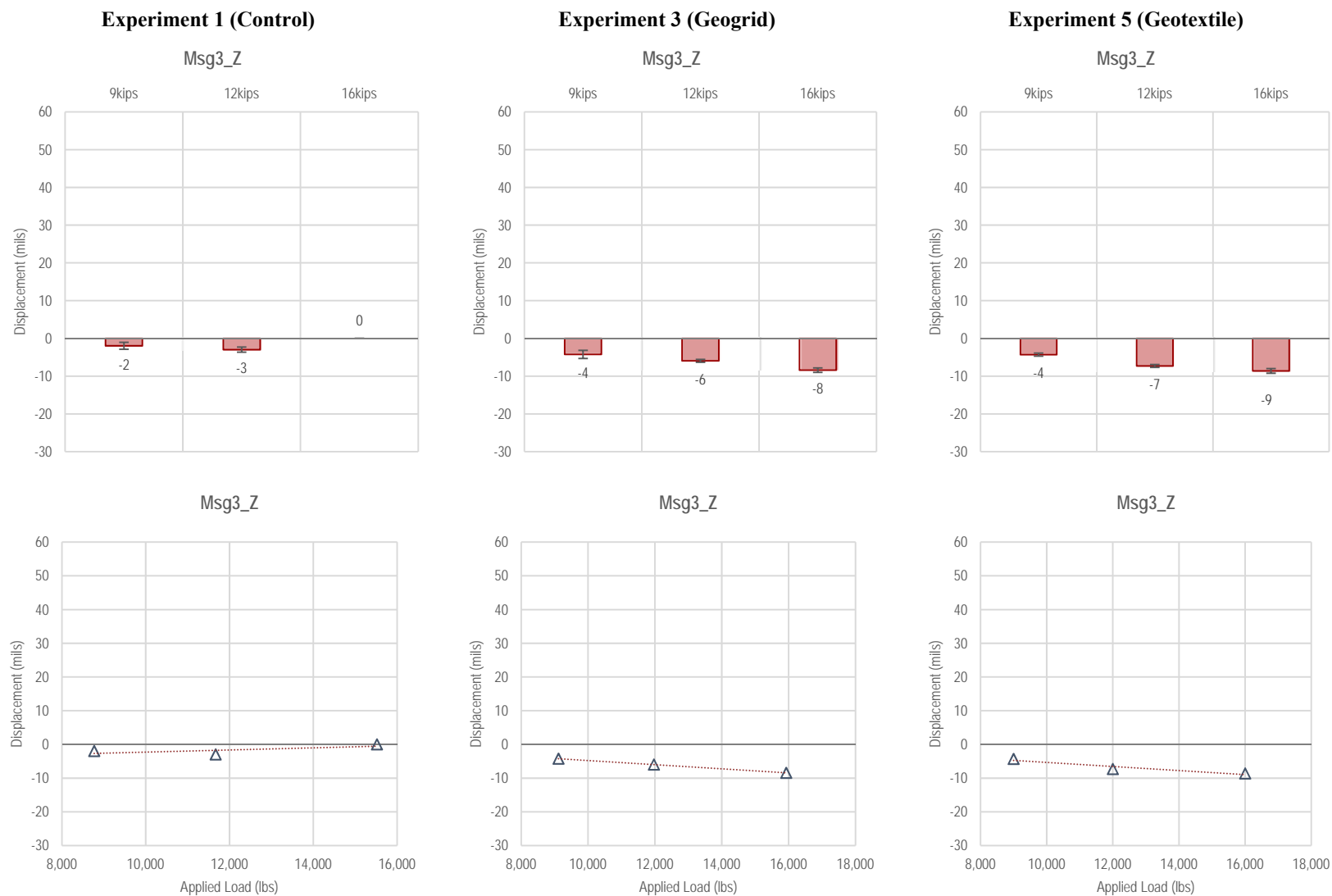


Figure F1-28. Summary of Msg3_Z measurements—Dynamic Loading

F-30

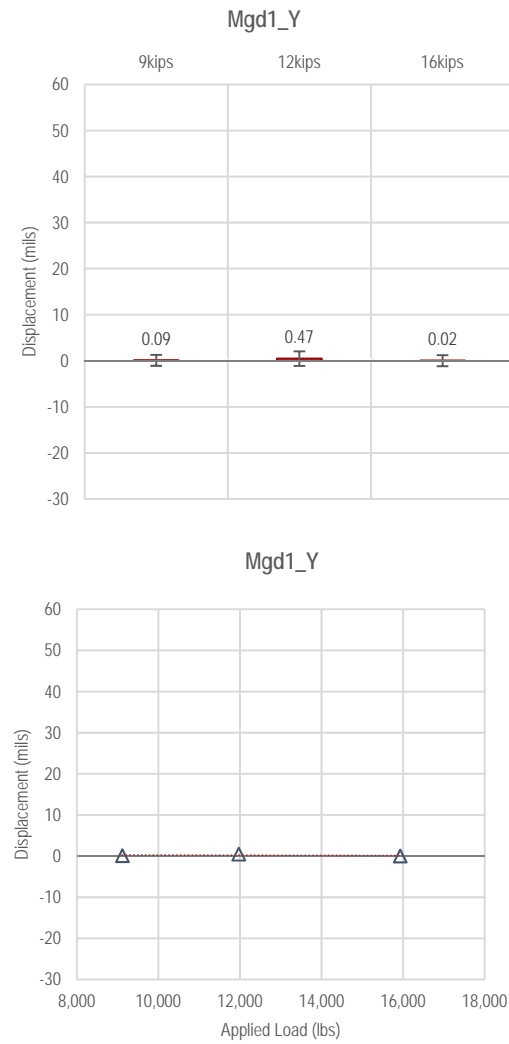
F-31

Experiment 1 (Control)

Not Available

Not Available

Experiment 3 (Geogrid)



Experiment 5 (Geotextile)

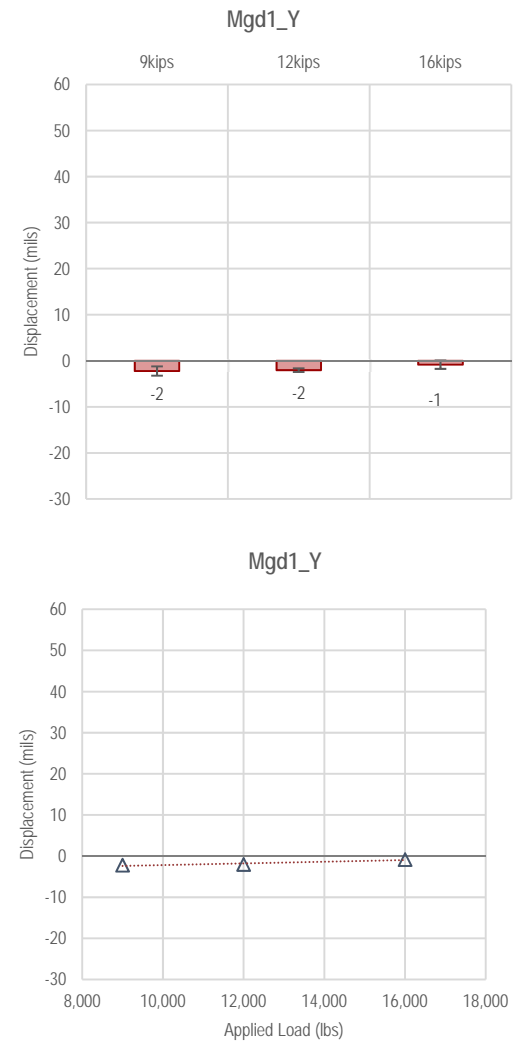
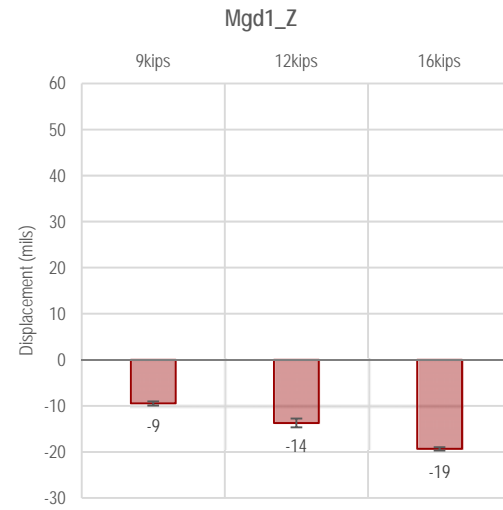


Figure F1-29. Summary of Mgd1_Y measurements—Dynamic Loading

Experiment 1 (Control)

Not Available

Experiment 3 (Geogrid)



Experiment 5 (Geotextile)

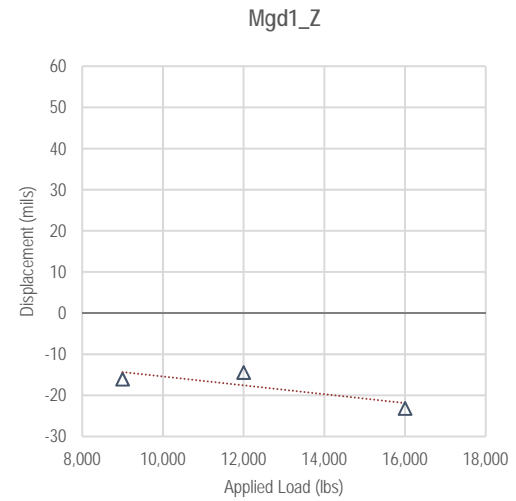
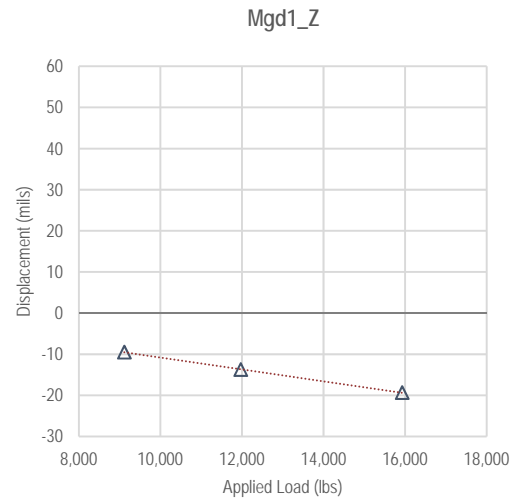
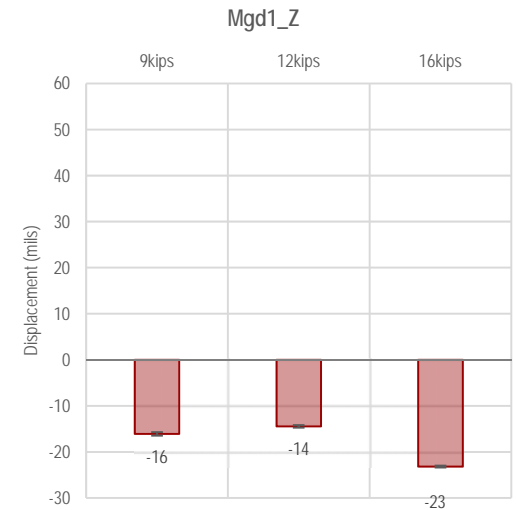
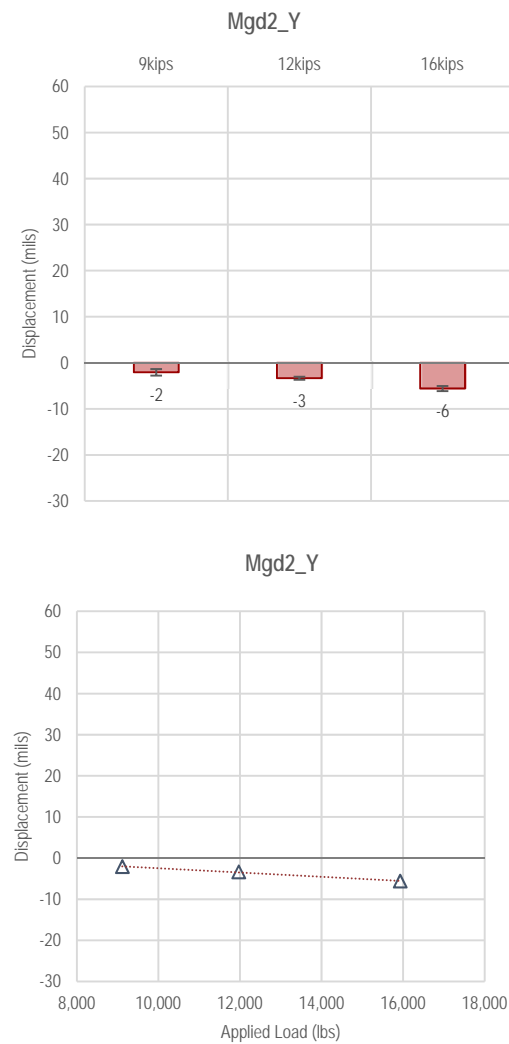


Figure F1-30. Summary of Mgd1_Z measurements—Dynamic Loading

Experiment 1 (Control)

Not Available

Experiment 3 (Geogrid)



Experiment 5 (Geotextile)

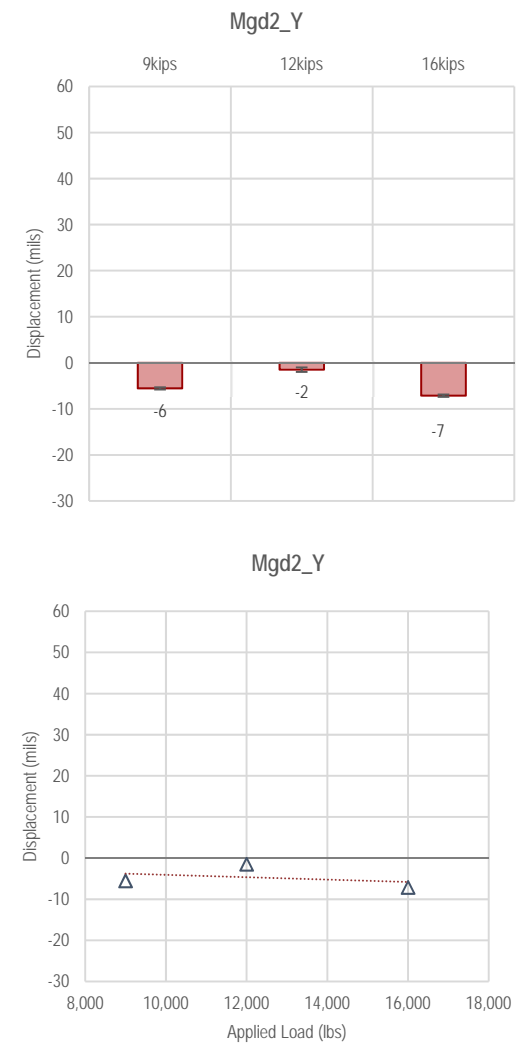
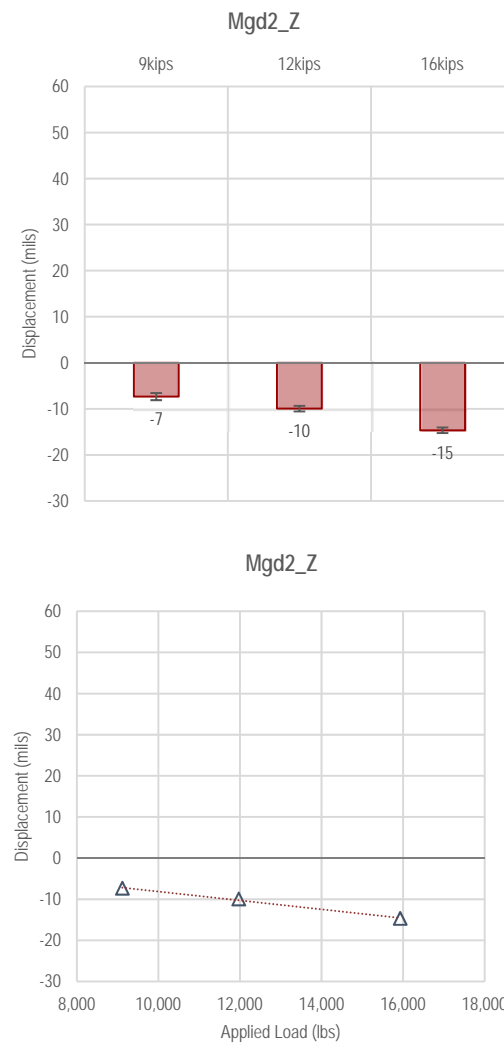


Figure F1-31. Summary of Mgd2_Y measurements—Dynamic Loading

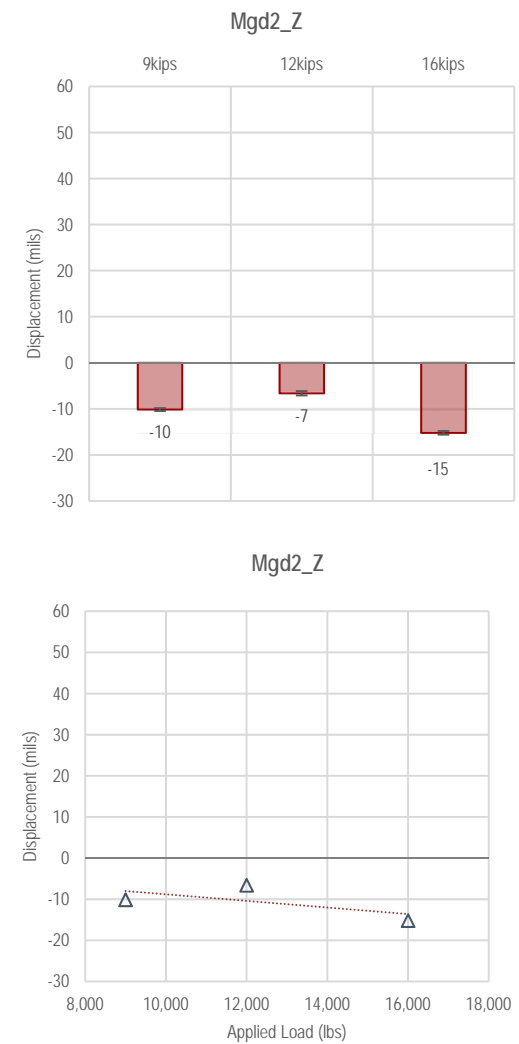
Experiment 1 (Control)

Not Available

Experiment 3 (Geogrid)



Experiment 5 (Geotextile)



Not Available

Figure F1-32. Summary of Mgd2_Z measurements—Dynamic Loading

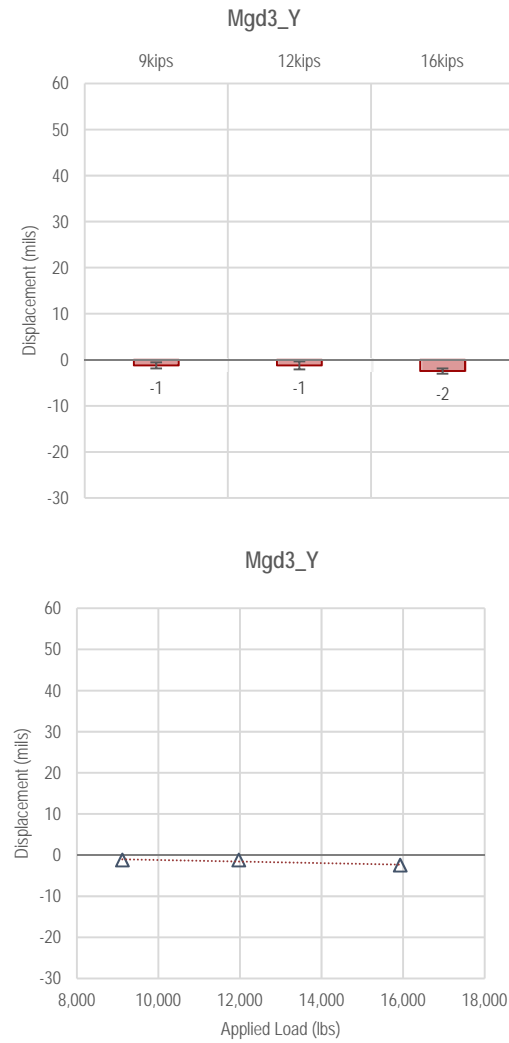
F-35

Experiment 1 (Control)

Not Available

Not Available

Experiment 3 (Geogrid)



Experiment 5 (Geotextile)

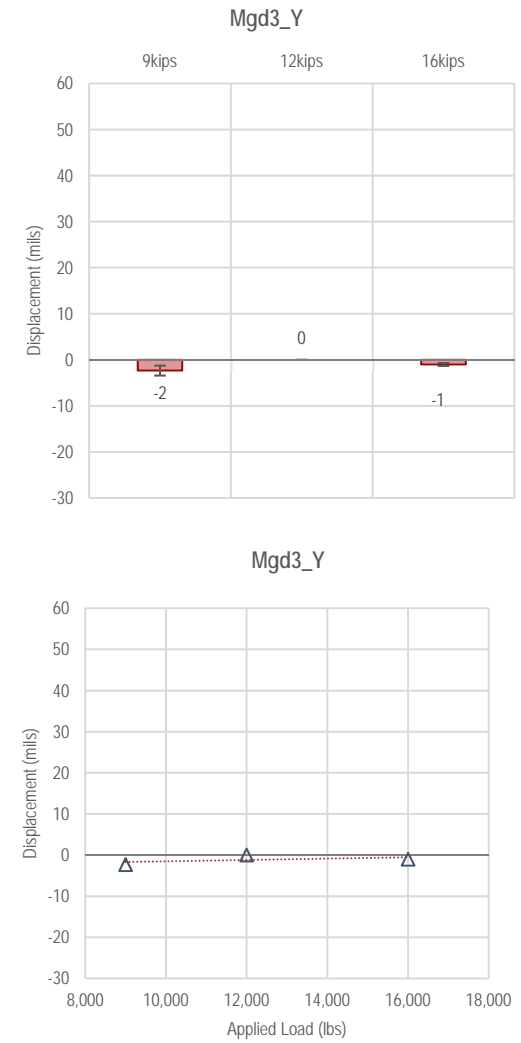
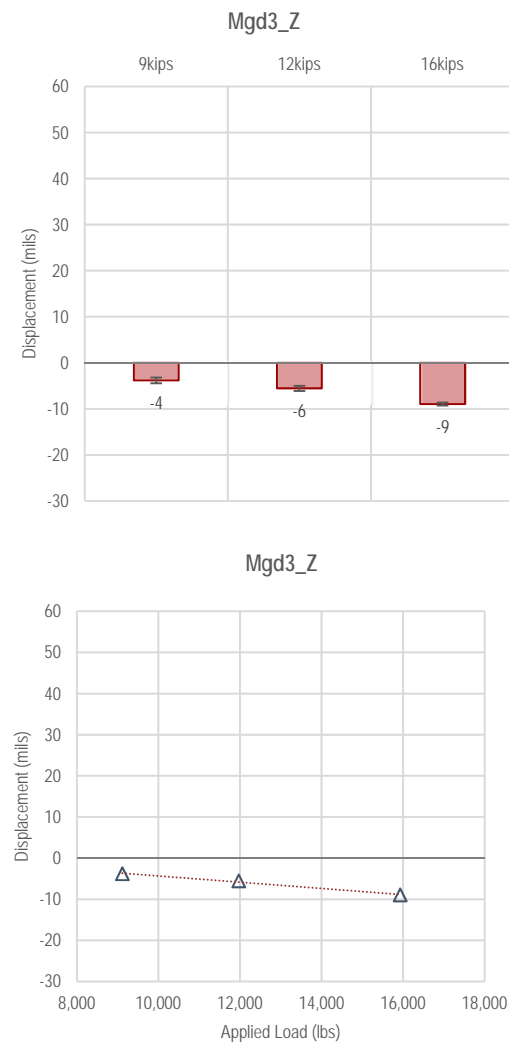


Figure F1-33. Summary of Mgd3_Y measurements—Dynamic Loading

Experiment 1 (Control)

Not Available

Experiment 3 (Geogrid)



Experiment 5 (Geotextile)

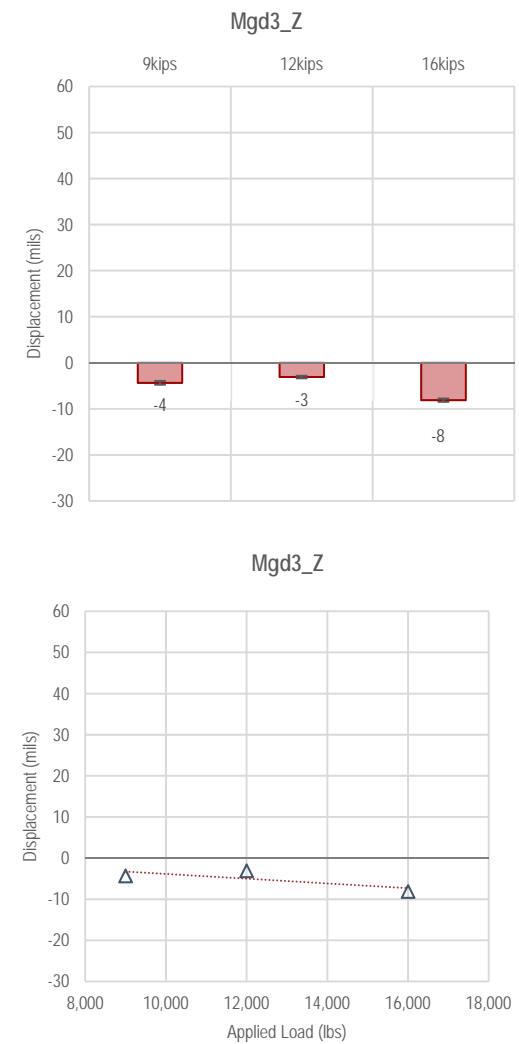


Figure F1-34. Summary of Mgd3_Z measurements—Dynamic Loading

**Appendix F2. Summary Charts for Flexible Pavement in Experiments: Static Loading—
Thin Base: No. 1 (Control), No. 3 (Geogrid), and No. 5 (Geotextile)**

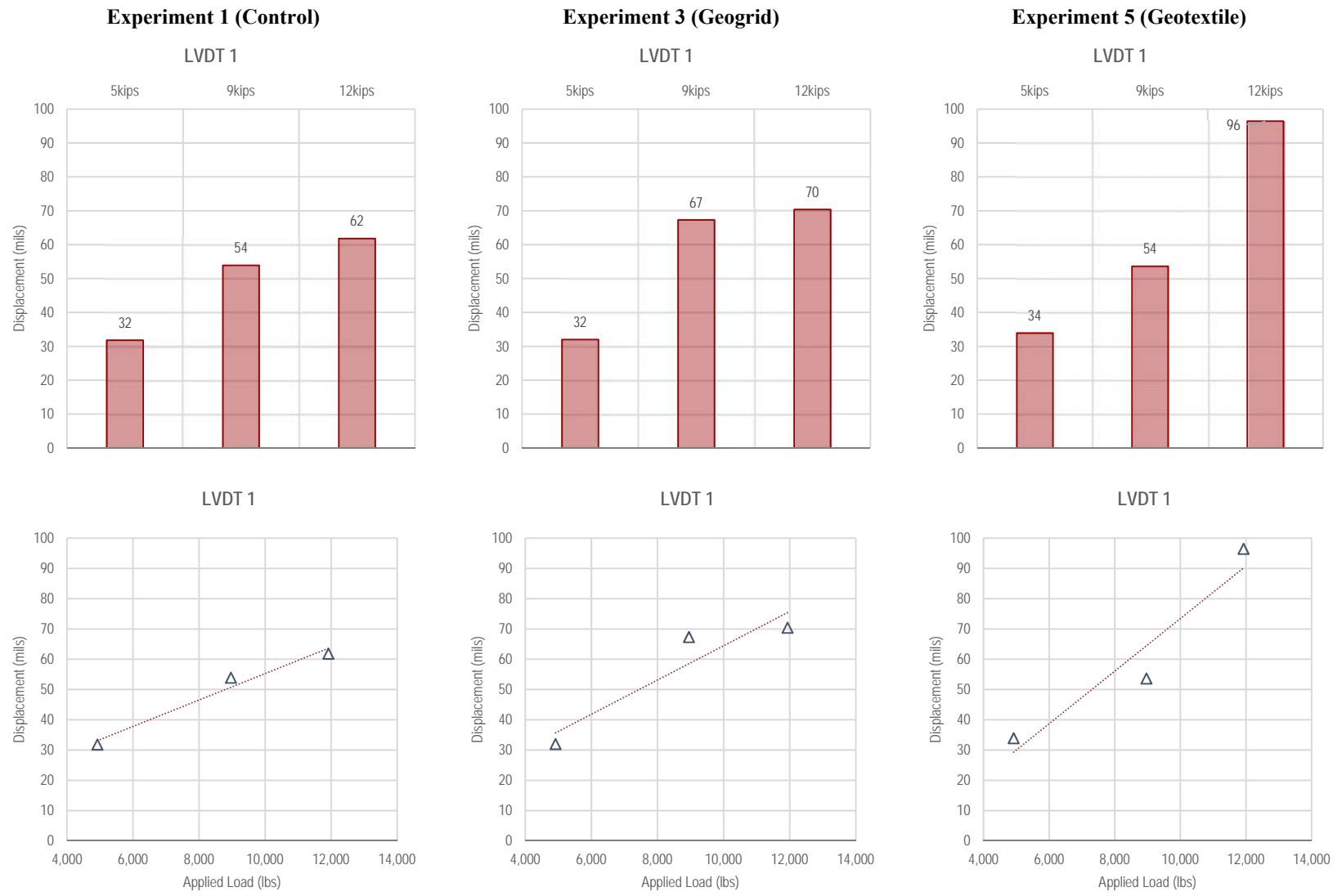


Figure F2-1. Summary of LVDT 1 measurements—Static Loading

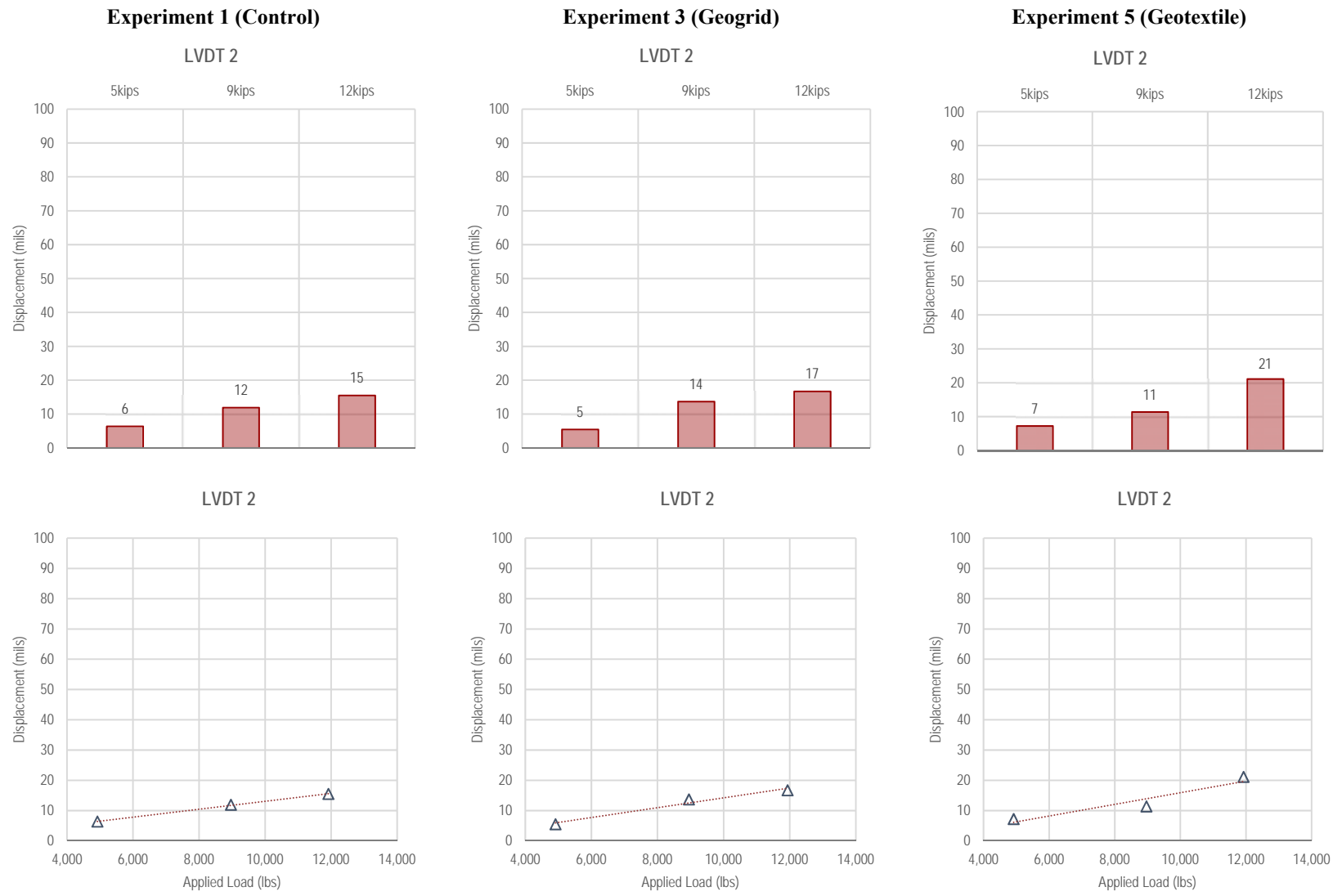


Figure F2-2. Summary of LVDT 2 measurements—Static Loading

F-39

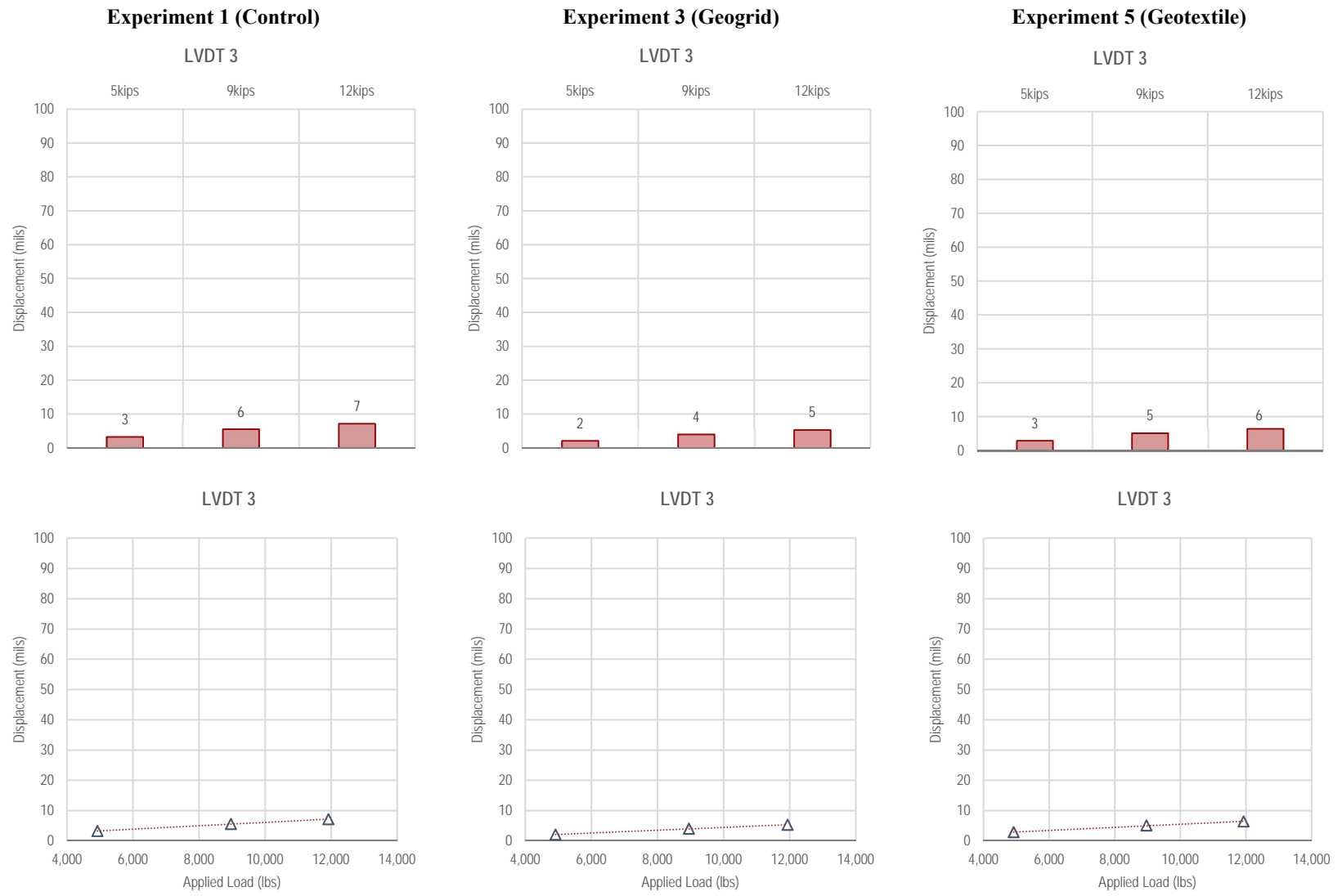


Figure F2-3. Summary of LVDT 3 measurements—Static Loading

F-40

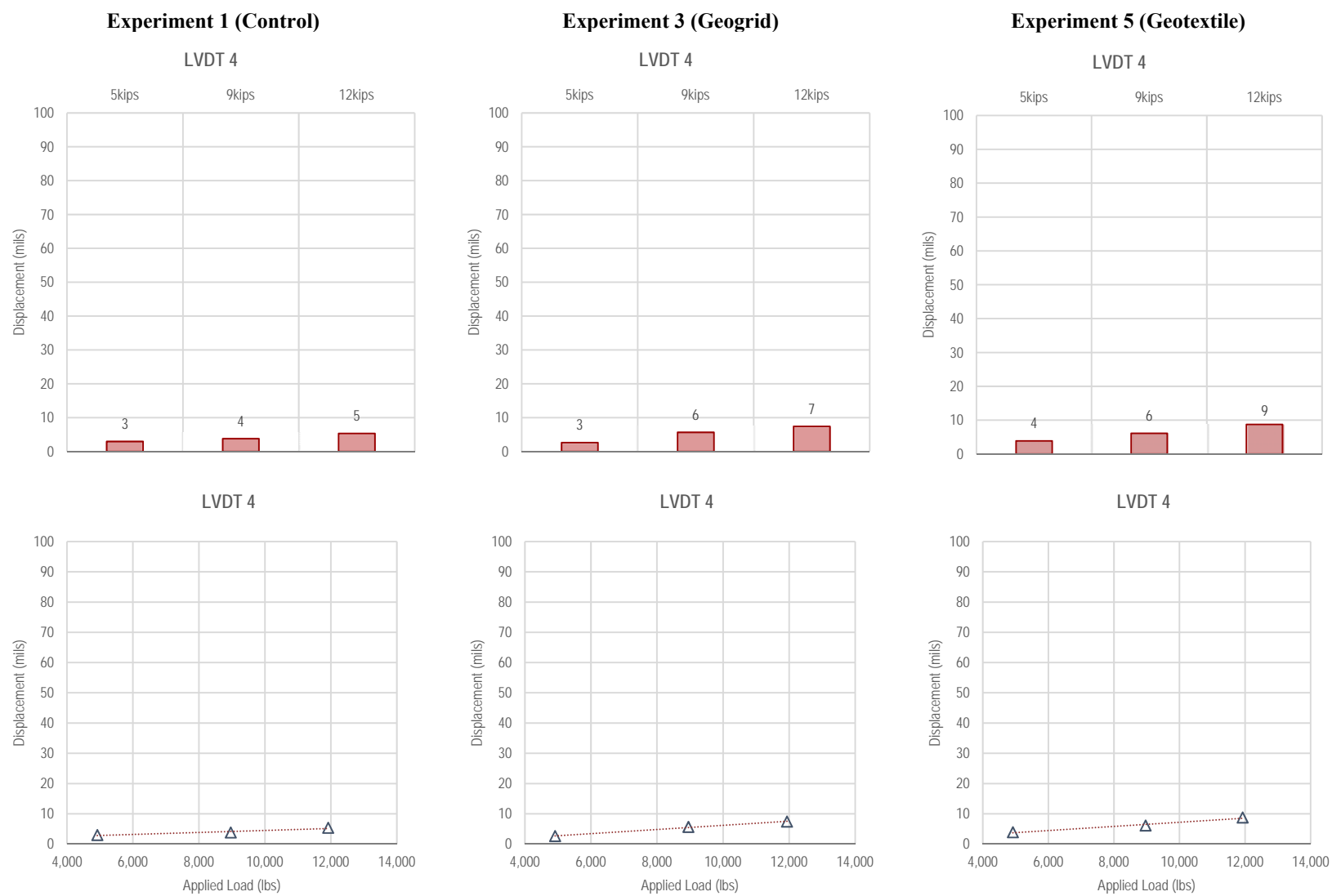


Figure F2-4. Summary of LVDT 4 measurements—Static Loading

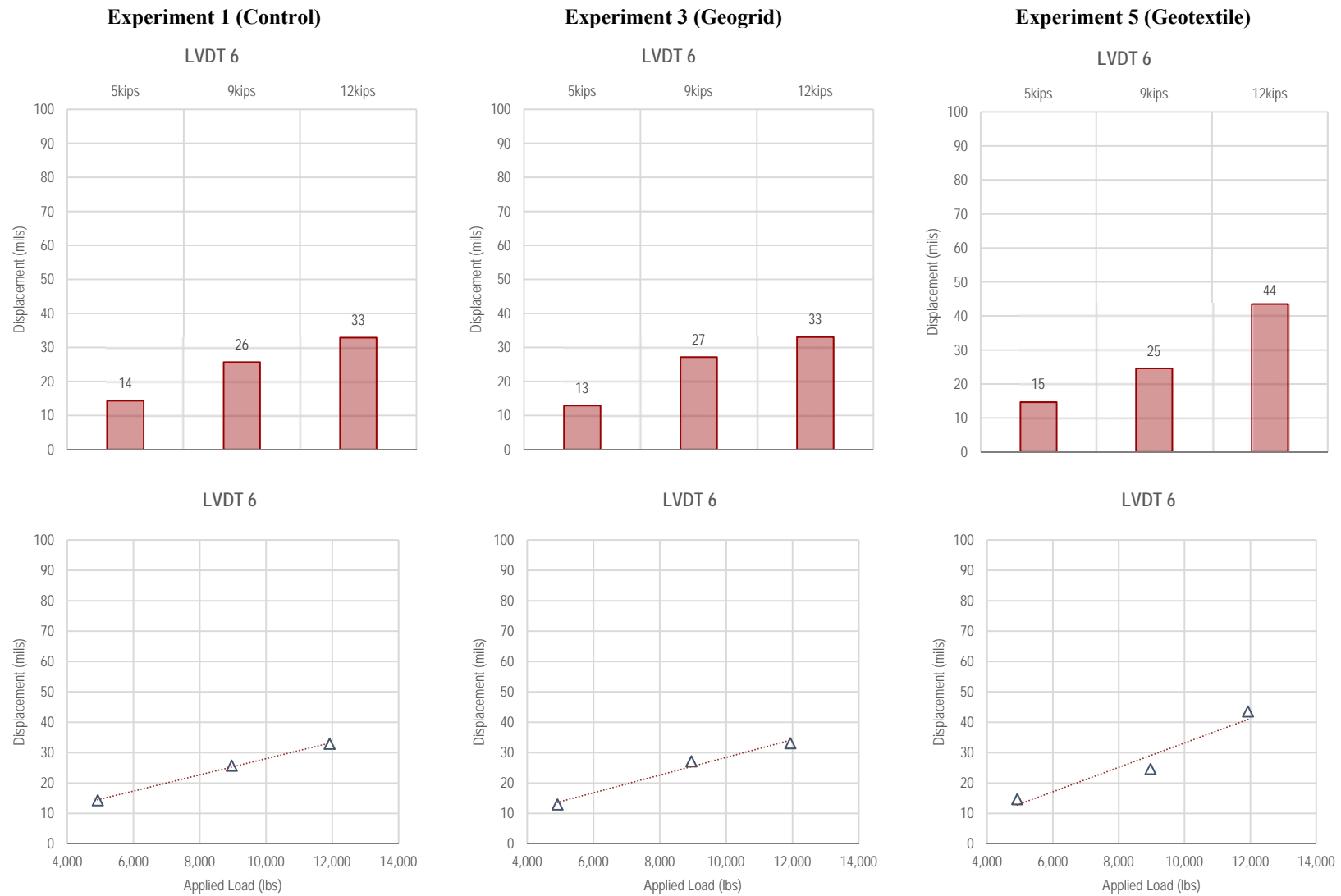


Figure F2-5. Summary of LVDT 6 measurements—Static Loading

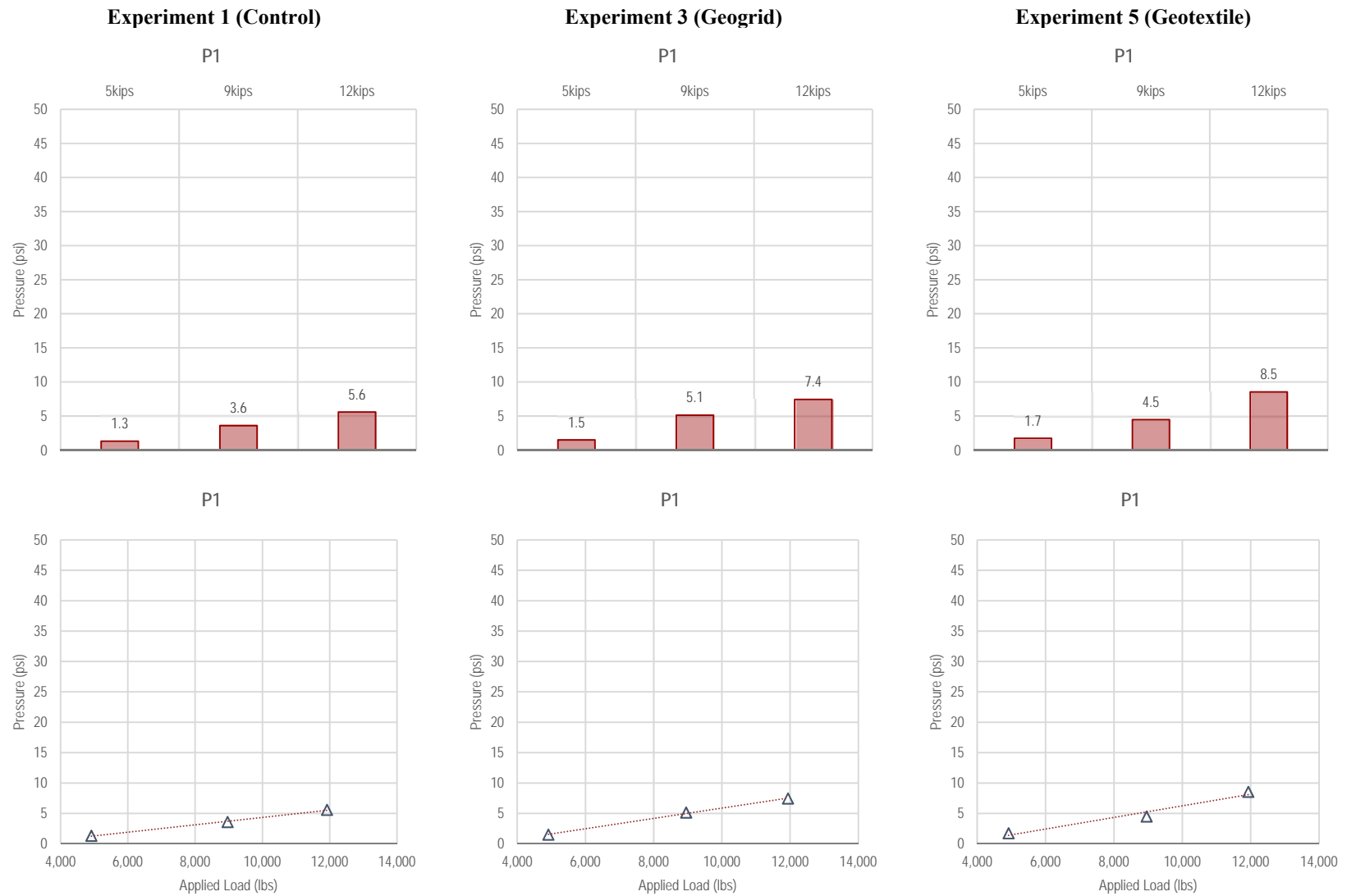


Figure F2-6. Summary of P1 measurements—Static Loading

F-43

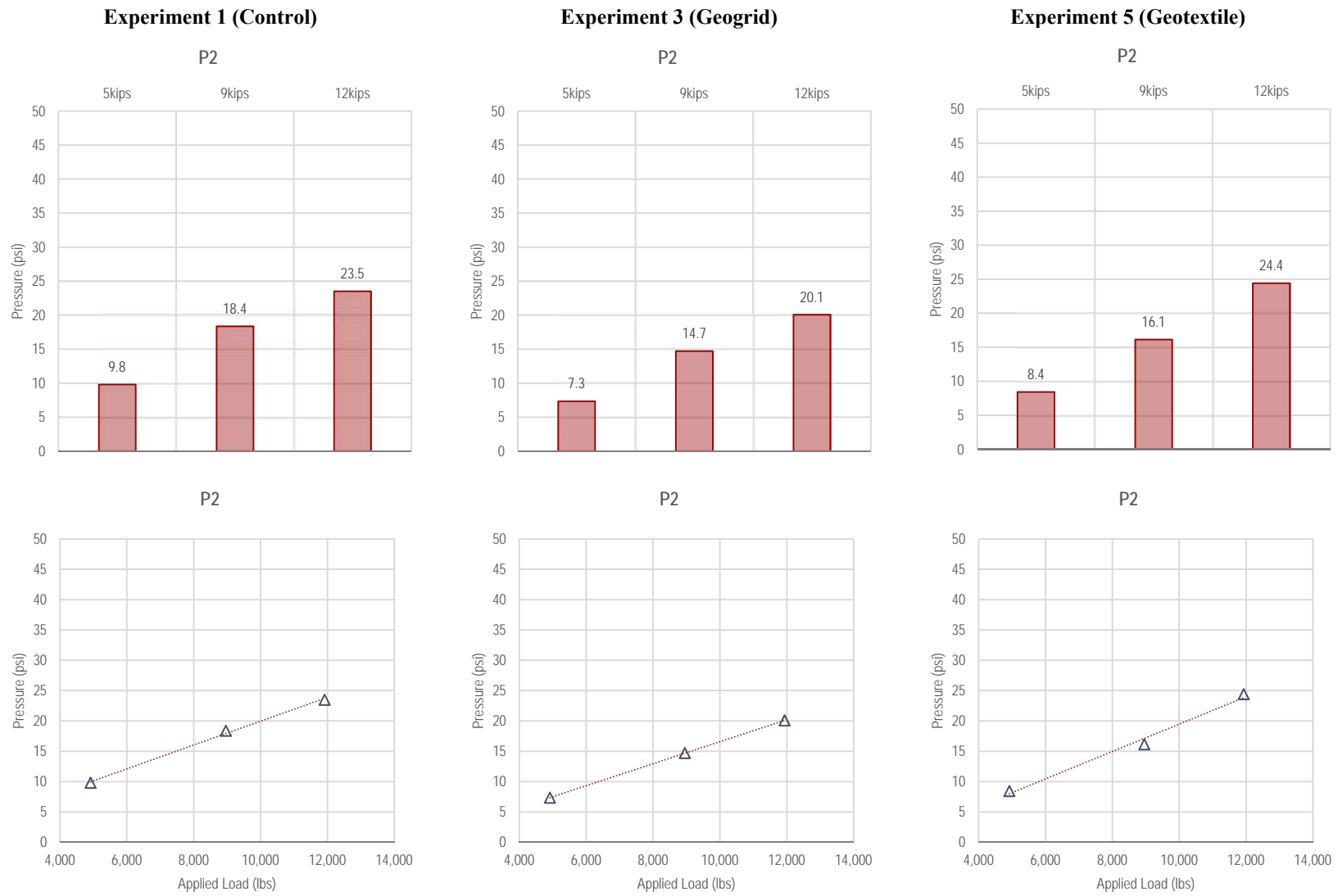


Figure F2-7. Summary of P2 measurements—Static Loading

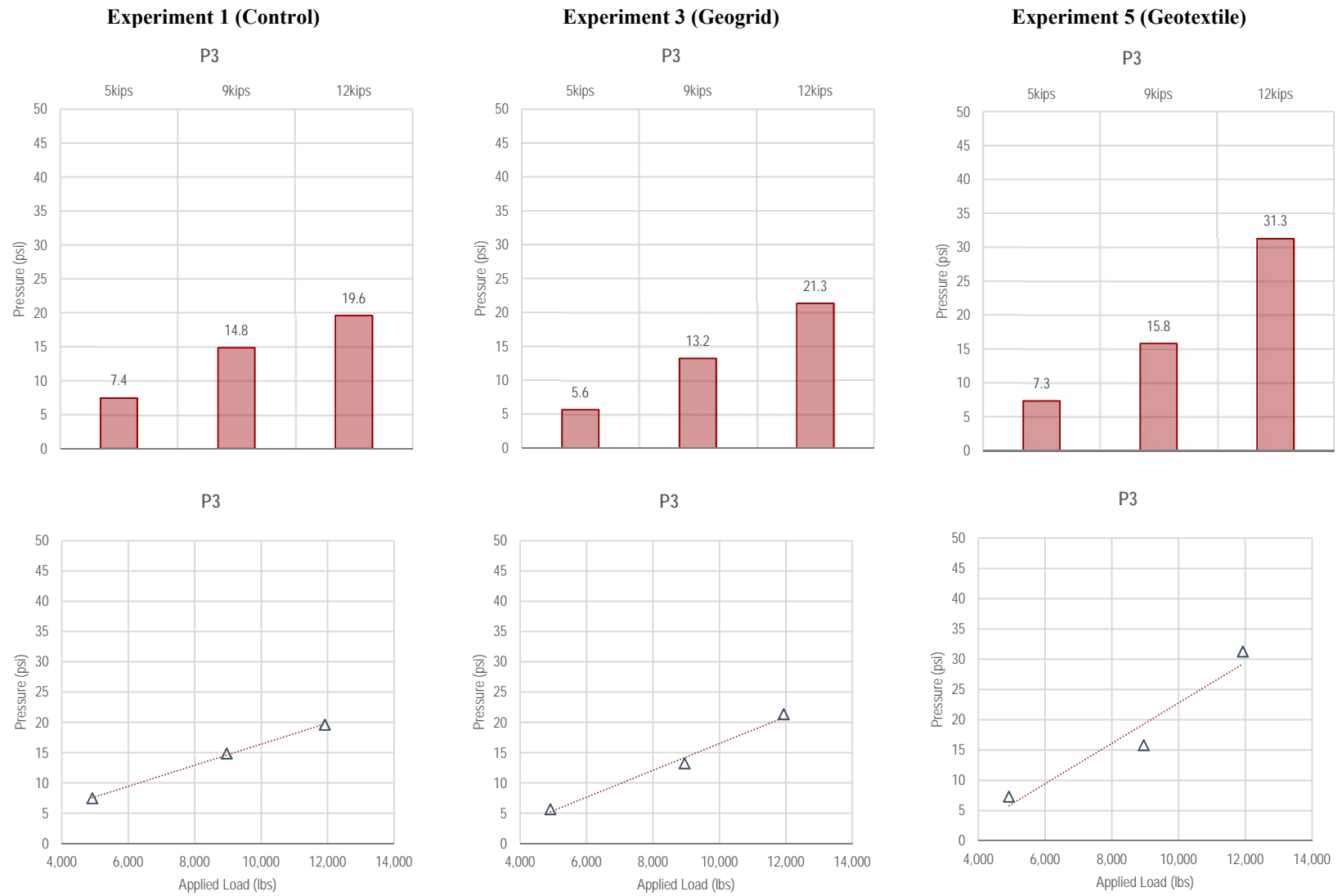


Figure F2-8. Summary of P3 measurements—Static Loading

F-45

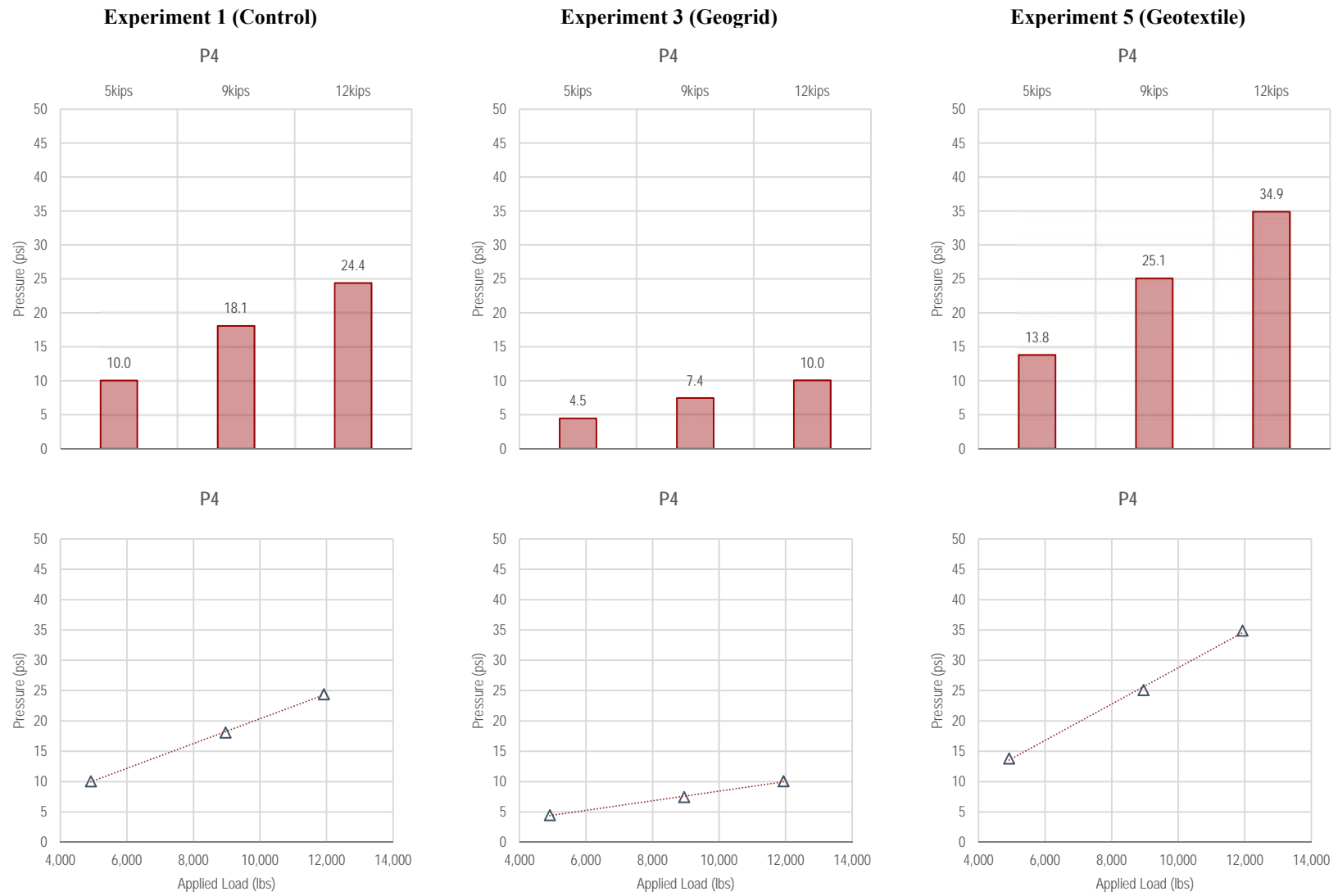


Figure F2-9. Summary of P4 measurements—Static Loading

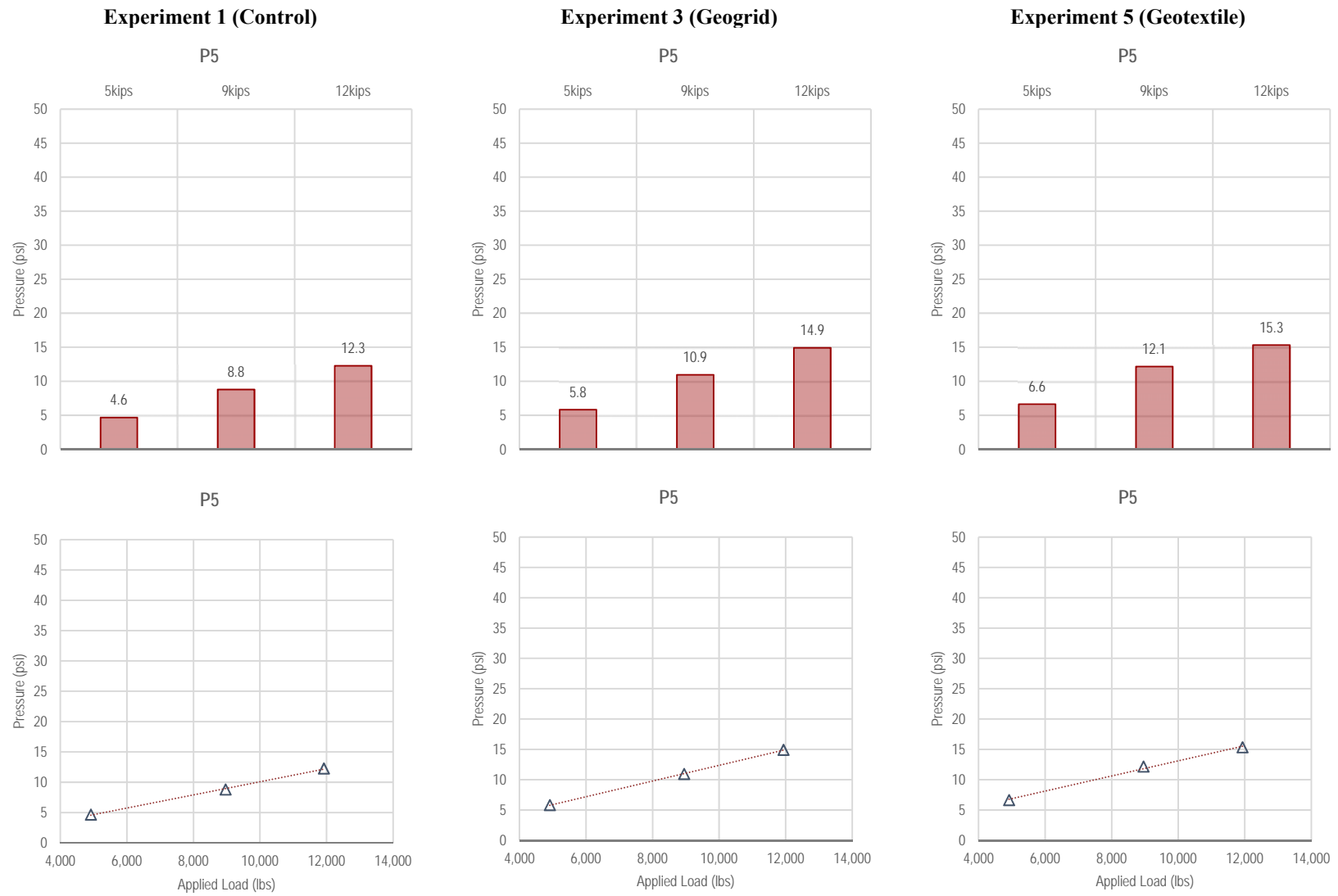
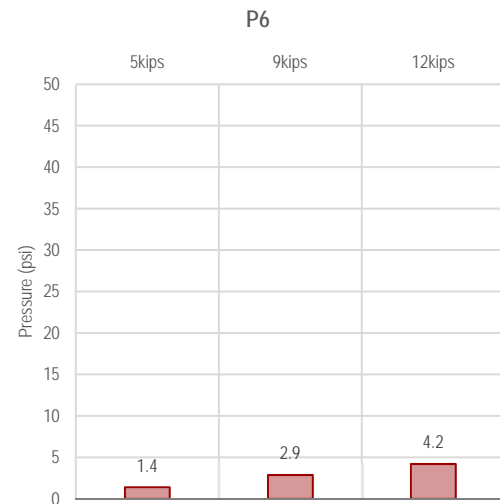


Figure F2-10. Summary of P5 measurements—Static Loading

Experiment 1 (Control)

Not Available

Experiment 3 (Geogrid)



Experiment 5 (Geotextile)

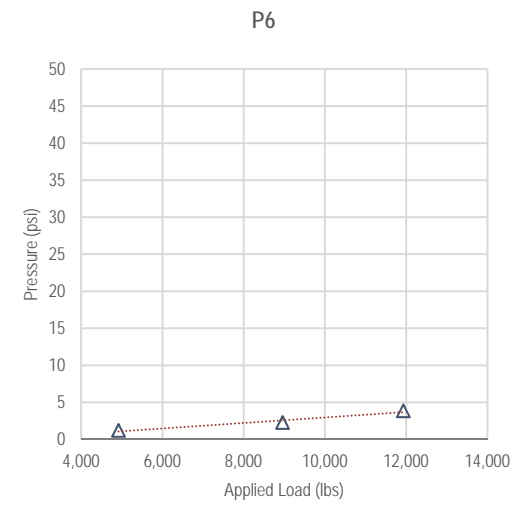
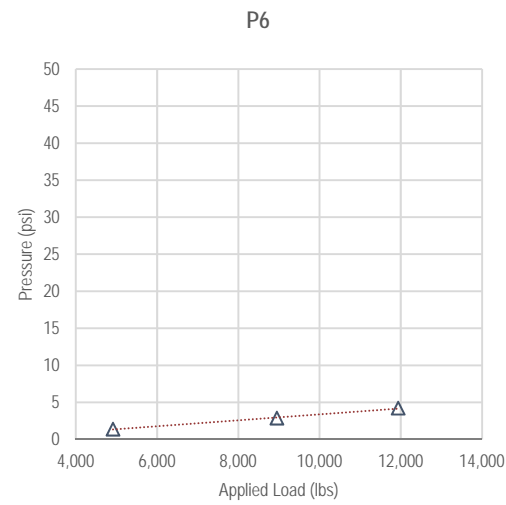
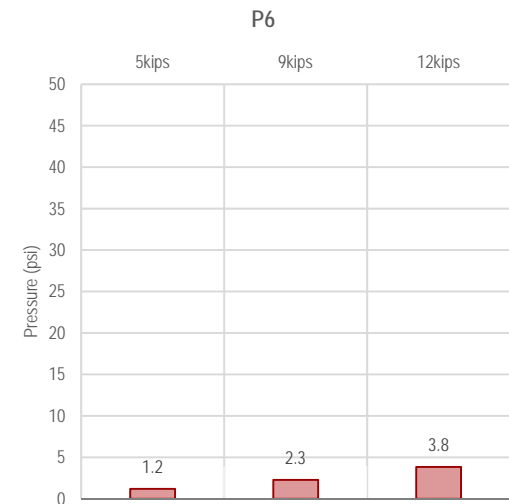
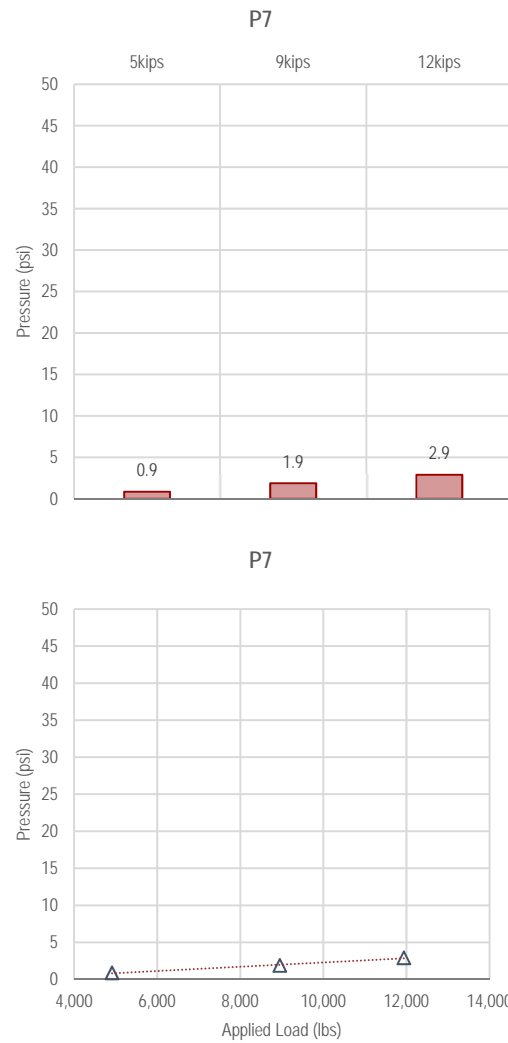


Figure F2-11. Summary of P6 measurements—Static Loading

Experiment 1 (Control)

Not Available

Experiment 3 (Geogrid)



Experiment 5 (Geotextile)

Not Available

Not Available

Figure F2-12. Summary of P7 measurements—Static Loading

F-50

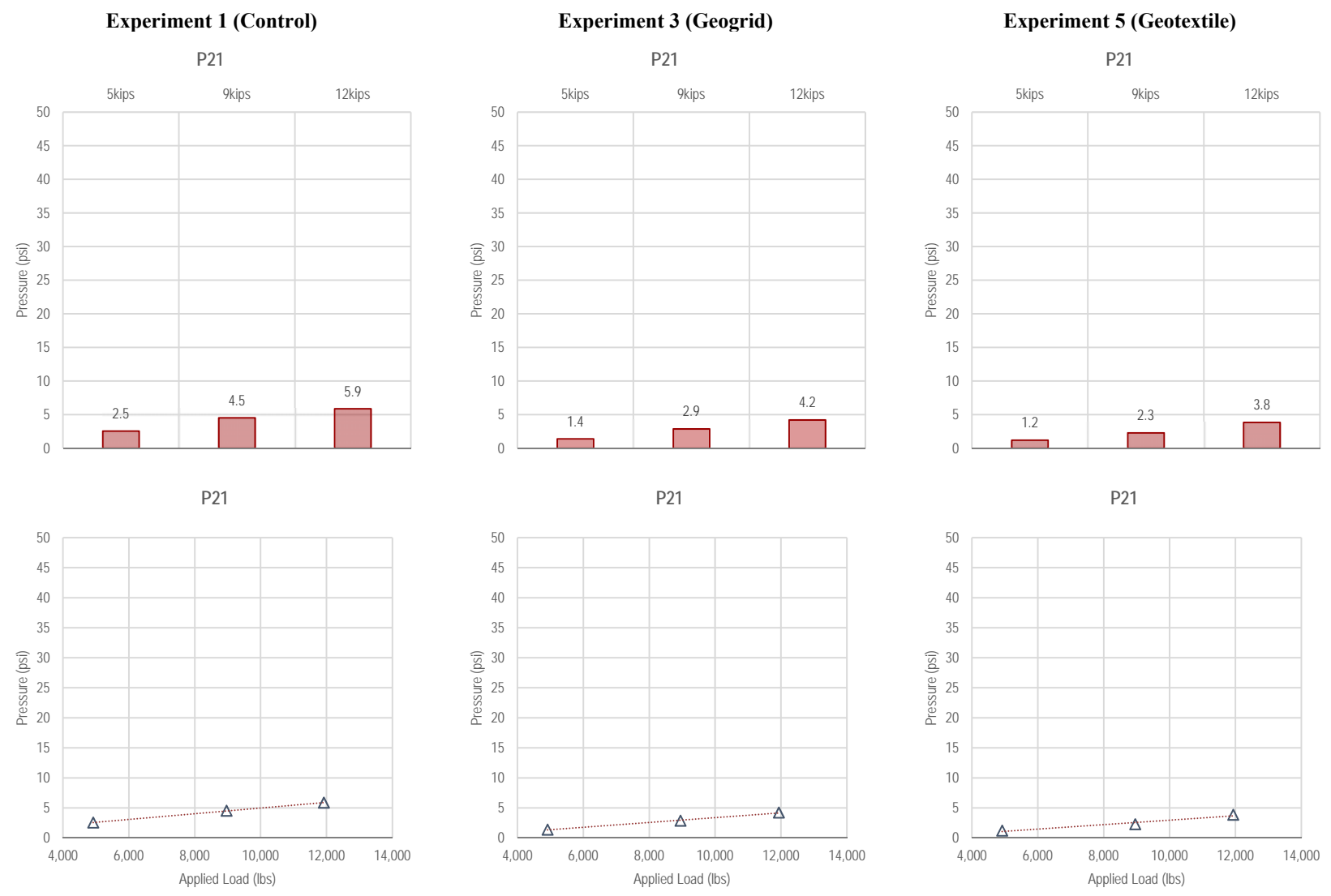


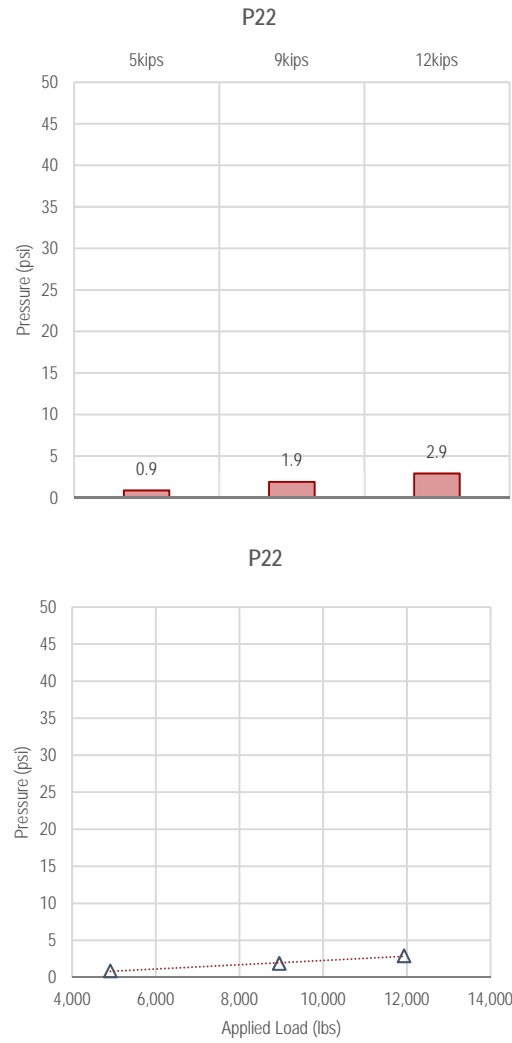
Figure F2-13. Summary of P21 measurements—Static Loading

F-51

Experiment 1 (Control)

Not Available

Experiment 3 (Geogrid)



Experiment 5 (Geotextile)

Not Available

Not Available

Figure F2-14. Summary of P22 measurements—Static loading

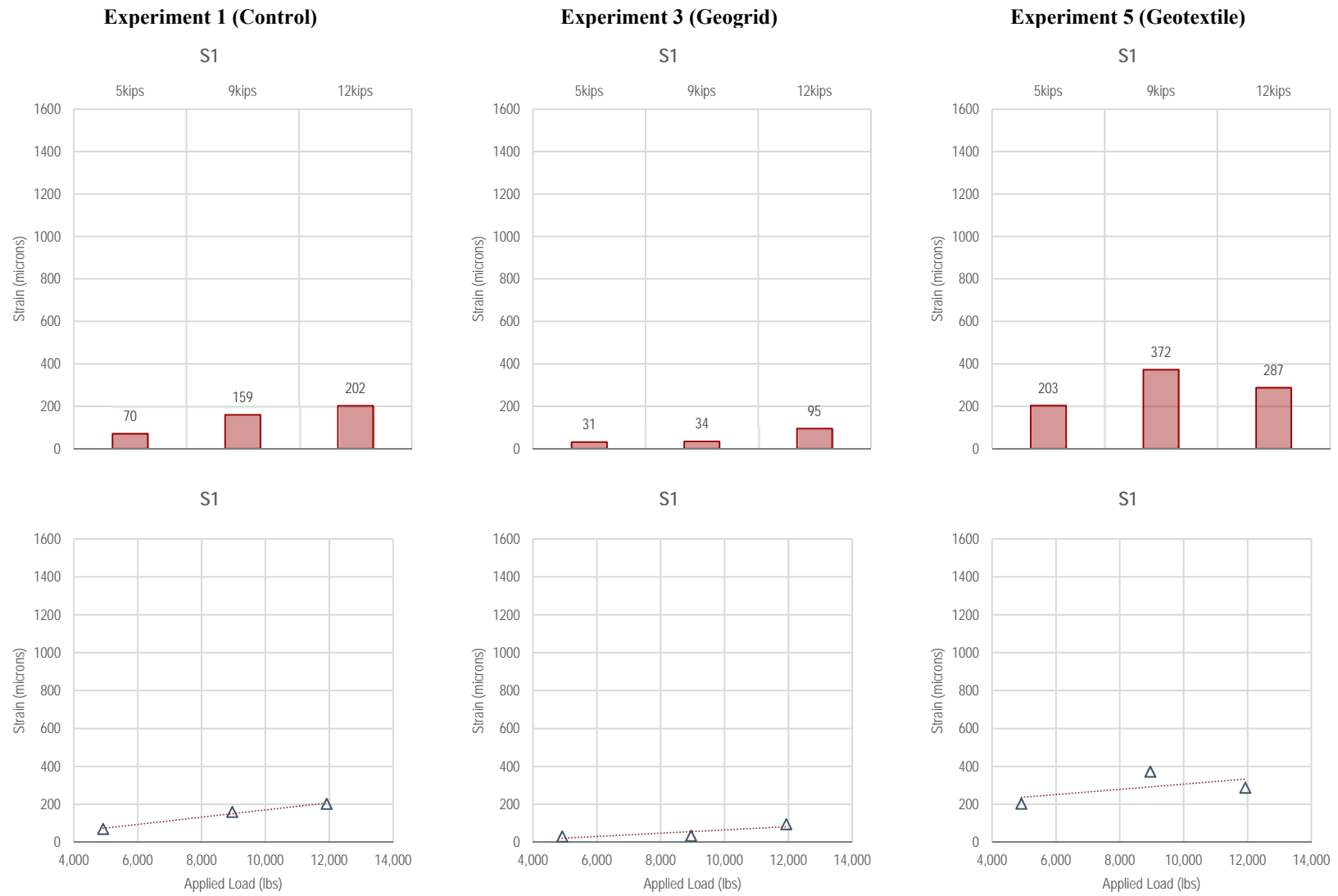


Figure F2-15. Summary of S1 measurements—Static Loading

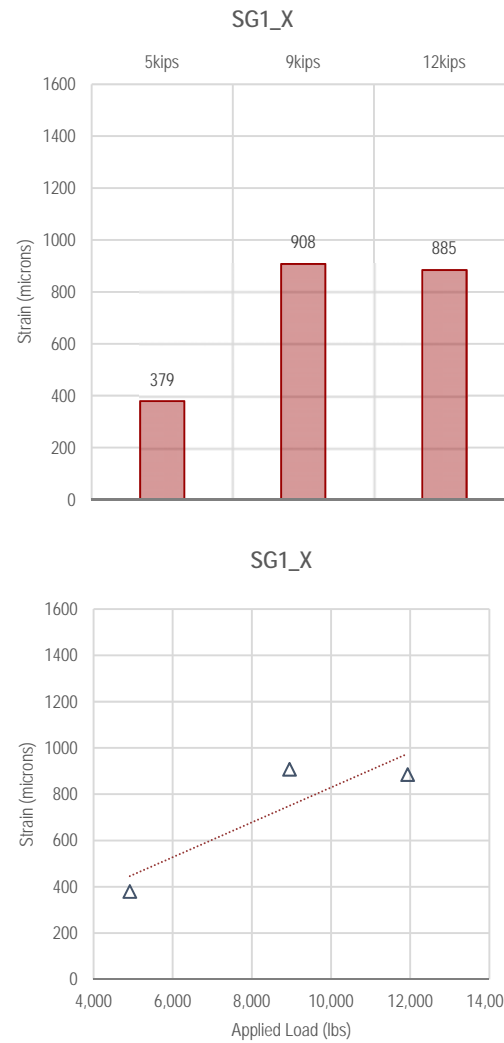
F-52

F-53

Experiment 1 (Control)

Not Available

Experiment 3 (Geogrid)



Experiment 5 (Geotextile)

Not Available

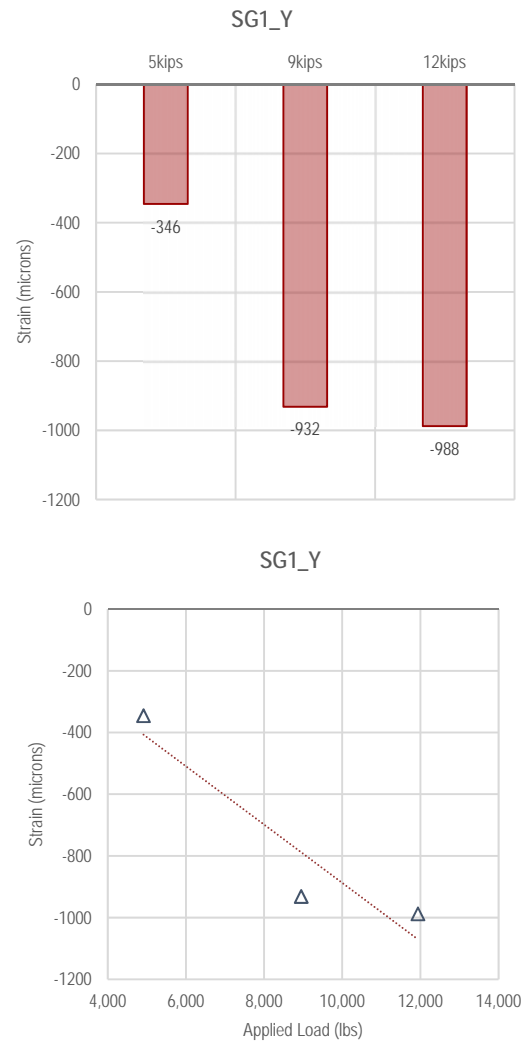
Not Available

Figure F2-16. Summary of SG1_X measurements—Static Loading

Experiment 1 (Control)

Not Available

Experiment 3 (Geogrid)



Experiment 5 (Geotextile)

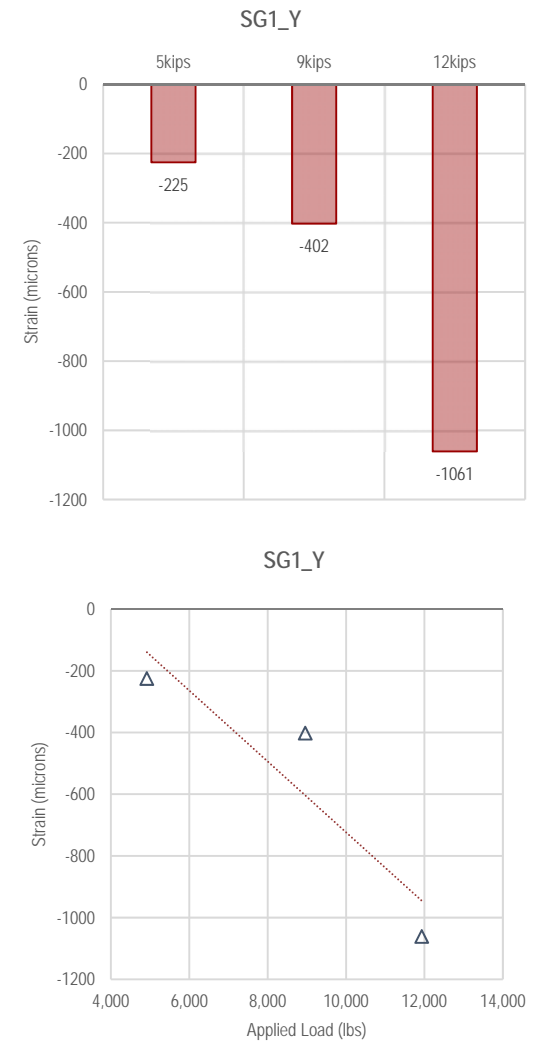
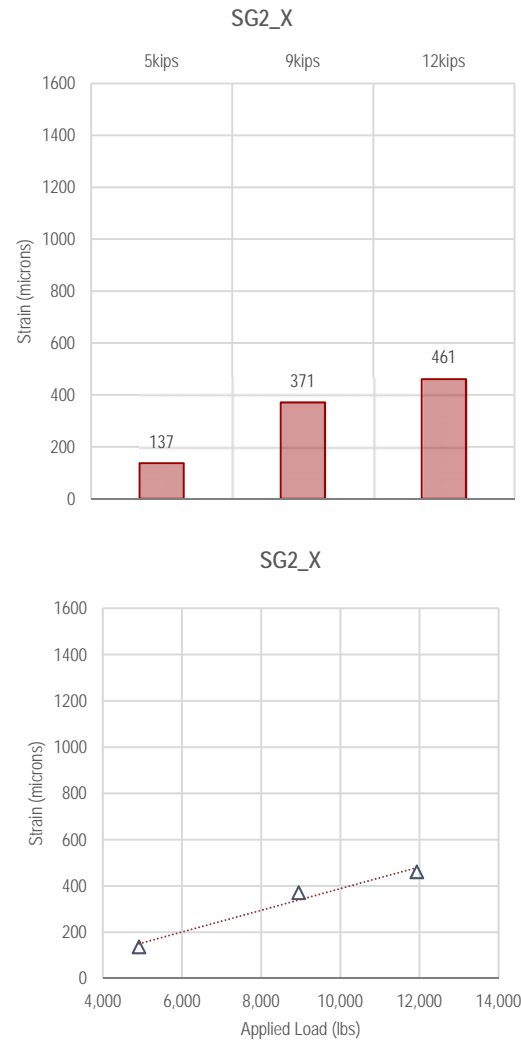


Figure F2-17. Summary of SG1_Y measurements—Static Loading

Experiment 1 (Control)

Not Available

Experiment 3 (Geogrid)



Experiment 5 (Geotextile)

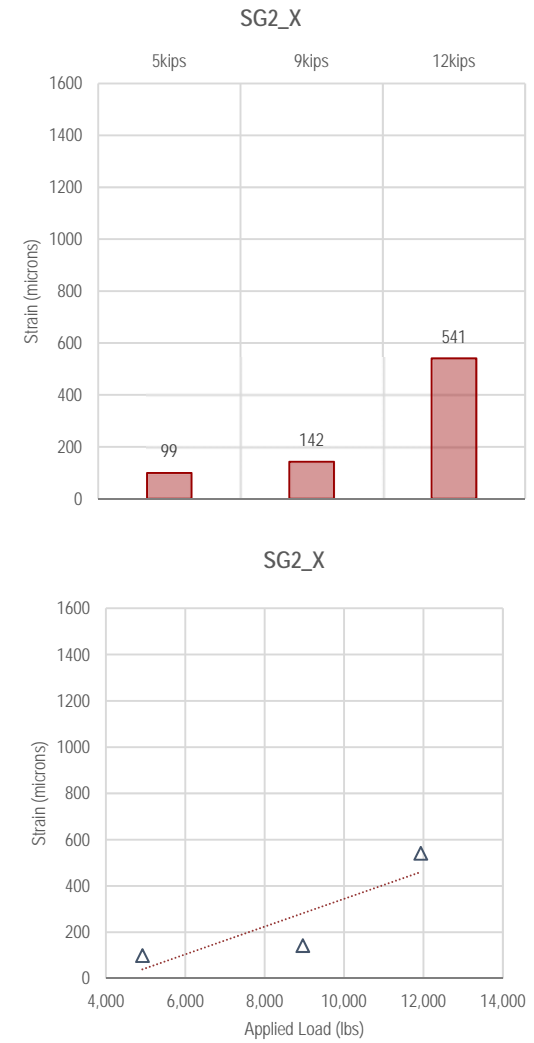
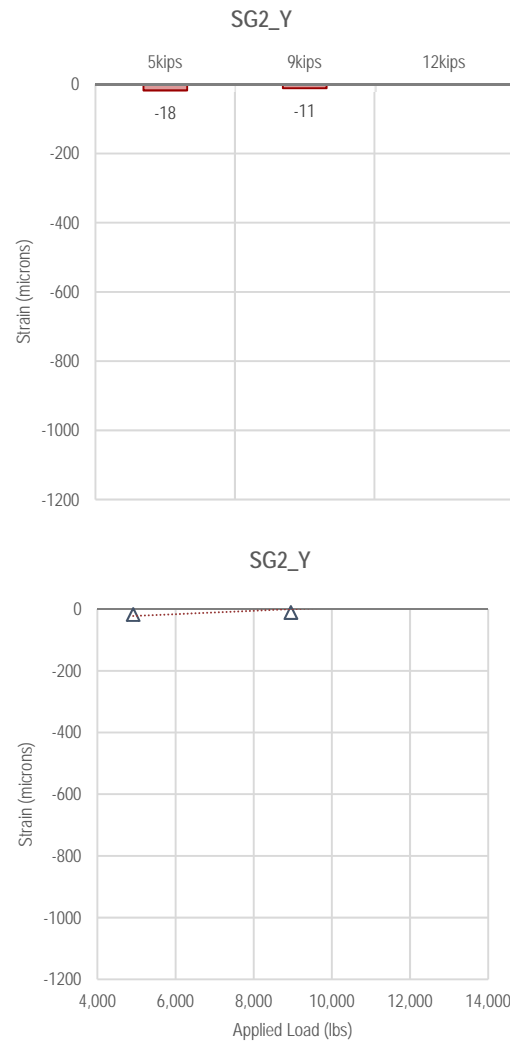


Figure F2-18. Summary of SG2_X measurements—Static Loading

Experiment 1 (Control)

Not Available

Experiment 3 (Geogrid)



Experiment 5 (Geotextile)

Not Available

Not Available

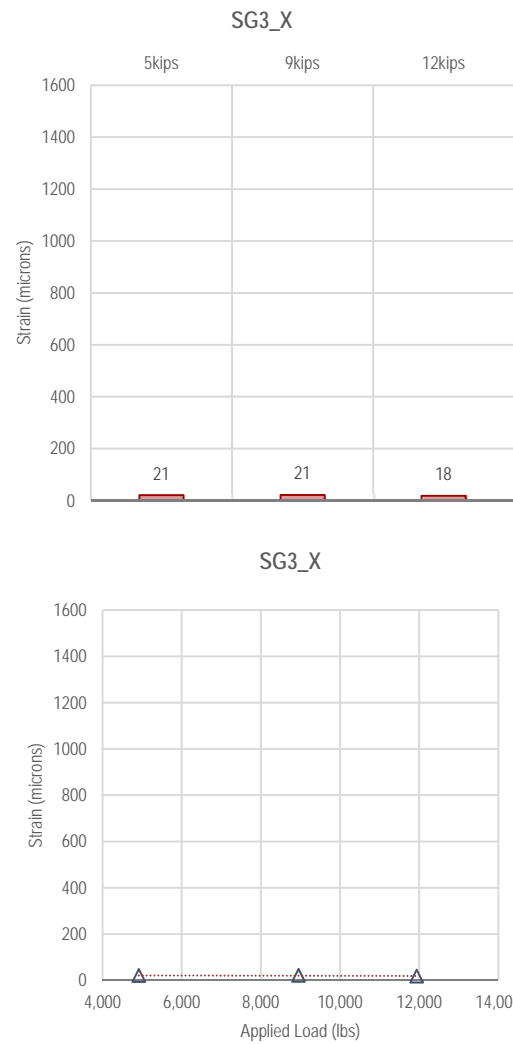
Figure F2-19. Summary of SG2_Y measurements—Static Loading

F-57

Experiment 1 (Control)

Not Available

Experiment 3 (Geogrid)



Experiment 5 (Geotextile)

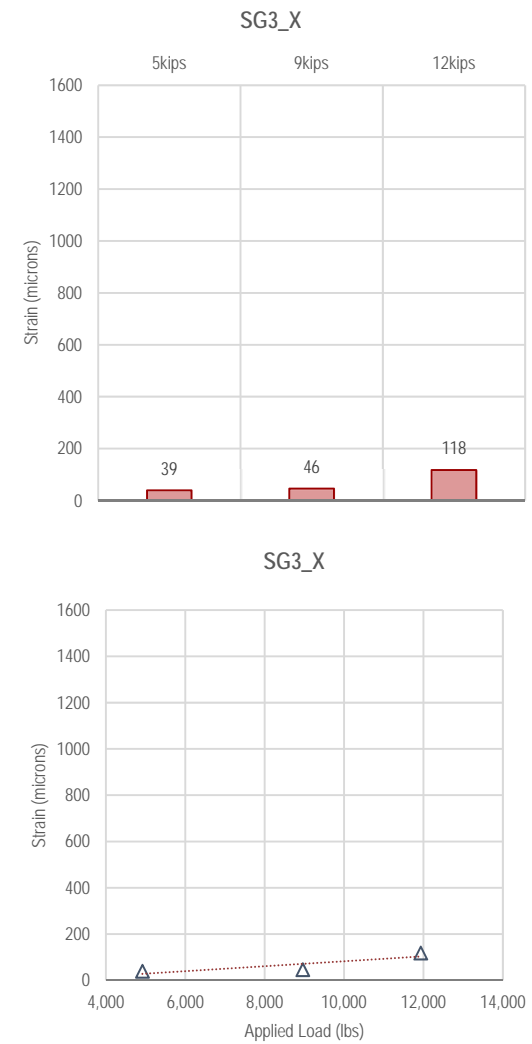


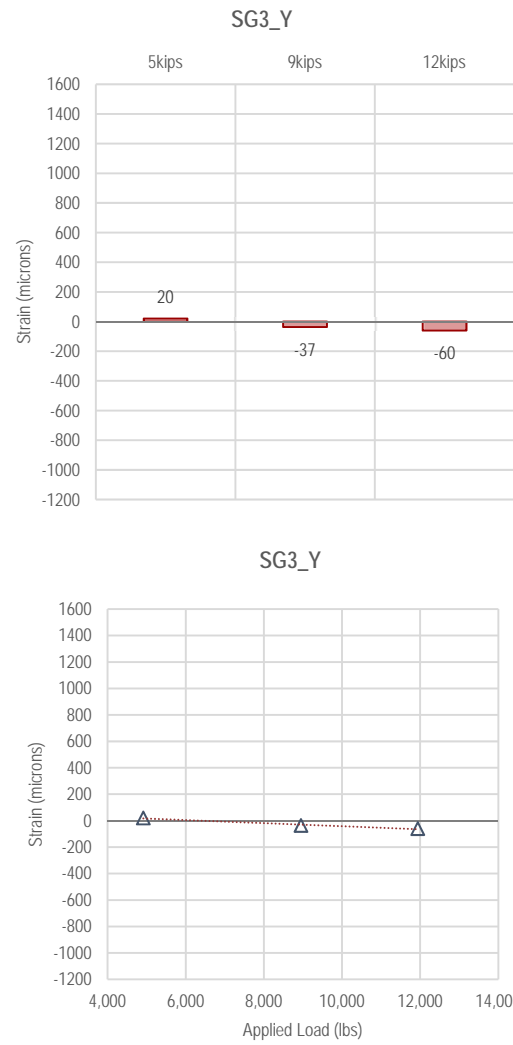
Figure F2-20. Summary of SG3_X measurements—Static Loading

Not Available

Experiment 1 (Control)

Not Available

Experiment 3 (Geogrid)



Experiment 5 (Geotextile)

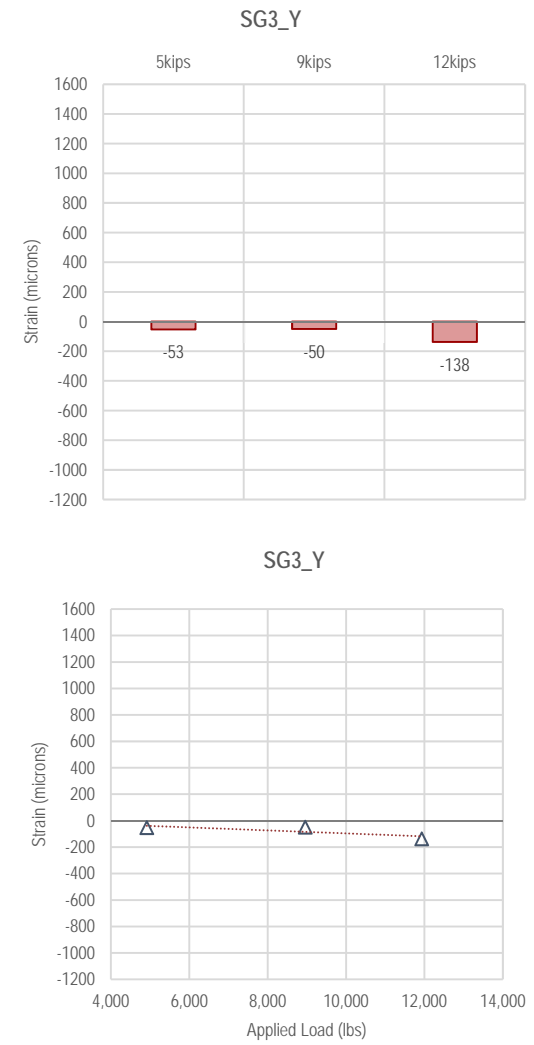


Figure F2-21. Summary of SG3_Y measurements—Static Loading

F-59

Experiment 1 (Control)

Experiment 3 (Geogrid)

Experiment 5 (Geotextile)

Not Available

Not Available

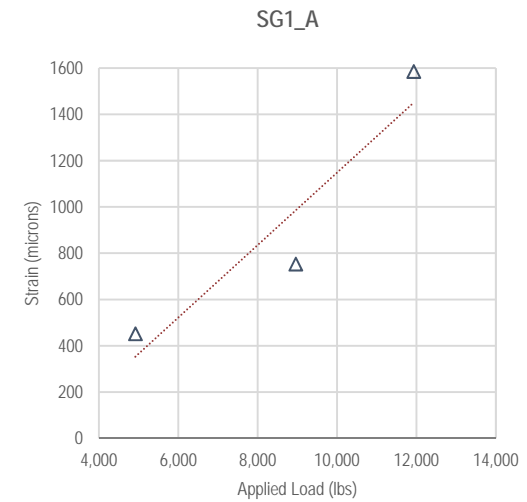
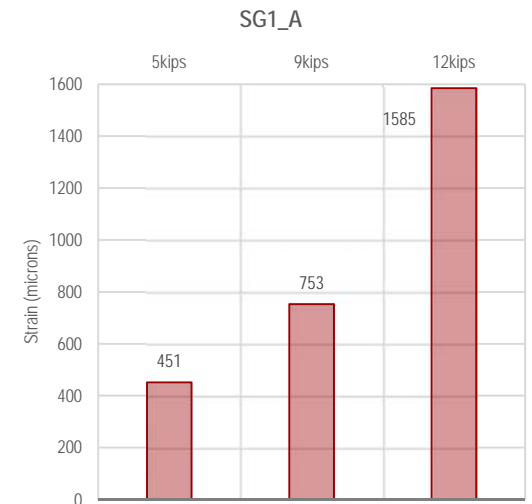


Figure F2-22. Summary of SG1_A measurements—Static Loading

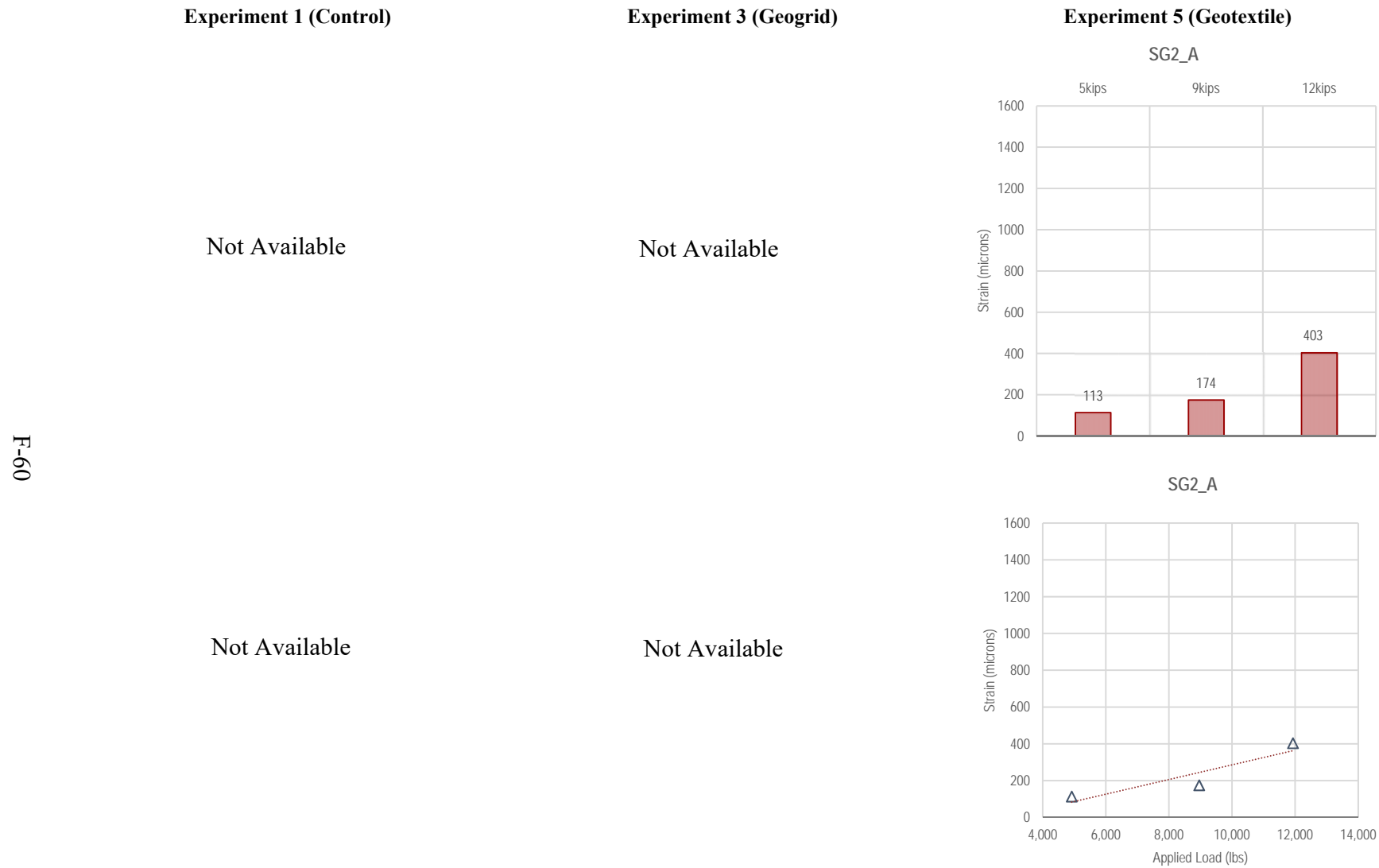


Figure F2-23. Summary of SG2_A measurements—Static Loading

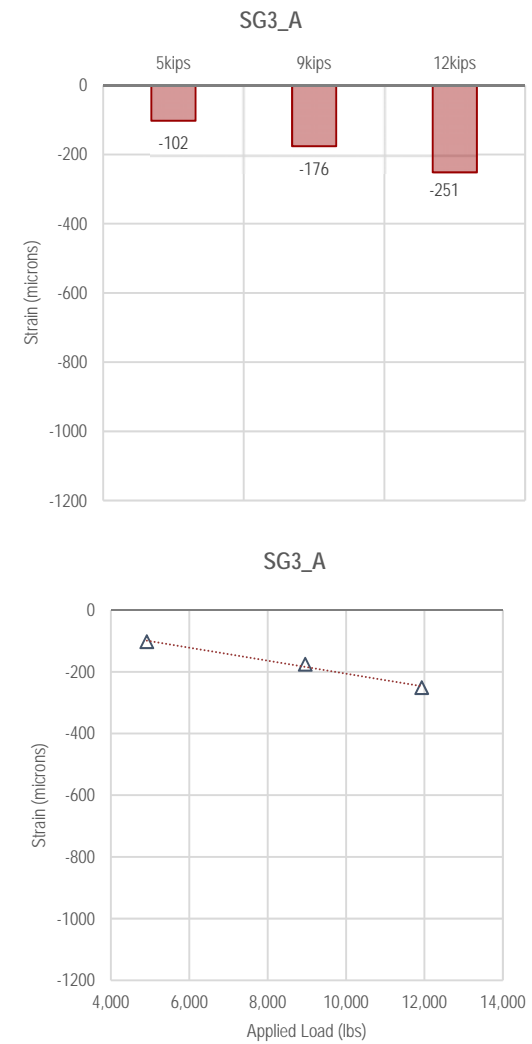
Experiment 1 (Control)

Experiment 3 (Geogrid)

Experiment 5 (Geotextile)

Not Available

Not Available



Not Available

Not Available

Figure F2-24. Summary of SG3_A measurements—Static Loading

**Appendix F3. Summary Charts for Flexible Pavement Experiments: Dynamic Loading—
Thick Base: No. 2 (Control), No. 4 (Geogrid), and No. 6 (Geotextile)**

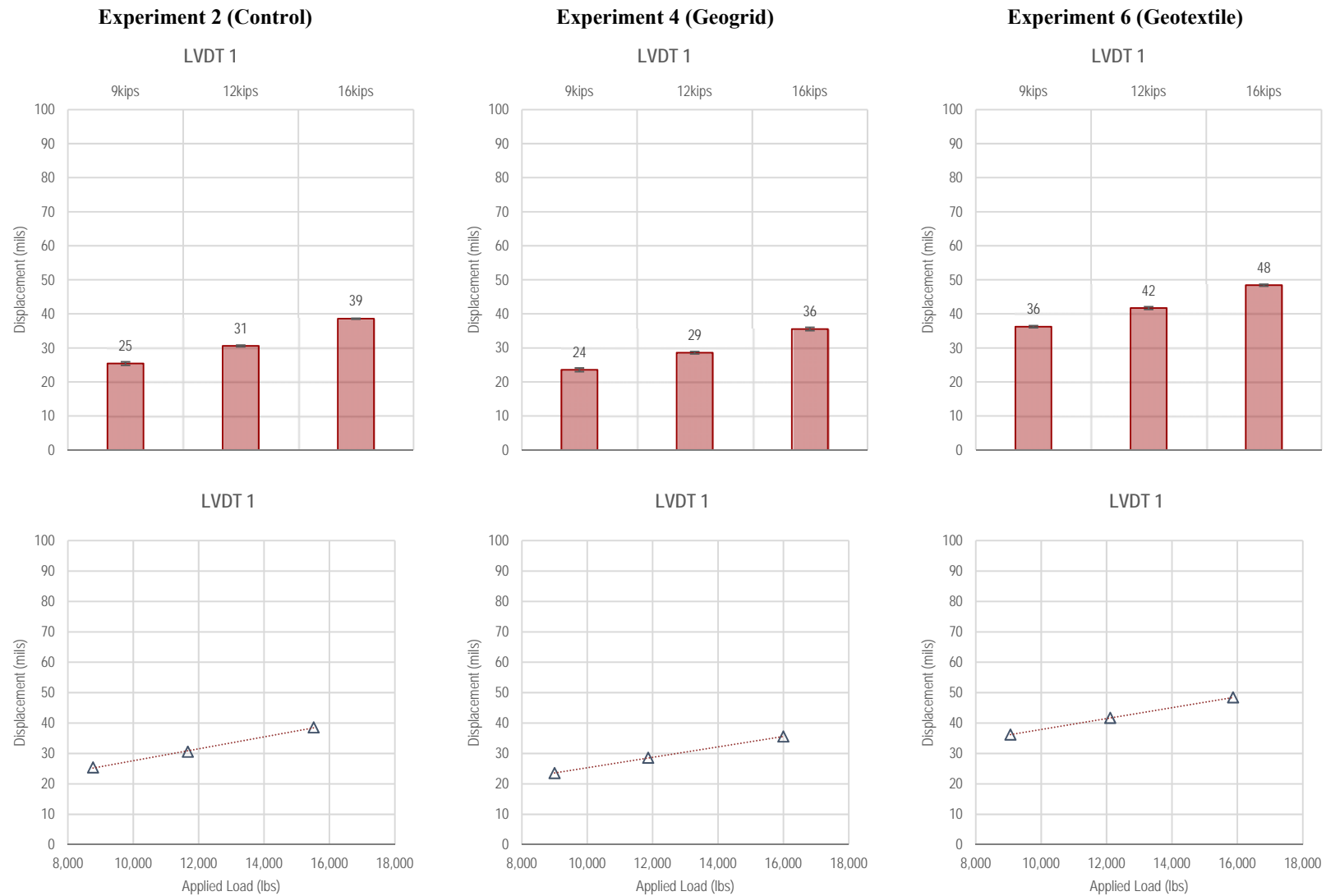


Figure F3-1. Summary of LVDT 1 measurements—Dynamic Loading

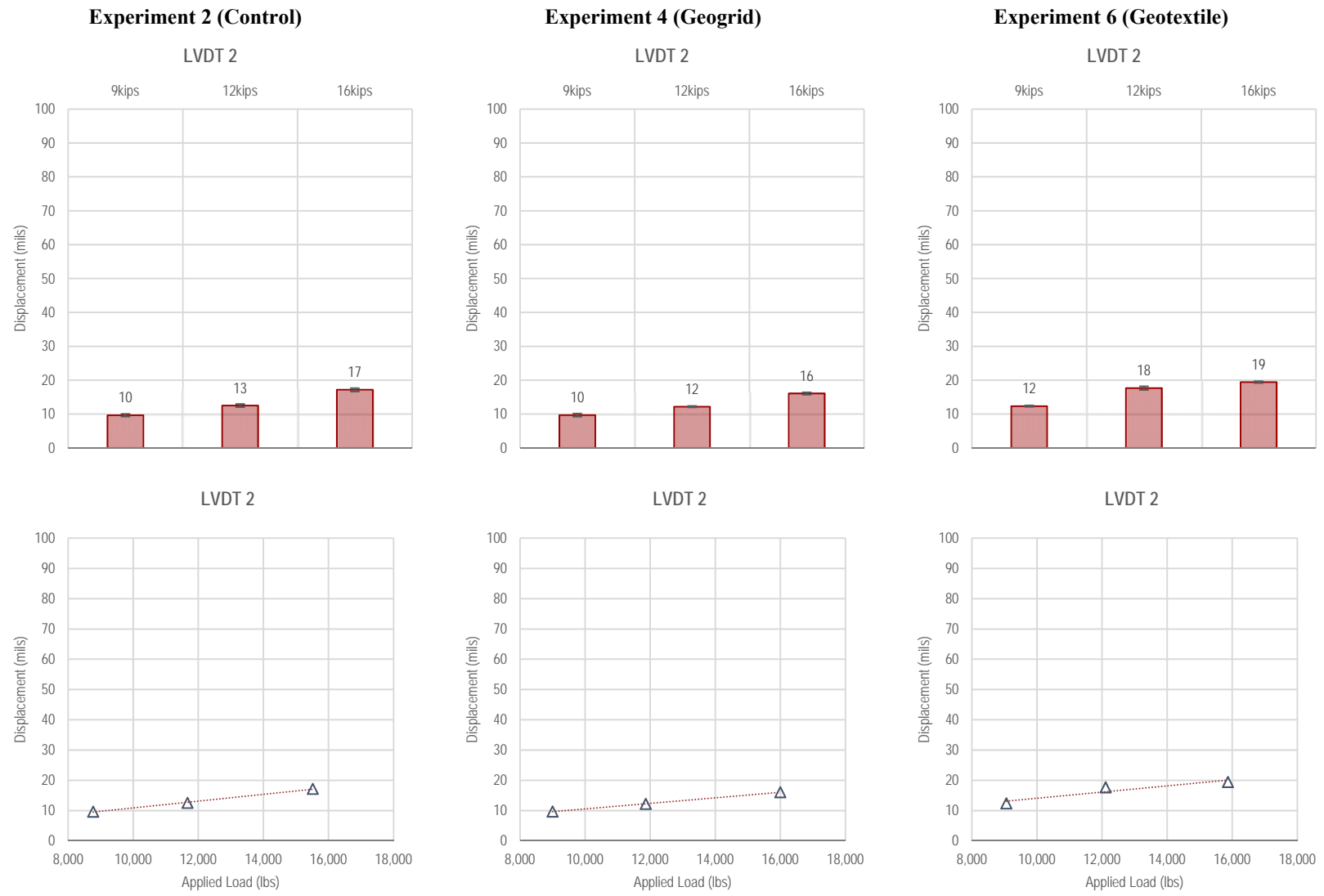


Figure F3-2. Summary of LVDT 2 measurements—Dynamic Loading

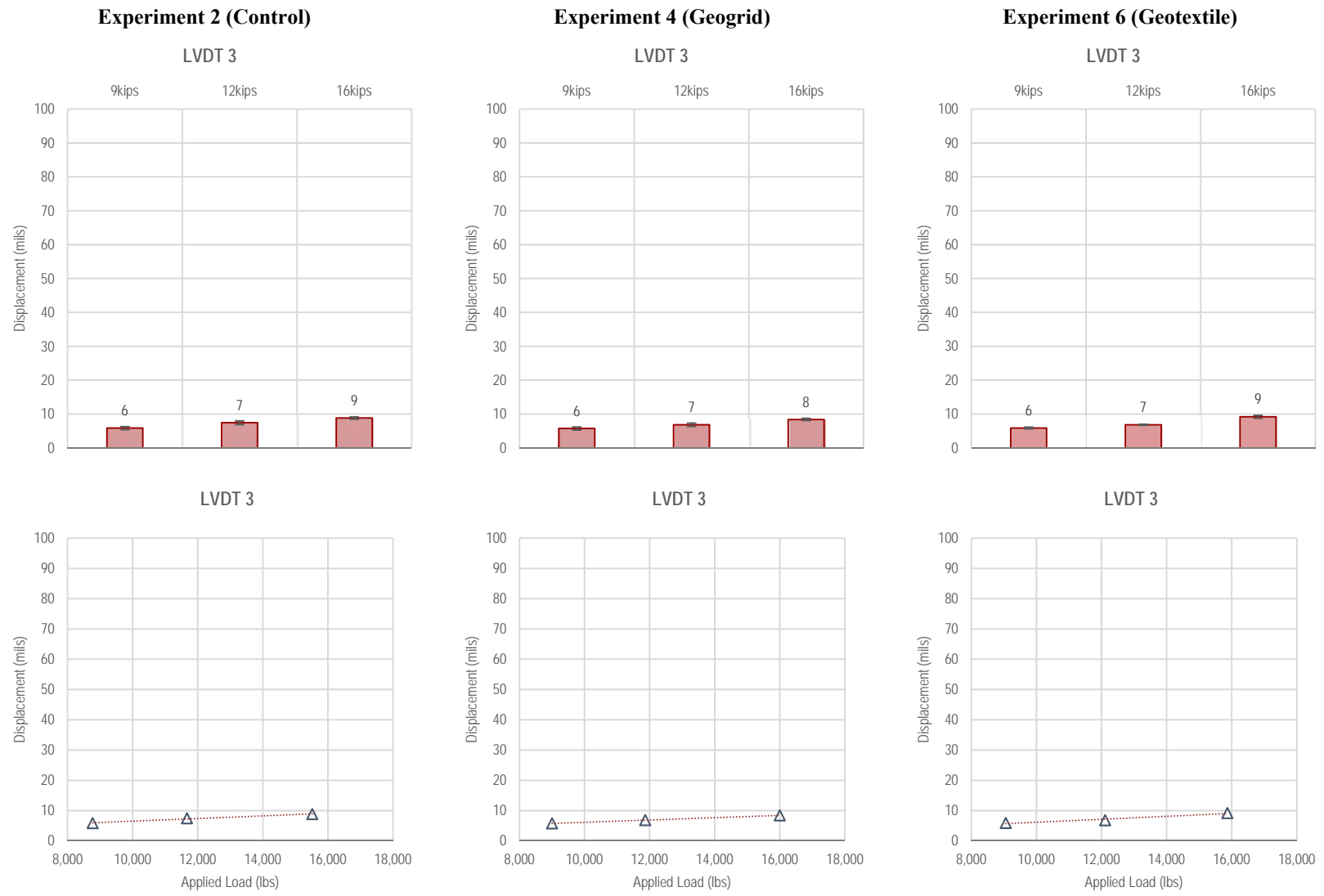


Figure F3-3. Summary of LVDT 3 measurements—Dynamic Loading

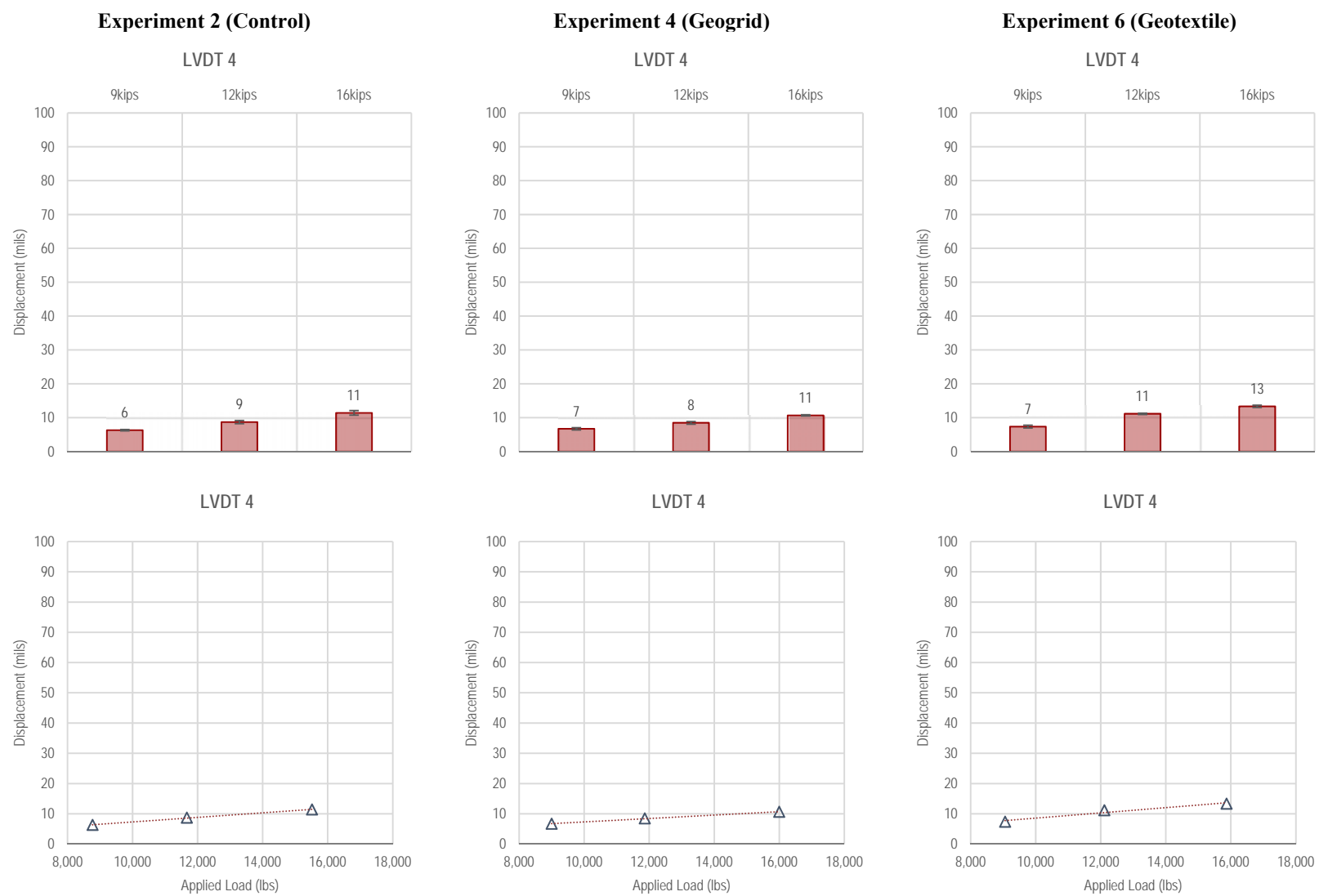
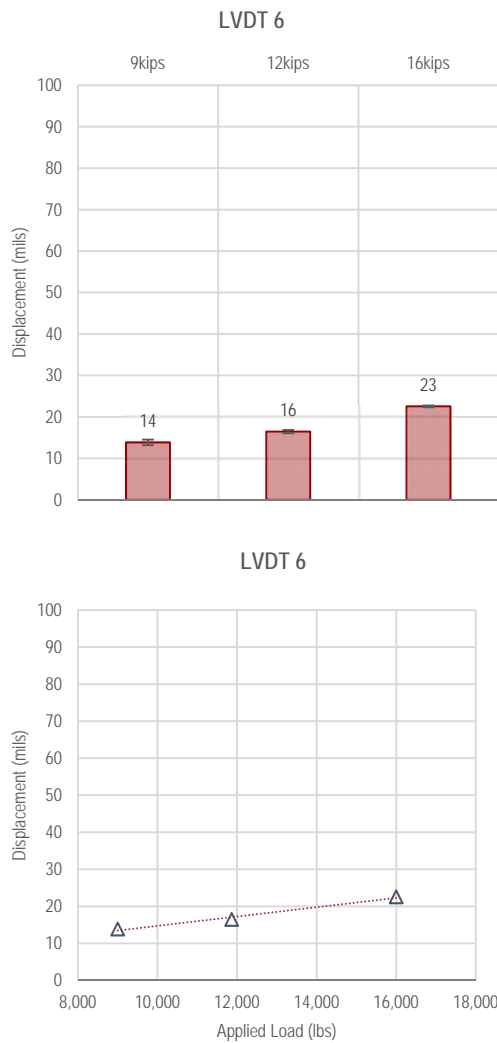


Figure F3-4. Summary of LVDT 4 measurements—Dynamic Loading

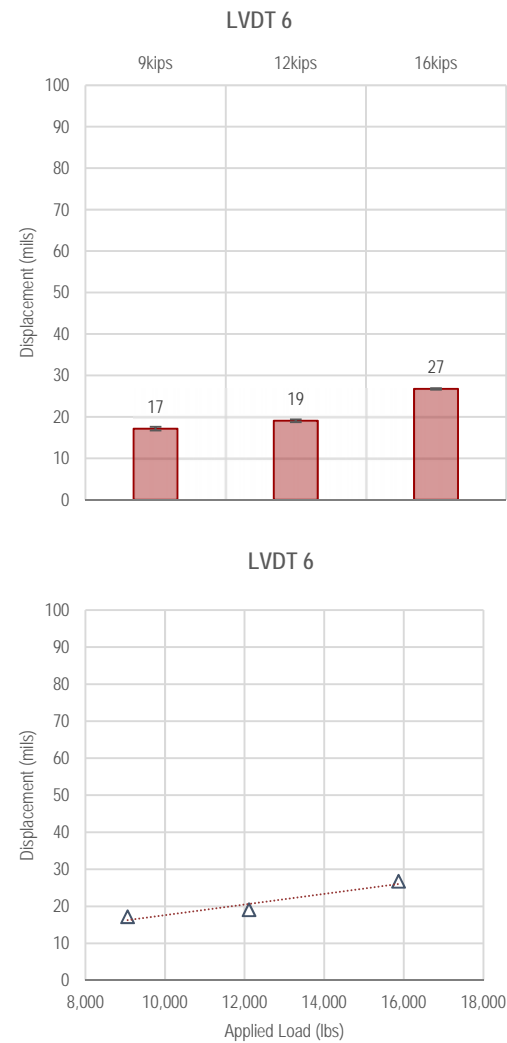
Experiment 2 (Control)

Not Available

Experiment 4 (Geogrid)



Experiment 6 (Geotextile)



Not Available

Figure F3-5. Summary of LVDT 6 measurements—Dynamic Loading

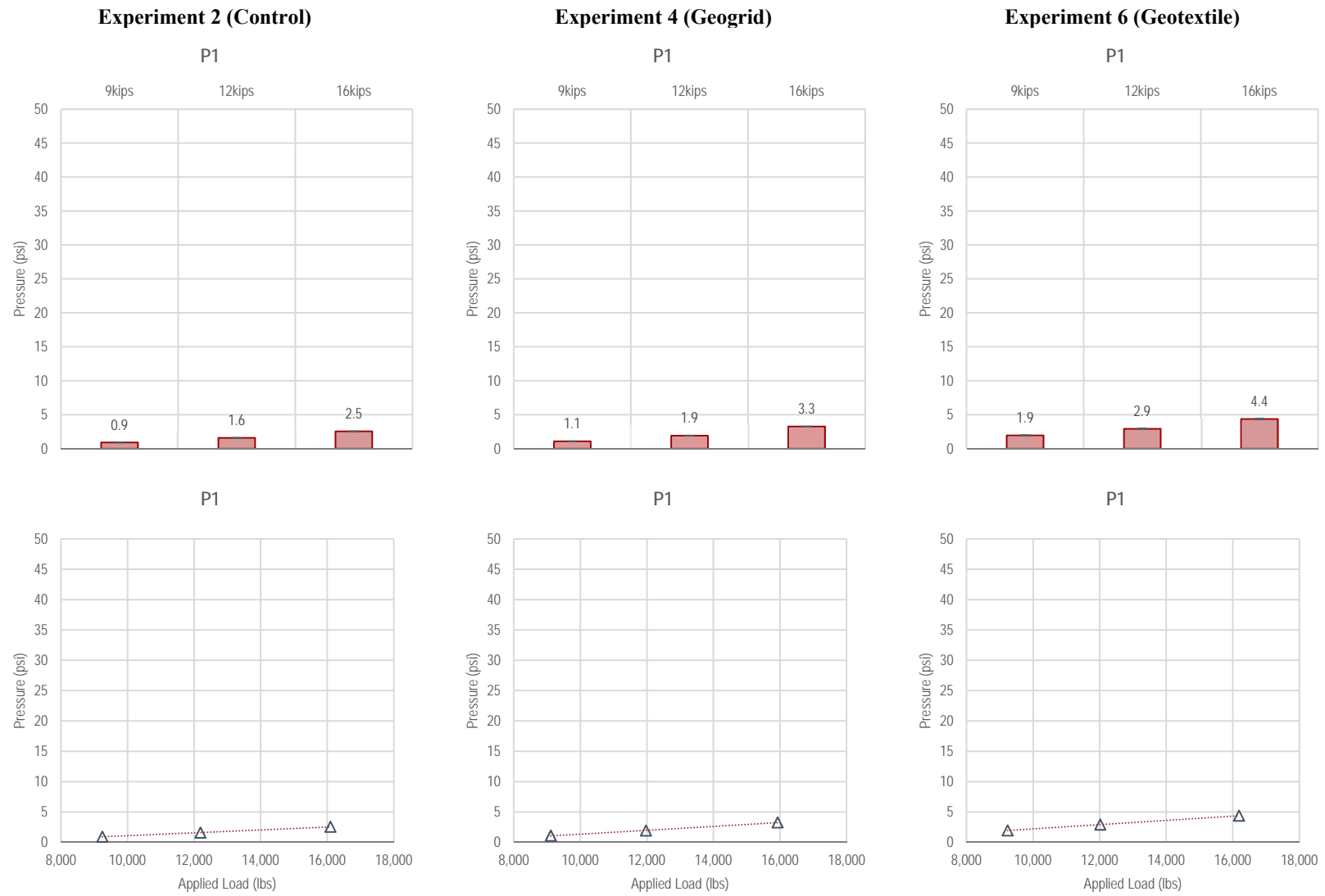
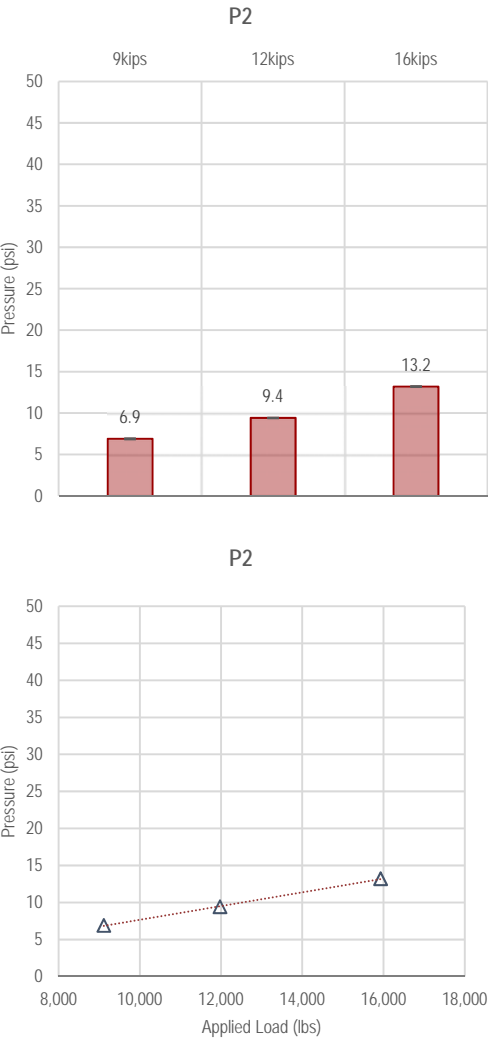


Figure F3-6. Summary of P1 measurements—Dynamic Loading

Experiment 2 (Control)

Not Available

Experiment 4 (Geogrid)



Experiment 6 (Geotextile)

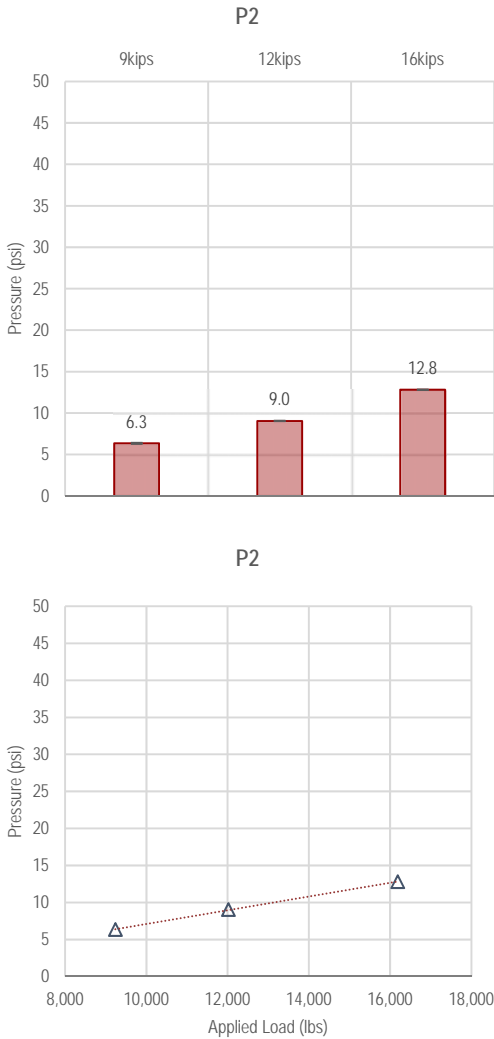
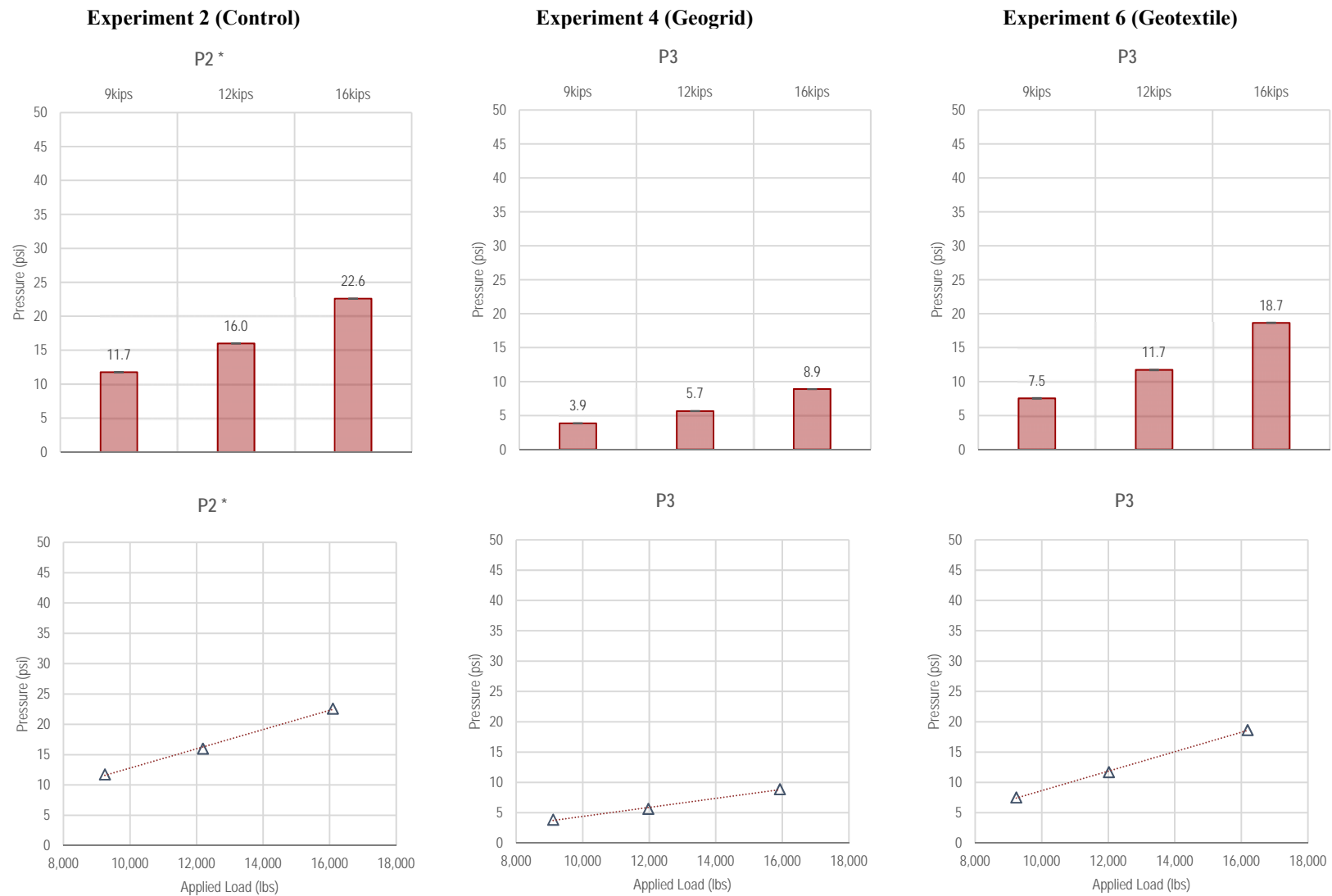


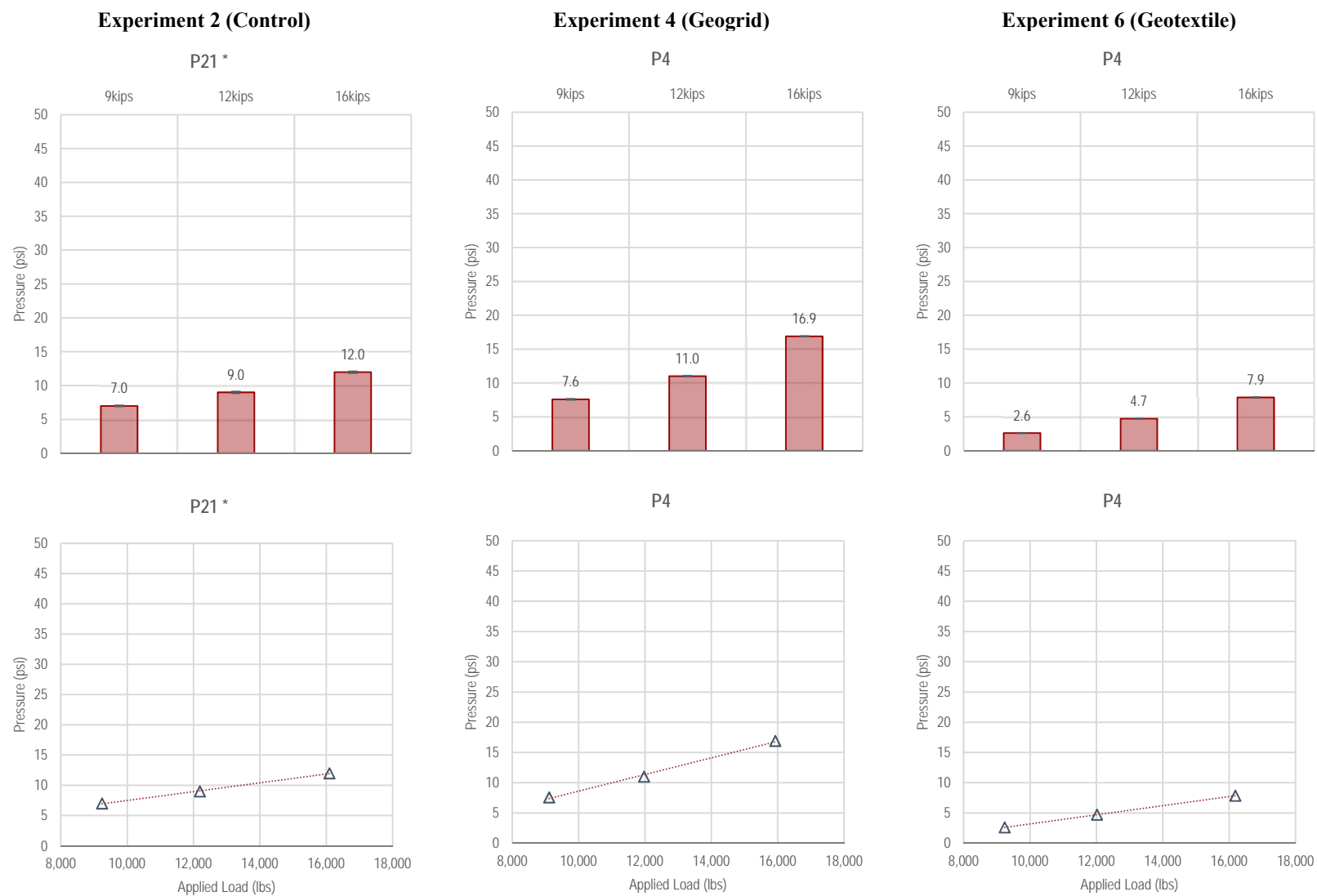
Figure F3-7. Summary of P2 measurements—Dynamic Loading

F-70



*For Control, P2 measurements are used since they are equivalent to P3 measurements in Reinforced experiments

Figure F3-8. Summary of P3 measurements—Dynamic Loading



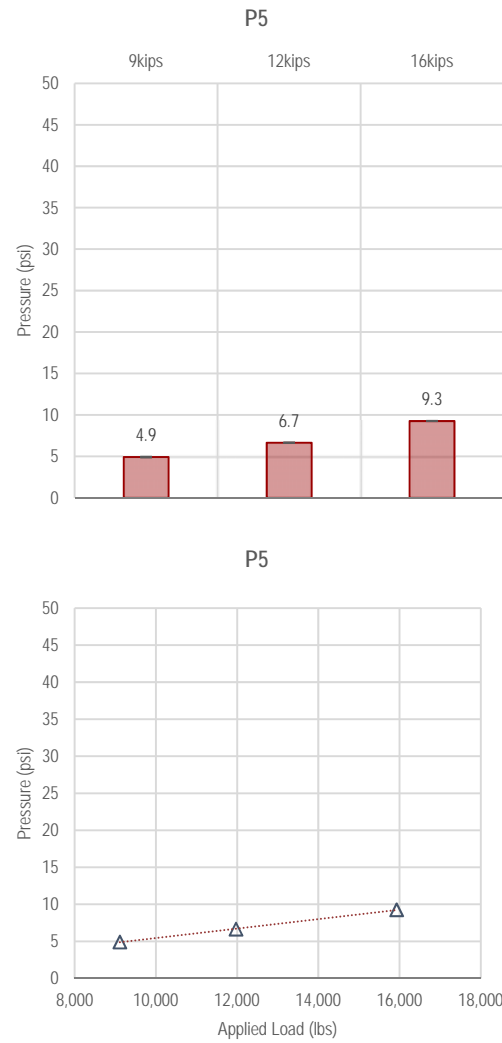
*For Control, P21 measurements are used since they are equivalent to P4 measurements in Reinforced experiments

Figure F3-9. Summary of P4 measurements—Dynamic Loading

Experiment 2 (Control)

Not Available

Experiment 4 (Geogrid)



Experiment 6 (Geotextile)

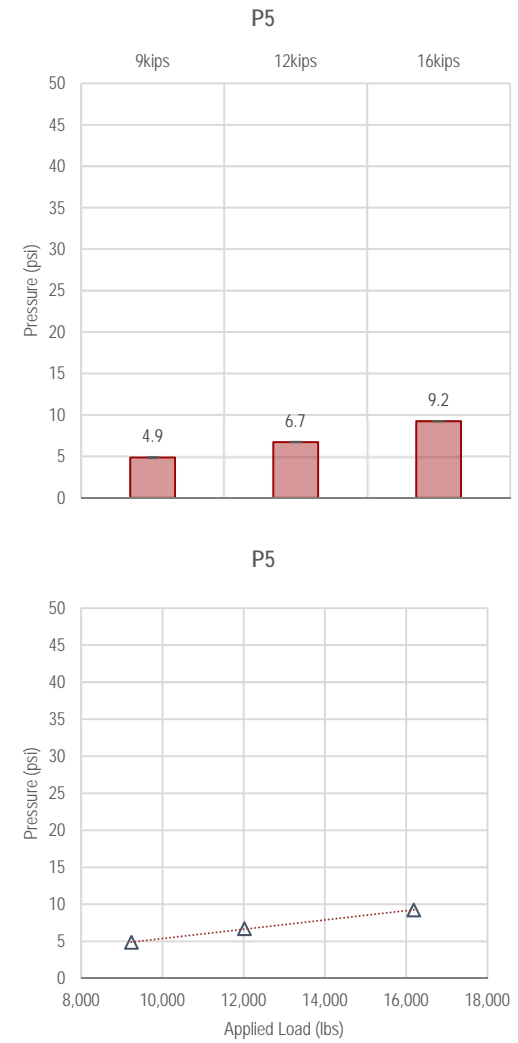
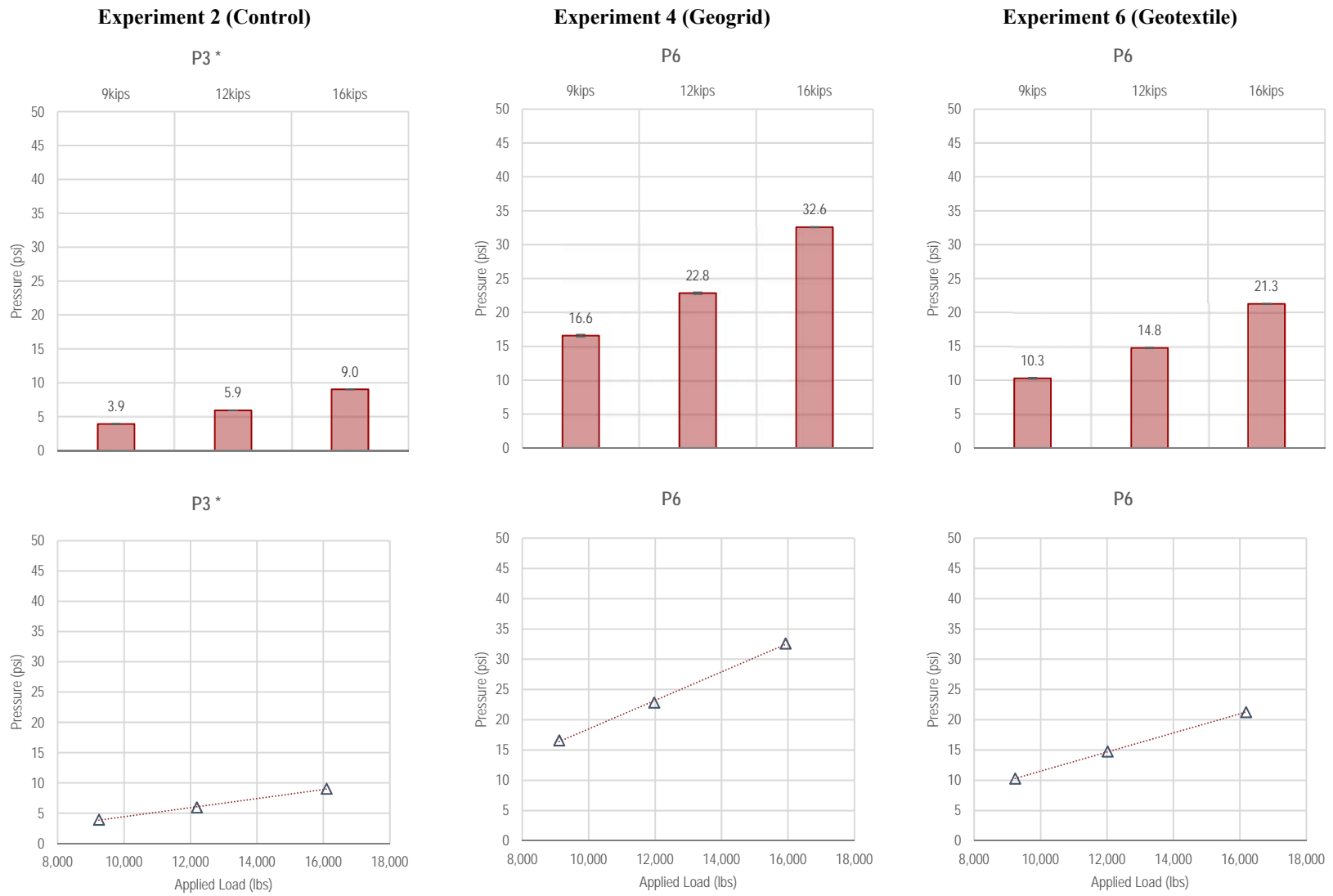
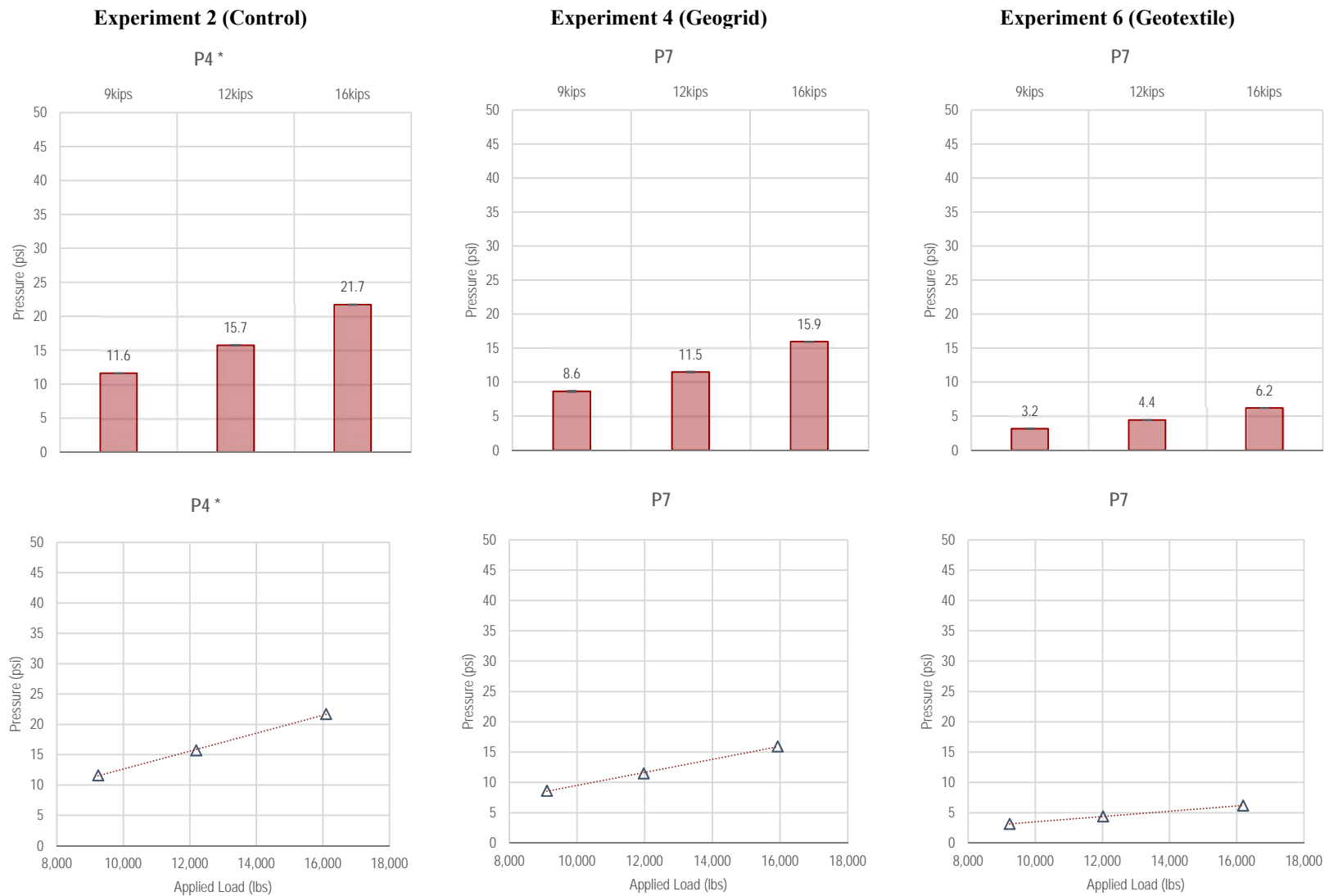


Figure F3-10. Summary of P5 measurements—Dynamic Loading



*For Control, P3 measurements are used since they are equivalent to P6 measurements in Reinforced experiments

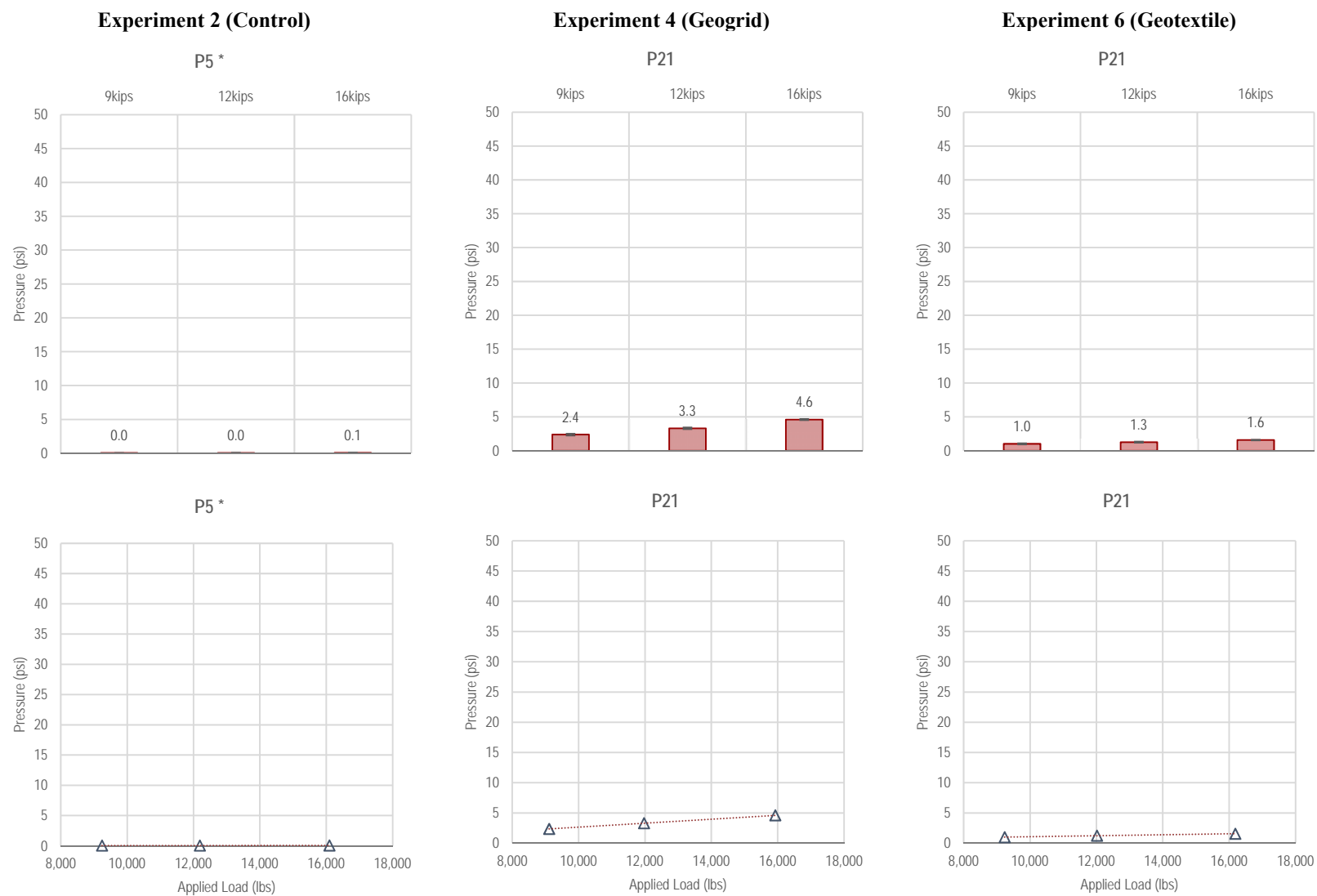
Figure F3-11. Summary of P6 measurements—Dynamic Loading



*For Control, P4 measurements are used since they are equivalent to P7 measurements in Reinforced experiments

Figure F3-12. Summary of P7 measurements—Dynamic Loading

F-74



*For Control, P5 measurements are used since they are equivalent to P21 measurements in Reinforced experiments

Figure F3-13. Summary of P21 measurements—Dynamic Loading

F-76

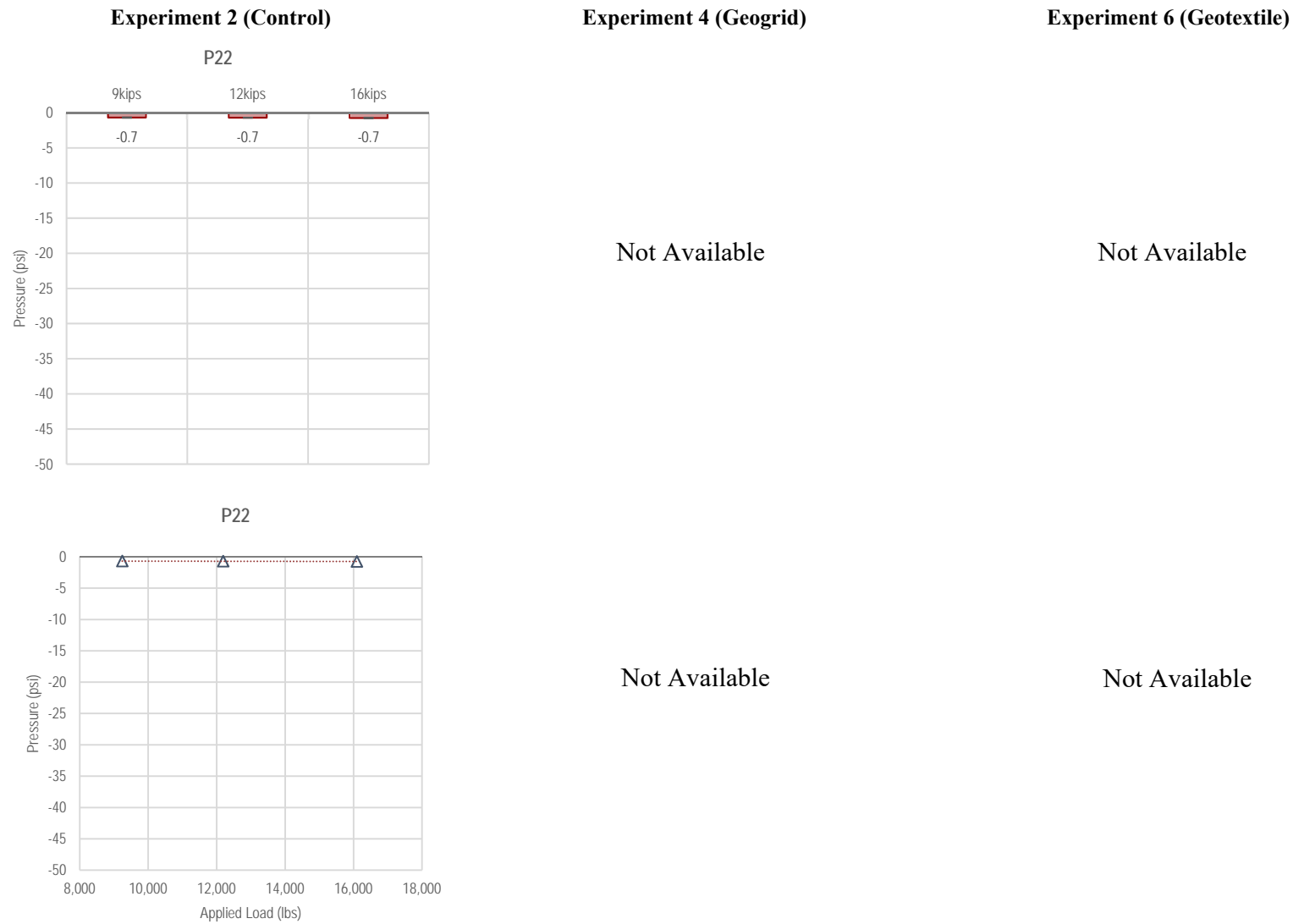


Figure F3-14. Summary of P22 measurements—Dynamic Loading

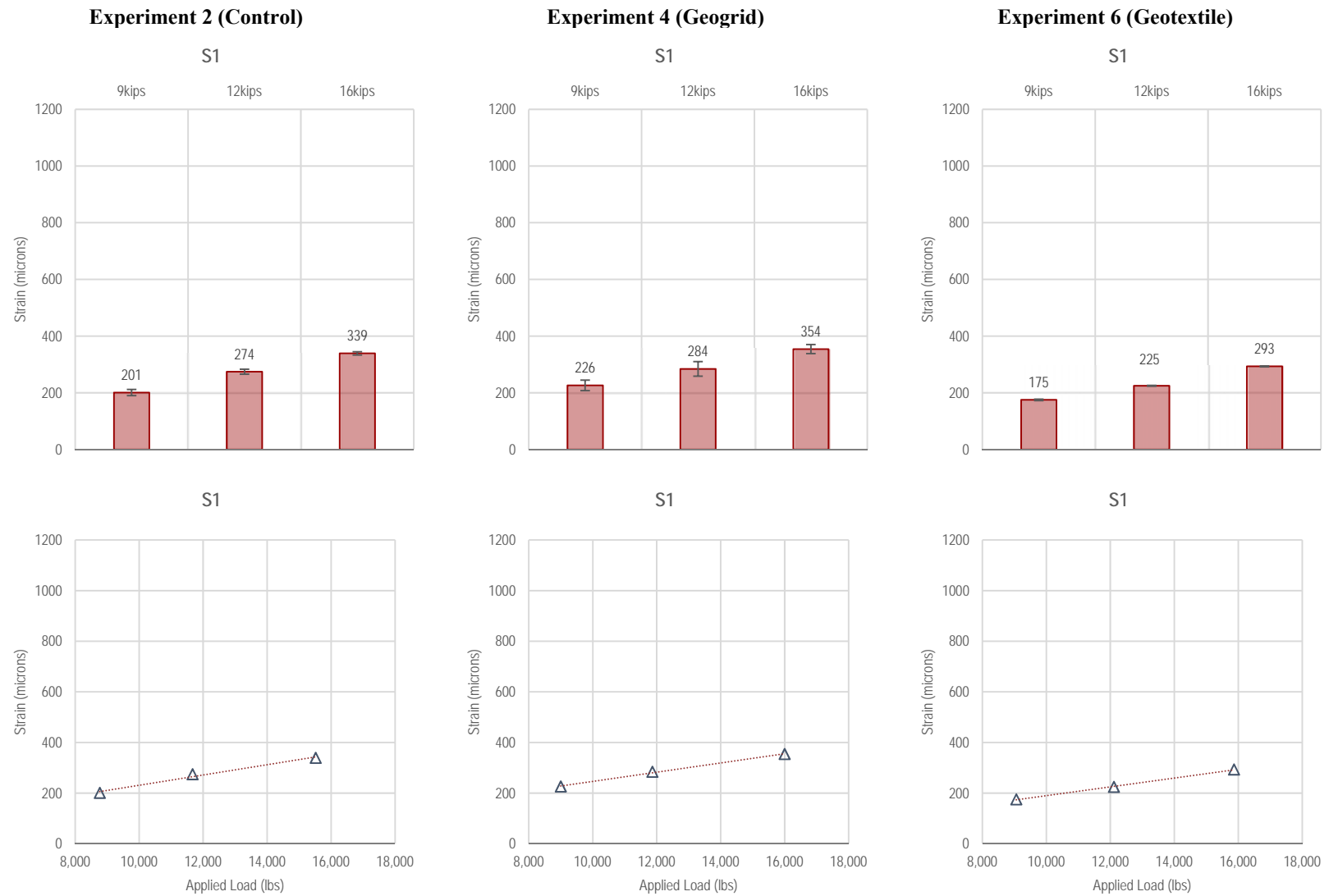
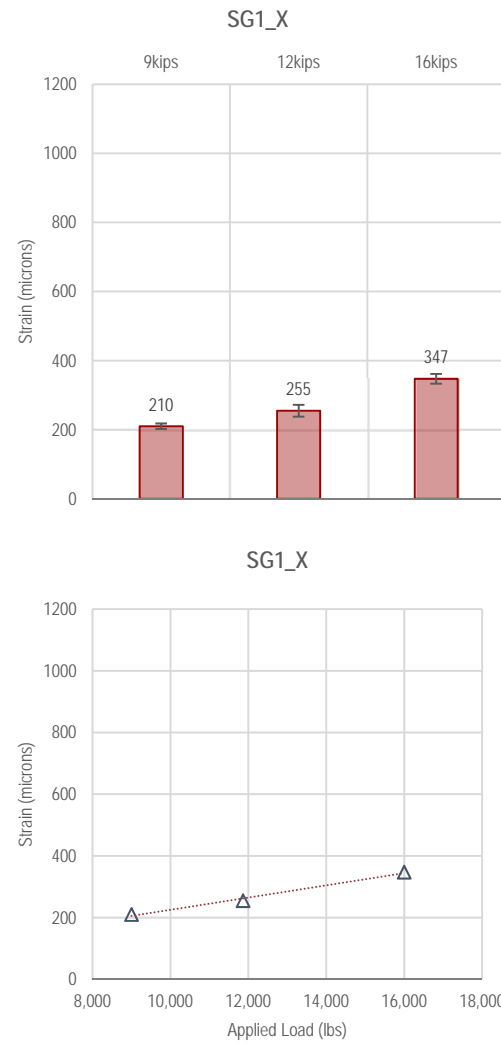


Figure F3-15. Summary of S1 measurements—Dynamic loading

Experiment 2 (Control)

Not Available

Experiment 4 (Geogrid)



Experiment 6 (Geotextile)

Not Available

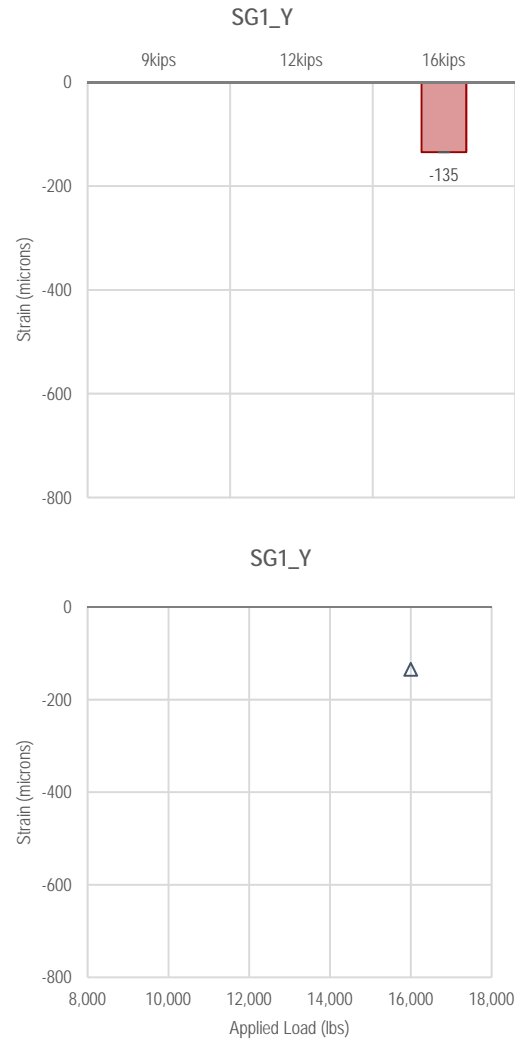
Not Available

Figure F3-16. Summary of SG1_X measurements—Dynamic Loading

Experiment 2 (Control)

Not Available

Experiment 4 (Geogrid)



Experiment 6 (Geotextile)

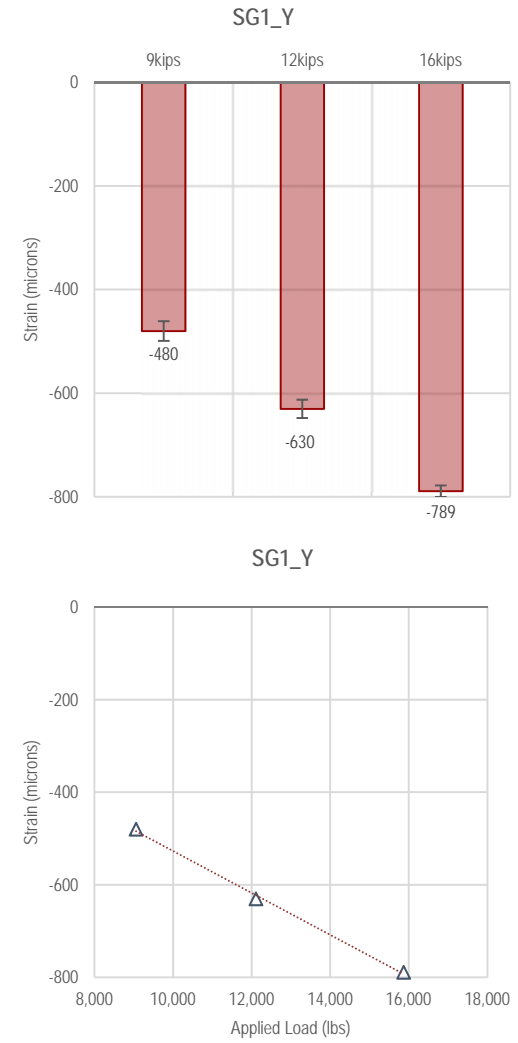


Figure F3-17. Summary of SG1_Y measurements—Dynamic Loading

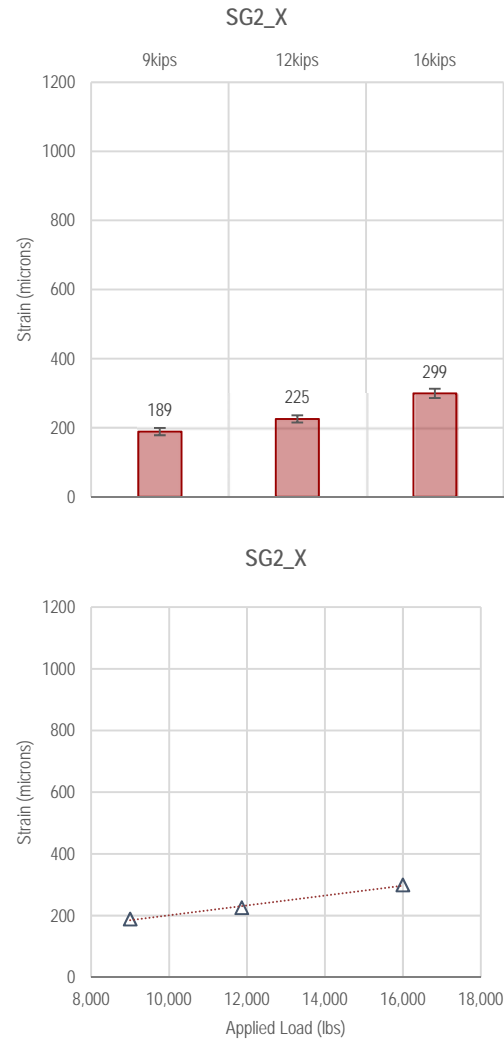
F-80

Experiment 2 (Control)

Not Available

Not Available

Experiment 4 (Geogrid)



Experiment 6 (Geotextile)

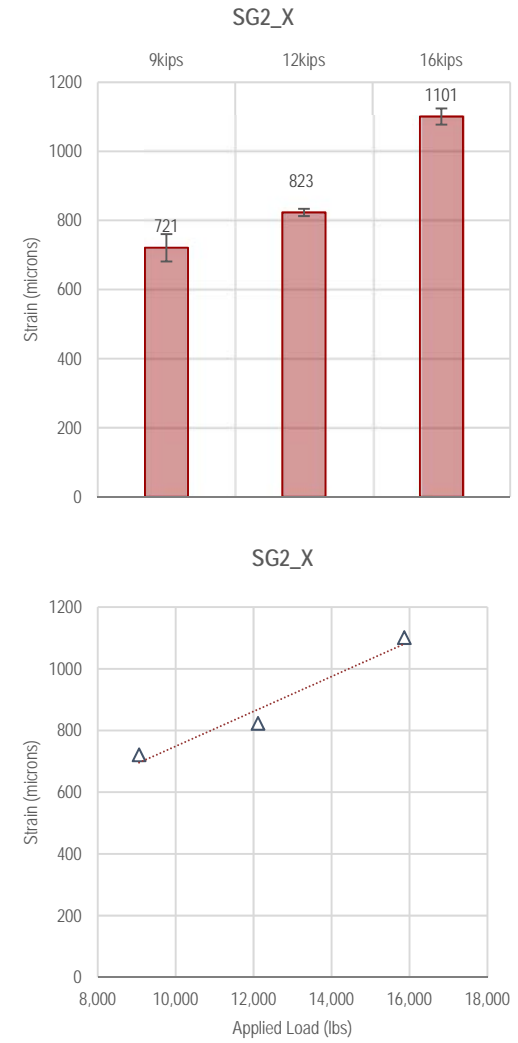


Figure F3-18. Summary of SG2_X measurements—Dynamic Loading

F-81

Experiment 2 (Control)

Not Available

Not Available

Experiment 4 (Geogrid)

Not Available

Not Available

Experiment 6 (Geotextile)

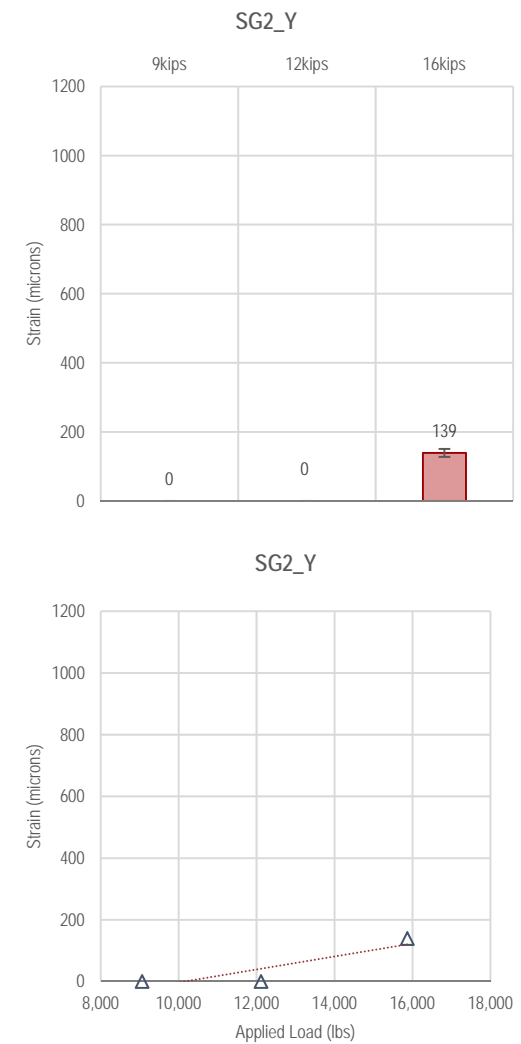
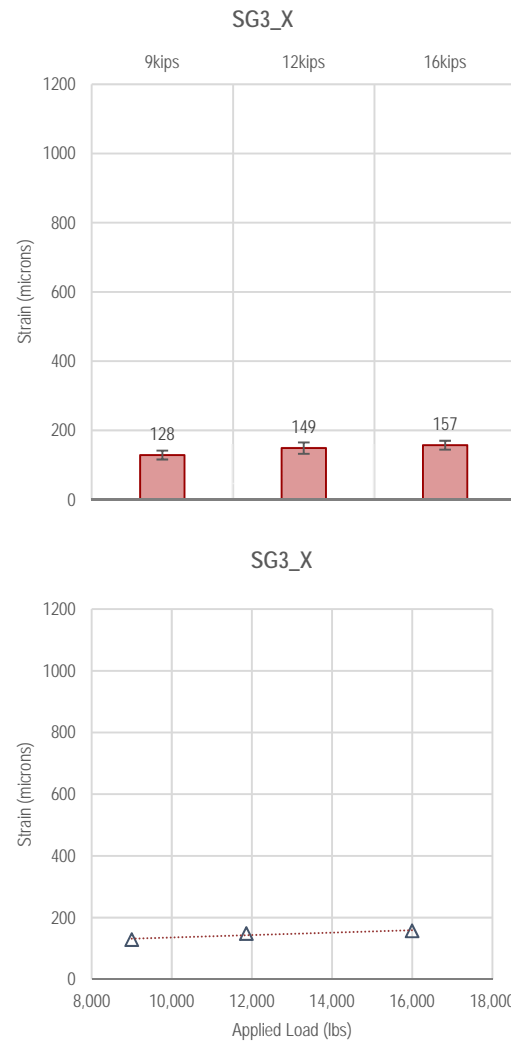


Figure F3-19. Summary of SG2_Y measurements—Dynamic Loading

Experiment 2 (Control)

Not Available

Experiment 4 (Geogrid)



Experiment 6 (Geotextile)

Not Available

Not Available

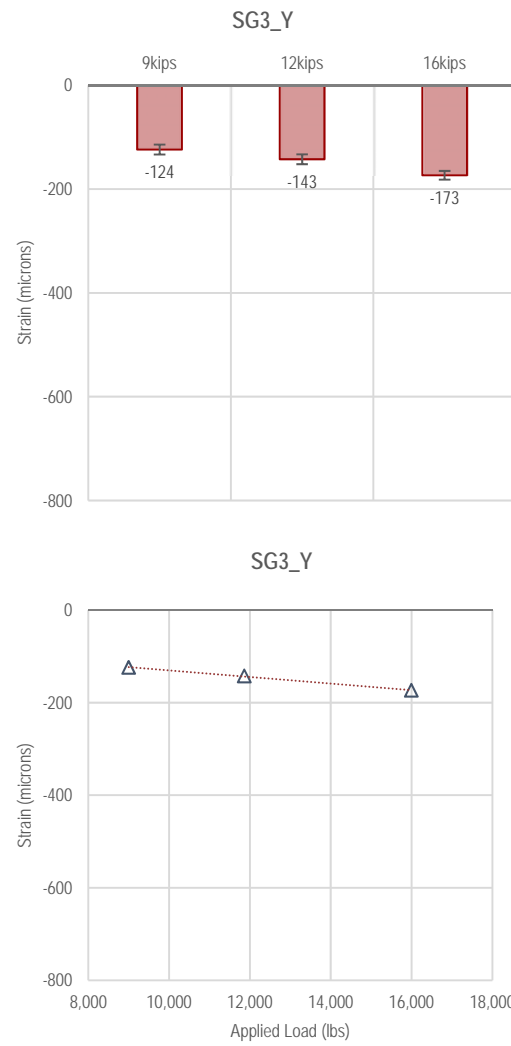
Not Available

Figure F3-20. Summary of SG3_X measurements—Dynamic Loading

Experiment 2 (Control)

Not Available

Experiment 4 (Geogrid)



Experiment 6 (Geotextile)

Not Available

Not Available

Figure F3-21. Summary of SG3_Y measurements—Dynamic Loading

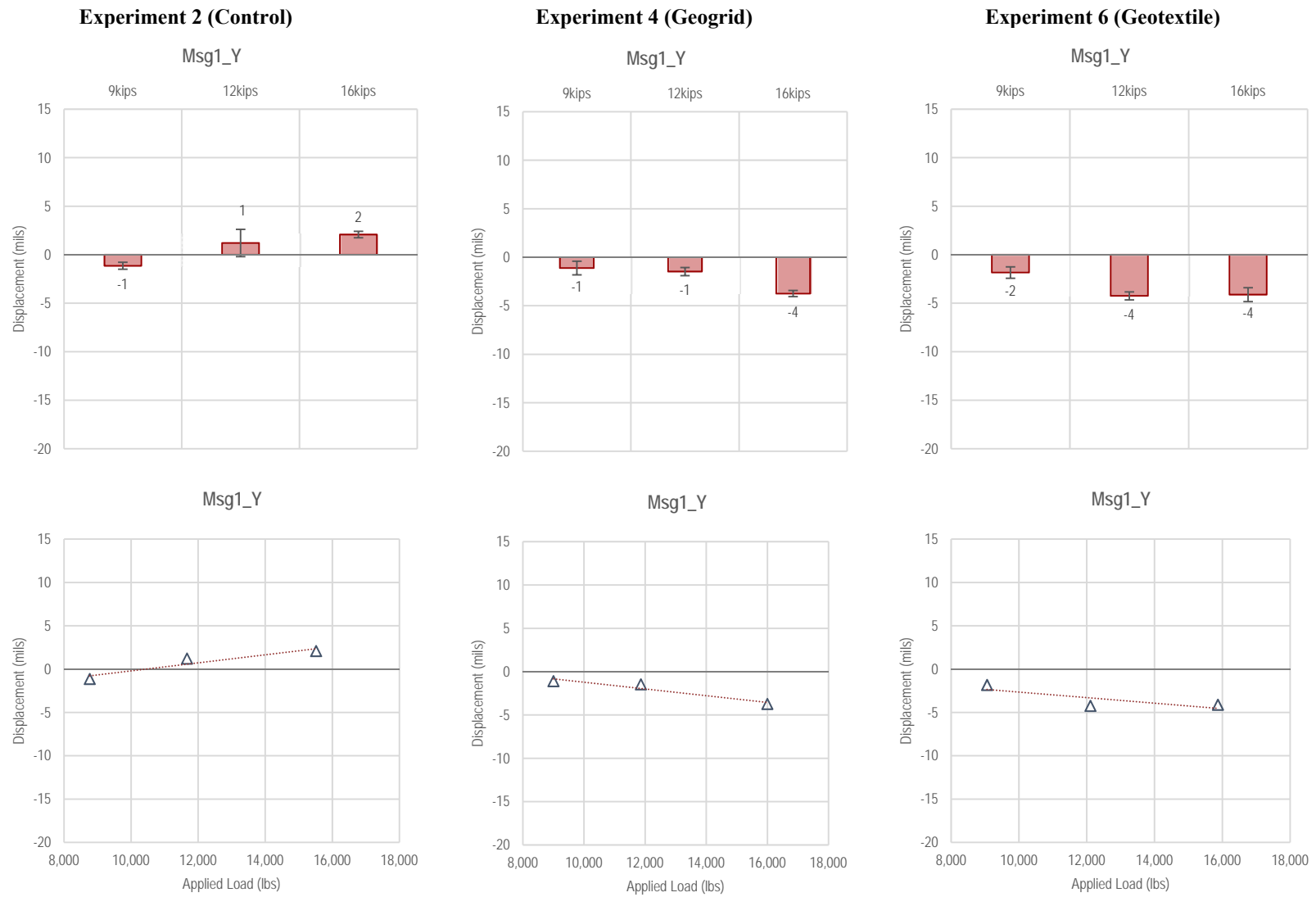


Figure F3-22. Summary of Msg1_Y measurements—Dynamic Loading

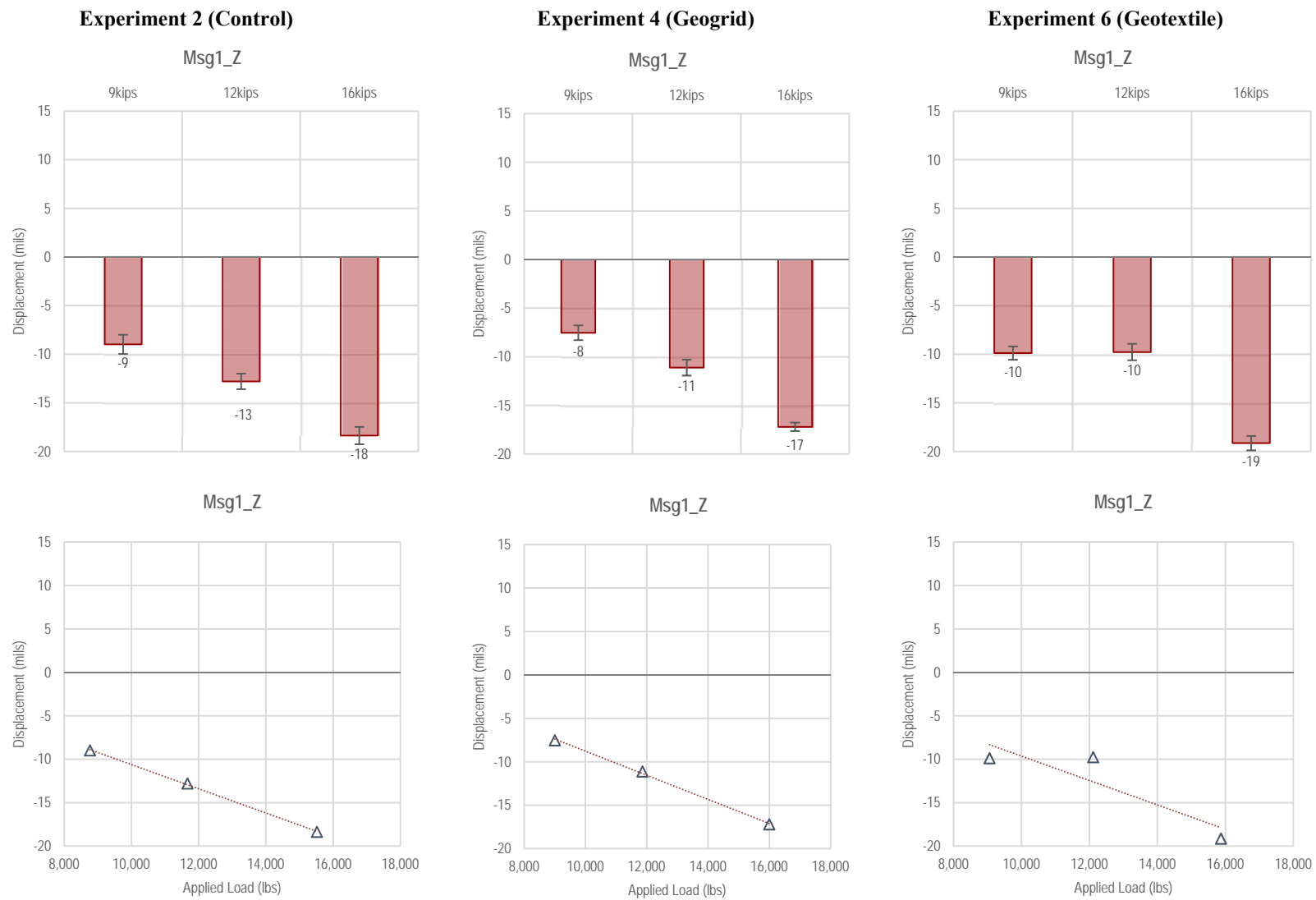


Figure F3-23. Summary of Msg1_Z measurements—Dynamic Loading

F-85

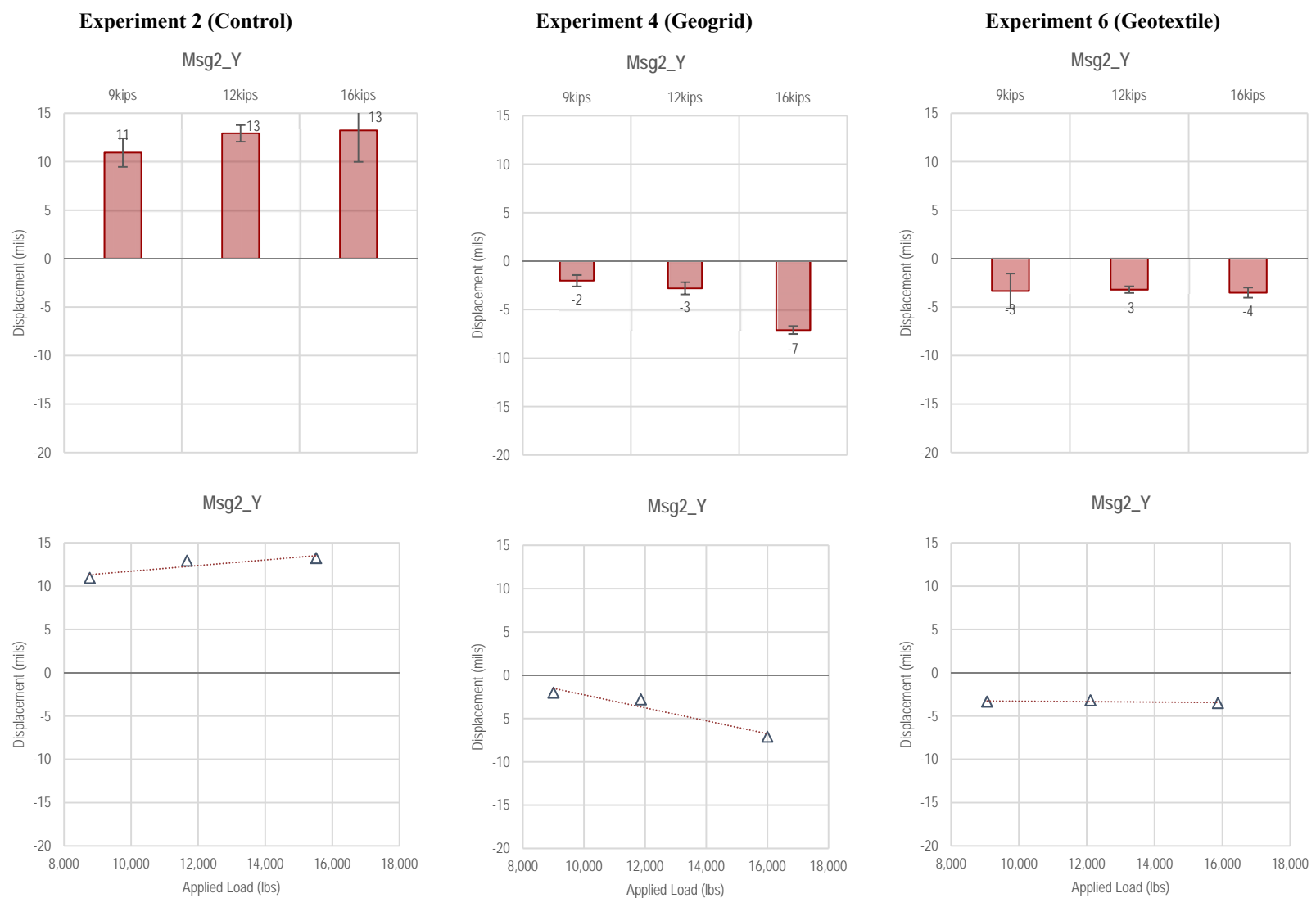


Figure F3-24. Summary of Msg2_Y measurements—Dynamic Loading

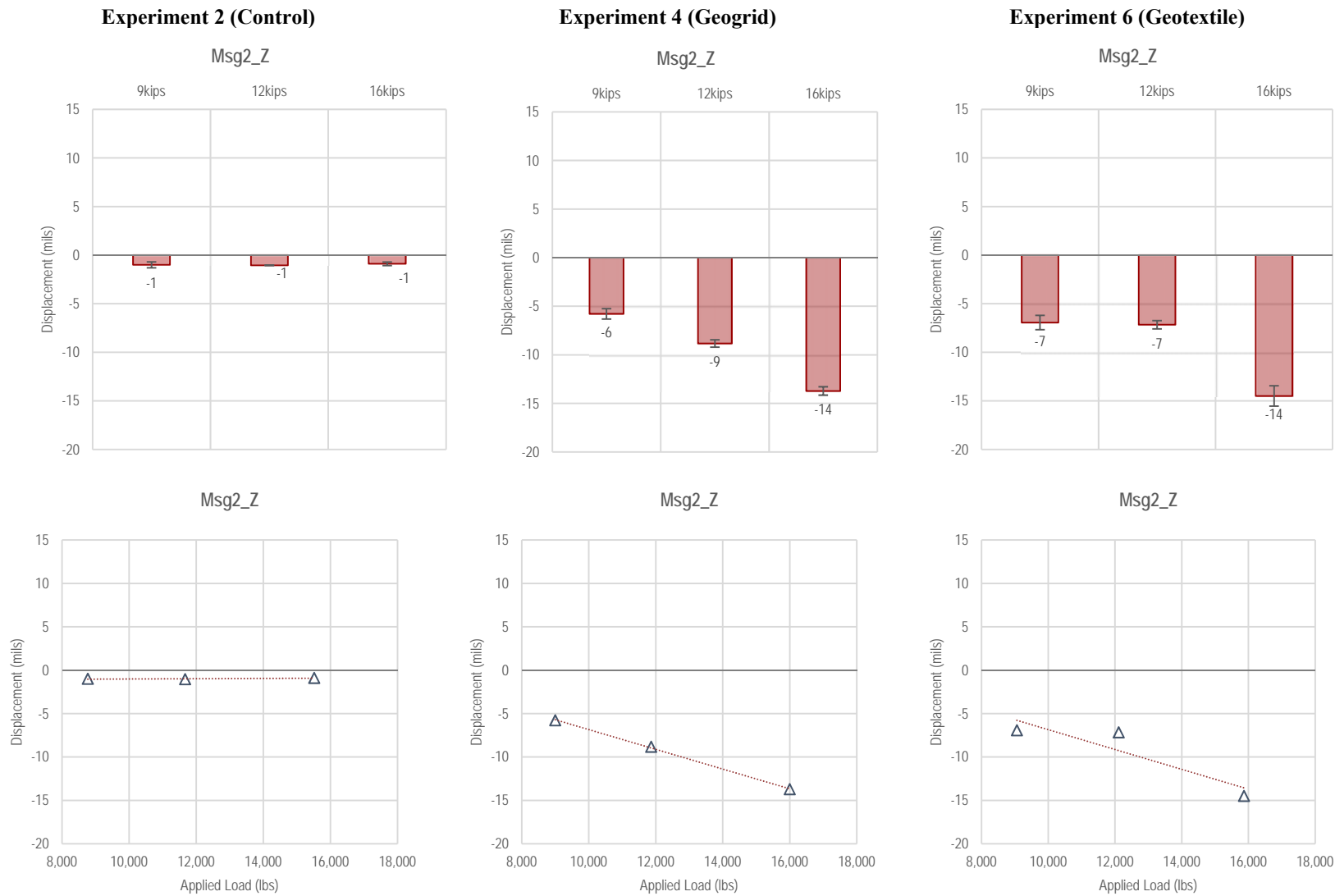


Figure F3-25. Summary of Msg2_Z measurements—Dynamic Loading

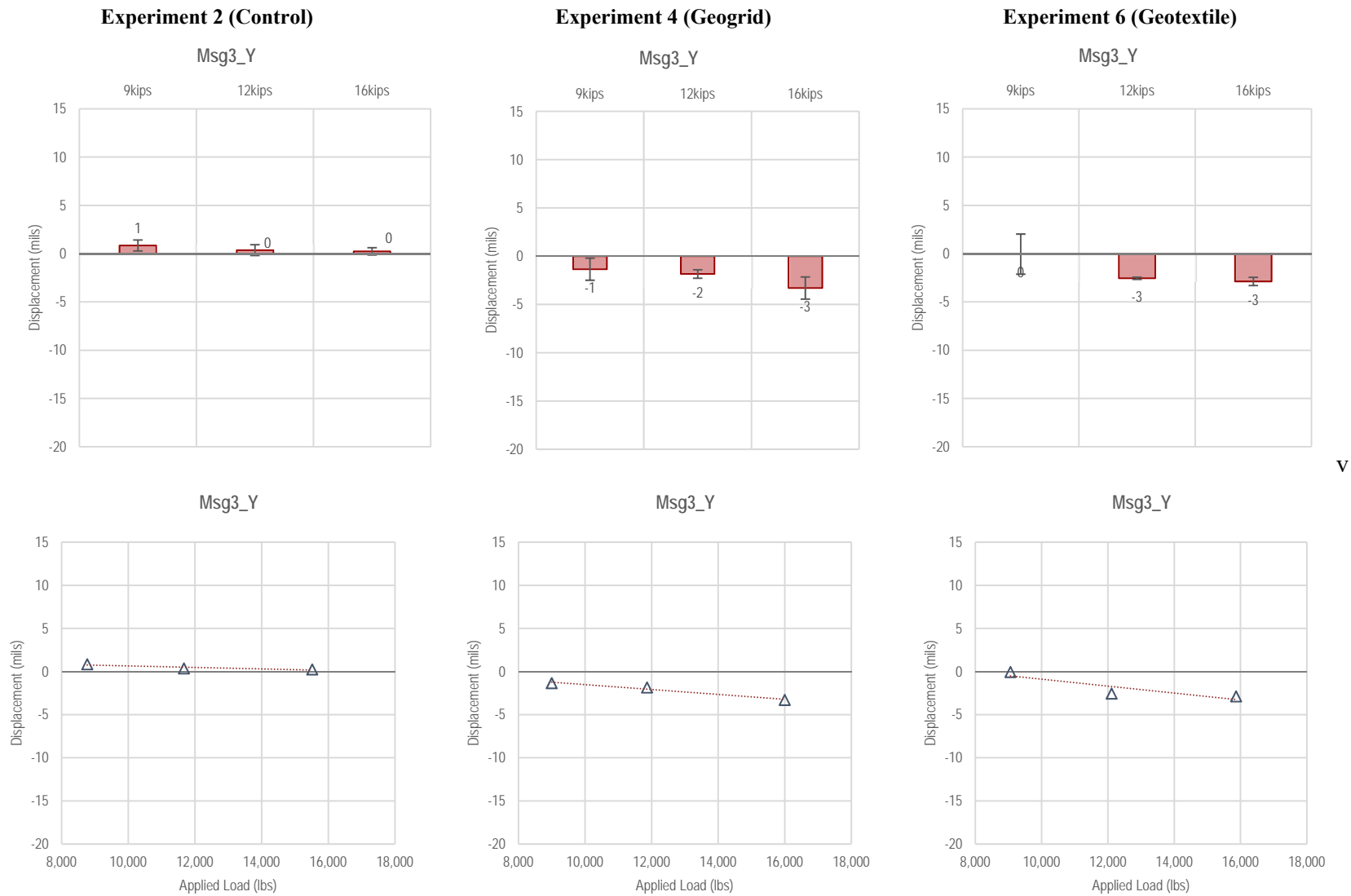


Figure F3-26. Summary of Msg3_Y measurements—Dynamic Loading

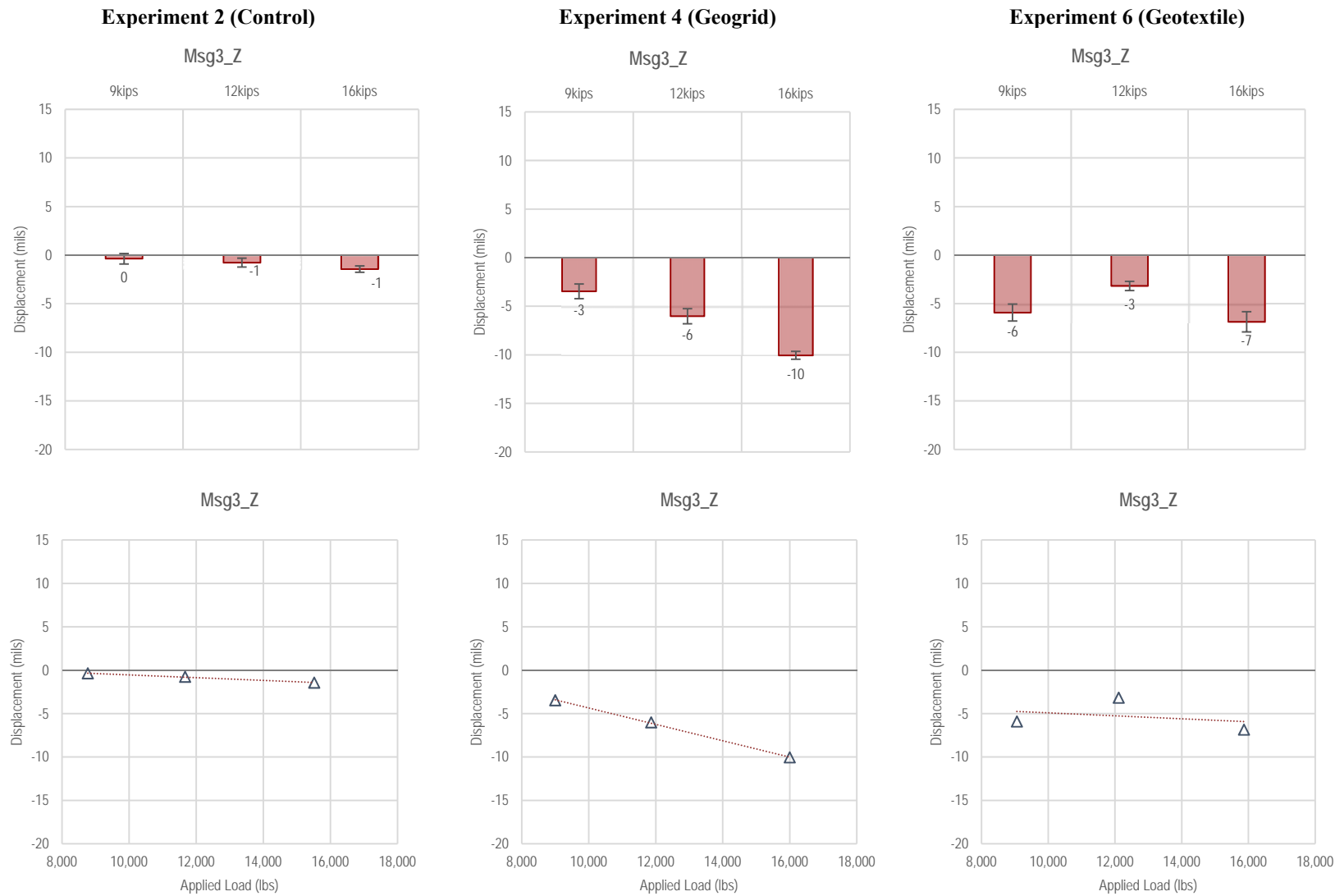
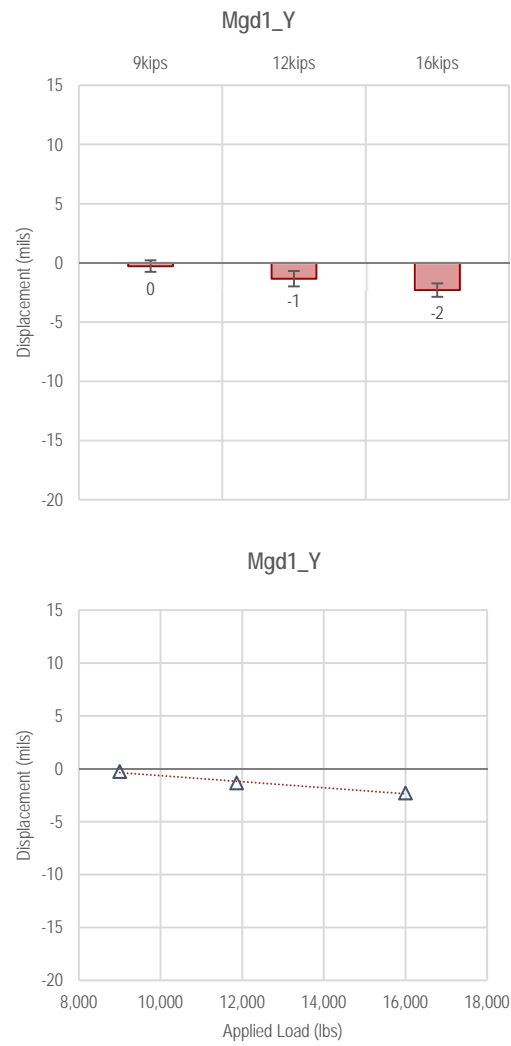


Figure F3-27. Summary of Msg3_Z measurements—Dynamic Loading

Experiment 2 (Control)

Not Available

Experiment 4 (Geogrid)



Experiment 6 (Geotextile)

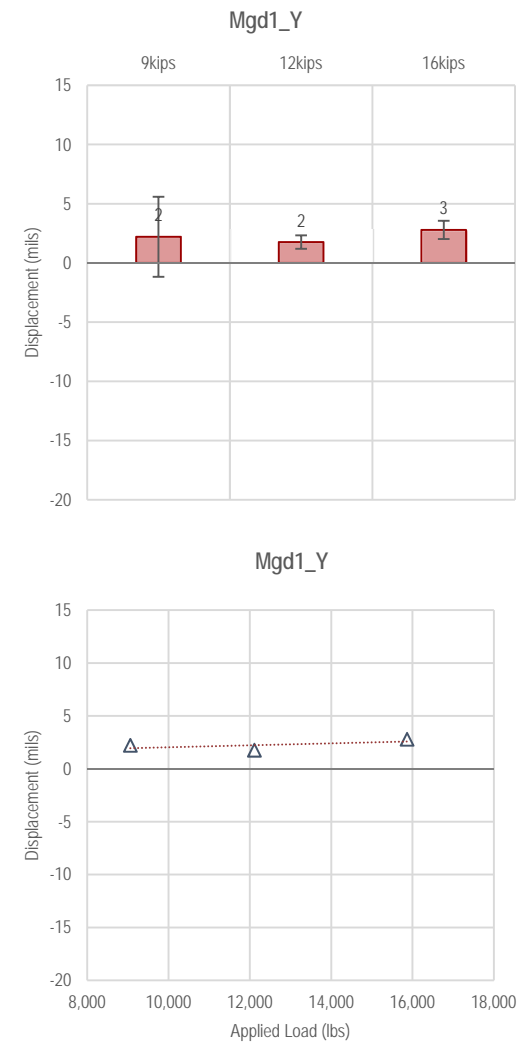
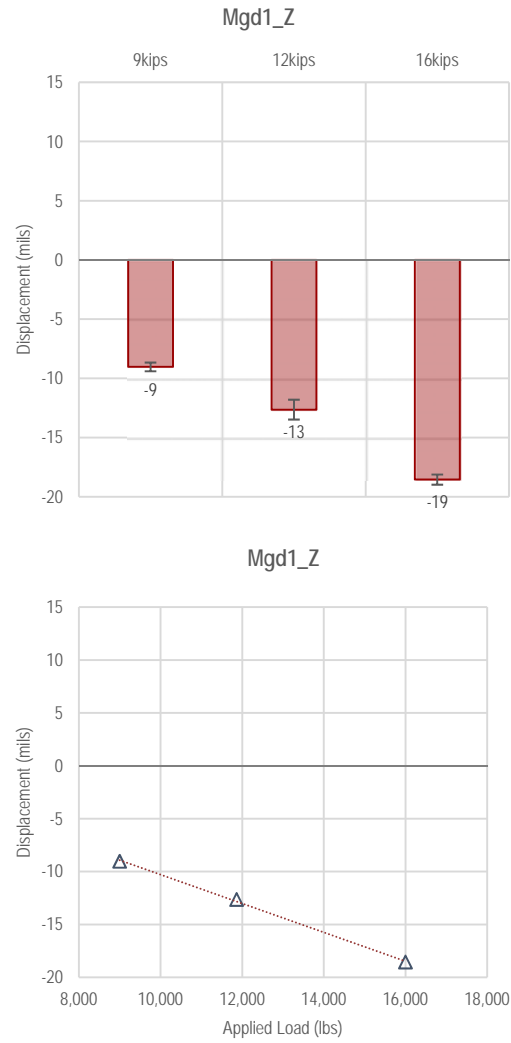


Figure F3-28. Summary of Mgd1_Y measurements—Dynamic Loading

Experiment 2 (Control)

Not Available

Experiment 4 (Geogrid)



Experiment 6 (Geotextile)

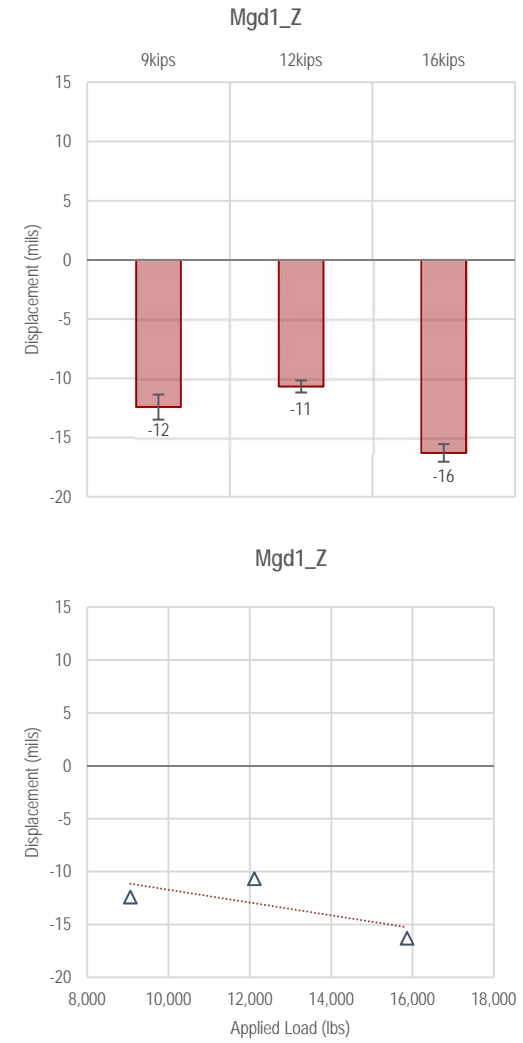
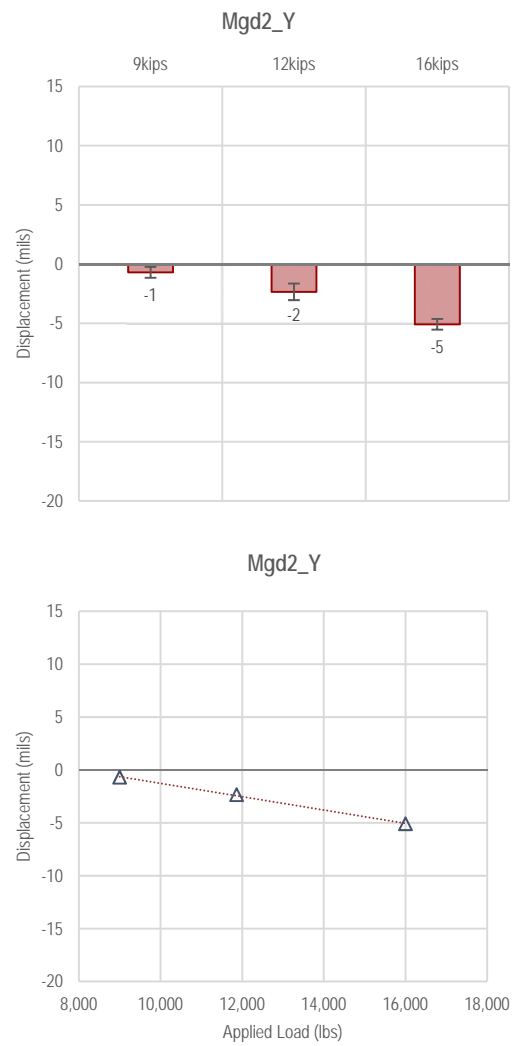


Figure F3-29. Summary of Mgd1_Z measurements—Dynamic Loading

Experiment 2 (Control)

Not Available

Experiment 4 (Geogrid)



Experiment 6 (Geotextile)

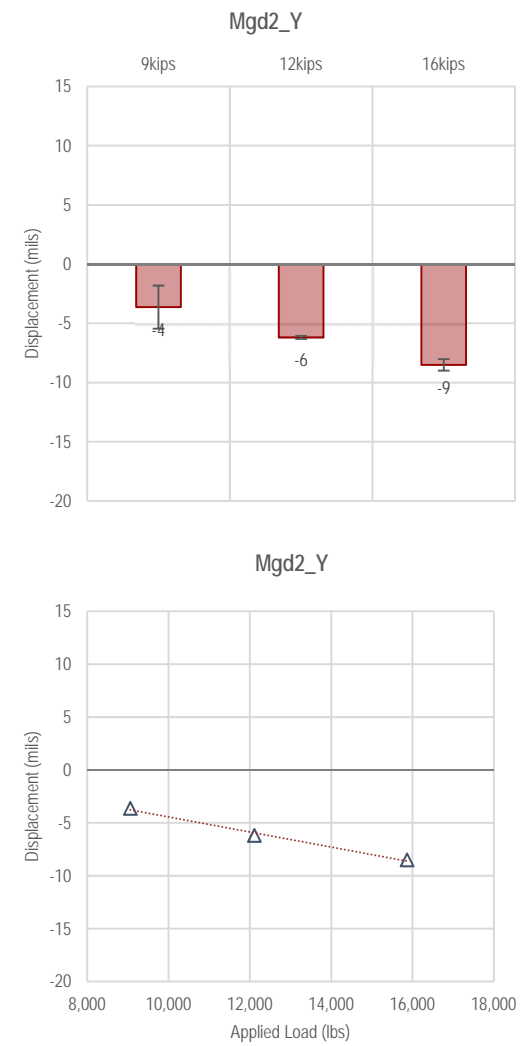
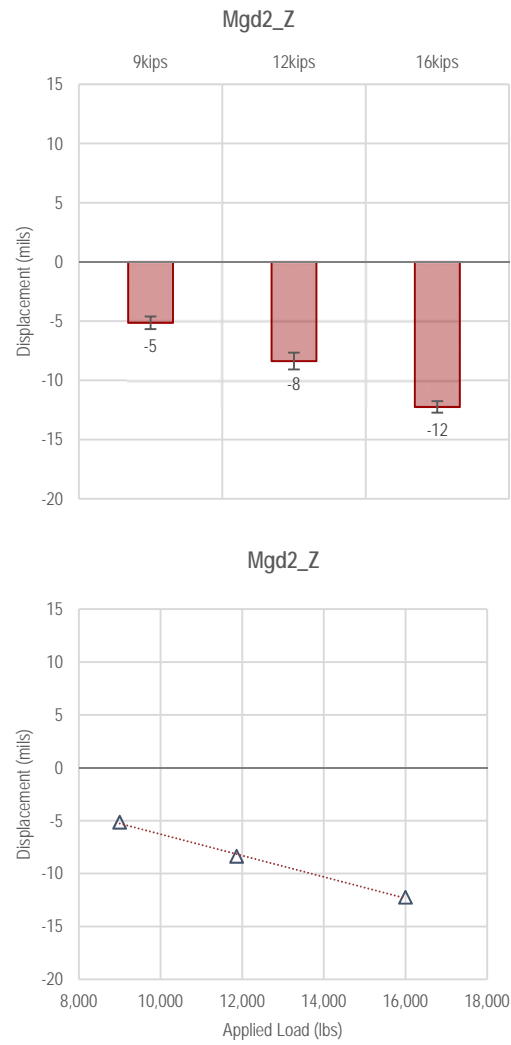


Figure F3-30. Summary of Mgd2_Y measurements—Dynamic Loading

Experiment 2 (Control)

Not Available

Experiment 4 (Geogrid)



Experiment 6 (Geotextile)

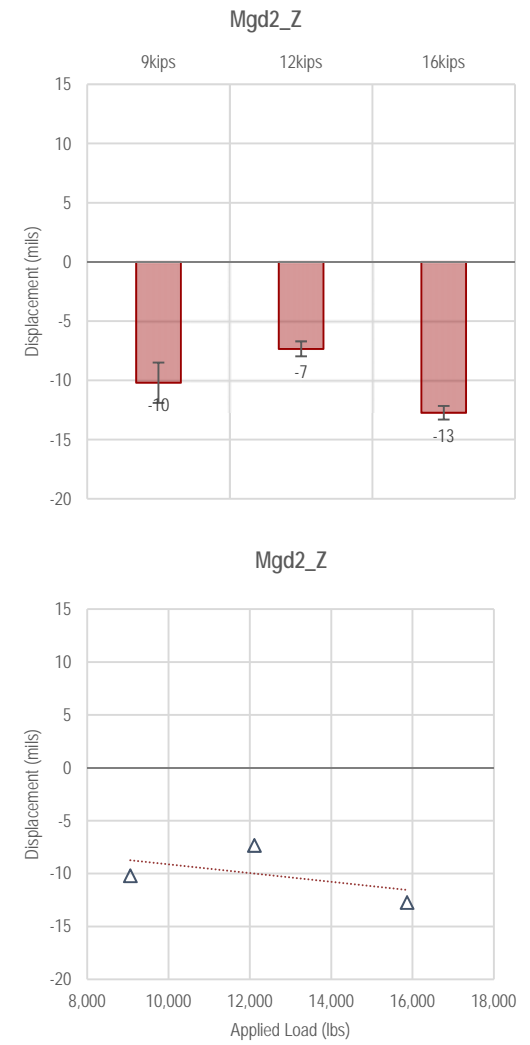


Figure F3-31. Summary of Mgd2_Z measurements—Dynamic Loading

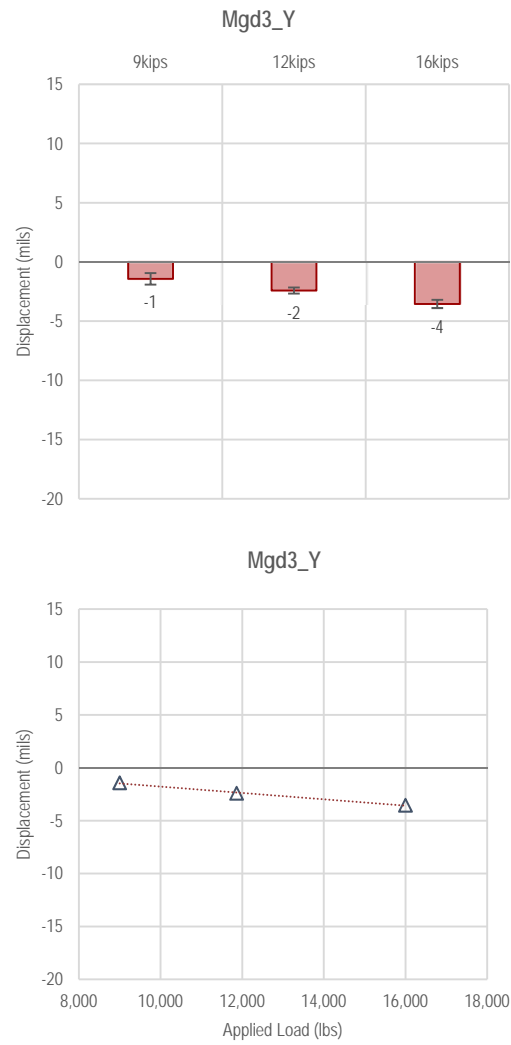
F-94

Experiment 2 (Control)

Not Available

Not Available

Experiment 4 (Geogrid)



Experiment 6 (Geotextile)

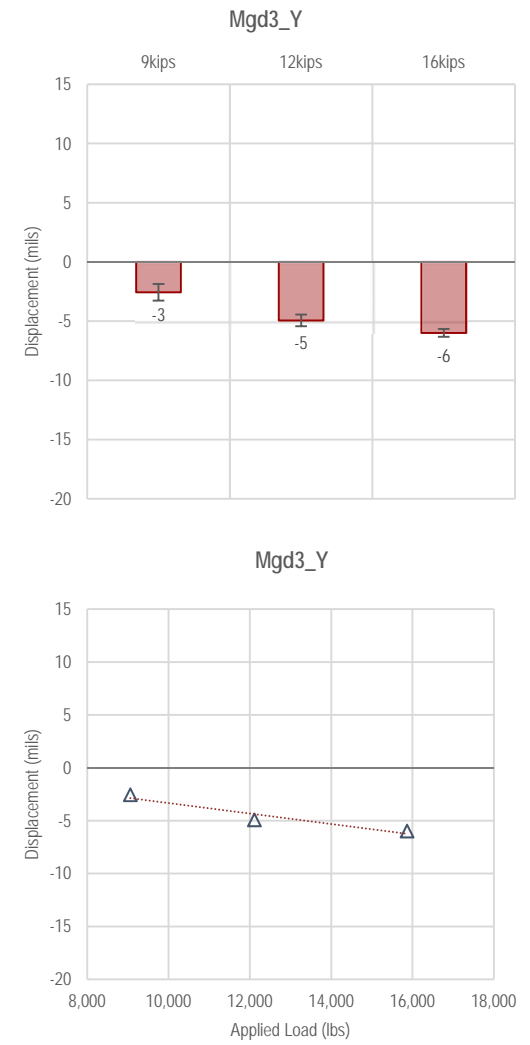


Figure F3-32. Summary of Mgd3_Y measurements—Dynamic Loading

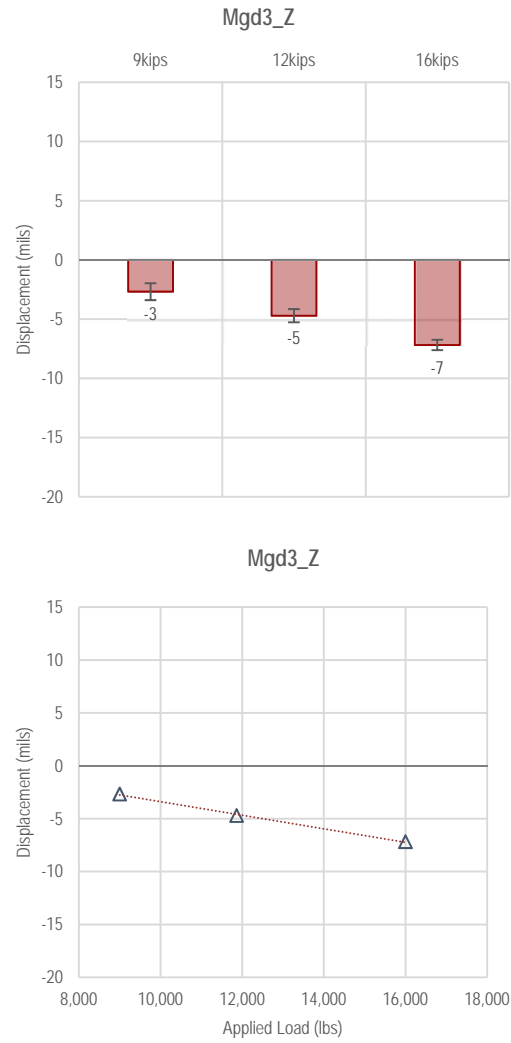
F-95

Experiment 2 (Control)

Not Available

Not Available

Experiment 4 (Geogrid)



Experiment 6 (Geotextile)

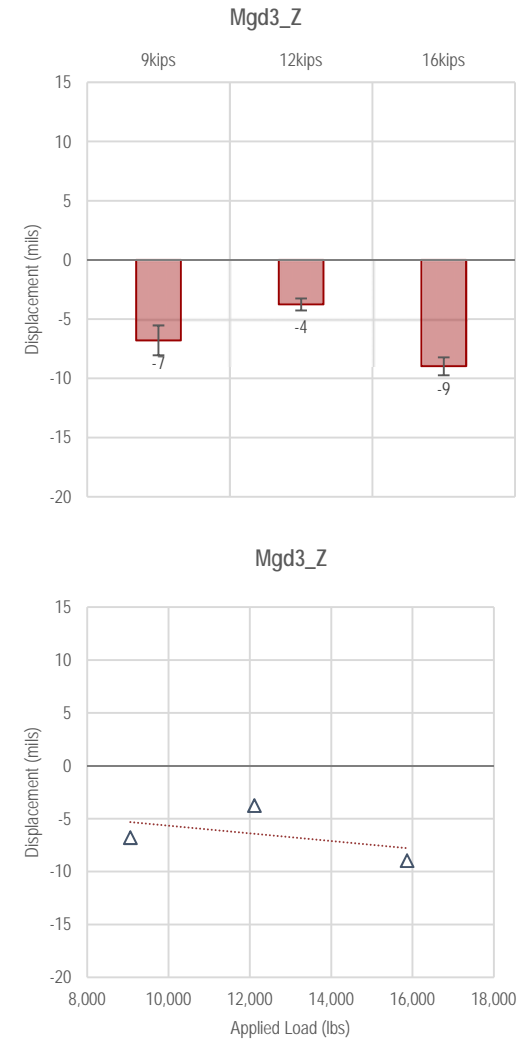


Figure F3-33. Summary of Mgd3_Z measurements—Dynamic Loading

**Appendix F4. Summary Charts for Flexible Pavement Experiments: Static Loading—
Thick Base: No. 2 (Control), No. 4 (Geogrid), and No. 6 (Geotextile)**

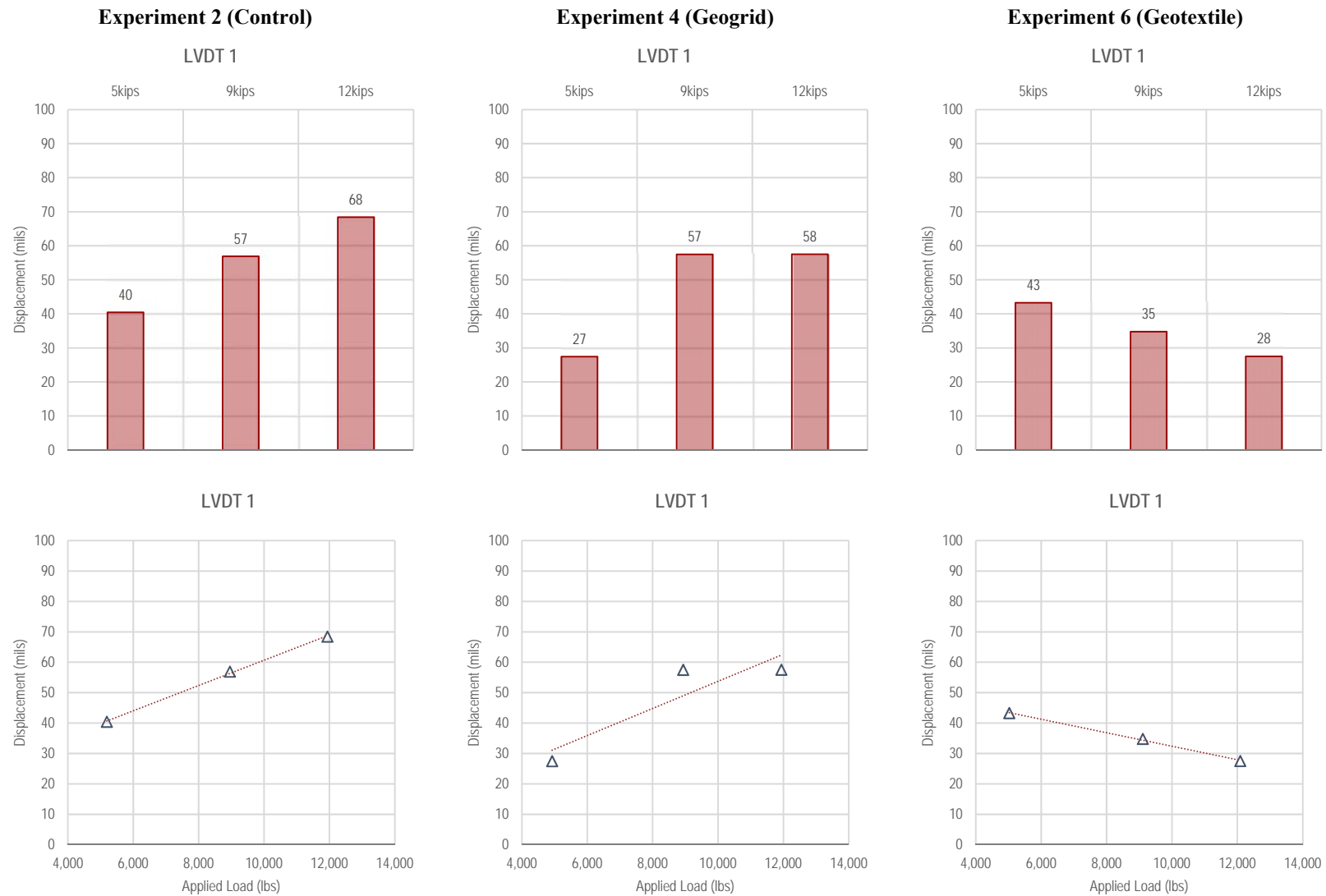


Figure F4-1. Summary of LVDT 1 measurements—Static Loading

F-97

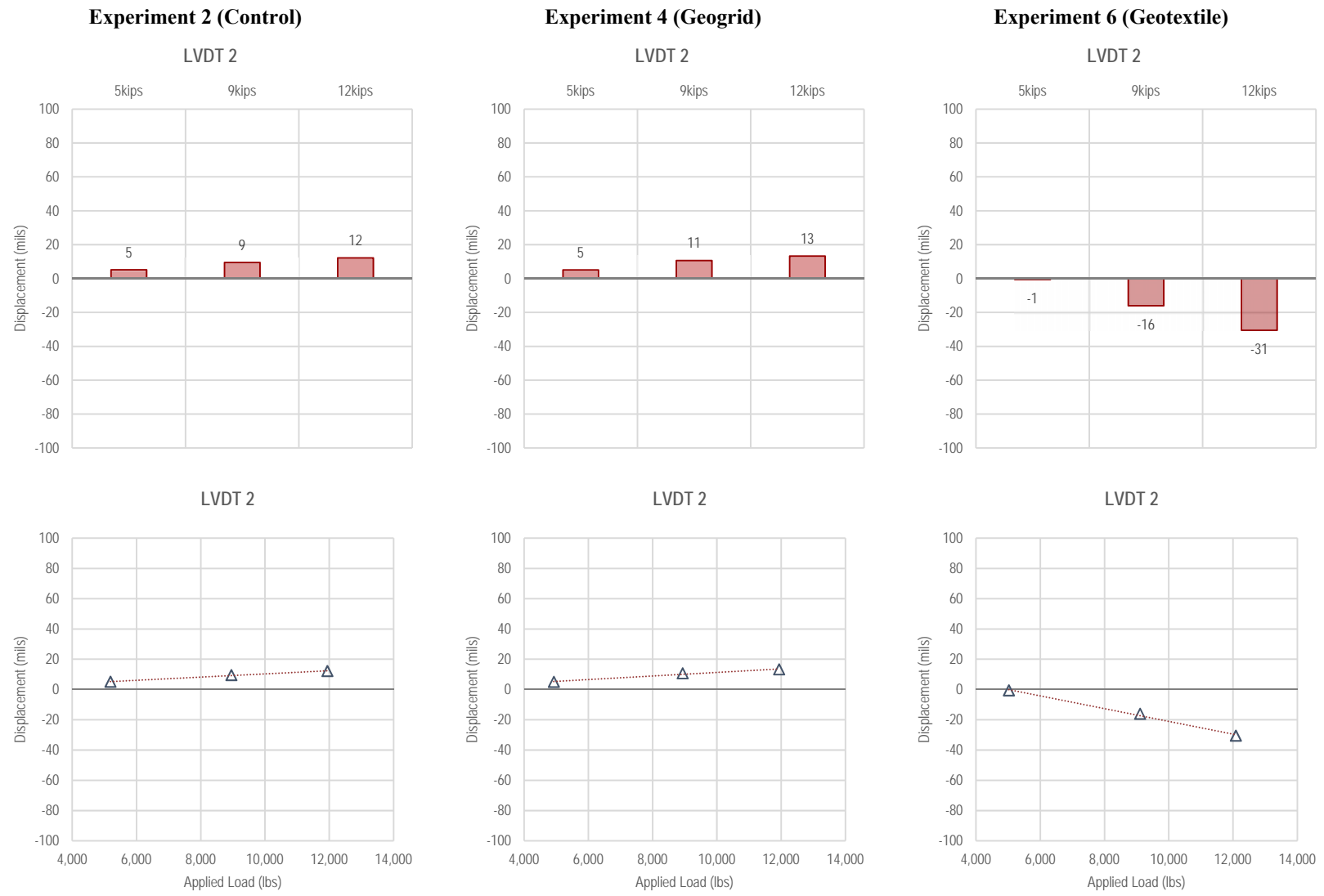


Figure F4-2. Summary of LVDT 2 measurements—Static Loading

F-98

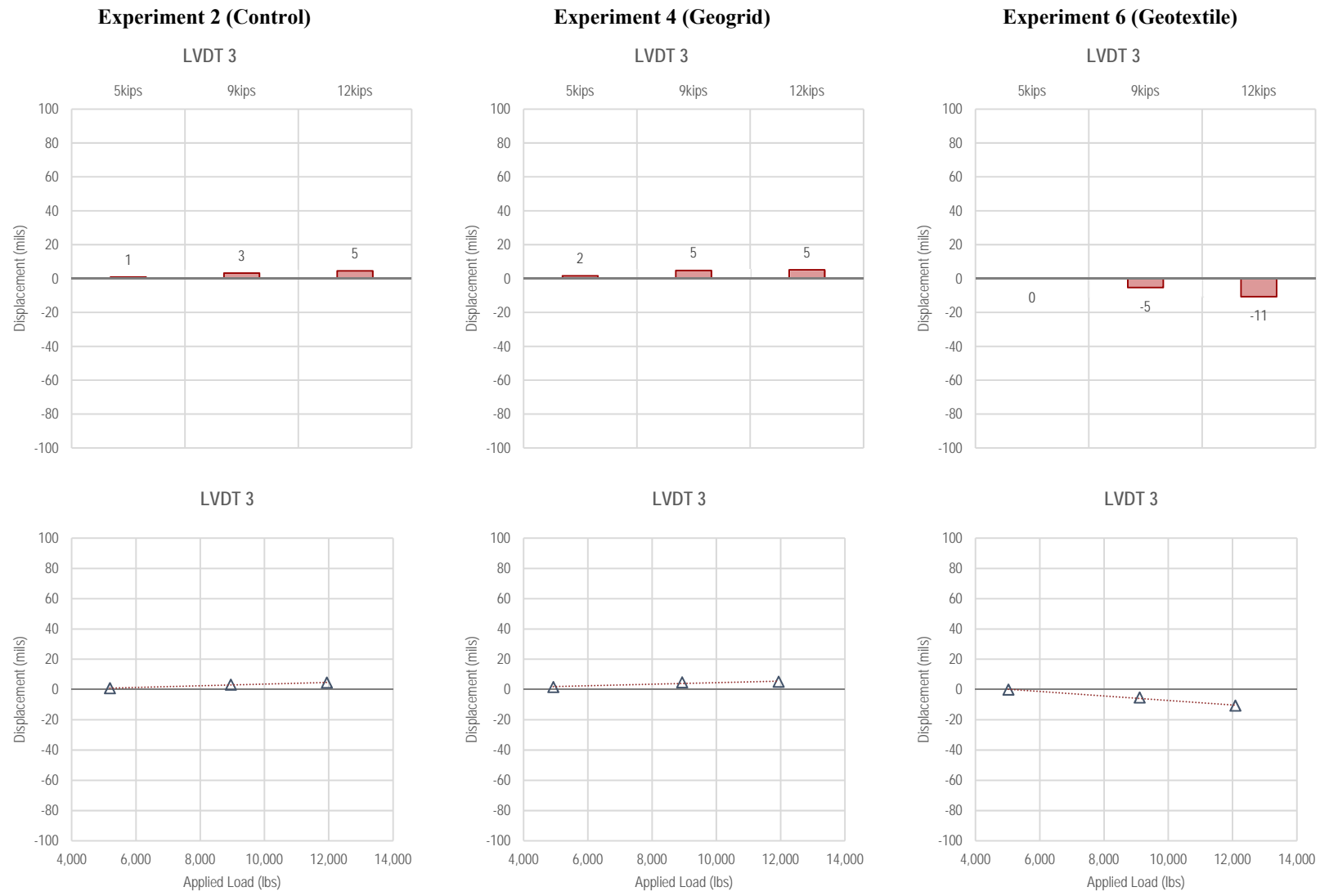


Figure F4-3. Summary of LVDT 3 measurements—Static Loading

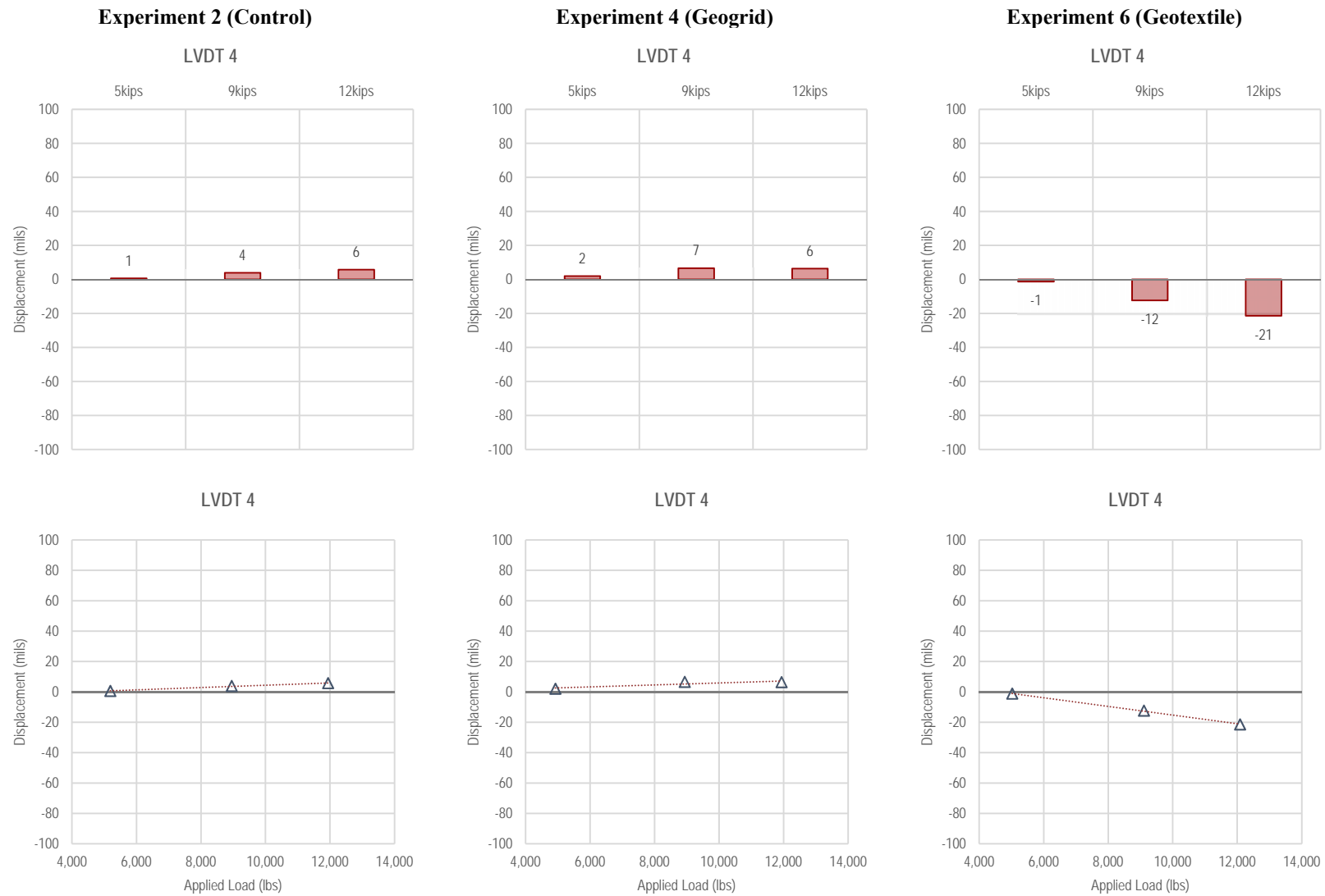
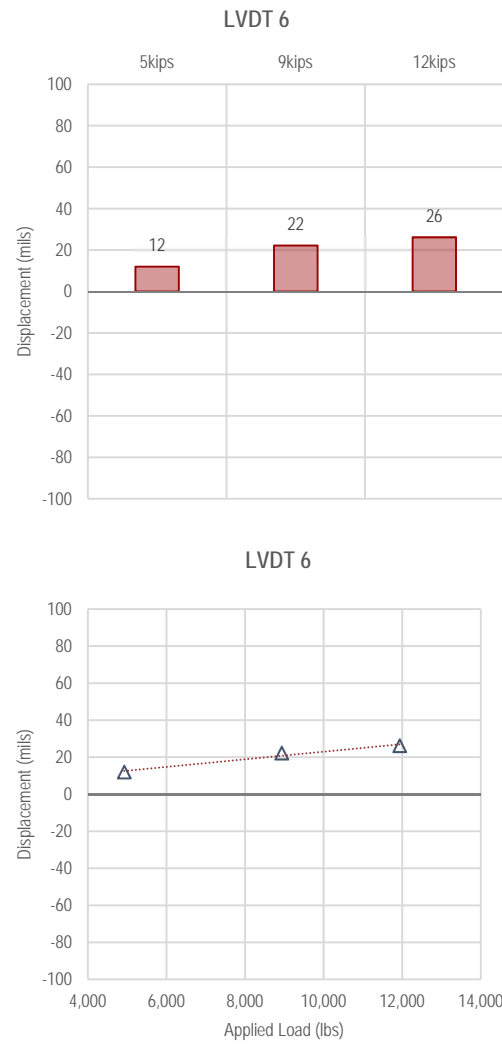


Figure F4-4. Summary of LVDT 4 measurements—Static Loading

Experiment 2 (Control)

Not Available

Experiment 4 (Geogrid)



Experiment 6 (Geotextile)

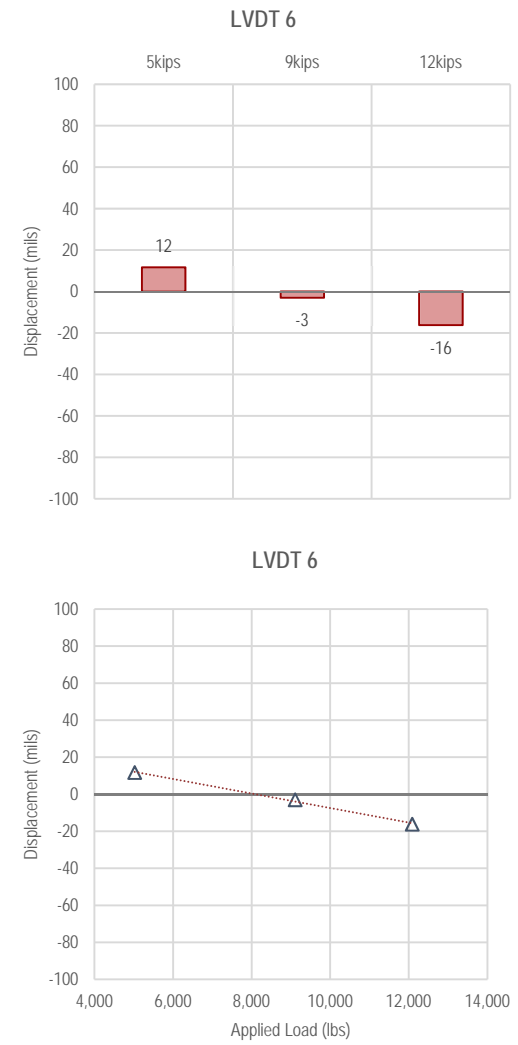


Figure F4-5. Summary of LVDT 6 measurements—Static Loading

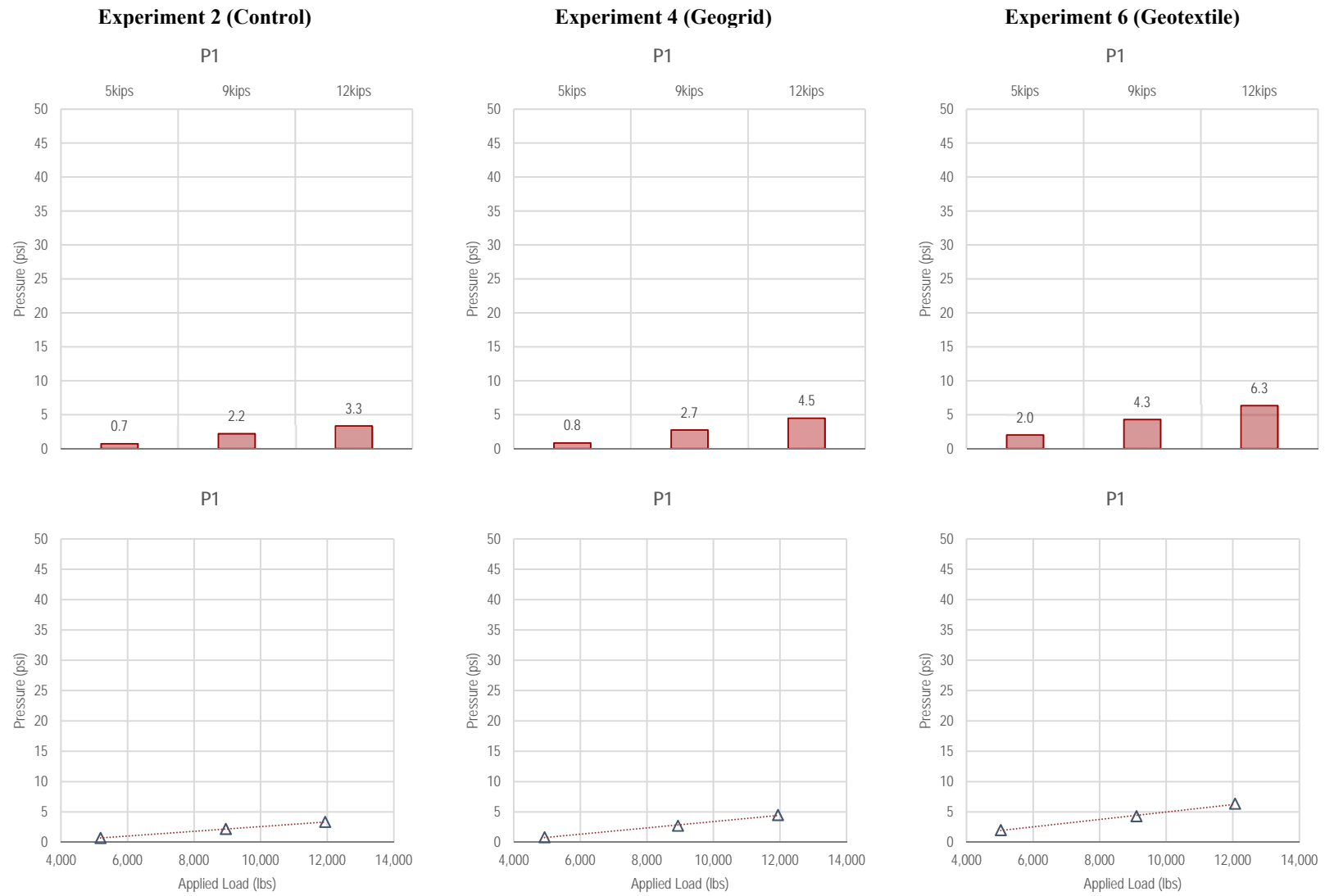
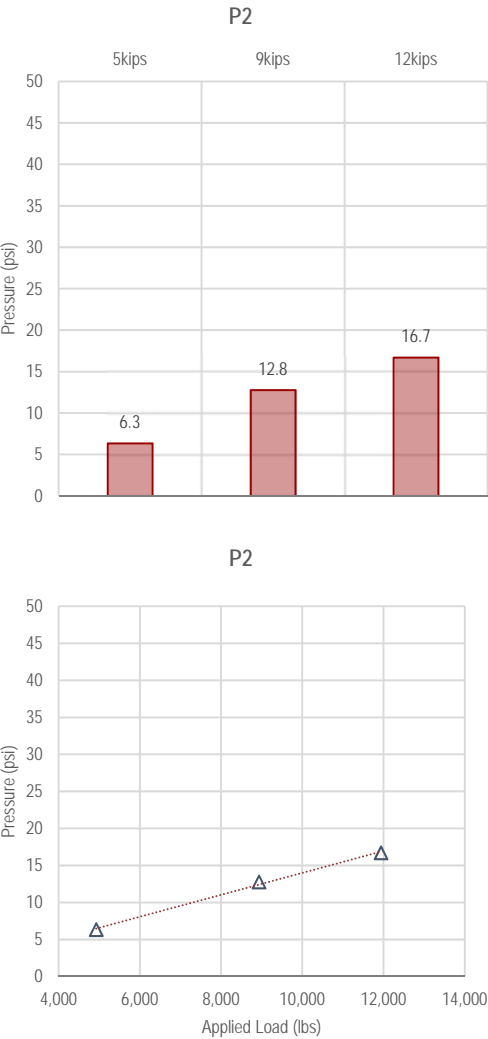


Figure F4-6. Summary of P1 measurements—Static Loading

Experiment 2 (Control)

Not Available

Experiment 4 (Geogrid)



Experiment 6 (Geotextile)

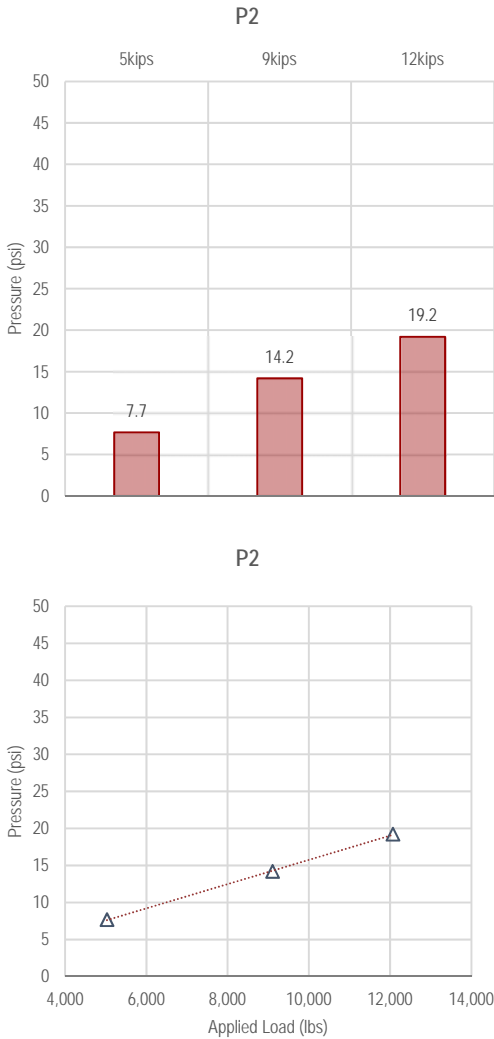
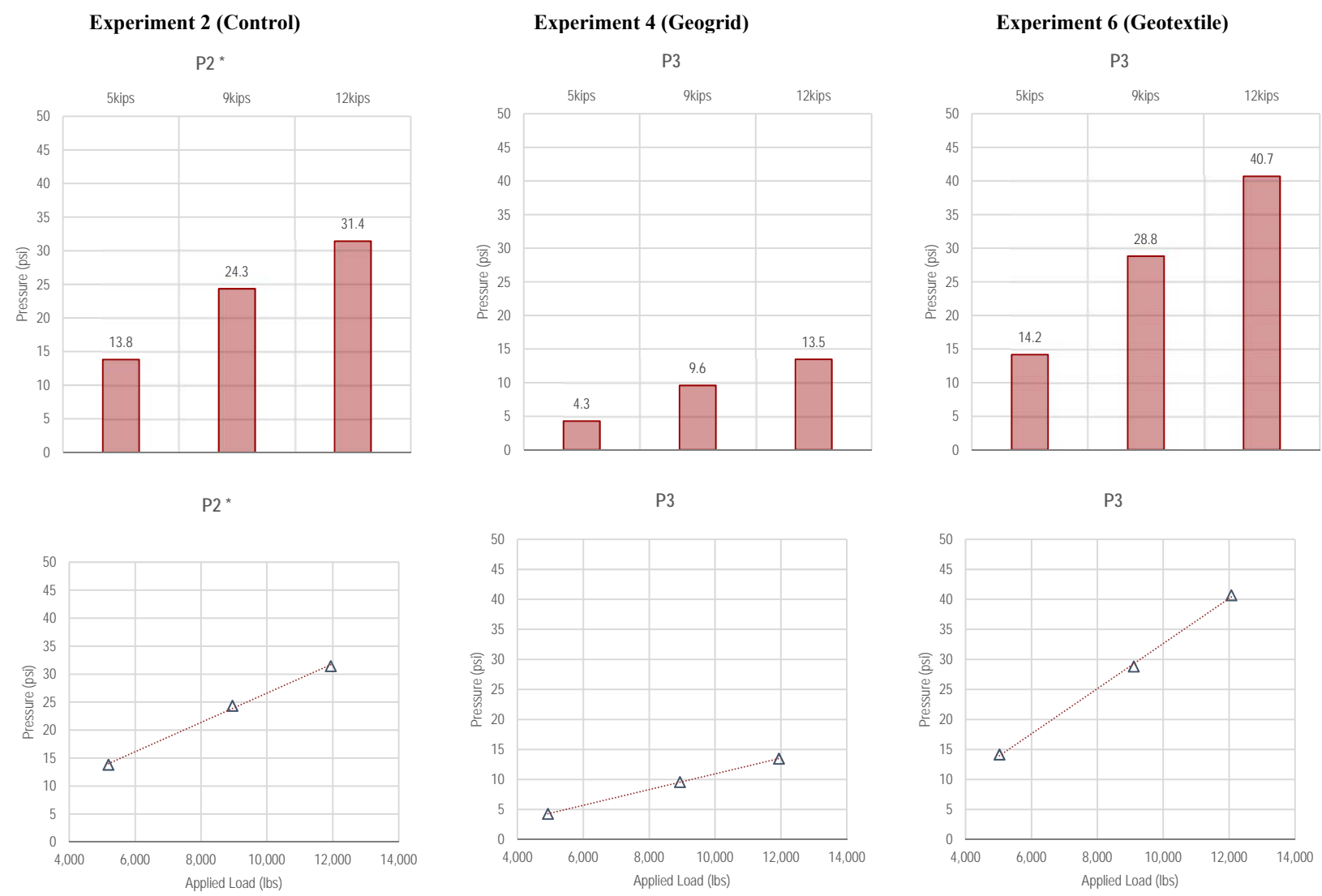


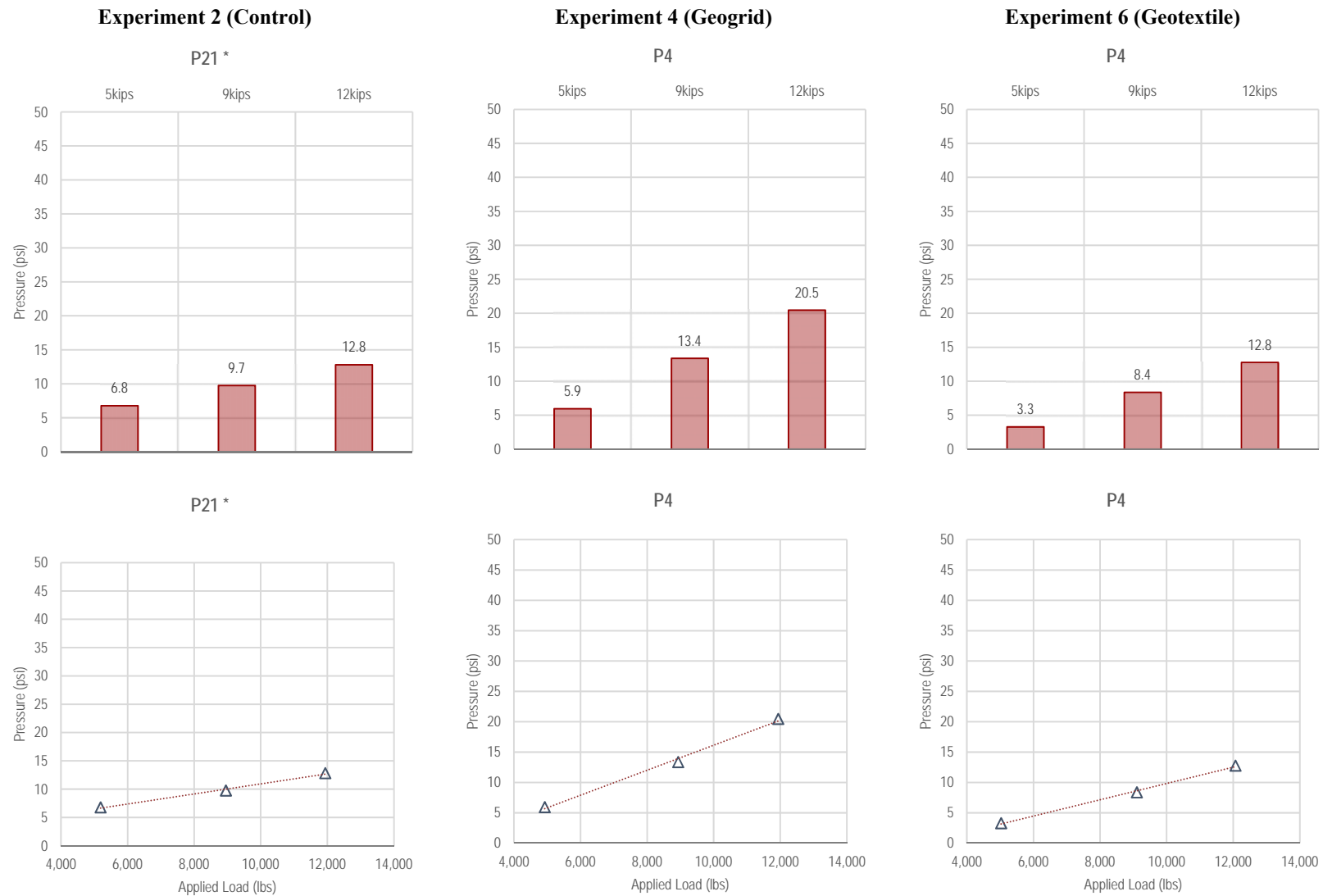
Figure F4-7. Summary of P2 measurements—Static Loading

F-104



*For Control, P2 measurements are used since they are equivalent to P3 measurements in Reinforced experiments

Figure F4-8. Summary of P3 measurements—Static Loading



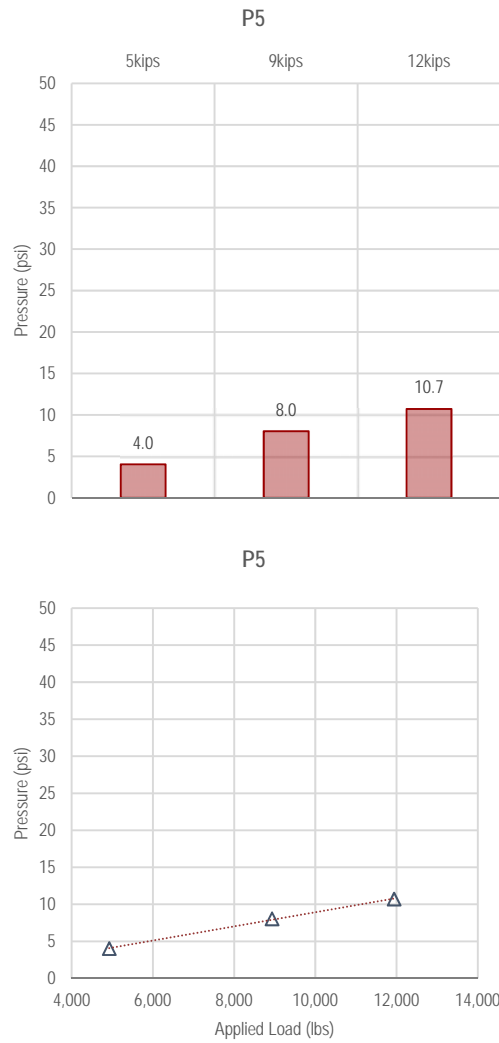
*For Control, P21 measurements are used since they are equivalent to P4 measurements in Reinforced experiments

Figure F4-9. Summary of P4 measurements—Static Loading

Experiment 2 (Control)

Not Available

Experiment 4 (Geogrid)



Experiment 6 (Geotextile)

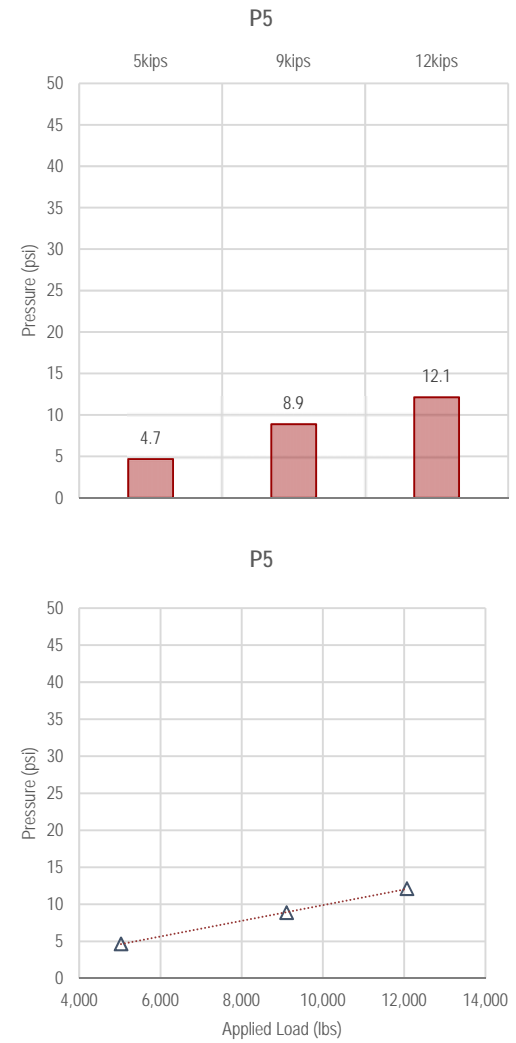
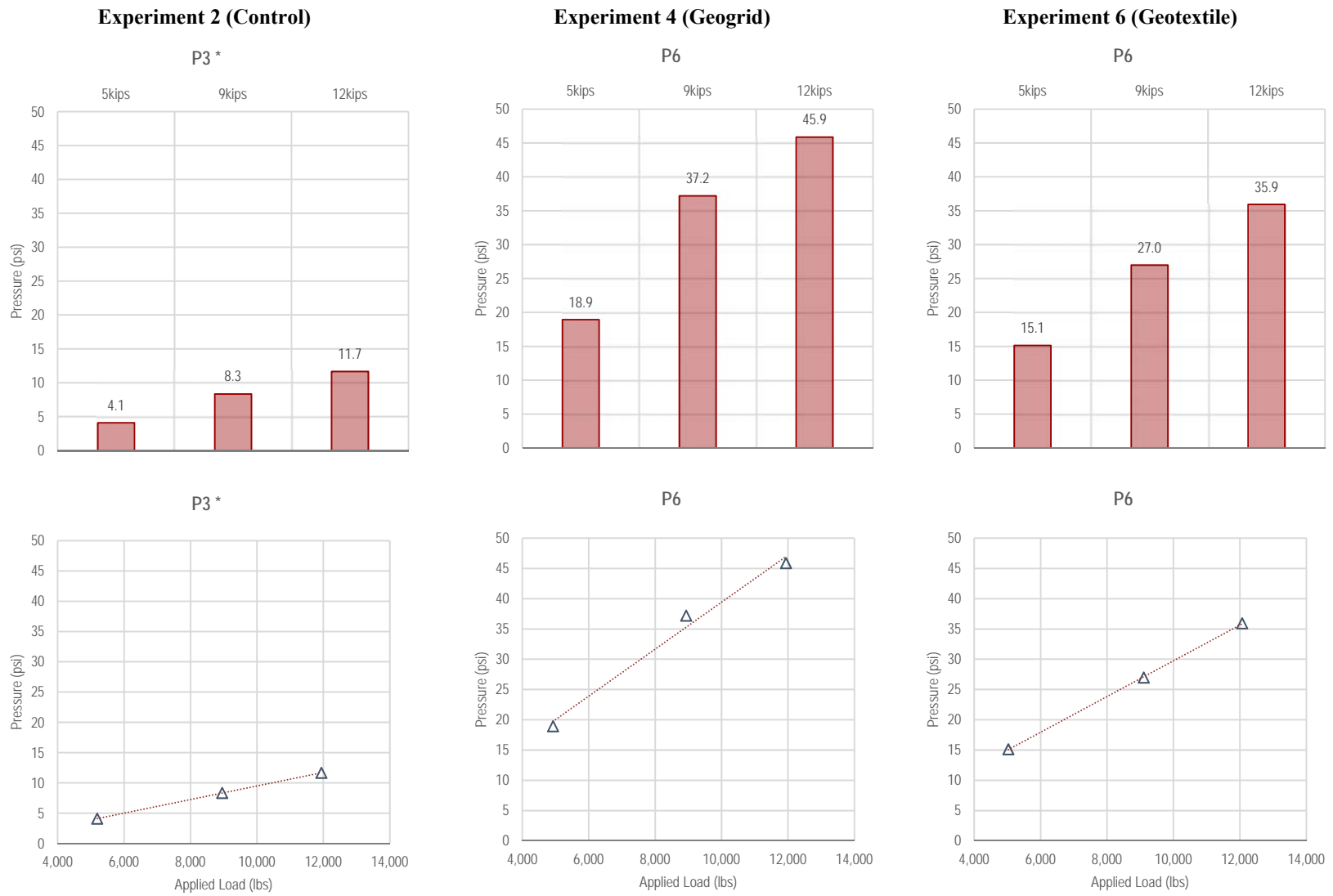


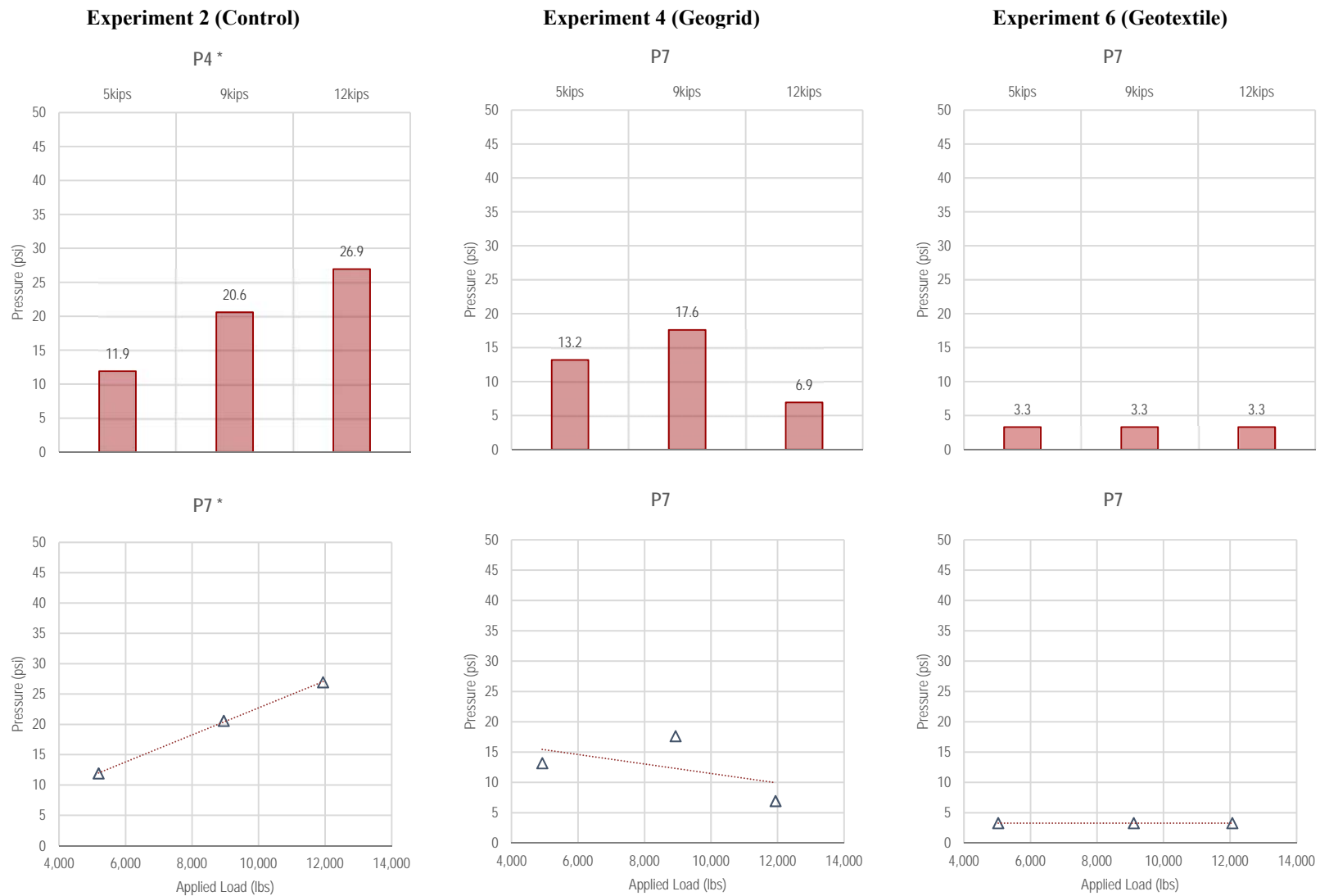
Figure F4-10. Summary of P5 measurements—Static Loading



*For Control, P3 measurements are used since they are equivalent to P6 measurements in Reinforced experiments

Figure F4-11. Summary of P6 measurements—Static Loading

F-108



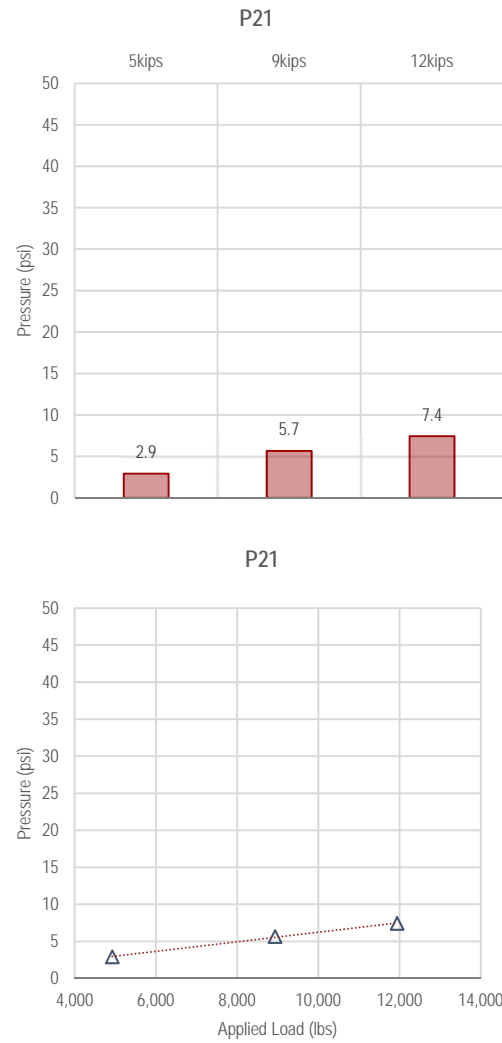
*For Control, P4 measurements are used since they are equivalent to P7 measurements in Reinforced experiments

Figure F4-12. Summary of P7 measurements—Static Loading

Experiment 2 (Control)

Not Available

Experiment 4 (Geogrid)



Experiment 6 (Geotextile)

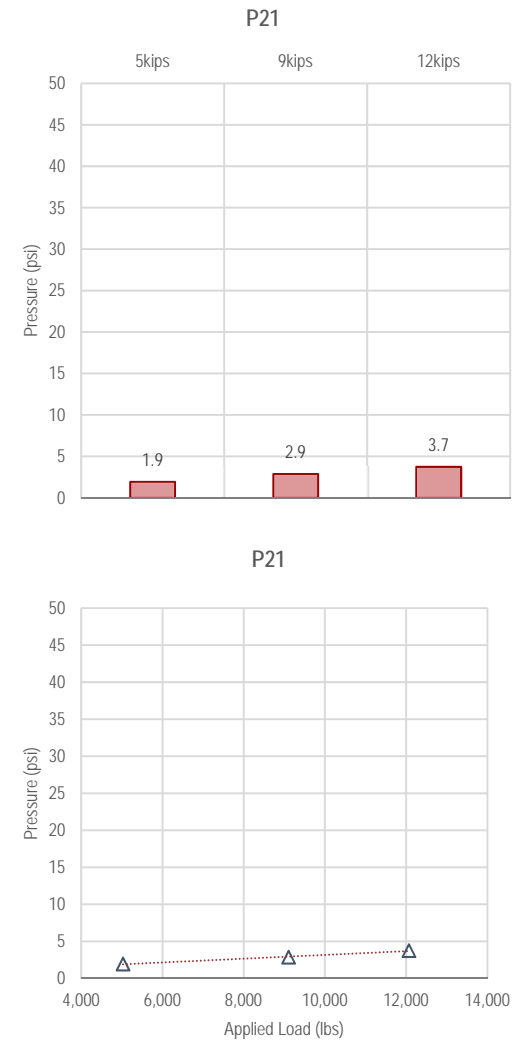


Figure F4-13. Summary of P21 measurements—Static Loading

F-110



Figure F4-14. Summary of P22 measurements—Static Loading

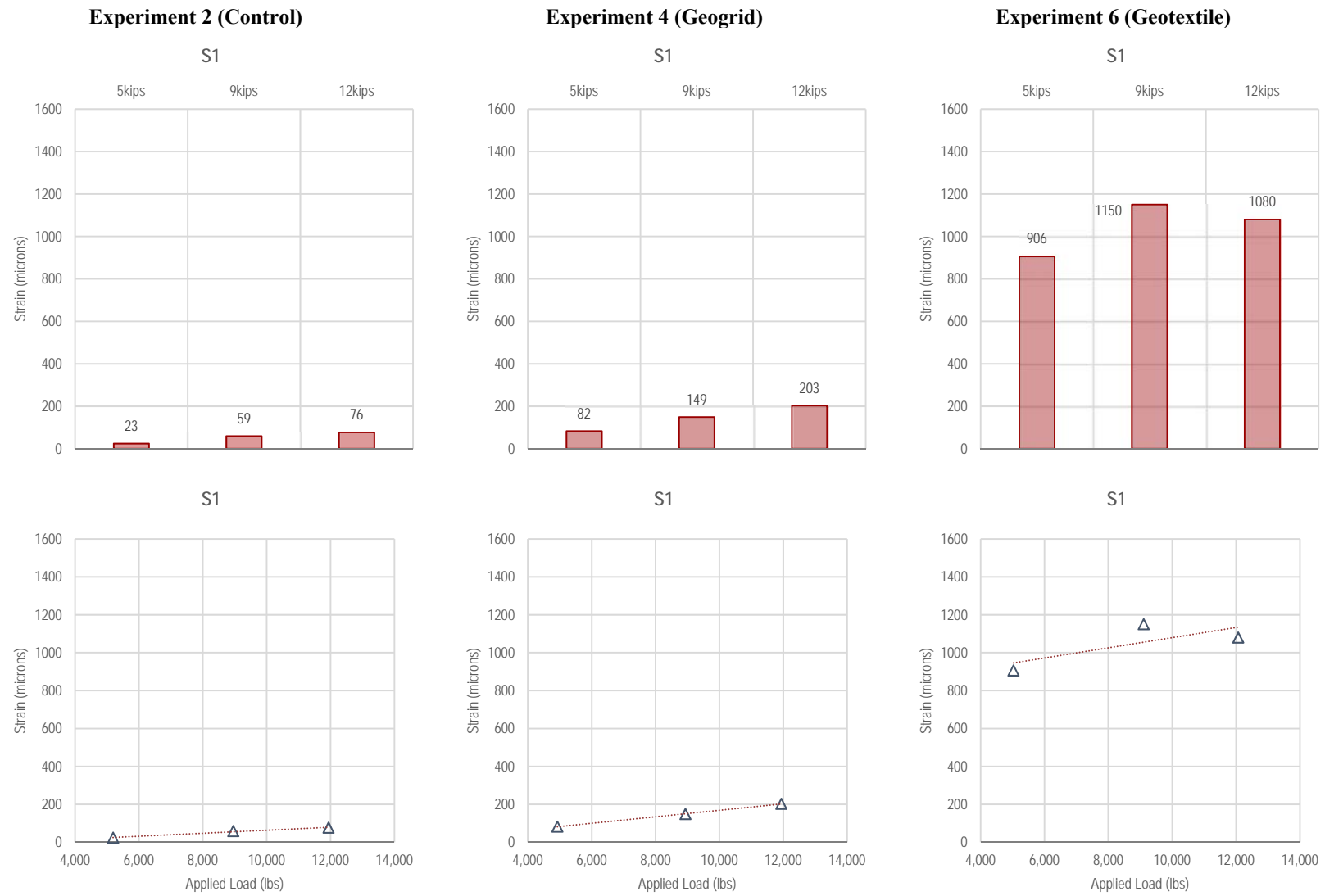
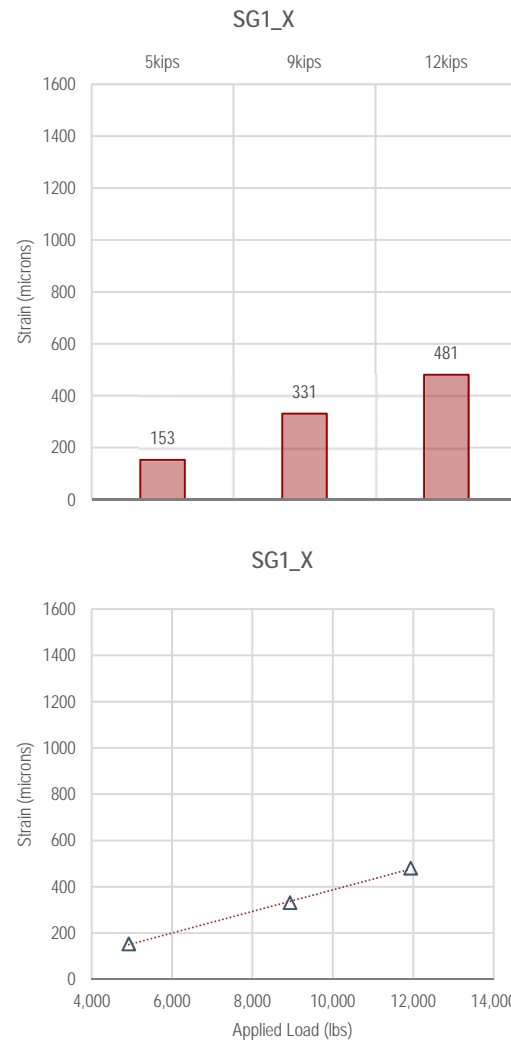


Figure F4-15. Summary of S1 measurements—Static Loading

Experiment 2 (Control)

Not Available

Experiment 4 (Geogrid)



Experiment 6 (Geotextile)

Not Available

Not Available

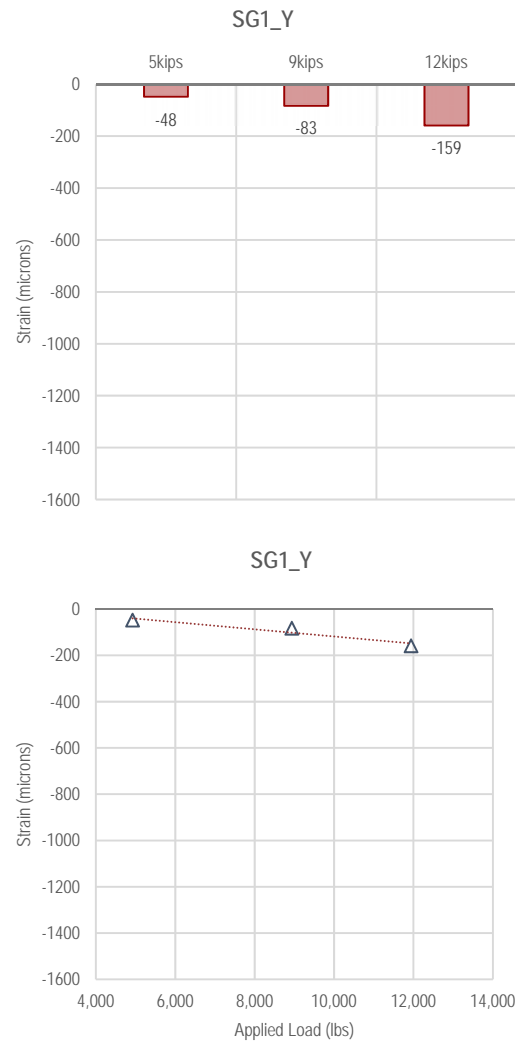
Figure F4-16. Summary of SG1_X measurements—Static Loading

Experiment 2 (Control)

Not Available

Not Available

Experiment 4 (Geogrid)



Experiment 6 (Geotextile)

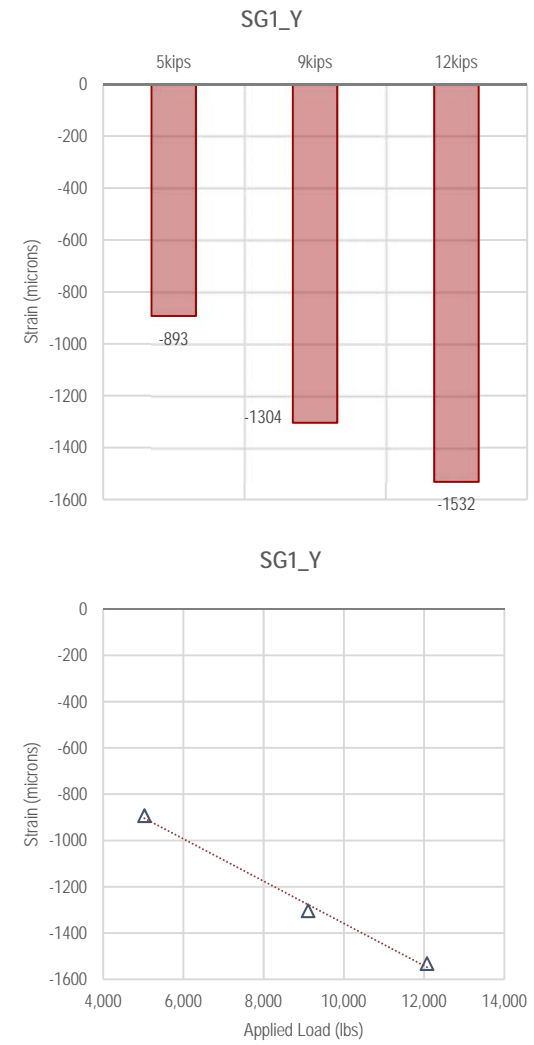


Figure F4-17. Summary of SG1_Y measurements—Static Loading

F-114

Experiment 2 (Control)

Not Available

Not Available

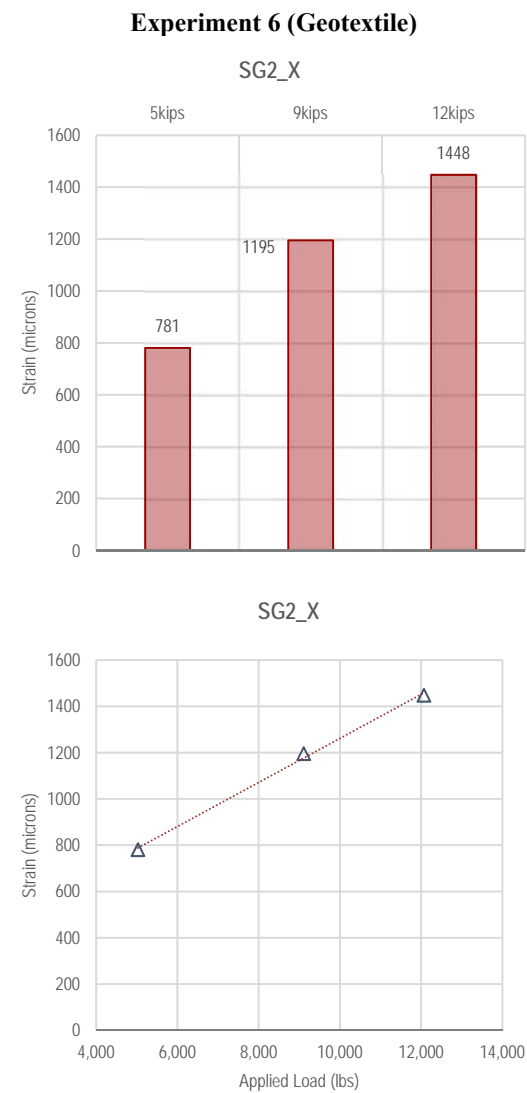
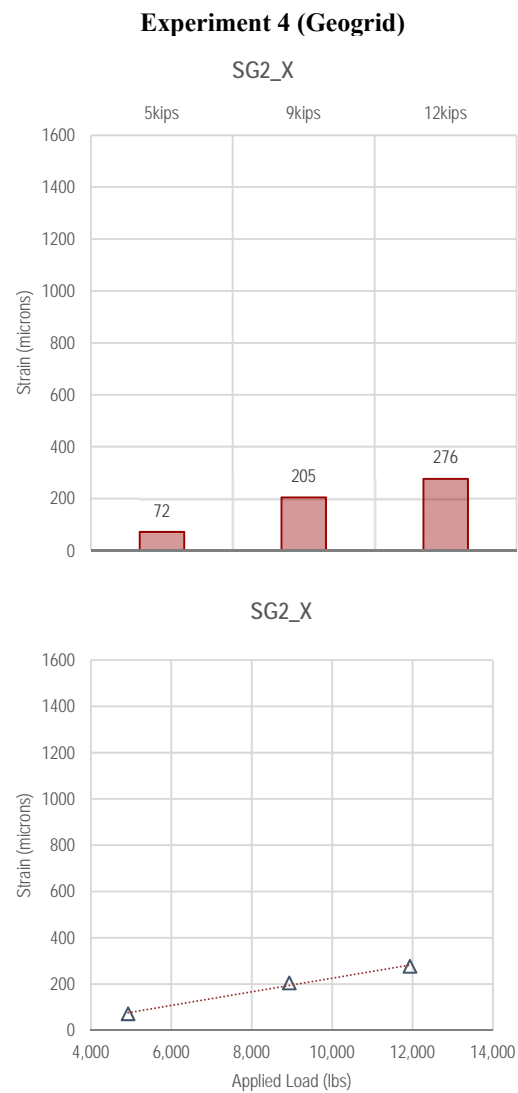


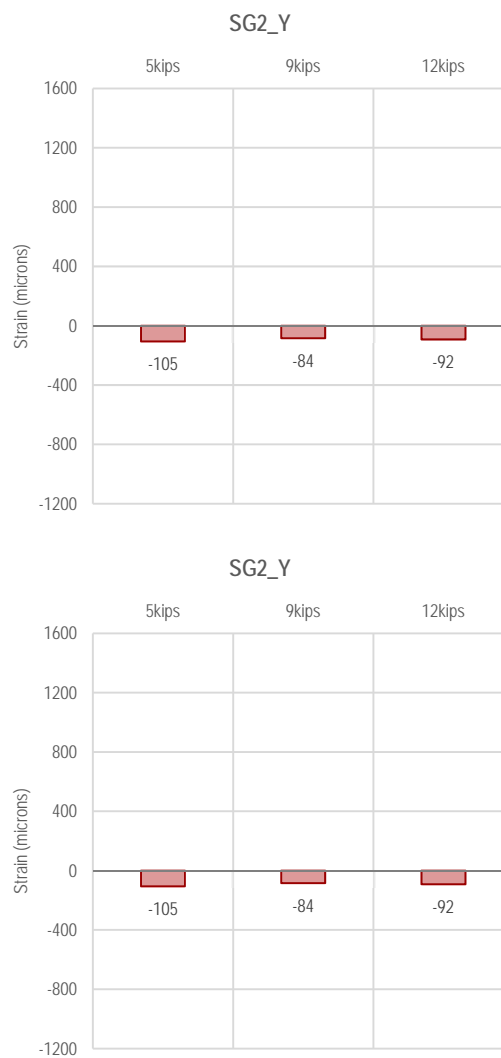
Figure F4-18. Summary of SG2_X measurements—Static Loading

Experiment 2 (Control)

Not Available

Not Available

Experiment 4 (Geogrid)



Experiment 6 (Geotextile)

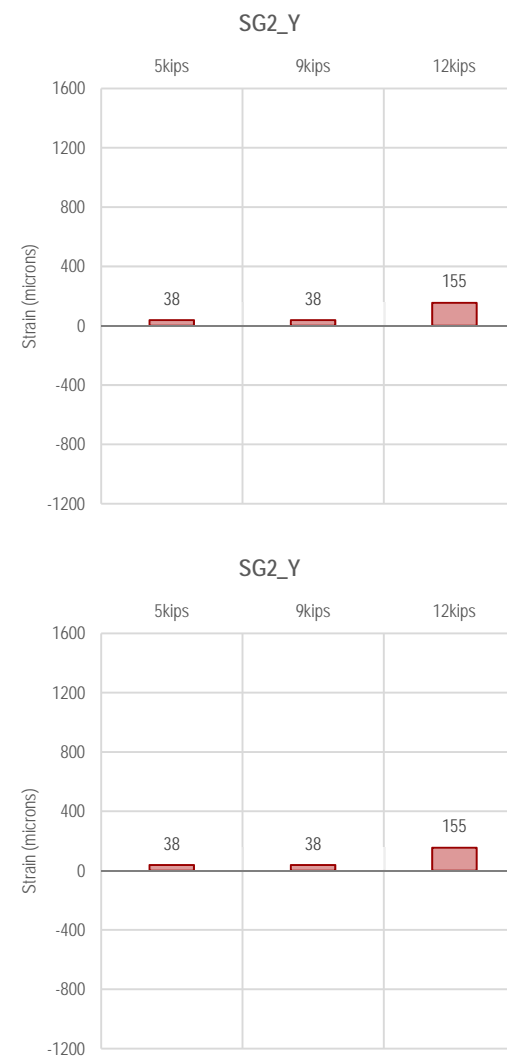
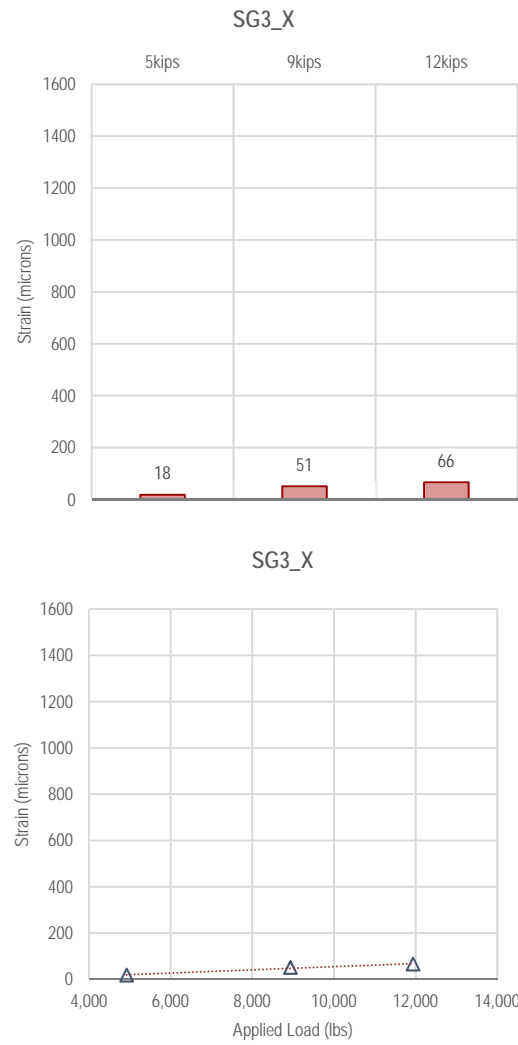


Figure F4-19. Summary of SG2_Y measurements—Static Loading

Experiment 2 (Control)

Not Available

Experiment 4 (Geogrid)



Experiment 6 (Geotextile)

Not Available

Not Available

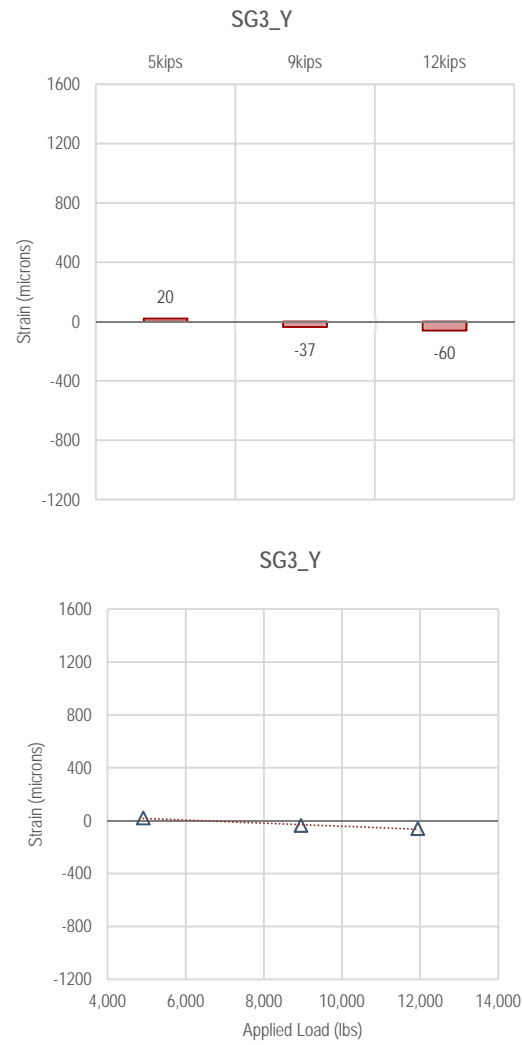
Not Available

Figure F4-20. Summary of SG3_X measurements—Static Loading

Experiment 2 (Control)

Not Available

Experiment 4 (Geogrid)



Experiment 6 (Geotextile)

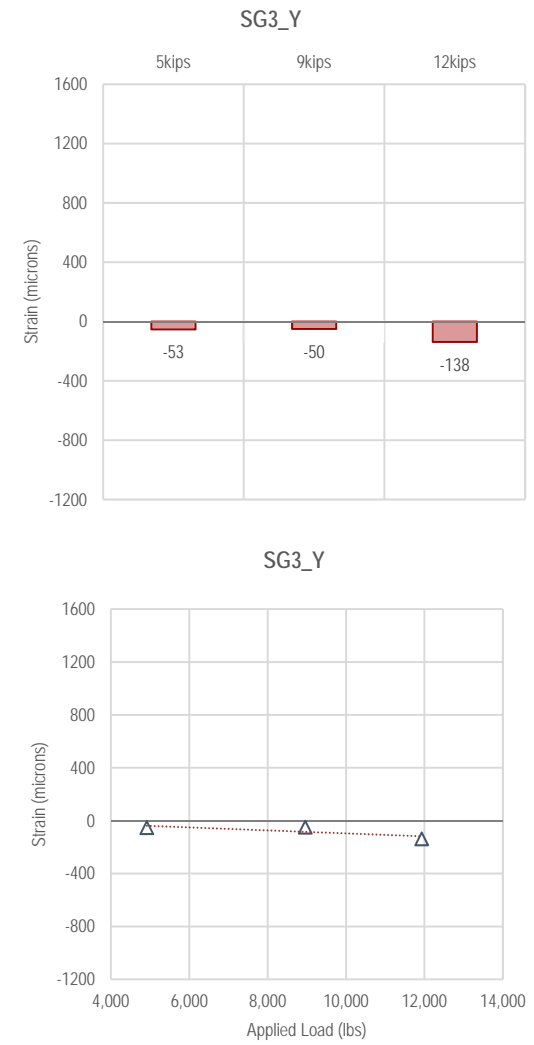


Figure F4-21. Summary of SG3_Y measurements—Static Loading

F-118

Experiment 2 (Control)

Not Available

Not Available

Experiment 4 (Geogrid)

Not Available

Not Available

Experiment 6 (Geotextile)



Figure F4-22. Summary of SG1_A measurements—Static Loading

Experiment 2 (Control)

Not Available

Experiment 4 (Geogrid)

Not Available

Experiment 6 (Geotextile)

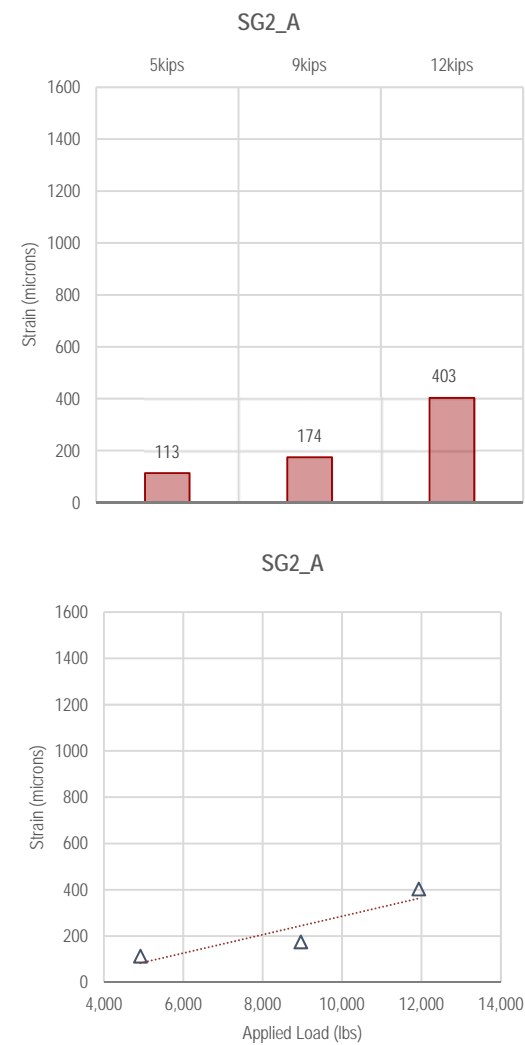


Figure F4-23. Summary of SG2_A measurements—Static Loading

Experiment 2 (Control)

Experiment 4 (Geogrid)

Experiment 6 (Geotextile)

Not Available

Not Available

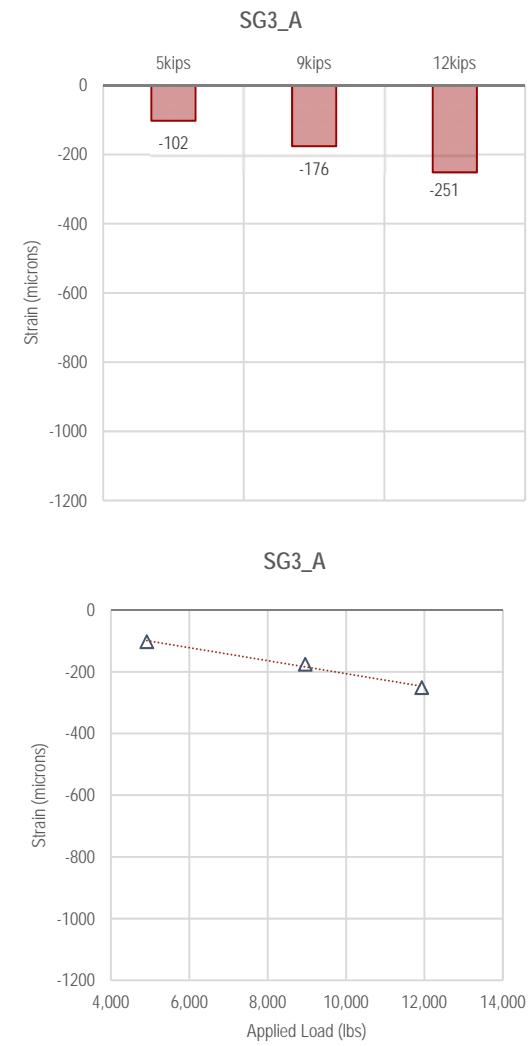


Figure F4-24. Summary of SG3_A measurements—Static Loading

APPENDIX G. FLEXIBLE PAVEMENT EXPERIMENTS: COMPARISON OF TEST MEASUREMENTS

Appendix G1. Flexible Pavements: Comparison of Test Measurements: Dynamic Loading—Thin Base: No. 1 (Control), No. 3 (Geogrid), and No. 5 (Geotextile)

Table G1-1. Comparison between Accelerometer Measurements

	Statistical Significant Difference between Instrumentation Results								
	Geogrid vs. Control			Geotextile vs. Control			Geotextile vs. Geogrid		
	Load (kip)								
	9	12	16	9	12	16	9	12	16
Instrumentation									
Msg1_Y	SH*	SH	SH	SH	SH	SH	NS	SL	NS
Msg1_Z	-	-	-	-	-	-	SH	SL	SL
Msg2_Y	SL*	SL	SL	-	SL	SL	-	NS	SL
Msg2_Z	-	-	-	-	-	-	SH	SL	NS
Msg3_Y	NS**	NS	-	SL	SL	-	NS	SL	NS
Msg3_Z	SL	SL	-	SL	SL	-	NS	SL	NS
Mgd1_Y	-	-	-	-	-	-	SL	SL	NS
Mgd1_Z	-	-	-	-	-	-	SL	NS	SL
Mgd2_Y	-	-	-	-	-	-	SL	SH	SL
Mgd2_Z	-	-	-	-	-	-	SL	SH	NS
Mgd3_Y	-	-	-	-	-	-	NS	-	SH
Mgd3_Z	-	-	-	-	-	-	NS	SH	SH

*SH/SL: Geogrid accelerometer measurement is statically higher/lower than the control accelerometer measurement at a significance level of 0.05.

**NS: Control accelerometer measurement and geogrid accelerometer measurement are not significantly different at a significance level of 0.05.

Table G1-2. Comparison between LVDT Measurements

	Statistical Significant Difference between Instrumentation Results								
	Geogrid vs. Control			Geotextile vs. Control			Geotextile vs. Geogrid		
	Load (kip)								
	Instrumentation	9	12	16	9	12	16	9	12
LVDT1	SH*	SH	SH	NS**	NS	SH	NS	SL	SH
LVDT2	SL*	SL	SL	SH	NS	SH	SH	NS	SH
LVDT3	SL	SL	SL	SL	SL	SL	NS	NS	SH
LVDT4	SH	SH	SH	SH	SH	SH	NS	SH	SH
LVDT6	SL	SL	SL	SH	NS	SH	SH	SH	SH

*SH/SL: Geogrid LVDT measurement is statically higher/lower than the control LVDT measurement at a significance level of 0.05.

**NS: Control LVDT measurement and geotextile LVDT measurement are not significantly different at a significance level of 0.05.

Table G1-3. Comparison between Pressure Cell Measurements

Instrumentation	Statistical Significant Difference between Instrumentation Results								
	Geogrid vs. Control			Geotextile vs. Control			Geotextile vs. Geogrid		
	Load (kip)								
	9	12	16	9	12	16	9	12	16
P1	SH*	SH	SH	SH	SH	SH	SH	SH	SH
P2	SL*	SL	SL	SL	SL	SL	SH	SH	SH
P3	SL	SL	SL	SL	SL	SL	SH	SH	SH
P4	SL	SL	SL	SH	SH	SH	SH	SH	SH
P5	SH	SH	SH	SH	SH	SH	SH	SH	SH
P21	SL	SL	SL	SL	SL	SL	SL	SL	SL
P22	SH	SH	SH	-	-	-	SL	SL	SL

*SH/SL: Geogrid pressure cell measurement is statically higher/lower than the control pressure cell measurement at a significance level of 0.05.

Table G1-4. Comparison between Strain Gauge Measurements

	Statistical Significant Difference between Instrumentation Results								
	Geogrid Vs Control			Geotextile vs Control			Geotextile vs Geogrid		
	Load (kip)								
Instrumentation	9	12	16	9	12	16	9	12	16
S1	SH	SH	SH	SL	SL	SL	SL	SL	SL
SG1_X	-	-	-	-	-	-	SL*	SL	SL
SG1_Y	-	-	-	-	-	-	SH*	SH	SH
SG2_X	-	-	-	-	-	-	SL	SL	SL
SG2_Y	-	-	-	-	-	-	SH	SH	SH
SG3_X	-	-	-	-	-	-	NS**	NS	NS
SG3_Y	-	-	-	-	-	-	SH	NS	SL

*SH/SL: Geotextile strain gauge measurement is statically higher/lower than the geogrid strain gauge measurement at a significance level of 0.05.

**NS: Geotextile strain gauge measurement and geogrid strain gauge measurement are not significantly different at a significance level of 0.05.

**Appendix G2. Flexible Pavements: Comparison of Test Measurements: Static Loading—
Thin Base: No. 1 (Control), No. 3 (Geogrid), and No. 5 (Geotextile)**

Table G2-1. Percent Difference in LVDT Measurements

	Percent Difference in Instrumentation Results								
	Geogrid vs. Control*			Geotextile vs. Control**			Geotextile vs. Geogrid***		
	Load (kip)								
	Instrumentation	5	9	12	5	9	12	5	9
LVDT1	0.6	24.9	13.8	6.7	-0.5	56.0	6.1	-20.3	37.1
LVDT2	-14.1	15.1	7.8	13.6	-4.5	36.2	32.4	-17.0	26.4
LVDT3	-36.2	-27.6	-26.0	-12.5	-8.3	-10.8	37.1	26.7	20.5
LVDT4	-12.1	49.1	39.0	30.8	61.4	64.0	48.8	8.3	17.9
LVDT6	-9.9	5.7	0.6	2.6	-4.3	32.3	13.8	-9.4	31.5

*Geogrid vs. Control:

$100 * [(LVDT \text{ Measurement in Experiment 3} - LVDT \text{ Measurement in Experiment 1}) / LVDT \text{ Measurement in Experiment 1}]$

**Geotextile vs. Control:

$100 * [(LVDT \text{ Measurement in Experiment 5} - LVDT \text{ Measurement in Experiment 1}) / LVDT \text{ Measurement in Experiment 1}]$

***Geotextile vs. Geogrid:

$100 * [(LVDT \text{ Measurement in Experiment 5} - LVDT \text{ Measurement in Experiment 3}) / LVDT \text{ Measurement in Experiment 3}]$

Table G2-2. Percent Difference in Pressure Cell Measurements

	Percent Difference in Instrumentation Results								
	Geogrid vs. Control*			Geotextile vs. Control**			Geotextile vs. Geogrid***		
	Load (kip)								
Instrumentation	5	9	12	5	9	12	5	9	12
P1	15.0	43.2	33.3	32.7	24.8	53.1	15.3	-12.8	14.8
P2	-25.1	-19.9	-14.5	-14.0	-12.2	3.9	14.8	9.6	21.6
P3	-24.2	-11.0	8.9	-1.8	6.3	59.6	29.6	19.5	46.5
P4	-55.6	-58.9	-58.8	37.5	38.7	43.1	209.3	237.1	247.0
P5	25.0	24.6	21.7	42.6	38.3	25.0	14.1	11.1	2.7
P21	-46.2	-36.5	-28.4	-53.2	-49.6	-34.5	-13.0	-20.7	-8.6

*Geogrid vs. Control:

$100 * [(\text{Pressure Cell Measurement in Experiment 3} - \text{Pressure Cell Measurement in Experiment 1}) / \text{Pressure Cell Measurement in Experiment 1}]$

**Geotextile vs. Control:

$100 * [(\text{Pressure Cell Measurement in Experiment 5} - \text{Pressure Cell Measurement in Experiment 1}) / \text{Pressure Cell Measurement in Experiment 1}]$

***Geotextile vs. Geogrid:

$100 * [(\text{Pressure Cell Measurement in Experiment 5} - \text{Pressure Cell Measurement in Experiment 3}) / \text{Pressure Cell Measurement in Experiment 3}]$

Table G2-3. Percent Difference in Strain Gauge Measurements

	Percent Difference in Instrumentation Results								
	Geogrid vs. Control*			Geotextile vs. Control**			Geotextile vs. Geogrid***		
	Load (kip)								
	5	9	12	5	9	12	5	9	12
Instrumentation	5	9	12	5	9	12	5	9	12
S1	-56.3	-78.8	-53.2	190.4	133.4	-100.0	563.9	1002.5	-100.0
SG1_X	-	-	-	-	-	-	-100.0	-100.0	-100.0
SG1_Y	-	-	-	-	-	-	-34.9	-56.8	7.4
SG2_X	-	-	-	-	-	-	-27.7	-61.7	17.3
SG2_Y	-	-	-	-	-	-	-100.0	-100.0	-100.0
SG3_X	-	-	-	-	-	-	89.4	115.0	547.9
SG3_Y	-	-	-	-	-	-	-364.7	35.8	128.1

*Geogrid vs. Control:

$$100 * [(\text{Strain Gauge Measurement in Experiment 3} - \text{Strain Gauge Measurement in Experiment 1}) / \text{Strain Gauge Measurement in Experiment 1}]$$

**Geotextile vs. Control:

$$100 * [(\text{Strain Gauge Measurement in Experiment 5} - \text{Strain Gauge Measurement in Experiment 1}) / \text{Strain Gauge Measurement in Experiment 1}]$$

***Geotextile vs. Geogrid:

$$100 * [(\text{Strain Gauge Measurement in Experiment 5} - \text{Strain Gauge Measurement in Experiment 3}) / \text{Strain Gauge Measurement in Experiment 3}]$$

Appendix G3. Flexible Pavements: Comparison of Test Measurements: Dynamic Loading—Thick Base: No. 2 (Control), No. 4 (Geogrid), and No. 6 (Geotextile)

Table G3-1. Comparison between Accelerometer Measurements

	Statistical Significant Difference between Instrumentation Results								
	Geogrid vs. Control			Geotextile vs. Control			Geotextile vs. Geogrid		
	Load (kip)								
	9	12	16	9	12	16	9	12	16
Instrumentation	9	12	16	9	12	16	9	12	16
Msg1_Y	NS**	NS	SL	NS	SL	SL	NS	SL	NS
Msg1_Z	SH*	SH	NS	NS	SH	NS	SL	NS	SL
Msg2_Y	SL*	SL	SL	SL	SL	SL	NS	NS	SH
Msg2_Z	SL	-	SL	SL	-	SL	SL	SH	NS
Msg3_Y	SL	SL	SL	NS	SL	SL	NS	NS	NS
Msg3_Z	SL	SL	SL	SL	SL	SL	SL	SH	SH
Mgd1_Y	-	-	-	-	-	-	NS	SH	SH
Mgd1_Z	-	-	-	-	-	-	SL	SH	SH
Mgd2_Y	-	-	-	-	-	-	SL	SL	SL
Mgd2_Z	-	-	-	-	-	-	SL	NS	NS
Mgd3_Y	-	-	-	-	-	-	NS	SL	SL
Mgd3_Z	-	-	-	-	-	-	SL	SH	SL

*SH/SL: Geogrid accelerometer measurement is statically higher/lower than the control accelerometer measurement at a significance level of 0.05.

**NS: Control accelerometer measurement and geogrid accelerometer measurement are not significantly different at a significance level of 0.05.

Table G3-2. Comparison between LVDT Measurements

	Statistical Significant Difference between Instrumentation Results								
	Geogrid vs. Control			Geotextile vs. Control			Geotextile vs. Geogrid		
	Load (kip)								
	9	12	16	9	12	16	9	12	16
Instrumentation	9	12	16	9	12	16	9	12	16
LVDT1	SL*	SL	SL	SH*	SH	SH	SH	SH	SH
LVDT2	NS**	NS	SL	SH	SH	SH	SH	SH	SH
LVDT3	NS	NS	NS	NS	NS	NS	NS	NS	SH
LVDT4	NS	NS	NS	SH	SH	SH	SH	SH	SH
LVDT6	-	-	-	-	-	-	SH	SH	SH

*SL: Geogrid LVDT measurement is statically higher/lower than the control LVDT measurement at a significance level of 0.05.

*SH: Geotextile LVDT measurement is statically higher/lower than the control LVDT measurement at a significance level of 0.05.

**NS: Control LVDT measurement and geogrid LVDT measurement are not significantly different at a significance level of 0.05.

Table G3-3. Comparison between Pressure Cell Measurements

	Statistical Significant Difference between Instrumentation Results								
	Geogrid vs. Control			Geotextile vs. Control			Geotextile vs. Geogrid		
	Load (kip)								
	9	12	16	9	12	16	9	12	16
Instrumentation									
P1	SH*	SH	SH	SH	SH	SH	SH	SH	SH
P2	-	-	-	-	-	-	SL	SL	SL
P3 (For Control, P2 measurements are used since they are equivalent to P3 measurements in Reinforced experiments)	SL*	SL	SL	SL	SL	SL	SH	SH	SH
P4 (For Control, P21 measurements are used since they are equivalent to P4 measurements in Reinforced experiments)	SH	SH	SH	SL	SL	SL	SL	SL	SL
P5	-	-	-	-	-	-	NS**	SH	NS
P6 (For Control, P3 measurements are used since they are equivalent to P6 measurements in Reinforced experiments)	-	-	-	-	-	-	SL	SL	SL
P7 (For Control, P4 measurements are used since they are equivalent to P7 measurements in Reinforced experiments)	-	-	-	-	-	-	SL	SL	SL
P21 (For Control, P5 measurements are used since they are equivalent to P21 measurements in Reinforced experiments)	SL	SL	SL	SL	SL	SL	SL	SL	SL

*SH/SL: Geogrid pressure cell measurement is statically higher/lower than the control pressure cell measurement at a significance level of 0.05.

**NS: Geotextile LVDT measurement and geogrid LVDT measurement are not significantly different at a significance level of 0.05.

Table G3-4. Comparison between Strain Gauge Measurements

	Statistical Significant Difference between Instrumentation Results								
	Geogrid vs. Control			Geotextile vs. Control			Geotextile vs. Geogrid		
	Load (kip)								
	9	12	16	9	12	16	9	12	16
Instrumentation									
S1	NS**	NS	NS	SL	SL	SL	SL*	SL	SL
SG1_Y	-	-	-	-	-	-	SL	SL	SL
SG2_X	-	-	-	-	-	-	SH*	SH	SH
SG2_Y	-	-	-	-	-	-	SH	SH	SH
SG3_X	-	-	-	-	-	-	SL	SL	SL
SG3_Y	-	-	-	-	-	-	SH	SH	SH

*SH/SL: Geotextile strain gauge measurement is statically higher/lower than the geogrid strain gauge measurement at a significance level of 0.05.

**NS: Geogrid strain gauge measurement and control strain gauge measurement are not significantly different at a significance level of 0.05.

**Appendix G4. Flexible Pavements: Comparison of Test Measurements: Static Loading—
Thick Base: No. 2 (Control), No. 4 (Geogrid), and No. 6 (Geotextile)**

Table G4-1. Percent Difference in LVDT Measurements

	Percent Difference in Instrumentation Results								
	Geogrid vs. Control*			Geotextile vs. Control**			Geotextile vs. Geogrid***		
	Load (kip)								
Instrumentation	5	9	12	5	9	12	5	9	12
LVDT1	-32.1	1.0	-15.9	7.0	-38.9	-59.8	57.6	-39.5	-52.2
LVDT2	-1.2	12.2	8.3	-112.0	-270.0	-350.2	-112.1	-251.5	-331.0
LVDT3	97.4	47.4	11.9	-110.1	-266.4	-335.6	-105.1	-212.9	-310.5
LVDT4	232.7	70.5	11.3	-305.1	-423.2	-475.5	-161.7	-289.5	-437.5
LVDT6	-	-	-	-	-	-	-2.4	-113.6	-161.9

*Geogrid vs. Control:

$100 * [(LVDT \text{ Measurement in Experiment 4} - LVDT \text{ Measurement in Experiment 2}) / LVDT \text{ Measurement in Experiment 2}]$

**Geotextile vs. Control:

$100 * [(LVDT \text{ Measurement in Experiment 6} - LVDT \text{ Measurement in Experiment 2}) / LVDT \text{ Measurement in Experiment 2}]$

***Geotextile vs. Geogrid:

$100 * [(LVDT \text{ Measurement in Experiment 6} - LVDT \text{ Measurement in Experiment 4}) / LVDT \text{ Measurement in Experiment 4}]$

Table G4-2. Percent Difference in Pressure Cell Measurements

	Percent Difference in Instrumentation Results								
	Geogrid vs. Control*			Geotextile vs. Control**			Geotextile vs. Geogrid***		
	Load (kip)								
	5	9	12	5	9	12	5	9	12
Instrumentation	5	9	12	5	9	12	5	9	12
P1	17.1	25.0	34.5	185.0	96.8	90.1	143.4	57.5	41.3
P2	-	-	-	-	-	-	21.0	11.2	15.1
P3 (For Control, P2 measurements are used since they are equivalent to P3 measurements in Reinforced experiments)	-68.9	-60.6	-57.1	2.6	18.4	29.5	230.3	200.8	202.2
P4 (For Control, P21 measurements are used since they are equivalent to P4 measurements in Reinforced experiments)	-12.2	37.2	59.9	-51.5	-14.1	-0.3	-44.8	-37.4	-37.6
P5	-	-	-	-	-	-	15.6	10.4	13.1
P6 (For Control, P3 measurements are used since they are equivalent to P6 measurements in Reinforced experiments)	-	-	-	-	-	-	-20.1	-27.5	-21.7
P7 (For Control, P4 measurements are used since they are equivalent to P7 measurements in Reinforced experiments)	-	-	-	-	-	-	-52.4	-49.7	-47.7
P21	-	-	-	-	-	-	-33	-49	-50

*Geogrid vs. Control:

$100 * [(\text{Pressure Cell Measurement in Experiment 4} - \text{Pressure Cell Measurement in Experiment 2}) / \text{Pressure Cell Measurement in Experiment 2}]$

**Geotextile vs. Control:

$100 * [(\text{Pressure Cell Measurement in Experiment 6} - \text{Pressure Cell Measurement in Experiment 2}) / \text{Pressure Cell Measurement in Experiment 2}]$

***Geotextile vs. Geogrid:

$100 * [(\text{Pressure Cell Measurement in Experiment 6} - \text{Pressure Cell Measurement in Experiment 4}) / \text{Pressure Cell Measurement in Experiment 4}]$

Table G4-3. Percent Difference in Strain Gauge Measurements

Instrumentation	Percent Difference in Instrumentation Results								
	Geogrid vs. Control*			Geotextile vs. Control**			Geotextile vs. Geogrid***		
	Load (kip)								
	5	9	12	5	9	12	5	9	12
S1	252.2	153.0	165.2	3774.2	1854.6	1312.7	1000.0	672.5	432.7
SG1_X	-	-	-	-	-	-	-	-	-
SG1_Y	-	-	-	-	-	-	1754.2	1476.6	862.2
SG2_X	-	-	-	-	-	-	990.6	483.9	424.2
SG2_Y	-	-	-	-	-	-	-135.9	-145.2	-268.6

*Geogrid vs. Control:

$100 * [(\text{Strain Gauge Measurement in Experiment 4} - \text{Strain Gauge Measurement in Experiment 2}) / \text{Strain Gauge Measurement in Experiment 2}]$

**Geotextile vs. Control:

$100 * [(\text{Strain Gauge Measurement in Experiment 6} - \text{Strain Gauge Measurement in Experiment 2}) / \text{Strain Gauge Measurement in Experiment 2}]$

***Geotextile vs. Geogrid:

$100 * [(\text{Strain Gauge Measurement in Experiment 6} - \text{Strain Gauge Measurement in Experiment 4}) / \text{Strain Gauge Measurement in Experiment 4}]$

APPENDIX H. INSTRUMENTATION PLANS FOR RIGID PAVEMENT EXPERIMENTS

Appendix H1. Experiment No. 7 (Control)

Experiment ID	Exp7-PCC
Description	Rigid pavement; 8-inch aggregate base

Average PCC Layer Thickness (inch)	6.00
Average CAB Layer Thickness (inch)	8.00

Pressure Cell ID	Pressure Cell Diameter	X Coordinate (in)	Y Coordinate (in)	Z Coordinate (in)	Comments
P1	4 inch	0	6	20	P1 measures vertical pressure at 20 inches below the subgrade surface and 6 inches from the centerline of the tank in positive Y-direction.
P2	4 inch	0	6	16	P2 measures vertical pressure at 16 inches below the subgrade surface and 6 inches from the centerline of the tank in positive Y-direction.
P3	4 inch	0	6	12	P3 measures vertical pressure at 12 inches below the subgrade surface and 6 inches from the centerline of the tank in positive Y-direction.
P4	4 inch	0	14	12	P4 measures vertical pressure at 12 inches below the base surface and 14 inches from the centerline of the tank in positive Y-direction.
P5	4 inch	0	14	16	P5 measures vertical pressure at 16 inches below the base surface and 14 inches from the centerline of the tank in positive Y-direction.
P6	4 inch	0	-2	12	P6 measures vertical pressure at 12 inches below the base surface and 2 inches from the centerline of the tank in negative Y-direction.
P7	4 inch	0	6	8	P7 measures vertical pressure at 8 inches below the base surface and 6 inches from main centerline in positive Y-direction.
P8	4 inch	0	18	8	P8 measures vertical pressure at 8 inches below the base surface and 18 inches from the centerline of the tank in positive Y-direction.
P9	4 inch	8	6	8	P9 measures vertical pressure at 8 inches below the surface and 8 inches from the centerline of the tank in positive X-direction and 6 inches from the centerline of the tank in positive Y-direction.
P10	4 inch	0	-6	8	P10 measures vertical pressure at 8 inches below the surface and 6 inches from the centerline of the tank in negative Y-direction.
P21	1 inch	7.75	8	8	P21 measures vertical pressure at 8 inches below the surface and 8 inches from the centerline of the tank in positive Y and 8 inches from the centerline of the tank in positive X-direction.

Strain Gauge	X Coordinate (in)	Y Coordinate (in)	Z Coordinate (in)	Comments
S1	0	0	6	Strain at the centerline of the load and at the bottom of the PCC layer.

LVDT ID	X Coordinate (in)	Y Coordinate (in)	Z Coordinate (in)	Comments
LVDT 1	0	12	0	At the pavement surface and 12 inches from the centerline of the tank in positive Y-direction, measuring the surface vertical deflection. Note: because of the plate configuration, the measurement is considered to be at the centerline of the load.
LVDT 2	0	18	0	At the pavement surface and 18 inches from the centerline of the tank in positive Y-direction, measuring the surface vertical deflection.
LVDT 3	0	30	0	At the pavement surface and 30 inches from main centerline in positive Y-direction, measuring the surface vertical deflection.
LVDT 4	0	42	0	At the pavement surface and 42 inches from the centerline of the tank in positive Y-direction, measuring the surface vertical deflection.
LVDT 5	0	48	0	On top of the Large-Scale Tank rim and 48 inches from the centerline of the tank in positive Y-direction, measuring the surface vertical deflection.

LVDT ID	X Coordinate (in)	Y Coordinate (in)	Z Coordinate (in)	Comments
LVDT 6	-12	0	6	At 6 inches below the surface and 12 inches from the centerline of the tank in negative X-direction, measuring base horizontal deflection (negative measurements for extension and positive measurements for compression).
LVDT 7	-24	0	6	At 6 inches below the surface and 24 inches from the centerline of the tank in negative X-direction, measuring base horizontal deflection (negative measurements for extension and positive measurements for compression).

Accelerometer	Accelerometer ID	X Coordinate (in)	Y Coordinate (in)	Z Coordinate (in)	Comments
A1	A1_Z	0	12	0	At the pavement surface and 12 inches from the centerline of the tank, measuring vertical acceleration in Z-direction. (It reports negative numbers when acceleration is in positive Z-direction.) Note: because of the plate configuration, the measurement is considered to be at the centerline of the load.
A2	A2_Z	0	18	0	At the pavement surface and 18 inches from the centerline of the tank in positive Y-direction, measuring vertical acceleration in Z-direction. (It reports negative numbers when acceleration is in positive Z-direction.)
A3	A3_Z	0	30	0	At the pavement surface and 30 inches from the centerline of the tank in positive Y-direction, measuring vertical acceleration in Z-direction. (It reports negative numbers when acceleration is in positive Z-direction.)
A4	A4_Z	-12	0	0	At the surface of the base and 12 inches from the centerline of the tank in negative X-direction, measuring vertical acceleration in Z-direction. (It reports negative numbers when acceleration is in positive Z-direction.)
A5	A5_Z	-12	6	0	At the pavement surface and 12 inches from the centerline of the tank in negative X-direction and 6 inches from the centerline of the tank in positive Y-direction, measuring vertical acceleration in Z-direction. (It reports negative numbers when acceleration is in positive Z-direction.)
A6	A6_Z	-24	0	0	At the surface of the base and 24 inches from the centerline of the tank in negative X-direction, measuring vertical acceleration in Z-direction. (It reports negative numbers when acceleration is in positive Z-direction.)
A7	A7_Z	-24	6	0	At the pavement surface and 24 inches from the centerline of the tank in negative X-direction and 6 inches from the centerline of the tank in positive Y-direction, measuring vertical acceleration in Z-direction. (It reports negative numbers when acceleration is in positive Z-direction.)
Msg1	M1_Y	0	6	10	In the middle of the base and at the centerline of the load, measuring horizontal acceleration in Y-direction.

Accelerometer	Accelerometer ID	X Coordinate (in)	Y Coordinate (in)	Z Coordinate (in)	Comments
Msg1	M1_Z	0	6	10	In the middle of the base and at the centerline of the load, measuring vertical acceleration in Z-direction. (It reports negative numbers when acceleration is in positive Z-direction.)
Msg1	M1_X	0	6	10	In the middle of the base and at the centerline of the load, measuring vertical acceleration in X-direction.
Msg2	M2_Y	0	18	10	In the middle of the base and 18 inches from the centerline of the tank, measuring horizontal acceleration in Y-direction.
Msg2	M2_Z	0	18	10	In the middle of the base and 18 inches from the centerline of the tank, measuring vertical acceleration in Z-direction. (It reports negative numbers when acceleration is in positive Z-direction.)
Msg3	M3_Y	0	30	10	In the middle of the base and 30 inches from the centerline of the tank, measuring horizontal acceleration in Y-direction.
Msg3	M3_Z	0	30	10	In the middle of the base and 30 inches from the centerline of the tank, measuring vertical acceleration in Z-direction. (It reports negative numbers when acceleration is in positive Z-direction.)
Msg4	M4_X	12	0	10	In the middle of the base and 12 inches from the centerline of the tank in positive X-direction, measuring horizontal acceleration in X-direction.
Msg4	M4_Z	12	0	10	In the middle of the base and 12 inches from the centerline of the tank in positive X-direction, measuring vertical acceleration in Z-direction. (It reports negative numbers when acceleration is in positive Z-direction.)
Msg5	M5_X	24	0	10	In the middle of the base and 24 inches from the centerline of the tank in positive X-direction, measuring horizontal acceleration in X-direction.
Msg5	M5_Z	24	0	10	In the middle of the base and 24 inches from the centerline of the tank in positive X-direction, measuring vertical acceleration in Z-direction. (It reports negative numbers when acceleration is in positive Z-direction.)
Msg6	M6_Z	-12	6	10	In the middle of the base and 12 inches from the centerline of the tank in negative X-direction, measuring vertical acceleration in Z-direction. (It reports negative numbers when acceleration is in positive Z-direction.)
Msg7	M7_X	-24	6	10	In the middle of the base and 24 inches from the centerline of the tank in negative X-direction, measuring horizontal acceleration in X-direction.
Msg7	M7_Z	-24	6	10	In the middle of the base and 24 inches from the centerline of the tank in negative X-direction, measuring vertical acceleration in Z-direction. (It reports negative numbers when acceleration is in positive Z-direction.)

Accelerometer	Accelerometer ID	X Coordinate (in)	Y Coordinate (in)	Z Coordinate (in)	Comments
Mb/c1	Mb1_X	0	6	6	At top of the base and 6 inches from the centerline of the tank in positive Y-direction, measuring horizontal acceleration in positive X-direction.
Mb/c1	Mb1_Y	0	6	6	At top of the base and 6 inches from the centerline of the tank in positive Y-direction, measuring horizontal acceleration in positive Y-direction.
Mb/c1	Mb1_Z	0	6	6	At top of the base and 6 inches from the centerline of the tank in positive Y-direction, measuring vertical acceleration in Z-direction. (It reports negative numbers when acceleration is in positive Z-direction.)
Mb/c1	Mc1_X	0	6	6	At bottom of the concrete layer and 6 inches from the centerline of the tank in positive Y-direction, measuring horizontal acceleration in positive X-direction.
Mb/c1	Mc1_Y	0	6	6	At bottom of the concrete layer and 6 inches from the centerline of the tank in positive Y-direction, measuring horizontal acceleration in positive Y-direction.
Mb/c1	Mc1_Z	0	6	6	At bottom of the concrete layer and 6 inches from the centerline of the tank in positive Y-direction, measuring vertical acceleration in Z-direction. (It reports negative numbers when acceleration is in positive Z-direction.)
Mb/c2	Mb2_Y	0	24	6	At top of the base and 24 inches from the centerline of the tank in positive Y-direction, measuring horizontal acceleration in positive Y-direction.
Mb/c2	Mb2_Z	0	24	6	At top of the base and 24 inches from the centerline of the tank in positive Y-direction, measuring vertical acceleration in Z-direction. (It reports negative numbers when acceleration is in positive Z-direction.)
Mb/c2	Mc2_Y	0	24	6	At bottom of the concrete layer and 24 inches from the centerline of the tank in positive Y-direction, measuring horizontal acceleration in positive Y-direction.
Mb/c2	Mc2_Z	0	24	6	At bottom of the concrete layer and 24 inches from the centerline of the tank in positive Y-direction, measuring vertical acceleration in Z-direction. (It reports negative numbers when acceleration is in positive Z-direction.)
Mb/c3	Mb2_Y	18	6	6	At top of the base, 18 inches from the centerline of the tank in positive X-direction and 6 inches from the centerline of the tank in positive Y-direction, measuring horizontal acceleration in positive Y-direction.
Mb/c3	Mb2_Z	18	6	6	At top of the base, 18 inches from the centerline of the tank in positive X-direction and 6 inches from the centerline of the tank in positive Y-direction, measuring horizontal acceleration in Z-direction. (It reports negative numbers when acceleration is in positive Z-direction.)

Accelerometer	Accelerometer ID	X Coordinate (in)	Y Coordinate (in)	Z Coordinate (in)	Comments
Mb/c3	Mc2_Y	18	6	6	At bottom of the concrete layer, 18 inches from the centerline of the tank in positive X-direction and 6 inches from the centerline of the tank in positive Y-direction, measuring horizontal acceleration in positive Y-direction.
Mb/c3	Mc2_Z	18	6	6	At bottom of the concrete layer, 18 inches from the centerline of the tank in positive X-direction and 6 inches from the centerline of the tank in positive Y-direction, measuring horizontal acceleration in Z-direction. (It reports negative numbers when acceleration is in positive Z-direction.)

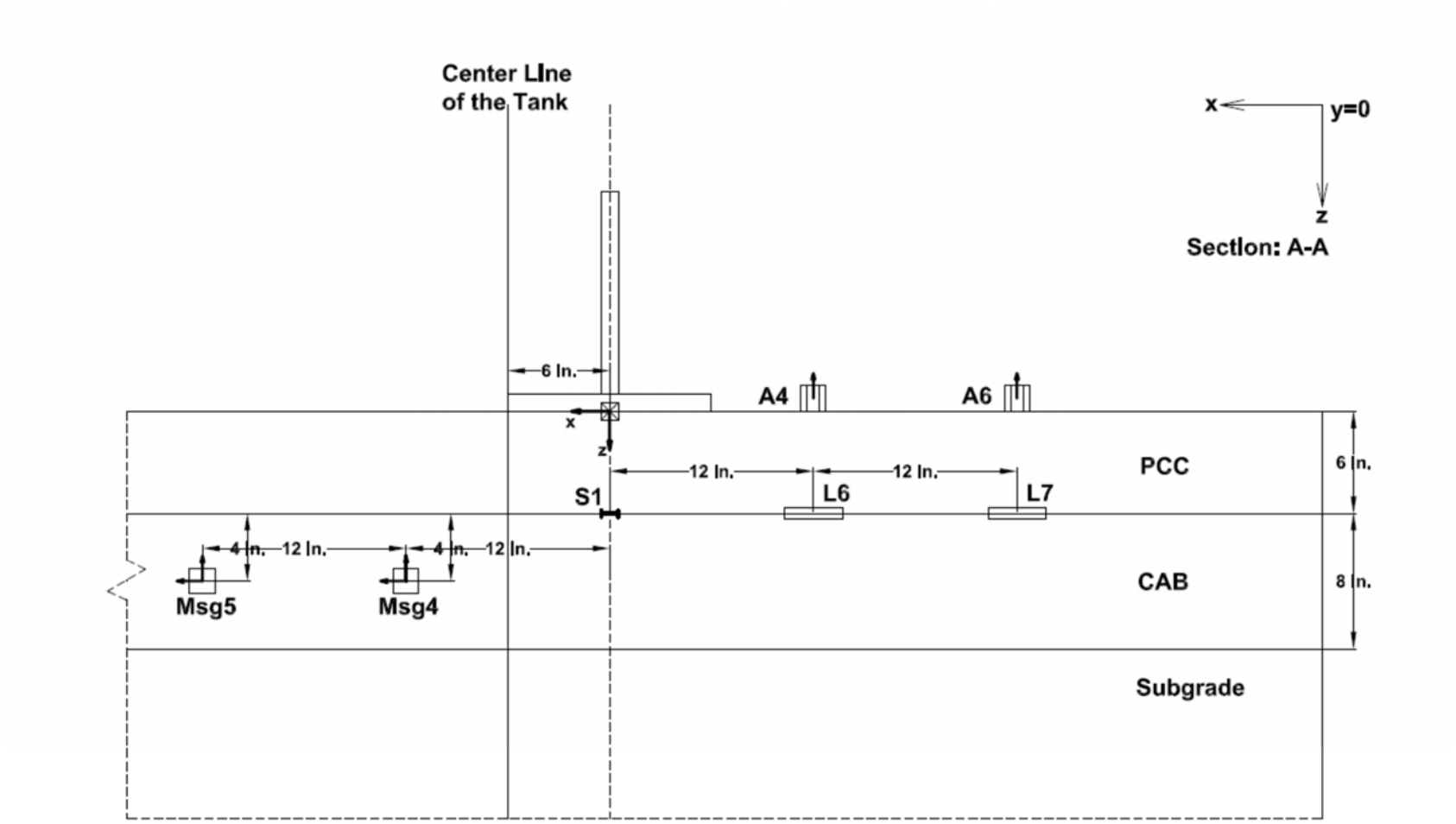


Figure H1-1. Instrumentation plan for experiment No. 7—Profile view, Y=0 inch

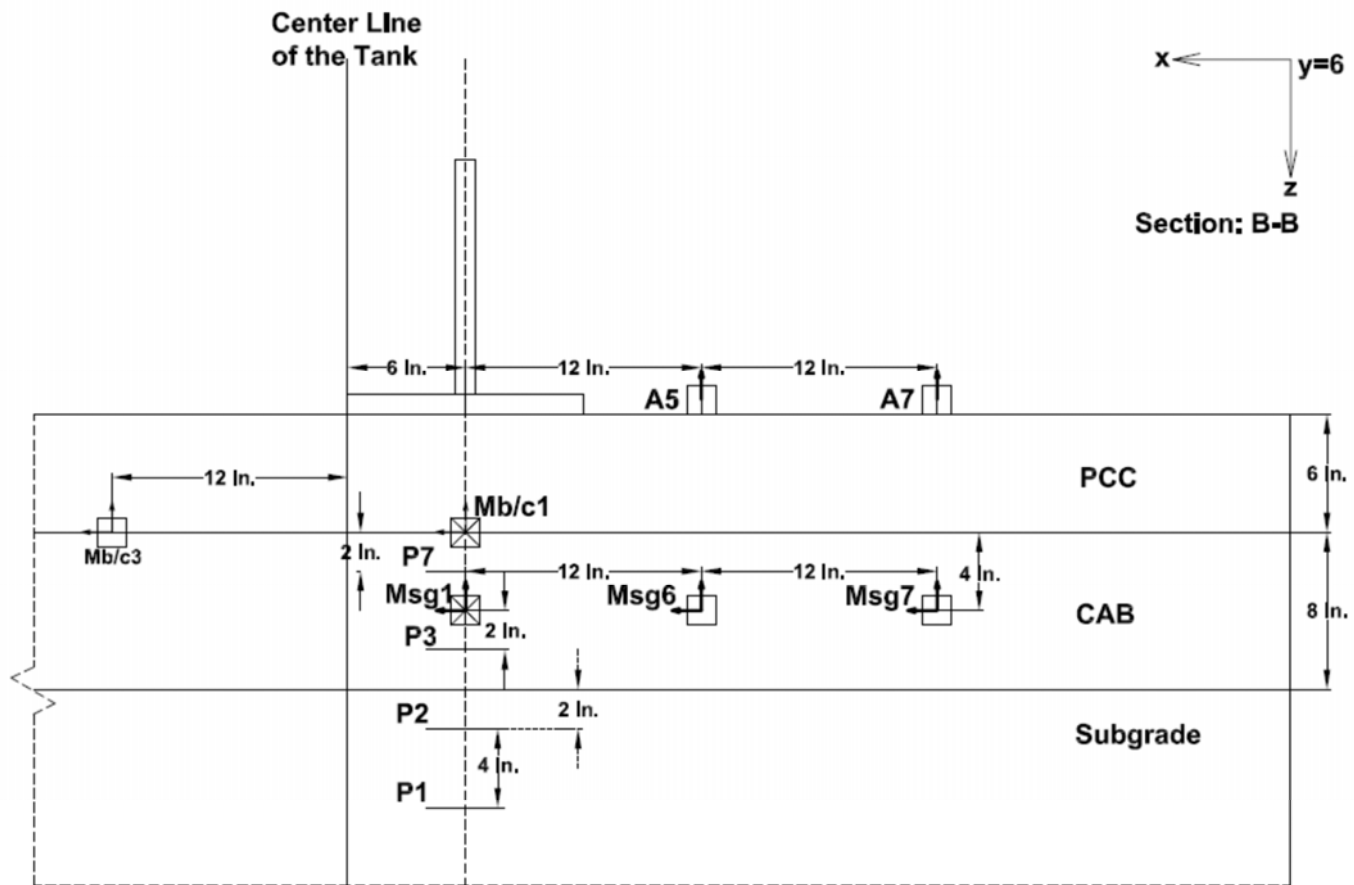


Figure H1-2. Instrumentation plan for experiment No. 7—Profile view, Y=6 inches

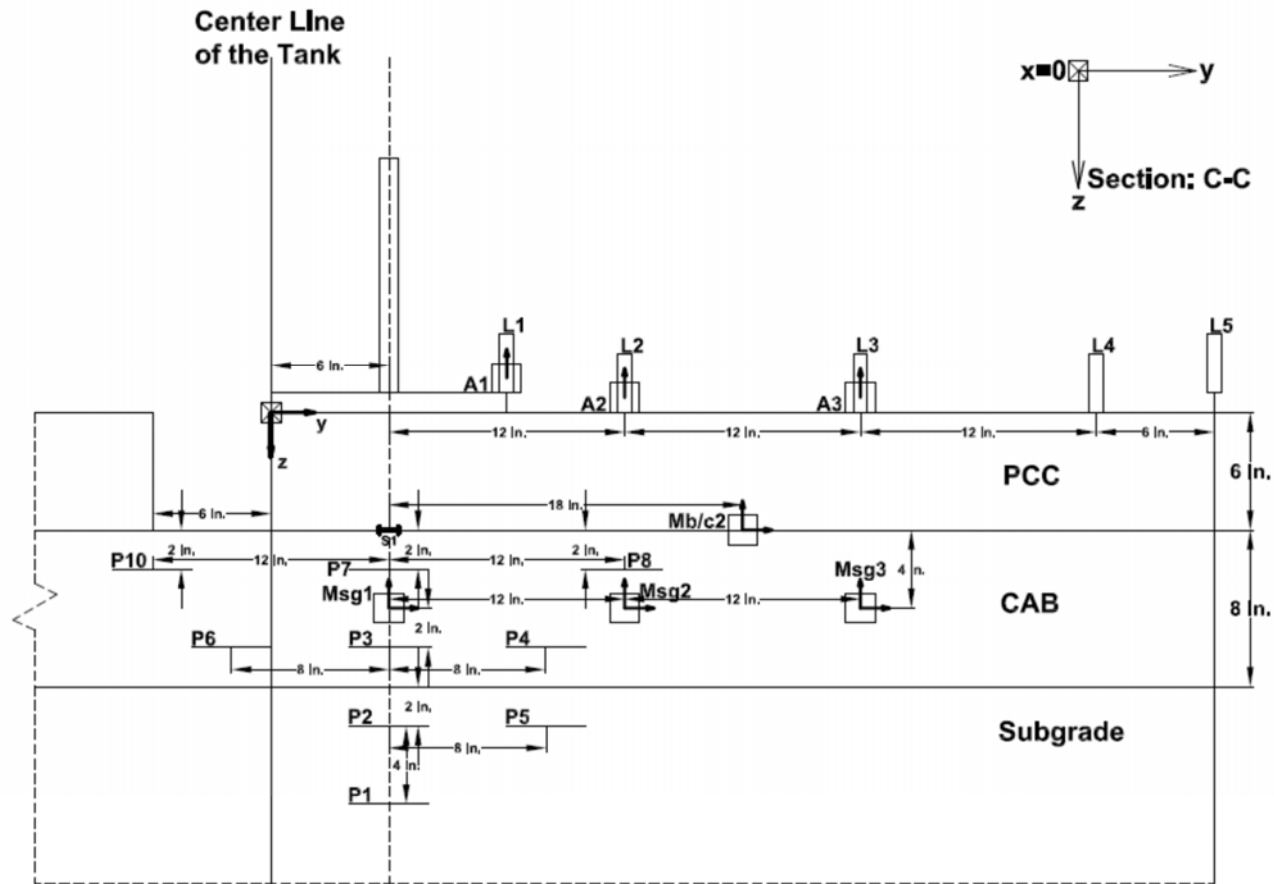


Figure H1-3. Instrumentation plan for experiment No. 7—Profile view, X=0 inch



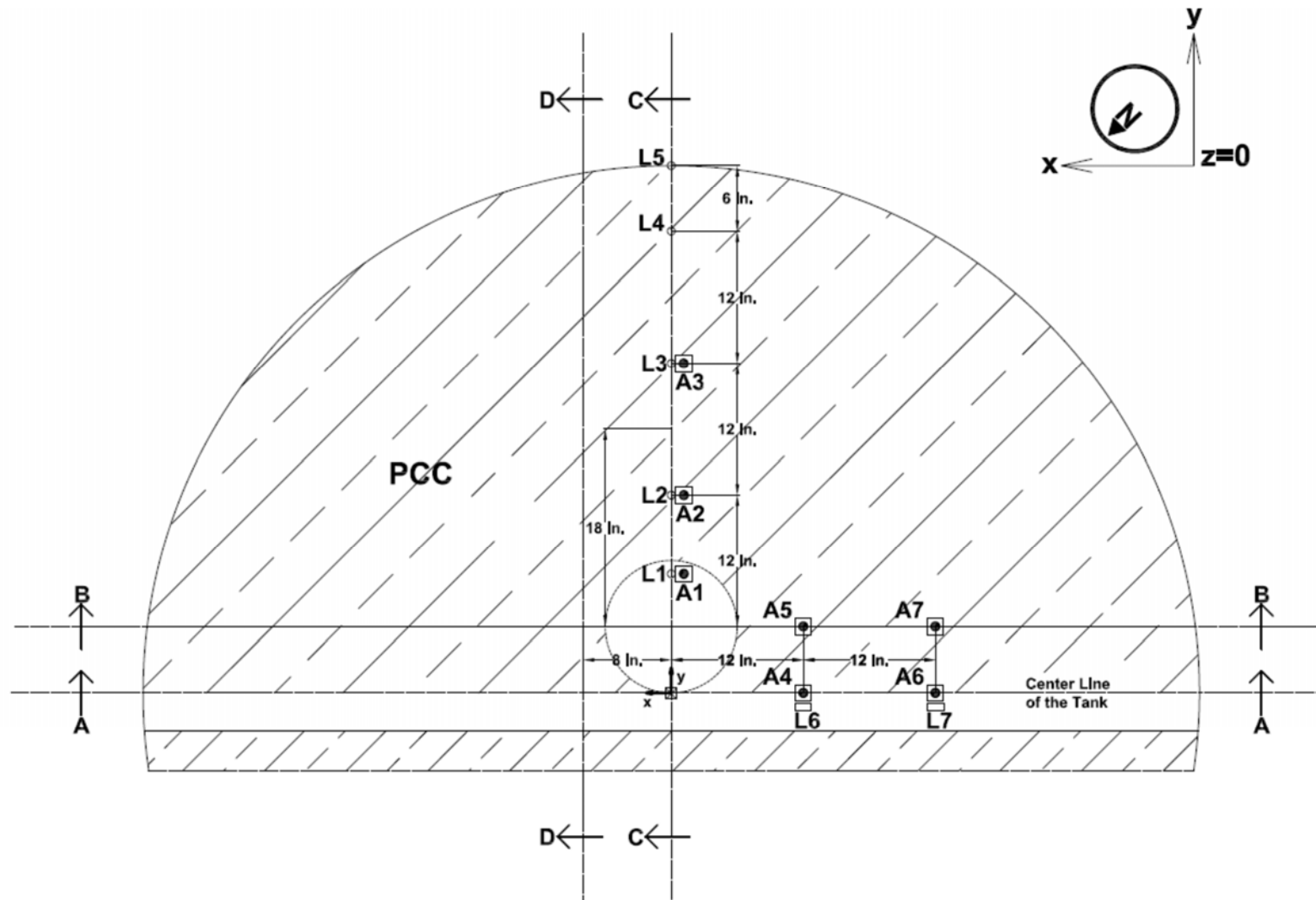


Figure H1-5. Instrumentation plan for experiment No. 7—Plan view, Z=0 inch

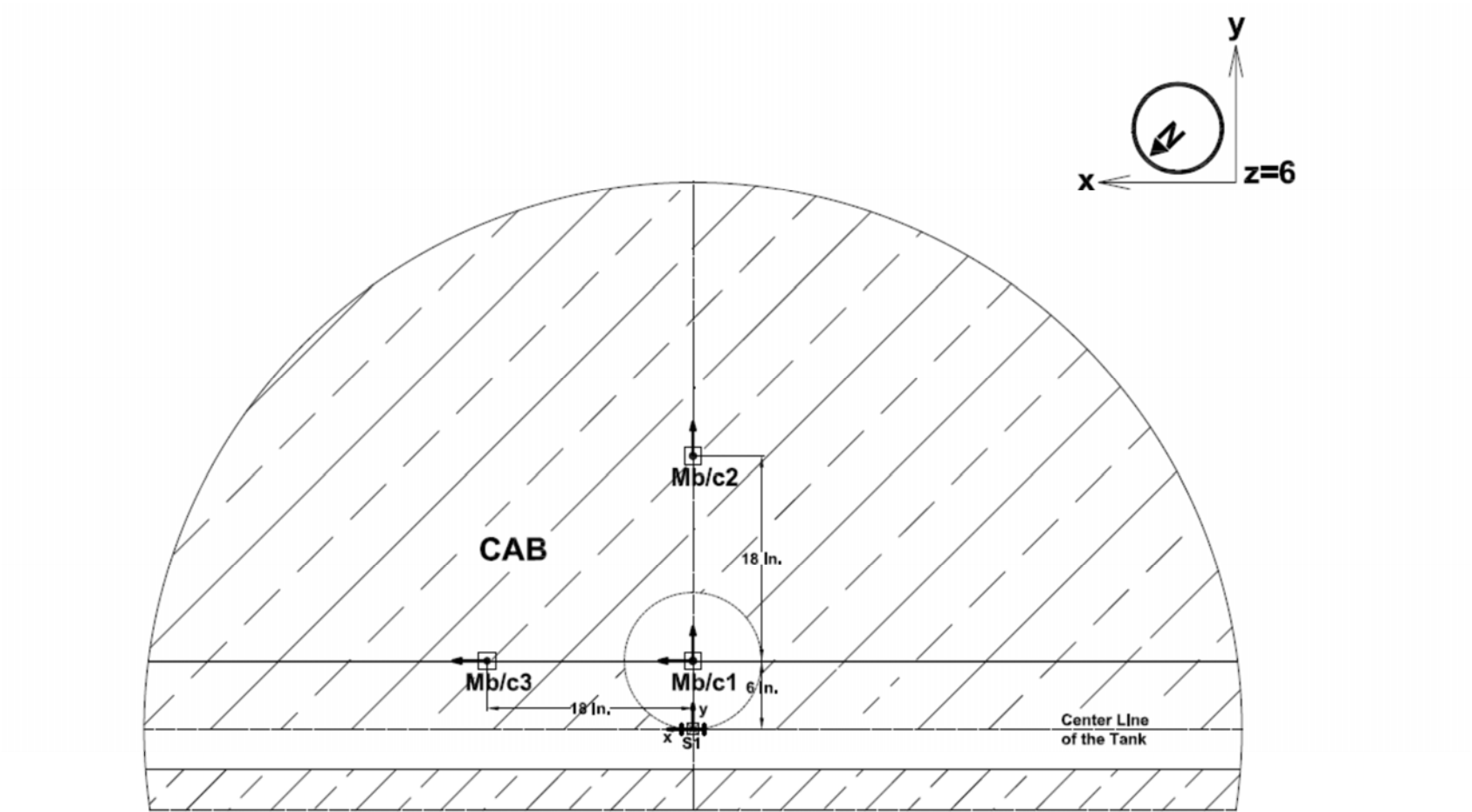


Figure H1-6. Instrumentation plan for experiment No. 7—Plan view, Z=6 inches

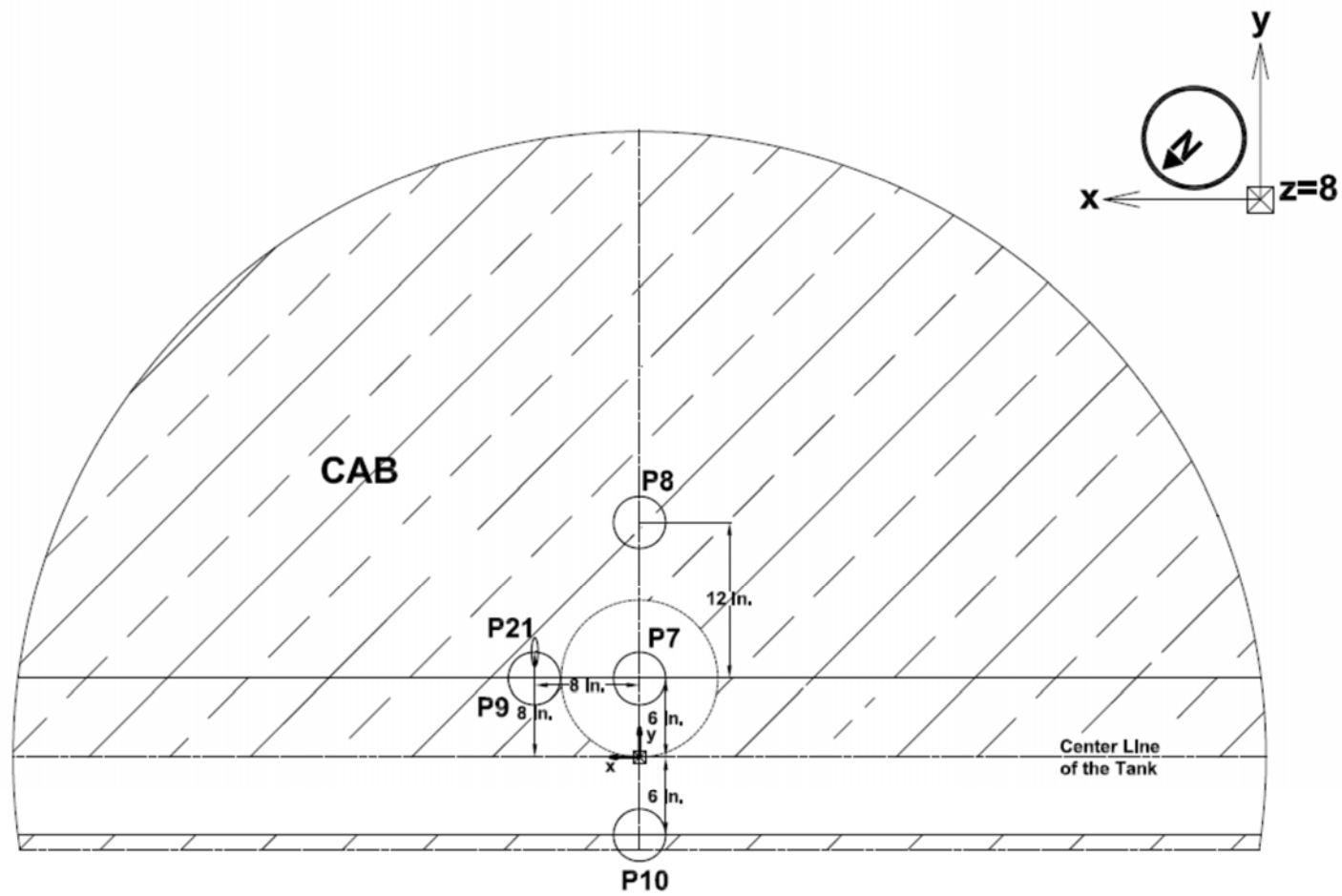


Figure H1-7. Instrumentation plan for experiment No. 7—Plan view, Z=8 inches

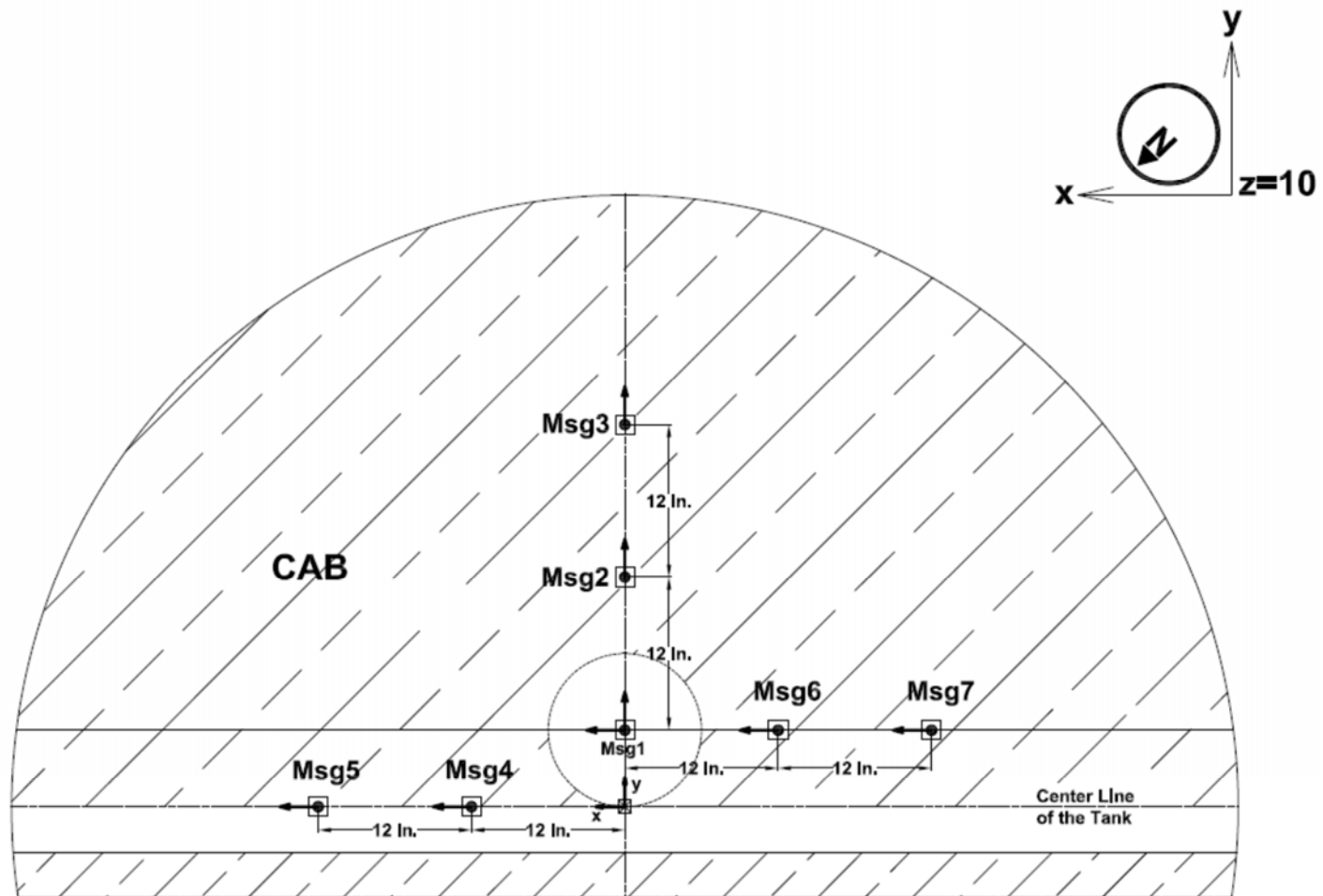


Figure H1-8. Instrumentation plan for experiment No. 7—Plan view, Z=10 inches

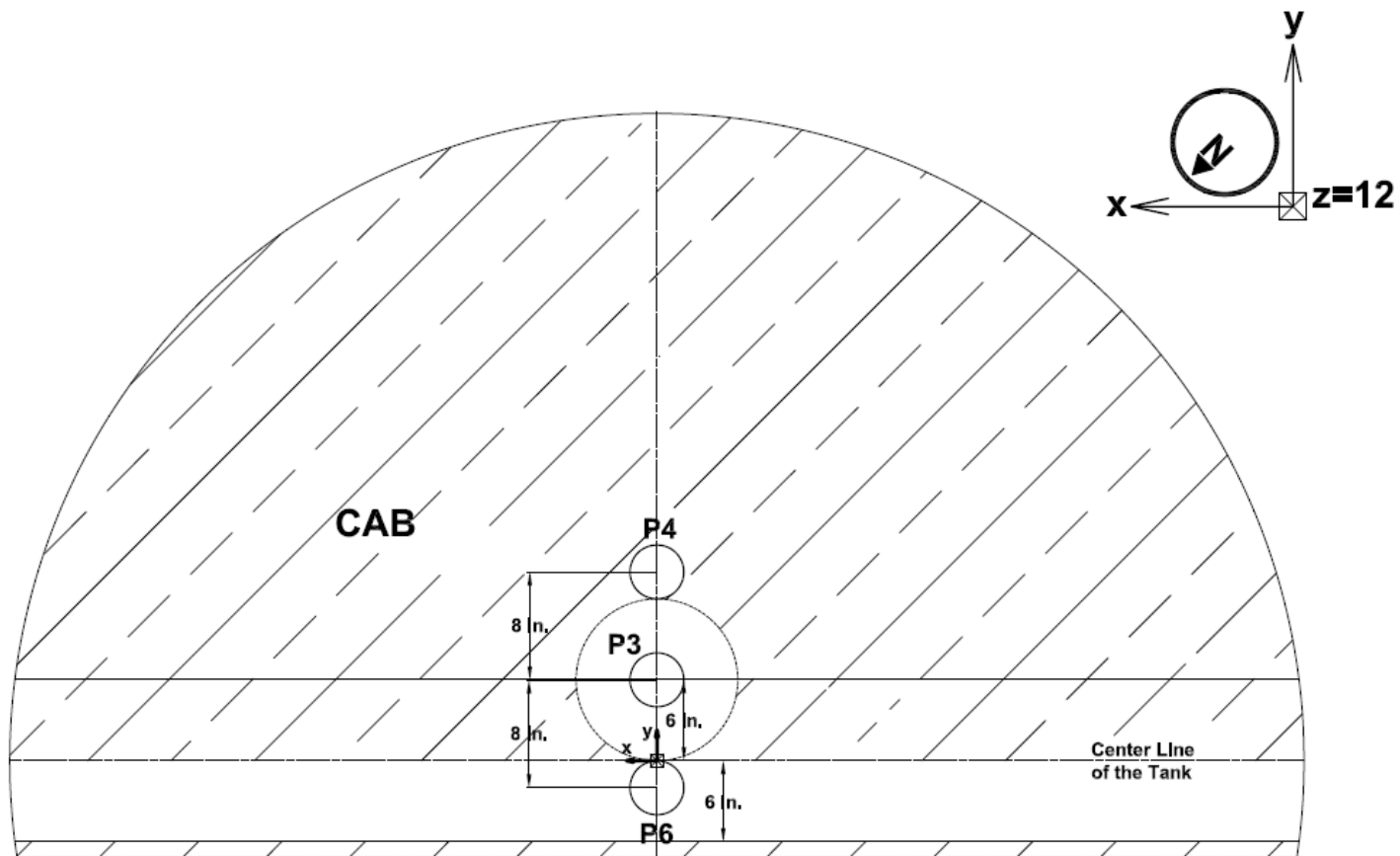


Figure H1-9. Instrumentation plan for experiment No. 7—Plan view, $Z=12$ inches

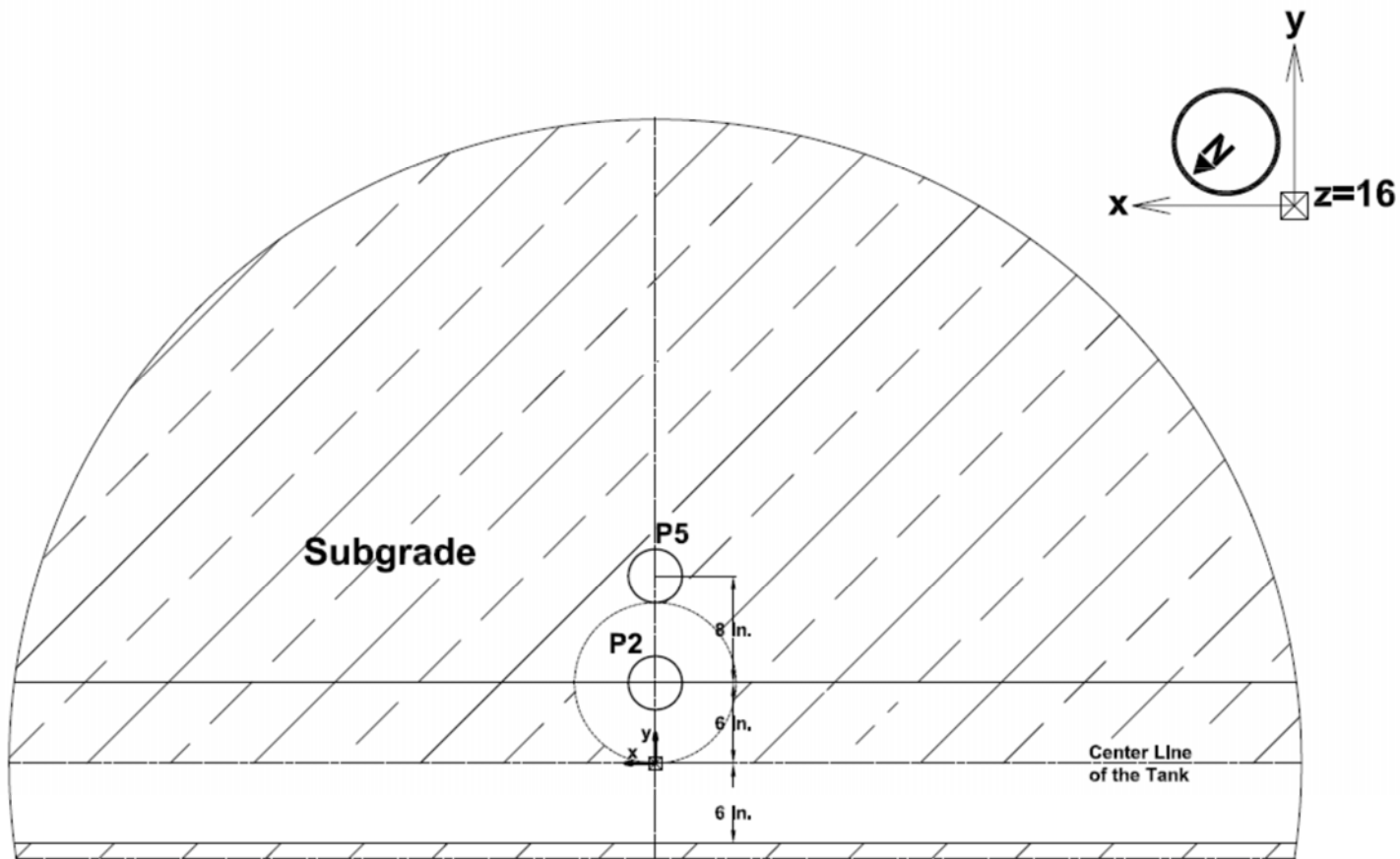


Figure H1-10. Instrumentation plan for experiment No. 7—Plan view, Z=16 inches

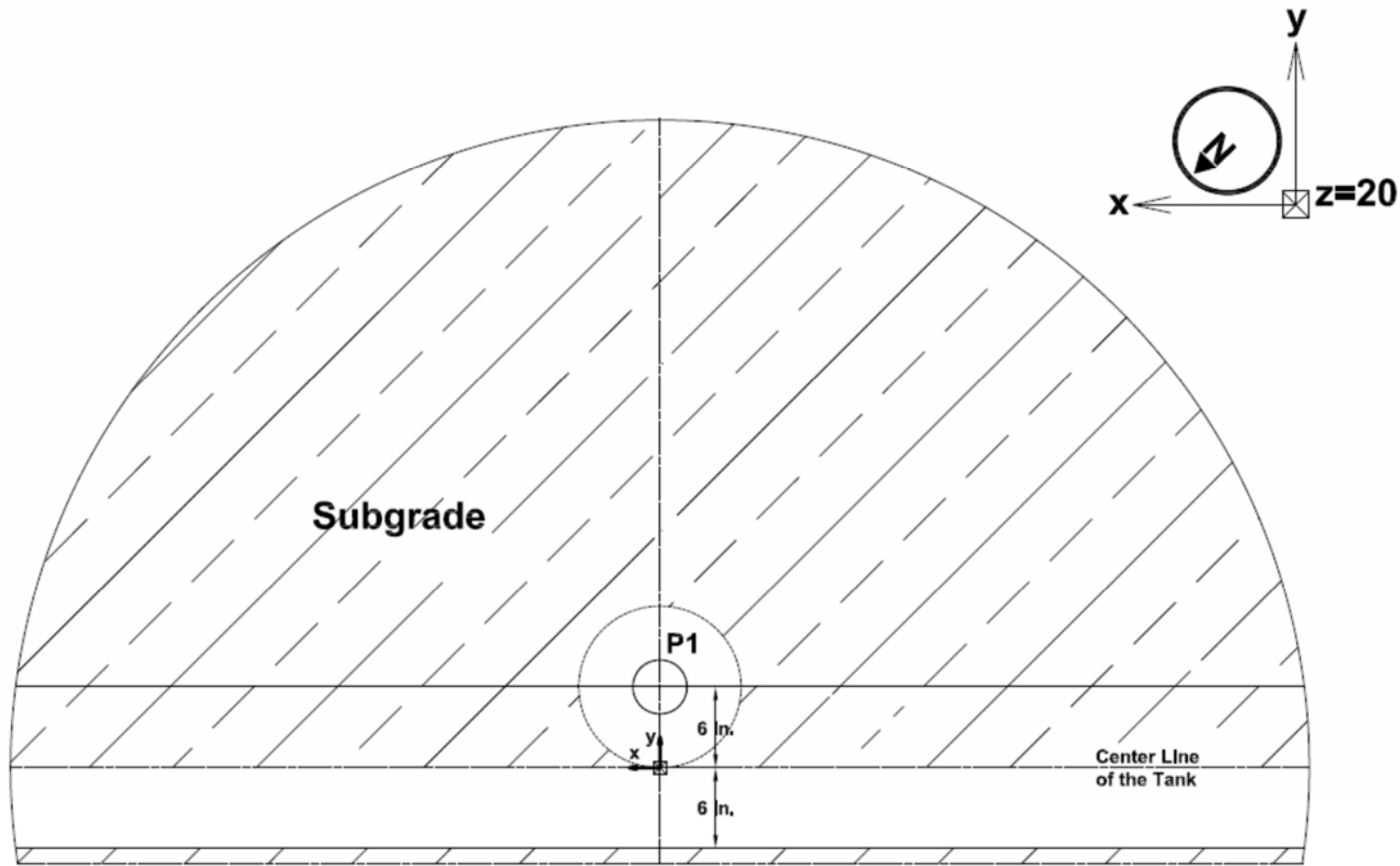


Figure H1-11. Instrumentation plan for experiment No. 7—Plan view, $Z=20$ inches

Appendix H2. Experiment No. 9 (Geogrid)

Experiment ID	Exp9-PCC
Description	Rigid pavement; 8-inch aggregate base with geogrid

Average PCC Layer Thickness (inch)	6.00
Average CAB Layer Thickness (inch)	8.00

Pressure Cell ID	Pressure Cell Diameter	X Coordinate (in)	Y Coordinate (in)	Z Coordinate (in)	Comments
P1	4 inch	0	6	20	P1 measures vertical pressure at 20 inches below the subgrade surface and 6 inches from the centerline of the tank in positive Y-direction.
P2	4 inch	0	6	16	P2 measures vertical pressure at 16 inches below the subgrade surface and 6 inches from the centerline of the tank in positive Y-direction.
P3	4 inch	0	6	12	P3 measures vertical pressure at 12 inches below the subgrade surface and 6 inches from the centerline of the tank in positive Y-direction.
P4	4 inch	0	14	12	P4 measures vertical pressure at 12 inches below the base surface and 14 inches from the centerline of the tank in positive Y-direction.
P5	4 inch	0	14	16	P5 measures vertical pressure at 16 inches below the base surface and 14 inches from the centerline of the tank in positive Y-direction.
P6	4 inch	0	-2	12	P6 measures vertical pressure at 12 inches below the base surface and 2 inches from the centerline of the tank in negative Y-direction.
P7	4 inch	0	6	8	P7 measures vertical pressure at 8 inches below the base surface and 6 inches from main centerline in positive Y-direction.
P8	4 inch	0	18	8	P8 measures vertical pressure at 8 inches below the base surface and 18 inches from the centerline of the tank in positive Y-direction.
P9	4 inch	8	6	8	P9 measures vertical pressure at 8 inches below the surface and 8 inches from the centerline of the tank in positive X-direction and 6 inches from the centerline of the tank in positive Y-direction.
P10	4 inch	0	-6	8	P10 measures vertical pressure at 8 inches below the surface and 6 inches from the centerline of the tank in negative Y-direction.
P21	1 inch	7.75	8	8	P21 measures vertical pressure at 8 inches below the surface and 8 inches from the centerline of the tank in positive Y and 8 inches from the centerline of the tank in positive X-direction.

Strain Gauge	X Coordinate (in)	Y Coordinate (in)	Z Coordinate (in)	Comments
S1	0	0	6	Strain at the centerline of the load and at the bottom of the PCC layer.
SG1-X	0	6	10	In the middle of the base and at the centerline of the load, measuring strain on geogrid.
SG1-Y	0	6	10	In the middle of the base and at the centerline of the load, measuring strain on geogrid.
SG2-X	0	18	10	In the middle of the base and 18 inches from the centerline of the tank, measuring strain on geogrid.
SG2-Y	0	18	10	In the middle of the base and 18 inches from the centerline of the tank, measuring strain on geogrid.
SG3-X	0	30	10	In the middle of the base and 30 inches from the centerline of the tank, measuring strain on geogrid.
SG3-Y	0	30	10	In the middle of the base and 30 inches from the centerline of the tank, measuring strain on geogrid.
SG4-X	-12	0	10	In the middle of the base and 12 inches from the centerline of the tank in negative X-direction, measuring strain on geogrid.
SG4-Y	-12	0	10	In the middle of the base and 12 inches from the centerline of the tank in negative X-direction, measuring strain on geogrid.
SG5-X	-24	0	10	In the middle of the base and 24 inches from the centerline of the tank in negative X-direction, measuring strain on geogrid.
SG5-Y	-24	0	10	In the middle of the base and 24 inches from the centerline of the tank in negative X-direction, measuring strain on geogrid.

LVDT ID	X Coordinate (in)	Y Coordinate (in)	Z Coordinate (in)	Comments
LVDT 1	0	12	0	At the pavement surface and 12 inches from the centerline of the tank in positive Y-direction, measuring the surface vertical deflection. Note: because of the plate configuration, the measurement is considered to be at the centerline of the load.
LVDT 2	0	18	0	At the pavement surface and 18 inches from the centerline of the tank in positive Y-direction, measuring the surface vertical deflection.
LVDT 3	0	30	0	At the pavement surface and 30 inches from main centerline in positive Y-direction, measuring the surface vertical deflection.
LVDT 4	0	42	0	At the pavement surface and 42 inches from the centerline of the tank in positive Y-direction, measuring the surface vertical deflection.
LVDT 5	0	48	0	On top of the Large-Scale Tank rim and 48 inches from the centerline of the tank in positive Y-direction, measuring the surface vertical deflection.
LVDT 6	-12	0	6	At 6 inches below the surface and 12 inches from the centerline of the tank in negative X-direction, measuring base horizontal deflection (negative measurements for extension and positive measurements for compression).
LVDT 7	-24	0	6	At 6 inches below the surface and 24 inches from the centerline of the tank in negative X-direction, measuring base horizontal deflection (negative measurements for extension and positive measurements for compression).

Accelerometer	Accelerometer ID	X Coordinate (in)	Y Coordinate (in)	Z Coordinate (in)	Comments
A1	A1_Z	0	12	0	At the pavement surface and 12 inches from the centerline of the tank, measuring vertical acceleration, measuring vertical acceleration in Z-direction. (It reports negative numbers when acceleration is in positive Z-direction.) Note: because of the plate configuration, the measurement is considered to be at the centerline of the load.
A2	A2_Z	0	18	0	At the pavement surface and 18 inches from the centerline of the tank in positive Y-direction, measuring vertical acceleration, measuring vertical acceleration in Z-direction. (It reports negative numbers when acceleration is in positive Z-direction.)
A3	A3_Z	0	30	0	At the pavement surface and 30 inches from the centerline of the tank in positive Y-direction, measuring vertical acceleration in Z-direction. (It reports negative numbers when acceleration is in positive Z-direction.)
A4	A4_Z	-12	0	0	At the surface of the base and 12 inches from the centerline of the tank in negative X-direction, measuring vertical acceleration in Z-direction. (It reports negative numbers when acceleration is in positive Z-direction.)
A5	A5_Z	-12	6	0	At the pavement surface and 12 inches from the centerline of the tank in negative X-direction and 6 inches from the centerline of the tank in positive Y-direction, measuring vertical acceleration in Z-direction. (It reports negative numbers when acceleration is in positive Z-direction.)
A6	A6_Z	-24	0	0	At the surface of the base and 24 inches from the centerline of the tank in negative X-direction, measuring vertical acceleration in Z-direction. (It reports negative numbers when acceleration is in positive Z-direction.)

Accelerometer	Accelerometer ID	X Coordinate (in)	Y Coordinate (in)	Z Coordinate (in)	Comments
A7	A7_Z	-24	6	0	At the pavement surface and 24 inches from the centerline of the tank in negative X-direction and 6 inches from the centerline of the tank in positive Y-direction, measuring vertical acceleration in Z-direction. (It reports negative numbers when acceleration is in positive Z-direction.)
Msg1	M1_Y	0	6	10	In the middle of the base and at the centerline of the load, measuring horizontal acceleration in Y-direction.
Msg1	M1_Z	0	6	10	In the middle of the base and at the centerline of the load, measuring vertical acceleration in Z-direction. (It reports negative numbers when acceleration is in positive Z-direction.)
Msg1	M1_X	0	6	10	In the middle of the base and at the centerline of the load, measuring vertical acceleration in X-direction.
Msg2	M2_Y	0	18	10	In the middle of the base and 18 inches from the centerline of the tank, measuring horizontal acceleration in Y-direction.
Msg2	M2_Z	0	18	10	In the middle of the base and 18 inches from the centerline of the tank, measuring vertical acceleration in Z-direction. (It reports negative numbers when acceleration is in positive Z-direction.)
Msg3	M3_Y	0	30	10	In the middle of the base and 30 inches from the centerline of the tank, measuring horizontal acceleration in Y-direction.
Msg3	M3_Z	0	30	10	In the middle of the base and 30 inches from the centerline of the tank, measuring vertical acceleration in Z-direction. (It reports negative numbers when acceleration is in positive Z-direction.)
Msg4	M4_X	12	0	10	In the middle of the base and 12 inches from the centerline of the tank in positive X-direction, measuring horizontal acceleration in X-direction.
Msg4	M4_Z	12	0	10	In the middle of the base and 12 inches from the centerline of the tank in positive X-direction, measuring vertical acceleration in Z-direction. (It reports negative numbers when acceleration is in positive Z-direction.)
Msg5	M5_X	24	0	10	In the middle of the base and 24 inches from the centerline of the tank in positive X-direction, measuring horizontal acceleration in X-direction.
Msg5	M5_Z	24	0	10	In the middle of the base and 24 inches from the centerline of the tank in positive X-direction, measuring vertical acceleration in Z-direction. (It reports negative numbers when acceleration is in positive Z-direction.)
Msg6	M6_X	-12	6	10	In the middle of the base and 12 inches from the centerline of the tank in negative X-direction, measuring horizontal acceleration is in X-direction.
Msg7	M7_X	-24	6	10	In the middle of the base and 24 inches from the centerline of the tank in negative X-direction, measuring horizontal acceleration in X-direction.
Msg7	M7_Z	-24	6	10	In the middle of the base and 24 inches from the centerline of the tank in negative X-direction, measuring vertical acceleration in Z-direction. (It reports negative numbers when acceleration is in positive Z-direction.)

Accelerometer	Accelerometer ID	X Coordinate (in)	Y Coordinate (in)	Z Coordinate (in)	Comments
Mgd1	Mgd1_X	0	6	10	In the middle of the base and at the centerline of the load, measuring horizontal acceleration on geogrid in X-direction.
Mgd1	Mgd1_Y	0	6	10	In the middle of the base and at the centerline of the load, measuring vertical acceleration on geogrid in Y-direction.
Mgd1	Mgd1_Z	0	6	10	In the middle of the base and at the centerline of the load, measuring vertical acceleration on geogrid in Z-direction. (It reports negative numbers when acceleration is in positive Z-direction.)
Mgd2	Mgd2_Y	0	18	10	In the middle of the base and 18 inches from the centerline of the tank, measuring horizontal acceleration on geogrid in Y-direction.
Mgd2	Mgd2_Z	0	18	10	In the middle of the base and 18 inches from the centerline of the tank, measuring vertical acceleration on geogrid in Z-direction.
Mgd3	Mgd3_Y	0	30	10	In the middle of the base and 30 inches from the centerline of the tank, measuring horizontal acceleration on geogrid in Y-direction.
Mgd3	Mgd3_Z	0	30	10	In the middle of the base and 30 inches from the centerline of the tank, measuring vertical acceleration on geogrid in Z-direction.
Mgd4	Mgd4_X	12	0	10	In the middle of the base and 12 inches from the centerline of the tank in positive X-direction, measuring horizontal acceleration on geogrid in X-direction.
Mgd4	Mgd4_Z	12	0	10	In the middle of the base and 12 inches from the centerline of the tank in positive X-direction, measuring vertical acceleration on geogrid in Z-direction. (It reports negative numbers when acceleration is in positive Z-direction.)
Mgd5	Mgd5_X	24	0	10	In the middle of the base and 24 inches from the centerline of the tank in positive X-direction, measuring horizontal acceleration on geogrid in X-direction.
Mgd5	Mgd5_Z	24	0	10	In the middle of the base and 24 inches from the centerline of the tank in positive X-direction, measuring vertical acceleration on geogrid in Z-direction. (It reports negative numbers when acceleration is in positive Z-direction.)
Mb/c1	Mb1_X	0	6	6	At top of the base and 6 inches from the centerline of the tank in positive Y-direction, measuring horizontal acceleration in positive X-direction.
Mb/c1	Mb1_Y	0	6	6	At top of the base and 6 inches from the centerline of the tank in positive Y-direction, measuring horizontal acceleration in positive Y-direction.
Mb/c1	Mb1_Z	0	6	6	At top of the base and 6 inches from the centerline of the tank in positive Y-direction, measuring vertical acceleration in Z-direction. (It reports negative numbers when acceleration is in positive Z-direction.)
Mb/c1	Mc1_X	0	6	6	At bottom of the concrete layer and 6 inches from the centerline of the tank in positive Y-direction, measuring horizontal acceleration in positive X-direction.
Mb/c1	Mc1_Y	0	6	6	At bottom of the concrete layer and 6 inches from the centerline of the tank in positive Y-direction, measuring horizontal acceleration in positive Y-direction.

Accelerometer	Accelerometer ID	X Coordinate (in)	Y Coordinate (in)	Z Coordinate (in)	Comments
Mb/c1	Mc1_Z	0	6	6	At bottom of the concrete layer and 6 inches from the centerline of the tank in positive Y-direction, measuring vertical acceleration in Z-direction. (It reports negative numbers when acceleration is in positive Z-direction.)
Mb/c2	Mb2_Y	0	24	6	At top of the base and 24 inches from the centerline of the tank in positive Y-direction, measuring horizontal acceleration in positive Y-direction.
Mb/c2	Mb2_Z	0	24	6	At top of the base and 24 inches from the centerline of the tank in positive Y-direction, measuring vertical acceleration in Z-direction. (It reports negative numbers when acceleration is in positive Z-direction.)
Mb/c2	Mc2_Y	0	24	6	At bottom of the concrete layer and 24 inches from the centerline of the tank in positive Y-direction, measuring horizontal acceleration in positive Y-direction.
Mb/c2	Mc2_Z	0	24	6	At bottom of the concrete layer and 24 inches from the centerline of the tank in positive Y-direction, measuring vertical acceleration in Z-direction. (It reports negative numbers when acceleration is in positive Z-direction.)
Mb/c3	Mb2_Y	18	6	6	At top of the base, 18 inches from the centerline of the tank in positive X-direction and 6 inches from the centerline of the tank in positive Y-direction, measuring horizontal acceleration in positive Y-direction.
Mb/c3	Mb2_Z	18	6	6	At top of the base, 18 inches from the centerline of the tank in positive X-direction and 6 inches from the centerline of the tank in positive Y-direction, measuring horizontal acceleration in Z-direction. (It reports negative numbers when acceleration is in positive Z-direction.)
Mb/c3	Mc2_Y	18	6	6	At bottom of the concrete layer, 18 inches from the centerline of the tank in positive X-direction and 6 inches from the centerline of the tank in positive Y-direction, measuring horizontal acceleration in positive Y-direction.
Mb/c3	Mc2_Z	18	6	6	At bottom of the concrete layer, 18 inches from the centerline of the tank in positive X-direction and 6 inches from the centerline of the tank in positive Y-direction, measuring horizontal acceleration in Z-direction. (It reports negative numbers when acceleration is in positive Z-direction.)



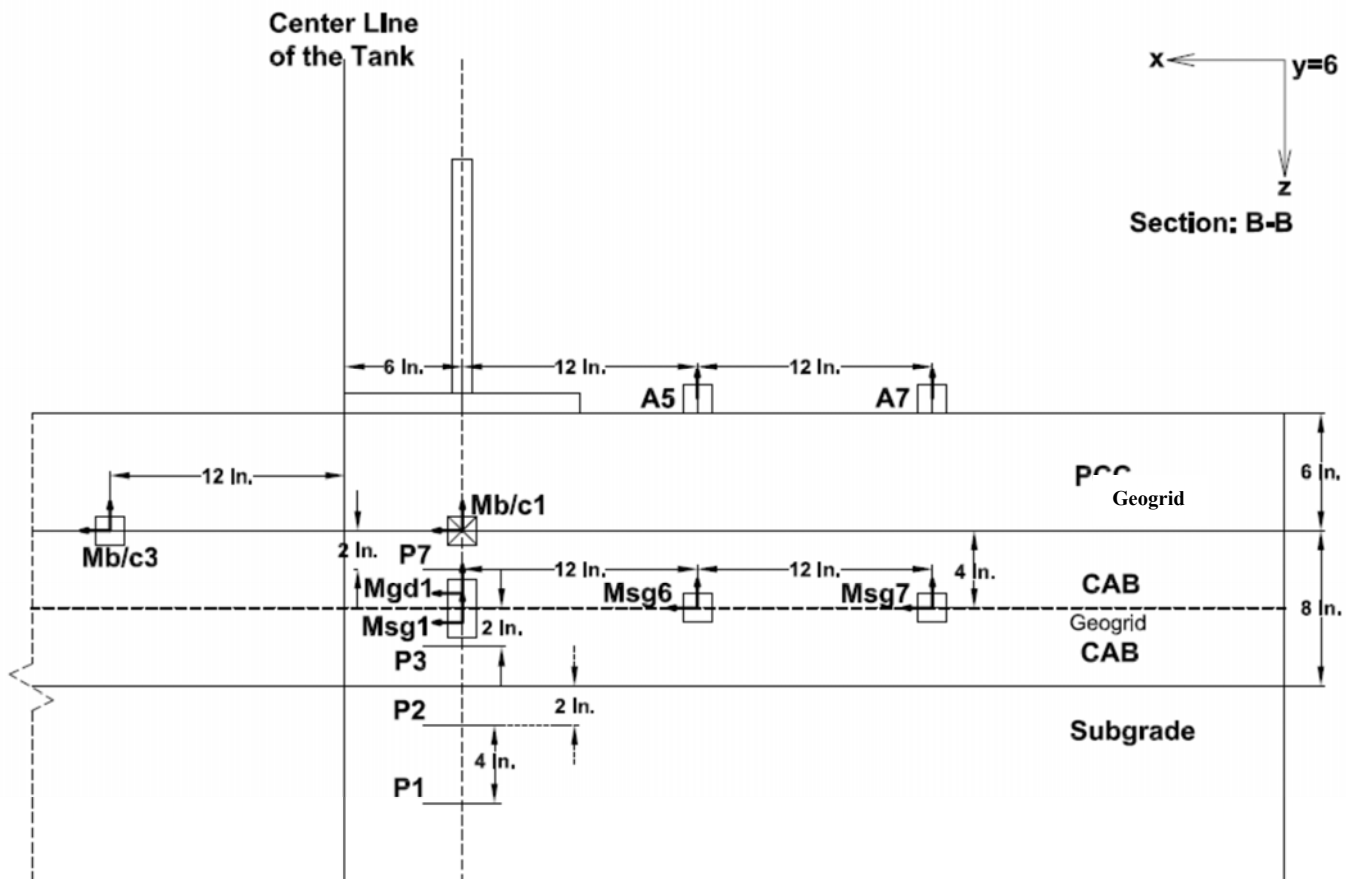


Figure H2-2. Instrumentation plan for experiment No. 9—Profile view, Y=6 inches

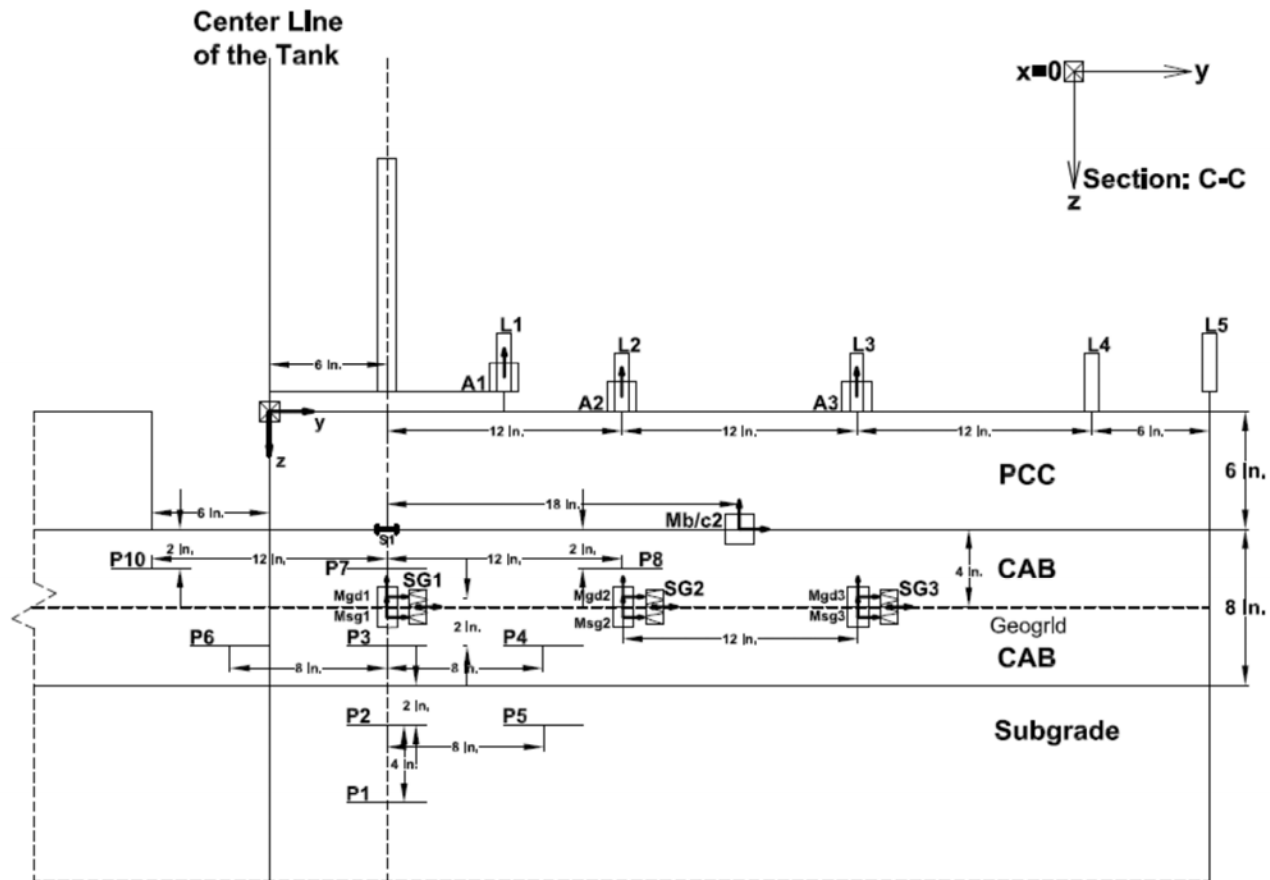


Figure H2-3. Instrumentation plan for experiment No. 9—Profile view, X=0 inch

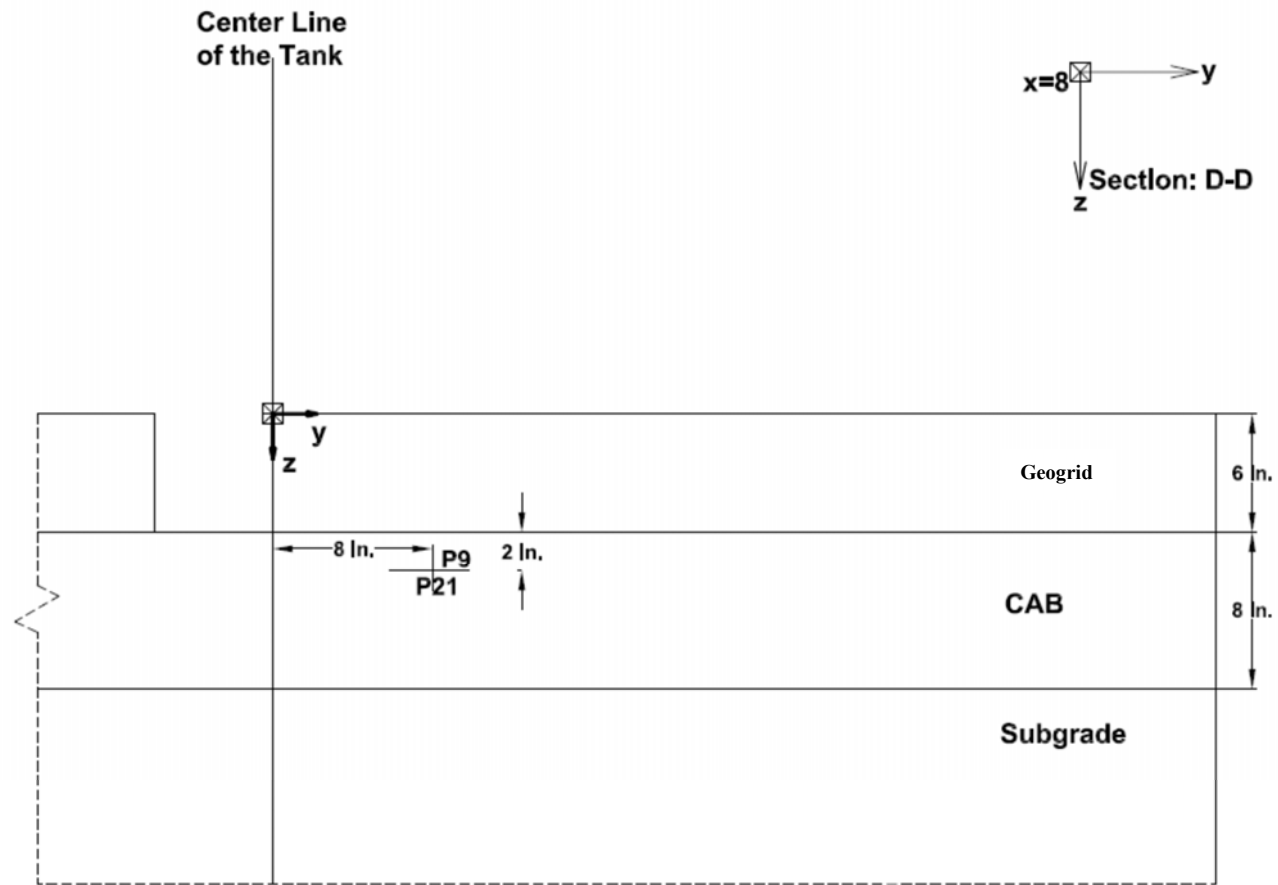


Figure H2-4. Instrumentation plan for experiment No. 9—Profile view, X=8 inches

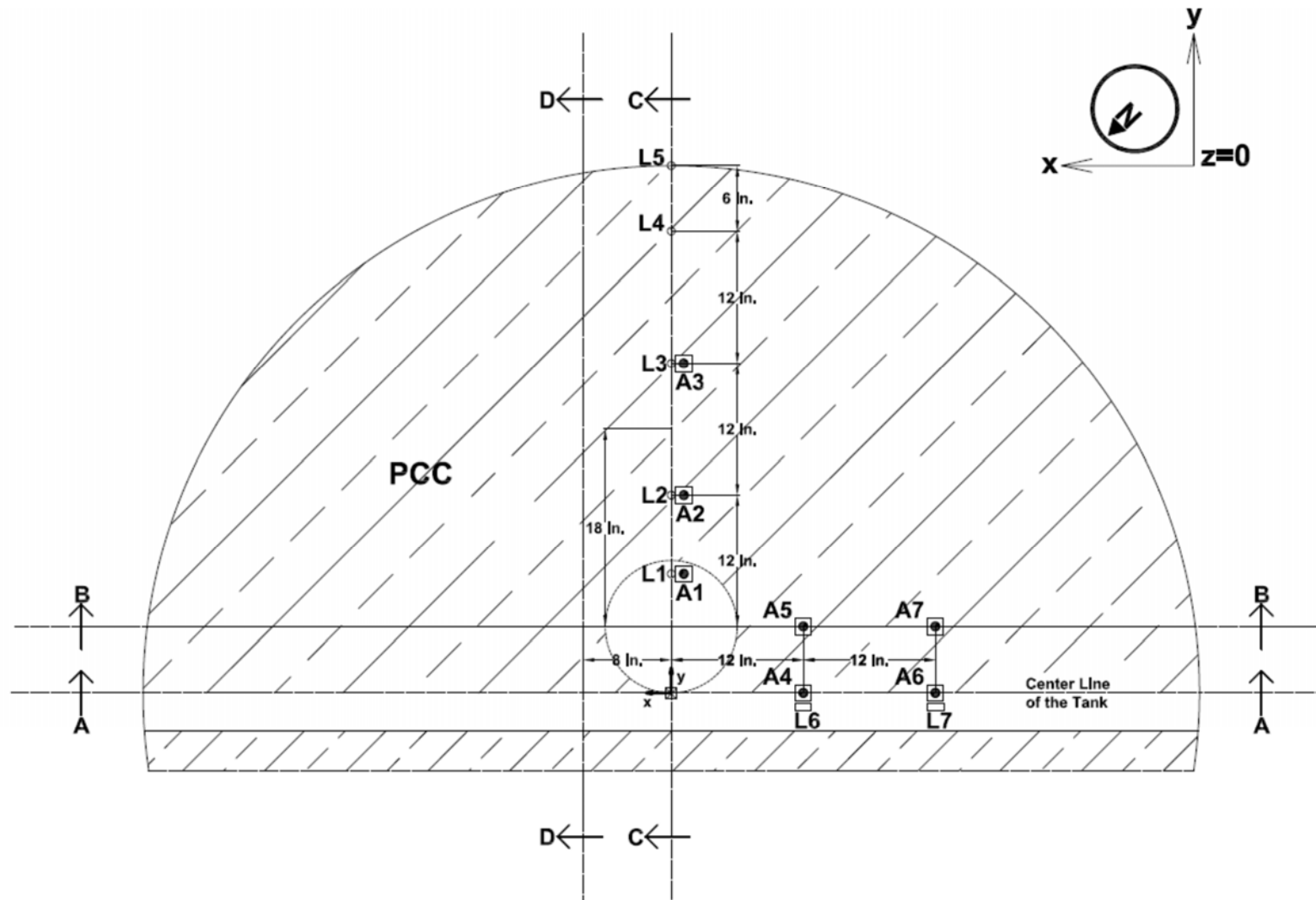


Figure H2-5. Instrumentation plan for experiment No. 9—Plan view, Z=0 inch

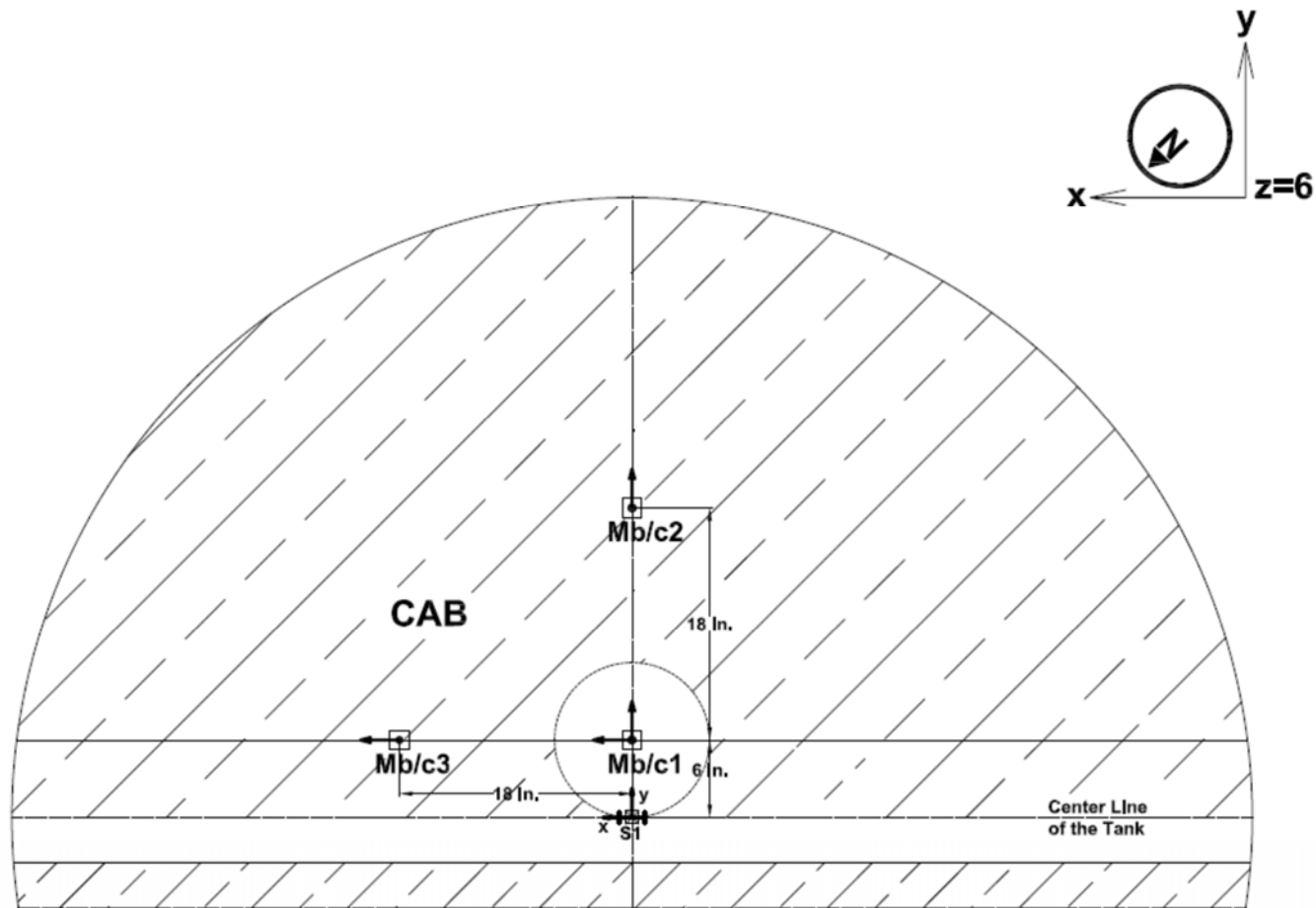


Figure H2-6. Instrumentation plan for experiment No. 9—Plan view, $Z=6$ inches



Figure H2-7. Instrumentation plan for experiment No. 9—Plan view, Z=8 inches

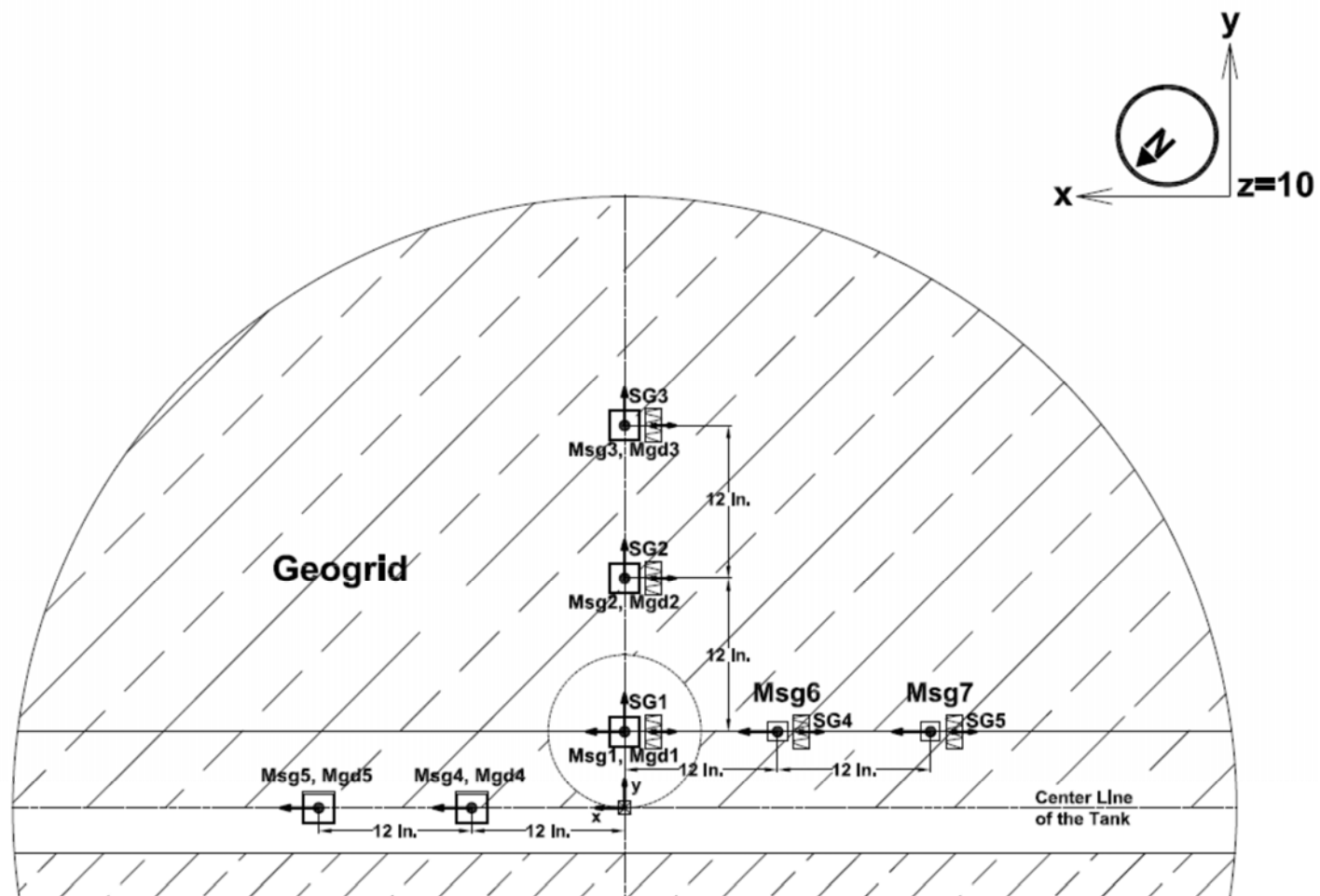


Figure H2-8. Instrumentation plan for experiment No. 9—Plan view, Z=10 inches

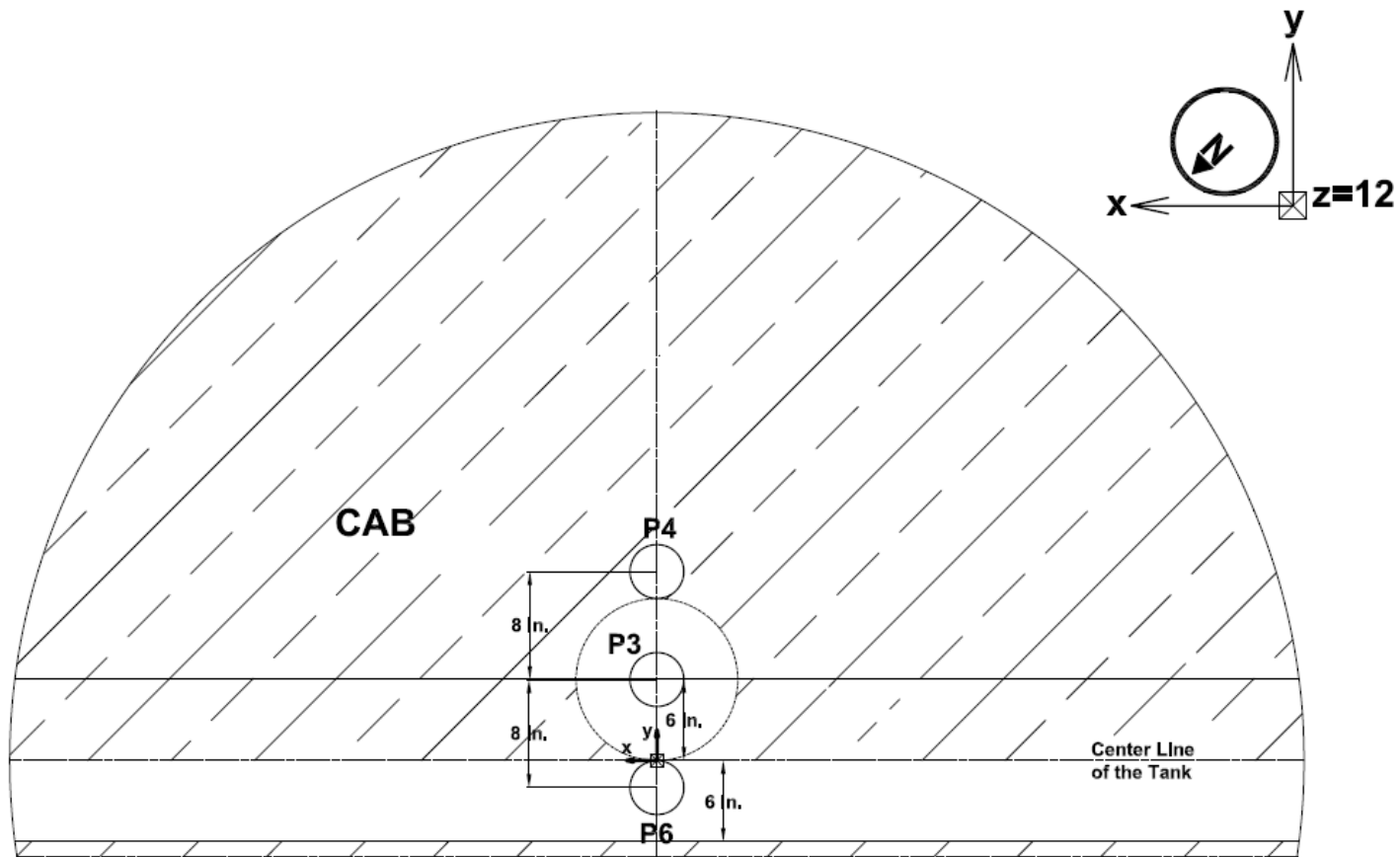


Figure H2-9. Instrumentation plan for experiment No. 9—Plan view, $Z=12$ inches

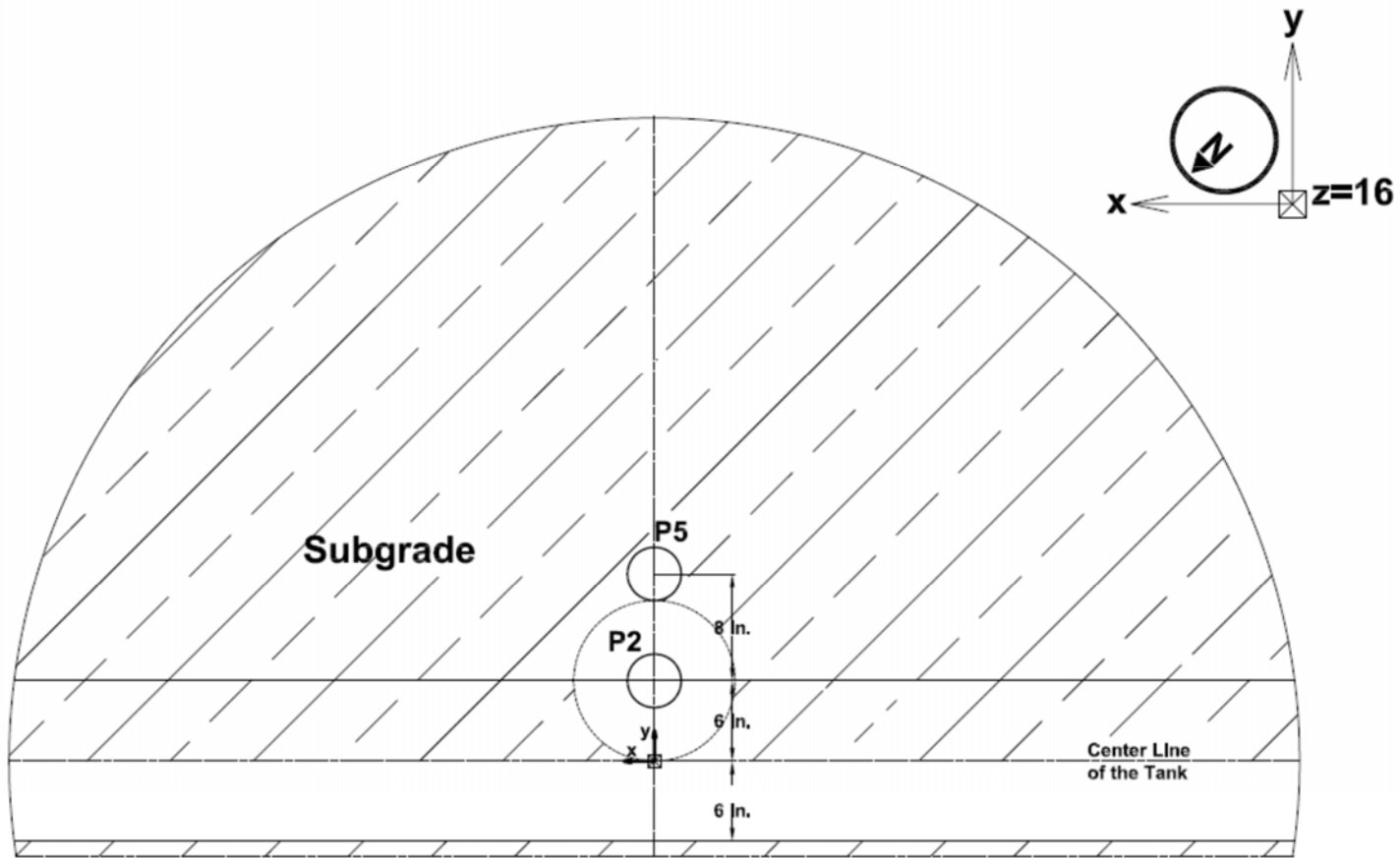


Figure H2-10. Instrumentation plan for experiment No. 9—Plan view, Z=16 inches

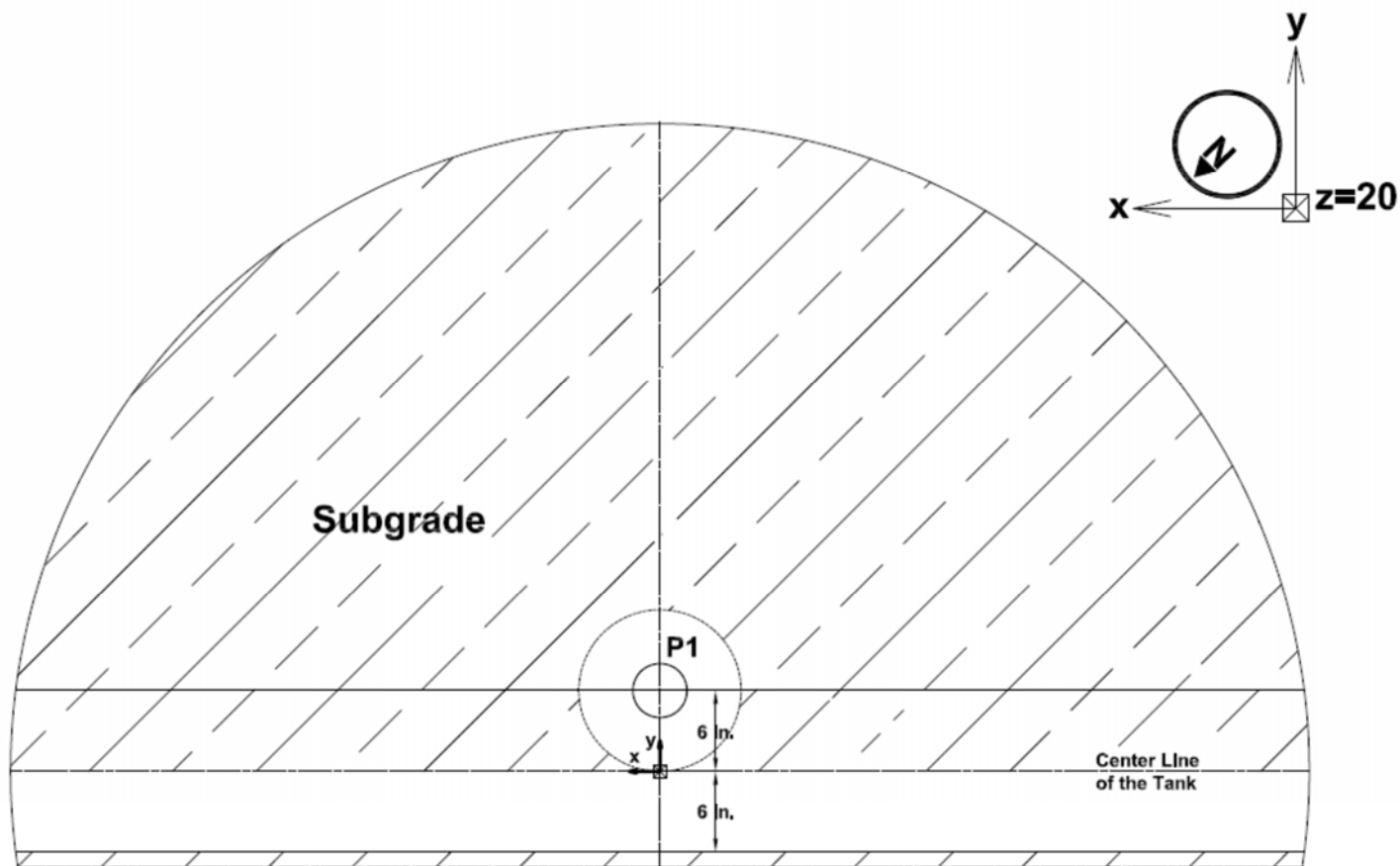


Figure H2-11. Instrumentation plan for experiment No. 9—Plan view, Z=20 inches

Appendix H3. Experiment No. 10 (Geotextile)

Experiment ID	Exp10-PCC
Description	Rigid pavement; 8-inch aggregate base with geotextile

Average PCC Layer Thickness (inch)	6.00
Average CAB Layer Thickness (inch)	8.00

Pressure Cell ID	Pressure Cell Diameter	X Coordinate (in)	Y Coordinate (in)	Z Coordinate (in)	Comments
P1	4 inch	0	6	20	P1 measures vertical pressure at 20 inches below the subgrade surface and 6 inches from the centerline of the tank in positive Y-direction.
P2	4 inch	0	6	16	P2 measures vertical pressure at 16 inches below the subgrade surface and 6 inches from the centerline of the tank in positive Y-direction.
P3	4 inch	0	6	12	P3 measures vertical pressure at 12 inches below the subgrade surface and 6 inches from the centerline of the tank in positive Y-direction.
P4	4 inch	0	14	12	P4 measures vertical pressure at 12 inches below the base surface and 14 inches from the centerline of the tank in positive Y-direction.
P5	4 inch	0	14	16	P5 measures vertical pressure at 16 inches below the base surface and 14 inches from the centerline of the tank in positive Y-direction.
P6	4 inch	0	-2	12	P6 measures vertical pressure at 12 inches below the base surface and 2 inches from the centerline of the tank in negative Y-direction.
P7	4 inch	0	6	8	P7 measures vertical pressure at 8 inches below the base surface and 6 inches from main centerline in positive Y-direction.
P8	4 inch	0	18	8	P8 measures vertical pressure at 8 inches below the base surface and 18 inches from the centerline of the tank in positive Y-direction.
P9	4 inch	8	6	8	P9 measures vertical pressure at 8 inches below the surface and 8 inches from the centerline of the tank in positive X-direction and 6 inches from the centerline of the tank in positive Y-direction.
P10	4 inch	0	-6	8	P10 measures vertical pressure at 8 inches below the surface and 6 inches from the centerline of the tank in negative Y-direction.
P21	1 inch	7.75	8	8	P21 measures vertical pressure at 8 inches below the surface and 8 inches from the centerline of the tank in positive Y and 8 inches from the centerline of the tank in positive X-direction.

Strain Gauge	X Coordinate (in)	Y Coordinate (in)	Z Coordinate (in)	Comments
S1	0	0	6	Strain at the centerline of the load and at the bottom of the PCC layer.
SG1-X	0	6	10	In the middle of the base and at the centerline of the load, measuring strain on geotextile.
SG1-Y	0	6	10	In the middle of the base and at the centerline of the load, measuring strain on geotextile.
SG2-X	0	18	10	In the middle of the base and 18 inches from the centerline of the tank, measuring strain on geotextile.
SG2-Y	0	18	10	In the middle of the base and 18 inches from the centerline of the tank, measuring strain on geotextile.
SG3-X	0	30	10	In the middle of the base and 30 inches from the centerline of the tank, measuring strain on geotextile.
SG3-Y	0	30	10	In the middle of the base and 30 inches from the centerline of the tank, measuring strain on geotextile.
SG4-X	-12	0	10	In the middle of the base and 12 inches from the centerline of the tank in negative X-direction, measuring strain on geotextile.
SG4-Y	-12	0	10	In the middle of the base and 12 inches from the centerline of the tank in negative X-direction, measuring strain on geotextile.
SG5-X	-24	0	10	In the middle of the base and 24 inches from the centerline of the tank in negative X-direction, measuring strain on geotextile.

Strain Gauge	X Coordinate (in)	Y Coordinate (in)	Z Coordinate (in)	Comments
SG5-Y	-24	0	10	In the middle of the base and 24 inches from the centerline of the tank in negative X-direction, measuring strain on geotextile.

LVDT ID	X Coordinate (in)	Y Coordinate (in)	Z Coordinate (in)	Comments
LVDT 1	0	12	0	At the pavement surface and 12 inches from the centerline of the tank in positive Y-direction, measuring the surface vertical deflection. Note: because of the plate configuration, the measurement is considered to be at the centerline of the load.
LVDT 2	0	18	0	At the pavement surface and 18 inches from the centerline of the tank in positive Y-direction, measuring the surface vertical deflection.
LVDT 3	0	30	0	At the pavement surface and 30 inches from main centerline in positive Y-direction, measuring the surface vertical deflection.
LVDT 4	0	42	0	At the pavement surface and 42 inches from the centerline of the tank in positive Y-direction, measuring the surface vertical deflection.
LVDT 5	0	48	0	On top of the Large-Scale Tank rim and 48 inches from the centerline of the tank in positive Y-direction, measuring the surface vertical deflection.
LVDT 6	-12	0	6	At 6 inches below the surface and 12 inches from the centerline of the tank in negative X-direction, measuring base horizontal deflection (negative measurements for extension and positive measurements for compression).
LVDT 7	-24	0	6	At 6 inches below the surface and 24 inches from the centerline of the tank in negative X-direction, measuring base horizontal deflection (negative measurements for extension and positive measurements for compression).

Accelerometer	Accelerometer ID	X Coordinate (in)	Y Coordinate (in)	Z Coordinate (in)	Comments
A1	A1_Z	0	12	0	At the pavement surface and 12 inches from the centerline of the tank, measuring vertical acceleration in Z-direction. (It reports negative numbers when acceleration is in positive Z-direction.) Note: because of the plate configuration, the measurement is considered to be at the centerline of the load.
A2	A2_Z	0	18	0	At the pavement surface and 18 inches from the centerline of the tank in positive Y-direction, measuring vertical acceleration in Z-direction. (It reports negative numbers when acceleration is in positive Z-direction.)
A3	A3_Z	0	30	0	At the pavement surface and 30 inches from the centerline of the tank in positive Y-direction, measuring vertical acceleration in Z-direction. (It reports negative numbers when acceleration is in positive Z-direction.)
A4	A4_Z	-12	0	0	At the surface of the base and 12 inches from the centerline of the tank in negative X-direction, measuring vertical acceleration in Z-direction. (It reports negative numbers when acceleration is in positive Z-direction.)
A5	A5_Z	-12	6	0	At the pavement surface and 12 inches from the centerline of the tank in negative X-direction and 6 inches from the centerline of the tank in positive Y-direction, measuring vertical acceleration in Z-direction. (It reports negative numbers when acceleration is in positive Z-direction.)
A6	A6_Z	-24	0	0	At the surface of the base and 24 inches from the centerline of the tank in negative X-direction, measuring vertical acceleration in Z-direction. (It reports negative numbers when acceleration is in positive Z-direction.)
A7	A7_Z	-24	6	0	At the pavement surface and 24 inches from the centerline of the tank in negative X-direction and 6 inches from the centerline of the tank in positive Y-

Accelerometer	Accelerometer ID	X Coordinate (in)	Y Coordinate (in)	Z Coordinate (in)	Comments
					direction, measuring vertical acceleration in Z-direction. (It reports negative numbers when acceleration is in positive Z-direction.)
Msg1	M1_Y	0	6	10	In the middle of the base and at the centerline of the load, measuring horizontal acceleration in Y-direction.
Msg1	M1_Z	0	6	10	In the middle of the base and at the centerline of the load, measuring vertical acceleration in Z-direction. (It reports negative numbers when acceleration is in positive Z-direction.)
Msg1	M1_X	0	6	10	In the middle of the base and at the centerline of the load, measuring vertical acceleration in X-direction.
Msg2	M2_Y	0	18	10	In the middle of the base and 18 inches from the centerline of the tank, measuring horizontal acceleration in Y-direction.
Msg2	M2_Z	0	18	10	In the middle of the base and 18 inches from the centerline of the tank, measuring vertical acceleration in Z-direction. (It reports negative numbers when acceleration is in positive Z-direction.)
Msg3	M3_Y	0	30	10	In the middle of the base and 30 inches from the centerline of the tank, measuring horizontal acceleration in Y-direction.
Msg3	M3_Z	0	30	10	In the middle of the base and 30 inches from the centerline of the tank, measuring vertical acceleration in Z-direction. (It reports negative numbers when acceleration is in positive Z-direction.)
Msg4	M4_X	12	0	10	In the middle of the base and 12 inches from the centerline of the tank in positive X-direction, measuring horizontal acceleration in X-direction.
Msg4	M4_Z	12	0	10	In the middle of the base and 12 inches from the centerline of the tank in positive X-direction, measuring vertical acceleration in Z-direction. (It reports negative numbers when acceleration is in positive Z-direction.)
Msg5	M5_X	24	0	10	In the middle of the base and 24 inches from the centerline of the tank in negative X-direction, measuring horizontal acceleration in X-direction.
Msg5	M5_Z	24	0	10	In the middle of the base and 24 inches from the centerline of the tank in positive X-direction, measuring vertical acceleration in Z-direction. (It reports negative numbers when acceleration is in positive Z-direction.)
Msg6	M6_X	-12	0	10	In the middle of the base and 12 inches from the centerline of the tank in negative X-direction, measuring horizontal acceleration in X-direction.
Msg6	M6_Z	-12	0	10	In the middle of the base and 12 inches from the centerline of the tank in negative X-direction, measuring vertical acceleration in Z-direction. (It reports negative numbers when acceleration is in positive Z-direction.)
Msg7	M7_X	-24	0	10	In the middle of the base and 24 inches from the centerline of the tank in negative X-direction, measuring horizontal acceleration in X-direction.
Msg7	M7_Z	-24	0	10	In the middle of the base and 24 inches from the centerline of the tank in negative X-direction, measuring vertical acceleration in Z-direction. (It reports negative numbers when acceleration is in positive Z-direction.)

Accelerometer	Accelerometer ID	X Coordinate (in)	Y Coordinate (in)	Z Coordinate (in)	Comments
Mgd1	Mgd1_X	0	6	10	In the middle of the base and at the centerline of the load, measuring horizontal acceleration on geotextile in X-direction.
Mgd1	Mgd1_Y	0	6	10	In the middle of the base and at the centerline of the load, measuring vertical acceleration on geotextile in Y-direction.
Mgd1	Mgd1_Z	0	6	10	In the middle of the base and at the centerline of the load, measuring vertical acceleration on geotextile in Z-direction. (It reports negative numbers when acceleration is in positive Z-direction.)
Mgd2	Mgd2_Y	0	18	10	In the middle of the base and 18 inches from the centerline of the tank, measuring horizontal acceleration on geotextile in Y-direction.
Mgd2	Mgd2_Z	0	18	10	In the middle of the base and 18 inches from the centerline of the tank, measuring vertical acceleration on geotextile in Z-direction.
Mgd3	Mgd3_Y	0	30	10	In the middle of the base and 30 inches from the centerline of the tank, measuring horizontal acceleration on geotextile in Y-direction.
Mgd3	Mgd3_Z	0	30	10	In the middle of the base and 30 inches from the centerline of the tank, measuring vertical acceleration on geotextile in Z-direction.
Mgd4	Mgd4_X	12	0	10	In the middle of the base and 12 inches from the centerline of the tank in positive X-direction, measuring horizontal acceleration on geotextile in X-direction.
Mgd4	Mgd4_Z	12	0	10	In the middle of the base and 12 inches from the centerline of the tank in positive X-direction, measuring vertical acceleration on geotextile in Z-direction. (It reports negative numbers when acceleration is in positive Z-direction.)
Mgd5	Mgd5_X	24	0	10	In the middle of the base and 24 inches from the centerline of the tank in positive X-direction, measuring horizontal acceleration on geotextile in X-direction.
Mgd5	Mgd5_Z	24	0	10	In the middle of the base and 24 inches from the centerline of the tank in positive X-direction, measuring vertical acceleration on geotextile in Z-direction. (It reports negative numbers when acceleration is in positive Z-direction.)
Mb/c1	Mb1_X	0	6	6	At top of the base and 6 inches from the centerline of the tank in positive Y-direction, measuring horizontal acceleration in positive X-direction.
Mb/c1	Mb1_Y	0	6	6	At top of the base and 6 inches from the centerline of the tank in positive Y-direction, measuring horizontal acceleration in positive Y-direction.
Mb/c1	Mb1_Z	0	6	6	At top of the base and 6 inches from the centerline of the tank in positive Y-direction, measuring vertical acceleration in Z-direction. (It reports negative numbers when acceleration is in positive Z-direction.)
Mb/c1	Mc1_X	0	6	6	At bottom of the concrete layer and 6 inches from the centerline of the tank in positive Y-direction, measuring horizontal acceleration in positive X-direction.
Mb/c1	Mc1_Y	0	6	6	At bottom of the concrete layer and 6 inches from the centerline of the tank in positive Y-direction, measuring horizontal acceleration in positive Y-direction.

Accelerometer	Accelerometer ID	X Coordinate (in)	Y Coordinate (in)	Z Coordinate (in)	Comments
Mb/c1	Mc1_Z	0	6	6	At bottom of the concrete layer and 6 inches from the centerline of the tank in positive Y-direction, measuring vertical acceleration in Z-direction. (It reports negative numbers when acceleration is in positive Z-direction.)
Mb/c2	Mb2_Y	0	24	6	At top of the base and 24 inches from the centerline of the tank in positive Y-direction, measuring horizontal acceleration in positive Y-direction.
Mb/c2	Mb2_Z	0	24	6	At top of the base and 24 inches from the centerline of the tank in positive Y-direction, measuring vertical acceleration in Z-direction. (It reports negative numbers when acceleration is in positive Z-direction.)
Mb/c2	Mc2_Y	0	24	6	At bottom of the concrete layer and 24 inches from the centerline of the tank in positive Y-direction, measuring horizontal acceleration in positive Y-direction.
Mb/c2	Mc2_Z	0	24	6	At bottom of the concrete layer and 24 inches from the centerline of the tank in positive Y-direction, measuring vertical acceleration in Z-direction. (It reports negative numbers when acceleration is in positive Z-direction.)
Mb/c3	Mb2_Y	18	6	6	At top of the base, 18 inches from the centerline of the tank in positive X-direction and 6 inches from the centerline of the tank in positive Y-direction, measuring horizontal acceleration in positive Y-direction.
Mb/c3	Mb2_Z	18	6	6	At top of the base, 18 inches from the centerline of the tank in positive X-direction and 6 inches from the centerline of the tank in positive Y-direction, measuring horizontal acceleration in Z-direction. (It reports negative numbers when acceleration is in positive Z-direction.)
Mb/c3	Mc2_Y	18	6	6	At bottom of the concrete layer, 18 inches from the centerline of the tank in positive X-direction and 6 inches from the centerline of the tank in positive Y-direction, measuring horizontal acceleration in positive Y-direction.
Mb/c3	Mc2_Z	18	6	6	At bottom of the concrete layer, 18 inches from the centerline of the tank in positive X-direction and 6 inches from the centerline of the tank in positive Y-direction, measuring horizontal acceleration in Z-direction. (It reports negative numbers when acceleration is in positive Z-direction.)



Figure H3-12. Instrumentation plan for experiment No. 10—Profile view, Y=0 inch

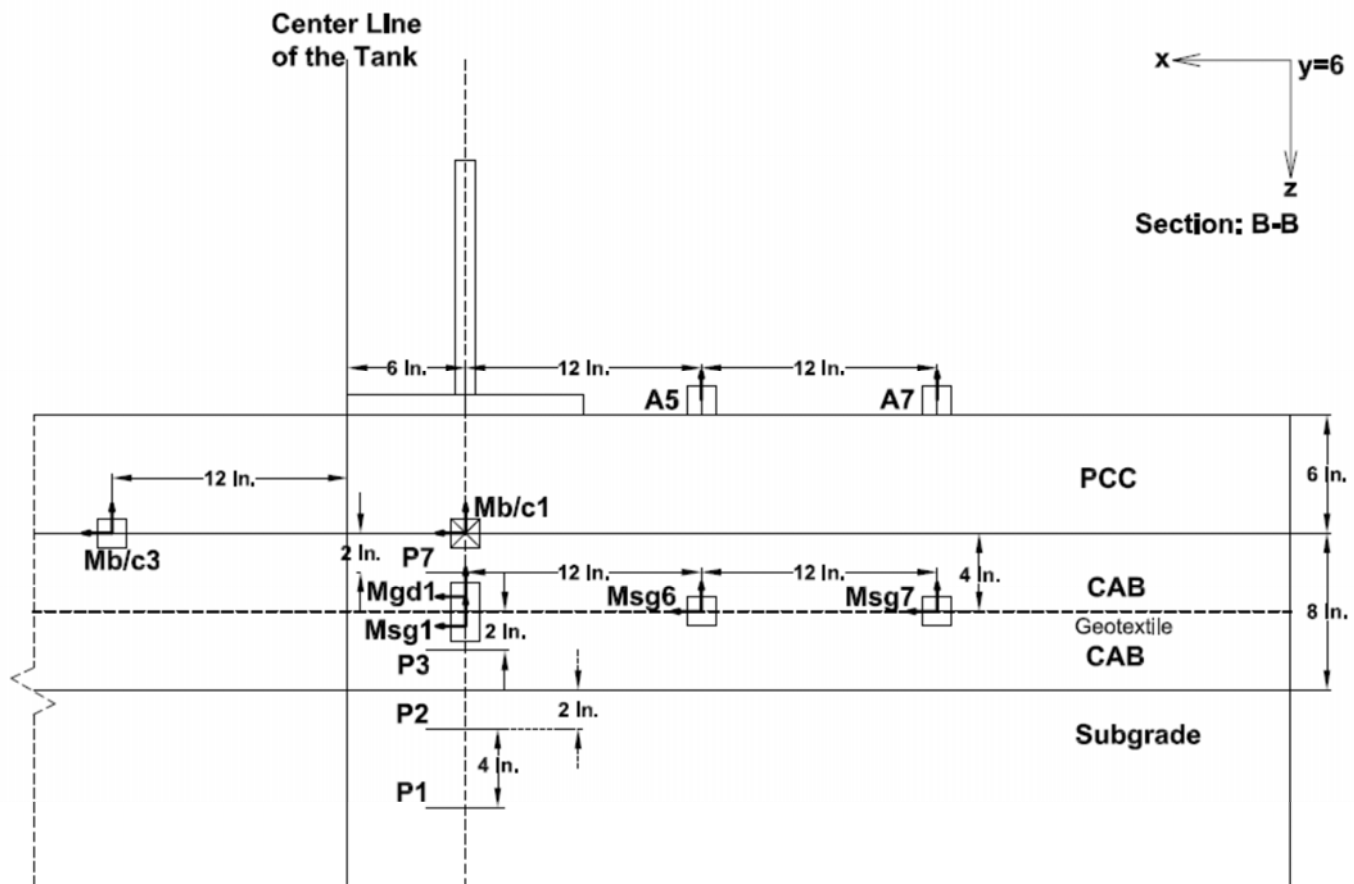


Figure H3-2. Instrumentation plan for experiment No. 10—Profile view, Y=6 inches

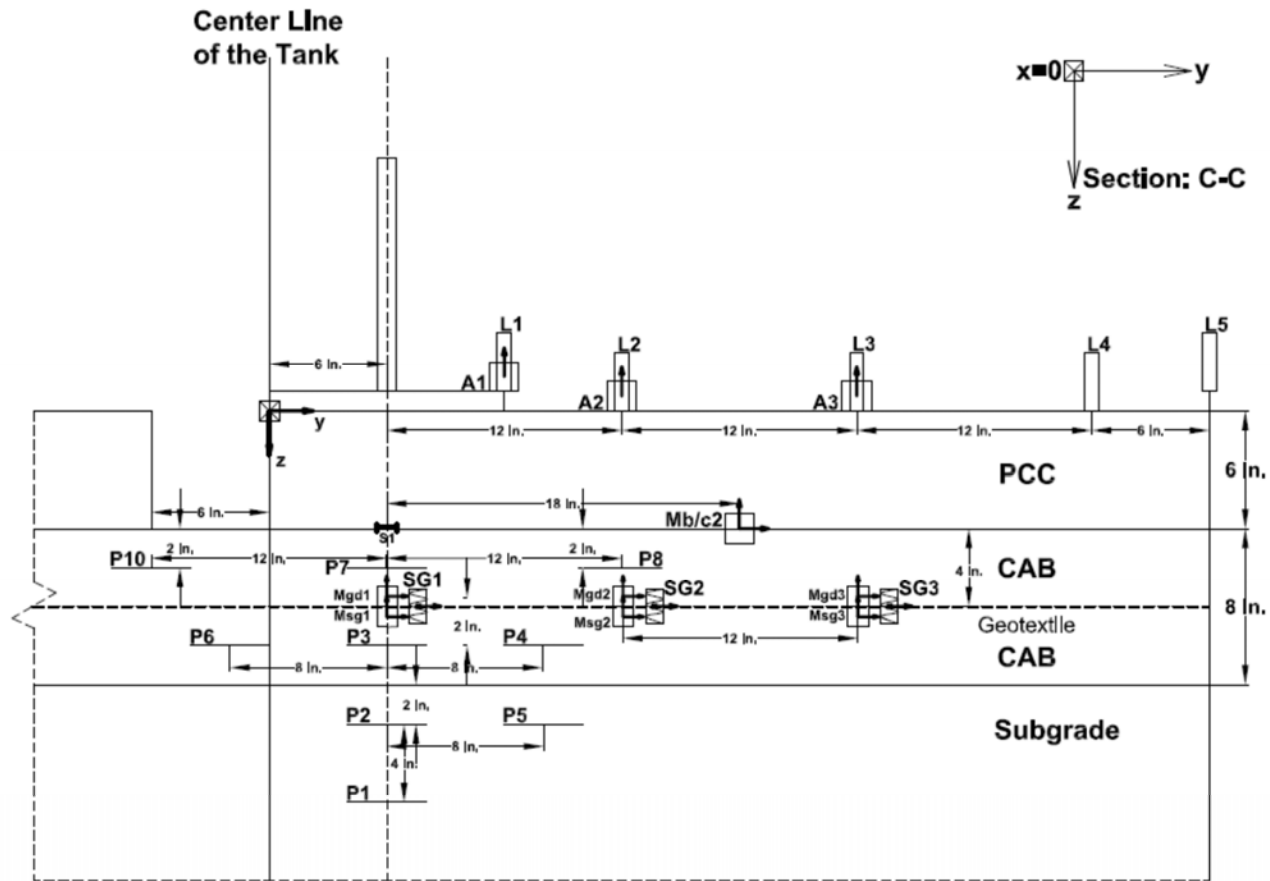


Figure H3-3. Instrumentation plan for experiment No. 10—Profile view, X=0 inch

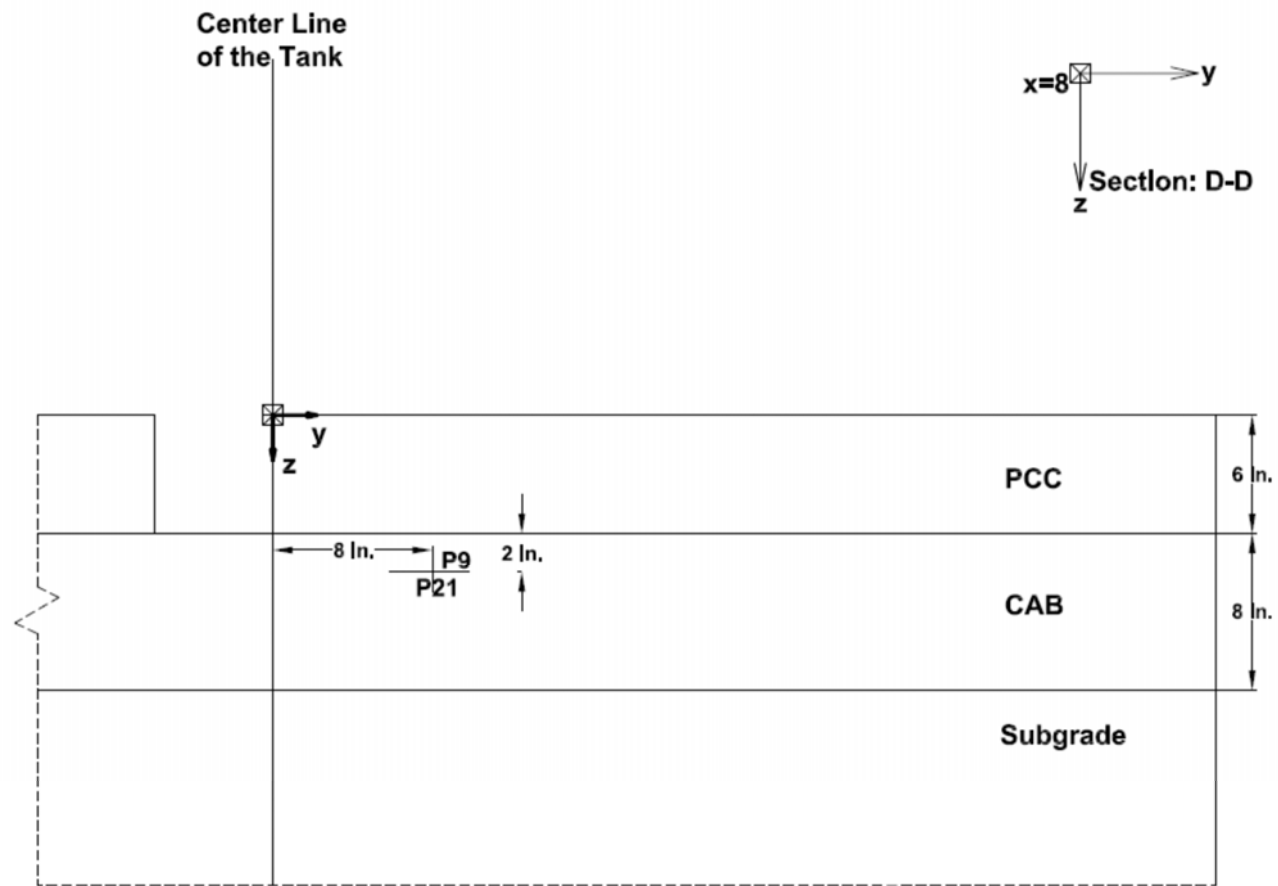


Figure H3-4. Instrumentation plan for experiment No. 10—Profile view, X=8 inches

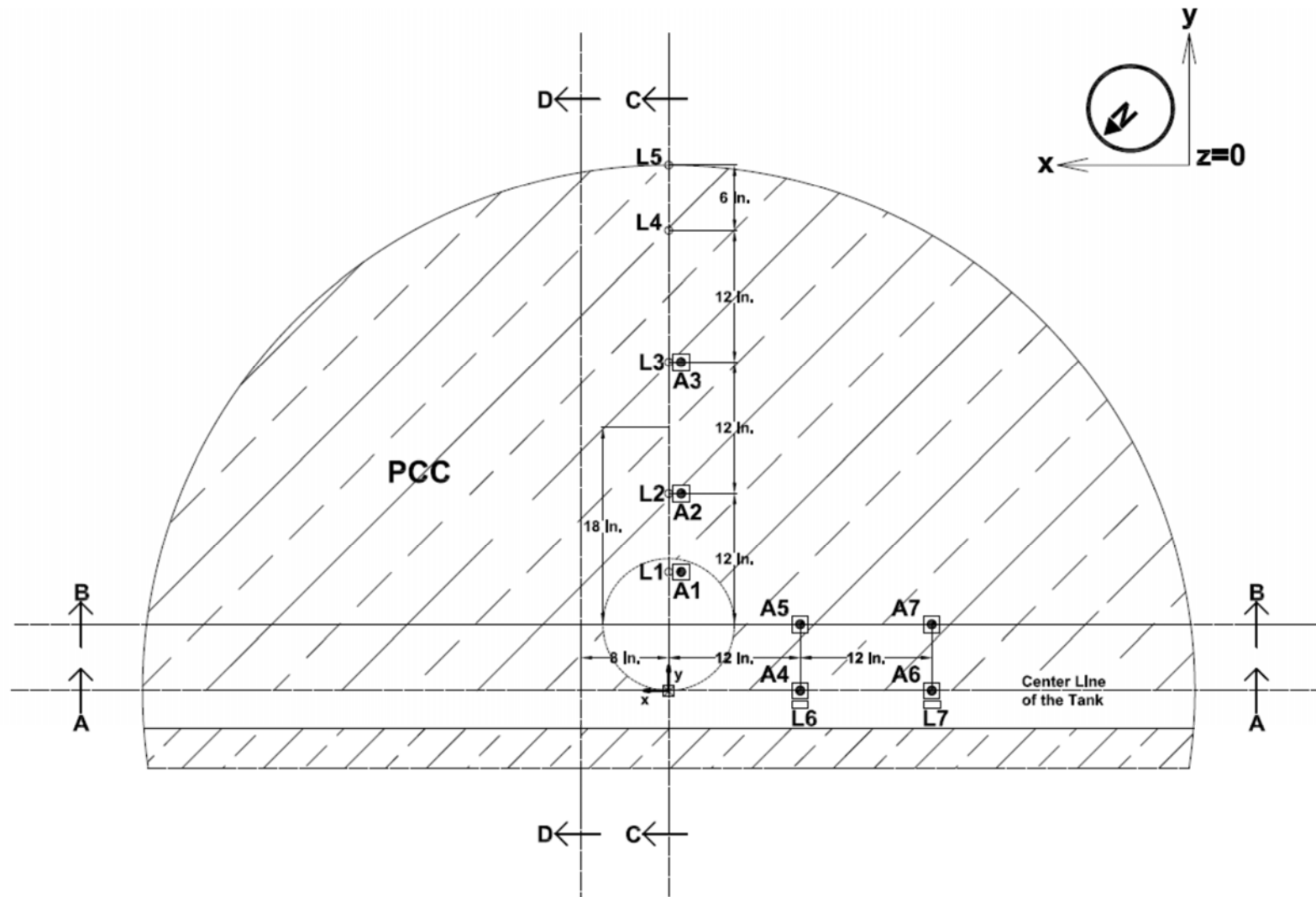


Figure H3-5. Instrumentation plan for experiment No. 10—Plan view, $Z=0$ inch

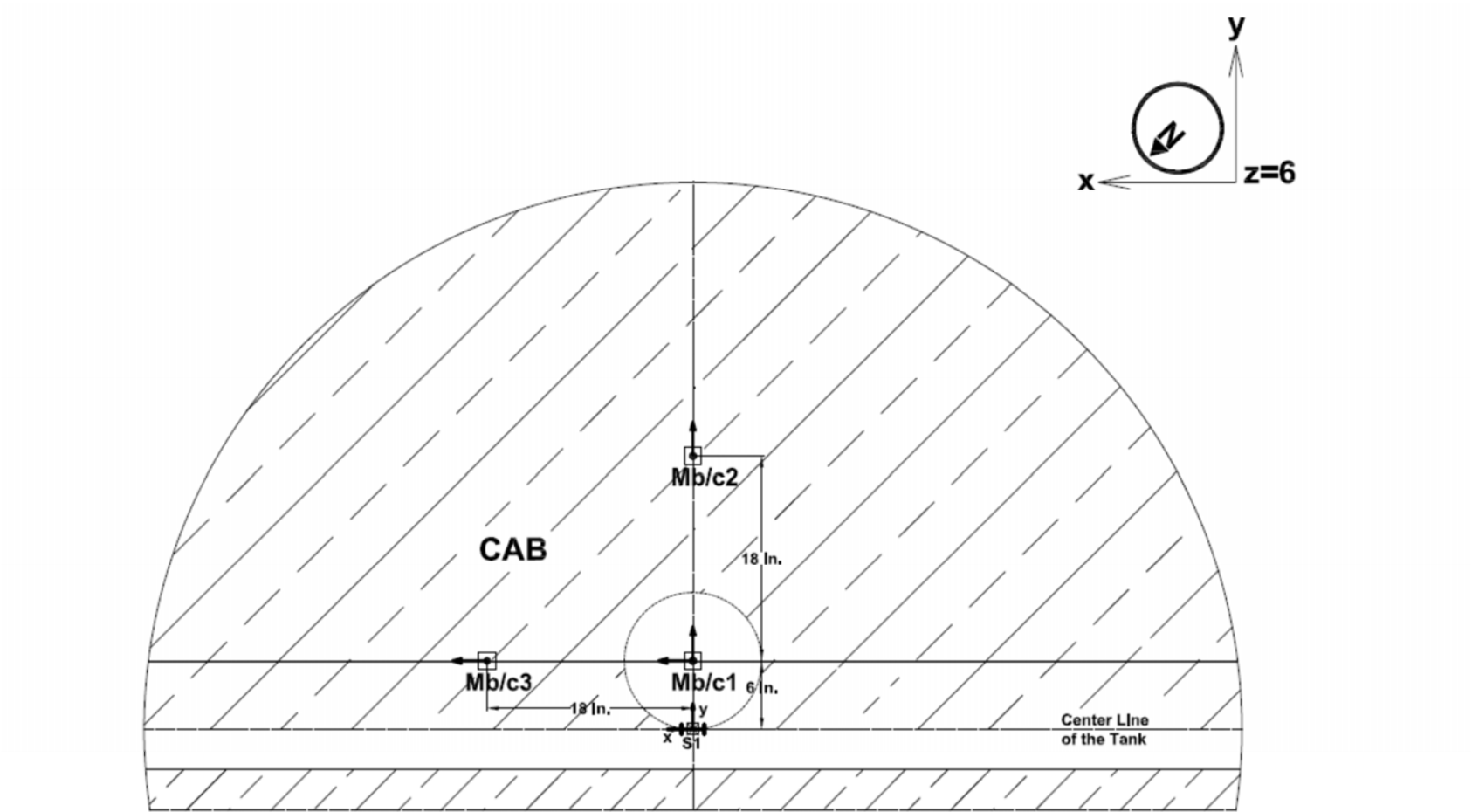


Figure H3-6. Instrumentation plan for experiment No. 10—Plan view, $Z=6$ inches

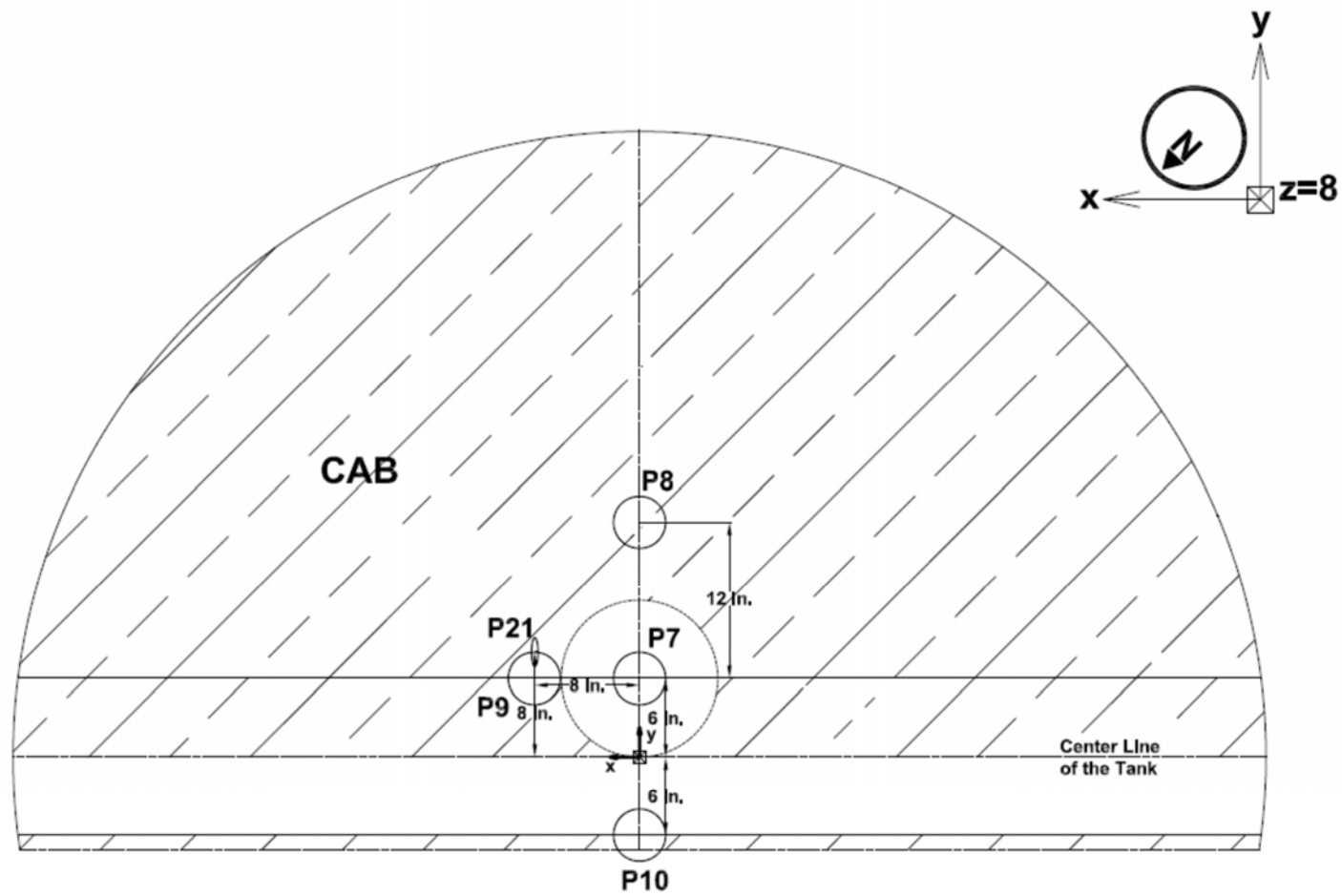


Figure H3-7. Instrumentation plan for experiment No. 10—Plan view, Z=8 inches

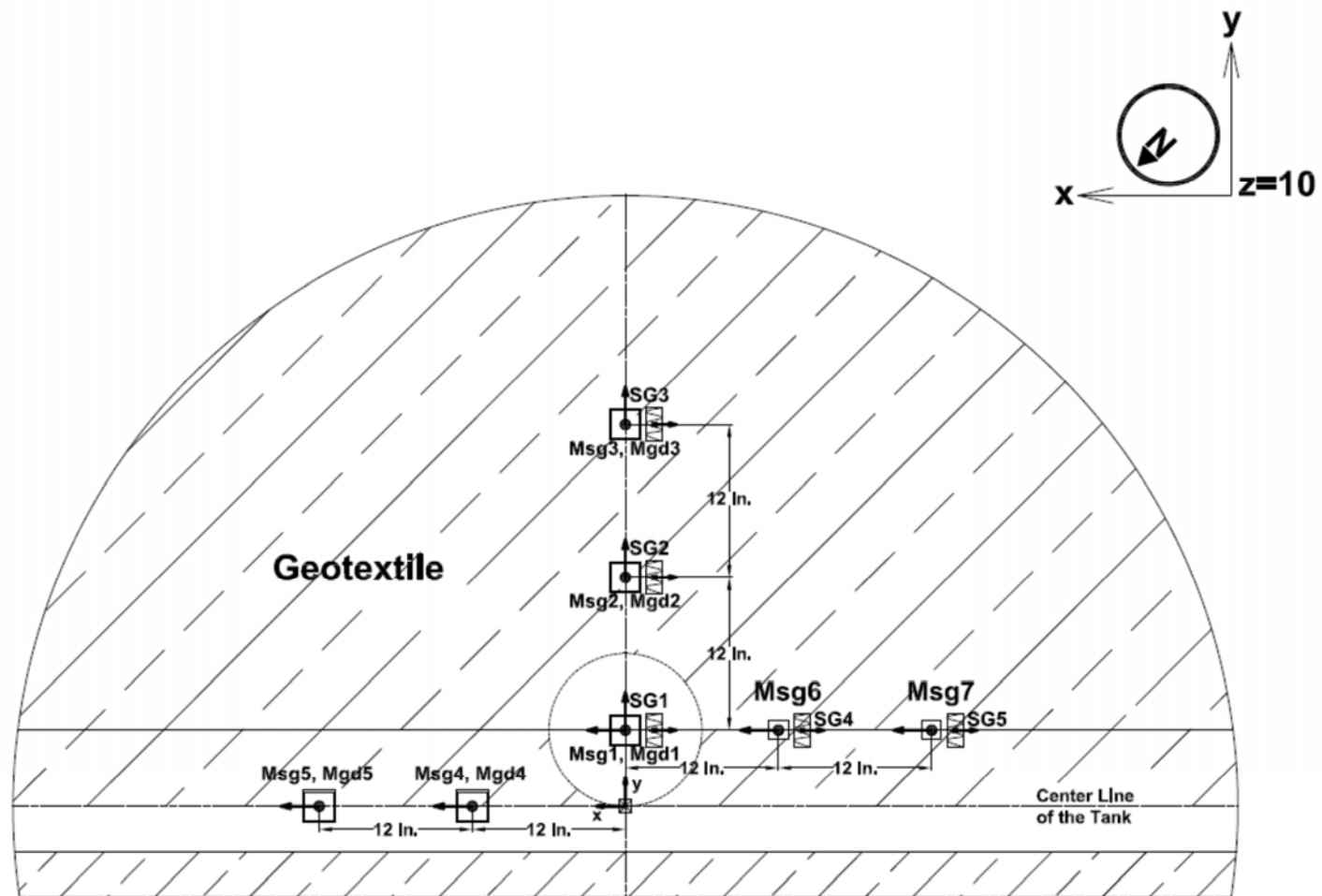


Figure H3-8. Instrumentation plan for experiment No. 10—Plan view, Z=10 inches

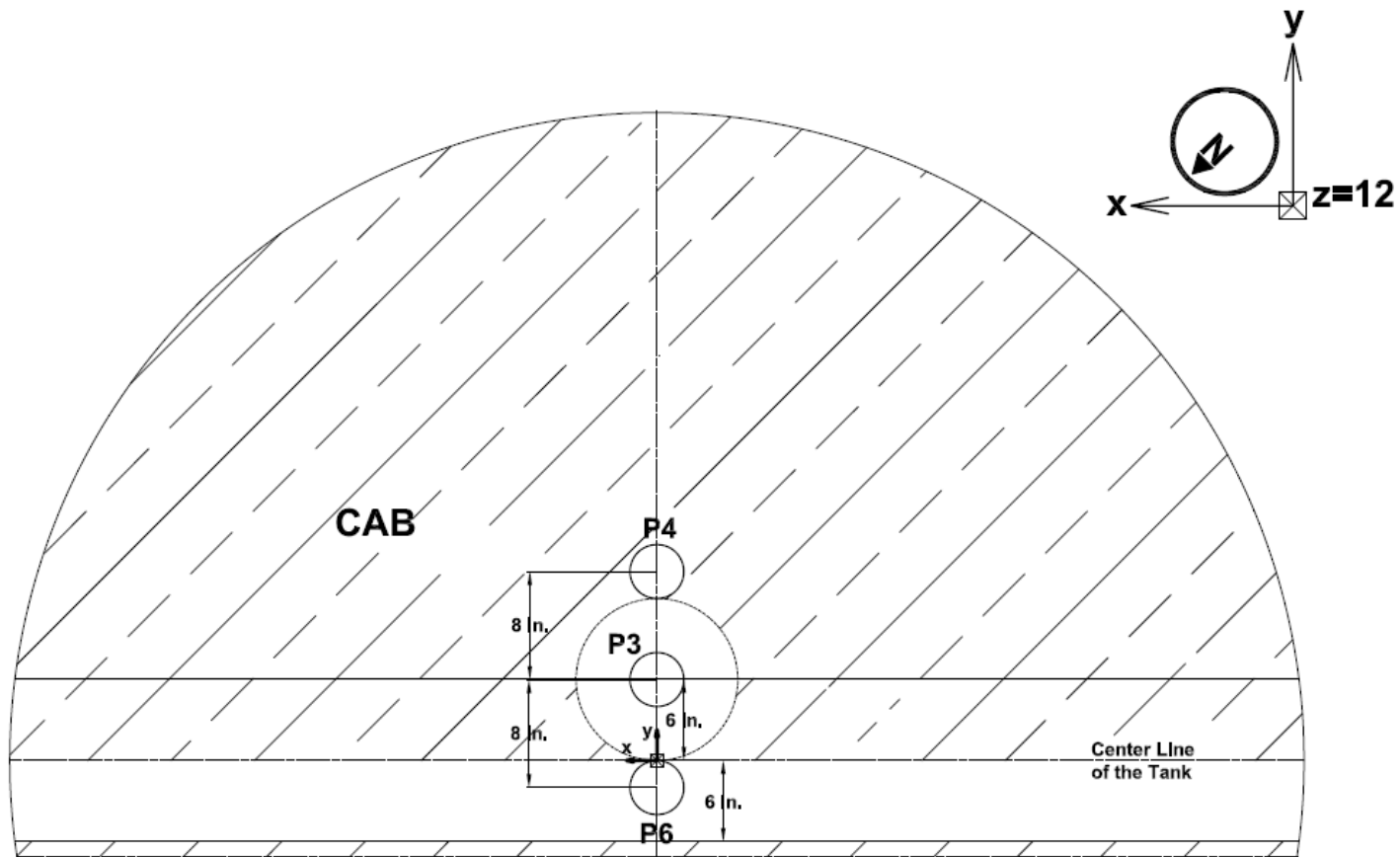


Figure H3-9. Instrumentation plan for experiment No. 10—Plan view, $Z=12$ inches

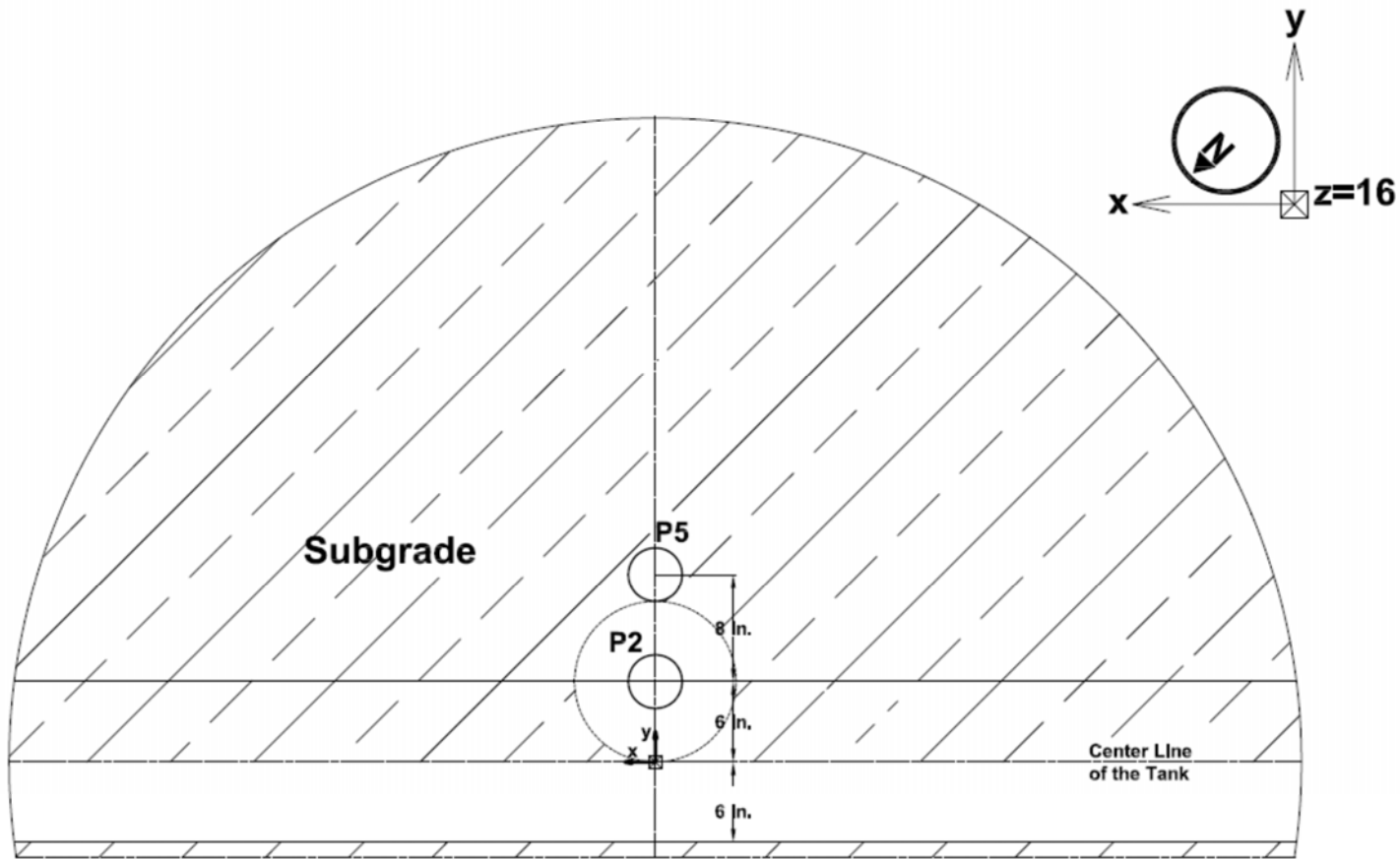


Figure H3-10. Instrumentation plan for experiment No. 10—Plan view, Z=16 inches

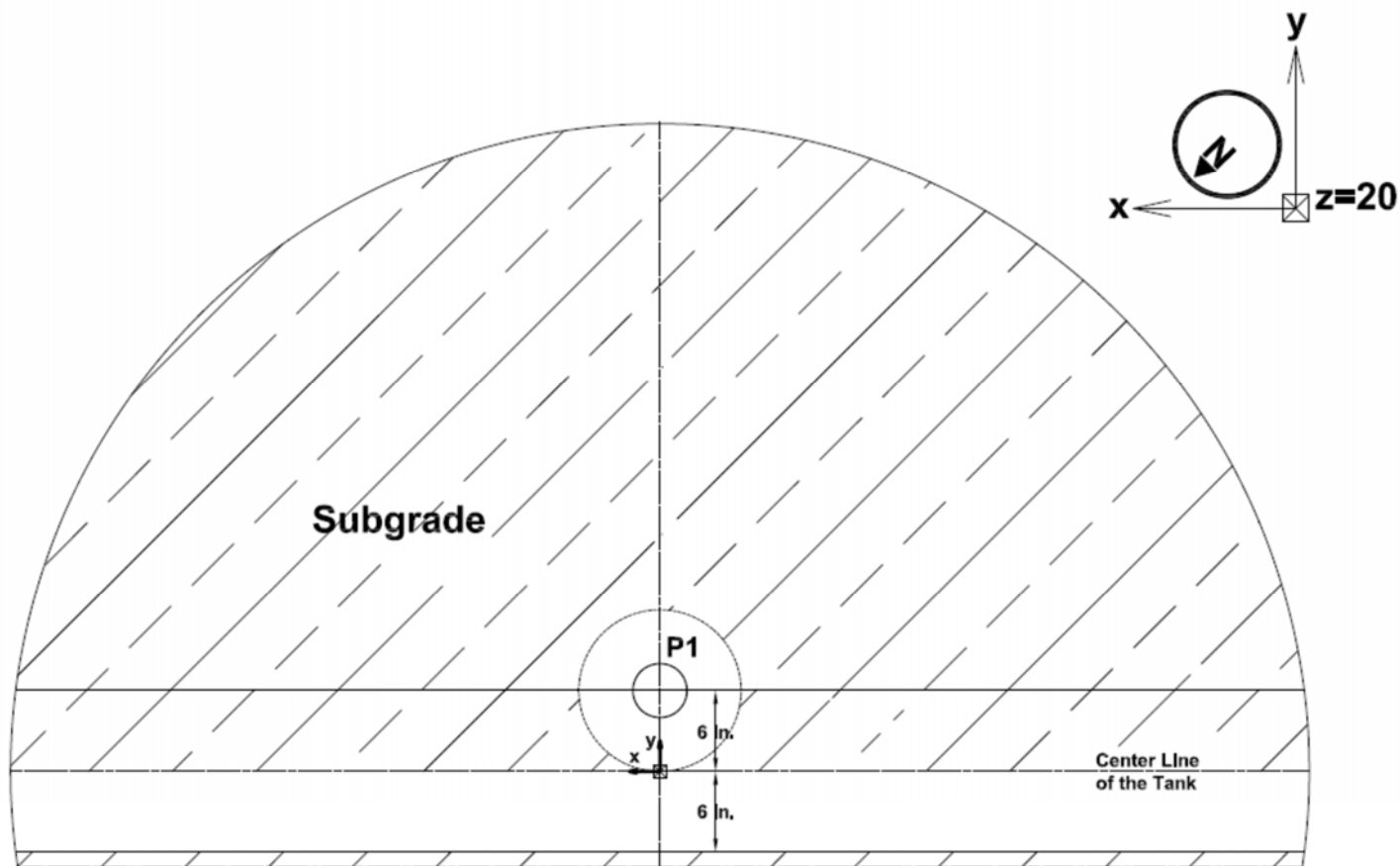


Figure H3-11. Instrumentation plan for experiment No. 10—Plan view, Z=20 inches

APPENDIX I. ANALYSIS METHODOLOGIES OF LARGE-SCALE TANK TEST DATA

The laboratory testing program for flexible and rigid pavements included a series of instrumentation that included accelerometers, LVDTs, earth pressure cells, and strain gauges. The instrumentation program was designed to assess several aspects of the influence of the base reinforcement on pavement responses under a variety of realistic pavement loading conditions. A database of pertinent pavement responses with and without reinforcement collected under dynamic and static pavement loading conditions was assembled. The pavement response database was used to assess the validity and applicability of the finite element numerical modeling of reinforced pavement structures. In particular, the instrumentation plan focused on the mechanisms associated with the interaction between the geosynthetic and the unbound materials, including (a) assessment of the deflection profile of the geosynthetic; (b) investigation of the slippage at the interface between the unbound material and the geosynthetic; (c) review of the stress transfer across the geosynthetic; and (d) examination of the load-induced strains in the geosynthetic. While the last two aspects could be addressed based on direct measurements from pressure cells (vertical and horizontal) and strain gauges, the first two aspects needed to be evaluated based on the deflections at many interior locations within the pavement. The slippage investigation at the interface required measurements for the deflections in the geosynthetic and in the adjacent unbound material to examine the relative movements between the two of them.

The role of the geosynthetic affecting the load transfer across the geosynthetic itself is generally referred to as shell/membrane action. Understanding the deformed shape of the geogrid or geotextile located within the unbound pavement layers during the application of the pulse loading is important to evaluate the shell/membrane action of the reinforced layer. The dynamic (instantaneous) deformation of the geosynthetic can be related to the change in vertical stress that can occur across the reinforced crushed aggregate base layer. Accordingly, high-gain accelerometers were used, with the recording measurements being twice integrated to get the displacement under dynamic loading. It was important to find the best methodology for the double integration of accelerometer readings to get the displacement. Subsequently, these displacements obtained from the integration could be used to assess the shell/membrane action of the embedded geogrid or geotextile.

Establishment of the Double-Integration Process

Many attempts to perform double integration of measured acceleration have been proposed by researchers, and they generally consist of (a) use of various types of filters, and (b) adoption of various baseline correction schemes. Though substantial research has been done to validate the applicability of integration procedures by seismologists and others, almost all of those efforts have focused on earthquake-induced acceleration histories. The earthquake acceleration histories have the bulk of the energy in the 0.02 to 30 Hz range. Unlike the acceleration histories recorded under seismic loading, the histories resulting from impact-type loading used in the LST program have a much wider frequency spectrum that is rich, especially in the higher frequency range (50 to 70 Hz). Without any correction, double integration clearly shows a noticeable drift with significantly large displacements that steadily increase even after the cessation of the load pulse. Many options are available with the integration procedures. For

example, features such as the use of low/high pass filters, baseline correction, and zero-th order correction significantly affect the results of the integration. The suitability of various options of the integration procedure for use with impact-type loading should be verified. Hence, it was important that a comparison between measured and double-integrated accelerograms be undertaken as part of this study to verify the applicability of any integration scheme being proposed. Accordingly, the deflections (LVDT measurements) and corresponding acceleration histories at three points on the pavement surface were measured during the laboratory testing program and were used for this purpose. The calibration of the integration scheme was based on the comparison between the measured LVDT surface deflection responses and those computed from the double integration.

A recently proposed FWD calibration method (use of only the acceleration history after the initiation of the pulse) gives an appropriate result for the maximum displacement, but the displacement history has a drift with time after the cessation of the pulse. The FWD approach can be seen as reasonable because the FWD requires only the maximum FWD displacement at the sensor locations rather than the complete displacement histories.

The initial phase of the laboratory testing program involved a pilot study in which many analyses with various integration schemes that involved many combinations of different correction procedures were examined. An overview of the attempts is presented here. High-gain accelerometers with maximum possible sampling rates (16 kHz) along with LVDTs were used to calibrate the suitability of various integration options. Figure I-1 shows the location of the sensors (LVDTs and accelerometers), and Figure I-2 shows the vertical acceleration measurements for the 49th to 55th loading cycles from all three accelerometers identified in Figure I-1. Figure I-3 shows the measured vertical displacements for the same loading cycles. The tests were conducted with the large-scale tank containing only the subgrade layer because the focus was on the double integration of acceleration records measured in the unbound layers. The accelerometers were located at 6 inches below the surface so that they were completely surrounded by the subgrade material, with the recordings representing the subgrade motions.

Sample plots of measured acceleration (ACC 1) and displacement (DIS 1) histories are shown in Figure I-4 and Figure I-5, respectively. The presence of higher frequencies in the acceleration histories as a result of the impact-type loading mixed with high-frequency noise can significantly affect the integration results. Without any correction, the double integration shows significant drifts that are large, as shown in Figure I-6. The Fourier transform of the measured acceleration data for ACC1 is shown in Figure I-7. The Fourier amplitudes up to about 60 Hz are stronger, possibly indicating the dominant frequency range attributable to the applied load pulse. After 60 Hz, the amplitudes are not as strong, and the signals above 60 Hz may be due to noise. It is apparent that many options that are available with integration of earthquake-induced acceleration histories may not work for the impulsive-type of loading under consideration.

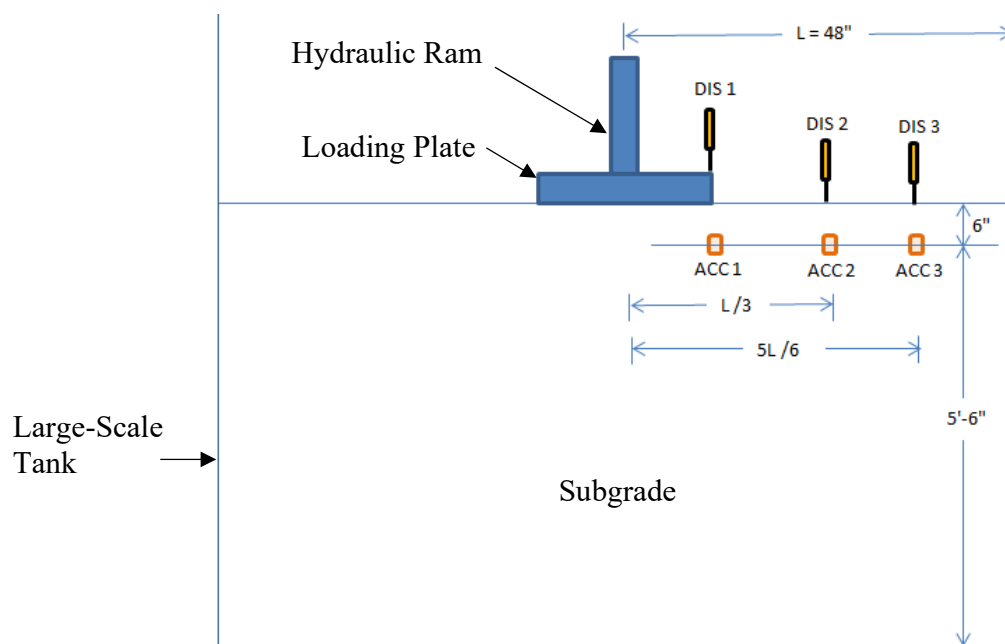


Figure I-1. Schematic of the pilot experimental study to calibrate the integration scheme

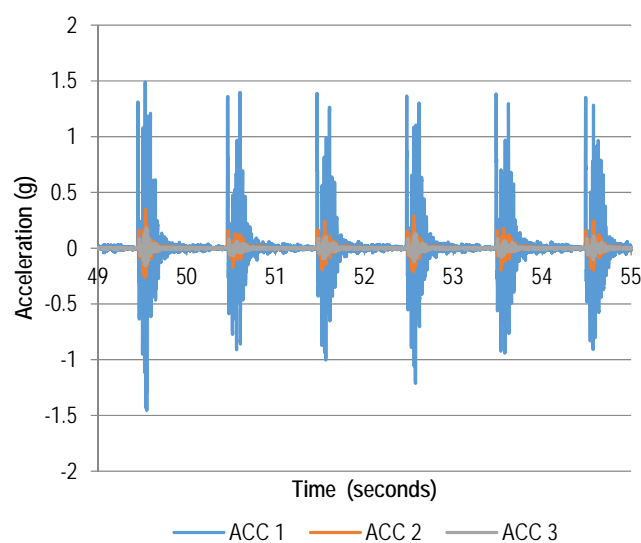


Figure I-2. Vertical acceleration measurements from pilot experimental study (loading cycles 49 to 55)

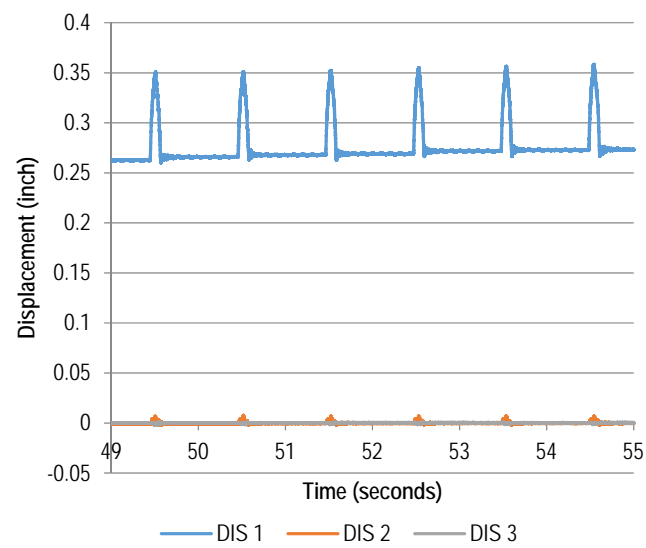


Figure I-3. Vertical LVDT measurements from pilot experimental study (loading cycles 49 to 55)

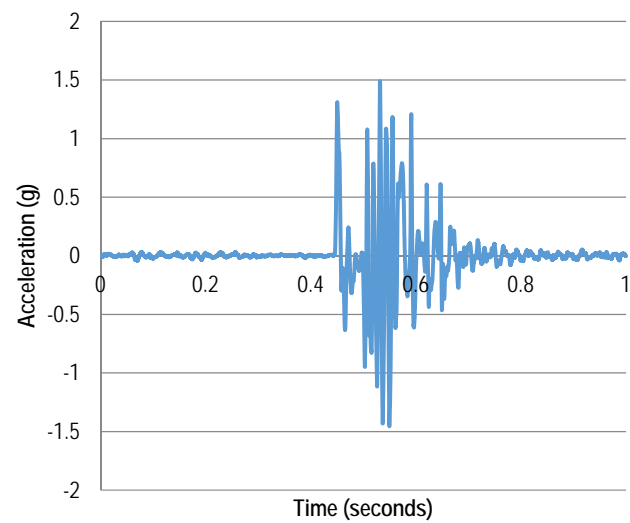


Figure I-4. Measured acceleration history from pilot experimental study (ACC 1)

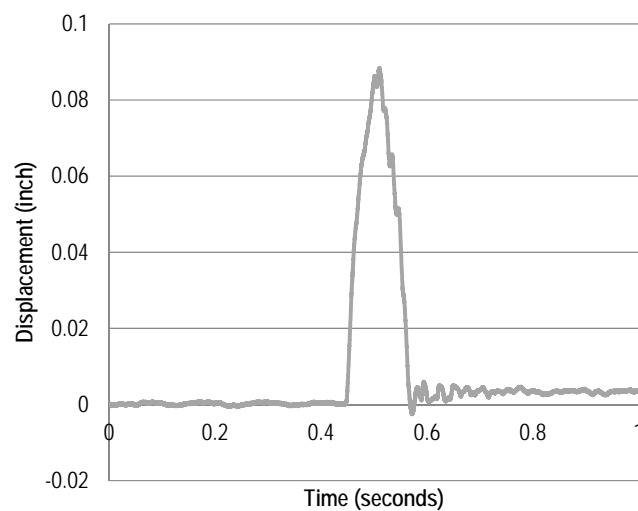


Figure I-5. Measured displacement history from pilot experimental study (DIS 1)

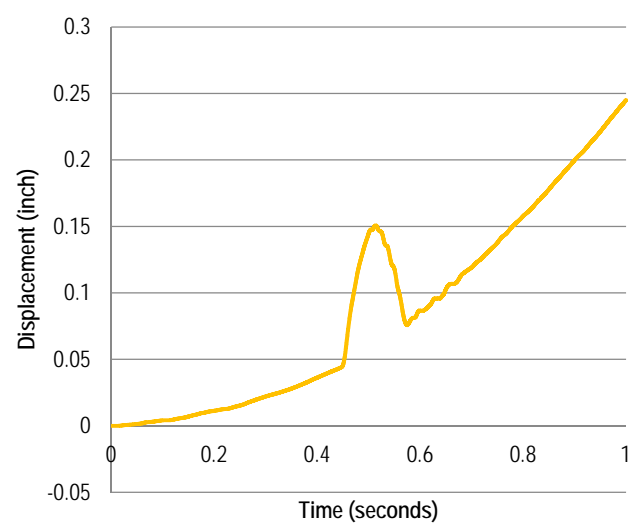


Figure I-6. Calculated displacement from the double integration of ACC 1 history without any corrections

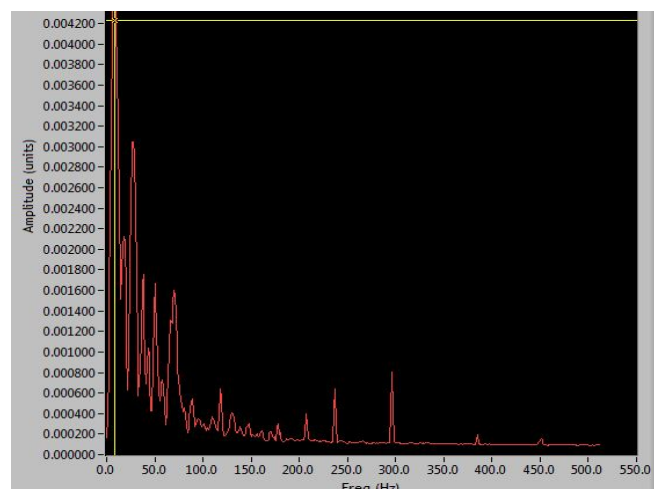


Figure I-7. Fourier transform of ACC 1 recording measurements

An attempt at integration with baseline correction (cubic polynomial) only without any filtering is compared with the measured displacement in Figure I-8. Though the shape of the pulse is captured well, the computed displacements prior to and after the cessation of the impact show noticeable negative values (upward movement). The origin of this occurrence can be traced to noise that is present in the accelerometer readings prior to the start and after the end of the displacement pulse. Another source for this may be the consequence of the use of the baseline correction routine. Figure I-9 shows the comparison of the measured and computed maximum pulse displacement for 18 recordings with this approach.

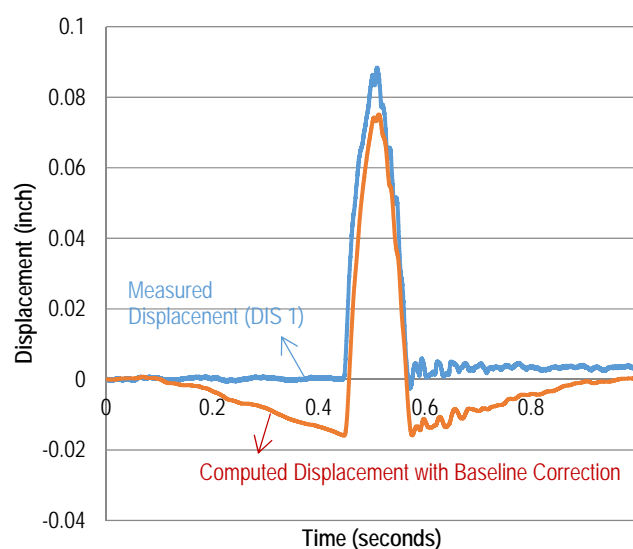


Figure I-8. Comparison between measured and computed (with baseline correction) displacement histories (DIS 1 and ACC 1)

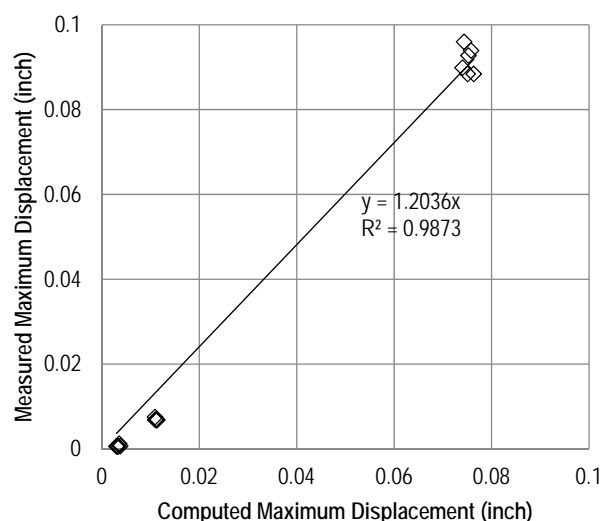


Figure I-9. Comparison between measured and computed maximum displacements for 18 recording measurements with baseline correction

Use of only the acceleration history after the initiation of the pulse as recommended by Irwin et al. (1) for integration of accelerations measured under FWD testing was another attempt to get reasonable displacement. In this approach, pulse initiation was correctly captured and the maximum pulse displacement was predicted well (within 5 percent). However, the displacement history still increased with time after the cessation of the pulse (see Figure I-10). This approach may be seen as reasonable for FWD testing because FWD requires only the maximum displacement at the sensor locations rather than the complete displacement histories. Figure I-11 shows the comparison of measured and computed maximum pulse displacements, and it is clear this procedure gives better results than the previous approach.

It has been found that a very effective way to get a reasonable displacement time history as well as maximum displacement is the correction of the acceleration history before double integration by subtracting the mean value from the entire acceleration record. This is known as the zero-th order correction. Figure I-12 shows the displacement history obtained using this approach. Figure I-13 shows a good agreement between the directly measured and the computed maximum displacements from the double integration for 18 data records.

As another attempt, only a portion of the data was considered by eliminating data at the start and at the end (for noise elimination), and then subtracting the mean acceleration value of the selected data range. This effort produced very good results. Figure I-14 shows the comparison of the measured displacement and computed displacement with this approach. As the figure shows, data between 0.3 second and 0.9 second (0.6 second time period) were considered. It is clear that this approach eliminates noise before strike (no displacement before pulse initiation) and provides good agreement with the measured displacement after the maximum displacement. This procedure seemed to match the entire measured displacement history well. However, it should be noted that the selection of the data range for integration was somewhat arbitrary. Therefore, it was recommended that a calibration of the integration scheme be

undertaken between measured and integrated displacements to verify the appropriateness of the integration scheme.

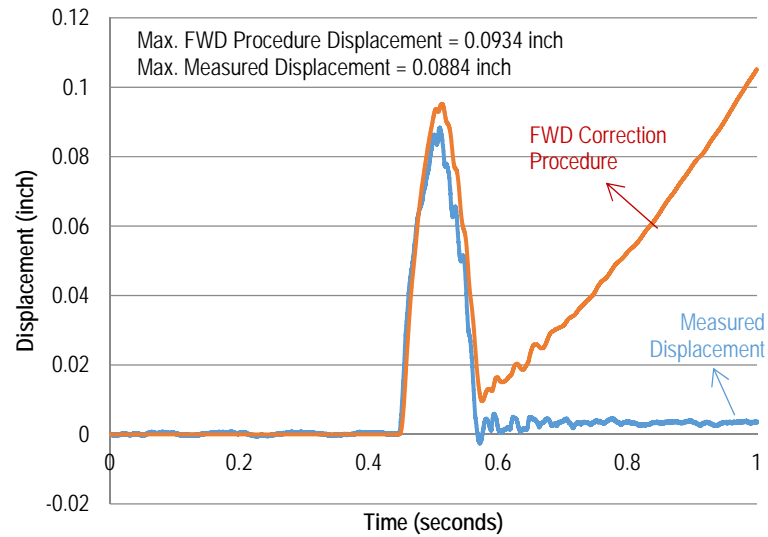


Figure I-10. Comparison between measured and computed displacement histories using FWD correction procedure (ignoring acceleration history before pulse initiation)

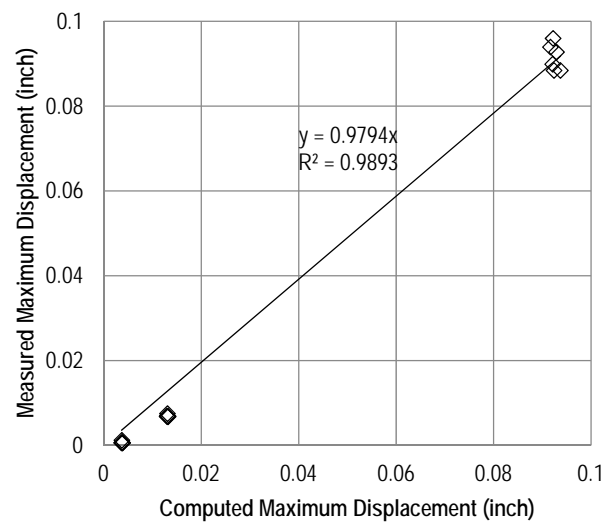


Figure I-11. Comparison between measured and computed maximum displacements for 18 recording measurements with FWD correction procedure

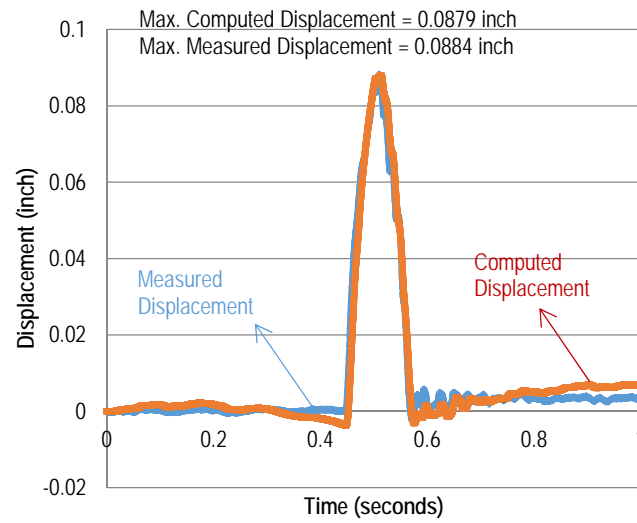


Figure I-12. Measured and double-integrated displacement history with zero-th order correction

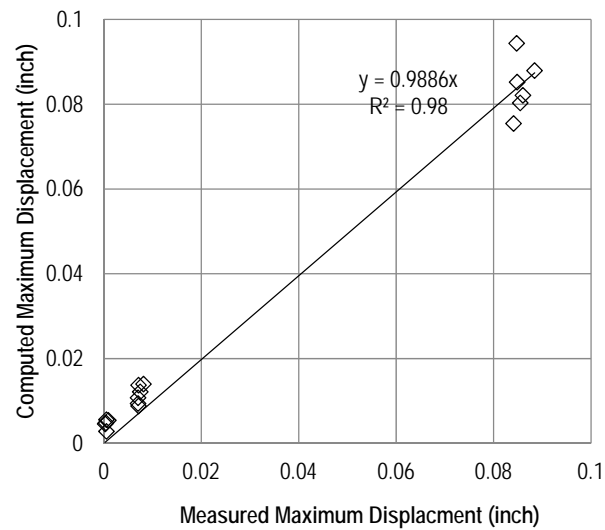


Figure I-13. Comparison between measured and computed maximum displacements for 18 recording measurements with zero-th order correction

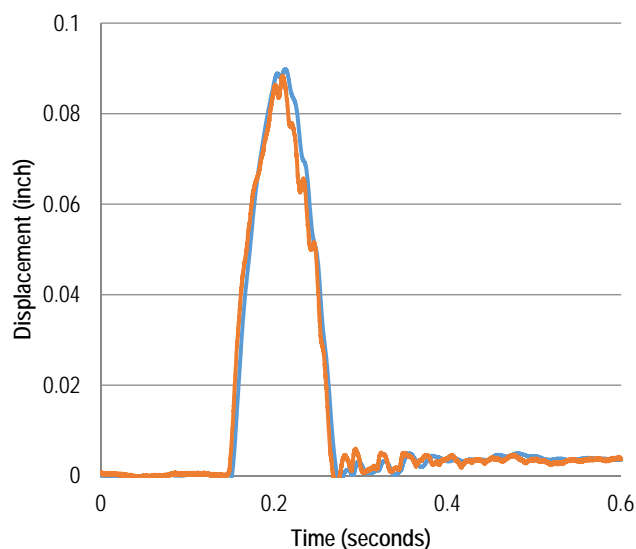


Figure I-14. Measured and double-integrated displacement histories for a sampling frequency of 16,666 Hz with selected time history interval (0.3 to 0.9 second) and zero-th correction

The pilot testing recorded only the surface responses, and therefore a much larger sampling rate was feasible ($f = 16,666$ Hz and $\Delta t = 0.00006$ sec) with the data acquisition system used in the laboratory testing program. However, in the subsequent experiments involving many more channels of recording, only a smaller sampling rate was possible. For finding the minimum sampling rate with a good agreement with the maximum measured displacement and entire displacement history, several analyses of double integration were completed by increasing the time interval of the measurements (i.e., skipping intermediate data). Table I-1 summarizes the results for the comparison of maximum displacements with various sampling frequencies. The original sampling frequency was 16,666 Hz, and the data show that the frequency of 2083 Hz can give very reasonable results (within 2 percent of the measured displacement at 16,666 Hz). Figure I-15 shows that the displacement history is also acceptable at this sampling frequency. Although the results for maximum displacement seemed to be good with 833 Hz, the displacement history was not appropriate (Figure I-16).

Table I-1. Comparison of Double-Integrated Displacement Results with Various Sampling Frequencies

Time Spacing (sec)	Frequency	Max Measured Displacement (mi)	Max Computed Displacement (mi)	% Difference with Measured Displacement	% Difference with Original Spacing
0.00006*	16,666*	88.40	89.81	1.58	0.00
0.00012	8,333		89.85	1.63	0.05
0.00018	5,555		89.93	1.73	0.14
0.00024	4,166		89.88	1.67	0.08
0.00030	3,333		90.15	1.97	0.38
0.00036	2,777		90.02	1.83	0.24
0.00042	2,380		90.06	1.87	0.28
0.00048	2,083		90.01	1.81	0.22
0.00054	1,851		90.83	2.74	1.14
0.00060	1,666		89.91	1.71	0.12
0.00120	833		89.82	1.60	0.02
0.00180	555		93.10	5.31	3.66
0.00240	416		86.96	1.63	3.17
0.00360	277		113.30	28.16	26.16

* Original spacing and frequency.

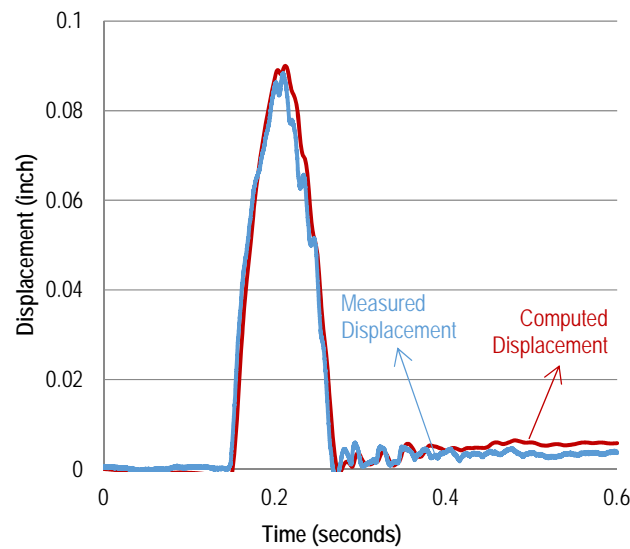


Figure I-15. Measured and double-integrated displacement histories for a sampling frequency of 2083 Hz with selected time history interval (0.3 to 0.9 second) and zero-th correction

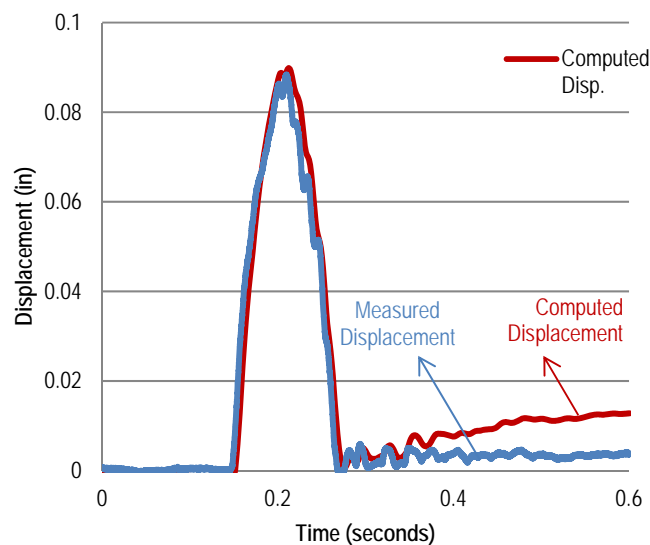


Figure I-16. Measured and double-integrated displacement histories for a sampling frequency of 833 Hz with selected time history interval (0.3 to 0.9 second) and zero-th correction

Another issue is the presence of noise in the signal. It should be noted that while the signal-to-noise ratio is higher near the loaded area, the ratio is much lower at locations farther away on the surface and interior locations. Sources of noise are many, and they include background noise (e.g., heater/AC) and vibrations trapped within the large-scale tank from previous load pulses. As a first step, an effort to characterize the noise was attempted. This entailed scrutinizing the measured acceleration data before and after each pulse and also the

measurements after the completion of the entire dynamic loading. However, this was not successful, mainly because it turned out that the noise was truly random. Noise is often associated with high-frequency signals, and therefore the elimination of such waves resulted in a better representation of the true signal. One of the correction schemes used in the past by researchers is band filters (band-pass or band-stop) in which certain frequencies of the excitation can be suppressed. Such suppressed frequencies are considered to be from noise. A proven method to get rid of noise is the use of low pass filters that eliminate the high-frequency signal. A range of low pass filters with cut-off (low pass filter) values of 55, 60, and 65 Hz were considered. Accordingly, the double integration consisted of first applying the filter followed by the zero-th order and baseline corrections. By comparing maximum displacement values and their times of occurrence under all load levels, it was found that using the 60 Hz filter produced the most consistent and closely comparable surface displacement predictions with those directly measured by the LVDTs. Table I-2 summarizes the results for the computed displacements when using different filters.

Table I-2. Typical Results When Using Low Pass Filter with Different Cut-Off Frequencies

Item	Values	Time at Max. Disp. (sec)
Cut-off Frequency = 55 Hz		
Max. Measured Displacement—LVDT (mi)	24.06	86.906
Max. Displacement from Integration (mi)	23.43	86.910
Difference (mi)	-0.63	0.004
Error (%)	-2.6	
Cut-off Frequency = 60 Hz		
Max. Measured Displacement—LVDT (mi)	24.13	86.906
Max. Displacement from Integration (mi)	23.43	86.909
Difference (mi)	-0.71	0.003
Error (%)	-2.9%	
Cut-off Frequency = 65 Hz		
Max. Measured Displacement—LVDT (mi)	24.21	86.906
Max. Displacement from Integration (mi)	23.43	86.909
Difference (mi)	-0.79	0.003
Error (%)	-3.3%	

Based on the attempts to perform double integration of the accelerometer measurements described above, the following iterative procedure was adopted for integration in this study:

- Step 1: From the entire plot of measured vertical acceleration response at the loading plate (referred to as A1 subsequently), select as many as seven consecutive cycles that look similar beyond 50 cycles of loading. The 50th loading cycle limit was chosen to allow the materials in the large-scale tank enough time to fully stabilize under the repeated loading.
- Step 2: Obtain the Fourier transform of the measured vertical acceleration response (A1) for one of the loading cycles (say 50th cycle) and determine the relative strength of signals and select a cut-off frequency (low pass filter) above which the noise is assumed to be prevalent.
- Step 3: Select the start and end of the time history interval for analysis. Consider the start time as 0.1 second before the measured peak vertical displacement from the LVDT (referred to as L1 subsequently) and the end time as 0.4 second after the peak.
- Step 4: Perform zero-th order and baseline corrections (cubic polynomial) and obtain the corrected acceleration history for double integration.
- Step 5: Compare the double-integrated (computed) corrected acceleration history with the measured vertical displacement.
- Step 6: If the comparison in Step 5 is not acceptable for the entire displacement history, repeat Steps 2 to 5 with another selection of a loading cycle until an acceptable match between displacements is obtained.
- Step 7: Repeat Steps 1 to 6 for the surface accelerometers that are located away from the loaded plate.

Illustration of Established Procedure

For better clarification, the steps associated with the proposed iterative procedure are exemplified below using, as an example, data from the large-scale tank Experiment No. 2 (flexible pavement with crushed aggregate base thickness of 10 inches; dynamic load of 9 kip), which is seen as a representative case. Acceleration (A1 to A3) and LVDT (L1 to L3) measurements were made on top of the asphalt concrete layer at three locations, as shown in Figure I-17. The readings from these sensors provided the important basis for the selection of the integration method to be used.

Figure I-18 shows the 50th to the 56th pulse cycles (seven cycles) for the recorded acceleration response of A1 (Step 1). The response of the 50th cycle (or pulse) was extracted from this plot and is shown in Figure I-19. The Fourier transform was then applied to the appropriate cut-off frequency (Step 2). After using the low pass filter, the start and end times of the acceleration response history were estimated to be 56.935 and 57.435 seconds, respectively, based on the LVDT time history of L1 (Step 3). Figure I-19 shows this selected window of the history. Step 4 involved zero-th order and baseline correction. In Step 5, the comparison between the measured and computed displacements was made (see Figure I-20). A close match between the measured and computed displacement histories was observed. However, if the match had been deemed not acceptable, Steps 2 to 5 would have been repeated with a different loading cycle.

The overall comparisons of the maximum displacements for all three surface locations and load levels are presented in Figure I-24 to Figure I-26. When displacements are higher (i.e., A1/L1 location), the comparison is very good, with the computed displacement being underpredicted by less than 3.6 percent. At the further location (i.e., A3/L3 location) where the displacements are the lowest, there is an overprediction by the computed values overall by as much as 10 percent. These deviations are not considered to be large and are within the range of expected deviations.

Copyright National Academy of Sciences. All rights reserved.

match was found between the computed (i.e., double-integrated acceleration) and the LVDT measurements at a surface location, the integration procedure was used for the accelerometers located directly below that location. Experiments with either a geogrid or geotextile had the respective data processed in the same fashion.

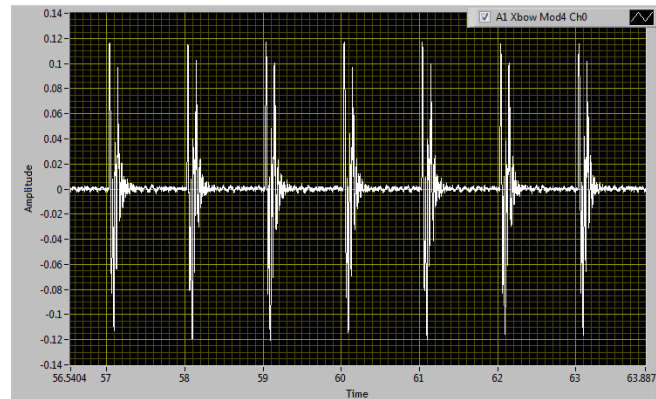


Figure I-18. Measured acceleration history for loading cycles 50 to 56 (Experiment No. 2, pulse load of 9 kip, A1)

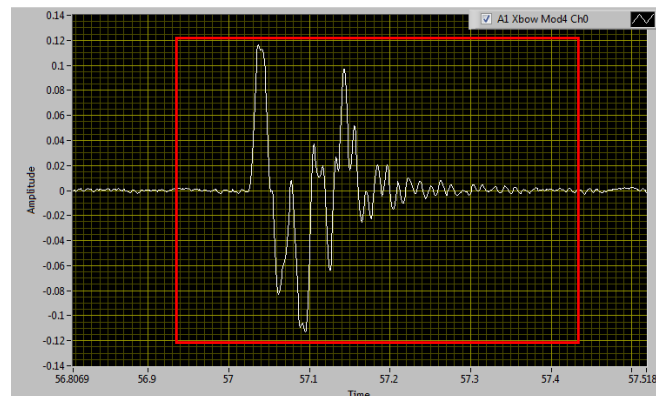


Figure I-19. Measured acceleration history for 50th loading cycle (Experiment No. 2, pulse load of 9 kip, A1)

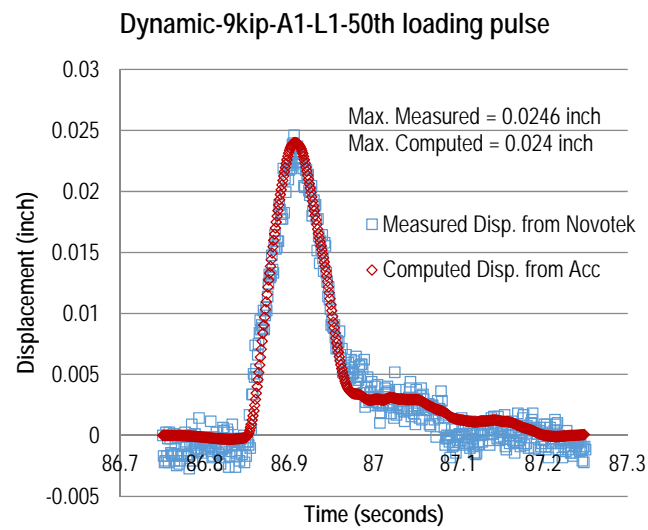


Figure I-20. Comparison between measured (L1) and computed (A1) displacements for 50th loading cycle (Experiment No. 2, pulse load of 9 kip)

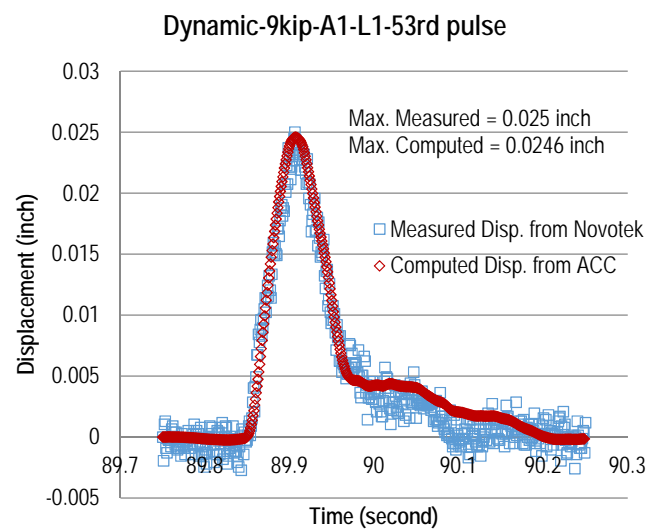


Figure I-21. Comparison between measured (L1) and computed (A1) displacements for 53rd loading cycle (Experiment No. 2, pulse load of 9 kip)

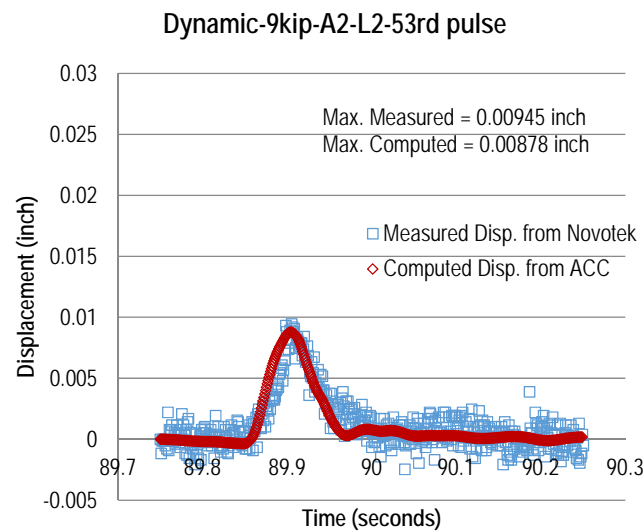


Figure I-22. Comparison between measured (L2) and computed (A2) displacements for 53rd loading cycle (Experiment No. 2, pulse load of 9 kip)

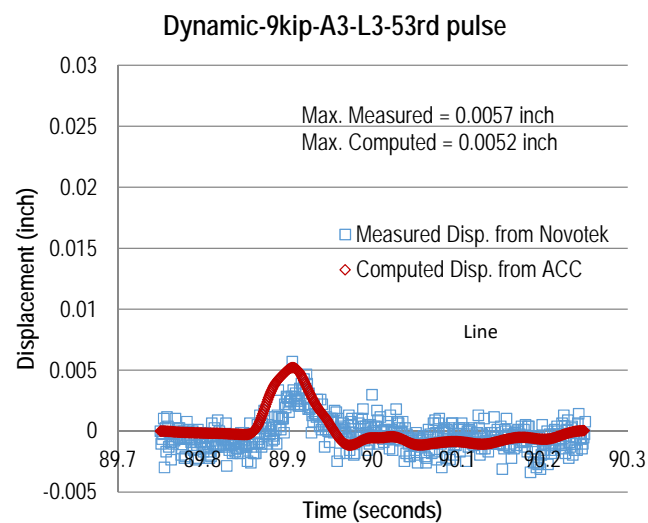


Figure I-23. Comparison between measured (L3) and computed (A3) displacements for 53rd loading cycle (Experiment No. 2, pulse load of 9 kip)

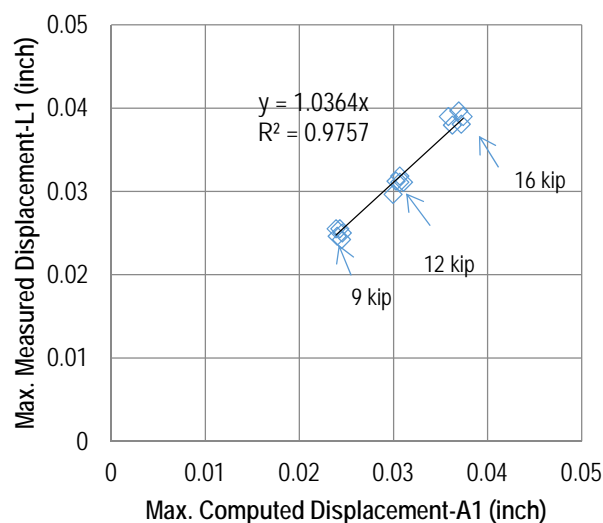


Figure I-24. Comparison between measured (L1) and computed (A1) maximum displacements for 53rd loading cycle and all load levels (Experiment No. 2)

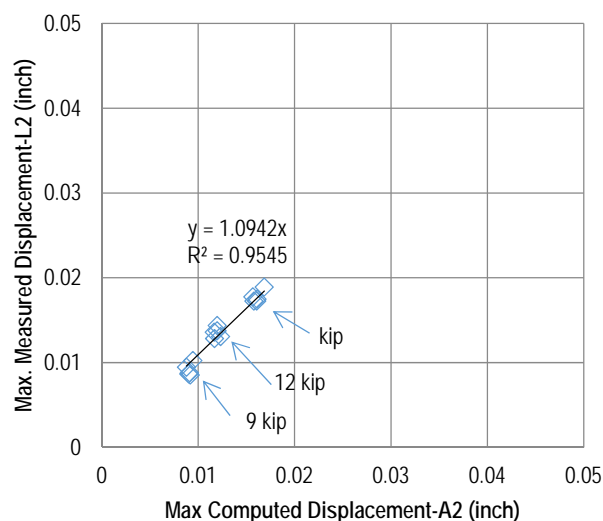


Figure I-25. Comparison between measured (L2) and computed (A2) maximum displacements for 53rd loading cycle and all load levels (Experiment No. 2)

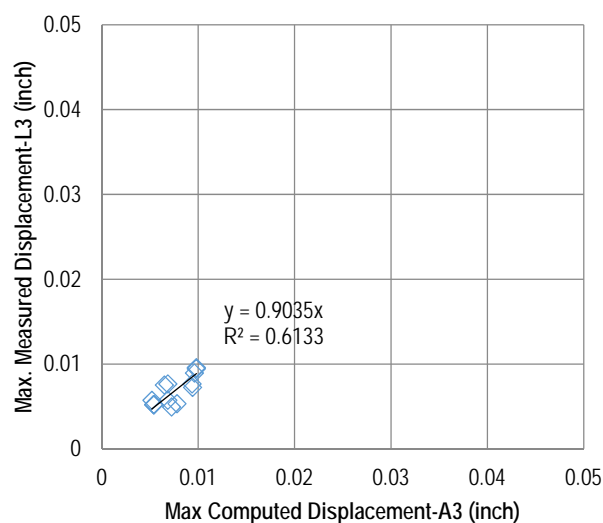


Figure I-26. Comparison between measured (L3) and computed (A3) maximum displacements for 53rd loading cycle and all load levels (Experiment No. 2)

References

1. Irwin, L.H., Orr, D.P., and Atkins, D. (2009). FWD Calibration Center and Operational Improvements: Redevelopment of the Calibration Protocol and Equipment. *Final Report FHWA-HRT-07-040*, FHWA, Washington D.C., 268p.

APPENDIX J. SUMMARY CHARTS OF RIGID PAVEMENT EXPERIMENTS

Appendix J1. Summary Charts for Rigid Pavement Experiments: Dynamic Loading—Dry and Wet: No. 7 (Control), No. 9 (Geogrid), and No. 10 (Geotextile)

J1-3

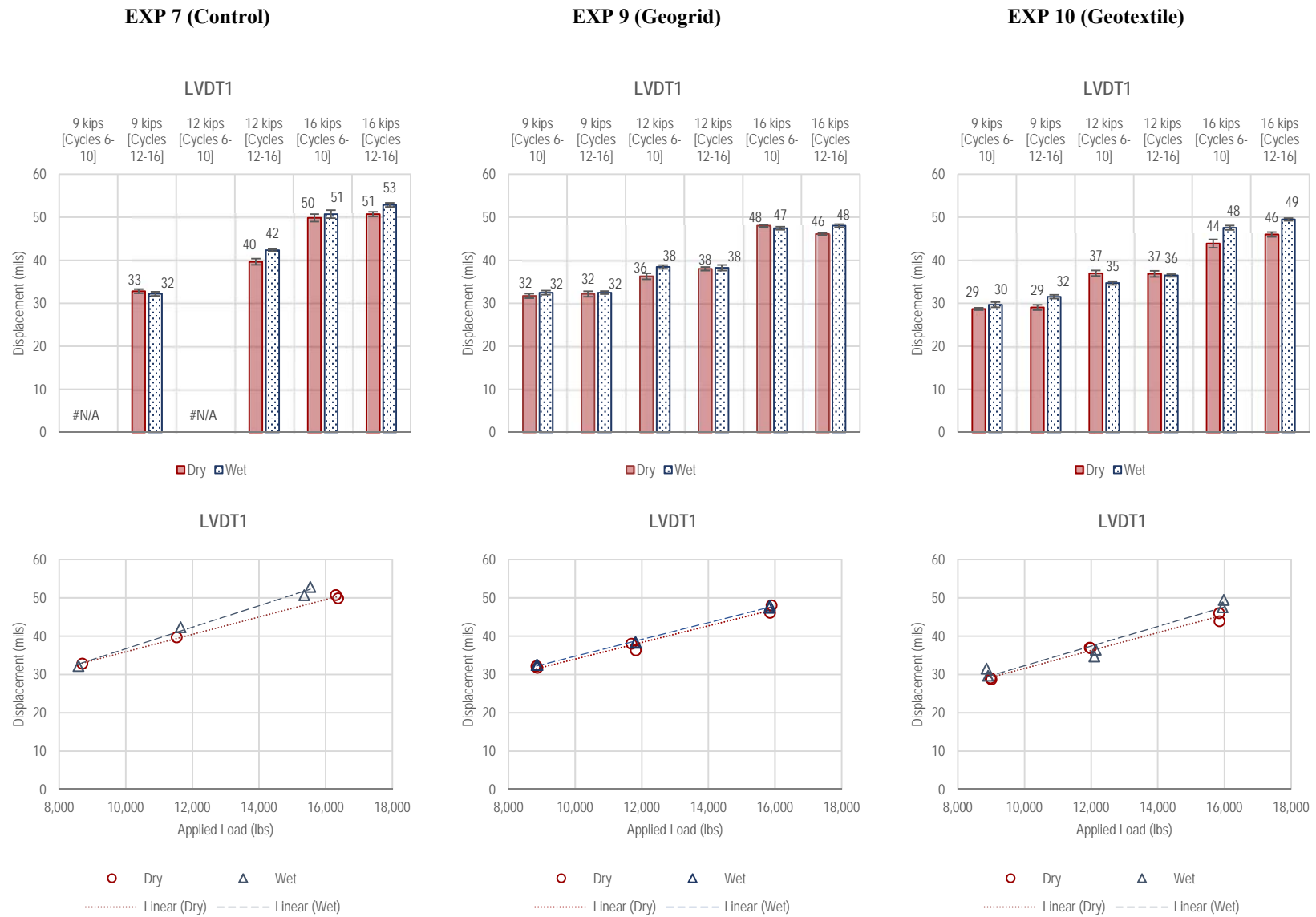


Figure J1-1. Summary of LVDT 1 measurements—Dynamic Loading

J-4

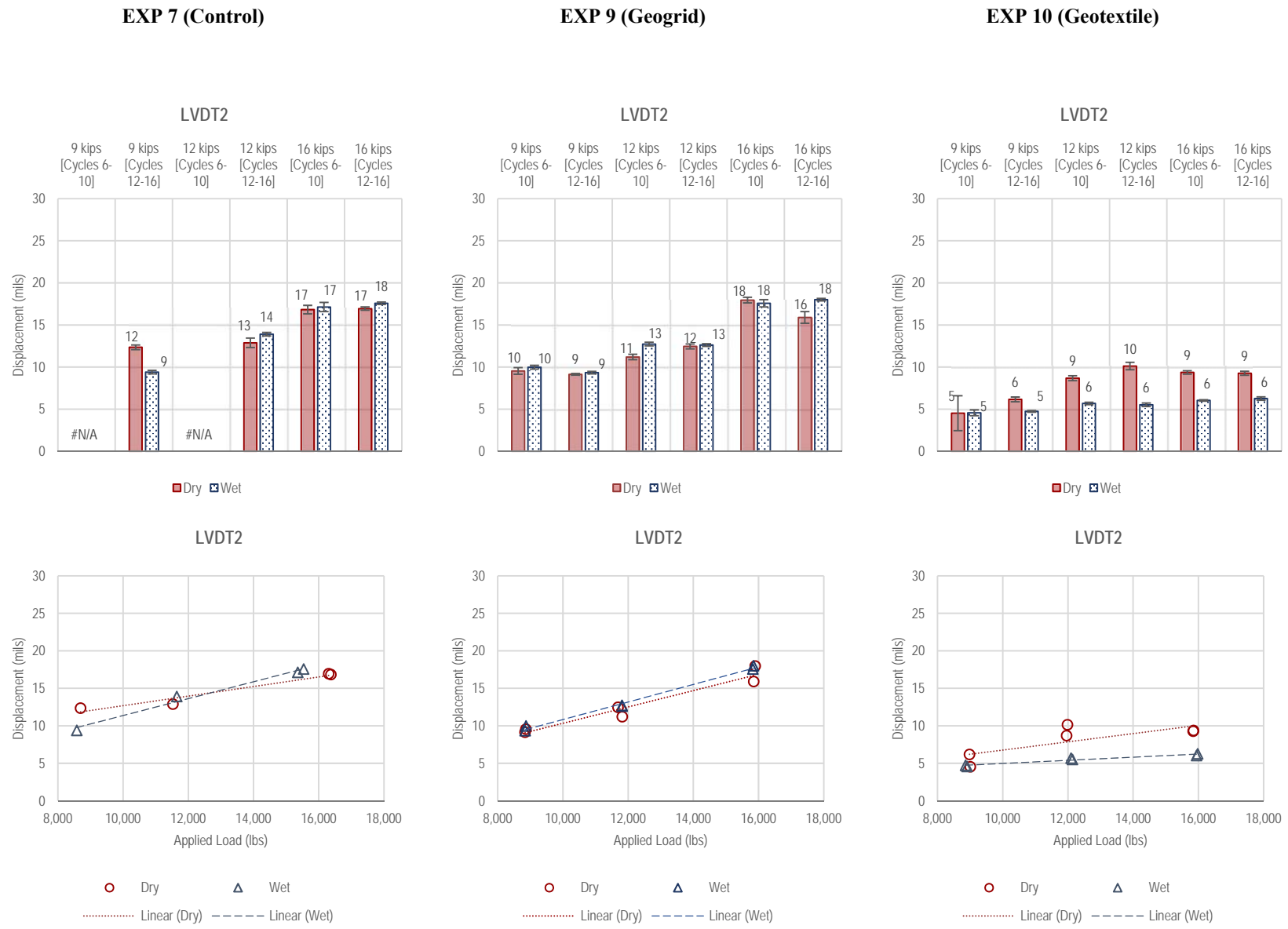


Figure J1-2. Summary of LVDT 2 measurements—Dynamic Loading

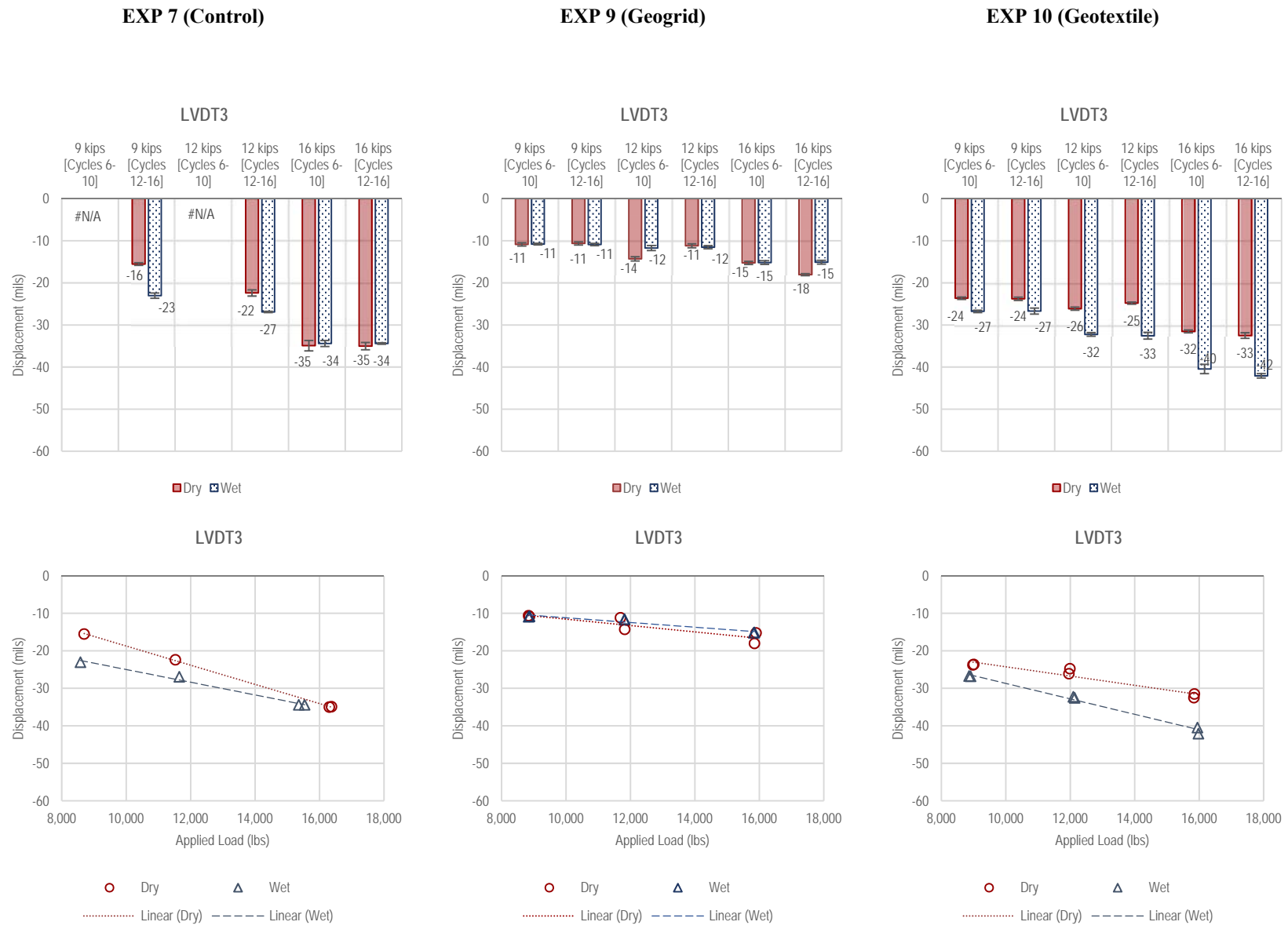


Figure J1-3. Summary of LVDT 3 measurements—Dynamic Loading

J-5

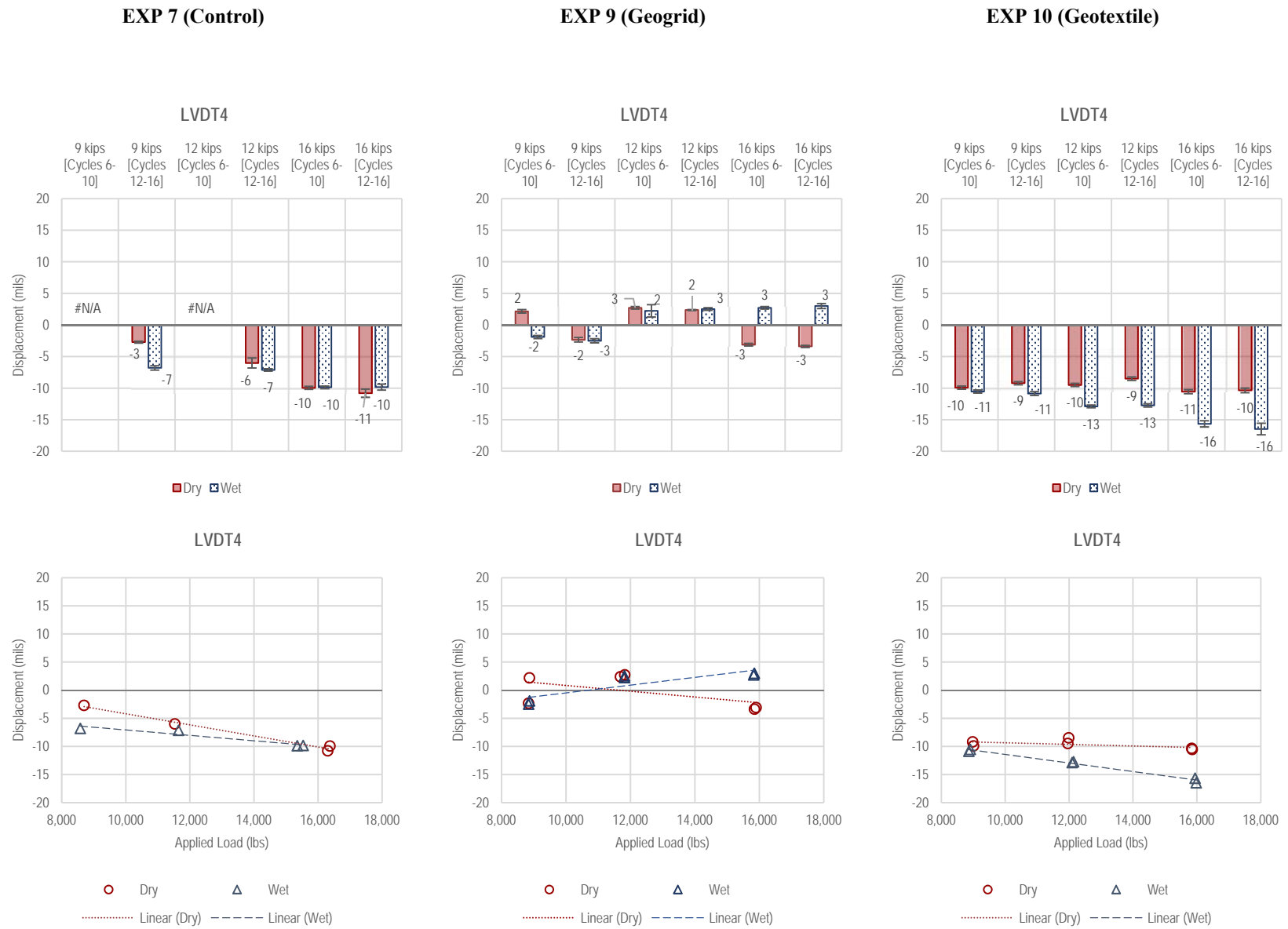


Figure J1-4. Summary of LVDT 4 measurements—Dynamic Loading

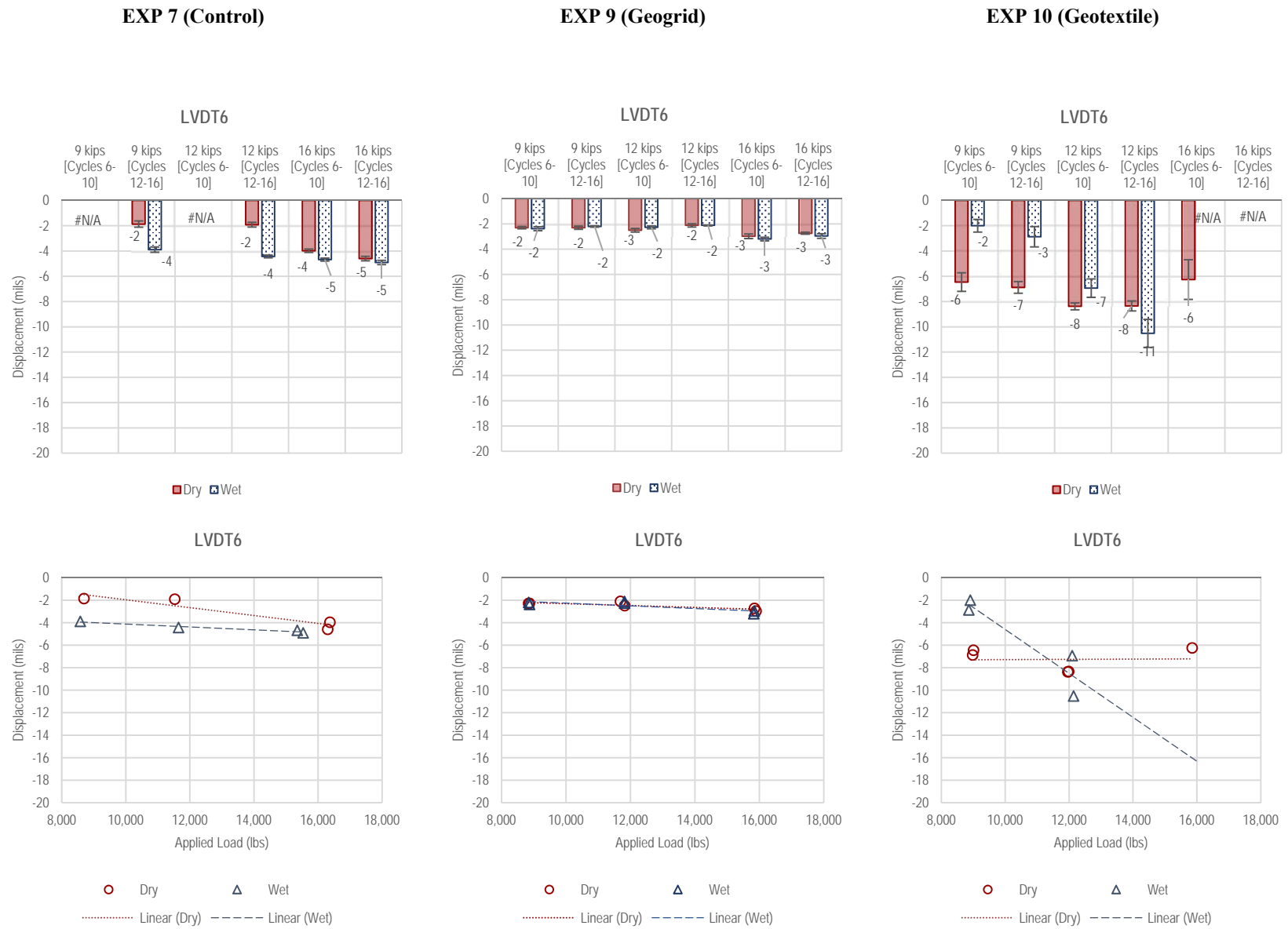
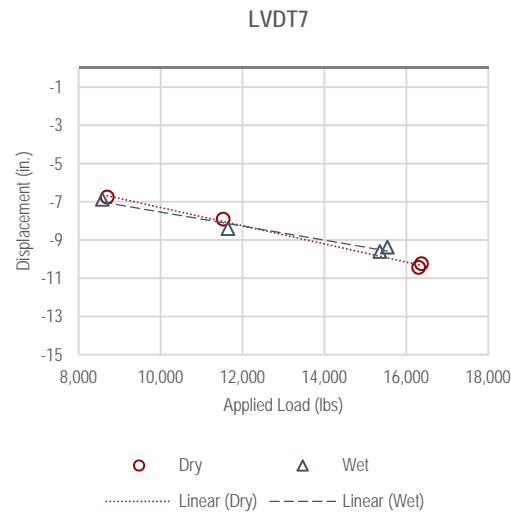
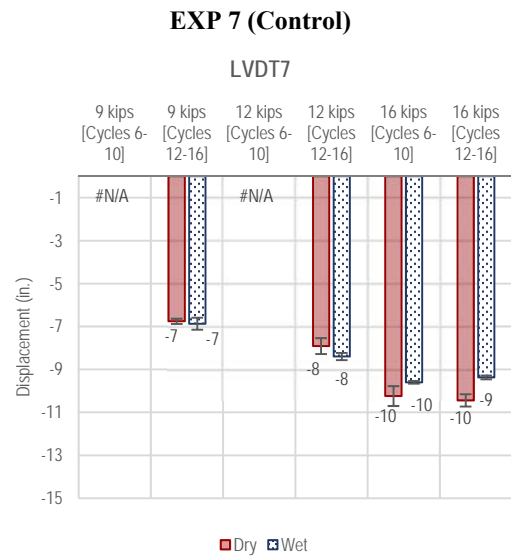


Figure J1-5. Summary of LVDT 6 measurements—Dynamic Loading

J-7

J-8



EXP 9 (Geogrid)

Not Available

Not Available

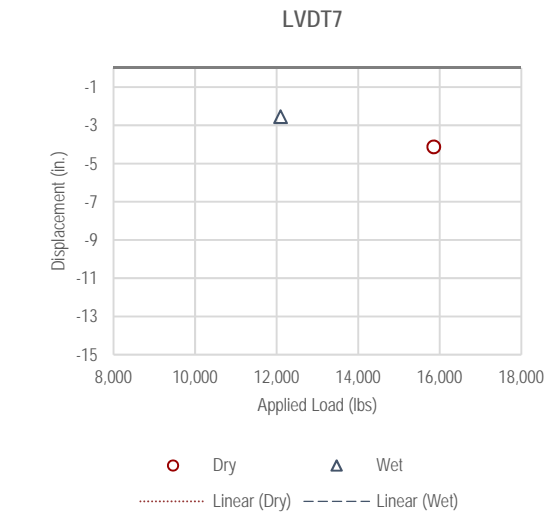
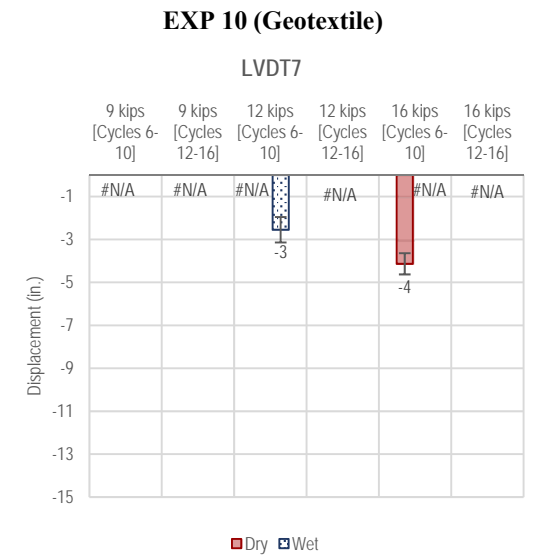
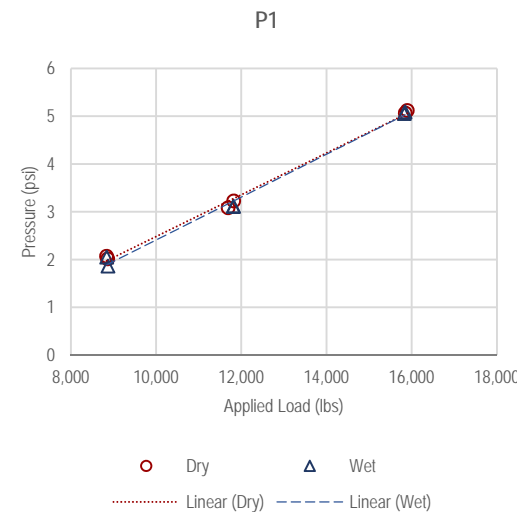
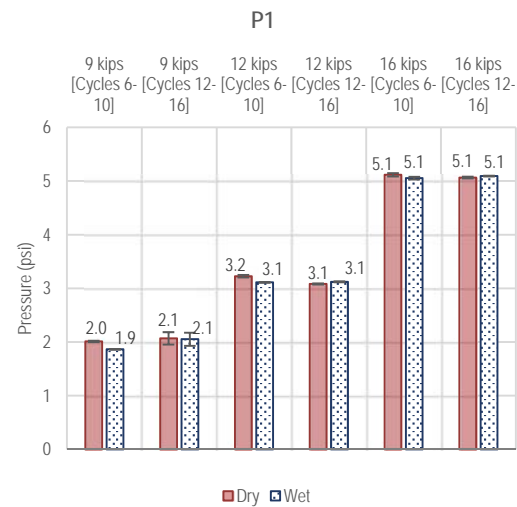


Figure J1-6. Summary of LVDT 7 measurements—Dynamic Loading

EXP 7 (Control)

Not Available

EXP 9 (Geogrid)



EXP 10 (Geotextile)

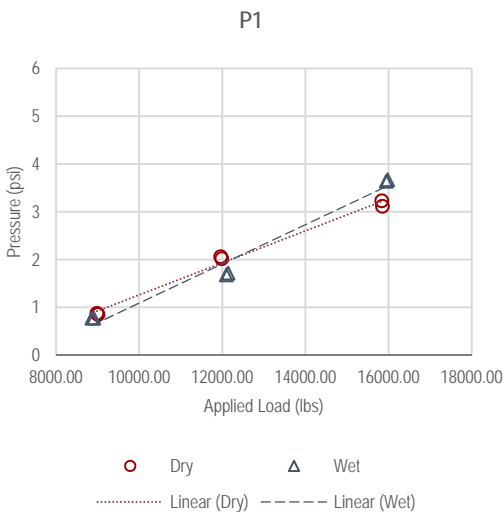
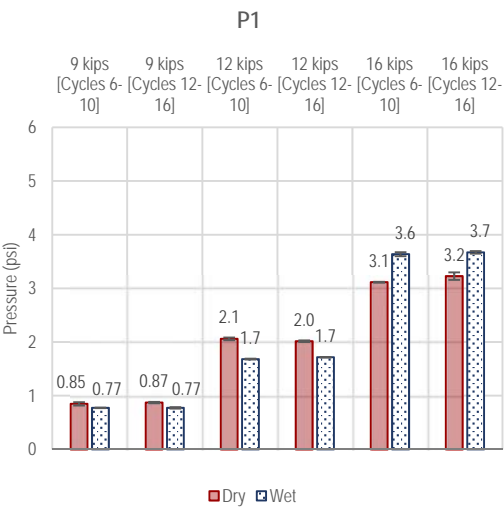


Figure J1-7. Summary of P1 measurements—Dynamic Loading

J-10

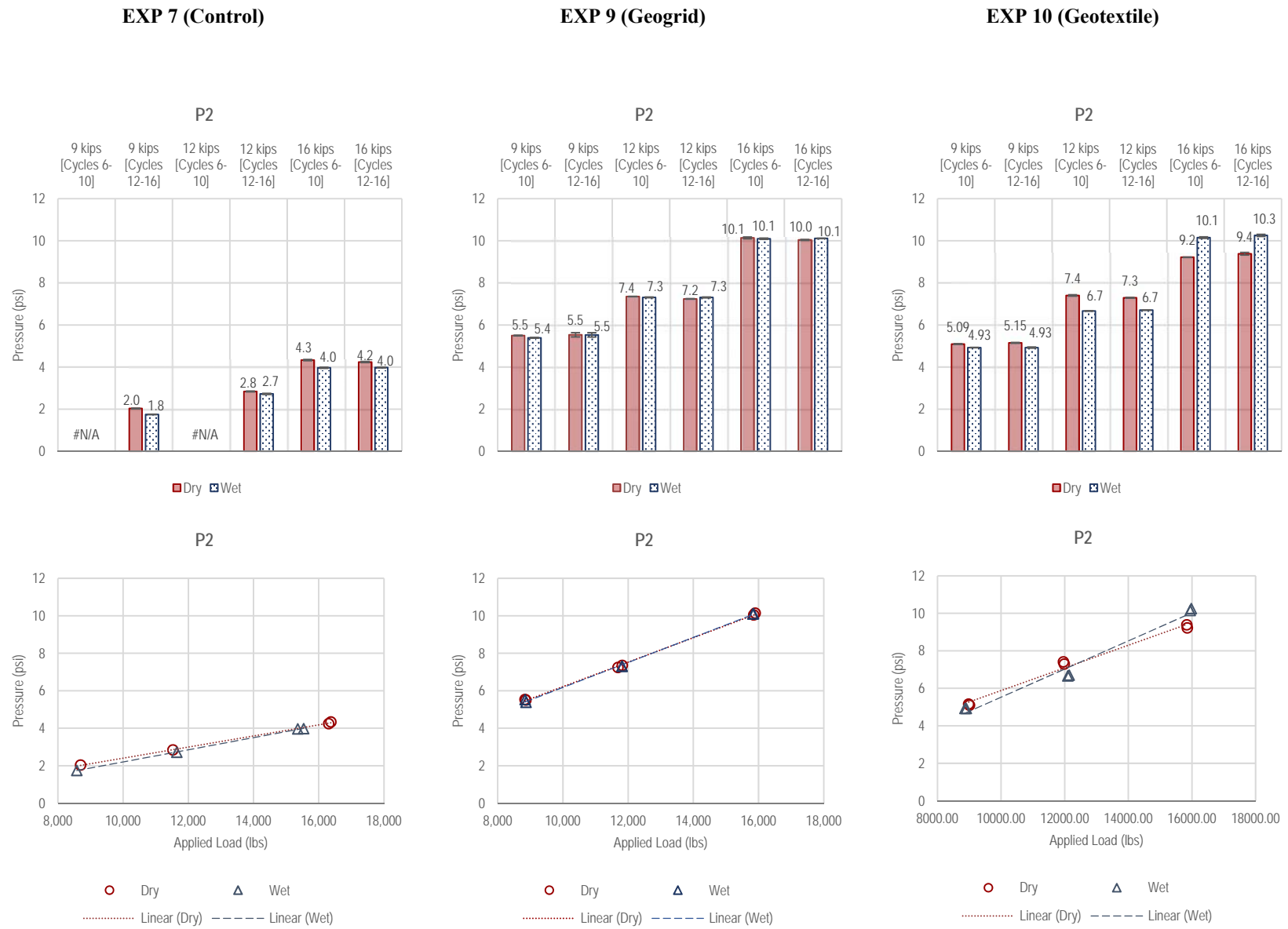
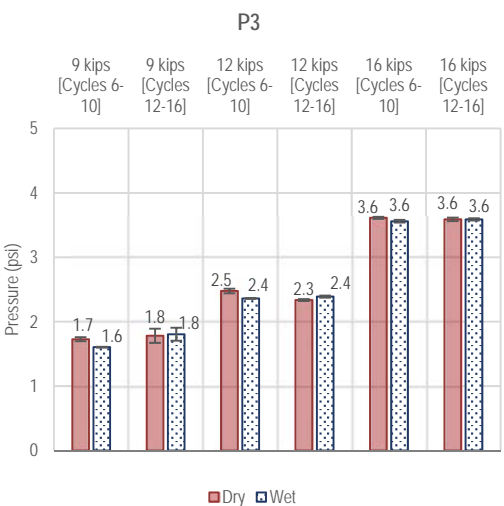


Figure J1-8. Summary of P2 measurements—Dynamic Loading

EXP 7 (Control)

Not Available

EXP 9 (Geogrid)



EXP 10 (Geotextile)

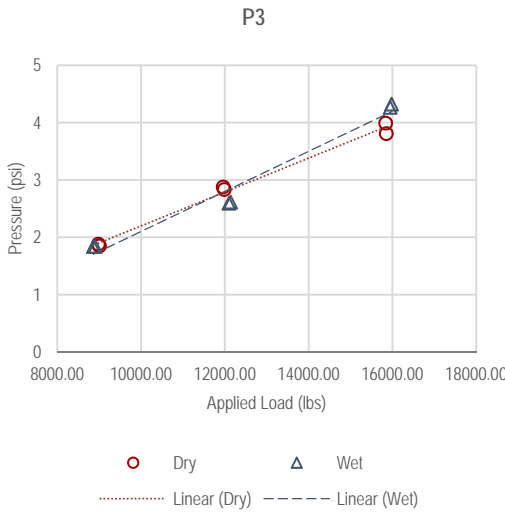
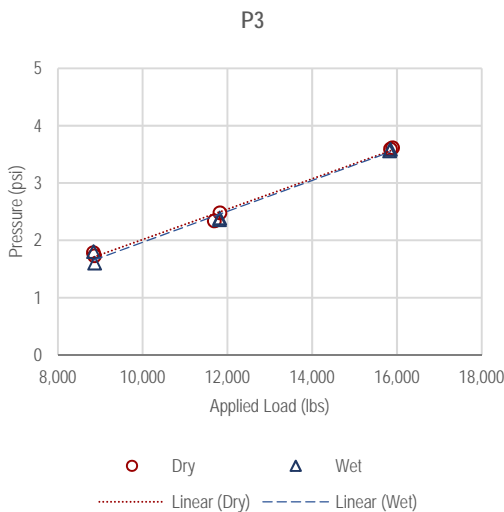
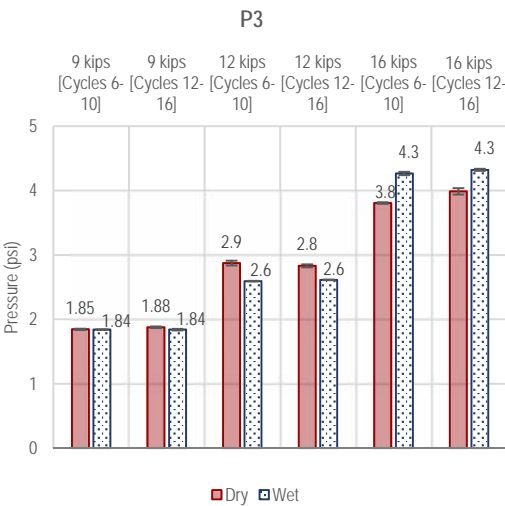


Figure J1-9. Summary of P3 measurements—Dynamic Loading

J-12

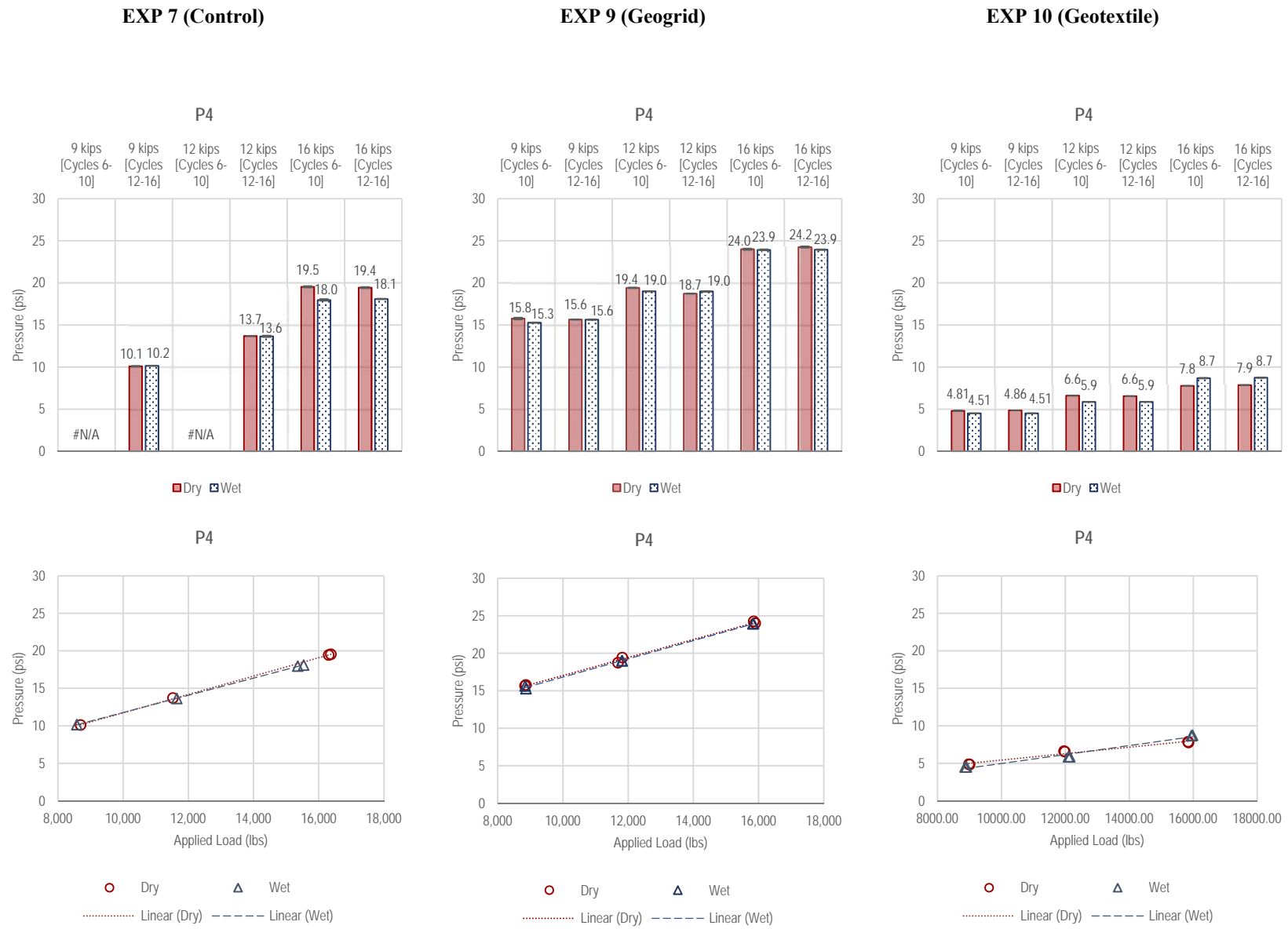


Figure J1-10. Summary of P4 measurements—Dynamic Loading

J-13

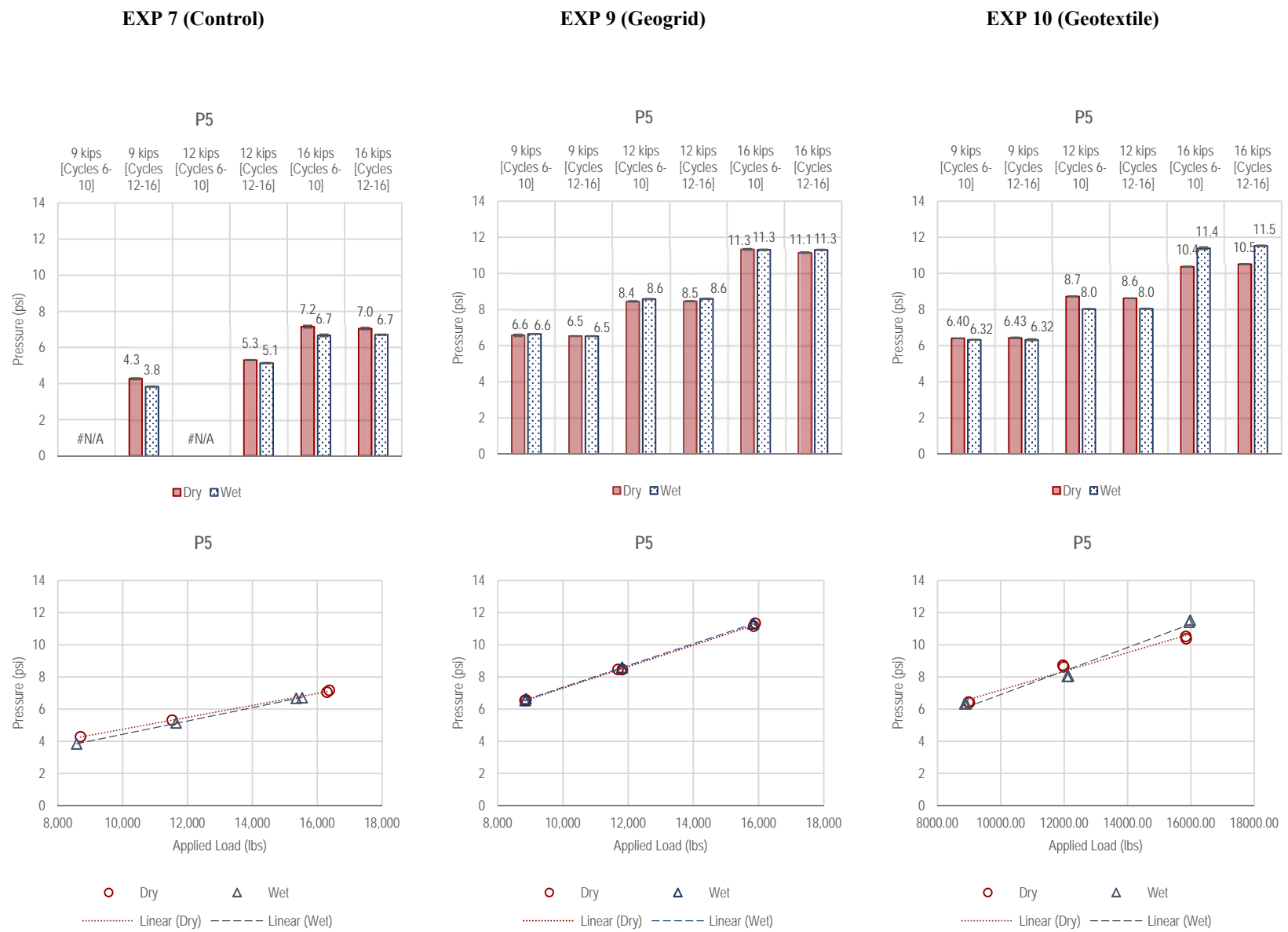


Figure J1-11. Summary of P5 measurements—Dynamic Loading

J-14

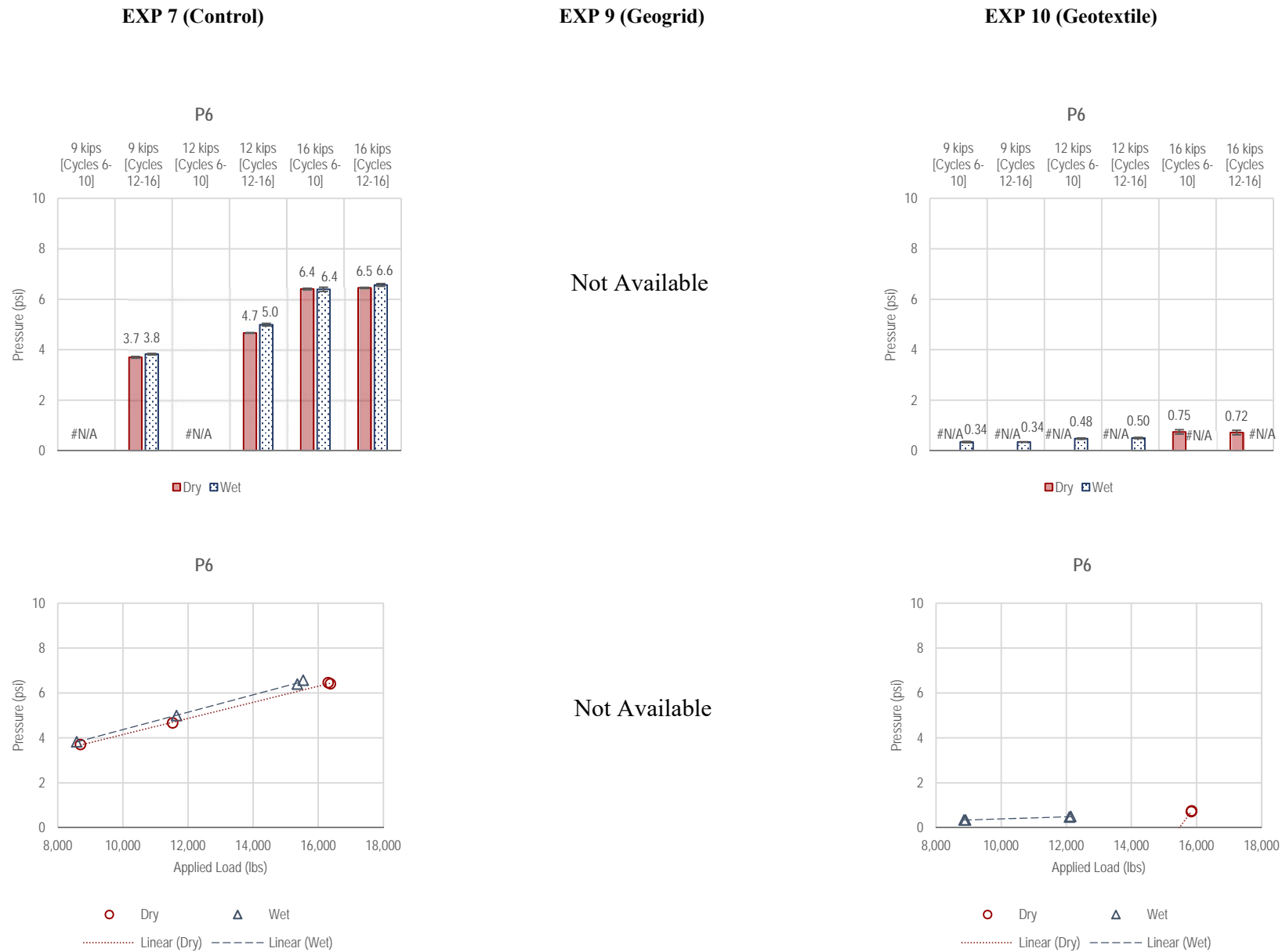


Figure J1-12. Summary of P6 measurements—Dynamic Loading

J-15

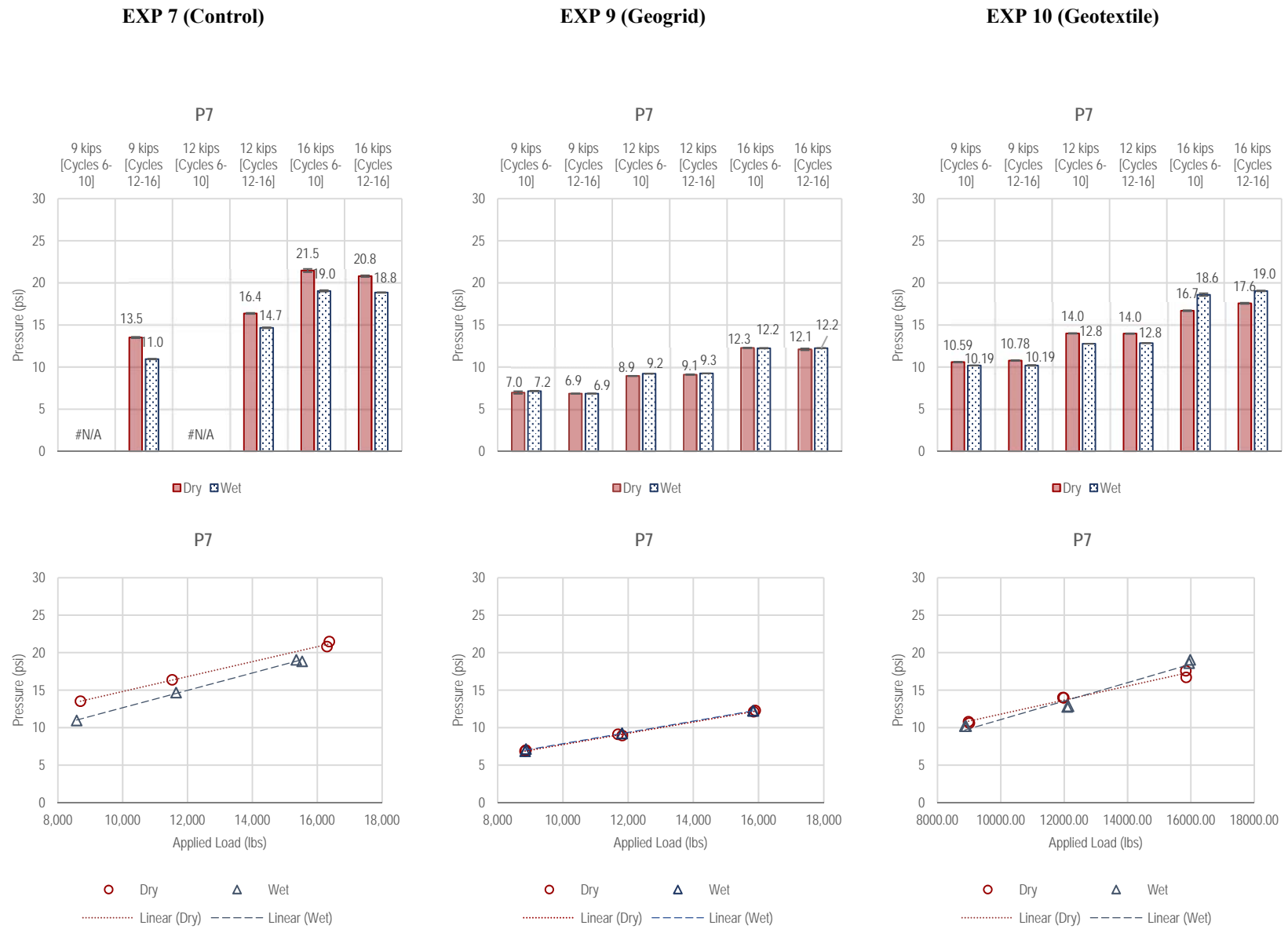


Figure J1-13. Summary of P7 measurements—Dynamic Loading

J-16

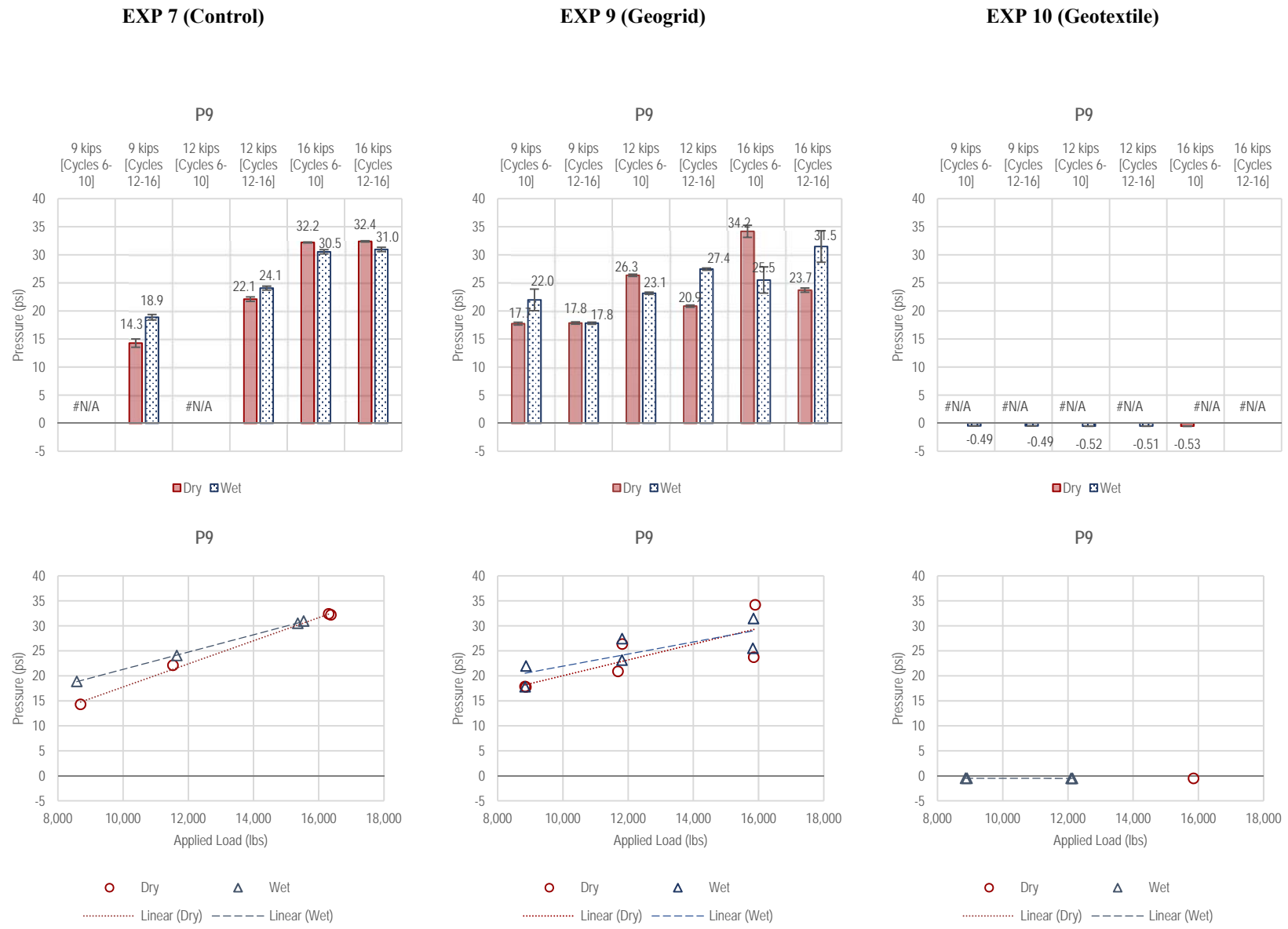


Figure J1-14. Summary of P9 measurements—Dynamic Loading

J-17

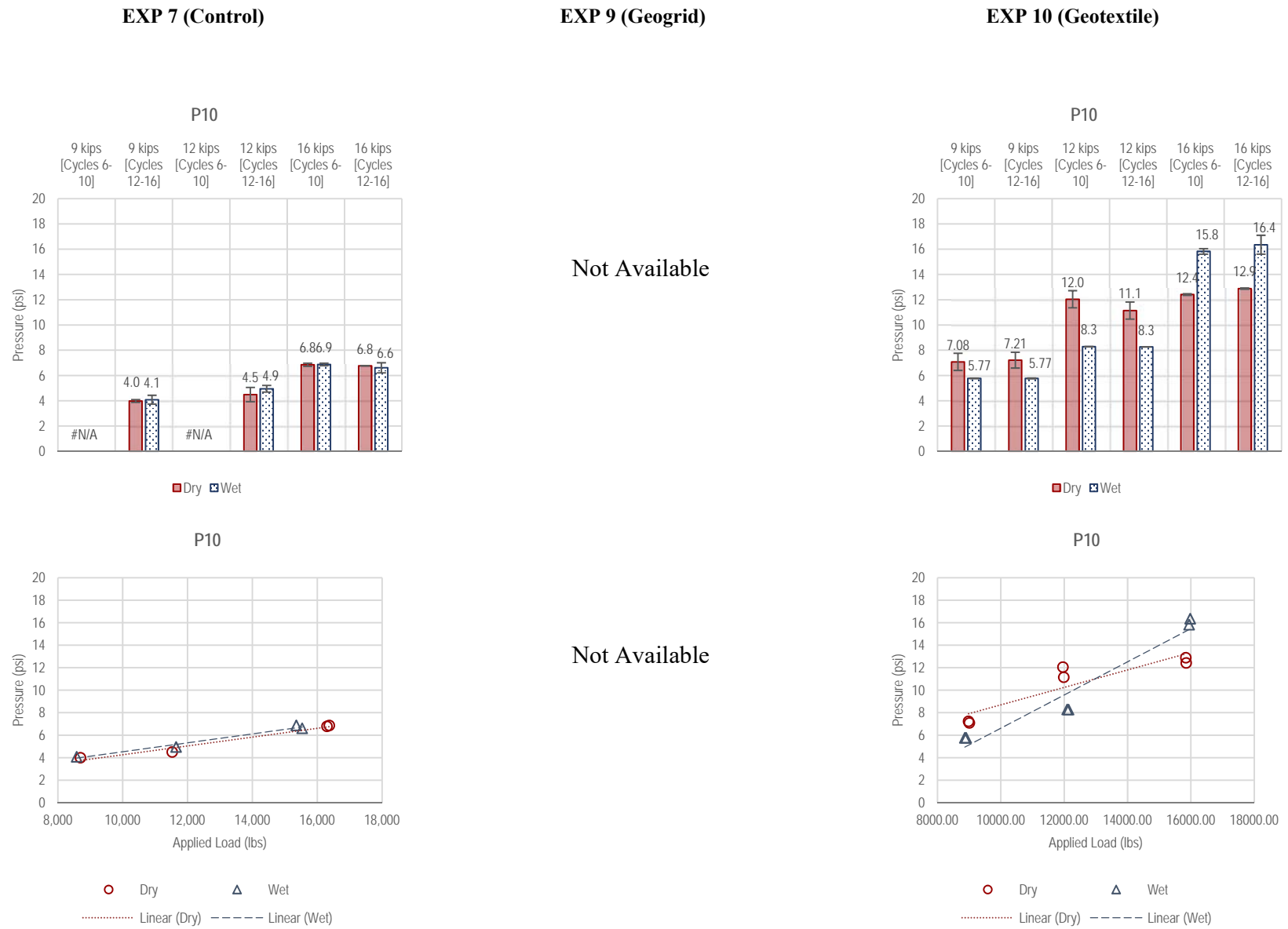


Figure J1-15. Summary of P10 measurements—Dynamic Loading

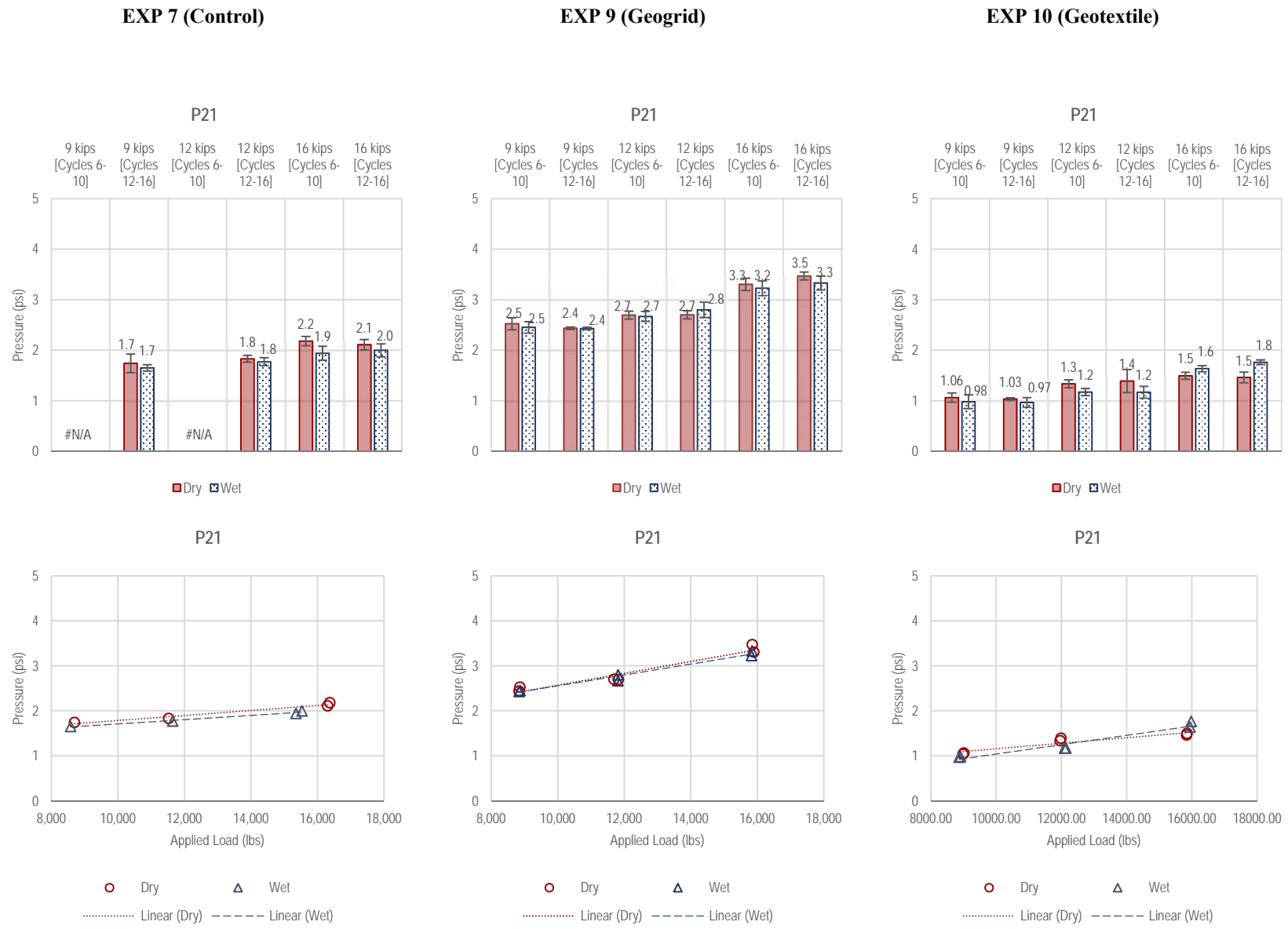


Figure J1-16. Summary of P21 measurements—Dynamic Loading

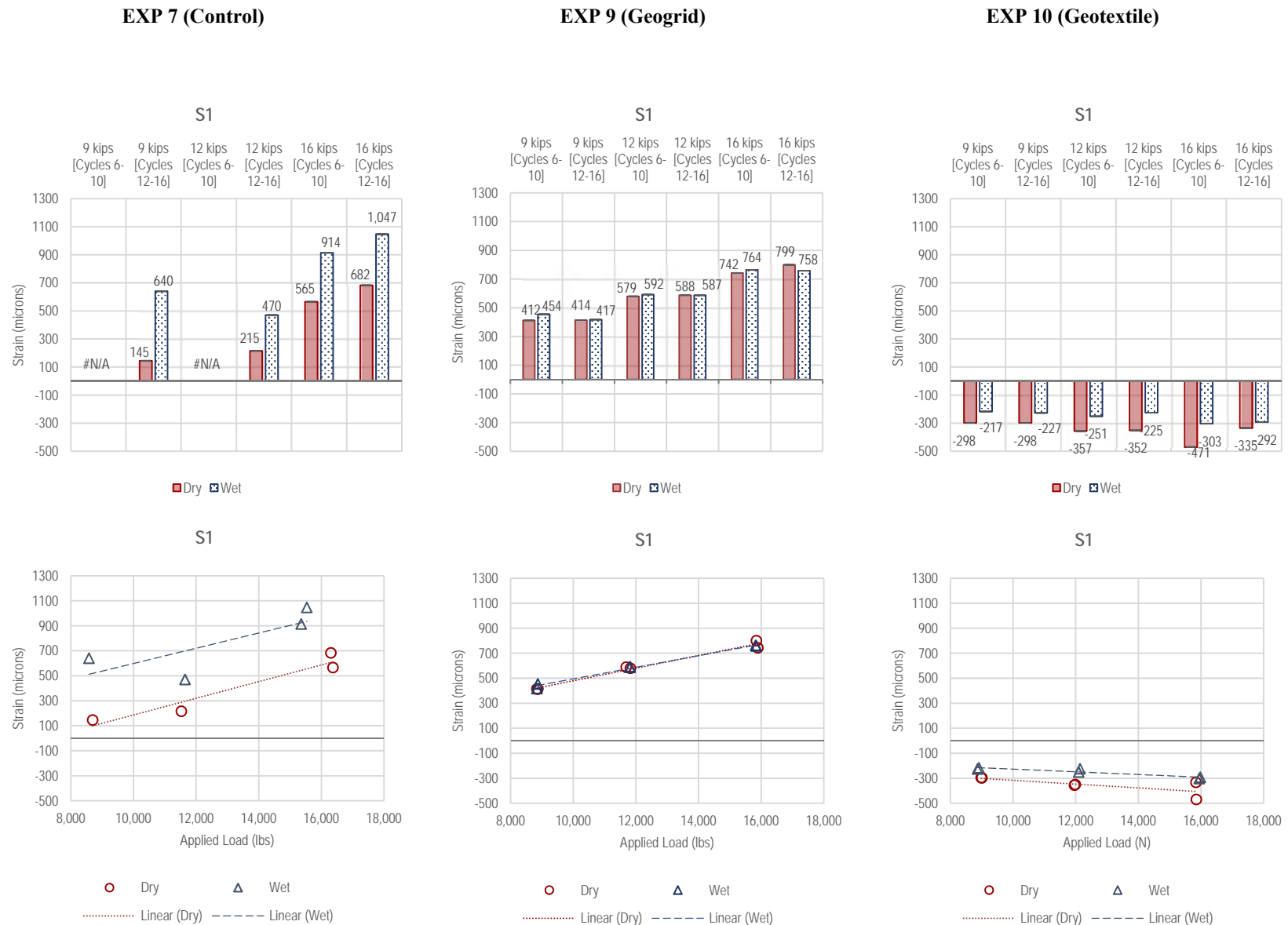


Figure J1-17. Summary of S1 measurements—Dynamic Loading

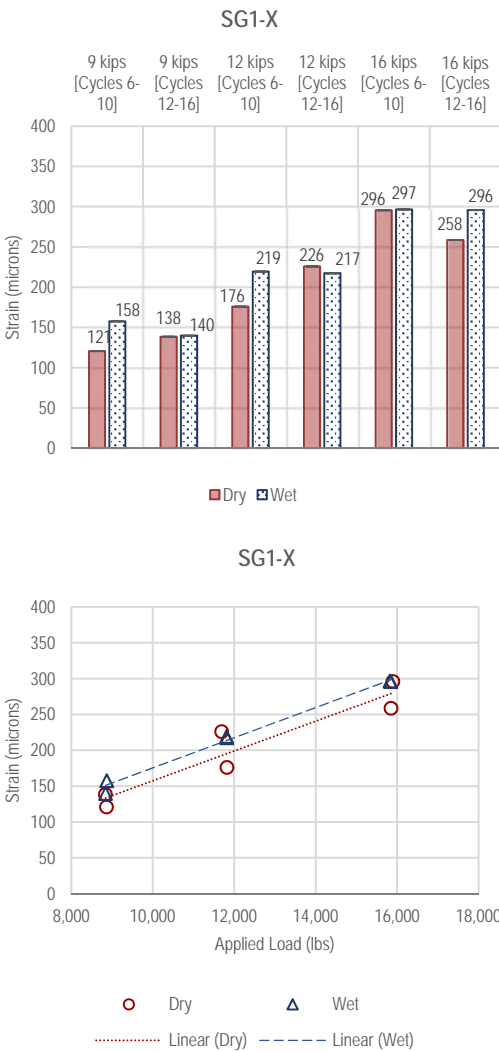
EXP 7 (Control)

EXP 9 (Geogrid)

EXP 10 (Geotextile)

Not Available

Not Available



Not Available

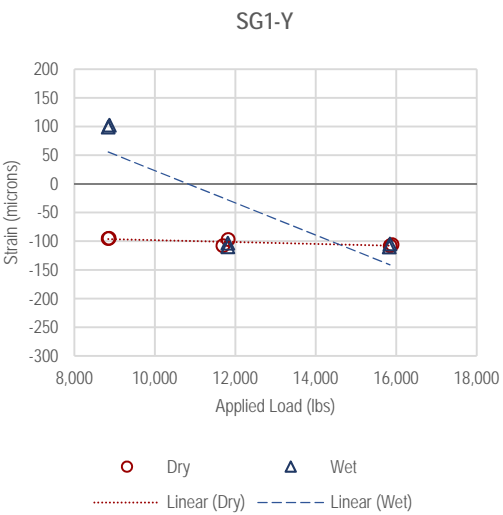
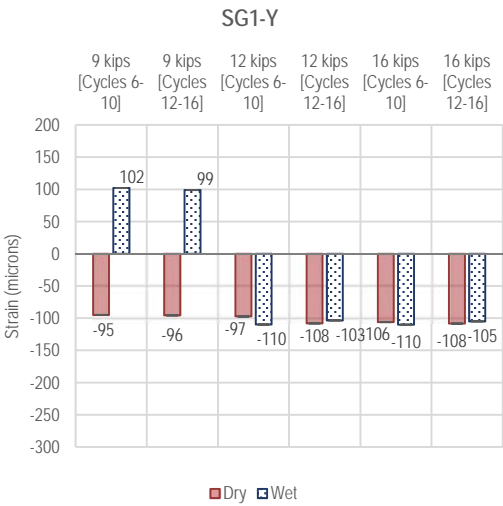
Not Available

Figure J1-18. Summary of SG1_X measurements—Dynamic Loading

EXP 7 (Control)

Not Available

EXP 9 (Geogrid)



EXP 10 (Geotextile)

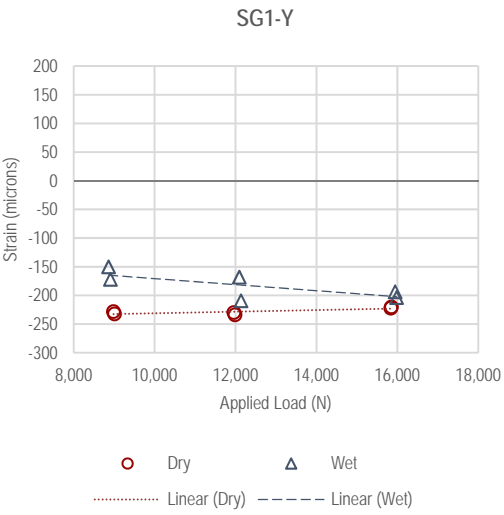
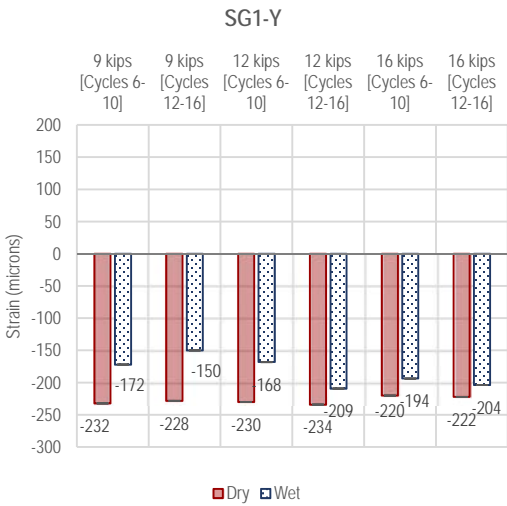


Figure J1-19. Summary of SG1_Y measurements—Dynamic Loading

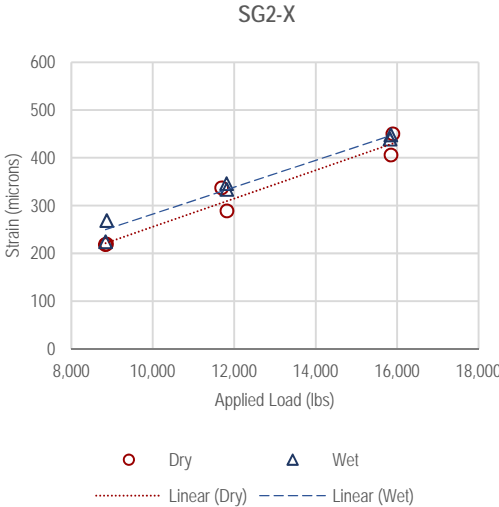
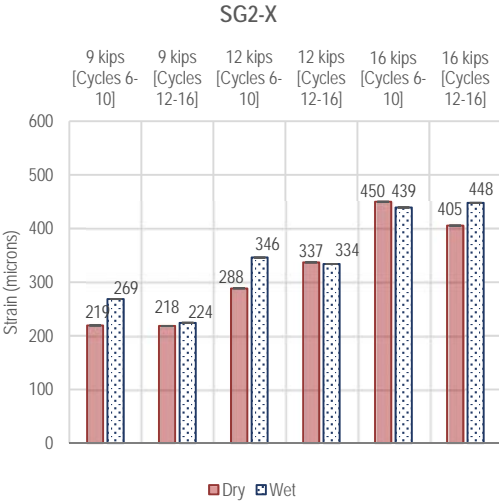
EXP 7 (Control)

EXP 9 (Geogrid)

EXP 10 (Geotextile)

Not Available

Not Available



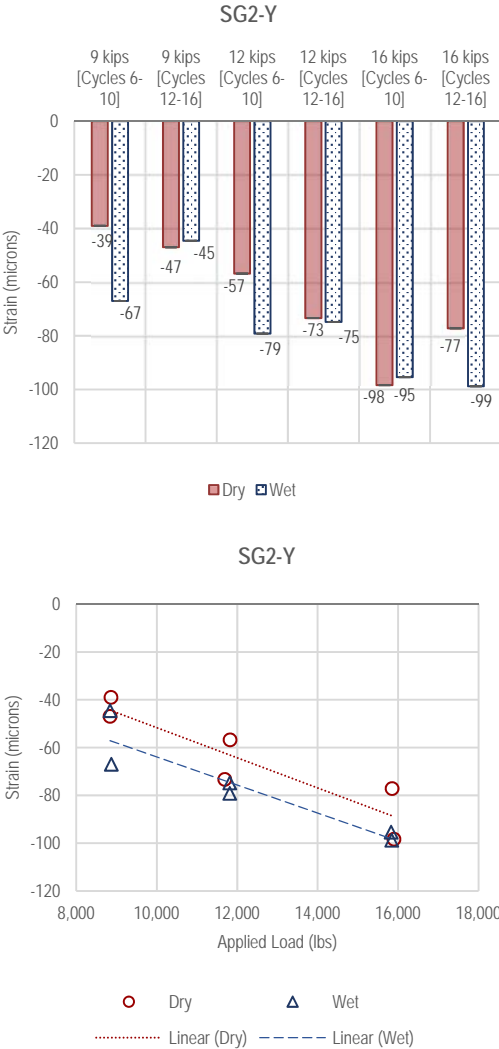
Not Available

Figure J1-20. Summary of SG2_X measurements—Dynamic Loading

EXP 7 (Control)

Not Available

EXP 9 (Geogrid)



EXP 10 (Geotextile)

Not Available

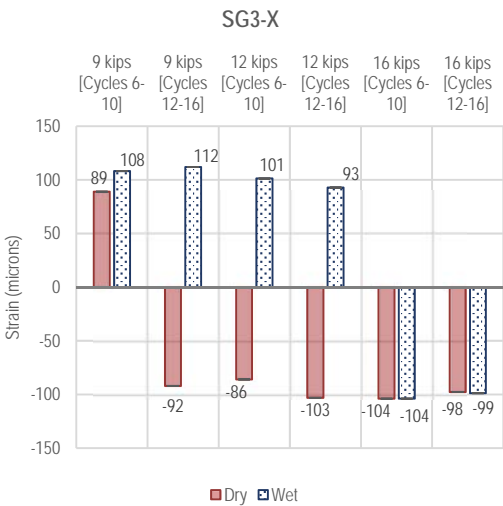
Not Available

Figure J1-21. Summary of SG2_Y measurements—Dynamic Loading

EXP 7 (Control)

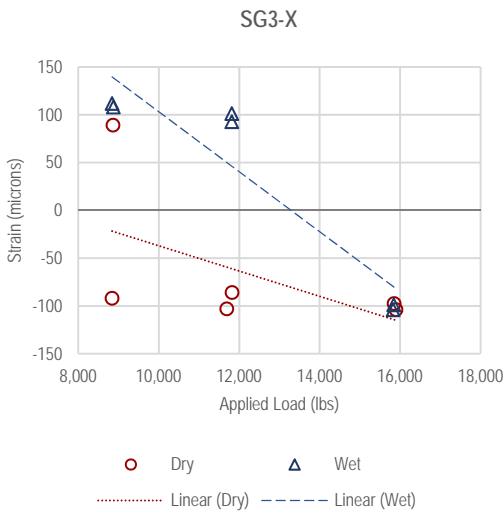
Not Available

EXP 9 (Geogrid)



EXP 10 (Geotextile)

Not Available



Not Available

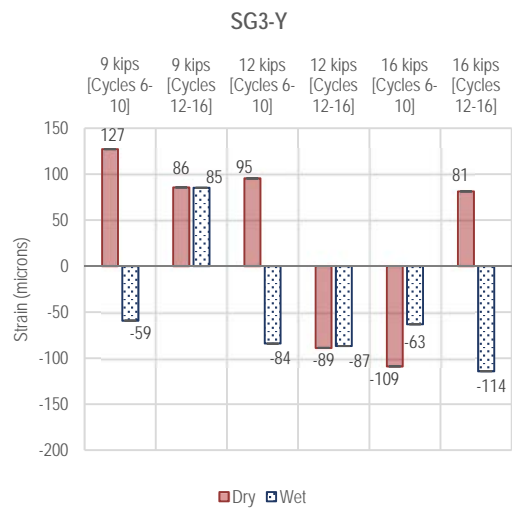
Not Available

Figure J1-22. Summary of SG3_X measurements—Dynamic Loading

EXP 7 (Control)

Not Available

EXP 9 (Geogrid)



EXP 10 (Geotextile)

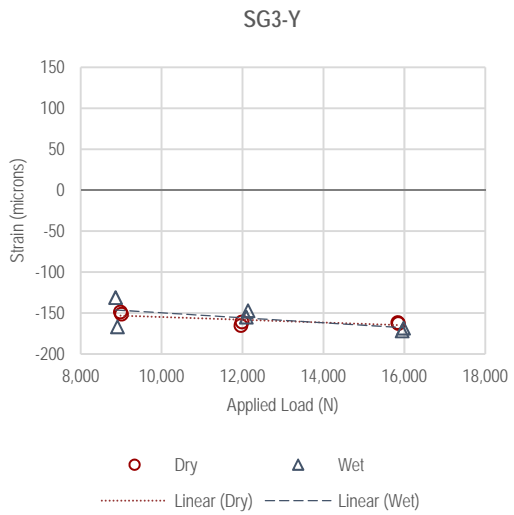
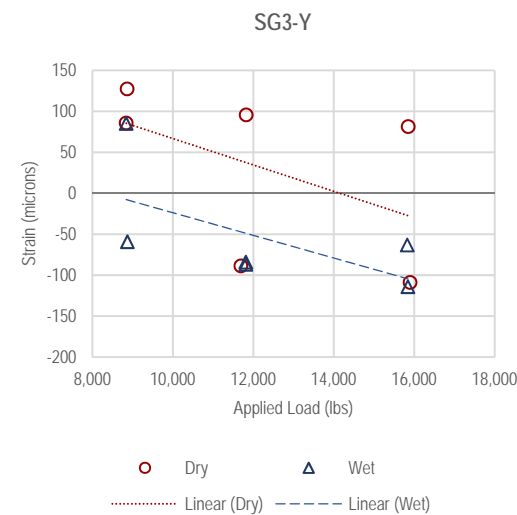
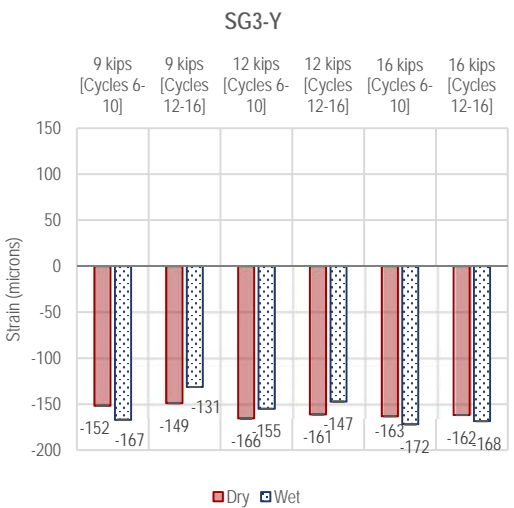
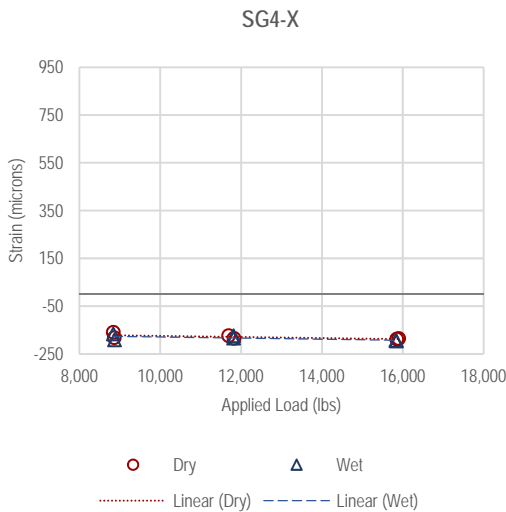
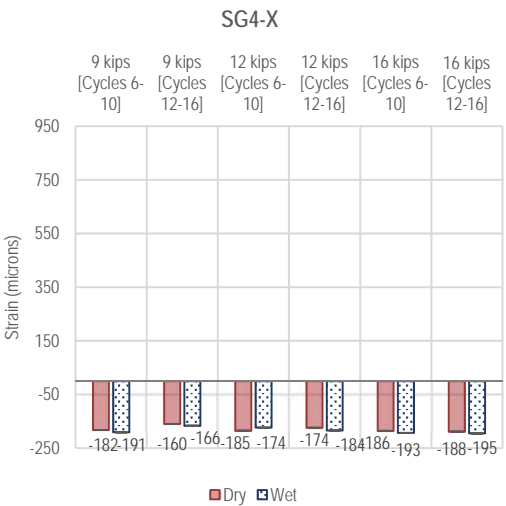


Figure J1-23. Summary of SG3_Y measurements—Dynamic Loading

EXP 7 (Control)

Not Available

EXP 9 (Geogrid)



EXP 10 (Geotextile)

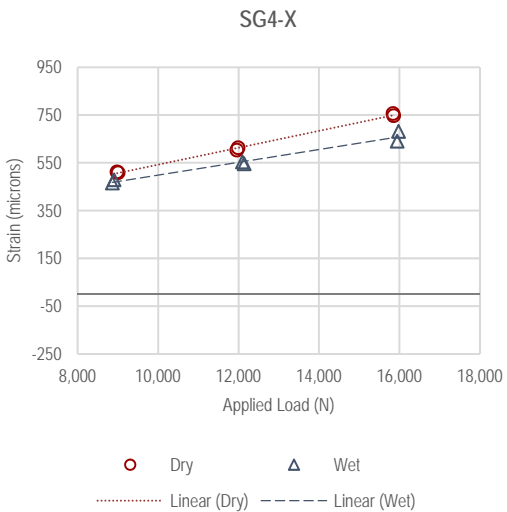
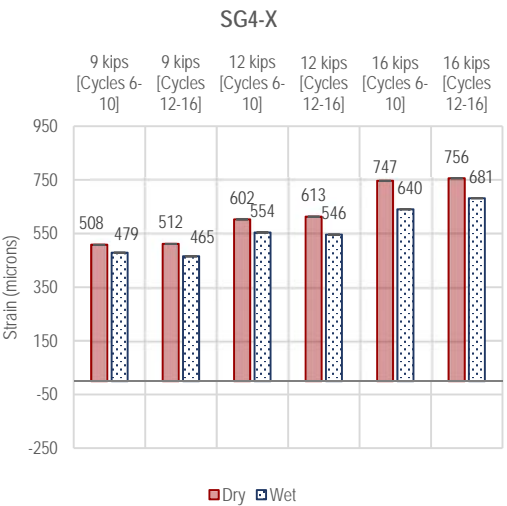


Figure J1-24. Summary of SG4_X measurements—Dynamic Loading

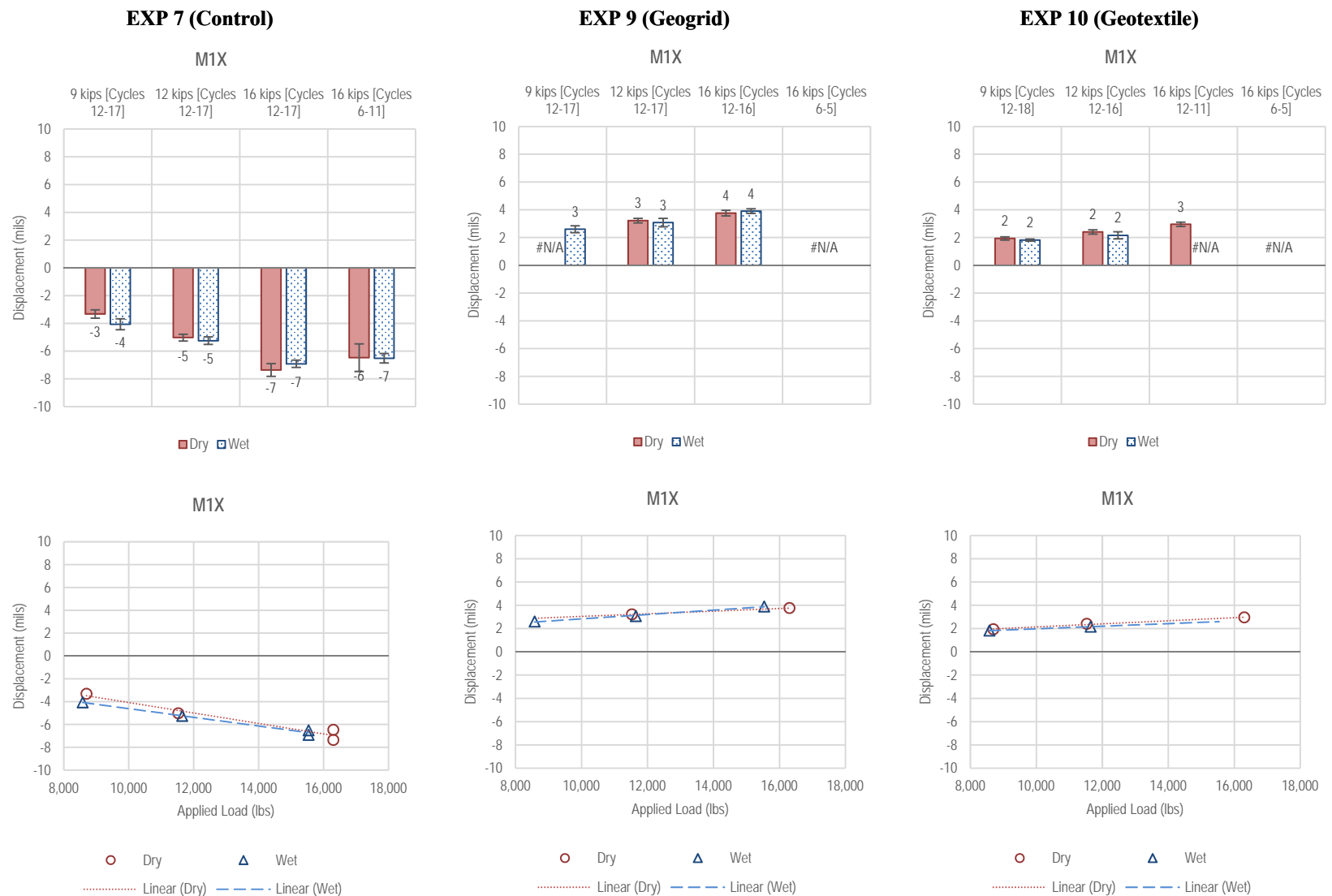


Figure J1-25. Summary of M1X measurements—Dynamic Loading

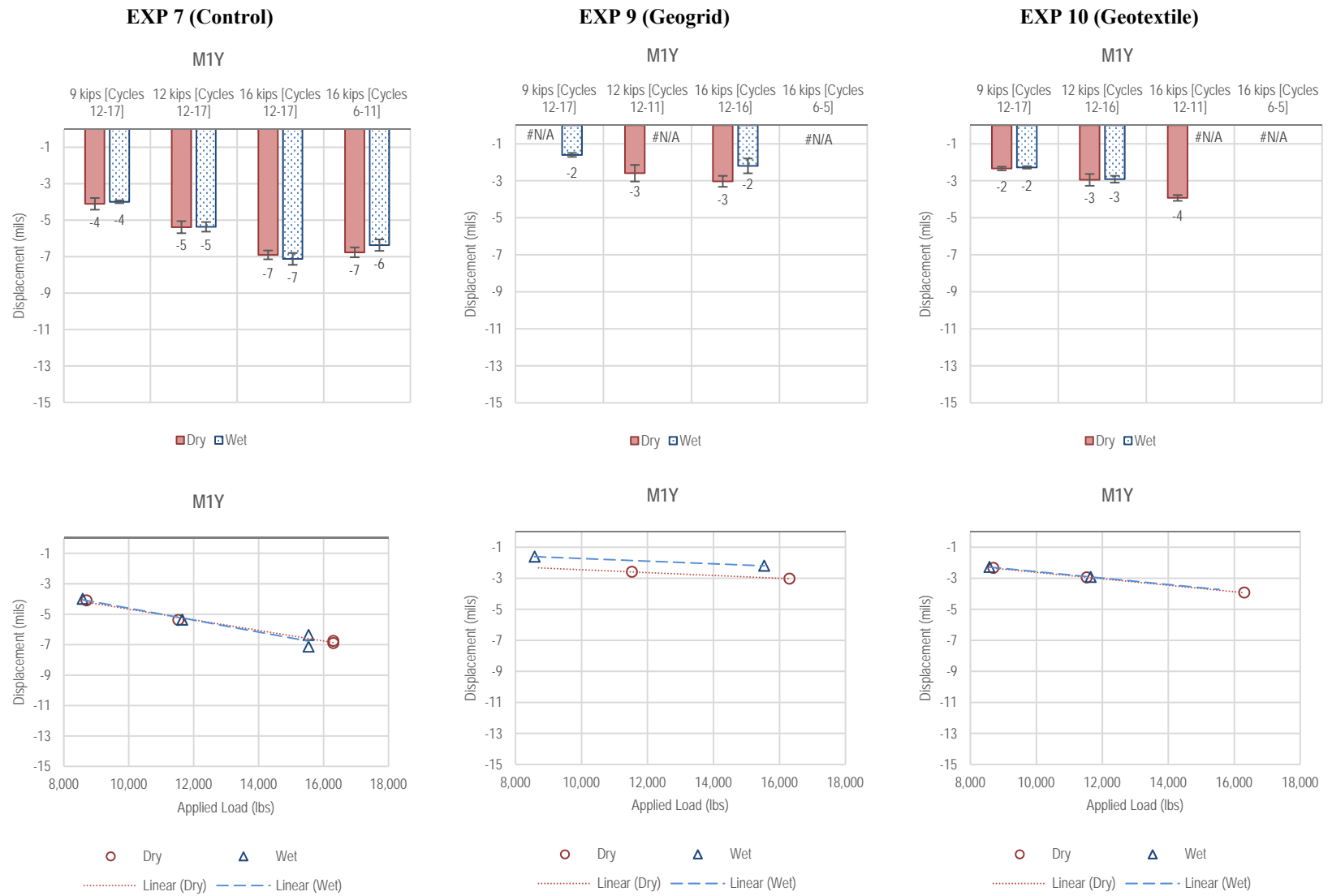


Figure J1-26. Summary of M1Y measurements—Dynamic Loading

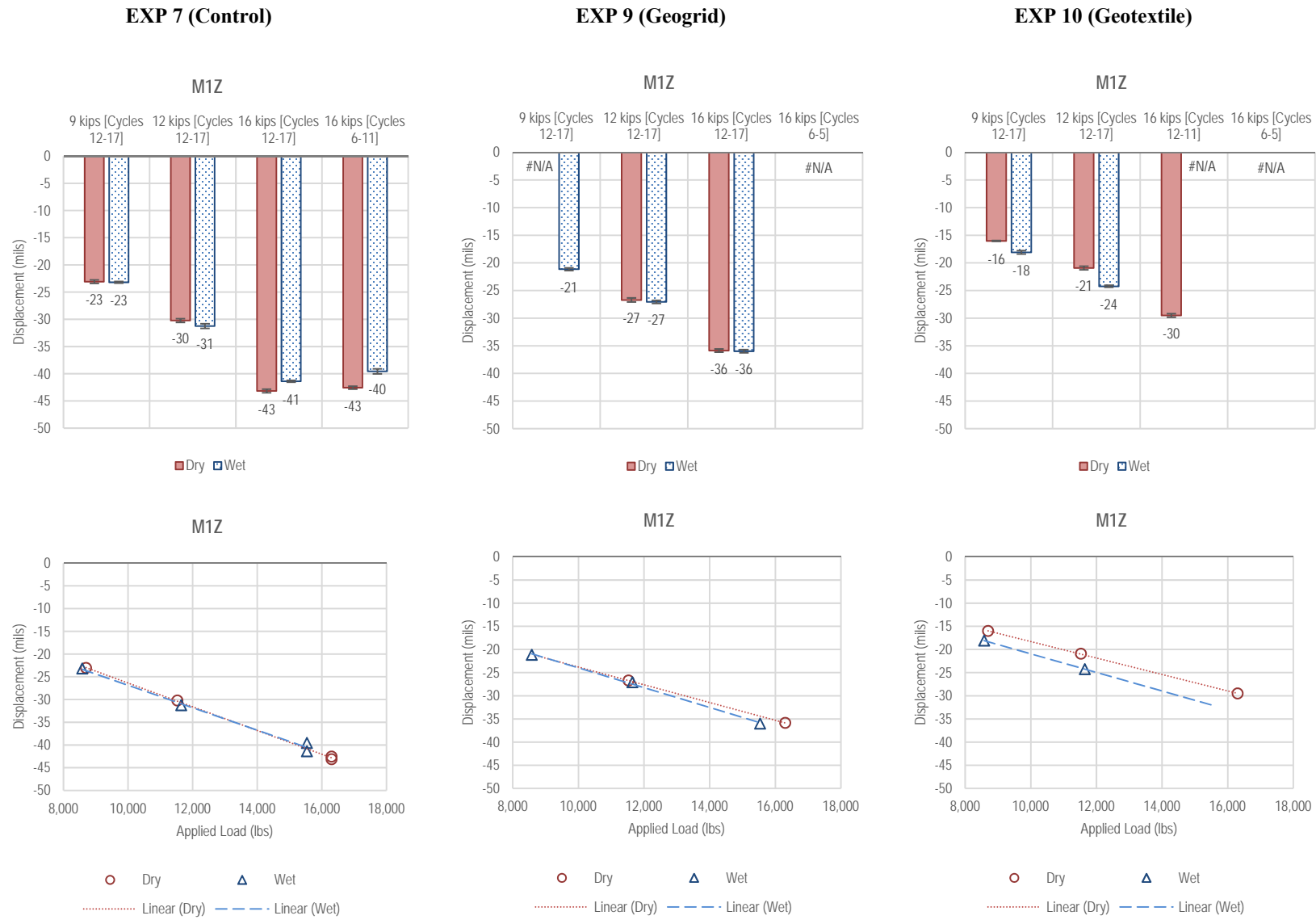


Figure J1-27. Summary of M1Z measurements—Dynamic Loading

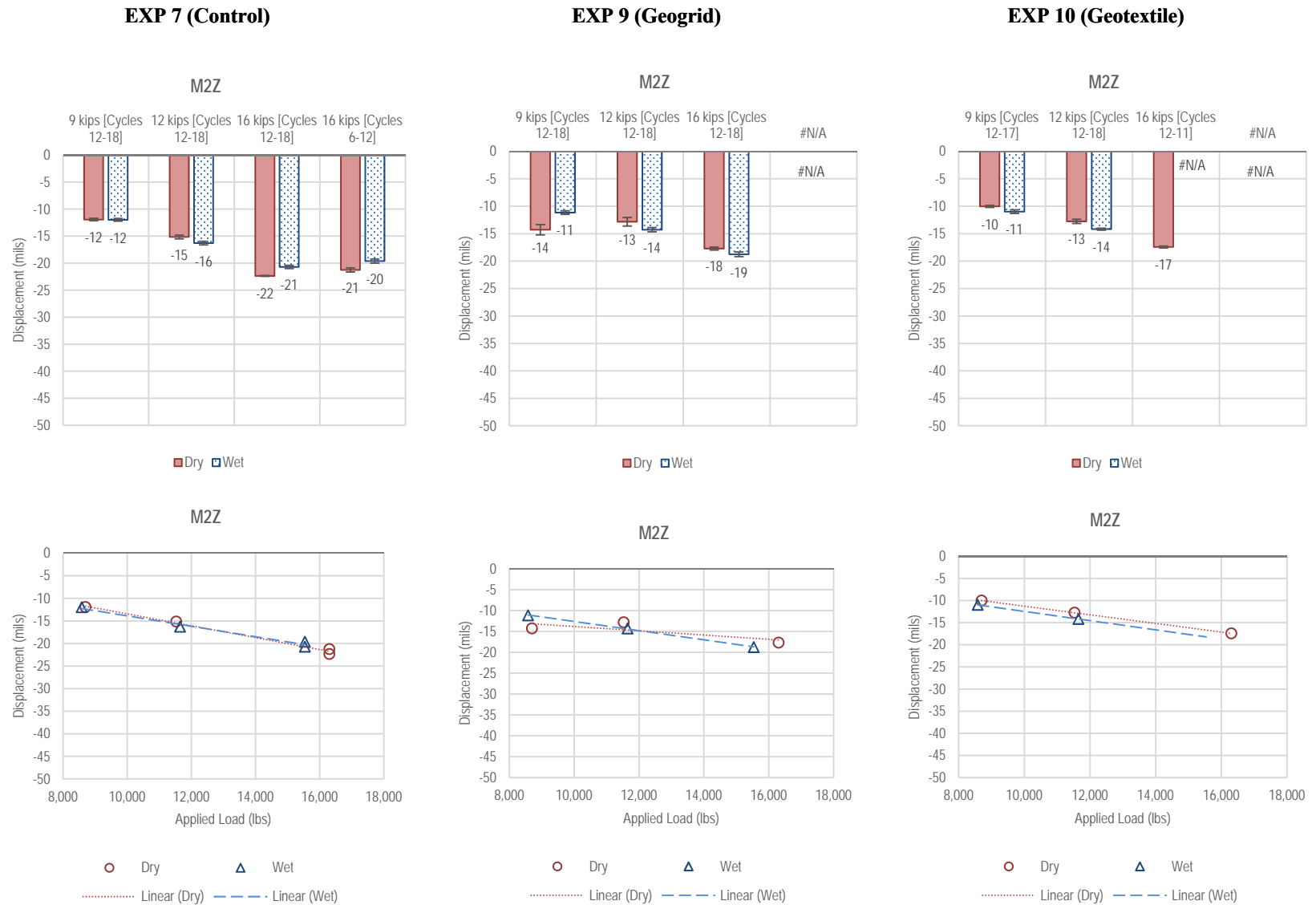


Figure J1-28. Summary of M2Z measurements—Dynamic Loading

J-31

EXP 7 (Control)

Not Available

Not Available

EXP 9 (Geogrid)

Not Available

Not Available

EXP 10 (Geotextile)

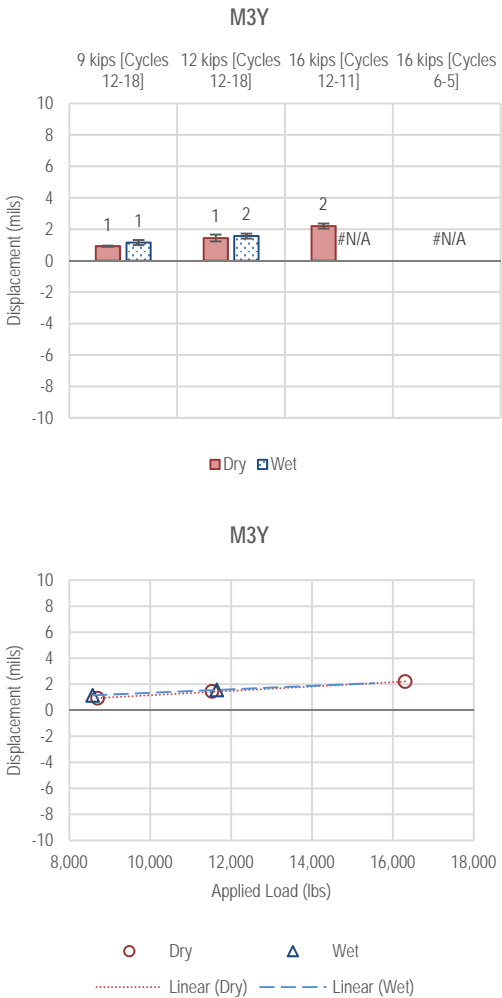
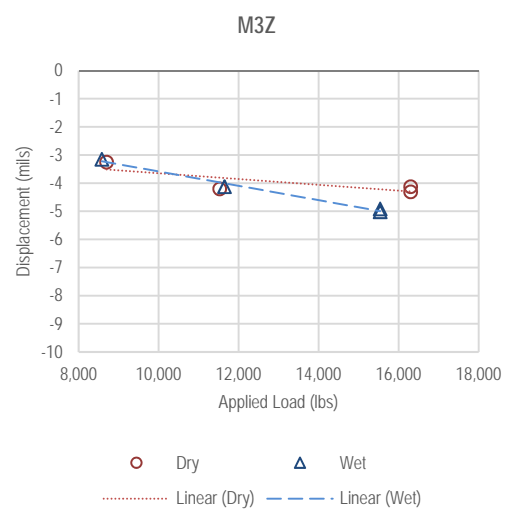
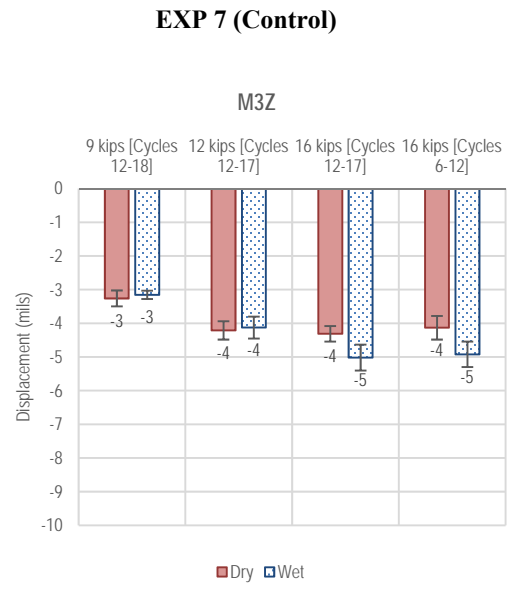


Figure J1-29. Summary of M3Y measurements—Dynamic Loading

J-32



EXP 9 (Geogrid)

Not Available

Not Available

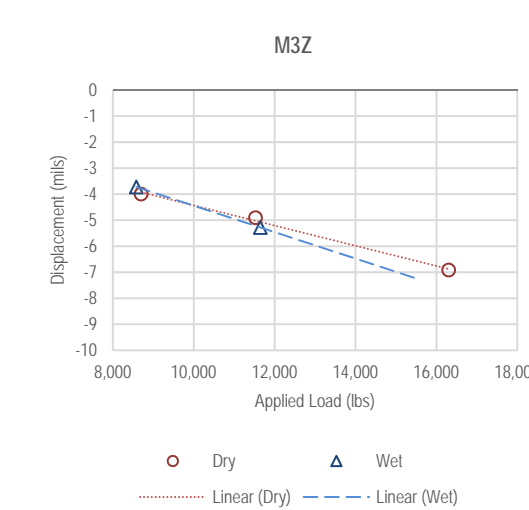
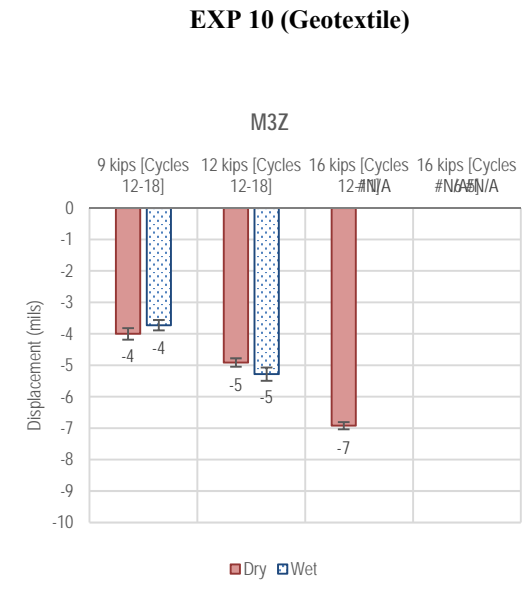


Figure J1-30. Summary of M3Z measurements—Dynamic Loading

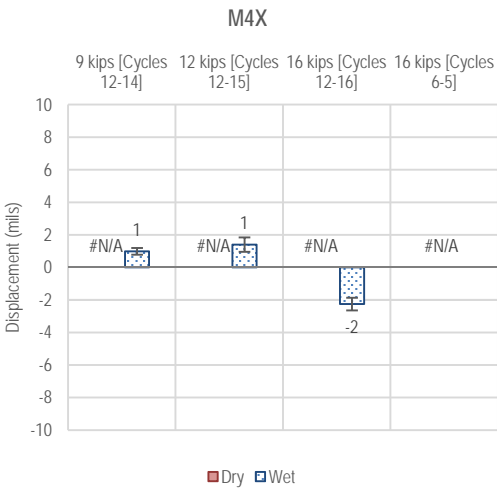
EXP 7 (Control)

EXP 9 (Geogrid)

EXP 10 (Geotextile)

Not Available

Not Available



Not Available

Not Available

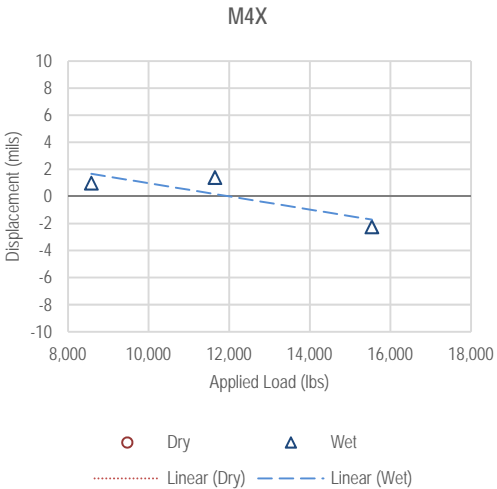
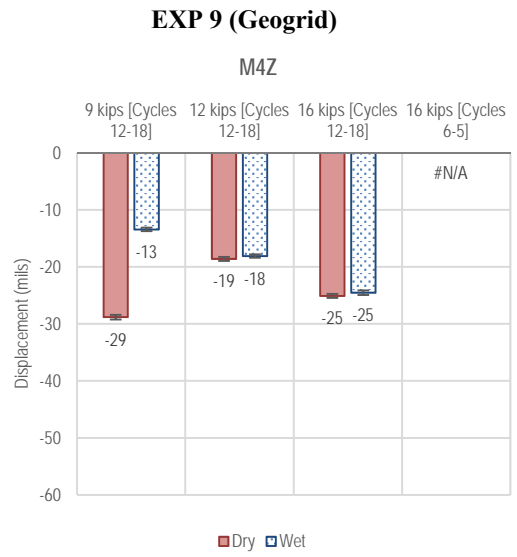
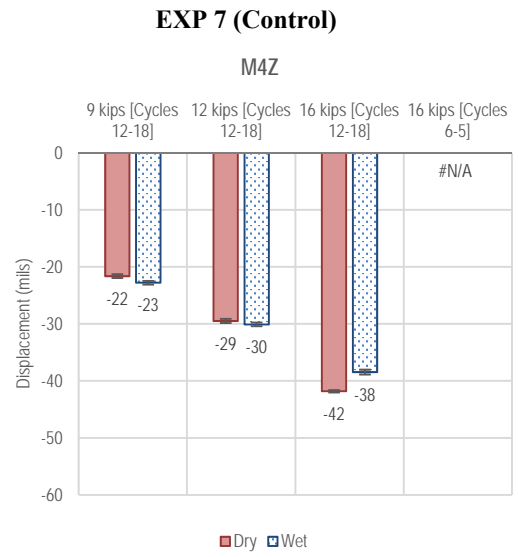
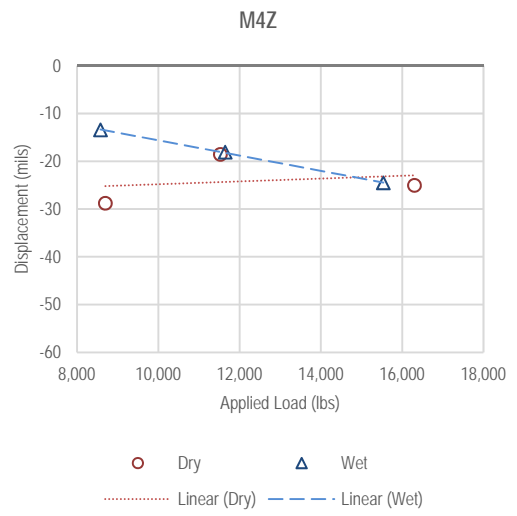
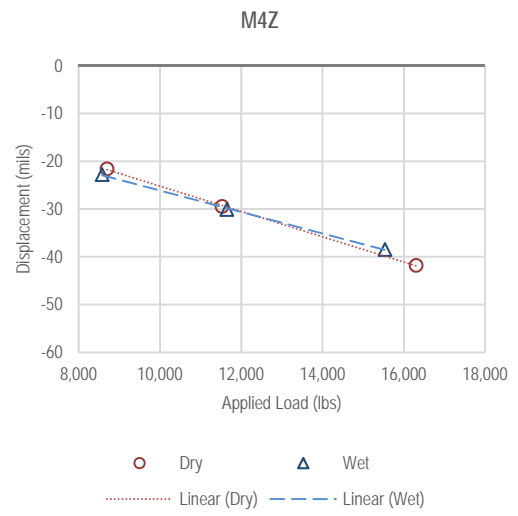


Figure J1-31. Summary of M4X measurements—Dynamic Loading



EXP 10 (Geotextile)

Not Available



Not Available

Figure J1-32. Summary of M4Z measurements—Dynamic Loading

J-34

EXP 7 (Control)

EXP 9 (Geogrid)

EXP 10 (Geotextile)

Not Available

Not Available

Not Available

Not Available

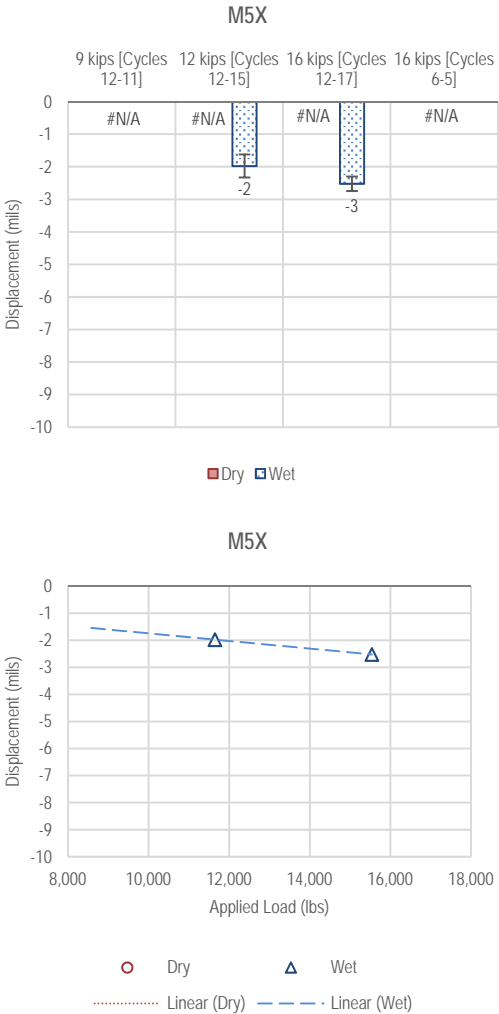
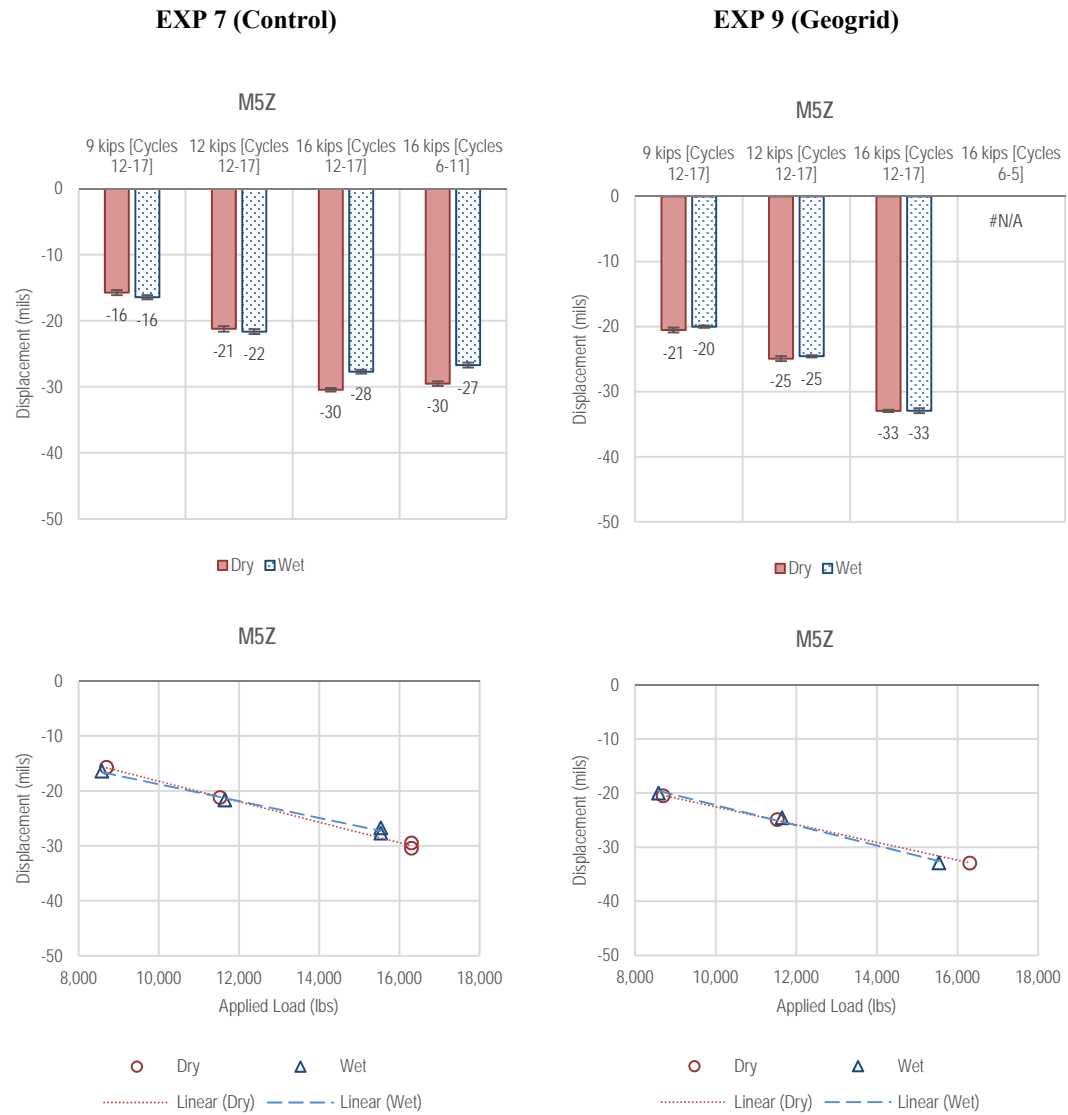


Figure J1-33. Summary of M5X measurements—Dynamic Loading

J-36

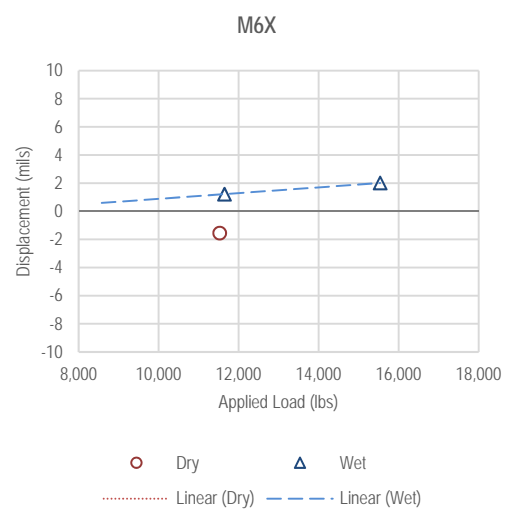
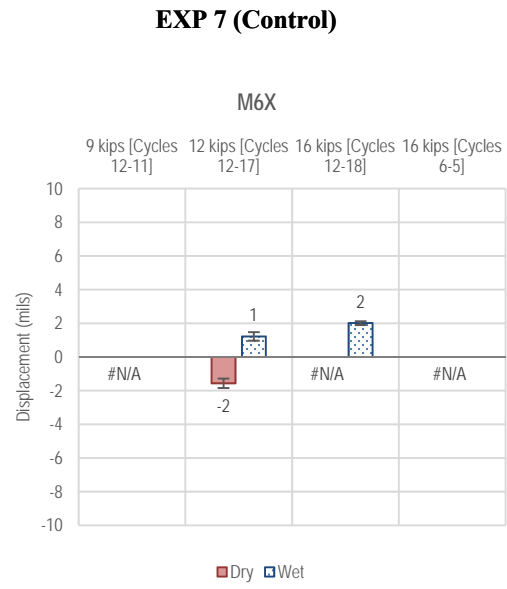


Not Available

Not Available

Figure J1-34. Summary of M5Z measurements—Dynamic Loading

J-37



EXP 9 (Geogrid)

Not Available

Not Available

EXP 10 (Geotextile)

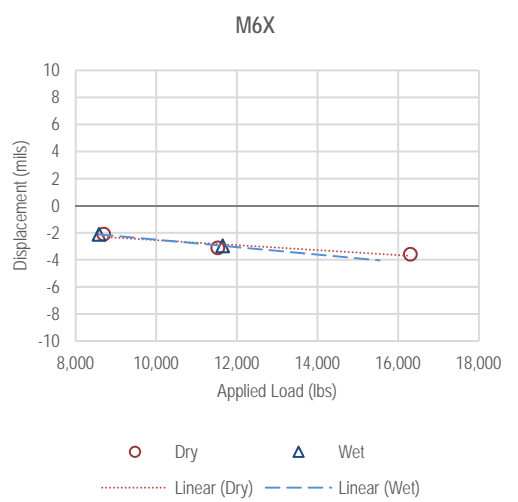
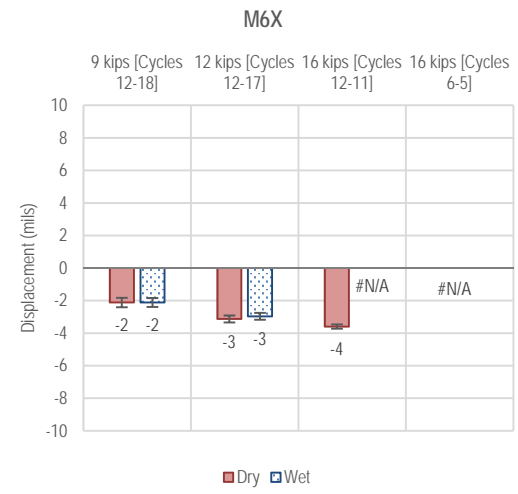
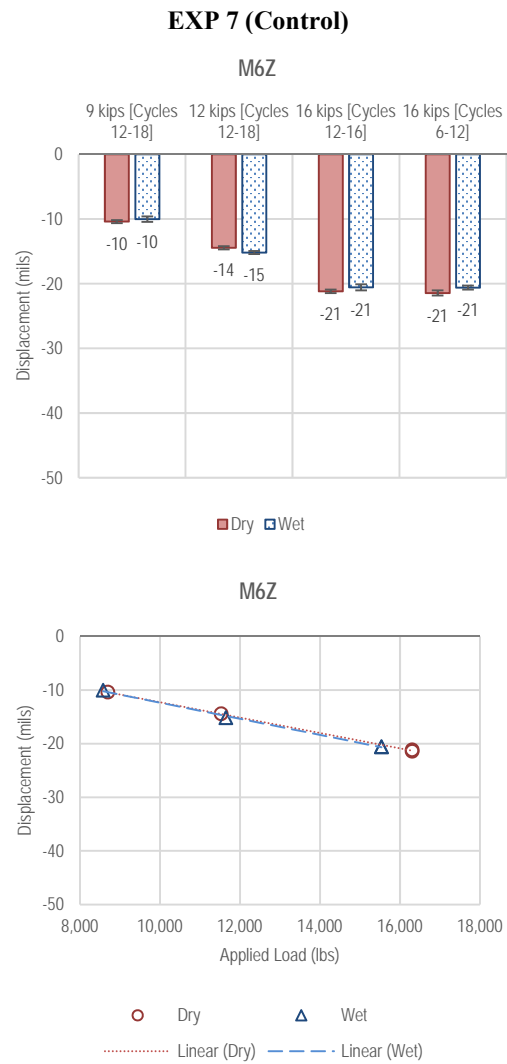


Figure J1-35. Summary of M6X measurements—Dynamic Loading

J-38



EXP 9 (Geogrid)

Not Available

Not Available

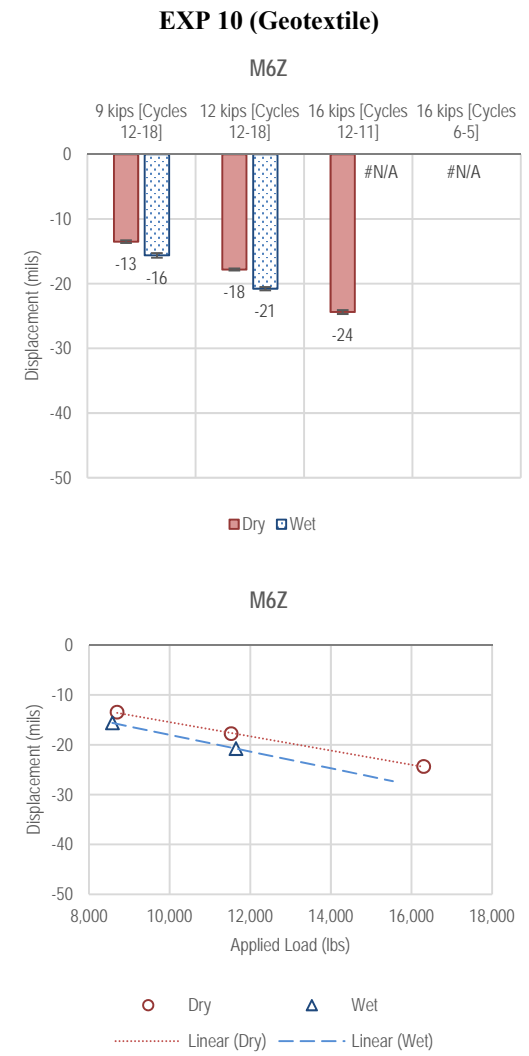


Figure J1-36. Summary of M6Z measurements—Dynamic Loading

J-39

EXP 7 (Control)

Not Available

Not Available

EXP 9 (Geogrid)

Not Available

Not Available

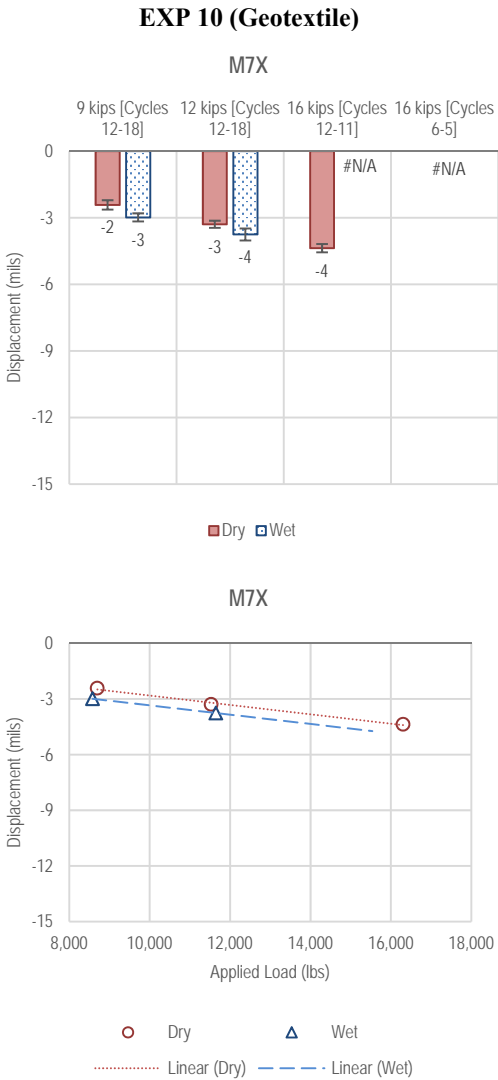


Figure J1-37. Summary of M7X measurements—Dynamic Loading

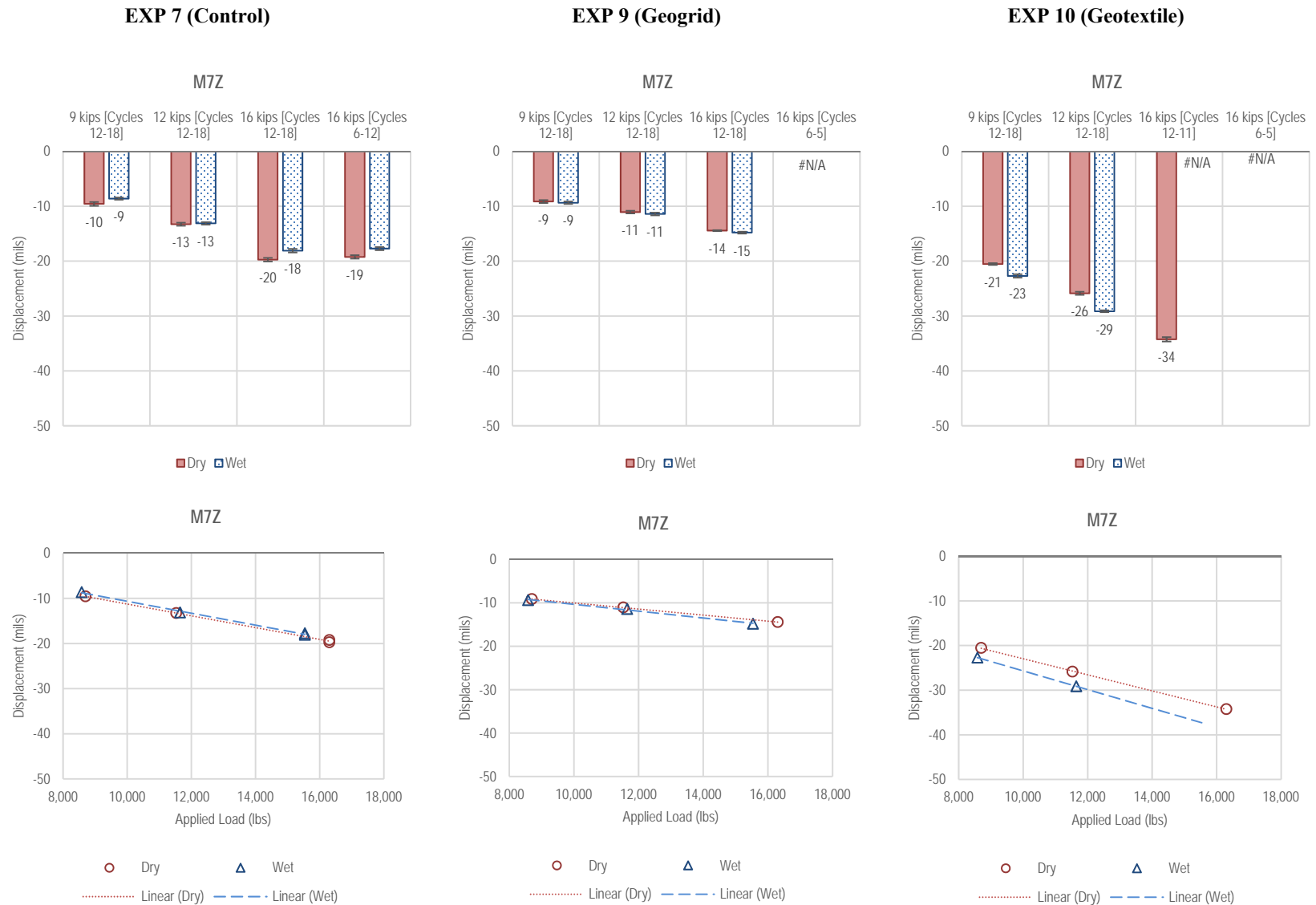
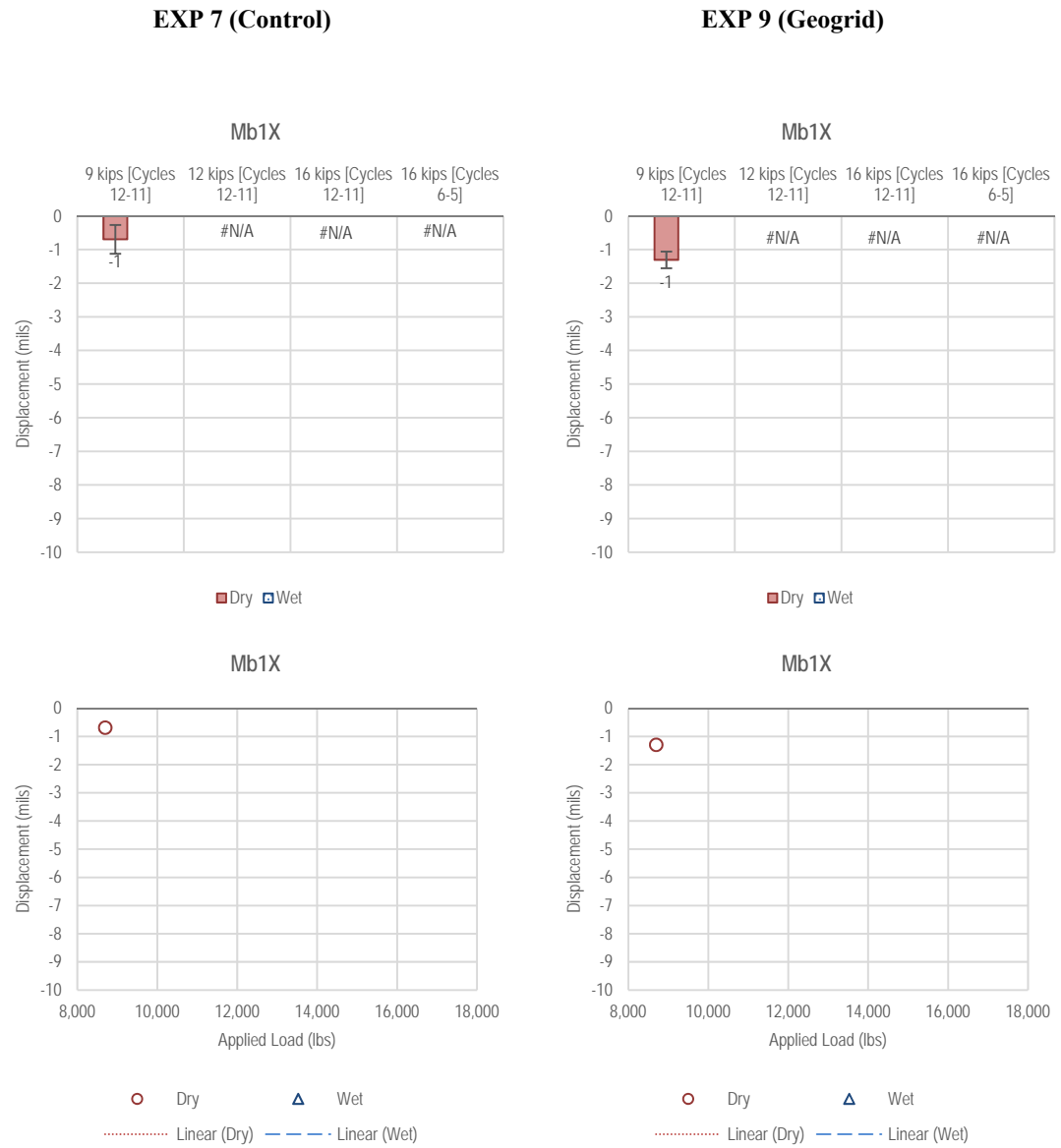


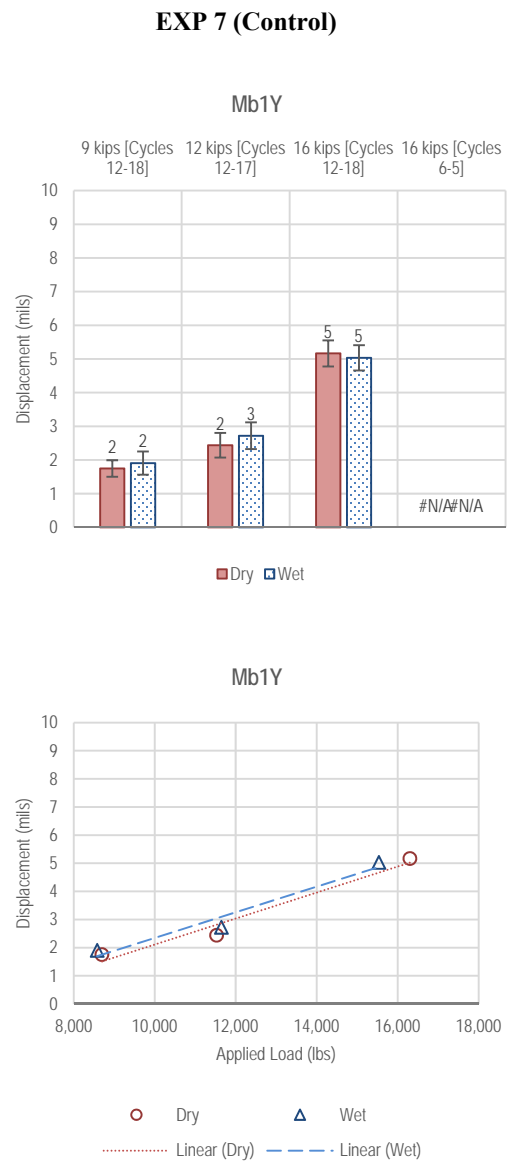
Figure J1-38. Summary of M7Z measurements—Dynamic Loading

J-40

J-41



J-42



EXP 9 (Geogrid)

Not Available

Not Available

EXP 10 (Geotextile)

Not Available

Not Available

Figure J1-40. Summary of Mb1Y measurements—Dynamic Loading

J-43

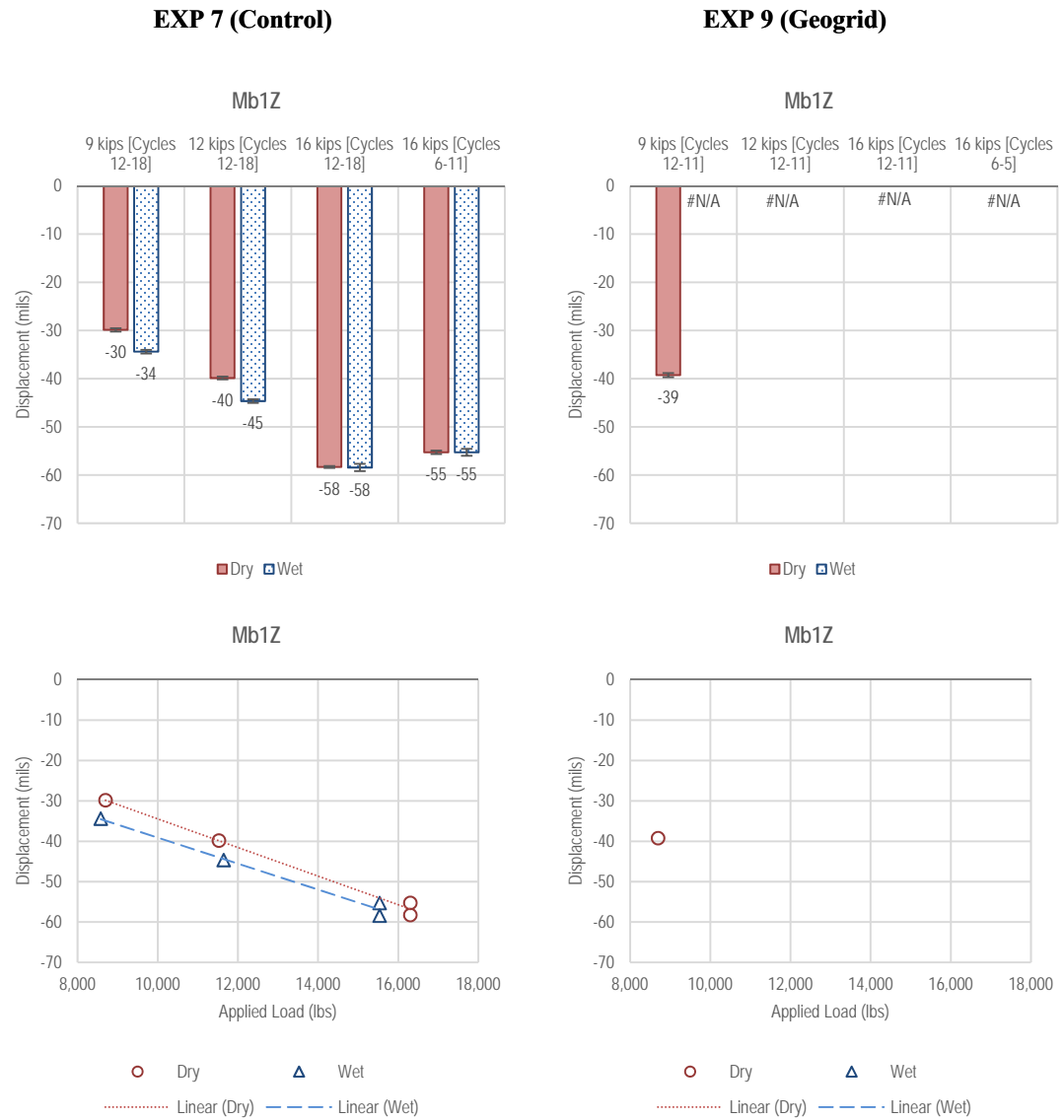


Figure J1-41. Summary of Mb1Z measurements—Dynamic Loading

J-44

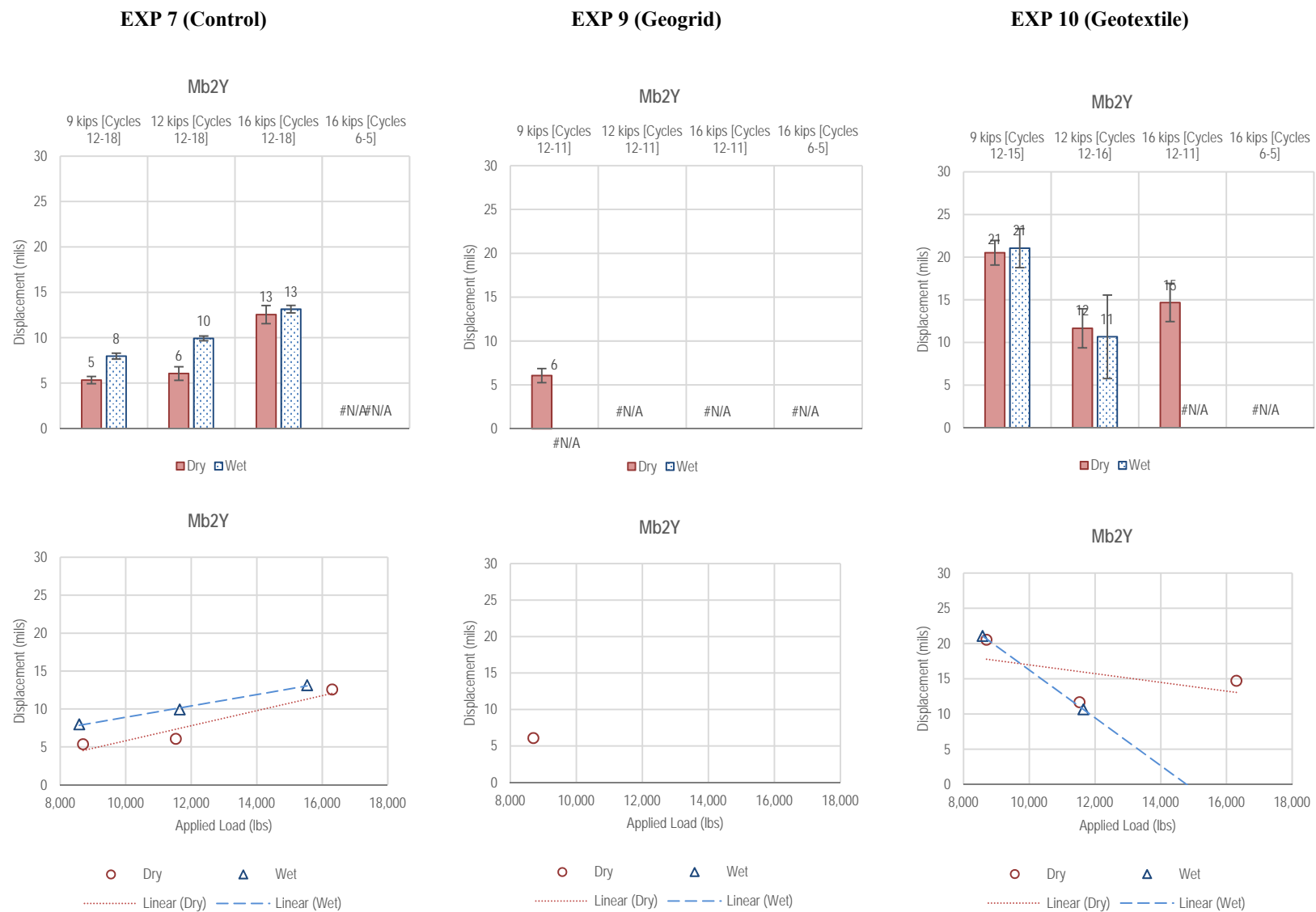


Figure J1-42. Summary of Mb2Y measurements—Dynamic Loading

J-45

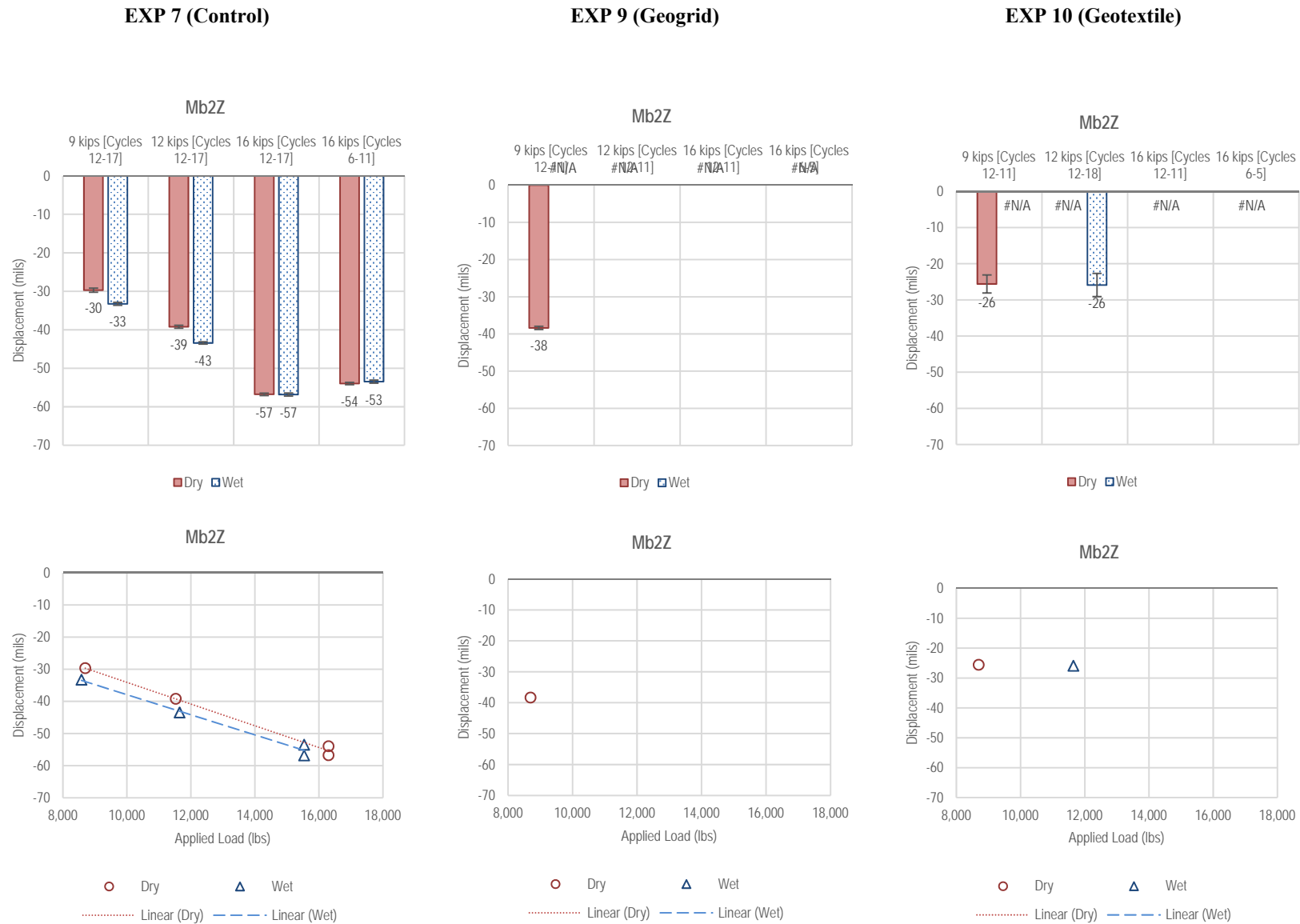


Figure J1-43. Summary of Mb2Z measurements—Dynamic Loading

J-46

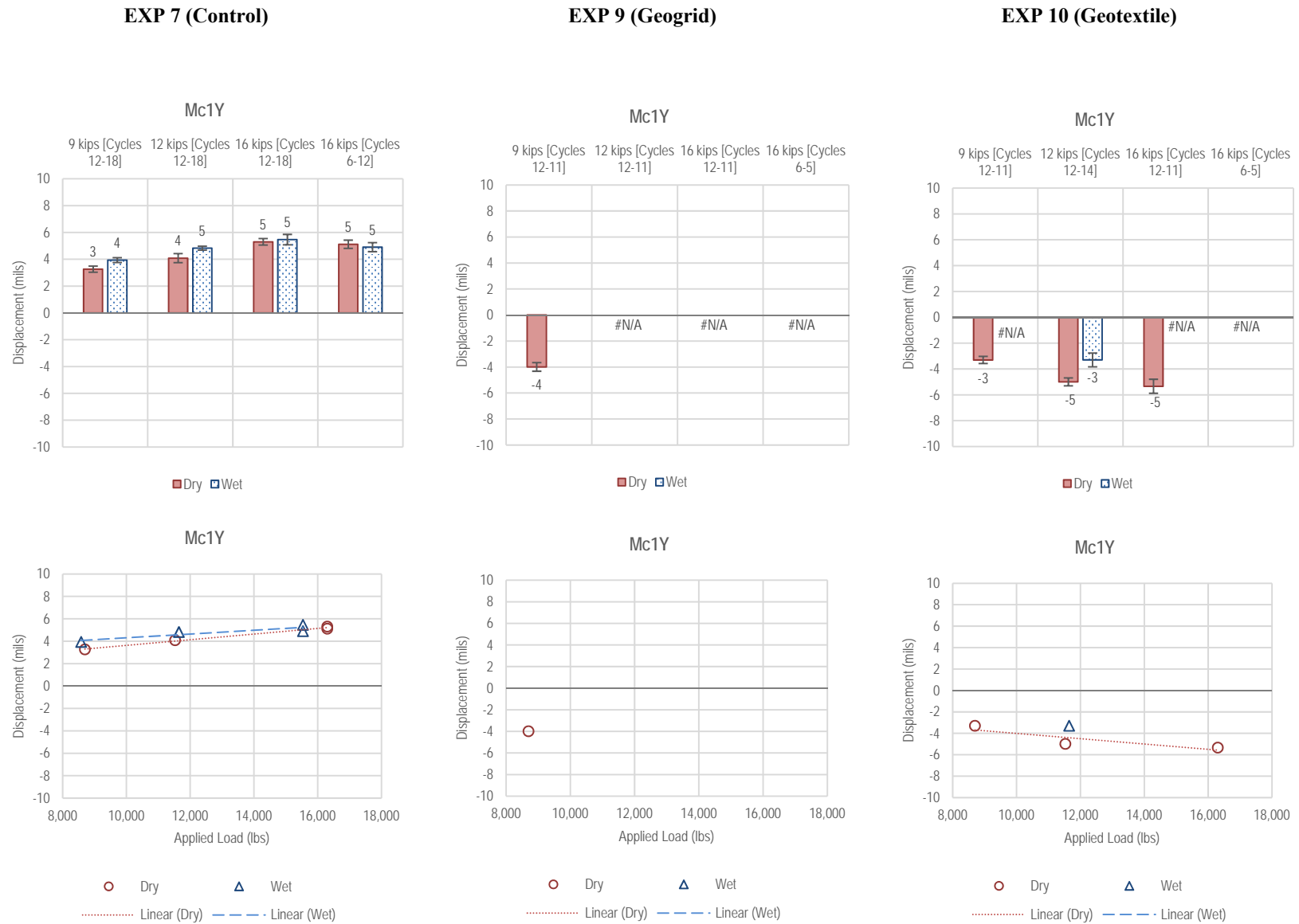


Figure J1-44. Summary of Mc1Y measurements—Dynamic Loading

J-47

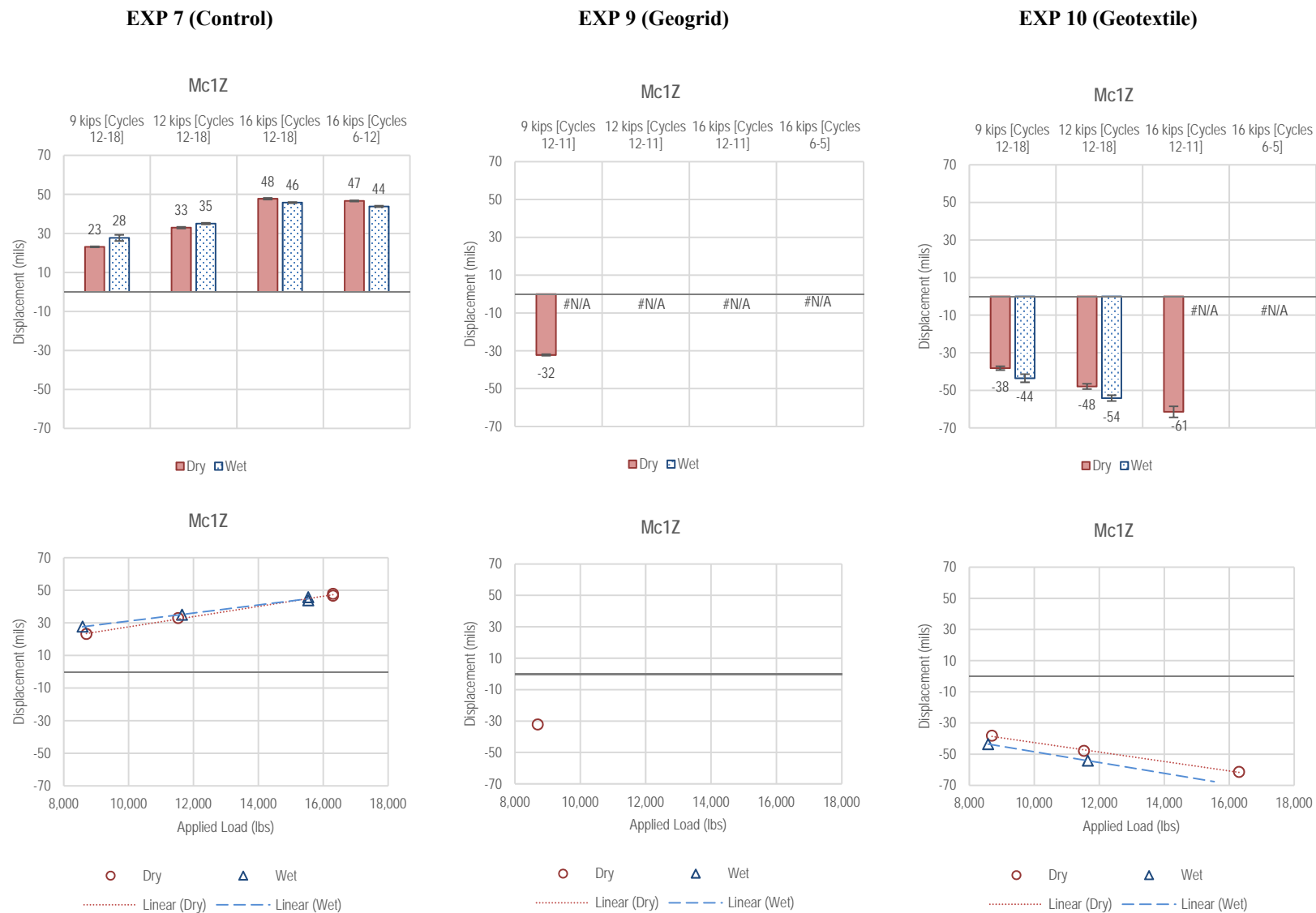


Figure J1-45. Summary of Mc1Z measurements—Dynamic Loading

J-48

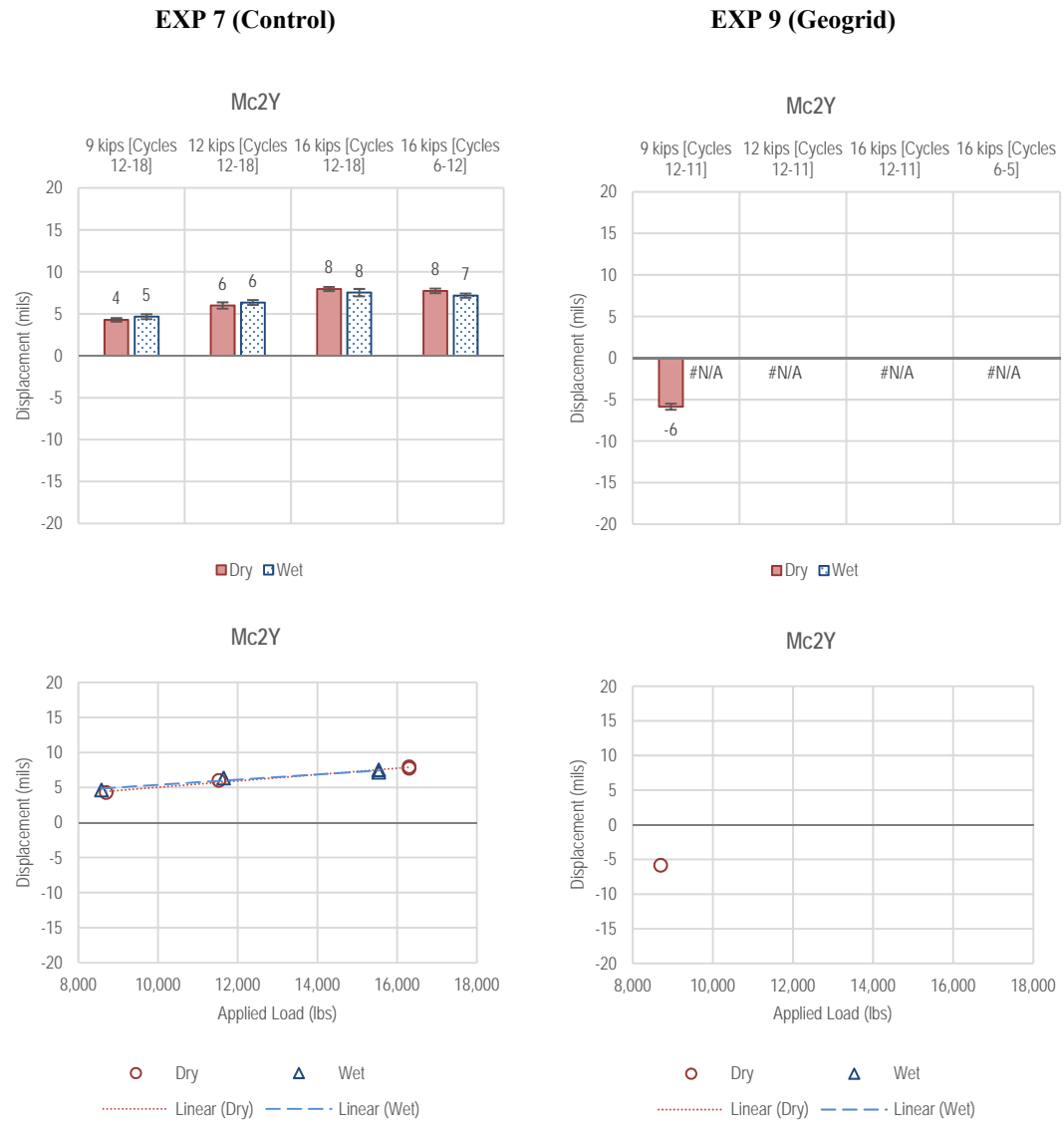


Figure J1-46. Summary of Mc2Y measurements—Dynamic Loading

J-49

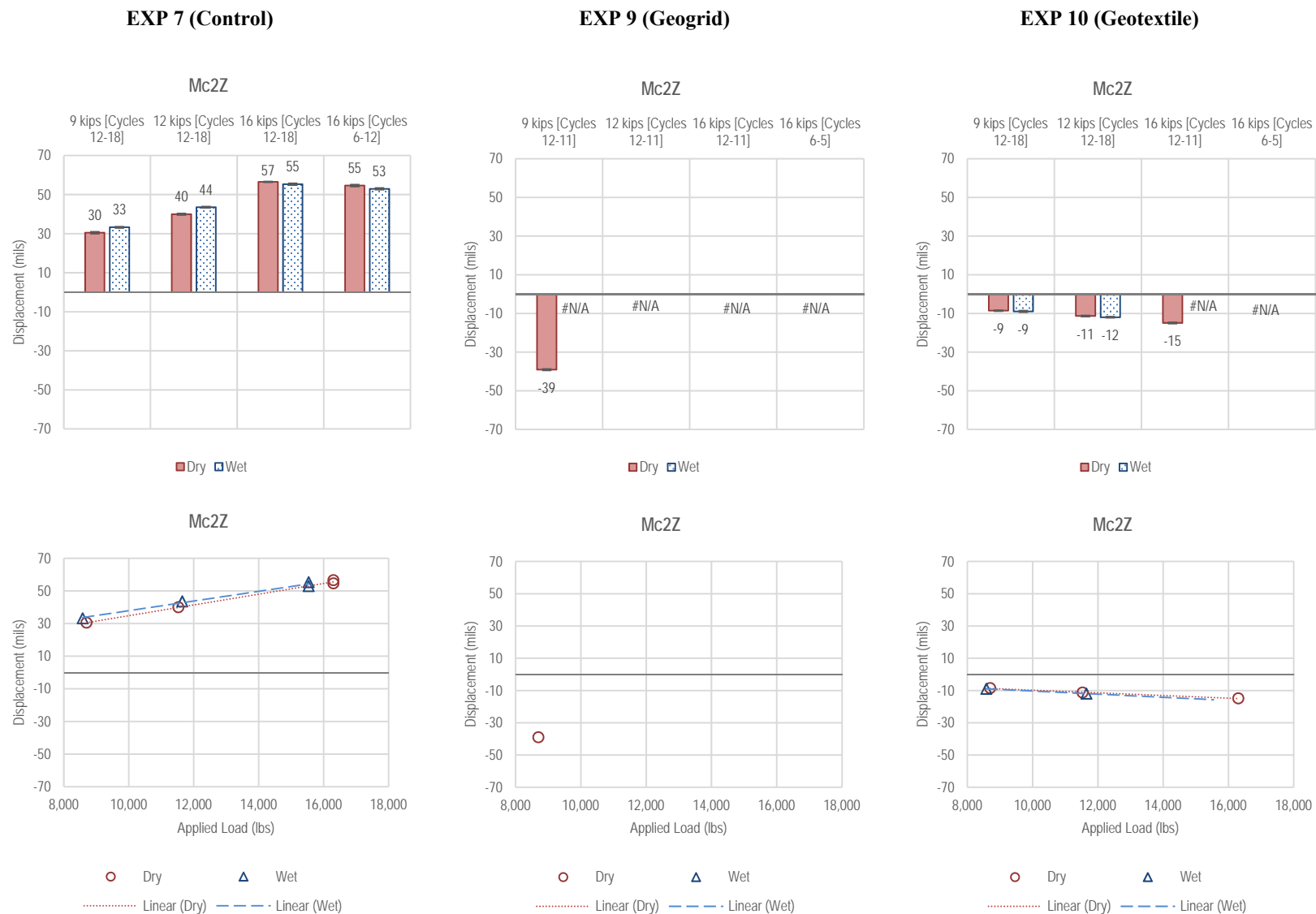


Figure J1-47. Summary of Mc2Z measurements—Dynamic Loading

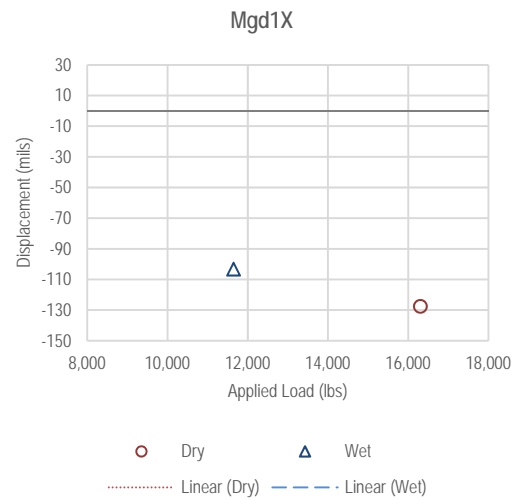
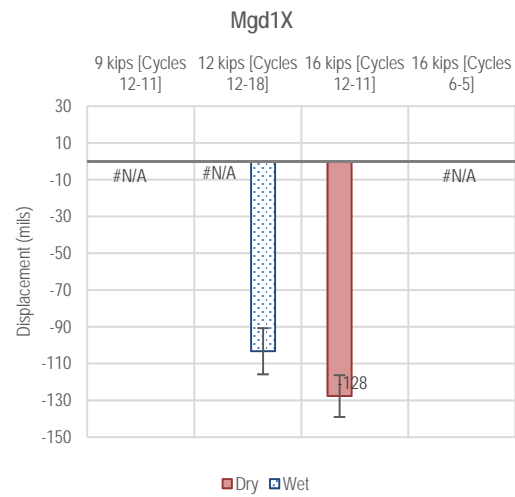
J-50

EXP 7 (Control)

Not Available

Not Available

EXP 9 (Geogrid)



EXP 10 (Geotextile)

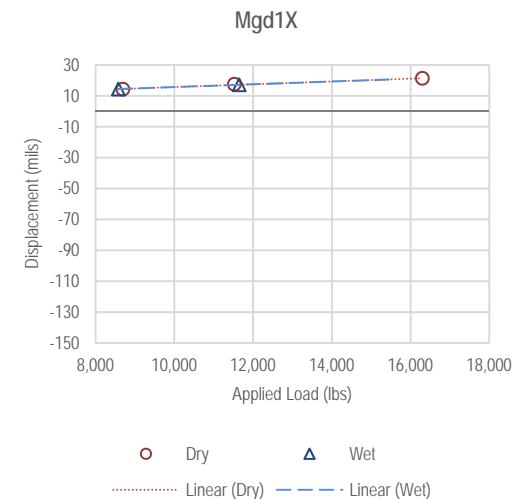
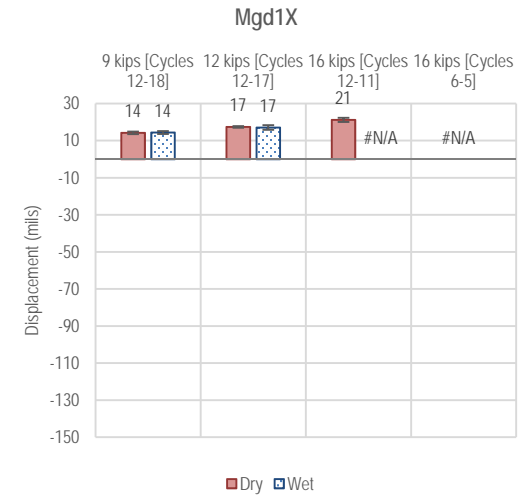


Figure J1-48. Summary of Mgd1X measurements—Dynamic Loading

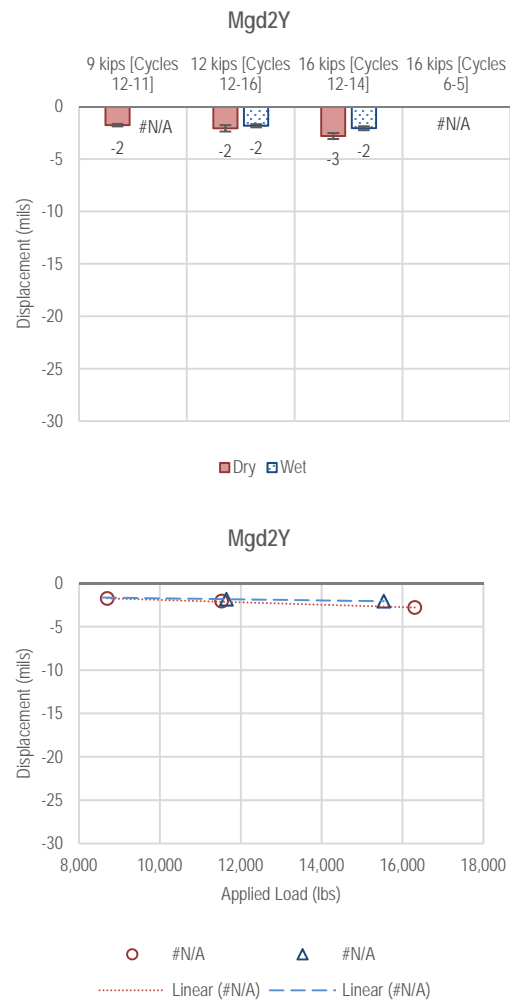
J-51

EXP 7 (Control)

Not Available

Not Available

EXP 9 (Geogrid)



EXP 10 (Geotextile)

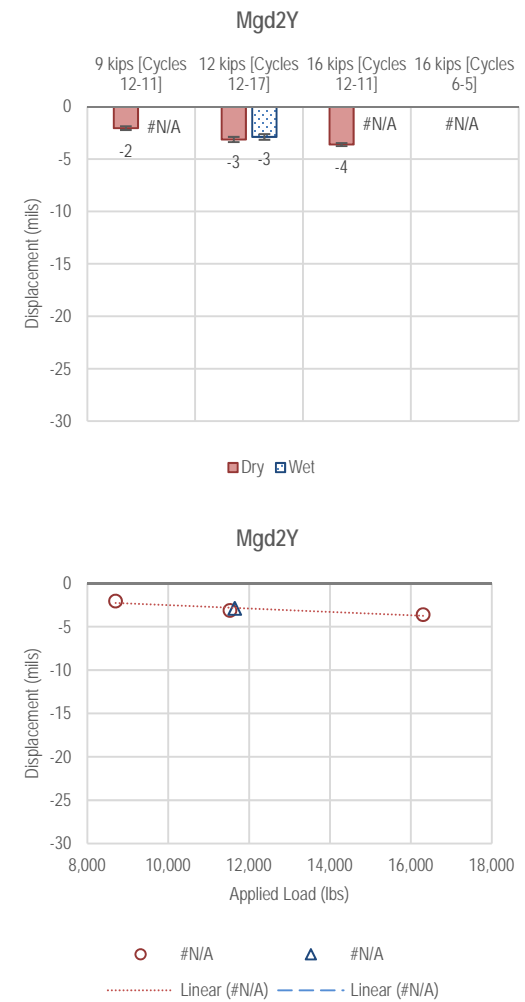
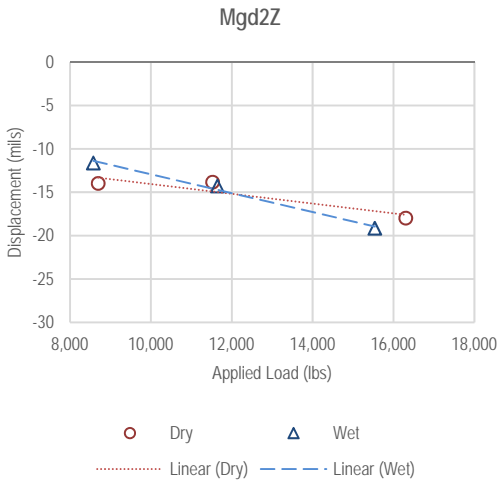
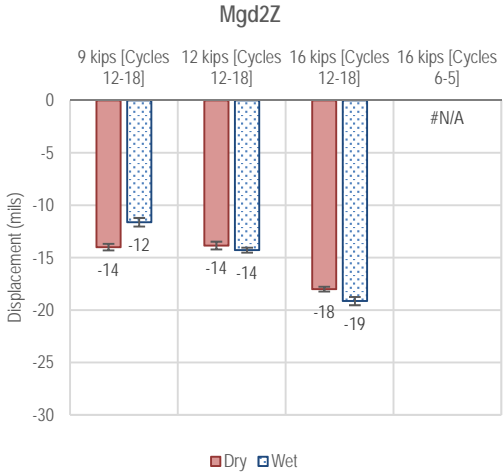


Figure J1-49. Summary of Mgd2Y measurements—Dynamic Loading

EXP 7 (Control)

Not Available

EXP 9 (Geogrid)



EXP 10 (Geotextile)

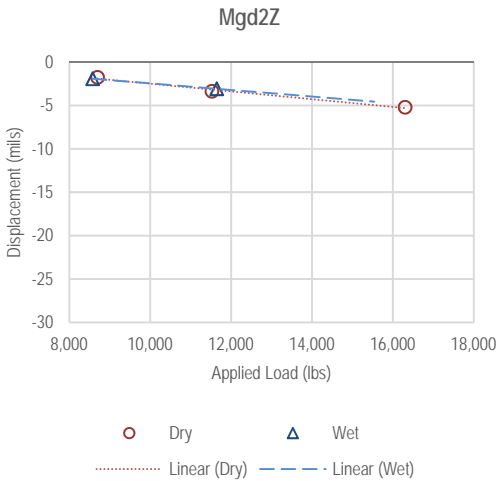
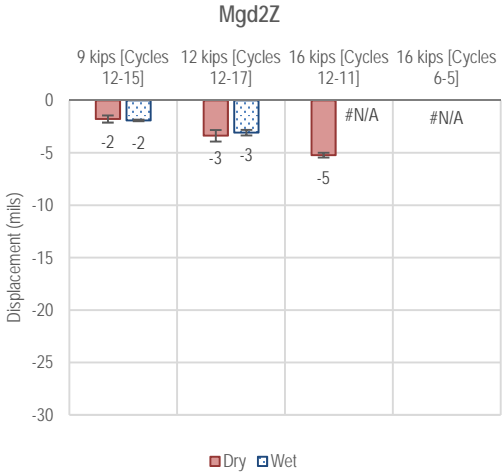


Figure J1-50. Summary of Mgd2Z measurements—Dynamic Loading

J-53

EXP 7 (Control)

EXP 9 (Geogrid)

EXP 10 (Geotextile)

Not Available

Not Available

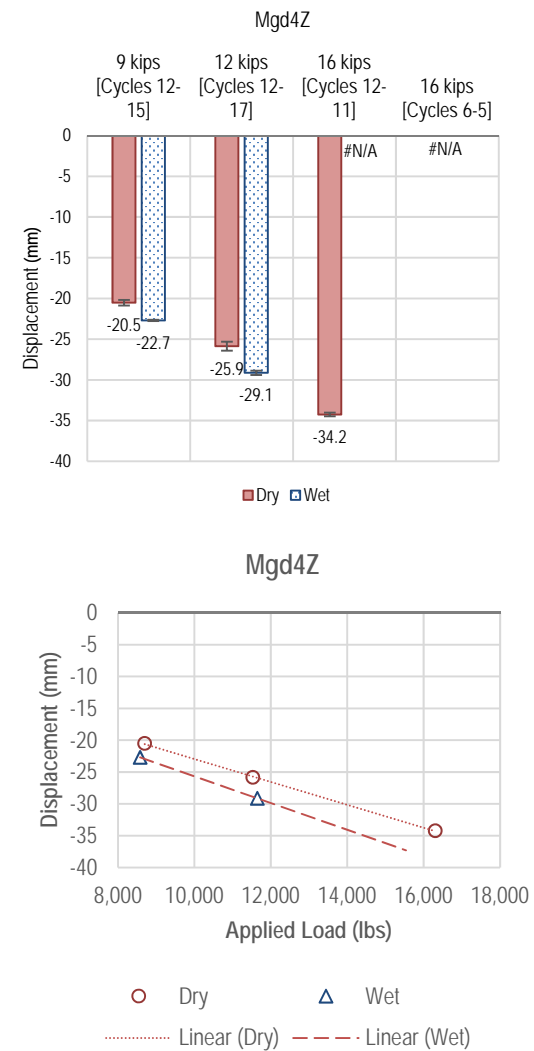


Figure J1-51. Summary of Mgd4Z measurements—Dynamic Loading

Appendix J2. Summary Charts for Rigid Pavement Experiments: Static Loading—Dry and Wet: No. 7 (Control), No. 9 (Geogrid), and No. 10 (Geotextile)

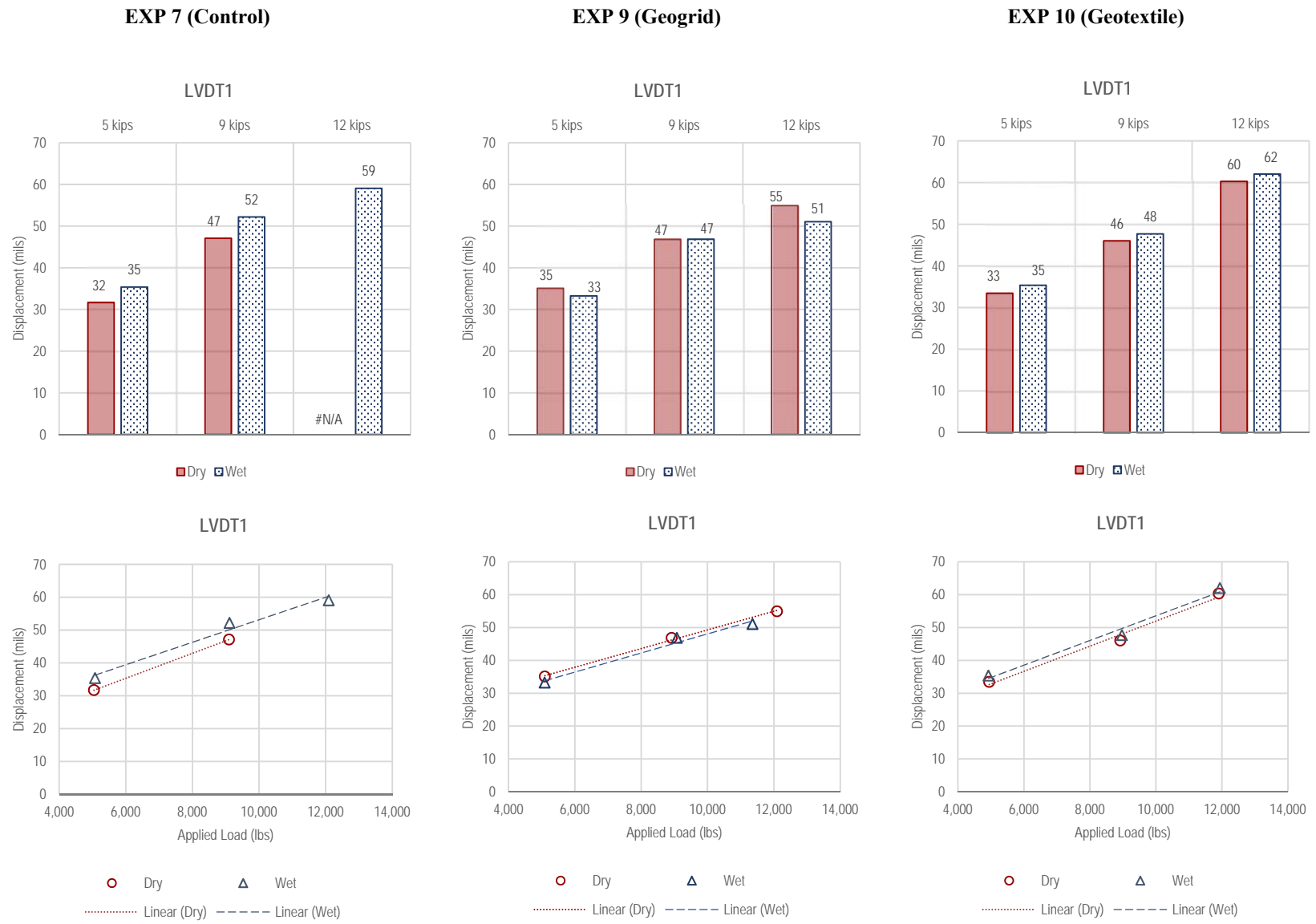


Figure J2-1. Summary of LVDT1 measurements—Static Loading

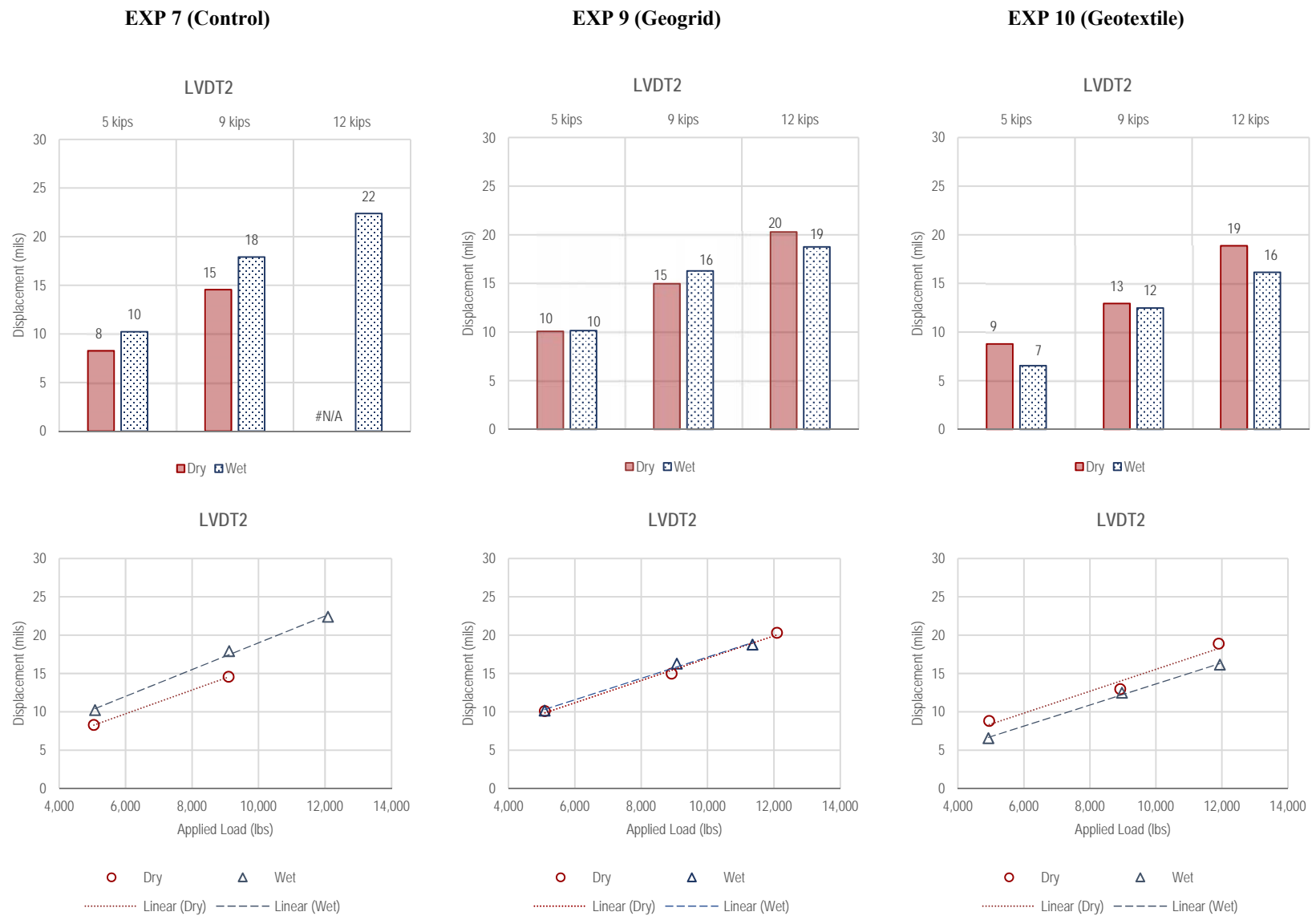


Figure J2-2. Summary of LVDT2 measurements—Static Loading

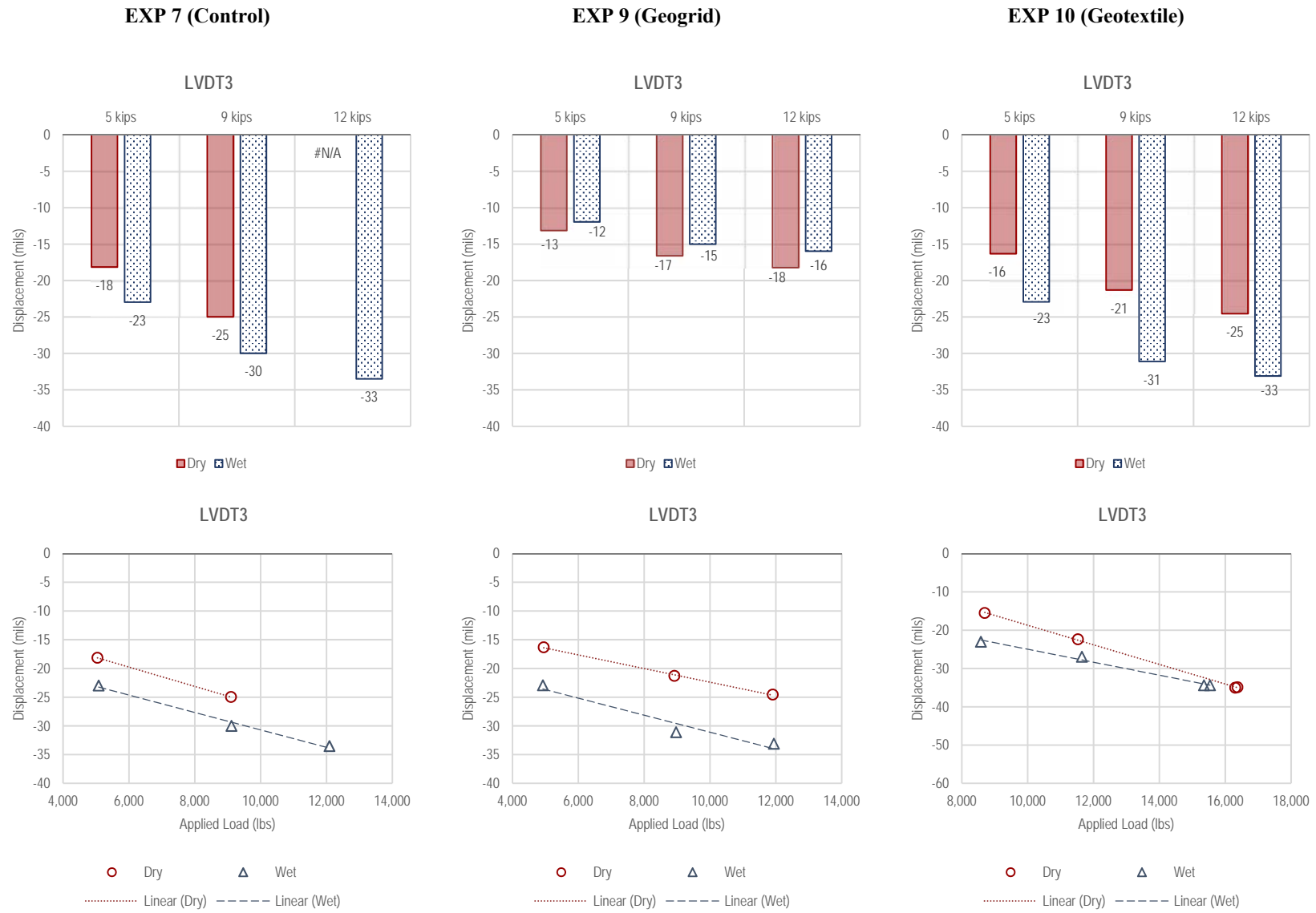


Figure J2-3. Summary of LVDT3 measurements—Static Loading

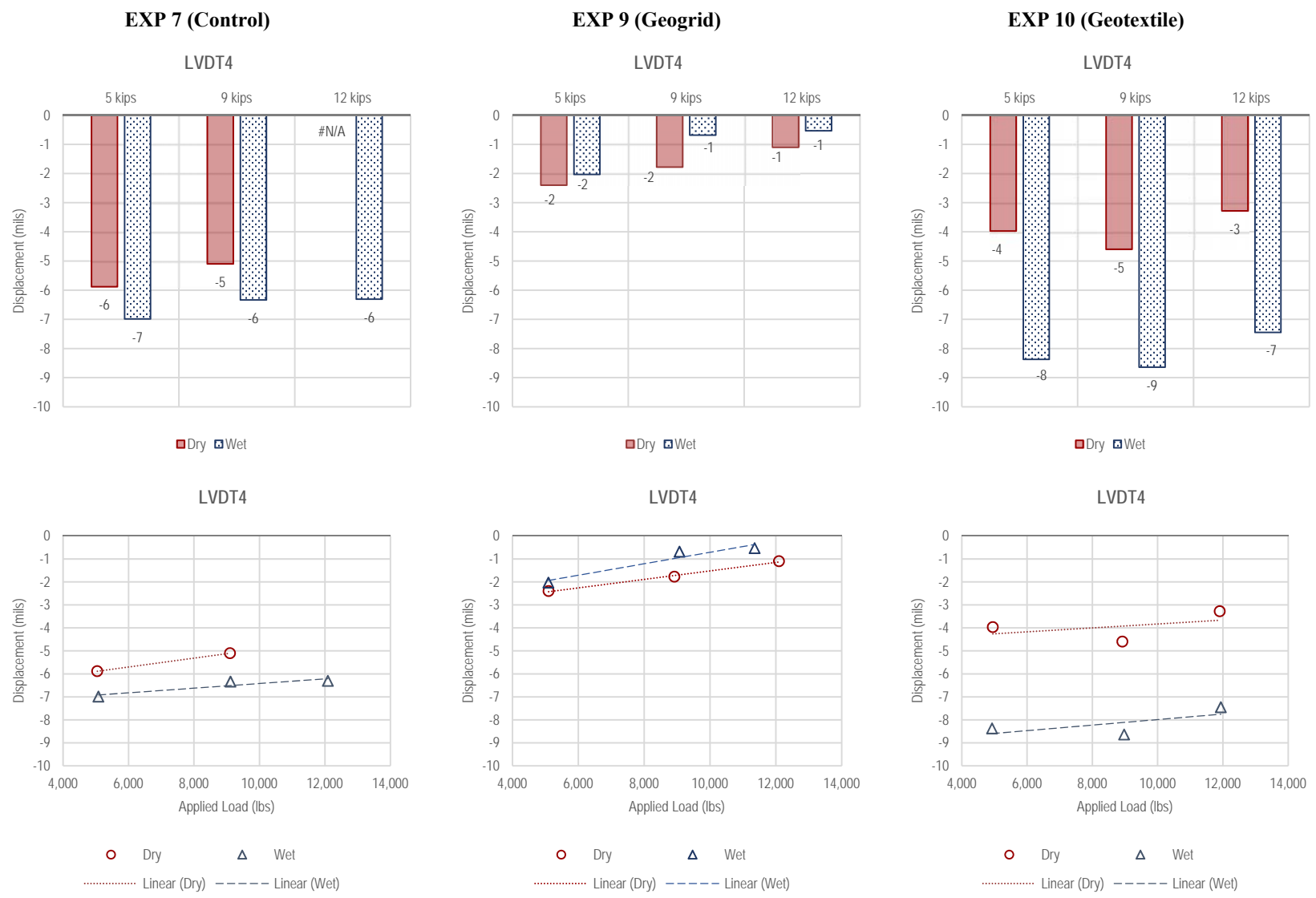


Figure J2-4. Summary of LVDT4 measurements—Static Loading

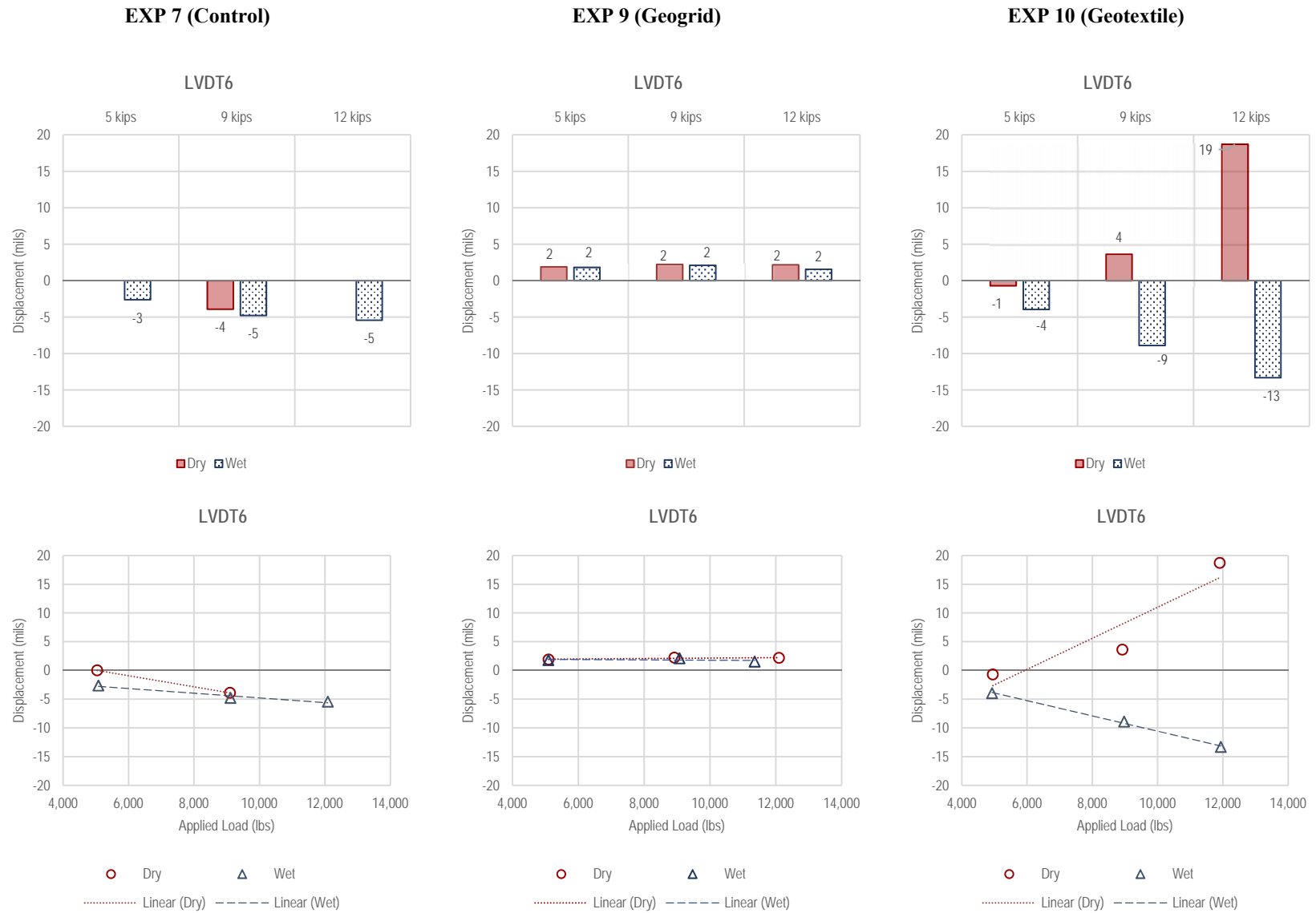


Figure J2-5. Summary of LVDT6 measurements—Static Loading

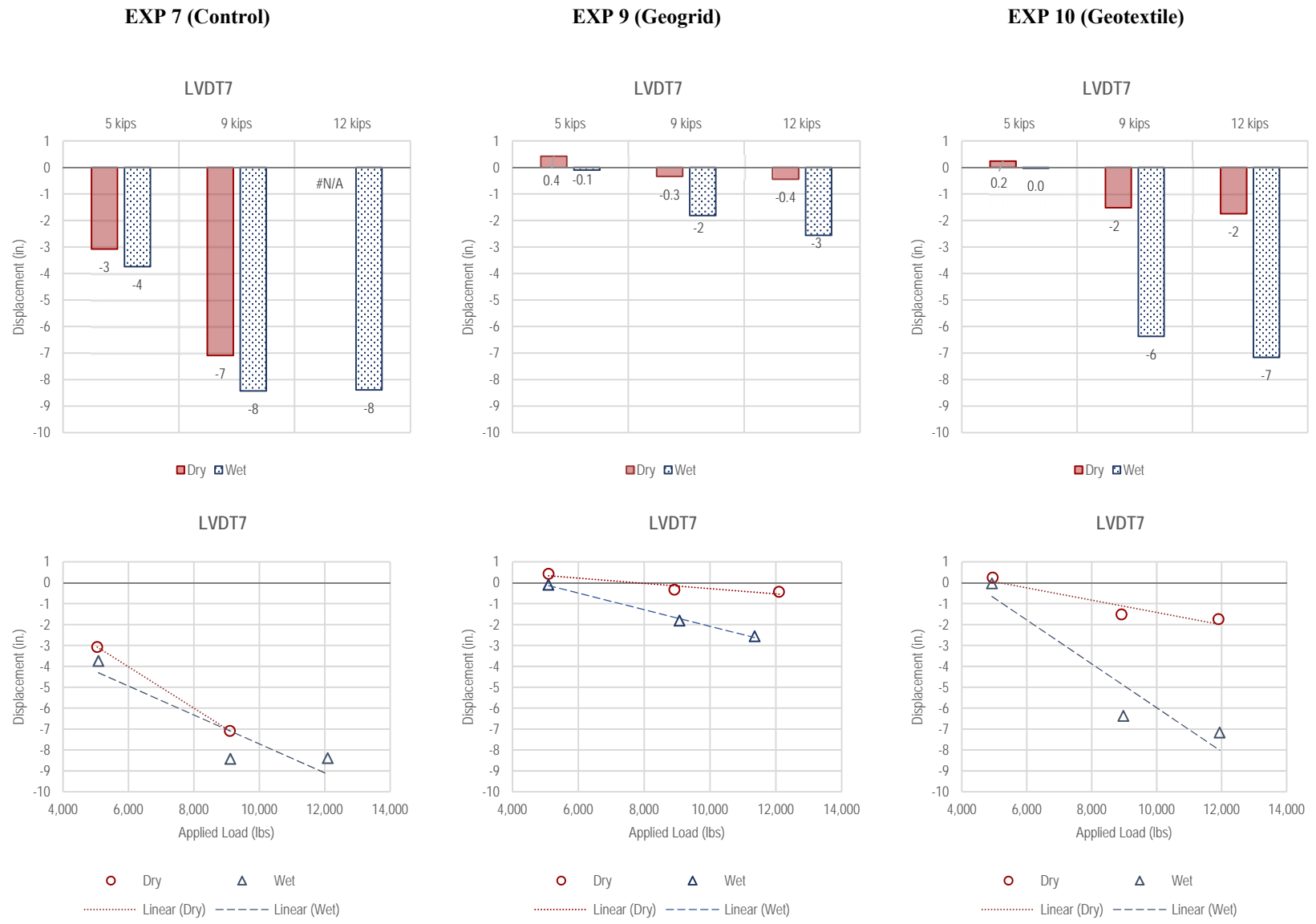


Figure J2-6. Summary of LVDT 7 measurements—Static Loading

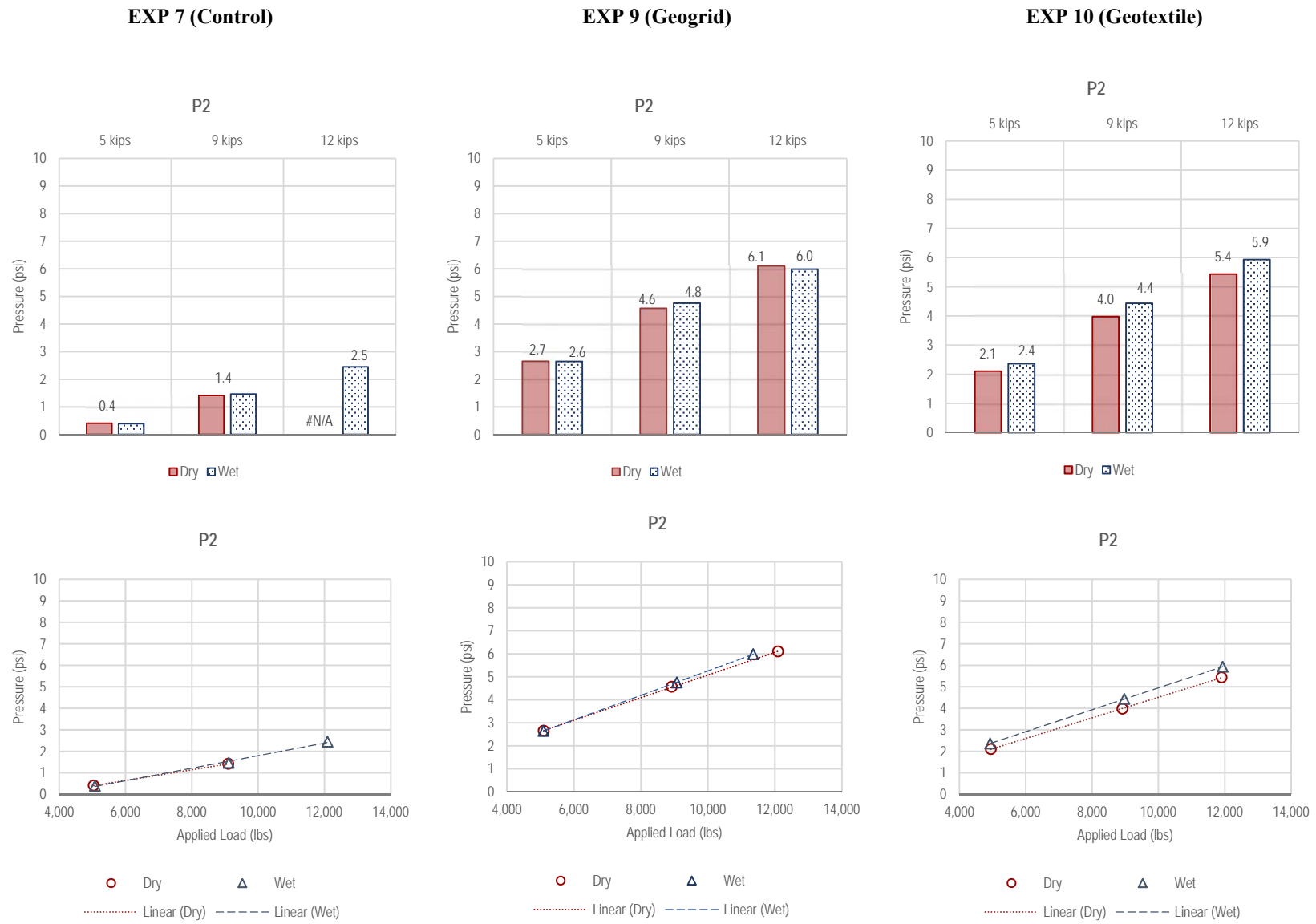


Figure J2-7. Summary of P2 measurements—Static Loading

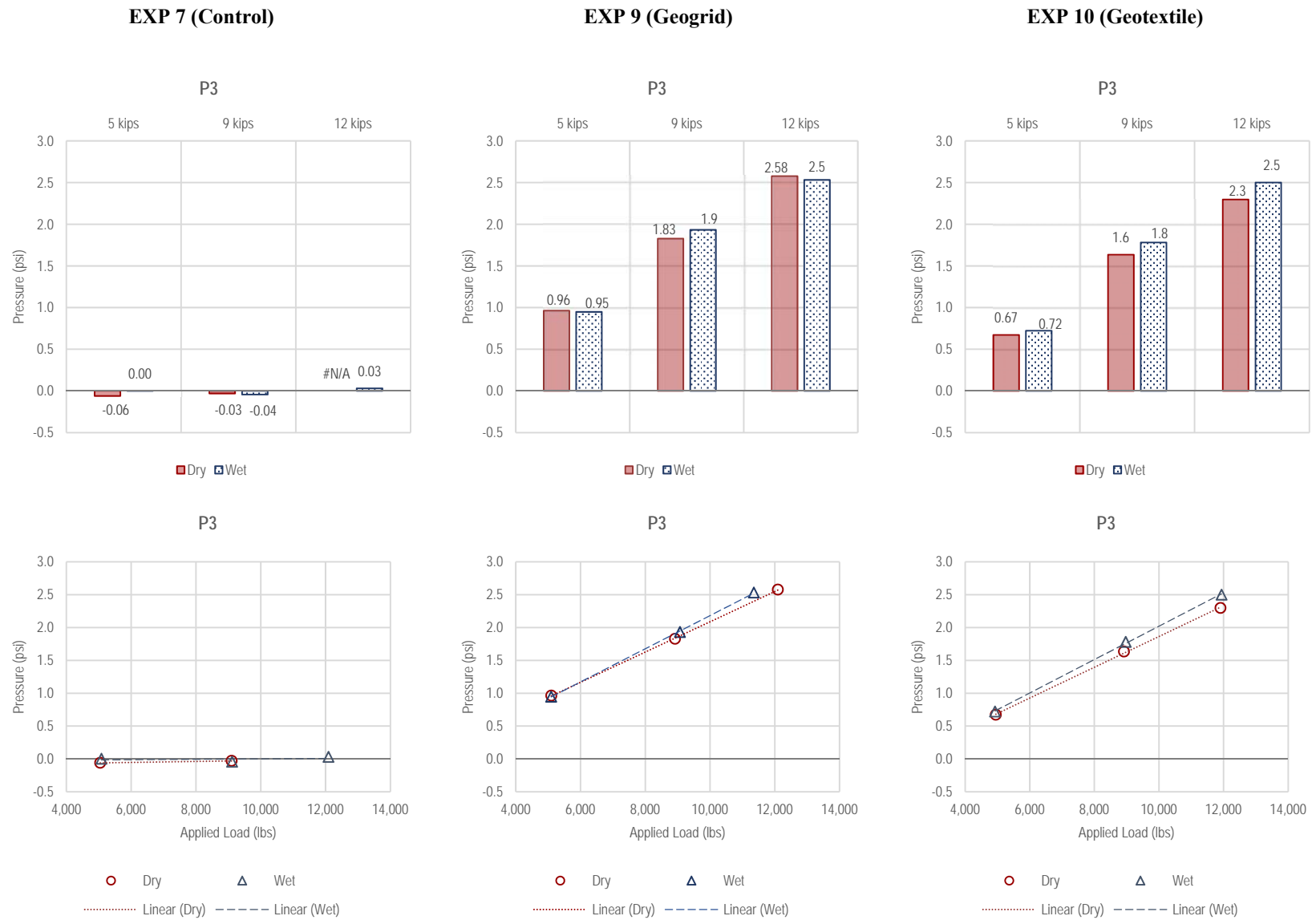


Figure J2-8. Summary of P3 measurements—Static Loading

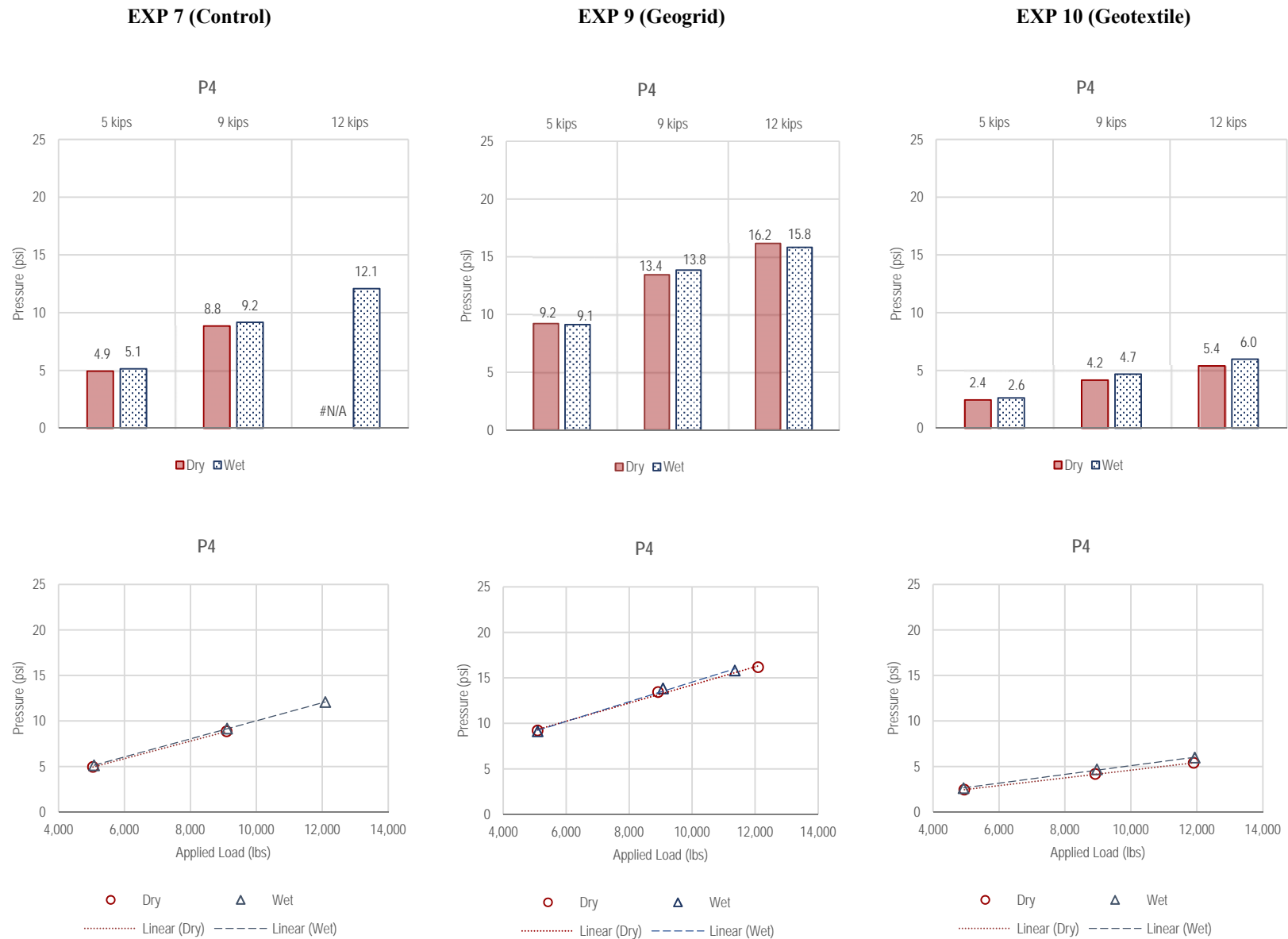


Figure J2-9. Summary of P4 measurements—Static Loading

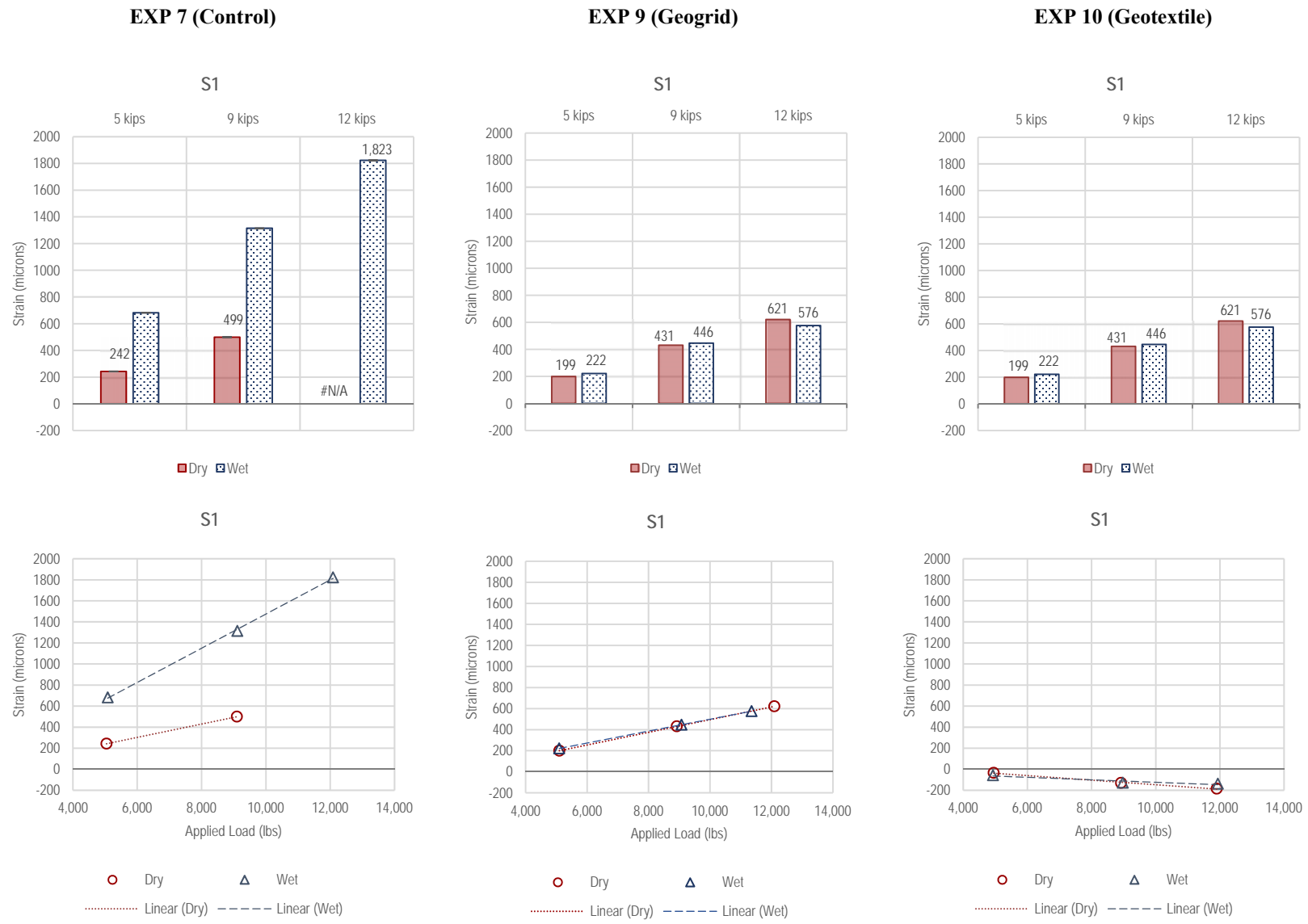


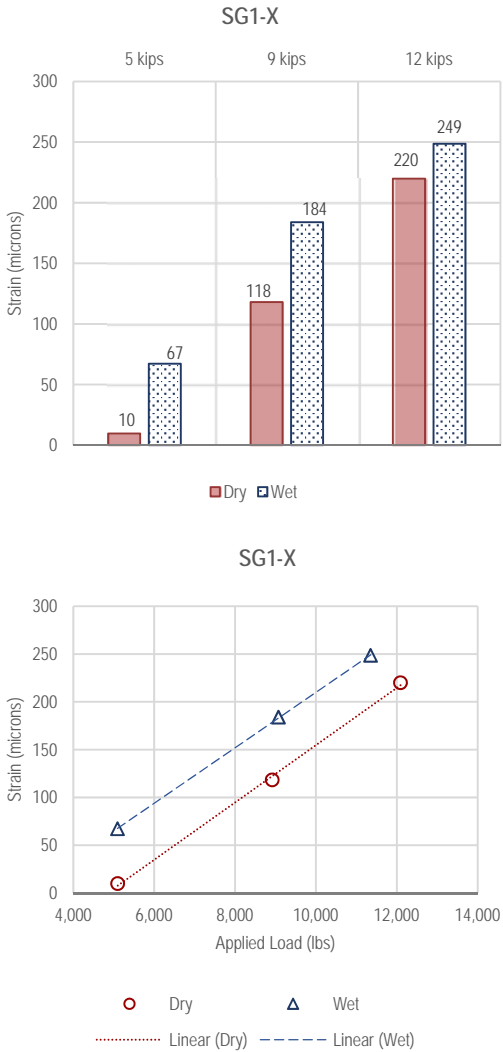
Figure J2-16. Summary of S1 measurements—Static Loading

EXP 7 (Control)

Not Available

Not Available

EXP 9 (Geogrid)



EXP 10 (Geotextile)

Not Available

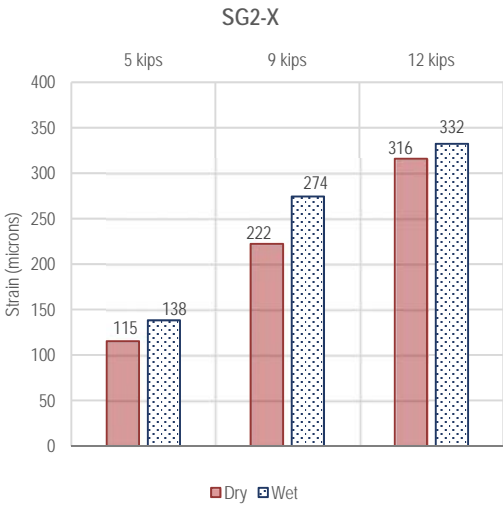
Not Available

Figure J2-17. Summary of SG1-X measurements—Static Loading

EXP 7 (Control)

Not Available

EXP 9 (Geogrid)



EXP 10 (Geotextile)

Not Available

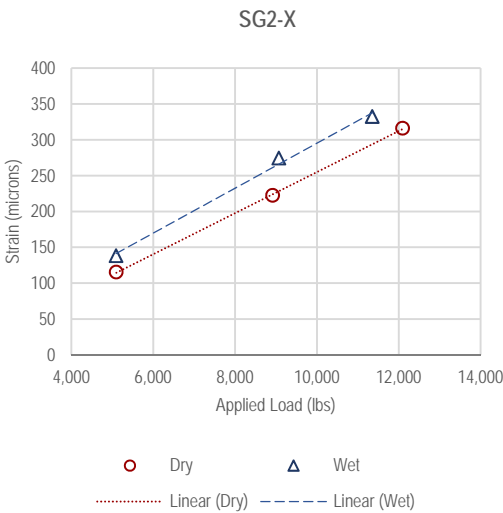
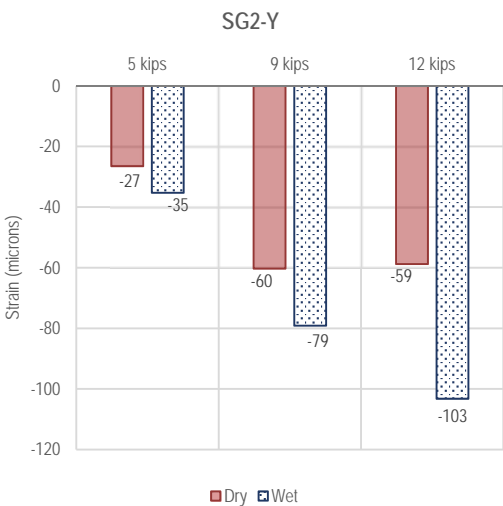


Figure J2-17. Summary of SG2-X measurements—Static Loading

EXP 7 (Control)

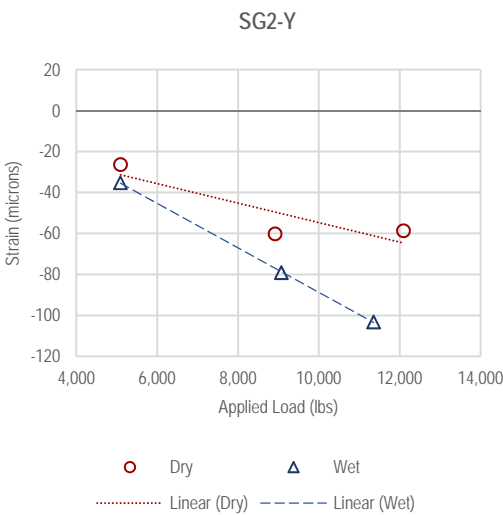
Not Available

EXP 9 (Geogrid)



EXP 10 (Geotextile)

Not Available



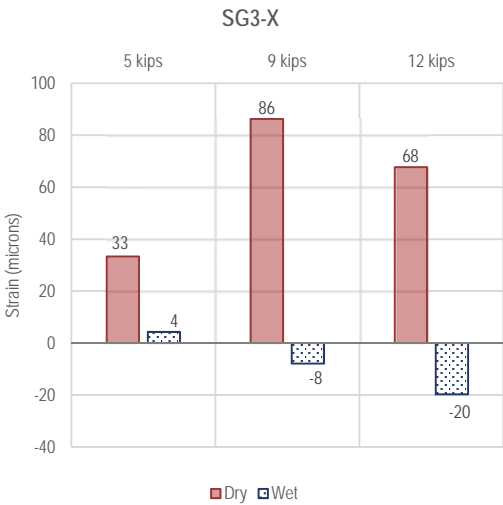
Not Available

Figure J2-18. Summary of SG2-Y measurements—Static Loading

EXP 7 (Control)

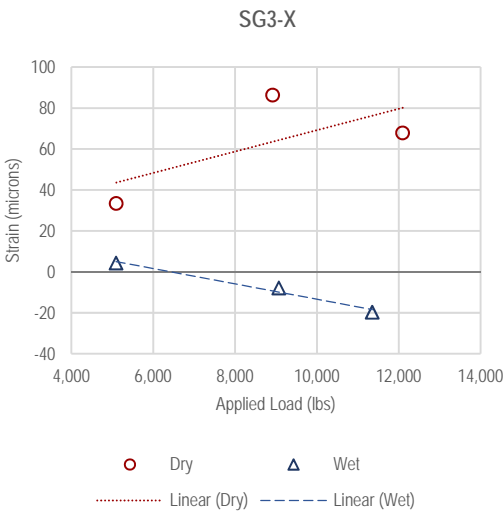
Not Available

EXP 9 (Geogrid)



EXP 10 (Geotextile)

Not Available



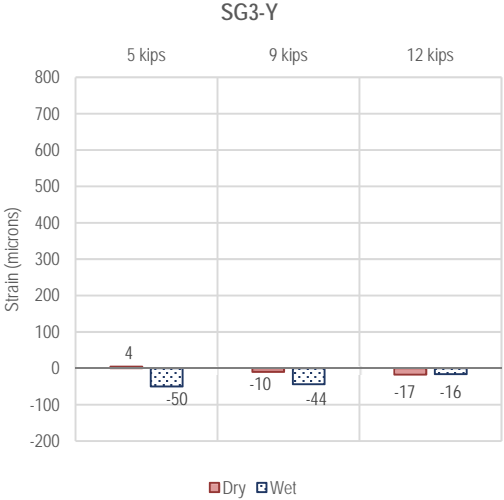
Not Available

Figure J2-19. Summary of SG3-X measurements—Static Loading

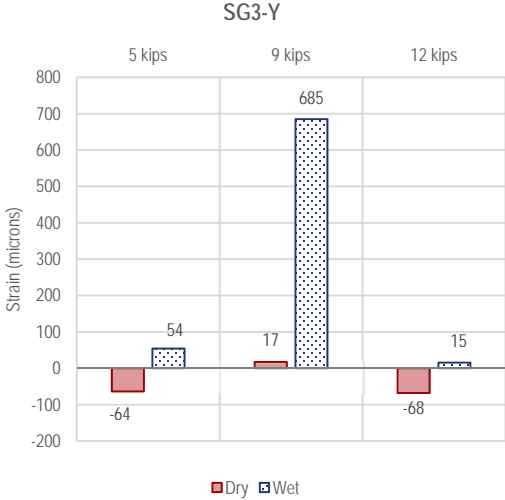
EXP 7 (Control)

Not Available

EXP 9 (Geogrid)



EXP 10 (Geotextile)



Not Available

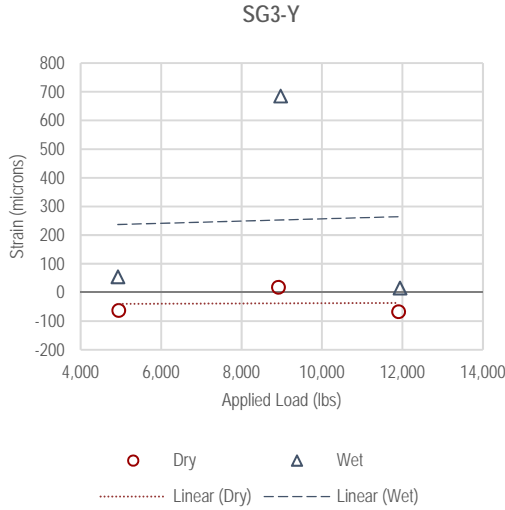
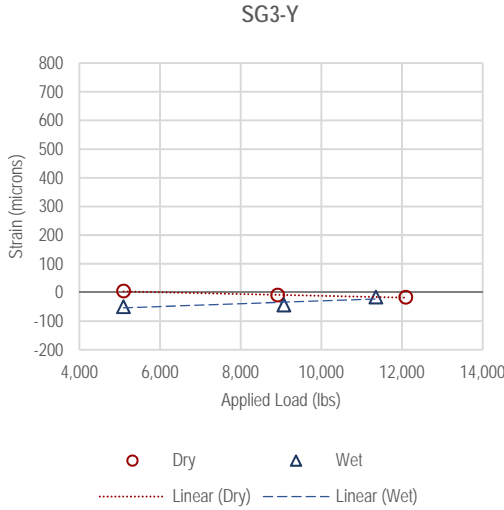
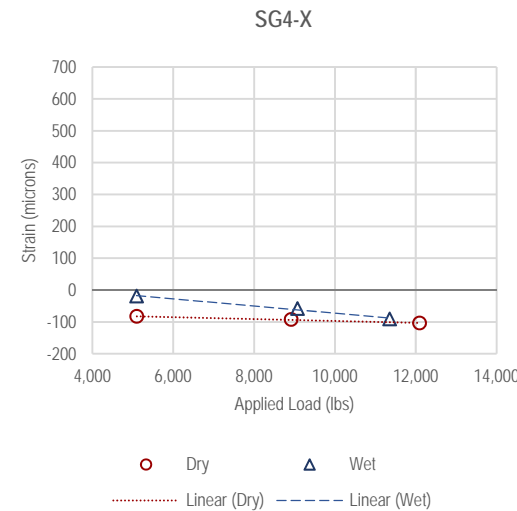
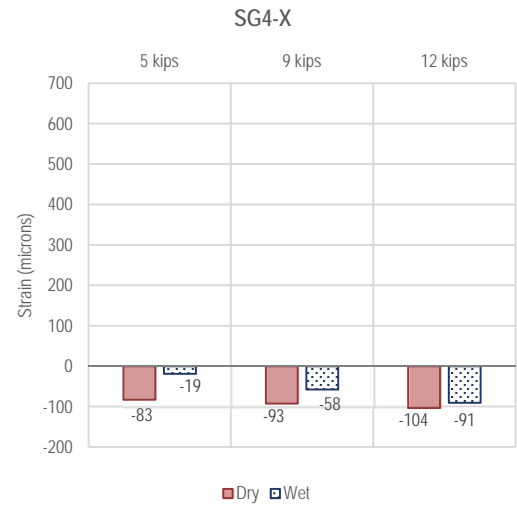


Figure J2-20. Summary of SG3-Y measurements—Static Loading

EXP 7 (Control)

Not Available

EXP 9 (Geogrid)



EXP 10 (Geotextile)

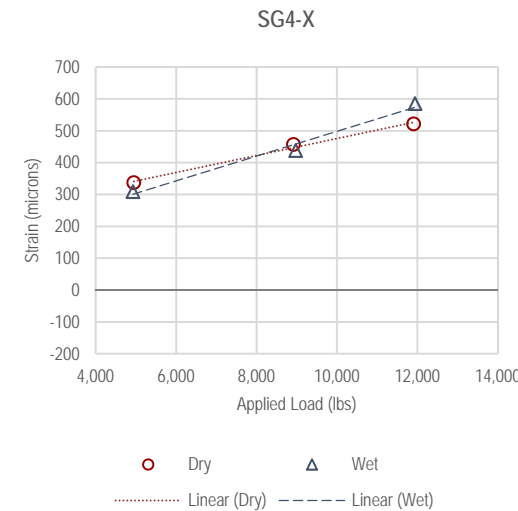
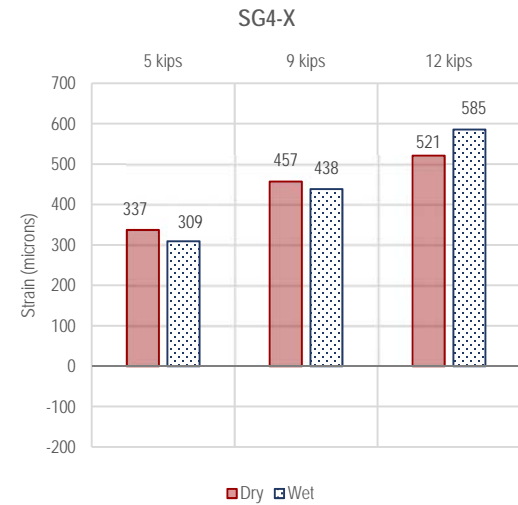


Figure J2-21. Summary of SG4-X measurements—Static Loading

APPENDIX K. RIGID PAVEMENT EXPERIMENTS: COMPARISON OF TEST MEASUREMENTS

**Appendix K1. Rigid Pavements: Comparison of Test Measurements: Dynamic Loading—
Dry and Wet: No. 7 (Control), No. 9 (Geogrid), and No. 10 (Geotextile)**

Table K1-1. Comparison between Accelerometer Measurements

	Statistical Significant Difference between Instrumentation Results								
	Geogrid vs. Control			Geotextile vs. Control			Geotextile vs. Geogrid		
	Load (kip)								
	Instrumentation	9	12	16	9	12	16	9	12
M1X-Dry	-	SH	-	SH	SH	SH	-	SL	-
M1X-Wet	SH*	SH	-	SH	SH	-	SL	SL	-
M1Y-Dry	-	SH	-	SH	SH	SH	-	NS	-
M1Y-Wet	SH	-	-	SH	SH	-	SL	-	-
M1Z-Dry	-	SH	-	SH	SH	SH	-	SH	-
M1Z-Wet	SH	SH	-	SH	SH	-	SH	SH	-
M2Z-Dry	SL*	SH	-	SH	SH	SH	SH	NS**	-
M2Z-Wet	SH	SH	-	SH	SH	-	NS	NS	-
M3Y-Dry	-	-	-	-	-	-	-	-	-
M3Y-Wet	-	-	-	-	-	-	-	-	-
M3Z-Dry	-	-	-	SL	SL	SL	-	-	-

*SH/SL: Geogrid accelerometer measurement is statically higher/lower than the control accelerometer measurement at a significance level of 0.05.

**NS: Geogrid accelerometer measurement and Geotextile accelerometer measurement are not significantly different at a significance level of 0.05.

Table K1-1. Comparison between Accelerometer Measurements (continued)

	Statistical Significant Difference between Instrumentation Results								
	Geogrid vs. Control			Geotextile vs. Control			Geotextile vs. Geogrid		
	Load (kip)								
	9	12	16	9	12	16	9	12	16
Instrumentation	9	12	16	9	12	16	9	12	16
M3Z-Wet	-	-	-	SL	SL	-	-	-	-
M4Z-Dry	SL*	SH	-	-	-	-	-	-	-
M4Z-Wet	SH*	SH	-	-	-	-	-	-	-
M5Z-Dry	SL	SL	-	-	-	-	-	-	-
M5Z-Wet	SL	SL	-	-	-	-	-	-	-
M6X-Dry	-	-	-	-	SL	-	-	-	-
M6X-Wet	-	-	-	-	SL	-	-	-	-
M6Z-Dry	-	-	-	SL	SL	SL	-	-	-
M6Z-Wet	-	-	-	SL	SL	-	-	-	-
M7X-Wet	-	-	-	-	-	-	SL	-	-
M7Z-Dry	NS**	SH	-	SL	SL	SL	SL	SL	-

*SH/SL: Geogrid accelerometer measurement is statically higher/lower than the control accelerometer measurement at a significance level of 0.05.

**NS: Control accelerometer measurement and geogrid accelerometer measurement are not significantly different at a significance level of 0.05.

Table K1-1. Comparison between Accelerometer Measurements (continued)

	Statistical Significant Difference between Instrumentation Results								
	Geogrid vs. Control			Geotextile vs. Control			Geotextile vs. Geogrid		
	Load (kip)								
	Instrumentation	9	12	16	9	12	16	9	12
M7Z-Dry	NS**	SH*	-	SL	SL	SL	SL	SL	-
M7Z-Wet	SL*	SH	-	SL	SL	-	SL	SL	-
Mb1X-Dry	NS	-	-	-	-	-	-	-	-
Mb1Z-Dry	SL	-	-	-	-	-	-	-	-
Mb2Y-Dry	NS	-	-	SH	SH	NS	SH	-	-
Mb2Y-Wet	-	-	-	SH	NS	-	-	-	-
Mb2Z-Dry	SL	-	-	SH	SH	-	SH	-	-
Mc1Y-Dry	SL	-	-	SL	SL	SL	SH	-	-
Mc1Z-Dry	-	-	-	SL	SL	SL	-	-	-
Mc1Z-Wet	-	-	-	SL	SL	-	-	-	-
Mc2Y-Dry	SL	-	-	-	-	-	-	-	-

*SH/SL: Geogrid accelerometer measurement is statically higher/lower than the control accelerometer measurement at a significance level of 0.05.

**NS: Control accelerometer measurement and geogrid accelerometer measurement are not significantly different at a significance level of 0.05.

Table K1-1. Comparison between Accelerometer Measurements (continued)

	Statistical Significant Difference between Instrumentation Results								
	Geogrid vs. Control			Geotextile vs. Control			Geotextile vs. Geogrid		
	Load (kip)								
	Instrumentation	9	12	16	9	12	16	9	12
Mc2Y-Wet	-	-	-	-	-	-	-	-	-
Mc2Z-Dry	SL*	-	-	SL	SL	SL	SH	-	-
Mc2Z-Wet	-	-	-	SL	SL	-	-	-	-
Mgd1X-Dry	-	-	-	-	-	-	-	SH	-
Mgd2Y-Dry	-	-	-	-	-	-	NS***	SL	-
Mgd2Y-Wet	-	-	-	-	-	-	-	SL	-
Mgd2Z-Dry	-	-	-	-	-	-	SH**	SH	-
Mgd2Z-Wet	-	-	-	-	-	-	SH	SH	-

*SL: Geogrid accelerometer measurement is statically lower than the control accelerometer measurement at a significance level of 0.05.

**SH: Geotextile accelerometer measurement is statically higher than the geogrid accelerometer measurement at a significance level of 0.05.

***NS: Geotextile accelerometer measurement and geogrid accelerometer measurement are not significantly different at a significance level of 0.05.

Table K1-2. Comparison between LVDT Measurements

	Statistical Significant Difference between Instrumentation Results								
	Geogrid vs. Control			Geotextile vs. Control			Geotextile vs. Geogrid		
	Load (kip)								
	Instrumentation	9	12	16	9	12	16	9	12
LVDT1-Dry	NS**	SL	SL	SL	SL	SL	SL	SL	NS
LVDT1-Wet	NS	SL	SL	NS	SL	SL	SL	SL	SH
LVDT2-Dry	SL*	NS	SL	SL	SL	SL	SL	SL	SL
LVDT2-Wet	NS	SL	SH	SL	SL	SL	SL	SL	SL
LVDT3-Dry	SH*	SH	SH	SL	SL	SH	SL	SL	SL
LVDT3-Wet	SH	SH	SH	SL	SL	SL	SL	SL	SL
LVDT4-Dry	NS	SH	SH	SL	SL	NS	SL	SL	SL
LVDT4-Wet	SH	SH	SH	SL	SL	SL	SL	SL	SL
LVDT6-Dry	SL	NS	SH	SL	SL	NS	SL	SL	NS
LVDT6-Wet	SH	SH	SH	NS	SL	SL	NS	SL	SL
LVDT7-Dry	SH	SH	SH	-	-	-	-	-	-
LVDT7-Wet	SH	SH	SH	-	-	-	-	-	-

*SH/SL: Geogrid LVDT measurement is statically higher/lower than the control LVDT measurement at a significance level of 0.05.

**NS: Control LVDT measurement and geotextile LVDT measurement are not significantly different at a significance level of 0.05.

Table K1-3. Comparison between Pressure Cell Measurements

	Statistical Significant Difference between Instrumentation Results								
	Geogrid vs. Control			Geotextile vs. Control			Geotextile vs. Geogrid		
	Load (kip)								
	9	12	16	9	12	16	9	12	16
Instrumentation	9	12	16	9	12	16	9	12	16
P1-Dry	SH*	SH	SH	SH	SH	SH	SL	SL	SL
P1-Wet	-	-	-	-	-	-	SL	SL	SL
P2-Dry	SH	SH	SH	SH	SH	SH	SL	SL	SL
P2-Wet	SH	SH	SH	SH	SH	SH	SL	SH	SH
P3-Dry	SH	SH	SH	SH	SH	SH	NS**	SH	SH
P3-Wet	SH	SH	SH	SH	SH	SH	NS	SH	SH
P4-Dry	SH	SH	SH	SL	SL	SL	SL	SL	SL
P4-Wet	SH	SH	SH	SL	SL	SL	SL	SL	SL
P5-Dry	SH	SH	SH	SH	SH	SH	SL	SL	SL
P5-Wet	SH	SH	SH	SH	SH	SH	SL	SH	SH
P6-Dry	SL*	SL	SL	SL	SL	SL	SH	SH	SH

*SH/SL: Geogrid LVDT measurement is statically higher/lower than the control LVDT measurement at a significance level of 0.05.

**NS: Geogrid LVDT measurement and geotextile LVDT measurement are not significantly different at a significance level of 0.05.

Table K1-3. Comparison between Pressure Cell Measurements (continued)

	Statistical Significant Difference between Instrumentation Results								
	Geogrid vs. Control			Geotextile vs. Control			Geotextile vs. Geogrid		
	Load (kip)								
	Instrumentation	9	12	16	9	12	16	9	12
P6-Wet	SL*	SL	SL	SL	SL	SL	SH	SH	SH
P7-Dry	SL	SL	SL	SL	SL	SL	SH	SH	SH
P7-Wet	SL	SL	SL	SL	SL	SH	SH	SH	SH
P8-Dry	SL	SL	SL	SL	SL	SL	SH	SH	NS
P8-Wet	SL	SL	SL	SL	SL	SL	NS	SH	SH
P9-Dry	SH*	SL	SL	SL	SL	SL	SL	SL	SL
P9-Wet	SL	SH	NS**	SL	SL	SL	SL	SL	SL
P10-Dry	-	-	-	SH	SH	SH	-	-	-
P10-Wet	-	-	-	SH	SH	SH	-	-	-
P21-Dry	SH	SH	SH	SL	SL	SL	SL	SL	SL
P21-Wet	SH	SH	SH	SL	SL	SH	SL	SL	SL

*SH/SL: Geogrid LVDT measurement is statically higher/lower than the control LVDT measurement at a significance level of 0.05.

**NS: Control LVDT measurement and geogrid LVDT measurement are not significantly different at a significance level of 0.05.

Table K1-4. Comparison between Strain Gauge Measurements

	Statistical Significant Difference between Instrumentation Results								
	Geogrid vs. Control			Geotextile vs. Control			Geotextile vs. Geogrid		
	Load (kip)								
Instrumentation	9	12	16	9	12	16	9	12	16
S1-Dry	SH*	SH	SH	-	-	-	-	-	-
S1-Wet	SL*	SL	SH	-	-	-	-	-	-
SG1_X-Dry	-	-	-	-	-	-	SL	SL	SL
SG1_X-Wet	-	-	-	-	-	-	SL	SL	SL
SG1_Y-Dry	-	-	-	-	-	-	SL	SL	SL
SG1_Y-Wet	-	-	-	-	-	-	SL	SL	SL
SG2_X-Dry	-	-	-	-	-	-	SL	SL	SL
SG2_X-Wet	-	-	-	-	-	-	SL	SL	SL
SG2_Y-Dry	-	-	-	-	-	-	SH	SH	SH
SG2_Y-Wet	-	-	-	-	-	-	SH	SH	SH
SG3_X-Dry	-	-	-	-	-	-	SH	SH	SH

*SH/SL: Geotextile strain gauge measurement is statically higher/lower than the geogrid strain gauge measurement at a significance level of 0.05.

Table K1-4. Comparison between Strain Gauge Measurements (continued)

	Statistical Significant Difference between Instrumentation Results								
	Geogrid vs. Control			Geotextile vs. Control			Geotextile vs. Geogrid		
	Load (kip)								
	9	12	16	9	12	16	9	12	16
Instrumentation	9	12	16	9	12	16	9	12	16
SG3_X-Wet	-	-	-	-	-	-	SL*	SL	SH*
SG3_Y-Dry	-	-	-	-	-	-	SL	SL	SL
SG3_Y-Wet	-	-	-	-	-	-	SL	NS**	NS
SG4_X-Dry	-	-	-	-	-	-	SH	SH	SH
SG4_X-Wet	-	-	-	-	-	-	SH	SH	SH

*SH/SL: Geotextile strain gauge measurement is statically higher/lower than the geogrid strain gauge measurement at a significance level of 0.05.

**NS: Control strain gauge measurement and geogrid strain gauge measurement are not significantly different at a significance level of 0.05.

Appendix K2. Rigid Pavements: Comparison of Test Measurements: Static Loading—Dry and Wet: No. 7 (Control), No. 9 (Geogrid), and No. 10 (Geotextile)

Table K2-1. Percent Difference in LVDT Measurements

Instrumentation	Percent Difference in Results of Instrumentations								
	Geogrid vs. Control*			Geotextile vs. Control**			Geotextile vs. Geogrid***		
	Load (kip)								
	5	9	12	5	9	12	5	9	12
LVDT1-Dry	10.7	-0.6	-	5.5	-2.3	-	-4.7	-1.7	9.8
LVDT1-Wet	-6.0	-10.2	-13.6	-0.1	-8.6	5.0	6.3	1.8	21.5
LVDT2-Dry	21.8	2.8	-	6.3	-11.1	-	-12.8	-13.5	-7.0
LVDT2-Wet	-0.7	-9.0	-16.2	-36.0	-30.3	-27.9	-35.5	-23.4	-13.9
LVDT3-Dry	-27.6	-33.5	-	-10.1	-14.7	-	24.2	28.3	34.5
LVDT3-Wet	-47.9	-50.0	-52.3	-0.2	3.7	-1.2	91.8	107.2	107.1
LVDT4-Dry	-59.2	-65.2	-	-32.6	-9.9	-	65.4	158.8	198.1
LVDT4-Wet	-71.0	-89.2	-91.5	19.8	36.3	18.1	312.5	1162.3	1293.0

*Geogrid vs. Control:

$$100 * [(LVDT \text{ Measurement in Experiment 9} - LVDT \text{ Measurement in Experiment 7}) / LVDT \text{ Measurement in Experiment 7}]$$

**Geotextile vs. Control:

$$100 * [(LVDT \text{ Measurement in Experiment 10} - LVDT \text{ Measurement in Experiment 7}) / LVDT \text{ Measurement in Experiment 7}]$$

***Geotextile vs. Geogrid:

$$100 * [(LVDT \text{ Measurement in Experiment 10} - LVDT \text{ Measurement in Experiment 9}) / LVDT \text{ Measurement in Experiment 9}]$$

Table K2-1. Percent Difference in LVDT Measurements (continued)

	Percent Difference in Results of Instrumentations								
	Geogrid vs. Control*			Geotextile vs. Control**			Geotextile vs. Geogrid***		
	Load (kip)								
	5	9	12	5	9	12	5	9	12
Instrumentation	5	9	12	5	9	12	5	9	12
LVDT6-Dry	-161.7	-156.8	-	-76.8	-191.9	-	-137.7	61.9	765.6
LVDT6-Wet	-168.8	-143.9	-128.6	50.7	86.5	145.2	-319.1	-524.6	-958.4
LVDT7-Dry	-114.1	-95.2	-	-108.1	-78.6	-	-42.9	346.0	295.4
LVDT7-Wet	-97.4	-78.5	-69.5	-99.1	-24.4	-14.6	-66.2	251.1	179.7

*Geogrid vs. Control:

$$100 * [(LVDT \text{ Measurement in Experiment 9} - LVDT \text{ Measurement in Experiment 7}) / LVDT \text{ Measurement in Experiment 7}]$$

**Geotextile vs. Control:

$$100 * [(LVDT \text{ Measurement in Experiment 10} - LVDT \text{ Measurement in Experiment 7}) / LVDT \text{ Measurement in Experiment 7}]$$

***Geotextile vs. Geogrid:

$$100 * [(LVDT \text{ Measurement in Experiment 10} - LVDT \text{ Measurement in Experiment 9}) / LVDT \text{ Measurement in Experiment 9}]$$

Table K2-2. Percent Difference in Pressure Cell Measurements

	Percent Difference in Results of Instrumentations								
	Geogrid vs. Control*			Geotextile vs. Control**			Geotextile vs. Geogrid***		
	Load (kip)								
	Instrumentation	5	9	12	5	9	12	5	9
P1-Dry	-	-	-	-	-	-	-	-	-
P1-Wet	-	-	-	-	-	-	-	-	-
P2-Dry	555.4	222.9	-	419.2	181.2	-	-20.8	-12.9	-10.9
P2-Wet	570.8	224.9	144.3	498.2	202.9	142.1	-10.8	-6.8	-0.9
P3-Dry	-1702.0	-6170.4	-	-1216.1	-5525.9	-	-30.3	-10.6	-10.9
P3-Wet	27755.3	-4589.2	7961.0	21101.7	-4237.4	7856.9	-23.9	-7.8	-1.3
P4-Dry	86.6	51.9	-	-50.5	-53.0	-	-73.5	-69.1	-66.7
P4-Wet	77.9	51.2	30.9	-49.0	-49.0	-50.6	-71.3	-66.3	-62.2
P5-Dry	86.3	62.8	-	65.1	48.8	-	-11.4	-8.6	-8.3

*Geogrid vs. Control:

$$100 * [(\text{Pressure Cell Measurement in Experiment 9} - \text{Pressure Cell Measurement in Experiment 7}) / \text{Pressure Cell Measurement in Experiment 7}]$$

**Geotextile vs. Control:

$$100 * [(\text{Pressure Cell Measurement in Experiment 10} - \text{Pressure Cell Measurement in Experiment 7}) / \text{Pressure Cell Measurement in Experiment 7}]$$

***Geotextile vs. Geogrid:

$$100 * [(\text{Pressure Cell Measurement in Experiment 10} - \text{Pressure Cell Measurement in Experiment 9}) / \text{Pressure Cell Measurement in Experiment 9}]$$

Table K2-3. Percent Difference in Pressure Cell Measurements

	Percent Difference in Results of Instrumentations								
	Geogrid vs. Control*			Geotextile vs. Control**			Geotextile vs. Geogrid***		
	Load (kip)								
	Instrumentation	5	9	12	5	9	12	5	9
P5-Wet	89.0	68.1	45.3	80.1	59.4	45.1	-4.7	-5.2	-0.1
P6-Dry	-113.3	-115.5	-	-94.4	-94.5	-	-141.6	-135.1	-151.2
P6-Wet	-110.1	-113.7	- 111.4	-97.0	-99.7	-98.2	-129.6	-102.5	-116.0
P7-Dry	-24.9	-37.4	-	1.1	-13.4	-	34.6	38.4	37.1
P7-Wet	-9.8	-28.6	-38.9	23.4	1.2	-9.9	36.8	41.7	47.4
P9-Dry	161.3	48.5	-	-106.5	-103.5	-	-102.5	-102.3	-102.0
P9-Wet	112.3	7.0	8.5	-124.2	-108.4	-100.7	-111.4	-107.8	-100.7
P10-Dry	-98.8	-101.2	-	0.4	35.3	-	8009.1	-11436.7	500.6
P10-Wet	-99.5	-88.7	-69.5	118.0	199.7	184.2	48245.2	2552.4	833.0
P21-Dry	-1.2	13.6	-	-67.4	-54.4	-	-67.0	-59.8	-41.8
P21-Wet	12.0	43.1	60.3	-57.9	-17.5	27.9	-62.4	-42.3	-20.2

*Geogrid vs. Control: $100 * [(\text{Strain Gauge Measurement in Experiment 9} - \text{Strain Gauge Measurement in Experiment 7}) / \text{Strain Gauge Measurement in Experiment 7}]$

**Geotextile vs. Control: $100 * [(\text{Strain Gauge Measurement in Experiment 10} - \text{Strain Gauge Measurement in Experiment 7}) / \text{Strain Gauge Measurement in Experiment 7}]$

***Geotextile vs. Geogrid: $100 * [(\text{Strain Gauge Measurement in Experiment 10} - \text{Strain Gauge Measurement in Experiment 9}) / \text{Strain Gauge Measurement in Experiment 9}]$

Table K2-4. Percent Difference in Strain Gauge Measurements

Instrumentation	Percent Difference in Results of Instrumentations								
	Geogrid vs. Control*			Geotextile vs. Control**			Geotextile vs. Geogrid***		
	Load (kip)								
	5	9	12	5	9	12	5	9	12
S1-Dry	-17.7	-13.6	-	-	-	-	-	-	-
S1-Wet	-67.4	-66.1	-68.4	-	-	-	-	-	-
SG3_Y-Wet	-	-	-	-	-	-	-208.6	-1659.7	-194.2
SG4_X-Dry	-	-	-	-	-	-	-505.5	-593.1	-601.6
SG4_X-Wet	-	-	-	-	-	-	-1722.5	-858.6	-745.5

*Geogrid vs. Control:

$$100 * [(\text{Strain Gauge Measurement in Experiment 9} - \text{Strain Gauge Measurement in Experiment 7}) / \text{Strain Gauge Measurement in Experiment 7}]$$

**Geotextile vs. Control:

$$100 * [(\text{Strain Gauge Measurement in Experiment 10} - \text{Strain Gauge Measurement in Experiment 7}) / \text{Strain Gauge Measurement in Experiment 7}]$$

***Geotextile vs. Geogrid:

$$100 * [(\text{Strain Gauge Measurement in Experiment 10} - \text{Strain Gauge Measurement in Experiment 9}) / \text{Strain Gauge Measurement in Experiment 9}]$$

APPENDIX L. CHARACTERIZATION OF MATERIALS USED IN LARGE-SCALE TANK TEST

Materials for the flexible and rigid pavements included typically used materials for dense-graded hot-mix asphalt (HMA) and Portland cement concrete (PCC), respectively. Both systems used the same crushed aggregate base and subgrade materials. The subgrade thickness was kept the same in all flexible and rigid experiments.

Subgrade Layer

The subgrade consisted of a high plasticity clay soil that was sampled from a local source. Before placing the subgrade material in the LST, a series of conventional characterizations were performed to determine swelling potential, moisture-density relation, and particle size distribution. To determine swelling potential of the clay soil, AASHTO T89 and T90 were followed. The soil was sampled, manually pulverized, and then washed over a standard number 40 sieve and allowed to dry for 24 hours at 100°C. Once the soil was ready for testing, standard methods were applied to find the Atterberg limits. The liquid limit curve for the clayey subgrade material is shown in Figure L-1a. Table L-1 summarizes the determined Atterberg limits.

AASHTO T11 and T88 were followed to plot a particle size distribution curve for the subgrade material. A laboratory compaction test using modified efforts was also performed in accordance with AASHTO T180 to determine the maximum dry density and the optimum moisture content of the subgrade material. Figure L-1b shows the proctor curve for the clay material.

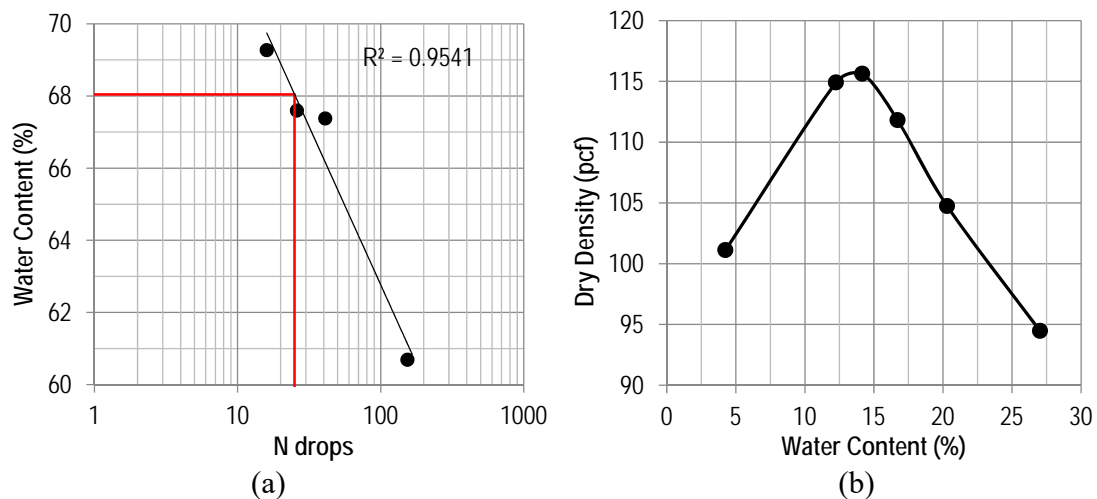


Figure L-1. (a) Liquid limit curve for the subgrade material; (b) modified proctor curve for the subgrade material

Table L-1. Atterberg Limits for Subgrade Material

Liquid Limit	Plastic Limit	Plasticity Index	Adjusted Plasticity Index
68.1	28.4	39.7	35.3

The shear strength parameters of the subgrade material were also determined. Direct shear testing was conducted on three sample replicates subjected to different normal stresses in accordance with ASTM D3080. The achieved density for the direct shear specimens was similar to the in-density of the subgrade material in the LST experiments (95 percent of the maximum dry density at 16 percent water content). The samples were not flooded during testing (i.e., tested unsaturated). Each sample was subjected to a different normal stress that was applied for 24 hours before the shearing phase to ensure proper consolidation. The applied normal stresses were 7.4, 14.8, and 29.7 psi. After consolidation, the samples were sheared at a very slow rate. Figure L-2 presents the normal–shear stress relationship. It was concluded that the subgrade had a peak friction angle of 22.9 degrees and an associated peak cohesion of 6.3 psi.

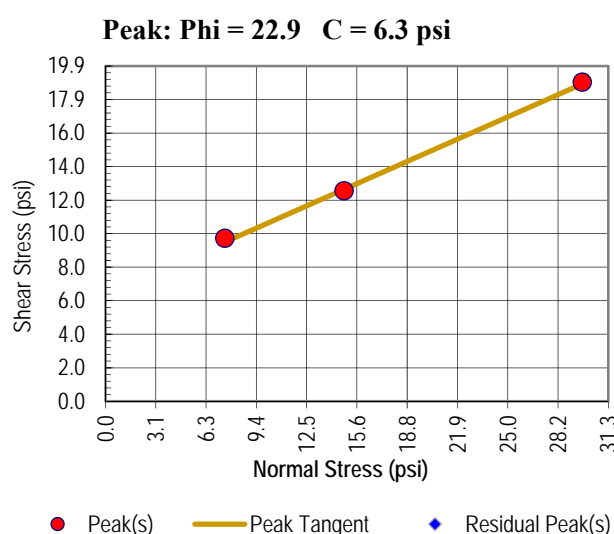


Figure L-2. Direct shear test results for the subgrade material

In order to place the required amount of clay in the LST, the task was divided into three days using a team of five people. The goal was to place the soil at 16 percent water content and 95 percent of the maximum dry density to a depth of 5.5 ft. The final thickness of the subgrade was kept at 4.5 ft for the various experiments. The additional 1 ft was placed to protect the clay from contamination and to reduce moisture evaporation. The top 1 ft of the subgrade was removed right before placing the crushed aggregate base in the LST.

The process of placing the subgrade material was fairly straightforward. The material was shoveled from the stockpile into 5-gal buckets. Four buckets, weighing 30 lb each, were then placed in a concrete mixer with enough water to reach the desired 16 percent moisture content. This subgrade-water mixture was mixed for approximately 30–40 seconds to maintain an even blend. The moist subgrade was then placed into the LST. To assure the proper amount of water was added to the sample, an average moisture content reading was taken at specified times two days before the filling began to analyze how the water content of the clay stockpile changed throughout the day. The weight of the water mixed with the subgrade was adjusted according to the change in water content of the stockpile. To achieve the required compaction, a gasoline-powered rammer proved to be the best option. Ten to 12 passes lasting approximately 5 to

7 minutes each were made to yield a 3-inch compacted lift. To assure the required 95 percent compaction was being reached, nuclear density gauge readings were taken at the 1-, 2-, and 3-ft levels in the LST. Figure L-3 shows the various phases of the placement and compaction of the subgrade material in the tank.

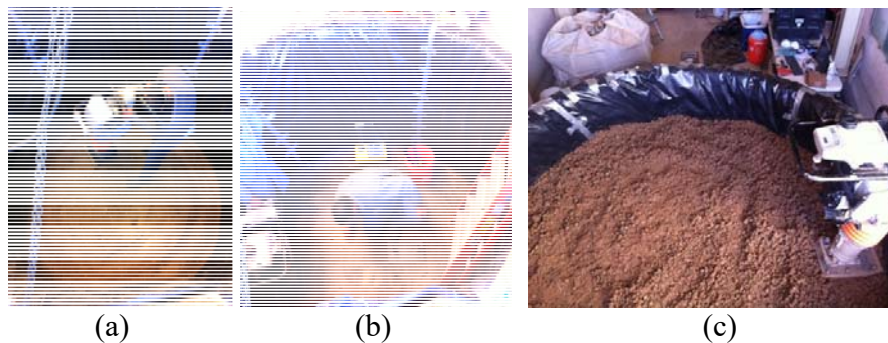


Figure L-3. Placement of the subgrade material in the LST: (a) compaction of the first lift; (b) nuclear density gauge testing; (c) completed placement for the 4.5 ft of subgrade material

While a nuclear density gauge was used to ensure achieving target density during the installation of the subgrade, limited dynamic cone penetrometer (DCP) testing was used to assess the density of the subgrade layer before and after the testing experiments. Thus, the DCP test was conducted after the placement of the subgrade layer for Experiment No. 1 to have a baseline reading. Then, before placing the new crushed aggregate base and asphalt layer for Experiment No. 2, another DCP test was conducted on the subgrade layer to determine if any changes to the density had occurred as a result of the pressures generated by the base, asphalt, and loading during placement and testing. In general, the results showed no significant difference between the densities of the pre-tested subgrade compared to the post-tested subgrade (see Figure L-4).

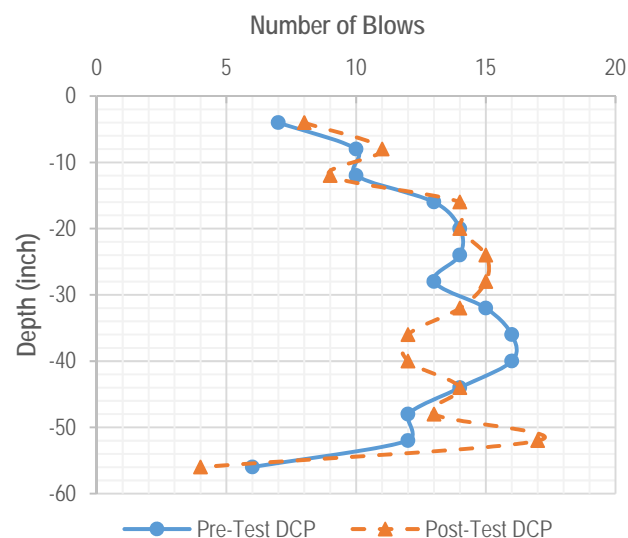


Figure L-4. DCP test results for subgrade layer in LST

Base Layer

A typical dense-graded crushed aggregate base was used in the LST experiments. The same material was used for all flexible and rigid pavement testing. Standard specifications for dense-graded crushed aggregate base (CAB) were reviewed for 19 different states throughout the country, and the requirements for liquid limit, plasticity index, Los Angeles abrasion loss, and resistance R-value are summarized in Table L-2. The minimum, median, and maximum for all reported values are also shown at the bottom of Table L-2. Overall, the specifications were very similar among the various surveyed states, with the Nevada Department of Transportation (NDOT) specification being very close to the median values of all the examined states' specifications. Accordingly, the selected crushed aggregate base material following the NDOT materials' specification was considered to be representative of a typical dense-graded crushed aggregate base.

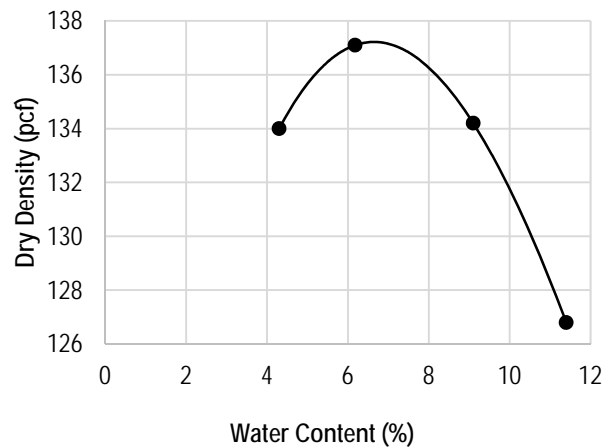
Table L-2. Summary of Selected State Specifications for Crushed Aggregate Base Material

State	Maximum Liquid Limit (LL)	Maximum Plasticity Index (PI)	Maximum Los Angeles Abrasion Loss (%)	Minimum R-Value
Alabama	25	6	60	70
Arizona	25	5	40	70
California	25	6	45	78
Colorado	35	6	45	70
Florida	25	6	45	70
Illinois	25	6	40	72
Indiana	25	5	40	70
Kansas	25	6	50	70
Massachusetts	25	6	45	75
Minnesota	25	6	40	75
Mississippi	25	6	45	70
Nevada	35	6	45	70
New York	25	6	35	70
North Dakota	25	5	50	70
Oklahoma	25	6	50	70
Texas	35	10	45	75
Pennsylvania	35	6	45	72
Virginia	25	6	45	70
Washington	25	6	35	72
Minimum	25	5	35	70
Median	25	6	45	70
Maximum	35	10	60	78

Aggregate base material from a local quarry in northern Nevada was sampled according to the AASHTO T2 protocol and brought back to the UNR facility for testing. Using AASHTO T248 splitting methods, the sample was reduced in size and blended until an adequate sample size and mix were achieved. From the blended sample, the AASHTO T27 and T180 protocols were followed to determine the gradation, maximum dry density, and optimum moisture content. Table L-3 and Figure L-5 show the gradation and moisture-density relationships, respectively.

Table L-3. Gradation for Crushed Aggregate Base Material

Sieve Size	Percent Passing	Lower Limit Specification	Upper Limit Specification
1 inch	100	100	100
3/4 inch	97	90	100
1/2 inch	86	-	-
3/8 inch	68	-	-
No. 4	46	35	65
No. 8	30	-	-
No. 10	26	25	53
No. 16	20	15	40
No. 30	15	-	-
No. 40	12	12	28
No. 50	10	-	-
No. 100	8	-	-
No. 200	3.1	2	10

**Figure L-5. Modified proctor curve for crushed aggregate base material**

The rapid triaxial test (RaTT) was employed to determine the cross-anisotropic properties of granular base material used in the Large-Scale Tank test. A total of 10 stress states associated with three test modes (i.e., compression, shear, and extension modes) were applied in the test protocol. Table L-4 presents the results of the anisotropic properties of the base material used in the Large-Scale Tank test.

Table L-4. Results of Rapid Triaxial Tests for Base Materials Used in Large-Scale Tank Test

σ_1 (kPa)	σ_3 (kPa)	E_x (MPa)	E_y (MPa)	G_{xy} (MPa)	ν_{xy}	ν_{xx}	E_x/E_y	G_{xy}/E_y
40	25	70.3	129.6	49.0	0.15	0.47	0.54	0.38
50	25	79.8	141.8	60.3	0.2	0.42	0.56	0.43
70	40	93.0	200.0	80.6	0.16	0.35	0.47	0.40
130	60	121.6	312.5	98.4	0.17	0.43	0.39	0.31
150	70	153.1	374.6	119.7	0.15	0.42	0.41	0.32
170	100	166.3	388.1	133.3	0.22	0.47	0.43	0.34
220	120	205.2	442.9	145.5	0.16	0.42	0.46	0.33
250	140	224.1	519.7	166.8	0.13	0.42	0.43	0.32
250	120	200.3	495.2	152.5	0.2	0.42	0.40	0.31
250	105	180.7	456.7	151.2	0.16	0.45	0.40	0.31
Average					0.17	0.43	0.45	0.35

The constitutive models of the base material used in this study are shown in Equations L-1 to L-3.

$$E_y = k_1 P_a \left(\frac{I_1}{P_a} \right)^{k_2} \left(\frac{\tau_{oct}}{P_a} + 1 \right)^{k_3} \quad (\text{L-1})$$

$$n = \frac{E_x}{E_y} \quad (\text{L-2})$$

$$m = \frac{G_{xy}}{E_y} \quad (\text{L-3})$$

where I_1 is the first invariant of the stress tensor; τ_{oct} is the octahedral shear stress; P_a is the atmospheric pressure; k_1 , k_2 , and k_3 are regression constants; E_x is the horizontal resilient modulus; E_y is the vertical resilient modulus; and G_{xy} is the shear modulus in the $x-y$ plane.

According to the results presented in Table L-4, the parameters in the constitutive models were determined by using the Solver function, and shown in Table L-5.

Table L-5. Determination of the Cross-Anisotropic Properties of the Base Material Used in Large-Scale Tank Test

Parameters	k_1	k_2	k_3	n	m	ν_{xy}	ν_{xx}
Determined Values	1545	0.75	-0.1	0.45	0.35	0.17	0.43

Geosynthetic Layer

A geogrid and a geotextile that are typical of such products and are currently being used in crushed aggregate base courses were selected for the LST testing. Both materials were installed according to the manufacturer specifications (i.e., no wrinkles or pretension).

For experiments where the geosynthetic was to be placed at the interface between the base and the subgrade, the top 1-inch layer of the subgrade was replaced to allow for a level,

even surface for the geosynthetic to contact. A 9-ft by 9-ft square section of geosynthetic was cut from the roll and then laid over the top of the tank. The edges were trimmed around the perimeter of the Large-Scale Tank to ensure a proper fit. Once the geosynthetic was in place, U-shaped tacks were placed around the edges to maintain activation tension. This approach worked extremely well and kept the geosynthetic firmly in place. A similar procedure was used for experiments where the geosynthetic was to be placed in the middle of the base.

The direct tension tests were conducted to determine the sheet modulus of geosynthetic products used in the Large-Scale Tank tests (see Figure L-6). Figure L-7 shows the relationships between the tensile force and the tensile strain for the tested geogrid and geotextile. “MD” is the abbreviation for machine direction. “XMD” is the abbreviation for cross-machine direction. Both the geogrid and geotextile in the machine direction had a smaller sheet modulus than those in the cross-machine direction. The ductility of geosynthetics in the machine direction was much higher than that in the cross-machine direction.



(a) Tensile Test Setup for Geogrid



(b) Tensile Test Setup for Geotextile

Figure L-6. Direct Tension Test for Determining Sheet Modulus of Geosynthetics

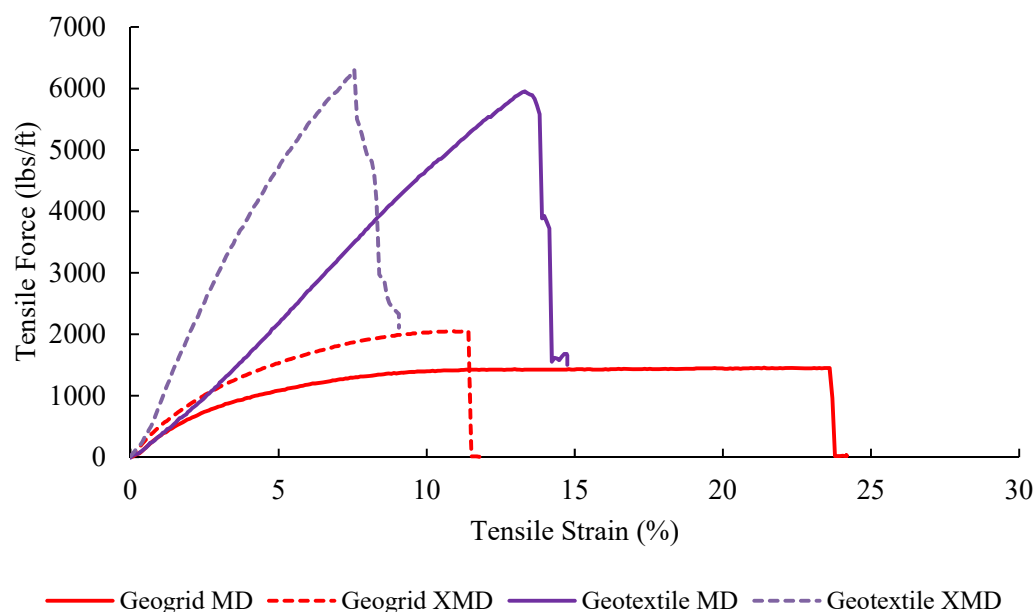


Figure L-7. Relationships between Tensile Force and Tensile Strain for Geosynthetics

Asphalt Concrete Layer

A typical dense-graded HMA with a PG 64-22 unmodified asphalt binder was used in all flexible pavement experiments. Before the final placement of the asphalt layer on top of the base layer in the LST, a trial asphalt placement was conducted to select the most appropriate compaction technique. Three methods of compaction were attempted to see which would yield the best in-place compaction. The first method used a vibro-plate with the HMA placed and compacted in two 3-inch lifts. The second used a mechanical rammer for compaction and placed the asphalt in two 3-inch lifts. The third was also with the rammer, but with three 2-inch lifts. It was decided after finishing that the mechanical rammer was not suitable for HMA compaction and would not be used due to excessive difficulty in achieving an even surface. As a result of the trial compaction, it was decided to place the asphalt mixture using three 2-inch lifts and compacting for a longer period of time using the vibro-plate in order to achieve a target in-place density of 92 to 96 percent.

The asphalt mixture was delivered with a dump truck from a local hot-mix plant supplier. The plant mix was dumped directly in front of the LST and shoveled in until 2.25 inches of uncompacted material was in place. A vibro-plate was then used for compaction of the lift by driving it around the perimeter of the tank from the outside edge to the inside for best compaction. This was repeated for a total of three 2-inch lifts after compaction. A thin lift nuclear density gauge was used at several locations around the surface of the tank to measure the in-place density of the compacted asphalt concrete surface layer. Figure L-8 shows pictures from the various steps during placement of the asphalt concrete layer.

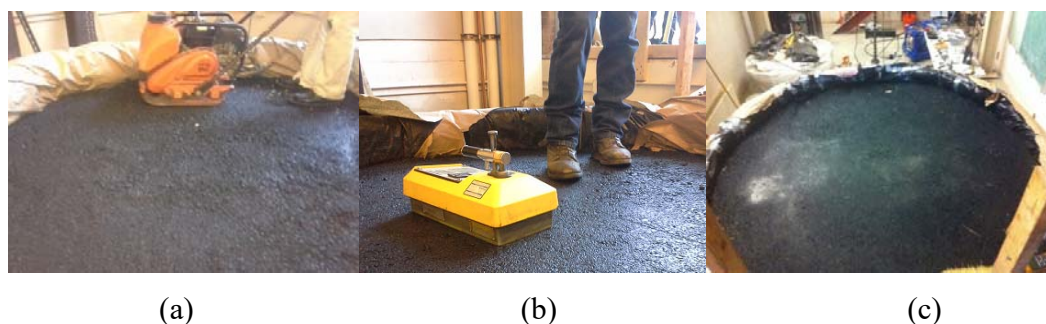


Figure L-8. (a) Compaction of the HMA top lift (from outside edge to the center of the tank); (b) thin lift nuclear density gauge measurement; (c) finished HMA surface layer

Plant-produced loose mixtures were sampled during placement of the material in the LST and were tested for theoretical maximum specific gravity (G_{mm}) in accordance with AASHTO T209. Table L-7 summarizes the test results for the maximum theoretical specific gravities. The data show that consistent G_{mm} values were obtained for the various materials and similar to the G_{mm} value from the mix design.

Loading of the pavement structure was conducted seven days after the placement of the HMA layer in all experimental cases. This was done to eliminate additional uncertainties due to variability in the asphalt material properties as a result of oxidative aging. Cores were taken immediately after the completion of testing for each experiment (see Figure L-9) to measure the thickness and verify the in-place asphalt layer density. A total of 10 cores were taken at various locations in the asphalt concrete layer. Five of the cores were extracted from pre-determined locations matching a nuclear gauge density test. Table L-8 summarizes the asphalt layer thicknesses and core densities for all six flexible pavement experiments.

Table L-7. Theoretical Maximum Specific Gravity Results for Plant-Produced Mixture

Experiment		Theoretical Maximum Specific Gravity, G_{mm}	
ID	No.	Measured	Mix Design
AC-Contr-B06	1	2.497	2.491
AC-Contr-B10	2	2.491	
AC-Grid-B06	3	2.502	
AC-Grid-B10	4	2.499	
AC-Textile-B06	5	2.499	
AC-Textile-B10	6	2.491	



Figure L-9. Coring of the asphalt concrete layer in the LST

Table L-8. Asphalt Layer Thicknesses and Core Densities

Experiment ^a		Asphalt Layer Thickness (inch)		Core Densities (%)	
ID	No.	Average	Standard Deviation	Average	Standard Deviation
AC-Contr-B06	1	5.8	0.4	93.7	1.3
AC-Contr-B10	2	5.6	0.1	92.7	2.2
AC-Grid-B06	3	5.7	0.2	93.4	1.3
AC-Grid-B10	4	5.7	0.3	95.3	1.5
AC-Textile-B06	5	5.9	0.1	94.0	1.9
AC-Textile-B10	6	5.9	0.3	96.9	0.9

^a Experiment No. 1 (control-thin CAB layer), 2 (control-thick CAB layer), 3 (geogrid-thin CAB layer), 4 (geogrid-thick CAB layer), 5 (geotextile-thin CAB layer), and 6 (geotextile-thick CAB layer).

Selected asphalt core specimens (referred to as plant-mixed, field-compacted [PMFC]) from each of the flexible experiments were also tested for dynamic modulus in accordance with AASHTO TP79-13. Plant-mixed, laboratory-compacted (PMLC) samples from each experiment were also prepared at a similar corresponding in-place air void level and tested for dynamic modulus. The developed dynamic modulus master curve for each of the PMLCs was compared to the associated PMFCs, as shown in Figure L-10. It should be noted that the master curves are all reported at the average asphalt layer temperature of 79°F that was recorded during the LST experiment.

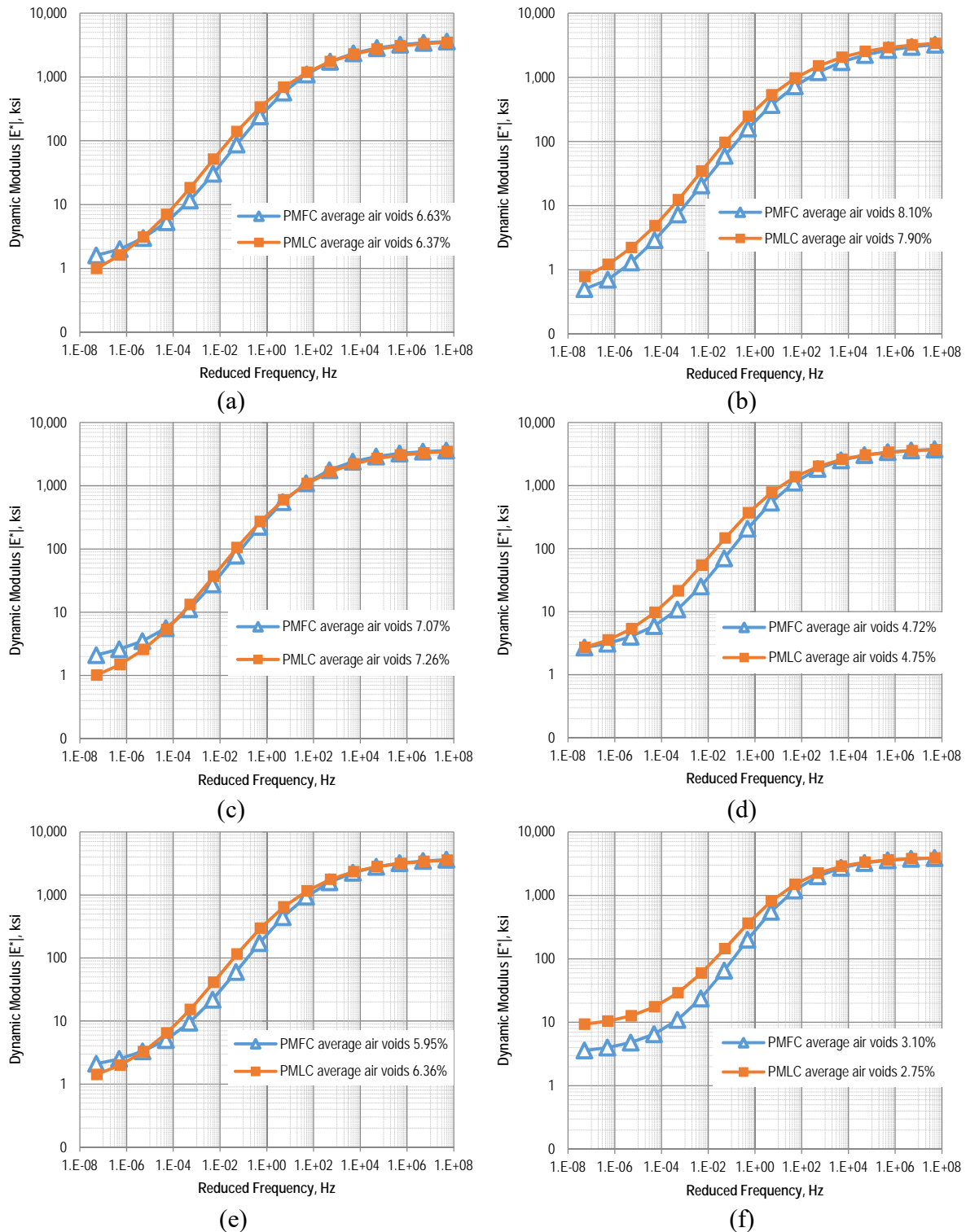


Figure L-10. Asphalt mixture dynamic modulus master curves at 79°F (average of three replicates): (a) Experiment No. 1; (b) Experiment No. 2; (c) Experiment No. 3; (d) Experiment No. 4; (e) Experiment No. 5; and (f) Experiment No. 6

Portland Cement Concrete Layer

The testing for rigid pavement in LST consisted of a half-slab PCC in order to allow for the measurements of slippage at the interface between the bottom of the PCC slab and the supporting base layer, as well as the deflection at the pavement edge. These two measurements were needed for modeling the properties of the composite concrete-base surface layer. Furthermore, an irrigation system was introduced to the rigid pavement experiments to model the effects of a wet base layer on the pavement responses, which is considered critical for modeling the mechanics of erosion in rigid pavements. The irrigation system consisted of a main plastic hose running around the diameter of the LST with holes placed every 6 inches and a set of quarter-inch soaker hoses attached to the main hose (on the side of the half tank) and running along the diameter of the tank. By connecting the hose to a water source, the base was flooded until it was evenly partially saturated. A picture of the irrigation system is shown in Figure L-11. The irrigation system was embedded in the crushed aggregate base layer at 1 inch below the top of the base.

In order to provide the necessary vertical pressure and confinement for the base layer during the loading of the pavement, a full PCC slab with a 6-inch gap in the middle of the tank was constructed. The 6-inch gap was selected to allow for the installation of the instrumentations needed for the assessment of slippage at the PCC-base interface. Figure L-12 shows a schematic of the setup for rigid pavement experiments.



Figure L-11. Completed irrigation system: soaker hose configuration

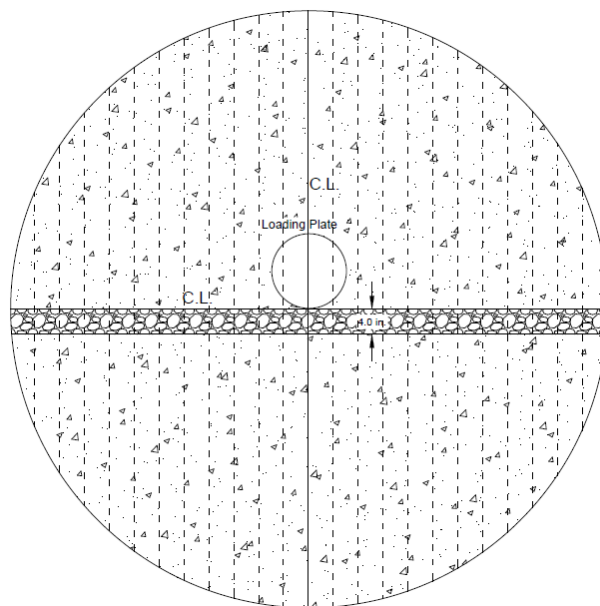


Figure L-12. LST top view for rigid pavement with irrigation system

The specification for a typical PCC material used for roadway paving was selected for the LST experiments. Table L-9 shows the requirements for the PCC material. A minimum 28-day flexural strength of 650 psi was required. A private local company was hired to provide the ready mix concrete for the rigid experiments. To verify the quality of the concrete delivered during each LST experiment, samples were taken during the placement of the concrete and tested for fresh and hardened properties. Limited core and slab samples were also collected and tested at the end of each experiment to verify that the concrete was being cured properly.

Placement of the concrete was performed using standard industry procedures. The PCC mix was brought in using a concrete truck. Slump, unit weight, and air content tests were conducted, and 21 compressive strength cylinders and seven flexural strength beams were prepared for curing and testing. While the test samples were being prepared, the concrete was poured directly into the LST ring. A standard vibrating rod was used to finalize the placement of the PCC mix. To ensure that the concrete cured properly, a curing blanket was placed over the slab and was hydrated throughout the day. The test results for fresh and hardened PCC properties are shown in Table L-10.

The LST testing of the concrete pavement initiated when at least 85 percent of the specified 28-day flexural strength was achieved (i.e., 552 psi). Based on the maturity testing measurements, it was determined that a 13-day curing period of the concrete slab was necessary before the start of the testing. The same curing technique and duration were implemented for all rigid pavement experiments. Table L-11 shows the test results for the PCC samples taken out of the slab right after the completion of each of the rigid experiments.

Table L-9. Mix Design Requirements for PCC Material

Test	Test Method	Requirements
Water to Cementitious Ratio	-	0.45 Maximum
Flexural Strength at 28 Days (psi)	ASTM C 78	650 Minimum
Slump (inches)	ASTM C 143	
Initial		2 Maximum
After Addition of HRWR ^a		4 Maximum
Air Content (percent)	ASTM C 173 or ASTM C231	
No. 467 Aggregate		5.5

^a High-range water reducer.**Table L-10. Hardened and Fresh Properties of PCC Sampled During Placement**

Property		Curing Duration (Days)	Experiment No. ^a		
			7	9	10
Hardened Properties	Compressive Strength, psi (ASTM C39)	5	4,501	4,438	4,387
		7	4,625	4,562	4,505
		9	4,785	4,672	4,598
		12	4,876	4,904	4,861
		14	5,203	5,128	5,024
		28	6,086	6,073	5,984
	Flexural Strength, psi (ASTM C78)	7	502	494	476
		9	545	535	521
		12	605	583	567
		14	619	601	598
Fresh Properties	Air Content, % (ASTM C138)		5.3	5.6	4.9
	Slump, inch (ASTM C143)		3.75	4.25	4.00
	Unit Weight (ASTM C173)		142.3	142.6	144.2

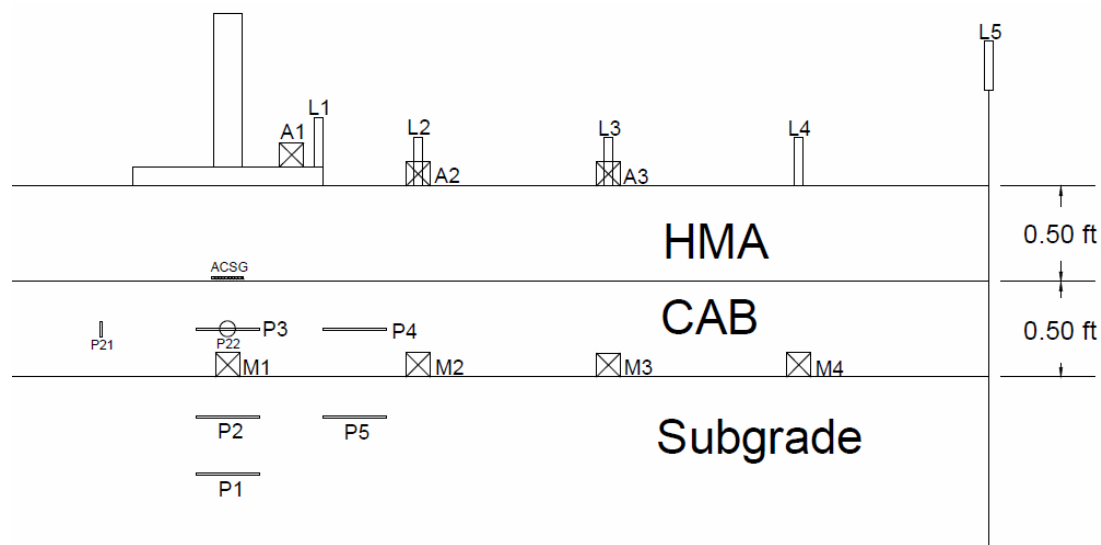
^a Experiment No. 7 (control), 9 (geogrid), and 10 (geotextile).**Table L-11. Post-Testing Properties of PCC (Core/Slab Specimens)**

Property	Exp. No. ^a	Test Results			
		Average	Standard Deviation	Minimum	Maximum
Core Thickness, inch	7	5.953	0.005	5.949	5.958
Compressive Strength, psi (ASTM C39)		4,679	23	4,661	4,705
Flexural Strength, psi (ASTM C78)		562	N/A ^b	557	567
Core Thickness, inch	9	6.075	0.003	6.072	6.077
Compressive Strength, psi (ASTM C39)		4,760	40	4,722	4,802
Flexural Strength, psi (ASTM C78)		566	N/A ^b	563	569
Core Thickness, inch	10	5.853	0.004	5.849	5.856
Compressive Strength, psi (ASTM C39)		4,901	79	4,826	4,984
Flexural Strength, psi (ASTM C78)		579	N/A ^b	577	581

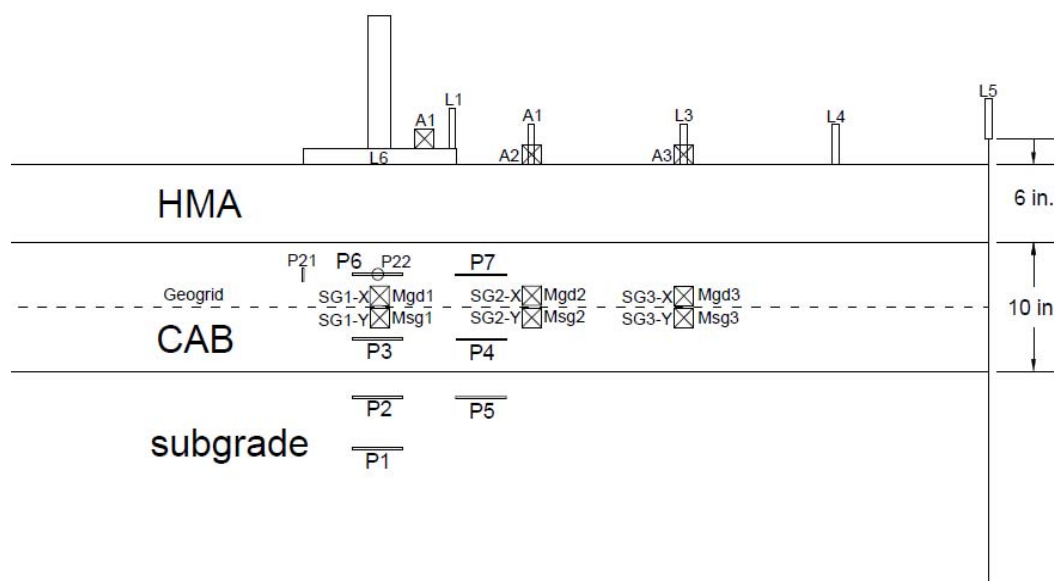
^a Experiment No. 7 (control), 9 (geogrid), and 10 (geotextile).^b Only two flexural strength beams were cut from each slab.

APPENDIX M. COMPARISON OF FINITE ELEMENT SIMULATIONS WITH LARGE-SCALE TANK MEASUREMENTS

The finite element simulation results of the developed geosynthetic-reinforced and unreinforced pavement models were validated by comparing them to the Large-Scale Tank test measurements in terms of the surface deflection, the tensile strain at the bottom of the asphalt concrete, and the vertical pressures within the base and subgrade layers. Figure M-1 illustrates the location of the instruments, such as the linear variable deflection transducers (LVDTs), the tensile strain gauge, and the pressure sensors in the flexible pavement structures. Four LVDTs were mounted on the surface of asphalt concrete (i.e., L1–L4). LVDT 5 was used to examine the movement of the Large-Scale Tank boundary. The pressure sensors P1, P2, P3, P4, P5, P6, and P7 were used to measure the vertical compressive pressure in the base course or subgrade. The pressure sensors P21 and P22 were installed to record the horizontal pressure in the base course.



(a) Flexible pavement with a 6-inch base course



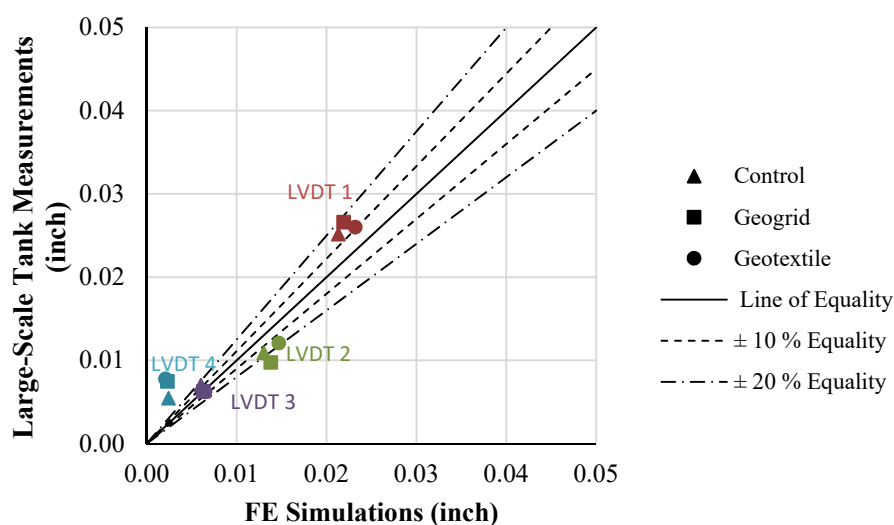
(b) Flexible pavement with a 10-inch base course

Figure M-1. Location of Instruments in Flexible Pavement Structures

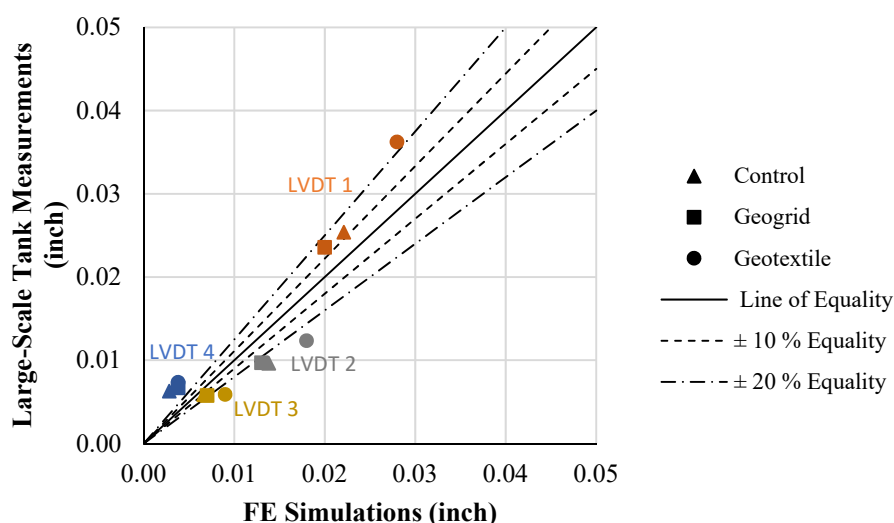
Figures M-2 to M-4 show the comparison of the surface deflections predicted by the finite element models and the Large-Scale Tank test measurements when the pavement structures were subjected to a 9-kip, 12-kip, and 16-kip load, respectively. The model-predicted surface deflections were in agreement with the Large-Scale Tank measurements from LVDTs 1, 2, and 3. The deviation between the measured surface deflection by LVDT 4 and that predicted by the finite element model existed because the surface deflection at this location was too small to be accurately captured by the LVDT. This indicates that the developed geosynthetic-reinforced and

unreinforced pavement models have high accuracy to predict the pavement surface deflections. The comparison of the tensile strain at the bottom of the asphalt concrete are plotted in Figures M-5 to M-7. The developed finite element models accurately predicted the tensile strain in the geogrid-reinforced and unreinforced pavement structures but slightly overestimated the tensile strain in the geotextile-reinforced pavement structures. Figures M-8 to M-10 present the comparison between the predicted vertical pressures within the base and subgrade layer and the measured results. Most of the measured pressure values were captured by the developed finite element models, except the measurement of pressure cells P1 and P7. There are a number of possible explanations for these discrepancies. For example, for sensor P1, the stress-dependent behavior of the subgrade was not taken into account (see Figures M-8a and M-8b). For sensor P7 shown in Figure M-8b, the fact that the measured pressure was lower than the predicted may be due to arching over the sensor.

In summary, the finite element simulation results were in good agreement with the Large-Scale Tank test measurements for both the reinforced and unreinforced pavement structures. Considering the paving material characterization, the geosynthetic-aggregate/soil interface characterization, and the reinforcement influence zone is important to develop accurate numerical models of geosynthetic-reinforced pavement structures.

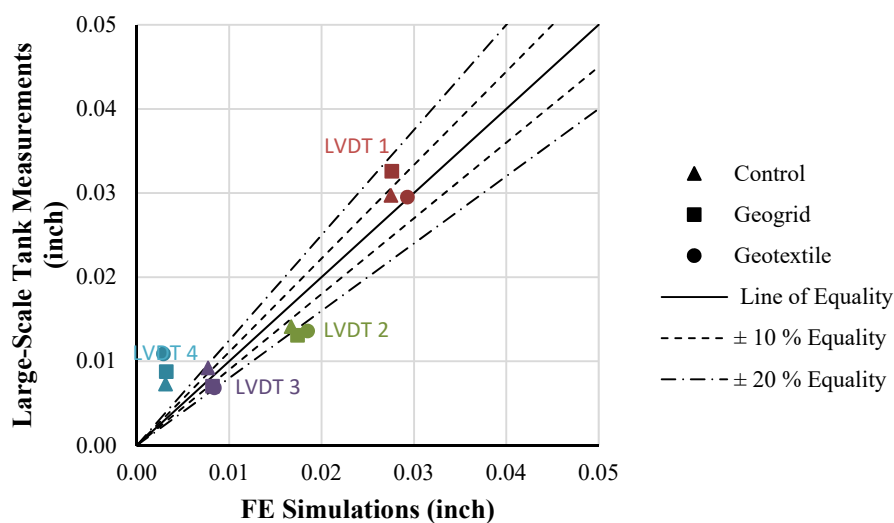


(a) Pavement Structures with 6-inch Base Course

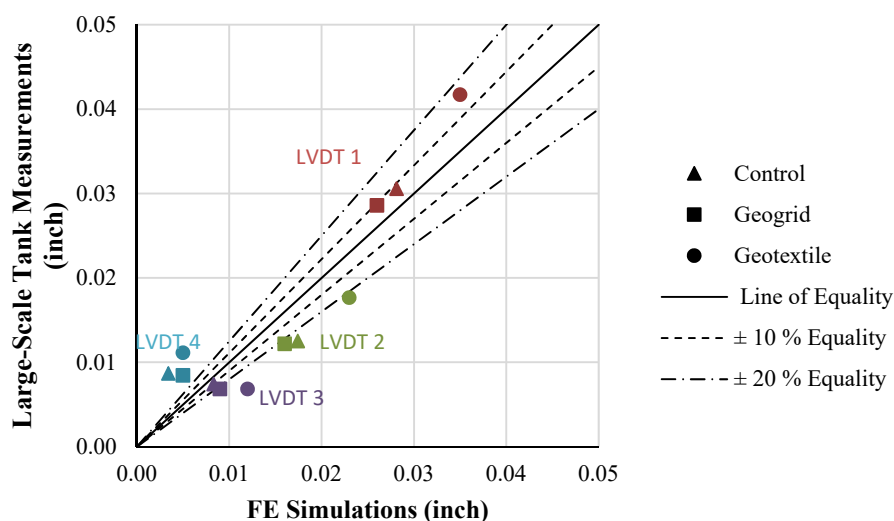


(b) Pavement Structures with 10-inch Base Course

Figure M-2. Comparison of Measured and Predicted Surface Deflections for Pavement Structures with and without Geosynthetic Subjected to a 9-kip Load

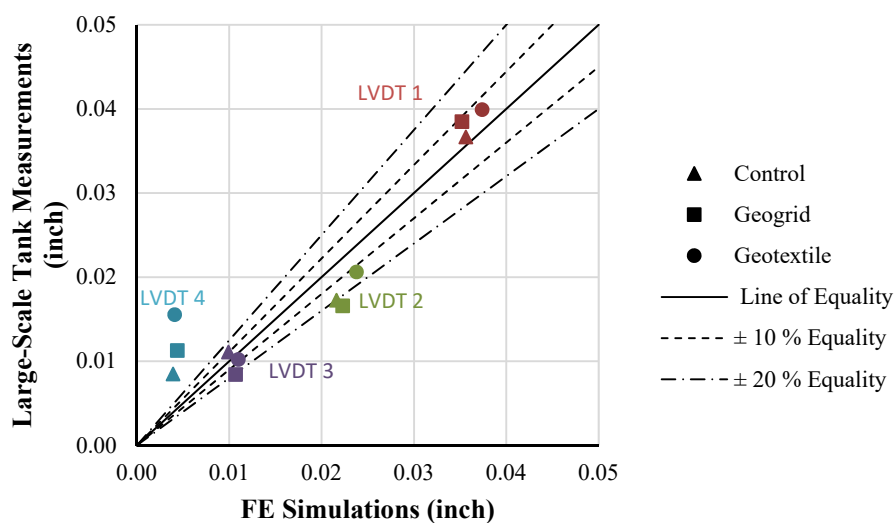


(a) Pavement Structures with 6-inch Base Course

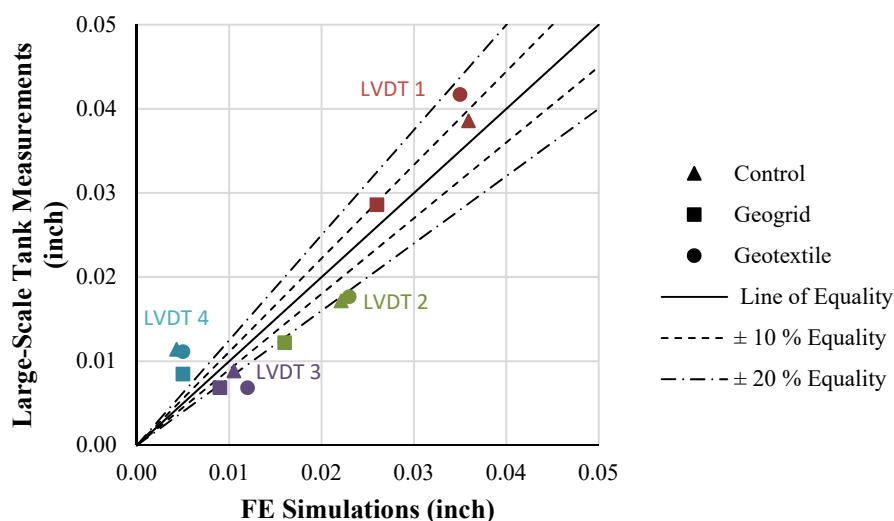


(b) Pavement Structures with 10-inch Base Course

Figure M-3. Comparison of Measured and Predicted Surface Deflections for Pavement Structures with and without Geosynthetic Subjected to a 12-kip Load

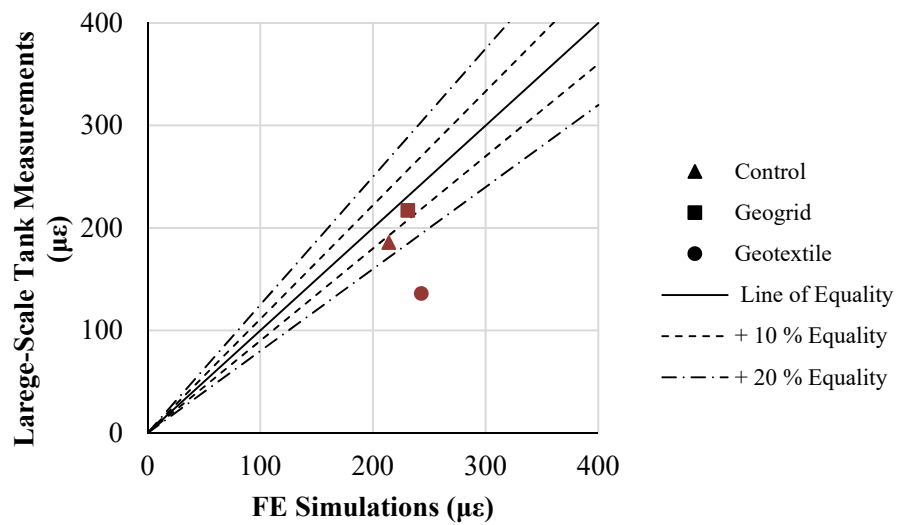


(a) Pavement Structures with 6-inch Base Course

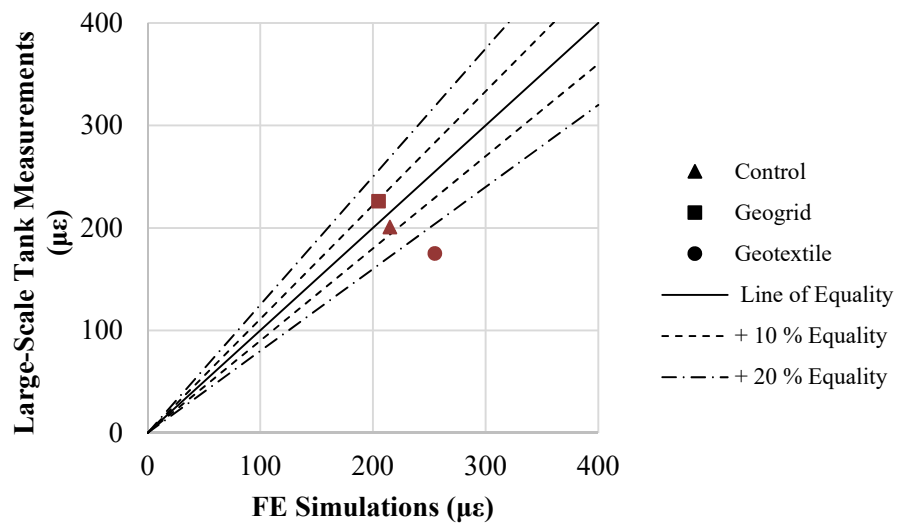


(b) Pavement Structures with 10-inch Base Course

Figure M-4. Comparison of Measured and Predicted Surface Deflections for Pavement Structures with and without Geosynthetic Subjected to a 16-kip Load

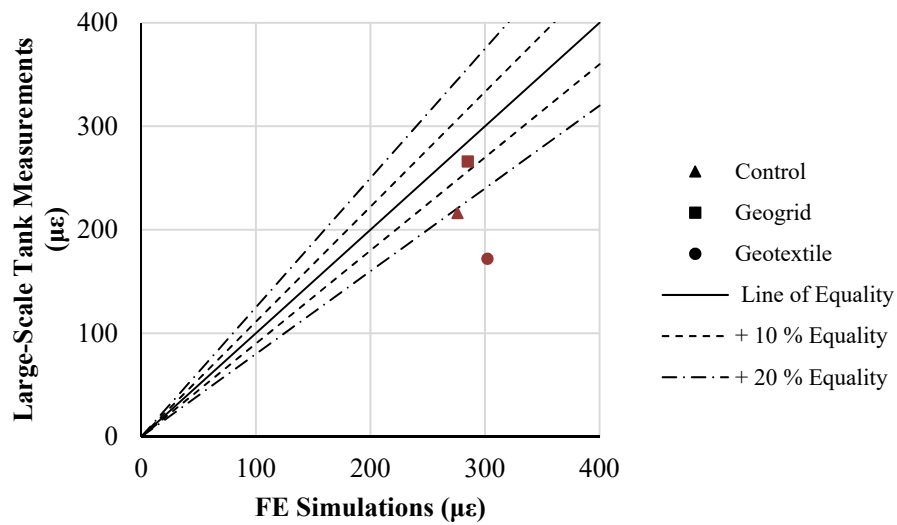


(a) Pavement Structures with 6-inch Base Course

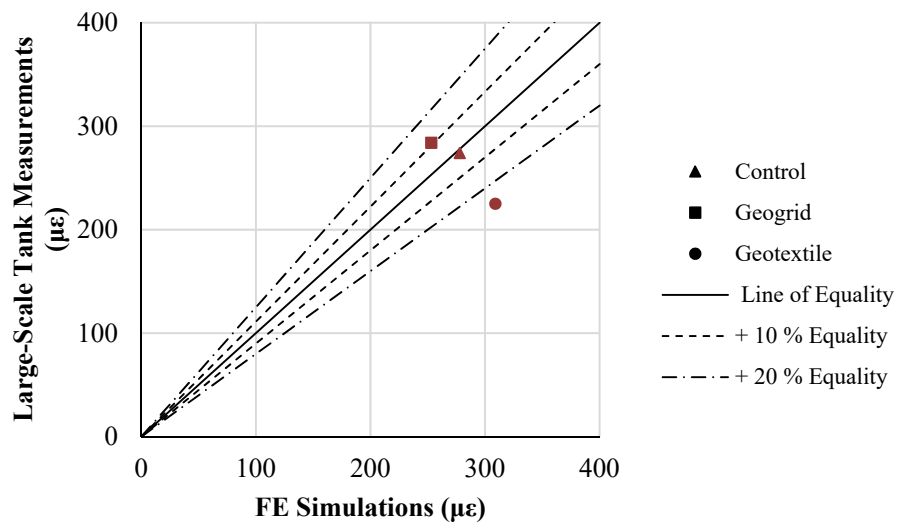


(b) Pavement Structures with 10-inch Base Course

M-5. Comparison of Measured and Predicted Tensile Strains at the Bottom of Asphalt Concrete for Pavement Structures with and without Geosynthetic Subjected to a 9-kip Load

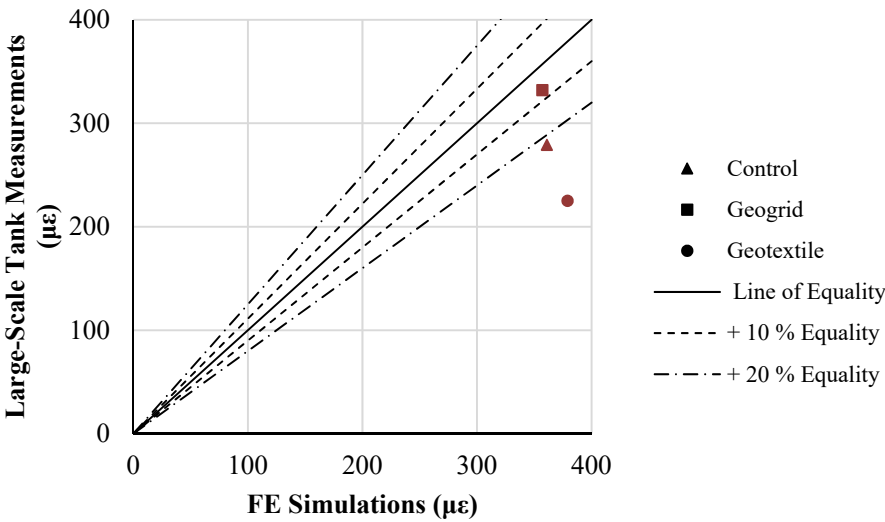


(a) Pavement Structures with 6-inch Base Course

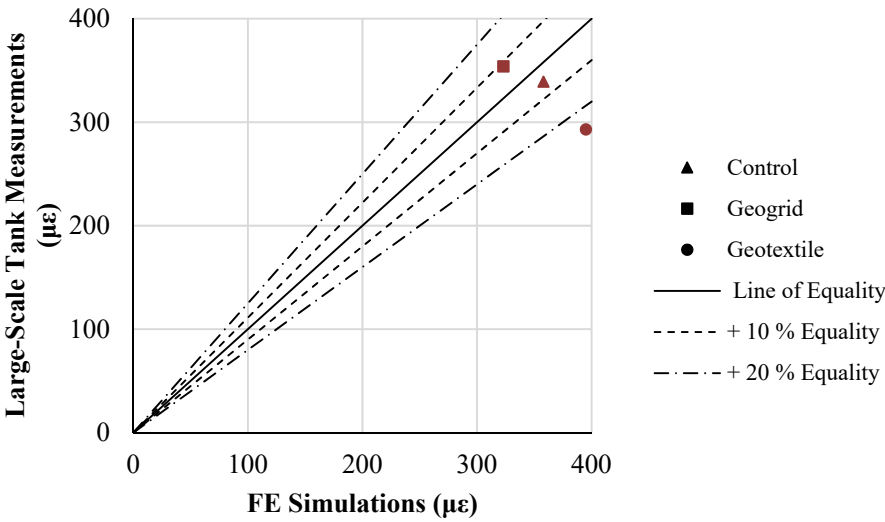


(b) Pavement Structures with 10-inch Base Course

M-6. Comparison of Measured and Predicted Tensile Strains at the Bottom of Asphalt Concrete for Pavement Structures with and without Geosynthetic Subjected to a 12-kip Load

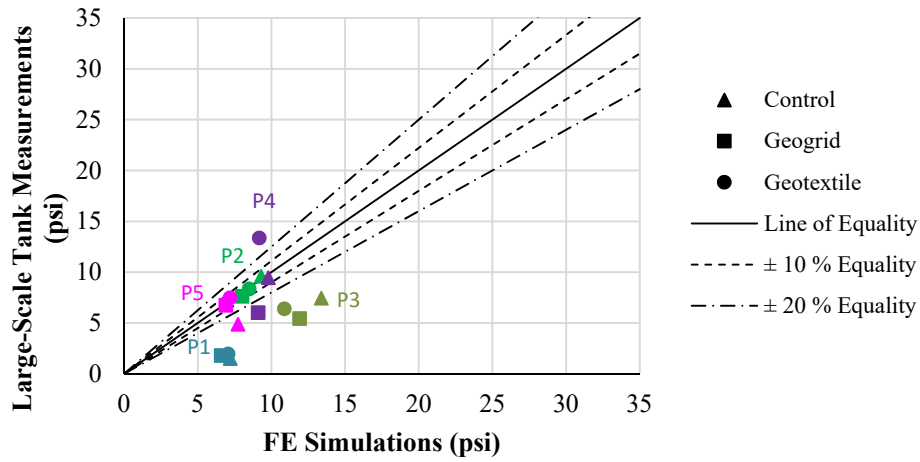


(a) Pavement Structures with 6-inch Base Course

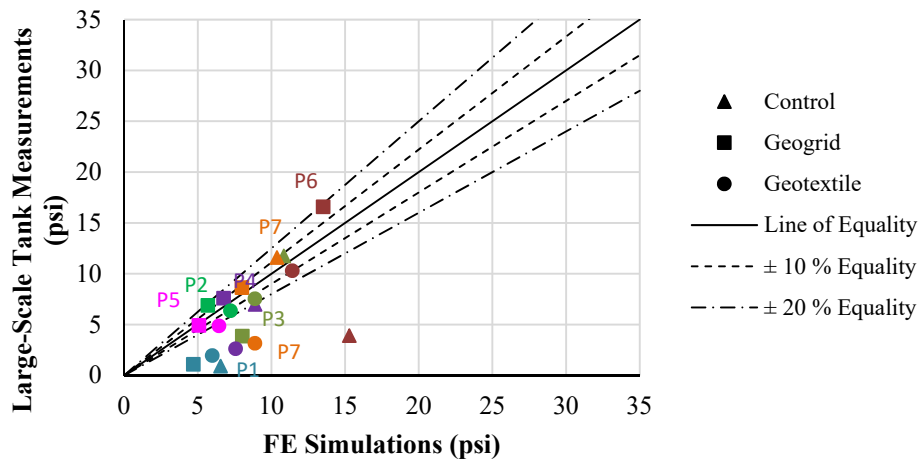


(b) Pavement Structures with 10-inch Base Course

M-7. Comparison of Measured and Predicted Tensile Strains at the Bottom of Asphalt Concrete for Pavement Structures with and without Geosynthetic Subjected to a 16-kip Load

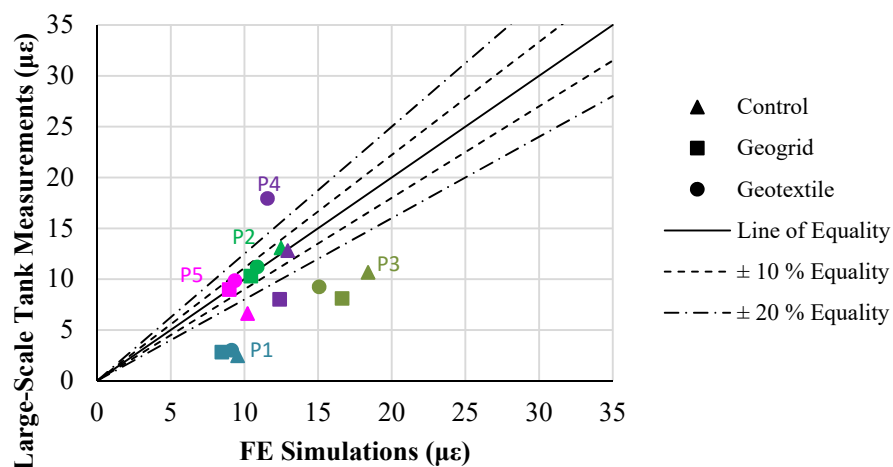


(a) Pavement Structures with 6-inch Base Course

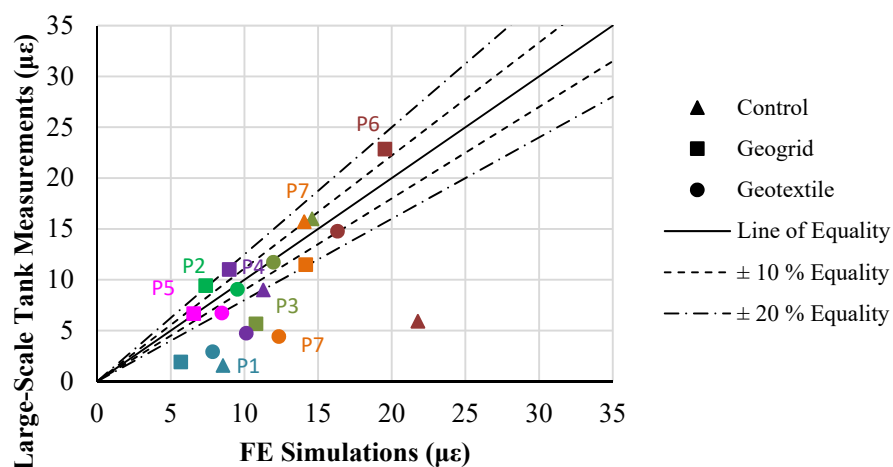


(b) Pavement Structures with 10-inch Base Course

M-8. Comparison of Measured and Predicted Vertical Stresses within the Base and Subgrade for Pavement Structures with and without Geosynthetic Subjected to a 9-kip Load

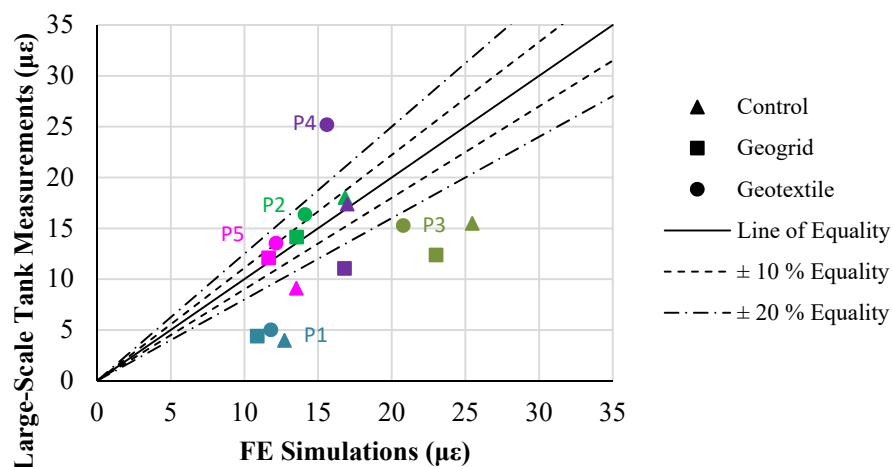


(a) Pavement Structures with 6-inch Base Course

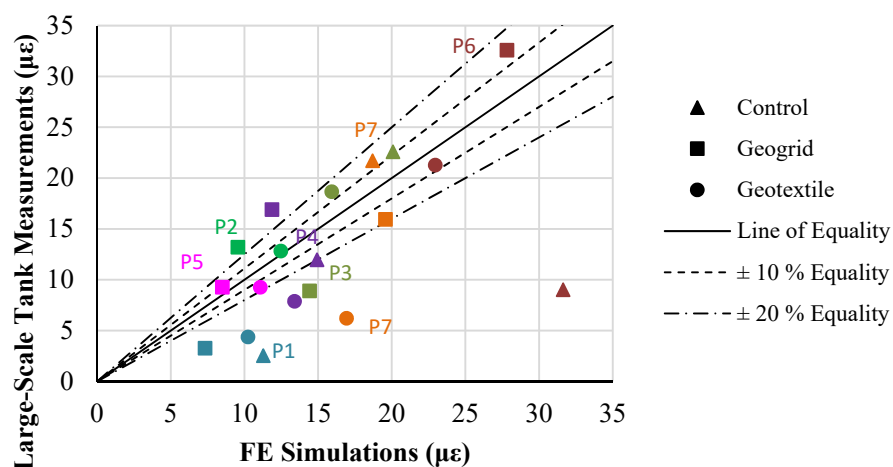


(b) Pavement Structures with 10-inch Base Course

M-9. Comparison of Measured and Predicted Vertical Stresses within the Base and Subgrade for Pavement Structures with and without Geosynthetic Subjected to a 12-kip Load



(a) Pavement Structures with 6-inch Base Course



(b) Pavement Structures with 10-inch Base Course

M-10. Comparison of Measured and Predicted Vertical Stresses within the Base and Subgrade for Pavement Structures with and without Geosynthetic Subjected to a 16-kip Load

APPENDIX N. DEVELOPMENT OF ARTIFICIAL NEURAL NETWORK MODELS FOR PREDICTING GEOSYNTHETIC-REINFORCED PAVEMENT PERFORMANCE

The current Pavement ME Design software predicts pavement performance based on the computed critical pavement responses from a linear isotropic and layered elastic program. In other words, the determination of critical pavement responses is the key to forecasting pavement performance. The finite element models developed in this project are sufficiently accurate to compute the critical responses of geosynthetic-reinforced pavement structures. However, these models were developed using the software ABAQUS, which is not compatible with the Pavement ME Design embedded software DARWin-ME. Furthermore, replacing the current Pavement ME Design software with the developed finite element models to compute the critical responses of the arbitrary user-inputted geosynthetic-reinforced pavement structures is impractical at the moment. Therefore, there is a need to predict the responses of any given geosynthetic-reinforced pavement structure based on computation by the developed finite element models for a wide range of geosynthetic-reinforced pavement structures.

To satisfy this need, the artificial neural network (ANN) approach is used to predict the critical responses of geosynthetic-reinforced pavement structures. The ANN models allow establishing the correlations between the input variables, X_i , and the output variables, Y_j , through the inter-connected neurons (i.e., weight factor, w_{ji}) (1). Note that the input variables, X_i , and the output variables, Y_j , are usually normalized to x_i and y_j , respectively, which are the values between 0 and 1. Herein, the output variables, Y_j , represent the computed critical pavement responses, including the tensile strain at the bottom of the asphalt concrete, and the compressive strain within the asphalt concrete, base layer, and subgrade. The selection of the input parameters, X_i , is based on the sensitivity analysis of the developed finite element models. The identified input parameters to the ANN model include the layer thickness, the modulus of the paving material, the location of the geosynthetic, and the type of geosynthetic. The correlations developed by the ANN models between the normalized input parameters, x_i , and the normalized output variables, y_j , are shown in Equation N-1.

$$y_j = f \left(\sum_{i=1}^n w_{ji} x_i \right) \quad (\text{N-1})$$

where f is a transfer function, which normally uses a sigmoidal, Gaussian, or threshold functional form; and w_{ji} is the unknown weight factors. Developing a neural network model specifically requires the determination of the weight factors, w_{ji} , in Equation 1. The ANN model determines these weight factors, w_{ji} , through two major functions: training and validating. The training dataset is used to determine the trial weight factors, w_{ji} , and the validating dataset is employed to examine the accuracy of the model prediction. A robust ANN model normally

requires a large database of input and output variables (2). Thus, generating the input and output variables database is the first step in developing the ANN model.

Experimental Computational Plan for ANN Models

To generate the database of the numerical model inputs and the corresponding computed critical pavement responses, the computation of multiple cases was performed based on the developed geosynthetic-reinforced and unreinforced finite element models. Tables N-1 and N-2 show the selected input parameters as well as their values for the geosynthetic-reinforced pavement structures and the corresponding unreinforced pavement structures, respectively. Based on these experimental computational plans, the number of the computed geosynthetic-reinforced pavement models was 5832, and the number of the computed unreinforced pavement models was 486. As shown in Table N-1, two geosynthetic types (geogrid and geotextile) and two geosynthetic locations (middle and bottom of base course) were taken into account in the computation of the multiple cases. The pavement responses database was divided into five categories, including

- The geogrid placed in the middle of the base layer (GG-M).
- The geogrid placed at the bottom of the base layer (GG-B).
- The geotextile placed in the middle of the base layer (GT-M).
- The geotextile placed at the bottom of the base layer (GT-B).
- The unreinforced one (NG).

Each category of pavement response database corresponded to one set of neural network models.

Table N-1. Selected Input Parameters for Geosynthetic-Reinforced Pavement Structures

Influential Factors	Level	Input Values
Load Magnitude	1	9 kip
HMA Thickness	3	2, 4, and 6 inches
HMA Modulus	3	300, 450, and 600 ksi
Base Thickness	3	6, 10, and 15 inches
Base Vertical Modulus	3	20, 40, and 60 ksi
Base Anisotropic Ratio	2	0.35 and 0.45
Geosynthetic Location	2	Middle and Bottom of Base Course
Geosynthetic Type	2	Geogrid and Geotextile
Geogrid Sheet Modulus	3	1200, 2400, and 3600 lb/in
Geotextile Sheet Modulus	3	1800, 3600, and 5400 lb/in
Subgrade Modulus	3	5, 15, and 25 ksi

Note: The number of total cases was 5832.

Table N-2. Selected Input Parameters for Unreinforced Pavement Structures

Influential Factors	Level	Input Values
Load Magnitude	1	9 kip
HMA Thickness	3	2, 4, and 6 inches
HMA Modulus	3	300, 450, and 600 ksi
Base Thickness	3	6, 10, and 15 inches
Base Vertical Modulus	3	20, 40, and 60 ksi
Base Anisotropic Ratio	2	0.35 and 0.45
Subgrade Modulus	3	5, 15, and 25 ksi

Note: The number of total cases was 486.

Selection of ANN Algorithms

A three-layered neural network architecture consisting of one input layer, one hidden layer, and one output layer was constructed as shown Figure N-1. The input parameters are listed in Tables 1 and 2, except the geosynthetic location and the geosynthetic type. The output variables were the critical pavement responses, including the tensile strain at the bottom of the asphalt concrete, and the compressive strains within the asphalt concrete, base course, and subgrade. The hidden layer assigned 20 neurons to establish the connection between the output layer and the input layer. In this study, the transfer function used a sigmoidal functional form, which is shown in Equation N-2 (3).

$$f(I_i) = \frac{1}{1 + \exp(-\phi I_i)} \quad (\text{N-2})$$

where I_i is the input quantity; and ϕ is a positive scaling constant, which controls the steepness between the two asymptotic values 0 and 1. The constructed neural network structure was programmed using the software MATLAB R2013a (4). The training algorithm used the Levenberg-Marquardt back-propagation method to minimize the mean squared error (MSE) (5). The gradient descent weight function was employed as a learning algorithm to adjust the weight factors, w_{ji} (6).

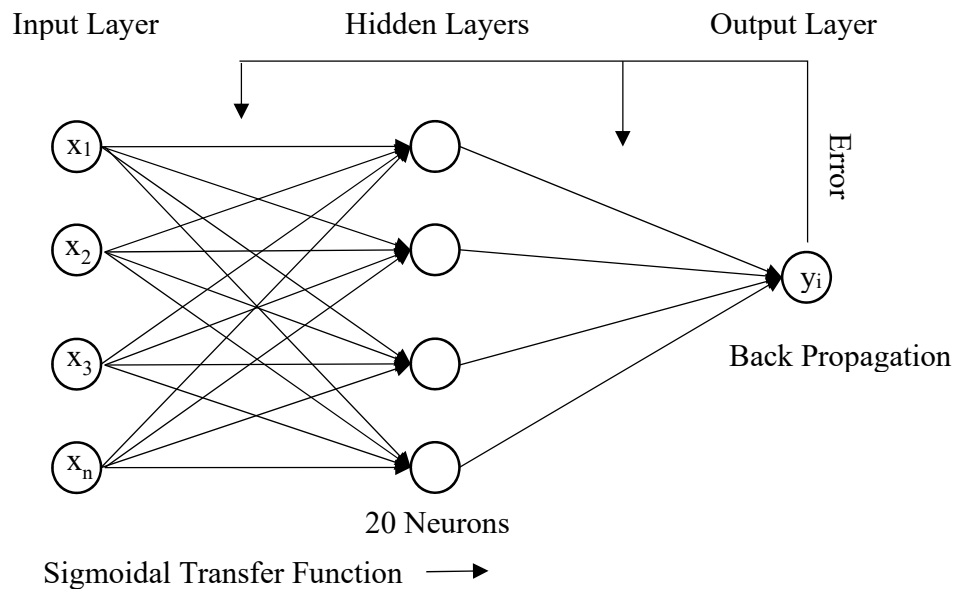


Figure N-1. Illustration of Three-Layered Neural Network Architecture

Prediction of Pavement Performance

The pavement response database was first randomly divided into a training dataset and a validating dataset as the ratio of 80 percent and 20 percent, respectively. The training dataset was used to determine the weight factors, w_{ji} , and the validating dataset was employed to examine the prediction accuracy of the developed neural network. Figures N-2–N-26 show the comprehensive comparisons between the finite element model computed pavement responses and the ANN model predicted pavement responses for the geosynthetic-reinforced and unreinforced pavement structures. The ANN models accurately predicted all of the pavement responses from the validating dataset after the training process. The developed ANN models can be used to interpolate the critical responses of any given geosynthetic-reinforced pavement structure.

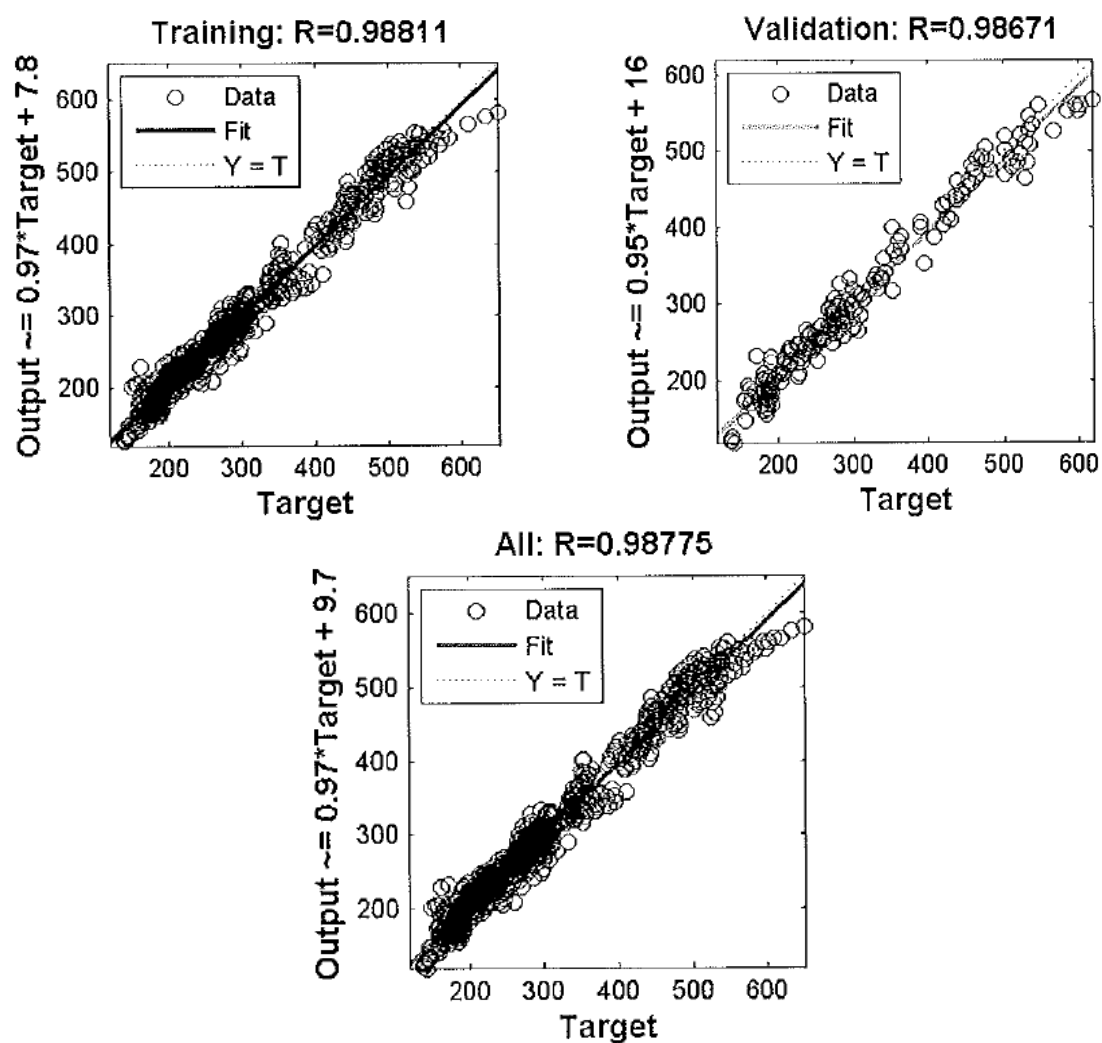


Figure N-2. Comparison of Tensile Strain at the Bottom of the Asphalt Concrete for GG-M Structure

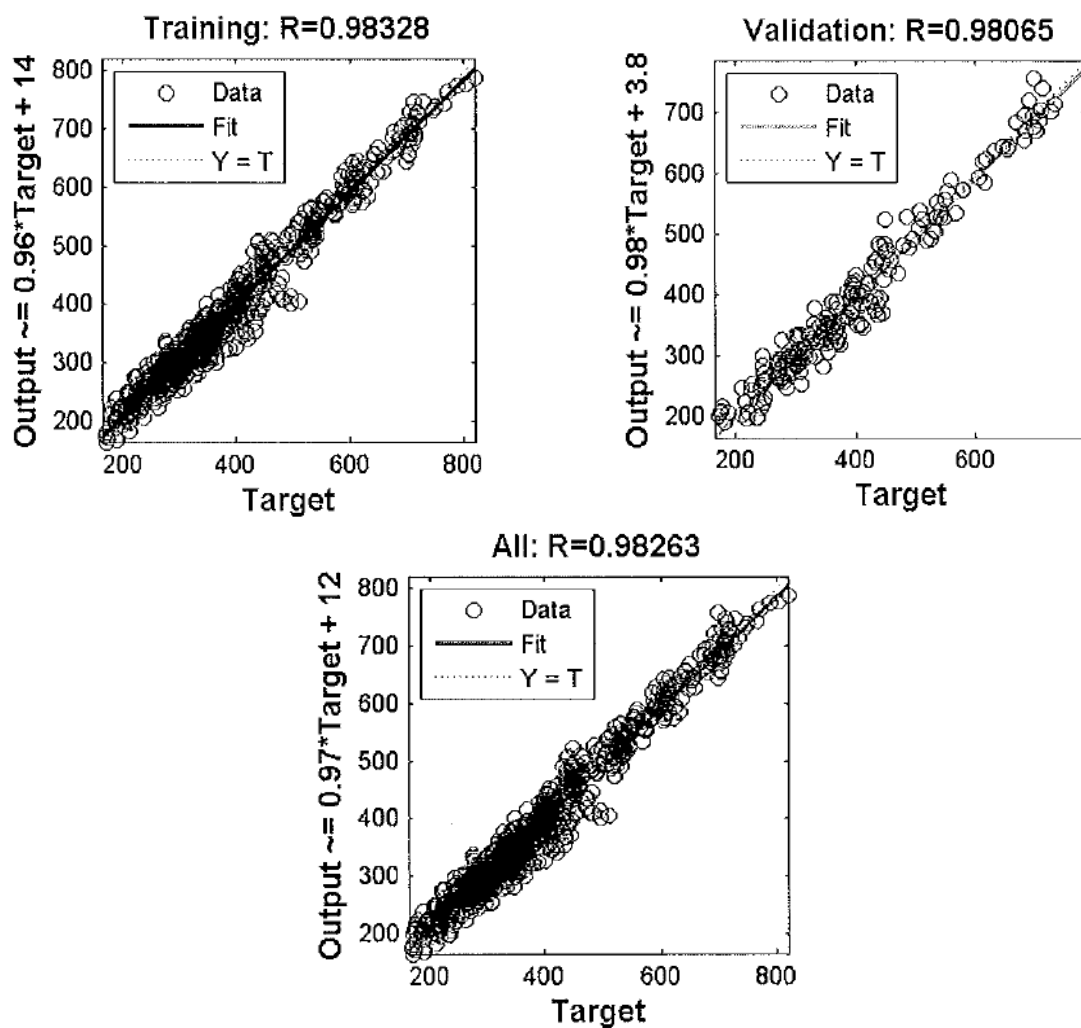


Figure N-3. Comparison of Average Vertical Strain in the Asphalt Concrete for GG-M Structure

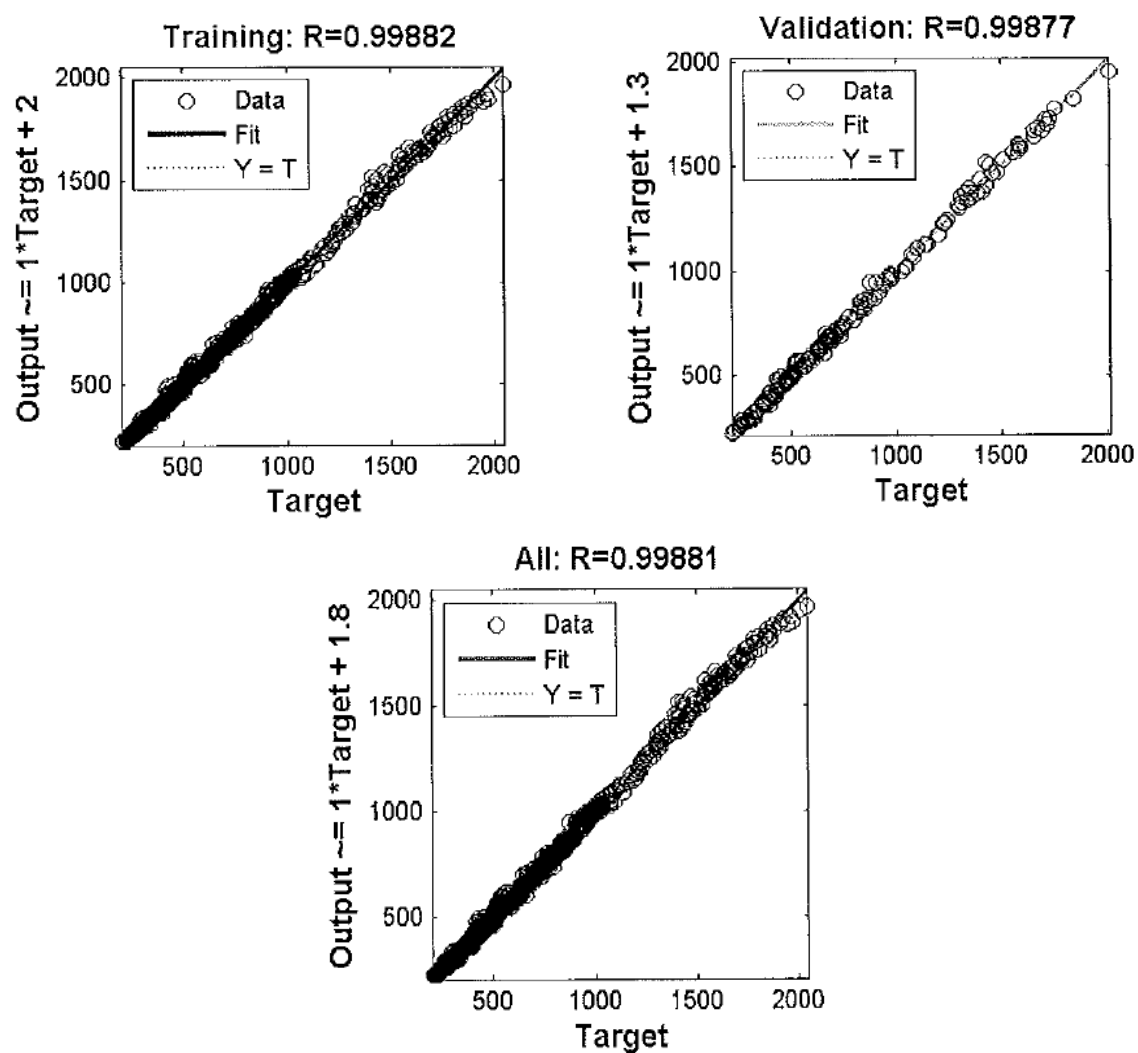


Figure N-4. Comparison of Average Vertical Strain in the Base Layer for GG-M Structure

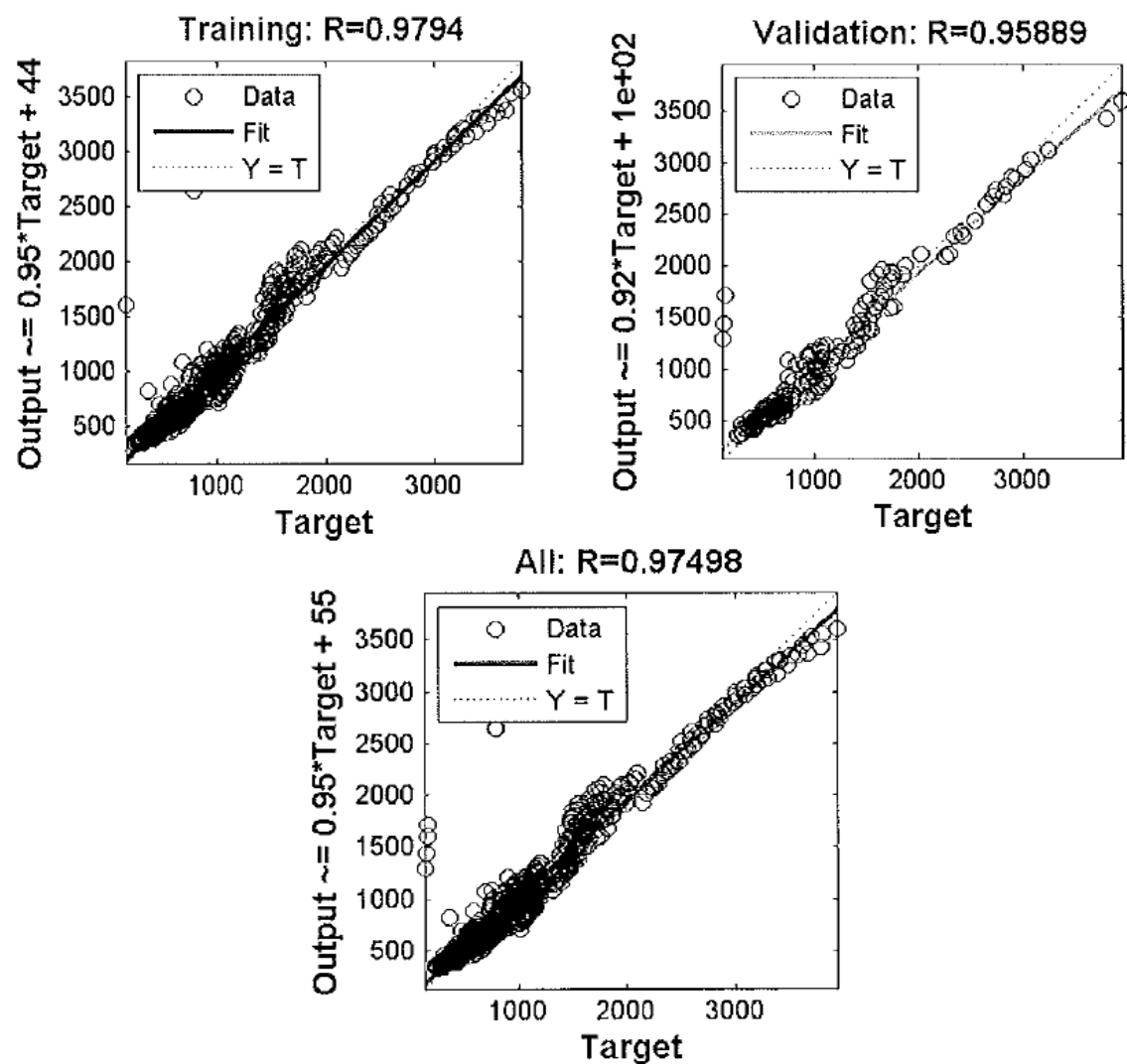


Figure N-5. Comparison of Vertical Strain at the Top of the Subgrade for GG-M Structure

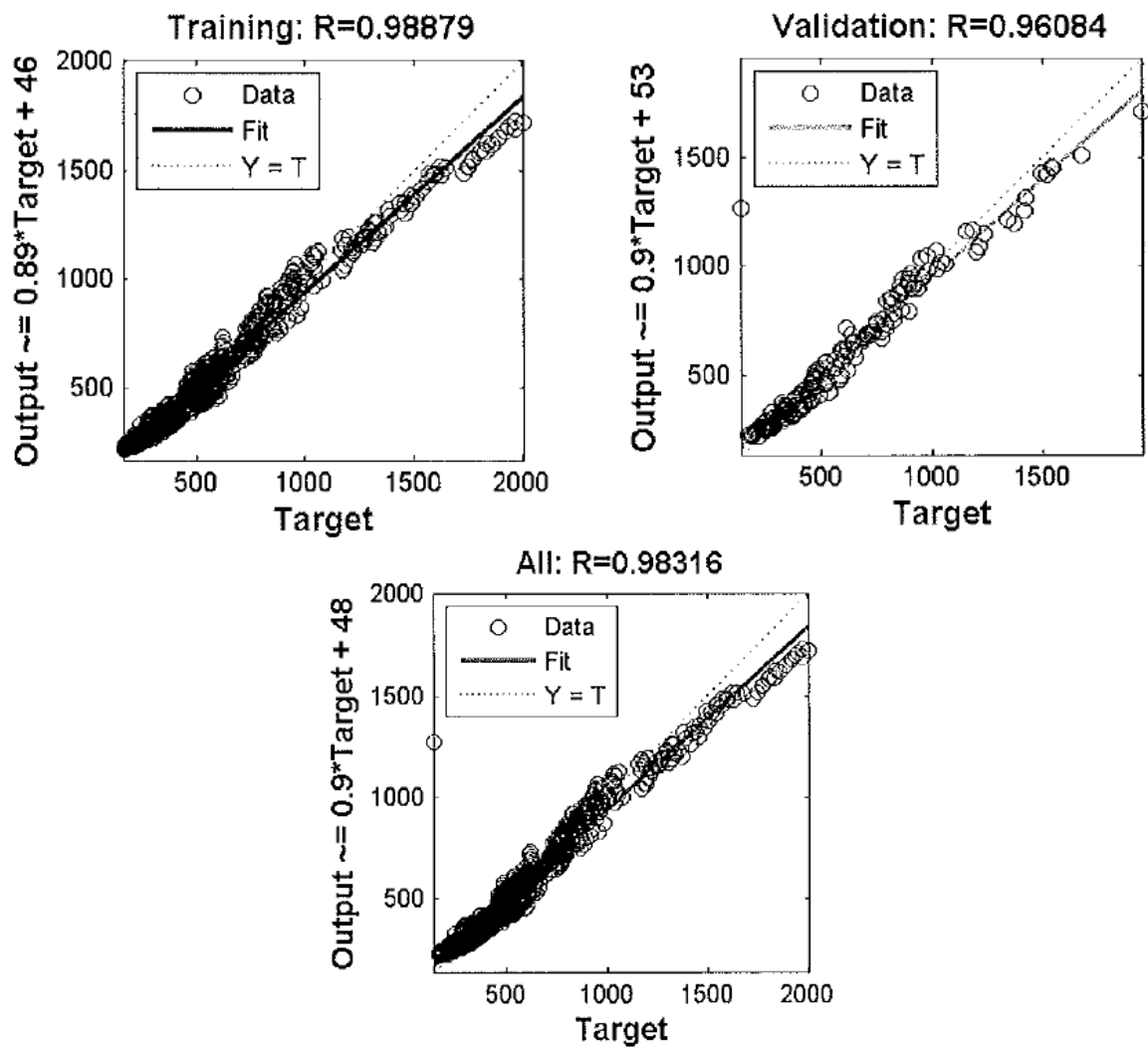


Figure N-6. Comparison of Vertical Strain at 6 inches below the Top of the Subgrade for GG-M Structure

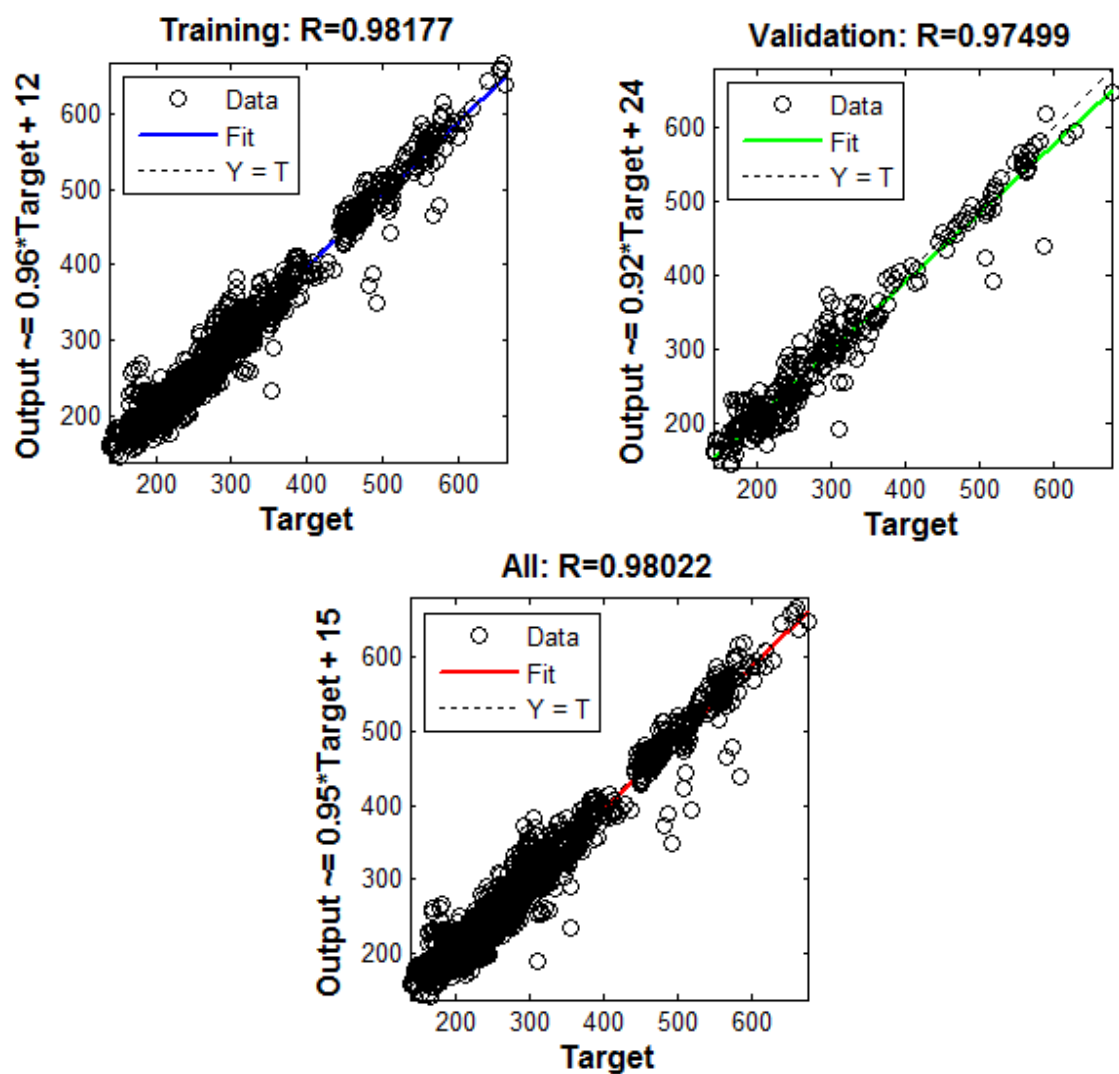


Figure N-7. Comparison of Tensile Strain at the Bottom of the Asphalt Concrete for GG-B Structure

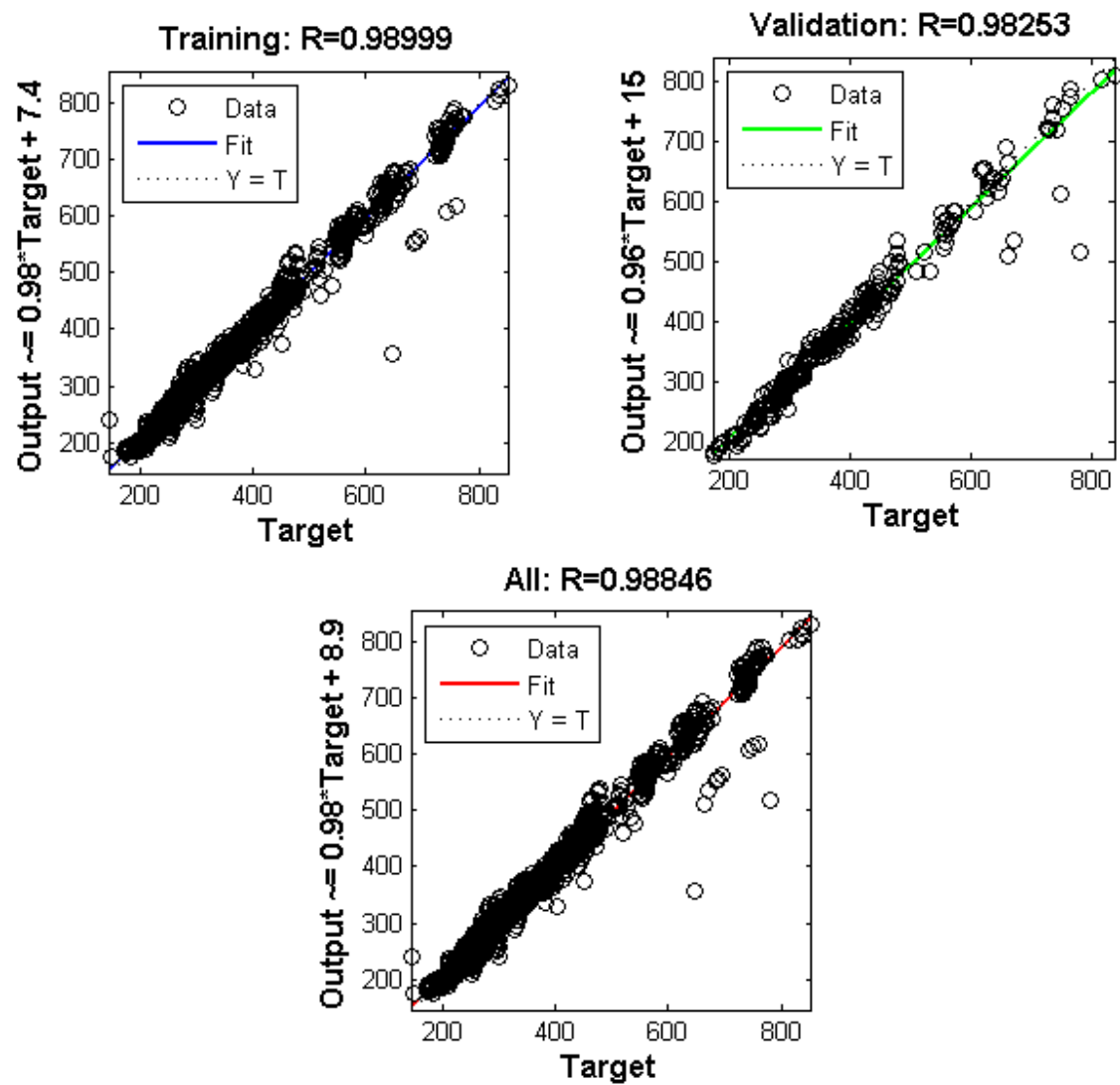


Figure N-8. Comparison of Average Vertical Strain in the Asphalt Concrete for GG-B Structure

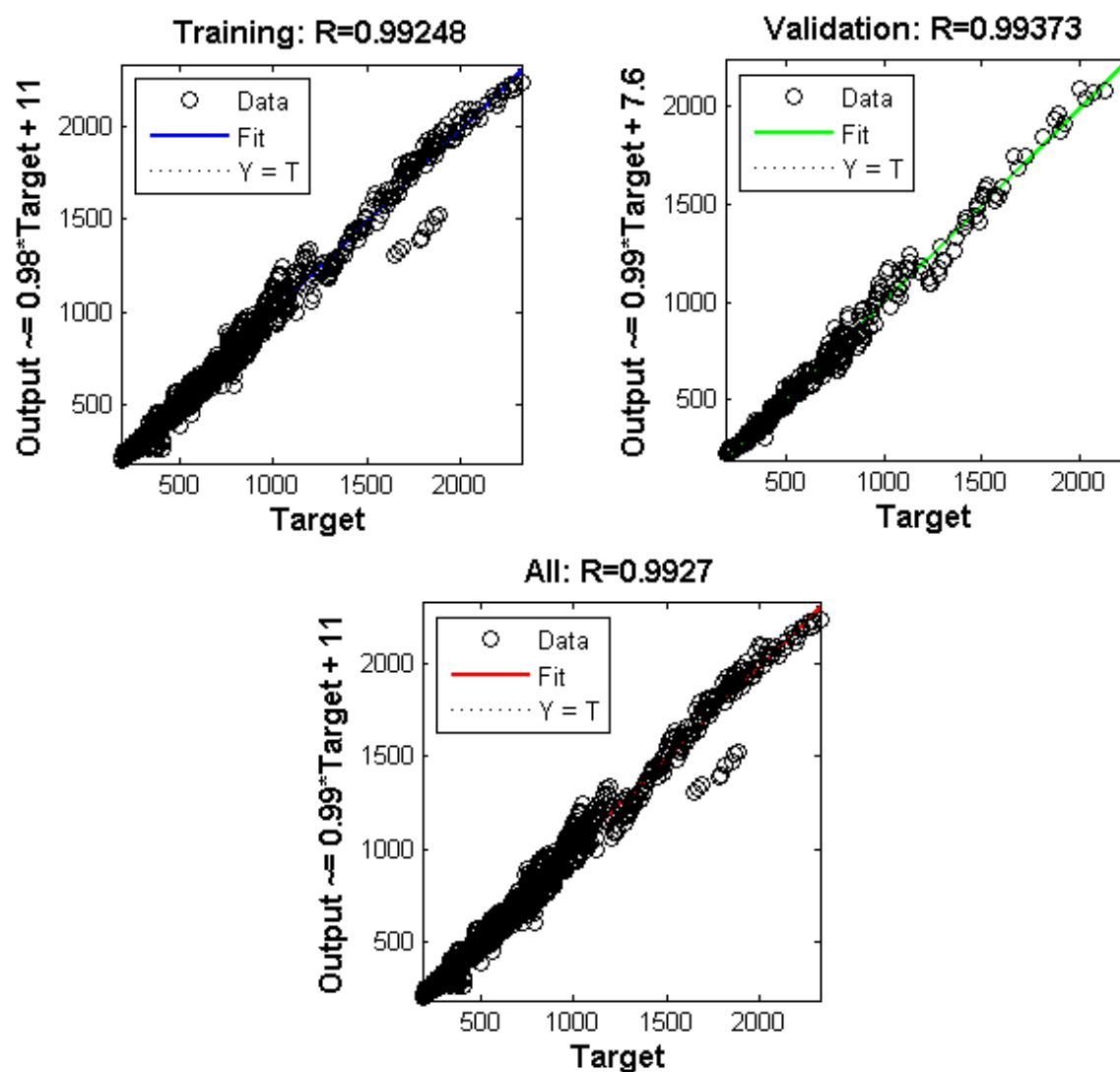


Figure N-9. Comparison of Average Vertical Strain in the Base Layer for GG-B Structure

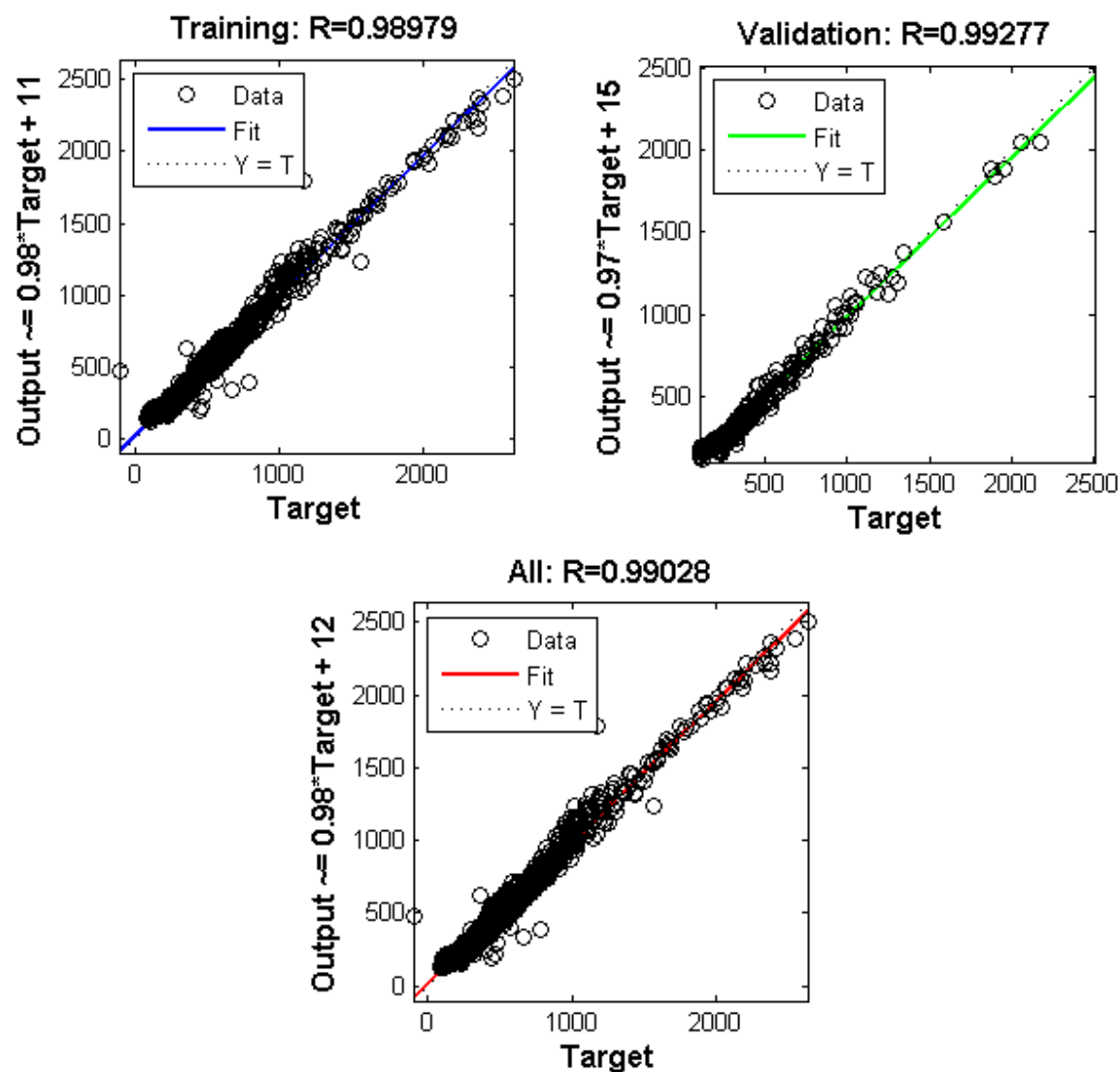


Figure N-10. Comparison of Vertical Strain at the Top of the Subgrade for GG-B Structure

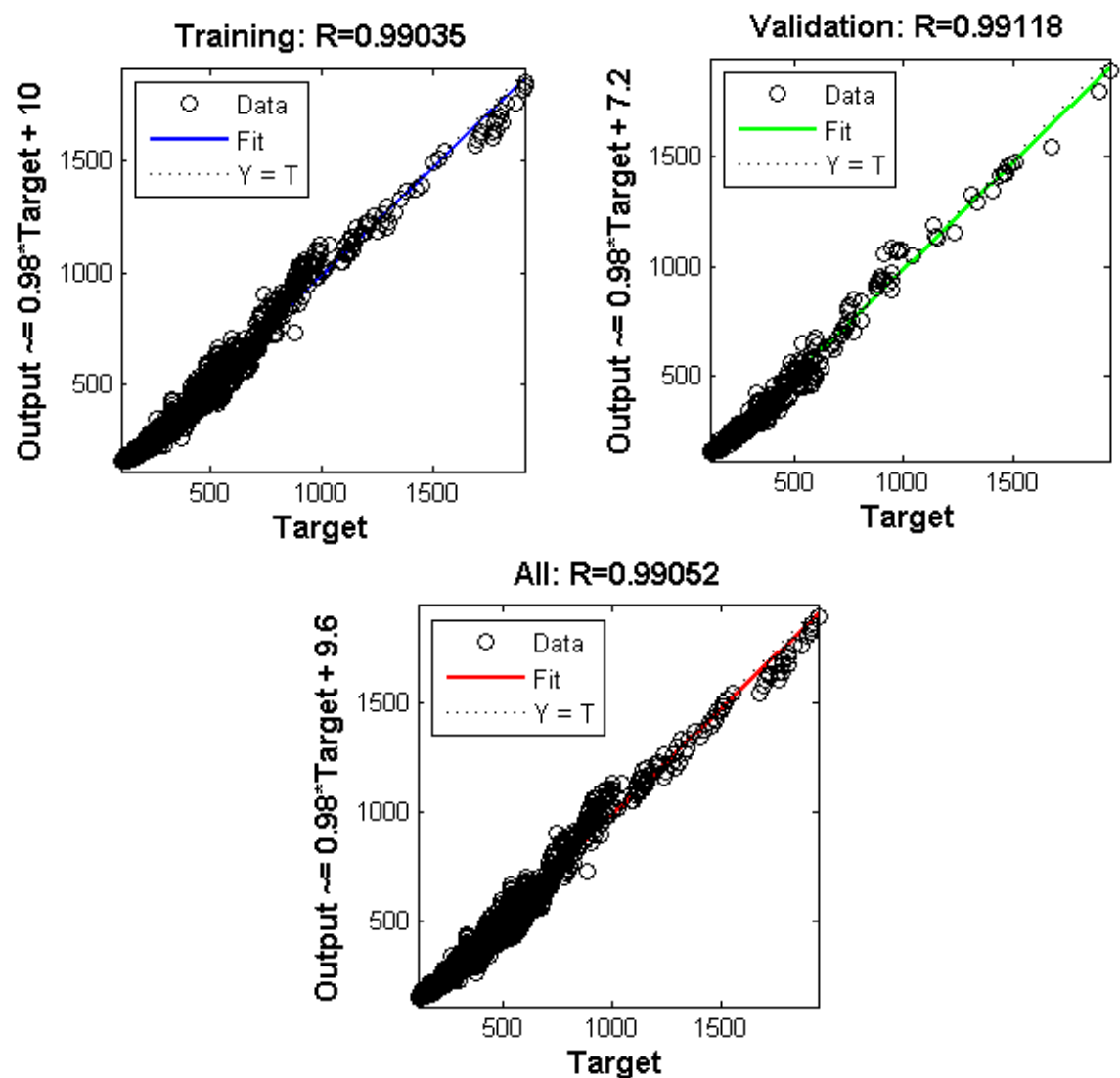


Figure N-11. Comparison of Vertical Strain at 6 inches below the Top of the Subgrade for GG-B Structure

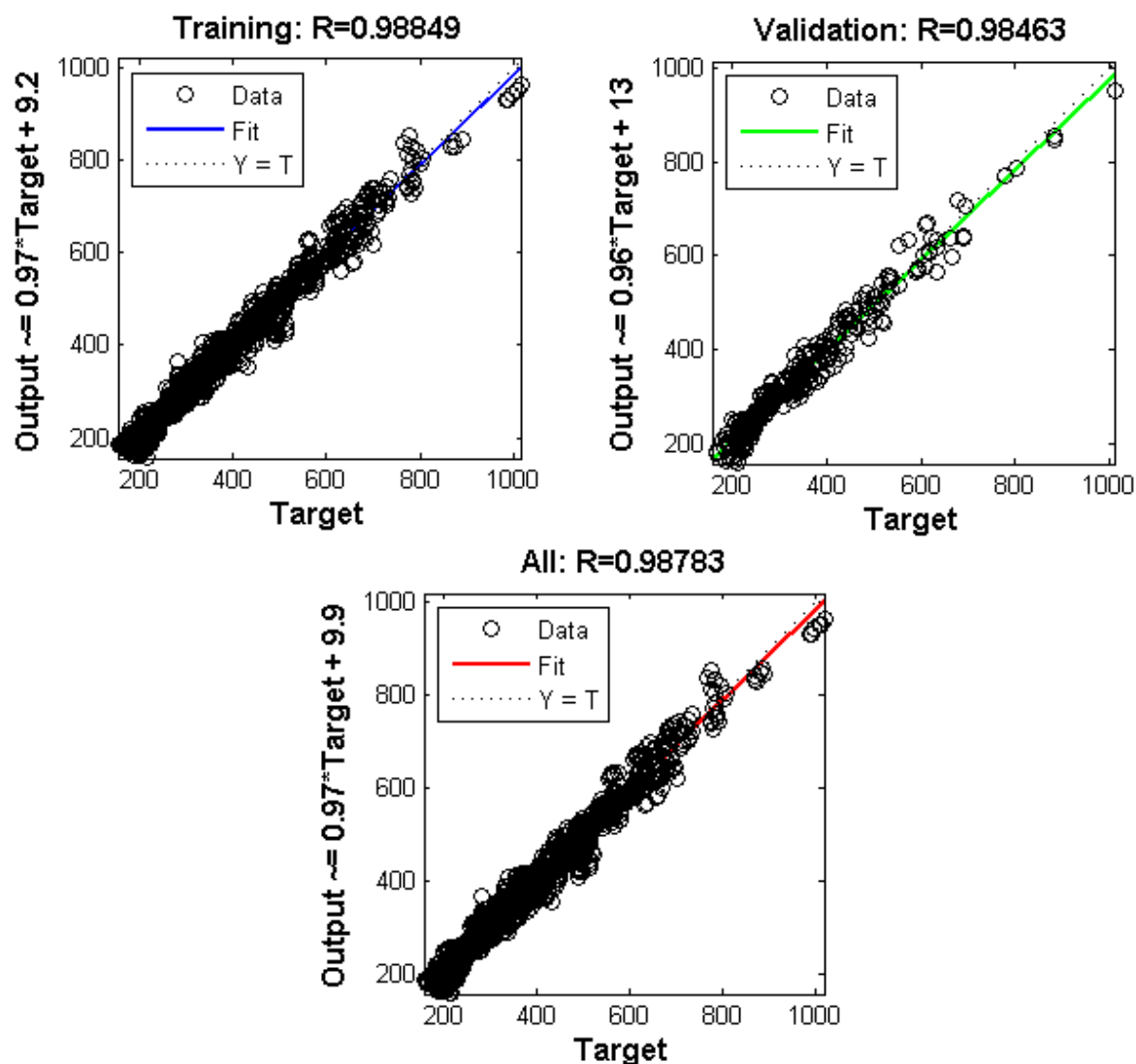


Figure N-12. Comparison of Tensile Strain at the Bottom of the Asphalt Concrete for GT-M Structure

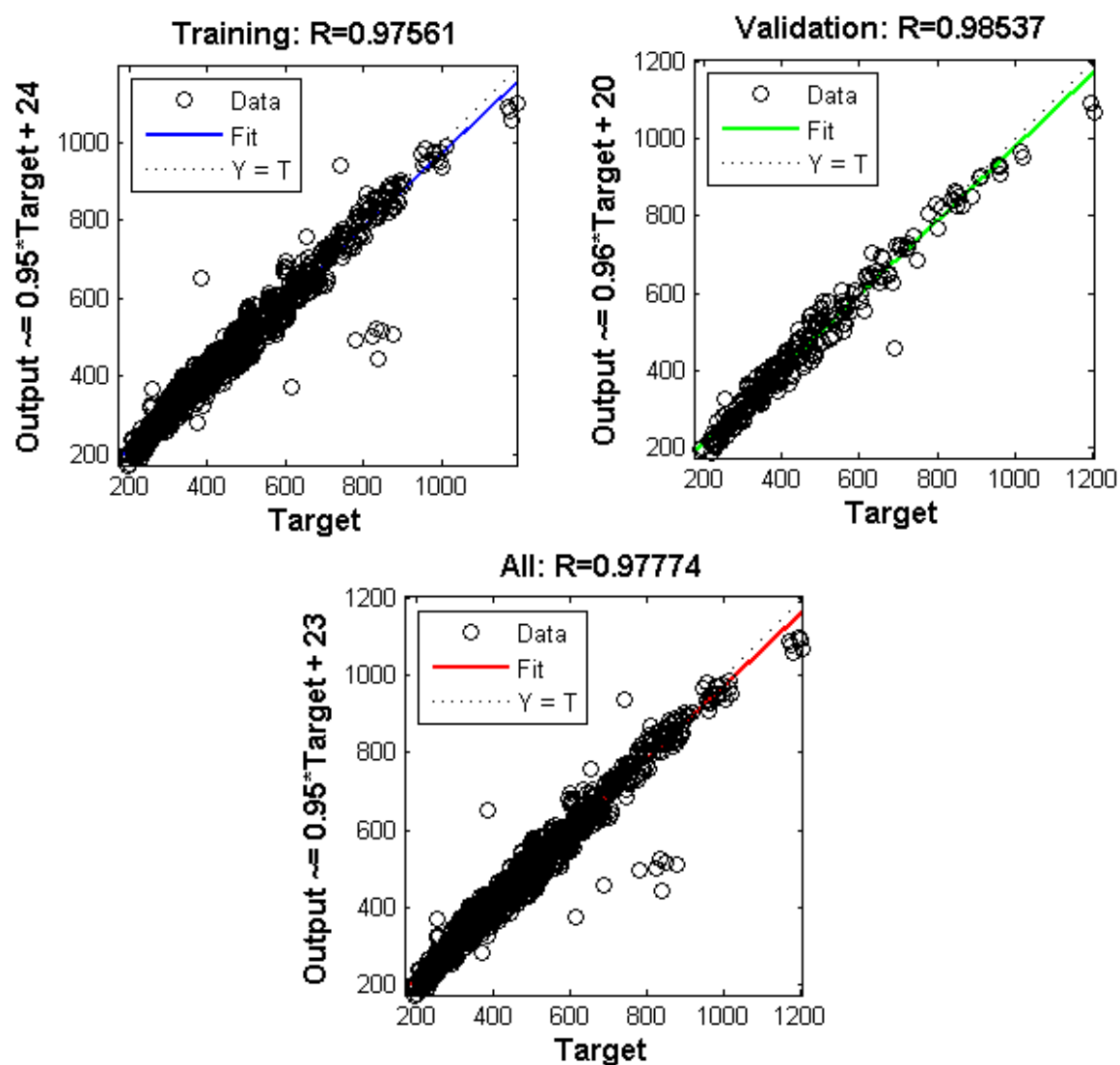


Figure N-13. Comparison of Average Vertical Strain in the Asphalt Concrete for GT-M Structure

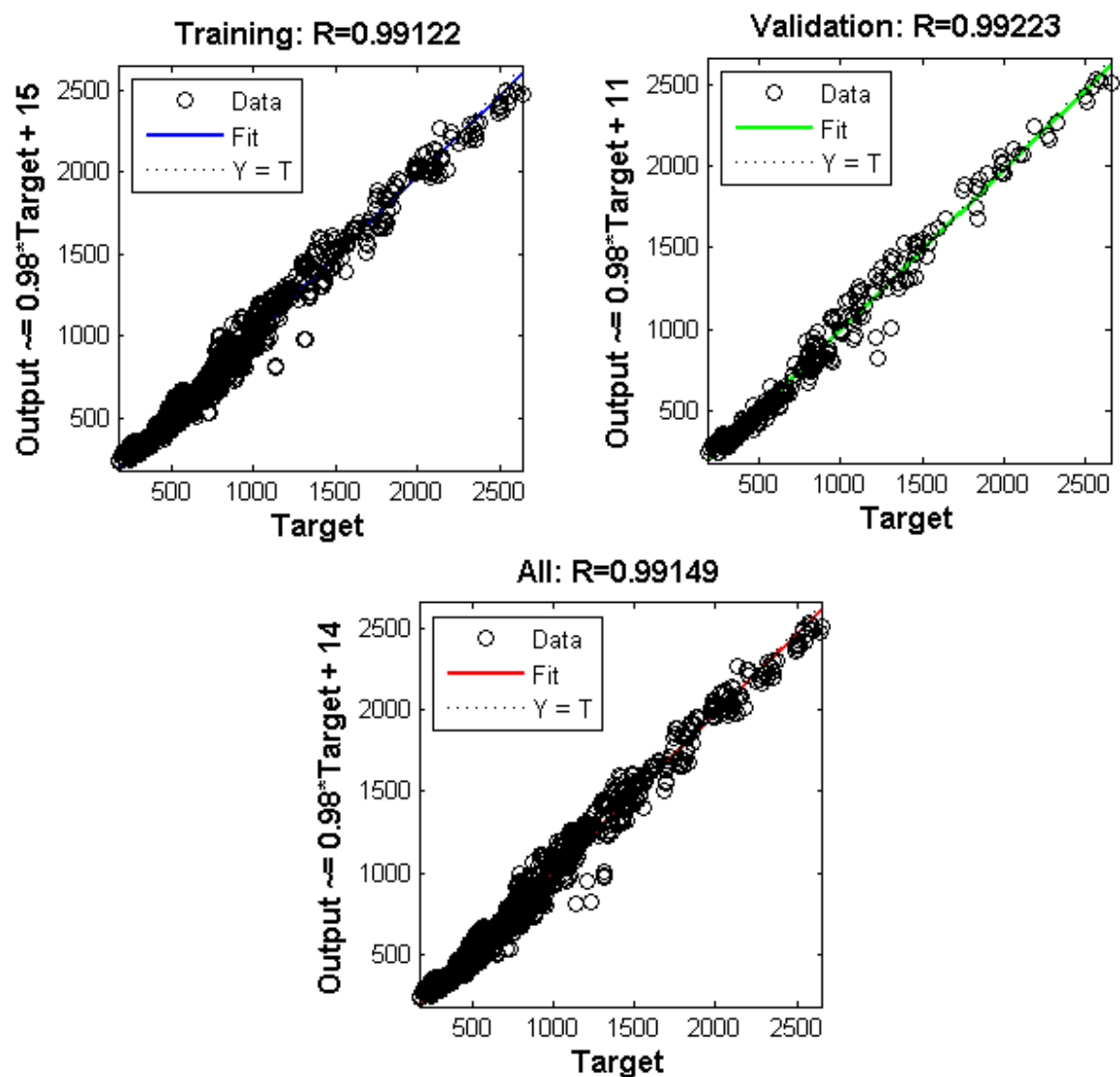


Figure N-14. Comparison of Average Vertical Strain in the Base Layer for GT-M Structure

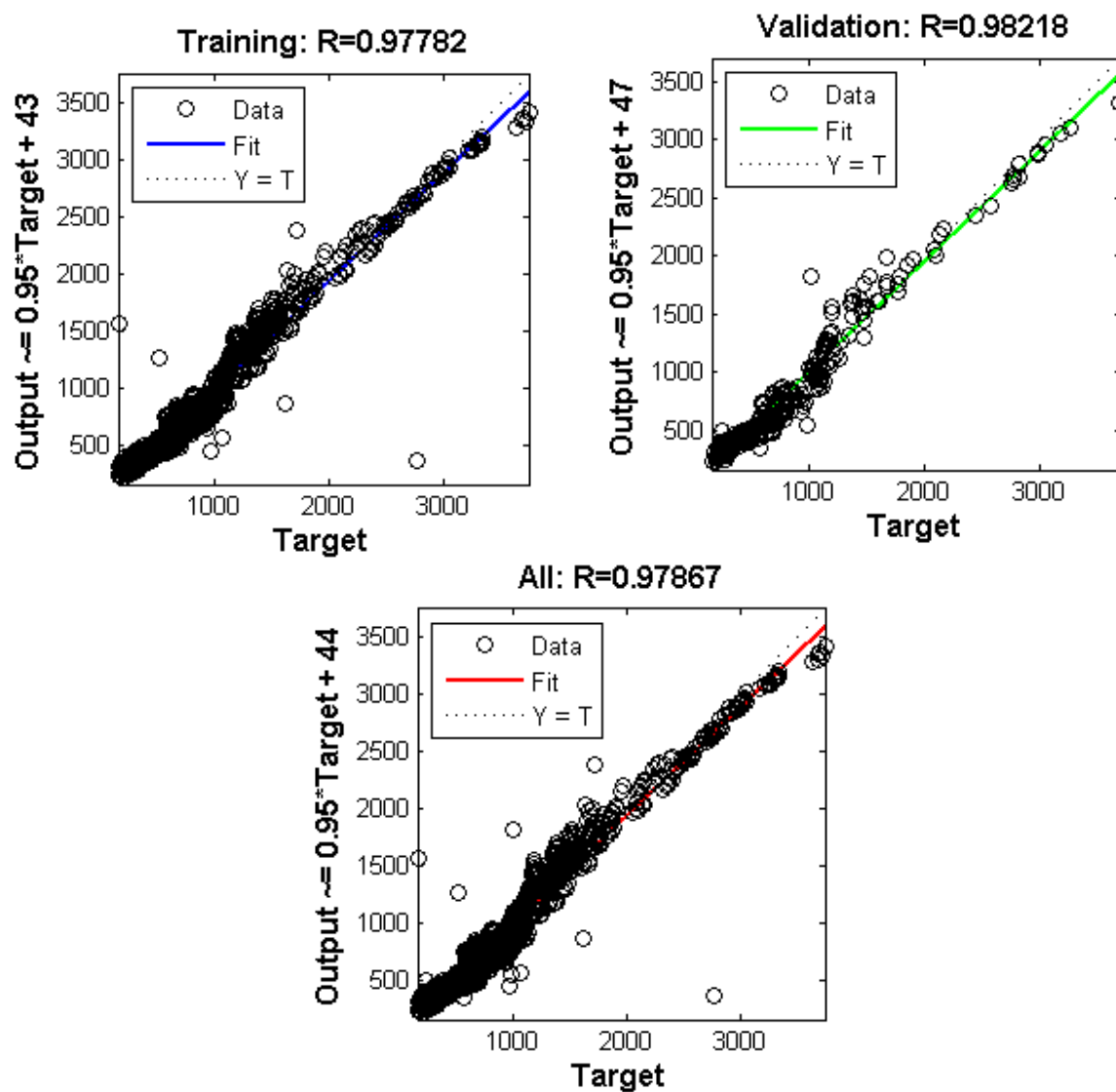


Figure N-15. Comparison of Vertical Strain at the Top of the Subgrade for GT-M Structure

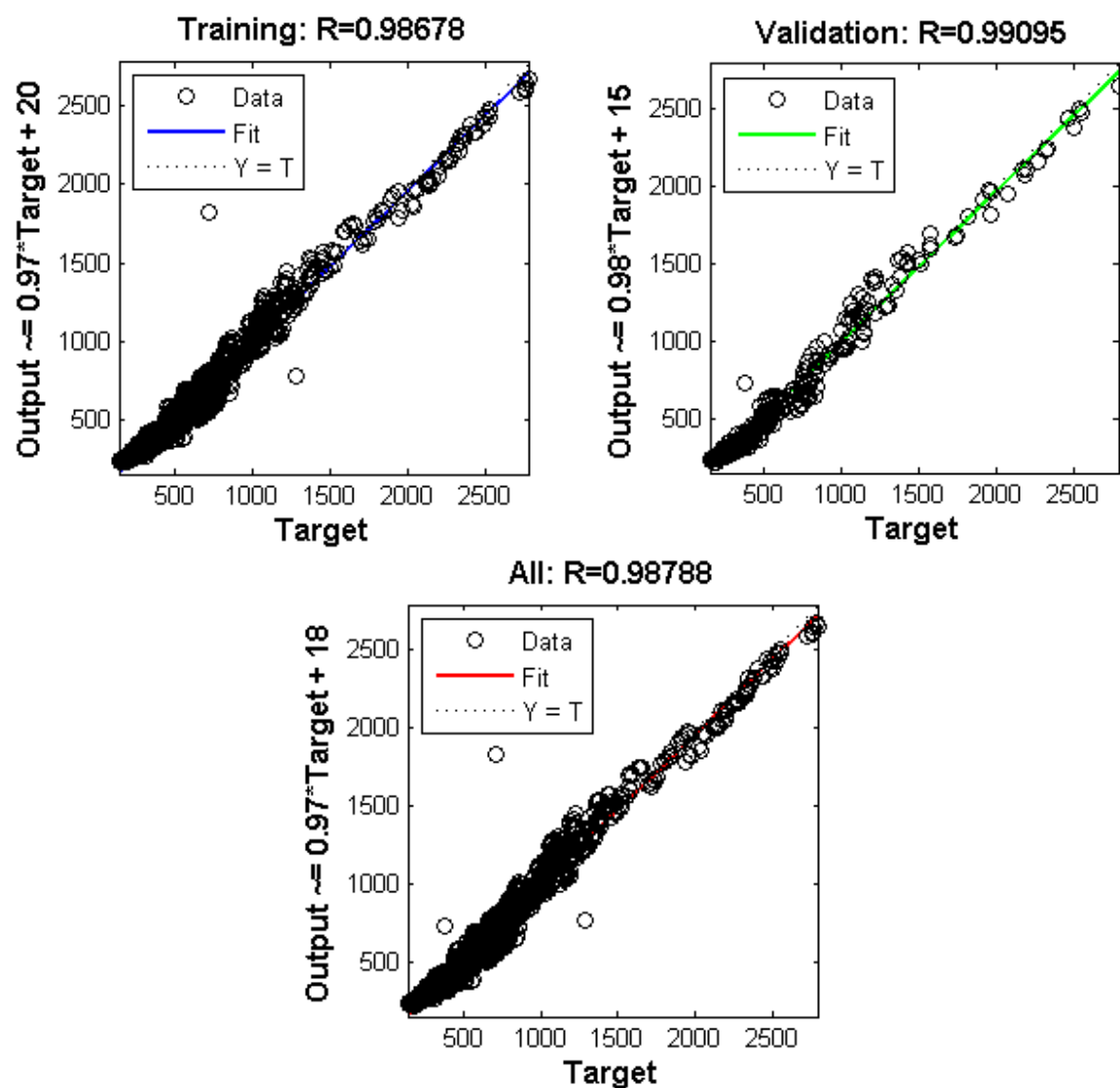


Figure N-16. Comparison of Vertical Strain at 6 inches below the Top of the Subgrade for GT-M Structure

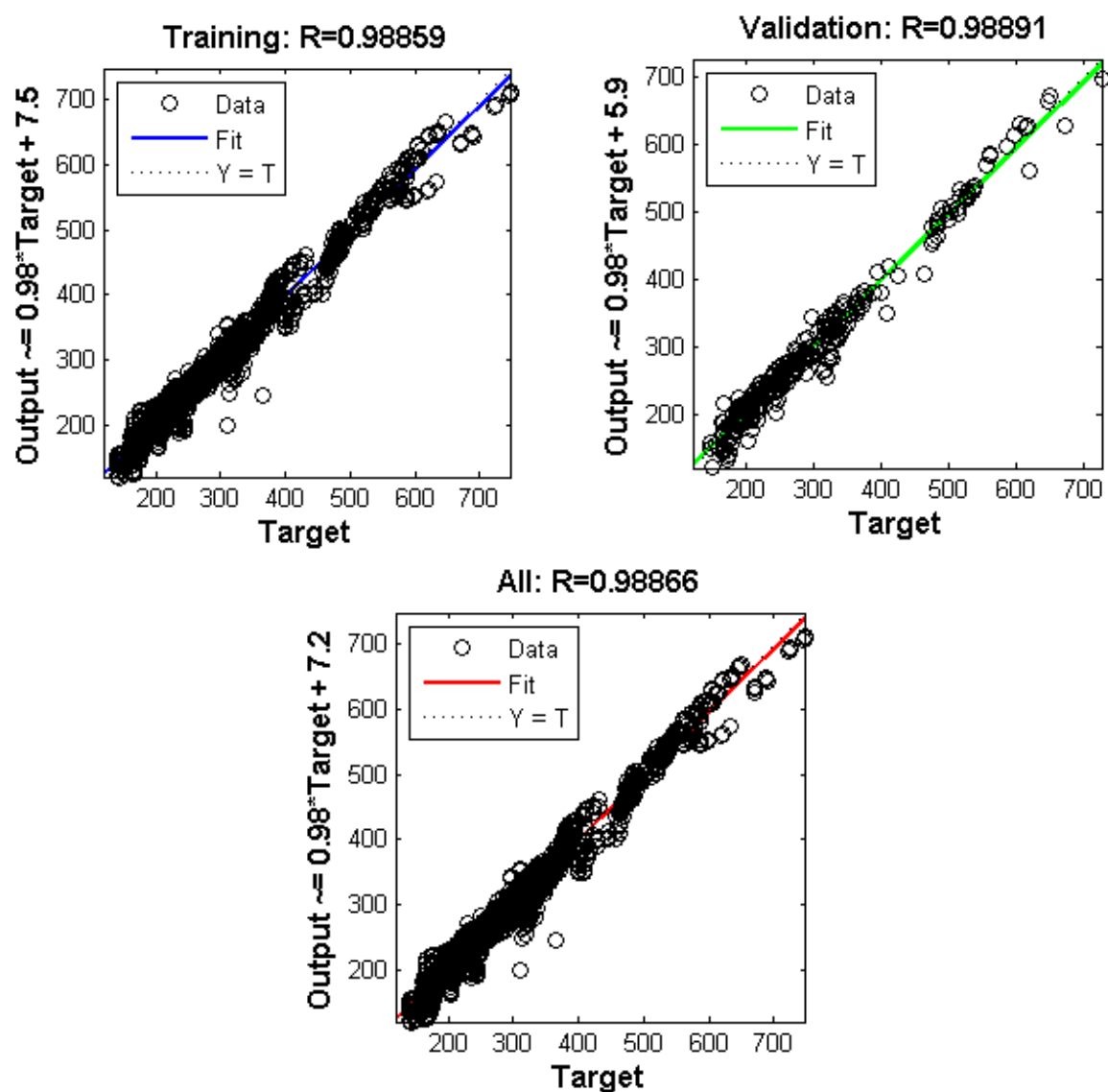


Figure N-17. Comparison of Tensile Strain at the Bottom of the Asphalt Concrete for GT-B Structure

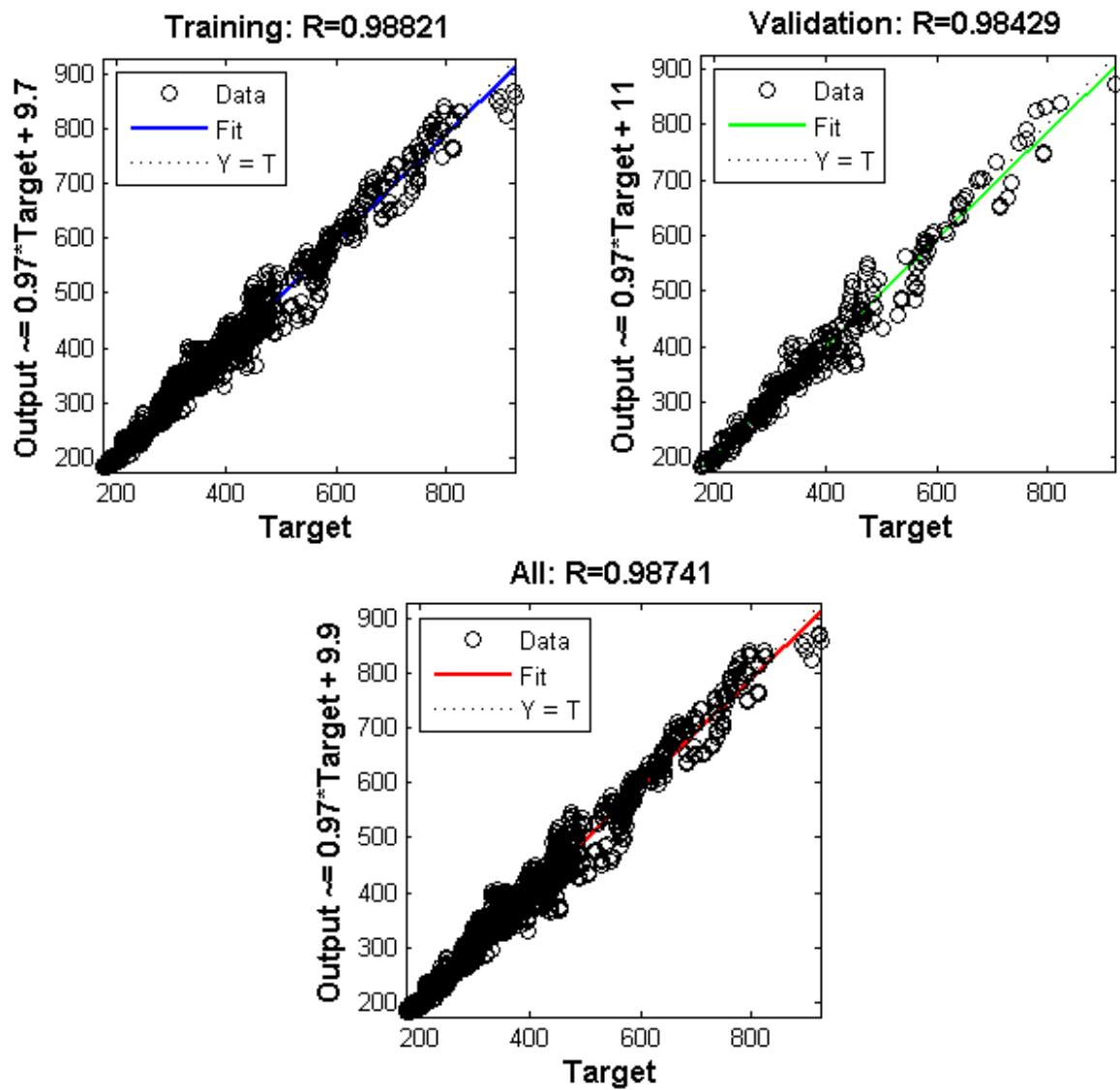


Figure N-18. Comparison of Average Vertical Strain in the Asphalt Concrete for GT-B Structure

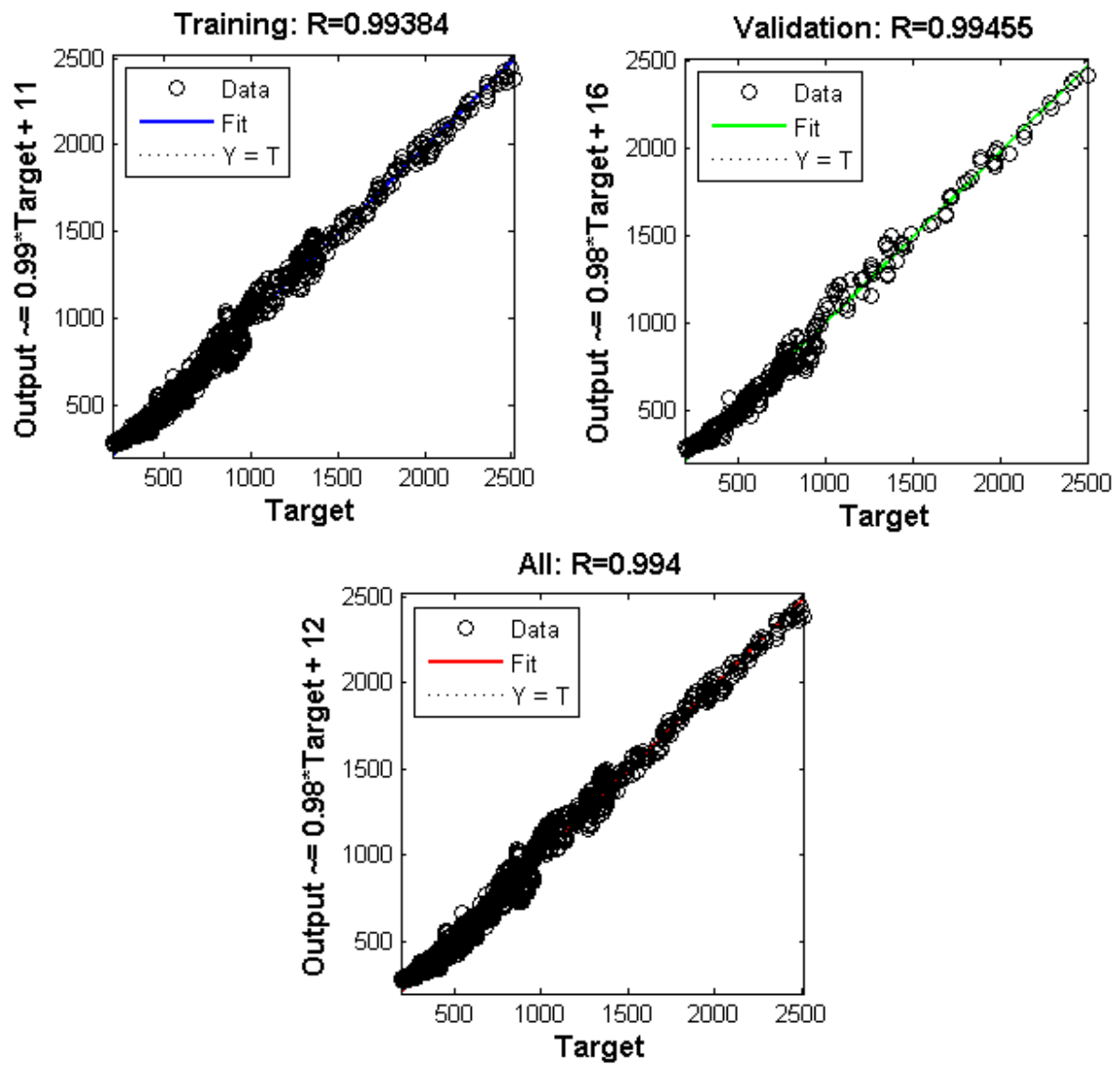


Figure N-19. Comparison of Average Vertical Strain in the Base Layer for GT-B Structure

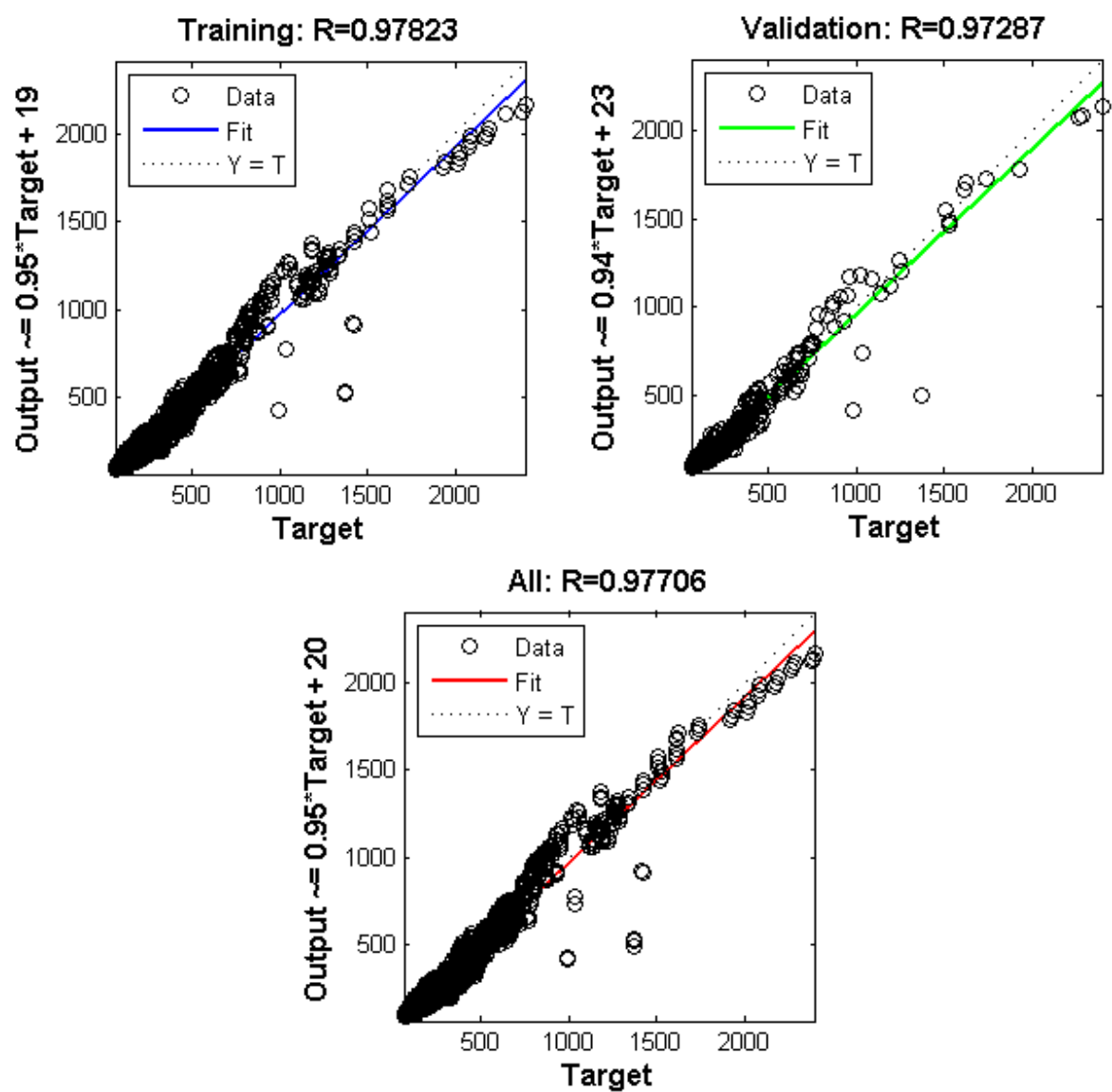


Figure N-20. Comparison of Vertical Strain at the Top of the Subgrade for GT-B Structure

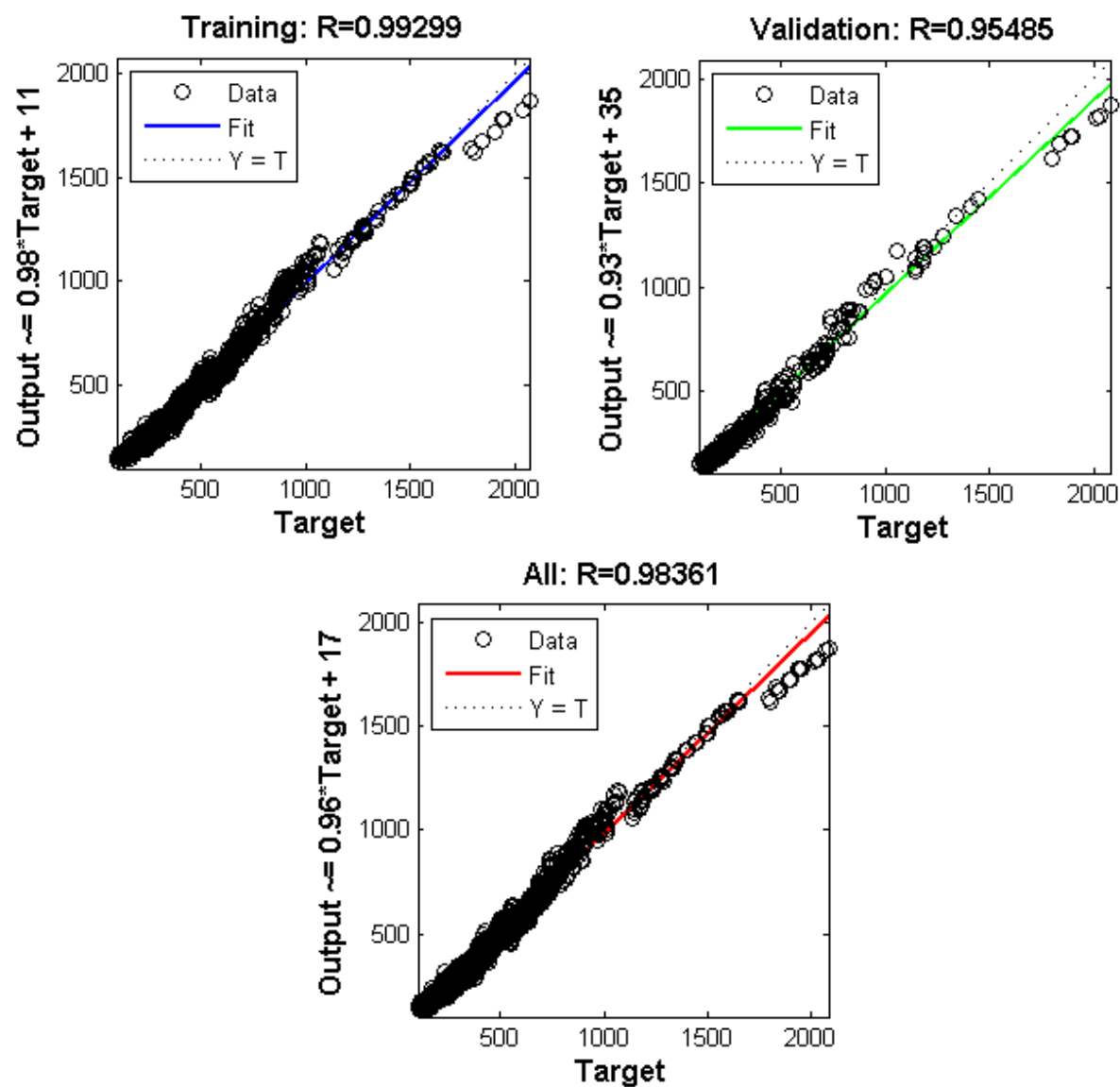


Figure N-21. Comparison of Vertical Strain at 6 inches below the Top of the Subgrade for GT-B Structure

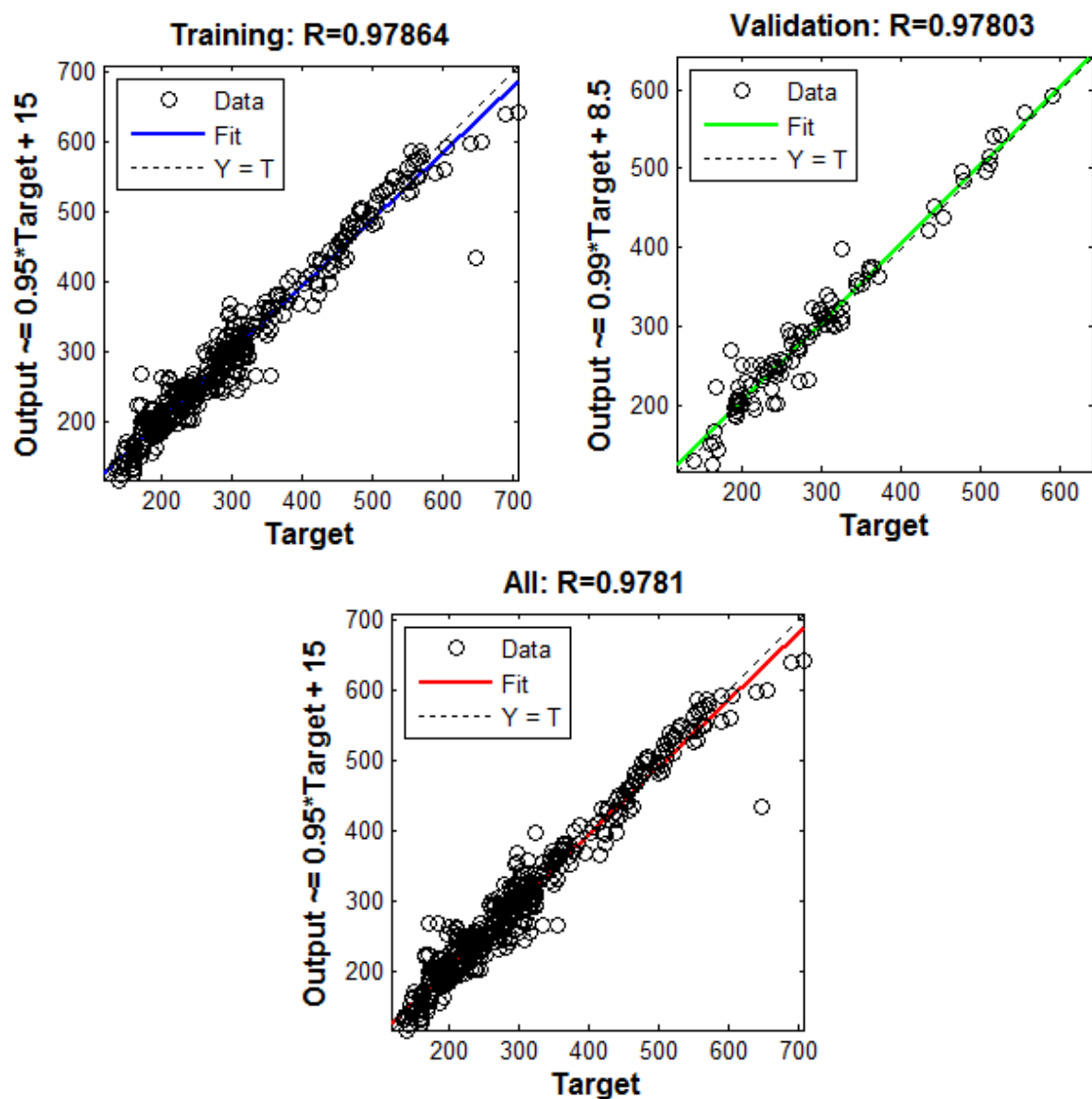


Figure N-22. Comparison of Tensile Strain at the Bottom of the Asphalt Concrete for NG Structure

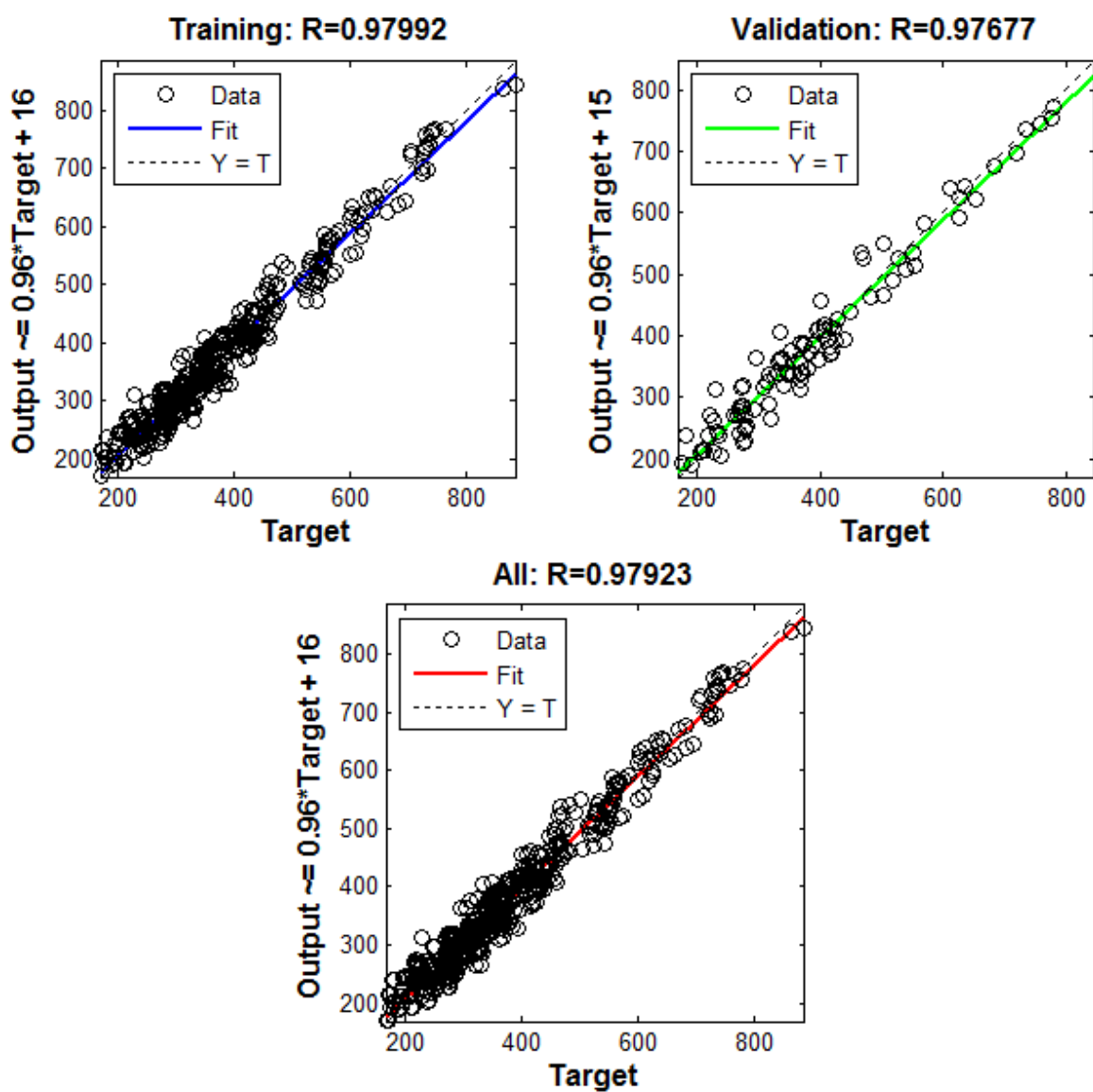


Figure N-23. Comparison of Average Vertical Strain in the Asphalt Concrete for NG Structure

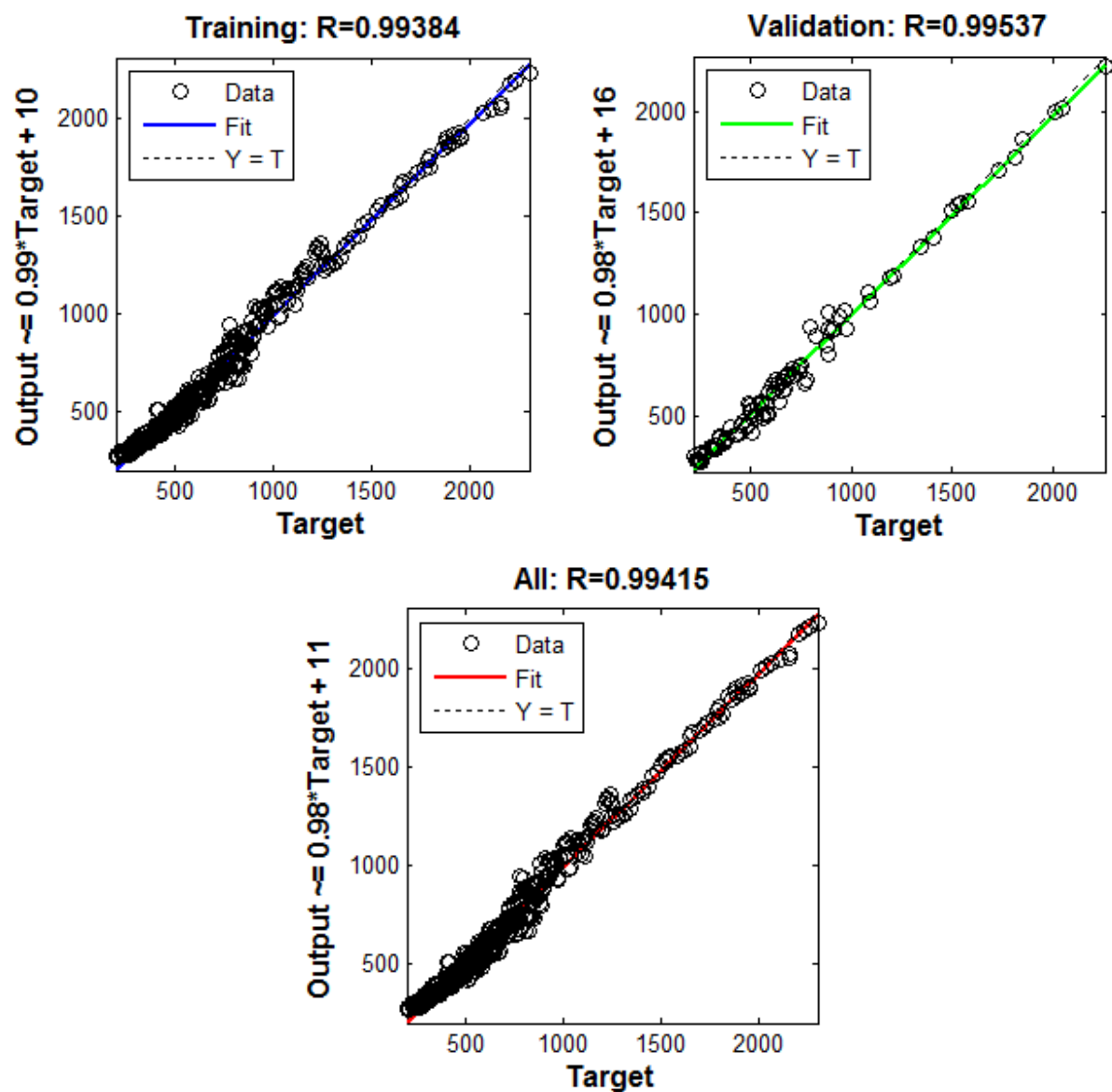


Figure N-24. Comparison of Average Vertical Strain in the Base Layer for NG Structure

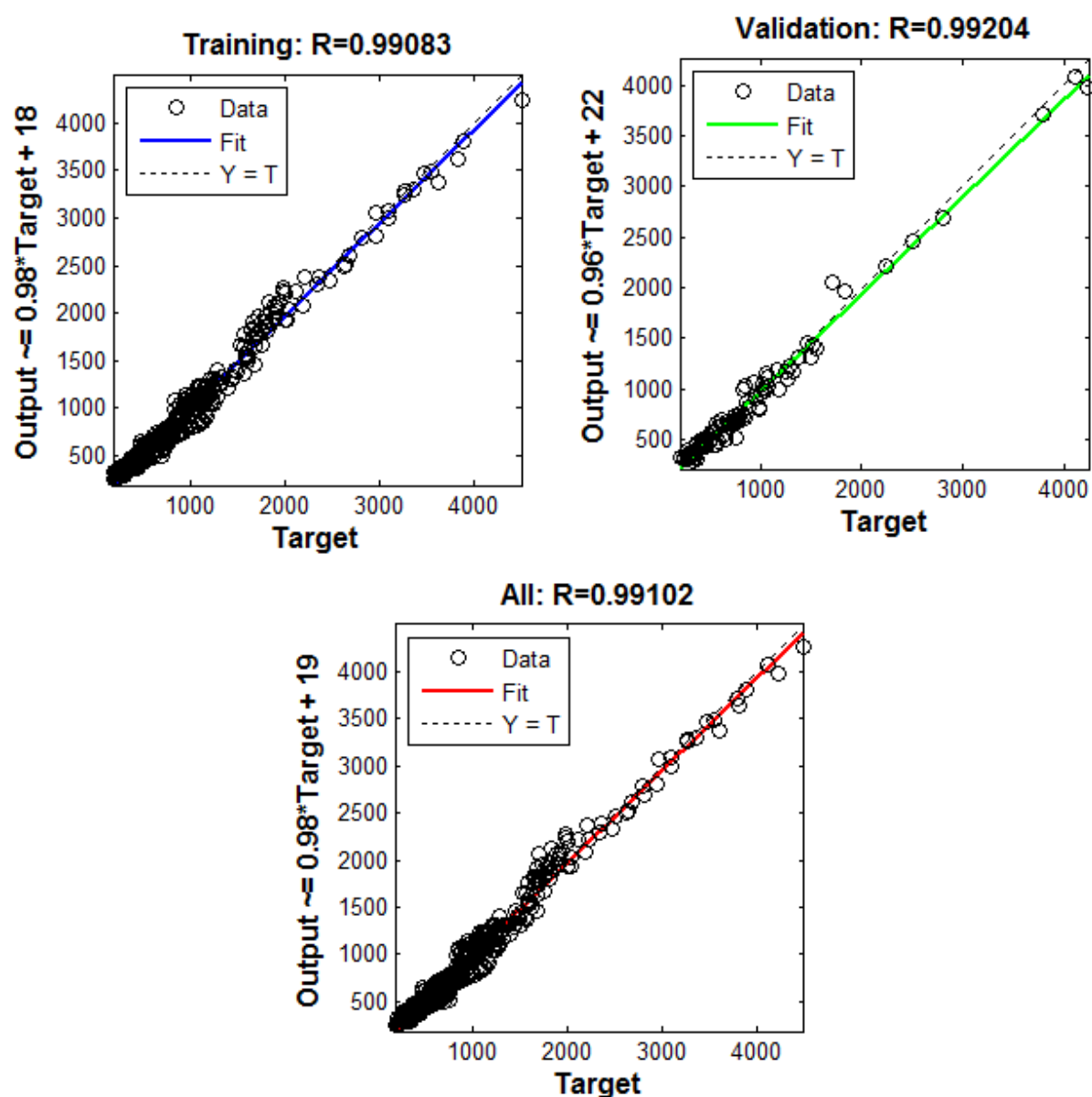


Figure N-25. Comparison of Vertical Strain at the Top of the Subgrade for NG Structure

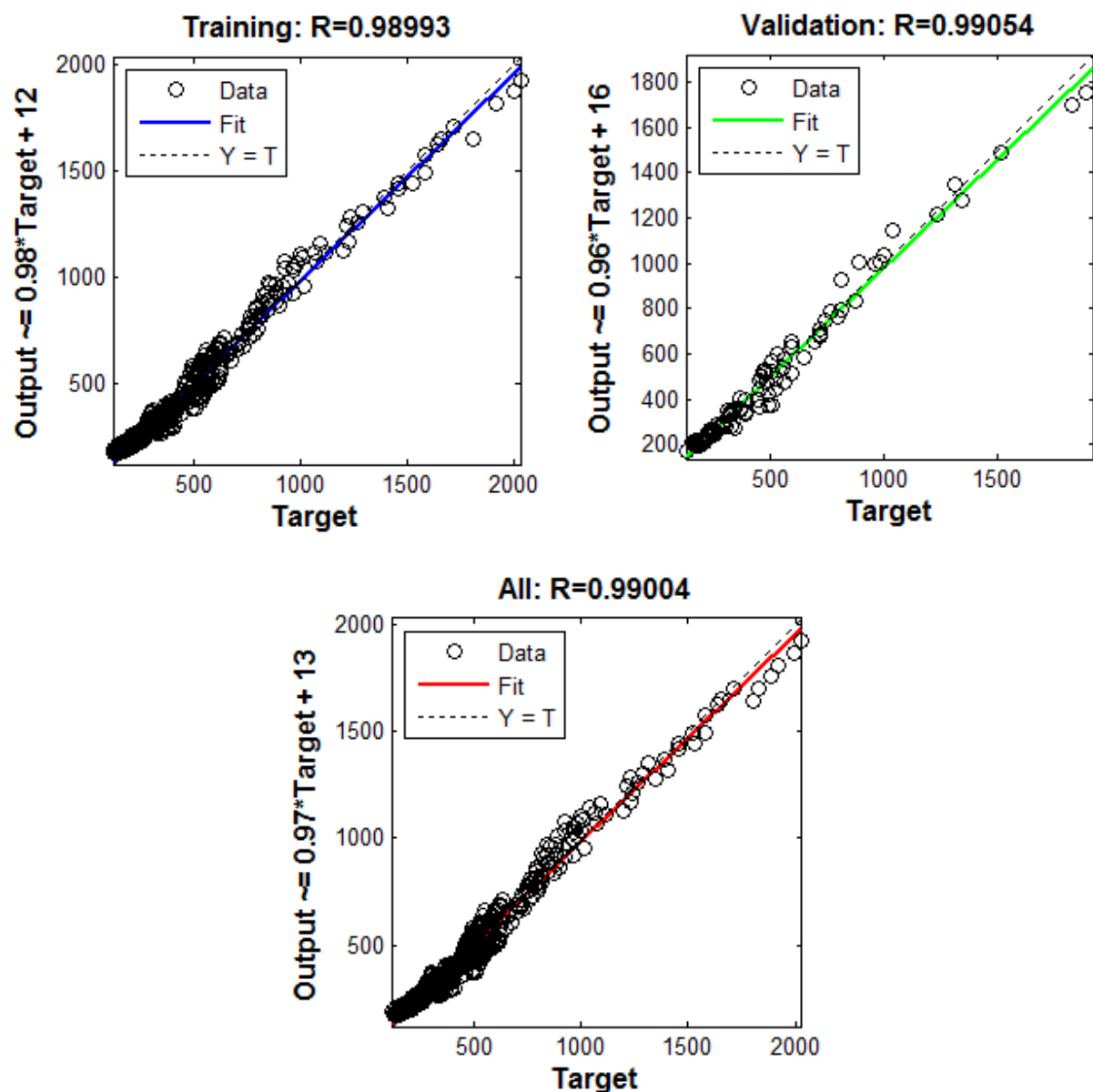


Figure N-26. Comparison of Vertical Strain at 6 inches below the Top of the Subgrade for NG Structure

References

1. Haykin, S.S. (1999). *Neural Networks: A Comprehensive Foundation*. Prentice Hall, Upper Saddle River, NJ.
2. Wu, Z., Hu, S., and Zhou, F. (2014). Prediction of Stress Intensity Factors in Pavement Cracking with Neural Networks Based on Semi-Analytical FEA. *Expert Systems with Applications*, Vol. 41, pp. 1021–1030.

3. Ceylan, H., Bayrak, M.B., and Gopalakrishnan, K. (2014). Neural Networks Applications in Pavement Engineering: A Recent Survey. *International Journal of Pavement Research and Technology*, Vol. 7, No. 6, pp. 434–444.
4. Demuth, H., and Beale, M. (1998). Neural Network Toolbox for Use with MATLAB. The MathWorks, Natick, MA.
5. More, J. (1978). The Levenberg-Marquardt Algorithm: Implementation and Theory. *Numerical Analysis*, Vol. 630, pp. 105–116.
6. Amari, S. (1998). Natural Gradient Works Efficiently in Learning. *Neural Computation*, Vol. 10, No. 2, pp. 251–276.

APPENDIX O. VALIDATION OF ARTIFICIAL NEURAL NETWORK APPROACH FOR PREDICTING GEOSYNTHETIC-REINFORCED PAVEMENT PERFORMANCE

The performance of geosynthetic-reinforced flexible pavements includes fatigue cracking, permanent deformation, and international roughness index (IRI). In this study, the artificial neural network (ANN) model was used to predict the critical responses of geosynthetic-reinforced pavements. A geosynthetic-reinforced pavement with any given material properties was then equivalent to an unreinforced pavement with the modified material properties to obtain the identical pavement responses. The process of validating this approach is illustrated in Figure O-1 and involves the following steps:

1. Identify the in-service geosynthetic-reinforced pavement sections from the long-term pavement performance (LTPP) database and Texas Pavement Management Information System (PMIS). This study focused on the in-service pavement sections with the placement of geosynthetics in conjunction with the unbound base courses.
2. Collect the pavement structure data, including layer thickness, construction dates, material design information, and falling weight deflectometer data.
3. Collect the traffic data from the identified pavement sections, which should be compatible with the input of traffic module in the Pavement ME Design software.
4. Collect the climatic data or weather station information from the identified pavement sections.
5. Collect the performance data from the identified pavement sections, including fatigue cracking, rutting, and IRI.
6. Employ the proposed ANN approach to determine the modified material properties of an unreinforced pavement.
7. Input the unreinforced pavement structure data, the collected traffic data and climatic data, and the determined modified material properties into the Pavement ME Design software to predict the pavement performance (i.e., fatigue cracking, rutting, and IRI).
8. Compare the predicted pavement performance with that measured from the field.

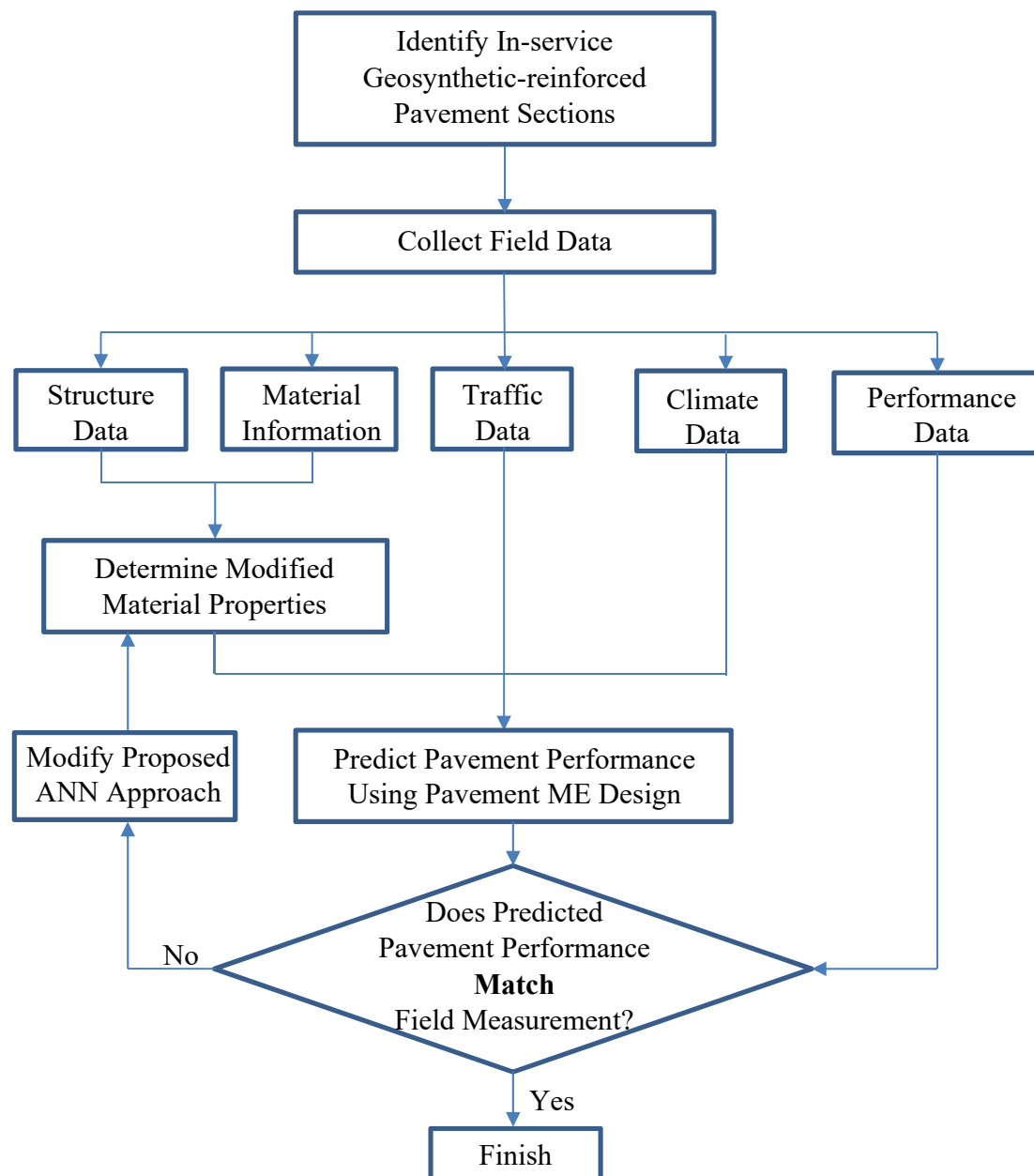


Figure O-1. Flow Chart of the Process of Validating the Proposed ANN Approach

After a thorough review of the in-service pavement sections in the LTPP database and PMIS, a total of 74 pavement sections containing geosynthetics were found in the LTPP database, and a total of 51 pavement sections containing geosynthetics were found in the PMIS. A full list of the identified pavement sections is presented in Appendix P. Of these identified pavement sections, most had stabilized base courses, which were not under consideration in this study. In the remaining pavement sections, a total of three qualified pavement sections were from the LTPP database, and a total of three qualified pavement sections were from the PMIS. Some

of these identified pavement sections had the stabilized soil over the untreated subgrade, as illustrated in Figure O-2.

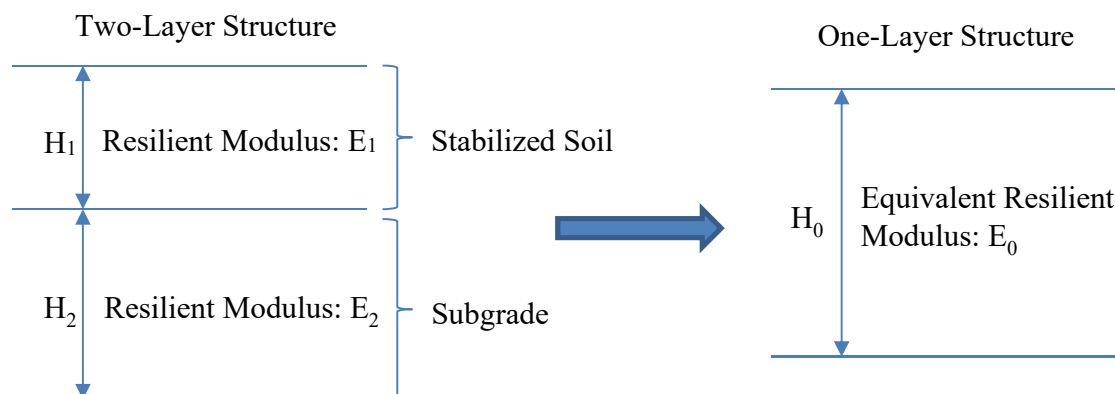


Figure O-2. Conversion of Resilient Moduli of Two-Layer Structure to Single Resilient Modulus of One-Layer Structure

Based on the Odemark's method, the resilient moduli of the two-layer structure are equivalent to the single resilient modulus of the one-layer structure using Equation O-1.

$$E_0 = \left[\frac{H_1 (E_1)^{1/3} + H_2 (E_2)^{1/3}}{H_1 + H_2} \right]^3 \quad (\text{O-1})$$

where E_0 is the resilient modulus of the one-layer structure, H_0 is the thickness of the one-layer structure, E_1 is the resilient modulus of the stabilized soil, H_1 is the thickness of the stabilized soil, E_2 is the resilient modulus of the subgrade, and H_2 is the thickness of the subgrade. The comparisons of the geosynthetic-reinforced pavement performances between the ANN approach predictions and the field measurements for these identified pavement sections are presented below.

LTPP Section 16-9032

The pavement section 16-9032 consists of a 6-inch hot-mixed and dense-graded asphalt concrete, a 23.2-inch crushed gravel unbound base, and a semi-infinite subgrade, which is classified as AASHTO 7-5 soil. A 0.1-inch woven geotextile is placed at the interface between the unbound base and subgrade. The comparisons of geosynthetic-reinforced pavement performance between the predictions by the proposed ANN approach and the field measurements are presented in Figures O-3–O-5. The predicted rutting depth and IRI results were in good agreement with the field measurements. The fatigue cracking of the geosynthetic-reinforced pavement was slightly overestimated by the proposed ANN approach. These findings indicate that the proposed ANN approach is capable of accurately predicting the performance of geosynthetic-reinforced pavements. Figures O-3–O-5 also present the predicted performance of the control pavement. It is demonstrated that the geotextile placed at the base/subgrade interface

has beneficial effects for reducing the rutting and international roughness index of flexible pavements.

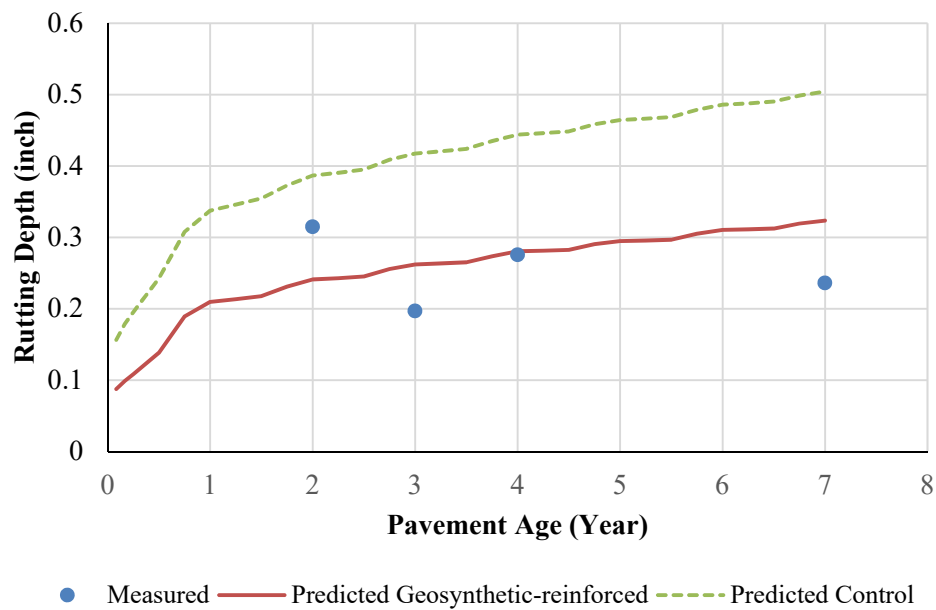


Figure O-3. Comparison of Rutting Depth between ANN Approach Prediction and Field Measurement for Pavement Section 16-9032

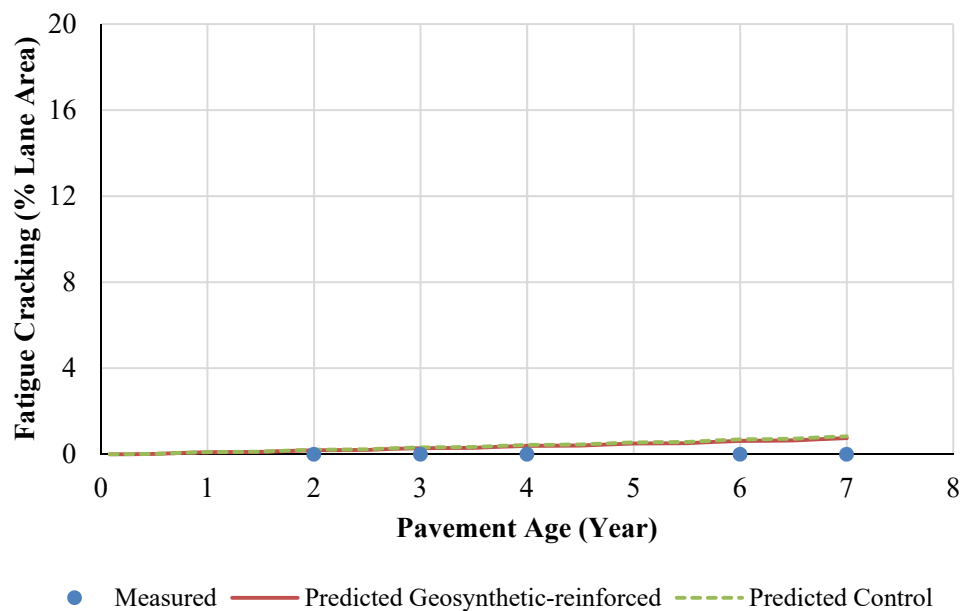


Figure O-4. Comparison of Fatigue Cracking between ANN Approach Prediction and Field Measurement for Pavement Section 16-9032

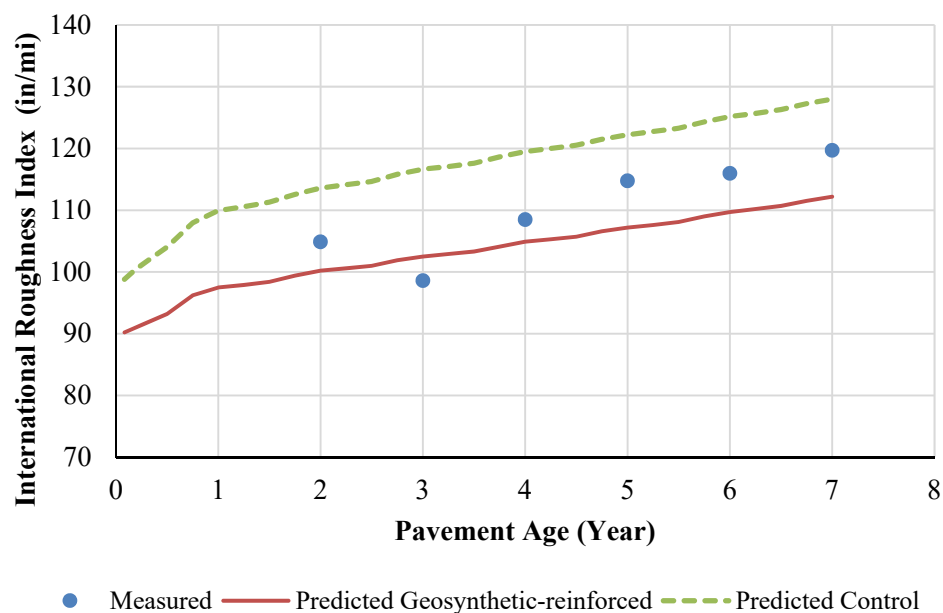


Figure O-5. Comparison of IRI between ANN Approach Prediction and Field Measurement for Pavement Section 16-9032

LTPP Section 48-0167

The pavement section 48-0167 consists of a 5.6-inch hot-mixed and dense-graded asphalt concrete, a 13-inch crushed gravel unbound base, a 12-inch lime-treated soil, and a semi-infinite subgrade sandy soil. A 0.3-inch geogrid is placed at the interface between the unbound base and lime-treated soil. The comparisons of geosynthetic-reinforced pavement performance between the predictions by the proposed ANN approach and the field measurements are presented in Figures O-6–O-7.

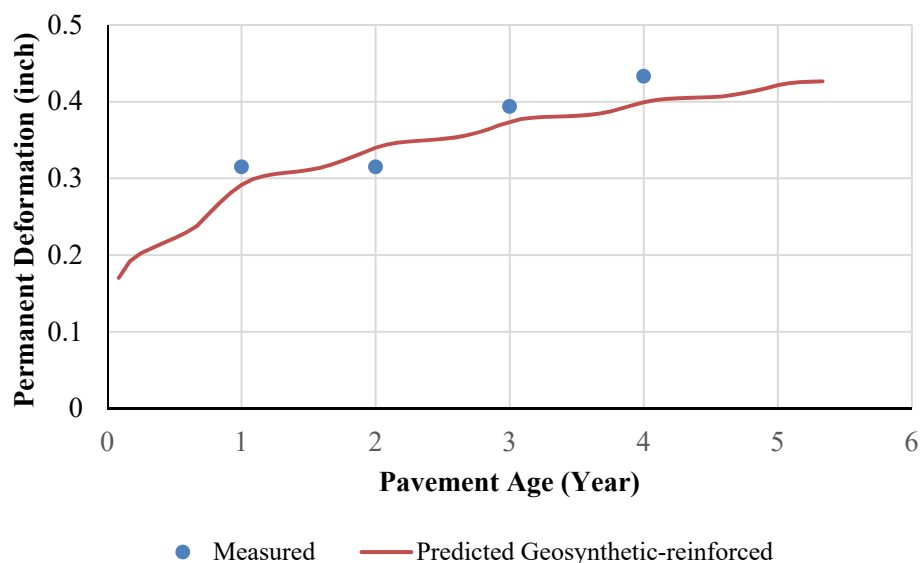


Figure O-6. Comparison of Rutting Depth between ANN Approach Prediction and Field Measurement for Pavement Section 48-0167

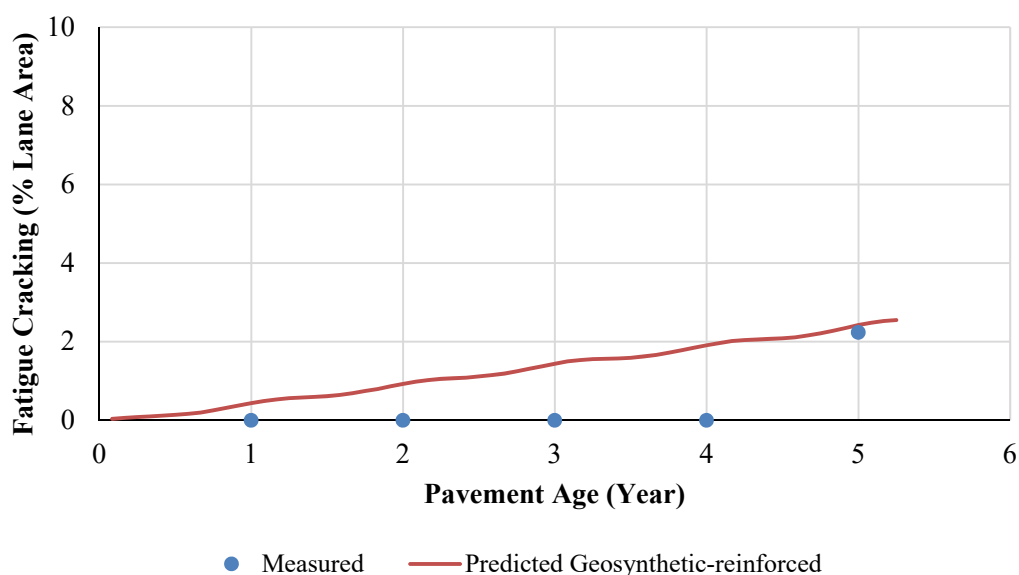


Figure O-7. Comparison of Fatigue Cracking between ANN Approach Prediction and Field Measurement for Pavement Section 48-0167

LTPP Section 20-0160

The pavement section 20-0160 consists of a 5.6-inch hot-mixed and dense-graded asphalt concrete, a 7-inch crushed stone unbound base, a 6-inch treated subbase, and a semi-infinite silty clay subgrade. A 0.3-inch geogrid is placed at the interface between the unbound base and pozzolanic treated subbase. The comparisons of geosynthetic-reinforced pavement performance

between the predictions by the proposed ANN approach and the field measurements are presented in Figures O-8–O-9.

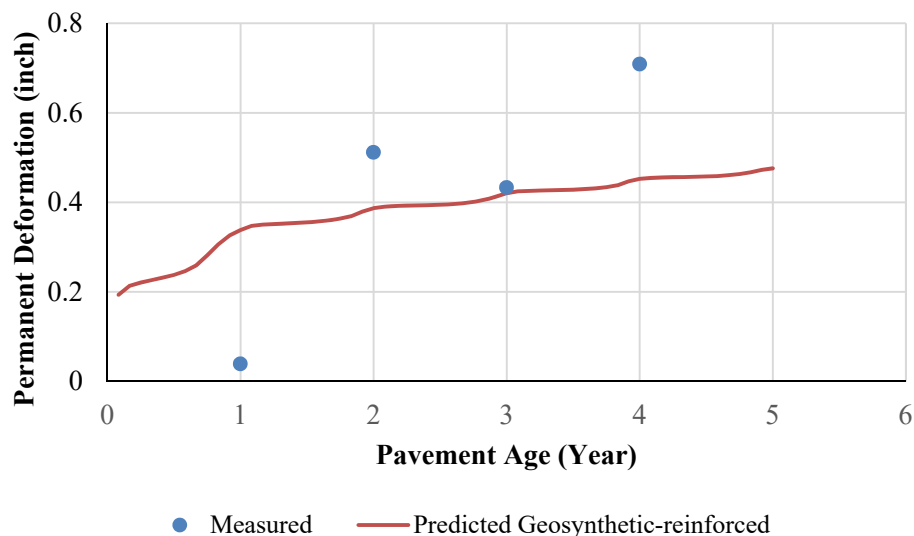


Figure O-8. Comparison of Rutting Depth between ANN Approach Prediction and Field Measurement for Pavement Section 20-0160

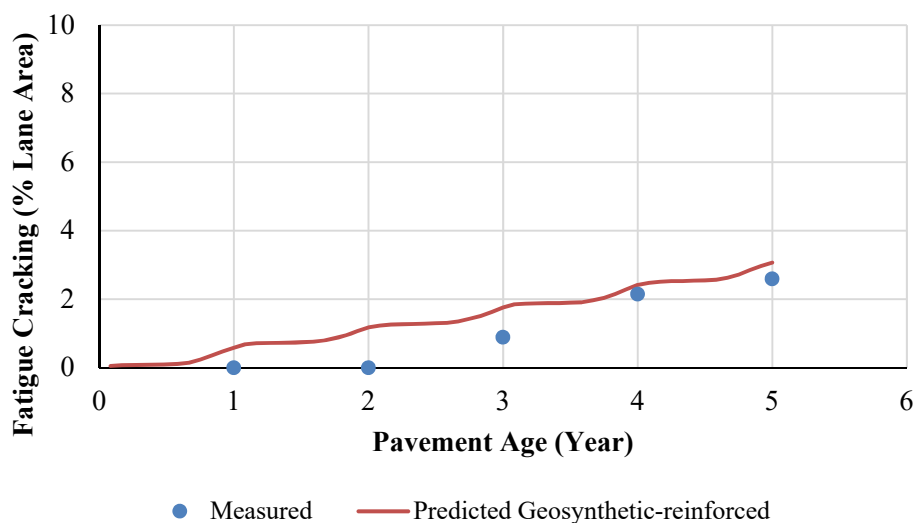


Figure Q-9. Comparison of Fatigue Cracking between ANN Approach Prediction and Field Measurement for Pavement Section 20-0160

PMIS Section FM 02

Texas Farm-to-Market Road No. 02 (FM 02) consists of a 1-inch asphalt seal coat, a 7-inch new base course, a 10-inch old base course, and a clay subgrade. The geosynthetic is placed at the interface between the new base course and the old base course. Two types of geogrids with different sheet stiffness are used in the sections of FM 02-2 and FM 02-3, respectively. One type of geotextile is used in the section of FM 02-4. The pavement sections

were constructed in January 2005. The average daily traffic is 800. The speed limit on FM 02 is 55 mph. The comparisons of geosynthetic-reinforced pavement performance between the predictions by the proposed ANN approach and the field measurements are presented in Figures O-10–O-15.

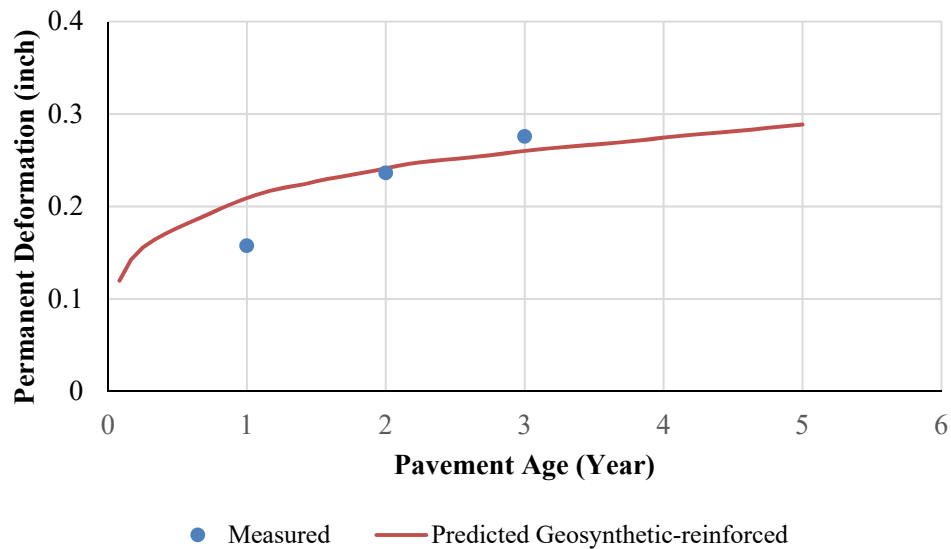


Figure O-10. Comparison of Rutting Depth between ANN Approach Prediction and Field Measurement for Pavement Section FM 02-2

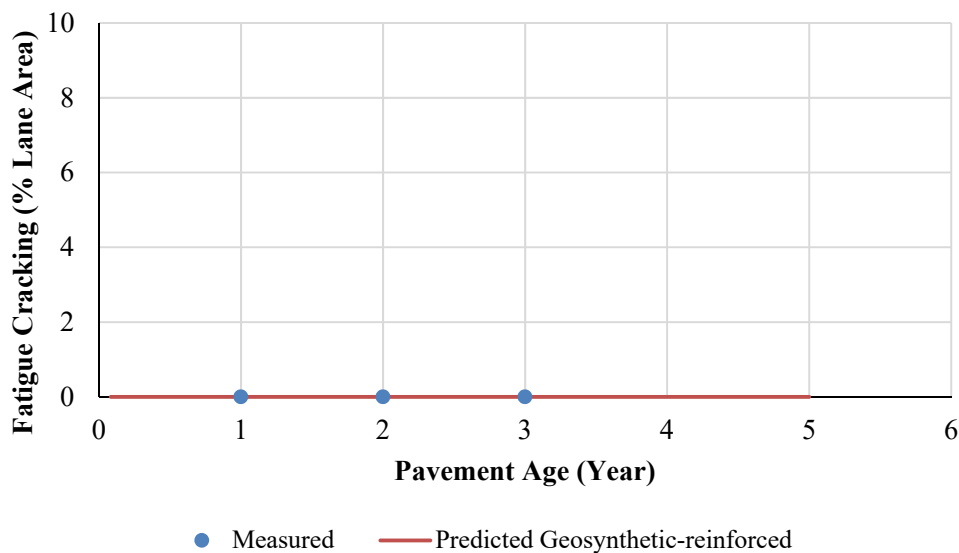


Figure O-11. Comparison of Fatigue Cracking between ANN Approach Prediction and Field Measurement for Pavement Section FM 02-2

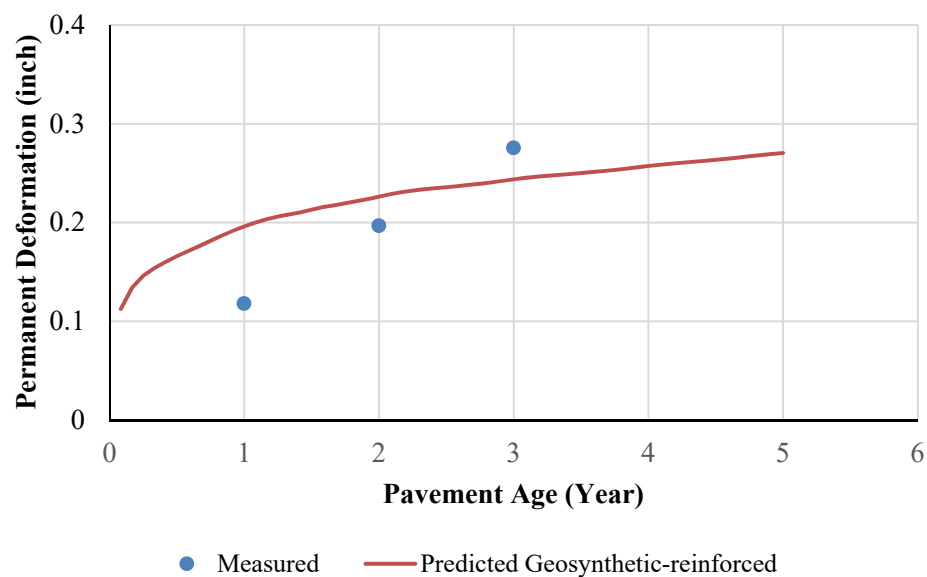


Figure O-12. Comparison of Rutting Depth between ANN Approach Prediction and Field Measurement for Pavement Section FM 02-3

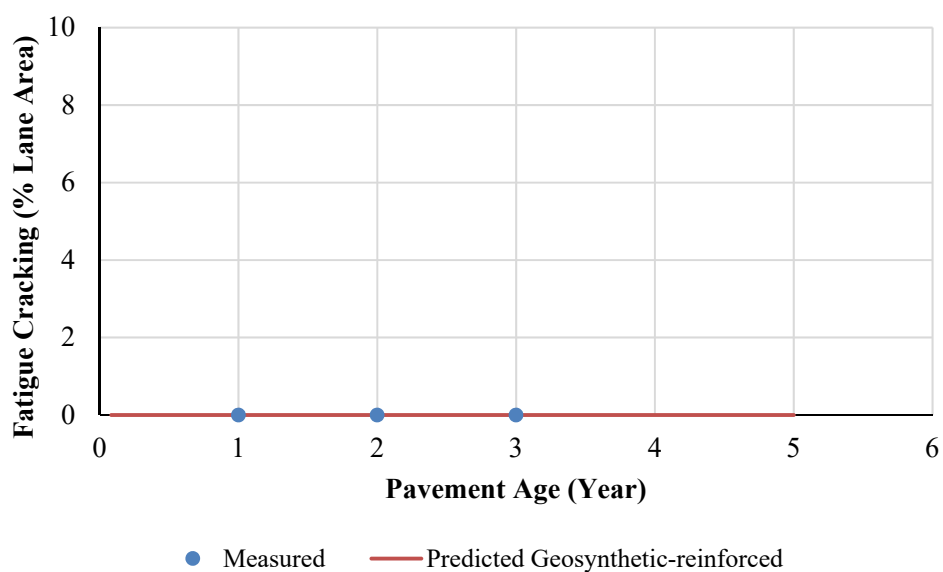


Figure O-13. Comparison of Fatigue Cracking between ANN Approach Prediction and Field Measurement for Pavement Section FM 02-3

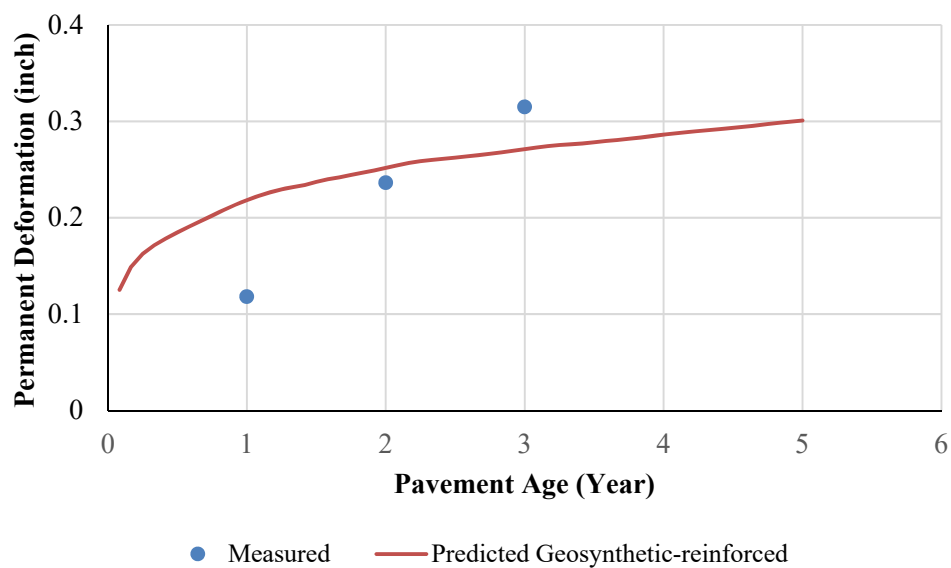


Figure O-14. Comparison of Rutting Depth between ANN Approach Prediction and Field Measurement for Pavement Section FM 02-4

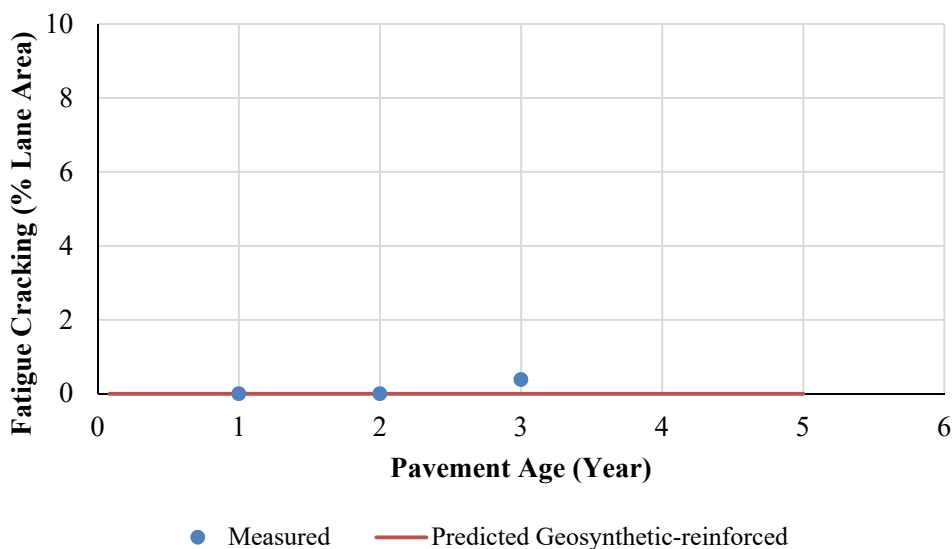


Figure O-15. Comparison of Fatigue Cracking between ANN Approach Prediction and Field Measurement for Pavement Section FM 02-4

**APPENDIX P. LIST OF GEOSYNTHETIC-REINFORCED IN-SERVICE PAVEMENT
SECTIONS IDENTIFIED FROM LONG-TERM PAVEMENT PERFORMANCE (LTPP)
DATABASE AND TEXAS PAVEMENT MANAGEMENT INFORMATION SYSTEM
(PMIS)**

Table P-1. List of Geosynthetic-Reinforced Pavement Sections from LTPP Database

Section Type	Pavement Section	Pavement Type	Traffic History	Pavement Structure	Geosynthetic Information	Distress History			FWD Data	Climatic Zone
						IRI	F/T Cracking	Rutting/Faulting		
GT	1-0110	ACP	√	√	Woven	√	√	√	√	WNF
GT	1-0111	ACP	√	√	Woven	√	√	√	√	WNF
GT	1-0112	ACP	√	√	Woven	√	√	√	√	WNF
GT	1-0163	ACP	√	√	Woven	√	√	√	√	WNF
C	1-0109	ACP	√	√		√	√	√	√	WNF
GT	5-0122	ACP	√	√	Woven	√	√	√	√	WNF
GT	5-0123	ACP	√	√	Woven	√	√	√	√	WNF
GT	5-0124	ACP	√	√	Woven	√	√	√	√	WNF
C	5-0121	ACP	√	√		√	√	√	√	WNF
GT	5-0213	JCP	√	√	Woven	√	√	√	√	WNF
GT	5-0214	JCP	√	√	Woven	√	√	√	√	WNF
GT	5-0215	JCP	√	√	Woven	√	√	√	√	WNF
GT	5-0126	JCP	√	√	Woven	√	√	√	√	WNF
GT	5-0217	JCP	√	√	Woven	√	√	√	√	WNF
GT	5-0218	JCP	√	√	Woven	√	√	√	√	WNF
GT	5-0219	JCP	√	√	Woven	√	√	√	√	WNF
GT	5-0220	JCP	√	√	Woven	√	√	√	√	WNF
GT	5-0221	JCP	√	√	Woven	√	√	√	√	WNF
GT	5-0222	JCP	√	√	Woven	√	√	√	√	WNF
GT	5-0223	JCP	√	√	Woven	√	√	√	√	WNF
GT	5-0224	JCP	√	√	Woven	√	√	√	√	WNF
GT	8-1057	ACP	√	√	Nonwoven	√	√	√	√	DF
GT	10-0110	ACP	√	√	Nonwoven	√	√	√	√	WF
GT	10-0111	ACP	√	√	Nonwoven	√	√	√	√	WF
GT	10-0112	ACP	√	√	Nonwoven	√	√	√	√	WF

Section Type	Pavement Section	Pavement Type	Traffic History	Pavement Structure	Geosynthetic Information	Distress History			FWD Data	Climatic Zone
						IRI	F/T Cracking	Rutting/Faulting		
C	10-0108	ACP	✓	✓		✓	✓	✓	✓	WF
GT	12-0110	ACP	✓	✓	Woven	✓	✓	✓	✓	WNF
GT	12-0111	ACP	✓	✓	Woven	✓	✓	✓	✓	WNF
GT	12-0112	ACP	✓	✓	Woven	✓	✓	✓	✓	WNF
C	12-0109	ACP	✓	✓		✓	✓	✓	✓	WNF
GT	16-9032	ACP	✓	✓	Woven	✓	✓	✓	✓	DF
GG	20-0160	ACP	✓	✓	Default	✓	✓	✓	✓	DF
C	20-0161	ACP	✓	✓		✓	✓	✓	✓	DF
GT	22-0122	ACP	✓	✓	Woven	✓	✓	✓	✓	WNF
GT	22-0123	ACP	✓	✓	Woven	✓	✓	✓	✓	WNF
GT	22-0124	ACP	✓	✓	Woven	✓	✓	✓	✓	WNF
C	22-0121	ACP	✓	✓		✓	✓	✓	✓	WNF
GT	26-0122	ACP	✓	✓	Woven	✓	✓	✓	✓	WF
GT	26-0123	ACP	✓	✓	Woven	✓	✓	✓	✓	WF
GT	26-0124	ACP	✓	✓	Woven	✓	✓	✓	✓	WF
C	26-0121	ACP	✓	✓		✓	✓	✓	✓	WF
GT	35-0110	ACP	✓	✓	Woven	✓	✓	✓	✓	DNF
GT	35-0111	ACP	✓	✓	Woven	✓	✓	✓	✓	DNF
GT	35-0112	ACP	✓	✓	Woven	✓	✓	✓	✓	DNF
C	35-0109	ACP	✓	✓		✓	✓	✓	✓	DNF
GT	40-0122	ACP	✓	✓	Woven	✓	✓	✓	✓	DNF
GT	40-0123	ACP	✓	✓	Woven	✓	✓	✓	✓	DNF
GT	40-0124	ACP	✓	✓	Woven	✓	✓	✓	✓	DNF
C	40-0120	ACP	✓	✓		✓	✓	✓	✓	DNF
GT	48-0119	ACP	✓	✓	Nonwoven	✓	✓	✓	✓	DNF
GT	48-0120	ACP	✓	✓	Nonwoven	✓	✓	✓	✓	DNF
GT	48-0121	ACP	✓	✓	Nonwoven	✓	✓	✓	✓	DNF

Section Type	Pavement Section	Pavement Type	Traffic History	Pavement Structure	Geosynthetic Information	Distress History			FWD Data	Climatic Zone
						IRI	F/T Cracking	Rutting/Faulting		
GT	48-0122	ACP	√	√	Nonwoven	√	√	√	√	DNF
GT	48-0123	ACP	√	√	Nonwoven	√	√	√	√	DNF
GT	48-0124	ACP	√	√	Nonwoven	√	√	√	√	DNF
C	48-0118	ACP	√	√		√	√	√	√	DNF
GG	48-0167	ACP	√	√	Default	√	√	√	√	DNF
GG	49-7086	ACP	√	√	Default	√	√	√	√	DF
GG	49-D410	JCP	√	√	Default	√	√	√	√	DF
GG	49-D430	JCP	√	√	Default	√	√	√	√	DF
GG	49-D431	JCP	√	√	Default	√	√	√	√	DF
GG	49-D440	JCP	√	√	Default	√	√	√	√	DF
GG	49-D441	JCP	√	√	Default	√	√	√	√	DF
GG	49-D443	JCP	√	√	Default	√	√	√	√	DF
GG	49-D444	JCP	√	√	Default	√	√	√	√	DF
GG	49-D445	JCP	√	√	Default	√	√	√	√	DF
GG	49-D446	JCP	√	√	Default	√	√	√	√	DF
GG	49-D448	JCP	√	√	Default	√	√	√	√	DF
GG	49-D449	JCP	√	√	Default	√	√	√	√	DF
GG	49-D450	JCP	√	√	Default	√	√	√	√	DF
GG	49-D451	JCP	√	√	Default	√	√	√	√	DF
GG	49-D452	JCP	√	√	Default	√	√	√	√	DF
GG	49-D454	JCP	√	√	Default	√	√	√	√	DF
GG	49-D455	JCP	√	√	Default	√	√	√	√	DF
GG	49-D459	JCP	√	√	Default	√	√	√	√	DF
GG	49-D460	JCP	√	√	Default	√	√	√	√	DF
GG	49-D461	JCP	√	√	Default	√	√	√	√	DF
GG	49-D462	JCP	√	√	Default	√	√	√	√	DF
GT	51-0122	ACP	√	√	Nonwoven	√	√	√	√	WF

Section Type	Pavement Section	Pavement Type	Traffic History	Pavement Structure	Geosynthetic Information	Distress History			FWD Data	Climatic Zone
						IRI	F/T Cracking	Rutting/Faulting		
GT	51-0123	ACP	√	√	Nonwoven	√	√	√	√	WF
GT	51-0124	ACP	√	√	Nonwoven	√	√	√	√	WF
C	51-0121	ACP	√	√		√	√	√	√	WF
GT	55-0122	ACP	√	√	Woven	√	√	√	√	WF
GT	55-0123	ACP	√	√	Woven	√	√	√	√	WF
GT	55-0124	ACP	√	√	Woven	√	√	√	√	WF
C	55-0121	ACP	√	√		√	√	√	√	WF

Note: GT = Geotextile, GG = Geogrid, C = Control.

Table P-2. State Code Dictionary in LTPP Database

State ID	State Name	State ID	State Name
1	Alabama	34	New Jersey
10	Delaware	35	New Mexico
11	District of Columbia	36	New York
12	Florida	37	North Carolina
13	Georgia	38	North Dakota
15	Hawaii	39	Ohio
16	Idaho	4	Arizona
17	Illinois	40	Oklahoma
18	Indiana	41	Oregon
19	Iowa	42	Pennsylvania
2	Alaska	44	Rhode Island
20	Kansas	45	South Carolina
21	Kentucky	46	South Dakota
22	Louisiana	47	Tennessee
23	Maine	48	Texas
24	Maryland	49	Utah
25	Massachusetts	5	Arkansas
26	Michigan	50	Vermont
27	Minnesota	51	Virginia
28	Mississippi	53	Washington
29	Missouri	54	West Virginia
30	Montana	55	Wisconsin
31	Nebraska	56	Wyoming
32	Nevada	6	California
33	New Hampshire	60	American Samoa
8	Colorado	9	Connecticut

Table P-3. List of Geosynthetic-Reinforced Pavement Sections from Texas PMIS Database

Section Type	Pavement Section	Pavement Type	Traffic History	Pavement Structure	Geosynthetic Type	Distress History			FWD Data	Climatic Zone
						IRI	F/T Cracking	Rutting/Faulting		
C	FM 02-1	ACP	√	√		√	√	√	√	WNF
GG	FM 02-2	ACP	√	√	GG PP	√	√	√	√	WNF
GG	FM 02-3	ACP	√	√	GG PET	√	√	√	√	WNF
GT	FM 02-4	ACP	√	√	GT	√	√	√	√	WNF
C	FM 02-5	ACP	√	√		√	√	√	√	WNF
GG	FM 02-6	ACP	√	√	GG PP	√	√	√	√	WNF
GG	FM 02-7	ACP	√	√	GG PET	√	√	√	√	WNF
GT	FM 02-8	ACP	√	√	GT	√	√	√	√	WNF
GG	FM 2331-292	ACP	√	√	GG2	√	√	√	√	DNF
GG	FM 2331-294	ACP	√	√	GG2	√	√	√	√	DNF
GG	FM 2331-296	ACP	√	√	GG2	√	√	√	√	DNF
C	FM 2331-290	ACP	√	√		√	√	√	√	DNF
GG	FM 917-558	ACP	√	√	GG2	√	√	√	√	DNF
GG	FM 917-560	ACP	√	√	GG2	√	√	√	√	DNF
C	FM 917-556	ACP	√	√		√	√	√	√	DNF
GG	FM 157-296	ACP	√	√	GG2	√	√	√	√	DNF
GG	FM 157-298	ACP	√	√	GG2	√	√	√	√	DNF
C	FM 157-294	ACP	√	√		√	√	√	√	DNF
GG	US 79-550	ACP	√	N/A	N/A	√	√	√	N/A	DNF
C	US 79-552	ACP	√	N/A		√	√	√	N/A	DNF
GG	SH 73-740	ACP	√	N/A	GG2	√	√	√	N/A	WNF
GG	SH 73-742	ACP	√	N/A	GG2	√	√	√	√	WNF
GG	SH 73-744	ACP	√	N/A	GG2	√	√	√	√	WNF
GG	SH 73-746	ACP	√	N/A	GG2	√	√	√	√	WNF
GG	SH 73-748	ACP	√	N/A	GG2	√	√	√	√	WNF

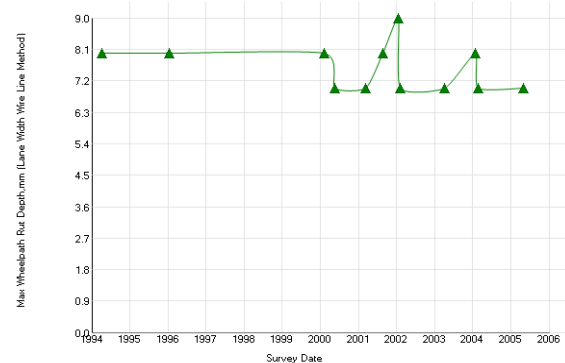
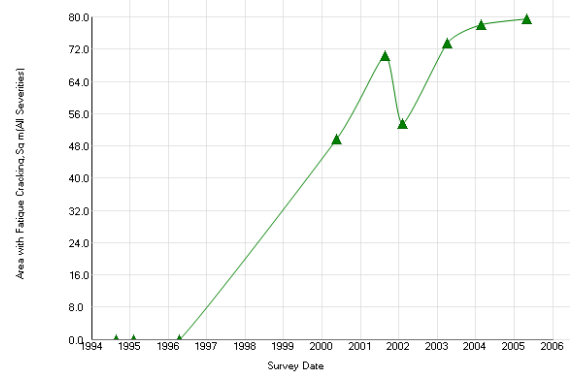
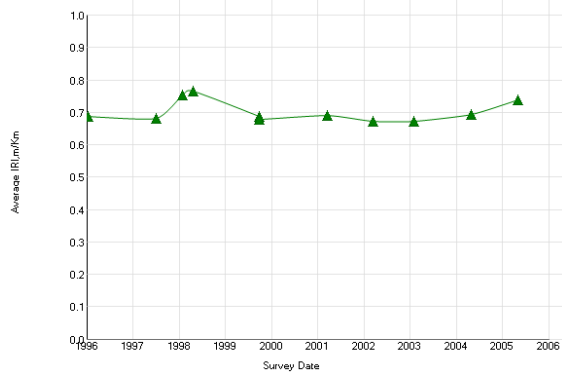
Section Type	Pavement Section	Pavement Type	Traffic History	Pavement Structure	Geosynthetic Type	Distress History			FWD Data	Climatic Zone
						IRI	F/T Cracking	Rutting/Faulting		
GG	SH 73-750	ACP	√	N/A	GG2	√	√	√	√	WNF
GG	SH 73-752	ACP	√	N/A	GG2	√	√	√	√	WNF
GG	SH 73-754	ACP	√	N/A	GG2	√	√	√	√	WNF
GG	SH 73-756	ACP	√	N/A	GG2	√	√	√	√	WNF
GG	SH 73-758	ACP	√	N/A	GG2	√	√	√	√	WNF
GG	SH 73-760	ACP	√	N/A	GG2	√	√	√	√	WNF
GG	SH 73-762	ACP	√	N/A	GG2	√	√	√	N/A	WNF
GG	SH 73-764	ACP	√	N/A	GG2	√	√	√	N/A	WNF
C	SH 73-766	ACP	√	N/A		√	√	√	N/A	WNF
GG	FM 357-688	ACP	√	N/A	GG1	√	√	√	√	WNF
GG	IH 45-218	JCP	√	N/A	N/A	√	√	N/A	√	WNF
GG	FM 123-740	ACP	√	N/A	GG1	√	√	√	√	WNF
GG	FM 699-304	ACP	√	N/A	GG1	√	√	√	N/A	WNF
GG	FM 699-306	ACP	√	N/A	GG1	√	√	√	N/A	WNF
C	FM 699-308	ACP	√	N/A		√	√	√	N/A	WNF
GG	FM 2517-736	ACP	√	N/A	GG1	√	√	√	N/A	WNF
GG	FM 2517-738	ACP	√	N/A	GG1	√	√	√	N/A	WNF
GG	FM 2517-744	ACP	√	N/A	GG1	√	√	√	N/A	WNF
C	FM 2517-740	ACP	√	N/A		√	√	√	N/A	WNF
GG	FM 1402-232	ACP	√	N/A	GG1	√	√	√	N/A	WNF
GG	FM 1696-672	ACP	√	N/A	GG1	√	√	√	N/A	WNF
C	FM 1696-670	ACP	√	N/A		√	√	√	N/A	WNF
GG	FM 39-406	ACP	√	N/A	GG1	√	√	√	√	WNF
GG	FM 39-408	ACP	√	N/A	GG1	√	√	√	√	WNF
GG	FM 39-410	ACP	√	N/A	GG1	√	√	√	√	WNF
GG	FM 39-412	ACP	√	N/A	GG1	√	√	√	√	WNF
C	FM 39-414	ACP	√	N/A		√	√	√	√	WNF

Section Type	Pavement Section	Pavement Type	Traffic History	Pavement Structure	Geosynthetic Type	Distress History			FWD Data	Climatic Zone
						IRI	F/T Cracking	Rutting/Faulting		
GG	FM 1428-646	ACP	√	N/A	GG1	√	√	√	√	WNF
GG	FM1428-648	ACP	√	N/A	GG1	√	√	√	√	WNF
C	FM 1428-650	ACP	√	N/A		√	√	√	√	WNF
GG	IH 45-182	ACP	√	N/A	GG1	√	√	√	√	WNF
GG	IH 45-184	ACP	√	N/A	GG1	√	√	√	√	WNF
GG	IH 45-186	ACP	√	N/A	GG1	√	√	√	√	WNF
C	IH 45-188	ACP	√	N/A		√	√	√	√	WNF
GG	FM 1375-664	ACP	√	N/A	GG1	√	√	√	√	WNF
GG	FM 1375-670	ACP	√	N/A	GG1	√	√	√	√	WNF
GG	US 67-770	ACP	√	N/A	GG1	√	√	√	√	DNF
C	US 67-772	ACP	√	N/A		√	√	√	√	DNF
GG	FM 1915-406	ACP	√	√	GG1	√	√	√	√	WNF
GG	FM 1915-408	ACP	√	√	GG1	√	√	√	√	WNF
C	FM 1915-410	ACP	√	√		√	√	√	√	WNF

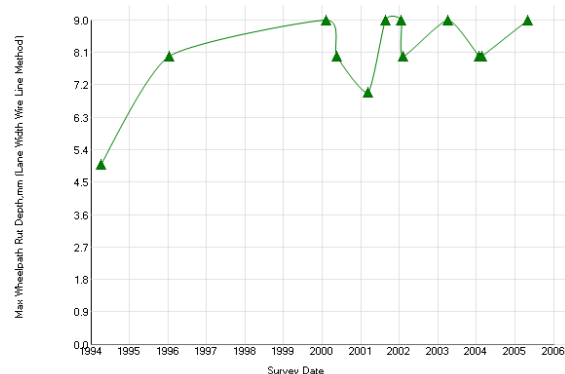
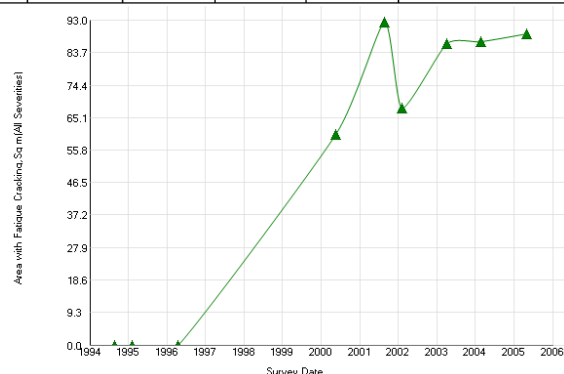
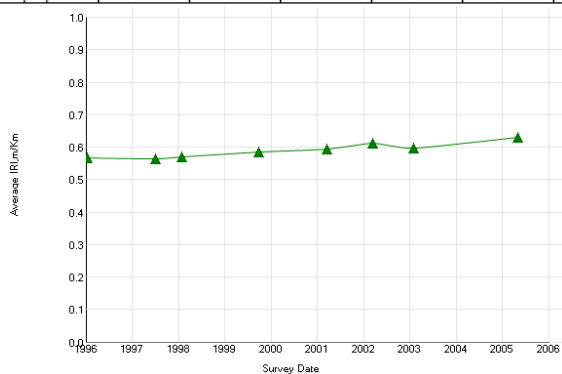
Note: FM = Farm to Market Road, IH = Interstate Highway, US = U.S. Highway, SH = State Highway, GG PP = Polypropylene Geogrid, GG PET = Polyester Geogrid, GT = Geotextile, GG1 = Tensar Geogrid Type 1, GG2 = Tensar Geogrid Type 2.

Appendix P1. LTPP Sections with Geotextile

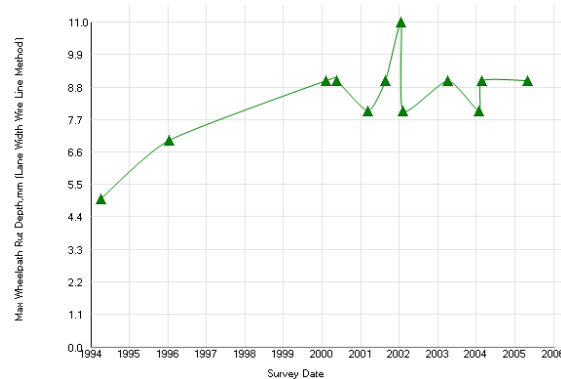
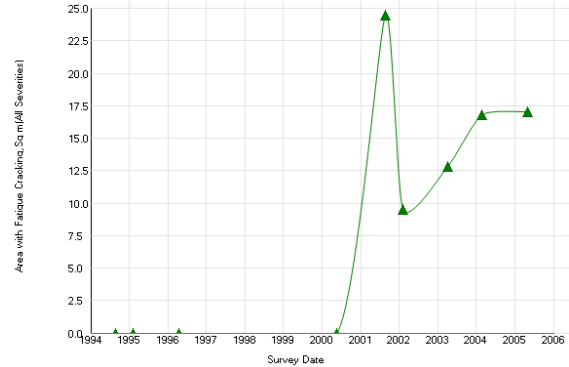
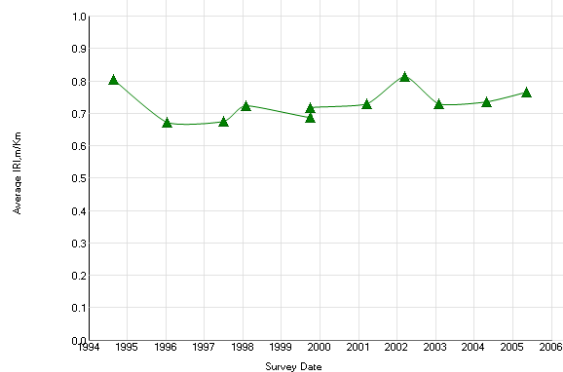
Experiment: SPS-1: Strategic Study of Structural Factors for Flexible Pavements, new/reconstructed AC pavements						Section ID: 01-0110						
Section# :			01-0110		Data :			ALL DATA				
REGION		Southern (Austin, TX, USA)			LATITUDE		32.61151		ROUTE/DIRECTION			
EXPERIMENT		SPS-1			LONGITUDE		-85.25871		NO. OF LANES			
STATE/PROVINCE		Alabama			ELEVATION				CONSTRUCTED			
COUNTY					MILEPOINT				OUT OF STUDY			
					FUNCTIONAL CLASS				04/30/1991			
									06/15/2005			
Layer Structure						Field Values		Laboratory Results				
LAYER		THICKNESS	MATERIAL			MOISTURE	DENSITY	SUBGRADE	COMPRESS	AIR	AC	MODULUS
NUMBER	TYPE	(mm)	DESCRIPTION			CONTENT (%)	(kg/m3)	P1	STR (kpa)	VOIDS(%)	CONTENT (%)	Mr.
1	SS		Fine-Grained Soils: Sandy Lean Clay									93
2	EF	2	Woven Geotextile									
3	TB	101	Open Graded, Hot Laid, Central Plant Mix									
4	TB	93	HMAC									
5	AC	152	Hot Mixed, Hot Laid AC, Dense Graded									
6	AC	35	Hot Mixed, Hot Laid AC, Dense Graded									
Distress Monitoring						Cross Profile		Monitored Traffic Data (Estimates)				
DISTRESS DATE	SURVEY METHOD	FATIGUE CRACKS (m2)	LOW TEMP. CRACKS (m)	LONG CRACKS (m)	POTHOLE/ PATCH (m2)	SURVEY DATE	RUT (mm) L/R	TRAFFIC YEAR	AADT (#)	TRUCKS (%)	CALCULATED ESALS	
											KESALS	
04/07/1994	AUTO			4	0.00	08/25/1994	3/4					
08/25/1994	MANUAL				0.00							
02/08/1995	MANUAL				0.00							
01/10/1996	AUTO		2		0.00							
04/18/1996	MANUAL				0.00							
02/05/2000	AUTO			112	0.00							
05/17/2000	MANUAL	49			0.00							
03/07/2001	AUTO		10	153	0.00							
08/24/2001	MANUAL	70	4		0.00							
01/14/2002	AUTO			152	0.00							
02/05/2002	MANUAL	53	5		0.00							
04/03/2003	MANUAL	73	6		0.00							
02/19/2004	MANUAL	78	3	1	0.00							
04/27/2005	MANUAL	79	2	1	0.00							



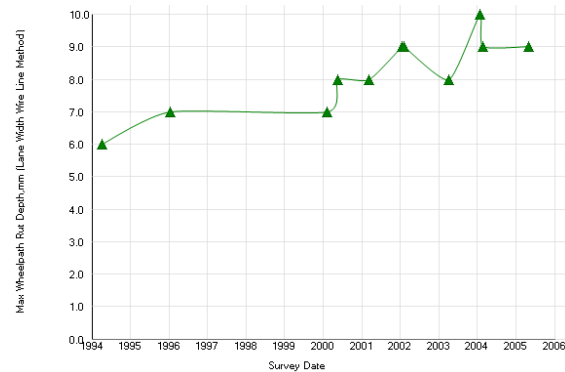
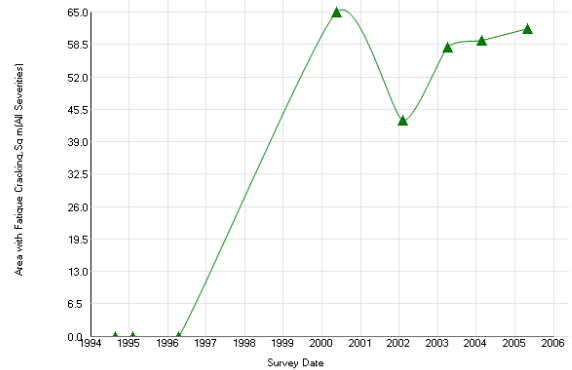
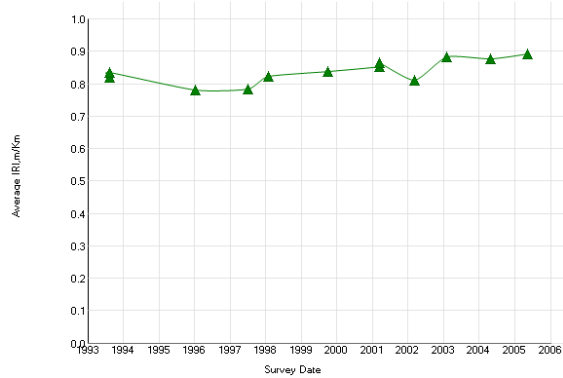
Experiment: SPS-1: Strategic Study of Structural Factors for Flexible Pavements, new/reconstructed AC pavements							Section ID: 01-0111				
Section# :			01-0111		Data :		ALL DATA				
REGION		Southern (Austin, TX, USA)		LATITUDE		32.61298		ROUTE/DIRECTION			
EXPERIMENT		SPS-1		LONGITUDE		-85.26083		NO. OF LANES			
STATE/PROVINCE		Alabama		ELEVATION				CONSTRUCTED		04/30/1991	
COUNTY				MILEPOINT				OUT OF STUDY		06/15/2005	
				FUNCTIONAL CLASS							
Layer Structure				Field Values			Laboratory Results				
LAYER		THICKNESS	MATERIAL DESCRIPTION			MOISTURE	DENSITY	SUBGRADE	COMPRESS	AIR	AC
NUMBER	TYPE	(mm)				CONTENT	(kg/m3)	P 1	STR	VOIDS(%)	CONTENT
						(%)			(kpa)		(%)
1	SS		Fine-Grained Soils: Silt with Sand								79
2	EF	2	Woven Geotextile								
3	TB	96	Open Graded, Hot Laid, Central Plant Mix								
4	TB	203	HMAC								
5	AC	58	Hot Mixed, Hot Laid AC, Dense Graded								
6	AC	33	Hot Mixed, Hot Laid AC, Dense Graded								
Distress Monitoring						Cross Profile		Monitored Traffic Data (Estimates)			
DISTRESS	SURVEY	FATIGUE	LOW TEMP.	LONG	POTHOLES/	SURVEY	RUT (mm)	TRAFFIC	AADT	TRUCKS	CALCULATED
DATE	METHOD	CRACKS	CRACKS	CRACKS	PATCH (m2)	DATE	L/R	YEAR	(#)	(%)	ESALS
		(m2)	(m)	(m)							KESALS
04/07/1994	AUTO				0.00	08/25/1994	4/3				
08/25/1994	MANUAL				0.00						
02/08/1995	MANUAL				0.00						
01/10/1996	AUTO				0.00						
04/18/1996	MANUAL				0.00						
02/05/2000	AUTO			108	0.00						
05/17/2000	MANUAL	60			0.00						
03/07/2001	AUTO		3	153	0.00						
08/24/2001	MANUAL	92			0.00						
01/14/2002	AUTO			152	0.00						
02/05/2002	MANUAL	67	1		0.00						
04/03/2003	MANUAL	86	2		0.00						
02/19/2004	MANUAL	86	3		0.00						
04/27/2005	MANUAL	89	3		0.00						



Experiment: SPS-1: Strategic Study of Structural Factors for Flexible Pavements, new/reconstructed AC pavements							Section ID: 01-0112					
REGION		Southern (Austin, TX, USA)		LATITUDE		32.61460	ROUTE/DIRECTION					
EXPERIMENT		SPS-1		LONGITUDE		-85.26314	NO. OF LANES					
STATE/PROVINCE		Alabama		ELEVATION			CONSTRUCTED		04/30/1991			
COUNTY				MILEPOINT			OUT OF STUDY		06/15/2005			
				FUNCTIONAL CLASS								
Layer Structure						Field Values		Laboratory Results				
LAYER		THICKNESS (mm)	MATERIAL DESCRIPTION			MOISTURE CONTENT (%)	DENSITY (kg/m3)	SUBGRADE P1	COMPRESS STR (kpa)	AIR VOIDS(%)	AC CONTENT (%)	MODULUS Mr.
NUMBER	TYPE											
1	SS		Fine-Grained Soils: Silt with Sand									
2	EF	2	Woven Geotextile									
3	TB	86	Open Graded, Hot Laid, Central Plant Mix									
4	TB	314	HMAC									
5	AC	55	Hot Mixed, Hot Laid AC, Dense Graded									
6	AC	27	Hot Mixed, Hot Laid AC, Dense Graded									
Distress Monitoring						Cross Profile		Monitored Traffic Data (Estimates)				
DISTRESS DATE	SURVEY METHOD	FATIGUE CRACKS (m2)	LOW TEMP. CRACKS (m)	LONG CRACKS (m)	POTHOLE/ PATCH (m2)	SURVEY DATE	RUT (mm) L/R	TRAFFIC YEAR	AADT (#)	TRUCKS (%)	CALCULATED ESALS	
											KESALS	
04/07/1994	AUTO			2	0.00	08/25/1994	4/3					
08/25/1994	MANUAL				0.00							
02/08/1995	MANUAL				0.00							
01/10/1996	AUTO			25	0.00							
04/18/1996	MANUAL				0.00							
02/05/2000	AUTO			131	0.00							
05/18/2000	MANUAL				0.00							
03/07/2001	AUTO		2	189	0.00							
08/24/2001	MANUAL	24		3	0.00							
01/14/2002	AUTO			153	0.00							
02/05/2002	MANUAL	9			0.00							
04/03/2003	MANUAL	12		1	0.00							
01/20/2004	AUTO		17	188	0.00							
02/20/2004	MANUAL	16		4	0.00							
04/27/2005	MANUAL	17		4	0.00							

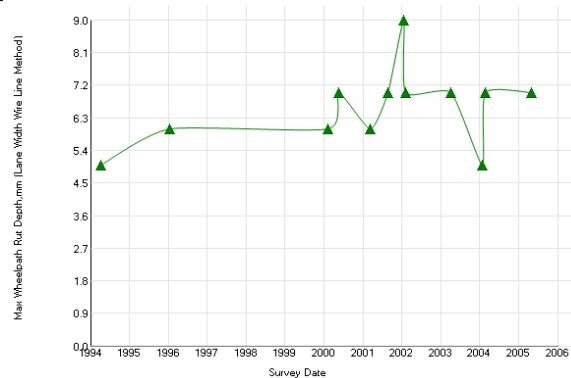
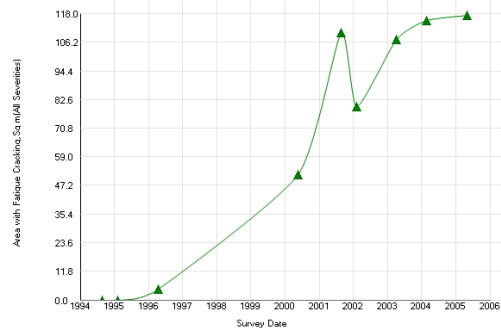
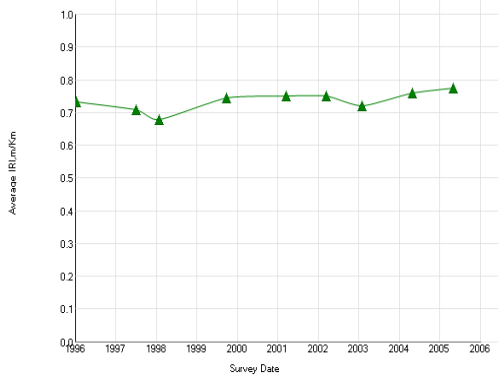


Experiment: SPS-1: Strategic Study of Structural Factors for Flexible Pavements, new/reconstructed AC pavements						Section ID: 01-0163						
Section# :			01-0163		Data :			ALL DATA				
REGION		Southern (Austin, TX, USA)			LATITUDE		32.60963		ROUTE/DIRECTION			
EXPERIMENT		SPS-1			LONGITUDE		-85.25599		NO. OF LANES			
STATE/PROVINCE		Alabama			ELEVATION				CONSTRUCTED			
COUNTY					MILEPOINT				04/30/1991			
					FUNCTIONAL CLASS				06/15/2005			
Layer Structure						Field Values		Laboratory Results				
LAYER		THICKNESS (mm)	MATERIAL DESCRIPTION			MOISTURE CONTENT (%)	DENSITY (kg/m3)	SUBGRADE P1	COMPRESS STR (kpa)	AIR VOIDS(%)	AC CONTENT (%)	MODULUS Mr.
NUMBER	TYPE											
1	SS		Fine-Grained Soils: Sandy Lean Clay									
2	GB	152	Crushed Stone									
3	EF	2	Woven Geotextile									
4	TB	109	Open Graded, Hot Laid, Central Plant Mix									
5	TB	152	HMAC									
6	AC	71	Hot Mixed, Hot Laid AC, Dense Graded									
7	AC	35	Hot Mixed, Hot Laid AC, Dense Graded									
Distress Monitoring						Cross Profile		Monitored Traffic Data (Estimates)				
DISTRESS DATE	SURVEY METHOD	FATIGUE CRACKS (m2)	LOW TEMP. CRACKS (m)	LONG CRACKS (m)	POTHOLE/ PATCH (m2)	SURVEY DATE	RUT (mm) L/R	TRAFFIC YEAR	AADT (#)	TRUCKS (%)	CALCULATED ESALS	
04/07/1994	AUTO			90	0.00	08/25/1994	4/3				KESALS	
08/25/1994	MANUAL				0.00							
02/08/1995	MANUAL				0.00							
01/10/1996	AUTO		5	111	0.00							
04/18/1996	MANUAL				0.00							
02/05/2000	AUTO		3	112	0.20							
05/17/2000	MANUAL	65			0.00							
03/07/2001	AUTO		3	153	0.00							
01/14/2002	AUTO			152	0.00							
02/04/2002	MANUAL	43		39	0.00							
04/02/2003	MANUAL	57		58	0.00							
02/19/2004	MANUAL	59		66	0.00							
04/27/2005	MANUAL	61		73	0.00							

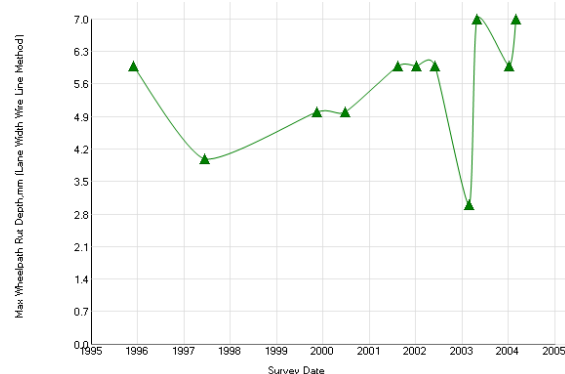
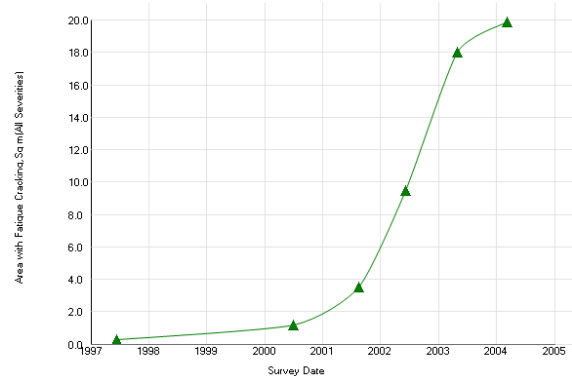
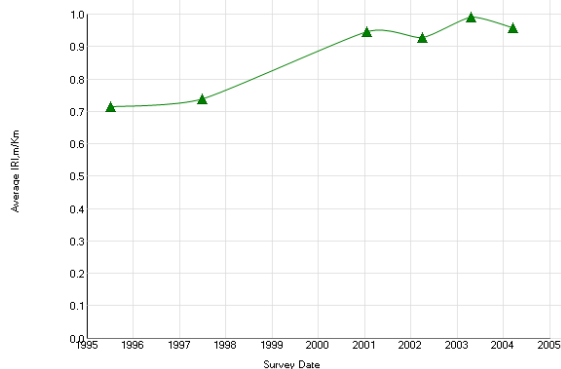


01-0109 Control

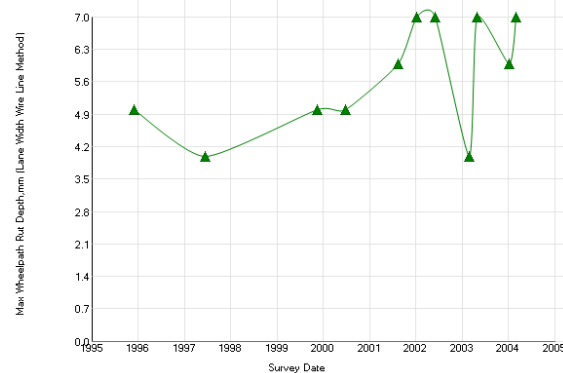
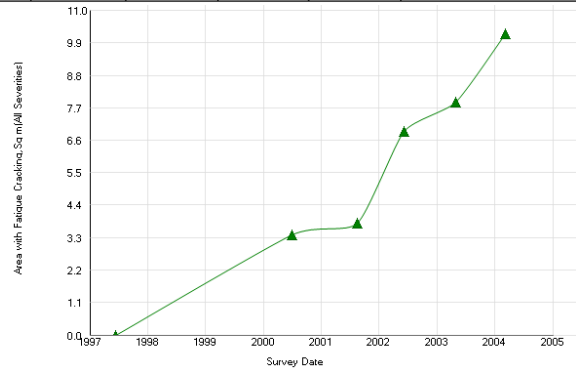
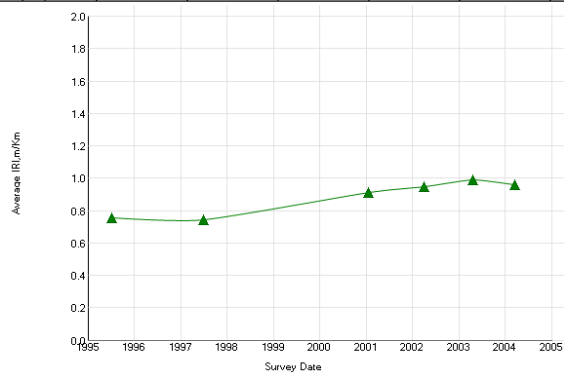
Experiment: SPS-1: Strategic Study of Structural Factors for Flexible Pavements, new/reconstructed AC pavements						Section ID: 01-0109			
Section# :			01-0109		Data : ALL DATA				
REGION		Southern (Austin, TX, USA)		LATITUDE		32.60833		ROUTE/DIRECTION	
EXPERIMENT		SPS-1		LONGITUDE		-85.25406		NO. OF LANES	
STATE/PROVINCE		Alabama		ELEVATION				CONSTRUCTED	
COUNTY				MILEPOINT				OUT OF STUDY	
				FUNCTIONAL CLASS				04/30/1991	
								06/15/2005	



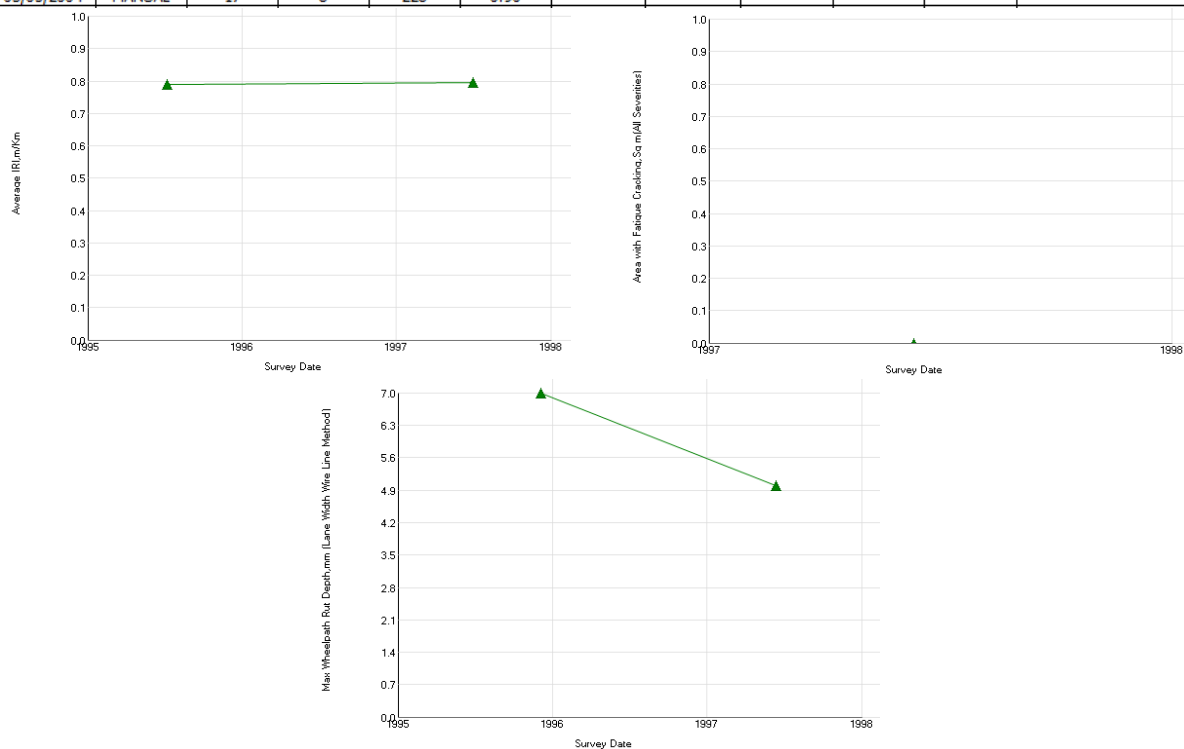
Experiment: SPS-1: Strategic Study of Structural Factors for Flexible Pavements, new/reconstructed AC pavements							Section ID: 05-0122					
REGION		Southern (Austin, TX, USA)		LATITUDE		35.72440		ROUTE/DIRECTION				
EXPERIMENT		SPS-1		LONGITUDE		-90.57977		NO. OF LANES				
STATE/PROVINCE		Arkansas		ELEVATION				CONSTRUCTED				
COUNTY				MILEPOINT				OUT OF STUDY				
				FUNCTIONAL CLASS				01/01/1993				
								11/15/2008				
Maintenance Rehabilitation/Rehabilitation Date							Activity Description					
04/26/2004							Crack Sealing (linear ft.)					
Layer Structure							Field Values		Laboratory Results			
LAYER		THICKNESS (mm)	MATERIAL DESCRIPTION		MOISTURE CONTENT (%)	DENSITY (kg/m3)	SUBGRADE P1	COMPRESS STR (kpa)	AIR VOIDS(%)	AC CONTENT (%)	MODULUS Mr.	
NUMBER	TYPE											
1	SS		Coarse-Grained Soil: Silty Sand		6	0.00						
2	EF	2	Woven Geotextile		7	0.00						
3	TB	88	Open Graded, Hot Laid, Central Plant Mix									
4	TB	104	HMAC									
5	AC	66	Hot Mixed, Hot Laid AC, Dense Graded									
6	AC	45	Hot Mixed, Hot Laid AC, Dense Graded									
Distress Monitoring							Cross Profile		Monitored Traffic Data (Estimates)			
DISTRESS DATE	SURVEY METHOD	FATIGUE CRACKS (m2)	LOW TEMP. CRACKS (m)	LONG CRACKS (m)	POTHOLES/ PATCH (m2)	SURVEY DATE	RUT (mm) L/R	TRAFFIC YEAR	AADT (#)	TRUCKS (%)	CALCULATED ESALS	
											KESALS	
12/05/1995	AUTO				0.00			1994	8200	849	257	
06/12/1997	MANUAL			138	0.00			1996	23000	3660	1969	
11/15/1999	AUTO			153	0.00			1998	10000	920	776	
06/27/2000	MANUAL	1		152	0.00							
08/14/2001	MANUAL	3		157	0.00							
01/08/2002	AUTO		15	315	0.00							
06/04/2002	MANUAL	9	3	156	0.00							
02/27/2003	AUTO		39	336	0.00							
04/30/2003	MANUAL	18	11	161	0.00							
01/09/2004	AUTO	1	75	320	0.00							
03/04/2004	MANUAL	19	14	162	0.00							
05/11/2005	MANUAL	18	26	166	0.00							
05/15/2007	MANUAL	27	29	173	0.00							



Experiment: SPS-1: Strategic Study of Structural Factors for Flexible Pavements, new/reconstructed AC pavements							Section ID: 05-0123				
REGION	Southern (Austin, TX, USA)		LATITUDE	35.72754		ROUTE/DIRECTION		01/01/1993 11/15/2008			
EXPERIMENT	SPS-1		LONGITUDE	-90.57977		NO. OF LANES					
STATE/PROVINCE	Arkansas		ELEVATION			CONSTRUCTED					
COUNTY			MILEPOINT			OUT OF STUDY					
			FUNCTIONAL CLASS								
Maintenance Rehabilitation/Rehabilitation Date					Activity Description						
04/26/2004					Crack Sealing (linear ft.)						
Layer Structure				Field Values		Laboratory Results					
LAYER		THICKNESS	MATERIAL DESCRIPTION		MOISTURE	DENSITY	SUBGRADE	COMPRESS	AIR	AC	MODULUS
NUMBER	TYPE	(mm)			CONTENT	(kg/m3)	P1	STR	VOIDS(%)	CONTENT	Mr.
1	SS		Coarse-Grained Soils: Poorly Graded Sand with Silt		6	0.00					
2	EF	2	Woven Geotextile								
3	TB	88	Open Graded, Hot Laid, Central Plant Mix								
4	TB	208	HMAC								
5	AC	139	Hot Mixed, Hot Laid AC, Dense Graded								
6	AC	43	Hot Mixed, Hot Laid AC, Dense Graded								
Distress Monitoring				Cross Profile		Monitored Traffic Data (Estimates)					
DISTRESS	SURVEY	FATIGUE	LOW TEMP.	LONG	POTHOLES/	SURVEY	RUT (mm)	TRAFFIC	AADT	TRUCKS	CALCULATED
DATE	METHOD	CRACKS	CRACKS	CRACKS	PATCH (m2)	DATE	L/R	YEAR	(#)	(%)	ESALS
		(m2)	(m)	(m)							
12/05/1995	AUTO				0.00			1994	8200	849	257
06/12/1997	MANUAL			152	0.00			1996	23000	3660	1969
11/15/1999	AUTO	1	1	154	0.00			1998	10000	920	776
06/27/2000	MANUAL	3		152	0.00						
08/14/2001	MANUAL	3	2	152	0.00						
01/08/2002	AUTO	2	21	314	0.00						
06/05/2002	MANUAL	6	4	158	0.00						
02/27/2003	AUTO	3	26	318	0.00						
04/30/2003	MANUAL	7	4	218	0.00						
01/09/2004	AUTO	3	68	315	0.00						
03/04/2004	MANUAL	10	9	228	0.00						
05/11/2005	MANUAL	10	13	250	0.00						
05/15/2007	MANUAL	13	23	243	0.00						

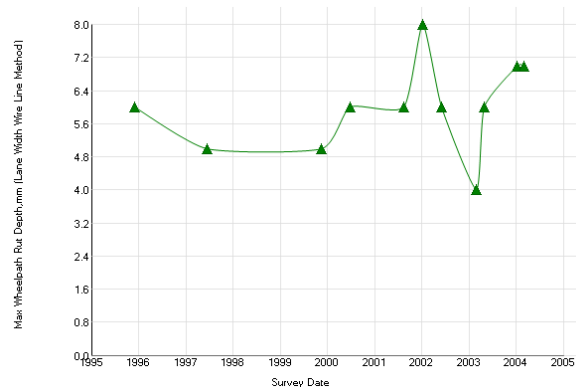
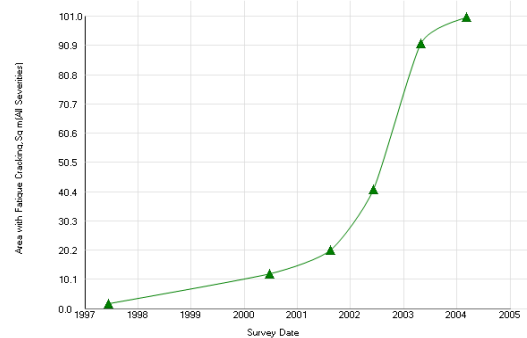
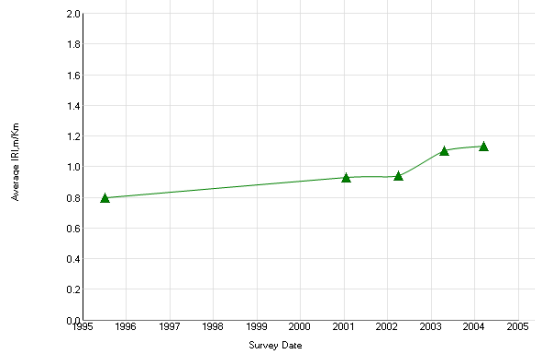


Experiment: SPS-1: Strategic Study of Structural Factors for Flexible Pavements, new/reconstructed AC pavements								Section ID: 05-0124			
REGION		Southern (Austin, TX, USA)		LATITUDE		35.72945		ROUTE/DIRECTION			
EXPERIMENT		SPS-1		LONGITUDE		-90.57983		NO. OF LANES			
STATE/PROVINCE		Arkansas		ELEVATION				CONSTRUCTED		01/01/1993	
COUNTY				MILEPOINT				OUT OF STUDY		11/15/2008	
				FUNCTIONAL CLASS							
Maintenance Rehabilitation/Rehabilitation Date						Activity Description					
05/15/1999						Patch Pot Holes - Hand Spread, Compacted with Truck (no. of holes)					
04/26/2004						Crack Sealing (linear ft.)					
Layer Structure				Field Values		Laboratory Results					
LAYER		THICKNESS (mm)	MATERIAL DESCRIPTION	MOISTURE CONTENT (%)	DENSITY (kg/m3)	SUBGRADE P1	COMPRESS STR (kpa)	AIR VOIDS(%)	AC CONTENT (%)	MODULUS Mr.	
NUMBER	TYPE										
1	SS		Coarse-Grained Soils: Poorly Graded Sand with Silt	6	0.00						
2	EF	2	Woven Geotextile								
3	TB	93	Open Graded, Hot Laid, Central Plant Mix								
4	TB	281	HMAC								
5	AC	134	Hot Mixed, Hot Laid AC, Dense Graded								
5	AC	139	Hot Mixed, Hot Laid AC, Dense Graded								
6	AC	35	Hot Mixed, Hot Laid AC, Dense Graded								
6	AC	40	Hot Mixed, Hot Laid AC, Dense Graded								
Distress Monitoring				Cross Profile		Monitored Traffic Data (Estimates)					
DISTRESS DATE	SURVEY METHOD	FATIGUE CRACKS (m2)	LOW TEMP. CRACKS (m)	LONG CRACKS (m)	POTHoles/ PATCH (m2)	SURVEY DATE	RUT (mm) L/R	TRAFFIC YEAR	AADT (#)	TRUCKS (%)	CALCULATED ESALS
											KESALS
12/05/1995	AUTO				0.00			1994	8200	849	257
06/12/1997	MANUAL			152	0.00			1996	23000	3660	1969
11/15/1999	AUTO	2	4	159	0.00			1998	10000	920	776
06/27/2000	MANUAL	4		152	1.90						
08/14/2001	MANUAL	6		179	1.90						
01/08/2002	AUTO	3	34		0.90						
06/05/2002	MANUAL	14	1	186	0.90						
02/27/2003	AUTO	4	34		0.90						
04/30/2003	MANUAL	16	6	215	0.90						
01/09/2004	AUTO	5	70		0.90						
03/05/2004	MANUAL	17	8	228	0.90						

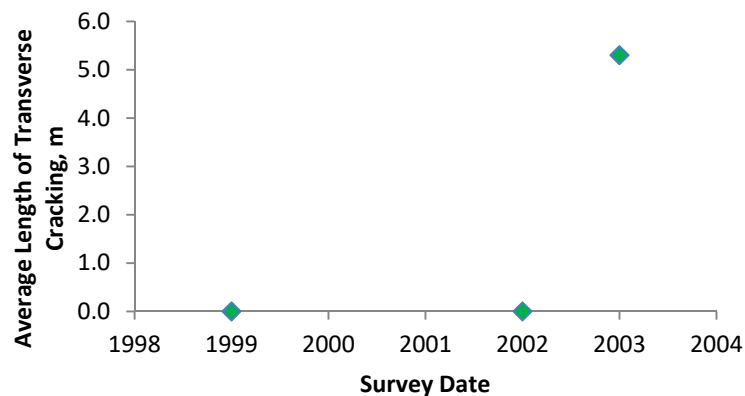
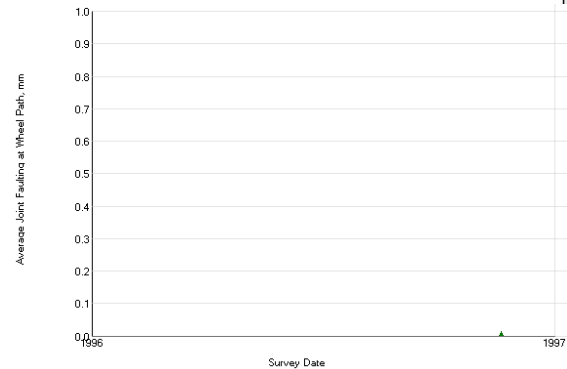
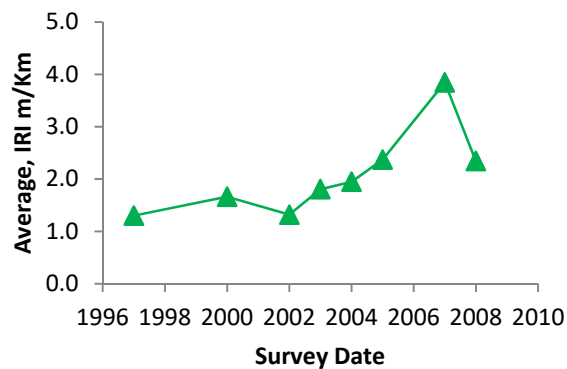


05-0121 Control

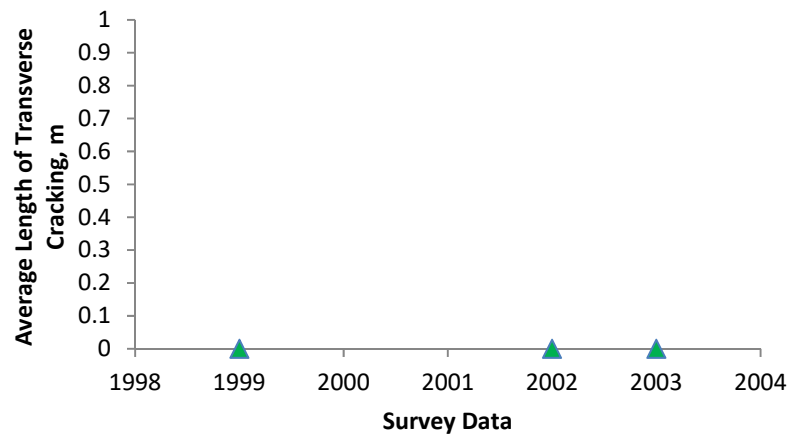
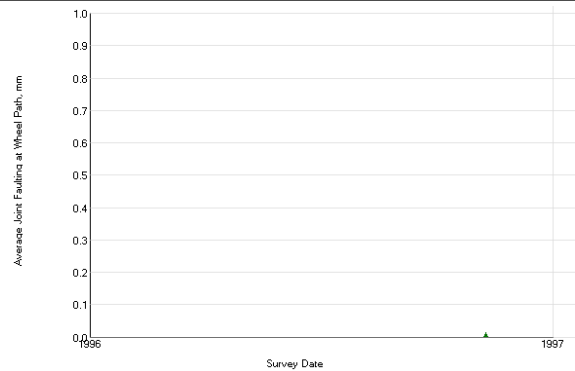
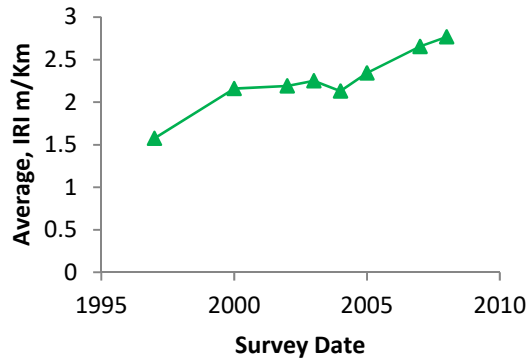
Experiment: SPS-1: Strategic Study of Structural Factors for Flexible Pavements, new/reconstructed AC pavements						Section ID: 05-0121					
Section# :			05-0121		Data :			ALL DATA			
REGION		Southern (Austin, TX, USA)		LATITUDE		35.72153		ROUTE/DIRECTION			
EXPERIMENT		SPS-1		LONGITUDE		-90.57973		NO. OF LANES			
STATE/PROVINCE		Arkansas		ELEVATION				CONSTRUCTED			
COUNTY				MILEPOINT				OUT OF STUDY			
				FUNCTIONAL CLASS				01/01/1993			
								06/15/2004			
Maintenance Rehabilitation/Rehabilitation Date						Activity Description					
04/26/2004						Crack Sealing (linear ft.)					
Layer Structure				Field Values		Laboratory Results					
LAYER		THICKNESS (mm)	MATERIAL DESCRIPTION	MOISTURE CONTENT (%)	DENSITY (kg/m3)	SUBGRADE P1	COMPRESS STR (kpa)	AIR VOIDS(%)	AC CONTENT (%)	MODULUS Mr.	
NUMBER	TYPE										
1	SS		Coarse-Grained Soil: Silty Sand	4	8.00						
2	GB	307	Crushed Stone	5	8.00						
3	TB	78	Open Graded, Hot Laid, Central Plant Mix	5	0.00						
4	AC	68	Hot Mixed, Hot Laid AC, Dense Graded	6	0.00						
5	AC	43	Hot Mixed, Hot Laid AC, Dense Graded								
Distress Monitoring						Cross Profile		Monitored Traffic Data (Estimates)			
DISTRESS DATE	SURVEY METHOD	FATIGUE CRACKS (m2)	LOW TEMP. CRACKS (m)	LONG CRACKS (m)	POTHOLE/ PATCH (m2)	SURVEY DATE	RUT (mm) L/R	TRAFFIC YEAR	AADT (#)	TRUCKS (%)	CALCULATED ESALS
											KESALS
12/05/1995	AUTO				0.00			1994	8200	849	257
06/12/1997	MANUAL	1	1	153	0.00			1996	23000	3660	1969
11/15/1999	AUTO		5	159	0.00			1998	10000	920	776
06/26/2000	MANUAL	12	3	154	0.00						
08/14/2001	MANUAL	20	1	156	0.00						
01/08/2002	AUTO	1	30	313	0.00						
06/04/2002	MANUAL	41	8	155	0.00						
02/27/2003	AUTO	2	31	316	0.00						
04/29/2003	MANUAL	91	11	140	0.00						
01/09/2004	AUTO	4	133	270	0.00						
03/04/2004	MANUAL	100	24	201	0.00						



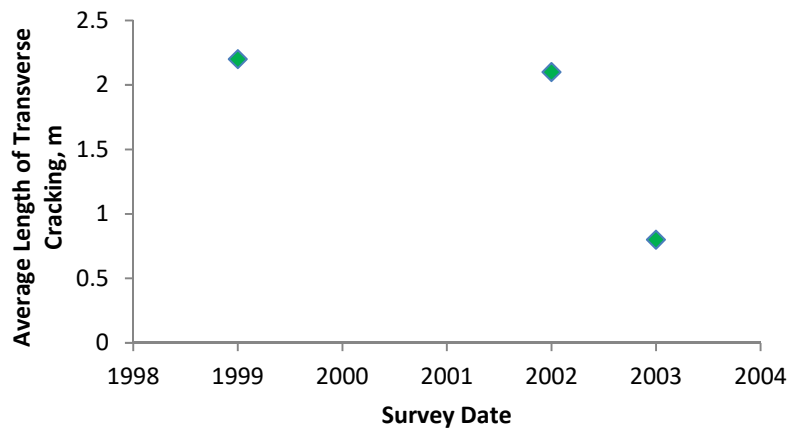
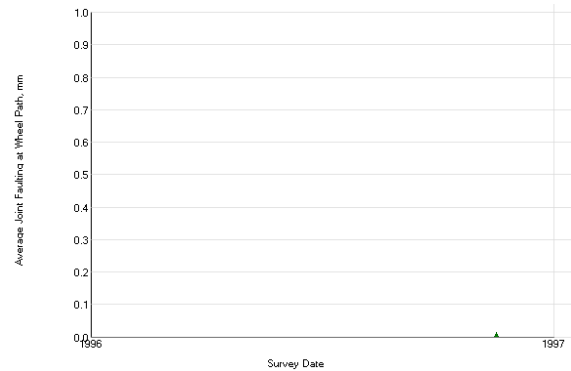
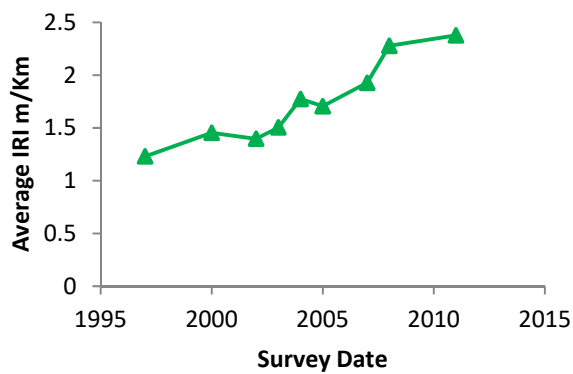
Experiment: SPS-2: Strategic Study of Structural Factors for Rigid Pavements, new/reconstructed JPCC pavements						Section ID: 05-0213					
Section# : 05-0213			Data : ALL DATA								
REGION	Southern (Austin, TX, USA)		LATITUDE	34.50536	ROUTE/DIRECTION						
EXPERIMENT	SPS-2		LONGITUDE	-92.70123	NO. OF LANES						
STATE/PROVINCE	Arkansas		ELEVATION		CONSTRUCTED 09/01/1993						
COUNTY			MILEPOINT		OUT OF STUDY 11/15/2008						
			FUNCTIONAL CLASS								
Maintenance Rehabilitation/Rehabilitation Date				Activity Description							
02/05/1997				Lane-Shoulder Longitudinal Joint Sealing (linear ft.)							
12/12/2002				Crack Sealing (linear ft.)							
11/15/2003				Partial Depth Patching of PCC Pavement Other Than at Joint (sq. yards)							
10/15/2006				Partial Depth Patching of PCC Pavement Other Than at Joint (sq. yards)							
Layer Structure			Field Values		Laboratory Results						
LAYER		THICKNESS (mm)	MATERIAL DESCRIPTION		MOISTURE CONTENT (%)	DENSITY (kg/m3)	SUBGRADE P1	COMPRESS STR (kpa)	AIR VOIDS(%)	AC CONTENT (%)	MODULUS Mr.
NUMBER	TYPE										
1	SS	762	Coarse-Grained Soil: Clayey Sand with Gravel			13.20					
2	EF	2	Woven Geotextile		8	7.20					
3	GB	152	Crushed Stone								295
4	PC	187	Portland Cement Concrete (JPCP)				42598	42598			
4	PC	215	Portland Cement Concrete (JPCP)				42598	42598			
Distress Monitoring					Cross Profile		Monitored Traffic Data (Estimates)				
DISTRESS DATE	SURVEY METHOD	FATIGUE CRACKS (m2)	LOW TEMP. CRACKS (m)	LONG CRACKS (m)	POTHOLE/ PATCH (m2)	SURVEY DATE	RUT (mm) L/R	TRAFFIC YEAR	AADT (#)	TRUCKS (%)	CALCULATED ESALS
											KESALS
								1996	23000	3660	1969
								1998	29000	6530	8882



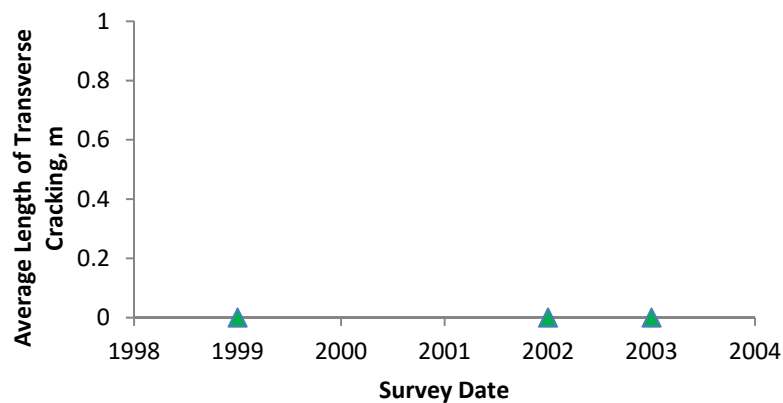
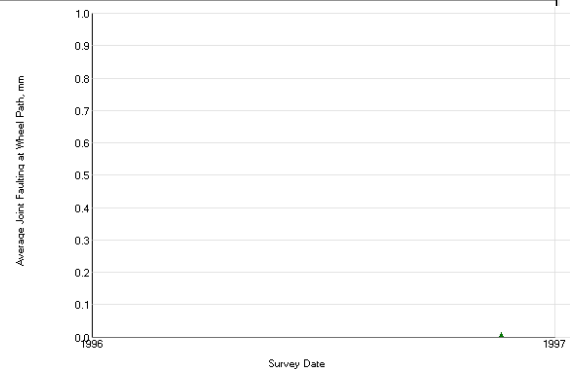
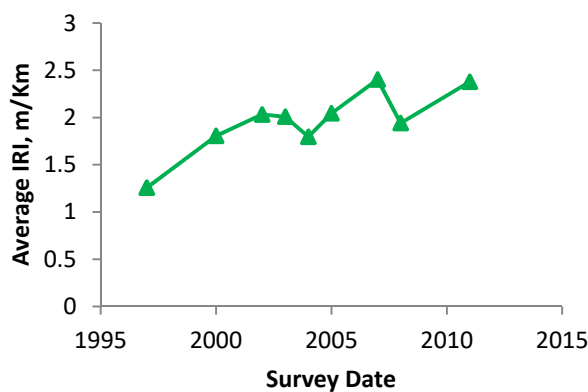
Experiment: SPS-2: Strategic Study of Structural Factors for Rigid Pavements, new/reconstructed JPCP pavements							Section ID: 05-0214					
Section# : 05-0214				Data : ALL DATA								
REGION		Southern (Austin, TX, USA)		LATITUDE		34.52304		ROUTE/DIRECTION NO. OF LANES CONSTRUCTED OUT OF STUDY 09/01/1993				
EXPERIMENT		SPS-2		LONGITUDE		-92.68468						
STATE/PROVINCE		Arkansas		ELEVATION								
COUNTY				MILEPOINT								
				FUNCTIONAL CLASS								
Maintenance Rehabilitation/Rehabilitation Date						Activity Description						
02/05/1997						Lane-Shoulder Longitudinal Joint Sealing (linear ft.)						
Layer Structure						Field Values		Laboratory Results				
LAYER		THICKNESS	MATERIAL DESCRIPTION			MOISTURE CONTENT (%)	DENSITY (kg/m3)	SUBGRADE P1	COMPRESS STR (kpa)	AIR VOIDS(%)	AC CONTENT (%)	MODULUS Mr.
NUMBER	TYPE	(mm)										
1	SS	3657	Coarse-Grained Soil: Silty Sand with Gravel			6	13.70					
2	EF	2	Woven Geotextile			8	7.70					
3	GB	254	Soil-Aggregate Mixture (Predominantly Coarse-Grained)			9	7.70					
4	PC	213	Portland Cement Concrete (JPCP)					74598	74598			
Distress Monitoring						Cross Profile		Monitored Traffic Data (Estimates)				
DISTRESS DATE	SURVEY METHOD	FATIGUE CRACKS (m2)	LOW TEMP. CRACKS (m)	LONG CRACKS (m)	POTHOLES/ PATCH (m2)	SURVEY DATE	RUT (mm) L/R	TRAFFIC YEAR	AADT (#)	TRUCKS (%)	CALCULATED ESALS	
											KESALS	
								1996	23000	3660	1969	
								1998	29000	6530	8882	



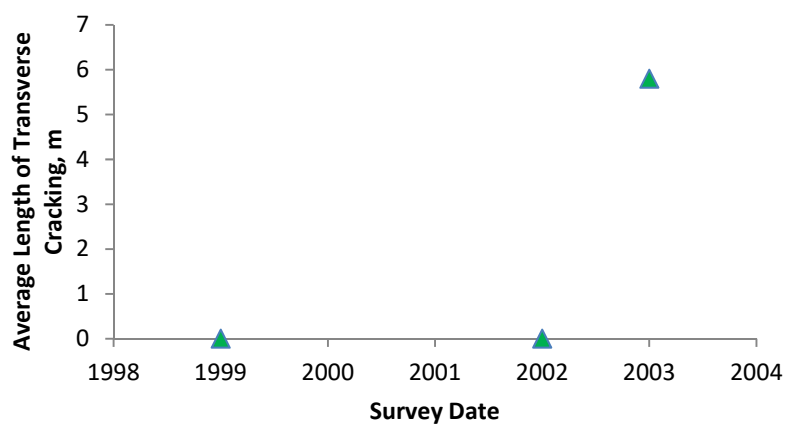
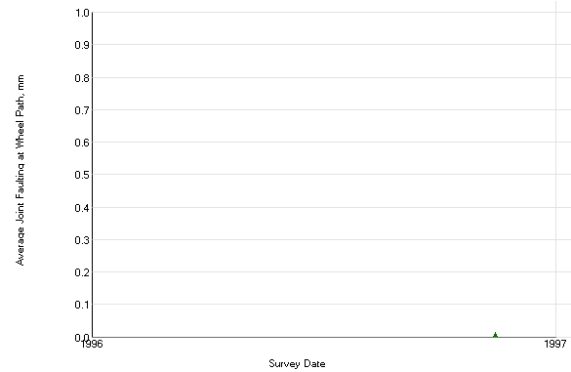
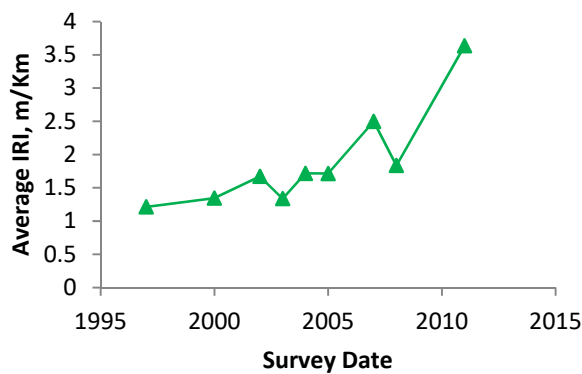
Experiment: SPS-2: Strategic Study of Structural Factors for Rigid Pavements, new/reconstructed JPCC pavements										Section ID: 05-0215			
Section# : 05-0215					Data : ALL DATA								
REGION		Southern (Austin, TX, USA)			LATITUDE		34.52874		ROUTE/DIRECTION NO. OF LANES CONSTRUCTED OUT OF STUDY 09/01/1993				
EXPERIMENT		SPS-2			LONGITUDE		-92.67982						
STATE/PROVINCE		Arkansas			ELEVATION								
COUNTY					MILEPOINT								
					FUNCTIONAL CLASS								
Maintenance Rehabilitation/Rehabilitation Date							Activity Description						
02/05/1997							Lane-Shoulder Longitudinal Joint Sealing (linear ft.)						
Layer Structure							Field Values		Laboratory Results				
LAYER		THICKNESS	MATERIAL DESCRIPTION				MOISTURE CONTENT (%)	DENSITY (kg/m3)	SUBGRADE P1	COMPRESS STR (kpa)	AIR VOIDS(%)	AC CONTENT (%)	MODULUS Mr.
NUMBER	TYPE	(mm)											
1	SS		Coarse-Grained Soil: Clayey Gravel with Sand				10	16.80					
2	EF	2	Woven Geotextile				7	10.80					
3	GB	152	Crushed Stone										
4	PC	292	Portland Cement Concrete (JPCP)						43952	43952			
Distress Monitoring							Cross Profile		Monitored Traffic Data (Estimates)				
DISTRESS DATE	SURVEY METHOD	FATIGUE CRACKS (m2)	LOW TEMP. CRACKS (m)	LONG CRACKS (m)	POTHOLE/PATCH (m2)	SURVEY DATE	RUT (mm) L/R	TRAFFIC YEAR	AADT (#)	TRUCKS (%)	CALCULATED ESALS		
											KESALS		
								1996	23000	3660	1969		
								1998	29000	6530	8882		



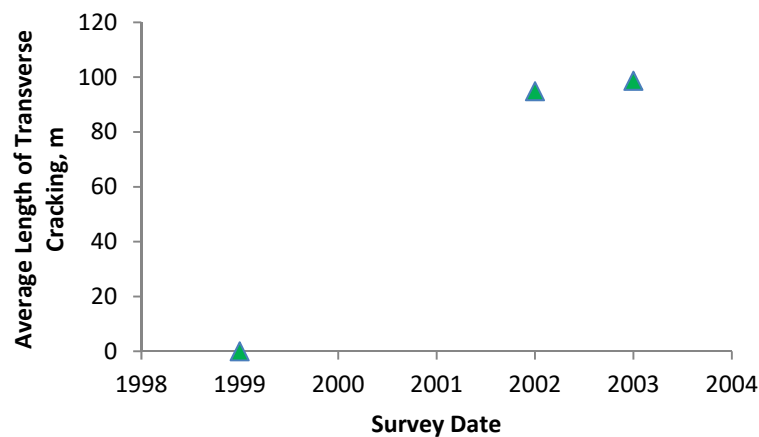
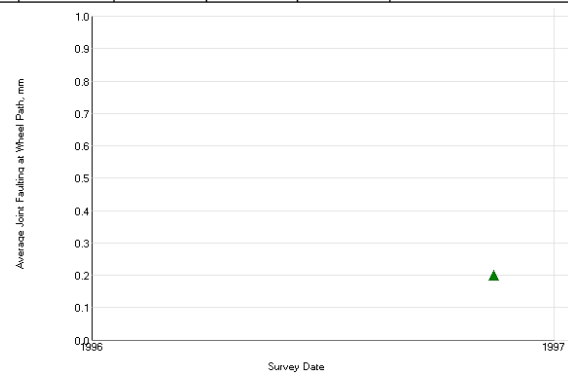
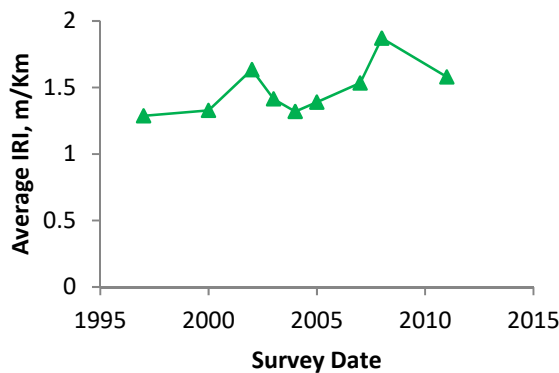
Experiment: SPS-2: Strategic Study of Structural Factors for Rigid Pavements, new/reconstructed JPCC pavements							Section ID: 05-0216					
Section# :			05-0216		Data :		ALL DATA					
REGION		Southern (Austin, TX, USA)		LATITUDE		34.50742		ROUTE/DIRECTION		09/01/1993		
EXPERIMENT		SPS-2		LONGITUDE		-92.69922		NO. OF LANES				
STATE/PROVINCE		Arkansas		ELEVATION				CONSTRUCTED				
COUNTY				MILEPOINT				OUT OF STUDY				
				FUNCTIONAL CLASS								
Maintenance Rehabilitation/Rehabilitation Date							Activity Description					
02/05/1997							Lane-Shoulder Longitudinal Joint Sealing (linear ft.)					
12/12/2002							Transverse Joint Sealing (linear ft.)					
12/12/2002							Lane-Shoulder Longitudinal Joint Sealing (linear ft.)					
Layer Structure							Field Values		Laboratory Results			
LAYER		THICKNESS (mm)	MATERIAL DESCRIPTION			MOISTURE CONTENT (%)	DENSITY (kg/m3)	SUBGRADE P1	COMPRESS STR (kpa)	AIR VOIDS(%)	AC CONTENT (%)	MODULUS Mr.
NUMBER	TYPE											
1	SS		Coarse-Grained Soil: Clayey Sand with Gravel			8	16.40					
2	EF	2	Woven Geotextile			8	10.40					
3	GB	152	Crushed Stone									
4	PC	279	Portland Cement Concrete (JPCP)					71032	71032			
Distress Monitoring							Cross Profile		Monitored Traffic Data (Estimates)			
DISTRESS DATE	SURVEY METHOD	FATIGUE CRACKS (m2)	LOW TEMP. CRACKS (m)	LONG CRACKS (m)	POTHOLES/ PATCH (m2)	SURVEY DATE	RUT (mm) L/R	TRAFFIC YEAR	AADT (#)	TRUCKS (%)	CALCULATED ESALS	
											KESALS	
								1996	23000	3660	1969	
								1998	29000	6530	8882	



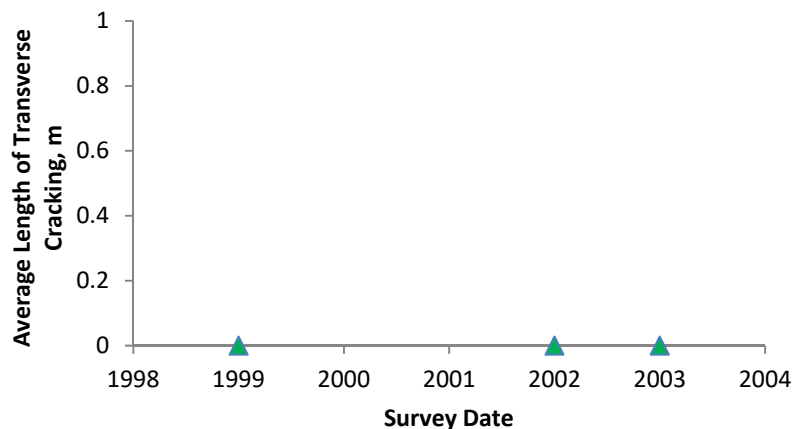
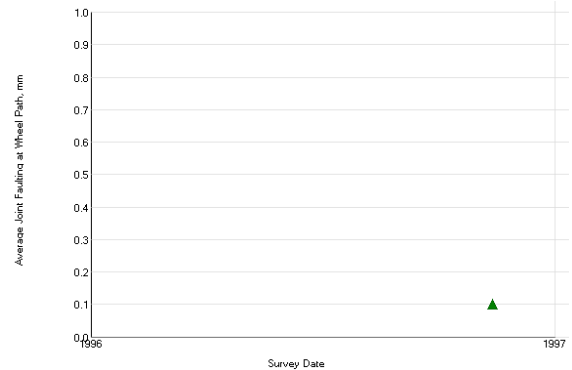
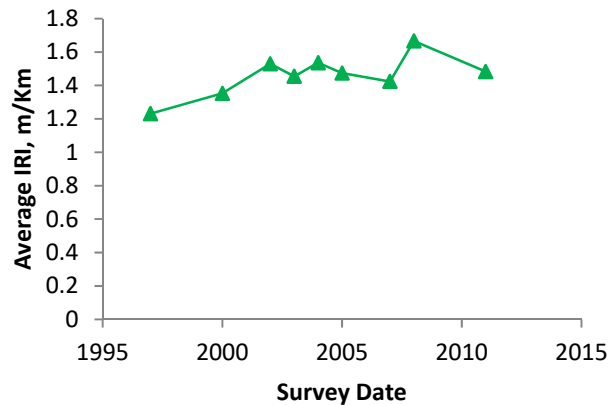
Experiment: SPS-2: Strategic Study of Structural Factors for Rigid Pavements, new/reconstructed JPCC pavements						Section ID: 05-0217						
Section# : 05-0217			Data : ALL DATA									
REGION		Southern (Austin, TX, USA)		LATITUDE		34.51267		ROUTE/DIRECTION				
EXPERIMENT		SPS-2		LONGITUDE		-92.69433		NO. OF LANES				
STATE/PROVINCE		Arkansas		ELEVATION				CONSTRUCTED				
COUNTY				MILEPOINT				OUT OF STUDY				
				FUNCTIONAL CLASS				09/01/1993				
Maintenance Rehabilitation/Rehabilitation Date						Activity Description						
02/05/1997						Lane-Shoulder Longitudinal Joint Sealing (linear ft.)						
12/03/2002						Crack Sealing (linear ft.)						
12/03/2002						Partial depth patching of PCC pavements at joints (sq. yards)						
06/15/2006						Partial depth patching of PCC pavements at joints (sq. yards)						
Layer Structure				Field Values			Laboratory Results					
LAYER		THICKNESS	MATERIAL		MOISTURE	DENSITY	SUBGRADE	COMPRESS	AIR	AC	MODULUS	
NUMBER	TYPE	(mm)	DESCRIPTION		CONTENT	(kg/m3)	P1	STR	VOIDS(%)	CONTENT	Mr.	
1	SS	3073	Coarse-Grained Soil: Poorly Graded Gravel with Silt and Sand		5	13.30						
2	EF	2	Woven Geotextile									
3	GB	101	Other									
4	TB	160	Lean Concrete				39355	39355				
5	PC	210	Portland Cement Concrete (JPCC)				39176	39176				
Distress Monitoring						Cross Profile		Monitored Traffic Data (Estimates)				
DISTRESS	SURVEY	FATIGUE	LOW TEMP.	LONG	POTHOLE	SURVEY	RUT (mm)	TRAFFIC	AADT	TRUCKS	CALCULATED ESALS	
DATE	METHOD	CRACKS	CRACKS	CRACKS	/PATCH	DATE	L/R	YEAR	(#)	(%)	KESALS	
		(m2)	(m)	(m)	(m2)							
								1996	23000	3660	1969	
								1998	29000	6530	8882	



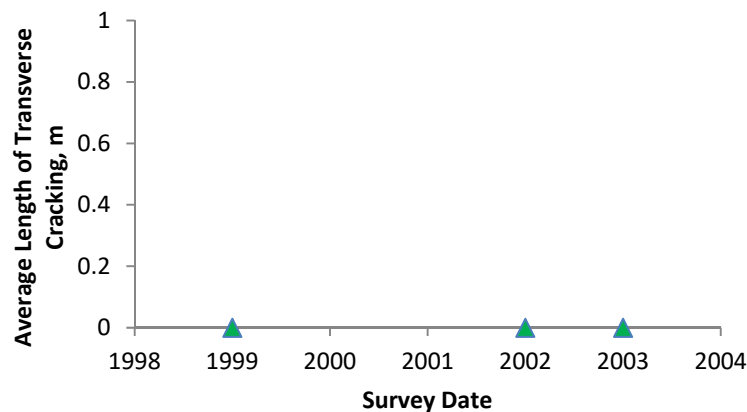
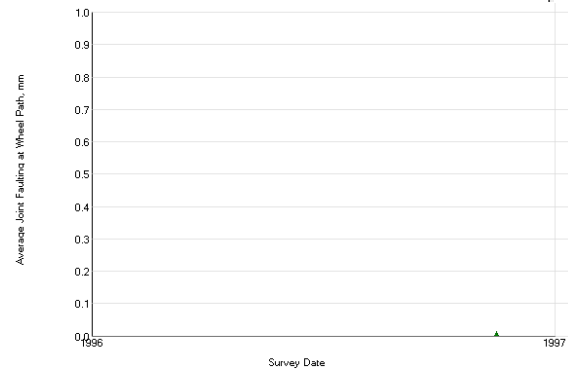
Experiment: SPS-2: Strategic Study of Structural Factors for Rigid Pavements, new/reconstructed JPCC pavements						Section ID: 05-0218					
Section# : 05-0218			Data : ALL DATA								
REGION		Southern (Austin, TX, USA)		LATITUDE		34.51594		ROUTE/DIRECTION NO. OF LANES CONSTRUCTED OUT OF STUDY 09/01/1993			
EXPERIMENT		SPS-2		LONGITUDE		-92.69125					
STATE/PROVINCE		Arkansas		ELEVATION							
COUNTY				MILEPOINT							
				FUNCTIONAL CLASS							
Maintenance Rehabilitation/Rehabilitation Date						Activity Description					
02/05/1997						Lane-Shoulder Longitudinal Joint Sealing (linear ft.)					
12/03/2002						Crack Sealing (linear ft.)					
12/03/2002						Transverse Joint Sealing (linear ft.)					
06/15/2006						Partial depth patching of PCC pavements at joints (sq. yards)					
Layer Structure				Field Values		Laboratory Results					
LAYER		THICKNESS (mm)	MATERIAL DESCRIPTION		MOISTURE CONTENT (%)	DENSITY (kg/m3)	SUBGRADE P 1	COMPRESS STR (kpa)	AIR VOIDS(%)	AC CONTENT (%)	MODULUS Mr.
NUMBER	TYPE										
1	SS	3200	Coarse-Grained Soil: Clayey Gravel with Sand		8	14.10					
2	EF	2	Woven Geotextile								
3	GB	101	Other								
4	TB	162	Lean Concrete				52825	52825			
5	PC	208	Portland Cement Concrete (JPCP)				74930	74930			
Distress Monitoring				Cross Profile		Monitored Traffic Data (Estimates)					
DISTRESS DATE	SURVEY METHOD	FATIGUE CRACKS (m2)	LOW TEMP. CRACKS (m)	LONG CRACKS (m)	POTHOLE/ PATCH (m2)	SURVEY DATE	RUT (mm) L/R	TRAFFIC YEAR	AADT (#)	TRUCKS (%)	CALCULATED ESALS
											KESALS
								1996	23000	3660	1969
								1998	29000	6530	8882



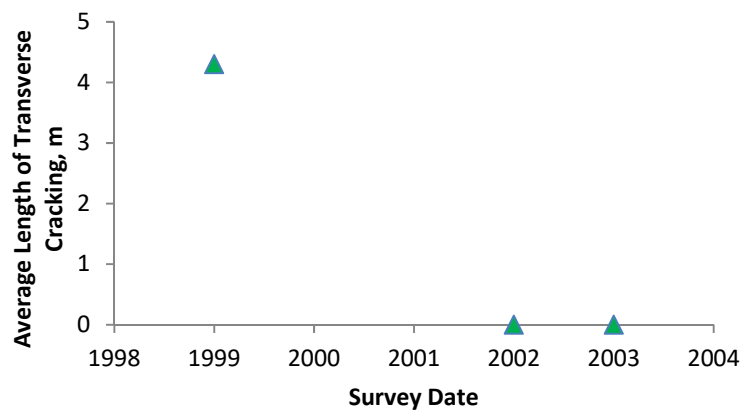
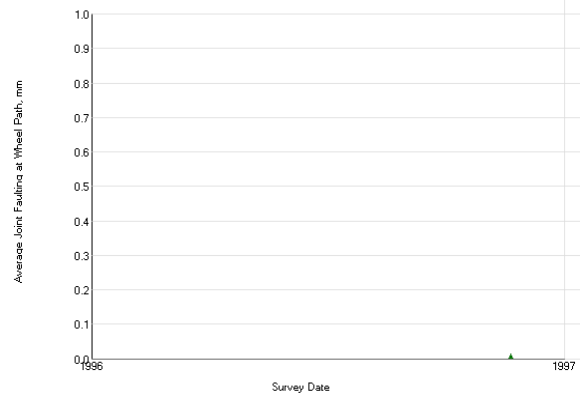
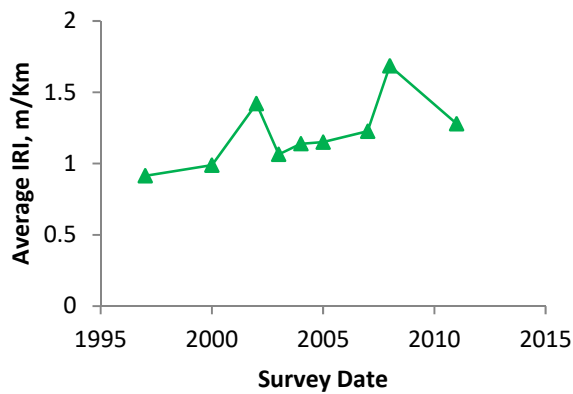
Experiment: SPS-2: Strategic Study of Structural Factors for Rigid Pavements, new/reconstructed JPCC pavements							Section ID: 05-0219					
Section# :			05-0219		Data :		ALL DATA					
REGION		Southern (Austin, TX, USA)		LATITUDE		34.51776		ROUTE/DIRECTION		09/01/1993		
EXPERIMENT		SPS-2		LONGITUDE		-92.68929		NO. OF LANES				
STATE/PROVINCE		Arkansas		ELEVATION				CONSTRUCTED				
COUNTY				MILEPOINT				OUT OF STUDY				
				FUNCTIONAL CLASS								
Maintenance Rehabilitation/Rehabilitation Date							Activity Description					
02/05/1997							Lane-Shoulder Longitudinal Joint Sealing (linear ft.)					
Layer Structure							Field Values		Laboratory Results			
LAYER		THICKNESS	MATERIAL			MOISTURE	DENSITY	SUBGRADE	COMPRESS	AIR	AC	MODULUS
NUMBER	TYPE	(mm)	DESCRIPTION			CONTENT (%)	(kg/m3)	P1	STR (kpa)	VOIDS(%)	CONTENT (%)	Mr.
1	SS		Coarse-Grained Soil: Clayey Gravel with Sand			7	17.10					
2	EF	2	Woven Geotextile									
3	GB	101	Other									
4	TB	154	Lean Concrete					52701	52701			
5	PC	281	Portland Cement Concrete (JPCP)					30212	30212			
Distress Monitoring							Cross Profile		Monitored Traffic Data (Estimates)			
DISTRESS DATE	SURVEY METHOD	FATIGUE CRACKS (m2)	LOW TEMP. CRACKS (m)	LONG CRACKS (m)	POTHOLE/ PATCH (m2)	SURVEY DATE	RUT (mm) L/R	TRAFFIC YEAR	AADT (#)	TRUCKS (%)	CALCULATED ESALS	
								1996	23000	3660	1969	
								1998	29000	6530	8882	



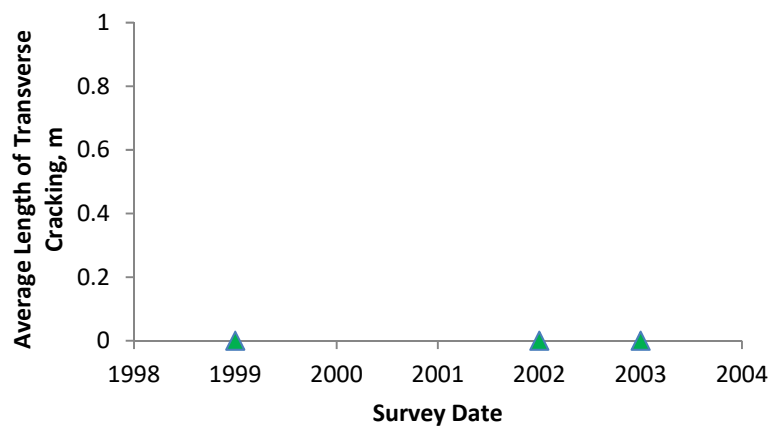
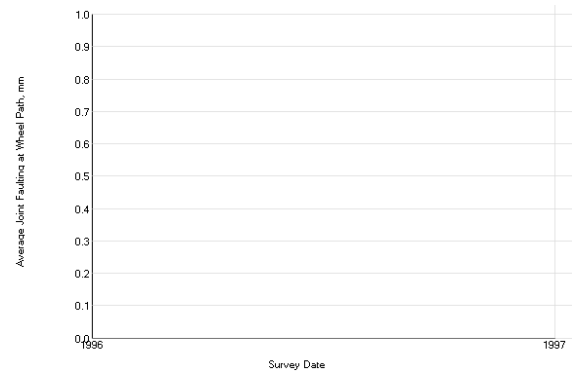
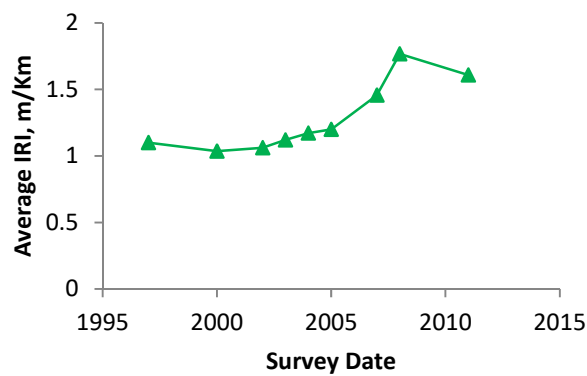
Experiment: SPS-2: Strategic Study of Structural Factors for Rigid Pavements, new/reconstructed JPCC pavements										Section ID: 05-0220		
Section# : 05-0220					Data : ALL DATA							
REGION		Southern (Austin, TX, USA)			LATITUDE		34.51081		ROUTE/DIRECTION		09/01/1993	
EXPERIMENT		SPS-2			LONGITUDE		-92.69624		NO. OF LANES			
STATE/PROVINCE		Arkansas			ELEVATION				CONSTRUCTED			
COUNTY					MILEPOINT				OUT OF STUDY			
					FUNCTIONAL CLASS							
Maintenance Rehabilitation/Rehabilitation Date							Activity Description					
02/05/1997							Lane-Shoulder Longitudinal Joint Sealing (linear ft.)					
12/03/2002							Transverse Joint Sealing (linear ft.)					
Layer Structure							Field Values		Laboratory Results			
LAYER		THICKNESS	MATERIAL			MOISTURE	DENSITY	SUBGRADE	COMPRESS	AIR	AC	MODULUS
NUMBER	TYPE	(mm)	DESCRIPTION			CONTENT	(kg/m ³)	P1	STR	VOIDS(%)	CONTENT	Mr.
1	SS		Coarse-Grained Soil: Poorly Graded Gravel with Silt and Sand			10	17.70					
2	EF	2	Woven Geotextile									
3	GB	152	Other									
4	TB	177	Lean Concrete					25409	25409			
5	PC	271	Portland Cement Concrete (JPCP)					69802	69802			
Distress Monitoring						Cross Profile		Monitored Traffic Data (Estimates)				
DISTRESS DATE	SURVEY METHOD	FATIGUE CRACKS (m2)	LOW TEMP. CRACKS (m)	LONG CRACKS (m)	POTHoles/PATCH (m2)	SURVEY DATE	RUT (mm) L/R	TRAFFIC YEAR	AADT (#)	TRUCKS (%)	CALCULATED ESALS	
								1996	23000	3660	1969	
								1998	29000	6530	8882	



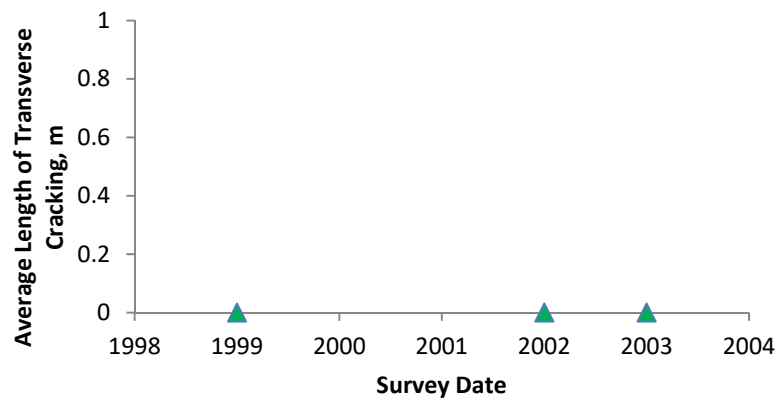
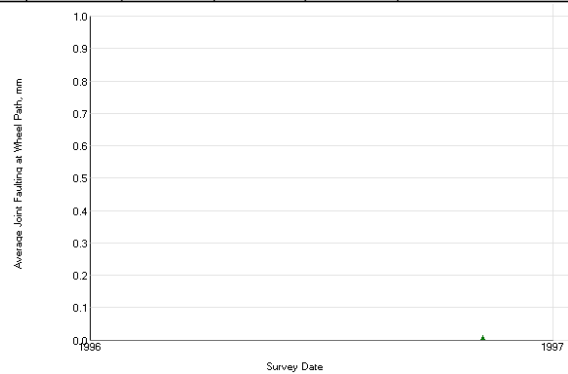
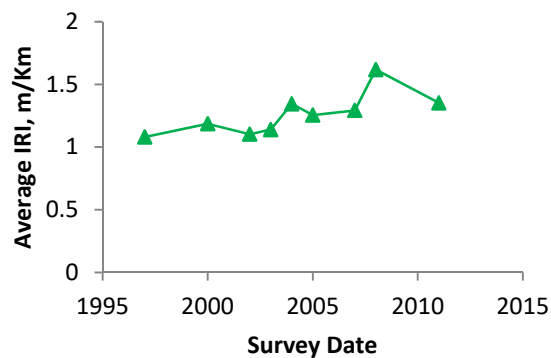
Experiment: SPS-2: Strategic Study of Structural Factors for Rigid Pavements, new/reconstructed JPCC pavements							Section ID: 05-0221					
Section# :			05-0221		Data :		ALL DATA					
REGION		Southern (Austin, TX, USA)		LATITUDE		34.50050		ROUTE/DIRECTION NO. OF LANES CONSTRUCTED OUT OF STUDY 09/01/1993				
EXPERIMENT		SPS-2		LONGITUDE		-92.70532						
STATE/PROVINCE		Arkansas		ELEVATION								
COUNTY				MILEPOINT								
				FUNCTIONAL CLASS								
Maintenance Rehabilitation/Rehabilitation Date							Activity Description					
02/05/1997							Lane-Shoulder Longitudinal Joint Sealing (linear ft.)					
12/12/2002							Transverse Joint Sealing (linear ft.)					
12/12/2002							Lane-Shoulder Longitudinal Joint Sealing (linear ft.)					
Layer Structure							Field Values		Laboratory Results			
LAYER		THICKNESS (mm)	MATERIAL DESCRIPTION		MOISTURE CONTENT (%)	DENSITY (kg/m3)	SUBGRADE P1	COMPRESS STR (kpa)	AIR VOIDS(%)	AC CONTENT (%)	MODULUS Mr.	
NUMBER	TYPE											
1	SS	2133	Coarse-Grained Soil: Clayey Sand with Gravel		10	16.00						
2	EF	2	Woven Geotextile									
3	GB	104	Crushed Stone									
4	TB	83	Open Graded, Hot Laid, Central Plant Mix									
4	TB	109	Open Graded, Hot Laid, Central Plant Mix									
5	PC	210	Portland Cement Concrete (JPCP)				41961	41961				
Distress Monitoring							Cross Profile		Monitored Traffic Data (Estimates)			
DISTRESS DATE	SURVEY METHOD	FATIGUE CRACKS (m2)	LOW TEMP. CRACKS (m)	LONG CRACKS (m)	POTHoles/ PATCH (m2)	SURVEY DATE	RUT (mm) L/R	TRAFFIC YEAR	AADT (#)	TRUCKS (%)	CALCULATED ESALS	
											KESALS	
								1996	23000	3660	1969	
								1998	29000	6530	8882	



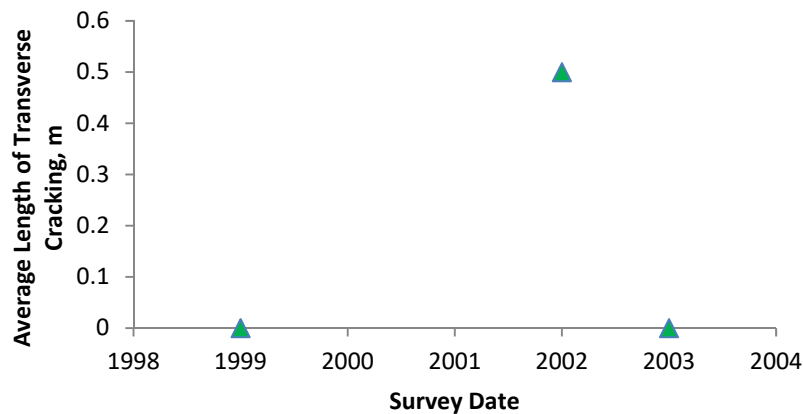
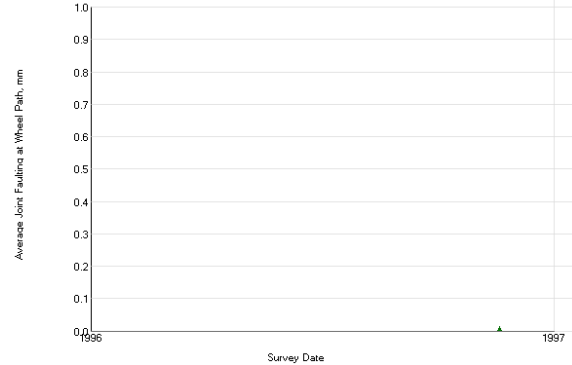
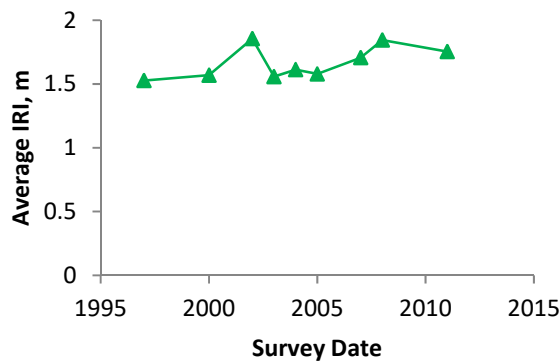
Experiment: SPS-2: Strategic Study of Structural Factors for Rigid Pavements, new/reconstructed JPCP pavements						Section ID: 05-0222						
Section# :			05-0222			Data :			ALL DATA			
REGION		Southern (Austin, TX, USA)		LATITUDE		34.52075		ROUTE/DIRECTION		09/01/1993		
EXPERIMENT		SPS-2		LONGITUDE		-92.68654		NO. OF LANES				
STATE/PROVINCE		Arkansas		ELEVATION				CONSTRUCTED				
COUNTY				MILEPOINT				OUT OF STUDY				
				FUNCTIONAL CLASS								
Maintenance Rehabilitation/Rehabilitation Date						Activity Description						
02/05/1997						Lane-Shoulder Longitudinal Joint Sealing (linear ft.)						
Layer Structure						Field Values		Laboratory Results				
LAYER		THICKNESS	MATERIAL DESCRIPTION			MOISTURE CONTENT (%)	DENSITY (kg/m3)	SUBGRADE P1	COMPRESS STR (kpa)	AIR VOIDS(%)	AC CONTENT (%)	MODULUS Mr.
NUMBER	TYPE	(mm)										
1	SS		Fine-Grained Soils: Fat Clay with Sand			8	14.00					
2	EF	2	Woven Geotextile									
3	GB	279	Crushed Stone									
4	TB	58	Open Graded, Hot Laid, Central Plant Mix									
5	PC	210	Portland Cement Concrete (JPCP)					73672	73672			
Distress Monitoring						Cross Profile		Monitored Traffic Data (Estimates)				
DISTRESS DATE	SURVEY METHOD	FATIGUE CRACKS (m2)	LOW TEMP. CRACKS (m)	LONG CRACKS (m)	POTHoles/PATCH (m2)	SURVEY DATE	RUT (mm) L/R	TRAFFIC YEAR	AADT (#)	TRUCKS (%)	CALCULATED ESALS	
											KESALS	
								1996	23000	3660	1969	
								1998	29000	6530	8882	



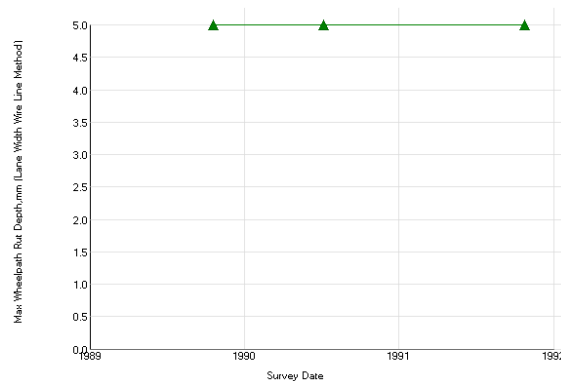
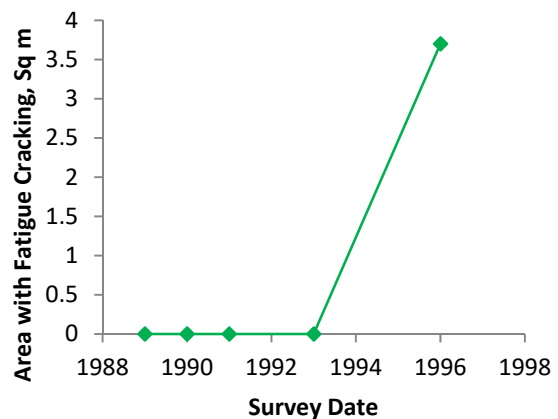
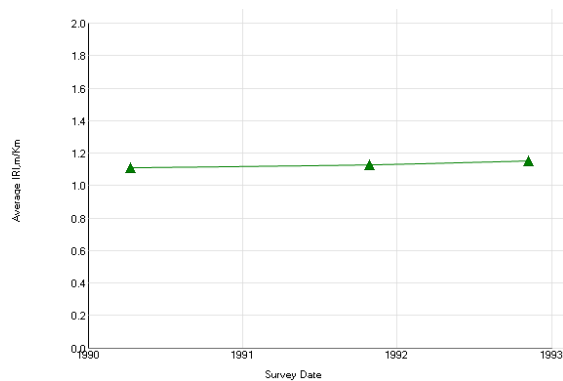
Experiment: SPS-2: Strategic Study of Structural Factors for Rigid Pavements, new/reconstructed JPCC pavements							Section ID: 05-0223				
Section# :			05-0223		Data :		ALL DATA				
REGION		Southern (Austin, TX, USA)		LATITUDE		34.52699		ROUTE/DIRECTION NO. OF LANES CONSTRUCTED OUT OF STUDY 09/01/1993			
EXPERIMENT		SPS-2		LONGITUDE		-92.68134					
STATE/PROVINCE		Arkansas		ELEVATION							
COUNTY				MILEPOINT							
				FUNCTIONAL CLASS							
Maintenance Rehabilitation/Rehabilitation Date							Activity Description				
02/05/1997							Lane-Shoulder Longitudinal Joint Sealing (linear ft.)				
Layer Structure					Field Values		Laboratory Results				
LAYER		THICKNESS (mm)	MATERIAL DESCRIPTION		MOISTURE CONTENT (%)	DENSITY (kg/m3)	SUBGRADE P1	COMPRESS STR (kpa)	AIR VOIDS(%)	AC CONTENT (%)	MODULUS Mr.
NUMBER	TYPE										
1	SS		Fine-Grained Soils: Sandy Lean Clay		8	19.30					
2	EF	2	Woven Geotextile								
3	GB	203	Crushed Stone								
4	TB	99	Open Graded, Hot Laid, Central Plant Mix								
5	PC	276	Portland Cement Concrete (JPCP)				38396	38396			
Distress Monitoring					Cross Profile		Monitored Traffic Data (Estimates)				
DISTRESS DATE	SURVEY METHOD	FATIGUE CRACKS (m2)	LOW TEMP. CRACKS (m)	LONG CRACKS (m)	POTHOLES/ PATCH (m2)	SURVEY DATE	RUT (mm) L/R	TRAFFIC YEAR	AADT (#)	TRUCKS (%)	CALCULATED ESALS
											KESALS
								1996	23000	3660	1969
								1998	29000	6530	8882



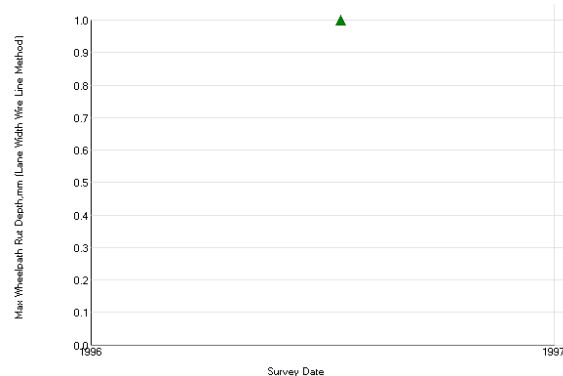
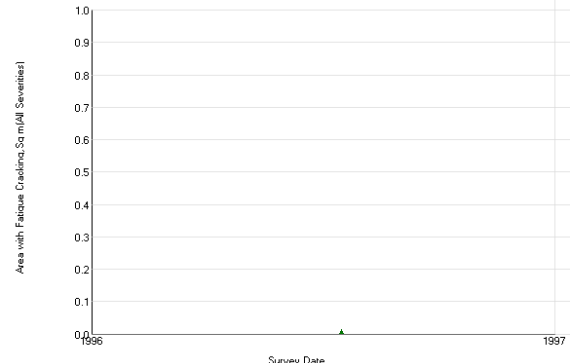
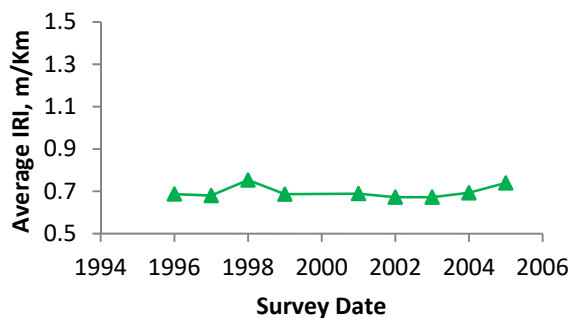
Experiment: SPS-2: Strategic Study of Structural Factors for Rigid Pavements, new/reconstructed JPCC pavements						Section ID: 05-0224						
Section# : 05-0224			Data : ALL DATA									
REGION		Southern (Austin, TX, USA)		LATITUDE		34.50928		ROUTE/DIRECTION				
EXPERIMENT		SPS-2		LONGITUDE		-92.69765		NO. OF LANES				
STATE/PROVINCE		Arkansas		ELEVATION				CONSTRUCTED				
COUNTY				MILEPOINT				OUT OF STUDY				
				FUNCTIONAL CLASS				09/01/1993				
Maintenance Rehabilitation/Rehabilitation Date						Activity Description						
06/15/1996						Partial depth patching of PCC pavements at joints (sq. yards)						
02/05/1997						Lane-Shoulder Longitudinal Joint Sealing (linear ft.)						
06/15/2001						Partial depth patching of PCC pavements at joints (sq. yards)						
12/03/2002						Transverse Joint Sealing (linear ft.)						
Layer Structure						Field Values		Laboratory Results				
LAYER		THICKNESS (mm)	MATERIAL DESCRIPTION			MOISTURE CONTENT (%)	DENSITY (kg/m ³)	SUBGRADE P1	COMPRESS STR (kpa)	AIR VOIDS(%)	AC CONTENT (%)	MODULUS Mr.
NUMBER	TYPE											
1	SS		Coarse-Grained Soil: Clayey Sand with Gravel			11	18.70					128
2	EF	2	Woven Geotextile									
3	GB	220	Soil-Aggregate Mixture (Predominantly Coarse-Grained)									
4	TB	63	Open Graded, Hot Laid, Central Plant Mix									
5	PC	276	Portland Cement Concrete (JPCP)					77430	77430			
Distress Monitoring						Cross Profile		Monitored Traffic Data (Estimates)				
DISTRESS DATE	SURVEY METHOD	FATIGUE CRACKS (m2)	LOW TEMP. CRACKS (m)	LONG CRACKS (m)	POTHOLE/ PATCH (m2)	SURVEY DATE	RUT (mm) L/R	TRAFFIC YEAR	AADT (#)	TRUCKS (%)	CALCULATED ESALS	
											KESALS	
								1996	23000	3660	1969	
								1998	29000	6530	8882	



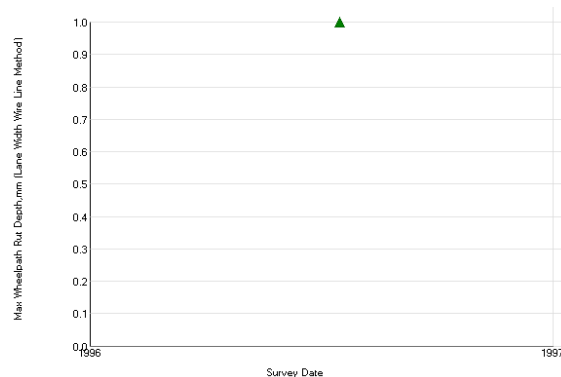
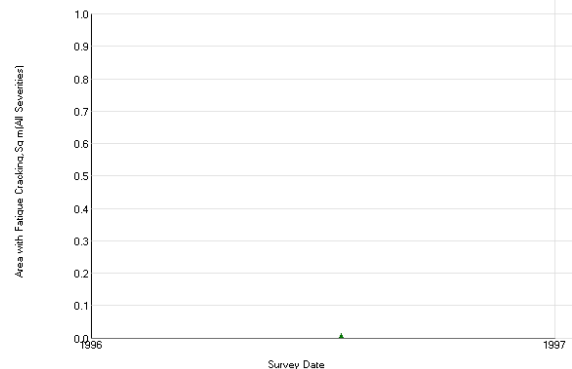
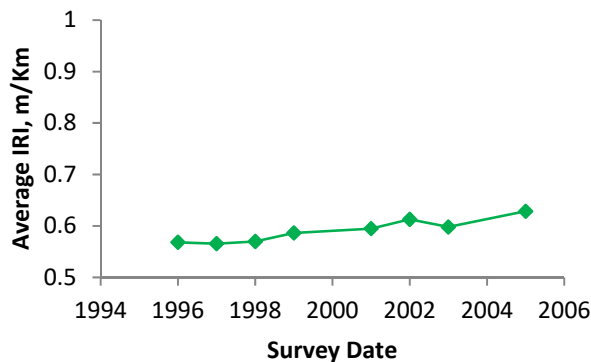
Experiment: GPS-1: Asphalt Concrete on Un-bound Granular Base						Section ID: 08-1057					
Section# :			08-1057			Data : ALL DATA					
REGION		Western (Reno, NV, USA)		LATITUDE		39.06638		ROUTE/DIRECTION		State	
EXPERIMENT		GPS-1		LONGITUDE		-108.45953		NO. OF LANES		2	
STATE/PROVINCE		Colorado		ELEVATION		4586		CONSTRUCTED		07/27/1988	
COUNTY		MESA		MILEPOINT		161		OUT OF STUDY		03/01/1997	
				FUNCTIONAL CLASS		Urban Other Principal Arterial					
Maintenance Rehabilitation/Rehabilitation Date						Activity Description					
08/13/1993						Aggregate Seal Coat (sq. yards)					
Layer Structure						Field Values		Laboratory Results			
LAYER		THICKNESS (mm)	MATERIAL DESCRIPTION	MOISTURE CONTENT (%)	DENSITY (kg/m3)	SUBGRADE P1	COMPRESS STR (kpa)	AIR VOIDS(%)	AC CONTENT (%)	MODULUS Mr.	
NUMBER	TYPE										
1	SS		Fine-Grained Soils: Lean Inorganic Clay	21	22.00					41	
2	EF	2	Other	3	7.50						
3	GS	347	Soil-Aggregate Mixture (Predominantly Coarse-Grained)	3	3.75					207	
4	EF	2	Other					4	5		
5	GB	96	Crushed Gravel								
6	AC	99	Hot Mixed, Hot Laid AC, Dense Graded								
7	AC	12	Chip Seal								
Distress Monitoring						Cross Profile		Monitored Traffic Data (Estimates)			
DISTRESS DATE	SURVEY METHOD	FATIGUE CRACKS (m2)	LOW TEMP. CRACKS (m)	LONG CRACKS (m)	POTHoles/ PATCH (m2)	SURVEY DATE	RUT (mm) L/R	TRAFFIC YEAR	AADT (#)	TRUCKS (%)	CALCULATED ESALS
											KESALS
10/19/1989	AUTO			12	0.00			1990	8800	240	49
07/07/1990	AUTO		1	118	0.00			1991	8400	230	88
10/24/1991	AUTO		3	100	0.00			1992	8500	250	87
11/04/1993	AUTO		8		0.00			1994	10600	245	41
07/18/1994	MANUAL		12		0.00			1996	11500	328	57
05/10/1996	AUTO	3	97	19	0.00			1997	12400	400	63
								1998	12800	410	66
								1999	13200	420	69



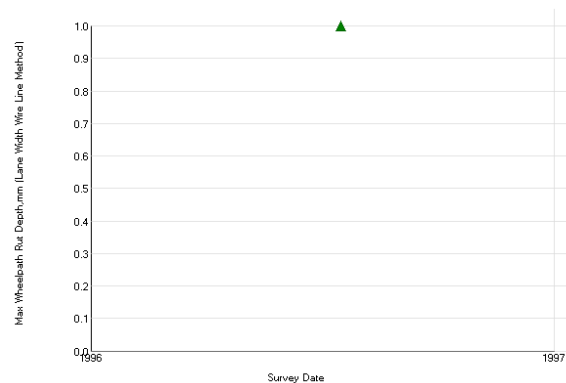
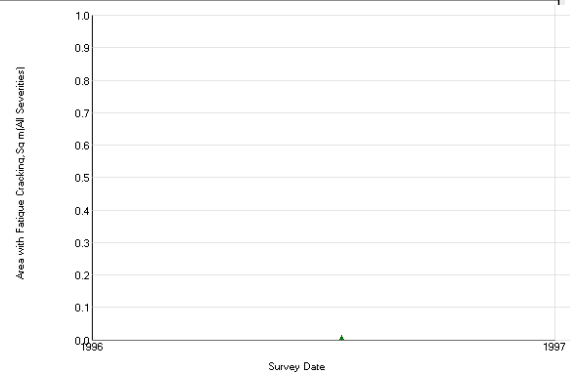
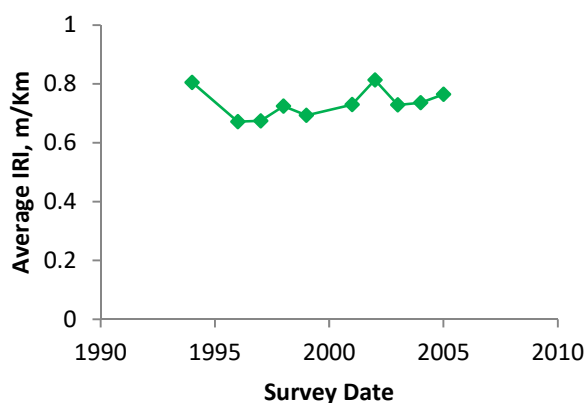
Experiment: SPS-1: Strategic Study of Structural Factors for Flexible Pavements, new/reconstructed AC pavements						Section ID: 10-0110						
REGION	North Atlantic (Amherst, NY, USA)			LATITUDE	38.77480	ROUTE/DIRECTION						
EXPERIMENT	SPS-1			LONGITUDE	-75.43859	NO. OF LANES						
STATE/PROVINCE	Delaware			ELEVATION		CONSTRUCTED			01/01/1992			
COUNTY				MILEPOINT		OUT OF STUDY			09/22/1996			
FUNCTIONAL CLASS												
Layer Structure						Field Values		Laboratory Results				
LAYER		THICKNESS (mm)	MATERIAL DESCRIPTION	MOISTURE CONTENT (%)	DENSITY (kg/m3)	SUBGRADE P1	COMPRESS STR (kpa)	AIR VOIDS(%)	AC CONTENT (%)	MODULUS Mr.		
NUMBER	TYPE											
1	SS		Coarse-Grained Soils: Poorly Graded Sand	5	16.00							
2	GS	1168	Soil-Aggregate Mixture (Predominantly Coarse-Grained)	6	16.00							
3	EF	2	Nonwoven Geotextile									
4	TB	91	Open Graded, Hot Laid, Central Plant Mix									
5	TB	104	HMAC									
6	AC	132	Hot Mixed, Hot Laid AC, Dense Graded									
7	AC	50	Hot Mixed, Hot Laid AC, Dense Graded									
8	AC	27	Hot Mixed, Hot Laid AC, Open Graded									
Distress Monitoring						Cross Profile		Monitored Traffic Data (Estimates)				
DISTRESS DATE	SURVEY METHOD	FATIGUE CRACKS (m2)	LOW TEMP. CRACKS (m)	LONG CRACKS (m)	POTHOLES/ PATCH (m2)	SURVEY DATE	RUT (mm) L/R	TRAFFIC YEAR	AADT (#)	TRUCKS (%)	CALCULATED ESALS	
											KESALS	
07/16/1996	MANUAL				0.00							
02/26/1997	MANUAL				0.00							
06/22/1999	AUTO		3		0.00							
10/13/1999	MANUAL				0.00							
11/01/2000	MANUAL				0.00							
08/26/2001	AUTO		1		0.00							
09/19/2001	MANUAL				0.00							
11/19/2002	MANUAL				0.00							
12/14/2002	AUTO				0.00							
06/23/2003	AUTO				0.00							
08/06/2003	MANUAL				0.00							
10/13/2004	MANUAL				0.00							
10/05/2005	MANUAL	56			0.00							



Experiment: SPS-1: Strategic Study of Structural Factors for Flexible Pavements, new/reconstructed AC pavements							Section ID: 10-0111				
REGION		North Atlantic (Amherst, NY, USA)		LATITUDE		38.77870		ROUTE/DIRECTION			
EXPERIMENT		SPS-1		LONGITUDE		-75.43858		NO. OF LANES			
STATE/PROVINCE		Delaware		ELEVATION				CONSTRUCTED		01/01/1992	
COUNTY				MILEPOINT				OUT OF STUDY		09/22/1996	
				FUNCTIONAL CLASS							
Layer Structure					Field Values		Laboratory Results				
LAYER		THICKNESS (mm)	MATERIAL DESCRIPTION		MOISTURE CONTENT (%)	DENSITY (kg/m3)	SUBGRADE P1	COMPRESS STR (kpa)	AIR VOIDS(%)	AC CONTENT (%)	MODULUS Mr.
NUMBER	TYPE										
1	SS		Coarse-Grained Soils: Poorly Graded Sand		6	17.00					
2	GS	1168	Soil-Aggregate Mixture (Predominantly Coarse-Grained)		7	17.00					80
3	EF	2	Nonwoven Geotextile			5.00					
4	TB	99	Open Graded, Hot Laid, Central Plant Mix			2.30					
5	TB	220	HMAC			1.00					
6	AC	63	Hot Mixed, Hot Laid AC, Dense Graded								
7	AC	30	Hot Mixed, Hot Laid AC, Dense Graded								
8	AC	27	Hot Mixed, Hot Laid AC, Open Graded								
Distress Monitoring					Cross Profile		Monitored Traffic Data (Estimates)				
DISTRESS DATE	SURVEY METHOD	FATIGUE CRACKS (m2)	LOW TEMP. CRACKS (m)	LONG CRACKS (m)	POTHoles/ PATCH (m2)	SURVEY DATE	RUT (mm) L/R	TRAFFIC YEAR	AADT (#)	TRUCKS (%)	CALCULATED ESALS
											KESALS
07/16/1996	MANUAL				0.00						
02/26/1997	MANUAL				0.00						
06/22/1999	AUTO				0.00						
10/12/1999	MANUAL				0.00						
11/01/2000	MANUAL				0.00						
08/26/2001	AUTO				0.00						
09/18/2001	MANUAL				0.00						
11/19/2002	MANUAL	45			0.00						
12/14/2002	AUTO				0.00						
06/23/2003	AUTO				0.00						
08/06/2003	MANUAL	45			0.00						
10/13/2004	MANUAL	39			0.00						
10/05/2005	MANUAL	122			0.00						

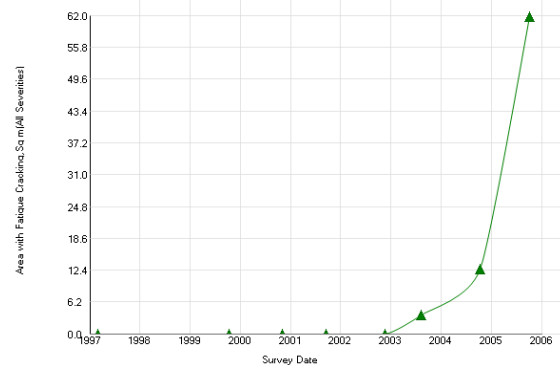
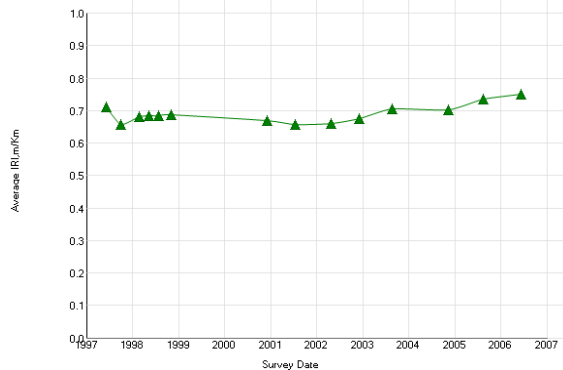


Experiment: SPS-1: Strategic Study of Structural Factors for Flexible Pavements, new/reconstructed AC pavements							Section ID: 10-0112				
REGION	North Atlantic (Amherst, NY, USA)		LATITUDE	38.77673		ROUTE/DIRECTION		01/01/1992 09/22/1996			
EXPERIMENT	SPS-1		LONGITUDE	-75.43865		NO. OF LANES					
STATE/PROVINCE	Delaware		ELEVATION			CONSTRUCTED					
COUNTY			MILEPOINT			OUT OF STUDY					
			FUNCTIONAL CLASS								
Layer Structure					Field Values		Laboratory Results				
LAYER		THICKNESS (mm)	MATERIAL DESCRIPTION	MOISTURE CONTENT (%)	DENSITY (kg/m3)	SUBGRADE P1	COMPRESS STR (kpa)	AIR VOIDS(%)	AC CONTENT (%)	MODULUS Mr.	
NUMBER	TYPE										
1	SS		Coarse-Grained Soils: Poorly Graded Sand	14	43.00					67	
2	GS	1168	Soil-Aggregate Mixture (Predominantly Coarse-Grained)	5	21.00						
3	EF	2	Nonwoven Geotextile	7	21.00						
4	TB	86	Open Graded, Hot Laid, Central Plant Mix								
5	TB	312	HMAC								
6	AC	78	Hot Mixed, Hot Laid AC, Dense Graded								
7	AC	35	Hot Mixed, Hot Laid AC, Dense Graded								
8	AC	30	Hot Mixed, Hot Laid AC, Open Graded								
Distress Monitoring					Cross Profile		Monitored Traffic Data (Estimates)				
DISTRESS DATE	SURVEY METHOD	FATIGUE CRACKS (m2)	LOW TEMP. CRACKS (m)	LONG CRACKS (m)	POTHOLHS/ PATCH (m2)	SURVEY DATE	RUT (mm) L/R	TRAFFIC YEAR	AADT (#)	TRUCKS (%)	CALCULATED ESALS KESALS
07/16/1996	MANUAL				0.00						
02/26/1997	MANUAL				0.00						
06/22/1999	AUTO				0.00						
10/12/1999	MANUAL				0.00						
11/01/2000	MANUAL				0.00						
08/26/2001	AUTO				0.00						
09/18/2001	MANUAL				0.00						
11/19/2002	MANUAL	13			0.00						
12/14/2002	AUTO				0.00						
06/23/2003	AUTO				0.00						
08/06/2003	MANUAL				0.00						
10/13/2004	MANUAL	31			0.00						
10/05/2005	MANUAL	90			0.00						

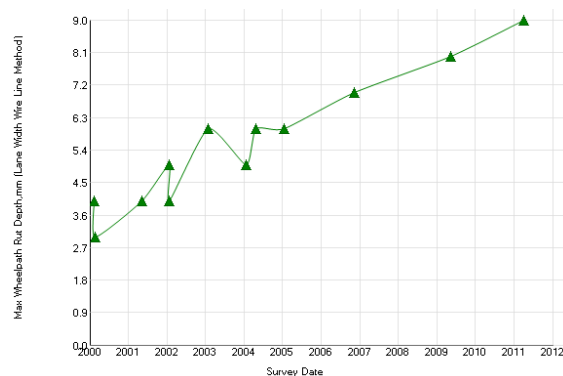
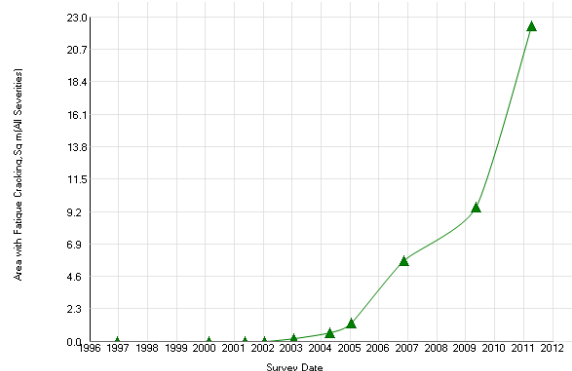
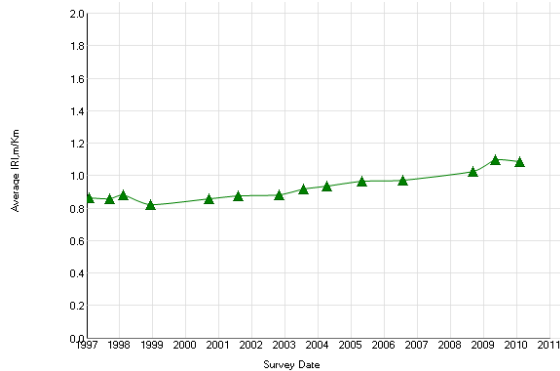


10-0108 Control

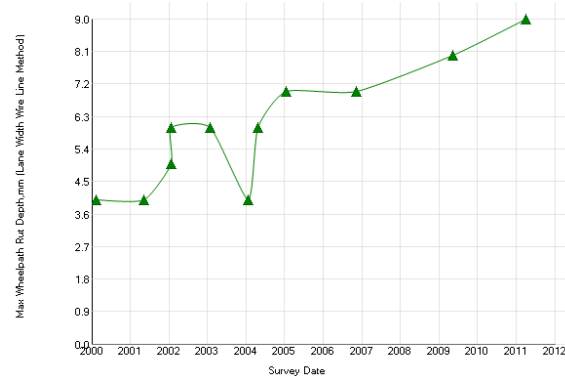
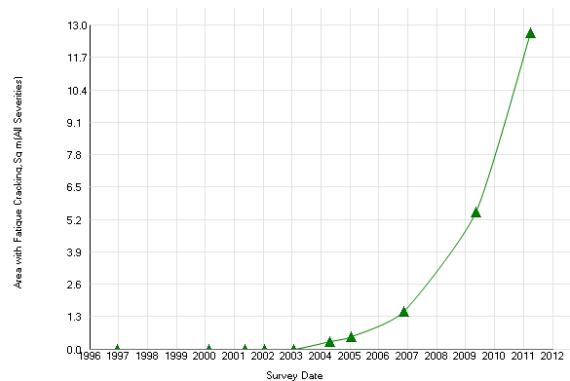
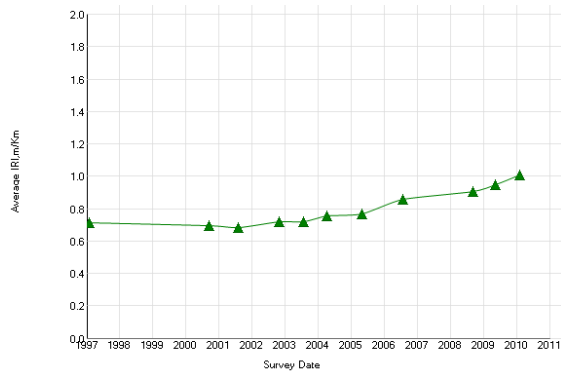
Experiment: SPS-1: Strategic Study of Structural Factors for Flexible Pavements, new/reconstructed AC pavements						Section ID: 10-0108						
Section# :			10-0108			Data :			ALL DATA			
REGION		North Atlantic (Amherst, NY, USA)			LATITUDE		38.77287		ROUTE/DIRECTION			
EXPERIMENT		SPS-1			LONGITUDE		-75.43859		NO. OF LANES			
STATE/PROVINCE		Delaware			ELEVATION				CONSTRUCTED			
COUNTY					MILEPOINT				01/01/1992			
					FUNCTIONAL CLASS				09/22/1996			
Layer Structure						Field Values		Laboratory Results				
LAYER		THICKNESS (mm)	MATERIAL DESCRIPTION			MOISTURE CONTENT (%)	DENSITY (kg/m3)	SUBGRADE P1	COMPRESS STR (kpa)	AIR VOIDS(%)	AC CONTENT (%)	MODULUS Mr.
NUMBER	TYPE											
1	SS		Coarse-Grained Soils: Poorly Graded Sand			14	40.00					57
2	GS	1092	Soil-Aggregate Mixture (Predominantly Fine-Grained)			6	20.00					83
3	GB	185	Crushed Stone			7	20.00					
4	TB	93	Open Graded, Hot Laid, Central Plant Mix			5	12.00					
5	AC	149	Hot Mixed, Hot Laid AC, Dense Graded			6	12.00					
6	AC	27	Hot Mixed, Hot Laid AC, Dense Graded				6.00					
7	AC	30	Hot Mixed, Hot Laid AC, Open Graded				2.30					
Distress Monitoring						Cross Profile		Monitored Traffic Data (Estimates)				
DISTRESS DATE	SURVEY METHOD	FATIGUE CRACKS (m2)	LOW TEMP. CRACKS (m)	LONG CRACKS (m)	POTHOLES/ PATCH (m2)	SURVEY DATE	RUT (mm) L/R	TRAFFIC YEAR	AADT (#)	TRUCKS (%)	CALCULATED ESALS	
											KESALS	
07/16/1996	MANUAL				0.00							
02/26/1997	MANUAL				0.00							
06/22/1999	AUTO				0.00							
10/13/1999	MANUAL				0.00							
11/01/2000	MANUAL				0.00							
08/26/2001	AUTO				0.00							
09/19/2001	MANUAL				0.00							
11/19/2002	MANUAL				0.00							
12/14/2002	AUTO				0.00							
06/23/2003	AUTO				0.00							
08/07/2003	MANUAL	3			0.00							
10/13/2004	MANUAL	12			0.00							
10/05/2005	MANUAL	61			0.00							



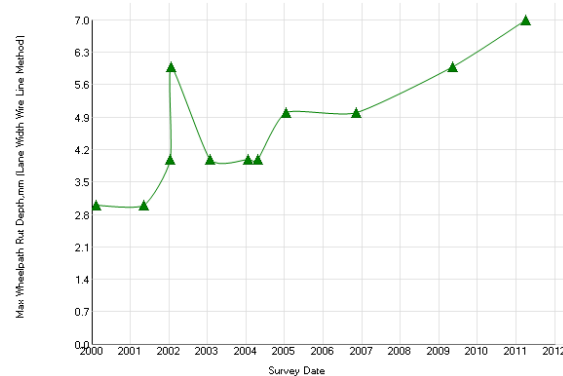
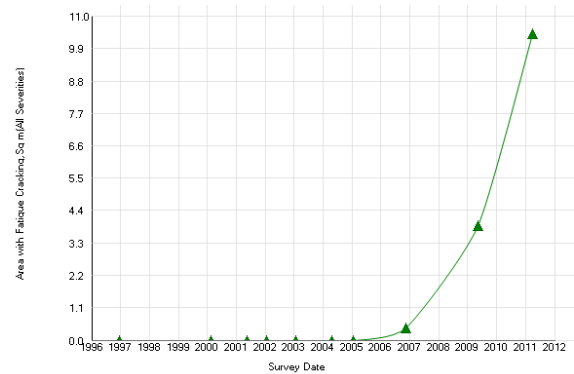
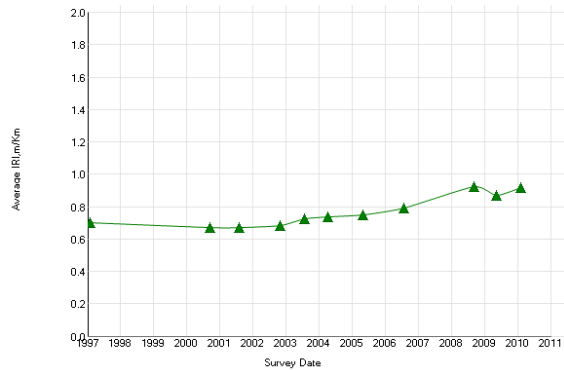
Experiment: SPS-1: Strategic Study of Structural Factors for Flexible Pavements, new/reconstructed AC pavements							Section ID: 12-0110					
Section# :			12-0110		Data :		ALL DATA					
REGION		Southern (Austin, TX, USA)		LATITUDE		26.49243		ROUTE/DIRECTION				
EXPERIMENT		SPS-1		LONGITUDE		-80.66008		NO. OF LANES				
STATE/PROVINCE		Florida		ELEVATION				CONSTRUCTED		01/01/1993		
COUNTY				MILEPOINT				OUT OF STUDY				
				FUNCTIONAL CLASS								
Layer Structure					Field Values		Laboratory Results					
LAYER		THICKNESS (mm)	MATERIAL DESCRIPTION			MOISTURE CONTENT (%)	DENSITY (kg/m3)	SUBGRADE P1	COMPRESS STR (kpa)	AIR VOIDS(%)	AC CONTENT (%)	MODULUS Mr.
NUMBER	TYPE											
1	SS	1950	Coarse-Grained Soil: Silty Sand with Gravel			5	15.63					
2	EF	2	Woven Geotextile			6	15.63					
3	TB	88	Open Graded, Hot Laid, Central Plant Mix			7	15.63					
4	TB	104	HMAC									
5	AC	132	Hot Mixed, Hot Laid AC, Dense Graded									
6	AC	53	Hot Mixed, Hot Laid AC, Dense Graded									
7	AC	12	Hot Mixed, Hot Laid AC, Open Graded									
Distress Monitoring					Cross Profile		Monitored Traffic Data (Estimates)					
DISTRESS DATE	SURVEY METHOD	FATIGUE CRACKS (m2)	LOW TEMP. CRACKS (m)	LONG CRACKS (m)	POTHOLE/ PATCH (m2)	SURVEY DATE	RUT (mm) L/R	TRAFFIC YEAR	AADT (#)	TRUCKS (%)	CALCULATED ESALS	
											KESALS	
12/19/1996	MANUAL				0.00							
02/09/2000	AUTO				0.00							
02/17/2000	MANUAL				0.00							
05/10/2001	MANUAL				0.00							
01/17/2002	MANUAL			2	0.00							
01/21/2002	AUTO				0.00							
01/23/2003	MANUAL			10	0.00							
04/22/2004	MANUAL		1	102	0.00							
01/18/2005	MANUAL	1	2	125	0.00							
11/09/2006	MANUAL	5	16	188	0.00							
05/07/2009	MANUAL	9	22	195	0.00							
04/04/2011	MANUAL	22	51	241	0.00							



Experiment: SPS-1: Strategic Study of Structural Factors for Flexible Pavements, new/reconstructed AC pavements						Section ID: 12-0111						
Section# :			12-0111		Data :			ALL DATA				
REGION		Southern (Austin, TX, USA)			LATITUDE		26.49582		ROUTE/DIRECTION			
EXPERIMENT		SPS-1			LONGITUDE		-80.66270		NO. OF LANES			
STATE/PROVINCE		Florida			ELEVATION				CONSTRUCTED			
COUNTY					MILEPOINT				01/01/1993			
					FUNCTIONAL CLASS							

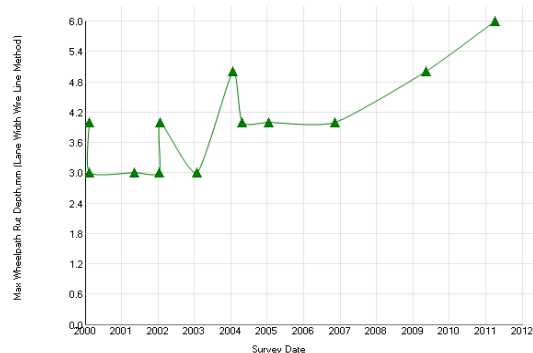
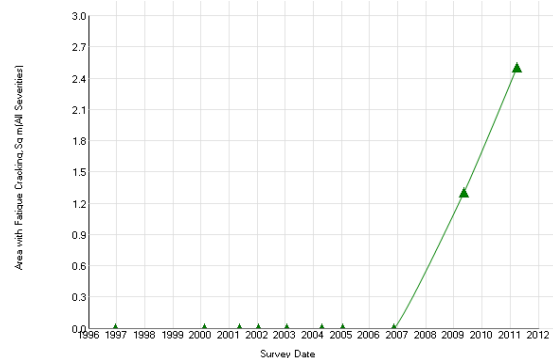
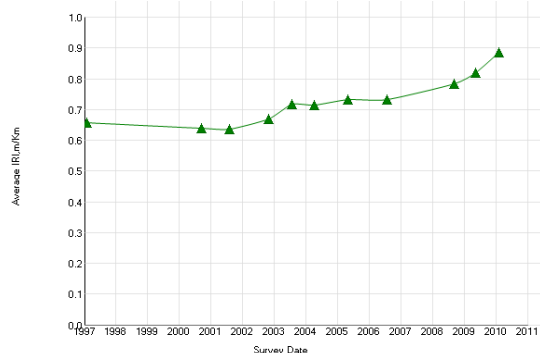


Experiment: SPS-1: Strategic Study of Structural Factors for Flexible Pavements, new/reconstructed AC pavements							Section ID: 12-0112				
Section# :			12-0112		Data :		ALL DATA				
REGION		Southern (Austin, TX, USA)		LATITUDE		26.49952		ROUTE/DIRECTION			01/01/1993
EXPERIMENT		SPS-1		LONGITUDE		-80.66560		NO. OF LANES			
STATE/PROVINCE		Florida		ELEVATION				CONSTRUCTED			
COUNTY				MILEPOINT				OUT OF STUDY			
				FUNCTIONAL CLASS							

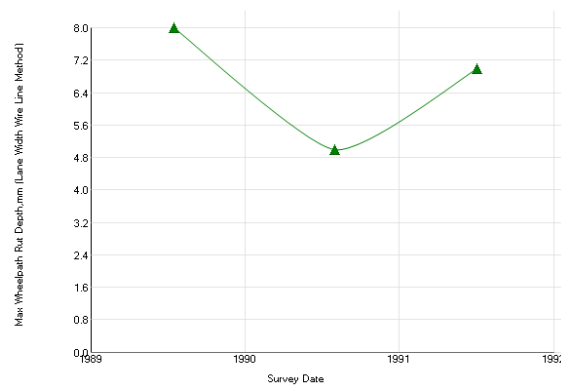
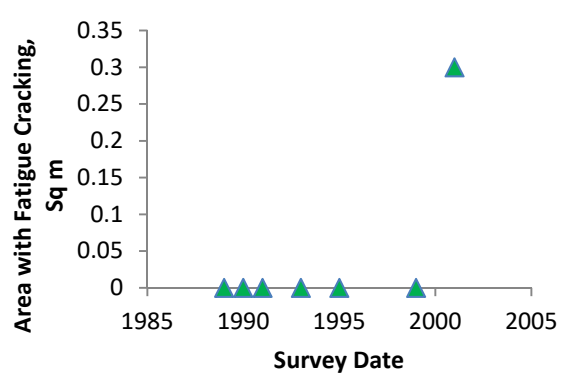


12-0109 Control

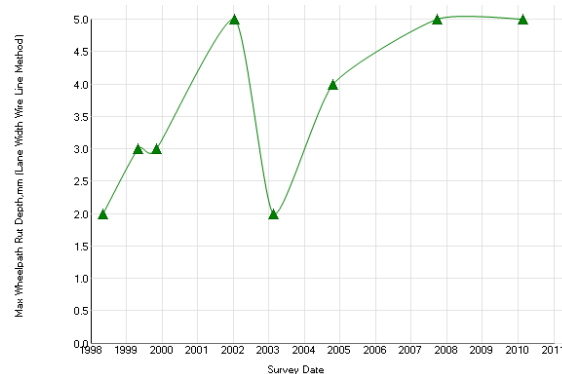
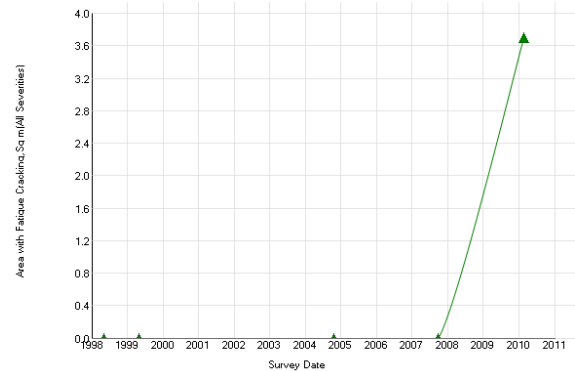
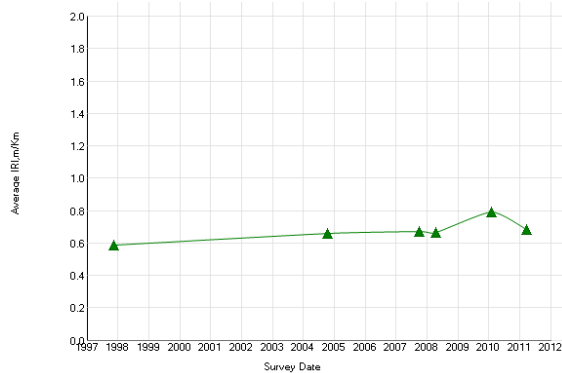
Experiment: SPS-1: Strategic Study of Structural Factors for Flexible Pavements, new/reconstructed AC pavements						Section ID: 12-0109						
Section# :			12-0109		Data : ALL DATA							
REGION		Southern (Austin, TX, USA)		LATITUDE		26.50282		ROUTE/DIRECTION				
EXPERIMENT		SPS-1		LONGITUDE		-80.66810		NO. OF LANES				
STATE/PROVINCE		Florida		ELEVATION				CONSTRUCTED		01/01/1993		
COUNTY				MILEPOINT				OUT OF STUDY				
				FUNCTIONAL CLASS								
Layer Structure						Field Values		Laboratory Results				
LAYER		THICKNESS (mm)	MATERIAL DESCRIPTION			MOISTURE CONTENT (%)	DENSITY (kg/m3)	SUBGRADE P1	COMPRESS STR (kpa)	AIR VOIDS(%)	AC CONTENT (%)	MODULUS Mr.
NUMBER	TYPE											
1	SS	2072	Coarse-Grained Soils: Poorly Graded Sand with Silt and Gravel			5	23.63					
2	GB	304	Crushed Stone			3	12.00					209
3	TB	93	Open Graded, Hot Laid, Central Plant Mix			3	11.63					
4	AC	129	Hot Mixed, Hot Laid AC, Dense Graded									
5	AC	50	Hot Mixed, Hot Laid AC, Dense Graded									
6	AC	12	Hot Mixed, Hot Laid AC, Open Graded									
Distress Monitoring						Cross Profile		Monitored Traffic Data (Estimates)				
DISTRESS DATE	SURVEY METHOD	FATIGUE CRACKS (m2)	LOW TEMP. CRACKS (m)	LONG CRACKS (m)	POTHOLE/ PATCH (m2)	SURVEY DATE	RUT (mm) L/R	TRAFFIC YEAR	AADT (#)	TRUCKS (%)	CALCULATED ESALS	
											KESALS	
12/20/1996	MANUAL				0.00							
02/09/2000	AUTO				0.00							
02/16/2000	MANUAL				0.00							
05/09/2001	MANUAL				0.00							
01/16/2002	MANUAL				0.00							
01/21/2002	AUTO				0.00							
01/22/2003	MANUAL			5	0.00							
04/21/2004	MANUAL			77	0.00							
01/18/2005	MANUAL			91	0.00							
11/08/2006	MANUAL		1	159	0.00							
05/07/2009	MANUAL	1	7	193	0.00							
03/30/2011	MANUAL	2	23	238	0.00							



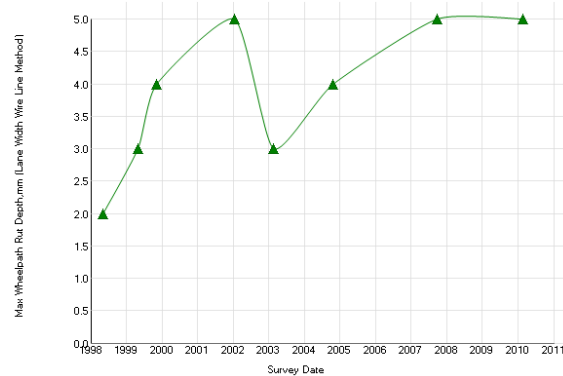
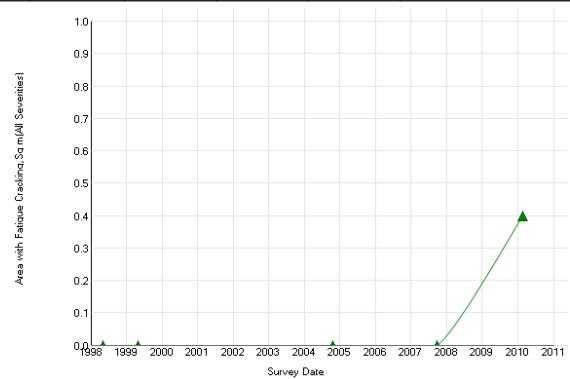
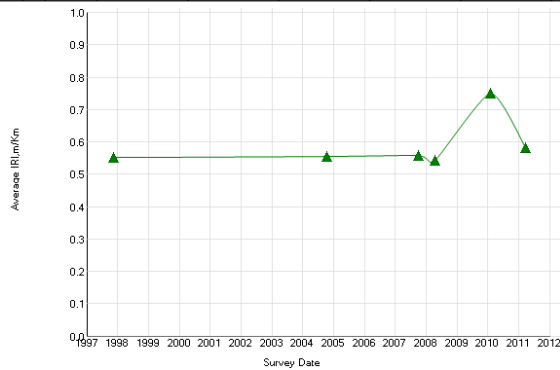
Experiment: GPS-1: Asphalt Concrete on Un-bound Granular Base							Section ID: 16-9032				
REGION		Western (Reno, NV, USA)		LATITUDE		47.63402		ROUTE/DIRECTION		U. S.	
EXPERIMENT		GPS-1		LONGITUDE		-116.86674		NO. OF LANES		1	
STATE/PROVINCE		Idaho		ELEVATION		2602		CONSTRUCTED		09/30/1987	
COUNTY		KOOTENAI		MILEPOINT		424		OUT OF STUDY		08/01/2002	
				FUNCTIONAL CLASS		Rural Principal Arterial - Other					
Maintenance Rehabilitation/Rehabilitation Date							Activity Description				
08/22/1994							Aggregate Seal Coat (sq. yards)				
06/01/2002							Patch Pot Holes - Hand Spread, Compacted with Truck (no. of holes)				
Layer Structure							Field Values		Laboratory Results		
LAYER		THICKNESS (mm)	MATERIAL DESCRIPTION	MOISTURE CONTENT (%)	DENSITY (kg/m3)	SUBGRADE P1	COMPRESS STR (kpa)	AIR VOIDS(%)	AC CONTENT (%)	MODULUS Mr.	
NUMBER	TYPE										
1	SS		Fine-Grained Soils: Sandy Silt	34	31.20					26	
2	EF	2	Woven Geotextile								
3	GB	589	Crushed Gravel								
4	AC	86	Hot Mixed, Hot Laid AC, Dense Graded					3	5		
5	AC	60	Hot Mixed, Hot Laid AC, Dense Graded								
6	AC	5	Chip Seal								
7	AC	10	Chip Seal								
Distress Monitoring							Cross Profile		Monitored Traffic Data (Estimates)		
DISTRESS DATE	SURVEY METHOD	FATIGUE CRACKS (m2)	LOW TEMP. CRACKS (m)	LONG CRACKS (m)	POTHOLES/ PATCH (m2)	SURVEY DATE	RUT (mm) L/R	TRAFFIC YEAR	AADT (#)	TRUCKS (%)	CALCULATED ESALS
											KESALS
07/17/1989	AUTO		8		0.00			1995	7200	395	111
08/02/1990	AUTO		13	2	0.00						
07/04/1991	AUTO		11	9	0.00						
06/30/1993	AUTO		20	17	0.00						
08/26/1994	MANUAL		11		0.00						
05/17/1995	AUTO		11	9	0.00						
07/09/1997	MANUAL		14	9	0.00						
09/22/1998	MANUAL		14		0.00						
09/15/1999	AUTO		18	9	0.00						
08/14/2001	MANUAL		18	32	0.00						
10/01/2001	AUTO		20	17	0.00						
07/11/2002	MANUAL	1	20		0.40						



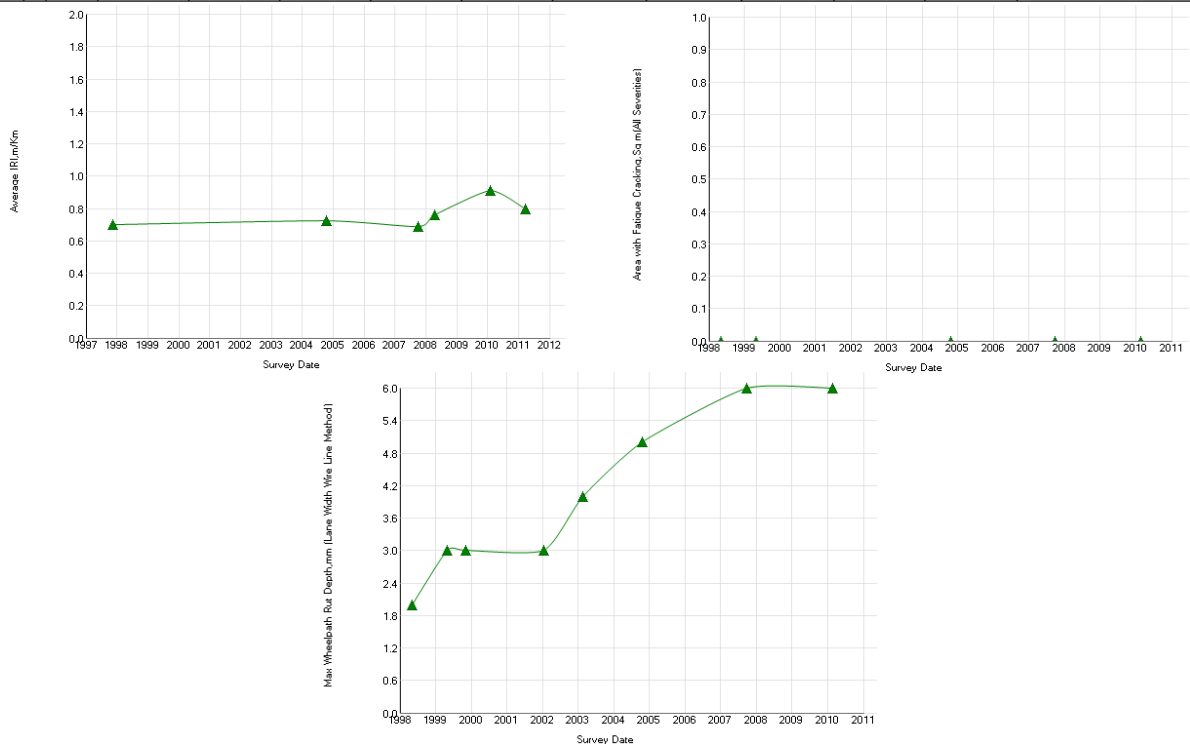
Experiment: SPS-1: Strategic Study of Structural Factors for Flexible Pavements, new/reconstructed AC pavements							Section ID: 22-0122					
Section# : 22-0122			Data : ALL DATA									
REGION		Southern (Austin, TX, USA)		LATITUDE		30.34633		ROUTE/DIRECTION NO. OF LANES CONSTRUCTED OUT OF STUDY 11/18/1992				
EXPERIMENT		SPS-1		LONGITUDE		-93.20016						
STATE/PROVINCE		Louisiana		ELEVATION								
COUNTY				MILEPOINT								
				FUNCTIONAL CLASS								
Layer Structure					Field Values		Laboratory Results					
LAYER		THICKNESS (mm)	MATERIAL DESCRIPTION			MOISTURE CONTENT (%)	DENSITY (kg/m3)	SUBGRADE P1	COMPRESS STR (kpa)	AIR VOIDS(%)	AC CONTENT (%)	MODULUS Mr.
NUMBER	TYPE											
1	SS		Fine-Grained Soils: Lean Inorganic Clay			8	11.70					
2	GS	320	Fine-Grained Soils: Silt with Sand			10	11.70					
3	TS	152	Cement-Treated Soil			14	11.70					
4	EF	2	Woven Geotextile			3	0.00					
5	TB	93	Open Graded, Hot Laid, Central Plant Mix									
6	TB	88	HMAC									
7	AC	78	Hot Mixed, Hot Laid AC, Dense Graded									
8	AC	35	Hot Mixed, Hot Laid AC, Dense Graded									
Distress Monitoring						Cross Profile		Monitored Traffic Data (Estimates)				
DISTRESS DATE	SURVEY METHOD	FATIGUE CRACKS (m2)	LOW TEMP. CRACKS (m)	LONG CRACKS (m)	POTHOLES/ PATCH (m2)	SURVEY DATE	RUT (mm) L/R	TRAFFIC YEAR	AADT (#)	TRUCKS (%)	CALCULATED ESALS	
											KESALS	
05/06/1998	MANUAL				0.00							
04/28/1999	MANUAL				0.00							
11/09/1999	AUTO				0.00							
01/12/2002	AUTO				0.00							
02/13/2003	AUTO				0.00							
10/19/2004	MANUAL				0.00							
09/25/2007	MANUAL			1	0.00							
02/18/2010	MANUAL	3	1	75	0.00							



Experiment: SPS-1: Strategic Study of Structural Factors for Flexible Pavements, new/reconstructed AC pavements							Section ID: 22-0123					
Section# :			22-0123		Data :		ALL DATA					
REGION		Southern (Austin, TX, USA)		LATITUDE		30.34846		ROUTE/DIRECTION				
EXPERIMENT		SPS-1		LONGITUDE		-93.20016		NO. OF LANES				
STATE/PROVINCE		Louisiana		ELEVATION				CONSTRUCTED		11/18/1992		
COUNTY				MILEPOINT				OUT OF STUDY				
				FUNCTIONAL CLASS								
Layer Structure				Field Values			Laboratory Results					
LAYER		THICKNESS (mm)	MATERIAL DESCRIPTION			MOISTURE CONTENT (%)	DENSITY (kg/m3)	SUBGRADE P1	COMPRESS STR (kpa)	AIR VOIDS(%)	AC CONTENT (%)	MODULUS Mr.
NUMBER	TYPE											
1	SS		Fine-Grained Soils: Lean Inorganic Clay			14	18.20					
2	GS	304	Fine-Grained Soils: Silt			15	18.20					
3	TS	152	Cement-Treated Soil			16	18.20					
4	EF	2	Woven Geotextile			3	0.00					
5	TB	106	Open Graded, Hot Laid, Central Plant Mix									
6	TB	185	HMAC									
7	AC	142	Hot Mixed, Hot Laid AC, Dense Graded									
8	AC	30	Hot Mixed, Hot Laid AC, Dense Graded									
Distress Monitoring						Cross Profile		Monitored Traffic Data (Estimates)				
DISTRESS DATE	SURVEY METHOD	FATIGUE CRACKS (m2)	LOW TEMP. CRACKS (m)	LONG CRACKS (m)	POTHOLES/ PATCH (m2)	SURVEY DATE	RUT (mm) L/R	TRAFFIC YEAR	AADT (#)	TRUCKS (%)	CALCULATED ESALS	
											KESALS	
05/06/1998	MANUAL				0.00							
04/28/1999	MANUAL				0.00							
11/09/1999	AUTO				0.00							
01/12/2002	AUTO				0.00							
02/13/2003	AUTO				0.00							
10/19/2004	MANUAL				0.00							
09/25/2007	MANUAL				0.00							
02/18/2010	MANUAL		2	39	0.00							

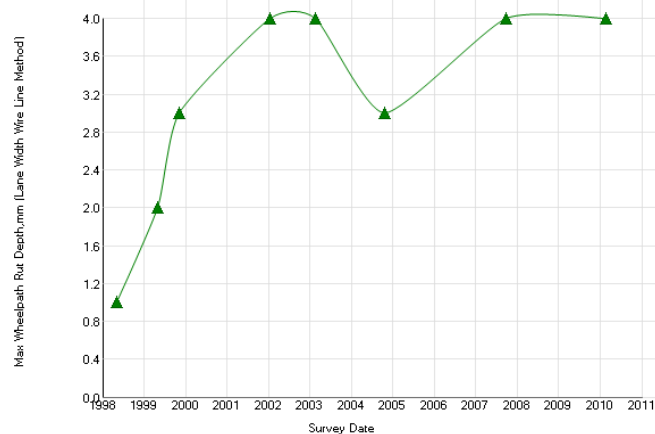
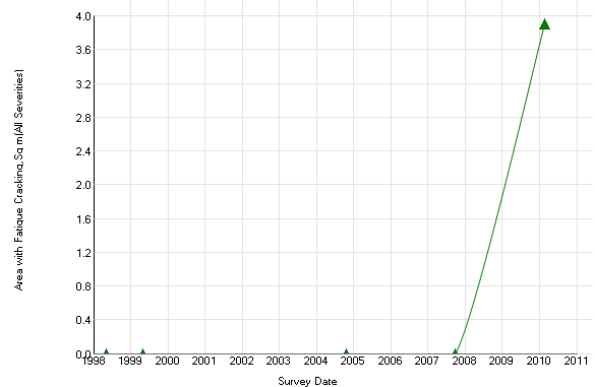
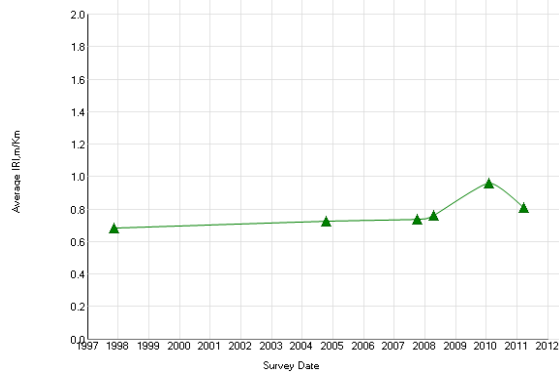


Experiment: SPS-1: Strategic Study of Structural Factors for Flexible Pavements, new/reconstructed AC pavements							Section ID: 22-0124					
Section# :			22-0124		Data :		ALL DATA					
REGION		Southern (Austin, TX, USA)		LATITUDE		30.35244		ROUTE/DIRECTION				
EXPERIMENT		SPS-1		LONGITUDE		-93.20019		NO. OF LANES				
STATE/PROVINCE		Louisiana		ELEVATION				CONSTRUCTED		11/18/1992		
COUNTY				MILEPOINT				OUT OF STUDY				
				FUNCTIONAL CLASS								
Layer Structure						Field Values		Laboratory Results				
LAYER		THICKNESS (mm)	MATERIAL DESCRIPTION			MOISTURE CONTENT (%)	DENSITY (kg/m3)	SUBGRADE P1	COMPRESS STR (kpa)	AIR VOIDS(%)	AC CONTENT (%)	MODULUS Mr.
NUMBER	TYPE											
1	SS		Fine-Grained Soils: Lean Inorganic Clay			9	21.40					89
2	GS	279	Fine-Grained Soils: Silt			15	21.40					58
3	TS	152	Cement-Treated Soil			16	21.40					
4	EF	2	Woven Geotextile			17	21.40					
5	TB	96	Open Graded, Hot Laid, Central Plant Mix			27	21.40					
6	TB	269	HMAC			3	0.00					
7	AC	149	Hot Mixed, Hot Laid AC, Dense Graded			4	0.00					
8	AC	33	Hot Mixed, Hot Laid AC, Dense Graded									
Distress Monitoring						Cross Profile		Monitored Traffic Data (Estimates)				
DISTRESS DATE	SURVEY METHOD	FATIGUE CRACKS (m2)	LOW TEMP. CRACKS (m)	LONG CRACKS (m)	POTHOLES/ PATCH (m2)	SURVEY DATE	RUT (mm) L/R	TRAFFIC YEAR	AADT (#)	TRUCKS (%)	CALCULATED ESALS	
											KESALS	
05/06/1998	MANUAL				0.00							
04/28/1999	MANUAL				0.00							
11/09/1999	AUTO				0.00							
01/12/2002	AUTO				0.00							
02/13/2003	AUTO				0.00							
10/19/2004	MANUAL				0.00							
09/26/2007	MANUAL				0.00							
02/18/2010	MANUAL			55	0.00							



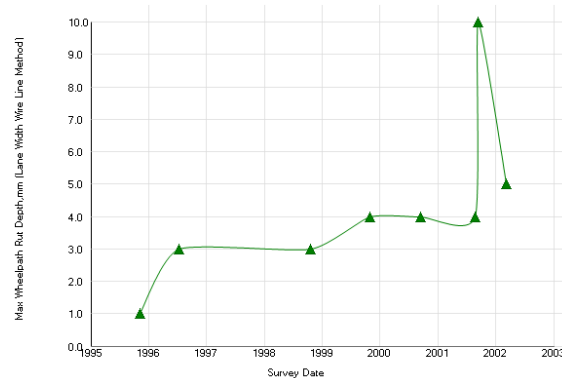
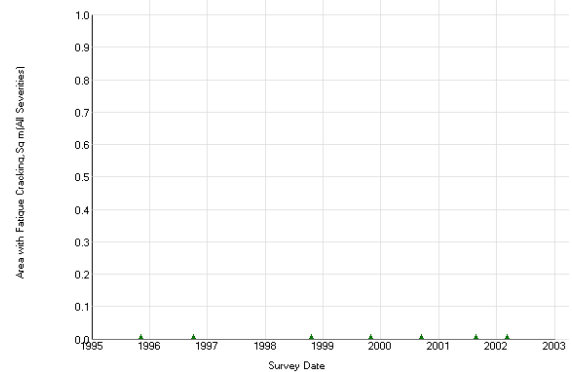
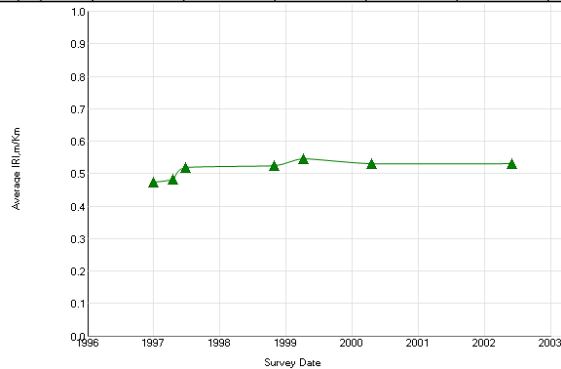
22-0121 Control

Experiment: SPS-1: Strategic Study of Structural Factors for Flexible Pavements, new/reconstructed AC pavements						Section ID: 22-0121					
Section# : 22-0121			Data : ALL DATA								
REGION		Southern (Austin, TX, USA)		LATITUDE		30.34359		ROUTE/DIRECTION			
EXPERIMENT		SPS-1		LONGITUDE		-93.20016		NO. OF LANES			
STATE/PROVINCE		Louisiana		ELEVATION				CONSTRUCTED		11/18/1992	
COUNTY				MILEPOINT				OUT OF STUDY			
				FUNCTIONAL CLASS							

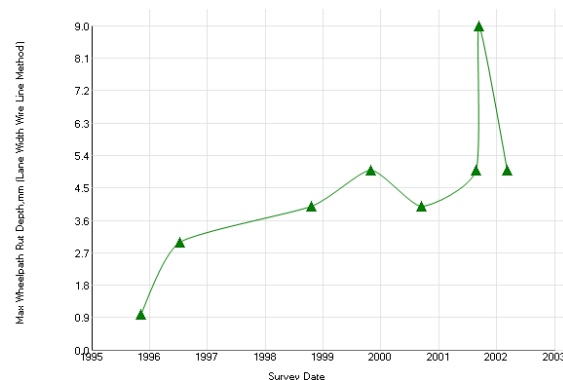
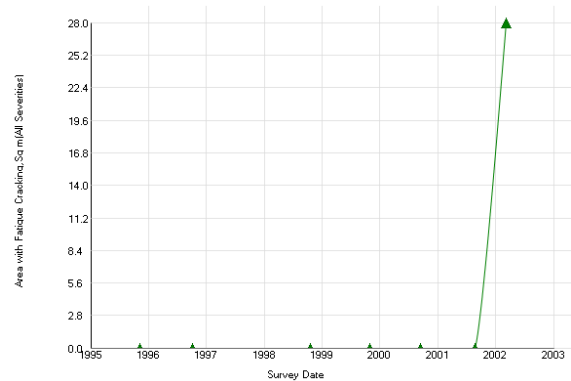
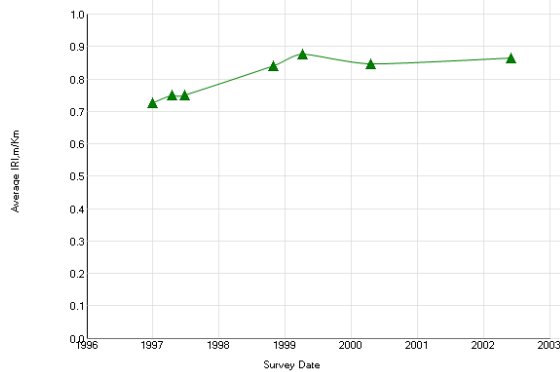


Experiment: SPS-1: Strategic Study of Structural Factors for Flexible Pavements, new/reconstructed AC pavements										Section ID: 26-0122		
Section#: 26-0122				Data: ALL DATA								
REGION		North Central (Champaign, IL, USA)			LATITUDE		42.96768		ROUTE/DIRECTION			
EXPERIMENT		SPS-1			LONGITUDE		-84.51900		NO. OF LANES			
STATE/PROVINCE		Michigan			ELEVATION				CONSTRUCTED			
COUNTY					MILEPOINT				OUT OF STUDY			
					FUNCTIONAL CLASS				01/01/1994			
									10/01/1995			
Layer Structure					Field Values		Laboratory Results					
LAYER		THICKNESS	MATERIAL			MOISTURE	DENSITY	SUBGRADE	COMPRESS	AIR	AC	MODULUS
NUMBER	TYPE	(mm)	DESCRIPTION			CONTENT	(kg/m3)	P1	STR	VOIDS(%)	CONTENT	Mr.
1	SS		Fine-Grained Soils: Sandy Clay			6	12.00					132
2	EF	2	Woven Geotextile			7	12.00					
3	TB	101	Open Graded, Hot Laid, Central Plant Mix			8	12.00					
4	TB	121	HMAC				4.00					
5	AC	50	Hot Mixed, Hot Laid AC, Dense Graded				2.00					
6	AC	43	Hot Mixed, Hot Laid AC, Dense Graded				0.00					
Distress Monitoring						Cross Profile		Monitored Traffic Data (Estimates)				
DISTRESS	SURVEY	FATIGUE	LOW TEMP.	LONG	POTHoles/	SURVEY	RUT (mm)	TRAFFIC	AADT	TRUCKS	CALCULATED ESALS	
DATE	METHOD	CRACKS	CRACKS	CRACKS	PATCH (m2)	DATE	L/R	YEAR	(#)	(%)	KESALS	
		(m2)	(m)	(m)								

Experiment: SPS-1: Strategic Study of Structural Factors for Flexible Pavements, new/reconstructed AC pavements								Section ID: 26-0123				
REGION		North Central (Champaign, IL, USA)		LATITUDE		42.97961		ROUTE/DIRECTION				
EXPERIMENT		SPS-1		LONGITUDE		-84.51906		NO. OF LANES				
STATE/PROVINCE		Michigan		ELEVATION				CONSTRUCTED		01/01/1994		
COUNTY				MILEPOINT				OUT OF STUDY		10/01/2002		
FUNCTIONAL CLASS												
Maintenance Rehabilitation/Rehabilitation Date						Activity Description						
05/01/2006						Crack Sealing (linear ft.)						
Layer Structure						Field Values		Laboratory Results				
LAYER		THICKNESS	MATERIAL DESCRIPTION			MOISTURE CONTENT (%)	DENSITY (kg/m3)	SUBGRADE P1	COMPRESS STR (kpa)	AIR VOIDS(%)	AC CONTENT (%)	MODULUS Mr.
NUMBER	TYPE	(mm)										
1	SS		Fine-Grained Soils: Sandy Clay			5	19.00					121
2	EF	2	Woven Geotextile			6	19.00					
3	TB	88	Open Graded, Hot Laid, Central Plant Mix			8	19.00					
4	TB	226	HMAC				7.00					
5	AC	50	Hot Mixed, Hot Laid AC, Dense Graded				4.00					
6	AC	48	Hot Mixed, Hot Laid AC, Dense Graded				2.00					
7	AC	12	Hot Mixed, Hot Laid AC, Dense Graded				0.00					
7	AC	43	Hot Mixed, Hot Laid AC, Dense Graded									
8	AC	40	Hot Mixed, Hot Laid AC, Dense Graded									
Distress Monitoring						Cross Profile		Monitored Traffic Data (Estimates)				
DISTRESS DATE	SURVEY METHOD	FATIGUE CRACKS (m2)	LOW TEMP. CRACKS (m)	LONG CRACKS (m)	POTHOLE/PATCH (m2)	SURVEY DATE	RUT (mm) L/R	TRAFFIC YEAR	AADT (#)	TRUCKS (%)	CALCULATED ESALS	
11/06/1995	MANUAL				0.00						KESALS	
07/08/1996	AUTO				0.00							
10/07/1996	MANUAL				0.00							
10/20/1998	MANUAL			43	0.00							
10/26/1999	MANUAL			55	0.00							
09/13/2000	MANUAL			54	0.00							
08/20/2001	MANUAL			116	0.00							
09/11/2001	AUTO			145	0.00							
03/05/2002	MANUAL			156	0.00							
03/18/2003	MANUAL				0.00							
07/12/2003	AUTO			171	0.00							
10/31/2006	MANUAL	3		182	0.00							
10/13/2009	MANUAL	12	41	425	0.00							
11/09/2010	MANUAL	187		305	0.00							

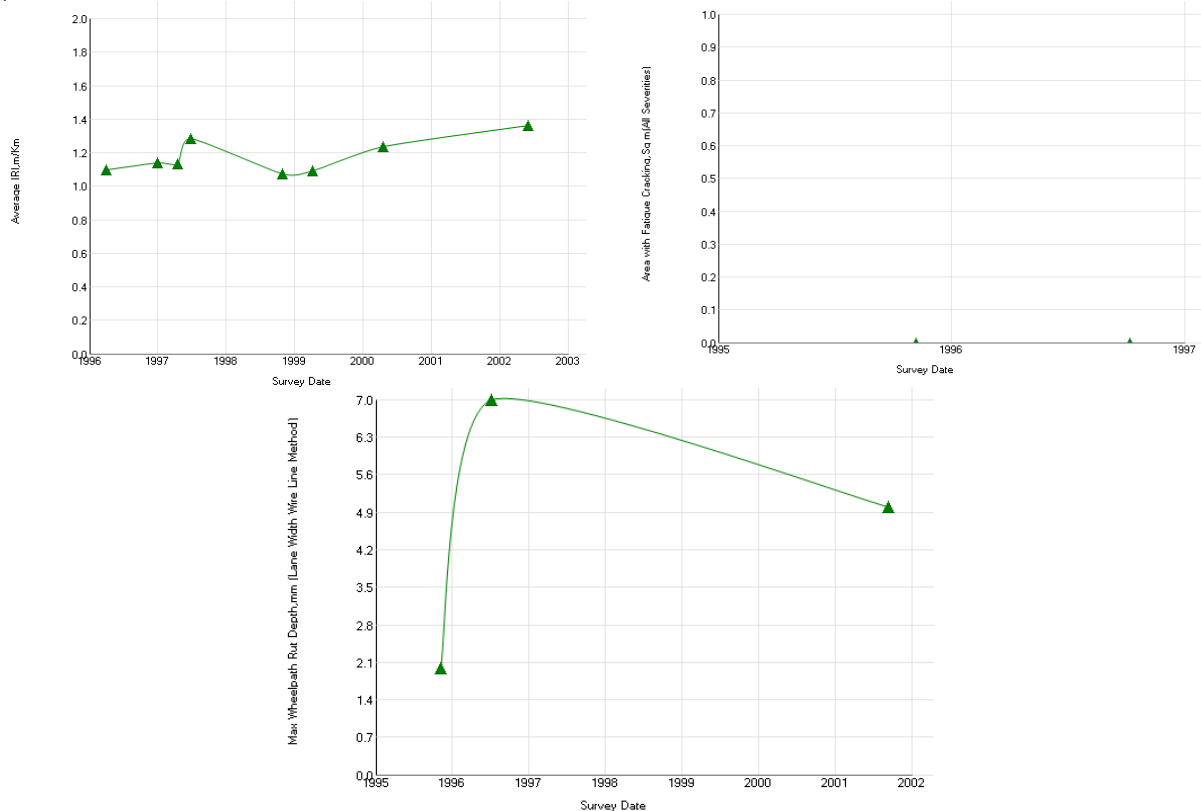


Experiment: SPS-1: Strategic Study of Structural Factors for Flexible Pavements, new/reconstructed AC pavements						Section ID: 26-0124						
REGION		North Central (Champaign, IL, USA)		LATITUDE		42.98267		ROUTE/DIRECTION				
EXPERIMENT		SPS-1		LONGITUDE		-84.51906		NO. OF LANES				
STATE/PROVINCE		Michigan		ELEVATION				CONSTRUCTED		01/01/1994		
COUNTY				MILEPOINT				OUT OF STUDY		10/01/2002		
				FUNCTIONAL CLASS								
Maintenance Rehabilitation/Rehabilitation Date						Activity Description						
05/01/2006						Crack Sealing (linear ft.)						
Layer Structure				Field Values		Laboratory Results						
LAYER		THICKNESS	MATERIAL			MOISTURE	DENSITY	SUBGRADE	COMPRESS	AIR	AC	MODULUS
NUMBER	TYPE	(mm)	DESCRIPTION			CONTENT (%)	(kg/m3)	P1	STR (kpa)	VOIDS(%)	CONTENT (%)	Mr.
1	SS		Fine-Grained Soils: Sandy Clay			6	23.00					
2	EF	2	Woven Geotextile				7.00					
3	TB	88	Open Graded, Hot Laid, Central Plant Mix				4.00					
4	TB	309	HMAC				2.00					
5	AC	58	Hot Mixed, Hot Laid AC, Dense Graded				0.00					
6	AC	48	Hot Mixed, Hot Laid AC, Dense Graded									
7	AC	12	Hot Mixed, Hot Laid AC, Dense Graded									
7	AC	50	Hot Mixed, Hot Laid AC, Dense Graded									
8	AC	40	Hot Mixed, Hot Laid AC, Dense Graded									
Distress Monitoring						Cross Profile		Monitored Traffic Data (Estimates)				
DISTRESS DATE	SURVEY METHOD	FATIGUE CRACKS (m2)	LOW TEMP. CRACKS (m)	LONG CRACKS (m)	POTHOLE/PATCH (m2)	SURVEY DATE	RUT (mm) L/R	TRAFFIC YEAR	AADT (#)	TRUCKS (%)	CALCULATED ESALS	
11/06/1995	MANUAL				47.00						KESALS	
07/08/1996	AUTO				50.10							
10/07/1996	MANUAL				42.70							
10/20/1998	MANUAL				44.30							
10/26/1999	MANUAL				44.30							
09/13/2000	MANUAL				44.20							
08/20/2001	MANUAL			102	46.10							
09/11/2001	AUTO			152	0.00							
03/05/2002	MANUAL	28		152	46.10							
03/18/2003	MANUAL				0.00							
07/12/2003	AUTO		2	159	0.00							
10/31/2006	MANUAL			157	0.00							
10/13/2009	MANUAL	30	29	358	0.00							
11/09/2010	MANUAL	98	12	318	0.00							

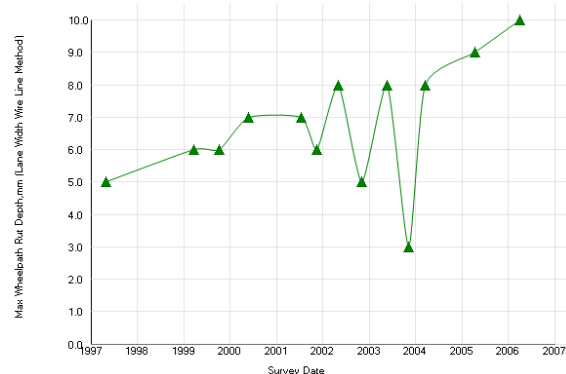
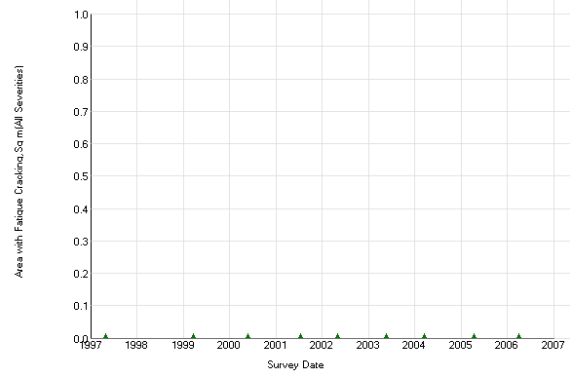
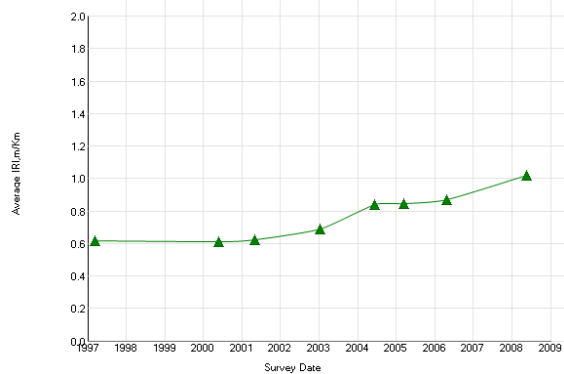


26-0121 Control

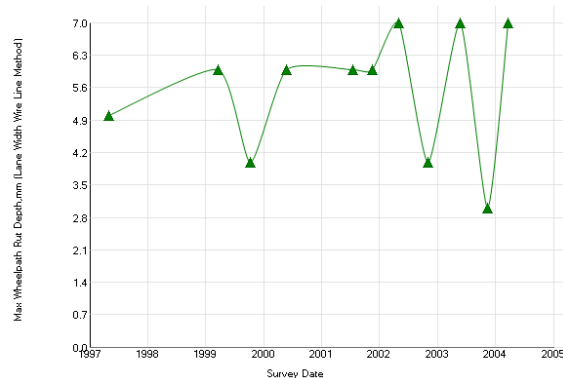
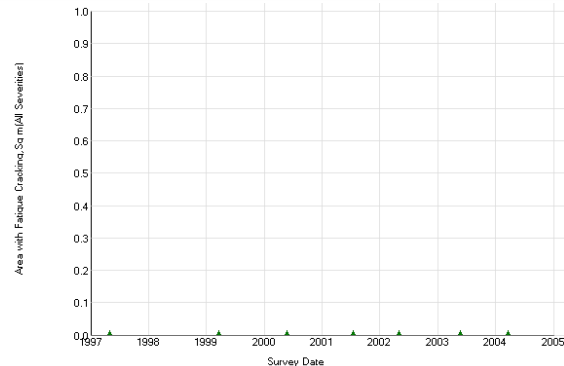
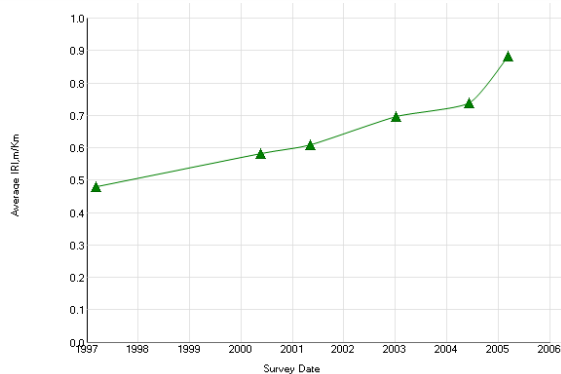
Experiment: SPS-1: Strategic Study of Structural Factors for Flexible Pavements, new/reconstructed AC pavements						Section ID: 26-0121						
Section# : 26-0121				Data : ALL DATA								
REGION		North Central (Champaign, IL, USA)		LATITUDE		42.99199		ROUTE/DIRECTION				
EXPERIMENT		SPS-1		LONGITUDE		-84.51910		NO. OF LANES				
STATE/PROVINCE		Michigan		ELEVATION				CONSTRUCTED		01/01/1994		
COUNTY				MILEPOINT				OUT OF STUDY		10/01/2002		
FUNCTIONAL CLASS												
Maintenance Rehabilitation/Rehabilitation Date						Activity Description						
05/01/2006						Crack Sealing (linear ft.)						
Layer Structure						Field Values		Laboratory Results				
LAYER		THICKNESS	MATERIAL			MOISTURE	DENSITY	SUBGRADE	COMPRESS	AIR	AC	MODULUS
NUMBER	TYPE	(mm)	DESCRIPTION			CONTENT	(kg/m3)	P1	STR	VOIDS(%)	CONTENT	Mr.
						(%)			(kpa)		(%)	
1	SS		Fine-Grained Soils: Sandy Clay			7	20.00					
2	GB	203	Crushed Stone			8	20.00					307
3	TB	101	Open Graded, Hot Laid, Central Plant Mix			1	8.00					
4	AC	50	Hot Mixed, Hot Laid AC, Dense Graded			2	8.00					
5	AC	10	Hot Mixed, Hot Laid AC, Dense Graded				2.00					
5	AC	48	Hot Mixed, Hot Laid AC, Dense Graded				0.00					
6	AC	38	Hot Mixed, Hot Laid AC, Dense Graded									
Distress Monitoring						Cross Profile		Monitored Traffic Data (Estimates)				
DISTRESS	SURVEY	FATIGUE	LOW TEMP.	LONG	POTHOLES/	SURVEY	RUT (mm)	TRAFFIC	AADT	TRUCKS	CALCULATED ESALS	
DATE	METHOD	CRACKS	CRACKS	CRACKS	PATCH (m2)	DATE	L/R	YEAR	(#)	(%)	KESALS	
		(m2)	(m)	(m)								
11/06/1995	MANUAL				0.00							
07/08/1996	AUTO		41	15	0.00							
10/07/1996	MANUAL			5	0.00							
09/11/2001	AUTO			2	0.00							
10/13/2009	MANUAL	76		307	0.00							
11/08/2010	MANUAL	193	1	161	0.00							



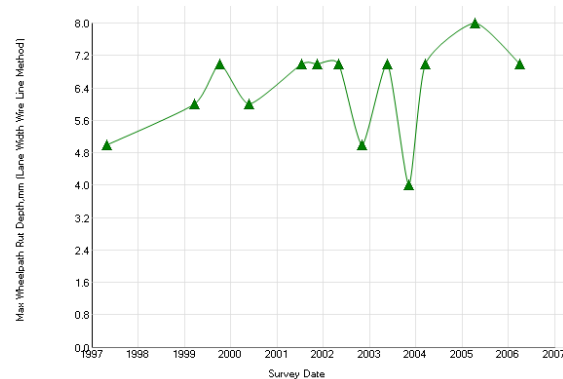
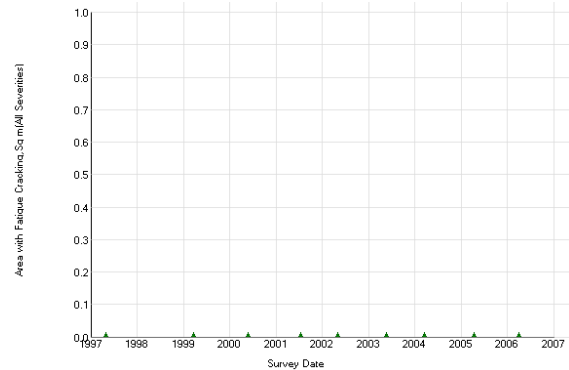
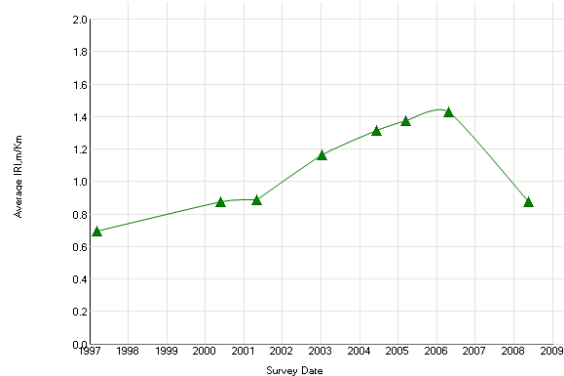
Experiment: SPS-1: Strategic Study of Structural Factors for Flexible Pavements, new/reconstructed AC pavements						Section ID: 35-0110						
Section# :			35-0110		Data :		ALL DATA					
REGION		Southern (Austin, TX, USA)		LATITUDE		32.67645		ROUTE/DIRECTION				
EXPERIMENT		SPS-1		LONGITUDE		-107.09330		NO. OF LANES				
STATE/PROVINCE		New Mexico		ELEVATION				CONSTRUCTED				
COUNTY				MILEPOINT				OUT OF STUDY				
				FUNCTIONAL CLASS				10/01/1994				
								06/15/2009				
Layer Structure				Field Values			Laboratory Results					
LAYER		THICKNESS	MATERIAL			MOISTURE	DENSITY	SUBGRADE	COMPRESS	AIR	AC	MODULUS
NUMBER	TYPE	(mm)	DESCRIPTION			CONTENT	(kg/m3)	P1	STR	VOIDS(%)	CONTENT	Mr.
						(%)			(kpa)		(%)	
1	SS		Fine-Grained Soils: Fat Inorganic Clay			24	15.00					84
2	TS	152	Lime-Treated Soil			26	15.00					
3	EF	2	Woven Geotextile				7.00					
4	TB	88	Open Graded, Hot Laid, Central Plant Mix				0.00					
5	TB	116	HMAC									
6	AC	182	Hot Mixed, Hot Laid AC, Dense Graded									
7	AC	20	Hot Mixed, Hot Laid AC, Open Graded									
Distress Monitoring						Cross Profile		Monitored Traffic Data (Estimates)				
DISTRESS	SURVEY	FATIGUE	LOW TEMP.	LONG	POTHOLES/	SURVEY	RUT (mm)	TRAFFIC	AADT	TRUCKS	CALCULATED ESALS	
DATE	METHOD	CRACKS	CRACKS	CRACKS	PATCH (m2)	DATE	L/R	YEAR	(#)	(%)	KESALS	
		(m2)	(m)	(m)								
05/02/1997	MANUAL				0.00			1996	6262	1152	147	
03/22/1999	MANUAL				0.00			1997	6459	1188	152	
10/08/1999	AUTO				0.00							
05/23/2000	MANUAL				0.00							
07/18/2001	MANUAL				0.00							
11/13/2001	AUTO				0.00							
05/02/2002	MANUAL				0.00							
11/03/2002	AUTO				0.00							
05/23/2003	MANUAL				0.00							
11/09/2003	AUTO			40	0.00							
03/19/2004	MANUAL				0.00							
04/12/2005	MANUAL				0.00							
03/29/2006	MANUAL				0.00							



Experiment: SPS-1: Strategic Study of Structural Factors for Flexible Pavements, new/reconstructed AC pavements						Section ID: 35-0111					
Section# : 35-0111			Data : ALL DATA								
REGION		Southern (Austin, TX, USA)		LATITUDE		32.67631		ROUTE/DIRECTION			
EXPERIMENT		SPS-1		LONGITUDE		-107.09541		NO. OF LANES			
STATE/PROVINCE		New Mexico		ELEVATION				CONSTRUCTED		10/01/1994	
COUNTY				MILEPOINT				OUT OF STUDY		06/15/2009	
				FUNCTIONAL CLASS							
Maintenance Rehabilitation/Rehabilitation Date						Activity Description					
03/15/2005						Grinding Surface (sq. yards)					
Layer Structure				Field Values		Laboratory Results					
LAYER		THICKNESS (mm)	MATERIAL DESCRIPTION	MOISTURE CONTENT (%)	DENSITY (kg/m3)	SUBGRADE P1	COMPRESS STR (kpa)	AIR VOIDS(%)	AC CONTENT (%)	MODULUS Mr.	
NUMBER	TYPE										
1	SS		Fine-Grained Soils: Fat Inorganic Clay	20	16.00					100	
2	TS	152	Lime-Treated Soil	22	16.00						
3	EF	2	Woven Geotextile	24	16.00						
4	TB	93	Open Graded, Hot Laid, Central Plant Mix		4.00						
5	TB	193	HMAC		0.00						
6	AC	109	Hot Mixed, Hot Laid AC, Dense Graded								
7	AC	15	Hot Mixed, Hot Laid AC, Open Graded								
7	AC	17	Hot Mixed, Hot Laid AC, Open Graded								
Distress Monitoring				Cross Profile		Monitored Traffic Data (Estimates)					
DISTRESS DATE	SURVEY METHOD	FATIGUE CRACKS (m2)	LOW TEMP. CRACKS (m)	LONG CRACKS (m)	POTHOLES/ PATCH (m2)	SURVEY DATE	RUT (mm) L/R	TRAFFIC YEAR	AADT (#)	TRUCKS (%)	CALCULATED ESALS
											KESALS
05/02/1997	MANUAL				0.00			1996	6262	1152	147
03/22/1999	MANUAL				0.00			1997	6459	1188	152
10/08/1999	AUTO				0.00						
05/23/2000	MANUAL				0.00						
07/18/2001	MANUAL				0.00						
11/13/2001	AUTO		1		0.00						
05/02/2002	MANUAL				0.00						
11/03/2002	AUTO				0.00						
05/23/2003	MANUAL				0.00						
11/09/2003	AUTO			11	0.00						
03/19/2004	MANUAL				0.00						
04/12/2005	MANUAL				0.00						
03/29/2006	MANUAL			5	0.00						

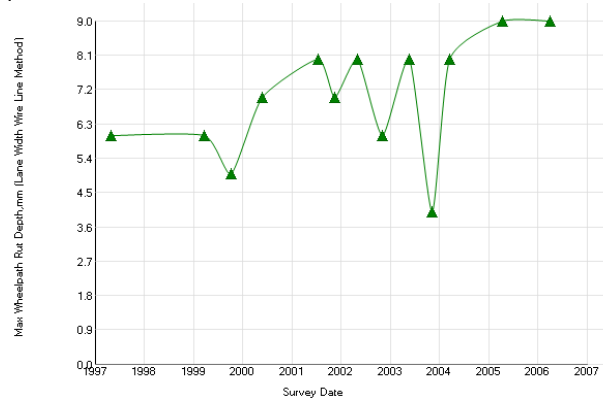
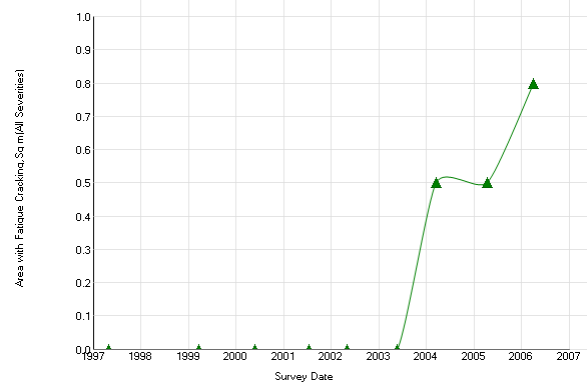
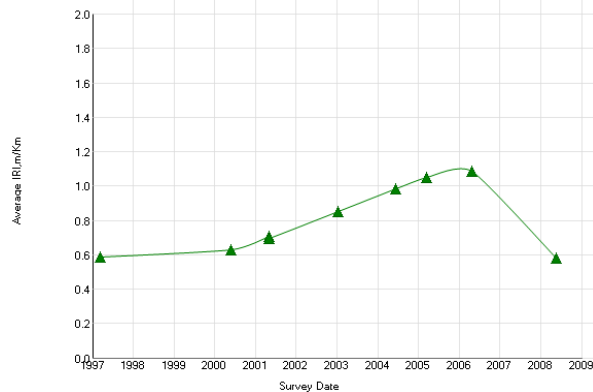


Experiment: SPS-1: Strategic Study of Structural Factors for Flexible Pavements, new/reconstructed AC pavements							Section ID: 35-0112					
Section# :			35-0112		Data :		ALL DATA					
REGION		Southern (Austin, TX, USA)		LATITUDE		32.67611		ROUTE/DIRECTION				
EXPERIMENT		SPS-1		LONGITUDE		-107.09897		NO. OF LANES				
STATE/PROVINCE		New Mexico		ELEVATION				CONSTRUCTED		10/01/1994		
COUNTY				MILEPOINT				OUT OF STUDY		06/15/2009		
				FUNCTIONAL CLASS								
Layer Structure					Field Values		Laboratory Results					
LAYER		THICKNESS (mm)	MATERIAL DESCRIPTION			MOISTURE CONTENT (%)	DENSITY (kg/m3)	SUBGRADE P1	COMPRESS STR (kpa)	AIR VOIDS(%)	AC CONTENT (%)	MODULUS Mr.
NUMBER	TYPE											
1	SS		Fine-Grained Soils: Lean Inorganic Clay			24	20.00					53
2	TS	152	Lime-Treated Soil			25	20.00					
3	EF	2	Woven Geotextile				4.00					
4	TB	81	Open Graded, Hot Laid, Central Plant Mix				0.00					
5	TB	297	HMAC									
6	AC	111	Hot Mixed, Hot Laid AC, Dense Graded									
7	AC	25	Hot Mixed, Hot Laid AC, Open Graded									
Distress Monitoring						Cross Profile		Monitored Traffic Data (Estimates)				
DISTRESS DATE	SURVEY METHOD	FATIGUE CRACKS (m2)	LOW TEMP. CRACKS (m)	LONG CRACKS (m)	POTHOLE/ PATCH (m2)	SURVEY DATE	RUT (mm) L/R	TRAFFIC YEAR	AADT (#)	TRUCKS (%)	CALCULATED ESALS	
											KESALS	
05/02/1997	MANUAL				0.00			1996	6262	1152	147	
03/22/1999	MANUAL				0.00			1997	6459	1188	152	
10/08/1999	AUTO				0.00							
05/23/2000	MANUAL				0.00							
07/18/2001	MANUAL				0.00							
11/13/2001	AUTO				0.00							
05/02/2002	MANUAL				0.00							
11/03/2002	AUTO				0.00							
05/23/2003	MANUAL				0.00							
11/09/2003	AUTO			7	0.00							
03/19/2004	MANUAL				0.00							
04/12/2005	MANUAL				0.00							
03/29/2006	MANUAL			1	0.00							

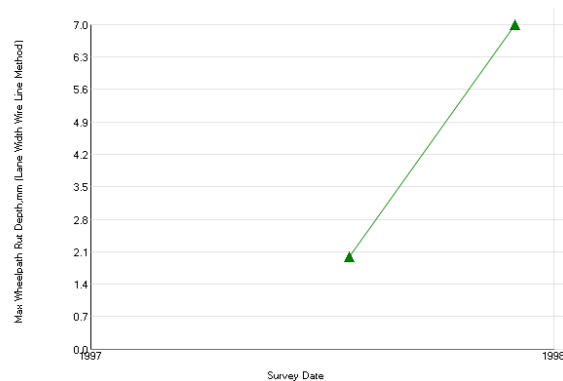
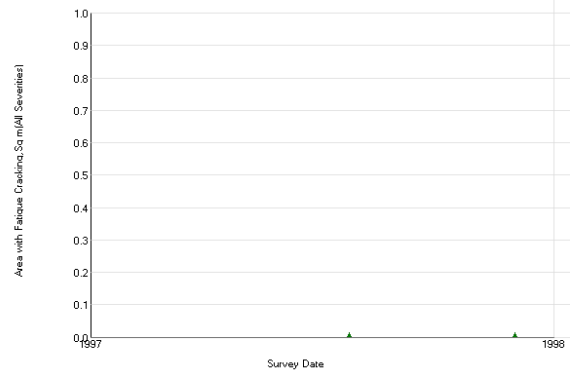
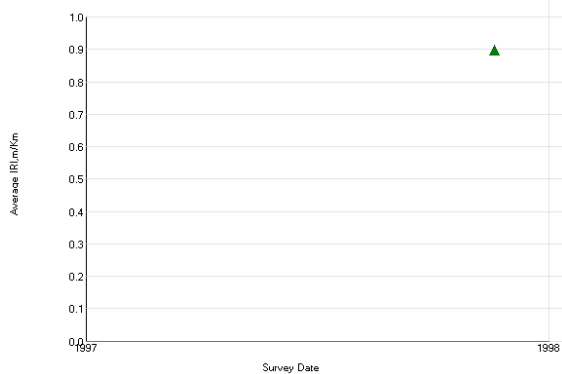


35-0109 Control

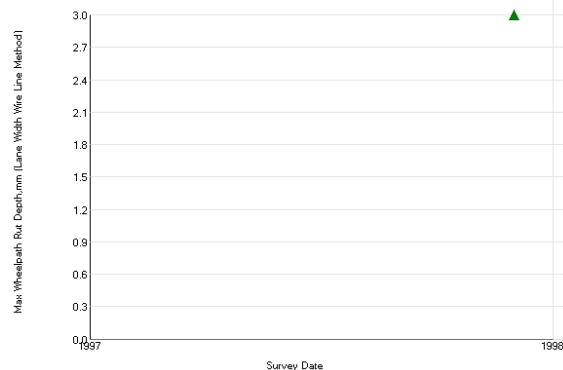
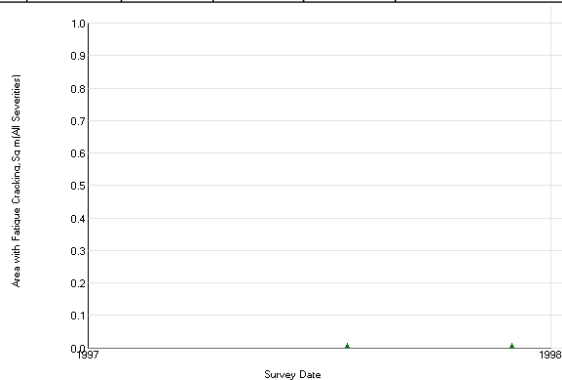
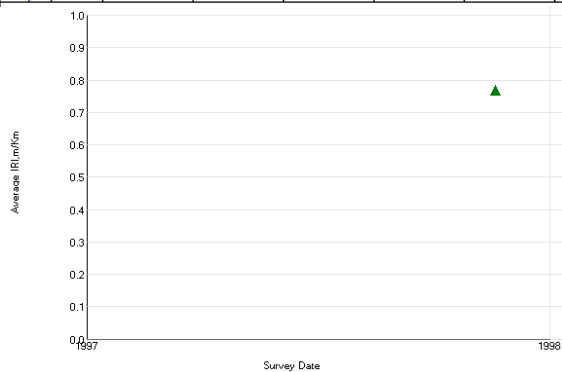
Experiment: SPS-1: Strategic Study of Structural Factors for Flexible Pavements, new/reconstructed AC pavements						Section ID: 35-0109					
Section# :			35-0109			Data :			ALL DATA		
REGION		Southern (Austin, TX, USA)		LATITUDE		32.67679		ROUTE/DIRECTION			
EXPERIMENT		SPS-1		LONGITUDE		-107.08810		NO. OF LANES			
STATE/PROVINCE		New Mexico		ELEVATION				CONSTRUCTED		10/01/1994	
COUNTY				MILEPOINT				OUT OF STUDY		06/15/2009	
				FUNCTIONAL CLASS							
Layer Structure						Field Values		Laboratory Results			
LAYER		THICKNESS	MATERIAL DESCRIPTION			MOISTURE	DENSITY	SUBGRADE	COMPRESS	AIR	AC
NUMBER	TYPE	(mm)				CONTENT					
					(%)					(%)	MODULUS
1	SS		Fine-Grained Soils: Sandy Fat Clay			18	23.00				73
2	TS	152	Lime-Treated Soil			19	23.00				154
3	GB	287	Crushed Gravel			2	11.00				
4	TB	109	Open Graded, Hot Laid, Central Plant Mix			3	11.00				
5	AC	187	Hot Mixed, Hot Laid AC, Dense Graded				0.00				
6	AC	17	Hot Mixed, Hot Laid AC, Open Graded								
Distress Monitoring						Cross Profile		Monitored Traffic Data (Estimates)			
DISTRESS DATE	SURVEY METHOD	FATIGUE CRACKS (m2)	LOW TEMP. CRACKS (m)	LONG CRACKS (m)	POTHOL/ PATCH (m2)	SURVEY DATE	RUT (mm) L/R	TRAFFIC YEAR	AADT (#)	TRUCKS (%)	CALCULATED ESALS
											KESALS
05/02/1997	MANUAL				0.00			1996	6262	1152	147
03/22/1999	MANUAL				0.00			1997	6459	1188	152
10/08/1999	AUTO				0.00						
05/23/2000	MANUAL				0.00						
07/18/2001	MANUAL				0.00						
11/13/2001	AUTO				0.00						
05/02/2002	MANUAL				0.00						
11/03/2002	AUTO				0.00						
05/23/2003	MANUAL				0.00						
11/09/2003	AUTO			32	0.00						
03/19/2004	MANUAL				0.00						
04/11/2005	MANUAL				0.00						
03/29/2006	MANUAL			4	0.00						



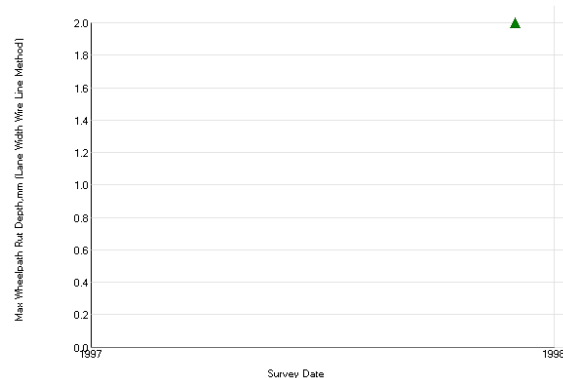
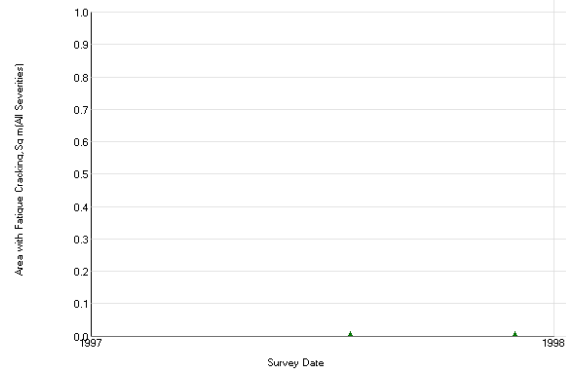
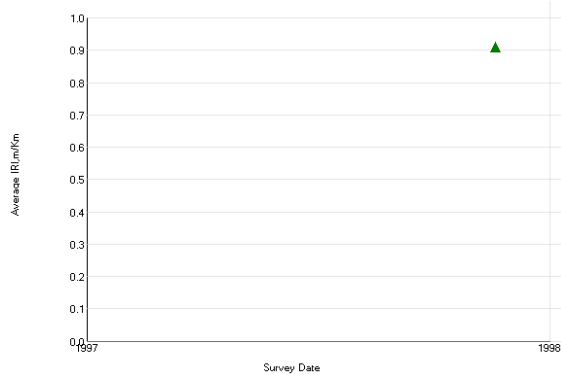
Experiment: SPS-1: Strategic Study of Structural Factors for Flexible Pavements, new/reconstructed AC pavements							Section ID: 40-0122					
Section# :			40-0122		Data :		ALL DATA					
REGION		Southern (Austin, TX, USA)			LATITUDE		34.63476		ROUTE/DIRECTION			
EXPERIMENT		SPS-1			LONGITUDE		-98.68243		NO. OF LANES			
STATE/PROVINCE		Oklahoma			ELEVATION				CONSTRUCTED			
COUNTY					MILEPOINT				OUT OF STUDY			
					FUNCTIONAL CLASS				01/01/1996			
									06/15/2008			
Maintenance Rehabilitation/Rehabilitation Date							Activity Description					
02/05/1999							Skin Patching (hand tools/hot pot to apply liquid asphalt and aggregate) (sq.yd)					
Layer Structure							Field Values		Laboratory Results			
LAYER		THICKNESS (mm)	MATERIAL DESCRIPTION			MOISTURE CONTENT (%)	DENSITY (kg/m3)	SUBGRADE P1	COMPRESS STR (kpa)	AIR VOIDS(%)	AC CONTENT (%)	MODULUS Mr.
NUMBER	TYPE											
1	SS	762	Coarse-Grained Soil: Clayey Sand			10	21.50					82
2	TS	203	Lime-Treated Soil			12	21.50					
3	EF	2	Woven Geotextile			13	21.50					
4	TB	121	Open Graded, Hot Laid, Central Plant Mix			15	13.50					
5	TB	99	HMAC			16	13.50					
6	AC	66	Hot Mixed, Hot Laid AC, Dense Graded			17	13.50					
7	AC	45	Hot Mixed, Hot Laid AC, Dense Graded			21	13.50					
Distress Monitoring						Cross Profile		Monitored Traffic Data (Estimates)				
DISTRESS DATE	SURVEY METHOD	FATIGUE CRACKS (m2)	LOW TEMP. CRACKS (m)	LONG CRACKS (m)	POTHOLFS/ PATCH (m2)	SURVEY DATE	RUT (mm) L/R	TRAFFIC YEAR	AADT (#)	TRUCKS (%)	CALCULATED ESALS	
											KESALS	
07/24/1997	MANUAL				0.00							
12/02/1997	MANUAL				0.00							
09/23/1999	MANUAL				0.00							
11/04/1999	AUTO				0.00							
09/11/2000	MANUAL				0.00							
12/18/2000	AUTO			55	0.00							
09/13/2001	MANUAL	1		56	0.00							
11/18/2001	AUTO			153	0.00							
07/24/2002	MANUAL	4		84	0.00							
11/07/2002	AUTO			123	0.00							
08/12/2003	MANUAL	8		94	0.00							
11/11/2003	AUTO	1	8	142	0.00							
08/24/2004	MANUAL	11	4	96	0.00							
08/22/2006	MANUAL	13	17	101	0.00							



Experiment: SPS-1: Strategic Study of Structural Factors for Flexible Pavements, new/reconstructed AC pavements						Section ID: 40-0123					
Section# :			40-0123			Data :			ALL DATA		
REGION		Southern (Austin, TX, USA)		LATITUDE		34.63691		ROUTE/DIRECTION		01/01/1996	
EXPERIMENT		SPS-1		LONGITUDE		-98.66400		NO. OF LANES			
STATE/PROVINCE		Oklahoma		ELEVATION				CONSTRUCTED			
COUNTY				MILEPOINT				OUT OF STUDY			
				FUNCTIONAL CLASS							
Maintenance Rehabilitation/Rehabilitation Date						Activity Description					
02/05/1999						Skin Patching (hand tools/hot pot to apply liquid asphalt and aggregate) (sq.yd)					
Layer Structure						Field Values		Laboratory Results			
LAYER		THICKNESS	MATERIAL			MOISTURE	DENSITY	SUBGRADE	COMPRESS	AIR	AC
NUMBER	TYPE	(mm)	DESCRIPTION			CONTENT	(kg/m3)	P 1	STR	VOIDS(%)	CONTENT
						(%)			(kpa)		(%)
											MODULUS
											Mr.
1	SS	914	Coarse-Grained Soil: Clayey Sand			14	27.10				112
2	TS	203	Lime-Treated Soil			15	27.10				
3	EF	2	Woven Geotextile			16	27.10				
4	TB	111	Open Graded, Hot Laid, Central Plant Mix			17	27.10				
5	TB	218	HMAC			20	19.10				
6	AC	139	Hot Mixed, Hot Laid AC, Dense Graded			23	19.10				
7	AC	40	Hot Mixed, Hot Laid AC, Dense Graded			24	19.10				
Distress Monitoring						Cross Profile		Monitored Traffic Data (Estimates)			
DISTRESS	SURVEY	FATIGUE	LOW TEMP.	LONG	POTHOLE	SURVEY	RUT (mm)	TRAFFIC	AADT	TRUCKS	CALCULATED
DATE	METHOD	CRACKS	CRACKS	CRACKS	/PATCH	DATE	L/R	YEAR	(#)	(%)	ESALS
		(m2)	(m)	(m)	(m2)						KESALS
07/25/1997	MANUAL				0.00						
12/02/1997	MANUAL				0.00						
09/24/1999	MANUAL				0.00						
11/04/1999	AUTO				0.00						
09/11/2000	MANUAL				0.00						
12/18/2000	AUTO				0.00						
09/13/2001	MANUAL			8	0.00						
11/18/2001	AUTO			108	0.00						
07/24/2002	MANUAL	3		91	0.00						
11/07/2002	AUTO			133	0.00						
08/13/2003	MANUAL	7		118	0.00						
11/11/2003	AUTO	4		176	0.00						
08/24/2004	MANUAL	9		131	0.00						
08/23/2006	MANUAL	10	8	128	0.00						
03/17/2010	MANUAL	19	53	140	0.00						

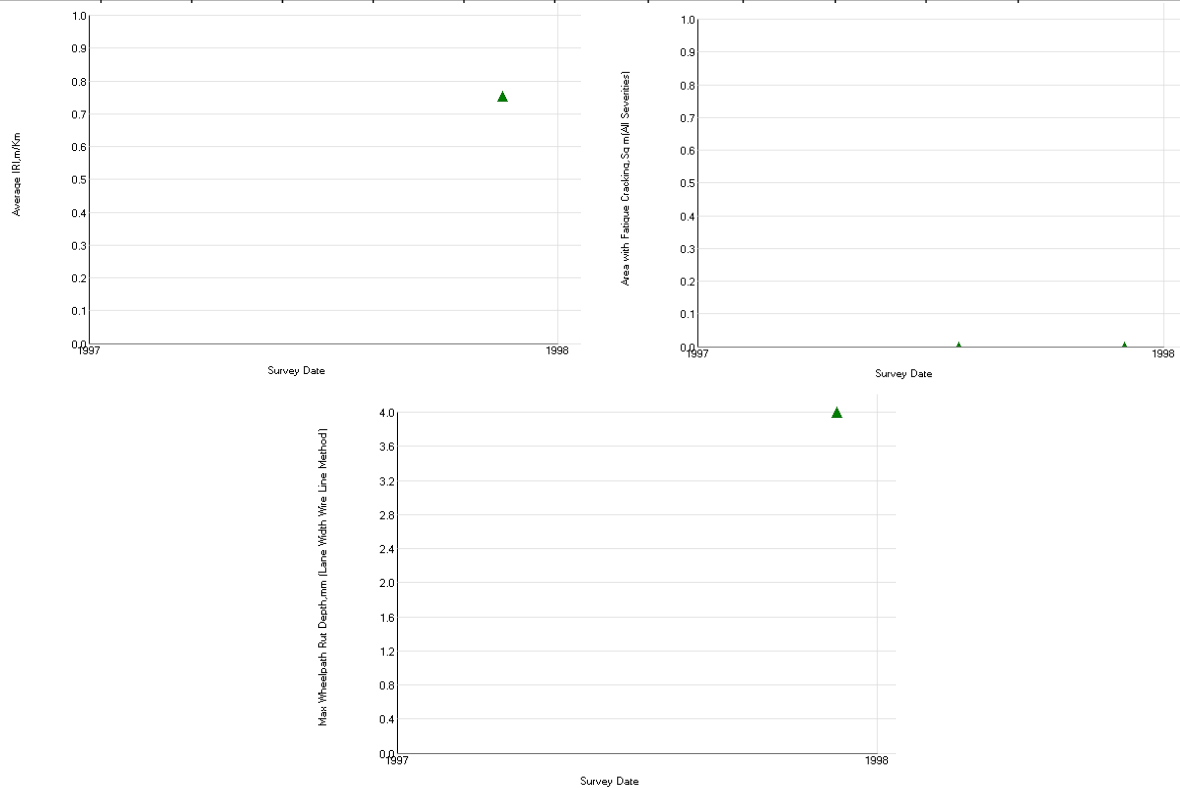


Experiment: SPS-1: Strategic Study of Structural Factors for Flexible Pavements, new/reconstructed AC pavements						Section ID: 40-0124							
Section# : 40-0124				Data : ALL DATA									
REGION		Southern (Austin, TX, USA)		LATITUDE		34.63726		ROUTE/DIRECTION NO. OF LANES CONSTRUCTED OUT OF STUDY 01/01/1996					
EXPERIMENT		SPS-1		LONGITUDE		-98.66103							
STATE/PROVINCE		Oklahoma		ELEVATION									
COUNTY				MILEPOINT									
				FUNCTIONAL CLASS									
Maintenance Rehabilitation/Rehabilitation Date						Activity Description							
02/05/1999						Skin Patching (hand tools/hot pot to apply liquid asphalt and aggregate) (sq.yd)							
Layer Structure						Field Values		Laboratory Results					
LAYER		THICKNESS	MATERIAL DESCRIPTION			MOISTURE CONTENT (%)	DENSITY (kg/m3)	SUBGRADE P1	COMPRESS STR (kpa)	AIR VOIDS(%)	AC CONTENT (%)	MODULUS Mr.	
NUMBER	TYPE	(mm)											
1	SS	5181	Coarse-Grained Soil: Clayey Sand			13	30.50					50	
2	TS	152	Lime-Treated Soil			14	30.50						
3	EF	2	Woven Geotextile			22	22.50						
4	TB	114	Open Graded, Hot Laid, Central Plant Mix			24	22.50						
5	TB	276	HMAC				7.20						
6	AC	137	Hot Mixed, Hot Laid AC, Dense Graded				0.00						
7	AC	48	Hot Mixed, Hot Laid AC, Dense Graded										
Distress Monitoring						Cross Profile		Monitored Traffic Data (Estimates)					
DISTRESS DATE	SURVEY METHOD	FATIGUE CRACKS (m2)	LOW TEMP. CRACKS (m)	LONG CRACKS (m)	POTHOLE/ PATCH (m2)	SURVEY DATE	RUT (mm) L/R	TRAFFIC YEAR	AADT (#)	TRUCKS (%)	CALCULATED ESALS		
07/25/1997	MANUAL				0.00						KESALS		
12/02/1997	MANUAL				0.00								
09/24/1999	MANUAL				0.00								
11/04/1999	AUTO				0.00								
09/11/2000	MANUAL				0.00								
12/18/2000	AUTO			9	0.00								
09/13/2001	MANUAL			4	0.00								
11/18/2001	AUTO			94	0.00								
07/24/2002	MANUAL			34	0.00								
11/07/2002	AUTO			101	0.00								
08/13/2003	MANUAL	1		80	0.00								
11/11/2003	AUTO			155	0.00								
08/24/2004	MANUAL	2		111	0.00								
08/23/2006	MANUAL	3	8	139	0.00								
03/17/2010	MANUAL	8	69	144	0.00								

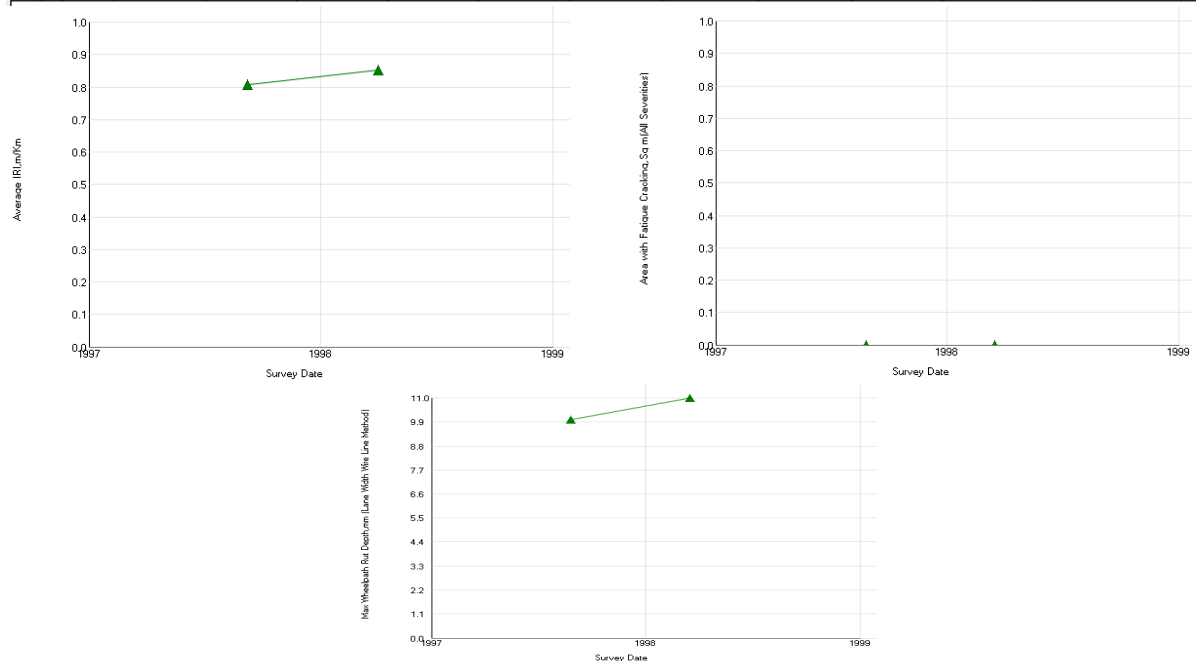


40-0120 Control

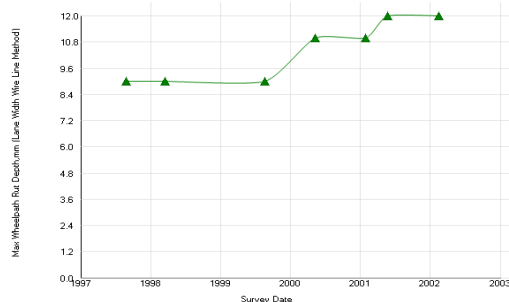
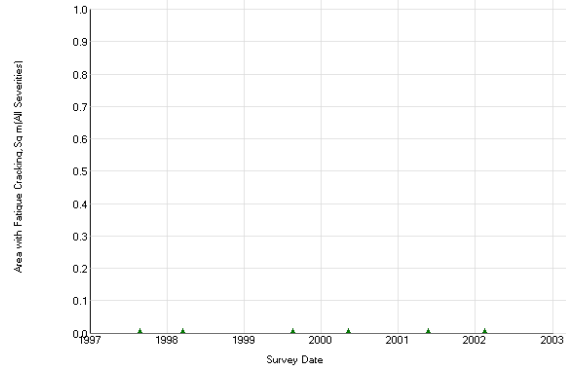
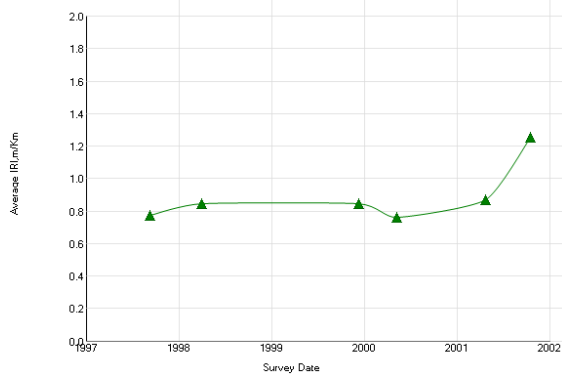
Experiment: SPS-1: Strategic Study of Structural Factors for Flexible Pavements, new/reconstructed AC pavements						Section ID: 40-0120						
Section# : 40-0120						Data : ALL DATA						
REGION		Southern (Austin, TX, USA)		LATITUDE		34.63599		ROUTE/DIRECTION		01/01/1996		
EXPERIMENT		SPS-1		LONGITUDE		-98.67161		NO. OF LANES				
STATE/PROVINCE		Oklahoma		ELEVATION				CONSTRUCTED				
COUNTY				MILEPOINT				OUT OF STUDY				
				FUNCTIONAL CLASS								
Maintenance Rehabilitation/Rehabilitation Date						Activity Description						
02/05/1999						Skin Patching (hand tools/hot pot to apply liquid asphalt and aggregate) (sq.yd)						
Layer Structure						Field Values		Laboratory Results				
LAYER		THICKNESS (mm)	MATERIAL DESCRIPTION			MOISTURE CONTENT (%)	DENSITY (kg/m3)	SUBGRADE P1	COMPRESS STR (kpa)	AIR VOIDS(%)	AC CONTENT (%)	MODULUS Mr.
NUMBER	TYPE											
1	SS	2743	Coarse-Grained Soil: Clayey Sand			14	17.80					91
2	TS	228	Lime-Treated Soil			16	17.80					
3	GB	200	Crushed Stone			19	17.80					185
4	TB	121	Open Graded, Hot Laid, Central Plant Mix			21	17.80					
5	AC	78	Hot Mixed, Hot Laid AC, Dense Graded			5	16.00					
6	AC	40	Hot Mixed, Hot Laid AC, Dense Graded			6	16.00					
Distress Monitoring						Cross Profile		Monitored Traffic Data (Estimates)				
DISTRESS DATE	SURVEY METHOD	FATIGUE CRACKS (m2)	LOW TEMP. CRACKS (m)	LONG CRACKS (m)	POTHOLES/ PATCH (m2)	SURVEY DATE	RUT (mm) L/R	TRAFFIC YEAR	AADT (#)	TRUCKS (%)	CALCULATED ESALS	
											KESALS	
07/25/1997	MANUAL				0.00							
12/02/1997	MANUAL				0.00							
09/24/1999	MANUAL				0.00							
11/04/1999	AUTO				0.00							
09/11/2000	MANUAL				0.00							
12/18/2000	AUTO			39	0.00							
09/13/2001	MANUAL	5		27	0.00							
11/18/2001	AUTO			116	0.00							
07/24/2002	MANUAL	9		69	0.00							
11/07/2002	AUTO		4	140	0.00							
08/13/2003	MANUAL	10		87	0.00							
11/11/2003	AUTO	1	27	147	0.00							



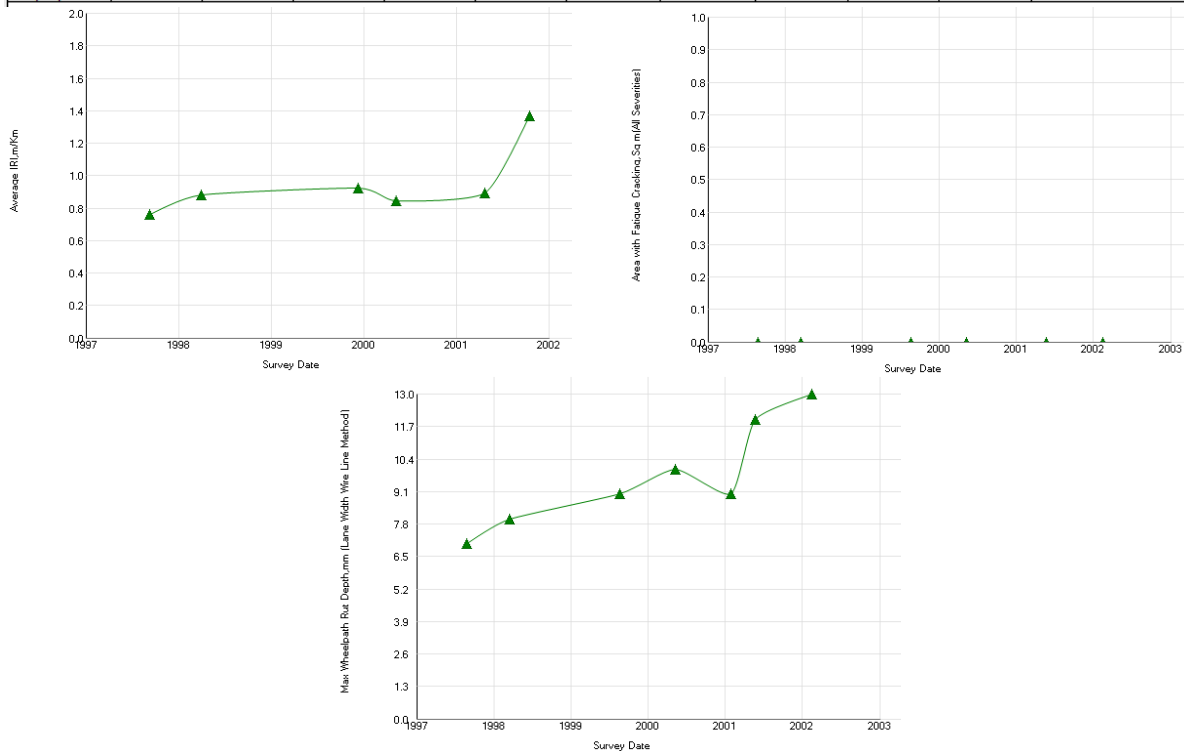
Experiment: SPS-1: Strategic Study of Structural Factors for Flexible Pavements, new/reconstructed AC pavements							Section ID: 48-0119					
Section# :			48-0119		Data :		ALL DATA					
REGION		Southern (Austin, TX, USA)			LATITUDE		26.70432		ROUTE/DIRECTION			
EXPERIMENT		SPS-1			LONGITUDE		-98.11115		NO. OF LANES			
STATE/PROVINCE		Texas			ELEVATION				CONSTRUCTED			
COUNTY					MILEPOINT				OUT OF STUDY			
					FUNCTIONAL CLASS				01/01/1995			
									04/29/2002			
Maintenance Rehabilitation/Rehabilitation Date							Activity Description					
07/09/1998							Grinding Surface (sq. yards)					
06/15/2006							Manual Premix Spot Patch (hand spreading and compacting with roller) (sq. yards)					
Layer Structure							Field Values		Laboratory Results			
LAYER		THICKNESS	MATERIAL			MOISTURE	DENSITY	SUBGRADE	COMPRESS	AIR	AC	MODULUS
NUMBER	TYPE	(mm)	DESCRIPTION			CONTENT (%)	(kg/m3)	P1	STR (kpa)	VOIDS(%)	CONTENT (%)	Mr.
1	SS		Coarse-Grained Soils: Poorly Graded Sand with Silt			8	26.90					66
2	TS	304	Lime-Treated Soil			9	26.90					
3	GB	101	Crushed Stone			10	26.90					263
4	EF	2	Nonwoven Geotextile			13	26.90					
5	TB	88	Open Graded, Hot Laid, Central Plant Mix			16	14.90					
6	AC	129	Hot Mixed, Hot Laid AC, Dense Graded			18	14.90					
6	AC	132	Hot Mixed, Hot Laid AC, Dense Graded			19	14.90					
6	AC	142	Hot Mixed, Hot Laid AC, Dense Graded			5	10.80					
7	AC	12	Hot Mixed, Hot Laid AC, Dense Graded			5	1.10					
7	AC	27	Hot Mixed, Hot Laid AC, Dense Graded			6	1.10					
7	AC	55	Hot Mixed, Hot Laid AC, Dense Graded			6	0.00					
8	AC	53	Hot Mixed, Hot Laid AC, Dense Graded			7	0.00					
9	AC	38	Hot Mixed, Hot Laid AC, Dense Graded									
Distress Monitoring						Cross Profile		Monitored Traffic Data (Estimates)				
DISTRESS DATE	SURVEY METHOD	FATIGUE CRACKS (m2)	LOW TEMP. CRACKS (m)	LONG CRACKS (m)	POTHOLES/ PATCH (m2)	SURVEY DATE	RUT (mm) L/R	TRAFFIC YEAR	AADT (#)	TRUCKS (%)	CALCULATED ESALS	
											KESALS	
08/26/1997	MANUAL				0.00							
03/17/1998	MANUAL				0.00							
08/19/1999	MANUAL				0.00							
05/10/2000	MANUAL				0.00							
01/27/2001	AUTO				0.00							
05/23/2001	MANUAL				0.00							
02/14/2002	MANUAL				0.00							
05/15/2002	MANUAL				0.00							
02/15/2003	AUTO				0.00							
11/12/2003	MANUAL				0.00							
12/21/2003	AUTO				0.00							
06/24/2004	MANUAL			25	0.00							
12/01/2005	MANUAL	1		52	0.00							
03/22/2007	MANUAL		4	194	1.10							



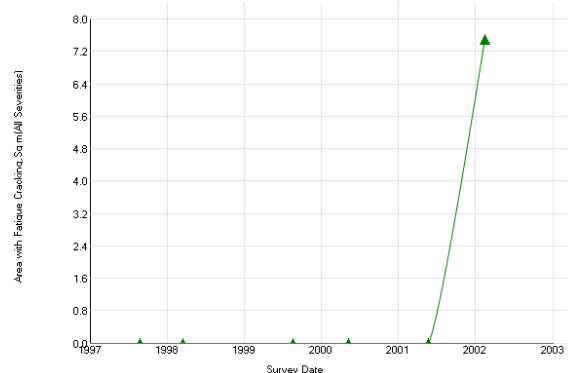
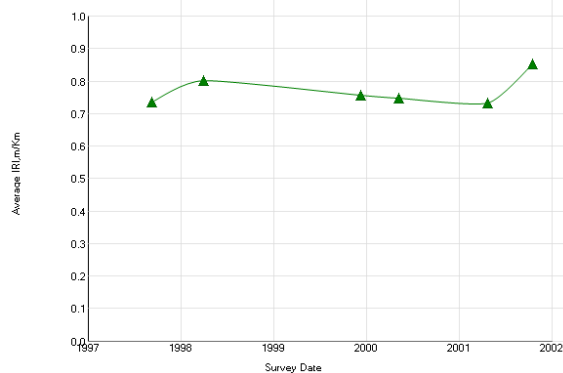
Experiment: SPS-1: Strategic Study of Structural Factors for Flexible Pavements, new/reconstructed AC pavements										Section ID: 48-0120		
Section# : 48-0120				Data : ALL DATA								
REGION		Southern (Austin, TX, USA)			LATITUDE		26.70649		ROUTE/DIRECTION			
EXPERIMENT		SPS-1			LONGITUDE		-98.11073		NO. OF LANES			
STATE/PROVINCE		Texas			ELEVATION				CONSTRUCTED			
COUNTY					MILEPOINT				01/01/1995			
					FUNCTIONAL CLASS				04/29/2002			
Maintenance Rehabilitation/Rehabilitation Date							Activity Description					
06/15/2006							Manual Premix Spot Patch (hand spreading and compacting with roller) (sq. yards)					
Layer Structure					Field Values		Laboratory Results					
LAYER		THICKNESS (mm)	MATERIAL DESCRIPTION			MOISTURE CONTENT (%)	DENSITY (kg/m3)	SUBGRADE P1	COMPRESS STR (kpa)	AIR VOIDS(%)	AC CONTENT (%)	MODULUS Mr.
NUMBER	TYPE											
1	SS		Coarse-Grained Soils: Poorly Graded Sand with Silt			7	27.90					
2	TS	388	Lime-Treated Soil			8	27.90					181
3	GB	180	Crushed Stone			9	27.90					216
4	EF	2	Nonwoven Geotextile			17	10.50					
5	TB	91	Open Graded, Hot Laid, Central Plant Mix			4	3.10					
5	TB	101	Open Graded, Hot Laid, Central Plant Mix			5	3.10					
6	AC	66	Hot Mixed, Hot Laid AC, Dense Graded			4	2.00					
6	AC	68	Hot Mixed, Hot Laid AC, Dense Graded			5	2.00					
7	AC	0	Hot Mixed, Hot Laid AC, Dense Graded			5	0.00					
7	AC	50	Hot Mixed, Hot Laid AC, Dense Graded			6	0.00					
8	AC	50	Hot Mixed, Hot Laid AC, Dense Graded									
9	AC	38	Hot Mixed, Hot Laid AC, Dense Graded									
Distress Monitoring					Cross Profile		Monitored Traffic Data (Estimates)					
DISTRESS DATE	SURVEY METHOD	FATIGUE CRACKS (m2)	LOW TEMP. CRACKS (m)	LONG CRACKS (m)	POTHOLE/ PATCH (m2)	SURVEY DATE	RUT (mm) L/R	TRAFFIC YEAR	AADT (#)	TRUCKS (%)	CALCULATED ESALS	
											KESALS	
08/26/1997	MANUAL				0.00							
03/17/1998	MANUAL				0.00							
08/19/1999	MANUAL				0.00							
05/10/2000	MANUAL				0.00							
01/27/2001	AUTO				0.00							
05/23/2001	MANUAL				0.00							
02/14/2002	MANUAL			10	0.00							
05/15/2002	MANUAL			15	0.00							
02/15/2003	AUTO				0.00							
11/12/2003	MANUAL				0.00							
11/21/2003	AUTO		7	3	0.00							
06/24/2004	MANUAL			80	0.00							
12/01/2005	MANUAL		1	179	0.00							
03/22/2007	MANUAL		7	325	21.80							



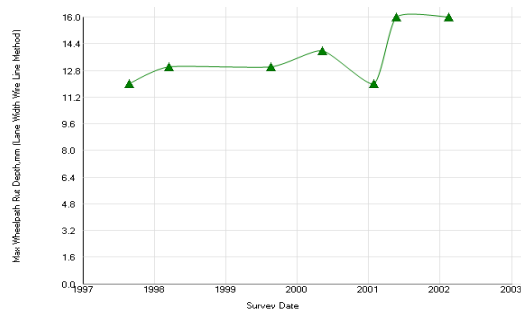
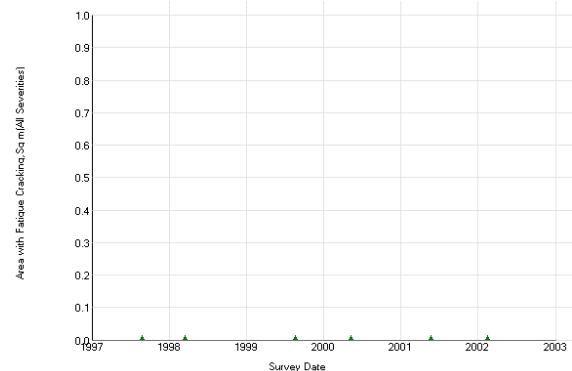
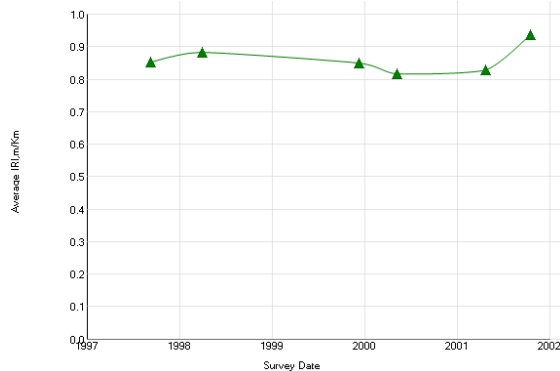
Experiment: SPS-1: Strategic Study of Structural Factors for Flexible Pavements, new/reconstructed AC pavements							Section ID: 48-0121				
Section# :			48-0121		Data :		ALL DATA				
REGION		Southern (Austin, TX, USA)		LATITUDE		26.70861		ROUTE/DIRECTION			
EXPERIMENT		SPS-1		LONGITUDE		-98.11034		NO. OF LANES			
STATE/PROVINCE		Texas		ELEVATION				CONSTRUCTED		01/01/1995	
COUNTY				MILEPOINT				OUT OF STUDY		04/29/2002	
				FUNCTIONAL CLASS							
Layer Structure				Field Values		Laboratory Results					
LAYER		THICKNESS (mm)	MATERIAL DESCRIPTION	MOISTURE CONTENT (%)	DENSITY (kg/m3)	SUBGRADE P1	COMPRESS STR (kpa)	AIR VOIDS(%)	AC CONTENT (%)	MODULUS Mr.	
NUMBER	TYPE										
1	SS		Coarse-Grained Soils: Poorly Graded Sand with Silt	11	31.20					65	
2	TS	596	Lime-Treated Soil	16	19.20					183	
3	GB	297	Crushed Stone	17	19.20					228	
4	EF	2	Nonwoven Geotextile	18	19.20						
5	TB	76	Open Graded, Hot Laid, Central Plant Mix	5	7.40						
5	TB	93	Open Graded, Hot Laid, Central Plant Mix	6	7.40						
6	AC	66	Hot Mixed, Hot Laid AC, Dense Graded	5	1.80						
7	AC	5	Hot Mixed, Hot Laid AC, Dense Graded	5	0.00						
7	AC	48	Hot Mixed, Hot Laid AC, Dense Graded	6	0.00						
8	AC	53	Hot Mixed, Hot Laid AC, Dense Graded								
9	AC	38	Hot Mixed, Hot Laid AC, Dense Graded								
Distress Monitoring					Cross Profile		Monitored Traffic Data (Estimates)				
DISTRESS DATE	SURVEY METHOD	FATIGUE CRACKS (m2)	LOW TEMP. CRACKS (m)	LONG CRACKS (m)	POTHOLE/ PATCH (m2)	SURVEY DATE	RUT (mm) L/R	TRAFFIC YEAR	AADT (#)	TRUCKS (%)	CALCULATED ESALS
											KESALS
08/26/1997	MANUAL				0.00						
03/17/1998	MANUAL				0.00						
08/19/1999	MANUAL				0.00						
05/10/2000	MANUAL				0.00						
01/27/2001	AUTO				0.00						
05/23/2001	MANUAL				0.00						
02/14/2002	MANUAL			8	0.00						
05/14/2002	MANUAL			17	0.00						
02/15/2003	AUTO				0.00						
11/12/2003	MANUAL			8	0.00						
11/21/2003	AUTO				0.00						
06/23/2004	MANUAL			37	0.00						
12/01/2005	MANUAL			76	0.00						
03/22/2007	MANUAL			192	0.00						



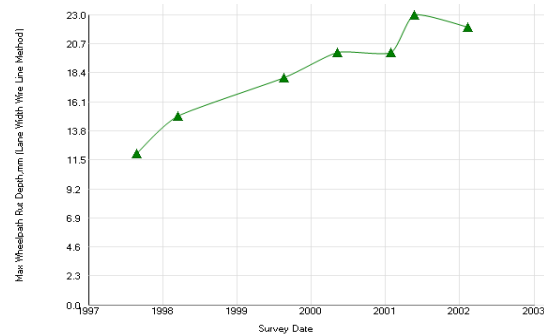
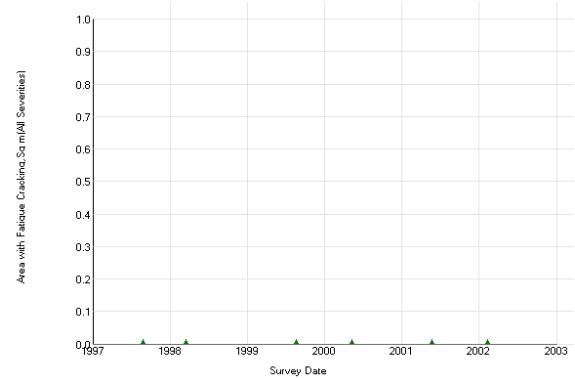
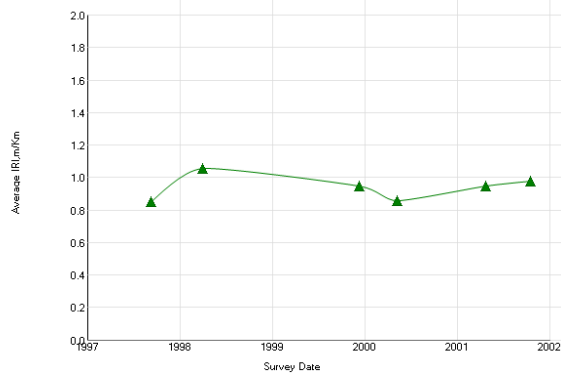
Experiment: SPS-1: Strategic Study of Structural Factors for Flexible Pavements, new/reconstructed AC pavements							Section ID: 48-0122				
Section# :			48-0122		Data :		ALL DATA				
REGION		Southern (Austin, TX, USA)		LATITUDE		26.72714		ROUTE/DIRECTION			
EXPERIMENT		SPS-1		LONGITUDE		-98.10696		NO. OF LANES			
STATE/PROVINCE		Texas		ELEVATION				CONSTRUCTED		01/01/1995	
COUNTY				MILEPOINT				OUT OF STUDY		04/29/2002	
				FUNCTIONAL CLASS							
Maintenance Rehabilitation/Rehabilitation Date					Activity Description						
06/15/2006					Manual Premix Spot Patch (hand spreading and compacting with roller) (sq. yards)						
Layer Structure					Field Values		Laboratory Results				
LAYER		THICKNESS	MATERIAL		MOISTURE	DENSITY	SUBGRADE	COMPRESS	AIR	AC	MODULUS
NUMBER	TYPE	(mm)	DESCRIPTION		CONTENT	(kg/m3)	P1	STR	VOIDS(%)	CONTENT	Mr.
1	SS		Coarse-Grained Soils: Poorly Graded Sand with Silt		8	24.80					
2	TS	508	Lime-Treated Soil		10	24.80					
3	EF	2	Nonwoven Geotextile		10	12.80					
4	TB	104	Open Graded, Hot Laid, Central Plant Mix		12	12.80					
4	TB	121	Open Graded, Hot Laid, Central Plant Mix		14	12.80					
5	TB	101	HMAC		4	4.20					
6	AC	60	Hot Mixed, Hot Laid AC, Dense Graded		5	4.20					
6	AC	71	Hot Mixed, Hot Laid AC, Dense Graded		5	2.10					
7	AC	5	Hot Mixed, Hot Laid AC, Dense Graded		5	0.00					
7	AC	43	Hot Mixed, Hot Laid AC, Dense Graded		6	0.00					
8	AC	55	Hot Mixed, Hot Laid AC, Dense Graded								
9	AC	38	Hot Mixed, Hot Laid AC, Dense Graded								
Distress Monitoring					Cross Profile		Monitored Traffic Data (Estimates)				
DISTRESS DATE	SURVEY METHOD	FATIGUE CRACKS (m2)	LOW TEMP. CRACKS (m)	LONG CRACKS (m)	POTHOLE/PATCH (m2)	SURVEY DATE	RUT (mm) L/R	TRAFFIC YEAR	AADT (#)	TRUCKS (%)	CALCULATED ESALS
											KESALS
08/26/1997	MANUAL				0.00						
03/16/1998	MANUAL				0.00						
08/18/1999	MANUAL				0.00						
05/09/2000	MANUAL				0.00						
01/27/2001	AUTO				0.00						
05/21/2001	MANUAL			2	0.00						
02/12/2002	MANUAL	7		31	0.00						
05/14/2002	MANUAL				0.00						
02/15/2003	AUTO				0.00						
11/11/2003	MANUAL				0.00						
11/21/2003	AUTO		2		0.00						
06/22/2004	MANUAL				0.00						
11/30/2005	MANUAL	2		80	0.00						
03/21/2007	MANUAL		9	227	18.60						



Experiment: SPS-1: Strategic Study of Structural Factors for Flexible Pavements, new/reconstructed AC pavements						Section ID: 48-0123						
Section#: 48-0123				Data : ALL DATA								
REGION		Southern (Austin, TX, USA)		LATITUDE		26.73063		ROUTE/DIRECTION				
EXPERIMENT		SPS-1		LONGITUDE		-98.10629		NO. OF LANES				
STATE/PROVINCE		Texas		ELEVATION				CONSTRUCTED				
COUNTY				MILEPOINT				OUT OF STUDY				
				FUNCTIONAL CLASS				01/01/1995				
								04/29/2002				
Maintenance Rehabilitation/Rehabilitation Date						Activity Description						
06/15/2006						Manual Premix Spot Patch (hand spreading and compacting with roller) (sq. yards)						
Layer Structure						Field Values		Laboratory Results				
LAYER		THICKNESS	MATERIAL			MOISTURE	DENSITY	SUBGRADE	COMPRESS	AIR	AC	MODULUS
NUMBER	TYPE	(mm)	DESCRIPTION			CONTENT (%)	(kg/m3)	P1	STR (kpa)	VOIDS(%)	CONTENT (%)	Mr.
1	SS		Coarse-Grained Soils: Poorly Graded Sand with Silt			6	31.00					65
2	TS	508	Lime-Treated Soil			10	31.00					
3	EF	2	Nonwoven Geotextile			13	31.00					
4	TB	111	Open Graded, Hot Laid, Central Plant Mix			13	19.00					
5	TB	195	HMAC			14	19.00					
5	TB	198	HMAC			16	19.00					
6	AC	78	Hot Mixed, Hot Laid AC, Dense Graded			6	6.70					
6	AC	101	Hot Mixed, Hot Laid AC, Dense Graded			7	6.70					
7	AC	0	Hot Mixed, Hot Laid AC, Dense Graded			6	2.00					
7	AC	53	Hot Mixed, Hot Laid AC, Dense Graded			6	0.00					
8	AC	53	Hot Mixed, Hot Laid AC, Dense Graded									
9	AC	38	Hot Mixed, Hot Laid AC, Dense Graded									
Distress Monitoring						Cross Profile		Monitored Traffic Data (Estimates)				
DISTRESS DATE	SURVEY METHOD	FATIGUE CRACKS (m2)	LOW TEMP. CRACKS (m)	LONG CRACKS (m)	POTHOLES/PATCH (m2)	SURVEY DATE	RUT (mm) L/R	TRAFFIC YEAR	AADT (#)	TRUCKS (%)	CALCULATED ESALS	
											KESALS	
08/25/1997	MANUAL				0.00							
03/16/1998	MANUAL				0.00							
08/18/1999	MANUAL				0.00							
05/09/2000	MANUAL				0.00							
01/27/2001	AUTO				0.00							
05/21/2001	MANUAL				0.00							
02/12/2002	MANUAL				0.00							
05/14/2002	MANUAL				0.00							
02/15/2003	AUTO			3	0.00							
11/11/2003	MANUAL				0.00							
11/21/2003	AUTO		4	1	0.00							
06/22/2004	MANUAL			14	0.00							
11/30/2005	MANUAL			131	0.00							
03/20/2007	MANUAL		3	220	23.00							

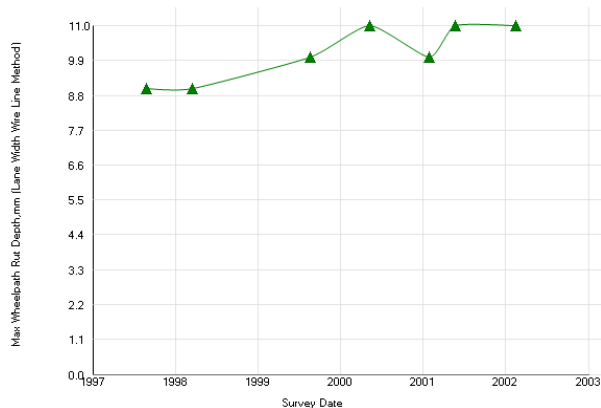
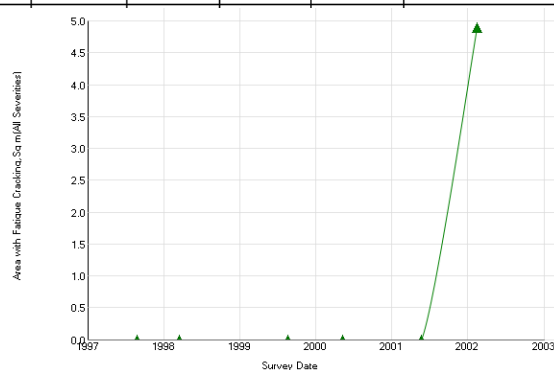
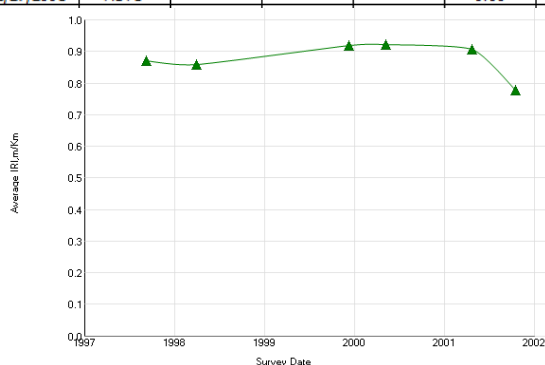


Experiment: SPS-1: Strategic Study of Structural Factors for Flexible Pavements, new/reconstructed AC pavements						Section ID: 48-0124					
Section# : 48-0124			Data : ALL DATA								
REGION		Southern (Austin, TX, USA)		LATITUDE		26.73281		ROUTE/DIRECTION			
EXPERIMENT		SPS-1		LONGITUDE		-98.10591		NO. OF LANES			
STATE/PROVINCE		Texas		ELEVATION				CONSTRUCTED			
COUNTY				MILEPOINT				OUT OF STUDY			
				FUNCTIONAL CLASS				01/01/1995			
								04/29/2002			
Maintenance Rehabilitation/Rehabilitation Date						Activity Description					
06/15/2006						Manual Premix Spot Patch (hand spreading and compacting with roller) (sq. yards)					
Layer Structure						Field Values		Laboratory Results			
LAYER		THICKNESS (mm)	MATERIAL DESCRIPTION		MOISTURE CONTENT (%)	DENSITY (kg/m3)	SUBGRADE P1	COMPRESS STR (kpa)	AIR VOIDS(%)	AC CONTENT (%)	MODULUS Mr.
NUMBER	TYPE										
1	SS		Coarse-Grained Soils: Poorly Graded Sand with Silt		6	34.30					
2	TS	508	Lime-Treated Soil		7	34.30					
3	EF	2	Nonwoven Geotextile		15	22.60					
4	TB	106	Open Graded, Hot Laid, Central Plant Mix		15	22.30					
5	TB	271	HMAC		16	22.30					
5	TB	274	HMAC		6	7.20					
6	AC	106	Hot Mixed, Hot Laid AC, Dense Graded		5	2.10					
7	AC	0	Hot Mixed, Hot Laid AC, Dense Graded		6	2.10					
7	AC	53	Hot Mixed, Hot Laid AC, Dense Graded		6	0.00					
8	AC	50	Hot Mixed, Hot Laid AC, Dense Graded		7	0.00					
9	AC	38	Hot Mixed, Hot Laid AC, Dense Graded								
Distress Monitoring						Cross Profile		Monitored Traffic Data (Estimates)			
DISTRESS DATE	SURVEY METHOD	FATIGUE CRACKS (m2)	LOW TEMP. CRACKS (m)	LONG CRACKS (m)	POTHOLES/ PATCH (m2)	SURVEY DATE	RUT (mm) L/R	TRAFFIC YEAR	AADT (#)	TRUCKS (%)	CALCULATED ESALS
											KESALS
08/25/1997	MANUAL				0.00						
03/16/1998	MANUAL				0.00						
08/18/1999	MANUAL				0.00						
05/08/2000	MANUAL				0.00						
01/27/2001	AUTO				0.00						
05/21/2001	MANUAL				0.00						
02/11/2002	MANUAL			2	0.00						
05/13/2002	MANUAL				0.00						
02/15/2003	AUTO		3		0.00						
11/10/2003	MANUAL				0.00						
11/21/2003	AUTO		5		0.00						
06/22/2004	MANUAL			22	0.00						
11/30/2005	MANUAL			42	0.00						
03/20/2007	MANUAL			82	27.70						

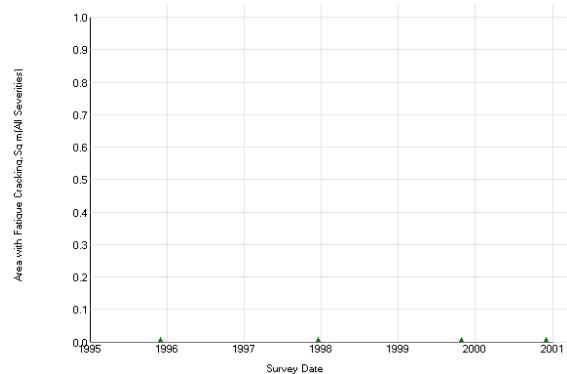
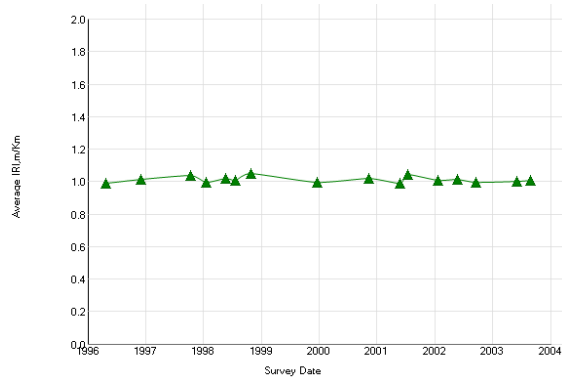


48-0118 Control

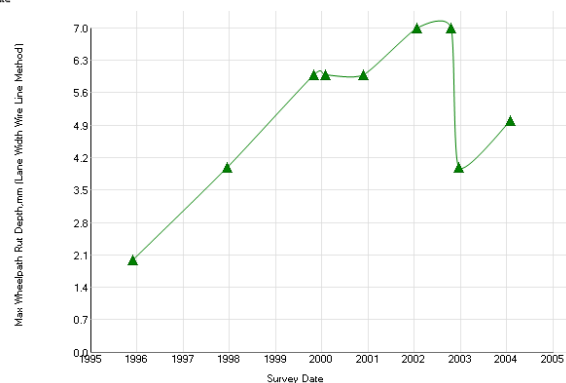
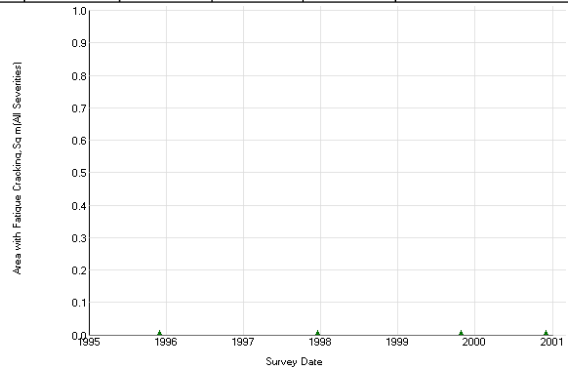
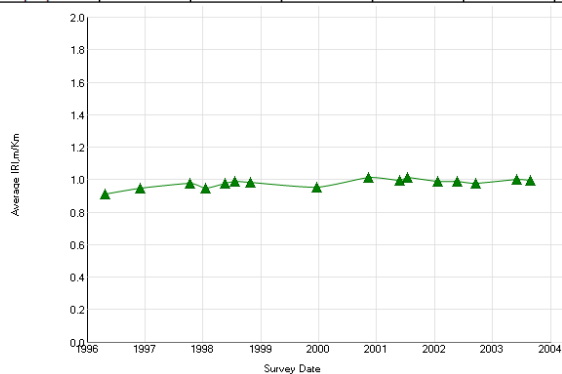
Experiment: SPS-1: Strategic Study of Structural Factors for Flexible Pavements, new/reconstructed AC pavements						Section ID: 48-0118																	
Section# :			48-0118		Data :			ALL DATA															
REGION		Southern (Austin, TX, USA)		LATITUDE		26.72278		ROUTE/DIRECTION															
EXPERIMENT		SPS-1		LONGITUDE		-98.10776		NO. OF LANES															
STATE/PROVINCE		Texas		ELEVATION				CONSTRUCTED															
COUNTY				MILEPOINT				OUT OF STUDY															
				FUNCTIONAL CLASS				01/01/1995															
								04/29/2002															
Maintenance Rehabilitation/Rehabilitation Date						Activity Description																	
06/15/2006						Manual Premix Spot Patch (hand spreading and compacting with roller) (sq. yards)																	
Layer Structure						Field Values		Laboratory Results															
LAYER		THICKNESS		MATERIAL		MOISTURE		SUBGRADE		COMPRESS		AIR		AC									
NUMBER		TYPE		DESCRIPTION		CONTENT		P1		STR		VOIDS		CONTENT									
		(mm)				(%)		(kg/m3)		(kpa)		(%)		(%)									
1		SS		Coarse-Grained Soils: Poorly Graded Sand with Silt		6		27.50															
2		TS		Lime-Treated Soil		7		27.50															
3		GB		Crushed Stone		11		15.50															
4		TB		HMAC		13		15.50															
4		TB		HMAC		14		15.50															
4		TB		HMAC		6		13.80															
5		AC		Hot Mixed, Hot Laid AC, Dense Graded		7		13.80															
5		AC		Hot Mixed, Hot Laid AC, Dense Graded		6		4.60															
6		AC		Hot Mixed, Hot Laid AC, Dense Graded		5		2.30															
6		AC		Hot Mixed, Hot Laid AC, Dense Graded		6		2.30															
7		AC		Hot Mixed, Hot Laid AC, Dense Graded		5		0.00															
7		AC		Hot Mixed, Hot Laid AC, Dense Graded		6		0.00															
8		AC		Hot Mixed, Hot Laid AC, Dense Graded																			
Distress Monitoring						Cross Profile		Monitored Traffic Data (Estimates)															
DISTRESS DATE		SURVEY METHOD		FATIGUE CRACKS		LOW TEMP. CRACKS		LONG CRACKS		POTHoles/PATCH		SURVEY DATE		RUT (mm)		TRAFFIC YEAR		AADT (#)		TRUCKS (%)		CALCULATED ESALS	
				(m2)		(m)		(m)		(m2)				L/R									
08/26/1997		MANUAL								0.00													
03/17/1998		MANUAL								0.00													
08/18/1999		MANUAL								0.00													
05/09/2000		MANUAL								0.00													
01/27/2001		AUTO								0.00													



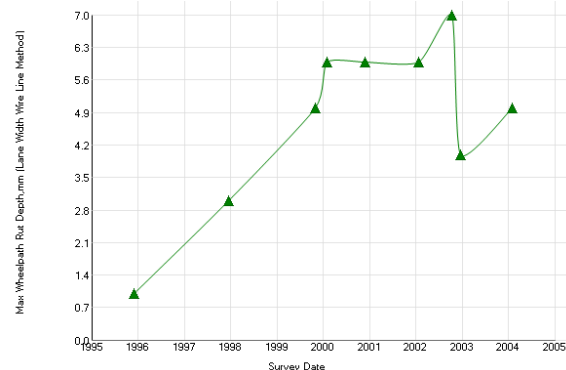
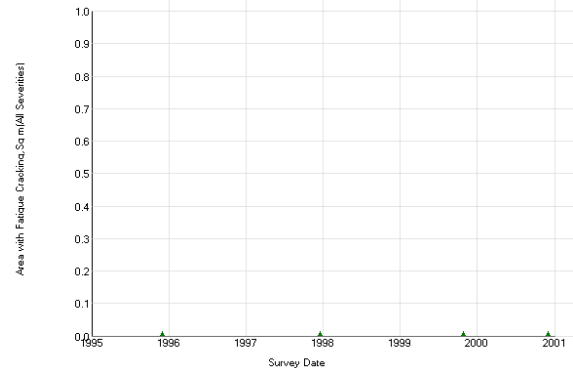
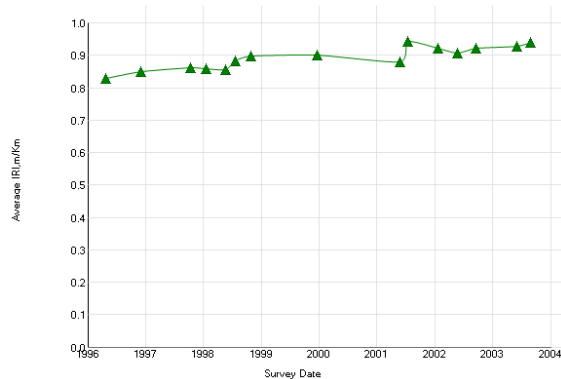
Experiment: SPS-1: Strategic Study of Structural Factors for Flexible Pavements, new/reconstructed AC pavements							Section ID: 51-0122					
Section# :			51-0122		Data :		ALL DATA					
REGION		North Atlantic (Amherst, NY, USA)			LATITUDE		36.64270		ROUTE/DIRECTION			
EXPERIMENT		SPS-1			LONGITUDE		-79.36474		NO. OF LANES			
STATE/PROVINCE		Virginia			ELEVATION				CONSTRUCTED			
COUNTY					MILEPOINT				07/26/1991			
					FUNCTIONAL CLASS							
Maintenance Rehabilitation/Rehabilitation Date							Activity Description					
10/01/2004							Strip Patching (using spreader and distributor to apply hot liquid asphalt and					
Layer Structure					Field Values		Laboratory Results					
LAYER		THICKNESS	MATERIAL			MOISTURE	DENSITY	SUBGRADE	COMPRESS	AIR	AC	MODULUS
NUMBER	TYPE	(mm)	DESCRIPTION			CONTENT	(kg/m3)	P1	STR	VOIDS(%)	CONTENT	Mr.
1	SS		Fine-Grained Soils: Sandy Silty Clay with Gravel			11	12.00					50
2	TS	152	Cement-Treated Soil			12	12.00					
3	EF	2	Nonwoven Geotextile			14	12.00					
4	TB	99	Open Graded, Hot Laid, Central Plant Mix			17	12.00					
5	TB	99	HMAC									
6	AC	55	Hot Mixed, Hot Laid AC, Dense Graded									
7	AC	43	Hot Mixed, Hot Laid AC, Dense Graded									
Distress Monitoring					Cross Profile		Monitored Traffic Data (Estimates)					
DISTRESS	SURVEY	FATIGUE	LOW TEMP.	LONG	POTHOLE/	SURVEY	RUT (mm)	TRAFFIC	AADT	TRUCKS	CALCULATED ESALS	
DATE	METHOD	CRACKS	CRACKS	CRACKS	PATCH (m2)	DATE	L/R	YEAR	(#)	(%)	KESALS	
		(m2)	(m)	(m)								
11/30/1995	MANUAL				0.00							
12/16/1997	MANUAL				0.00							
10/27/1999	MANUAL				0.00							
02/02/2000	AUTO	30	1	3	0.00							
11/29/2000	MANUAL				0.00							
01/25/2002	AUTO	124	2	262	0.00							
12/16/2002	AUTO	96	3	157	0.00							
01/29/2004	AUTO	165	1	246	0.00							
12/01/2004	MANUAL	84		145	122.00							
03/27/2007	MANUAL	122		137	122.00							
07/14/2010	MANUAL	136		152	113.00							



Experiment: SPS-1: Strategic Study of Structural Factors for Flexible Pavements, new/reconstructed AC pavements						Section ID: 51-0123						
Section# : 51-0123			Data: ALL DATA									
REGION EXPERIMENT STATE/PROVINCE COUNTY		North Atlantic (Amherst, NY, USA) SPS-1 Virginia		LATITUDE LONGITUDE ELEVATION MILEPOINT FUNCTIONAL CLASS		36.64031 -79.36480 		ROUTE/DIRECTION NO. OF LANES CONSTRUCTED OUT OF STUDY		07/26/1991		
Maintenance Rehabilitation/Rehabilitation Date						Activity Description						
10/01/2004						Strip Patching (using spreader and distributor to apply hot liquid asphalt and						
Layer Structure						Field Values		Laboratory Results				
LAYER		THICKNESS (mm)	MATERIAL DESCRIPTION			MOISTURE CONTENT (%)	DENSITY (kg/m3)	SUBGRADE P1	COMPRESS STR (kpa)	AIR VOIDS(%)	AC CONTENT (%)	MODULUS Mr.
NUMBER	TYPE											
1	SS		Fine-Grained Soils: Sandy Silt with Gravel			10	19.00					
2	TS	152	Cement-Treated Soil			12	19.00					
3	EF	2	Nonwoven Geotextile									
4	TB	104	Open Graded, Hot Laid, Central Plant Mix									
5	TB	205	HMAC									
6	AC	121	Hot Mixed, Hot Laid AC, Dense Graded									
7	AC	43	Hot Mixed, Hot Laid AC, Dense Graded									
Distress Monitoring						Cross Profile		Monitored Traffic Data (Estimates)				
DISTRESS DATE	SURVEY METHOD	FATIGUE CRACKS (m2)	LOW TEMP. CRACKS (m)	LONG CRACKS (m)	POTHOLES/ PATCH (m2)	SURVEY DATE	RUT (mm) L/R	TRAFFIC YEAR	AADT (#)	TRUCKS (%)	CALCULATED ESALS	
											KESALS	
11/30/1995	MANUAL				0.00							
12/16/1997	MANUAL				0.00							
10/27/1999	MANUAL				0.00							
02/02/2000	AUTO	52		4	0.00							
11/29/2000	MANUAL				0.00							
01/25/2002	AUTO	58	3	157	0.00							
12/16/2002	AUTO	92	1	157	0.00							
01/29/2004	AUTO	150		306	0.00							
12/02/2004	MANUAL	48		152	152.40							
03/28/2007	MANUAL	61		152	152.50							
07/14/2010	MANUAL	207		152	152.50							

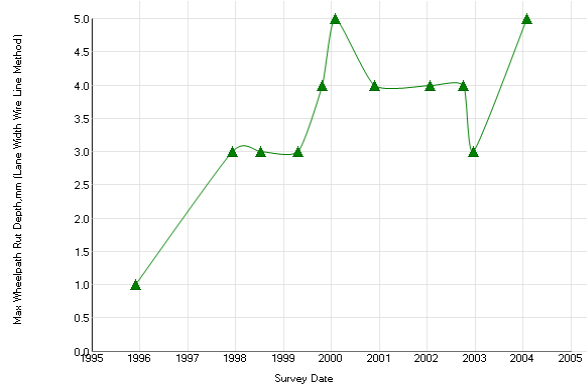
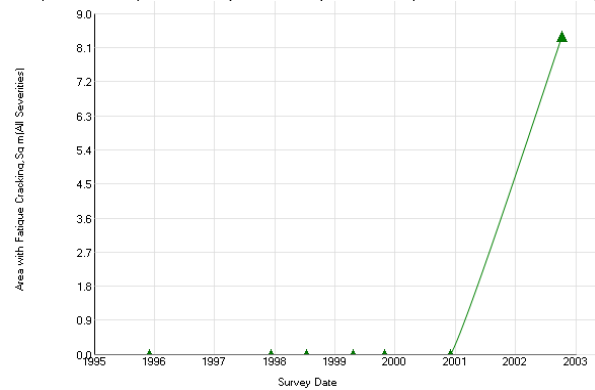
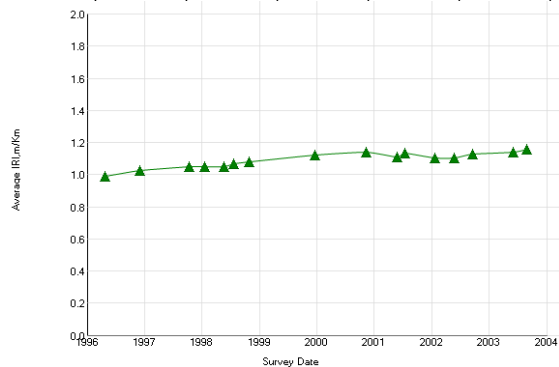


Experiment: SPS-1: Strategic Study of Structural Factors for Flexible Pavements, new/reconstructed AC pavements						Section ID: 51-0124						
Section# :			51-0124		Data :			ALL DATA				
REGION		North Atlantic (Amherst, NY, USA)			LATITUDE		36.63808		ROUTE/DIRECTION NO. OF LANES CONSTRUCTED OUT OF STUDY 07/26/1991			
EXPERIMENT		SPS-1			LONGITUDE		-79.36482					
STATE/PROVINCE		Virginia			ELEVATION							
COUNTY					MILEPOINT							
					FUNCTIONAL CLASS							
Maintenance Rehabilitation/Rehabilitation Date						Activity Description						
10/01/2004						Strip Patching (using spreader and distributor to apply hot liquid asphalt and						
Layer Structure						Field Values		Laboratory Results				
LAYER		THICKNESS		MATERIAL DESCRIPTION		MOISTURE CONTENT (%)	DENSITY (kg/m3)	SUBGRADE P1	COMPRESS STR (kpa)	AIR VOIDS(%)	AC CONTENT (%)	MODULUS Mr.
NUMBER	TYPE	(mm)										
1	SS			Fine-Grained Soils: Sandy Silt with Gravel		10	23.00					54
2	TS	152		Fine-Grained Soils		13	23.00					133
3	EF	2		Nonwoven Geotextile		14	23.00					
4	TB	86		Open Graded, Hot Laid, Central Plant Mix		19	23.00					
5	TB	317		HMAC								
6	AC	119		Hot Mixed, Hot Laid AC, Dense Graded								
7	AC	40		Hot Mixed, Hot Laid AC, Dense Graded								
Distress Monitoring						Cross Profile		Monitored Traffic Data (Estimates)				
DISTRESS DATE	SURVEY METHOD	FATIGUE CRACKS (m2)	LOW TEMP. CRACKS (m)	LONG CRACKS (m)	POTHOLE/ PATCH (m2)	SURVEY DATE	RUT (mm) L/R	TRAFFIC YEAR	AADT (#)	TRUCKS (%)	CALCULATED ESALS	
											KESALS	
11/30/1995	MANUAL				0.00							
12/16/1997	MANUAL				0.00							
10/27/1999	MANUAL				0.00							
02/02/2000	AUTO	103	1	31	0.00							
11/29/2000	MANUAL				0.00							
01/25/2002	AUTO	55		157	0.00							
12/16/2002	AUTO	86		157	0.00							
01/29/2004	AUTO	145	2	306	0.00							
12/02/2004	MANUAL	25		152	167.80							
03/28/2007	MANUAL	44		152	167.80							
07/14/2010	MANUAL	176		152	152.50							

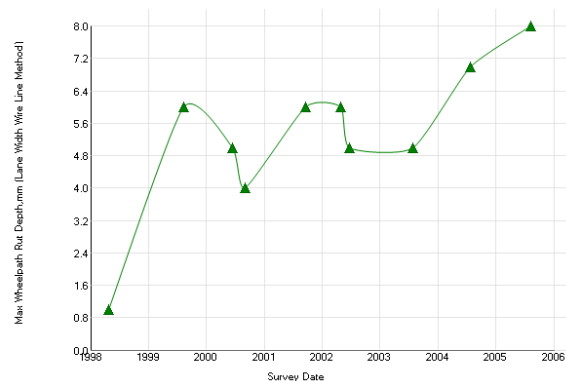
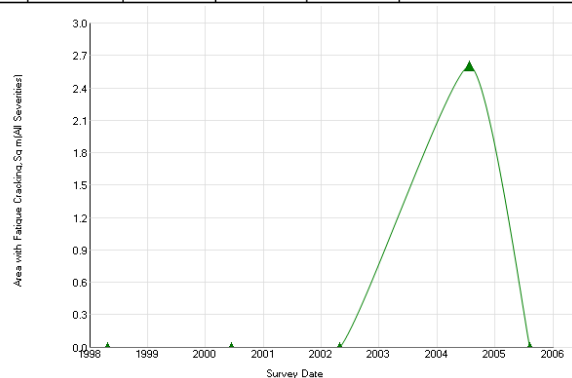
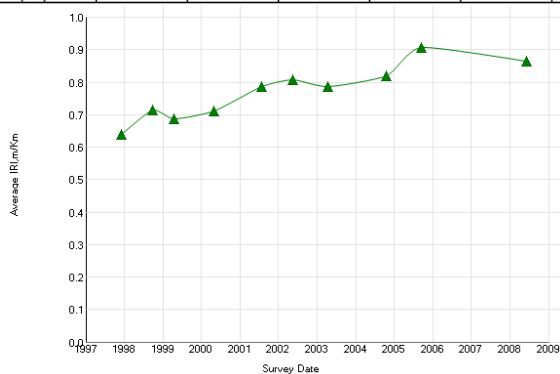


51-0121 Control

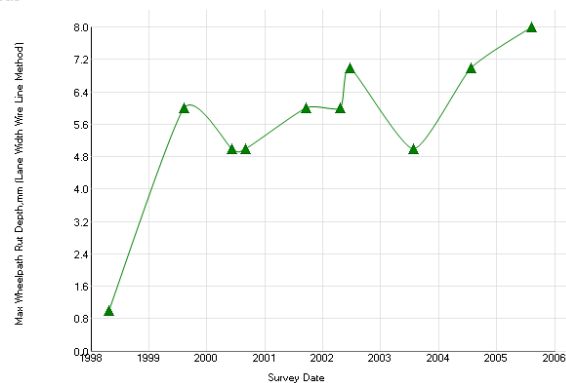
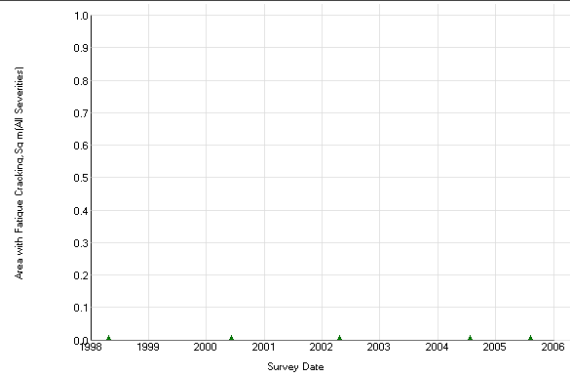
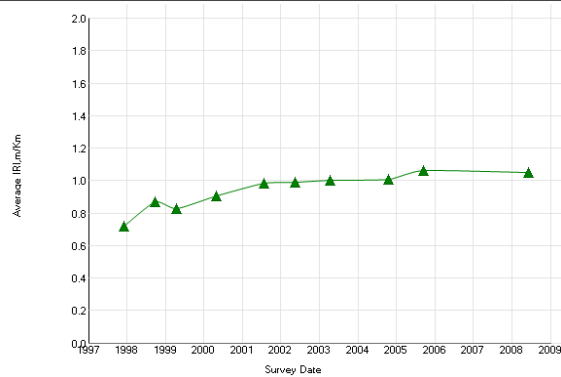
Experiment: SPS-1: Strategic Study of Structural Factors for Flexible Pavements, new/reconstructed AC pavements						Section ID: 51-0121						
Section# :			51-0121		Data :			ALL DATA				
REGION		North Atlantic (Amherst, NY, USA)			LATITUDE		36.65115		ROUTE/DIRECTION			
EXPERIMENT		SPS-1			LONGITUDE		-79.36469		NO. OF LANES			
STATE/PROVINCE		Virginia			ELEVATION				CONSTRUCTED			
COUNTY					MILEPOINT				OUT OF STUDY			
					FUNCTIONAL CLASS				07/26/1991			
Maintenance Rehabilitation/Rehabilitation Date						Activity Description						
10/01/2004						Strip Patching (using spreader and distributor to apply hot liquid asphalt and						
Layer Structure						Field Values		Laboratory Results				
LAYER		THICKNESS	MATERIAL			MOISTURE	DENSITY	SUBGRADE	COMPRESS	AIR	AC	MODULUS
NUMBER	TYPE	(mm)	DESCRIPTION			CONTENT	(kg/m3)	P1	STR	VOIDS(%)	CONTENT	Mr.
						(%)			(kpa)		(%)	
1	SS		Fine-Grained Soils: Sandy Silty Clay with Gravel			11	20.00					62
2	TS	152	Cement-Treated Soil			15	20.00					
3	GB	317	Crushed Stone			4	8.00					105
4	TB	109	Open Graded, Hot Laid, Central Plant Mix			5	8.00					
5	AC	53	Hot Mixed, Hot Laid AC, Dense Graded									
6	AC	40	Hot Mixed, Hot Laid AC, Dense Graded									
Distress Monitoring						Cross Profile		Monitored Traffic Data (Estimates)				
DISTRESS DATE	SURVEY METHOD	FATIGUE CRACKS (m2)	LOW TEMP. CRACKS (m)	LONG CRACKS (m)	POTHOLES/PATCH (m2)	SURVEY DATE	RUT (mm) L/R	TRAFFIC YEAR	AADT (#)	TRUCKS (%)	CALCULATED ESALS	
11/30/1995	MANUAL				0.00						KESALS	
12/11/1997	MANUAL				0.00							
07/14/1998	MANUAL				0.00							
04/22/1999	MANUAL				0.00							
10/26/1999	MANUAL				0.00							
02/02/2000	AUTO	2		13	0.00							
11/28/2000	MANUAL				0.00							
01/25/2002	AUTO	24	1	159	0.00							
10/05/2002	MANUAL	8			0.00							
12/16/2002	AUTO	46	1	162	0.00							
01/29/2004	AUTO	118	4	193	0.00							
12/01/2004	MANUAL	62			152.50							



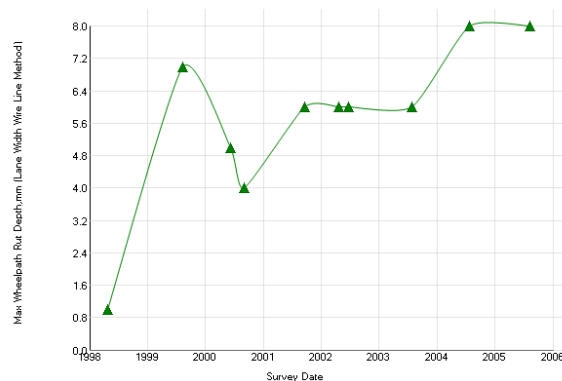
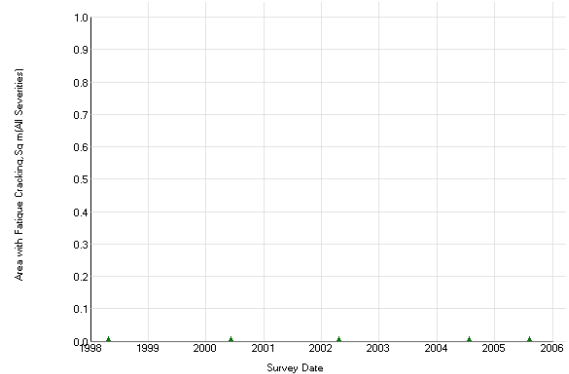
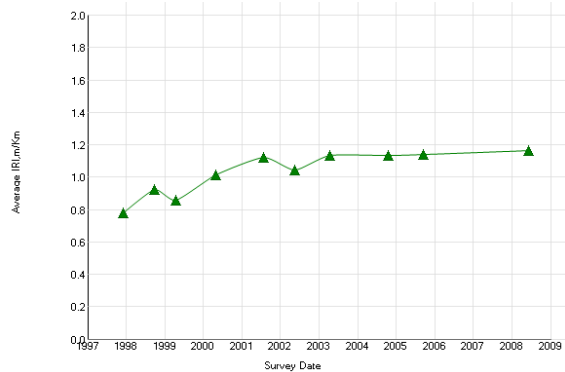
Experiment: SPS-1: Strategic Study of Structural Factors for Flexible Pavements, new/reconstructed AC pavements							Section ID: 55-0122				
Section# : 55-0122			Data : ALL DATA								
REGION		North Central (Champaign, IL, USA)		LATITUDE		44.87826		ROUTE/DIRECTION			
EXPERIMENT		SPS-1		LONGITUDE		-89.30523		NO. OF LANES			
STATE/PROVINCE		Wisconsin		ELEVATION				CONSTRUCTED		01/01/1997	
COUNTY				MILEPOINT				OUT OF STUDY		09/01/2008	
FUNCTIONAL CLASS											
Layer Structure				Field Values		Laboratory Results					
LAYER		THICKNESS (mm)	MATERIAL DESCRIPTION		MOISTURE CONTENT (%)	DENSITY (kg/m3)	SUBGRADE P 1	COMPRESS STR (kpa)	AIR VOIDS(%)	AC CONTENT (%)	MODULUS Mr.
NUMBER	TYPE										
1	SS		Coarse-Grained Soil: Silty Sand		2	16.75					83
2	GS	254	Soil-Aggregate Mixture (Predominantly Coarse-Grained)			4.00					210
3	GB	121	Crushed Rock			1.75					208
4	EF	2	Woven Geotextile			0.00					
5	TB	106	Open Graded, Hot Laid, Central Plant Mix								
6	TB	116	HMAC								
7	AC	66	Hot Mixed, Hot Laid AC, Dense Graded								
8	AC	48	Hot Mixed, Hot Laid AC, Dense Graded								
Distress Monitoring					Cross Profile		Monitored Traffic Data (Estimates)				
DISTRESS DATE	SURVEY METHOD	FATIGUE CRACKS (m2)	LOW TEMP. CRACKS (m)	LONG CRACKS (m)	POTHOLE/ PATCH (m2)	SURVEY DATE	RUT (mm) L/R	TRAFFIC YEAR	AADT (#)	TRUCKS (%)	CALCULATED ESALS
											KESALS
04/23/1998	MANUAL				0.00						
08/13/1999	AUTO				0.00						
06/12/2000	MANUAL				0.00						
09/03/2000	AUTO				0.00						
09/19/2001	AUTO			127	0.00						
04/25/2002	MANUAL			239	0.00						
06/23/2002	AUTO			153	0.00						
07/27/2003	AUTO			152	0.00						
07/21/2004	MANUAL	2		264	0.00						
08/10/2005	MANUAL			284	0.00						



Experiment: SPS-1: Strategic Study of Structural Factors for Flexible Pavements, new/reconstructed AC pavements						Section ID: 55-0123					
Section# : 55-0123				Data : ALL DATA							
REGION		North Central (Champaign, IL, USA)		LATITUDE		44.86979		ROUTE/DIRECTION			
EXPERIMENT		SPS-1		LONGITUDE		-89.29307		NO. OF LANES			
STATE/PROVINCE		Wisconsin		ELEVATION				CONSTRUCTED			
COUNTY				MILEPOINT				OUT OF STUDY			
				FUNCTIONAL CLASS				01/01/1997			
								09/01/2008			
</											

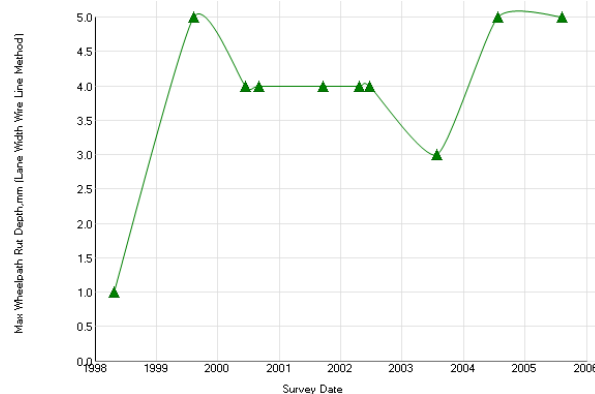
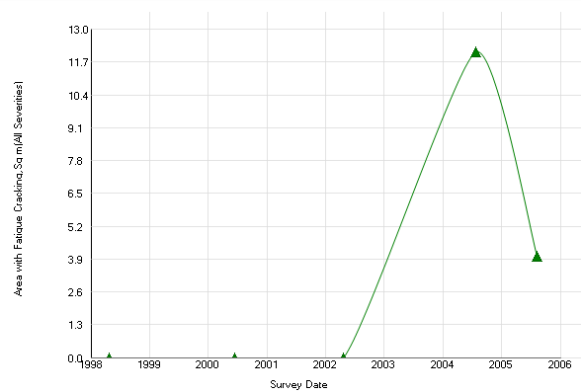
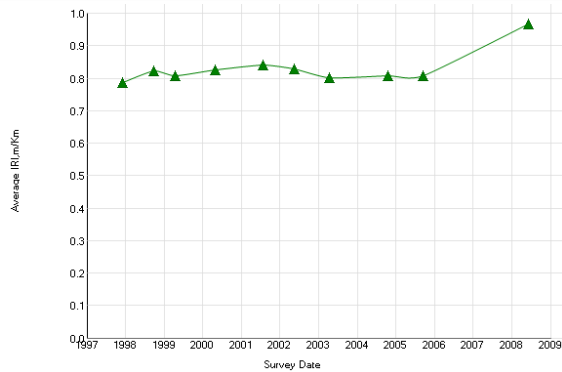


Experiment: SPS-1: Strategic Study of Structural Factors for Flexible Pavements, new/reconstructed AC pavements						Section ID: 55-0124						
Section# :			55-0124		Data :			ALL DATA				
REGION		North Central (Champaign, IL, USA)			LATITUDE		44.87118		ROUTE/DIRECTION			
EXPERIMENT		SPS-1			LONGITUDE		-89.29498		NO. OF LANES			
STATE/PROVINCE		Wisconsin			ELEVATION				CONSTRUCTED			
COUNTY					MILEPOINT				01/01/1997			
					FUNCTIONAL CLASS				09/01/2008			



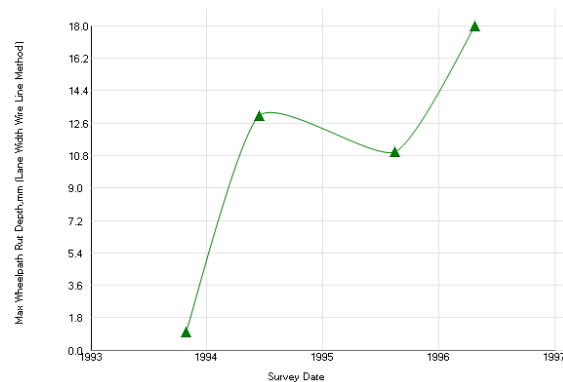
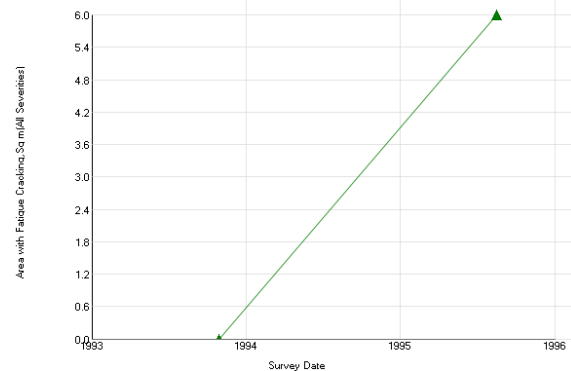
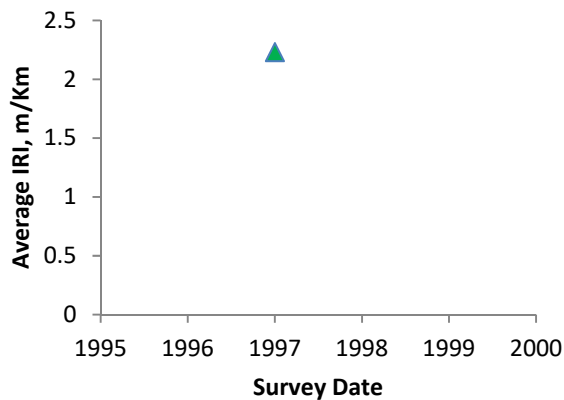
55-0121 Control

Experiment: SPS-1: Strategic Study of Structural Factors for Flexible Pavements, new/reconstructed AC pavements						Section ID: 55-0121						
Section# : 55-0121				Data : ALL DATA								
REGION		North Central (Champaign, IL, USA)			LATITUDE		44.87449		ROUTE/DIRECTION			
EXPERIMENT		SPS-1			LONGITUDE		-89.29955		NO. OF LANES			
STATE/PROVINCE		Wisconsin			ELEVATION				CONSTRUCTED			
COUNTY					MILEPOINT				01/01/1997			
					FUNCTIONAL CLASS				09/01/2008			
Layer Structure						Field Values		Laboratory Results				
LAYER		THICKNESS (mm)	MATERIAL DESCRIPTION			MOISTURE CONTENT (%)	DENSITY (kg/m3)	SUBGRADE P1	COMPRESS STR (kpa)	AIR VOIDS(%)	AC CONTENT (%)	MODULUS Mr.
NUMBER	TYPE											
1	SS		Coarse-Grained Soil: Silty Sand			4	20.00					
2	GS	172	Soil-Aggregate Mixture (Predominantly Coarse-Grained)			2	8.00					
3	GB	340	Crushed Stone			3	8.00					
4	TB	106	Open Graded, Hot Laid, Central Plant Mix				1.75					
5	AC	50	Hot Mixed, Hot Laid AC, Dense Graded				0.00					
6	AC	45	Hot Mixed, Hot Laid AC, Dense Graded									
Distress Monitoring						Cross Profile		Monitored Traffic Data (Estimates)				
DISTRESS DATE	SURVEY METHOD	FATIGUE CRACKS (m2)	LOW TEMP. CRACKS (m)	LONG CRACKS (m)	POTHOLE/ PATCH (m2)	SURVEY DATE	RUT (mm) L/R	TRAFFIC YEAR	AADT (#)	TRUCKS (%)	CALCULATED ESALS	
											KESALS	
04/23/1998	MANUAL				0.00							
08/13/1999	AUTO				0.00							
06/12/2000	MANUAL				0.00							
09/03/2000	AUTO				0.00							
09/19/2001	AUTO				0.00							
04/23/2002	MANUAL			130	0.00							
06/23/2002	AUTO				0.00							
07/27/2003	AUTO			14	0.00							
07/21/2004	MANUAL	12	1	210	0.00							
08/10/2005	MANUAL	4	6	243	0.00							



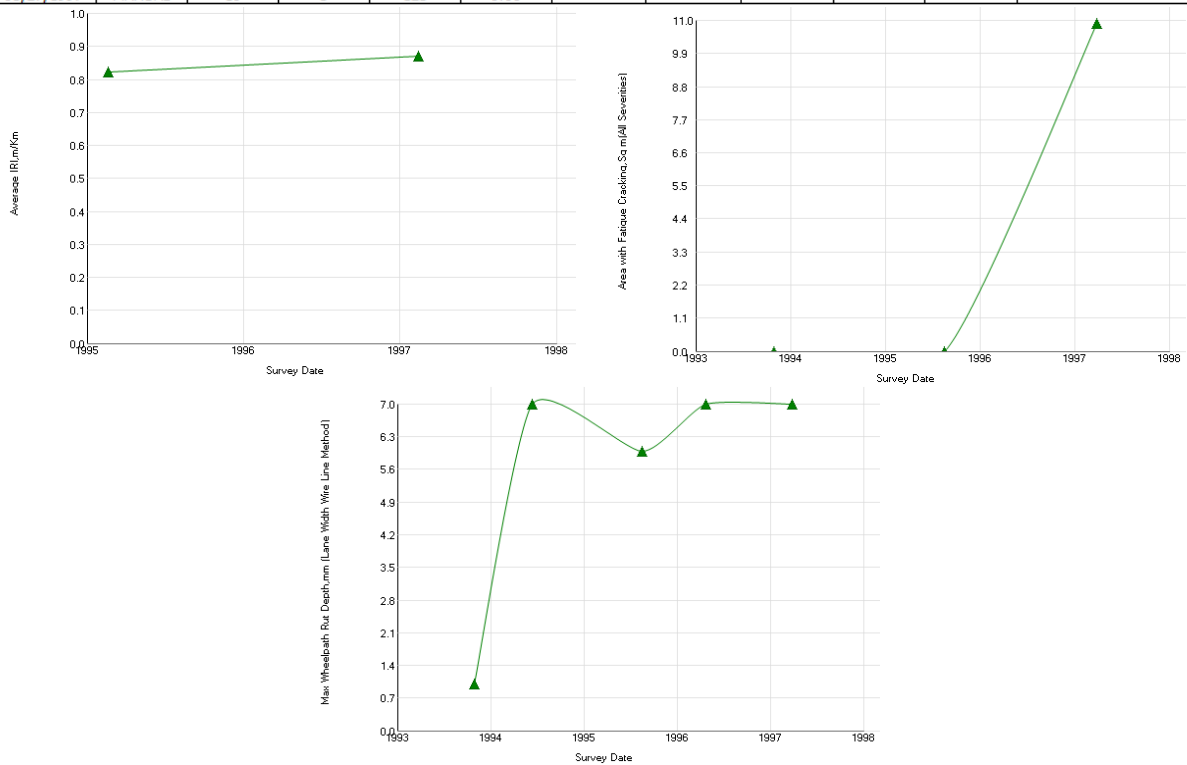
Appendix P2. LTPP Sections with Geogrid

Experiment: SPS-1: Strategic Study of Structural Factors for Flexible Pavements, new/reconstructed AC pavements							Section ID: 20-0160				
Section# :			20-0160		Data :		ALL DATA				
REGION		North Central (Champaign, IL, USA)		LATITUDE		37.61522		ROUTE/DIRECTION			
EXPERIMENT		SPS-1		LONGITUDE		-99.09271		NO. OF LANES			
STATE/PROVINCE		Kansas		ELEVATION				CONSTRUCTED		01/01/1992	
COUNTY				MILEPOINT				OUT OF STUDY		07/25/1997	
				FUNCTIONAL CLASS							
Maintenance Rehabilitation/Rehabilitation Date							Activity Description				
09/01/1996							Manual Premix Spot Patch (hand spreading and compacting with roller) (sq. yards)				
Layer Structure					Field Values		Laboratory Results				
LAYER		THICKNESS (mm)	MATERIAL DESCRIPTION	MOISTURE CONTENT (%)	DENSITY (kg/m ³)	SUBGRADE P1	COMPRESS STR (kpa)	AIR VOIDS(%)	AC CONTENT (%)	MODULUS Mr.	
NUMBER	TYPE										
1	SS		Fine-Grained Soils: Silty Clay	12	12.50						
2	TS	152	Pozzolanic-Aggregate Mixture	13	12.50						
3	EF	2	Woven Geotextile								
4	GB	177	Crushed Stone								
5	AC	101	Hot Mixed, Hot Laid AC, Dense Graded								
6	AC	40	Hot Mixed, Hot Laid AC, Dense Graded								
Distress Monitoring					Cross Profile		Monitored Traffic Data (Estimates)				
DISTRESS DATE	SURVEY METHOD	FATIGUE CRACKS (m2)	LOW TEMP. CRACKS (m)	LONG CRACKS (m)	POTHOLE/ PATCH (m2)	SURVEY DATE	RUT (mm) L/R	TRAFFIC YEAR	AADT (#)	TRUCKS (%)	CALCULATED ESALS
10/28/1993	MANUAL				0.00						
06/15/1994	AUTO				0.00						
08/17/1995	MANUAL	6		29	0.10						
04/23/1996	AUTO	14	34	79	0.00						
03/27/1997	MANUAL	147	8	130	2.30						

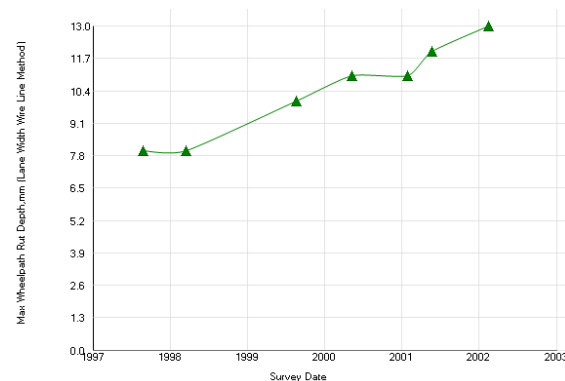
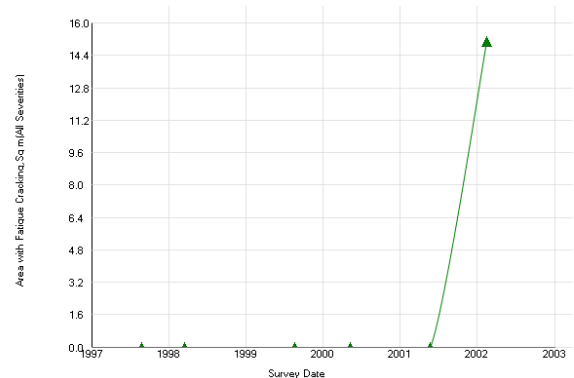
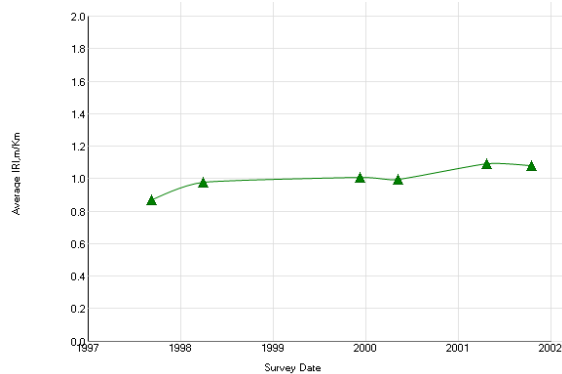


20-0161 Control

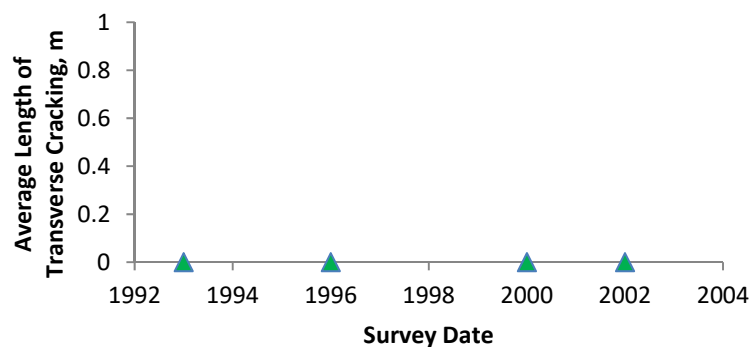
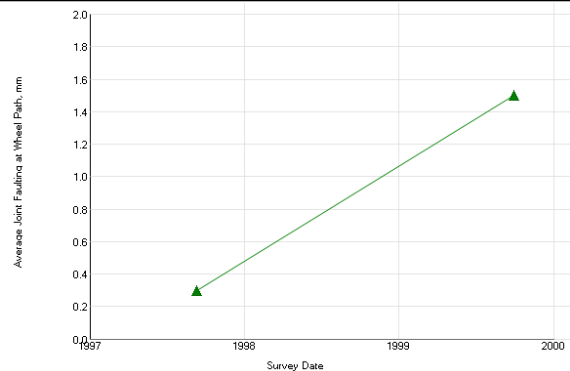
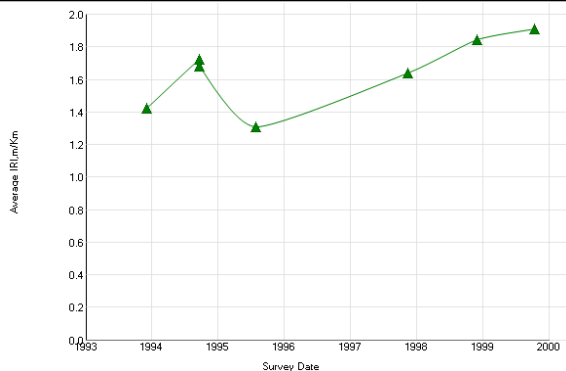
Experiment: SPS-1: Strategic Study of Structural Factors for Flexible Pavements, new/reconstructed AC pavements						Section ID: 20-0161					
Section# : 20-0161						Data : ALL DATA					
REGION		North Central (Champaign, IL, USA)		LATITUDE		37.61689		ROUTE/DIRECTION			
EXPERIMENT		SPS-1		LONGITUDE		-99.06952		NO. OF LANES			
STATE/PROVINCE		Kansas		ELEVATION				CONSTRUCTED		01/01/1992	
COUNTY				MILEPOINT				OUT OF STUDY		07/25/1997	
				FUNCTIONAL CLASS							
Layer Structure						Field Values		Laboratory Results			
LAYER		THICKNESS	MATERIAL			MOISTURE	DENSITY	SUBGRADE	COMPRESS	AIR	AC
NUMBER	TYPE	(mm)	DESCRIPTION			CONTENT	(kg/m3)	P1	STR	VOIDS(%)	CONTENT
						(%)			(kpa)		(%)
1	SS		Fine-Grained Soils: Sandy Clay			10	16.50				
2	TS	152	Pozzolanic-Aggregate Mixture								
3	GB	279	Crushed Stone								
4	AC	106	Hot Mixed, Hot Laid AC, Dense Graded								
5	AC	40	Hot Mixed, Hot Laid AC, Dense Graded								
Distress Monitoring						Cross Profile		Monitored Traffic Data (Estimates)			
DISTRESS	SURVEY	FATIGUE	LOW TEMP.	LONG	POTHOLES/	SURVEY	RUT (mm)	TRAFFIC	AADT	TRUCKS	CALCULATED
DATE	METHOD	CRACKS	CRACKS	CRACKS	PATCH (m2)	DATE	L/R	YEAR	(#)	(%)	ESALS
		(m2)	(m)	(m)							
10/28/1993	MANUAL				0.00						
06/15/1994	AUTO				0.00						
08/17/1995	MANUAL				0.00						
04/23/1996	AUTO		11	86	0.00						
03/27/1997	MANUAL	10	3	123	0.00						



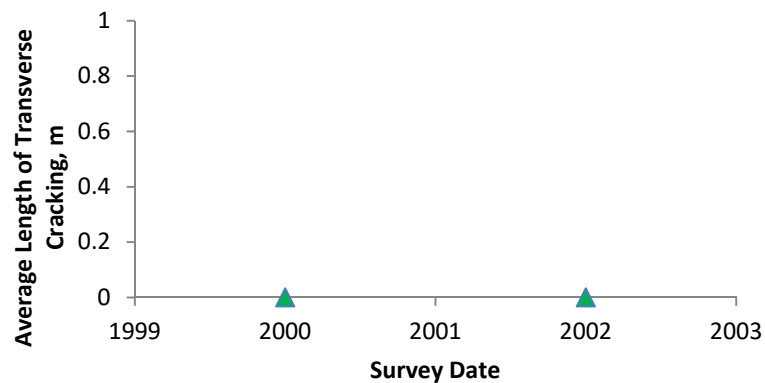
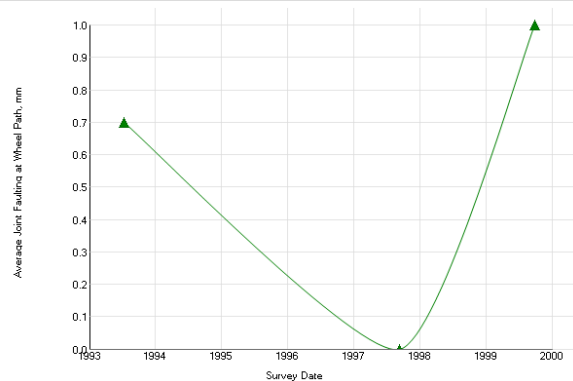
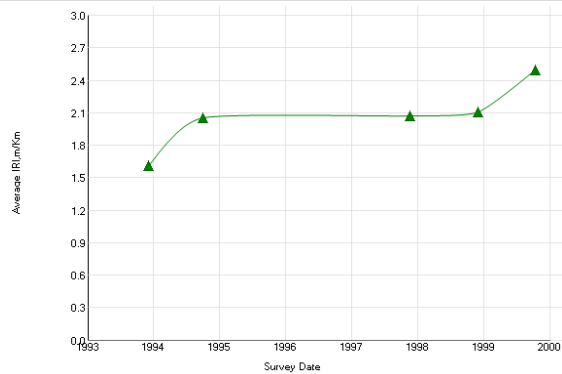
Experiment: SPS-1: Strategic Study of Structural Factors for Flexible Pavements, new/reconstructed AC pavements						Section ID: 48-0167						
REGION	Southern (Austin, TX, USA)		LATITUDE	26.71299		ROUTE/DIRECTION						
EXPERIMENT	SPS-1		LONGITUDE	-98.10946		NO. OF LANES						
STATE/PROVINCE	Texas		ELEVATION			CONSTRUCTED						
COUNTY			MILEPOINT			OUT OF STUDY						
			FUNCTIONAL CLASS			01/01/1995						
						04/29/2002						
Layer Structure					Field Values		Laboratory Results					
LAYER		THICKNESS (mm)	MATERIAL DESCRIPTION	MOISTURE CONTENT (%)	DENSITY (kg/m3)	SUBGRADE P1	COMPRESS STR (kpa)	AIR VOIDS(%)	AC CONTENT (%)	MODULUS Mr.		
NUMBER	TYPE											
1	SS		Coarse-Grained Soils: Poorly Graded Sand with Silt	11	26.70					64		
2	TS	304	Lime-Treated Soil	17	26.70							
3	EF	7	Other	18	26.70							
4	GB	330	Limerock, Caliche	21	26.70					148		
5	AC	66	Hot Mixed, Hot Laid AC, Dense Graded	15	14.70							
6	AC	0	Hot Mixed, Hot Laid AC, Dense Graded	16	14.70							
6	AC	60	Hot Mixed, Hot Laid AC, Dense Graded	16	4.80							
7	AC	55	Hot Mixed, Hot Laid AC, Dense Graded	17	4.80							
8	AC	38	Hot Mixed, Hot Laid AC, Dense Graded	18	4.80							
Distress Monitoring						Cross Profile		Monitored Traffic Data (Estimates)				
DISTRESS DATE	SURVEY METHOD	FATIGUE CRACKS (m2)	LOW TEMP. CRACKS (m)	LONG CRACKS (m)	POTHOLFS/ PATCH (m2)	SURVEY DATE	RUT (mm) L/R	TRAFFIC YEAR	AADT (#)	TRUCKS (%)	CALCULATED ESALS	
08/26/1997	MANUAL				0.00							
03/17/1998	MANUAL				0.00							
08/19/1999	MANUAL				0.00							
05/10/2000	MANUAL				0.00							
01/27/2001	AUTO			1	0.00							
05/22/2001	MANUAL			5	0.00							
02/13/2002	MANUAL	15			0.00							
05/14/2002	MANUAL			6	0.00							
02/15/2003	AUTO		5	2	0.00							
11/11/2003	MANUAL	4			0.00							
11/21/2003	AUTO		1		0.00							
06/23/2004	MANUAL	12		16	0.00							



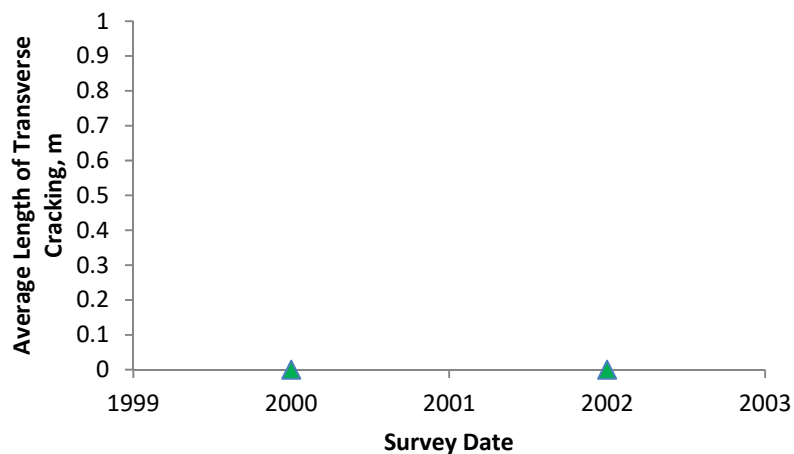
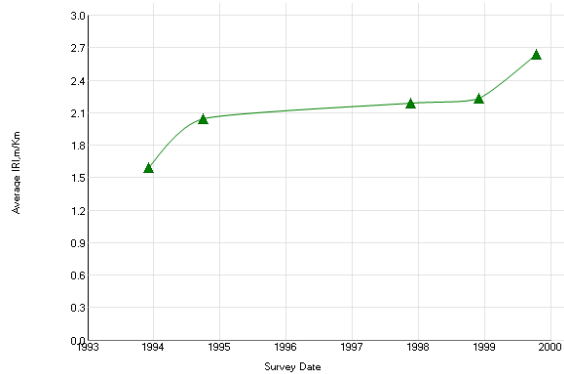
Experiment: GPS-3: Jointed Plain Concrete Pavement (JPCP)						Section ID: 49-7086							
Section# : 49-7086						Data : ALL DATA							
REGION		Western (Reno, NV, USA)		LATITUDE		40.71588		ROUTE/DIRECTION		State			
EXPERIMENT		GPS-3		LONGITUDE		-111.98435		NO. OF LANES		3			
STATE/PROVINCE		Utah		ELEVATION		4242		CONSTRUCTED		06/07/1991			
COUNTY		SALT LAKE		MILEPOINT		19		OUT OF STUDY					
				FUNCTIONAL CLASS		Urban Other Principal Arterial							
Maintenance Rehabilitation/Rehabilitation Date						Activity Description							
05/01/2001						Transverse Joint Sealing (linear ft.)							
05/01/2001						Lane-Shoulder Longitudinal Joint Sealing (linear ft.)							
Layer Structure						Field Values		Laboratory Results					
LAYER		THICKNESS	MATERIAL DESCRIPTION			MOISTURE CONTENT (%)	DENSITY (kg/m3)	SUBGRADE P1	COMPRESS STR (kpa)	AIR VOIDS(%)	AC CONTENT (%)	MODULUS Mr.	
NUMBER	TYPE	(mm)											
1	SS		Coarse-Grained Soil: Clayey Gravel with Sand									106	
2	EF	2	Woven Geotextile										
3	GS	304	Crushed Gravel										
4	EF	12	Nonwoven Geotextile										
5	GS	304	Soil-Aggregate Mixture (Predominantly Coarse-Grained)									272	
6	GS	101	Soil-Aggregate Mixture (Predominantly Coarse-Grained)										
7	TB	137	Lean Concrete										
8	PC	256	Portland Cement Concrete (JPCP)					51676	51676				
Distress Monitoring						Cross Profile		Monitored Traffic Data (Estimates)					
DISTRESS DATE	SURVEY METHOD	FATIGUE CRACKS (m2)	LOW TEMP. CRACKS (m)	LONG CRACKS (m)	POTHOLE/ PATCH (m2)	SURVEY DATE	RUT (mm) L/R	TRAFFIC YEAR	AADT (#)	TRUCKS (%)	CALCULATED ESALS		
											KESALS		
								1991	9795	288	102		
								1992	19810	448	105		
								1993	28375	175	107		
								1994	37590	175	110		
								1995	39715	298	138		
								1996	40735	310	193		
								1997	47627	1132	618		
								1998	45350	1450	224		
								1999	43010	1375	213		
								2000	40795	1304	202		
								2001	40295	861	451		
								2002	39010	834	436		
								2003	39000	598	228		
								2004	51295	642	192		



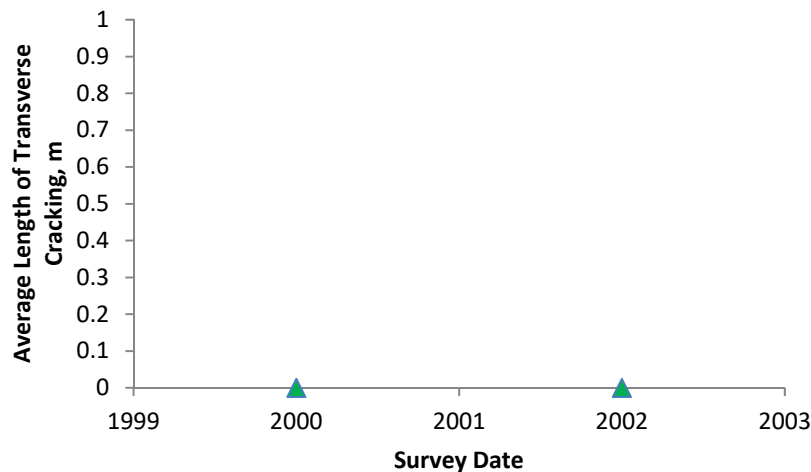
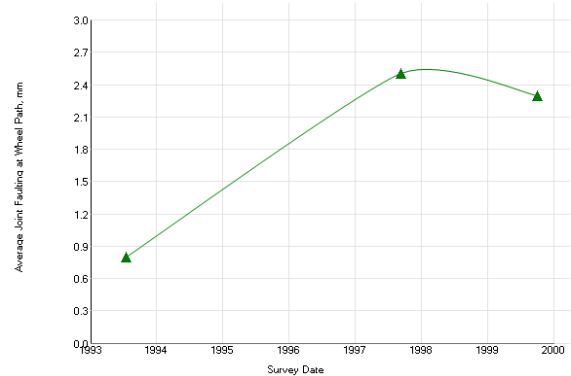
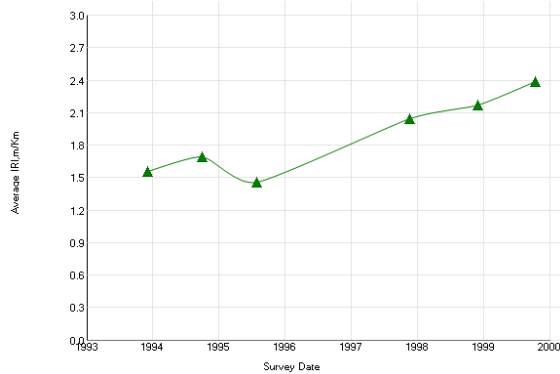
Experiment: SPS-4: Preventive Maintenance of Jointed Concrete Pavement						Section ID: 49-D410						
Section# :			49-D410			Data :			ALL DATA			
REGION		Western (Reno, NV, USA)		LATITUDE		ROUTE/DIRECTION						
EXPERIMENT		SPS-4		LONGITUDE		NO. OF LANES						
STATE/PROVINCE		Utah		ELEVATION		CONSTRUCTED				01/01/1988		
COUNTY				MILEPOINT		OUT OF STUDY				09/15/2002		
				FUNCTIONAL CLASS								
Maintenance Rehabilitation/Rehabilitation Date						Activity Description						
05/19/1992						Transverse Joint Sealing (linear ft.)						
05/19/1992						Lane-Shoulder Longitudinal Joint Sealing (linear ft.)						
05/01/2001						Transverse Joint Sealing (linear ft.)						
05/01/2001						Lane-Shoulder Longitudinal Joint Sealing (linear ft.)						
Layer Structure						Field Values		Laboratory Results				
LAYER		THICKNESS	MATERIAL			MOISTURE	DENSITY	SUBGRADE	COMPRESS	AIR	AC	MODULUS
NUMBER	TYPE	(mm)	DESCRIPTION			CONTENT (%)	(kg/m3)	P1	STR (kpa)	VOIDS(%)	CONTENT (%)	Mr.
1	SS		Coarse-Grained Soil: Clayey Gravel with Sand									
2	EF	2	Woven Geotextile									
3	GS	304	Crushed Gravel									
4	EF	12	Woven Geotextile									
5	GS	304	Soil-Aggregate Mixture (Predominantly Coarse-Grained)									
6	GS	101	Soil-Aggregate Mixture (Predominantly Coarse-Grained)									
7	TB	137	Lean Concrete									
8	PC	256	Portland Cement Concrete (JPCP)									
Distress Monitoring						Cross Profile		Monitored Traffic Data (Estimates)				
DISTRESS DATE	SURVEY METHOD	FATIGUE CRACKS (m2)	LOW TEMP. CRACKS (m)	LONG CRACKS (m)	POTHOLE/ PATCH (m2)	SURVEY DATE	RUT (mm) L/R	TRAFFIC YEAR	AADT (#)	TRUCKS (%)	CALCULATED ESALS	
											KESALS	



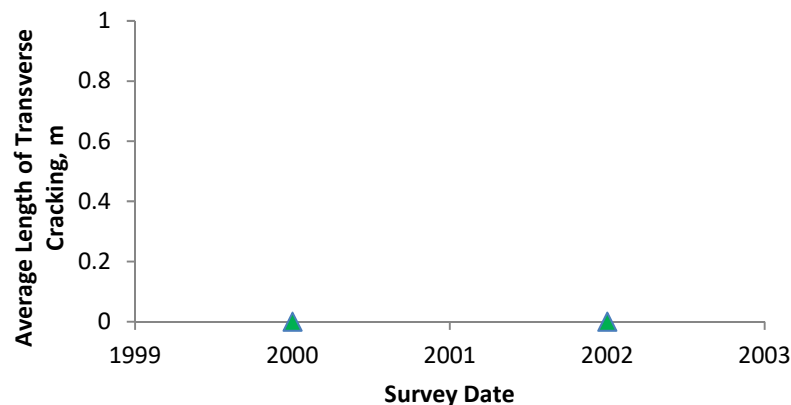
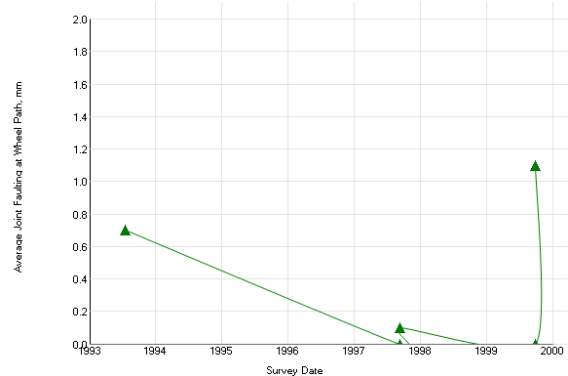
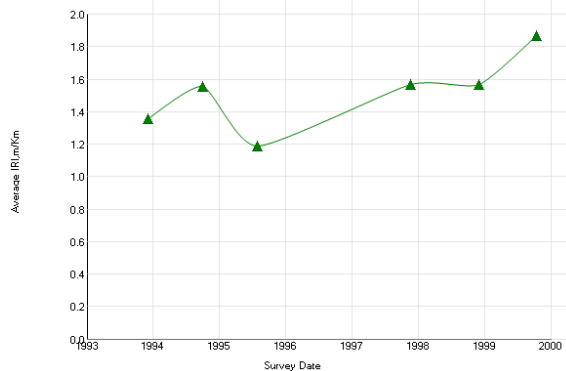
Experiment: SPS-4: Preventive Maintenance of Jointed Concrete Pavement							Section ID: 49-D430					
Section# :			49-D430		Data :		ALL DATA					
REGION		Western (Reno, NV, USA)			LATITUDE		ROUTE/DIRECTION					
EXPERIMENT		SPS-4			LONGITUDE		NO. OF LANES					
STATE/PROVINCE		Utah			ELEVATION		CONSTRUCTED					
COUNTY					MILEPOINT		OUT OF STUDY					
					FUNCTIONAL CLASS		01/01/1988					
							09/15/2002					
Maintenance Rehabilitation/Rehabilitation Date							Activity Description					
05/01/2001							Transverse Joint Sealing (linear ft.)					
05/01/2001							Lane-Shoulder Longitudinal Joint Sealing (linear ft.)					
Layer Structure							Field Values		Laboratory Results			
LAYER		THICKNESS (mm)	MATERIAL DESCRIPTION		MOISTURE CONTENT (%)	DENSITY (kg/m3)	SUBGRADE P1	COMPRESS STR (kpa)	AIR VOIDS(%)	AC CONTENT (%)	MODULUS Mr.	
NUMBER	TYPE											
1	SS		Coarse-Grained Soil: Clayey Gravel with Sand									
2	EF	2	Woven Geotextile									
3	GS	304	Crushed Gravel									
4	EF	12	Woven Geotextile									
5	GS	304	Soil-Aggregate Mixture (Predominantly Coarse-Grained)									
6	GS	101	Soil-Aggregate Mixture (Predominantly Coarse-Grained)									
7	TB	137	Lean Concrete									
8	PC	256	Portland Cement Concrete (JPCP)									
Distress Monitoring							Cross Profile		Monitored Traffic Data (Estimates)			
DISTRESS DATE	SURVEY METHOD	FATIGUE CRACKS (m2)	LOW TEMP. CRACKS (m)	LONG CRACKS (m)	POTHoles/ PATCH (m2)	SURVEY DATE	RUT (mm) L/R	TRAFFIC YEAR	AADT (#)	TRUCKS (%)	CALCULATED ESALS	
											KESALS	



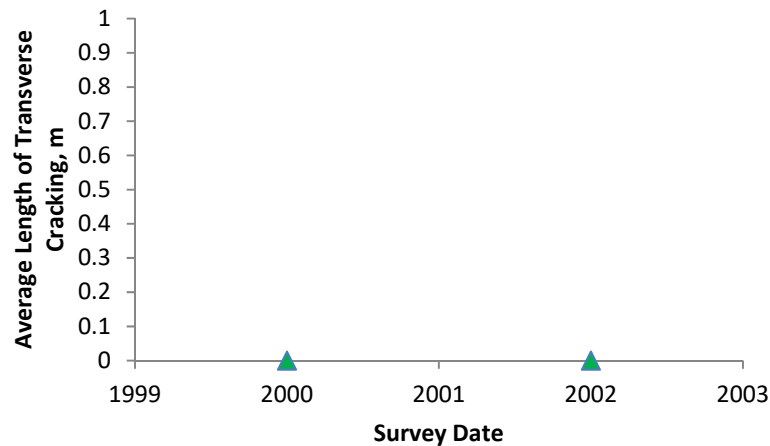
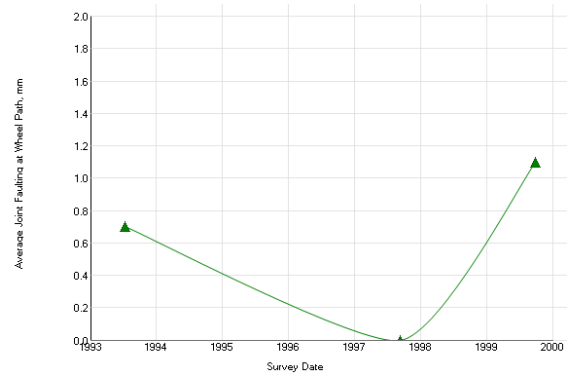
Experiment: SPS-4: Preventive Maintenance of Jointed Concrete Pavement							Section ID: 49-D431					
Section# : 49-D431			Data : ALL DATA									
REGION		Western (Reno, NV, USA)		LATITUDE		ROUTE/DIRECTION						
EXPERIMENT		SPS-4		LONGITUDE		NO. OF LANES						
STATE/PROVINCE		Utah		ELEVATION		CONSTRUCTED		01/01/1988				
COUNTY				MILEPOINT		OUT OF STUDY		09/15/2002				
				FUNCTIONAL CLASS								
Maintenance Rehabilitation/Rehabilitation Date							Activity Description					
05/01/2001							Transverse Joint Sealing (linear ft.)					
05/01/2001							Lane-Shoulder Longitudinal Joint Sealing (linear ft.)					
Layer Structure							Field Values		Laboratory Results			
LAYER		THICKNESS	MATERIAL			MOISTURE	DENSITY	SUBGRADE	COMPRESS	AIR	AC	MODULUS
NUMBER	TYPE	(mm)	DESCRIPTION			CONTENT (%)	(kg/m3)	P1	STR (kpa)	VOIDS(%)	CONTENT (%)	Mr.
1	SS		Coarse-Grained Soil: Clayey Gravel with Sand									
2	EF	2	Woven Geotextile									
3	GS	304	Crushed Gravel									
4	EF	12	Woven Geotextile									
5	GS	304	Soil-Aggregate Mixture (Predominantly Coarse-Grained)									
6	GS	101	Soil-Aggregate Mixture (Predominantly Coarse-Grained)									
7	TB	137	Lean Concrete									
8	PC	256	Portland Cement Concrete (JPCP)									
Distress Monitoring							Cross Profile		Monitored Traffic Data (Estimates)			
DISTRESS DATE	SURVEY METHOD	FATIGUE CRACKS (m2)	LOW TEMP. CRACKS (m)	LONG CRACKS (m)	POTHOLE/ PATCH (m2)	SURVEY DATE	RUT (mm) L/R	TRAFFIC YEAR	AADT (#)	TRUCKS (%)	CALCULATED ESALS	
											KESALS	



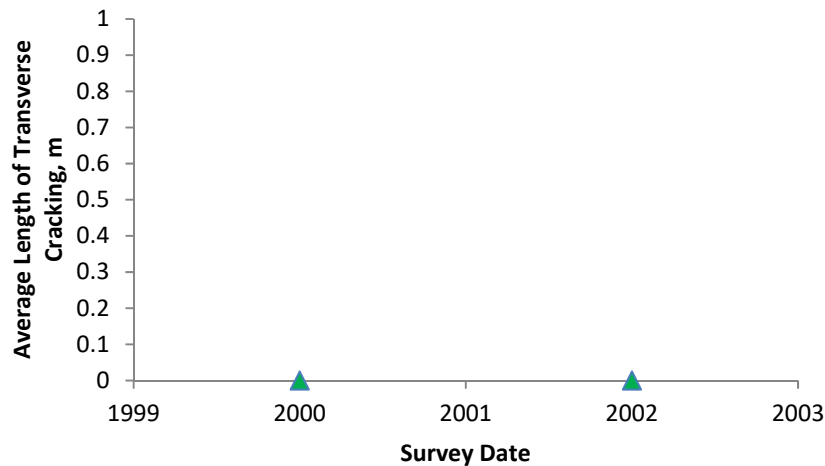
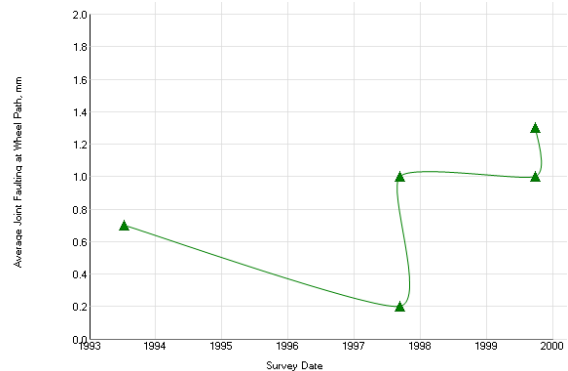
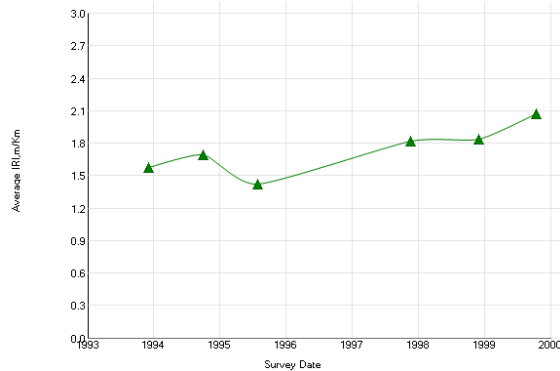
Experiment: SPS-4: Preventive Maintenance of Jointed Concrete Pavement							Section ID: 49-D440				
Section# : 49-D440			Data : ALL DATA								
REGION		Western (Reno, NV, USA)		LATITUDE		ROUTE/DIRECTION					
EXPERIMENT		SPS-4		LONGITUDE		NO. OF LANES					
STATE/PROVINCE		Utah		ELEVATION		CONSTRUCTED					
COUNTY				MILEPOINT		01/01/1988					
				FUNCTIONAL CLASS		09/15/2002					
Maintenance Rehabilitation/Rehabilitation Date							Activity Description				
05/19/1992							Transverse Joint Sealing (linear ft.)				
05/19/1992							Lane-Shoulder Longitudinal Joint Sealing (linear ft.)				
05/01/2001							Transverse Joint Sealing (linear ft.)				
05/01/2001							Lane-Shoulder Longitudinal Joint Sealing (linear ft.)				
Layer Structure				Field Values		Laboratory Results					
LAYER		THICKNESS (mm)	MATERIAL DESCRIPTION		MOISTURE CONTENT (%)	DENSITY (kg/m3)	SUBGRADE P1	COMPRESS STR (kpa)	AIR VOIDS(%)	AC CONTENT (%)	MODULUS Mr.
NUMBER	TYPE										
1	SS		Coarse-Grained Soil: Clayey Gravel with Sand								
2	EF	2	Woven Geotextile								
3	GS	304	Crushed Gravel								
4	EF	12	Woven Geotextile								
5	GS	304	Soil-Aggregate Mixture (Predominantly Coarse-Grained)								
6	GS	101	Soil-Aggregate Mixture (Predominantly Coarse-Grained)								
7	TB	137	Lean Concrete								
8	PC	256	Portland Cement Concrete (JPCP)								
Distress Monitoring					Cross Profile		Monitored Traffic Data (Estimates)				
DISTRESS DATE	SURVEY METHOD	FATIGUE CRACKS (m2)	LOW TEMP. CRACKS (m)	LONG CRACKS (m)	POTHOLE/ PATCH (m2)	SURVEY DATE	RUT (mm) L/R	TRAFFIC YEAR	AADT (#)	TRUCKS (%)	CALCULATED ESALS
											KESALS



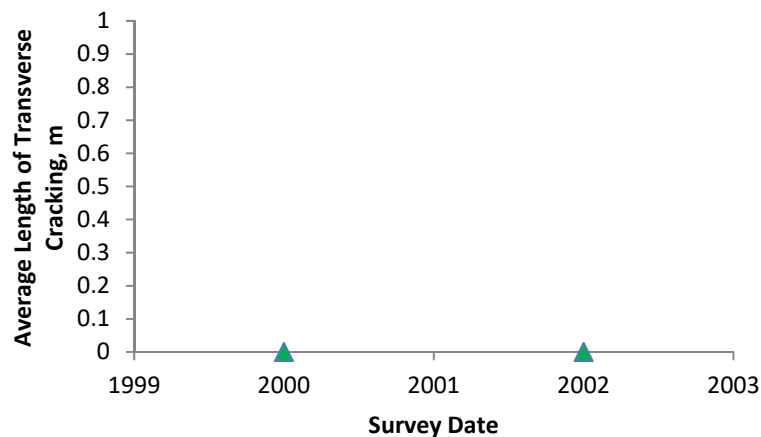
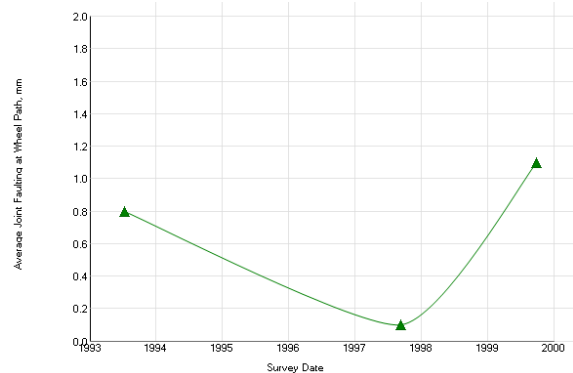
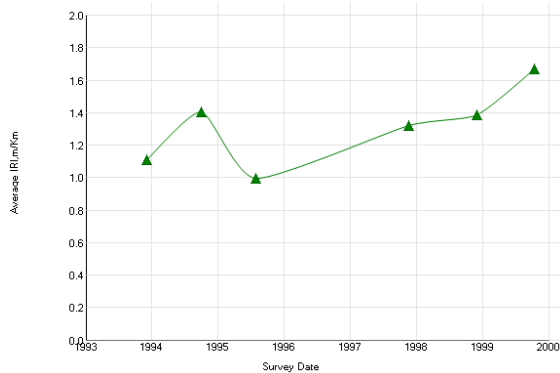
Experiment: SPS-4: Preventive Maintenance of Jointed Concrete Pavement							Section ID: 49-D441						
Section# : 49-D441				Data : ALL DATA									
REGION		Western (Reno, NV, USA)			LATITUDE		ROUTE/DIRECTION						
EXPERIMENT		SPS-4			LONGITUDE		NO. OF LANES						
STATE/PROVINCE		Utah			ELEVATION		CONSTRUCTED 01/01/1988						
COUNTY					MILEPOINT		OUT OF STUDY 09/15/2002						
					FUNCTIONAL CLASS								
Maintenance Rehabilitation/Rehabilitation Date							Activity Description						
05/19/1992							Transverse Joint Sealing (linear ft.)						
05/19/1992							Lane-Shoulder Longitudinal Joint Sealing (linear ft.)						
05/01/2001							Transverse Joint Sealing (linear ft.)						
05/01/2001							Lane-Shoulder Longitudinal Joint Sealing (linear ft.)						
Layer Structure							Field Values		Laboratory Results				
LAYER		THICKNESS (mm)	MATERIAL DESCRIPTION			MOISTURE CONTENT (%)	DENSITY (kg/m3)	SUBGRADE P1	COMPRESS STR (kpa)	AIR VOIDS(%)	AC CONTENT (%)	MODULUS Mr.	
NUMBER	TYPE												
1	SS		Coarse-Grained Soil: Clayey Gravel with Sand										
2	EF	2	Woven Geotextile										
3	GS	304	Crushed Gravel										
4	EF	12	Woven Geotextile										
5	GS	304	Soil-Aggregate Mixture (Predominantly Coarse-Grained)										
6	GS	101	Soil-Aggregate Mixture (Predominantly Coarse-Grained)										
7	TB	137	Lean Concrete										
8	PC	256	Portland Cement Concrete (JPCP)										
Distress Monitoring							Cross Profile		Monitored Traffic Data (Estimates)				
DISTRESS DATE	SURVEY METHOD	FATIGUE CRACKS (m2)	LOW TEMP. CRACKS (m)	LONG CRACKS (m)	POTHOLE/ PATCH (m2)	SURVEY DATE	RUT (mm) L/R	TRAFFIC YEAR	AADT (#)	TRUCKS (%)	CALCULATED ESALS		
											KESALS		



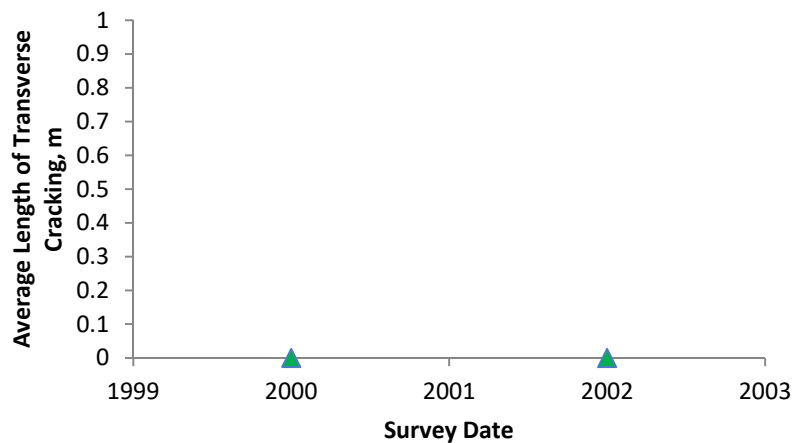
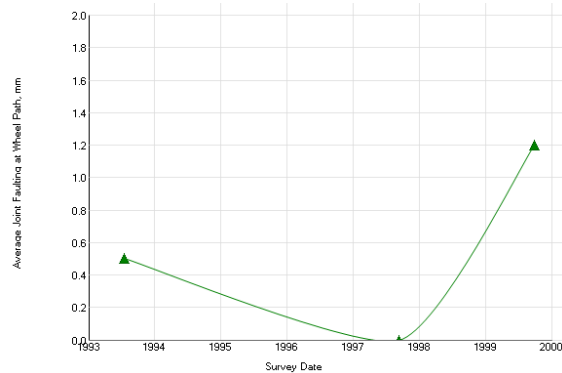
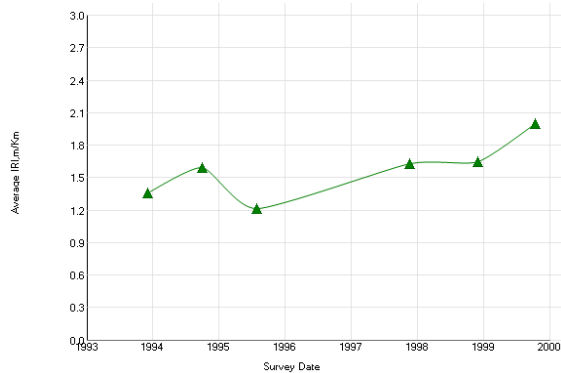
Experiment: SPS-4: Preventive Maintenance of Jointed Concrete Pavement						Section ID: 49-D443							
Section# :			49-D443		Data :			ALL DATA					
REGION		Western (Reno, NV, USA)			LATITUDE		ROUTE/DIRECTION						
EXPERIMENT		SPS-4			LONGITUDE		NO. OF LANES						
STATE/PROVINCE		Utah			ELEVATION		CONSTRUCTED						
COUNTY					MILEPOINT		01/01/1988						
					FUNCTIONAL CLASS		09/15/2002						
Maintenance Rehabilitation/Rehabilitation Date							Activity Description						
05/19/1992							Transverse Joint Sealing (linear ft.)						
05/19/1992							Lane-Shoulder Longitudinal Joint Sealing (linear ft.)						
05/01/2001							Transverse Joint Sealing (linear ft.)						
05/01/2001							Lane-Shoulder Longitudinal Joint Sealing (linear ft.)						
Layer Structure					Field Values		Laboratory Results						
LAYER		THICKNESS (mm)	MATERIAL DESCRIPTION			MOISTURE CONTENT (%)	DENSITY (kg/m3)	SUBGRADE P1	COMPRESS STR (kpa)	AIR VOIDS(%)	AC CONTENT (%)	MODULUS Mr.	
NUMBER	TYPE												
1	SS		Coarse-Grained Soil: Clayey Gravel with Sand										
2	EF	2	Woven Geotextile										
3	GS	304	Crushed Gravel										
4	EF	12	Woven Geotextile										
5	GS	304	Soil-Aggregate Mixture (Predominantly Coarse-Grained)										
6	GS	101	Soil-Aggregate Mixture (Predominantly Coarse-Grained)										
7	TB	137	Lean Concrete										
8	PC	256	Portland Cement Concrete (JPCP)										
Distress Monitoring						Cross Profile		Monitored Traffic Data (Estimates)					
DISTRESS DATE	SURVEY METHOD	FATIGUE CRACKS (m2)	LOW TEMP. CRACKS (m)	LONG CRACKS (m)	POTHOLE/ PATCH (m2)	SURVEY DATE	RUT (mm) L/R	TRAFFIC YEAR	AADT (#)	TRUCKS (%)	CALCULATED ESALS		
											KESALS		



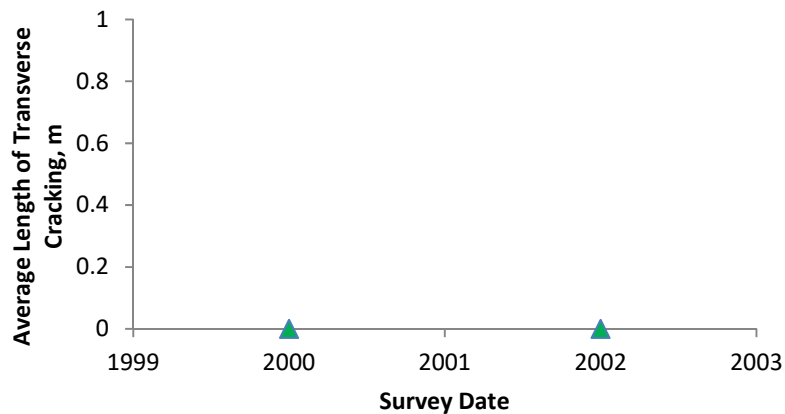
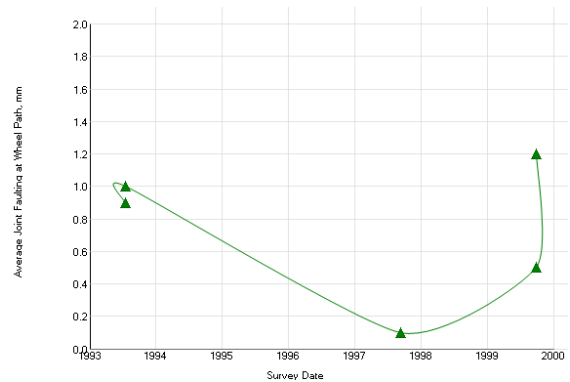
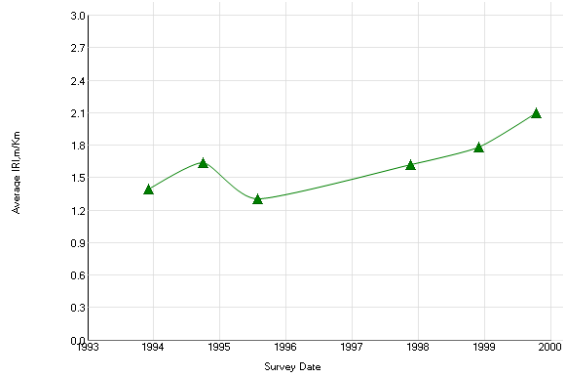
Experiment: SPS-4: Preventive Maintenance of Jointed Concrete Pavement							Section ID: 49-D444					
Section# : 49-D444				Data : ALL DATA								
REGION		Western (Reno, NV, USA)		LATITUDE			ROUTE/DIRECTION					
EXPERIMENT		SPS-4		LONGITUDE			NO. OF LANES					
STATE/PROVINCE		Utah		ELEVATION			CONSTRUCTED 01/01/1988					
COUNTY				MILEPOINT			OUT OF STUDY 09/15/2002					
				FUNCTIONAL CLASS								
Maintenance Rehabilitation/Rehabilitation Date							Activity Description					
05/27/1992							Transverse Joint Sealing (linear ft.)					
05/27/1992							Lane-Shoulder Longitudinal Joint Sealing (linear ft.)					
05/01/2001							Transverse Joint Sealing (linear ft.)					
05/01/2001							Lane-Shoulder Longitudinal Joint Sealing (linear ft.)					
Layer Structure				Field Values			Laboratory Results					
LAYER		THICKNESS	MATERIAL DESCRIPTION			MOISTURE CONTENT	DENSITY	SUBGRADE	COMPRESS STR	AIR VOIDS	AC CONTENT	MODULUS
NUMBER	TYPE	(mm)				(%)	(kg/m3)	P1	(kpa)	(%)	(%)	Mr.
1	SS		Coarse-Grained Soil: Clayey Gravel with Sand									
2	EF	2	Woven Geotextile									
3	GS	304	Crushed Gravel									
4	EF	12	Woven Geotextile									
5	GS	304	Soil-Aggregate Mixture (Predominantly Coarse-Grained)									
6	GS	101	Soil-Aggregate Mixture (Predominantly Coarse-Grained)									
7	TB	137	Lean Concrete									
8	PC	256	Portland Cement Concrete (JPCP)									
Distress Monitoring						Cross Profile		Monitored Traffic Data (Estimates)				
DISTRESS DATE	SURVEY METHOD	FATIGUE CRACKS (m2)	LOW TEMP. CRACKS (m)	LONG CRACKS (m)	POTHOLFS/PATCH (m2)	SURVEY DATE	RUT (mm) L/R	TRAFFIC YEAR	AADT (#)	TRUCKS (%)	CALCULATED ESALS	
											KESALS	



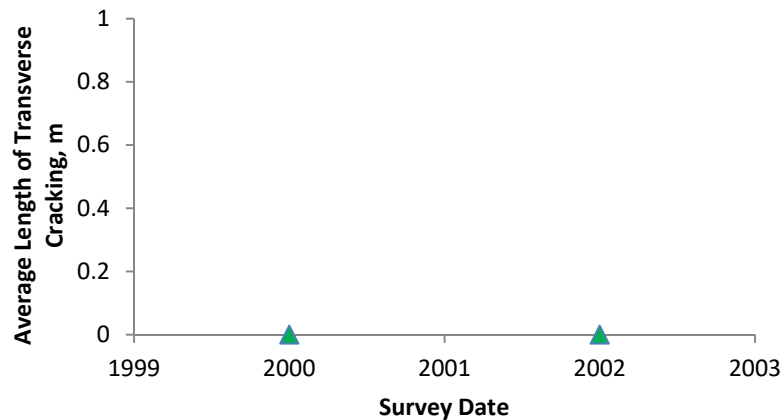
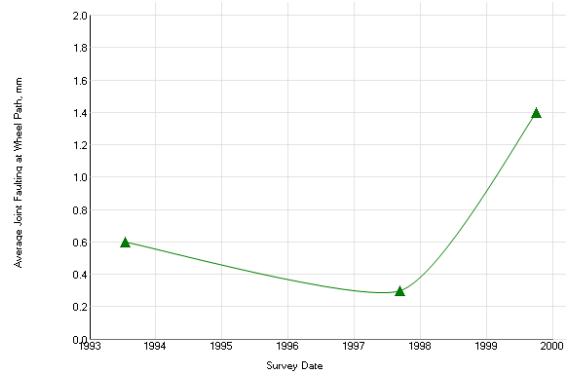
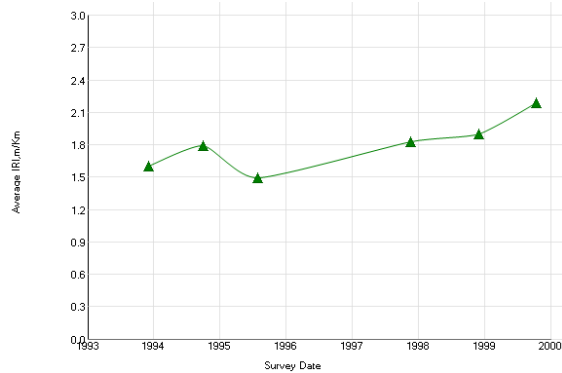
Experiment: SPS-4: Preventive Maintenance of Jointed Concrete Pavement						Section ID: 49-D445							
Section# :			49-D445		Data :			ALL DATA					
REGION		Western (Reno, NV, USA)			LATITUDE		ROUTE/DIRECTION						
EXPERIMENT		SPS-4			LONGITUDE		NO. OF LANES						
STATE/PROVINCE		Utah			ELEVATION		CONSTRUCTED			01/01/1988			
COUNTY					MILEPOINT		OUT OF STUDY			09/15/2002			
					FUNCTIONAL CLASS								
Maintenance Rehabilitation/Rehabilitation Date						Activity Description							
05/22/1992						Transverse Joint Sealing (linear ft.)							
05/22/1992						Lane-Shoulder Longitudinal Joint Sealing (linear ft.)							
05/01/2001						Transverse Joint Sealing (linear ft.)							
05/01/2001						Lane-Shoulder Longitudinal Joint Sealing (linear ft.)							
Layer Structure						Field Values		Laboratory Results					
LAYER		THICKNESS	MATERIAL DESCRIPTION			MOISTURE CONTENT (%)	DENSITY (kg/m3)	SUBGRADE P1	COMPRESS STR (kpa)	AIR VOIDS(%)	AC CONTENT (%)	MODULUS Mr.	
NUMBER	TYPE	(mm)											
1	SS		Coarse-Grained Soil: Clayey Gravel with Sand										
2	EF	2	Woven Geotextile										
3	GS	304	Crushed Gravel										
4	EF	12	Woven Geotextile										
5	GS	304	Soil-Aggregate Mixture (Predominantly Coarse-Grained)										
6	GS	101	Soil-Aggregate Mixture (Predominantly Coarse-Grained)										
7	TB	137	Lean Concrete										
8	PC	256	Portland Cement Concrete (JPCP)										
Distress Monitoring						Cross Profile		Monitored Traffic Data (Estimates)					
DISTRESS DATE	SURVEY METHOD	FATIGUE CRACKS (m2)	LOW TEMP. CRACKS (m)	LONG CRACKS (m)	POTHOLES/ PATCH (m2)	SURVEY DATE	RUT (mm) L/R	TRAFFIC YEAR	AADT (#)	TRUCKS (%)	CALCULATED ESALS		
											KESALS		



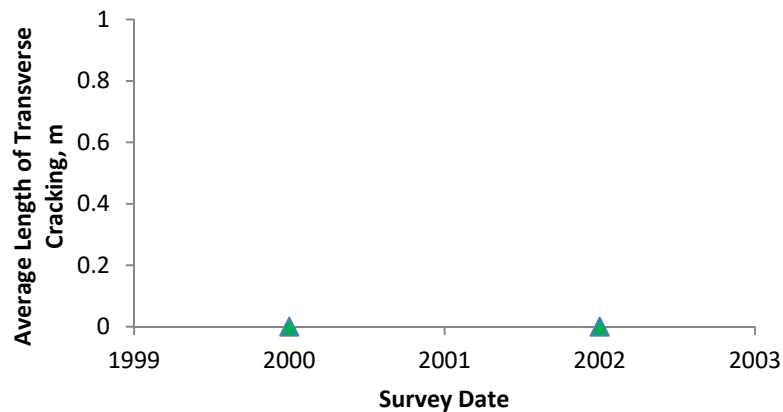
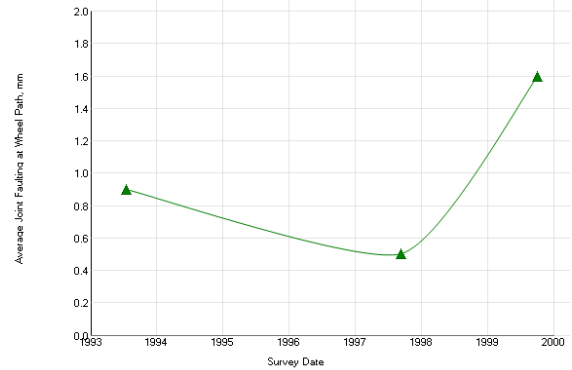
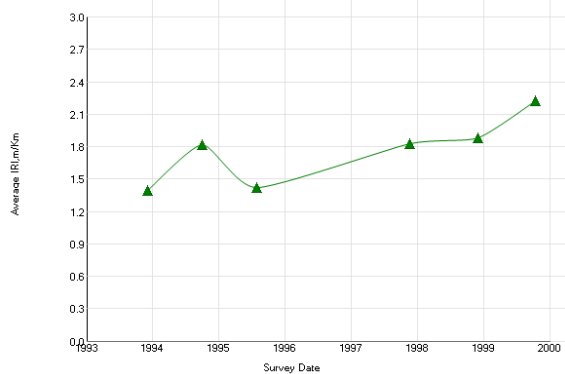
Experiment: SPS-4: Preventive Maintenance of Jointed Concrete Pavement							Section ID: 49-D446					
Section# :			49-D446		Data :		ALL DATA					
REGION		Western (Reno, NV, USA)			LATITUDE		ROUTE/DIRECTION					
EXPERIMENT		SPS-4			LONGITUDE		NO. OF LANES					
STATE/PROVINCE		Utah			ELEVATION		CONSTRUCTED					
COUNTY					MILEPOINT		OUT OF STUDY					
					FUNCTIONAL CLASS		01/01/1988 09/15/2002					
Maintenance Rehabilitation/Rehabilitation Date							Activity Description					
05/22/1992							Transverse Joint Sealing (linear ft.)					
05/22/1992							Lane-Shoulder Longitudinal Joint Sealing (linear ft.)					
05/01/2001							Transverse Joint Sealing (linear ft.)					
05/01/2001							Lane-Shoulder Longitudinal Joint Sealing (linear ft.)					
Layer Structure					Field Values		Laboratory Results					
LAYER		THICKNESS (mm)	MATERIAL DESCRIPTION			MOISTURE CONTENT (%)	DENSITY (kg/m3)	SUBGRADE P1	COMPRESS STR (kpa)	AIR VOIDS(%)	AC CONTENT (%)	MODULUS Mr.
NUMBER	TYPE											
1	SS		Coarse-Grained Soil: Clayey Gravel with Sand									
2	EF	2	Woven Geotextile									
3	GS	304	Crushed Gravel									
4	EF	12	Woven Geotextile									
5	GS	304	Soil-Aggregate Mixture (Predominantly Coarse-Grained)									
6	GS	101	Soil-Aggregate Mixture (Predominantly Coarse-Grained)									
7	TB	137	Lean Concrete									
8	PC	256	Portland Cement Concrete (JPCP)									
Distress Monitoring						Cross Profile		Monitored Traffic Data (Estimates)				
DISTRESS DATE	SURVEY METHOD	FATIGUE CRACKS (m2)	LOW TEMP. CRACKS (m)	LONG CRACKS (m)	POTHOLE/ PATCH (m2)	SURVEY DATE	RUT (mm) L/R	TRAFFIC YEAR	AADT (#)	TRUCKS (%)	CALCULATED ESALS	
											KESALS	



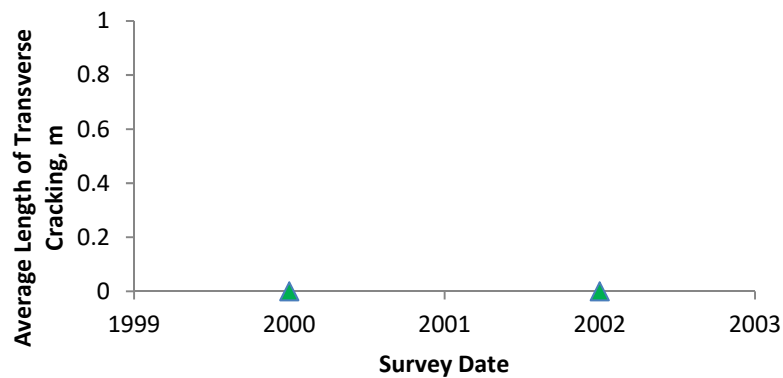
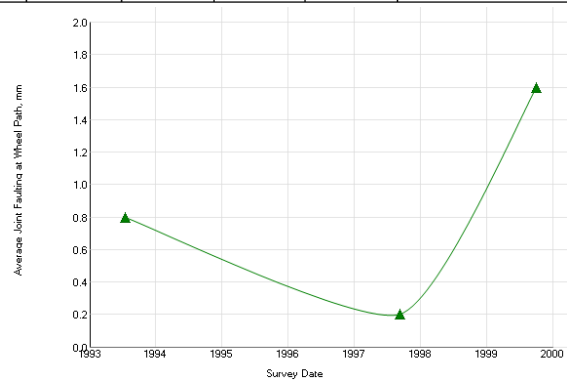
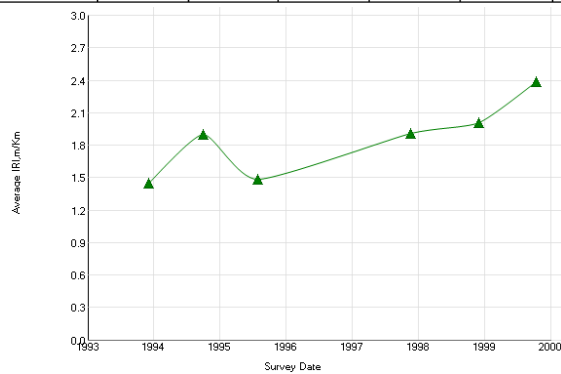
Experiment: SPS-4: Preventive Maintenance of Jointed Concrete Pavement							Section ID: 49-D448						
Section# : 49-D448				Data : ALL DATA									
REGION		Western (Reno, NV, USA)			LATITUDE		ROUTE/DIRECTION						
EXPERIMENT		SPS-4			LONGITUDE		NO. OF LANES						
STATE/PROVINCE		Utah			ELEVATION		CONSTRUCTED 01/01/1988						
COUNTY					MILEPOINT		OUT OF STUDY 09/15/2002						
					FUNCTIONAL CLASS								
Maintenance Rehabilitation/Rehabilitation Date							Activity Description						
07/02/1992							Transverse Joint Sealing (linear ft.)						
07/02/1992							Lane-Shoulder Longitudinal Joint Sealing (linear ft.)						
05/01/2001							Transverse Joint Sealing (linear ft.)						
05/01/2001							Lane-Shoulder Longitudinal Joint Sealing (linear ft.)						
Layer Structure							Field Values		Laboratory Results				
LAYER		THICKNESS	MATERIAL DESCRIPTION				MOISTURE CONTENT (%)	DENSITY (kg/m ³)	SUBGRADE P1	COMPRESS STR (kpa)	AIR VOIDS(%)	AC CONTENT (%)	MODULUS Mr.
NUMBER	TYPE	(mm)											
1	SS		Coarse-Grained Soil: Clayey Gravel with Sand										
2	EF	2	Woven Geotextile										
3	GS	304	Crushed Gravel										
4	EF	12	Woven Geotextile										
5	GS	304	Soil-Aggregate Mixture (Predominantly Coarse-Grained)										
6	GS	101	Soil-Aggregate Mixture (Predominantly Coarse-Grained)										
7	TB	137	Lean Concrete										
8	PC	256	Portland Cement Concrete (JPCP)										
Distress Monitoring							Cross Profile		Monitored Traffic Data (Estimates)				
DISTRESS DATE	SURVEY METHOD	FATIGUE CRACKS (m2)	LOW TEMP. CRACKS (m)	LONG CRACKS (m)	POTHOLES/PATCH (m2)	SURVEY DATE	RUT (mm) L/R	TRAFFIC YEAR	AADT (#)	TRUCKS (%)	CALCULATED ESALS		
											KESALS		



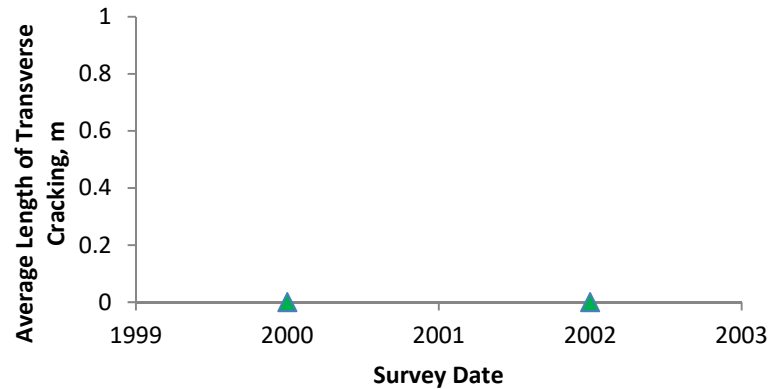
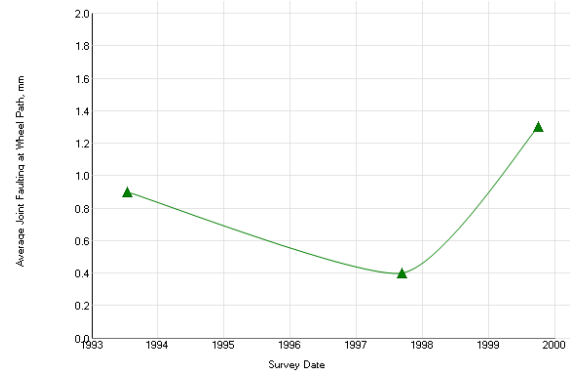
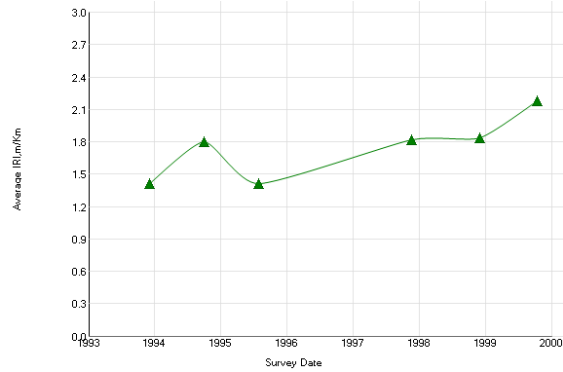
Experiment: SPS-4: Preventive Maintenance of Jointed Concrete Pavement						Section ID: 49-D449						
Section# :			49-D449			Data :			ALL DATA			
REGION		Western (Reno, NV, USA)			LATITUDE		ROUTE/DIRECTION					
EXPERIMENT		SPS-4			LONGITUDE		NO. OF LANES					
STATE/PROVINCE		Utah			ELEVATION		CONSTRUCTED			01/01/1988		
COUNTY					MILEPOINT		OUT OF STUDY			09/15/2002		
					FUNCTIONAL CLASS							
Maintenance Rehabilitation/Rehabilitation Date						Activity Description						
05/27/1992						Transverse Joint Sealing (linear ft.)						
05/27/1992						Lane-Shoulder Longitudinal Joint Sealing (linear ft.)						
05/01/2001						Transverse Joint Sealing (linear ft.)						
05/01/2001						Lane-Shoulder Longitudinal Joint Sealing (linear ft.)						
Layer Structure						Field Values		Laboratory Results				
LAYER		THICKNESS	MATERIAL			MOISTURE	DENSITY	SUBGRADE	COMPRESS	AIR	AC	MODULUS
NUMBER	TYPE	(mm)	DESCRIPTION			CONTENT (%)	(kg/m3)	P1	STR (kpa)	VOIDS(%)	CONTENT (%)	Mr.
1	SS		Coarse-Grained Soil: Clayey Gravel with Sand									
2	EF	2	Woven Geotextile									
3	GS	304	Crushed Gravel									
4	EF	12	Woven Geotextile									
5	GS	304	Soil-Aggregate Mixture (Predominantly Coarse-Grained)									
6	GS	101	Soil-Aggregate Mixture (Predominantly Coarse-Grained)									
7	TB	137	Lean Concrete									
8	PC	256	Portland Cement Concrete (JPCP)									
Distress Monitoring						Cross Profile		Monitored Traffic Data (Estimates)				
DISTRESS DATE	SURVEY METHOD	FATIGUE CRACKS (m2)	LOW TEMP. CRACKS (m)	LONG CRACKS (m)	POTHOLE/ PATCH (m2)	SURVEY DATE	RUT (mm) L/R	TRAFFIC YEAR	AADT (#)	TRUCKS (%)	CALCULATED ESALS	
											KESALS	



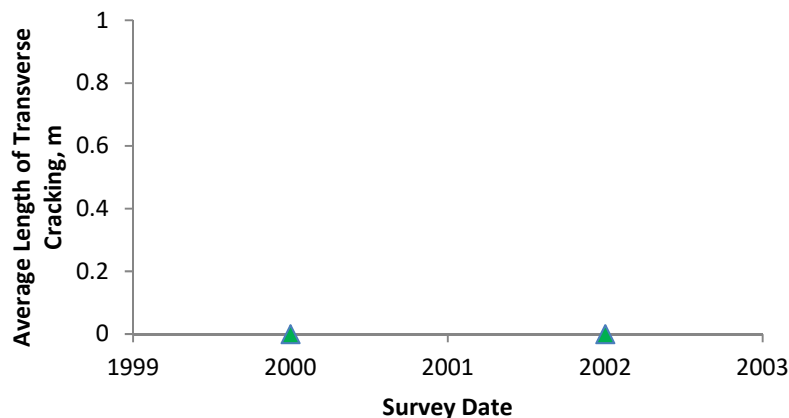
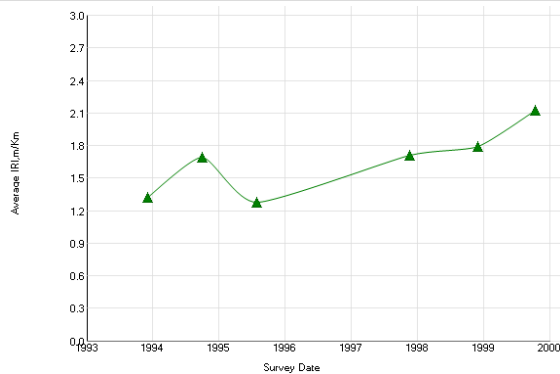
Experiment: SPS-4: Preventive Maintenance of Jointed Concrete Pavement						Section ID: 49-D450						
Section# :			49-D450			Data :			ALL DATA			
REGION		Western (Reno, NV, USA)		LATITUDE		ROUTE/DIRECTION						
EXPERIMENT		SPS-4		LONGITUDE		NO. OF LANES						
STATE/PROVINCE		Utah		ELEVATION		CONSTRUCTED				01/01/1988		
COUNTY				MILEPOINT		OUT OF STUDY				09/15/2002		
				FUNCTIONAL CLASS								
Maintenance Rehabilitation/Rehabilitation Date						Activity Description						
05/27/1992						Transverse Joint Sealing (linear ft.)						
05/27/1992						Lane-Shoulder Longitudinal Joint Sealing (linear ft.)						
05/01/2001						Transverse Joint Sealing (linear ft.)						
05/01/2001						Lane-Shoulder Longitudinal Joint Sealing (linear ft.)						
Layer Structure						Field Values		Laboratory Results				
LAYER		THICKNESS	MATERIAL DESCRIPTION			MOISTURE CONTENT (%)	DENSITY (kg/m3)	SUBGRADE P1	COMPRESS STR (kpa)	AIR VOIDS(%)	AC CONTENT (%)	MODULUS Mr.
NUMBER	TYPE	(mm)										
1	SS		Coarse-Grained Soil: Clayey Gravel with Sand									
2	EF	2	Woven Geotextile									
3	GS	304	Crushed Gravel									
4	EF	12	Woven Geotextile									
5	GS	304	Soil-Aggregate Mixture (Predominantly Coarse-Grained)									
6	GS	101	Soil-Aggregate Mixture (Predominantly Coarse-Grained)									
7	TB	137	Lean Concrete									
8	PC	256	Portland Cement Concrete (JPCP)									
Distress Monitoring						Cross Profile		Monitored Traffic Data (Estimates)				
DISTRESS DATE	SURVEY METHOD	FATIGUE CRACKS (m2)	LOW TEMP. CRACKS (m)	LONG CRACKS (m)	POTHOLE/ PATCH (m2)	SURVEY DATE	RUT (mm) L/R	TRAFFIC YEAR	AADT (#)	TRUCKS (%)	CALCULATED ESALS	
											KESALS	



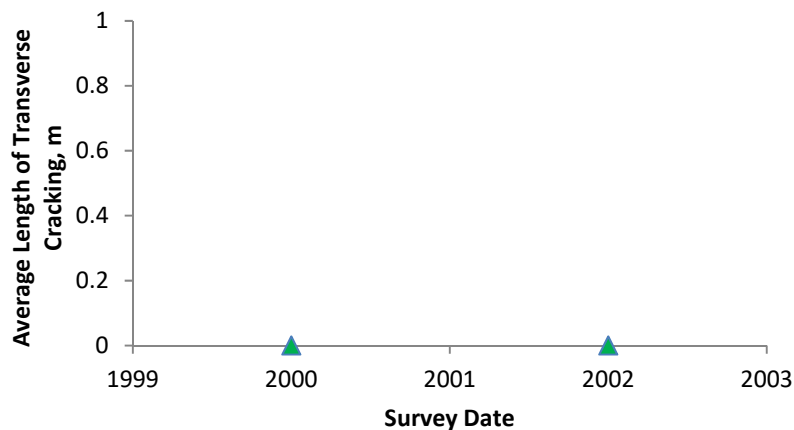
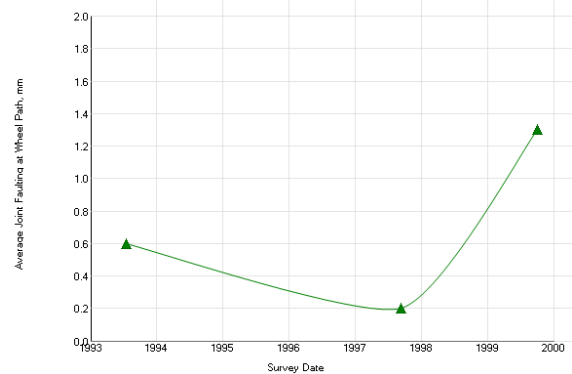
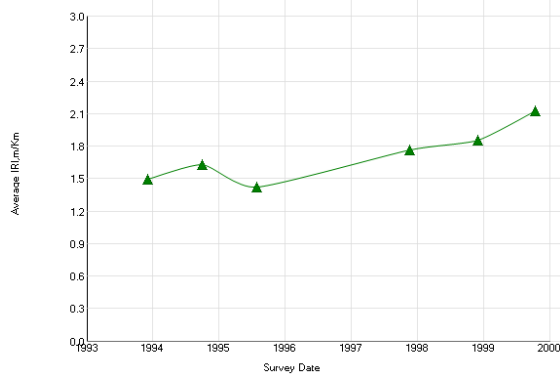
Experiment: SPS-4: Preventive Maintenance of Jointed Concrete Pavement						Section ID: 49-D451				
Section# :			49-D451		Data :		ALL DATA			
REGION		Western (Reno, NV, USA)		LATITUDE		ROUTE/DIRECTION				
EXPERIMENT		SPS-4		LONGITUDE		NO. OF LANES				
STATE/PROVINCE		Utah		ELEVATION		CONSTRUCTED		01/01/1988		
COUNTY				MILEPOINT		OUT OF STUDY		09/15/2002		
				FUNCTIONAL CLASS						
Maintenance Rehabilitation/Rehabilitation Date						Activity Description				
06/29/1992						Transverse Joint Sealing (linear ft.)				
06/29/1992						Lane-Shoulder Longitudinal Joint Sealing (linear ft.)				
05/01/2001						Transverse Joint Sealing (linear ft.)				
05/01/2001						Lane-Shoulder Longitudinal Joint Sealing (linear ft.)				
Layer Structure				Field Values		Laboratory Results				
LAYER		THICKNESS	MATERIAL	MOISTURE	DENSITY	SUBGRADE	COMPRESS	AIR	AC	MODULUS
NUMBER	TYPE	(mm)	DESCRIPTION	CONTENT (%)	(kg/m3)	P1	STR (kpa)	VOIDS(%)	CONTENT (%)	Mr.
1	SS		Coarse-Grained Soil: Clayey Gravel with Sand							
2	EF	2	Woven Geotextile							
3	GS	304	Crushed Gravel							
4	EF	12	Woven Geotextile							
5	GS	304	Soil-Aggregate Mixture (Predominantly Coarse-Grained)							
6	GS	101	Soil-Aggregate Mixture (Predominantly Coarse-Grained)							
7	TB	137	Lean Concrete							
8	PC	256	Portland Cement Concrete (JPCP)							



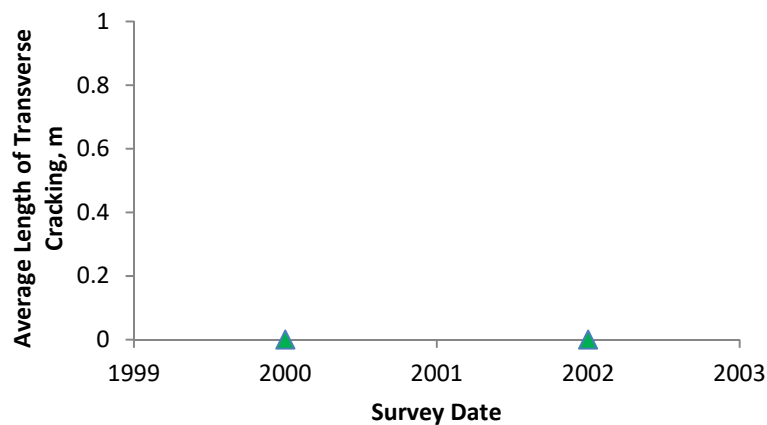
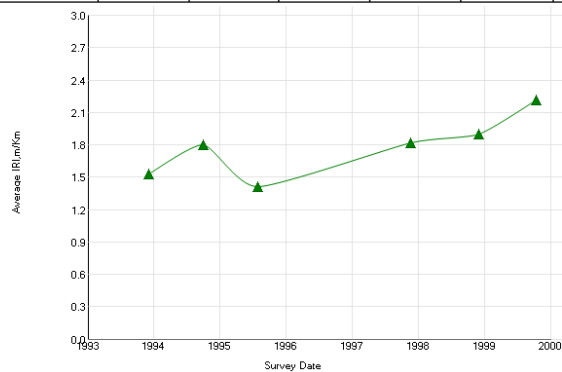
Experiment: SPS-4: Preventive Maintenance of Jointed Concrete Pavement						Section ID: 49-D452						
Section# :			49-D452			Data :			ALL DATA			
REGION		Western (Reno, NV, USA)		LATITUDE		ROUTE/DIRECTION						
EXPERIMENT		SPS-4		LONGITUDE		NO. OF LANES						
STATE/PROVINCE		Utah		ELEVATION		CONSTRUCTED				01/01/1988		
COUNTY				MILEPOINT		OUT OF STUDY				09/15/2002		
				FUNCTIONAL CLASS								
Maintenance Rehabilitation/Rehabilitation Date						Activity Description						
08/14/1992						Transverse Joint Sealing (linear ft.)						
08/14/1992						Lane-Shoulder Longitudinal Joint Sealing (linear ft.)						
05/01/2001						Transverse Joint Sealing (linear ft.)						
05/01/2001						Lane-Shoulder Longitudinal Joint Sealing (linear ft.)						
Layer Structure						Field Values		Laboratory Results				
LAYER		THICKNESS (mm)	MATERIAL DESCRIPTION			MOISTURE CONTENT (%)	DENSITY (kg/m3)	SUBGRADE P1	COMPRESS STR (kpa)	AIR VOIDS(%)	AC CONTENT (%)	MODULUS Mr.
NUMBER	TYPE											
1	SS		Coarse-Grained Soil: Clayey Gravel with Sand									
2	EF	2	Woven Geotextile									
3	GS	304	Crushed Gravel									
4	EF	12	Woven Geotextile									
5	GS	304	Soil-Aggregate Mixture (Predominantly Coarse-Grained)									
6	GS	101	Soil-Aggregate Mixture (Predominantly Coarse-Grained)									
7	TB	137	Lean Concrete									
8	PC	256	Portland Cement Concrete (JPCP)									
Distress Monitoring						Cross Profile		Monitored Traffic Data (Estimates)				
DISTRESS DATE	SURVEY METHOD	FATIGUE CRACKS (m2)	LOW TEMP. CRACKS (m)	LONG CRACKS (m)	POTHOLE/ PATCH (m2)	SURVEY DATE	RUT (mm) L/R	TRAFFIC YEAR	AADT (#)	TRUCKS (%)	CALCULATED ESALS	
											KESALS	



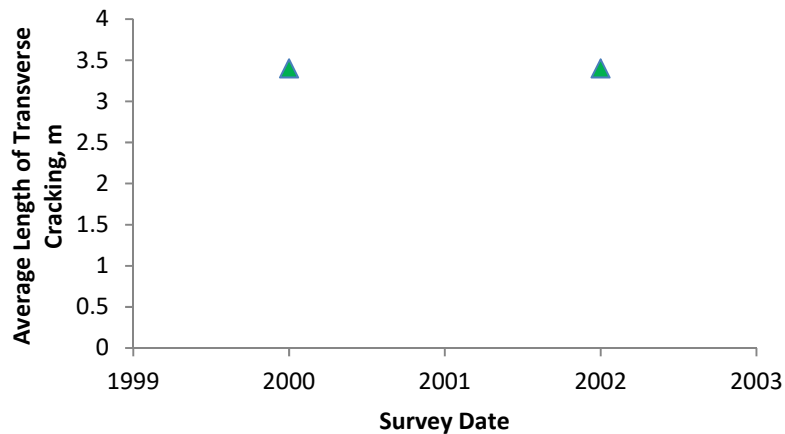
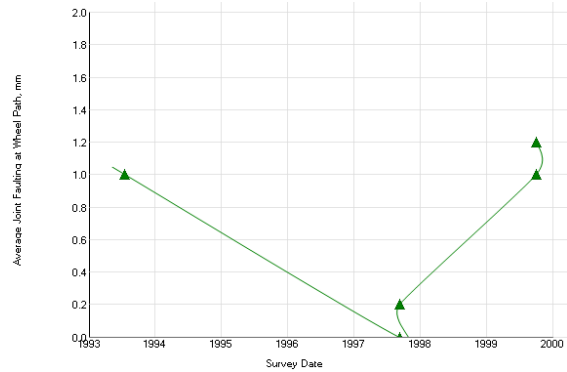
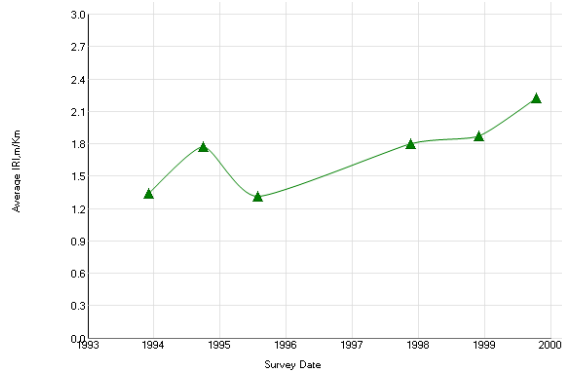
Experiment: SPS-4: Preventive Maintenance of Jointed Concrete Pavement							Section ID: 49-D454				
Section# :			49-D454		Data :		ALL DATA				
REGION		Western (Reno, NV, USA)		LATITUDE		ROUTE/DIRECTION					
EXPERIMENT		SPS-4		LONGITUDE		NO. OF LANES					
STATE/PROVINCE		Utah		ELEVATION		CONSTRUCTED					
COUNTY				MILEPOINT		01/01/1988					
				FUNCTIONAL CLASS		09/15/2002					
Maintenance Rehabilitation/Rehabilitation Date							Activity Description				
07/03/1992							Transverse Joint Sealing (linear ft.)				
07/03/1992							Lane-Shoulder Longitudinal Joint Sealing (linear ft.)				
05/01/2001							Transverse Joint Sealing (linear ft.)				
05/01/2001							Lane-Shoulder Longitudinal Joint Sealing (linear ft.)				
Layer Structure				Field Values		Laboratory Results					
LAYER		THICKNESS	MATERIAL DESCRIPTION		MOISTURE	DENSITY	SUBGRADE	COMPRESS	AIR	AC	MODULUS
NUMBER	TYPE	(mm)			CONTENT (%)	(kg/m3)	P1	STR (kpa)	VOIDS(%)	CONTENT (%)	Mr.
1	SS		Coarse-Grained Soil: Clayey Gravel with Sand								
2	EF	2	Woven Geotextile								
3	GS	304	Crushed Gravel								
4	EF	12	Woven Geotextile								
5	GS	304	Soil-Aggregate Mixture (Predominantly Coarse-Grained)								
6	GS	101	Soil-Aggregate Mixture (Predominantly Coarse-Grained)								
7	TB	137	Lean Concrete								
8	PC	256	Portland Cement Concrete (JPCP)								
Distress Monitoring					Cross Profile		Monitored Traffic Data (Estimates)				
DISTRESS DATE	SURVEY METHOD	FATIGUE CRACKS (m2)	LOW TEMP. CRACKS (m)	LONG CRACKS (m)	POTHOLE/ PATCH (m2)	SURVEY DATE	RUT (mm) L/R	TRAFFIC YEAR	AADT (#)	TRUCKS (%)	CALCULATED ESALS
											KESALS



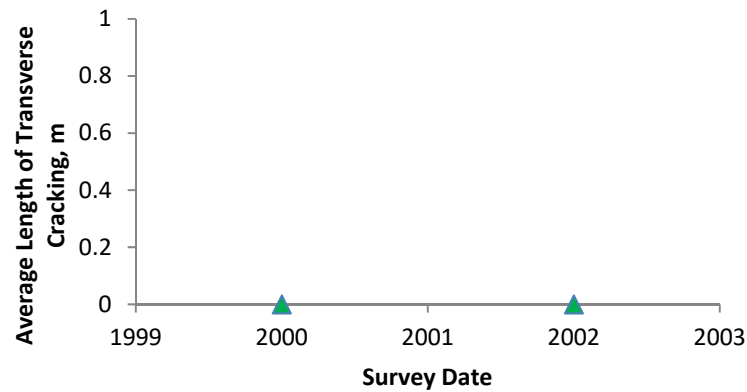
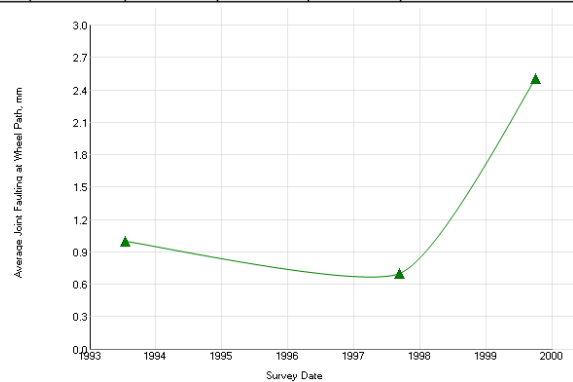
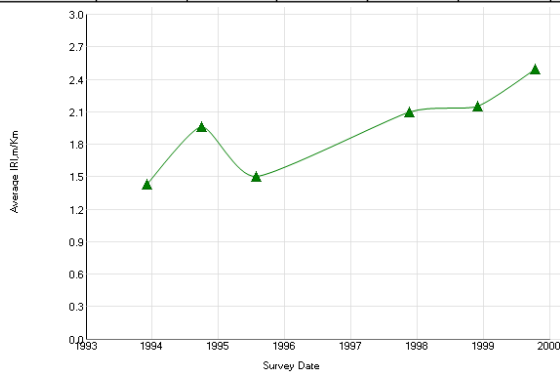
Experiment: SPS-4: Preventive Maintenance of Jointed Concrete Pavement						Section ID: 49-D455						
Section# :			49-D455		Data :			ALL DATA				
REGION		Western (Reno, NV, USA)			LATITUDE		ROUTE/DIRECTION					
EXPERIMENT		SPS-4			LONGITUDE		NO. OF LANES					
STATE/PROVINCE		Utah			ELEVATION		CONSTRUCTED					
COUNTY					MILEPOINT		OUT OF STUDY					
					FUNCTIONAL CLASS		01/01/1988					
							09/15/2002					
Maintenance Rehabilitation/Rehabilitation Date						Activity Description						
07/03/1992						Transverse Joint Sealing (linear ft.)						
07/03/1992						Lane-Shoulder Longitudinal Joint Sealing (linear ft.)						
05/01/2001						Transverse Joint Sealing (linear ft.)						
05/01/2001						Lane-Shoulder Longitudinal Joint Sealing (linear ft.)						
05/01/2001						Partial depth patching of PCC pavements at joints (sq. yards)						
Layer Structure						Field Values		Laboratory Results				
LAYER		THICKNESS (mm)	MATERIAL DESCRIPTION			MOISTURE CONTENT (%)	DENSITY (kg/m3)	SUBGRADE P1	COMPRESS STR (kpa)	AIR VOIDS(%)	AC CONTENT (%)	MODULUS Mr.
NUMBER	TYPE											
1	SS		Coarse-Grained Soil: Clayey Gravel with Sand									
2	EF	2	Woven Geotextile									
3	GS	304	Crushed Gravel									
4	EF	12	Woven Geotextile									
5	GS	304	Soil-Aggregate Mixture (Predominantly Coarse-Grained)									
6	GS	101	Soil-Aggregate Mixture (Predominantly Coarse-Grained)									
7	TB	137	Lean Concrete									
8	PC	256	Portland Cement Concrete (JPCP)									
Distress Monitoring						Cross Profile		Monitored Traffic Data (Estimates)				
DISTRESS DATE	SURVEY METHOD	FATIGUE CRACKS (m2)	LOW TEMP. CRACKS (m)	LONG CRACKS (m)	POTHOLE/ PATCH (m2)	SURVEY DATE	RUT (mm) L/R	TRAFFIC YEAR	AADT (#)	TRUCKS (%)	CALCULATED ESALS	
											KESALS	



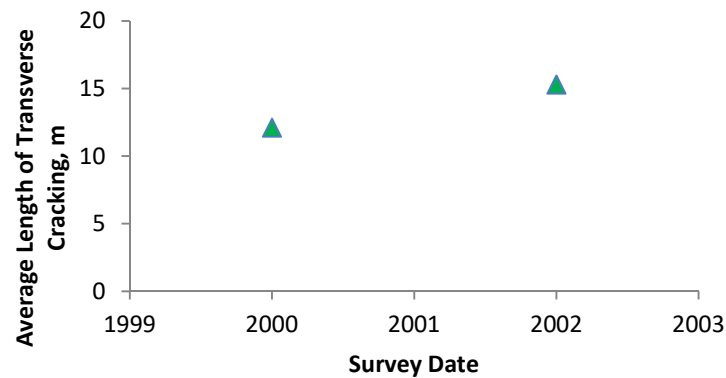
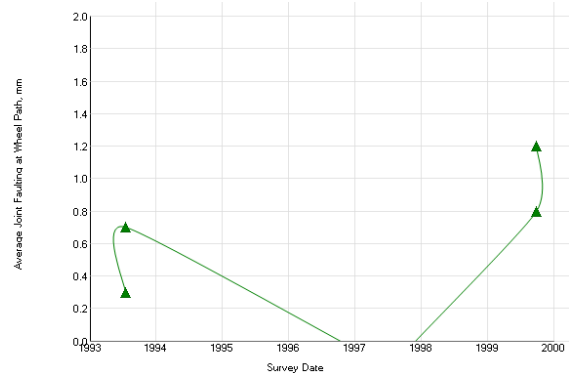
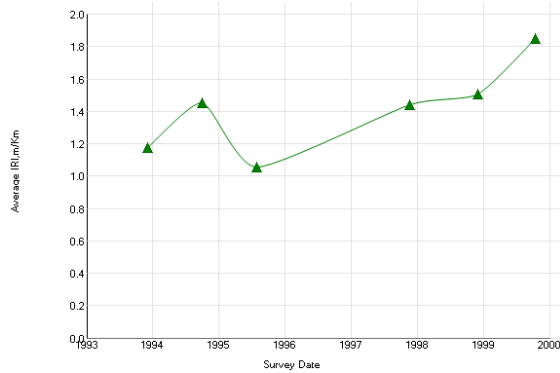
Experiment: SPS-4: Preventive Maintenance of Jointed Concrete Pavement						Section ID: 49-D459						
Section# :			49-D459			Data :			ALL DATA			
REGION		Western (Reno, NV, USA)			LATITUDE		ROUTE/DIRECTION					
EXPERIMENT		SPS-4			LONGITUDE		NO. OF LANES					
STATE/PROVINCE		Utah			ELEVATION		CONSTRUCTED			01/01/1988		
COUNTY					MILEPOINT		OUT OF STUDY			09/15/2002		
					FUNCTIONAL CLASS							
Maintenance Rehabilitation/Rehabilitation Date						Activity Description						
07/03/1992						Transverse Joint Sealing (linear ft.)						
07/03/1992						Lane-Shoulder Longitudinal Joint Sealing (linear ft.)						
05/01/2001						Transverse Joint Sealing (linear ft.)						
05/01/2001						Lane-Shoulder Longitudinal Joint Sealing (linear ft.)						
Layer Structure						Field Values		Laboratory Results				
LAYER		THICKNESS	MATERIAL			MOISTURE	DENSITY	SUBGRADE	COMPRESS	AIR	AC	MODULUS
NUMBER	TYPE	(mm)	DESCRIPTION			CONTENT (%)	(kg/m3)	P1	STR (kpa)	VOIDS(%)	CONTENT (%)	Mr.
1	SS		Coarse-Grained Soil: Clayey Gravel with Sand									
2	EF	2	Woven Geotextile									
3	GS	304	Crushed Gravel									
4	EF	12	Woven Geotextile									
5	GS	304	Soil-Aggregate Mixture (Predominantly Coarse-Grained)									
6	GS	101	Soil-Aggregate Mixture (Predominantly Coarse-Grained)									
7	TB	137	Lean Concrete									
8	PC	256	Portland Cement Concrete (JPCP)									
Distress Monitoring						Cross Profile		Monitored Traffic Data (Estimates)				
DISTRESS DATE	SURVEY METHOD	FATIGUE CRACKS (m2)	LOW TEMP. CRACKS (m)	LONG CRACKS (m)	POTHoles/ PATCH (m2)	SURVEY DATE	RUT (mm) L/R	TRAFFIC YEAR	AADT (#)	TRUCKS (%)	CALCULATED ESALS	
											KESALS	



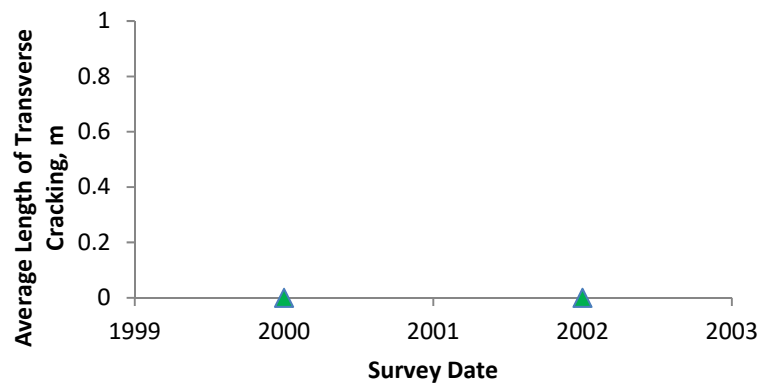
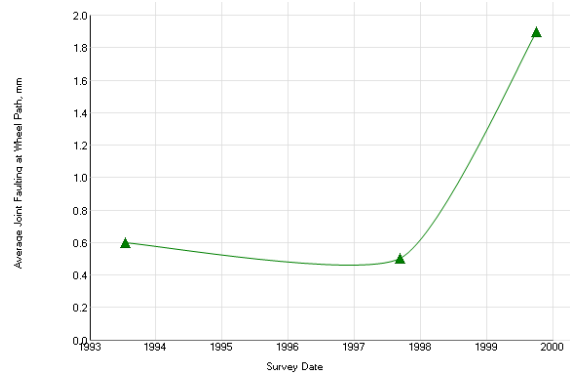
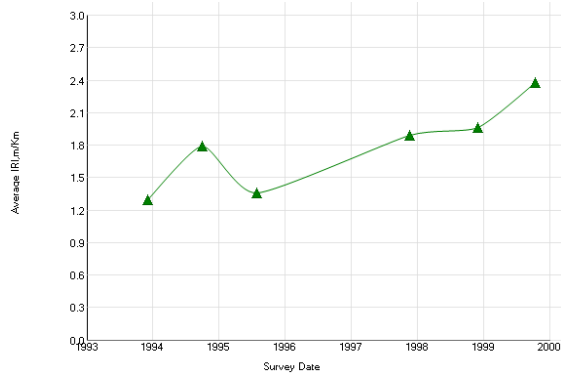
Experiment: SPS-4: Preventive Maintenance of Jointed Concrete Pavement							Section ID: 49-D460					
Section# :			49-D460		Data :		ALL DATA					
REGION		Western (Reno, NV, USA)			LATITUDE		ROUTE/DIRECTION					
EXPERIMENT		SPS-4			LONGITUDE		NO. OF LANES					
STATE/PROVINCE		Utah			ELEVATION		CONSTRUCTED		01/01/1988			
COUNTY					MILEPOINT		OUT OF STUDY		09/15/2002			
					FUNCTIONAL CLASS							
Maintenance Rehabilitation/Rehabilitation Date							Activity Description					
05/01/2001							Transverse Joint Sealing (linear ft.)					
05/01/2001							Lane-Shoulder Longitudinal Joint Sealing (linear ft.)					
Layer Structure							Field Values		Laboratory Results			
LAYER		THICKNESS (mm)	MATERIAL DESCRIPTION			MOISTURE CONTENT (%)	DENSITY (kg/m3)	SUBGRADE P1	COMPRESS STR (kpa)	AIR VOIDS(%)	AC CONTENT (%)	MODULUS Mr.
NUMBER	TYPE											
1	SS		Coarse-Grained Soil: Clayey Gravel with Sand									
2	EF	2	Woven Geotextile									
3	GS	304	Crushed Gravel									
4	EF	12	Woven Geotextile									
5	GS	304	Soil-Aggregate Mixture (Predominantly Coarse-Grained)									
6	GS	101	Soil-Aggregate Mixture (Predominantly Coarse-Grained)									
7	TB	137	Lean Concrete									
8	PC	256	Portland Cement Concrete (JPCP)									
Distress Monitoring							Cross Profile		Monitored Traffic Data (Estimates)			
DISTRESS DATE	SURVEY METHOD	FATIGUE CRACKS (m2)	LOW TEMP. CRACKS (m)	LONG CRACKS (m)	POTHOLFS/ PATCH (m2)	SURVEY DATE	RUT (mm) L/R	TRAFFIC YEAR	AADT (#)	TRUCKS (%)	CALCULATED ESALS	
											KESALS	



Experiment: SPS-4: Preventive Maintenance of Jointed Concrete Pavement						Section ID: 49-D461							
Section# :			49-D461			Data :			ALL DATA				
REGION		Western (Reno, NV, USA)			LATITUDE		ROUTE/DIRECTION						
EXPERIMENT		SPS-4			LONGITUDE		NO. OF LANES						
STATE/PROVINCE		Utah			ELEVATION		CONSTRUCTED			01/01/1988			
COUNTY					MILEPOINT		OUT OF STUDY			09/15/2002			
					FUNCTIONAL CLASS								
Maintenance Rehabilitation/Rehabilitation Date					Activity Description								
05/20/1992					Transverse Joint Sealing (linear ft.)								
05/20/1992					Lane-Shoulder Longitudinal Joint Sealing (linear ft.)								
05/01/2001					Transverse Joint Sealing (linear ft.)								
05/01/2001					Lane-Shoulder Longitudinal Joint Sealing (linear ft.)								
Layer Structure						Field Values		Laboratory Results					
LAYER		THICKNESS (mm)	MATERIAL DESCRIPTION			MOISTURE CONTENT (%)	DENSITY (kg/m3)	SUBGRADE P1	COMPRESS STR (kpa)	AIR VOIDS(%)	AC CONTENT (%)	MODULUS Mr.	
NUMBER	TYPE												
1	SS		Coarse-Grained Soil: Clayey Gravel with Sand										
2	EF	2	Woven Geotextile										
3	GS	304	Crushed Gravel										
4	EF	12	Woven Geotextile										
5	GS	304	Soil-Aggregate Mixture (Predominantly Coarse-Grained)										
6	GS	101	Soil-Aggregate Mixture (Predominantly Coarse-Grained)										
7	TB	137	Lean Concrete										
8	PC	256	Portland Cement Concrete (JPCP)										
Distress Monitoring						Cross Profile		Monitored Traffic Data (Estimates)					
DISTRESS DATE	SURVEY METHOD	FATIGUE CRACKS (m2)	LOW TEMP. CRACKS (m)	LONG CRACKS (m)	POTHOLE/ PATCH (m2)	SURVEY DATE	RUT (mm) L/R	TRAFFIC YEAR	AADT (#)	TRUCKS (%)	CALCULATED ESALS		
											KESALS		



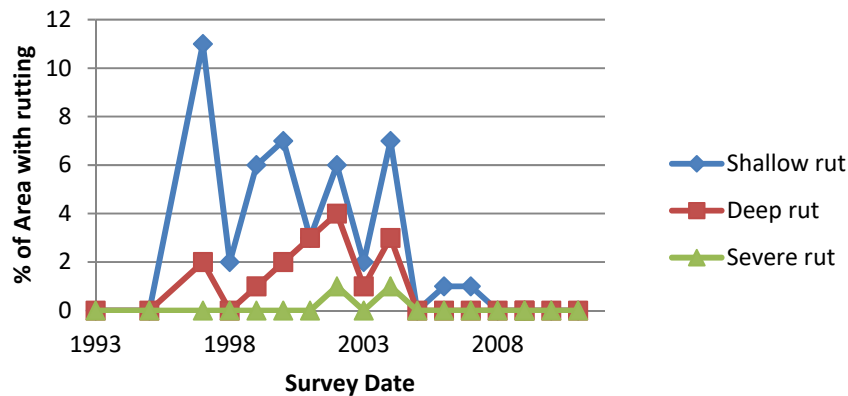
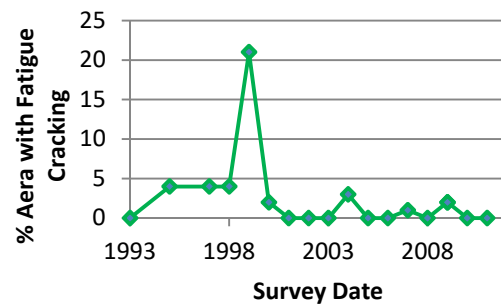
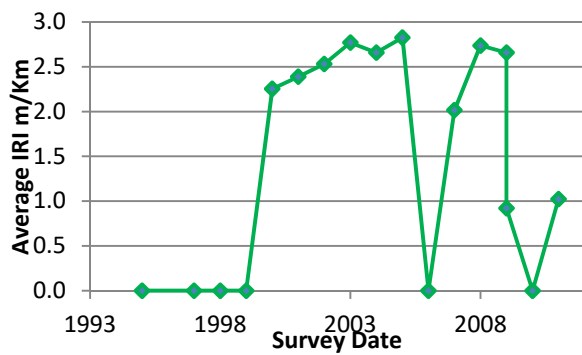
Experiment: SPS-4: Preventive Maintenance of Jointed Concrete Pavement						Section ID: 49-D462						
Section# :			49-D462		Data :			ALL DATA				
REGION		Western (Reno, NV, USA)			LATITUDE		ROUTE/DIRECTION					
EXPERIMENT		SPS-4			LONGITUDE		NO. OF LANES					
STATE/PROVINCE		Utah			ELEVATION		CONSTRUCTED					
COUNTY					MILEPOINT		01/01/1988					
					FUNCTIONAL CLASS		09/15/2002					
Maintenance Rehabilitation/Rehabilitation Date							Activity Description					
05/29/1992							Transverse Joint Sealing (linear ft.)					
05/29/1992							Lane-Shoulder Longitudinal Joint Sealing (linear ft.)					
05/01/2001							Transverse Joint Sealing (linear ft.)					
05/01/2001							Lane-Shoulder Longitudinal Joint Sealing (linear ft.)					
Layer Structure					Field Values		Laboratory Results					
LAYER		THICKNESS	MATERIAL			MOISTURE	DENSITY	SUBGRADE	COMPRESS	AIR	AC	MODULUS
NUMBER	TYPE	(mm)	DESCRIPTION			CONTENT (%)	(kg/m3)	P1	STR (kpa)	VOIDS(%)	CONTENT (%)	Mr.
1	SS		Coarse-Grained Soil: Clayey Gravel with Sand									
2	EF	2	Woven Geotextile									
3	GS	304	Crushed Gravel									
4	EF	12	Woven Geotextile									
5	GS	304	Soil-Aggregate Mixture (Predominantly Coarse-Grained)									
6	GS	101	Soil-Aggregate Mixture (Predominantly Coarse-Grained)									
7	TB	137	Lean Concrete									
8	PC	256	Portland Cement Concrete (JPCP)									
Distress Monitoring						Cross Profile		Monitored Traffic Data (Estimates)				
DISTRESS DATE	SURVEY METHOD	FATIGUE CRACKS (m2)	LOW TEMP. CRACKS (m)	LONG CRACKS (m)	POTHoles/PATCH (m2)	SURVEY DATE	RUT (mm) L/R	TRAFFIC YEAR	AADT (#)	TRUCKS (%)	CALCULATED ESALS	
												KESALS



Appendix P3. Texas PMIS Sections with Geosynthetics

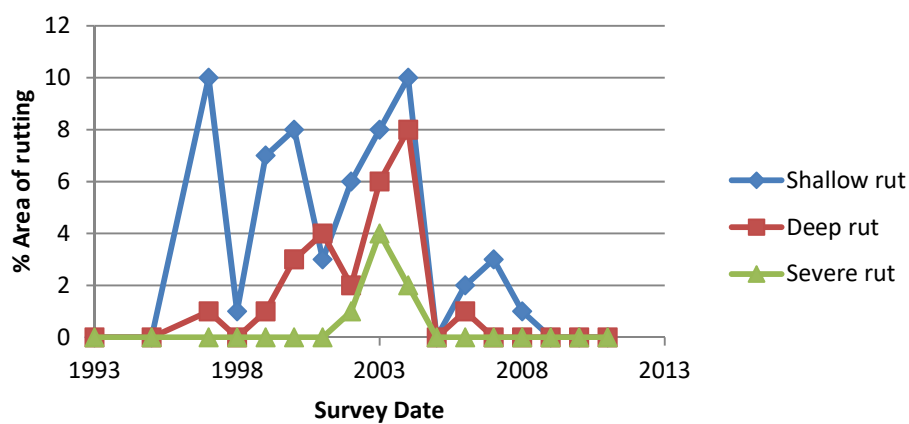
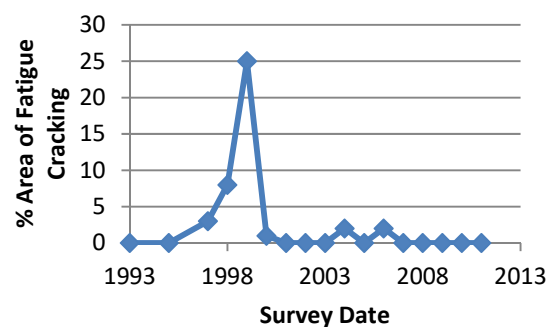
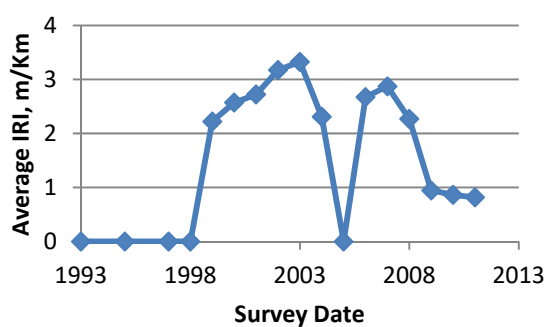
Section No.: FM 2331-292

Layer Number	Layer Type	Thickness (mm)	Material Description	Modulus
1	SS		High PI	
2	EF		Tensar Geogrid Type 2	
3	CTB	203.2	Cement Stabilized Base	
4	Seal Coat			
5	AC	50.8		



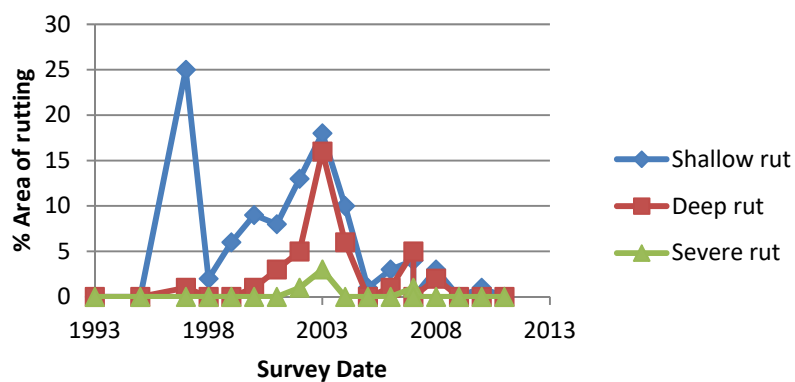
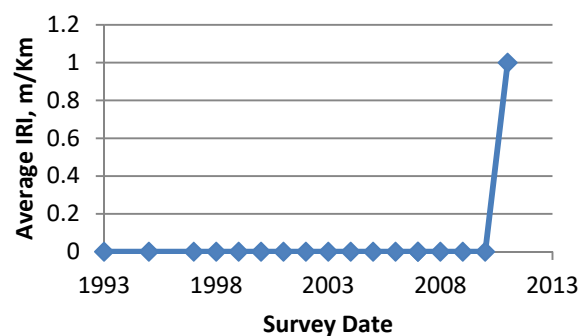
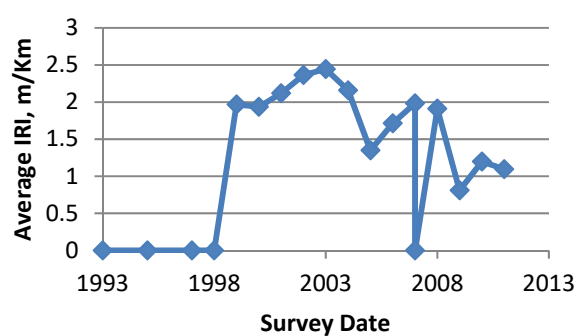
Section No.: FM 2331-294

Layer Number	Layer Type	Thickness (mm)	Material Description	Modulus
1	SS		High PI	
2	EF		Tensar Geogrid Type 2	
3	CTB	203.2	Cement Stabilized Base	
4	Seal Coat			
5	AC	50.8		



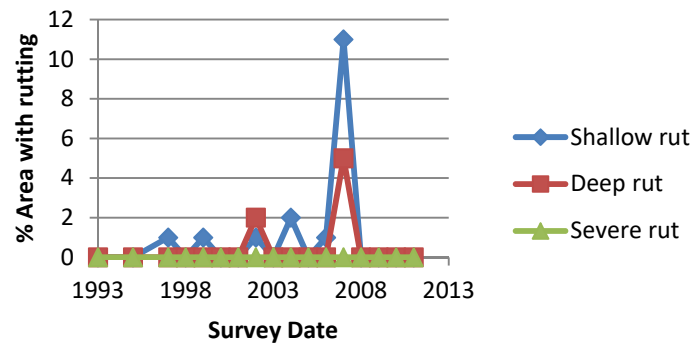
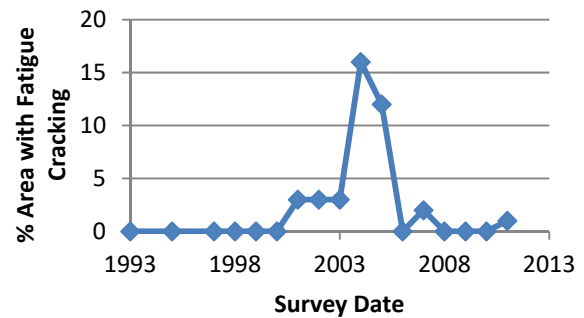
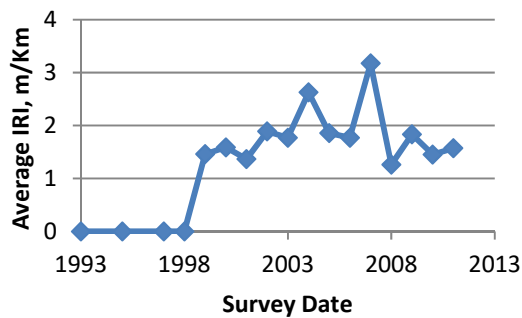
Section No.: FM 2331-296

Layer Number	Layer Type	Thickness (mm)	Material Description	Modulus
1	SS		High PI	
2	EF		Tensar Geogrid Type 2	
3	CTB	203.2	Cement Stabilized Base	
4	Seal Coat			
5	AC	50.8		



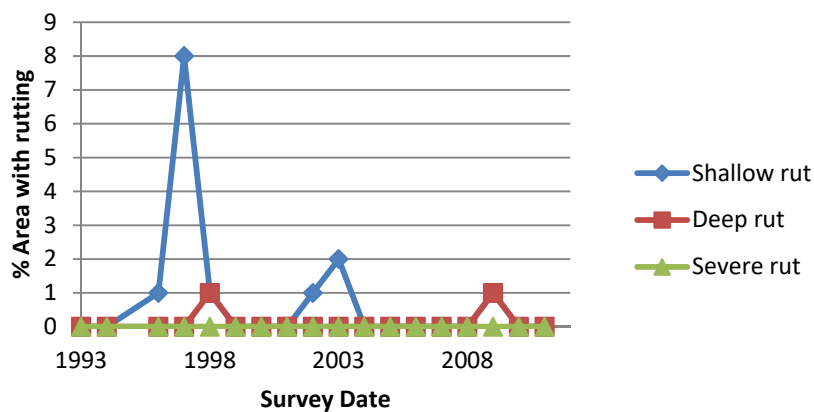
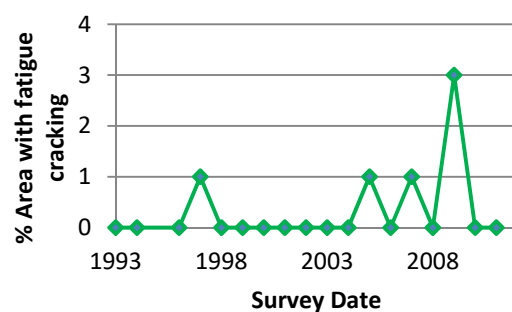
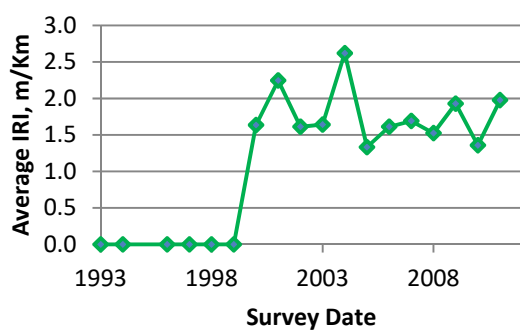
Section No.: FM 2331-290 Control

Layer Number	Layer Type	Thickness (mm)	Material Description	Modulus
1	SS		High PI	
2	CTB	203.2	Cement Stabilized Base	
3	Seal Coat			
4	AC	50.8		



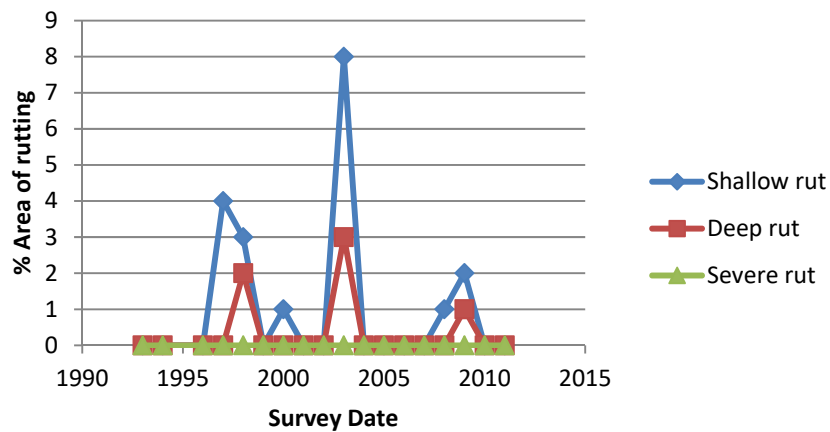
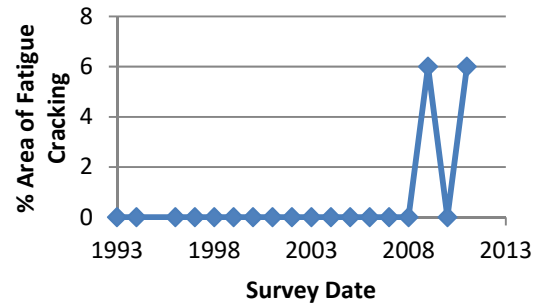
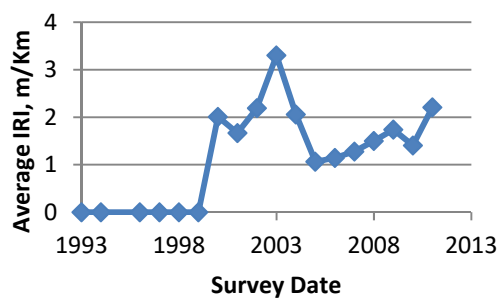
Section No.: Fort Worth FM 0917-558

Layer Number	Layer Type	Thickness (mm)	Material Description	Modulus
1	SS		High PI	
2	EF		Tensor geogrid type 2	
3	CTB	203.2	Cement stabilized base	
4	Seal Coat			
5	AC	50.8		



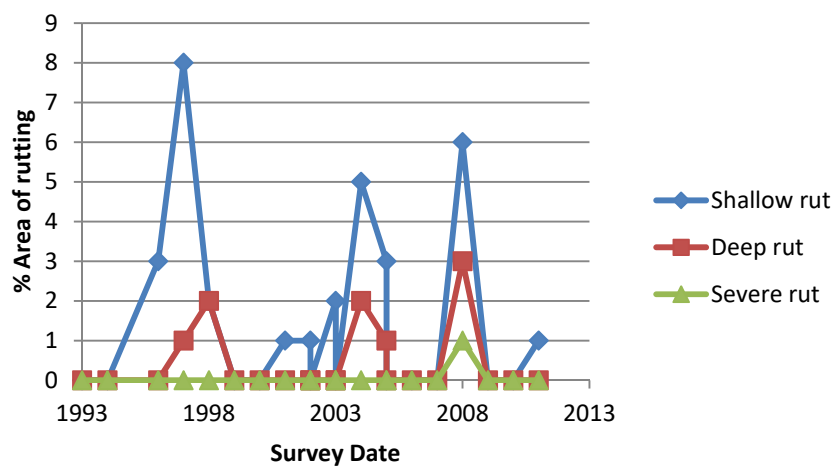
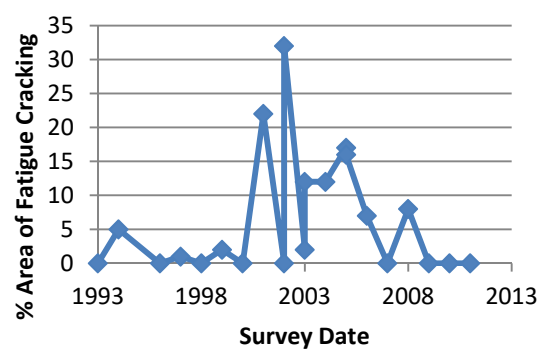
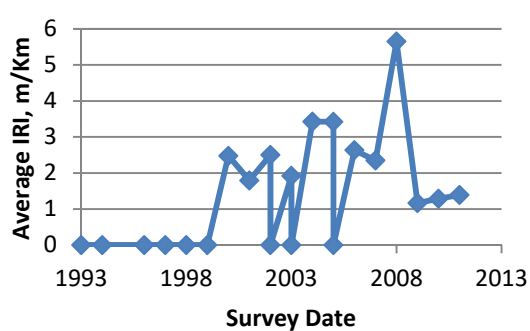
Section No.: Fort Worth FM 0917-560

Layer Number	Layer Type	Thickness (mm)	Material Description	Modulus
1	SS		High PI	
2	EF		Tensor geogrid type 2	
3	CTB	203.2	Cement stabilized base	
4	Seal Coat			
5	AC	50.8		



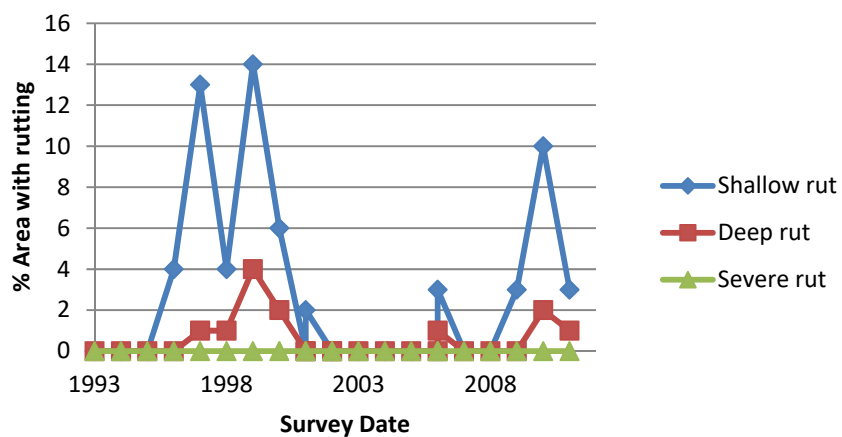
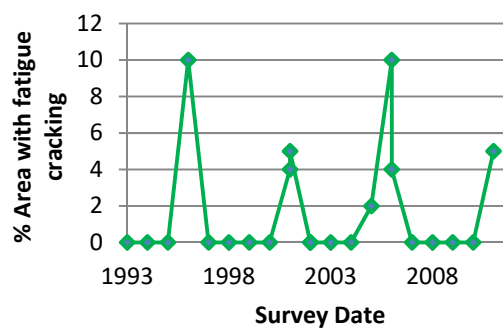
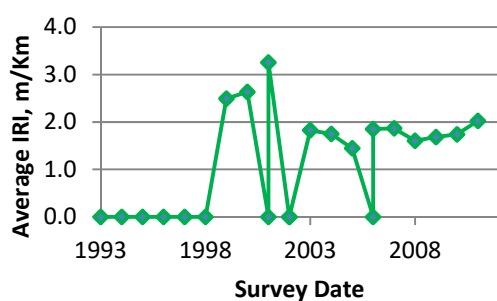
Section No.: Fort Worth FM 0917-556 Control

Layer Number	Layer Type	Thickness (mm)	Material Description	Modulus
1	SS		High PI	
2	CTB	203.2	Cement stabilized base	
3	Seal Coat			
4	AC	50.8		



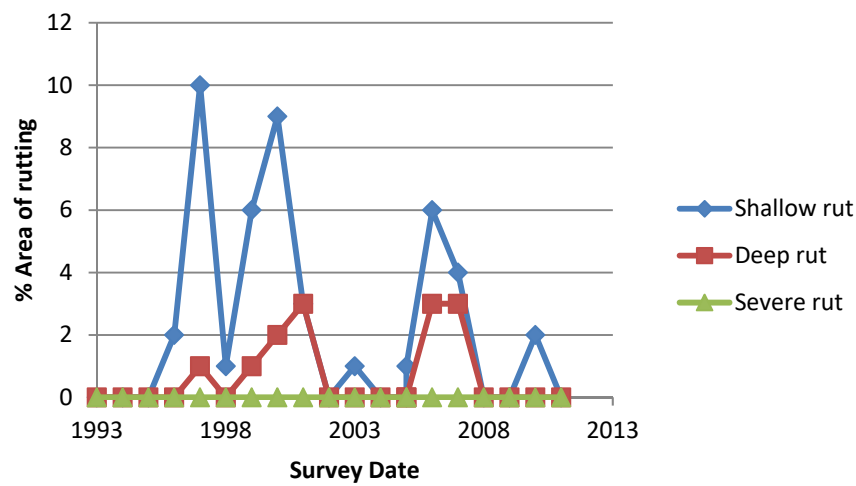
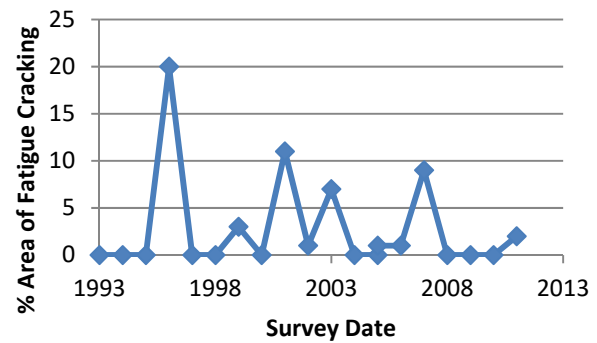
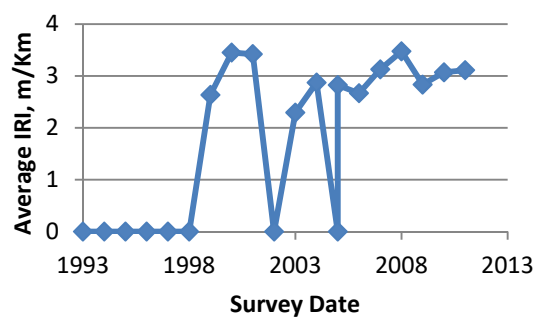
Section No.: Fort Worth FM 0157-296

Layer Number	Layer Type	Thickness (mm)	Material Description	Modulus
1	SS		High PI	
2	EF		Tensar geogrid type 2	
3	CTB	203.2	Cement stabilized base	
4	Seal Coat			
5	AC	50.8		



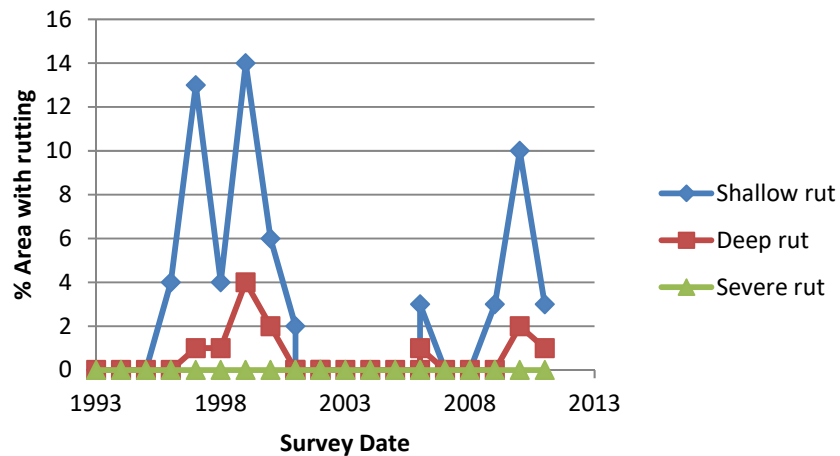
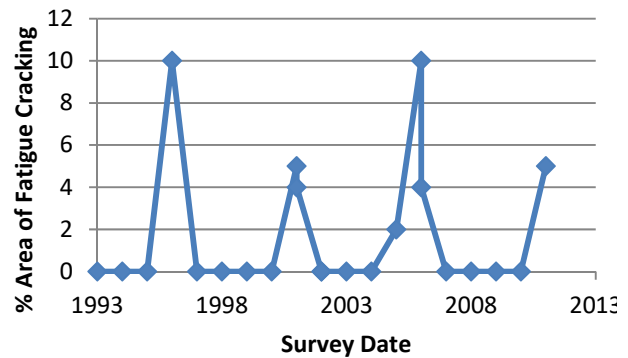
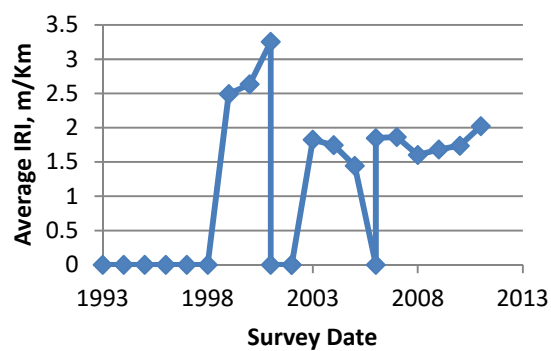
Section No.: Fort Worth FM 0157-298

Layer Number	Layer Type	Thickness (mm)	Material Description	Modulus
1	SS		High PI	
2	EF		Tensar geogrid type 2	
3	CTB	203.2	Cement stabilized base	
4	Seal Coat			
5	AC	50.8		



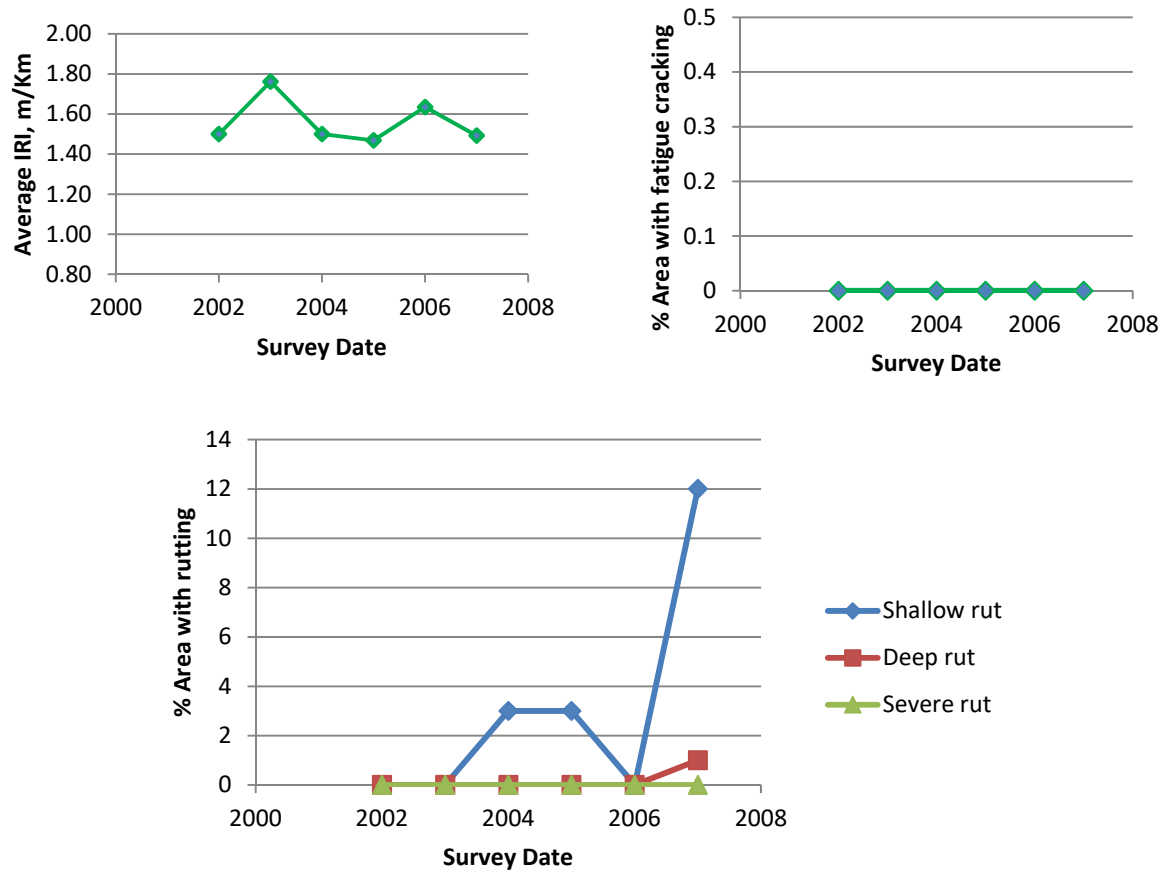
Section No.: Fort Worth FM 0157-294 Control

Layer Number	Layer Type	Thickness (mm)	Material Description	Modulus
1	SS		High PI	
2	CTB	203.2	Cement stabilized base	
3	Seal Coat			
4	AC	50.8		



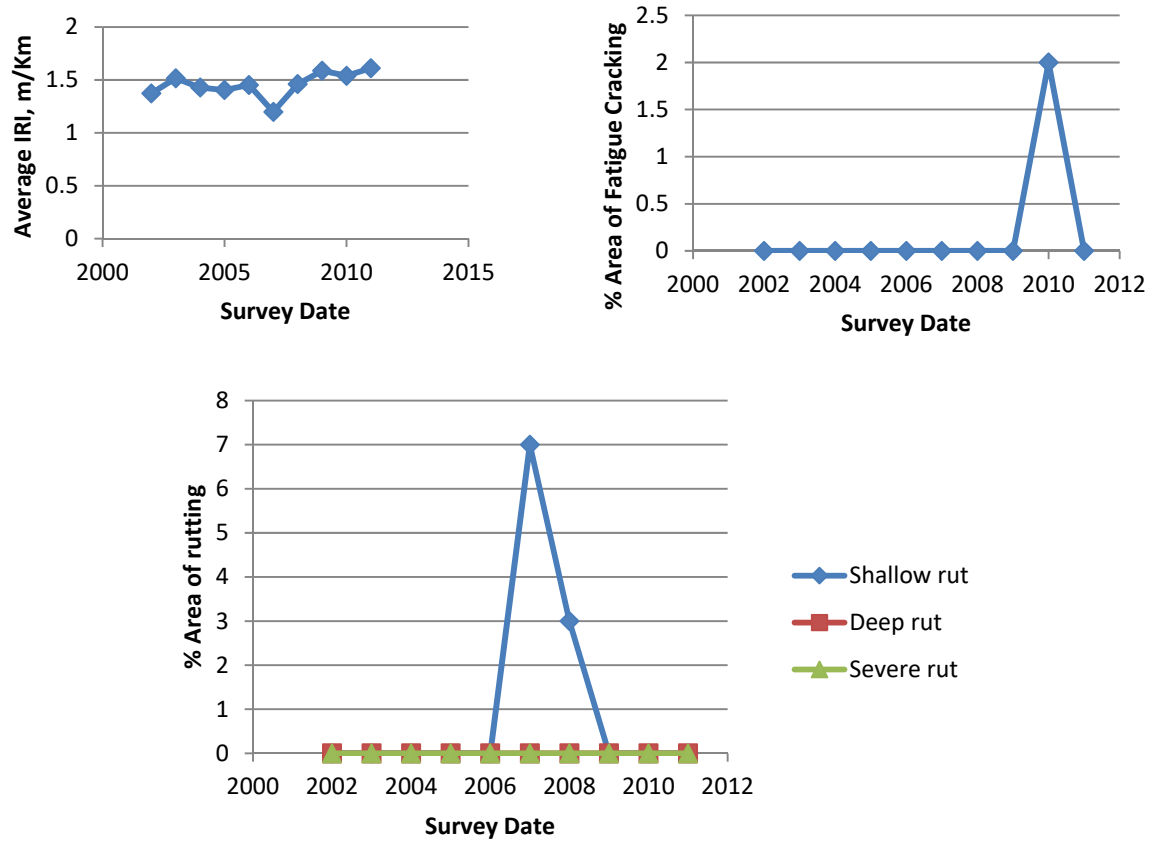
Section No.: Williamson US 0079-550

Layer Structure (N/A)



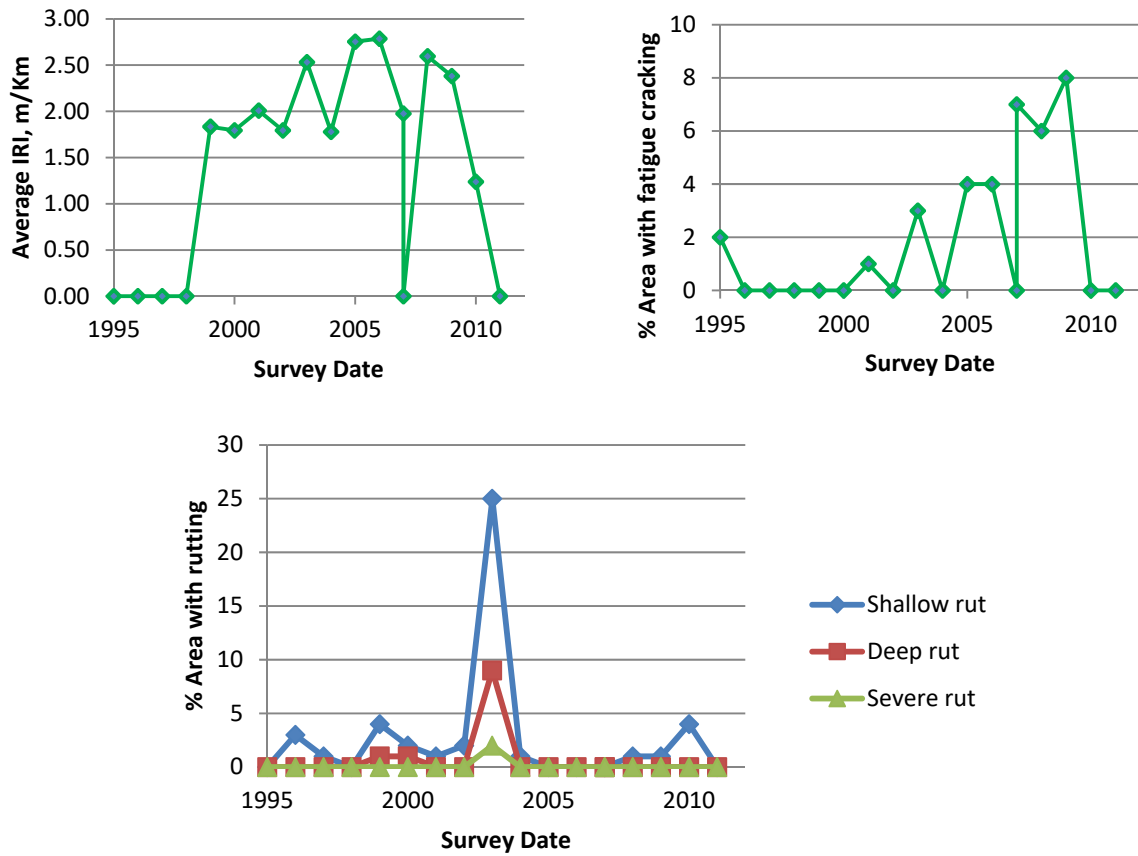
Section No.: Williamson US 0079-552 Control

Layer Structure (N/A)



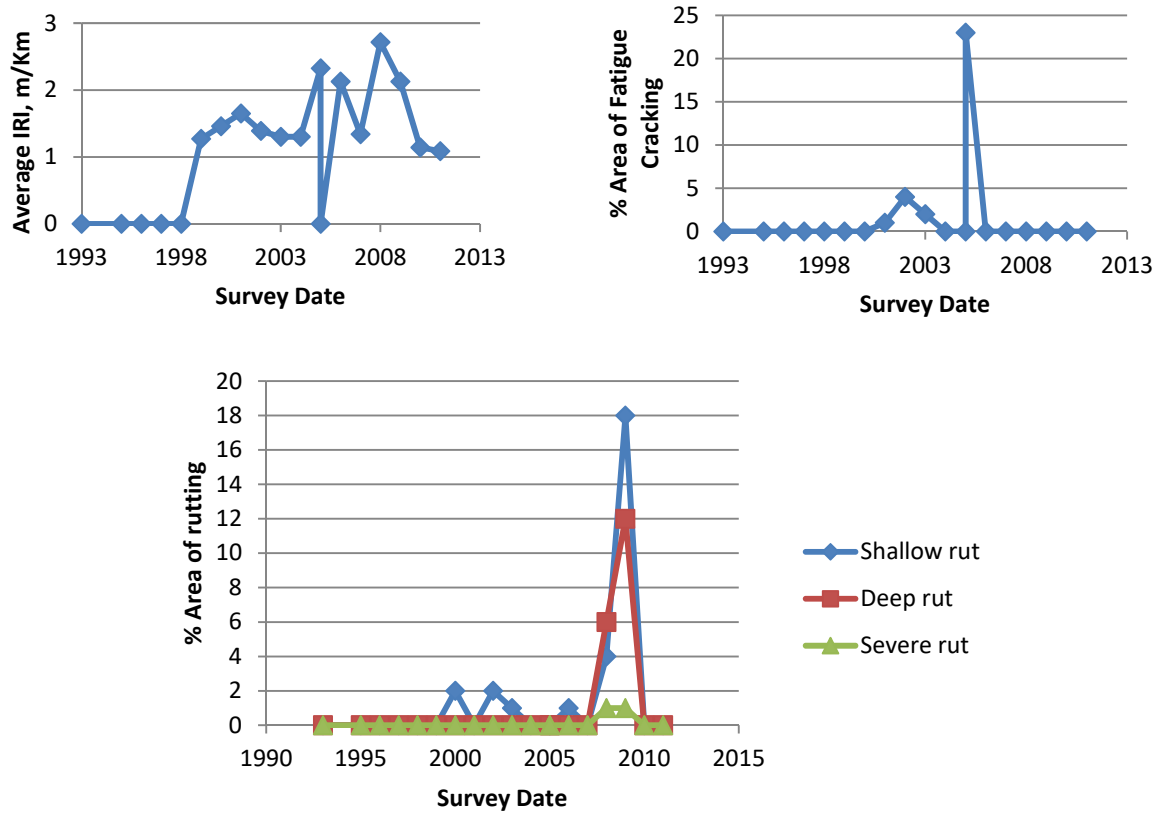
Section No.: Jefferson SH 0073-740

Layer Structure (N/A)



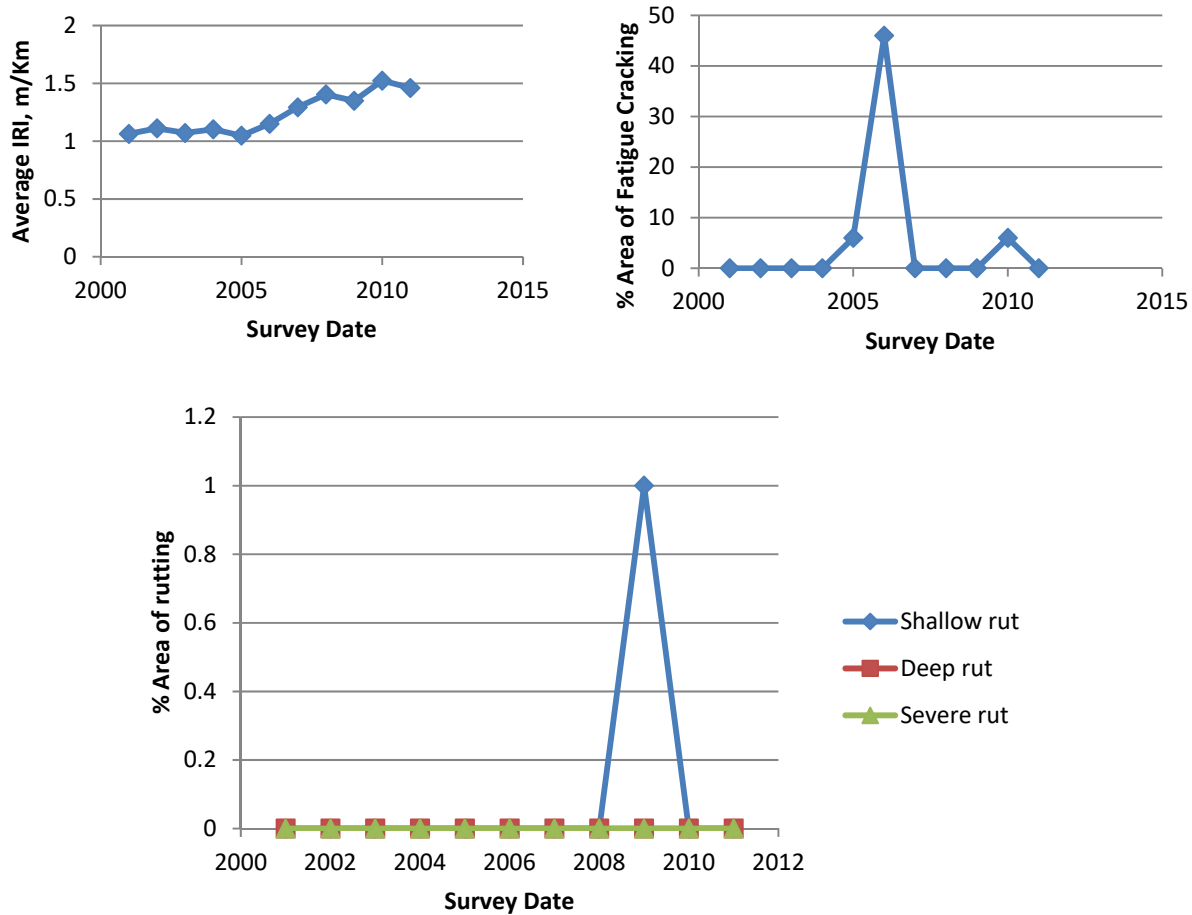
Section No.: Jefferson SH 0073-742

Layer Structure (N/A)



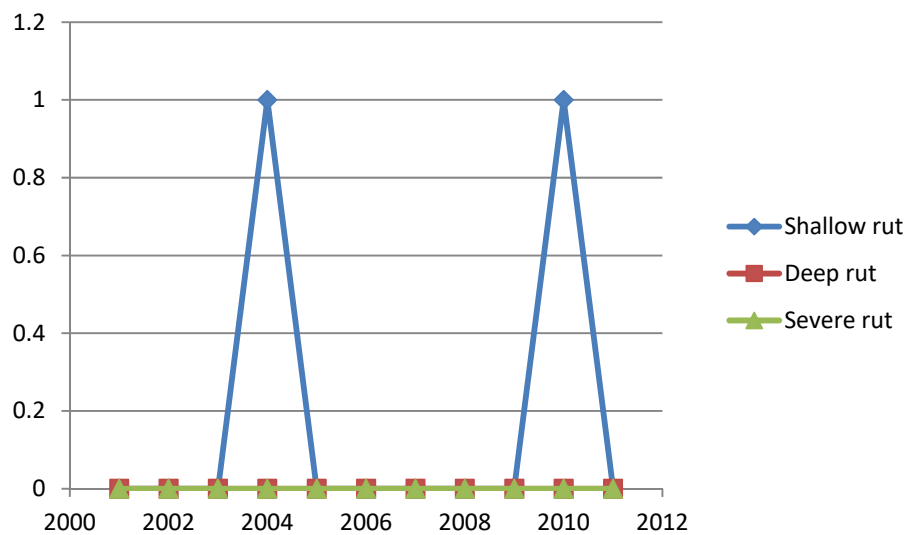
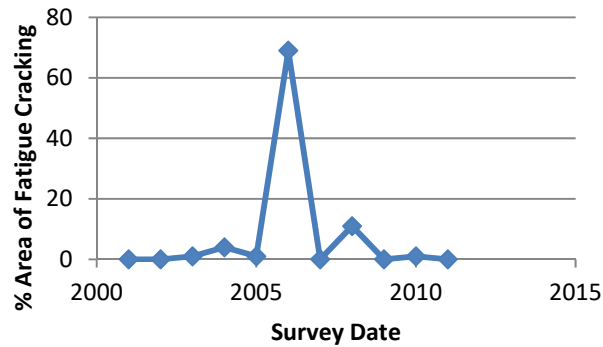
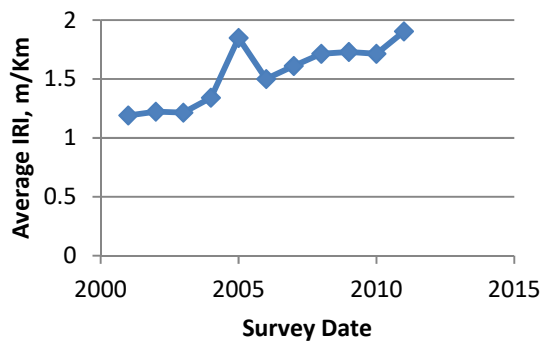
Section No.: Jefferson SH 0073-744

Layer Structure (N/A)



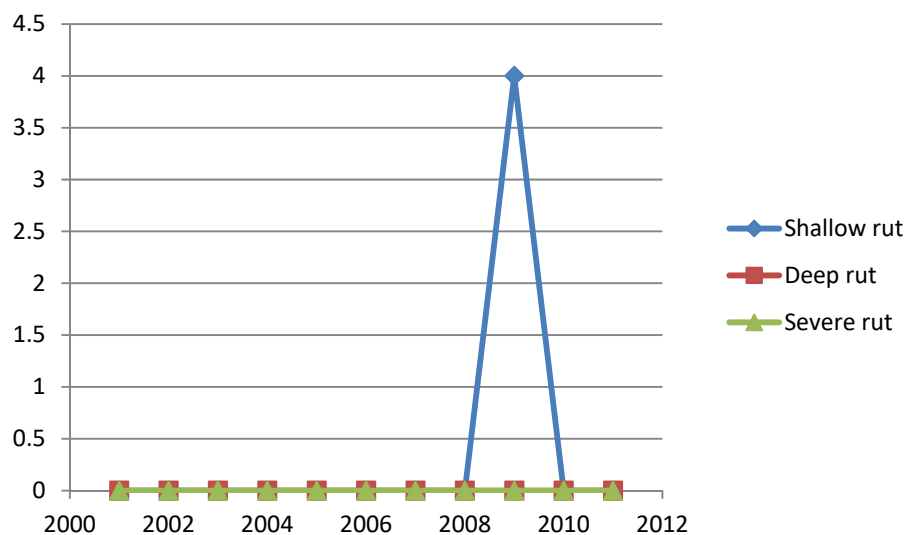
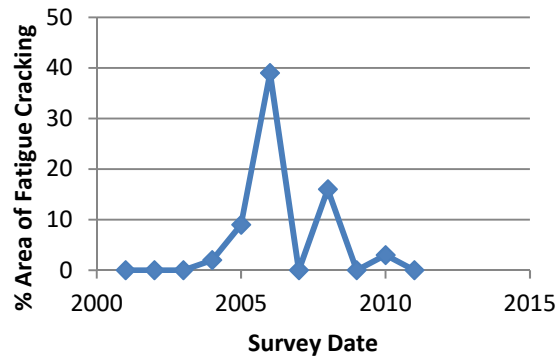
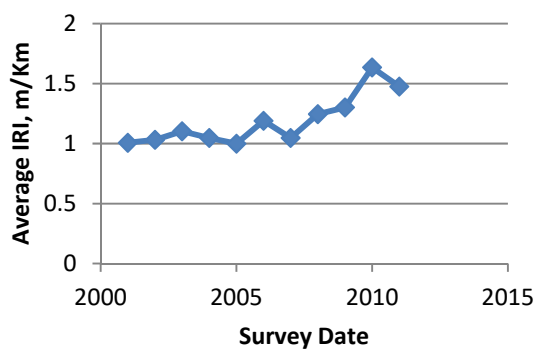
Section No.: Jefferson SH 0073-746

Layer Structure (N/A)



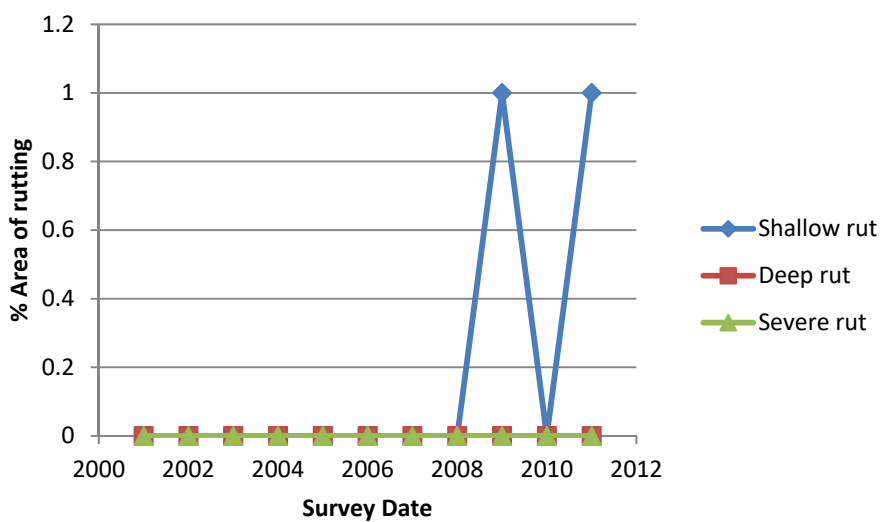
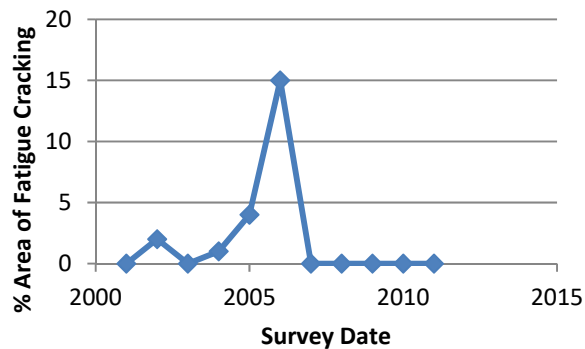
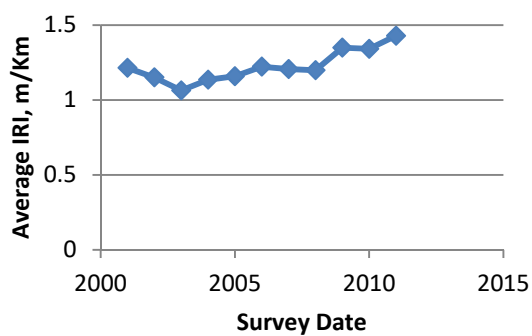
Section No.: Jefferson SH 0073-748

Layer Structure (N/A)



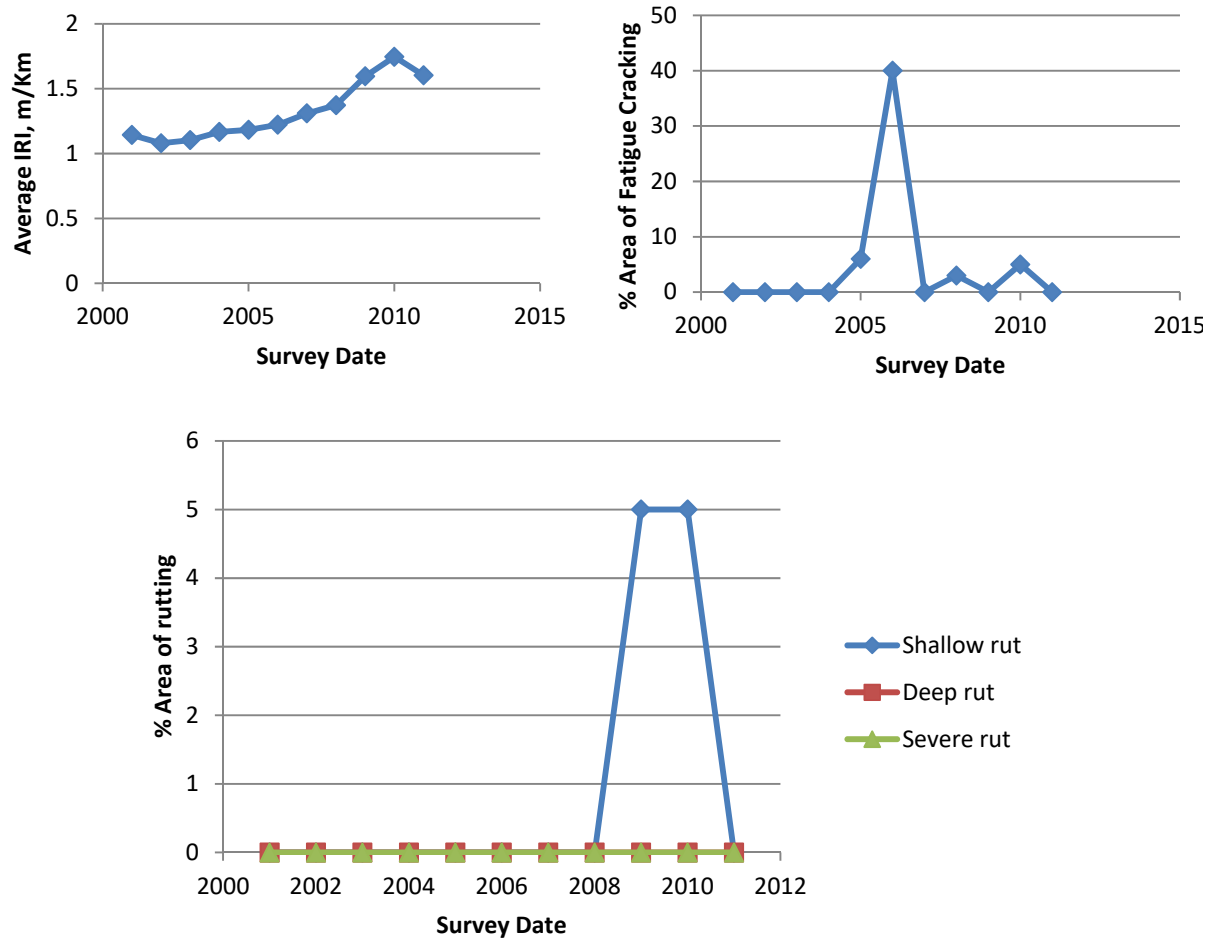
Section No.: Jefferson SH 0073-750

Layer Structure (N/A)



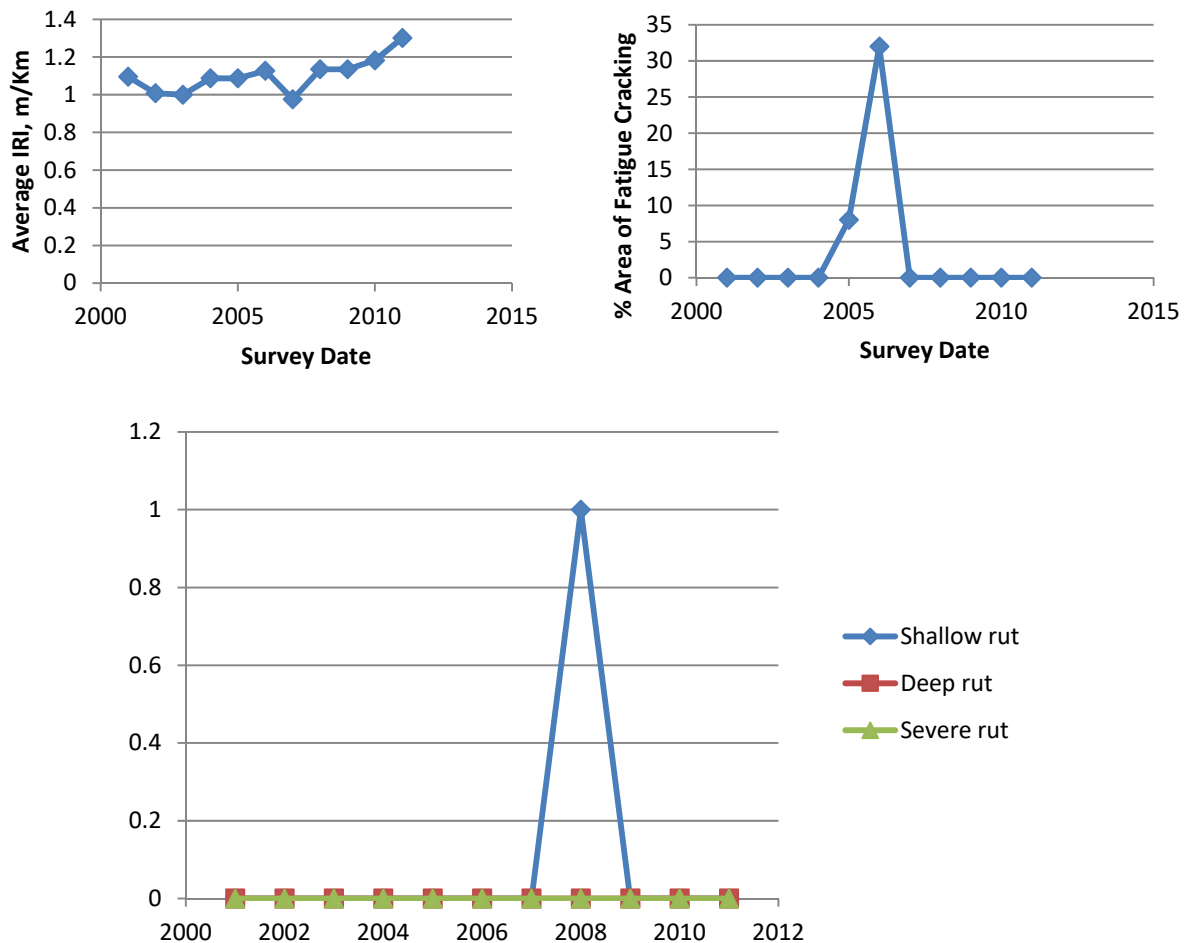
Section No.: Jefferson SH 0073-752

Layer Structure (N/A)



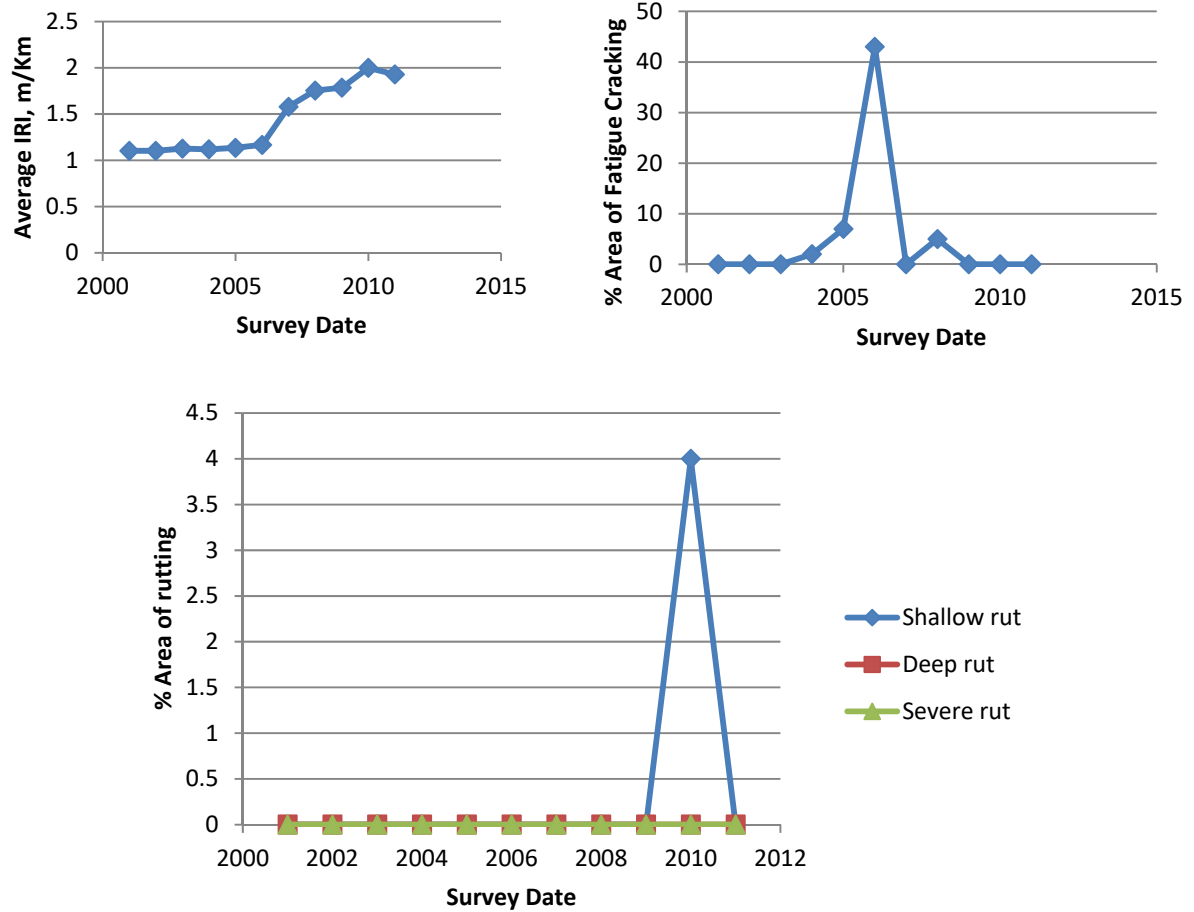
Section No.: Jefferson SH 0073-754

Layer Structure (N/A)



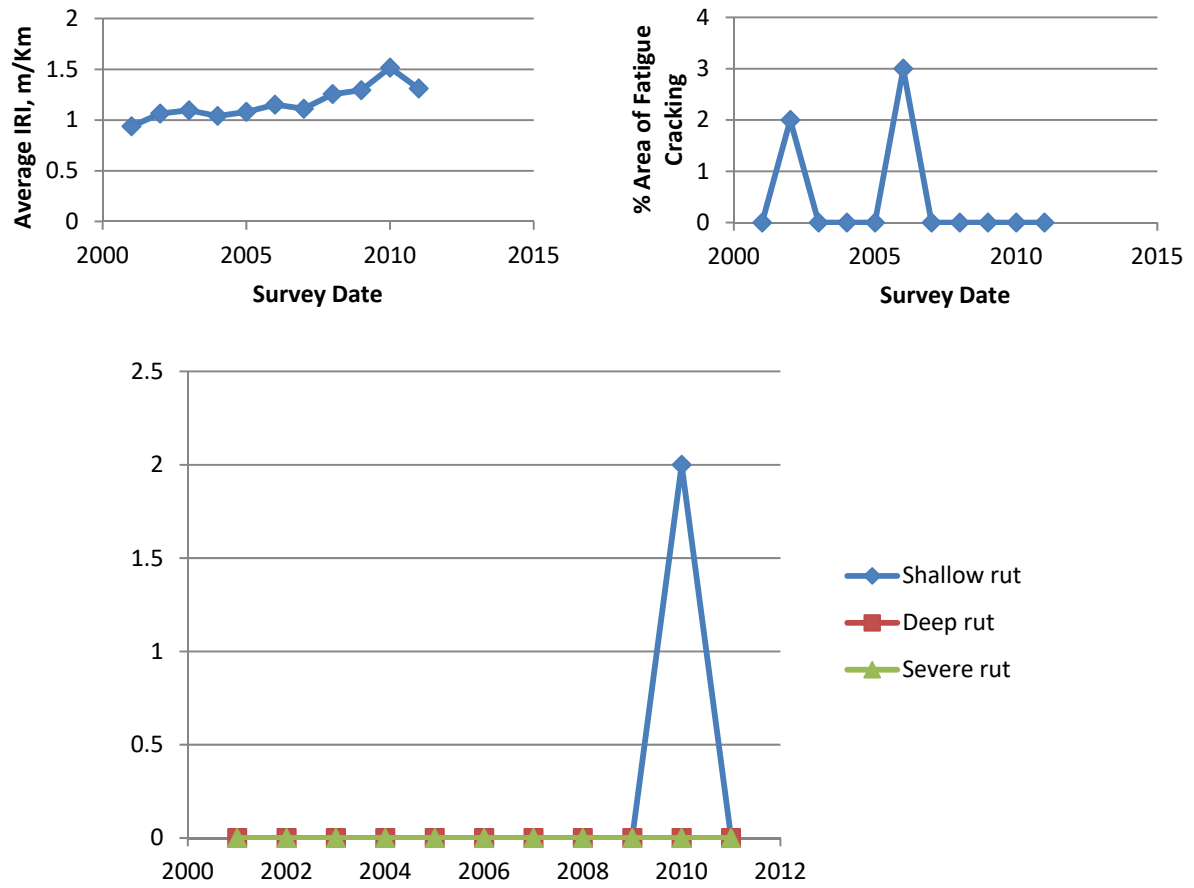
Section No.: Jefferson SH 0073-756

Layer Structure (N/A)



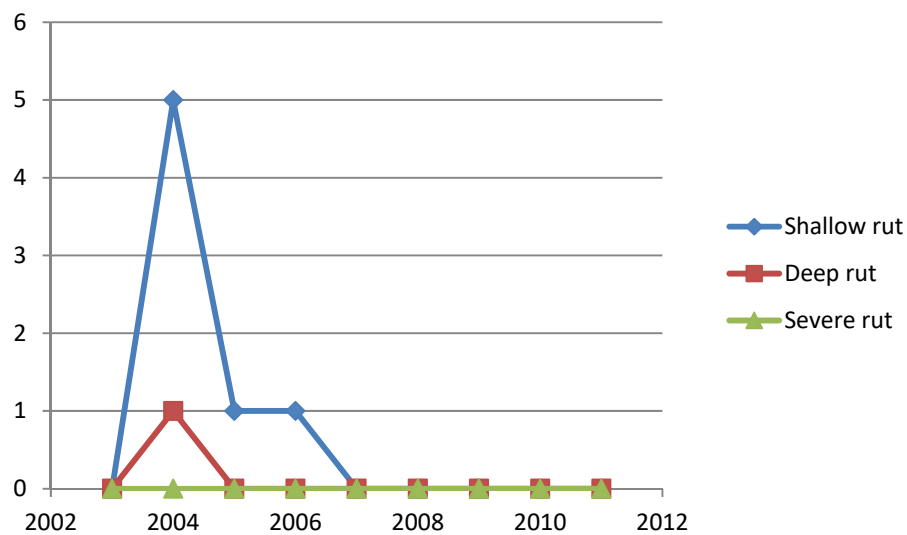
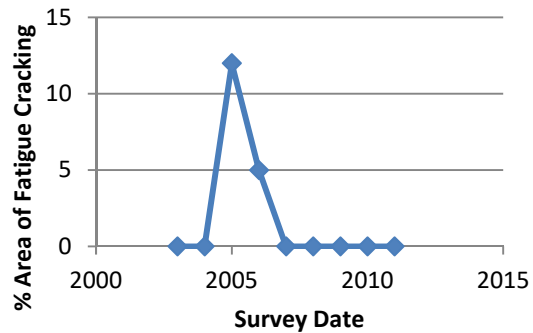
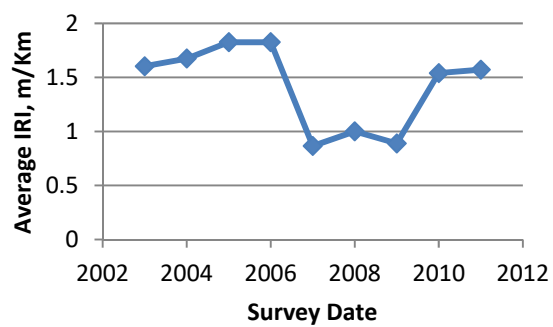
Section No.: Jefferson SH 0073-758

Layer Structure (N/A)



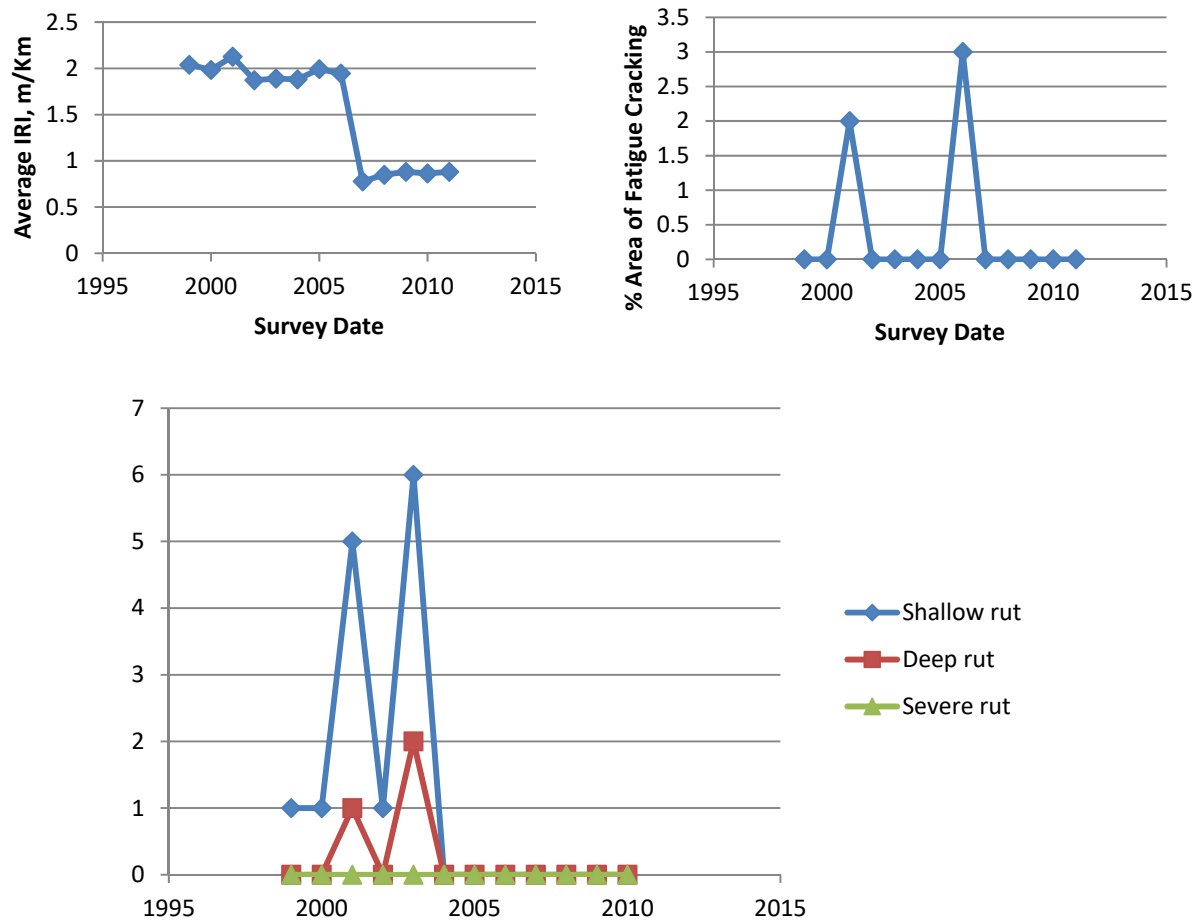
Section No.: Jefferson SH 0073-760

Layer Structure (N/A)



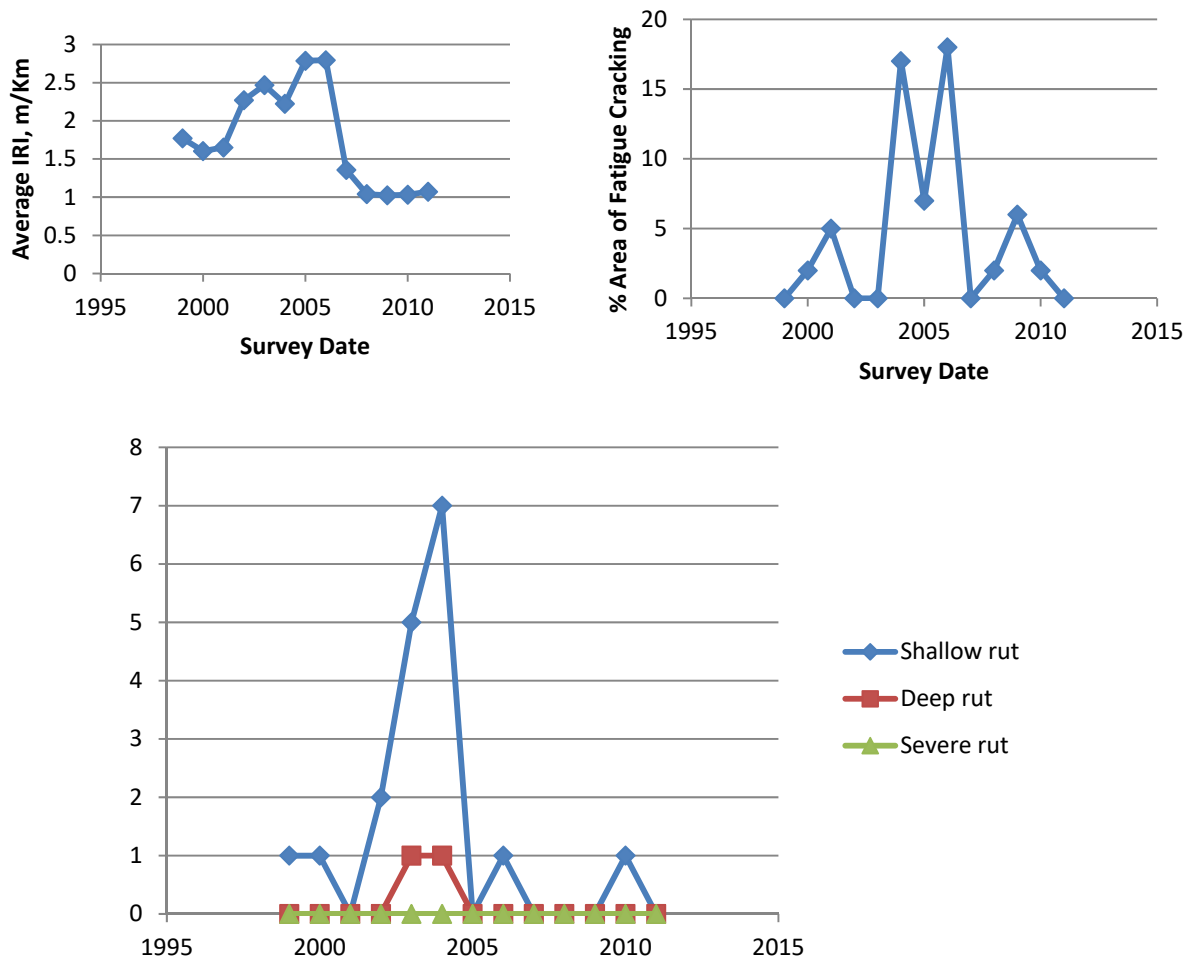
Section No.: Jefferson SH 0073-762

Layer Structure (N/A)



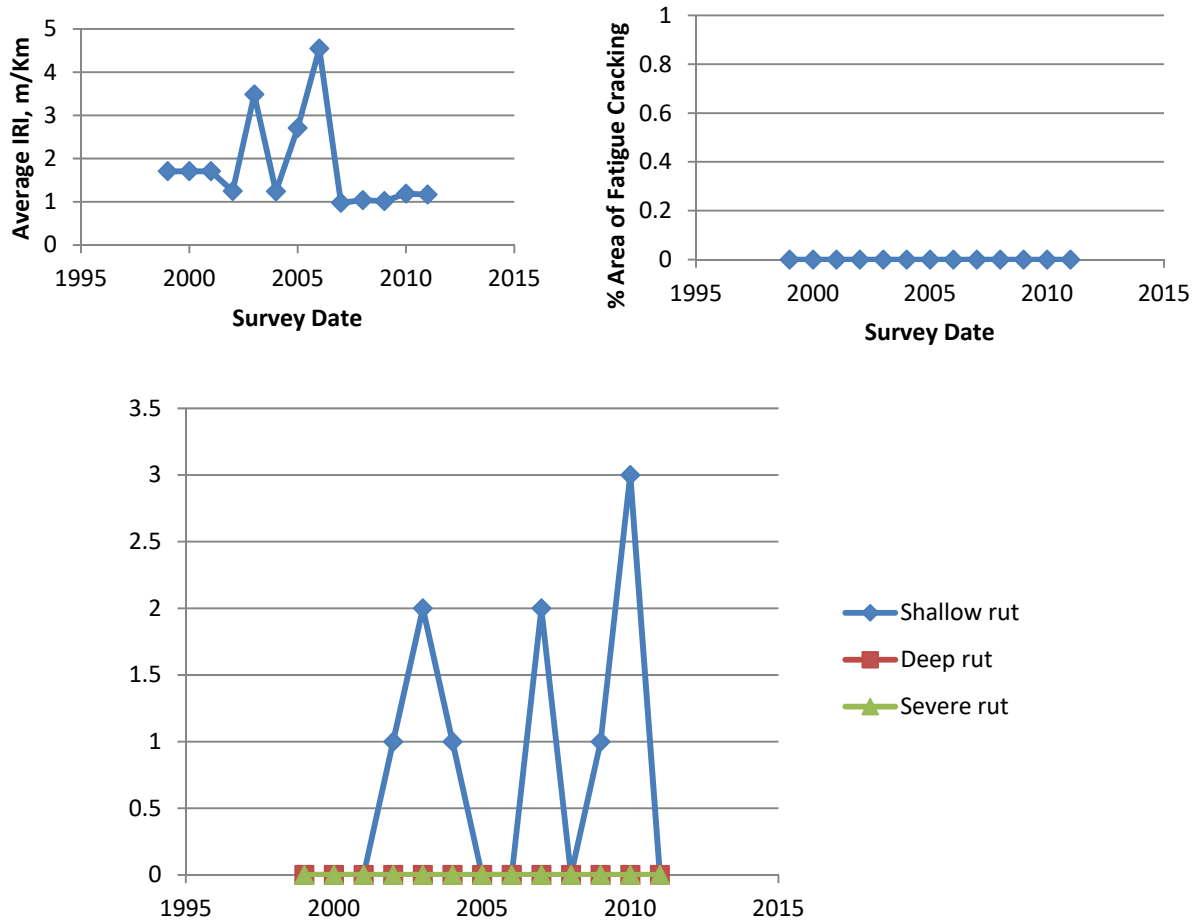
Section No.: Jefferson SH 0073-764

Layer Structure (N/A)



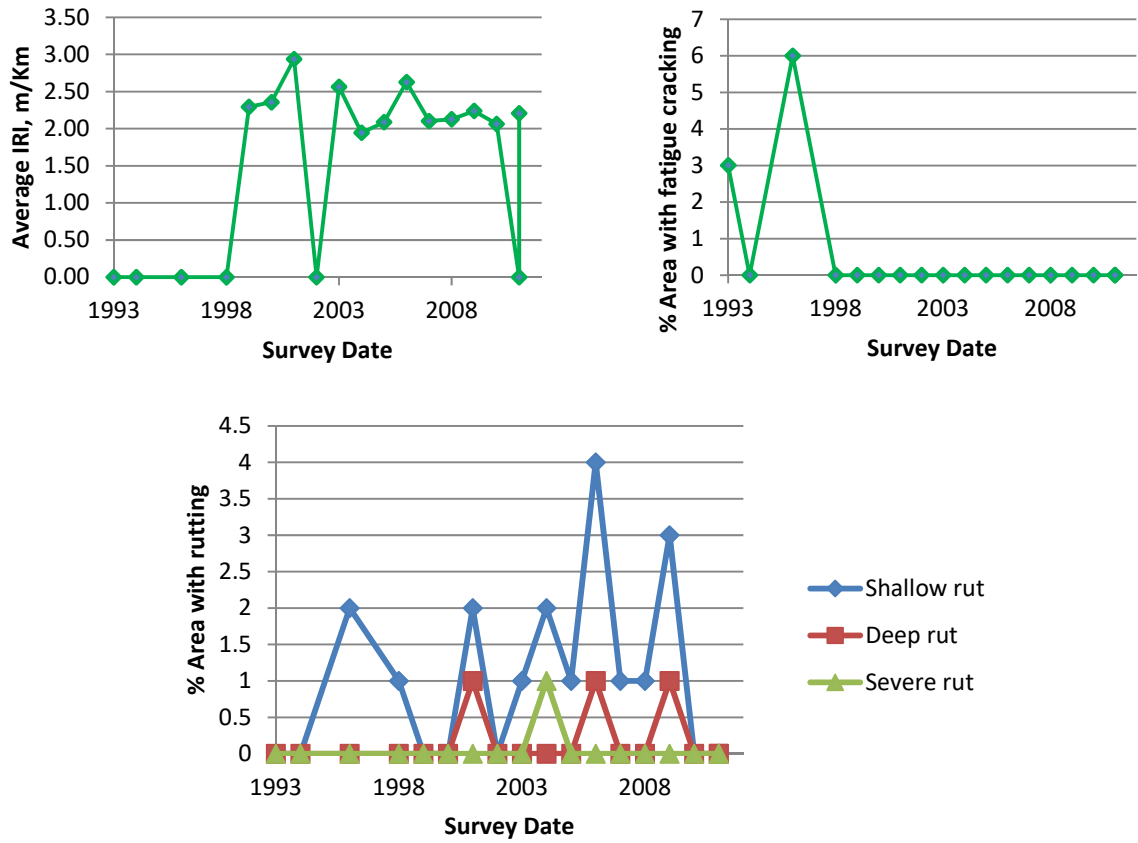
Section No.: Jefferson SH 0073-766 Control

Layer Structure (N/A)



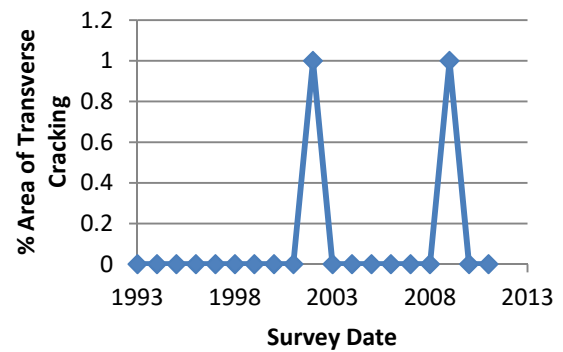
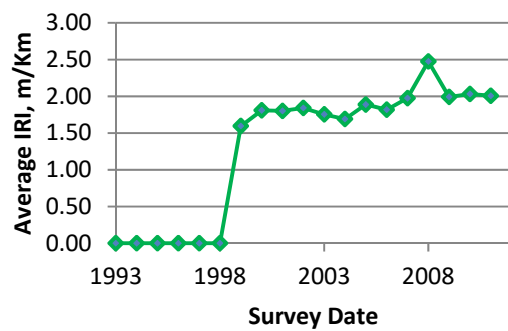
Section No.: Houston FM 0357-688

Layer Structure (N/A)



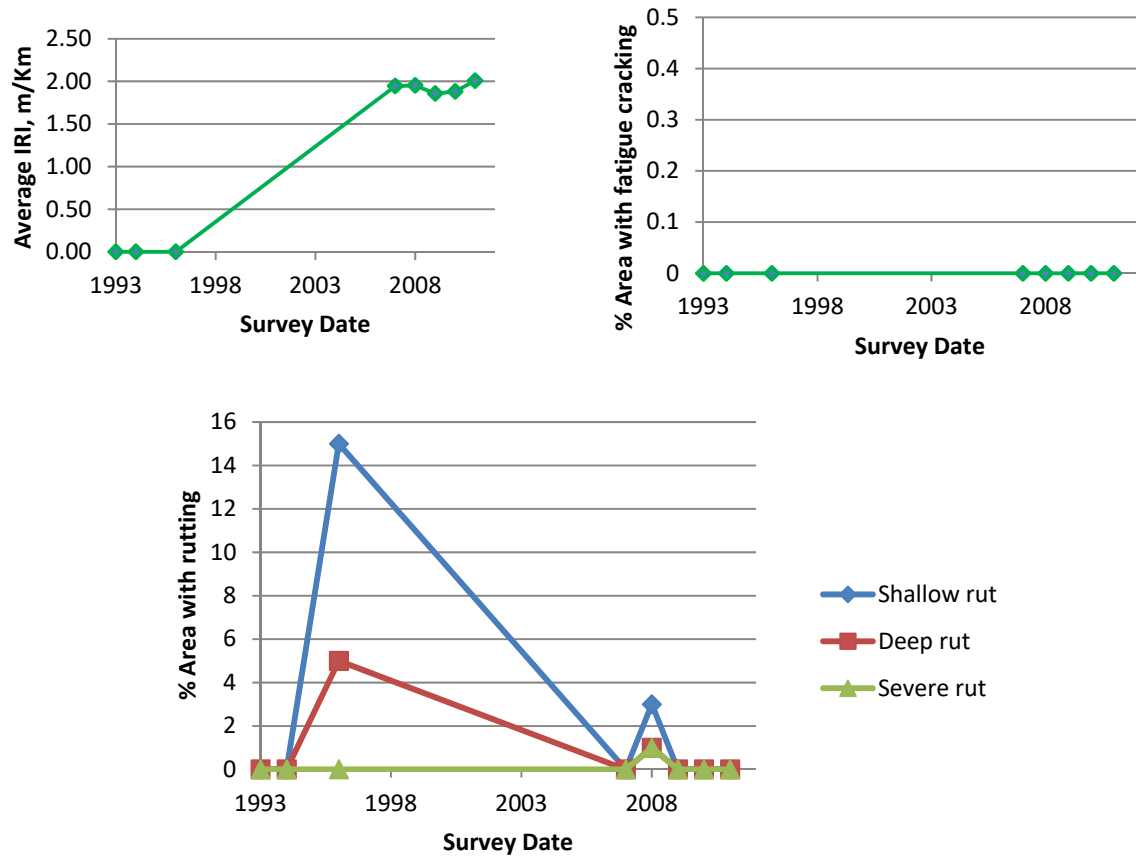
Section No.: Navarro IH 0045-218

Layer Number	Layer Type	Thickness (mm)	Material Description	Modulus
1	SS			
2	EF			
3	GB	152.4–254	Flexible base	
4	PC		JPCP	



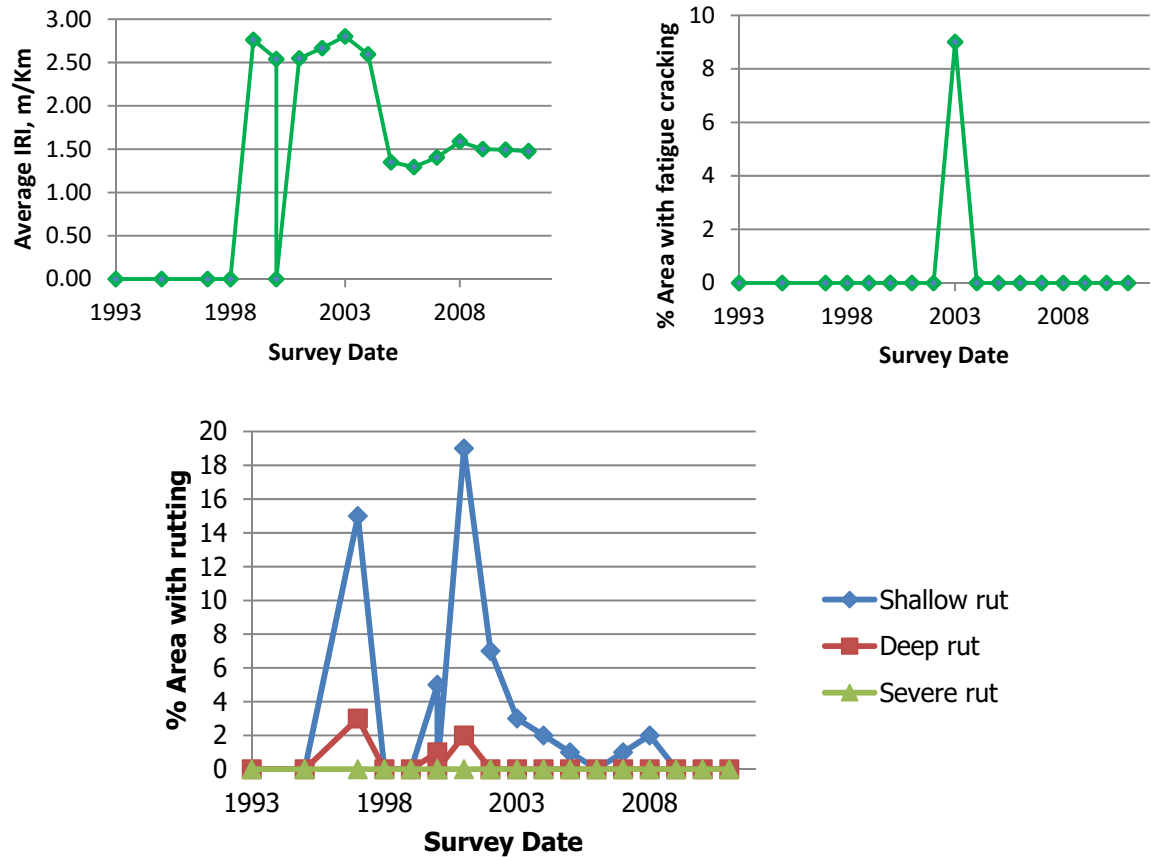
Section No.: Panola FM 0123-740

Layer Structure (N/A)



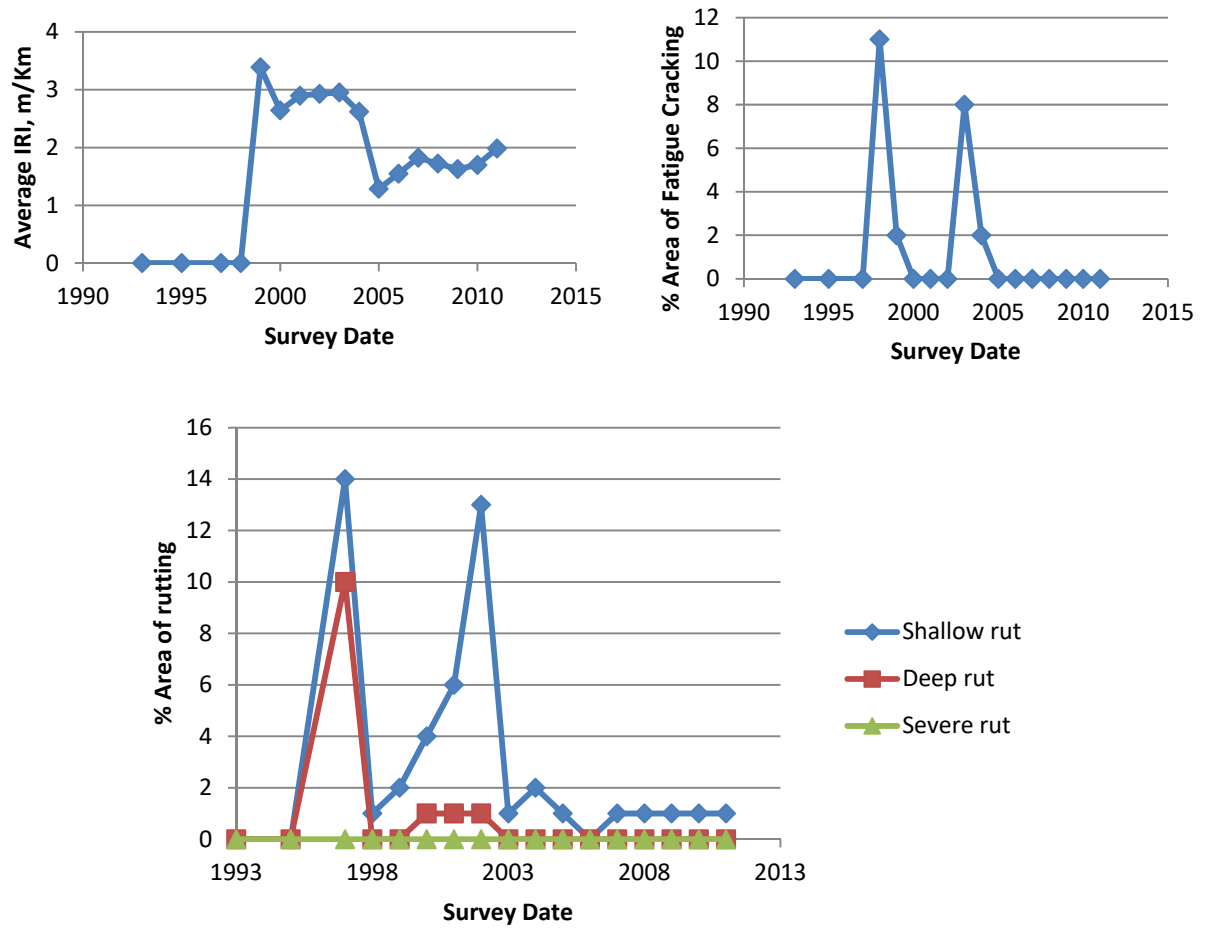
Section No.: Panola FM 0699-304

Layer Structure (N/A)

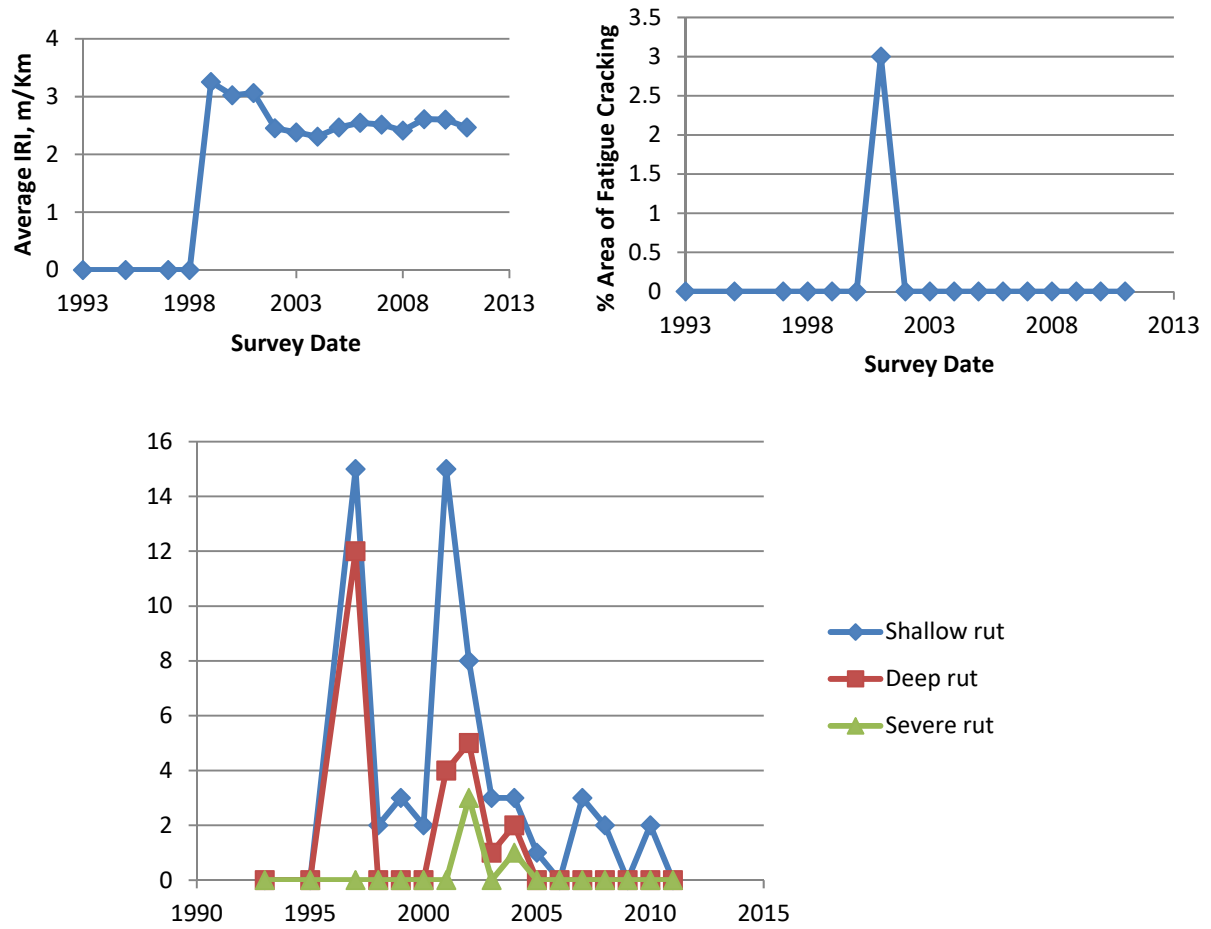


Section No.: Panola FM 0699-306

Layer Structure (N/A)

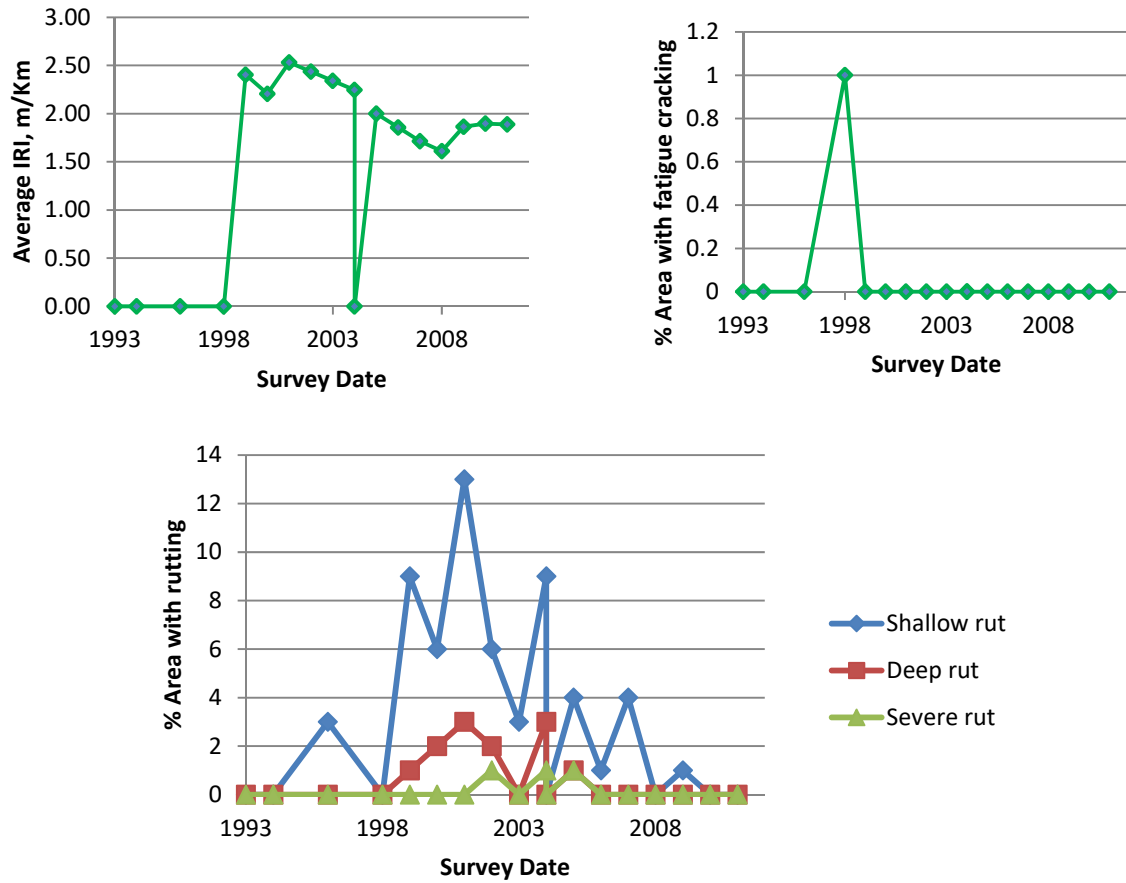


Section No.: Panola FM 0699-308 Control
Layer Structure (N/A)



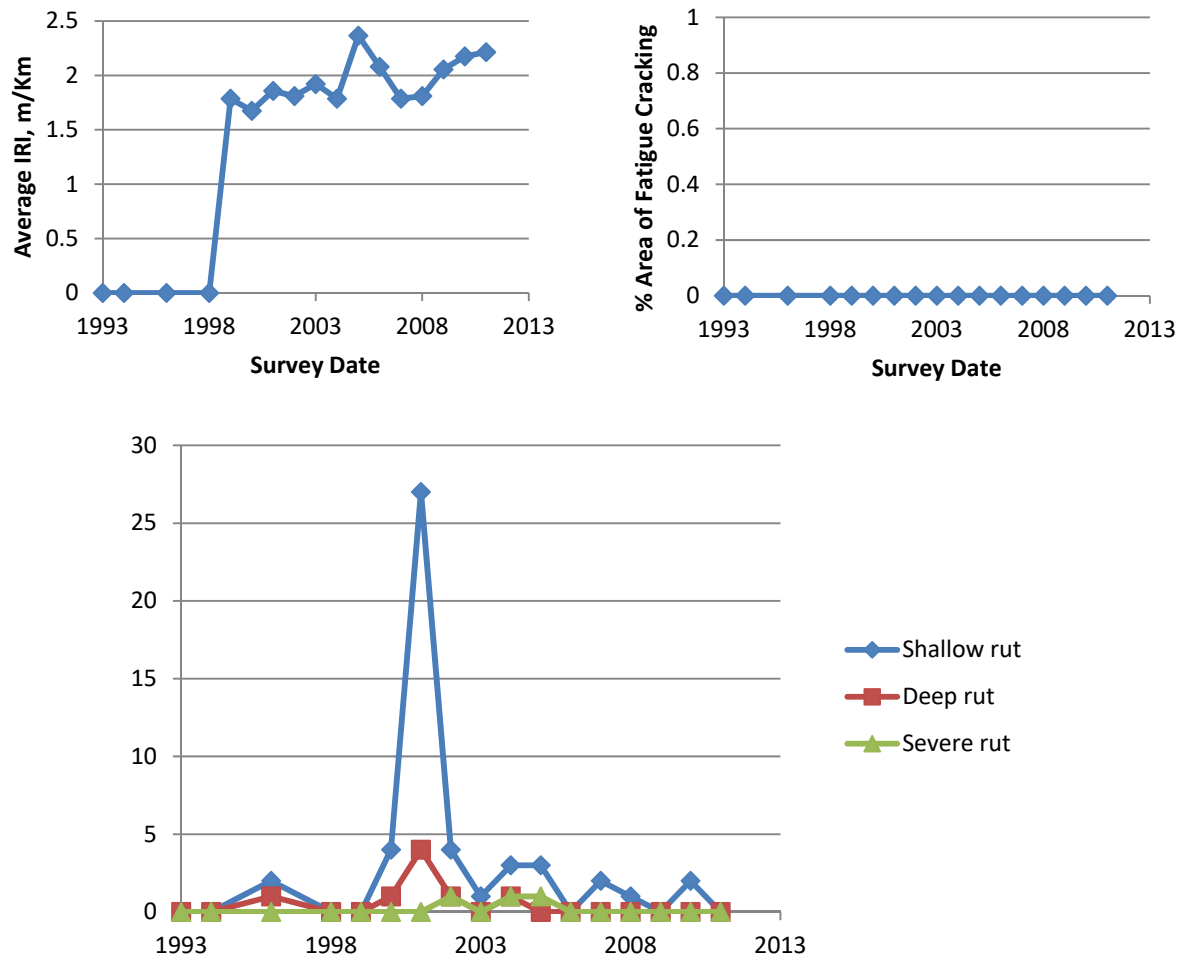
Section No.: Panola FM 2517-736

Layer Structure (N/A)



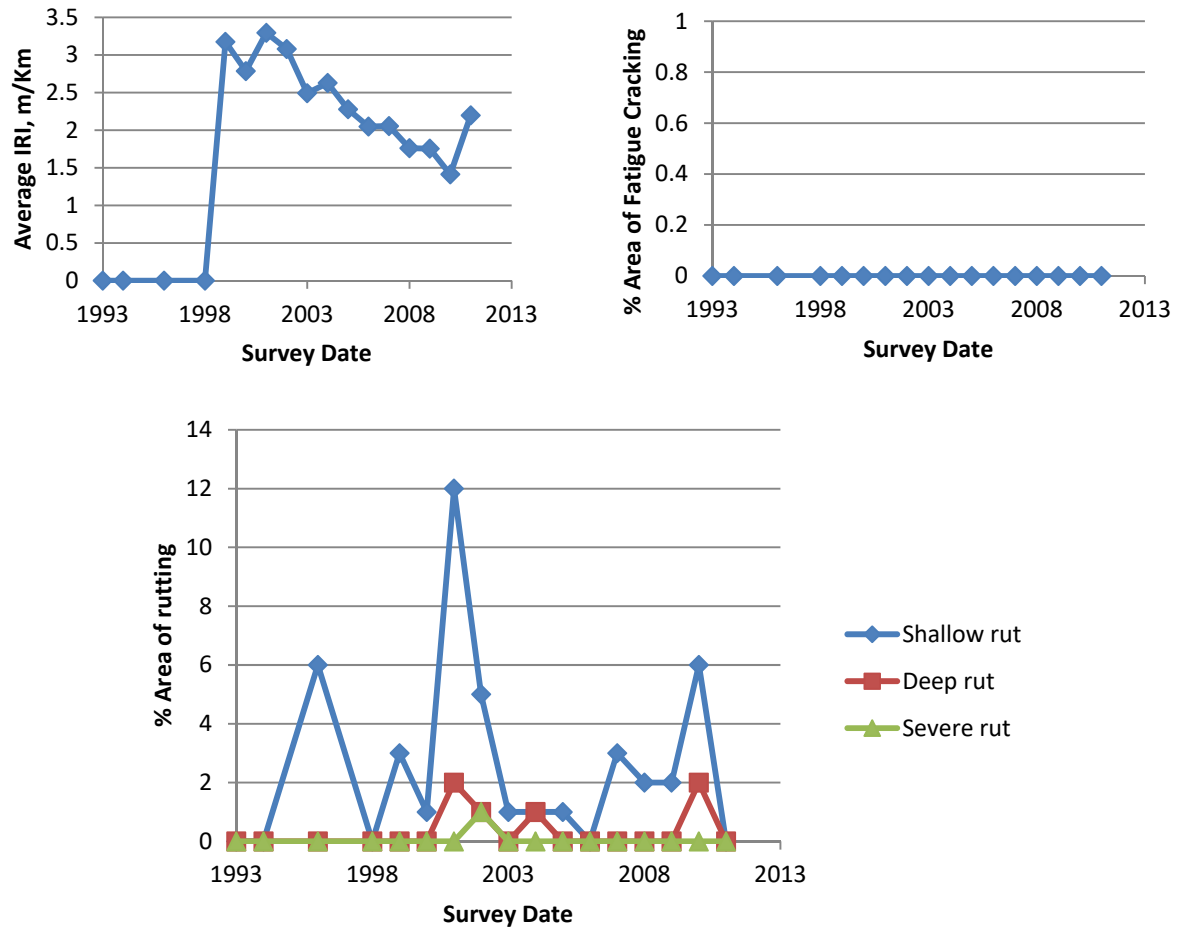
Section No.: Panola FM 2517-738

Layer Structure (N/A)



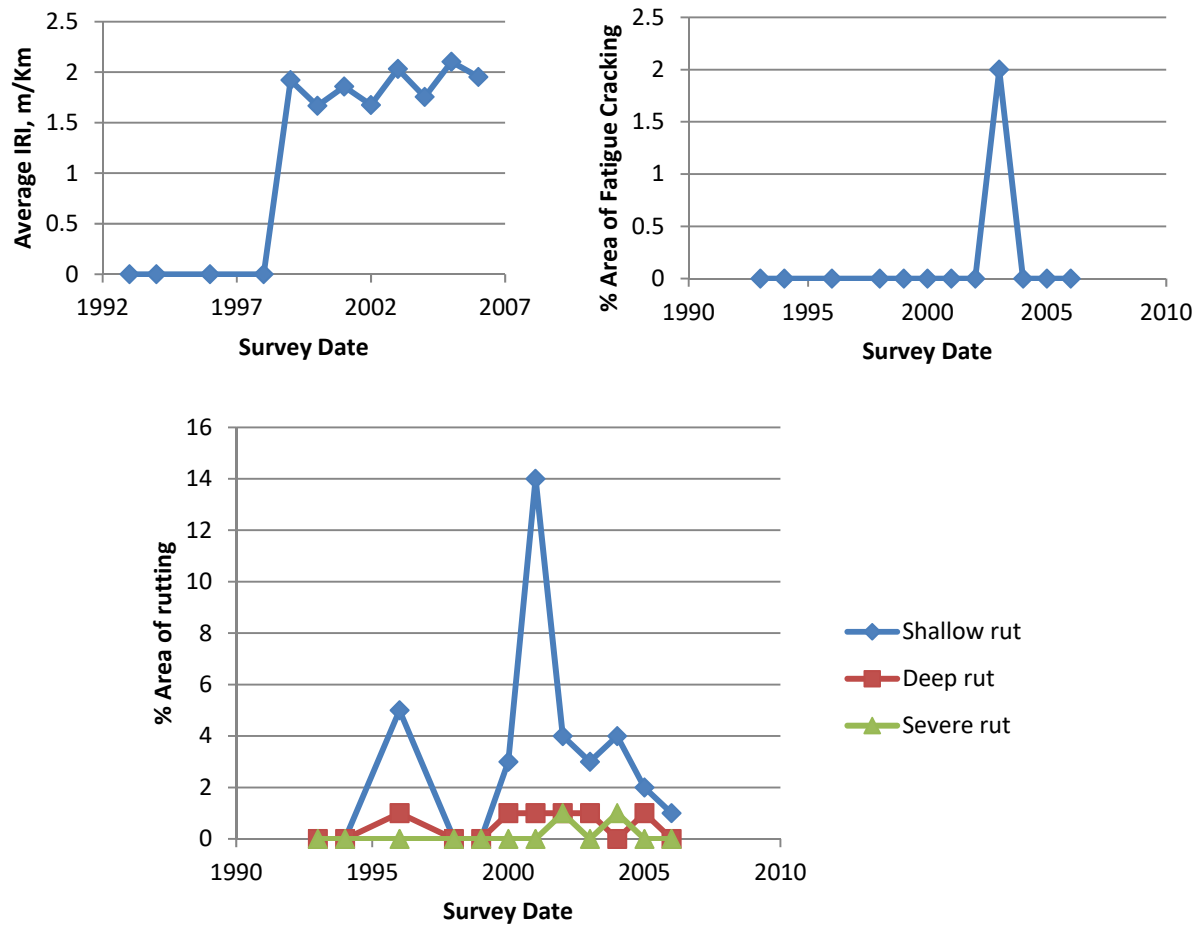
Section No.: Panola FM 2517-744

Layer Structure (N/A)



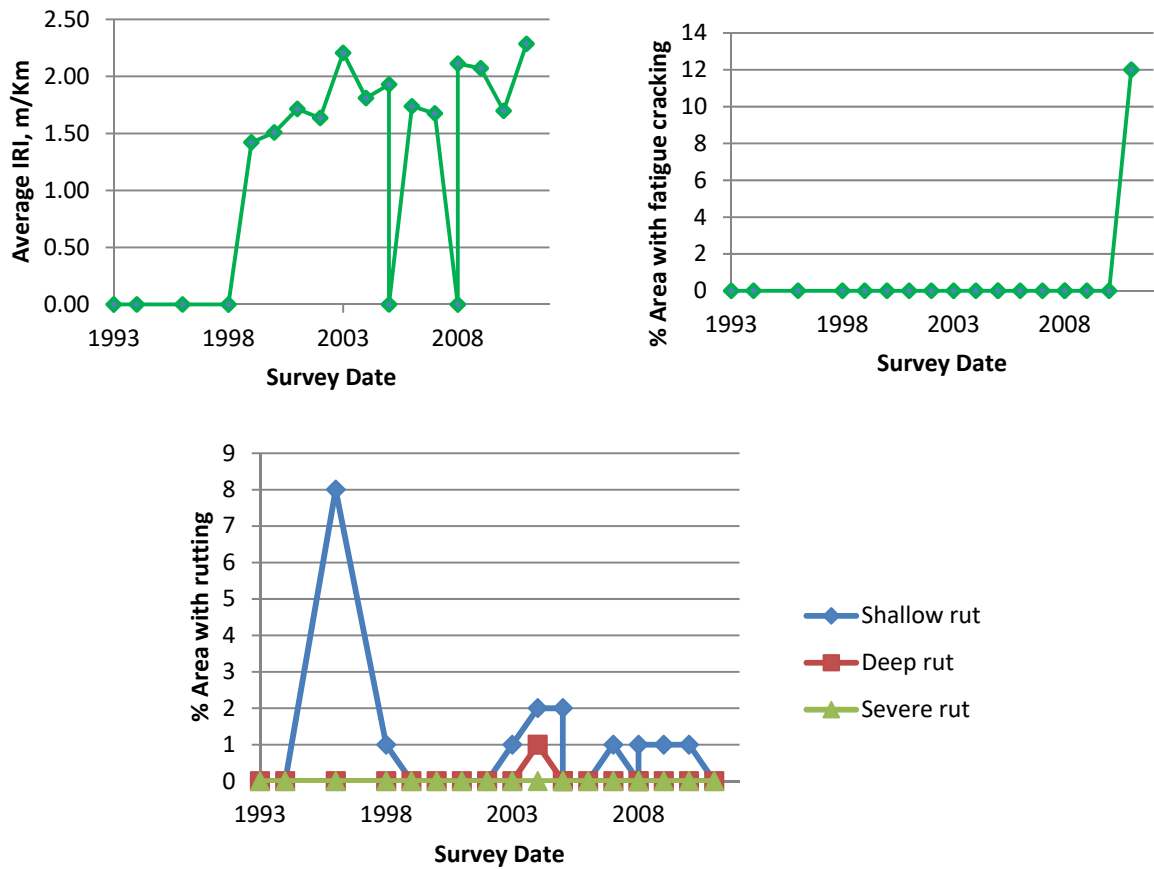
Section No.: Panola FM 2517-740 Control

Layer Structure (N/A)



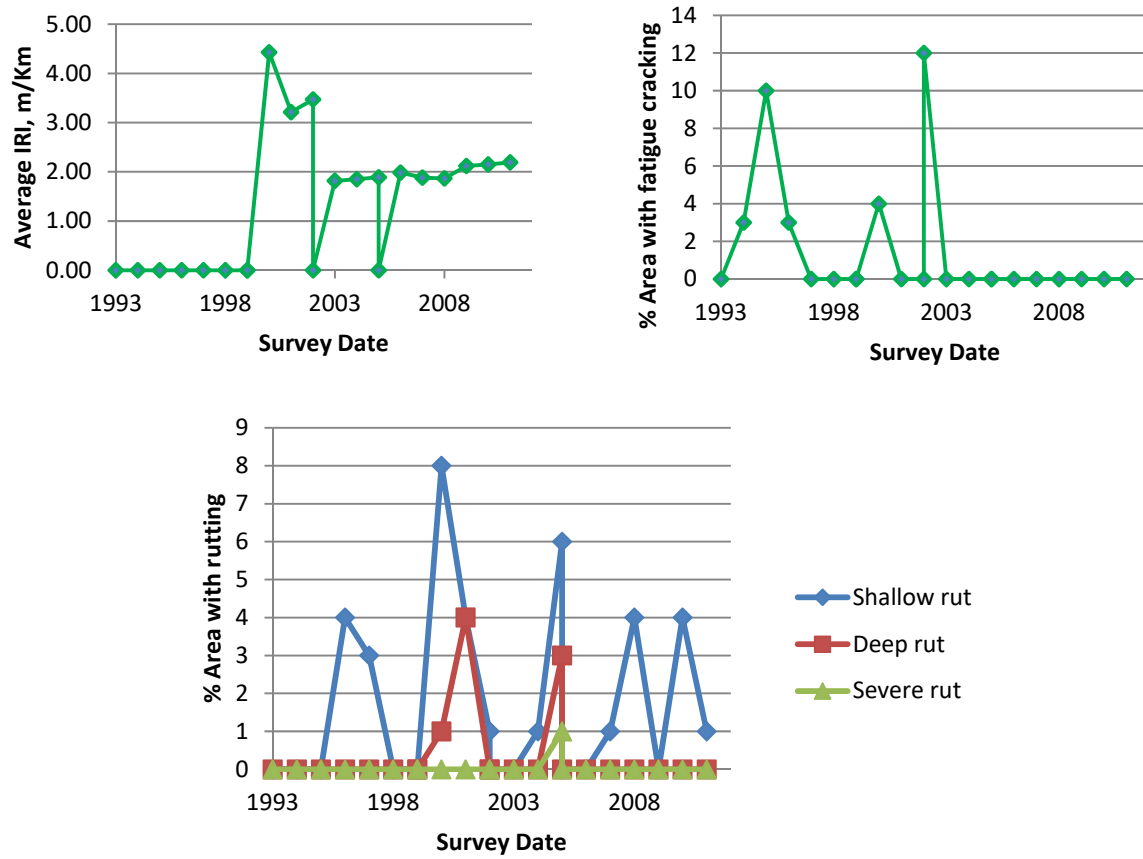
Section No.: Titus FM 1402-232

Layer Structure (N/A)



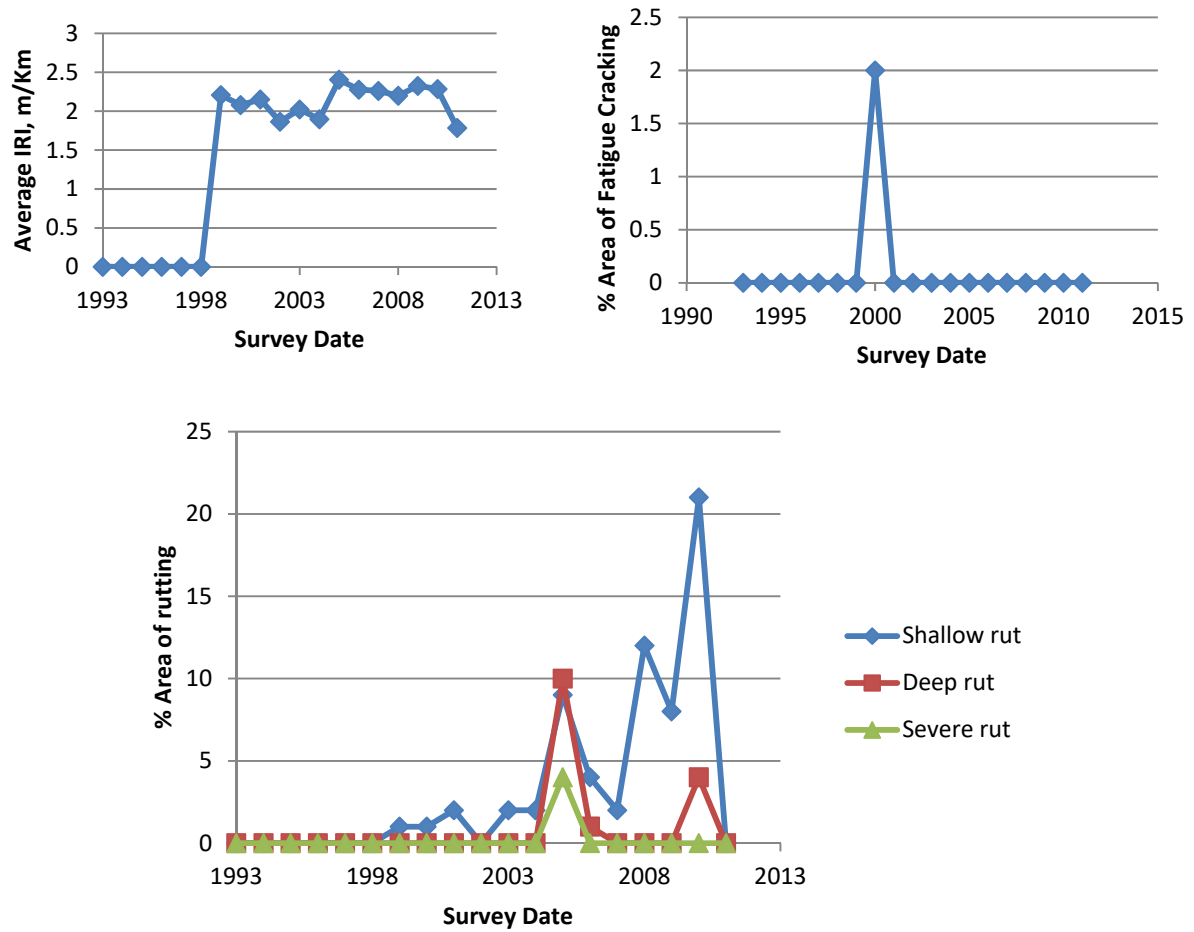
Section No.: Walker FM 1696-672

Layer Structure (N/A)



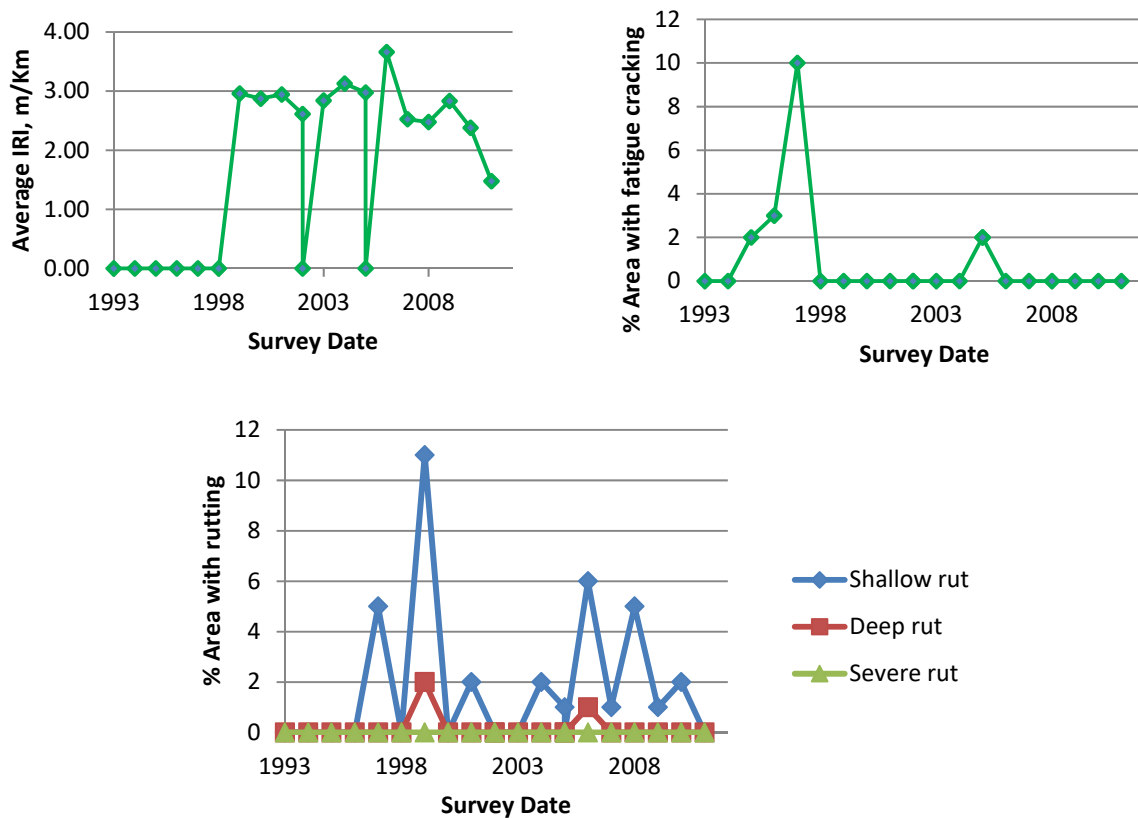
Section No.: Walker FM 1696-670 Control

Layer Structure (N/A)



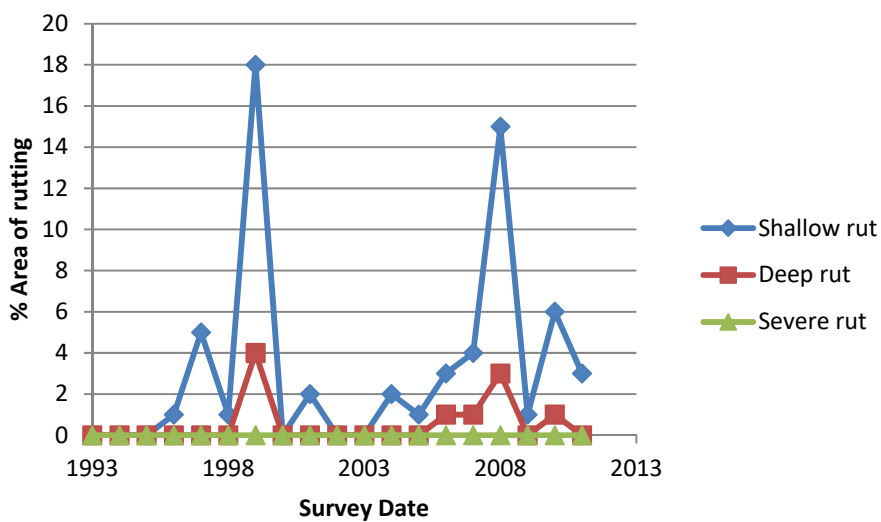
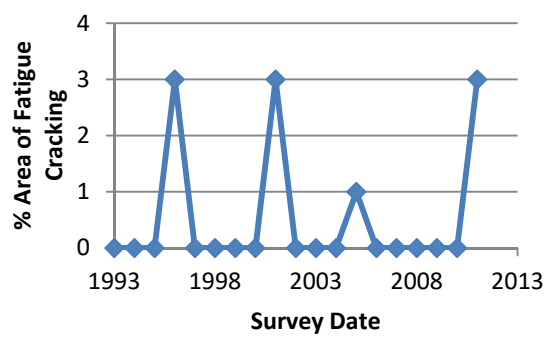
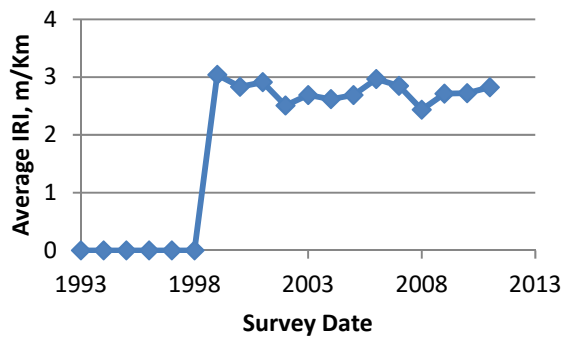
Section No.: Madison FM 0039-406

Layer Structure (N/A)



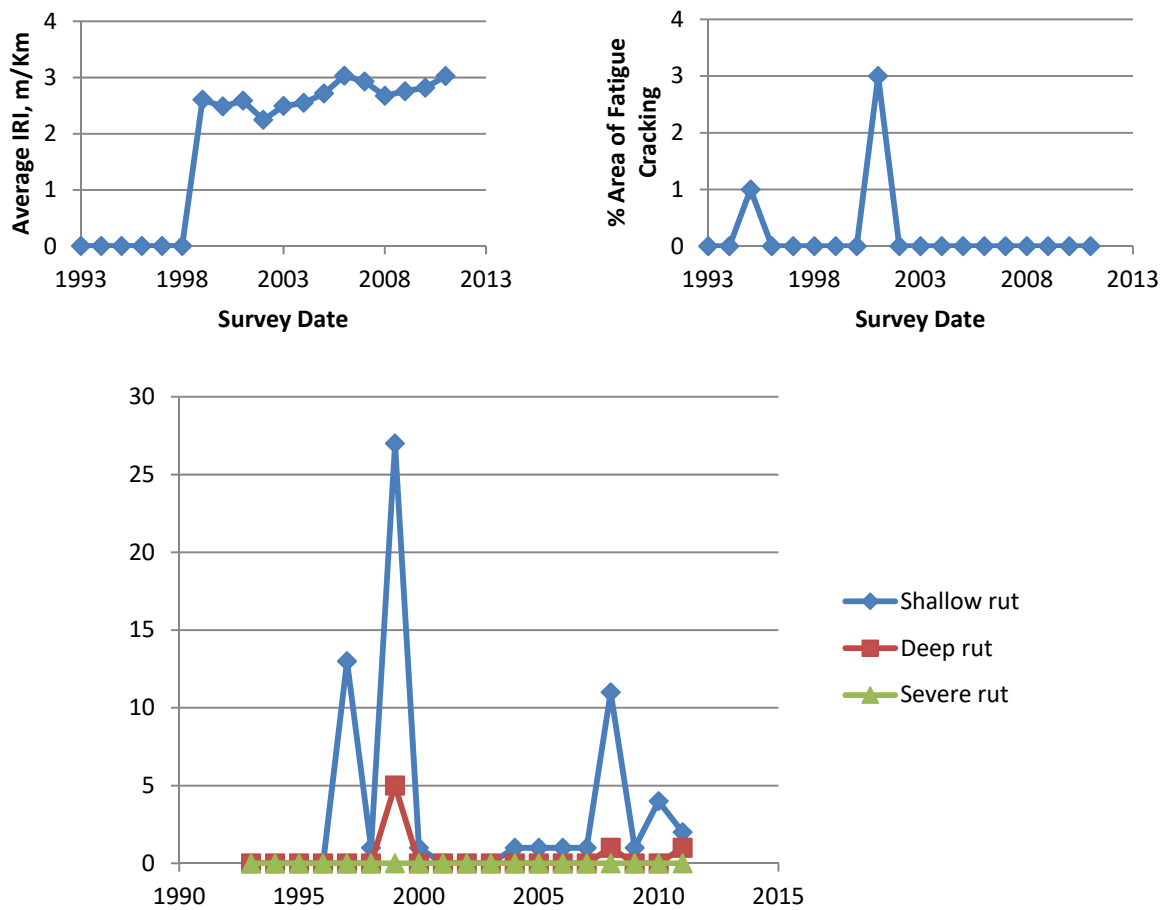
Section No.: Madison FM 0039-408

Layer Structure (N/A)



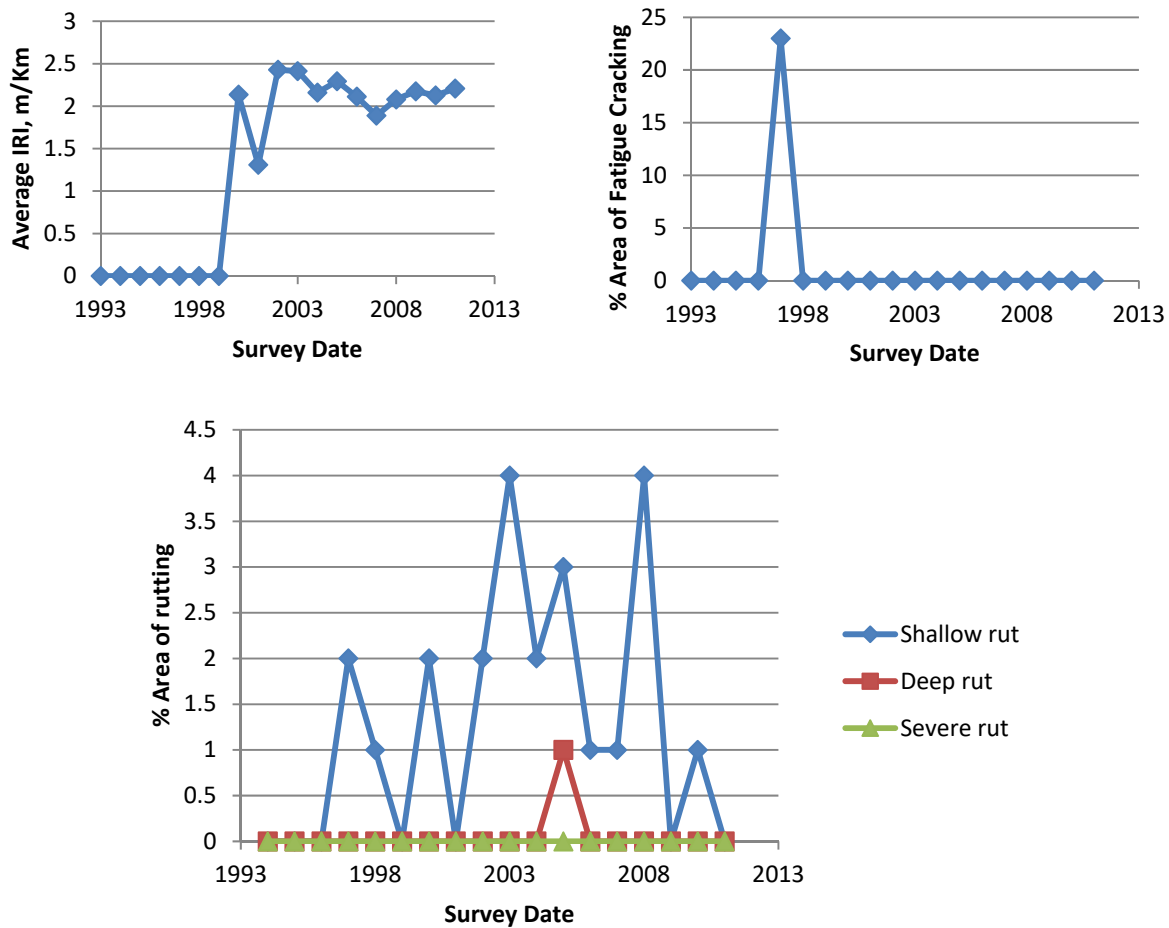
Section No.: Madison FM 0039-410

Layer Structure (N/A)



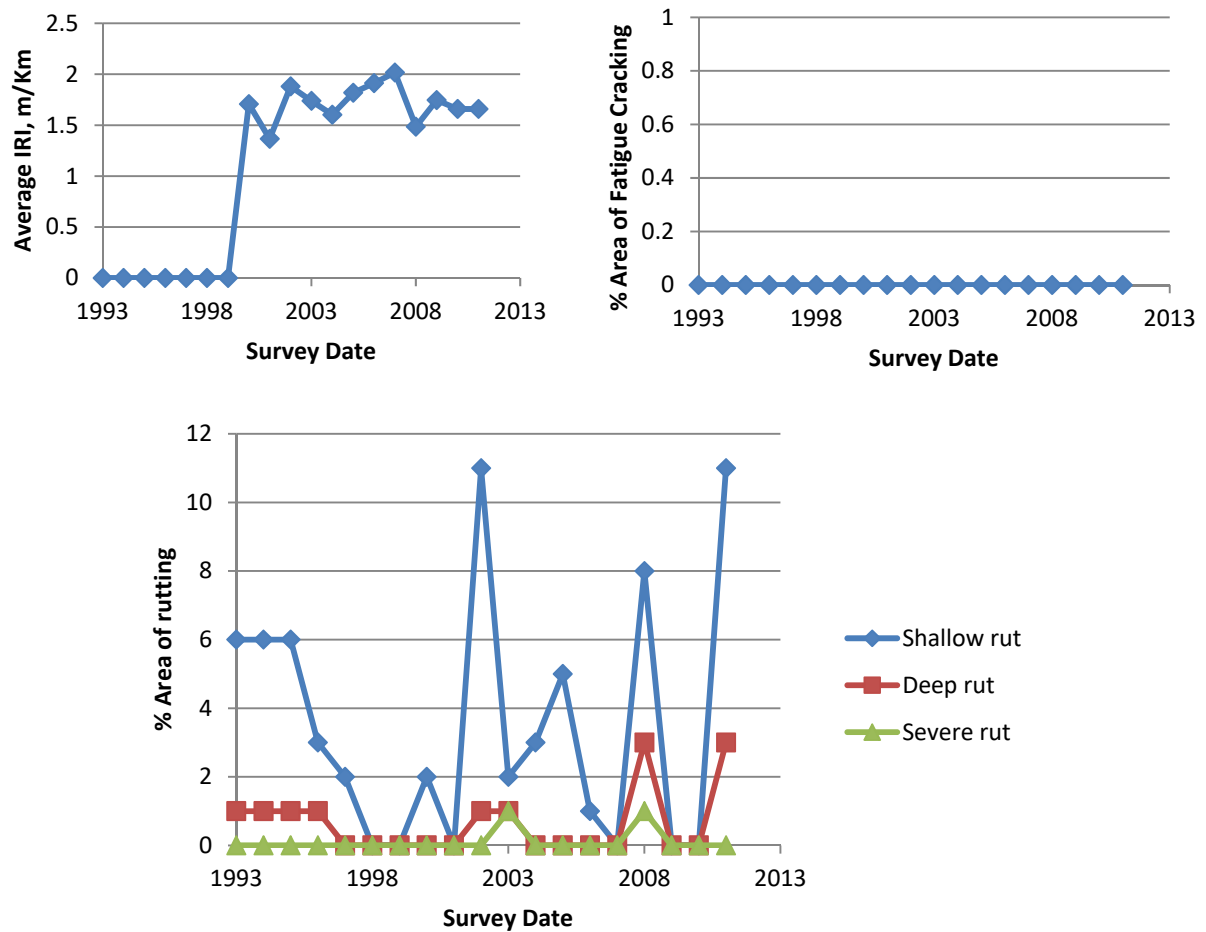
Section No.: Madison FM 0039-412

Layer Structure (N/A)



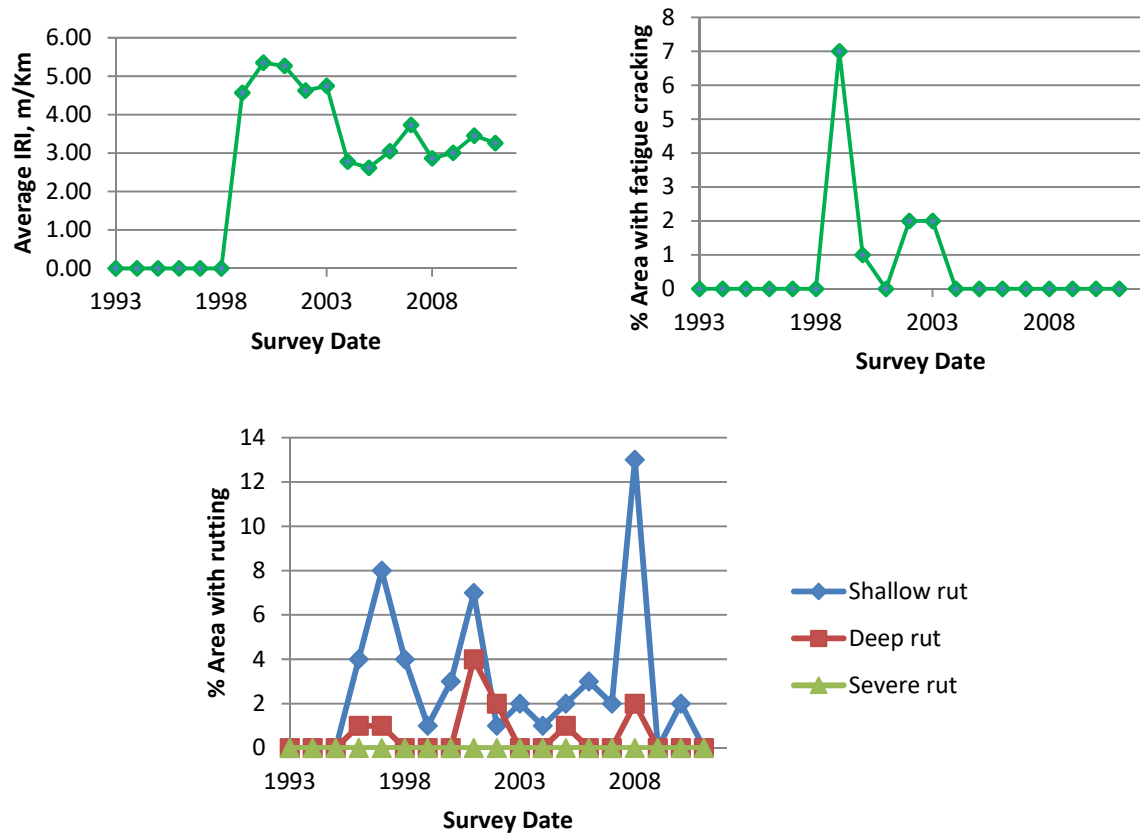
Section No.: Madison FM 0039-414 Control

Layer Structure (N/A)



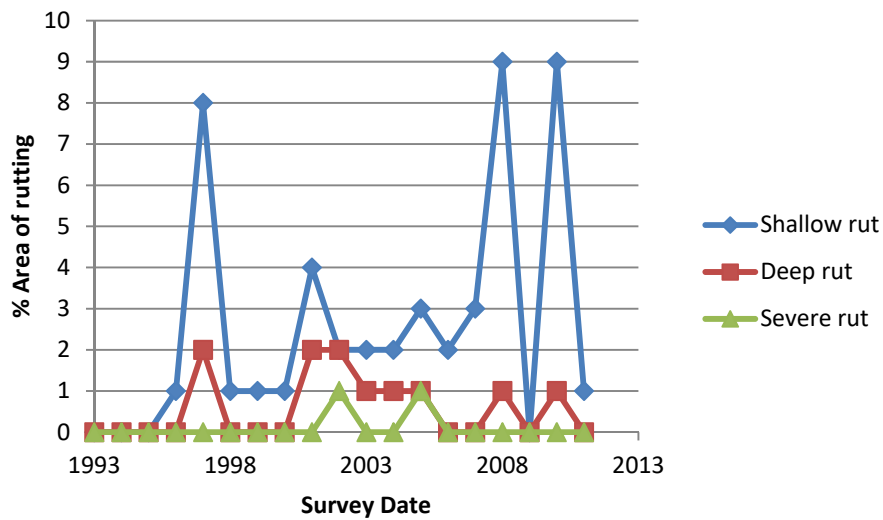
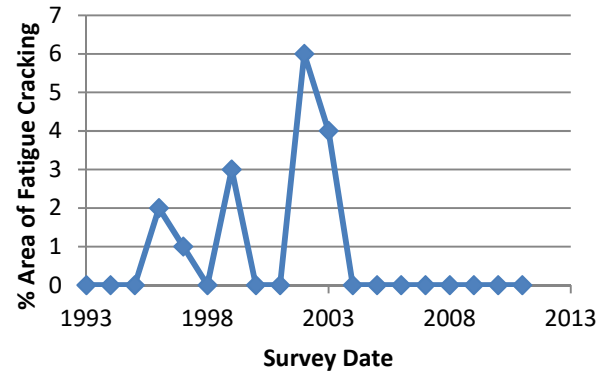
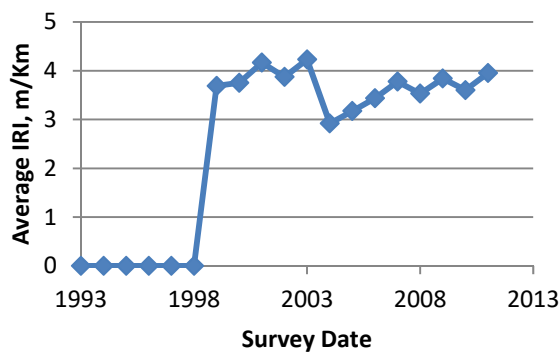
Section No.: Madison FM 1428-646

Layer Structure (N/A)



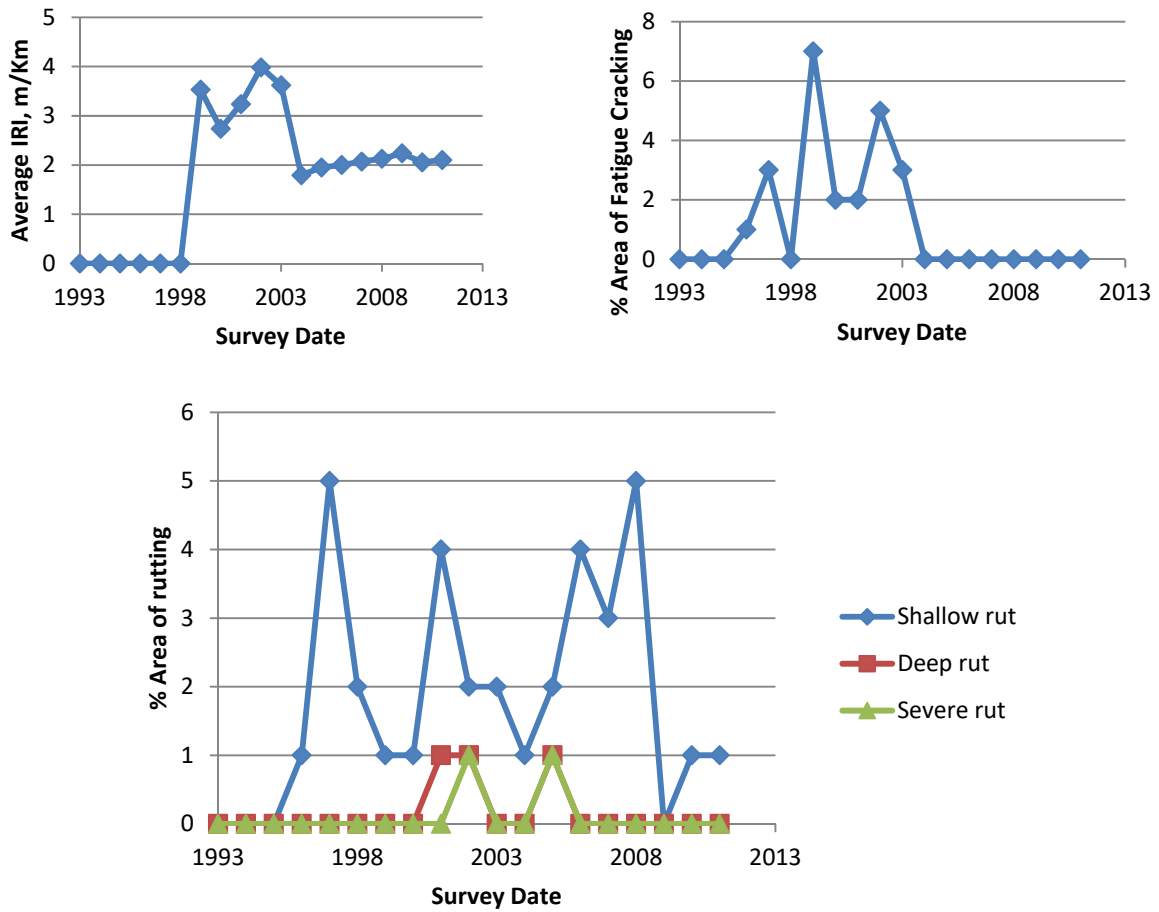
Section No.: Madison FM 1428-648

Layer Structure (N/A)



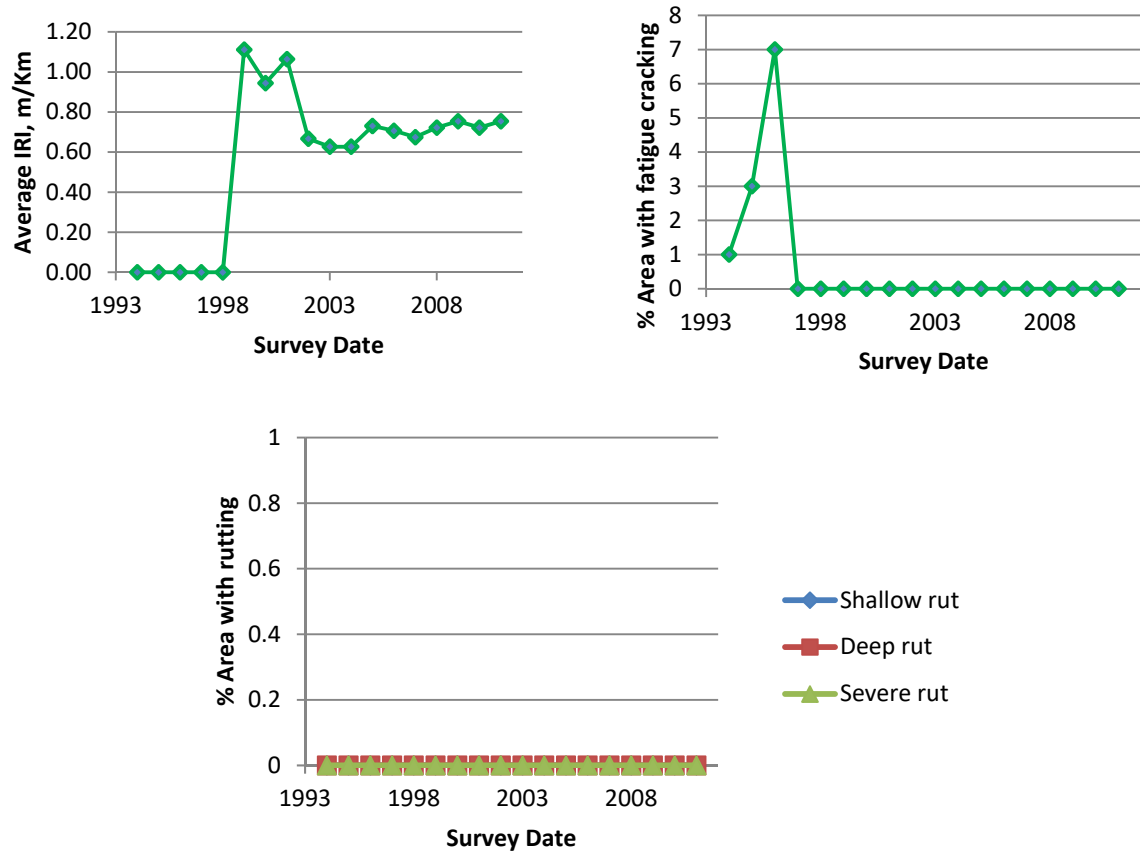
Section No.: Madison FM 1428-650 Control

Layer Structure (N/A)



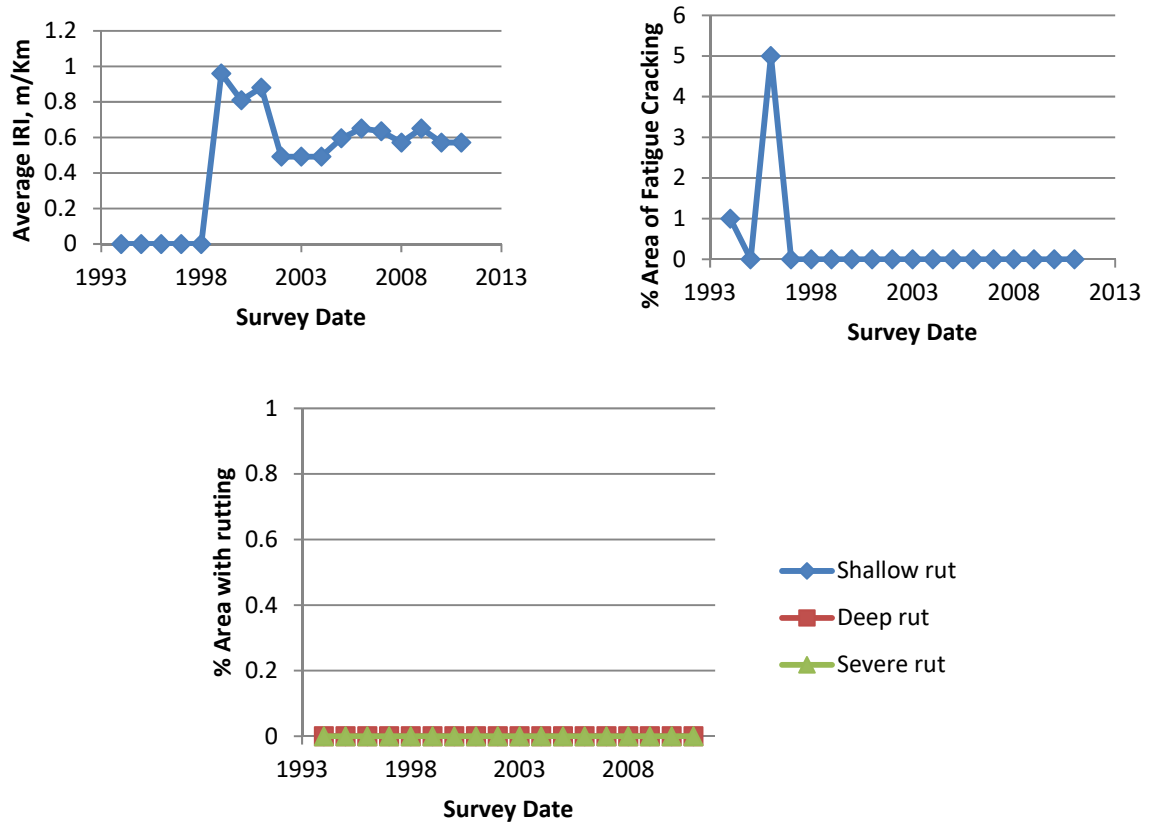
Section No.: Madison IH 0045-182

Layer Structure (N/A)



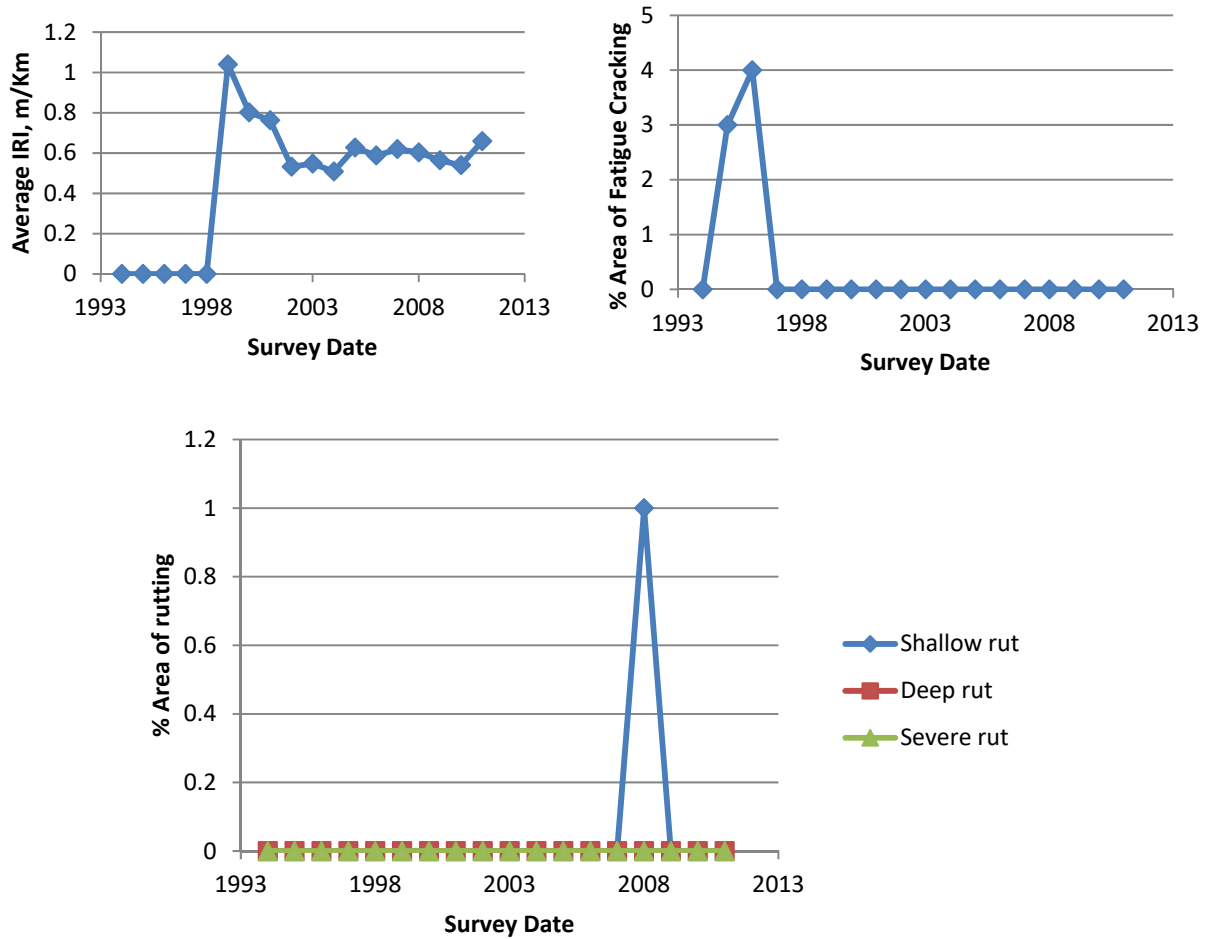
Section No.: Madison IH 0045-184

Layer Structure (N/A)



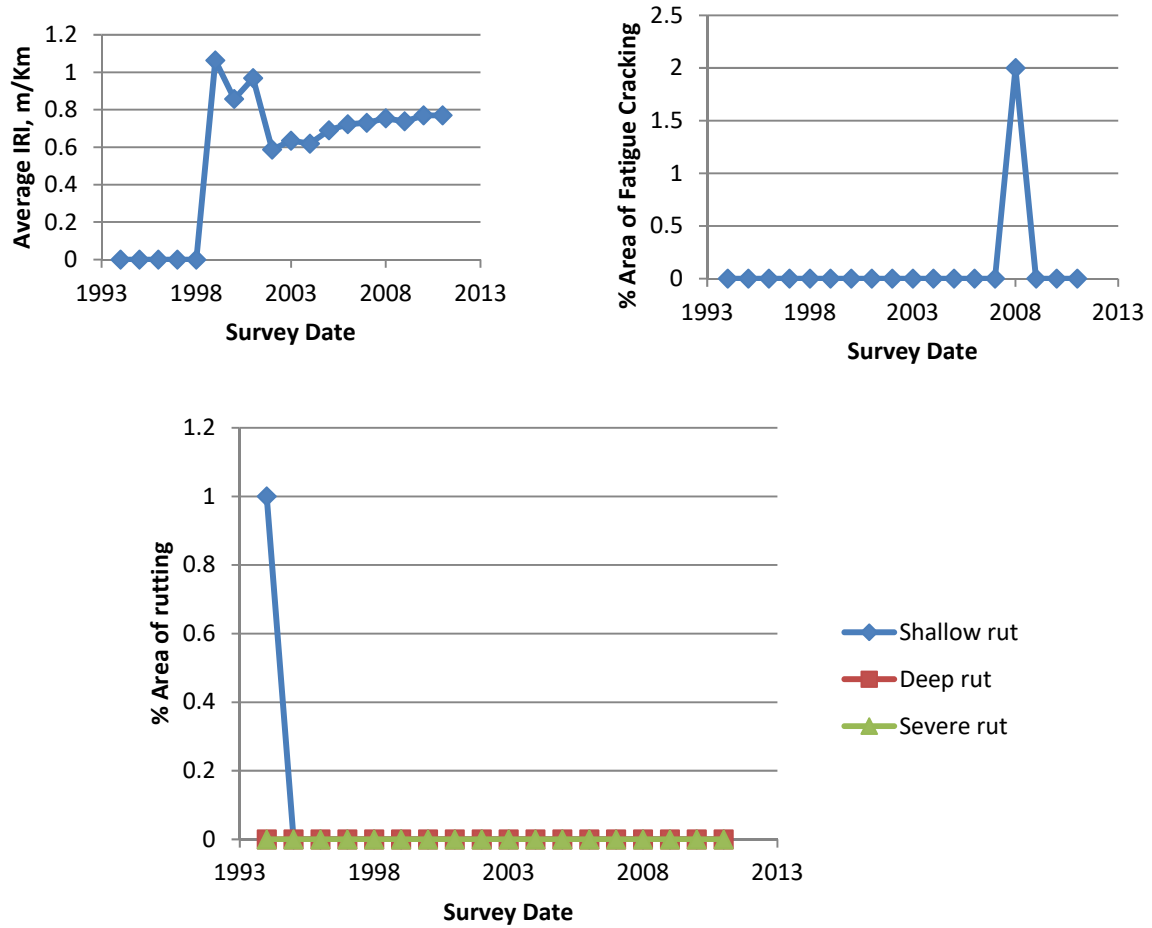
Section No.: Madison IH 0045-186

Layer Structure (N/A)



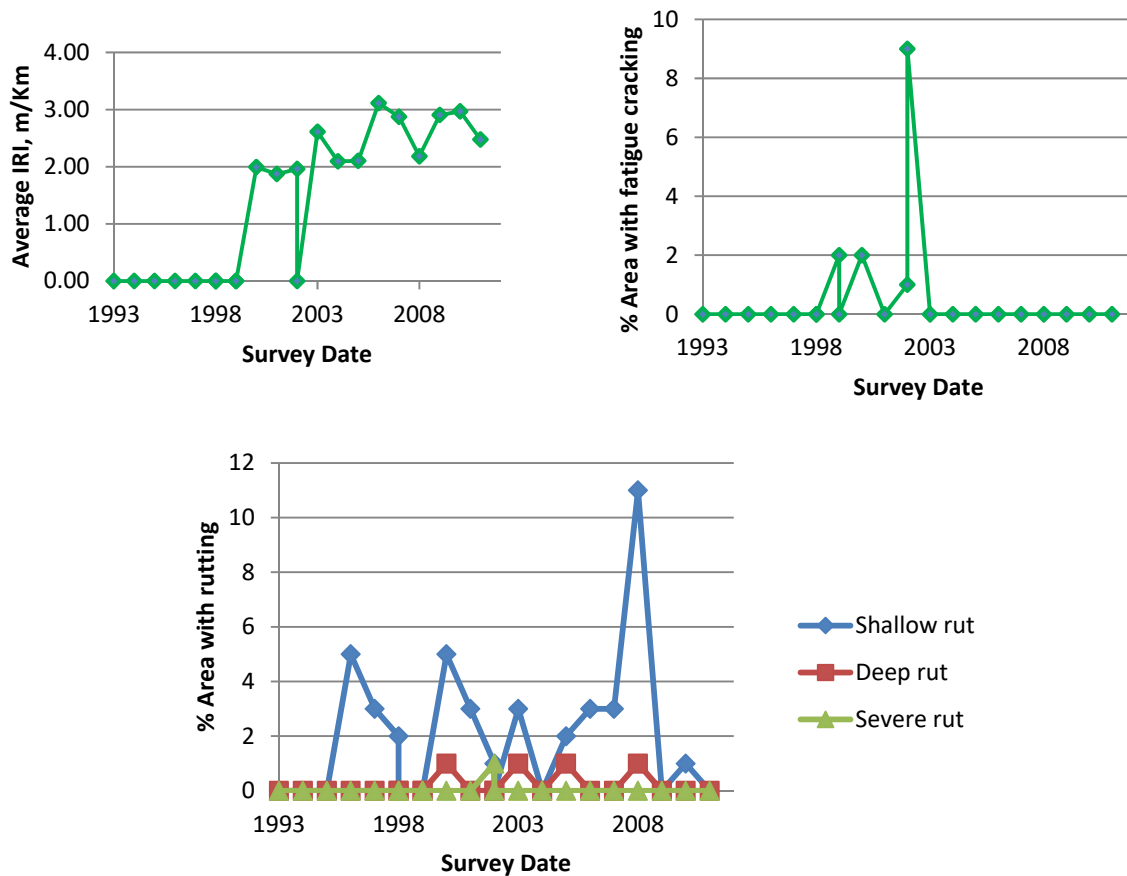
Section No.: Madison IH 0045-188

Layer Structure (N/A)



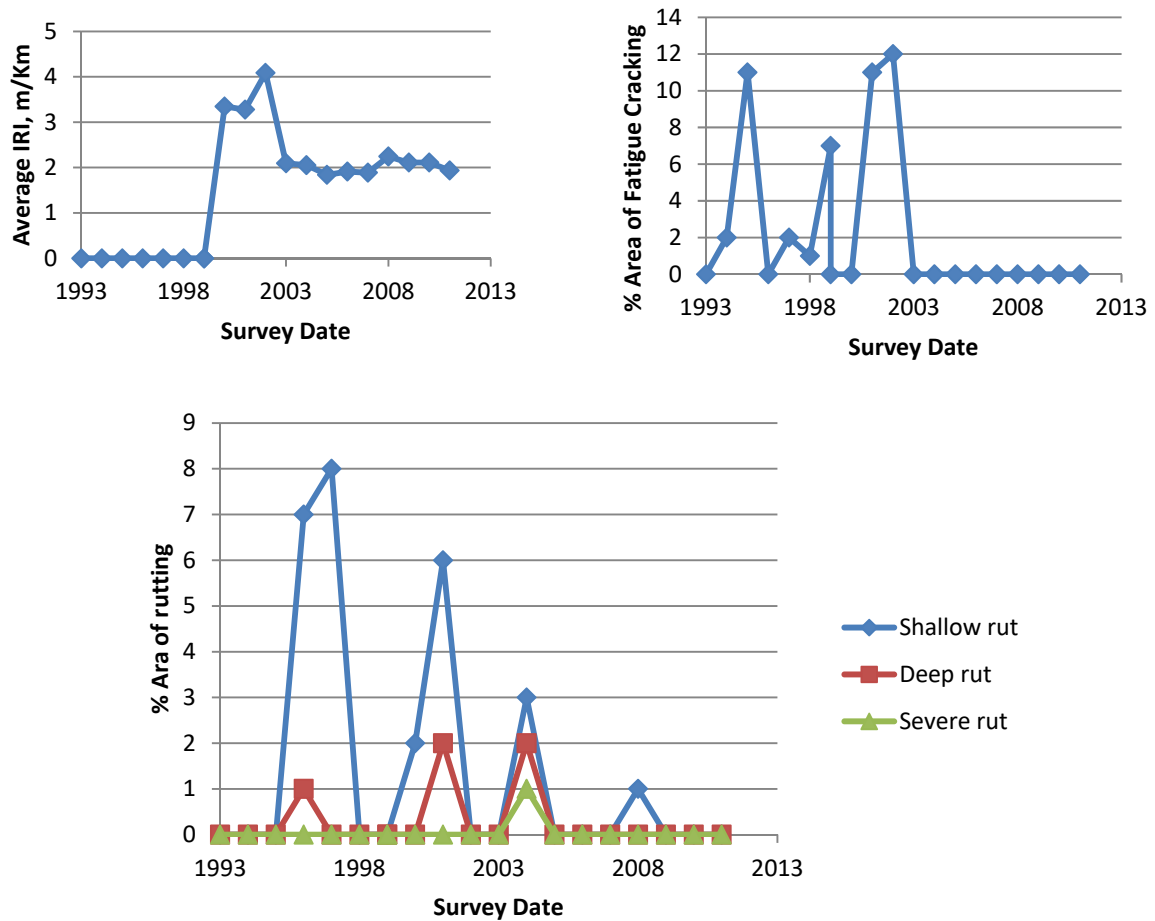
Section No.: Madison FM 1375-664

Layer Structure (N/A)



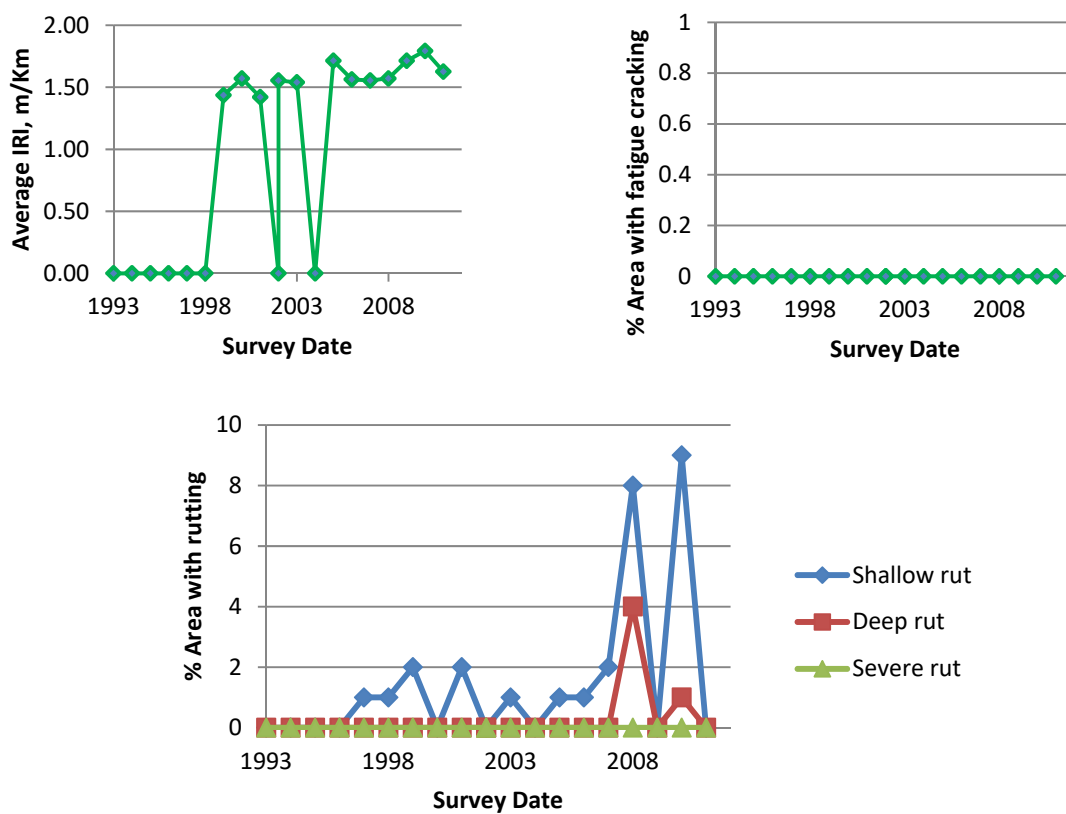
Section No.: Madison FM 1375-670

Layer Structure (N/A)



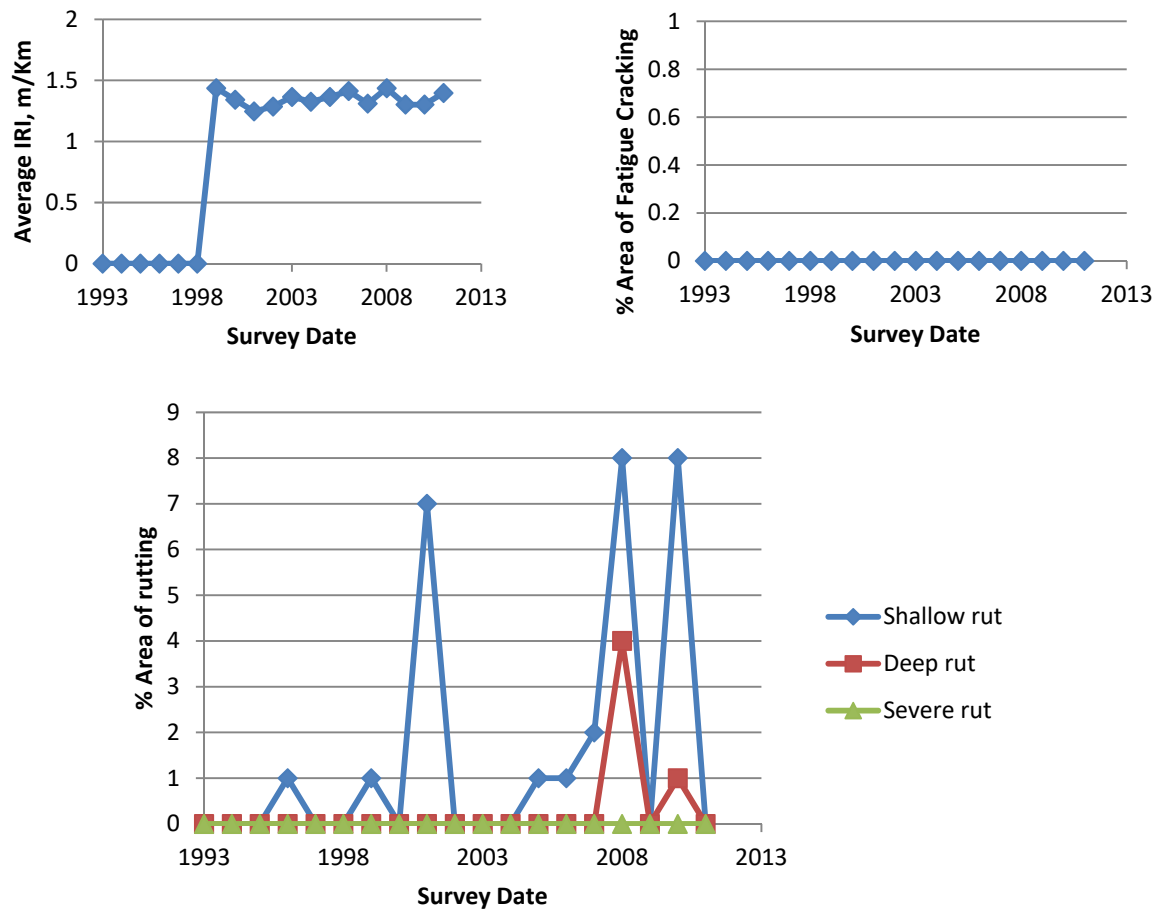
Section No.: Upton US 0067-770

Layer Structure (N/A)



Section No.: Upton US 0067-772 Control

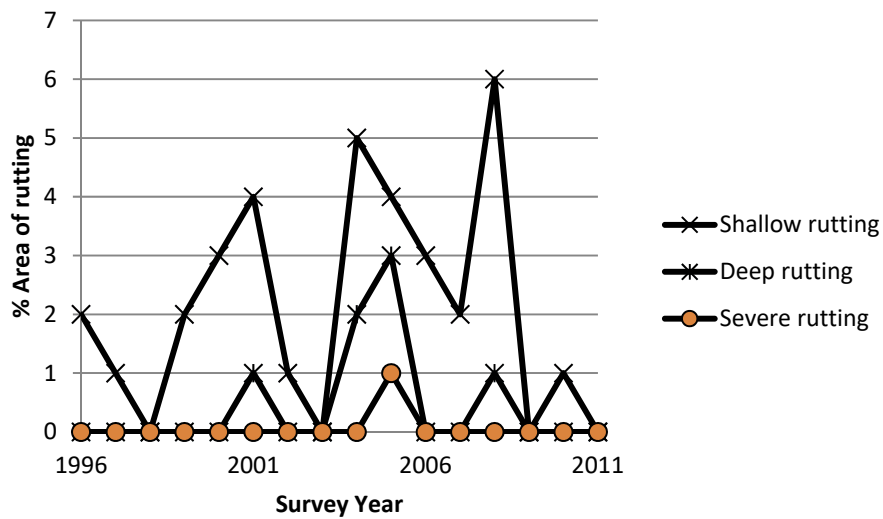
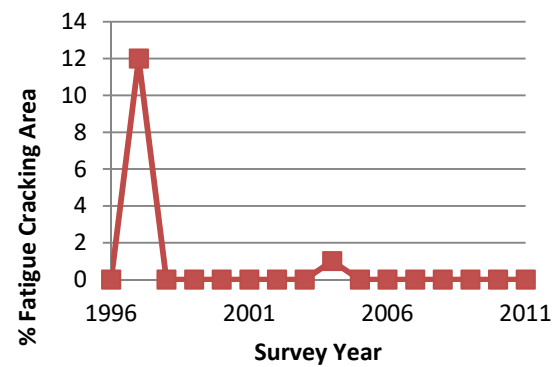
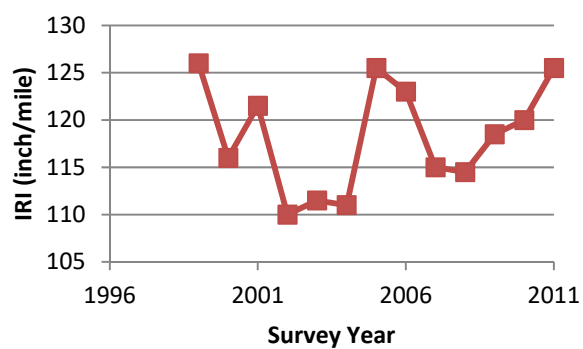
Layer Structure (N/A)



Section No.: Milam FM 1915-406

Layer Structure

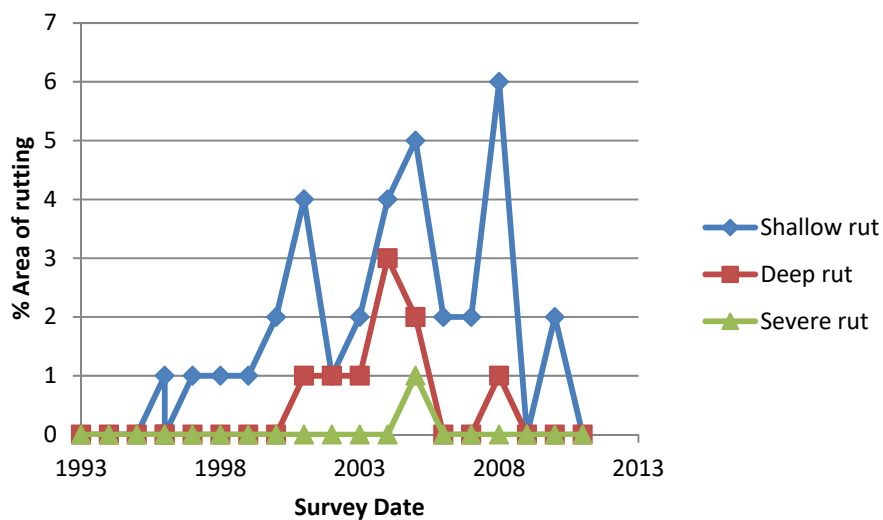
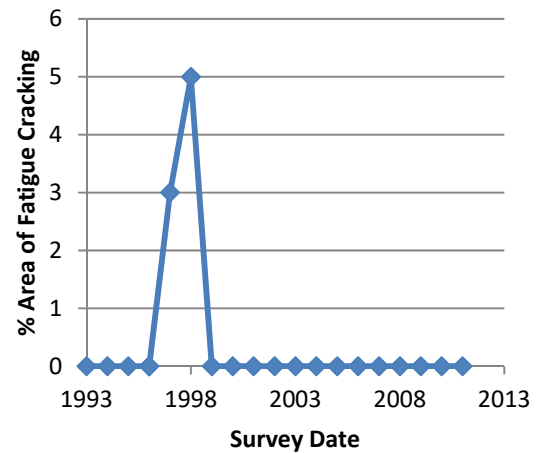
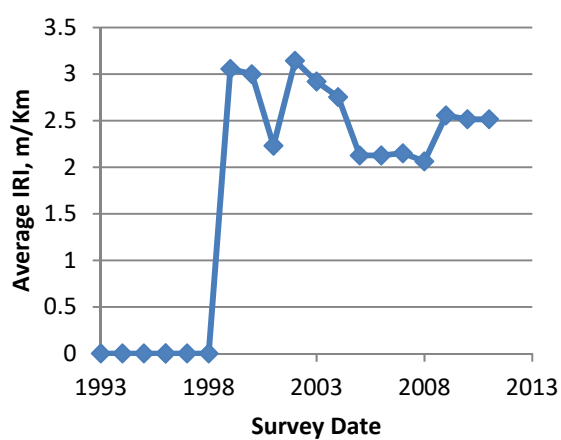
Layer Number	Layer Type	Thickness (mm)	Material Description	Modulus
1	SS			
2	TS	254	Lime treated subgrade	
3	EF		Geogrid	
4	GB	203.2	Flexible base	
5	AC		Seal coat	



Section No.: Milam FM 1915-408

Layer Structure

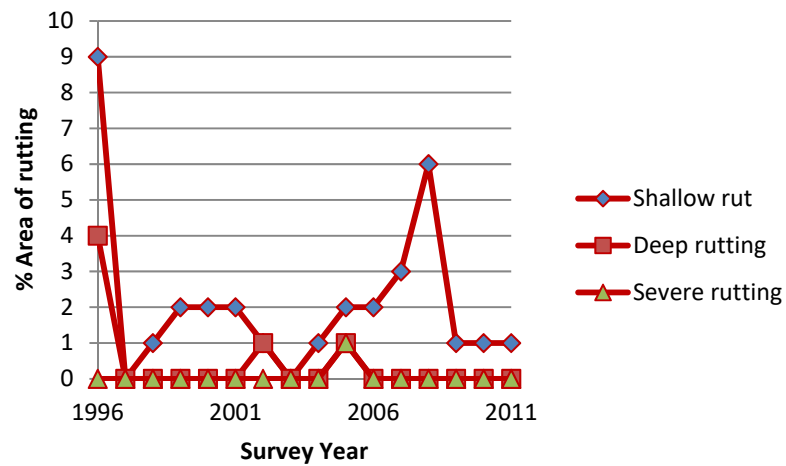
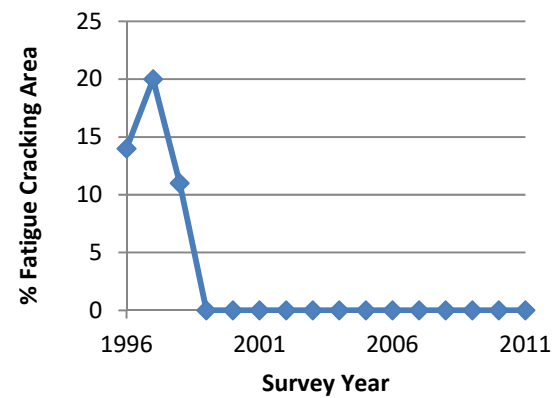
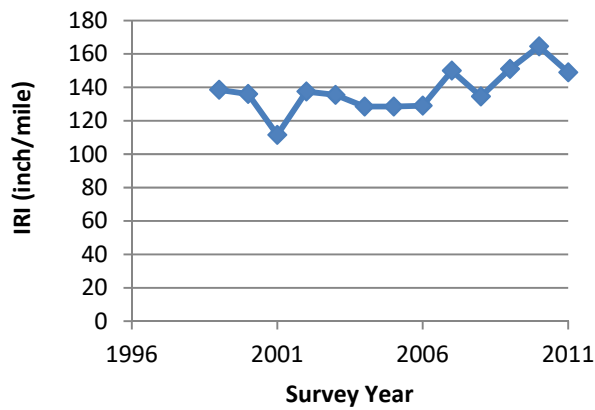
Layer Number	Layer Type	Thickness (mm)	Material Description	Modulus
1	SS			
2	TS	254	Lime treated subgrade	
3	EF		Geogrid	
4	GB	203.2	Flexible base	
5	AC		Seal coat	



Section No.: Milam FM 1915-410 Control

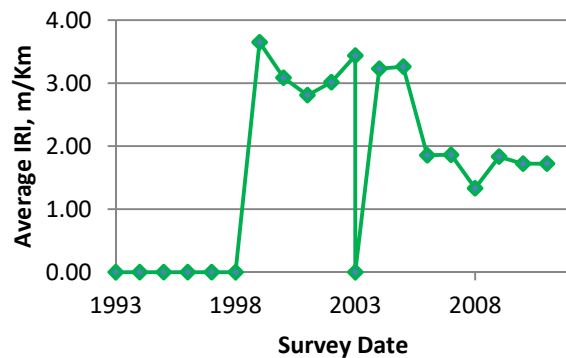
Layer Structure

Layer Number	Layer Type	Thickness (mm)	Material Description	Modulus
1	SS			
2	TS	254	Lime treated subgrade	
3	EF		Geogrid	
4	GB	203.2	Flexible base	
5	AC		Seal coat	

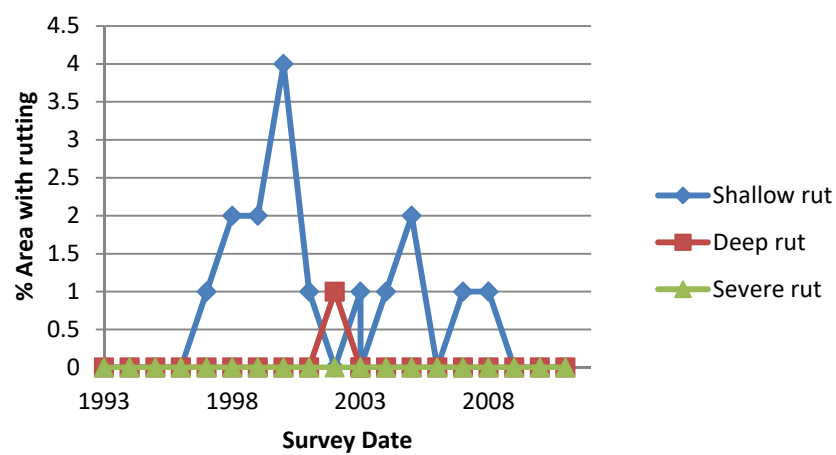


Section No.: FM 02-1 Control

Layer Number	Layer Type	Thickness (mm)	Material Description	Modulus
1	SS		Black clay	
2	GB	381	Old flexible base	
3	GB	177.8	New flexible base	
4	AC	25.4	Seal coat	

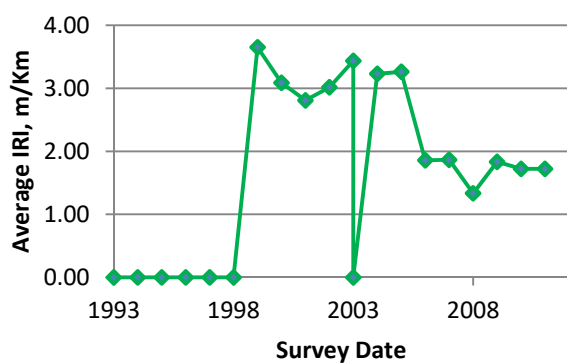


Fatigue cracking is observed data

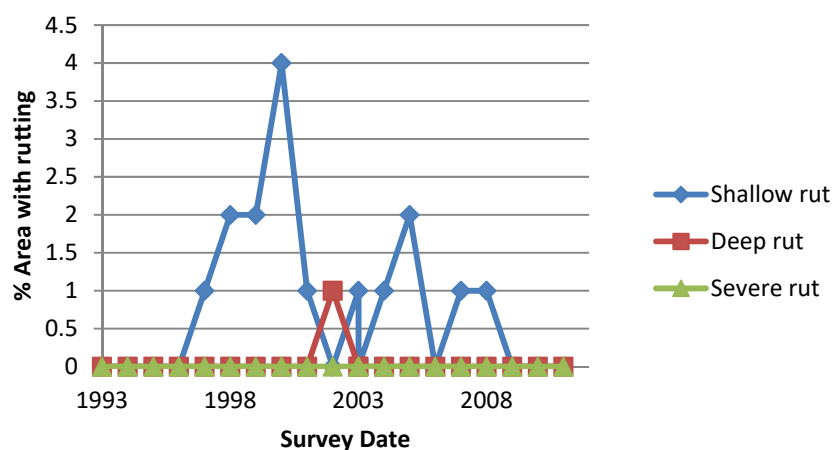


Section No.: FM 02-2

Layer Number	Layer Type	Thickness (mm)	Material Description	Modulus
1	SS		Black clay	
2	GB	381	Old flexible base	
3	EF		Polypropylene Geogrid	
4	GB	177.8	New flexible base	
5	AC	25.4	Seal coat	

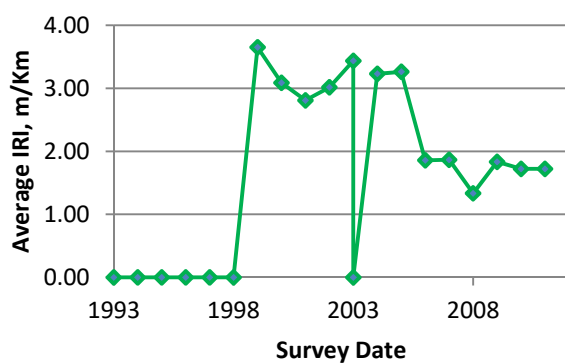


Fatigue cracking is observed data

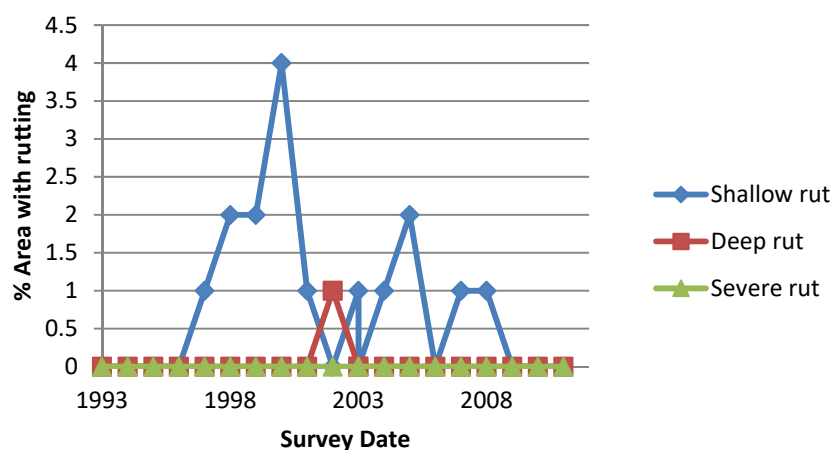


Section No.: FM 02-3

Layer Number	Layer Type	Thickness (mm)	Material Description	Modulus
1	SS		Black Clay	
2	GB	381	Old flexible base	
3	EF		Polyester geogrid	
4	GB	177.8	New flexible base	
5	AC	25.4	Seal coat	

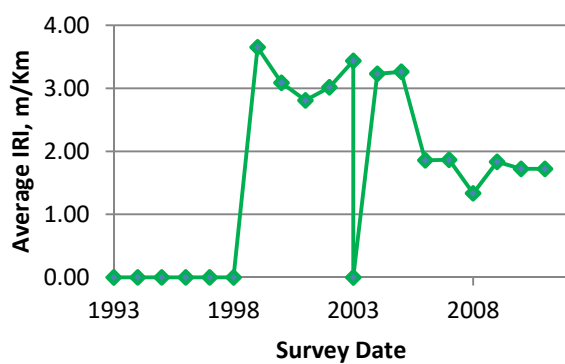


Fatigue cracking is observed data

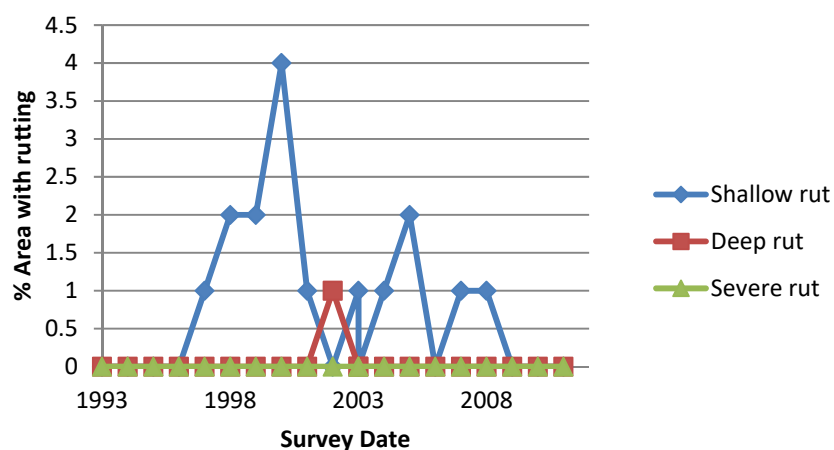


Section No.: FM 02-4

Layer Number	Layer Type	Thickness (mm)	Material Description	Modulus
1	SS		Black Clay	
2	GB	381	Old flexible base	
3	EF		Geotextile	
4	GB	177.8	New flexible base	
5	AC	25.4	Seal coat	

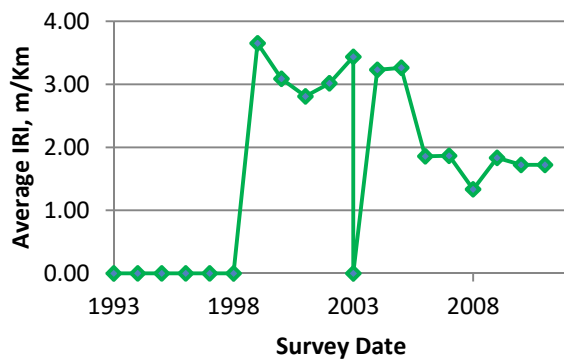


Fatigue cracking is observed data

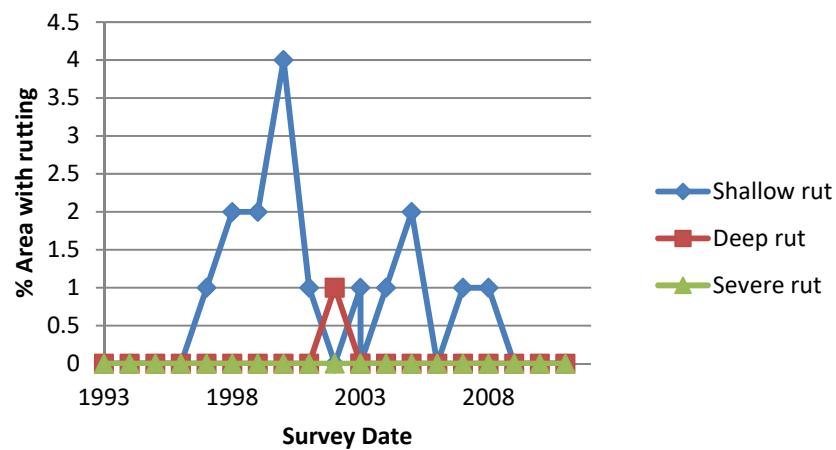


Section No.: FM 02-5 Control

Layer Number	Layer Type	Thickness (mm)	Material Description	Modulus
1	SS		Black Clay	
2	GB	127	Old flexible base	
3	TB	254	Lime stabilized	
4	GB	177.8	New flexible base	
5	AC	25.4	Seal coat	

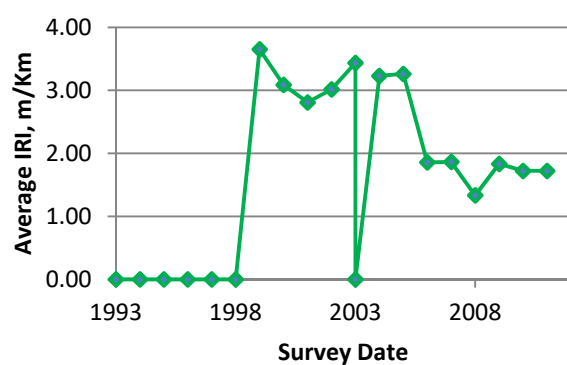


Fatigue cracking is observed data

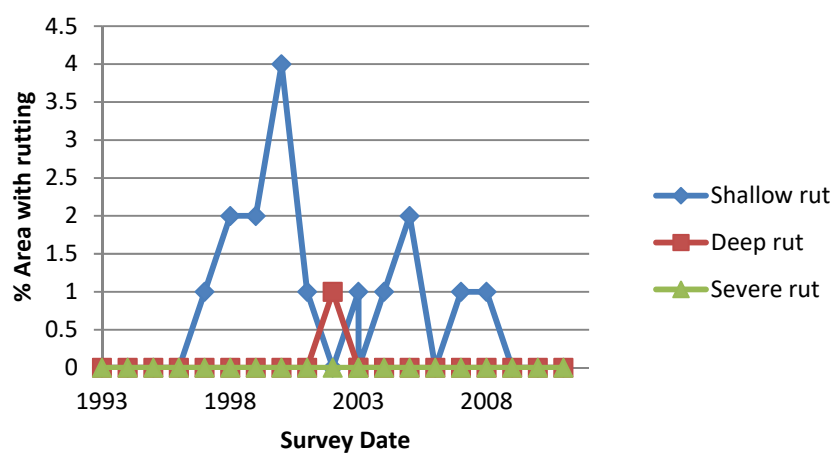


Section No.: FM 02-6

Layer Number	Layer Type	Thickness (mm)	Material Description	Modulus
1	SS		Black Clay	
2	GB	127	Old flexible base	
3	TB	254	Lime stabilized	
4	EF		Polypropylene geogrid	
5	GB	177.8	New flexible base	
6	AC	25.4	Seal coat	

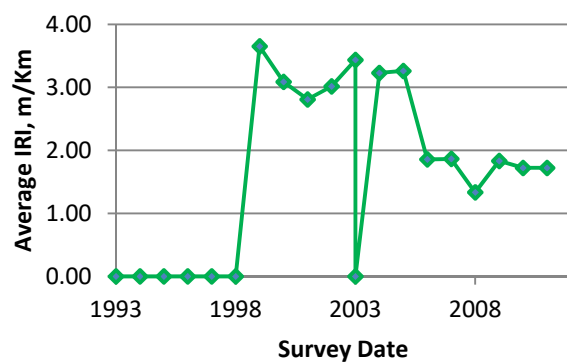


Fatigue cracking is observed data

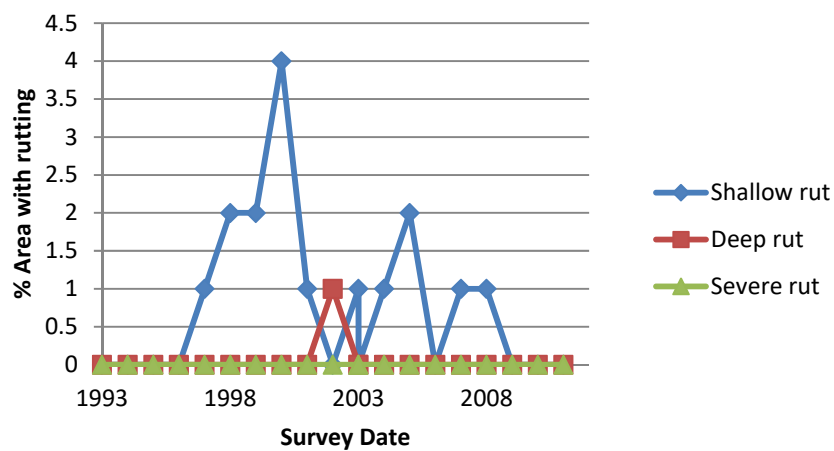


Section No.: FM 02-7

Layer Number	Layer Type	Thickness (mm)	Material Description	Modulus
1	SS		Black Clay	
2	GB	127	Old flexible base	
3	TB	254	Lime stabilized	
4	EF		Polyester geogrid	
5	GB	177.8	New flexible base	
6	AC	25.4	Seal coat	

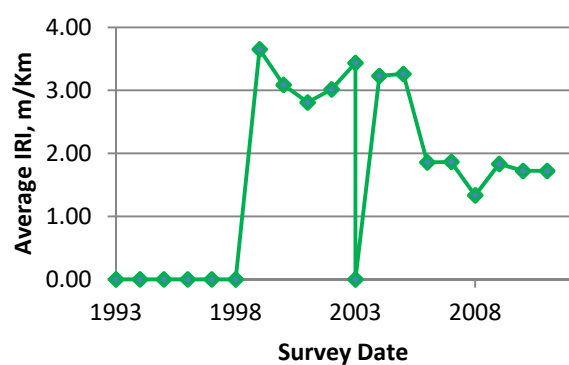


Fatigue cracking is observed data

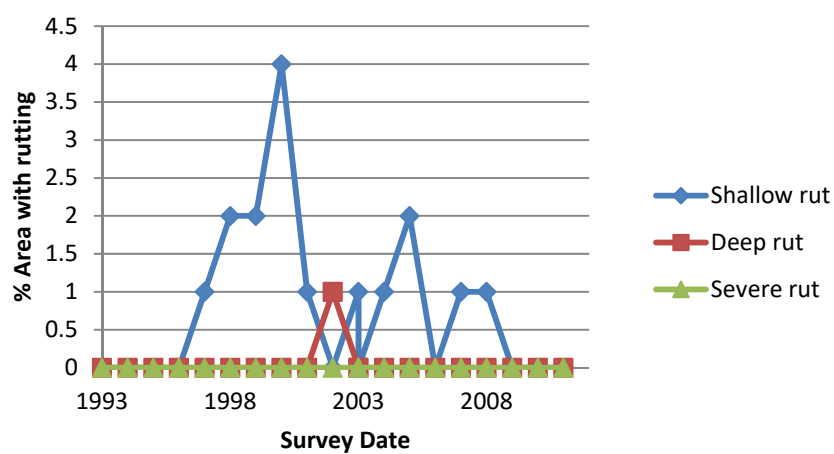


Section No.: FM 02-8

Layer Number	Layer Type	Thickness (mm)	Material Description	Modulus
1	SS		Black Clay	
2	GB	127	Old flexible base	
3	TB	254	Lime stabilized	
4	EF		Geotextile	
5	GB	177.8	New flexible base	
6	AC	25.4	Seal coat	



Fatigue cracking is observed data



Appendix P4. Collection of FWD Data from Identified Pavement Sections

Table R4-1. Collection of FWD Data from LTPP Database

Pavement Section	Drop Load (kPa)	Peak Deflection 1 (Microns)	Peak Deflection 2 (Microns)	Peak Deflection 3 (Microns)	Peak Deflection 4 (Microns)	Peak Deflection 5 (Microns)	Peak Deflection 6 (Microns)	Peak Deflection 7 (Microns)	Peak Deflection 8 (Microns)	Peak Deflection 9 (Microns)
1-0110	389	89	81	74	69	64	51	43	35	76
	574	134	120	112	105	99	79	67	53	115
	785	193	172	160	148	141	112	94	73	164
	964	243	215	199	183	176	141	117	91	204
1-0111	386	78	66	61	55	53	39	32	25	62
	573	123	102	93	84	86	61	47	40	97
	784	177	148	136	124	125	90	76	62	141
	955	224	191	166	159	157	115	98	76	178
1-0112	403	45	34	31	36	34	26	31	19	38
	602	67	62	59	53	50	44	36	33	57
	800	98	80	75	74	70	59	55	44	79
	1028	121	96	88	91	86	70	70	52	97
1-0163	387	62	54	43	40	38	27	22	19	50
	581	97	82	69	63	59	45	37	29	77
	794	139	118	100	93	87	65	54	42	111
	967	174	148	132	119	109	83	66	54	139
1-0109	380	150	105	89	74	62	36	23	20	99
	574	227	163	141	115	97	59	37	31	152
	788	323	236	204	167	140	90	57	44	217
	967	405	295	257	209	174	113	75	57	273
5-0122	389	66	56	51	46	42	35	26	23	50
	574	96	82	75	67	62	51	43	34	77
	796	137	116	105	94	88	70	61	48	107
	980	169	143	131	117	107	88	72	59	133
5-0123	380	39	33	31	29	30	24	22	20	32
	576	59	49	46	43	44	36	32	30	47
	793	84	71	67	62	58	51	45	38	66
	992	104	86	82	76	73	63	55	48	82
5-0124	381	45	32	29	28	27	23	22	20	32
	569	67	46	43	42	41	35	34	31	46

Pavement Section	Drop Load (kPa)	Peak Deflection 1 (Microns)	Peak Deflection 2 (Microns)	Peak Deflection 3 (Microns)	Peak Deflection 4 (Microns)	Peak Deflection 5 (Microns)	Peak Deflection 6 (Microns)	Peak Deflection 7 (Microns)	Peak Deflection 8 (Microns)	Peak Deflection 9 (Microns)
	786	95	66	62	57	54	47	41	36	61
	981	117	80	74	70	66	57	51	45	75
5-0121	384	132	110	91	73	60	41	30	25	90
	565	191	158	132	109	92	66	48	37	135
	752	247	207	174	143	121	87	65	51	173
	984	320	267	225	186	155	113	87	69	220
5-0213	595	86	79	68	70	58	55	40	36	81
	780	114	104	93	91	78	70	54	47	108
	1005	148	136	127	118	107	91	74	61	143
5-0214	676	87	84	81	78	74	68	64	61	78
	1096	138	133	130	123	118	107	100	96	126
5-0215	570	135	90	85	77	71	58	48	38	102
	978	213	151	143	130	120	97	81	66	169
5-0126	637	136	116	108	96	88	70	52	42	90
	1020	223	191	177	159	141	110	84	64	148
5-0217	653	91	82	77	70	63	51	40	33	71
	1051	147	132	125	114	103	83	67	54	119
5-0218	647	156	82	80	74	68	58	49	41	106
	1046	239	136	131	121	110	91	73	58	167
5-0219	649	66	65	63	60	57	50	41	34	61
	1040	108	105	101	98	91	80	66	55	98
5-0220	637	345	294	273	241	209	155	108	73	33
	1048	461	391	362	317	275	201	141	95	37
5-0221	625	122	115	113	106	99	83	66	53	112
	988	198	190	184	173	161	135	108	87	182
5-0222	650	314	270	253	225	199	156	122	98	57
	1051	469	405	379	340	301	237	187	151	83
5-0223	573	83	72	68	62	56	48	38	30	34
	971	148	129	122	110	100	84	68	56	67
5-0224	644	137	52	51	48	44	40	34	29	108
	1043	215	80	79	73	67	61	53	46	171

P-168

Pavement Section	Drop Load (kPa)	Peak Deflection 1 (Microns)	Peak Deflection 2 (Microns)	Peak Deflection 3 (Microns)	Peak Deflection 4 (Microns)	Peak Deflection 5 (Microns)	Peak Deflection 6 (Microns)	Peak Deflection 7 (Microns)	Peak Deflection 8 (Microns)	Peak Deflection 9 (Microns)
8-1057	372	313	239	185	137	113	82	67		
	527	431	334	267	200	163	118	92		
	700	576	451	369	281	229	164	128		
	943	770	615	511	396	326	232	177		
10-0110	387	94	72	63	55	48	37	28	22	63
	585	142	111	98	86	75	59	44	35	98
	786	190	149	132	116	102	80	61	47	131
	1055	250	198	176	156	136	107	82	63	175
10-0111	375	92	68	62	54	47	36	29	22	61
	579	148	112	101	89	78	60	46	36	100
	773	199	152	137	121	107	83	63	49	137
	1008	260	200	181	160	142	109	84	65	180
10-0112	375	71	49	44	39	36	29	23	19	42
	582	114	79	70	63	57	46	37	29	68
	779	151	107	94	85	77	62	50	40	92
	1020	197	139	124	112	102	82	66	53	122
10-0108	376	128	103	87	69	55	37	27	20	86
	573	202	161	138	110	88	60	43	32	137
	778	276	220	189	152	121	84	59	46	188
	1060	367	294	255	205	165	114	81	61	254
12-0110	397	70	43	30	24	19	11	6	4	30
	595	111	63	46	36	28	17	10	6	45
	783	146	82	61	47	37	21	13	9	59
	1078	188	110	82	65	51	30	18	11	83
12-0111	395	84	32	28	24	18	11	8	5	31
	592	122	51	43	34	27	17	10	7	43
	817	168	70	58	48	37	23	15	10	59
	1072	223	94	78	63	50	31	19	13	78
12-0112	395	41	24	18	15	12	8	5	4	18
	598	65	37	28	23	19	11	7	7	28
	797	90	50	38	31	25	18	12	8	37

P-169

Pavement Section	Drop Load (kPa)	Peak Deflection 1 (Microns)	Peak Deflection 2 (Microns)	Peak Deflection 3 (Microns)	Peak Deflection 4 (Microns)	Peak Deflection 5 (Microns)	Peak Deflection 6 (Microns)	Peak Deflection 7 (Microns)	Peak Deflection 8 (Microns)	Peak Deflection 9 (Microns)
	1089	119	69	53	44	37	24	16	12	52
12-0109	404	42	28	21	14	10	7	4	4	20
	599	64	43	32	23	17	10	7	6	31
	805	87	59	45	31	23	14	10	8	43
	1092	118	79	61	44	33	20	14	11	59
16-9032	380	191	175	157	110	95	65	41		
	545	286	262	239	170	146	99	64		
	694	375	348	315	225	194	132	83		
20-0160	356	694	498	354	163	83	23	22		
	533	948	702	525	265	135	36	34		
	720	1161	881	692	369	194	50	49		
	938	1414	1045	880	476	266	67	68		
20-0161	363	189	149	121	89	64	37	20		
	543	270	215	175	132	96	55	30		
	739	352	279	231	174	128	76	40		
	991	567	455	382	197	230	137	64		
22-0122	369	97	82	74	68	60	48	39	30	77
	600	157	136	124	113	100	79	63	49	127
	772	206	179	163	150	132	103	81	62	167
	950	261	227	207	188	167	131	103	78	211
22-0123	370	43	37	34	33	30	27	24	20	33
	606	71	59	54	54	50	44	38	34	54
	777	93	77	69	70	63	55	47	42	70
	958	115	97	87	87	79	69	59	52	88
22-0124	385	26	22	21	21	20	17	16	13	21
	626	40	35	33	33	31	27	24	21	33
	800	53	45	42	42	40	36	31	28	42
	1011	66	56	54	51	49	45	39	34	52
22-0121	368	100	87	78	67	59	45	36	27	77
	600	163	144	128	111	96	73	58	47	127
	770	210	184	163	141	120	89	69	54	164

P-170

Pavement Section	Drop Load (kPa)	Peak Deflection 1 (Microns)	Peak Deflection 2 (Microns)	Peak Deflection 3 (Microns)	Peak Deflection 4 (Microns)	Peak Deflection 5 (Microns)	Peak Deflection 6 (Microns)	Peak Deflection 7 (Microns)	Peak Deflection 8 (Microns)	Peak Deflection 9 (Microns)
	954	264	233	208	180	155	119	94	77	206
26-0122	N/A									
26-0123	385	48	45	42	39	36	29	24	18	41
	572	72	65	63	58	54	43	34	25	60
	765	94	87	83	77	70	57	46	36	82
	1013	131	118	111	103	93	77	61	48	112
26-0124	393	37	32	30	29	27	23	19	16	31
	577	55	47	44	41	38	32	27	22	43
	776	72	62	59	54	50	43	36	30	59
	1038	97	84	79	73	67	58	49	40	79
26-0121	383	123	91	77	62	48	34	20	12	77
	582	186	147	126	103	80	54	33	20	127
	757	246	192	168	137	107	71	43	28	169
	1044	343	270	236	193	153	102	63	40	238
35-0110	383	59	51	46	42	36	28	20	16	46
	571	91	79	72	65	58	43	32	25	72
	761	125	108	99	88	78	59	44	33	97
	994	168	147	134	120	105	81	61	45	132
35-0111	385	55	46	42	37	32	24	18	15	41
	571	84	69	63	56	48	37	28	22	62
	763	113	94	84	75	65	50	38	30	83
	997	147	123	110	98	86	66	50	40	108
35-0112	383	41	30	25	22	18	14	10	6	25
	573	63	47	40	33	27	20	14	10	39
	764	84	65	54	46	37	27	19	13	53
	1001	115	85	74	64	55	40	28	20	73
35-0109	372	124	100	86	74	62	46	34	28	86
	561	179	146	127	109	92	70	52	41	126
	750	236	191	167	143	123	92	70	55	165
	982	305	247	216	186	160	119	93	73	214
40-0122	386	80	70	63	54	46	34	26	21	62

P-171

Pavement Section	Drop Load (kPa)	Peak Deflection 1 (Microns)	Peak Deflection 2 (Microns)	Peak Deflection 3 (Microns)	Peak Deflection 4 (Microns)	Peak Deflection 5 (Microns)	Peak Deflection 6 (Microns)	Peak Deflection 7 (Microns)	Peak Deflection 8 (Microns)	Peak Deflection 9 (Microns)
	574	116	105	94	81	69	51	39	31	93
	751	158	143	127	110	93	70	51	41	128
	965	214	192	173	148	127	94	71	56	170
40-0123	378	37	33	29	27	25	20	17	13	29
	587	59	52	48	43	40	34	26	21	46
	785	83	71	66	61	56	47	36	30	65
	972	106	91	85	78	72	60	48	37	83
40-0124	375	32	29	27	26	24	22	20	18	28
	585	52	45	44	41	40	35	32	28	43
	781	73	64	61	59	55	50	45	40	61
	962	90	80	75	72	68	61	54	47	75
40-0120	363	139	130	115	96	71	49	34	22	103
	570	209	193	171	145	111	78	52	33	155
	768	276	255	227	193	148	105	74	47	207
	965	340	313	280	238	185	132	94	60	256
48-0119	394	96	71	54	47	37	28	21	13	54
	565	139	104	79	69	54	42	32	18	78
	753	184	137	106	92	73	56	43	24	105
	982	245	181	141	122	98	75	56	33	139
48-0120	388	87	73	50	38	34	29	18	13	50
	566	123	104	72	56	50	43	26	21	71
	754	160	129	96	76	64	55	33	27	94
	988	211	163	127	100	83	65	47	39	125
48-0121	402	114	79	63	48	37	25	19	15	63
	579	161	111	90	69	54	37	30	23	89
	749	196	142	116	90	71	51	39	31	115
	971	249	179	148	116	93	67	52	41	145
48-0122	399	62	53	48	43	37	30	23	20	49
	583	94	78	72	63	56	44	35	28	72
	771	124	105	96	85	74	59	46	38	95
	998	163	137	125	110	98	77	61	49	125

P-172

Pavement Section	Drop Load (kPa)	Peak Deflection 1 (Microns)	Peak Deflection 2 (Microns)	Peak Deflection 3 (Microns)	Peak Deflection 4 (Microns)	Peak Deflection 5 (Microns)	Peak Deflection 6 (Microns)	Peak Deflection 7 (Microns)	Peak Deflection 8 (Microns)	Peak Deflection 9 (Microns)
48-0123	395	50	31	24	25	21	20	14	12	25
	572	73	45	32	39	33	30	21	16	35
	753	97	60	46	51	44	40	28	22	49
	975	133	81	66	64	55	48	38	32	67
48-0124	399	46	25	19	16	15	13	11	9	19
	575	67	37	27	24	22	20	15	12	28
	754	90	49	37	33	29	25	20	18	37
	985	123	65	50	44	40	33	27	24	51
48-0118	394	66	48	37	33	31	23	19	14	40
	570	96	71	56	50	45	35	28	20	60
	759	132	97	79	69	61	47	37	29	82
	1000	176	130	107	93	83	63	49	38	110
48-0167	379	194	146	108	77	56	33	21	17	109
	557	256	194	145	103	79	48	31	23	144
	749	316	238	178	129	100	63	42	32	176
	989	393	297	220	161	132	85	57	45	218
49-7086	569	136	127	123	115	107	90	78	64	130
	765	181	168	160	150	139	117	98	79	172
	1026	238	219	213	197	182	156	129	106	227
49-D410	538	206	176	162	141	123	92	69	50	118
	765	286	244	224	195	171	127	96	70	184
	989	356	303	281	242	212	160	118	89	247
49-D430	538	239	105	102	95	86	72	59	48	184
	769	340	128	126	118	109	93	78	66	262
	1002	413	149	146	137	127	109	93	80	316
49-D431	530	99	96	94	91	88	80	71	62	89
	754	140	136	134	129	125	113	101	89	126
	999	181	176	173	167	161	145	130	114	163
49-D440	538	81	81	76	69	63	53	45	37	70
	764	122	121	114	104	95	78	65	54	103
	998	163	159	151	138	126	102	85	70	137

Pavement Section	Drop Load (kPa)	Peak Deflection 1 (Microns)	Peak Deflection 2 (Microns)	Peak Deflection 3 (Microns)	Peak Deflection 4 (Microns)	Peak Deflection 5 (Microns)	Peak Deflection 6 (Microns)	Peak Deflection 7 (Microns)	Peak Deflection 8 (Microns)	Peak Deflection 9 (Microns)
49-D441	536	80	78	75	71	66	57	48	38	76
	760	118	112	108	102	95	82	69	57	109
	1001	150	142	138	129	122	104	87	71	139
49-D443	538	72	71	70	65	60	51	41	32	71
	764	111	105	103	95	88	76	61	49	103
	996	145	137	134	125	116	99	79	64	135
49-D444	538	85	70	65	64	57	49	42	33	72
	758	126	102	96	92	84	71	57	47	105
	1003	172	132	126	118	109	91	72	60	138
49-D445	534	106	105	103	99	94	82	70	57	100
	758	153	149	146	140	132	115	98	79	142
	995	196	191	187	177	169	147	124	101	183
49-D446	544	65	61	59	54	49	41	28	24	62
	773	95	88	84	78	71	59	41	35	88
	1004	124	116	111	103	95	78	53	45	115
49-D448	537	110	109	101	96	93	85	69	59	103
	762	157	154	145	137	132	119	98	82	146
	998	204	197	189	177	171	152	125	104	189
49-D449	535	97	98	94	88	84	73	64	54	87
	756	137	140	133	124	118	104	90	77	123
	999	178	180	173	163	153	133	116	99	160
49-D450	531	129	121	116	108	101	85	71	58	124
	758	183	170	163	152	141	119	99	80	175
	996	235	217	209	194	181	153	126	102	222
49-D451	542	99	97	90	81	77	64	53	44	86
	765	145	142	131	119	111	92	77	65	124
	1001	188	185	172	156	145	119	100	83	161
49-D452	548	135	118	111	100	90	73	59	48	116
	774	185	165	154	138	125	101	83	67	158
	1012	237	209	196	176	159	129	105	85	198
49-D454	572	107	102	100	96	91	82	62		

P-174

Pavement Section	Drop Load (kPa)	Peak Deflection 1 (Microns)	Peak Deflection 2 (Microns)	Peak Deflection 3 (Microns)	Peak Deflection 4 (Microns)	Peak Deflection 5 (Microns)	Peak Deflection 6 (Microns)	Peak Deflection 7 (Microns)	Peak Deflection 8 (Microns)	Peak Deflection 9 (Microns)
	780	141	133	131	127	119	108	82		
	1016	179	170	169	162	154	139	107		
49-D455	529	115	111	108	101	95	82	71	59	107
	757	163	161	154	146	137	119	102	86	153
	991	210	206	199	187	177	153	132	110	195
49-D459	538	100	92	88	81	75	63	53	43	84
	765	141	129	124	114	106	89	75	62	119
	1001	179	165	157	146	135	114	96	79	152
49-D460	542	173	72	69	65	61	54	46	42	136
	770	231	105	100	95	89	77	67	55	182
	1007	287	134	129	121	114	99	85	72	226
49-D461	534	142	136	133	124	119	104	90	80	127
	754	203	193	188	177	168	148	128	110	179
	998	258	249	241	229	216	191	167	143	228
49-D462	536	109	105	101	94	88	76	65	55	97
	757	154	147	141	131	123	106	92	78	136
	1001	200	185	177	166	154	134	116	99	175
51-0122	386	138	104	95	83	71	55	44	33	97
	595	204	160	142	125	110	85	66	51	149
	787	275	212	192	169	147	115	87	68	199
	1004	346	269	243	214	187	146	110	85	253
51-0123	390	155	99	82	73	66	54	43	34	81
	593	222	147	122	106	95	81	65	53	126
	798	286	192	160	142	127	108	88	70	164
	1011	351	237	202	179	160	135	110	89	206
51-0124	378	74	38	29	26	24	22	18	15	29
	587	112	58	45	41	39	34	28	23	45
	796	152	81	64	58	55	47	40	33	63
	1008	199	105	85	77	73	63	54	44	83
51-0121	354	225	171	137	97	69	39	21	19	136
	549	316	243	195	142	101	59	35	27	193

P-175

Pavement Section	Drop Load (kPa)	Peak Deflection 1 (Microns)	Peak Deflection 2 (Microns)	Peak Deflection 3 (Microns)	Peak Deflection 4 (Microns)	Peak Deflection 5 (Microns)	Peak Deflection 6 (Microns)	Peak Deflection 7 (Microns)	Peak Deflection 8 (Microns)	Peak Deflection 9 (Microns)
	747	401	307	249	182	132	81	52	40	245
	1001	501	383	312	230	170	108	73	58	308
55-0122	379	107	63	55	48	37	24	19	15	55
	556	159	98	84	72	56	36	28	24	84
	767	219	134	115	98	78	52	40	33	116
	998	281	174	150	127	101	70	52	43	150
55-0123	370	106	50	44	42	37	29	23	19	45
	558	154	75	66	63	55	43	36	29	67
	750	202	101	89	84	74	58	48	40	90
	1015	267	133	117	111	98	78	65	53	119
55-0124	380	84	28	27	26	23	18	16	12	30
	565	123	45	43	41	37	28	24	19	44
	769	166	63	59	56	49	38	33	27	61
	1006	214	85	80	74	65	52	43	35	78
55-0121	369	132	93	81	57	41	32	24	17	81
	561	193	140	122	89	65	50	37	27	122
	767	256	184	162	119	91	67	50	40	162
	1001	319	232	204	152	118	88	66	51	203

Table P4-2. Collection of FWD Data from Texas PMIS Database

Pavement Section	Drop Load (lb)	Peak Deflection 1 (Mils)	Peak Deflection 2 (Mils)	Peak Deflection 3 (Mils)	Peak Deflection 4 (Mils)	Peak Deflection 5 (Mils)	Peak Deflection 6 (Mils)	Peak Deflection 7 (Mils)
FM 02-1	Layer moduli have been calculated in Report FHWA/TX-08/0-4829-1							
FM 02-2								
FM 02-3								
FM 02-4								
FM 02-5								
FM 02-6								
FM 02-7								
FM 02-8								
FM 2331-292	9010	28.09	17.78	10.31	5.74	3.19	1.91	1.37
FM 2331-294	9494	18.48	13.7	9.03	5.2	3.04	1.9	1.31
FM 2331-296	8946	40.84	19.09	6.63	3.24	2.01	1.5	1.26
FM 2331-290	8740	40.07	18.8	8.76	5.06	3.16	2.24	1.6
FM 917-558	9621	9.02	7.19	5.07	3.37	2.29	1.67	1.28
FM 917-560	9490	22.06	12.93	6.8	3.81	2.28	1.45	1.1
FM 917-556	9403	15.79	10.38	6.31	4.04	2.78	2.08	1.63
FM 157-296	11020	9.83	8.35	6.89	5.39	4.17	3.11	2.3
FM 157-298	10452	29.59	13.78	7.03	5.08	3.99	3.15	2.57
FM 157-294	10885	9.15	7.4	5.61	4.24	3.04	2.21	1.64
US 79-550	N/A							
US 79-552	N/A							
SH 73-740	N/A							
SH 73-742	9057	15.93	9.48	5.28	3.22	2.22	1.79	1.48
SH 73-744	9006	21	12.38	6.93	4.49	3.32	2.74	2.3
SH 73-746	8751	24.28	9.69	3.64	2.66	2.23	1.85	1.46
SH 73-748	9065	18.98	12.09	7.01	4.54	3.36	2.78	2.32
SH 73-750	8954	24.19	14.87	7.93	4.78	3.44	2.88	2.4
SH 73-752	9038	24.15	16.19	9.55	5.75	3.86	3.05	2.52
SH 73-754	9268	9.98	6.63	4.26	2.99	2.24	1.88	1.63
SH 73-756	9034	19.74	12.37	7.22	4.63	3.31	2.55	2.12
SH 73-758	9065	21.37	15.28	9.41	6.02	4.13	3.17	2.48
SH 73-760	9208	12.73	9.56	6.56	4.65	3.43	2.76	2.28

P-177

Pavement Section	Drop Load (lb)	Peak Deflection 1 (Mils)	Peak Deflection 2 (Mils)	Peak Deflection 3 (Mils)	Peak Deflection 4 (Mils)	Peak Deflection 5 (Mils)	Peak Deflection 6 (Mils)	Peak Deflection 7 (Mils)
SH 73-762	N/A							
SH 73-764	N/A							
SH 73-766	N/A							
FM 357-688	8394	71.2	37.47	17.9	8.78	5.44	4.16	3.58
IH 45-218	9586	17.22	12.81	8.45	5.67	3.74	2.53	1.91
FM 123-740	N/A							
FM 699-304	N/A							
FM 699-306	N/A							
FM 699-308	N/A							
FM 2517-736	N/A							
FM 2517-738	N/A							
FM 2517-744	N/A							
FM 2517-740	N/A							
FM 1402-232	N/A							
FM 1696-672	9621	33.11	13.03	5.38	3.37	2.35	2	1.58
FM 1696-670	9482	55.17	24.54	10.02	5.17	3.13	2.22	1.72
FM 39-406	7643	6.21	4.76	4.05	3.5	1.46	1.24	1.12
	10253	23.15	18.19	11.75	7.25	4.44	2.97	2.28
FM 39-408	7393	20.59	10.38	4.96	2.85	1.86	1.23	0.97
	10102	39.78	25.12	12.95	7.46	5.01	3.48	2.72
FM 39-410	7699	10.51	6.39	4.78	3.7	2.83	2.12	1.74
	10074	33.47	21.28	11	6.72	4.79	3.59	2.93
FM 39-412	8851	27.05	14.41	6.41	3.73	2.49	1.8	1.52
FM 39-414	8914	26.39	13.66	7.63	4.93	3.5	2.59	2.19
FM 1428-646	9395	28.39	20.14	12.37	7.42	4.95	3.48	2.74
FM1428-648	9419	30.34	18.92	8.48	3.84	2.61	2.1	1.73
FM 1428-650	9471	42.7	22.65	10.28	4.96	2.91	2.14	1.81
IH 45-182	9836	5.56	3.89	3.3	2.62	1.99	1.64	1.27
IH45-184	9896	3.53	2.95	2.58	2.09	1.72	1.39	1.15
IH 45-186	9911	3.34	2.37	2.03	1.73	1.49	1.3	1.11
IH 45-188	9888	5.01	3.3	2.83	2.46	1.93	1.63	1.36
FM 1375-664	10098	30.3	18.47	8.86	4.92	3.21	2.48	1.93

Pavement Section	Drop Load (lb)	Peak Deflection 1 (Mils)	Peak Deflection 2 (Mils)	Peak Deflection 3 (Mils)	Peak Deflection 4 (Mils)	Peak Deflection 5 (Mils)	Peak Deflection 6 (Mils)	Peak Deflection 7 (Mils)
FM 1375-670	9570	26.91	18.4	10.73	6.78	4.52	3.31	2.68
US 67-770	9308	17.33	10.28	5.27	3.11	2.12	1.66	1.35
US 67-772	8497	27.27	13.35	6.25	4.33	3.39	2.81	2.28
FM 1915-406	9761	17.93	6.2	3.06	1.87	1.36	1.1	0.87
FM 1915-408	10201	22	7.31	3.2	1.76	1.31	1.07	0.71
FM 1915-410	9705	31.46	10.1	4.06	2.24	1.44	1.05	0.73

Appendix P5. Collection of Geosynthetic Information

Table P5-1. Defaulted Material Properties of Nonwoven Geotextile

Property	Test Method	Magnitude	Unit
Thickness	ASTM D-5199	2	mm
Tensile Strength	ASTM D-4632	912	N
Puncture Strength	ASTM D-4833	579	N
Apparent Opening Size	ASTM D-4751	0.18	mm
Permittivity	ASTM D-4491	1.35	Sec ⁻¹

Table P5-2. Defaulted Material Properties of Woven Geotextile

Property	Test Method	Magnitude	Unit
Thickness	ASTM D-5199	2	mm
Tensile Strength	ASTM D-4632	1402	N
Puncture Strength	ASTM D-4833	533	N
Apparent Opening Size	ASTM D-4751	0.425	mm
Permittivity	ASTM D-4491	0.05	Sec ⁻¹

Table P5-3. Defaulted Material Properties of Geogrid

Property	Test Method	Magnitude	Unit
Rib Thickness	ASTM D-1777	0.76*0.76	mm
Tensile Strength @ 2% Strain	ASTM D-6637	4.1*6.6	kN/m
Tensile Strength @ 5% Strain	ASTM D-6637	8.5*13.4	kN/m
Ultimate Tensile Strength	ASTM D-6637	12.4*19.0	kN/m
Junction Efficiency	GRI-GG2-05	93%	1
Aperture Stability	US Army Corps Method	0.32	m-N/deg

Table P5-4. Material Properties of Polypropylene Geogrid

Property	Test Method	Magnitude	Unit
Rib Thickness	ASTM D-1777	0.76*0.76	mm
Aperture Dimension	Measured	25.0*33.0	mm
Tensile Strength @ 2% Strain	ASTM D-6637	4.1*6.6	kN/m
Tensile Strength @ 5% Strain	ASTM D-6637	8.5*13.4	kN/m
Ultimate Tensile Strength	ASTM D-6637	12.4*19.0	kN/m

Table P5-5. Material Properties of Polyester Geogrid

Property	Test Method	Magnitude	Unit
Rib Thickness	ASTM D-1777	0.76*0.76	mm
Aperture Dimension	Measured	25.4*25.4	mm
Tensile Strength @ 2% Strain	ASTM D-6637	7.3*7.3	kN/m
Tensile Strength @ 5% Strain	ASTM D-6637	13.4*13.4	kN/m
Ultimate Tensile Strength	ASTM D-6637	29.2*29.2	kN/m

Table P5-6. Material Properties of Geotextile in FM 02-4 and FM 02-8

Property	Test Method	Magnitude	Unit
Thickness	ASTM D-5199	2	mm
Apparent Opening Size	ASTM D-4751	0.6	mm
Tensile Strength @ 2% Strain	ASTM D-6637	14.0	kN/m
Tensile Strength @ 5% Strain	ASTM D-6637	35.0	kN/m
Ultimate Tensile Strength	ASTM D-6637	70.0	kN/m

Table P5-7. Material Properties of Geogrid Type 1

Property	Test Method	Magnitude	Unit
Rib Thickness	ASTM D-1777	0.76*0.76	mm
Aperture Dimension	Measured	25.0*33.0	mm
Tensile Strength @ 2% Strain	ASTM D-6637	4.1*6.6	kN/m
Tensile Strength @ 5% Strain	ASTM D-6637	8.5*13.4	kN/m
Ultimate Tensile Strength	ASTM D-6637	12.4*19.0	kN/m
Junction Efficiency	GRI-GG2-05	94%	1

Table P5-8. Material Properties of Geogrid Type 2

Property	Test Method	Magnitude	Unit
Rib Thickness	ASTM D-1777	1.27*1.27	mm
Aperture Dimension	Measured	25.0*33.0	mm
Tensile Strength @ 2% Strain	ASTM D-6637	6.0*9.0	kN/m
Tensile Strength @ 5% Strain	ASTM D-6637	11.8*19.6	kN/m
Ultimate Tensile Strength	ASTM D-6637	19.2*28.8	kN/m
Junction Efficiency	GRI-GG2-05	94%	1

APPENDIX Q. EXAMPLES OF PROGRAM RUNS OF THE COMPOSITE GEOSYNTHETIC–BASE COURSE MODEL

Four examples are presented in this appendix to illustrate using the program named “Composite Geosynthetic–Base Course Model” to analyze the pavement structure with/without geogrid or geotextile within the base course. The model analysis provides the following results:

1. Critical strains in the unreinforced pavement structure, including:
 - a. Compressive strain at the bottom of the base course;
 - b. Average strain in the base course;
 - c. Tensile strain at the bottom of the asphalt layer;
2. Critical strains in the pavement with a geosynthetic layer, including:
 - a. Compressive strain at the bottom of the base course;
 - b. Average strain in the base course;
 - c. Tensile strain at the bottom of the asphalt layer;
3. Modified moduli of the base and the subgrade with the geosynthetic reinforcement that are equivalent to those of an unreinforced pavement.

Example 1: Geogrid at the Bottom of the Base Course

If the users would like to analyze a pavement structure reinforced using the geogrid at the bottom of the base course, as illustrated in Figure Q-1, they may take the following steps to perform the analysis:

1. Double click the application file “Composite Geosynthetic–Base Course Model.exe” to start the program;
2. Tick “Geogrid at the Bottom” on the left side of the program interface under “Geosynthetic Location” (see Figure Q-2);
3. Input the properties of the pavement layers and the geogrid on the right side of the program interface under “Pavement Structure” (see Figure Q-2); and
4. Click “Run Analysis”.

The “Results” window will then pop up, as shown in Figure Q-3. It can be observed from Figure Q-3 that the subgrade modulus has been increased from 5.0 ksi to 13.1 ksi and base modulus has been increased from 20.0 ksi to 22.5 ksi with placing the geogrid at the bottom of the base course.

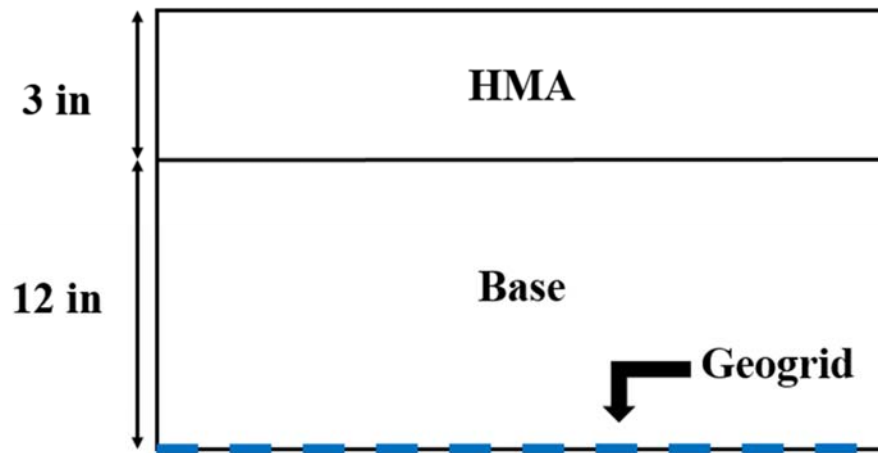


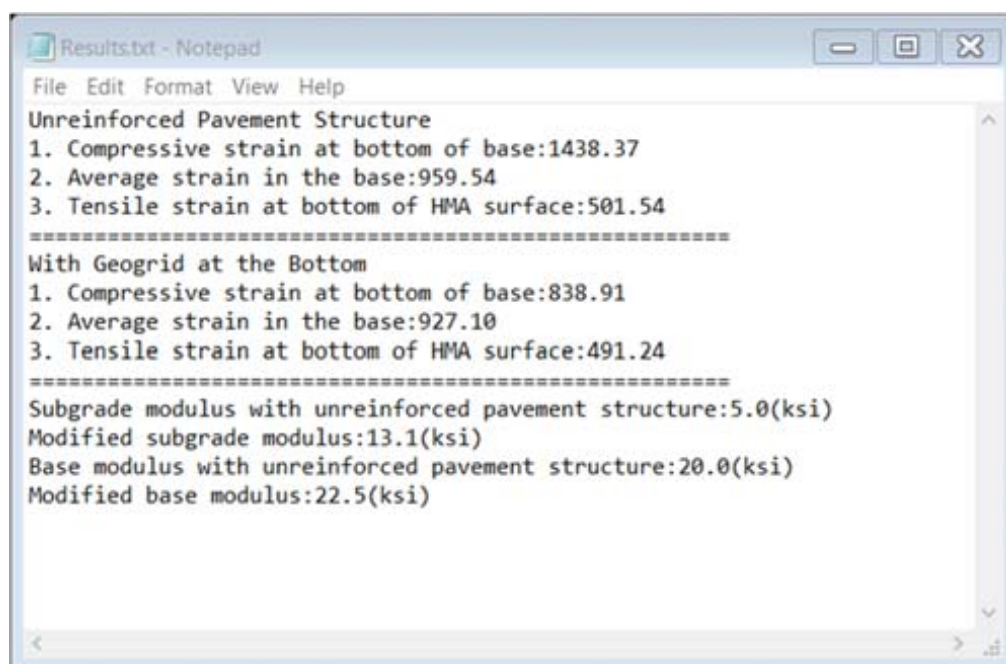
Figure Q-1. Placing Geogrid at the Bottom of Base Course

The screenshot shows the 'Composite Geosynthetic-Base Course Model' software interface. It features two main sections: 'Geosynthetics Location' and 'Pavement Structure'. The 'Geosynthetics Location' section has four radio button options, with 'Geogrid at the Bottom of Base Course' selected. The 'Pavement Structure' section contains input fields for various material properties.

Geosynthetics Location	Pavement Structure
<input checked="" type="radio"/> Geogrid at the Bottom of Base Course	HMA Thickness (in): 4
<input type="radio"/> Geogrid in the Middle of Base Course	Base Thickness (in): 10
<input type="radio"/> Geotextile at the Bottom of Base Course	HMA Modulus (ksi): 300
<input type="radio"/> Geotextile in the Middle of Base Course	Base Modulus (ksi): 20
	Base Anisotropic Ratio: 0.35
	Geosynthetic Sheet Stiffness (lb/in): 1200
	Subgrade Modulus (ksi): 5

At the bottom of the interface are two buttons: 'Run Analysis' and 'Exit'.

Figure Q-2. Select “Geogrid at the Bottom” and Input Material Properties



```

Results.txt - Notepad
File Edit Format View Help
Unreinforced Pavement Structure
1. Compressive strain at bottom of base:1438.37
2. Average strain in the base:959.54
3. Tensile strain at bottom of HMA surface:501.54
=====
With Geogrid at the Bottom
1. Compressive strain at bottom of base:838.91
2. Average strain in the base:927.10
3. Tensile strain at bottom of HMA surface:491.24
=====
Subgrade modulus with unreinforced pavement structure:5.0(ksi)
Modified subgrade modulus:13.1(ksi)
Base modulus with unreinforced pavement structure:20.0(ksi)
Modified base modulus:22.5(ksi)

```

Figure Q-3. Analysis Results for Example 1

Example 2: Geogrid in the Middle of the Base Course

If the users desire to analyze a pavement with a geogrid in the middle of the base course, as exhibited in Figure Q-4, the steps listed below can be followed to complete the analysis:

1. Double click the application file “Composite Geosynthetic–Base Course Model.exe” to start the program;
2. Tick “Geogrid in the Middle” on the left side of the program interface under “Geosynthetic Location” (see Figure Q-5);
3. Input the properties of the pavement layers and the geogrid on the right side of the program interface under “Pavement Structure” (see Figure Q-5); and
4. Click “Run Analysis”.

The “Results” file will then open up, as shown in Figure Q-6, which indicates that the base modulus has been increased from 20.0 ksi to 20.8 ksi with a geogrid layer in the middle of the base course.

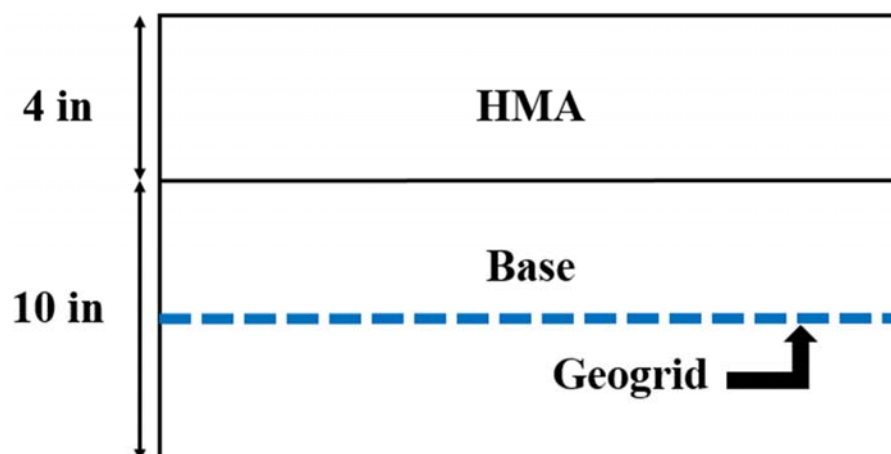


Figure Q-4. Placing Geogrid in the Middle of Base Course

The screenshot shows the 'Composite Geosynthetic-Base Course Model' software interface. It has two main sections: 'Geosynthetics Location' and 'Pavement Structure'. In the 'Geosynthetics Location' section, four radio buttons are present: 'Geogrid at the Bottom of Base Course', 'Geogrid in the Middle of Base Course' (which is selected), 'Geotextile at the Bottom of Base Course', and 'Geotextile in the Middle of Base Course'. The 'Pavement Structure' section contains input fields for: 'HMA Thickness (in)' (4), 'Base Thickness (in)' (10), 'HMA Modulus (ksi)' (300), 'Base Modulus (ksi)' (20), 'Base Anisotropic Ratio' (0.35), 'Geosynthetic Sheet Stiffness (lb/in)' (1200), and 'Subgrade Modulus (ksi)' (5). At the bottom, there are two buttons: 'Run Analysis' and 'Exit'.

Figure Q-5. Select “Geogrid in the Middle” and Input Material Properties

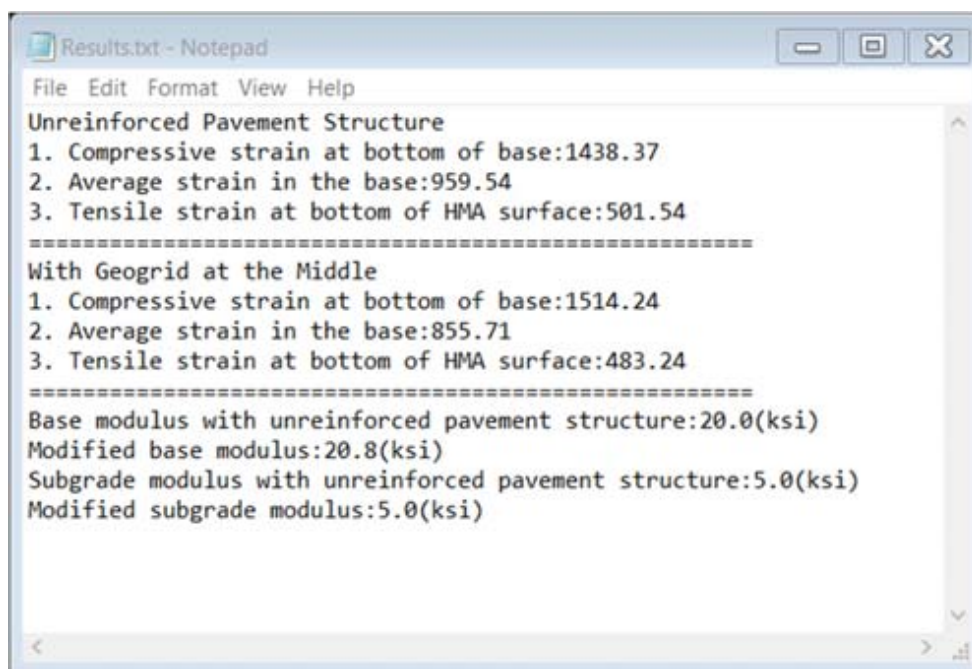


Figure Q-6. Analysis Results for Example 2

Example 3: Geotextile at the Bottom of the Base Course

If a geotextile layer is used at the bottom of the base course, as displayed in Figure Q-7, the users may take the following steps to analyze the pavement structure:

1. Double click the application file “Composite Geosynthetic–Base Course Model.exe” to start the program;
2. Tick “Geotextile at the Bottom” on the left side of the program interface under “Geosynthetic Location” (see Figure Q-8);
3. Input the properties of the pavement layers and the geotextile on the right side of the program interface under “Pavement Structure” (see Figure Q-8); and
4. Click “Run Analysis”.

As can be seen from the “Results” file (see Figure Q-9), the subgrade modulus has been increased from 5.0 ksi to 7.7 ksi when placing the geotextile layer at the bottom of the base course.

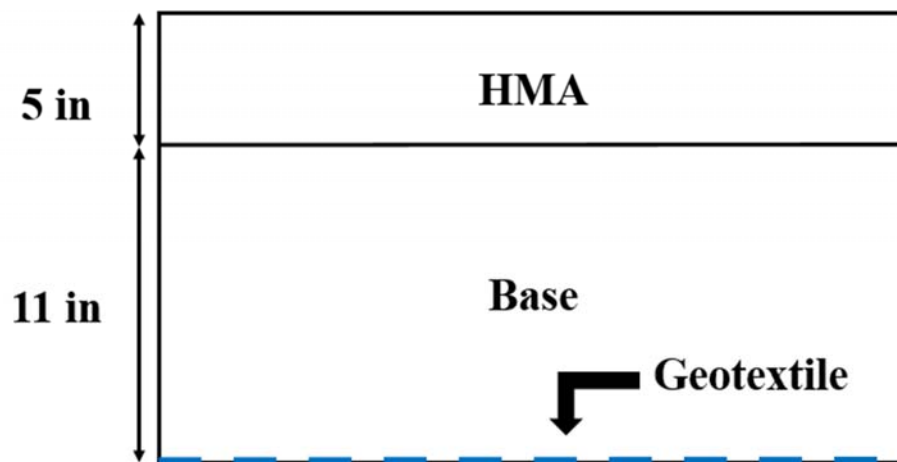
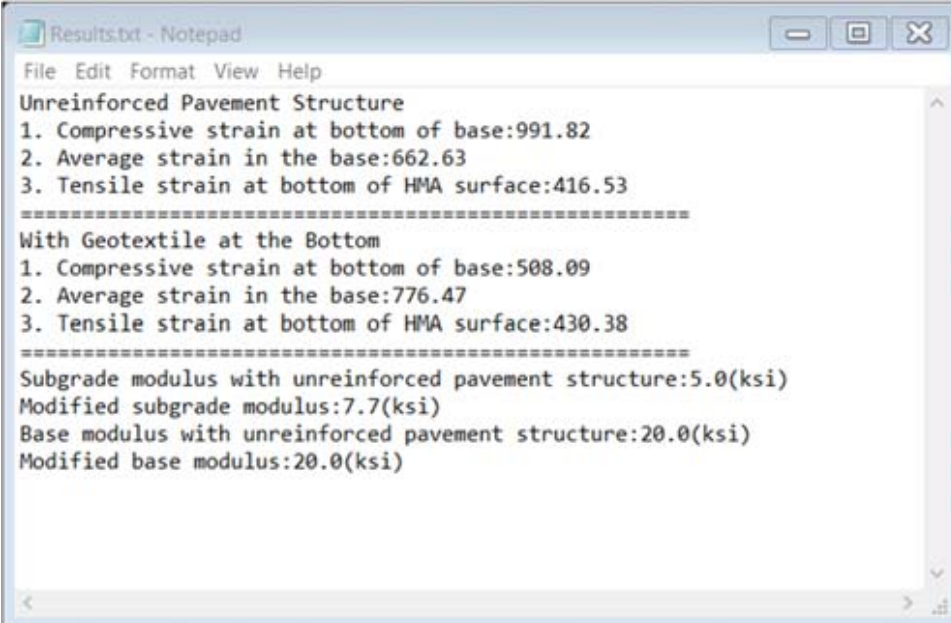


Figure Q-7. Placing Geotextile at the Bottom of Base Course

The screenshot shows the 'Composite Geosynthetic-Base Course Model' software interface. It has two main sections: 'Geosynthetics Location' and 'Pavement Structure'. In the 'Geosynthetics Location' section, four radio buttons are present: 'Geogrid at the Bottom of Base Course', 'Geogrid in the Middle of Base Course', 'Geotextile at the Bottom of Base Course' (which is selected), and 'Geotextile in the Middle of Base Course'. The 'Pavement Structure' section contains input fields for: 'HMA Thickness (in)' (5), 'Base Thickness (in)' (11), 'HMA Modulus (ksi)' (300), 'Base Modulus (ksi)' (20), 'Base Anisotropic Ratio' (0.35), 'Geosynthetic Sheet Stiffness (lb/in)' (1200), and 'Subgrade Modulus (ksi)' (5). At the bottom, there are two buttons: 'Run Analysis' and 'Exit'.

Figure Q-8. Select “Geotextile at the Bottom” and Input Material Properties



```

Results.txt - Notepad
File Edit Format View Help
Unreinforced Pavement Structure
1. Compressive strain at bottom of base:991.82
2. Average strain in the base:662.63
3. Tensile strain at bottom of HMA surface:416.53
=====
With Geotextile at the Bottom
1. Compressive strain at bottom of base:508.09
2. Average strain in the base:776.47
3. Tensile strain at bottom of HMA surface:430.38
=====
Subgrade modulus with unreinforced pavement structure:5.0(ksi)
Modified subgrade modulus:7.7(ksi)
Base modulus with unreinforced pavement structure:20.0(ksi)
Modified base modulus:20.0(ksi)

```

Figure Q-9. Analysis Results for Example 3

Example 4: Geotextile in the Middle of the Base Course

The last example is the pavement structure with a geotextile layer placed in the middle of the base course, as shown in Figure Q-10. The following steps may be taken to analyze this pavement structure:

1. Double click the application file “Composite Geosynthetic–Base Course Model.exe” to start the program;
2. Tick “Geotextile in the Middle” on the left side of the program interface under “Geosynthetic Location” (see Figure Q-11);
3. Input the properties of the pavement layers and the geotextile on the right side of the program interface under “Pavement Structure” (see Figure Q-11); and
4. Click “Run Analysis”.

As shown in Figure Q-12, the “Results” file indicates that placing a geotextile layer in the middle of the base course in fact decreases the modulus of the base course from 40.0 ksi to 26.2 ksi.

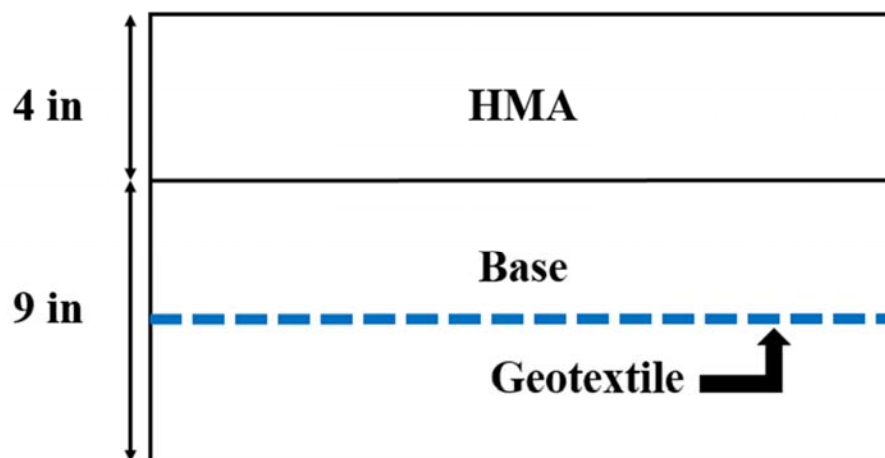
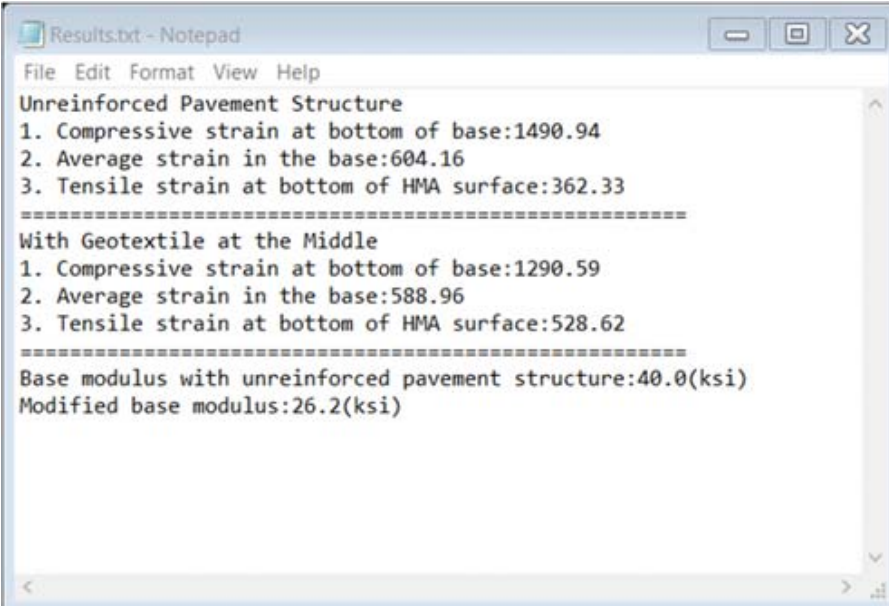


Figure Q-10. Placing Geotextile in the Middle of Base Course

The screenshot shows the 'Composite Geosynthetic-Base Course Model' software interface. It features two main sections: 'Geosynthetics Location' and 'Pavement Structure'. In the 'Geosynthetics Location' section, four radio buttons are present, with the last one, 'Geotextile in the Middle of Base Course', being selected. The 'Pavement Structure' section contains several input fields with numerical values: HMA Thickness (in) is 4, Base Thickness (in) is 9, HMA Modulus (ksi) is 300, Base Modulus (ksi) is 40, Base Anisotropic Ratio is 0.35, Geosynthetic Sheet Stiffness (lb/in) is 1200, and Subgrade Modulus (ksi) is 5. At the bottom, there are two buttons: 'Run Analysis' and 'Exit'.

Figure Q-11. Select “Geotextile in the Middle” and Input Material Properties



```

Results.txt - Notepad
File Edit Format View Help
Unreinforced Pavement Structure
1. Compressive strain at bottom of base:1490.94
2. Average strain in the base:604.16
3. Tensile strain at bottom of HMA surface:362.33
=====
With Geotextile at the Middle
1. Compressive strain at bottom of base:1290.59
2. Average strain in the base:588.96
3. Tensile strain at bottom of HMA surface:528.62
=====
Base modulus with unreinforced pavement structure:40.0(ksi)
Modified base modulus:26.2(ksi)
    
```

Figure Q-12. Analysis Results for Example 4